JOURNAL OF THE KOREAN PHYSICAL SOCIETY

June 1999

PROCEEDINGS OF the 9th Seoul International Symposium on the Physics of Semiconductors and Applications-1998

November 6–7, 1998,
Engineering Building
Ahn-Am Campus, Korea University
Seoul, Korea

Volume 34
Supplementary Issue

Published by the
KOREAN PHYSICAL SOCIETY
Seoul, Korea

Journal of the Korean Physical Society

Published monthly by the Korean Physical Society and devoted to original papers in experimental and theoretical physics

Office Address

The Korean Physical Society

635-4, Yuksam-Dong, Kangnam-Ku,

Seoul 135-703, Korea

Tel.: 82-2-556-4737

Fax.: 82-2-554-1643

http://mulli.kps.or.kr

Contributions

Manuscripts for publication should be sent in triplicate to the Korean Physical Society. Manuscripts from countries outside Korea may be submitted through the appropriate overseas editor depending on the subject area, or directly to the Korean Physical Society.

A Submitted Manuscript is accepted with the understanding that the manuscript is not currently under consideration by another journal and that it has not been copyrighted or accepted for publication elsewhere.

The Letter section is provided for short communications of timely and important results which warrant prompt publication.

The Brief Report section is for short accounts of original results which are not appropriate for regular research papers.

General Style. Manuscripts must be prepared in accordance with the general requirements that are summarized in the Regulation for Publication published in the back of the first issue of every volume.

The author's institution is requested to contribute a Publication Charge of U.S.$40.00 per page which, if honored, entitles them to 50 free reprints. Instructions for ordering reprints will be sent with the galley proofs.

Alteration in Proof. A limited number of alterations in proof are allowed, but the cost of making extensive corrections and changes after an article has been set in type will be charged to the author. Proofs and all correspondence concerning papers in the process of publication should be returned to the same address as that to which the initial manuscript was sent.

Subscriptions, renewals, and changes of address should be addressed to the General Affairs Secretary of the Society. For a change of address, please send both the old and new addresses.

The Annual Subscription Prices for libraries and non-members are U.S.$200 and $100, respectively.

Proceedings of
The 9th Seoul International Symposium on the Physics of Semiconductors and Applications-1998

November 6-7, 1998
Engineering Building
Ahn-Am Campus, Korea University
Seoul, Korea

Symposium Organizations

HONORARY CHAIRMAN

Chairman:	Choong Hyun Chung, Yonsei University
Co-Chairman:	Y. S. Park, Office of Naval Research(U.S.A.)

ISPSA-98 ORGANIZING COMMITTEE

Symposium Chairman:	Suk-Ki Min, Korea University
General Secretary:	Dong Hyuk Shin, Dongguk University
Program Committee Chariman:	Hyung Jae Lee, Jeonbuk National University
Publication Chairman:	Jin Jang, Kyung Hee University
Financial Chairman:	Tae Won Kang, Dongguk University
Publication Secretary:	Young Dong Kim, Kyung Hee University
Treasurer:	Young Kyun Park, KIST
Local:	Jichai Jeong, Korea University
	Eun Kyu Kim, KIST
U. S. Contacts:	Yung Kee Yeo, American Physicist Association(U.S.A.)

INTERNATIONAL ADVISORY COMMITTEE

M. Cardona, Max-Planck-Inst., Germany
D. I. Choi, Korean Physical Society, Korea
H. L. Hwang, National Tsing Hua University, Taiwan
Choochon Lee, KAIST, Korea
J. L. Merz, University of Notre dame, U. S. A.
J. Nishizawa, Tohoku University, Japan
M. H. Pilkhun, University of Stuttgart, Germany
T. Sugano, Toyo University, Japan
H. Z. Zheng, Institute for Semiconductors, China
Byung-Doo Choe, Seoul National University, Korea
I. Esaki, Tsukuba University, Japan
K. von Klitzing, Max-Planck-Inst., Germany
Y. Marfaing, CNRS, France
S. Namba, Nagasaki Institute of Applied Science, Japan
M. J. Park, Korea University, Korea
B. W. Rah, Kyoungpook National University, Korea
J. Thomas Ratchford, George Mason University, U.S.A.
T. S. Park, Kyoungpook National University, Korea

PROGRAM COMMITTEE

B. H. Chang, Chung Ang University
I. H. Choi, Korea University
K. S. Chung, Kyung Hee University
W. K. Chung, Sungkyunkwan University
J. Ihm, Seoul National University
K. N. Kang, KIST
B. M. Kim, POSTEC
C. O. Kim, Hanyang University
J. M. Kim, ADD
S. K. Chang, Yonsei University
M. S. Choi, LG Semicon
S. Chung, Ajou University
C. H. Hong, Korea Maritime University
H. S. Kang, Jeonbuk National University
M. H. Kang, Korea Telecom
C. K. Kim, KAIST
D. M. Kim, POSTEC
S. J. Kim, Hyundai Electronics

S. U. Kim, Korea University
W. T. Kim, Cheonnam National University
Y. S. Kwon, KAIST
E. Lee, ETRI
I. H. Lee, Korea Electronics
J. G. Lee, Samsung Electronics
S. J. Lee, Korea Military Academy
Y. W. Lee, Samsung Electronics
D. C. Moon, Kwangwoon University
S. K. Noh, KRISS
C. H. Park, Korea University
H. L. Park, Yonsei University
K. O. Park, Anam Semiconductors
S. J. Park, K-JIST
J. K. Rhee, Dongguk University
B. K. Sohn, Kyungpook National University
J. S. Song, KIER
I. S. Whang, Hyundai Electronics
K. C. Yoo, LG Electronics
P. W. Yu, K-JIST
T. I. Kim, SAIT
Y. K. Kim, Jeonbuk National University
Y. Kuk, Seoul National University
H. K. Lee, LG Semicon
J. D. Lee, Seoul National University
J. W. Lee, Sammi Technology and Industries
Y. T. Lee, K-JIST
H. Lim, Ajou University
E. S. Min, Hyundai Electronics
K. H. Oh, Hyundai Electronics
G. Park, Sogang University
H. M. Park, ETRI
S. C. Park, ETRI
Y. J. Park, Seoul National University
Y. J. Shin, Jeonbuk National University
K. S. Sohn, Kyungpook National University
I. K. Whang, Anam Semiconductors
K. W. Whang, Seoul National University
S. I. Yoon, Pusan National University

SPONSORS
Office of Naval Research
Korea-U.S. Science Cooperation Center

Preface

The 9th Seoul International Symposium on the Physics of Semiconductors and Applications (Seoul ISPSA-98) was held at Korea University, Seoul, Korea, on November 6-7, 1998.

This Symposium was organized by the Korean Physical Society in collaboration with the Korea-U.S. Science Cooperation Center and the Office of Naval Research. The purpose of this Symposium is to provide scientists, engineers, and researchers with chances to exchange technical information and to gain insight into the state of the art and the future R & D directions in the rapidly advancing semiconductor science and technologies. In light of the exciting developments currently being made in the wide bandgap semiconductors including III-nitrides, silicon carbide, and carbon-related materials, the ISPSA-98 put special emphasis on the wide bandgap materials and their applications, both in optoelectronics and electronic devices. 20 leading scientists and researchers were invited from all over the world to give the overview of the state of the art and recent achievements. And 151 contributed papers were presented. In the supplement of Journal of the Korean Physical Society, 81 papers selected by the Program Committee are included.

I wish to express my sincere thanks to the invited speakers for their cooperation and to attendees, especially the Committee members and the Advisory members who helped to make this Symposium successful. Finally, I would like to express my sincere appreciation to Dr. Yoon-Soo Park at the Office of Naval Research for his kind help.

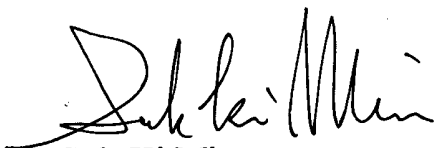

Suk-Ki Min
Chairman, Organizing Committee

ISSN 0374-4884

CONTENTS

June 1999

Journal of the Korean Physical Society, Vol. 34, June 1999, pp. S199~S219

Current Status of Group III-Nitride Semiconductors and Future Prospects

Yoon-Soo PARK

Office of Naval Research, 800 N. Quincy Street, Arlington, VA 22217-5660, U.S.A.

During the past decade, group III-Nitride wide bandgap semiconductors have become the focus of extremely intensive research because of their exceptional physical properties and their high potential for use in countless numbers of applications. Nearly all aspects have been investigated, from the fundamental physical understanding of these materials to the development of the fabrication technology and demonstration of commercial devices. This purpose of this paper is to review the physical properties of III-Nitrides, their areas of application, the current status of the material technology including synthesis and processing. The state-of-the-art of III-Nitride material quality, as well as the devices which have been demonstrated, including electronic devices, ultraviolet photodetectors, visible light emitting diodes (LEDs) and ultraviolet-blue laser diodes, will also be presented.

I. INTRODUCTION

Aluminum nitride (AlN), gallium nitride (GaN), indium nitride (InN) and their alloys are commonly known as 'III-Nitride materials' or 'III-Nitrides'. These materials have exceptional physical properties, chiefly their wide energy bandgap, which make them the ideal building blocks for numerous optical and electronic devices to be used in many applications. The III-Nitrides have existed for many years: AlN was synthesized by 1907 [1], InN by 1910 [2], and GaN by 1932 [3]. However, because the material was polycrystalline, it was not useful for semiconductor devices. Only limited research had been conducted on III-Nitrides until the 1980~1990's when two major breakthroughs led to renewed interest in III-Nitrides: the development of a buffer layer technique to obtain smooth and non-polycrystalline films and the demonstration of p-type doping. This opened the door to the control of the material structural, electrical and optical quality. Now, research in III-Nitrides has become a field of its own, whereas it used to be part of the 'wide bandgap semiconductor' field, and commercial devices have become available.

This paper will first review the physical properties of III-Nitride materials, followed by a non-exhaustive description of the areas of applications. Technological details will then be discussed, including the material growth and the substrates used. The current state-of-the-art in III-Nitride thin films and heterostructures will be presented. The technology for the material processing will also be reviewed, including etching and metal contacts. Finally, the state-of-the-art for III-Nitride based devices will be presented, including electronic devices, ultraviolet photodetectors, visible light emitting diodes (LEDs) and ultraviolet-blue laser diodes.

II. PHYSICAL PROPERTIES OF III-NITRIDE MATERIALS

Unlike more conventional semiconductors, such as silicon (Si) or gallium arsenide (GaAs) which have a diamond or zinc-blende structure with a cubic symmetry, III-Nitride crystals are wurtzite in their stable form with a hexagonal symmetry, belonging to the point group 6 mm. III-Nitrides are thus polar crystals because they do not have a center of symmetry [4]. They thus possess many other potentially useful properties such as piezoelectricity, pyroelectricity [5] and second harmonic generation [6,7]. The large difference in electronegativity between the group III and group V elements (Al=1.18, Ga=1.13, In=0.99, N=3.0) results in very strong chemical bonds in the III-Nitride material system, which are at

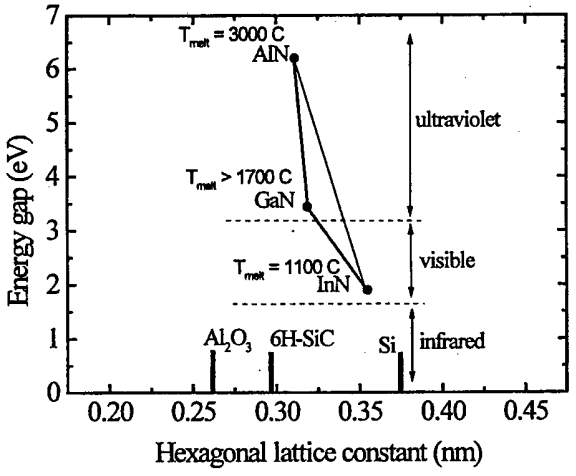

Fig. 1. Energy gap versus hexagonal lattice constant for III-Nitride and selected substrate materials.

Table 1. Physical properties of III-Nitrides (from references [8,9], except a from [10]).

	GaN	AlN	InN
Room temperature energy gap (eV)	3.44	6.2	1.9
Lattice constant, a (Å)	3.189[a]	3.112	3.545
Thermal expansion coefficient, α_a (10^{-6} K^{-1})	4.2 (17-477 C)[a]	5.27 (20-800 C)	5.6 (280 C)
Thermal expansion coefficient, α_c (10^{-6} K^{-1})	4.0 (17-477 C)[a]	4.15 (20-800 C)	3.8 (280 C)
Electron effective mass, m_e (m_0)	0.2		0.11
Hole effective mass, m_h (m_0)	0.8		0.5 (m_{hh} calculated) 0.17 (m_{hh} calculated)
Refractive index, n	2.35 (1.0 μm) 2.60 (0.38 μm)	2.2 (0.60 μm) 2.5 (0.23 μm)	2.56 (1.0 μ) 3.12 (0.66 μ)
ϵ (0)	10.4 ($E\|\|c$), 9.5 ($E \perp c$)	9.14	
ϵ (∞)	5.8 ($E\|\|c$), 5.4 ($E \perp c$)	4.84	9.3
Thermal conductivity, κ (W/cm K)	1.3	2.0	
Bulk modulus (GPa)	207[a]		
TO (meV)	69.3 (TO$\perp$), 66.1 (TO$\|\|$)	82.6	59.3
LO (meV)	92.5 (LO$\perp$)	112.8	86.1
Melting point (C)	>1700	3000	1100
Nitrogen partial pressure at meltin point (atmospheres)	3000	100	$\gg 10^5$
ΔG^0 (kcal/mol)	−33.0	−68.2	−23.0
Heat capacity, C_p (cal mol^{-1} K^{-1})	9.7	7.6	10.0

the origin of most of the interesting III-Nitride physical properties.

A direct result of this is the wide bandgap. III-Nitrides have a bandgap energy ranging from 6.2 to 1.9 eV, corresponding to a wavelength from 200 to 650 nm. This spectral range covers the visible spectrum (blue, green, yellow and red) as well as the near ultraviolet region in which the atmosphere transmits, as shown in Figure 1. The bandgap is direct which is most appropriate for optical devices. Because the intrinsic carrier concentration is an exponential function of the energy gap and the temperature, a wider bandgap semiconductor has a much lower intrinsic carrier concentrations over a large temperature range:

$$n_i(\mathrm{cm}^{-3}) = 4.9 \times 10^{15} \left(\frac{m_{de} m_{dh}}{m_0^2}\right)^{3/4} T^{3/2} e^{-E_g/2kT}$$

where all the parameters have conventional meaning. This results in lower leakage and dark currents in devices, which is especially important in photodetectors and high temperature electronics. Another consequence of the strong chemical bonding is the physical (high melting points, mechanical strength) and chemical stability of these materials. These also enjoy high thermal conductivity. Their effective masses are higher than conventional semiconductors, thus leading to lower carrier mobilities, but this is made up for by the high saturated electron drift velocities predicted for this material system. The refractive indices of III-Nitrides are lower compared to narrower gap semiconductors, which results in a lower reflectivity at the interface. This is an advantage for photodetector efficiency, but a disadvantage when trying to achieve lasers with low threshold currents.

All these properties yields III-Nitrides a very high potential for operation in the visible-to-ultraviolet spectral region as well as in harsh environments (radiation, heat) such as those typical of space applications, high frequency, high power and high temperature electronics. Details of the physical properties of III-Nitrides are summarized in Table 1. Although III-Nitride based devices are being rapidly demonstrated and commercialized, there are many barriers that must be overcome before the full potential of these materials can be realized as reliable devices. First, the high melting point of III-Nitrides and the extremely high nitrogen partial pressures near the melting point make their bulk growth very difficult. Therefore, high quality III-Nitride substrates do not exist. The synthesis of nitride crystals has thus to be carried in the form of thin films on a non-native substrate. The dissimilarity between the substrate material and III-Nitrides generally lead to poor structural quality as a result of the lattice and thermal mismatch. Moreover, nitride alloys with different compositions are also lattice mismatched, which leads to dislocations in III-Nitride heterostructures. Finally, high free electron and hole concentrations are often difficult to achieve because most dopant elements form deep levels in wide bandgap nitride semiconductors. The addition of more dopant source during the growth process frequently results in degradation of the structural and optical properties [8–10].

III. AREAS OF APPLICATION

The driving force behind the exceptional interest in III-Nitride materials has been their potential for numerous

significant device applications, both civilian and military. The majority of such devices can be divided into two categories: electronic and optoelectronic (photodetectors and light emitters) devices.

Electronic devices using III-Nitrides are needed for both high power and high temperature applications. High power and high temperature devices are in demand by the automotive, aerospace, and power industries. Power electronics have potential applications in the power industry and in any equipment which uses significant power, such as all electric vehicles, ships and aircraft. High temperature electronics would allow control directly in harsh environments, such as in engines, making them important in the automotive and aerospace industries. Because III-Nitride devices are expected to better withstand high temperatures while at the same time operate adequately, these electronics could be operated uncooled, thus reducing the cost and weight of systems.

Solar-blind UV photodetectors are devices which are sensitive to UV radiation while being (ideally) insensitive to longer wavelength radiation. Such devices have applications where there is a need to detect or control the source of UV radiation in an existing background of visible or infrared radiation [11]. Examples of such applications include flame detection, furnace and engine monitoring for the automotive, aerospace and petroleum industry, undersea communications, UV astronomy [12], space-to-space communications secure from Earth, early missile threat warning and airborne UV countermeasures, and portable battlefield reagent/chemical analysis system. Thanks to their wide energy gap, III-Nitrides have been successfully used in UV photodetectors with very promising characteristics. Because of their theoretical intrinsic solar blindness and low dark currents, III-Nitride based devices are expected to work without optical filters and complex electronics, thus significantly reducing the launch weight for space and airborne applications.

Thanks to their ideally suited bandgap energy range, III-Nitrides have been successfully used in commercial bright blue and green light emitting diodes (LEDs). When used with the already available red AlGaAs based LEDs, these new LEDs complete the primary colors (red, green, blue) for large, high brightness, outdoor full-color displays. Traffic lights are starting to use green LEDs because of their superior efficiency and reliability in comparison to incandescent light sources. Solid state white light sources using a combination of red, green, and blue LEDs or using phosphors excited by blue or ultraviolet (UV) LEDs may soon replace conventional light bulbs with better efficiency and reliability. UV LEDs could also replace the inefficient and hot "black" lights that are used in fun houses, tanning salons, and in more mundane applications such as killing bacteria in water.

The main thrust in recent III-Nitride research has been the fabrication of a reliable, short-wavelength (ultraviolet to green spectral region) laser diode. The primary advantage of shorter wavelengths is the ability to focus the beam to smaller spot sizes which scale as λ^{-2}, thus quadrupling the storage density of optical media by reducing the laser wavelength in half. The objective will be to achieve a digital video disk (DVD) system capable of storing 15 gigabytes by the year 2000. A DVD-RAM system would require a laser diode operating in continuous wave (CW) at 60 °C, with an output power of 30~40 mW, and an operating voltage of 3 V at 100 mA. The requirements for a DVD-ROM system would only be a 4~5 mW CW laser. In both cases, the laser should have a wavelength of 400~430 nm. It must not be too short to avoid transmission losses in air. Visible laser diodes are also expected to be used in projective displays, optical communications and chemical analysis because the wavelength could be tuned to correspond to absorption lines of specific airborne chemicals to be detected. For example, a 55 inch large display needs a luminosity of 500 cd/m^2, which requires at least a 6.6 W, 1.8 W and 1.2 W red, green and blue lasers. Finally, laser printing is also an important applications for short wavelength laser diodes. These would need to emit at a wavelength higher than 430 nm to avoid the decomposition of the toner components, with a single mode CW output power higher than 6 mW for fast printing.

Table 2. Comparison of the GaN and GaAs-based laser properties.

Material	GaN (InGaN/GaN MQW)	GaAs (InGaAs/GaAs MQW)
Transparency carier density n_o	10^{19} cm^{-3}	2×10^{18} cm^{-3}
Optical confinement factor Γ	5 %	5 %
Differential gain β	5×10^{-16} cm^2	1×10^{-15} cm^2
Typical total active layer thickness d	300 Å	100 Å
α_i	50 cm^{-1}	2 cm^{-1}
Radiative recombination coeff. B	3×10^{-11} cm^3/sec	6×10^{-11} cm^3/sec
J_{th}	2000 A/cm^2	40 A/cm^2

Theoretical calculations have been conducted to compare the lasing threshold characteristics of GaN and GaAs based semiconductor lasers and the results are shown in Table 2. The theoretical threshold current densities were calculated using the formula:

$$J_{th} = edBn_{th}^2 = edB\left(n_o + \frac{\alpha_{tot}}{\Gamma\beta}\right)^2$$

where the parameters are defined in Table 2, and assuming no non-radiative recombination (η_i=1). The threshold for GaN based lasers was found to be

IV. SUBSTRATES AND GROWTH TECHNIQUES FOR III-NITRIDES

Because of their extreme physical properties, bulk III-Nitride single crystals are barely available and their quality is not good enough to be used as a substrates. Many non-native substrates have been investigated over the years for the epitaxy or growth of III-Nitride thin films. A non exhaustive list of potential substrates and their physical properties is given in Table 3 and Table 4. Reported values typically vary widely, so these numbers should be treated with caution.

A substrate must satisfy several properties in order to be suitable for epitaxial growth. First, it must be "compatible" with III-Nitrides, *i.e.* have a crystal structure (bulk and surface arrangement of atoms) which lends to the proper initial nucleation of oriented III-Nitride crystals during growth. The substrate lattice constant and the resulting lattice mismatch with the epilayer are important quantitative measures of this "compatibility" between substrate and epilayer, are useful in predicting the amount of stress for the epilayer. The data is tabulated in Table 3. The thermal expansion coefficient of the substrate is also an important parameter because a mismatch in these coefficients with other materials will result in mechanical stresses and cracks from cooling from the growth temperature and from cycling during processing and operation of the device. An estimate of the mismatch between the epilayer and the substrate caused by cooling 1000 °C is given assuming the layer is relaxed at the growth temperature. The substrate must also be stable under the growth conditions typically used for III-Nitrides [13]. This is best quantified by the melting point of the substrate. Other substrate properties, such as thermal conductivity, energy gap and optical transparency in the visible spectrum, possibility to dope, maximum wafer size available and price are also given. All these properties will affect the choice of substrate for III-

Table 3. Structural properties of III-Nitride and potential substrate materials.

Formula	Name	Symmetry	Point group	Space group	Stacking sequence (Wyckoff)	Lattice constants (Å)	Plane with nearest match to (0001)GaN	Effective a lattice constant (Å)	da/a with GaN
GaN	Gallium nitride	Hexagonal	6 mm	$P6_3mc$ (186)	AB (HH)	a=3.1891 c=5.1855	(0001)	3.1891	0 %
AlN	Aluminum nitride	Hexagonal	6 mm	$P6_3mc$ (186)	AB (HH)	a=3.112 c=4.982	(0001)	3.112	2.47 %
InN	Indium nitride	Hexagonal	6 mm	$P6_3mc$ (186)	AB (HH)	a=3.5446 c=5.7034	(0001)	3.5446	−10.03 %
4H-SiC	4H silicon carbide	Hexagonal	6 mm	$P6_3mc$ (186)	ABCB (CHCH)	a=3.073 c=10.053	(0001)	3.073	3.77 %
6H-SiC	6H silicon carbide	Hexagonal	6 mm	$P6_3mc$ (186)	ABCACB (CCHCCH)	a=3.081 c=14.117	(0001)	3.081	3.51 %
15R-SiC	15R silicon carbide	Trigonal	3 m	R3m (160)	$(CCHCH)_3$				
Al_2O_3	Sapphire, corundum	Trigonal	$\bar{3}$ m	$R\bar{3}c$ (167)		a=4.758 c=12.991	(0001) rotated 30°	2.747	16.09 %
$LiGaO_2$	LGO, lithium gallate	Orthorhombic	mm^2	$Pna2_1$ (33)		a=5.402 b=6.372 c=5.007	(001)	3.119 3.186	2.25 % 0.10 %
$LiAl_2$	LAO, lithium aluminate	Tetragonal	422	$P42_1$ (90)		a=5.1715 c=6.2840	(100)	2.986 3.142	6.81 % 1.50 %
$NdGaO_3$	NGO, neodymium galate	Orthorhombic	mmm	Pbmm (62)		a=5.431 b=5.499 c=7.710 a=5.431 b=5.499 c=7.710	(101) (011)	3.175 3.144 3.136 3.1857	0.45 % 1.45 % 1.71 % 0.03 %
ZnO	Zinc oxide	Hexagonal	6 mm	$P6_3mc$ (186)	AB (HH)	a=3.253 c=5.213	(0001)	3.253	−1.97 %
MgO	Magnesium oxide	Cubic	$m\bar{3}m$	$Fm\bar{3}m$ (225)		a=4.216	(111)	2.981	4.93 %
Si	Silicon	Cubic	$m\bar{3}m$	$Fd\bar{3}m$ (227)		a=5.4310202	(111)	3.8403112	−16.96 %
GaAs	Gallium arsenide	Cubic	$\bar{4}3m$	$F\bar{4}3m$ (216)	ABC (CCC)	a=5.65325	(111)	3.99745	−20.22 %

Table 4. Other physical properties of III-Nitride and potential substrate materials.

Formula name	$\bar{\alpha}_a$ (10^{-6} K^{-1}) 0 to 1000 °C	Mismatch with GaN by colling 1000 °C (TEC_{GaN}-TEC_{sub})x (−1000 K)	Thermal conductivity (W/cm K)	Melting temperature (°C)	Energy gap (eV)	Transparent in visible?	Doping?	Maximum diameter (cm)	Low end price (to 1 significant fig.) ($/cm^2)
GaN	5.6 (0 to 600 °C)	0 %	1.3	>1700	3.44	Yes	n, p	–	–
AlN	5.7	0.01 %	2.0	3000	6.2	Yes	Extremely difficult	–	–
InN	5.7 (300 °C)	0.01 %			1.9	No	n	–	–
4H-SiC	4.46	−0.11 %	4.9	1100	3.20	Impurity absorption	n, p	3.5	100
6H-SiC	4.44	−0.12 %	4.9		2.86	Impurity absorption	n, p	3.5	100
15R-SiC			4.9			Impurity absorption	n, p	–	–
Al_2O_3	8.6	0.30 %	0.3	2015	>8.5	Yes	Insulator	10[c]	6[c]
$LiGaO_2$	∼7	0.14 %		∼1600		Yes		5	20
$LiAlO_2$				∼1700		Yes		2	60
$NdGaO_3$ (101)	6.6 7.8	0.10 % 0.22 %		∼1600				5	
$NdGaO_3$ (011)	11.9 6.1	0.63 % 0.05 %		∼1600					
ZnO	7.8	0.22 %		∼2000	3.44 (1.6 K)	Yes	N?	2	300
MgO	13.85	0.83 %	0.36[f]	2800	7.9	Yes	Insulator	5	20
Si	3.90	−0.17 %	1.3	1412	1.1242	No	n, p	30	
GaAs	6.7	0.11 %	0.5	1240	1.424	No	n, p	5	4

Nitride epitaxy depending on the application sought for.

To date, three substrates stand out as the most promising for III-Nitride growth: silicon, silicon carbide (SiC) and sapphire (Al_2O_3). Silicon is the most widely available substrate in the semiconductor industry and can come in sizes up to 10 inch diameter. It is also the cheapest one and the highest quality. However, it suffers from a poor "compatibility" with III-Nitride crystals. Also, it has a very narrow bandgap in comparison to nitrides, which makes it ill-suited for optical devices. At the other extreme, SiC offers the closest match with III-Nitrides, in terms of crystal symmetry, lattice and thermal mismatch with the nitrides. The lattice constant is smaller, resulting in compressive strain of the epilayer. On the other hand, the low thermal expansion coefficient of SiC results in tensile strain in the film upon cooling. It is a wide bandgap semiconductor being developed for applications in high power electronics and other demanding applications. Its drawback is its limited availability, small available size, its quality is still not as good as other Si or Al_2O_3 substrates [14], and its prohibitively high price. Sapphire offers a compromise between the Si and SiC, and has become the most often used substrate for III-Nitride epitaxial growth. The appealing features include the high thermal and chemical stability, the large high quality wafers available, and the reasonable cost. However, there are large lattice and thermal mismatches. The thermal expansion coefficient is much larger than that of the III-Nitrides, resulting in a compressive strain in the epilayer upon cooling. The III-Nitrides generally grow on (0001) sapphire substrates with a 30° rotation about the c-axis with respect to the sapphire lattice, resulting in the alignment of the directions [00.1]||[00.1] and [10·0]||[11·0]. This results in a compressive strain on the III-Nitride layer since the effective lattice constant of the substrate given below is smaller than that of III-Nitride:

$$a_{effective} = \frac{a_{Al_2O_3}}{\sqrt{3}}$$

The comparison of Si, SiC and Al_2O_3 as potential substrate for III-Nitride epitaxy is summarized in Table 5. GaN has been included in the table to reflect the proper-

Table 5. Comparison of the most promising substrates for III-Nitride growth.

Substrate issues for III-Nitride growth	GaN	Si	6H-SiC	Al_2O_3
Crystal symmetry	++	-	+	+
Compatibility of process	++	-	+	+v
Lattice of process	+	- -	-	- -
Thermal mismatch	+	-	-	-
High quality	+	++	-	++
Availability	- -	+	-	+
Size (large area)	- -	++	-	+v
Cheap ($)?	n/a	+	-	+

ties of the bulk GaN single crystals which are currently being grown at high pressure by a few research groups in Poland [15]. At the present time, sapphire is the most viable substrate material in terms of quality, availability and cost.

Crystallographic models for the growth of III-Nitride thin films on these substrates have been developed to understand the atomic arrangements at the epilayer/substrate interface [16–20]. The comparison of different natures and orientations of substrates has been conducted [21].

Although the growth of III-Nitrides has been conducted on non-native substrates, high quality films have been achieved which led to the demonstration of high performance devices, as will be discussed later in this paper. The dissimilarity between the substrates and nitride materials has been alleviated through the successful development of the growth technology, and more precisely the use of buffer layers [22].

One of the reason why III-Nitrides have suffered from a lack of interest until the 1980s is because of the lack of suitable growth techniques. For example, because of their higher melting points, these materials required higher growth temperatures than conventional semiconductors, which then resulted in significant buoyancy in the gas flow pattern in chemical vapor deposition techniques.

Table 6 summarizes the strengths and weaknesses of the currently most common growth techniques used to grow III-Nitride crystals, including metalorganic chemical vapor deposition (MOCVD), molecular beam epitaxy (MBE), vapor phase epitaxy (VPE), high pressure growth and sublimation sandwich method (SSM).

Currently, MOCVD and MBE are the most widely used techniques. MOCVD is undoubtedly the method of choice for the growth of high quality III-Nitrides films for mass production and particularly for devices. However, recently, VPE growth of III-Nitrides has gained attention for the growth of very thick GaN films for use as substrates after original substrate lift-off [23]. High pressure growth remains limited to a few research groups in Poland for the direct growth of bulk GaN crystals. Finally, SSM has gained recently interest for the growth of bulk single crystal AlN. The III-Nitride material properties grown using these techniques will be presented in the next section.

All these growth techniques make use of precursors which are the source materials for each element (Al, Ga, In, N). These can come in the form of solid, liquid or gas depending on the growth technique used. A non-exhaustive list is tabulated in Table 7. It is worth to note that all group III element precursors are commonly used for the growth of other more conventional III-V semiconductors. Different group III sources have been compared for the growth of GaN [24]. The group V (nitrogen) sources are much more common than AsH_3 or PH_3 which makes them much safer to use, more avail-

Table 6. Strengths and weaknesses of most common growth technologies for III-Nitride.

Growth technolog	Strengths	Weaknesses	Frontier for 21st century
Metal-Organic Chemical Vapor Deposition MOCVD MOVPE	o Well developed technology o Atomically sharp interfaces o In-situ thickness monitoring o High growth rater (<4 m/hr) o Easily scaleable for mass production o Short run cycles (heat+growth+cool) o Possibility to use plasma or laser assiste growth	o Lack of precise in-situ characterization o Large quantities of NH_3 are needed	mass procuction of high quality III-Nitride thin films and devices
Molecular Beam Epitaxy MBE, GSMBE, MOMBE	o Well developed technology o Atomically sharp interfaces o Precise in-situ characterization o High purity growth enviromment o Hydrogen free enviromment o Scalable for mass procuction	o Need for ultra-high vacuum (cryogenics) o Long run cycle (heat+growth+cool) o Growth temperature is limited on the high end o Efficiency of nitrogen source or cracker (ECR, RF) is limited o Low growth rates (<1~1.5 m/hr) o Not as high throughput as MOCVD	Growth in Hydrogen-free environment
Vapor Phase Epitaxy VPE, HVPE	o Simple growth technique o Very high growth rate (<100 m/hr) o Reasonably good quality films	o No sharp interfaces o Long run cycles (heat+growth+cool) o small area growth o Better films are obtained for lower growth	Thick GaN films for substrates
High pressure growth	o Bulk GaN single crystals	o Only for GaN single crystals o Small size crystals (few mm^2 area) o Extreme temperature & pressure conditions	Bulk GaN single crystals for substrate use
Sublimation sandwich method SSM	o Very simple growth technique o Extremely high growth rate (<300 m/hr)	o Poor quality of films o Need a GaN powder source o Small area growth	Bulk AlN single crystals for substrate use

Table 7. Most common chemical precursors for the growth and doping of III-Nitride.

Element group	Chemical formula	Chemical name	Chemical family	Physical state at 20 °C	Growth technique	Toxicity
III	(CH_3)-, $(C_2H_5)_3$-Al	Trimethy, triethyl-aluminum (TMAl, TEAl)	organometallic	liquid	MOCVD, MBE	pyrophoric
	$AlH_3N(CH_3)_3$	Alane trimethylamine	organometallic	solid	MOCVE, MBE, VPE	
	$(CH_3)_3$-, $(C_2H_5)_3$-Ga	Trimethy, triethyl-gallium (TMGa, TEGa)	organometallic	liquid	MOCVD, MBE	pyrophoric
	$GaCl_3$	Gallium chloride	metal chloride	solid	VPE	
	$(CH_3)_3$-In	Trimethy-indium (TMIn)	organometalic	solid	MOCVD, MEB	pyrophoric
	$(CH_2H_5)_3$-In	Trimethy-indium (TEIn)	organometalic	liquid	MOCVD, MEB	pyrophoric
	$InCl_3$	Indium chloride	metal chloride	solid	VPE	
	Al, Ga, In	Aluminum, gallium, indium	metal	solid	MBE, VPE	no
V	N_2	Nitrogen	inorganic gas	gas	MOCVD, MBE	no
	NH_3	Ammonia	nitrogen hydride	gas	MOCVD, MBE, VPE, sublimation	corrosive
	N_2H_4	Hydrazine	nitrogen hydride	gas		
	$(CH_3)_3CNH_2$	Tertiarybutylammine	organometallic	~liquid		
	CH_6H_5	Phenylhydrazine	organometallic	liquid		
III-V	AlN	Aluminum nitride	powder	solid	sublimation	no
	GaN	Gallium nitride	powder	solid	sublimation	no
II (P-type dopant)	Cp_2Mg	Biscyclopentadienyl-magnesium	organometalic	solid	MOCVD, MBE, VPE	pyrophoric
	Mg	Magnesium	metal	solid	MBE	no
	DEZn	Diethyl-zinc	organometalic	liquid	MOCVD, MBE, VPE	pyrophoric
	DMZn	Dimethyl-zinc	organometalic	liquid	MOCVD, MBE, VPE	pyrophoric
	Zn	Zinc	metal	solie	MBE	no
	SiH_4	Silane	hydride	gas	MOCVD	pyrophoric
	Si_2H_6	Disiland	hydride	gas	MOCVD	
	Si	Silicon	metal	solid	MBE	no
	GeH_4	Germane	hydride	gas	MOCVD	toxic
	H_2S	Hydrogen sulfide	nonmetal hydride	gas	MOCVD	toxic
	H_2Se	Hydrogen selenide	nonmetal hydride	gas	MOCVD	

able and much cheaper. However, there is still intense research to develop a better group V source, in terms of ease of cracking, purity and efficiency [25].

V. STATE-OF-THE-ART OF III-NITRIDE THIN FILMS

1. Aluminum Nitride (AlN)

Aluminum nitride thin films have been synthesized for many years for use as a ceramic for coating because of their high physical strength. These films were all amorphous and were generally grown using RF sputtering.

It is only after the growing interest in GaN that more monocrystalline AlN films have been synthesized. Bulk AlN single crystals are being investigated using the sublimation sandwich method. Bulk AlN represents a future direction for the research on this material. However, AlN thin films are generally grown on basal plane Al_2O_3 or SiC substrates, without a buffer layer. This is due to the fact sapphire and AlN share a common element: aluminum, which makes the bonding at the interface much easier. Epitaxial films are rarely thicker than 1~1.5 μm. High crystalline quality films have been achieved on Al_2O_3 and SiC substrates with open detec-

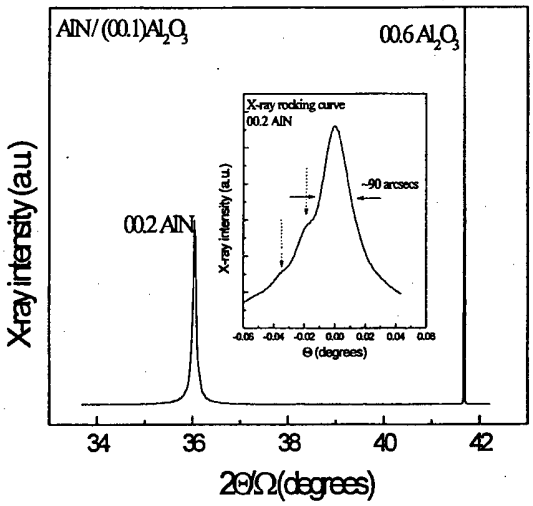

Fig. 2. Symmetric x-ray diffraction spectra of an AlN film on basal plane sapphire [27].

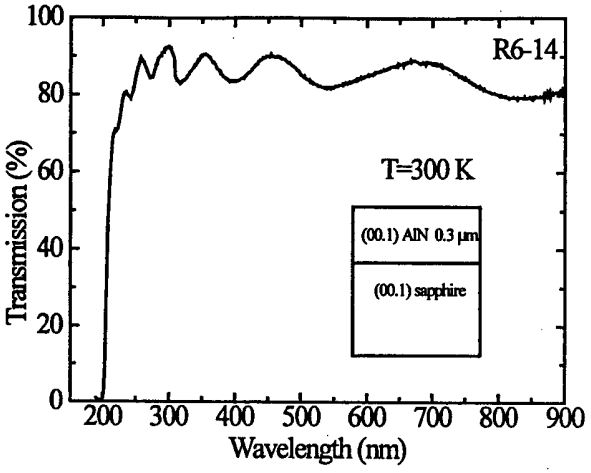

Fig. 3. Room temperature optical absorption of AlN film on basal plane sapphire [27].

tor symmetric x-ray rocking curve linewidths as low as 90 and 60 arcsecs respectively, as shown in Figure 2 [26,27].

As grown AlN films are almost always insulating. The origins of this behavior are still controversial and much research work is needed to understand the insulating behavior of AlN. Negative electron affinity (NEA) has also been reported from AlN films [28]. This effect has been used to demonstrate cold cathode structures using AlN films [29]. The piezoelectric properties of AlN has been investigated for a number of years for Surface Acoustic Wave (SAW) applications [30]. The optical properties of AlN are assessed through optical absorption (Figure 3) and cathodoluminescence. The nonlinear optical properties of AlN are an interesting field for future research which has been little touched, although second harmonic generation from AlN films were conducted and yielded the non linear coefficients:

$$\chi^{(2)}_{zzz} = 10 \text{ pm/V} \quad \text{and} \quad \chi^{(2)}_{zxx} = 0.5 \text{ pm/V}.$$

2. Gallium Nitride (GaN)

GaN is by far the most studied III-Nitride material. A thin AlN, GaN or AlGaN buffer layer is generally used for the growth. Basal plane Al_2O_3 and SiC substrates are most commonly used. Films as thick as 100 μm have been reported, depending on the growth technique utilized. In face of the growing interest in these materials, there has been an effort to grow bulk GaN single crystals using high pressure growth or hydride VPE followed by substrate lift-off. This is undoubtedly a promising topic for future research.

High crystalline quality GaN thin films have been achieved, with open detector x-ray rocking curve linewidths as low as 30 arcsecs (Figure 4) and asymmetric x-ray rocking curve linewidths as low as 400 arcsecs [27]. The thermal stability of GaN has been reported [31].

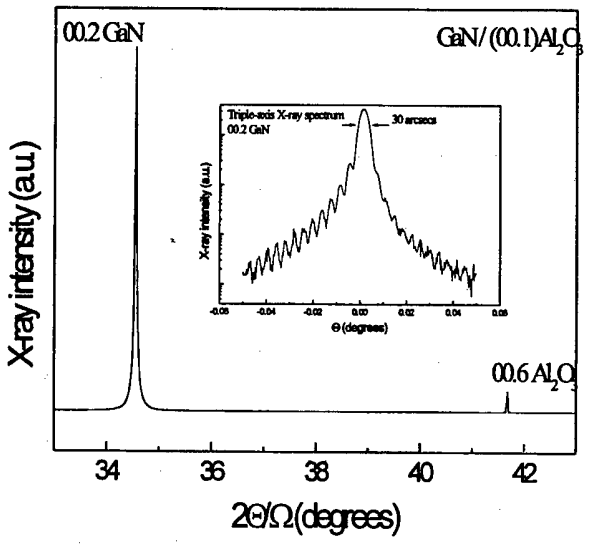

Fig. 4. Symmetric x-ray diffraction spectrum of an GaN film on basal plane sapphire [27].

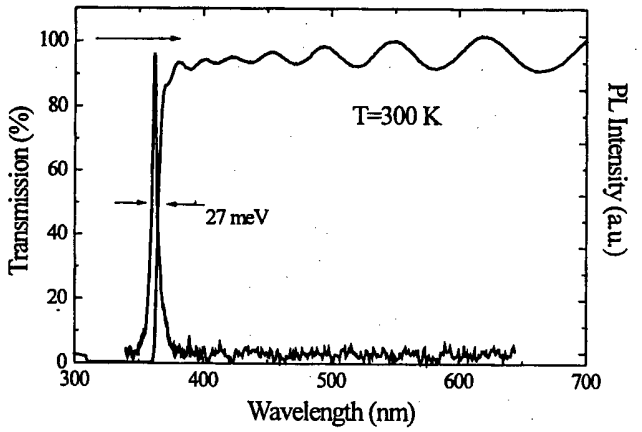

Fig. 5. Room temperature optical transmission and photoluminescence from a GaN film on Al_2O_3 substrate [27].

Undoped GaN films are usually either highly resistive or exhibiting n-type conduction with a residual carrier concentration $\sim 10^{16}$ cm^{-3} at room temperature and an electron mobility as high as 900 cm^2/Vs. Theoretical calculations showed that the maximum 300 K electron mobility in GaN was 2,350 cm^2/Vs. The pyroelectricity properties of GaN have been measured and yielded a pyroelectric voltage coefficient of $\sim 10^4$ V/mK.

The optical properties of GaN are usually assessed through optical transmission and photoluminescence (PL), as shown in Figure 5. Free excitons A, B and C have been observed with peak linewidths of ~1-3 meV at 2 K using photoluminescence (PL). The room temperature PL linewidths are typically as low as ~30 meV, as shown in Figure 5. Residual acceptor and donor related luminescence transitions are often observed as well. A broad 'yellow' luminescence is sometimes observed

and has been attributed to defects in GaN (see Section 7). Transition metal (*e.g.* Fe, V) have been observed by infrared spectroscopy. Second harmonic generation from GaN films have yielded the non linear coefficients: $\chi^{(2)}_{xzx} = \chi^{(2)}_{zxx}$ which was 11 times the $\chi^{(2)}_{xxx}$ of quartz, and $\chi^{(2)}_{zzz}$ which was -22 times the $\chi^{(2)}_{xxx}$ of quartz [6].

3. Ternary $Al_xGa_{1-x}N$

Ternary $Al_xGa_{1-x}N$ has been grown over the entire compositional range. Generally an AlN or GaN buffer layer is used, although there are some reports of AlGaN buffers. Here again, basal plane Al_2O_3 and SiC are the preferred substrates. The films are typically thinner than 1~1.5 μm. High crystallinity AlGaN films have been achieved on sapphire substrates, with open detector symmetric x-ray rocking curve linewidths as low as 100 arcsecs [32].

The resistivity of $Al_xGa_{1-x}N$ was found to increase exponentially with Al concentration (x) [32]. This behavior still needs to be understood and is an important area of future research. Low Al concentration alloys sometimes show limited n-type conduction due to residual donors as in the case of GaN. $Al_xGa_{1-x}N$ are reported to exhibit negative electron affinity for $x > 0.75$ and have been used in cold cathode applications [29].

The optical properties of $Al_xGa_{1-x}N$ have been assessed using cathodoluminescence and optical absorption, in particular to determine the bandgap energy as shown in Figure 6. A bandgap bowing parameter

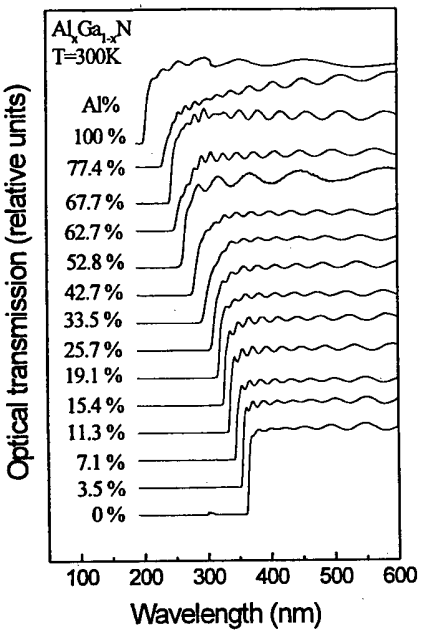

Fig. 6. Room temperature optical transmission of $Al_xGa_{1-x}N$ for $0 < x < 1$ [32].

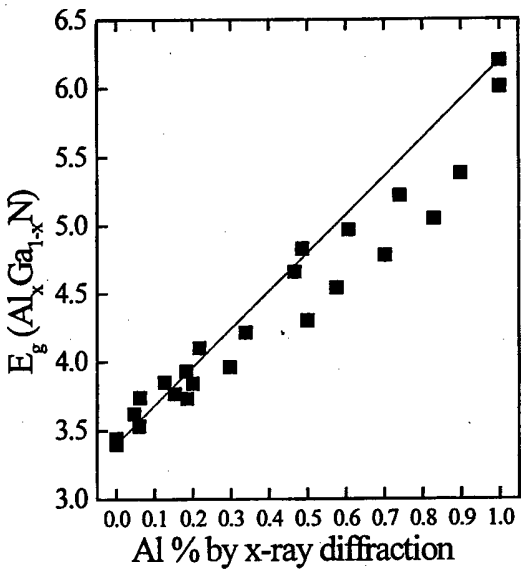

Fig. 7. Room temperature energy gap of $Al_xGa_{1-x}N$ determined by optical absorption as a function alloy composition as determined by x-ray diffraction [33].

has been measured to be between -1.0 and 1.0 eV, as shown in Figure 7 [33]. Calculations (for zinc blende $Al_xGa_{1-x}N$) have predicted this parameter to be 0.53 eV. There is some uncertainty on the exact alloy composition due to the presence of strain in the thin films. Ellipsometry and photoreflectance measurements have been conducted and yielded the refractive index of a few $Al_xGa_{1-x}N$ alloys (*e.g.* 0.1 lower than GaN for x=0.1).

4. AlGaN/GaN heterostructures

One of the main advantages of the III-Nitrides over other wide bandgap materials such as SiC is the potential to fabricate heterostructures and achieve bandgap engineering within the same material system. However, AlGaN/GaN heterostructures are still in their infancy and much remains to be done.

Two dimensional electron gas (2DEG) has been demonstrated at the AlGaN/GaN interface. Room temperature electron mobilities as high as 2,000 cm^2/Vs have been measured for a sheet carrier density of 10^{13} cm^{-2}. At 20 K, the electron mobilities were as high as 5,700 cm^2/Vs and 7,500 cm^2/Vs for structures on sapphire and SiC substrates for a sheet carrier of 5×10^{12} cm^{-2} [34]. Theoretical modelings showed that piezoelectric scattering, as well as polar optical and ionized impurity scattering, played an important role in the mobility of 2DEG in GaN [35].

Calculations of the strain induced piezoeffect at lattice mismatched III-Nitrides have been carried out. The piezoelectrically induced charge in GaN/AlGaN has been measured in field effect transistor structures [36].

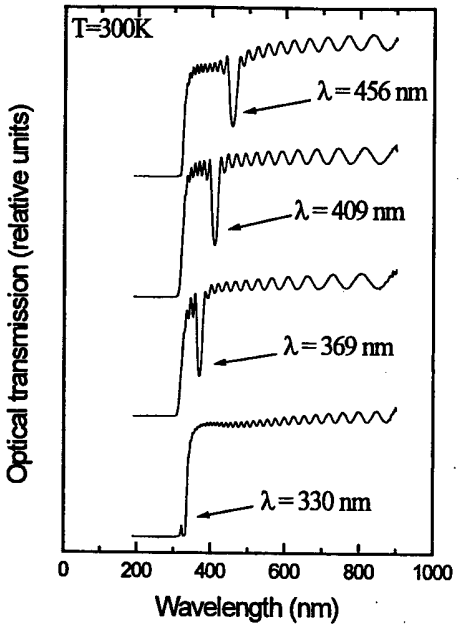

Fig. 8. Room temperature optical transmission of $Al_xGa_{1-x}N/Al_yGa_{1-y}N$ multilayer Bragg reflectors [32].

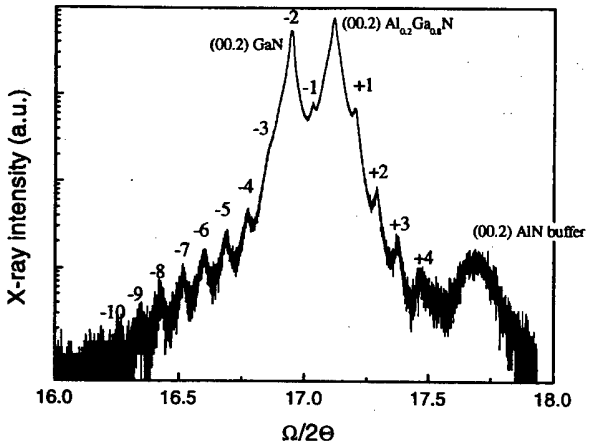

Fig. 9. Open detector x-ray diffraction spectrum of a 13 period 500 Å $Al_{0.2}Ga_{0.8}N$/50 Å GaN superlattice.

Band alignments in the III-Nitride material system have been investigated and remain a controversial issue. Theoretical calculations estimated that the valence band offsets of (wurtzite) AlN, GaN and InN to be : AlN/GaN=0.7~0.81 eV and GaN/InN=0.3~0.48 eV. Experimental measurements of the valence band offsets yielded: AlN/GaN=0.70~1.36 eV, GaN/InN=1.05 eV and AlN/InN=1.81 eV [37].

Bragg reflectors using $Al_xGa_{1-x}N/Al_yGa_{1-y}N$ multilayers have been demonstrated. The peak reflectivity could be tuned by varying the periods of the multilayer structures, as shown by the a sudden decrease in the optical transmission spectrum in Figure 8 [32].

X-ray diffraction from AlGaN/GaN superlattices have revealed clear satellite peaks, as shown in Figure 9. This confirms that high structural quality interfaces can be achieved in this material system.

5. Ternary $Ga_{1-x}In_xN$

Ternary $Ga_{1-x}In_xN$ have been grown in the entire composition range. However, the material quality significantly deteriorates as the In concentration increases. It was shown that the $Ga_{1-x}In_xN$ alloy composition and material quality very strong depended on the growth conditions, in particular the growth temperature, growth pressure, V/III ratio, growth rate. To grow alloys with higher In concentration, it is generally necessary to lower the growth temperature, raise the growth pressure, increase the V/III ratio and growth rate [38].

Moreover, it has been reported that GaN and InN have a miscibility gap [39]. $Ga_{1-x}In_xN$ films are generally thin (<0.5 μm) and are grown on thick GaN films (>1 μm) on basal plane Al_2O_3 or SiC substrates. The x-ray rocking curve linewidths can be as low as 480 arcsecs (for 14 % In) [40].

As grown $Ga_{1-x}In_xN$ films generally show n-type conduction ($n > 10^{17}$ cm^{-3} at 300 K). Room temperature photoluminescence measurements showed that $Ga_{1-x}In_xN$ can have a linewidth as low as 70 meV (for 14 % In). The bandgap bowing parameter has been measured to be between 1.0 and 3.2 eV, as shown in Figure 10 [33]. Theoretical calculations (for zinc-blende $Ga_{1-x}In_xN$) predicted a value of 1.02 eV. Ellipsometry has yielded the refractive index of $Ga_{1-x}In_xN$ to be ~0.05 higher (for x=0.06) than that of GaN.

Improving the quality of $Ga_{1-x}In_xN$ compounds for $x > 0.5$, as well as enhancing the uniformity of the growth

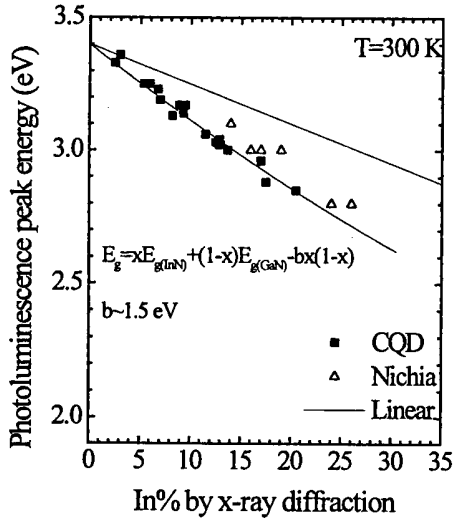

Fig. 10. Room temperature energy gap of $Ga_{1-x}In_xN$ determined by photoluminescence as a function alloy composition as determined by x-ray diffraction [33]. Data points labeled "Nichia" are taken from reference [40]. Data points labeled "CQD" are taken from reference [33].

over large areas remain a challenge for the future.

6. GaInN/GaN Heterostructures

GaInN/GaN heterostructures and quantum wells have been reported, although they have been more often characterized in actual devices [41,42].

The cathodoluminescence intensity was shown to increase by several orders for GaInN/GaN multi-quantum wells compared to bulk GaInN films [43]. There have been reports of "composition pulling effect" in thin GaInN films grown on GaN [44]. It was shown that the lattice mismatch between the growing GaInN layer and the underlying GaN prevented the incorporation of indium into the lattice. This can have significant effect in the control of the emission wavelength from GaInN/GaN quantum wells. Finally, quantum confined Stark effect in GaInN/GaN multiquantum wells due to piezoelectric effects has been recently reported to influence the optical properties of these structures [45]. This effect can be minimized by adequately doping the structures with Si.

VI. DOPING OF III-NITRIDES

In order to fabricate devices, it is necessary to control the doping of III-Nitrides. The n-type doping in these materials has generally been much easier than the p-type doping. this is mainly because III-Nitrides have the tendency to exhibit n-type conductivity as grown. Like other III-V semiconductors, the n-type doping can be achieved using group VI elements, while the p-type doping is achieved by incorporating group II elements. Group IV elements, such as Si and Ge, act as donors in III-Nitrides, whereas C seems to act as an acceptor. This is due to the fact that Si and Ge have an electronegativity closer to Al, Ga and In than N, and thus would be more likely to replace Al, Ga and In than N. The electronegativity of C is closer to N than to the group III elements, and thus would more likely to replace N in the III-Nitride lattice.

1. N-type Doping

There have been a few reports of Ge doped AlN films which exhibited n-type conductivity, although not much information is available.

The n-type doping of GaN films has been much more investigated using Si, Ge [46], Se, sulfur [47] and oxygen. The most successful dopants have been Si and Ge. Doping control has been achieved up to a carrier concentration of 10^{20} cm^{-3}. The Si level in the bandgap was estimated to be $\sim$22 $\pm$4 meV below the bottom of the conduction band [48]. Impurity band conduction is usually observed at low temperatures.

The n-type doping of $Al_xGa_{1-x}N$ compounds has been successfully carried out using Si and Ge [49]. N-type conduction has been observed up to an Al concentration of $x < 0.6$. Future research will be oriented towards enhancing the n-type conductivity for alloys with $x > 0.6$. The n-type doping of $Ga_{1-x}In_xN$ alloys using Si has also been conducted, although this has not been done to enhance the electrical properties of the films but rather the optical properties. It was shown that Si doping of $Ga_{1-x}In_xN$ significantly increased the photoluminescence intensity [50].

2. P-type Doping

There have been only very few reports of doping of AlN films by incorporating unusually high amounts of C into the lattice [51].

The p-type doping of GaN films has been achieved using Mg. The doping control is not easy at all as it is very sensitive to dopant flow rate. As doped films are generally insulating (except a few reports of as grown p-type GaN by MBE) and require post-growth treatment such as thermal annealing (>600 °C under nitrogen or vacuum) or low energy electron beam irradiation (LEEBI) to activate the p-type dopant [52,53]. The mechanism by which this happens has been identified as the breaking of Mg-H bond [54]. The concentration of Mg atoms in the lattice is typically $<10^{19}$ cm^{-3}, but the room temperature free hole concentrations are generally $<5\times10^{18}$ cm^{-3} for a mobility <20 cm^2/Vs. The activation energy of Mg has been estimated to be 150$\sim$200 meV. Impurity band conduction is also observed at low temperatures in p-type GaN films.

The p-type doping of $Al_xGa_{1-x}N$ has been carried out using Mg and the alloys showed p-type conductivity up to $x < 0.3$ [32]. $Ga_{1-x}In_xN$ alloys have also been p-type doped using Mg for $x < 0.09$ [55].

Much more research work in the p-type doping of III-Nitrides is necessary in the future, in particular for GaN and for $Al_xGa_{1-x}N$ for $x > 0.3$. Research directions include new doping sources, new doping scheme involving co-doping [56].

VII. DEFECTS STUDY IN III-NITRIDES

Because nearly all III-Nitride films used in devices are grown on a foreign substrate, defects will necessarily form at the epilayer/substrate interface. The high densities of defects generally lead to much confusion and has made it difficult to separate the effects due to one type of defect from those due to another.

The GaN films grown on sapphire exhibit a limited

coherence length which is at the origin of the GaN x-ray diffraction peak broadening, as determined through reciprocal space maps of GaN films on Al_2O_3. This was consistent with transmission electron microscopy (TEM) measurements [57].

Threading dislocations and stacking faults are one of the most common defects in III-Nitrides and are visualized using TEM. AlN films on sapphire generally exhibit threading dislocation densities $\sim 10^{10}$ cm^{-2} with Burgers vectors of the type 1/3<11-20> [58]. Threading dislocations densities in GaN are generally higher than 10^8 cm^{-2}, even for GaN on limited bulk GaN substrate. The Burgers vectors are of the type 1/3<11-20> (pure edge) and 1/3<11-23> (mixed screw-edge) [59].

Some of these defects can be visualized through etch pit revelation after wet chemical etching. Etch pits have been studied and compared in GaN grown using different Ga precursors [24]. Different etch pit sizes and shapes were observed. An etch pit density of $\sim 10^4$ cm^{-2} could be determined. Atomic force microscopy and TEM have also been used to reveal pits in GaInN [60].

Point defects are usually experimentally observed indirectly using optical methods such as photoluminescence or cathodoluminescence. For example, Ga vacancies have been shown, both experimentally and theoretically, to be one cause for the yellow photoluminescence in GaN films [61]. Spatially resolved cathodoluminescence also revealed that this yellow luminescence was stronger at grain boundaries [62].

Obviously, the ultimate objective will be to achieve defect-free III-Nitride films. Unless high quality bulk III-Nitride substrates become available, other approaches have to be developed to reach this goal.

The first will be to use of compliant substrates with wafer bonding and substrate lift-off [63]. This has been achieved for InSb on GaAs. However, several issues, such as the stiffness of III-Nitride materials, Al_2O_3 or SiC substrates are likely to limit the applicability of this technique for III-Nitrides. Lateral epitaxial overgrowth, followed by substrate lift-off as well, is a promising technique to achieve nearly dislocation free films. This requires the capability to apply a dielectric pattern onto a template layer, followed by single or multiple-step regrowth [64]. Finally, multilayer techniques can also be used to minimize the propagation of threading screw dislocations to a density below 10^7 cm^{-2} [65].

VIII. PROCESSING TECHNOLOGIES

The methods of fabrication for III-Nitride devices have always been challenging due to the wide bandgap of the Nitrides which makes them physically and chemically stable and which limits the number of metals that can form good ohmic contacts.

1. Etching

Because most devices are grown on sapphire which is insulating, it is not possible to make back electrical contact through the substrate. Etching is therefore a critical and necessary step for the fabrication of most optical and electronic nitride-based devices, in particular to be able to reach both electrical contacts.

Conventional wet chemical etchants have not been successful for use in the fabrication of GaN-based devices due to the low chemical reactivity of the nitrides. Many dry etching techniques have been found to be successful, but ion-induced damage to the etched surface, such as gate recessing for FETs, is unacceptable. Some study has been done using a photoenhanced wet etching technique, which achieved etch rates of 50 nm/min and a surface roughness of 1.5 nm [66]. Unfortunately, this etching method does not seem as efficient for p-type GaN due to the nature of the surface oxidation reaction involved.

A more universal procedure for etching nitride material involves a low ion energy, high density plasma etching technique such as inductively coupled plasma reactive ion etching (RIE), electron cyclotron resonance (ECR), and chemically assisted ion beam etching (CAIBE). These methods offer low energy ion bombardment and smooth, anisotropic etching at high rates. Important parameters in such processes include the chamber pressure, electrode temperature, ion energy, ion density, electromagnet current, gas chemistry, and ion bombardment angle. Several plasma chemistries have been utilized in these high density plasma systems, which provide varying levels of etch rate matching between binary compounds. A few popular chemistries, along with their attributes are listed in Table 8 [67–69].

Beside etching the III-Nitride device structure in order to be able to achieve electrical contact, dry etching has also been a promising method to fabricate mirror facets in nitride based lasers.

Indeed, because of the 30 degree rotation between the crystal lattices of III-Nitrides and sapphire substrate, the cleaving planes of the epilayers and substrates do not coincide. Mechanical polishing has been a popular method to achieve mirrors in III-Nitrides, but it is a time-consuming, cumbersome task that rarely achieves the smoothness desired and is not a viable option for mass production.

Dry-etching still is the most popular technique for mirrors in III-Nitrides, because it is easy and fast; although, the cleaving of sapphire after substantial substrate thinning is recently making a growing case. Using dry etching, to attain a smooth vertical mirror, it is important that the etch be non composition dependent in order to attain similar etch rates for each layer in the laser structure, thus ensuring that there will be no undercutting, protrusions or other significant flaws in the etched verti-

Table 8. Plasma etch chemistries, their etch rates for various Nitride-based binary compounds and advantages.

Chemistry	Material	Typical etch rate*	Comments
$SiCl_4/Ar$	GaN	2850 Å/min	This chemistry does not allow for the incorporation of hydrogen. At hight temp, 170 °C, inN and GaN are both ~2350 Å/min.
	AlN	1245 Å/min	
	InN	3840 Å/min	
$CH_2/(H_2)/Ar$	GaN	4800 Å/min	If H_2 used the etch rates will be slightly higher, but the different compounds will have more unequal rates of etching.
	AlN	1150 Å/min	
	InN	5850 Å/min	
	InGaN	3200 Å/min	
$CH_4/h_2/Ar$	GaN	1450 Å/min	CH_4 provides polymer sidewall protection for additional anisotropy, but coats the chamber walls and requires extensive conditioning of chamber.
	AlN	1150 Å/min	
	InN	3300 Å/min	
	InGaN	3500 Å/min	
$Cl_2/BCl_3/Ar$	GaN	6000 Å/min	Dose not introduce hydrogen. Vergy fast etch rates for all three binary compounds.
	AlN	5000 Å/min	
	InN	6500 Å/min	

*Etch rates are dependent on recipe parameters. These numbers should only be viewed as a comparison index for within each chemistry.

cal plane. Furthermore, with the advances in high density plasma control and directional ion bombardment systems such as CAIBE, the ability to achieve an anisotropic sidewall to the etch is developing rapidly. The standard roughness for these mirrors is about 50 nm. Recent investigations have placed the reflection coefficient at about 15 % [70]. Although this value is what is expected for a GaN-air interface, it is not sufficient for high-power, long-lifetime lasers and high reflectivity coatings are usually used in nitride lasers.

Although the dry etching technology of III-Nitride materials has been successfully developed, the results are still not consistent, *i.e.* there are no standard etch recipes that work universally. This may be due to the fact that the etches are conducted on materials with very dissimilar quality. The future in dry etching of III-Nitrides will be to develop such a standard etch. Important qualities of this ideal etching recipe are high etch rate, minimum structural and electrical damage, and reproducibility.

IX. METAL CONTACTS

When a metal is applied to a semiconductor, the junction can be ohmic or rectifying, leading to an ohmic or a Schottky contact.

High quality, low-resistance ohmic contacts are a necessary component in the fabrication of nitride based devices in order to electrically connect the semiconductor device structure. For example, a high metal-GaN contact resistance would result in a voltage drop and thus hinder the performance of these devices. This is even more important in lasers where high contact resistance is a common cause for the high threshold voltages and Joule heating which leads to early device failure. Low-resistance metal contacts on both p- and n-type III-Nitrides are therefore much sought for, but because of their wide bandgap, not many metals have the adequate work function to form a ohmic contact to III-Nitrides.

Electrical contacts to n-GaN are well-studied, and several different schemes have been found to be acceptable for use. The ohmic/rectifying nature of the metal contact is usually easily predicted because the barrier directly depends on the work function difference between the metal and the semiconductor. Any metal with a work function less than that of n-GaN is expected to form an ohmic contact to it provided that there are no surface states.

However, this is not always the case because of contamination and oxide which can exist on GaN surfaces. These problems can be solved by utilizing some surface preparation techniques, which, when performed before the formation of the contact metal, can improve the contact performance greatly. The simplest method of preparing a surface for metal evaporation to prevent either an oxide film or debris on the surface to affect the electrical properties of the junction involves cleaning, including standard degreasing techniques, dipping the wafer into a dilute HCl solution or dry etching. The latter may actually serve a three-fold purpose: cleaning the surface of the wafer by sputtering off any native oxide, increasing the roughness of the surface and increasing the contact area, increasing the number of point defects at the surface due to damage and thus creating an effective n^+ layer near the surface.

All the metals which are in direct contact with the semiconductor surface share the common characteristic of low work function. Bilayers and compound metal structures are carefully designed to utilize the electrical and mechanical properties of the alloys that are formed during their heating, as well as to provide a top contact metal layer on the surface for wire bonding purposes. Ohmic contacts can be fabricated very effectively using either a low or high temperature post-evaporation annealing. For example at low temperatures, between 400

Table 9. A list of ohmic metal contact schemes for use with n-GaN.

Nitride material	Contact material	Resistivity
n-GaN	Nd/Al	9.8×10^{-6} Ω/cm^2 (RTA)
	Ti/Au	3×10^{-6} Ω/cm^3
	Pd/Al	1.2×10^{-5} Ω/cm^2 (650 °C anneal)
	Ti/Al	5×10^{-5} Ω/cm^2 (600 °C anneal)
	Al	8×10^{-6} Ω/cm^2
	Ti/Al/Ni/Au	8.9×10^{-8} Ω/cm^2 (RTA+RIE)

to 600 °C, Ti acts as an oxygen getter, thus reducing the native oxide on the surface, and an Ti-Al intermetallic phase can form and come into contact with the GaN [71]. Aluminum alone, when heated, could also reduce the native oxide, but is limited by the formation of an AlN layer which accompanies excessive annealing. At higher temperatures (>900 °C), if Ti is used as the first contact material, it has been found that TiN will form at the junction of Ti and GaN [72]. This semi-metal, coupled with the nitrogen vacancies near the interface, forms a very low resistance ohmic contact.

Some common contact schemes used in attaining ohmic contacts to n-GaN are such as RIE damage and post-evaporation annealing (rapid thermal annealing or RTA) are indicated in Table 9 [71–75].

While much work has been done to achieve the realization of a low resistance, ohmic contact to n-GaN, the investigation into the p-GaN metal contact has been limited and sparse. Ni/Au is the most popular bilayer contact scheme used currently in many blue laser designs. It is chosen due to the large work function of Ni, as well as its ability to adhere well to the surface of the material, and the thermal quality and wire bonding continuity that Au offers. Some insight into the mechanisms behind p-GaN interaction and Ni/Au is necessary to determine whether this is indeed the best choice of material. Many different metals with high work functions have been investigated, and a definite correlation between resistivity and work function was demonstrated [76]. Unfortunately, no work has been published yet which illustrates achievement of the low contact resistance required for blue lasers.

Also essential for many devices are Schottky contacts.

Table 10. A list of contact material, built in potential, barrier height, and ideality factor for Schottky contacts to p-GaN.

Nitride material	Contact material	Built in potential	Barrier height	Ideality factor
n-GaN	Cr	0.52 V	0.55 eV	1.05
	Au	1.00 V	1.03 eV	1.15
	Ni	1.12 V	1.13 eV	1.17
	Ag		0.82 eV	1.01
	Pb		0.73 eV	1.01

For example, Schottky barrier photodiodes and JFETs make use of a high-quality rectifying contact to the semiconductor material. Thermal stability is very important for use in high temperature applications. A short list of some tested materials is shown in Table 10 [77,78].

Low resistance ohmic metal contacts to n-type GaN are well developed and do not need much work in the near future. By contrast, ohmic metal contacts to p-type GaN will receive the most attention. The development of Schottky contacts is still immature. Although interest in this area of research is growing, the contact quality must be improved to support the evolution of current devices.

X. DEVICES

1. Electronic Devices

Not only are III-Nitrides suitable for optical devices, they are also promising for electronic devices. Unlike optical devices which make use of $Ga_{1-x}In_xN$ alloys to span the visible optical spectrum, electronic devices use $Al_xGa_{1-x}N$ compounds to make use of the large breakdown voltage, high saturation velocity and thermal conductivity of these materials, in order to fabricate devices which could operate at high-frequency, high power and high temperature. AlN is also a promising insulating material as an alternative to oxides [79]. Four figures of merit are generally used to characterize materials for electronic devices.

1. The Johnson figure of merit (JFM) is related to the electronic properties of materials. It characterizes the frequency-power trade-off, since high frequency usually requires small device dimension while high power need large device size. JFM is calculated as:

$$\mathrm{JFM} = \left(\frac{E_m V_s}{2\pi}\right)^2,$$

where E_m is the breakdown voltage, V_s is the saturation velocity.

2. The Keyes figure of merit (KFM) is related to the material thermal properties. It characterizes the device size and thermal resistance trade-off, and is calculated as:

$$\mathrm{KFM} = \lambda\left(\frac{cv_s}{2\pi\epsilon}\right)^{1/2},$$

where λ is the thermal conductivity of the materials, c is the speed of light, and ϵ is the material dielectric constant.

3. The Baliga figure of merit (BFM) addresses conduction losses of low frequency power devices and is calculated as:

$$\mathrm{BFM} = \epsilon\mu E_m^3,$$

where μ is the carrier mobility in the material.

Table 11. Comparison of the Johnson figures of merit of different materials.

Material	E_b (V/cm)	V_s (cm/s)	$[(E_bV_s)/\pi]^2$ (V^2/s^2)	Ratio to Silicon
Si	3×10^5	1.0×10^7	9.1×10^{23}	1.0
GaAs	4×10^5	2.0×10^7	64.8×10^{23}	7.1
GaN	50×10^5	2.7×10^7	18466×10^{23}	2029
6H-SiC	40×10^5	2.0×10^7	6485×10^{23}	712
3C-SiC	40×10^5	2.0×10^7	6485×10^{23}	71
Diamond	100×10^5	2.7×10^7	73863×10^{23}	8117

Table 12. Comparison of the Keyes figures of merit of different materials.

Material	σ_T (300 K) (W/cm)	V_s (cm/s)	ϵ_r	$\sigma_T\,(V_s/\epsilon_r)^{1/2}$ ($W/cm^{1/2}s^{1/2}$)	Ratio to Silicon
Si	1.5	1.0×10^7	11.8	13.8×10^2	1.0
GaAs	0.5	2.0×10^7	12.8	6.25×10^2	0.45
GaN	1.3	2.7×10^7	9	22.5×10^2	1.6
6H-SiC	5.0	2.0×10^7	9.7	71.8×10^2	5.2
3C-SiC	5.0	2.0×10^7	9.7	71.8×10^2	5.2
Diamond	20.0	2.7×10^7	5.5	443.1×10^2	32.1

4. The Baliga high-frequency figure of merit (BHFM) addresses switching losses of high- frequency power devices, due to charging and discharging, and is calculated as:

$$\text{BHFM} = \epsilon\mu E_m^2$$

These figures of merit allow give some type of comparison between III-Nitrides and other semiconductors for high-frequency, high-power and high-temperature electronic devices. The values are generally normalized to Si. The values for the JFM and KFM are listed in Table 11 and respectively. From these tables, it can be seen that GaN, AlN are promising materials for high-performance electronic devices.

To date, III-Nitrides-based metal-insulator, metal-semiconductor and heterojunction field effect transistors (MISFET, MESFET, HFET), as well as GaN/SiC hybrid heterojunction bipolar transistors have been demonstrated. More recently, AlGaN/GaN modulation doped field effect transistors (MODFET) with cut-off frequency as high as 50 GHz and maximum frequency of 92 GHz have been achieved. These devices were able to operate up to 500 °C.

Piezoelectric effect between AlGaN and GaN interfaces has been investigated to generate two-dimensional electron gas at the interface without doping of the barrier. HFET based on this piezoelectric effect has been demonstrated with cut-off frequency as high as 62 GHz and a maximum frequency up to 140 GHz.

In spite of these successes, the development of III-Nitride based electronic devices is still in its infancy. Much research work will be necessary to enhance the performance and reliability of these devices and fulfill the expected potential of III-Nitrides for high frequency, high power and high temperature electronic devices. This will mostly rely on improvement of the material quality and metal contact technology.

2. Ultraviolet Photodetectors

There are many types of types of photodetectors. Photoconductors, metal-semiconductor-metal (MSM), Schottky barrier, and photovoltaic diodes are the most common. They are all considered useful for certain applications. The advantages and disadvantages of each type

Table 13. Comparison of different types of UV photodetectors.

Photodetecotor type	Advantages	Disadvantages	Challenges
Photoconductors	o Easy to fabricate o Internal photoelectric gain	o Low speed o Large dark current o Large Johnson noise	o Interdigitated patterns require enhanced resolution.
P-n or p-i-n photodiodes	o Low or zero dark current o High-speed o High impedance (good for FPA readout circuitry) o Compatible with planar processin technology (for FPA) o For p-i-n photodiodes, easey optimization of quantum efficiency and speed with I layer	o Speed is limited by minority carrier diffusion time and storage time o Speed and quantum effciency trade-off	o Etching in nessary to expose various layers o Ohmic contacts necessary to both n- and p-type material
Schottky photodiodes	o High efficiency o High speed o Easy to fabricate	o Require high absorption coefficient o No-sharp cut-off (below bandgap res.) o Front side illumination needed	o Schottky contact is needed

of photodetectors are summarized in Table 13 [11].

The development of photodetectors based on III-Nitride material began with the most simple device design, the photoconductor. This device required no p-GaN layer to operate, and therefore simplified not only the growth demands, but also the fabrication steps because etching steps were not needed to define the device or contact two electrically different types of GaN layers. Both single stripe devices and interdigitated contact designs have been pioneered to explore the limits of current responsivity, noise equivalent power (NEP), temporal response, and rejection ratio. The current responsivity depends on two main factors: the quantum efficiency, η, and the photoconductive gain, G, which are assumed to be constant over the volume of the device. The quantum efficiency is a measure of how well the input radiation is coupled to the electrical area of the photodetector. It is usually defined as the number of electron-hole pairs generated for each incident photon. Photoconductive gain is a concept that simplifies the idea of a photoconductive phenomenon. The responsivity is significantly higher for devices utilizing the closely spaced interdigitated contacts due to the photoconductive gain mechanism exploited in the design. The noise equivalent power (NEP) is also a parameter used to measure the performance of a detector. It is the ratio of the current noise to the responsivity of the device. Another popular metric used to quantify the performance of a UV detector is the UV-to-visible rejection ratio, which is the ratio of the photoresponse of UV light to the photoresponse of visible light. These parameters are outlined with their appropriate values in Table 14 for several types of photodetectors reported in the literature [80–89].

The characteristics of current photoconductor devices include very fast response detectors [82], $Al_xGa_{1-x}N$ detectors over the entire range ($0 \leq x \leq 1$) [80], and demonstration of gain mechanism in an MSM detector by using interdigitated contact design with a gain over 3000 A/W [83]. GaN detector arrays have also been demonstrated. The kinetics of photoconductivity has also been investigated in GaN photodetectors [90].

Schottky diodes are the most simple detectors to fabricate and are capable of being extremely fast. Several groups have combined efforts to develop Schottky photodetectors with high responsivity and low NEP [84]. They have also fabricated the first GaN-based photodetector grown on a Si substrate rather than the popular c-plane sapphire substrate [85].

The last part of Table 14 highlights the reported results for p-n and p-i-n photodiodes [91]. To date, all the p-n junctions in the photodiodes were formed using GaN, leading to a cut-off wavelength of 365 nm corresponding to the bandgap of GaN. The temporal response for these detector designs led to carrier lifetimes as low as 20 ns, with very low NEP, good responsivities (0.10~0.14 A/W) and rejection ratios of about three orders of magnitude. The latest advancement in this field was a GaN p-i-n photodiode which not only has a high responsivity of 0.15 A/W, but made a jump from the typical rejection ratio of 10^3 to a much larger 10^6, as shown in Figure 11 [89].

The progression to faster response, higher rejection of visible light, lower noise interference, and better response are all indicative of not only improved designs, but also a

Table 14. Major accomplishments in Nitride based detectors: photoconductors, MSM and Schottky diodes, and photovoltaic detectors.

Detector	R (A/W)	G·η	NEP (N)	τ	Rejection Ratio	Research Group
GaN PC	125	600		20 ns		Boston University
$Al_xGa_{1-x}N$	18~300	64~150	$< 10^{-8}$	1~2 ms	10^3	APA Optics
AlN, GaN PC $Al_xGa_{1-x}N$ PC ($0 < x < 1$)	> 10 (single stripe)		$< 10^{-9}$	< 3 ms	10^3	CQD-Northwestern University
GaN MSA	0.3				$> 10^2$	University of Texas-Austin
GaN MSA	3200 (interdigitated)			300 μs	$> 10^2$	NASA-Goddard Space Flight Center
n-GaN Schottky PD	0.18	0.65	5×10^{-9}	120 μs	10	APA Optics Texas Tech Univ.
n-GaN Schottky on Si (111)	0.10		4×10^{-9}		10^2	APA Optics, Texas Tech Univ., NC State
GaN p-i-n PD	0.11	0.48		8.2 μs		SVT Associates, U of Minnesota
GaN p-π-n PD	0.10		4×10^{-11}	18 ns	10^3	APA Optics, Texas Tech
AlGaN/GaN p-i-n PD	0.14	0.5	8×10^{-12}	12 ns	10^3	University of Illinois-Wright Laboratory
GaN p-i-n PD	0.15	0.5		2.5 μs	10^6	CQD-Northwestern University

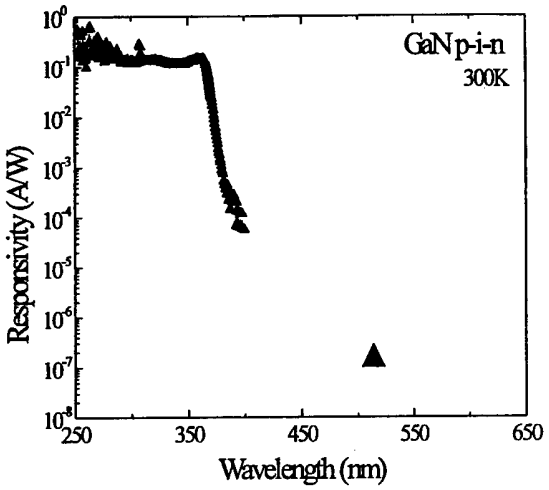

Fig. 11. Room temperature spectral response from a GaN p-i-n photodiode. The responsivity at 514 nm was measured using a high power argon laser, while the rest of the spectrum was measured using a Xe lamp [89].

continued increase in the quality of material. III-Nitride based UV photodetectors remain a very promising field for research and development for the future.

3. Visible Light Emitting Diodes

To generate visible light using III-Nitride materials, one has to use $Ga_{1-x}In_xN$ alloys in the active layer.

The first generation of blue and blue/green LEDs were fabricated from GaInN/AlGaN double-heterostructures (DH) [92]. Although these provided high optical output, higher than 1 candela (cd), they had a broad spectrum with linewidths typically ~70 nm, while the emission spectrum ranged from the violet to the yellow-orange spectral range, making the output appear "whitish-blue" to the human eye. Greatly improved LED performance, in terms of both color purity and intensity, have been achieved using single quantum-well (SQW) structures [93–95]. The emission peak linewidths for blue LEDs (450 nm) have been reduced to 20 nm, with brightness as high as 2 cd. Green LEDs (520 nm) exhibited a emission peak linewidth of 30 nm and luminous intensity of 12 cd. The latest record has been achieved by using strained single quantum wells of $Ga_{1-x}In_xN$. Violet (405 nm), blue (450 nm) and green (520 nm) LEDs has been demonstrated with efficiencies of 9.2 %, 8.7 % and 6.3 % respectively (see Table 15). These LEDs give better performance than those made from other materials and join the mainstream of LED evolution as shown in Table 16. White LED have also been demonstrated by combining a blue nitride LED with a phosphorescent coating of the LED packaging. All these LEDs are now commercially available.

In addition to these high brightness LEDs, devices with longer emission peak wavelengths, up to 600 nm (orange),

Table 15. Nichia LED performances at forward current I_f=20 mA [93–95] (predicted lifetime ~60,000 hrs [96]).

Color	Peak λ (nm)	Peak FWHM (nm)	P_{out} (mW)	η (%)
Violet	405	20	5.8	9.2
Blue	450	20	5	9.1
Green	520	30	3	6.3
Yellow	590	90	0.5	1.2

Table 16. Comparison of visible III-Nitride LEDs and those fabricated from other semiconductor materials.

Color	Material	Peak wavelength (nm)	Luminous intensity (mcd)	Output power (μW)	External quantum efficiency (%)
Green	AlInGaP	570	1000	400	1.0
	GaP	555	100	40	0.1
	ZnTeSe*	512	400	1300	5.3
	InGaN	520	12000	3000	6.3
Blue	SiC	470	20	20	0.04
	ZnCdSe*	489	700	327	1.3
	InGaN	450	2500	5000	9.1

*At forward curren I_f=10 mA, All others I_f=20 mA.

have been achieved by increasing the indium composition (Table 15) [96]. However, the performance of these devices are not as satisfactory because the quality of GaInN tends to deteriorate for higher indium compositions due to the dissociation of GaInN at high temperatures, and because of the higher lattice and thermal mismatch between the well and the barrier layers [97].

Despite the successful commercialization of III-Nitride based LEDs, there remain some important issues.

First is the reliability of the devices. These LEDs are still fragile and require careful handling. They can be easily damaged by reverse bias greater than 5 Volts or forward current higher than 100 mA. This is surprising because III-Nitrides are expected to have high breakdown voltages. An improper doping profile or high background carrier concentration in GaInN could be the cause of failure at high reverse bias or large forward current.

Second is their thermal handling capability. The recommended operation temperature is <80 °C to avoid early degradation of the devices. Ideally, III-Nitrides based devices are suitable for much higher temperature operation because of their thermal properties. The unusual low operation temperature could be due to the high defect density in the materials and the thermal instability of GaInN active layer.

Third is the price. Commercial III-Nitride based LEDs cost more than US$ 6 apiece, which is still too high for large volume applications.

4. Violet-blue Laser Diodes

The realization of III-Nitride based laser diodes has

Table 17. Current GaN-based blue laser diode players.

Research group	Date	Structure	Operation mode	Threshold	λ_0 (nm) $\Delta\lambda$ (nm)	Output power	Fabrication	Lifetime
Nichia	Nov, 1995	GaInN MQW on sapphire	pulsed @RT	1.7 A@34 V 4 kA/cm^2	417 1.6	215 mW@ 2.3 A&34 V	RIE etching for mirrors with HR coating (60~70 %)	not tested (>24 hrs)
Meijo University	Mar, 1996	GaInN SQW-SCH on sapphire	Pulsed @RT	16 V 2.9 kA/cm^2	376 0.15	not given	RIE etching for mirror without coating	not given
Toshiba	Sept, 1996	GaInN MQW on sapphire	Pulsed@ RT	5 A@20 V 50 kA/cm^2	417.5 0.15	not given	cleaved along <1120> on c-sapphire	not given
Cree	1997	no details						
Fujitsu	July, 1997	10 GaInN MQW on SiC	Pulsed@RT (1 %)	500 mA@22 V 12 kA/cm^2	405~425	80 mW	HR coated	Not given
UCSB	Sept, 1997	GaInN MQW on sapphire	Pulsed, RT	50 V 12.7 kA/cm^2	420	Not given	RIE	Not given
Xerox	Oct, 1997	10 GaInN MQW on sapphire	Pulsed@RT 400 ns @1 kHz	25 kA/cm^2	422~432	Not given	Dry etching	Not given
Sony		5 GaInN MQW on sapphire	Pulsed, RT, 500 ns, 1 kHz	9.5 kA/cm^2	417.5	<0.2 nm	Cleaving	Not give
Northwes- tern Univ.	Dec, 1997	GaInN MQW	Pulsed, CW, RT	1.4 kA/cm^2 @77 K	405~410	2 mW/facets (Pulsed)	Mechanical polishing	140 hrs @RT
Nichia	Oct, 1997	GaInN MQW	CW@RT	16 mA 1.5 kA/cm^2	390~420	2 mW	RIE mirror with HR coating	10,000 hrs@RT

eluded the research community for many years. It is only after thorough development of the material, processing and device fabrication technology that such lasers have been made possible.

There has been outstanding success in GaN-based blue laser diodes in the past few years. To date, nine research groups worldwide have demonstrated GaInN/GaN multiple quantum well based violet-blue laser diodes and some of the device characteristics are summarized in Table 17. Blue laser diodes operating at room temperature and in continuous wave mode with a projected lifetime of 20,000 hours have been demonstrated and are nearing commercialization. Most of the recent nitride lasers share the following characteristics.

- The active layer consists of a $Ga_{1-x}In_xN/Ga_{1-y}In_yN$ or GaInN/GaN multi-quantum well (MQW) with an emission peak ranging from 400 to 430 nm.
- The MQW is not uniform, but has a quantum dot-like structure. These quantum dots are formed most likely because of indium composition fluctuation and segregation.
- Laser performances are enhanced when Si doping the wells and barriers of the MQW.
- The general structure of the laser consists of a separate confinement heterostructure, using AlGaN as the cladding layers, although there has been report of Al-free III-Nitride lasers [42].
- The p-type contact layer has a hole concentration in the range of 10^{18} cm^{-3}.

The dislocation density in early generation of III-Nitride based lasers is measured to be higher than 10^7 cm^{-2}, which led to very short lifetime and low output power. It is only recently that much higher output power and longer lifetime have been achieved by reducing the dislocation density through lateral epitaxial overgrowth (LEO).

From the above discussion, it can be seen that there are still many fundamental issues that need to be addressed.

First, there is currently no real understanding of the lasing mechanism in III-Nitride lasers. There are experimental evidences that recombination in the MQW active layer is enhanced in these laser diodes by self-formed quantum-dot like structures, or by localization of excitons by potential fluctuation [98–102]. Theoretical work is necessary to study how these structures are affecting material and modal gain [103], recombination efficiency, emission wavelength (tunable by adjusting the dot or potential feature sizes), and how lasing can be improved by intentionally control the formation of such structures.

Secondly, the mechanism for the formation of the aforementioned quantum-dot structure or local potentials is also unknown. Is it due to the intrinsic nature of GaInN ternary alloys since compositional modulation due to phase separation would be energetically favored in this material system? [39] Or is it due to compressive strain introduced by lattice mismatch? The understanding of the mechanism would inevitably lead to better devices.

The effect of doping in III-Nitride based lasers is not entirely clear. Generally lasers have intrinsic active layers in order to enhance carrier diffusion and reduce free carrier absorption in the active layer. However, Si doping in III-Nitride lasers enhances the laser diode performance [100]. It is believed that the doping effectively screens the piezoelectric field in the MQW active region [104].

The p-type doping needs to be increased in order to minimize device resistance. Searching for other dopants seems hopeless because of the deep-level nature of acceptor dopants in III-Nitrides, which may be an intrinsic nature of wide bandgap nitride materials, just like ZnSe-based materials. However, new doping schemes such as piezoelectric effect, which can enhance the ionization of impurities by built-in electrical field, or tunneling-assisted carrier injection should be studied.

Finally, the failure mechanisms in III-Nitride lasers need to be determined and minimized. Potential causes of failure include heat generation due to high series resistance, dislocations and other threading defects, as well as optical damage due to reabsorption of stimulated emission at defects which are formed during growth [105]. Reduction of defects is now rapidly being conducted through lateral epitaxy overgrowth [106]. With the progress of bulk GaN growth either by high-pressure technique or hydride VPE or LEO grown, homoepitaxy of III-Nitride devices may be soon available.

XI. CONCLUSIONS

This review has showed that indeed much has already been achieved in the III-Nitride material system over the past two decades, in particular the realization of commercial optical devices. Much more fundamental work still needs to be conducted in order to understand the very rich and unexplored physical properties of III-Nitrides. A better understanding of all the physical parameters would allow in turn a better design of existing devices and the potential discovery of novel devices.

REFERENCES

[1] F. Fichter and Z. Anorg, Chem. **54**, 322 (1971).

[2] F. Fischer and F. Schroter, Ber. Deutschen Chemischen Gesellschaft **43**, 1465 (1910).

[3] W. C. Johnson, J. B. Parsons and M. C. Crew, J. Phys. Chem. **36**, 2561 (1932).

[4] B. Daudin, J. L. Rouviere and M. Arlery, Appl. Phys. Lett. **69**, 2480 (1996).

[5] A. D. Bykhovski, V. V. Kaminski, M. S. Shur, Q. C. Chen and M. A. Khan, Appl. Phys. Lett. **69**, 3254 (1996).

[6] J. Miragliotta, D. K. Wickenden, T. J. Kistenmacher and W. A. Bryden, J. Opt. Soc. Am. **B10**, 1447 (1993).

[7] H. Y. Zhang, X. H. He, Y. H. Shih, M. Schurman, Z. C. Feng and R. A. Stall, Appl. Phys. Lett. **69**, 2953 (1996).

[8] *Semiconductors: Group IV Elements and III-V Compounds*, ed. by O. Madelung (Springer-Verlag, Berlin, 1991).

[9] O. Madelung, *Semiconductors-Basic Data*, 2nd ed. (Springer-Verlag, Berlin, 1996).

[10] M. Leszczynski, T. Suski, P. Perlin, H. Teisseyre, I. Grzegory, M. Bockowski, J. Jun, S. Porowski and J. Major, J. Phys. **D28**, A149 (1995).

[11] M. Razeghi and A. Rogalski, J. Appl. Phys. **79**, 7433 (1996).

[12] P. Kung, A. Saxler, X. Zhang, D. Walker and M. Razeghi, In *Photodetectors: Materials and Devices*, ed. Gail J. Brown and Manijeh Razeghi, SPIE Proceedings Series (Bellingham, Wash.: SPIE-The International Society for Optical Engineering, 1996), Vol. 2685, p. 126.

[13] P. Kung, A. Saxler, X. Zhang, D. Walker, R. Lavado and M. Razeghi, Appl. Phys. Lett. **69**, 2116 (1996).

[14] H. Ohsato and M. Razeghi, In *Photodetectors: Materials and Devices II*, ed. Gail J. Brown and Manijeh Razeghi, SPIE Proceedings Series (Bellingham, Wash.: SPIE-The International Society for Optical Engineering, 1997), Vol. 2999, p. 288.

[15] S. Porowski, J. Cryst. Growth **166**, 583 (1996).

[16] C. J. Sun, P. Kung, A. Saxler, H. Ohsato, K. Haritos and M. Razeghi, J. Appl. Phys. **75**, 3964 (1994).

[17] P. Kung, C. J. Sun, A. Saxler, H. Ohsato and M. Razeghi, J. Appl. Phys. **75**, 4515 (1994).

[18] T. Kato, P. Kung, A. Saxler, C. J. Sun, H. Ohsato, M. Razeghi and T. Solid-State Electronics **41**, 227 (1997).

[19] T. Kato, H. Ohsato, T. Okuda, P. Kung, A. Saxler, C. J. Sun and M. Razeghi, J. Cryst. Growth **173**, 244 (1997).

[20] T. Kato, P. Kung, A. Saxler, C. J. Sun, H. Ohsato, M. Razeghi and T. Okuda, J. Cryst. Growth **183**, 131 (1998).

[21] C. J. Sun and M. Razeghi, Appl. Phys. Lett. **63**, 973 (1993).

[22] H. Amano, N. Sawaki, I. Akasaki and Y. Toyoda, Appl. Phys. Lett. **48**, 353 (1986).

[23] L. T. Romano, B. S. Krusor and R. J. Molnar, Appl. Phys. Lett. **71**, 2283 (1997).

[24] A. Saxler, D. Walker, P. Kung, X. Zhang, M. Razeghi, J. Solomon, W. C. Mitchel and H. R. Vydyanath, Appl. Phys. Lett. **71**, 3272 (1997).

[25] B. Beaumont, P. Gibart and J. P. Faurie, J. Cryst. Growth **156**, 140 (1995).

[26] A. Saxler, P. Kung, C. J. Sun, E. Bigan and M. Razeghi, Appl. Phys. Lett. **64**, 339 (1994).

[27] P. Kung, A. Saxler, X. Zhang, D. Walker, T. C. Wang, I. Ferguson and M. Razeghi, Appl. Phys. Lett. **66**, 2958 (1995).

[28] M. C. Benjamin, C. Wang, R. F. Davis and R. J. Nemanich, Appl. Phys. Lett. **64**, 3288 (1994).

[29] A. T. Sowers, J. A. Christman, M. D. Bremser, B. L. Ward, R. F. Davis and R. J. Nemanich, Appl. Phys. Lett. **71**, 2289 (1997).

[30] K. Kaya, H. Takahashi, Y. Shibata, Y. Kanno and T. Hirai, Jpn. J. Appl. Phys. **36**, 307 (1997).

[31] C. J. Sun, P. Kung, A. Saxler, H. Ohsato, E. Bigan, M. Razeghi and D. K. Gaskill, Journal of Applied Physics **76**, 236 (1994).

[32] P. Kung, A. Saxler, D. Walker, X. Zhang, R. Lavado, K. S. Kim and M. Razeghi, In *III-V Nitrides*, ed. by F. A. Ponce, T. D. Moustakas, I. Akasaki and B. A. Monemar, Materials Research Society Symposium Proceedings (Materials Research Society, Pittsburgh, 1997), Vol. 449, p. 79.

[33] M. Razeghi, unpublished.

[34] J. M. Redwing, M. A. Tischler, J. S. Flynn, S. Elhamri, M. Ahoujja, R. S. Newrock and W. C. Mitchel, Appl. Phys. Lett. **69**, 963 (1996).

[35] M. Shur, B. Gelmont and M. A. Khan, J. Electron. Mater. **25**, 777 (1996).

[36] E. T. Yu, G. J. Sullivan, P. M. Asbeck, C. D. Wang, D. Qiao and S. S. Lau, Appl. Phys. Lett. **71**, 2794 (1997).

[37] G. Martin, A. Botchkarev, A. Rockett and H. Morko, Appl Phys. Lett. **68**, 2541 (1996).

[38] A. Koukitu, N. Takahashi, T. Taki and H. Seki, J. Cryst. Growth **170**, 306 (1997).

[39] I. H. Ho and G. B. Stringfellow, Appl. Phys. Lett. **69**, 2701 (1996).

[40] S. Nakamura and T. Mukai, Jpn. J. Appl. Phys. **31**, L1457 (1992).

[41] A. Sohmer, J. Off, H. Bolay, V. Harle, V. Syganow, Jin Seo Im, V. Wagner, F. Adler, Andreas Hangleiter, A. Dornen, F. Scholz, D. Brunner, O. Ambacher and H. Lakner, MRS Internet Journal Nitride Semiconductor Research **2**, 14 (1997).

[42] P. Kung, A. Saxler, D. Walker, A. Rybaltowski, X. Zhang, J. Diaz and M. Razeghi, MRS Internet Journal Nitride Semiconductor Research **3**, 1 (1998).

[43] M. Koike, S. Yamasaki, S. Nagai, N. Koide, S. Asami, H. Amano and I. Akasaki, Appl. Phys. Lett. **68**, 1403 (1996).

[44] K. Hiramatsu, Y. Kawaguchi, M. Shimizu, N. Sawaki, T. Zheleva, Robert F. Davis, H. Tsuda, W. Taki, N. Kuwano and K. Oki, MRS Internet Journal Nitride Semiconductor Research **2**, 6 (1997).

[45] T. Deguchi, A. Shikanai, K. Torii, T. Sota, S. Chichibu and S. Nakamura, Appl. Phys. Lett. **72**, 3329 (1998).

[46] X. Zhang, P. Kung, A. Saxler, D. Walker and M. Razeghi, J. Appl. Phys. **80**, 6544 (1996).

[47] A. Saxler, P. Kung, X. Zhang, D. Walker, J. Solomon, M. Ahoujja, W. C. Mitchel, H. R. Vydyanath and M. Razeghi, *GaN Doped with Sulfur. In Defects in Semiconductors ICDS-19*, ed. Gordon Davies and Maria Helena Nazare, Materials Science Forum, 1161 (Trans Tech Publications, Switzerland, 1998), Vols. 258-263.

[48] W. Gotz, N. M. Johnson, C. Chen, H. Liu, C. Kuo and W. Imler, Appl. Phys. Lett. **68**, 3144 (1996).

[49] X. Zhang, P. Kung, A. Saxler, D. Walker, T. C. Wang and M. Razeghi, Appl. Phys. Lett. **67**, 1745 (1995).

[50] S. Nakamura, T. Mukai and M. Senoh, Jpn. J. Appl. Phys. **32**, L16 (1993).

[51] K. Wongchotique, N. Chen, D. P. Zhang, X. Tang and M. G. Spencer, In *Gallium Nitride and Related Materials*, ed. F. A. Ponce, R. D. Dupuis, S. Nakamura and J. A. Edmond, Materials Research Society Symposium Proceedings, (Materials Research Society, Pittsburgh, 1996), Vol. 395, p. 279.

[52] S. Nakamura, T. Mukai, M. Senoh and N. Iwasa, Jpn. J. Appl. Phys. **31**, L139 (1992).

[53] H. Amano, M. Kito, K. Hiramatsu and I. Akasaki, Jpn. J. Appl. Phys. **28**, L2112 (1989).

[54] S. Nakamura, N. Iwasa, M. Senoh and T. Mukai, Jpn. J. Appl. Phys. **31**, 1258 (1992).

[55] S. Yamasaki, S. Asami, N. Shibata, M. Koike, K. Manabe, T. Tanaka, H. Amano and I. Akasaki, Appl Phys. Lett. **66**, 1112 (1995).

[56] O. Brandt, H. Yang, H. Kostial and K. H. Ploog, Appl. Phys. Lett. **69**, 2707 (1996).

[57] A. Saxler, M. A. Capano, W. C. Mitchel, P. Kung, X. Zhang, D. Walker and M. Razeghi, In *III-V Nitrides*, ed. F. A. Ponce, T. D. Moustakas, I. Akasaki and B. A. Monemar, Materials Research Society Symposium Proceedings (Materials Research Society, Pittsburgh, 1997), Vol. 449, p. 477.

[58] K. Dovidenko, S. Oktyabrsky, J. Narayan and M. Razeghi, J. Appl. Phys. **79**, 2439 (1996).

[59] X. H. Wu, L. M. Brown, D. Kapolnek, S. Keller, B. Keller, S. P. DenBaars and J. S. Speck, J. Appl. Phys. **80**, 3228 (1996).

[60] Y. Chen, T. Takeuchi, H. Amano, I. Akasaki, N. Yamada, Y. Kaneko and S. Y. Wang, Appl. Phys. Lett. **72**, 710 (1998).

[61] X. Zhang, P. Kung, A. Saxler, D. Walker and M. Razeghi, In *Gallium Nitride and Related Materials*, ed. F. A. Ponce, R. D. Dupuis, S. Nakamura and J. A. Edmond, Materials Research Society Symposium Proceedings (Materials Research Society, Pittsburgh, 1996), Vol. 395, p. 625.

[62] F. A. Ponce, D. P. Bour, W. Gotz and P. J. Wright, Appl. Phys. Lett. **68**, 57 (1996).

[63] F. E. Ejeckam, M. Seaford, Y. H. Lo, H. Q. Hou and B. E. Hammons, Appl. Phys. Lett. **71**, 776 (1997).

[64] O. H. Nam, M. D. Bremser, T. S. Zheleva and R. F. Davis, Appl. Phys. Lett. **71**, 2638 (1997).

[65] P. Kung, X. Zhang, A. Saxler, D. Walker, M. Razeghi, W. Qian and V. P. Dravid, Journal of the European Ceramic Society **17**, 1781 (1997).

[66] C. Youtsey, I. Adesida, L. T. Romano and G. Bulman, Appl. Phys. Lett. **72**, 560 (1998).

[67] C. B. Vartuli, J. D. MacKenzie, J. W. Lee, C. R. Abernathy, S. J. Pearton and R. J. Shul, J. Appl. Phys. **80**, 3705 (1996).

[68] R. J. Shul, C. I. H. Ashby, C. G. Willison, L. Zhang, J. Han, M. M. Bridges, S. J. Pearton, J. W. Lee and L. F. Lester, In *Wide-Bandgap Semiconductors for High Power, High Frequency and High Temperature*, ed. By S. Denbaars, M. S. Shur, J. Palmour, M. Spencer, Materials Research Society Proceedings (Materials Research Society, Pittsburgh, 1998), Vol. 512, p. 449.

[69] M. Razeghi, unpublished.

[70] F. Binet, J. Y. Duboz, N. Laurent, C. Bonnat, P. Collot, F. Hanauer, O. Briot and R. L. Aulomnard, Appl. Phys. Lett. **72**, 960 (1998).

[71] B. P. Luther, S. E. Mohney, T. N. Jackson, M. Asif Khan, Q. Chen and J. W. Yang, Appl. Phys. Lett. **70**, 57 (1997).

[72] Z. Fan, S. N. Mohammad, W. Kim, O. Aktas, A. E. Botchkarev and H. Morkoc, Appl. Phys. Lett. **68**, 1672 (1996).

[73] C. T. Lee, M. Y. Yeh, C. D. Tsai and Y. T. Lyu, J. of Electron. Mater. **26**, 262 (1997).

[74] Y. F. Wu, W. N. Jiang, B. P. Keller, S. Keller, D. Kapolnek, S. P. Denbaars, U. K. Mishra and B. Wilson, Solid State Electron. **41**, 165 (1997).

[75] A. T. Ping, M. Asif Khan and I. Adesida, J. of Electron. Mater. **25**, 819 (1996).

[76] H. Ishikawa, S. Kobayashi, Y. Koide, S. Yamasaki, S. Nagai, J. Umezaki, M. Koike and M. Murakami, J. Appl. Phys. **81**, 1315 (1997).

[77] E. V. Kalinina, N. I. Kuznetsov, V. A. Dmitriev, K. G. Irvine and C. H. Carter, Jr., J. of Electron. Mater. **25**, 831 (1996).

[78] T. U. Kampen and W. Monch, MRS Internet J. **1**, 41 (1997).
[79] X. Zhang, D. Walker, A. Saxler, P. Kung, J. Xu and M. Razeghi, Electron. Lett. **32**, 1622 (1996).
[80] D. Walker, X. Zhang, P. Kung, A. Saxler, S. Javadpour, J. Xu and M. Razeghi, Appl. Phys. Lett. **68**, 2100 (1996).
[81] D. Walker, X. Zhang, A. Saxler, P. Kung, J. Xu and M. Razeghi, Appl. Phys. Lett. **70**, 949 (1997).
[82] J. C. Carrano, P. A. Grudowski, C. J. Eiting, R. D. Dupuis and J. C. Campbell, Appl. Phys. Lett. **70**, 1992 (1997).
[83] Z. C. Huang, D. B. Mott, P. K. Shu, J. C. Chen and D. K. Wickenden, J. of Electron. Mater. **26**, 330 (1997).
[84] Q. Chen, J. W. Yang, A. Osinsky, S. Gangopadhyay, B. Lim, M. Lim, A. Anwar, M. Asif Khan, D. Kuksenkov and H. Temkin, Appl. Phys. Lett. **70**, 2277 (1997).
[85] A. Osinsky, S. Gangopadhyay, J. W. Yang, R. Gaska, D. Kuksenkov, H. Temkin, I. K. Shmagin, Y. C. Chang, J. F. Muth and R. M. Kolbas, Appl. Phys. Lett. **72**, 551 (1998).
[86] J. M. Van Hove, R. Hickman, J. J. Klaassen, P. P. Chow and P. P. Ruden, Appl. Phys. Lett. **70**, 2282 (1997).
[87] A. Osinsky, S. Gangopadhyay, R. Gaska, B. Williams, M. A. Khan, D. Kuksenkov and H. Temkin, Appl. Phys. Lett. **71**, 2334 (1997).
[88] G. Y. Xu, A. Salvador, W. Kim, Z. Fan, C. Lu, H. Tang, H. Morkoc, G. Smith, M. Estes, B. Goldenberg, W. Yang and S. Krishnankutty, Appl. Phys. Lett. **71**, 2154 (1997).
[89] D. Walker, A. Saxler, P. Kung, X. Zhang, M. Hamilton, J. Diaz and M. Razeghi, Appl. Phys. Lett. **72**, 3303 (1998).
[90] P. Kung, X. Zhang, D. Walker, A. Saxler, J. Piotrowski, A. Rogalski and M. Razeghi, Appl. Phys. Lett. **67**, 3792 (1995).
[91] X. Zhang, P. Kung, D. Walker, J. Piotrowski, A. Rogalski, A. Saxler and M. Razeghi, Appl. Phys. Lett. **67**, 2028 (1995).
[92] A. Saxler, K. S. Kim, D. Walker, P. Kung, X. Zhang, G. Brown, W. C. Mitchel and M. Razeghi, In *Defects in Semiconductors ICDS-19*, ed. Gordon Davies and Maria Helena Nazare, Materials Science Forum (Trans Tech Publications, Switzerland, 1998), Vols. 258-263, p. 1229.
[93] S. Nakamura, M. Senoh, N. Iwasa and S. Nagahama, Appl. Phys. Lett. **67**, 1868 (1995).
[94] S. Nakamura, M. Senoh, N. Iwasa and S. Nagahama, Jpn. J. Appl. Phys. **34**, L797 (1995).
[95] S. Nakamura, M. Senoh, N. Iwasa, S. Nagahama, T. Yamada and T. Mukai, Jpn. J. Appl. Phys. **34**, L1332 (1995).
[96] G. Fasol, oral presentation in ATIP (Asian Technology Information Program)-seminar, Tokyo, Japan, August, 1995.
[97] Q. Guo, O. Kato and A. Yoshida, J. Appl. Phys. **73**, 7969 (1993).
[98] S. Nakamura, M. Senoh, S. Nagahama, N. Iwasa, T. Yamada, T. Matsushita, Y. Sugimoto and H. Kiyoku, Appl. Phys. Lett. **70**, 616 (1996).
[99] S. Nakamura, M. Senoh, S. Nagahama, N. Iwasa, T. Yamada, T. Matsushita, H. Kiyoku and Y. Sugimoto, Appl. Phys. Lett. **70**, 1417 (1996).
[100] S. Nakamura, M. Senoh, S. Nagahama, N. Iwasa, T. Yamada, T. Matsushita, Y. Sugimoto and H. Kiyoku, Appl. Phys. Lett. **70**, 2753 (1997).
[101] S. Chichibu, K. Wada and S. Nakamura, Appl. Phys. Lett. **71**, 2346 (1997).
[102] Y. Narukawa, Y. Kawakami, M. Funato, S. Fujita, S. Fujita and S. Nakamura, Appl. Phys. Lett. **70**, 981 (1997).
[103] Y.-K. Song, M. Kuball, A. V. Nurmikko, G. E. Bulman, K. Doverspike, S. T. Sheppard, T. W. Weeks, M. Leonard, H. S. Kong, H. Dieringer and J. Edmond, Appl. Phys. Lett. **72**, 1418 (1998).
[104] T. Deguchi, A. Shikanai, K. Torii, T. Sota, S. Chichibu and S. Nakamura, Appl. Phys. Lett. **72**, 3329 (1998).
[105] D. A. Cohen, T. Margalith, A. C. Abare, M. P. Mack, L. A. Coldren, S. P. DenBaars and D. R. Clarke, Appl. Phys. Lett. **72**, 3267 (1998).
[106] S. Nakamura, M. Senoh, S. Nagahama, N. Iwasa, T. Yamada, T. Matsushita, H. Kiyoku, Y. Sugimoto, T. Kozaki, H. Umemoto, M. Sano and K. Chocho, Appl. Phys. Lett. **72**, 2014 (1998).

Journal of the Korean Physical Society, Vol. 34, June 1999, pp. S220~S223

InGaN/GaN Quantum Well Structures Grown on Bulk GaN and Sapphire Substrates

Shiro SAKAI*

Department of Electrical and Electrionic Engineering, and the Satellite Venture Business Laboratory of the University Tokushima, Tokushima 770-8506, Japan

This paper describes properties of InGaN films grown on a dislocated GaN on sapphire and on a dislocation-free bulk GaN substrates prepared by the sublimation technique. We demonstrated that a dislocation in an InGaN worked as a non-radiative recombination center and that the dislocation made the indium composition at dislocation site higher. By the comparison of sapphire and bulk GaN as substrates, GaN bulk substrate was found to make InGaN layer much more uniform.

I. INTRODUCTION

GaN based blue-to green light emitting diodes (LEDs) with InGaN active layer have been already developed and commercialized and laser diode (LD) also has been developed. However in spite of a lot of dislocations (density of $10^8 \sim 10^{11}$ cm^{-2}) in InGaN layer produced by hetero-epitaxy with a sapphire substrate, the light emission efficiency of these devices is very high. Recently we reported that dislocations works as non-radiative recombination centers in GaN [1] and proposed the InGaN phase separation model formed by different indium incorporation rate at the dislocation site [2]. Keller *et al.* reported that the dislocations strongly influence the growth mechanism and the morphology of InGaN SQWs and bulk films [3]. More recently, we showed by spatially resolved cathodeluminescence images that dislocations work as non-radiative recombination centers in InGaN, and that the spiral growth due to mixed dislocation completely separates high- and low-indium compositional InGaN [4].

This paper reports optical and structural properties of GaN and InGaN grown on sapphire and on bulk GaN substrates by MOCVD.

II. SAMPLE PREPARATION

The InGaN/GaN MQW (multiple quantum well) and SQW (single quantum well) structures with indium content of less than 20 % were grown by horizontal atmospheric metal organic chemical vapor deposition (MOCVD) system on a (0001) sapphire substrate and on a (101_0) plane of a bulk GaNwhich was prepared by the sublimation method [5]. The dislocation density in homoepitaxial GaN and heteroepitaxial GaN on sapphire are less than 10^6 cm^{-2} and $5\times10^8\sim5\times10^9$ cm^{-2}, respectively. Flow rate of trimethylgallium (TMG), trimethylindium (TMI) and NH_3 used as source gases in InGaN growth were 44 μmol/min, 116 μmol/min, and 10 SLM, respectively. The structure of the samples prepared in this study is GaN (0.1 μm)/SQW or MQW/GaN (1.5 μm)/buffer GaN (2.5 nm)/sapphire (0001).

Two different series of samples were grown. In one series, only growth time and hence thickness of InGaN in 10 period of MQW was changes while keeping growth temperature of 715 °C and GaN barrier layer thickens of 7.5 nm. Three samples had InGaN well with thicknesses of 1.25 nm, 2.5 nm and 5 nm. The indium composition determined by x-ray diffraction satellite peaks was 0.126. In the other series of samples, only growth temperature of MQW layer was changed from 675 °C to 715 °C, and the InGaN growth time was fixed to make InGaN thickness of about 2~2.5 nm. The growth temperature of GaN layers were 1050 °C. The samples were characterized by cathode luminescence (CL) and transmission electron microscope (TEM). CL measurements were performed with an acceleration voltage of 5 kV using a JEOL 6400 scanning electron microscopy (SEM) equipped with an Oxford Instrument Mono CL2. Plan-view and cross-sectional CL images were taken using as-grown and thinned TEM sample, respectively.

III. RESULTS AND DISCUSSION

Figure 1 shows 79 K CL spectra of three 10 MQW samples with different well thicknesses. 2.5 nm sample has the strongest emission. The spectra were taken at several different points on the same wafer. The peak position and half width did not depend on the measurement point in 1.25 nm and 2.5 nm samples, but the peak po-

*E-mail: sakai@ee.tokushima-u.ac.jp,
Phone: +81-88-656-7446, Fax: +81-88-656-9060

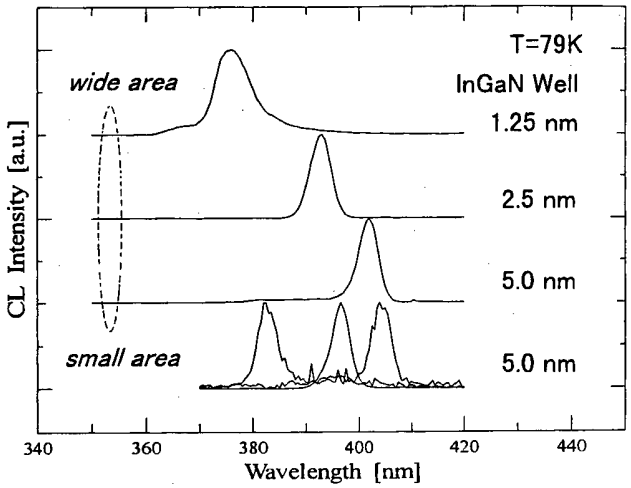

Fig. 1. 79 K CL spectra of three 10 MQW samples with different well thicknesses of 1.25 nm, 2.5 nm and 5 nm.

sition changed from position to position in 5 nm sample, as shown by the bottom spectrum of Fig. 1.

Figure 2 shows plan-view CL images taken at wavelength corresponding to the InGaN band edge at room temperature. The surfaces of all samples are smooth and featureless, but a high density of dark spots of the order of $10^8 \sim 10^9$ cm^{-2} are observed in 1.25 nm and 2.5 nm samples. Two pictures of 1.25 nm sample taken at two different wavelengths are almost identical, *i.e.* bright spots in 367 nm image is also bright in 376 nm image. These dark spots are caused by the dislocation as described later. Therefore, the indium composition is uniform without any phase separation in 1.25 nm and 2.5 nm samples. However, the situation seems very different in 5 nm sample. Three pictures taken at three different wavelength are complemental. Combining the result of Fig. 1, it can be concluded that 5 nm sample is phase separated into several regions with different indium composition.

Figure 3 is the CL spectra of 10 MQW sample grown at 675 °C. Lowering InGaN growth temperature to 675 °C increased indium composition to 0.14, although all flow rates during MOCVD growth were the same as those of the samples shown in Figs. 1 and 2. The different spectrum shape and peak position at different measurement position indicate that this sample is phase separated, in spite that InGaN is as thin as 2 nm.

Figure 4 is the CL images of SQW and 10 MQW with 2 nm (growth temperature 675 °C) and 2.5 nm (growth

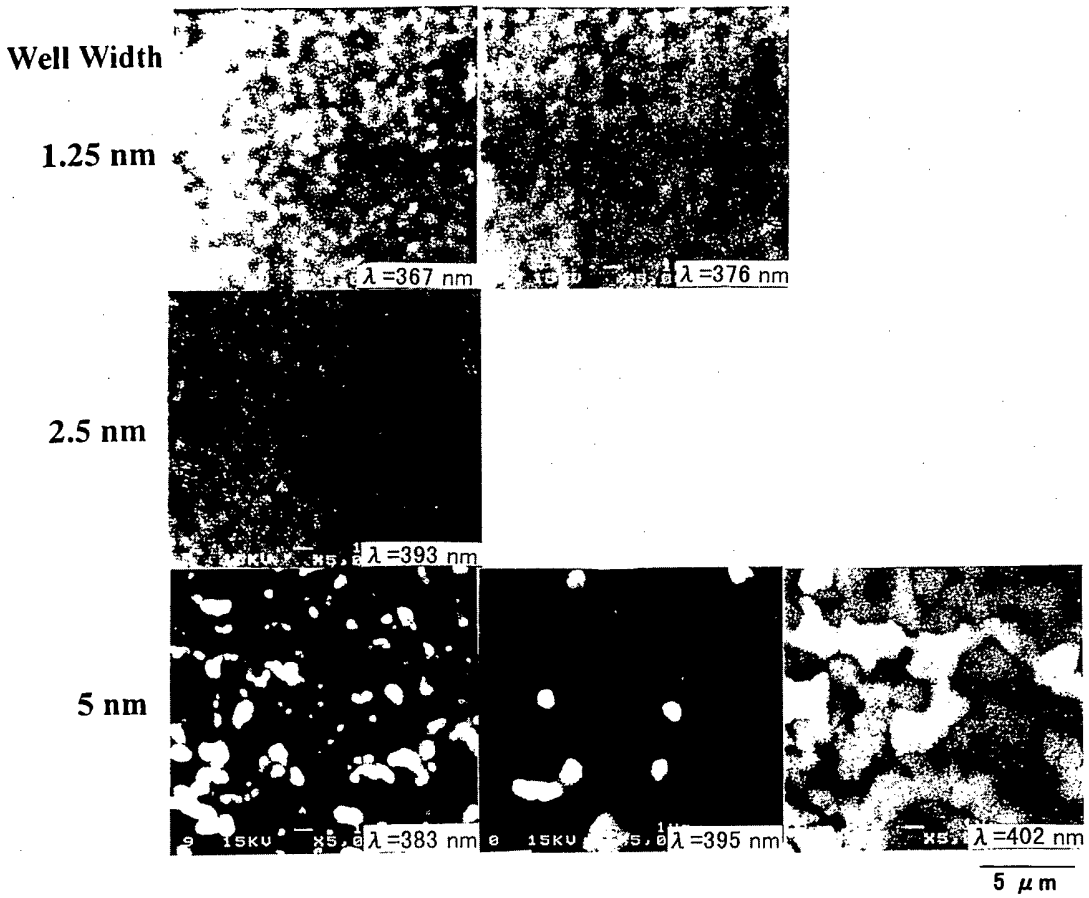

Fig. 2. Plan-view CL images taken at wavelength corresponding to the InGaN band edge at room temperature. The samples are 10 MQW grown at 715 °C on sapphire substrate.

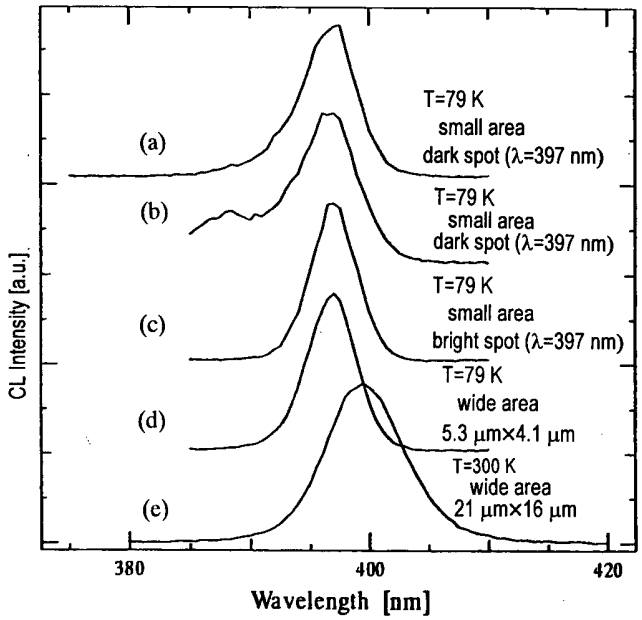

Fig. 3. CL spectra of 10 MQW sample grown at 675 °C. InGaN thickness and indium composition are 2 nm and 0.14, respectively.

temperature 715 °C) InGaN layers taken at wavelength corresponding to the band edges of GaN and InGaN. In the CL image of the SQW sample, a dark spot in CL image taken at GaN wavelength is also a dark spot in those taken at InGaN wavelength. Considering that dark spots in CL image taken at GaN wavelength correspond to dislocations, dislocation is a non-radiative recombination center also in InGaN. Comparing SQW and MQW grown at 715 °C, we found that MQW CL is just a superimpose of SQW CL. Both MQW and SQW grown at 715 °C is not phase separated. However, MQW grown at 675 °C is clearly phase separated as shown by the bottom pictures. In magnified CL image shown in Fig. 5, it is observed that a pair of dark spot exist in all of the bright area in 397 nm CL image. This paired dark spot were identified as a mixed screw and pure edge dislocation [3,4]. Therefore, the mixed dislocation is nucleating indium rich region resulting in the phase separation.

Figure 6 is the CL image of 10 MQW with 2 nm InGaN well grown at 675 °C on a GaN bulk substrate. Under these growth conditions, InGaN is phase separated, if it is grown on a sapphire, however this is not the case on bulk GaN substrate. The CL image is very uniform

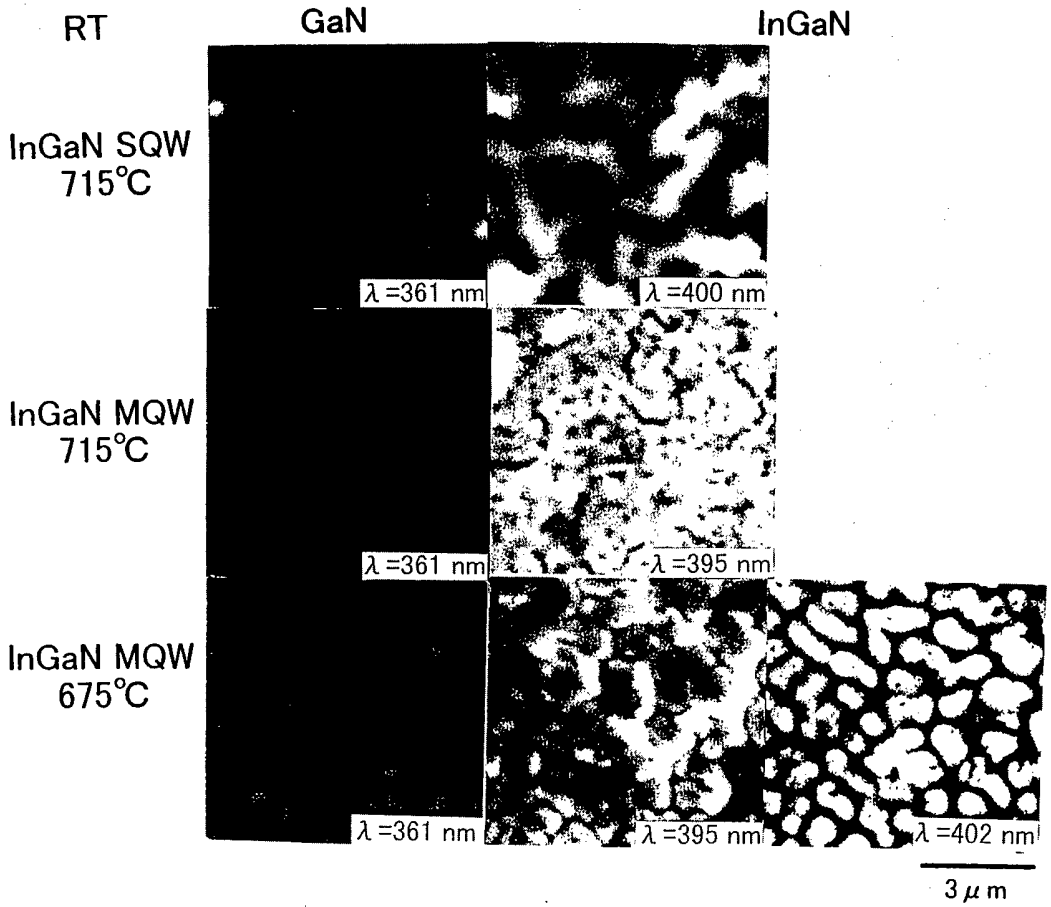

Fig. 4. CL images of SQW and 10 MQW with 2 nm (growth temperature 675 °C) and 2.5 nm (growth temperature 715 °C) InGaN layers taken at wavelength corresponding to the band edges of GaN and InGaN.

Fig. 5. Magnified CL image of 10 MQW sample grown at 675 °C with InGaN thickness of 2 nm.

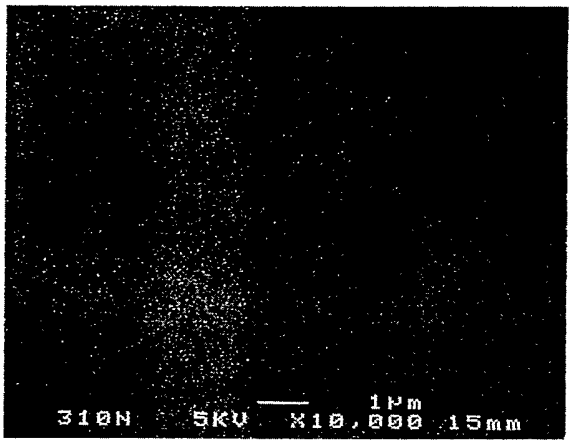

Fig. 6. Room temperature CL image of (2 nm-thick InGaN/4 nm-thick GaN) 10 MQW grown at 675 °C on a GaN bulk substrate taken at wavelength of 403 nm.

without any dark spot. This result also supports that dislocation triggers occurrence of phase separation in InGaN. The InGaN nucleates at the dislocation site, and the incorporation rate at the dislocation is faster at this site.

IV. SUMMARY AND CONCLUSION

Role of dislocation in InGaN SQW and MQW structures with different well thickness and different growth temperatures were investigated by cathodoluminescence (CL). Same emission patterned CL images of both GaN and InGaN showed that dislocations works as non-radiative recombination centers even in InGaN. The phase separation due to dislocations were not confirmed in those InGaN with thickness less than 2.5 nm if it is grown at 715 °C, but that could be clearly observed when the thick ness of InGaN grown at 715 °C is 5 nm or growth temperature is lowered to 675 °C. These results mean that the phase separation in InGaN is caused by the spiral growth due to mixed dislocation. In fact, no such phase separation was observed in homoepitaxial InGaN grown on dislocation-free bulk GaN substrate. By the comparison of sapphire and bulk GaN as substrates, bulk GaN substrate was found to make InGaN layer much more uniform. Therefore, a bulk GaN substrate gives a big advantage over sapphire when it is used as a laser substrate. Uniform indium composition provides much larger optical gain, whereas the gain at a fixed wavelength is available only in the restricted area in an inhomogeneous InGaN films.

ACKNOWLEDGMENTS

Author wishes to acknowledge fo llowing peoples for discussion. Dr. Y. Naoi, Dr. K. Nishino, Mr. S. Tottori, Mr. T. Sugahara, Dr. T. Wang, Dr. M. Hao, Dr. S. Mohanty, Dr. M. Lachab at Tokushima University, L. Romano at Xerox, and Prof. J. Orton at Nottingham University. This work was partly suppor ted by the grant-in-aid from the ministry of education, Science Sports and culture.

REFERENCES

[1] T. Sugahara, H. Sato, M. Hao, Y. Naoi, S. Kurai, S. Tottori, K. Yamashita, K. Nishino, L. T. Romano and S. Sakai, Jpn. J. Appl. Phys. **37**, L398 (1998).

[2] H. Sato, T. Sugahara, Y. Naoi and S. Sakai, Jpn. J. Appl. Phys. **37**, 2013 (1998).

[3] S. Keller, U. K. Mishra, S. P. Denbaars and W. Seifert, Jpn. J. Appl. Phys. **37**, L431 (1998).

[4] T. Sugahara, M. Hao, T. Wang, D. Nakagawa, Y. Naoi, K. Nishino and S. Sakai, Jpn. J. Appl. Phys. Part **237**, L1195 (1998).

[5] H. Sato, T. Sugahara, M. Hao, Y. Naoi, S. Kurai, K. Yamashita, K. Nishino and S. Sakai, Jpn. J. Appl. Phys. **37**, 626 (1998).

Journal of the Korean Physical Society, Vol. 34, June 1999, pp. S224~S233

Spontaneous Polarization and Piezoelectric Field in Nitride Semiconductor Heterostructures

Hadis MORKOÇ and Roberto CINGOLANI*
Virginia Commonwealth University, P.O. Box 843072 Richmond, USA 23284-3072

Walter LAMBRECHT
Case Western University, Cleveland, OH 44106, U.S.A.

Bernard GIL
Montpellier University II, 34095 Montpellier, CEDEX 5, France

D. PAVLIDIS
University of Michigan, Ann Arbor, MI 48109-2122, U.S.A.

H.-X. JIANG and J. LIN
Kansas State University, Manhattan, Kansas 66506-2601, U.S.A.

Wide bandgap nitride semiconductors have recently attracted a great level of attention owing to their direct bandgaps in the visible to ultraviolet regions of the spectrum. A number of scientific challenges remain, however, including important issues such as the determination and control of film polarity and relative extent of various polarization effects. Polarization effects arise from two sources: 1) spontaneous polarization at heterointerfaces due to the ionic wurtzite nitride bonds, and 2) strain-induced piezoelectric polarization caused by lattice misfit or thermal strain. Polarization effects can impact heterojunction structures such as MODFETs and quantum wells. In quantum wells, the fundamental electron-heavy-hole transition in GaN/AlGaN quantum wells is observed to red-shift *well below* the GaN bulk gap for well widths larger than 3 nm for the specific quantum wells investigated. Polarization effects as pertained to nitride semiconductor heterostructures and devices will be treated.

I. INTRODUCTION

Gallium nitride and its alloys with InN and AlN have recently emerged as important semiconductor materials with applications to emitters and detectors (visible to UV range) and high power/temperature electronics [1–6]. The production of nitride LEDs with acceptable longevity and brightness have already made possible full color displays, signs, and lighting. This material system is also used for semiconductor lasers in blue and UV wavelengths, which will help provide data storage capabilities well in excess of 1 Gbyte/cm^2. In addition to light emitter applications, GaN devices can be used as UV sensors in jet engines and automobiles to optimize fuel efficiency [7–9]. The large bandgap of GaN also leads to a large dielectric breakdown field and good thermal conductivity, making it desirable for high power electronic devices [10]. For example, modulation doped FETs with a record power density of 6 W/mm have been reported at frequencies up to 10 GHz [11]. Other applications include amplifiers operating at high temperature and low-cost amplifiers for space applications.

Despite the above success stories, many fundamental problems remain with nitride materials. Chief among them, are polarization effects and the control of film polarity, *i.e.* the anion and cation ordering. This polarity determines both the spontaneous polarization present at interfaces and any piezoelectric fields in strained films. These two effects can strongly impact device operation due to band offsets, carrier concentration variations, *etc.* Historically, piezoelectric effects have been studied extensively in concept and in other II-VI semiconductors. The GaN device literature, however, tends to lump all polarization effects under piezoelectric effects. Experimental investigations are made more difficult by the presence of inversion-domains which cause any piezoelectric field direction to change from one domain to the next. Re-

*Permanent address: Dept. Material Science, University of Lecce, Lecce Italy

cent evidence suggests that the spontaneous polarization actually plays a dominant role. As a result of polarization, a sizable red shift of the ground level transitions of GaN/AlGaN and InGaN/GaN [12,13] and AlGaN/GaN [14–16] quantum wells have been observed by various groups with increasing well width in the range of a few monolayers to a few tens of nm. This phenomenon is sometimes accompanied by the concomitant reduction of the oscillator strength and by the increase of the characteristic decay time of the emission due to the spatial separation of electron and hole wavefunctions. All together, these effects point towards the existence of a strong built-in electric field in the heterostructures that causes a substantial quantum confined Stark effect. The current interpretation in the literature for the observed Stark effect is that it is caused by a strain induced strong piezoelectric field [17]. Similarly, polarization effects have important ramifications in modulation doped FETs also due to the misfit and thermal strain and heterointerfaces involved. For example, field caused polarization effects can increase or decrease carrier interfacial free carrier concentrations. As in the case of quantum wells, the literature interpretation of the polarization effects have been lumped into piezoelectric effects [18,19]. In fact the exuberance has progressed so much so that terms such as piezoelectric doping have been coined.

II. POLARIZATION EFFECTS

As alluded to earlier, experimental evidence exists that supports the presence of electric field in GaN-based heterostructures. The question, which in our opinion has not yet been fully answered, is what is the origin of these fields? Basically, there are two possible origins to consider: piezoelectric effects and the difference in spontaneous polarization between AlGaN and GaN even in the absence of strain.

Spontaneous polarization is a somewhat elusive quantity that was only recently fully understood thanks to the work of King-Smith and Vanderbilt [20] and Resta [21]. Wurtzite and zincblende III-V semiconductors lack inversion symmetry and as such exhibit piezoelectric effects when strained along the (0001) and (111) directions, respectively. These effects are particularly strong in nitrides because of their large piezoelectric coefficients (almost an order of magnitude larger than in traditional III-V, see Ref. 22 and table below) and because of the high ionicity and hence less efficient screening of the resulting electric fields. In addition, wurtzite symmetry has a unique axis, thus allowing for spontaneous polarization ($\boldsymbol{P}_0$) even in the absence of strain; values of $\boldsymbol{P}_0$ are given below in table. This can manifest itself in polarization charge at hetero-interfaces. Note that for a reasonable strain of 0.1 %, spontaneous polarization, $\boldsymbol{P}_0$, effects dominate if abrupt interfaces of a well-determined

Table 1. Piezoelectric coefficients in nitrides and some other III-V.

	AlN	GaN	InN	AlAs	GaAs	InAs
e_{33} (C/m^2)	1.46	0.73	0.97	−0.01	−0.12	−0.03
e_{31} (C/m^2)	−0.60	−0.49	−0.57	0.01	0.06	0.01
P_0 (C/m^2)	−0.081	−0.029	−0.032			

Note: for Arsenides which are zincblende crystals, the values given are e_{33}=2, $e_{14}/3e_{31}$=$-e_{14}/3$ from Bernardini *et al.* Ref. 22.

polarity are assumed. The fundamental scientific question is how abrupt are real interfaces and how strong are changes in spontaneous polarization across them. Once this question is understood, the practical question becomes: how can these factors be controlled to exploit the beneficial effects of charge build-up and their associated fields on transport in FET's and related devices or avoid the detrimental effects of the fields on radiative recombination efficiency in optical devices.

Spontaneous polarization implies that a polarization vector can be present even in the absence of any external electric field. There are some problems in defining the polarization $\boldsymbol{P}_0$ uniquely directly in terms of the dipole moment of the charge distribution for an infinite bulk system. These difficulties can be overcome by instead formulating $\boldsymbol{P}$ in terms of the current operator $\boldsymbol{j}$. Techniques for calculating it in terms of a quantum mechanical Berry phase were developed by King-Smith and Vanderbilt. Nevertheless, it is generally agreed that this polarization cannot be directly observed for a given bulk material. The typical statement one would find in textbooks (if the subject matter is treated at all) is that surface charges on the sample will produce a compensating field. Only differences in spontaneous polarization *e.g.* differences induced by temperature (pyroelectric effect) or strain (piezoelectric effect) can be measured. However, one can also measure a difference in spontaneous polarization between two materials. The reason is that what one essentially measures is a $\Delta\boldsymbol{P}$ which according to Gauss's law of electrostatics corresponds to a induced polarization charge at the interface. Bernardini and Fiorentini [23] showed indeed that for an abrupt heterojunction between GaN and AlN, the field in the quantum well can be written to a very good approximation in terms of the difference in bulk spontaneous polarizations obtained from the Berry phase calculations for each bulk material [22]. In other words, the size effects of the quantum well play a minor role and the additional effect of possible transfer of charge from one interface to the other appears to be negligible. This is not obvious a prior but borne out by their calculations.

One possibility for explaining the above-mentioned effects in nitride devices is spontaneous polarization differences. In fact, the calculated values by Bernardini and Fiorentini indicate that these could be dominant

over or at least comparable to piezo-effects. The difference between AlN and GaN $\boldsymbol{P}_0$ is about 0.05 C/m^2, (about 3.3×10^{13} carriers cm^{-2}) so for $Al_{.15}Ga_{.85}N$/GaN one might expect a value of 0.0075 C/m^2 (about 5×10^{12} carriers cm^{-2}). On the other hand, for a typical strain level of 0.1 % the piezoelectrically induced polarization is only 0.0015 C/m^2 (about 1×10^{12} carriers cm^{-2}).

The alternative point of view, followed so far by most experimental groups, is *to ignore the spontaneous polarization* and to explain the fields as resulting from piezoelectric fields. The latter would in their turn result from the strain due to the lattice mismatch or from thermal expansion coefficient mismatch between the layers in a heterostructure. In fact, in most cases, the biaxial strain present in the layers, in conjunction with the elastic constants and the piezoelectric coefficient relating the induced field to stress, were shown to lead to effects of the magnitude observed. Thus, there seemed no need to invoke any spontaneous polarization effects, which to some people appear still to be somewhat exotic effects. However, one should recognize that independent measurements of the actual strain present in the film are difficult and carry a rather large uncertainty.

The observed increases in charge density at the interface indicate that the field points away from the AlGaN/GaN interface towards the free surface or the contact with the metal, the polarization pointing the opposite way. The spontaneous polarization $\boldsymbol{P}_0$ calculated by Bernardini and Fiorentini is larger in AlN than in GaN in magnitude and points from the N to the cation in the bonds oriented along the c-axis. This is consistent with the direction of the field if we assume the AlGaN layer has a polarity such that the nitrogen atoms in the N-cation bonds oriented along $\boldsymbol{c}$ are closer to the free surface. *This should be distinguished from the surface termination* which depends on whether we end the system in a surface with a single dangling bond or with three dangling bonds (if unreconstructed) and which can further be modified by additional layers of either atom on the surface depending on the surface chemical potential. If, for the moment and for simplicity, we assume the system to end in a surface exposing a single dangling bond, it means a cation face polarity is consistent with the observed direction of the fields (which indicate electron accumulation at the AlGaN/GaN) interface and with the calculated direction of $\boldsymbol{P}_0$. Experimental nitride films are typically found to have a domain structure with slight misalignments between the grains so as to relieve interface mismatch strain. If these domains would also have opposite polarity (which could for example result from inversion domain boundaries), then obviously, on average all the spontaneous polarization effect would be wiped out. That may well be the case in poor quality samples. But, even in high quality samples, one might expect there to be a certain degree of interdiffusion at the interfaces, at least at the level of one or two atomic layers. In fact, this type of interdiffusion or interface roughness is very difficult to detect even by HREM unless special techniques are used to filter out such information [24]. The presently unanswered question is how much this interdiffusion will affect the polarization difference induced polarization charge build-up at the interface. This question is the central question, which we will try to answer by first principles computational studies.

A factor, which complicates the analysis of the experimental data, is that the strength of the electric fields is also strongly influenced by the free carrier concentration present in the layers, contacts and any surface charge. Let us consider the following thought experiment. We bring the AlGaN layer in contact with the GaN layer, properly polarized but keep the charge carriers from flowing and finding their equilibrium distribution. In that case a polarization charge density would result from the difference in $\boldsymbol{P}_0$ between AlGaN and GaN. This would lead to a very strong field leading to potential differences of order 0.1 V/nm even for a 15 % AlGaN layer. Clearly, this is unsustainable and would lead to charge flow towards the interface from whatever source of free carriers is available (the metal/AlGaN contact on top, for example, or carriers resulting from doping in the AlGaN layer). This will produce a field of opposite sign until the actual net field is screened and some equilibrium is found. In other words, the actual field and the actual charge accumulating at the interface results from a complicated self-consistent screening taking place over the length scale of the device, not only the atomistic scale of the interface. This means that self-consistent device simulations of the charge distribution are required which take into account the fields resulting from the atomistic polarization difference as input but also take into account the relations imposed between charge and potential by Poisson's equation and the overall charge density resulting from solving some approximate form of the Schrodinger equation. In other words an "interface" must be developed between the macroscopic or mesoscopic level device simulations and the atomistic ab-initio theory of the polarization and interface electronic structure. So far, simulations have typically used plausible values of the field consistent with the data. Therefore it is very difficult to judge whether the original effect arises from piezoelectricity or from the spontaneous polarization, the final fields being at least an order of magnitude smaller than the original fields because of the screening by carriers. In fact, this also means that when one considers a device in operation, in which the carrier concentration varies appreciably, this will dynamically change the whole effect. Typically, for example, under laser injection conditions, one expects these effects to be totally wiped out.

III. PIEZO AND PYROELECTRIC EFFECTS

The point must be clearly made that in ideal wide-

bandgap nitride semiconductors, the free carrier concentrations are minuscule and the polarization charge is a bound charge. The polarization charge can not produce a dc current through the external circuit, only a displacement current which is an ac effect. The polarization field, however, would redistribute the free and weakly bound charge (field aided ionization) along with band discontinuities. In positive strain, tensile strain, the direction of the piezolectric polarization is from the anion, B face, to the cation, A face, sites meaning the electric field would be from the A (cation) face to the B (anion) face. As can be easily imagined, if the growing nitride contains both polarities, the direction of the polarization vector would follow suit. The polarity of the growing surface is somewhat controversial at the time of writing that is in part fueled by the lack of commercial GaN substrates. It appears that low quality films may contain both polarities. Borrowing from the II-VI widebandgap semiconductor field that the anion surface is more conducive to high quality layer growth with uniform polarity, one could predict that high quality GaN films can be grown on the N face of GaN (0001) in which case the strain polarization vector would be toward the surface under compressive strain. If the strain is tensile, then the polarization vector would be from the surface toward the substrate with piezoelectric field being towards the surface.

Anisotropy in widebandgap semiconductors is expected to cause thermal stimulus and thermal gradients. The latter is quite likely in devices where the junction temperatures are high against a relatively cool bulk. In such a case, the thermally induced electric field, pyroelectric effect, would be present with effects similar to those described above [25]. This phenomenon has not been studied in detail in nitride semiconductors. Contrary to this lack of attention, the electric field generated by thermal gradients, occurs readily in power devices, is comparable to the fields caused by applied voltages in nitride based FET like devices.

The large Stark shifts in quantum wells lead to reduced effective bandgaps. This in turn exacerbates efforts to determine the mole fraction-bandgap relationship, particularly in InGaN quantum wells. This is in part due to the fact that preparation of high quality bulk InGaN is complicated because of phase segregation and re-evaporation of In from the growing surface. Consequently, high quality films are limited to thin films straddled by low mole fraction InGaN, GaN or AlGaN. Even the bulk layers, being not completely relaxed on non-native substrates, pave the way to the piezoelectric effect. The related field, unless accounted for, causes errors in the determination of mole fractions of the barrier and well layers in quantum wells, and of band discontinuities. In fact, the field induced by the piezoelectric effect could in many cases be larger than the effect of engineered charge separation. Such may be the case in modulation doped structures where the piezoelectric polarization induced charge could be as large if not larger than those caused by the intentionally added donors. We must, however, remember that the strain-induced field by itself does not lead to free carriers unless there exist shallow impurity and defect centers, and surface charge. Unless the strain present in the films is coherent and/or the inhomogeneities can be modeled, an accurate description will not be possible.

As mentioned previously, nitride films do not necessarily grow with single polarity. In some domains the films have Ga domain, meaning the bonds in [0001] directions are Ga-N bonds and in some others they are N-Ga bonds [26,27]. In such as case, strained GaN would exhibit polarization vectors in opposing directions each time the polarity is reversed. This means that polarity of charge would also have change sign. This also means that carriers would be subjected to alternating fields as they traverse in the basal plane, the net result of which would be a reduction of carrier mobility and velocity.

While physics appears to be converging, reports on FETs appear to suggest that free carriers can be provided by polarization and that the experimental results agree with theory [28,29]. Results obtained in our laboratory, in conjunction with band discontinuities, with respect to polarization effects point to the importance of spontaneous polarization ordering of the barrier layer with respect to the smaller bandgap material, and polarization in general [30–32]. Physics indicates that the polarization charge can be due to weakly bound and free carriers present in a system. This is due to the fact that polarization can occur in perfect insulators, as well with negligible free carriers. The complicating factor is the lack of control on the polarity of the film, Ga or N polarity discussed above, and lack of uniform polarity, meaning presence of inversion domains. We have developed some means that are preliminary at this stage of producing single polarity films that need the furthered significantly [26]. In the proposed research, we aim to grow layers with known and uniform polarity with unique deposition tool at our disposal.

As a result of polarization, the static potential at the GaN/AlN interface is different from that at the AlN/GaN interface giving rise to interface charge comparable to charge densities used in devices and asymmetry in quantum wells which are compositionally square as shown in Fig. 1. Keep in mind that spontaneous polarization does not require any strain and effects the barrier discontinuity, again underscoring the need for a clear and an in-depth investigation of the problem. A substantial level of research that led to first experimental figures for band discontinuities have already been performed by our team, but the field is in desperate need of more in depth investigations in improved structures. The asymmetry in AlN/GaN and GaN/AlN interfaces caused by spontaneous polarization [2]3 was within the experimental errors of Martin *et al.* [30–32]. The errors had their genesis in measurement techniques as well as the inhomogeneities,

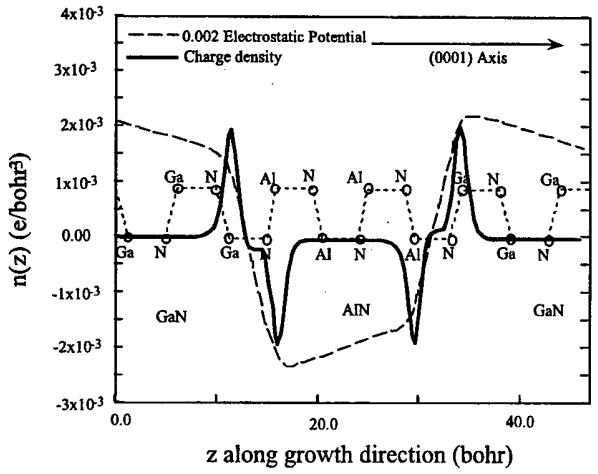

Fig. 1. Total charge density and Electrostatic Potential in a GaN/AlN SL, by Bernardini and V. Fiorentini 23.

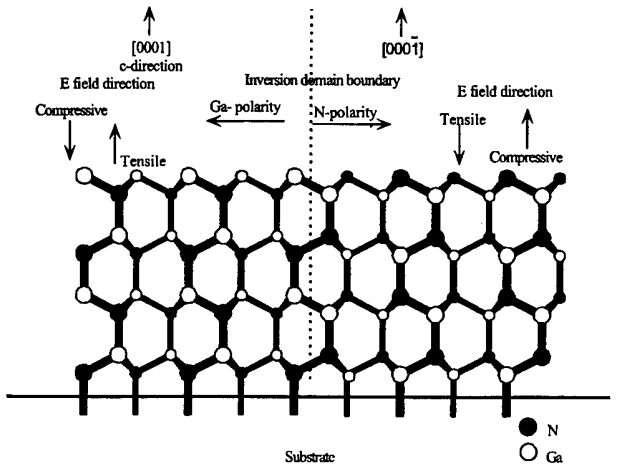

Fig. 2. Schematic representation of an inversion domain boundary formed in growth along the [0001] direction.

namely strain, in these heterostructures. However, that in AlN/InN and InN/AlN interfaces was too large to be obscured by experimental and sample related uncertainties as shown in table below.

For GaN/AlN

	GaN/AlN	AlN/GaN	Substrate
Martin *et al.* (1994)	0.8±0.3	0.8±0.3	SiC, Al_2O_3
Martin *et al.* (1996)	0.60±0.24	0.57±0.22	SiC, Al_2O_3
Bernardini and Fiorentini(1998, ref. 23):			
Relaxed/Theory	0.85	0.20	
Strained/Theory	1.0	0.29	Coherent

For GaN/InN and AlN/InN

InN/GaN = 0.93±0.25 eV	InN/AlN = 1.71±0.20 eV
GaN/InN = 0.59±0.24 eV	AlN/InN = 1.32±0.14 eV

(values in eV)

Fig. 2 shows a schematic representation of an inversion domain boundary formed in growth along the [0001] direction. On the left of the boundary, the growth initiates with N, and on the right, it begins with Ga. On the left side the nature of the bond along the [0001] direction is from Ga to N. Therefore, this polarity is called the Ga polarity. On the other hand, the [000$\bar{1}$] bond is from N to Ga that means that the polarity is N polarity. In nitrogen polarity and under tensile strain the PE field generated points away from the surface where that for the Ga polarity region points towards the surface. When the sign of the strain is changed to compressive, then the direction of the field changes also. Currently, a great deal of controversy exists to which polarity, whether cation on top or anion on top, the GaN films prefer to grow and whether this polarity is uniform across the film.

There are reports by convergent beam electron diffraction techniques [33] that indicate that some MBE grown films may be of, inversion mixed polarity domains [34] on sapphire substrates. In addition there are also reports that the MBE films grown on [0001] SiC(Si face) allows single N bonds to form at the interface with SiC that cause the polarity of the film to be of Ga [35]. If so, it is consistent with all the preferred growth polarity in many of the compound semiconductors including all the III-Vs and II-VIs. However, even on SiC and with all the precautions, the inversion domains may not be eliminated alltogether [36]. Having said so, it should be reiterated that proper cleaning of SiC to remove damage and troughs caused by polishing would go a long way to reduce the inversion domains. We should mention for comparison that good MOCVD grown films generally have the cation up (Ga polarity) configuration with some cases of mixed polarity.

Inversion domains combined with any strain in nitride based films lead to flipping PE fields with untold adverse effect our ability to characterize the films let alone using them for devices. Such flipping field would also cause much increased scattering of carrier as they traverse in the c-plane. Fig. 3(a) depicts a case of compressively strained GaN where the polarity uniformity is not maintained. Simply put, identical device structures with different polarity layers would have widely differing performance underscoring the importance that these issues will have to be investigated and reconciled.

That shown in Fig. 3(b) depicts the case where an AlGaN/GaN modulation doped structure is considered. It is assumed that the GaN layer is the buffer layer also and is completely relaxed which is not the case in experimental layers that are grown on SiC and sapphire as these substrates cause residual tensile and compressive strain, respectively. The polarity mixing from one domain to the other which are reported to about 100 Å in size causes the PE induced electric field to flip, causing a variation in the sheet carrier concentration along the channel. It is also clear that the carrier, as they traverse in the substrate plane, will be scattered along the PE field with a

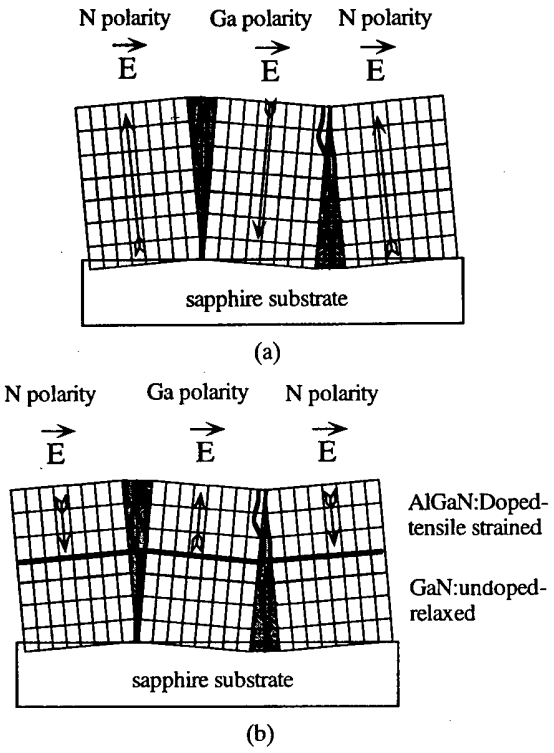

Fig. 3. (a) compressive residual strain: mixed cation/anion order; (b) AlGaN/GaN heterostructure such as that in a normal modulation doped structures. It is assumed that the GaN buffer layer is relaxed and AlGaN layer is under tensile strain. The nature of the growth is such that a mixed cation/anion order is present.

net reduction in the carrier mobility in the plane of the layer.

The defective nature of the present day GaN is such it tends to relax the entire heterostructure at the growth temperature, leaving the films under compressive strain due to thermal mismatch between sapphire and the layers. The same applies to SiC substrates with generally tensile strain resulting. The observation that the epitaxial layers show the exciton energies within a range is indicative that each film may be under different strain as determined how partially the films are relaxed at growth temperature. The Hall measurements in modulation doped structures point to a picture which is very complex and needs further investigation which will require films with uniform polarity and strain. In any case, doped modulation structures exhibited higher sheet carrier concentrations, better transconductances, and larger currents when fabricated into MODFETs than the undoped layers.

However, time resolved photoluminescence measurements performed in GaN/AlGaN MQWs [14] indicated that temporal evolution of the PL A exciton peak undergoes a red shift as the recombination depletes the excess carriers as shown in Fig. 4. The results are consistent with residual field in the GaN quantum-well which are

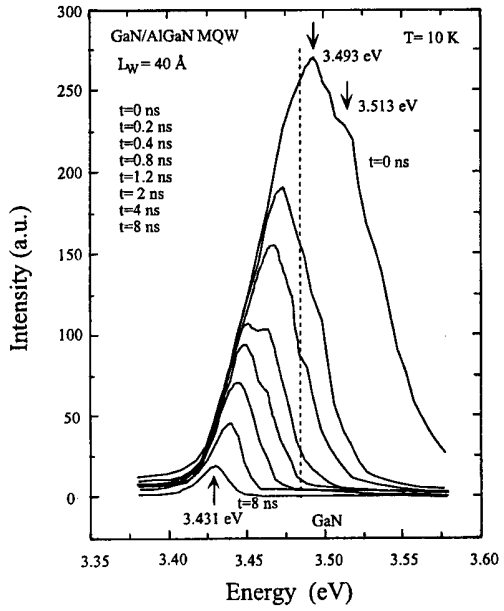

Fig. 4. Time resolved PL signal from a 40 Å well AlGaN/GaN MQW structure grown by MBE.

under compressive strain due to thermal mismatch with the substrates. While the intensity of the field can be estimated from the shift, assuming one knows the piezoelectric constant and the elastic stiffness coefficient as well as the dielectric constant of GaN, its direction can not be determined by this technique.

Fig. 5 shows the effect of the field where (a) depicts the case *e.g.* shortly after the excitation pulse with large numbers of excess carriers. The case (b) depicts the evolution of the band structure some time later as the excess carriers are allowed to recombine. The screening effect is reduced and full force of the PE field is felt leading to a temporal red shift of the A exciton energy. In addition, the spatial separation of the electron and hole wavefunctions is increased leading to a reduced recombination rate. The picture may be more complex and or suffer from variation in samples as blue shift too has been observed which may have to do with interwell excitons and oblique excitons [37]. Though controversial, in lasers the injected carrier concentrations even at transparency are comparable to polarization induced charge, 10^{13} cm^{-2}, which means the PE induced field is screened. However, the PE effect reduces the gain at lower injection levels due, among others, to reduced oscillator strength.

Using optical transitions in GaN/AlGaN, we revisited the physical origin of the built-in field and its effect on quantum wells. We believe that we can demonstrate that the built-in field originates primarily from the spontaneous polarization charge formed at the GaN/AlGaN interfaces, with a minor contribution from the piezoelectric field induced by the strain (either lattice mismatch and thermal strain). Such a built-in electric field causes: (i) a band bending and a red-shift of the gap, which

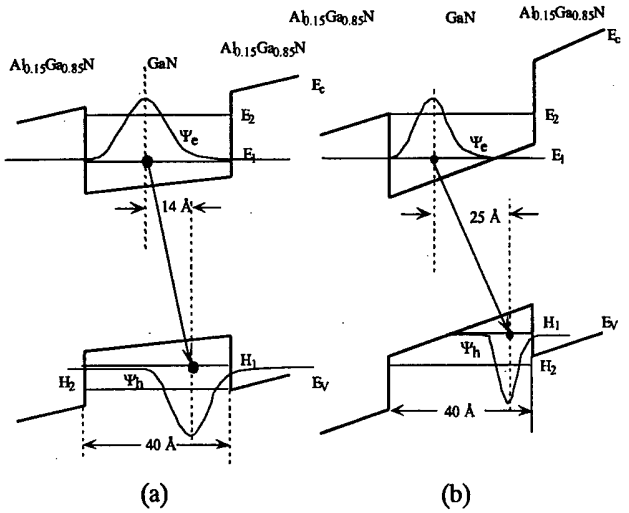

Fig. 5. The effect of the field where (a) depicts the case, *e.g.*, shortly after the excitation pulse with large numbers of excess carriers. The case (b) depicts the evolution of the band structure some time later as the excess carriers are allowed to recombine.

largely overcome the blue-shift expected from the quantum size effect, and, (ii) a progressive separation of the electron and hole wavefunctions with increasing the well width, resulting in the decrease of the emission strength and in the increase of the decay times. The experiments reveal that the fundamental transition of the quantum wells occurs at an energy well below the bulk GaN gap for well width larger than 3 nm (for the specific case of $GaN/Al_{0.15}Ga_{0.85}N$). A total built in field of the order of MV/cm is found and used to explain qualitatively the optical data. Moreover, a quantitative description of the red-shift and oscillator strength is obtained by means of a self-consistent tight-binding (TB) model which specifically accounts for the total built-in field and for the screening, either dielectric or induced by the photogenerated carriers. The impact of the built-in field on the actual electrostatic stability of the exciton quasi-particle in GaN quantum wells is also addressed at the end of the manuscript.

One and two-photon absorption photoluminescence spectroscopy methods have been applied to investigate $GaN/Al_{0.15}Ga_{0.85}N$ quantum wells of increasing thickness. The samples were grown by reactive molecular beam epitaxy on sapphire substrates. Following a chemical and *in situ* cleaning of c-plane sapphire substrates, a thin AlN buffer layer was grown at 850 °C with ammonia as the active nitrogen source. This was followed by the growth of a 1 μm thick GaN buffer layer grown at 800 °C. Finally, the quantum well region was grown. Each sample consisted of 10 GaN quantum. Five samples of well width L_w=2 nm, 3 nm, 4 nm 5 nm, 9 nm, were grown and analyzed. The barrier width and composition were kept constant in all samples ($Al_{0.15}Ga_{0.85}N$ barriers of thickness L_b=10 nm).

Linear luminescence was excited either by the 325 nm line of a cw He-Cd laser (10 mW power) or by the 337.1 nm line of a pulsed N_2 laser (300 kW peak power), in order to get rid of extrinsic emission bands and to study the density dependent screening of the built-in field generated by the photogenerated carriers. Two-photon absorption induced luminescence was also measured in order to make sure that the observed blue-shift was not due to band-filling of hot electron-hole pairs, and to avoid once again the undesired occurrence of localized-states and impurities emission in the spectra. In these experiments the half-gap excitation provided by the tunable output of a pulsed parametric oscillator, was tuned at the fundamental n=1 electron-heavy-hole resonance ($2\hbar = E_{1e1h}$) of the quantum well. Time resolved luminescence was also measured by using the third harmonic of a ps Ti:Sapphire laser and a streak-camera. All measurements were performed at 10 K.

In Fig. 6 we display a few representative PL spectra recorded at 10 K under one- and two-photon absorption excitation and for different power densities. First of all we note that the quantum well emission is dominant and no barrier luminescence or impurity related emission is observed under pulsed excitation. The emission energy decreases with increasing well width, as expected

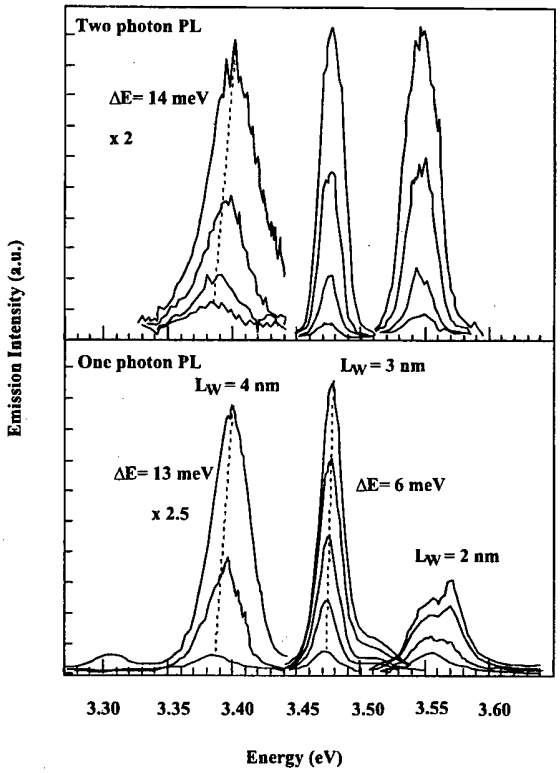

Fig. 6. One and Two-photon spectra in GaN/AlGaN multiple quantum wells and their evolution with injection intensity. Two points to be garnered. The substantial overall redshift with respect to even bulk GaN and some blue shift with injection intensity.

from the quantum size effect. However, we note that for large well widths the E_{1e1h} transition falls below the bulk GaN gap (3.51 eV @ 10 K). In order to eliminate possible extrinsic recombination processes, we have performed two-photon absorption experiments with approximately half-gap excitation ($2\hbar\omega \approx E_{1e1h}$). Both the linear and non-linear spectra exhibit the same energy positions and linewidths for the quantum well structures under investigation, indicating that carrier heating or any possible extrinsic effects do not influence the luminescence spectra of these samples. Furthermore, we note that all samples exhibit a substantial blue-shift with increasing photogeneration rate, under both one- and two-photon absorption excitation. This suggests a screening induced blue shift caused by the partial compensation of the Stark effect by the photogenerated carriers. It is important to mention that the emission spectra do not show any significant intensity dependence under low-power cw excitation, suggesting that at low photogeneration rates the screening of the built-in field is negligible and of no consequence.

In Fig. 7, we display the progressive reduction of the emission efficiency and the increase of the decay times occurring with increasing well width. In an effort to shed light on the polarization issue, the total polarization charge can be written as $P_{tot}=P_{piezo}+P_{spont}$, where P_{piezo} is the piezoelectric charge caused by the lattice mismatch (lm) strain and by the thermal strain (ts) [$P_{piezo}=P_{lm}+P_{ts}$], whereas P_{spont} represents from the spontaneous polarizability of the GaN/AlGaN interface, as clearly demonstrated by the recent works of Bernardini *et al.* [22,23]. For an alternating sequence of wells (w) and barriers (b) the total electric field in the well can be calculated as [23]

$$F_w = -4\pi L_b(P^w_{tot} - P^b_{tot})/(L_w\epsilon_b + L_b\epsilon_w) \qquad (1)$$

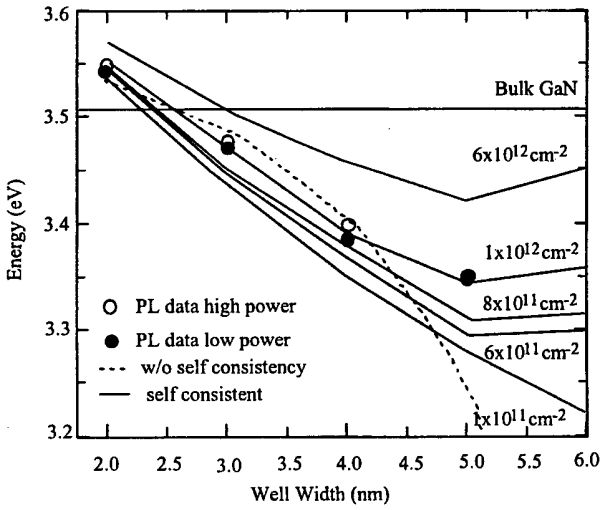

Fig. 7. Transition energies in GaN/AlGaN quantum wells vs. the well thickness indicating the substantial red shift due to polarization effects.

ϵ being the dielectric constant of the layer. The piezoelectric charge induced by the in-plane lattice mismatch ($\epsilon_{//}$) can be calculated as $P_{lm} = 2\left(e_{33}\frac{C_{11}}{C} - e_{31}\right)\epsilon_{//}$ where e_{ij} and C_{ij} are the piezoelectric tensor components and the elastic constants, respectively. Since, the layers are grown on thick GaN buffer layers, we expect that the GaN quantum well is relaxed and takes the bulk GaN lattice constant of the buffer (3.189 Å). Moreover, since the $Al_{0.15}Ga_{0.85}N$ layers are thin and grow pseudomorphically for thicknesses in the range of few nm [38]. The $Al_{0.15}Ga_{0.85}N$ barriers undergo a tensile in-plane strain $\sigma_{||}$=0.37 %. This results in a piezoelectric polarization charge P^w_{lm}=0 in the quantum well and P^b_{lm}=3.2×10^{12} cm^{-2} in the $Al_{0.15}Ga_{0.85}N$ barrier. On the other hand, the thermal strain in our experimental conditions amounts to some 0.003 %, resulting in an additional polarization charge of the order of P^w_{ts}=2×10^{11} cm^{-2}. As far as the spontaneous polarization charge is concerned, we take the recent data of Ref. 22, 23 leading to P^w_{sp}=−1.8×10^{13} cm^{-2} and P^b_{sp}=−2.3×10^{13} cm^{-2}, the latter value being obtained by linear interpolation of the GaN and AlN values (P_{sp}=−5×10^{13} cm^{-2} in AlN). By using these data and eq. (1) we can calculate the built-in field in the different samples, which turns out to vary in the range 1∼3 MV/cm depending on the actual well width.

At first order, neglecting high-field effects and corrections for self-consistency, we might expect that the built-in field causes a red-shift of the quantum well gap given by the quadratic Stark effect [39,40]

$$\Delta E = -D\frac{m^* e^2 F^2 L_w^4}{\hbar^2} \qquad (2)$$

where the constant D≈0.0022.

In Fig. 7, we compare the measured ground level transition energies with those calculated in the square well approximation with the inclusion of the Stark shift (Eq. (2)) caused by the calculated built-in field F (dotted curve). Clearly the inclusion of the spontaneous polarization in the built-in field is crucial to reproduce the overall well-width dependence of the E_{1e1h} transition and its red-shift below the bulk energy gap for well width L_w>3 nm. The agreement between theoretical and experimental data is very reasonable, especially if we take into account that the nominal growth parameters were used in the calculations, without any fitting parameter. Nonetheless, we note that the simple model potential adopted here is quantitatively not very accurate, in that (i) large deviations from the experimental trend are observed for wide wells, and (ii) it does not account for the intensity dependent blue-shift of the optical transitions.

The agreement between the calculated and measured data can in fact be substantially improved by the use of a self-consistent tight-binding (TB) model [41]. The tight-binding model is used to describe the electronic structure in the entire Brillouin zone, up to several eV above the

fundamental gap, thus overcoming the well-known limitations of the envelope function approach. For the specific case of nitrides, the parameters of our empirical TB model were determined by fitting the band-structure of Ref. 42. For the self-consistent calculations the electron and hole quasi-Fermi levels are calculated for a given photo-injected charge density. The resulting electron and hole distribution functions (n and p, respectively) are used to solve the Poisson equation

$$\frac{d}{dz}D = \frac{d}{dz}\left(-\epsilon\frac{d}{dz}V + P_{tot}\right) = e(p-n) \qquad (3)$$

where D and V are the displacement field and the potential, and P_{tot} is the total polarization charge discussed above. The Poisson equation is solved assuming zero field at the boundaries. The obtained potential is thus inserted into the TB Schroedinger equation which is solved to get the energies and wavefunctions. The new quasi-Fermi levels are thus recalculated and the procedure is iterated until self-consistency is achieved. The results of the self-consistent calculations are shown by the solid curves in Fig. 7. The agreement with the experimental data is very good both in terms of the trend and absolute values. The effect of screening is clearly observed in the progressive blue-shift of the eigenstates occurring with increasing injected carrier density. For the present experimental conditions, we expect that the photogenerated carrier density is around 1×10^{12} cm^{-2}.

IV. CONCLUSIONS

Evidence has been provided to show that polarization effects are important phenomena in wurtzite semiconductors and heterojunctions. Spontaneous polarization which is caused by ionic bonding coupled with wurtzitic symmetry occurs at heterointerface and does not require strain. Piezoelectric polarization requires strain and is important in nitride semiconductors because of large piezoelectric coefficients as compared to other semiconductors. With data from quantum wells, we have shown that the optical properties of GaN/AlGaN are strongly affected by the built-in electric field originated by the spontaneous polarization charge, and, to a much lesser extent, by strain. The well width dependence of the fundamental 1e-1h transition, and of its strength and temporal evolution are consistent with the Quantum Confined Stark Effect (QCSE) induced by the built-in field. The first quantitative analysis of these effects is provided based on a sophisticated self-consistent tight-binding model accounting for screening (either dielectric and of free-carriers) and for the spontaneous polarization charge existing at the GaN/AlGaN interfaces.

ACKNOWLEDGMENTS

One of the authors, R. C. gratefully acknowledges Virginia Commonwealth University for the hospitality. The work at Lecce is partially sponsored by INFM-Italia through Progetto Sud, and that at VCU by the Office of Naval Research and Air Force Office of Scientific Research.

REFERENCES

[1] S. T. Strite and H. Morkoç, J. Vac. Sci. and Tech. **B10**, 1237 (1992).
[2] H. Morkoç, S. Strite, G. B. Gao, M. E. Lin, B. Sverdlov and M. Burns, J. Appl. Phys. Rev. **76**, 1363 (1994).
[3] S. N. Mohammad and H. Morkoç, Progress in Quantum Electronics **20**, 361 (1996).
[4] *Group III Nitride Semiconductor Compounds*, Edited by B. Gil (Clarendon Press, Oxford, 1998), ISBN 0-19-850159-5.
[5] H. Morkoç, *Nitrides Semiconductors and Devices*, Springer, in press.
[6] S. Nakamura and G. Fosol, *The Blue Laser* (Springer Verlag, 1997).
[7] M. Razeghi and A. Rogalski, J. Appl. Phys. **79**, 7433 (1996).
[8] G. Y. Xu, A. Salvador, W. Kim, Z. Fan, C. Lu, H. Tang, H. Morkoç, G. Smith, M. Estes, B. Goldenberg, W. Yang and S. Krishnankutty, Appl. Phys. Lett. **71**, 2154 (1997).
[9] H. Morkoç, *Wurtzite GaN-Based Heterostructures by Molecular Beam Epitaxy*, IEEE J. Selected topics in Quantum Electronics (Eds. Richard Miles and I. Akasaki, 1998), Vol. 4, No. 3, p. 537.
[10] H. Morkoç, *SiC Materials and Devices*, Ed. Y. S. Park (Academic Press, 1998), Vol. 52, p. 307.
[11] S. T. Sheppard *et al.*, Presented at Device Research Conference, June 1998, Charlottesville, VA. Other GaN MODFETs references include; Y.-F. Wu, IEEE Electron Device Letters **19**, 50 (1998); A. T. Ping *et al.*, IEEE Electron Device Letters **19**, 54 (1998).
[12] T. Takeuchi, C. Wetzel, S. Yamaguchi, H. Sakai, H. Amano, I. Akasaki, Y. Kaneko, S. Nakagawa, Y. Yamaoka and N. Yamada, Appl. Phys. Lett. **73**, 1691 (1998).
[13] J. S. Im, H. Kollmer, J. Off, A. Sohmer, F. Scholz and A. Hangleiter, Phys. Rev. **B57**, R9435 (1998).
[14] H. S. Kim, J. Y. Lin, H. X. Jiang, W. W. Chow, A. E. Botchkarev and H. Morkoç, Appl. Phys. Letts.
[15] M. Leroux, N. Grandjean, J. Massies, B. Gil, P. Lefebvre and P. Bigenwald, Phys. Rev. B. (in press).
[16] Roberto Cingolani, A. Botchkarev, H. Tang, Hadis Morkoç, Giuliano Coli, Mauro Lomascolo, A. Di Carlo and P. Lugli, Appl. Phys. Letts, submitted.
[17] A. Bykhovski, B. Gelmont and M. Shur, Appl. Phys. Lett. **63**, 2243 (1993).
[18] E. T. Yu, G. J. Sullivan, P. M. Asbeck, C. D. Wang, D. Qiao and S. S.Lau, Appl. Phys. Lett. **71**, 2794 (1997).
[19] P. M. Asbeck, E. T. Yu, S. S. Lau, G. J. Sullivan, J. Van Hove and J. Redwing, Elec. Lett. **33**, 1230 (1997).
[20] R. D. King-Smith and D. Vanderbilt, Phys. Rev. **B47**, 1651 (1990).
[21] R. Resta, Rev. Mod. Phys. **66**, 899 (1994).
[22] F. Bernardini, V. Fiorentini and D. Vanderbilt, Phys.

Rev. **B56**, R10024 (1997),
[23] F. Bernardini and V. Fiorentini, Phys. Rev. **B57**, 1 (1998).
[24] A. Ourmazd, D. W. Taylor, J. Cunningham and C. W. Tu, Phys. Rev. Lett. **62**, 933 (1989).
[25] A. D. Bykhovski, V. V. Kaminski, M. S. Shur, Q. C. Chen and M. A. Khan, Appl. Phys. Lett. **69**, 3254 (1996).
[26] B. Daudin, J. L. Rouviere and M. Arley, Appl. Phys. Lett. **69**, 2480 (1996),
[27] P. Vermaut, P. Ruterana, G. Nouet, A. Salvador and H. Morkoç, Phil. Mag. 4/14/96, V. Potin, P. Ruterana, G. Nouet, A. Salvador and H. Morkoç, *Proc. of Gallium Nitride and Related Materials II Symposium*, p. 323, Edited by C. R. Abernathy, H. Amano and J. C. Zolper, Vol. 468, p. 323 (1997), Mater. Res. Soc; Pittsburgh, PA, USA, San Francisco, CA, USA; 1-4 April 1997.
[28] P. M. Asbeck, E. T. Yu, S. S. Lau, G. J. Sullivan, J. Van Hove and J. Redwing, Electronics Lett. **33**, 1230 (1997).
[29] E. T. Yu, G. J. Sullivan, P. M. Asbeck, C. D. Wang, D. Qiao and S. S. Lau, Appl. Phys. Lett. **71**, 2794 (1997).
[30] G. A. Martin, S. Strite, A. Botchkarev, A. Agarwal, A. Rockett, H. Morkoç, W. R. L. Lambrecht and B. Segall, Appl. Phys. Lett. **65**, 610 (1994).
[31] G. A. Martin, PhD. Thesis, *Semiconductor Electronic Band Alignment at Heterojunctions of Wurtzite AlN, GaN and InN*, Department of Physics, University of Illinois, 1996.
[32] G. A. Martin, A. Botchkarev, A. Agarwal, A. Rockett and H. Morkoç, Appl. Phys. Lett. **68**, 2541, (1996).
[33] P. Vermaut, P. Ruterana, G. Nouet, A. Salvador and H. Morkoç, International Conference on Microscopy of Semiconducting Materials, Oxford, 7-10 April, 1997, *Proceedings of the Royal Microscopical Society Conference*, I. O. P. Conference Series, Vol. 157, p. 183, Eds. A. G. Cullis and J. L. Hutchison, Oxford, UK; 7-10 April 1997.
[34] V. Potin, P. Ruterana, G. Nouet, A. Salvador and H. Morkoç, *Proc. of Gallium Nitride and Related Materials II Symposium*, p. 323, Edited by C. R. Abernathy, H. Amano and J. C. Zolper, Vol. 468, p. 323 (1997); Mater. Res. Soc; Pittsburgh, PA, USA., San Francisco, CA, USA; 1-4 April 1997.
[35] P. Vermaut, P. Ruterana, G. Nouet, A. Salvador and H. Morkoç, Phil. Mag. 4/14/96.
[36] B. Sverdlov, G. A. Martin, H. Morkoç and D. J. Smith, Appl. Phys. Lett. **67**, 2063 (1995).
[37] B. Gil, P. Lefebvre, J. Allegre, H. Mathieu, N. Grandjean, M. Leroux, J. Massies, P. Bigenwald and P. Christol, Phys. Rev. B., submitted.
[38] T. Takeuchi, C. Wetzel, S. Yamaguchi, H. Sakai, H. Amano, I. Akasaki, Y. Kaneko, S. Nakagawa, Y. Yamaoka and N. Yamada, Appl. Phys. Lett. **73**, 1691 (1998).
[39] G. Bastard, *Wave Mechanics Applied to Semiconductor Heterostructures* (Edition de Physique, Paris, France, 1987).
[40] J. Singh, *Semiconductor Optoelectronics* (1995).
[41] F. Della Sala, A. DiCarlo, P. Lugli, F. Bernardini, V. Fiorentini, R. Scholz and J. M. Jancu, Appl. Phys. Lett., in press (1998).
[42] J. M. Jancu, R. Scholz, F. Beltram and F. Bassani, Phys. Rev. **B57**, 6493 (1995).

Journal of the Korean Physical Society, Vol. 34, June 1999, pp. S234~S243

Development of High-performance III-Nitride-based Semiconductor Devices

M. RAZEGHI*, P. KUNG, D. WALKER, E. MONROY†,
M. HAMILTON and P. SANDVIK

Center for Quantum Devices, Department of Electrical and Computer Engineering, Northwestern University, Evanston, IL 60208, U.S.A.

In the past decade, research work in AlGaInN wide band gap semiconductors has continuously intensified, mainly because of their exceptional expected material properties which make them the ideal materials for numerous devices, including solar blind ultraviolet photodetectors. In this paper, the growth and characterization of AlGaInN thin films on sapphire and silicon substrates by metalorganic chemical vapor deposition is presented. The fabrication and testing results of GaN and $Al_xGa_{1-x}N$ based ultraviolet photodetectors are discussed, including high speed low noise GaN based Schottky metal-semiconductor-metal photodetectors with high ratio of rejection of visible light to UV light, high visible blindness GaN p-i-n photodiodes, $Al_xGa_{1-x}N$ photoconductors in the entire Al compositional range, and the first $Al_xGa_{1-x}N$ p-i-n photodiodes ($0 \leq x \leq 0.15$) ever reported. Finally, in an on-going effort to improve the quality of AlGaInN materials, the LEO growth and characterization of low defect density GaN films on both (00.1) sapphire and (111) silicon substrates is described.

I. INTRODUCTION

Gallium nitride based semiconductors have been the focus of intense interest in recent years due to advances in crystal growth technology and device fabrication procedures. Their direct, wide band gaps make them an ideal choice for use in various photodetector applications such as ultraviolet (UV) astronomy, flame detection and engine monitoring, space-to-space communications or solar UV monitoring, where it would be advantageous to exploit the natural material durability in harsh environments and the material visible-blindness [1]. The impressive development of nitride technology in these last few years has led to the fabrication of simple GaN based photodetectors [2–6]. Several types of photodetectors have been reported, including photoconductors [3,7,8], photovoltaic p-i-n photodiodes [4], GaN single Schottky barrier devices [9], and more recently, Schottky-based metal-semiconductor-metal (MSM) photodetectors which consist of two Schottky contacts on a planar surface [10].

To date, nearly all the research work on GaN semiconductor materials has been carried out using sapphire substrates because of the lack of another suitable substrate. This has resulted in materials containing an impressive number of defects, in particular threading dislocations, in spite of which high performance devices have been achieved. Lateral epitaxial overgrowth (LEO) has recently emerged as a promising growth method to achieve quasi defect free GaN-based materials on potentially any type of substrate [11]. LEO was successfully used to reduce dislocation density in GaN-based laser diodes on (00.1) Al_2O_3 and enhance their lifetime [12].

In this paper, we first briefly present the growth and characterization of AlGaInN thin films on sapphire and silicon substrates by metalorganic chemical vapor deposition (MOCVD). The fabrication and characterization of GaN and $Al_xGa_{1-x}N$ based ultraviolet (UV) photodetectors will then be discussed. These include high speed low noise GaN based Schottky metal-semiconductor-metal (MSM) photodetectors with high ratio of rejection of visible light to UV light, high visible blindness GaN p-i-n photodiodes, $Al_xGa_{1-x}N$ photoconductors in the entire Al compositional range, and the first $Al_xGa_{1-x}N$ p-i-n photodiodes ($0 \leq x \leq 0.15$) ever reported. Finally, the LEO growth of high quality GaN films on both (00.1) sapphire and (111) silicon substrates will be presented.

II. ALGAINN WIDE BANDGAP THIN FILMS AND HETEROSTRUCTURES

$Al_xGa_{1-x}N$ and $Ga_{1-x}In_xN$ thin films were grown in a horizontal low pressure metalorganic chemical vapor deposition (MOCVD) reactor. The chemical precursors included trimethyl-aluminum, trimethyl- and triethyl-gallium, trimethyl-indium and purified ammonia. Biscy-

*E-mail: razeghi@ece.nwu.edu
†Dpto. Ingeniería Electronica, Universidad Politécnica de Madrid, 28015 Madrid, Spain

clopentadienylmagnesium was used for the p-type doping source, while silane and germane were used for the n-type doping sources. Pd diffused hydrogen and purified nitrogen were used as carrier gases. The growth was performed on basal plane sapphire and (111) silicon substrates. The epilayer growth temperature was about 1000 °C [13–15].

High quality ternary $Al_xGa_{1-x}N$ alloys were achieved on sapphire substrates for the entire alloy composition range. Open detector symmetric x-ray diffraction linewidths as low as 30 arcsecs were obtained. The Al concentrations were determined by applying Vegard's law to both by x-ray diffraction and optical absorption measurements. A bowing parameter close to 0 eV was estimated. Room temperature photoluminescence linewidths narrower than 35 meV were measured for GaN. The n-type and p-type doping control of GaN was achieved for n up to 10^{20} cm^{-3} and p up to 2×10^{17} cm^{-3}. The n-type doping control of $Al_xGa_{1-x}N$ was achieved up to 60 % Al, while the p-type doping of $Al_xGa_{1-x}N$ was achieved for up to 30 % Al.

High quality $Al_xGa_{1-x}N$/GaN heterostructures were successfully achieved on sapphire substrates. Open detector x-ray diffraction of $Al_xGa_{1-x}N$/GaN superlattice structures exhibited clear satellite peaks. Two dimensional electron gas at the $Al_xGa_{1-x}N$/GaN interface exhibited mobilities as high as 1000 cm^2/Vs at 300 K and 2000 cm^2/Vs at 77 K. $Al_xGa_{1-x}N/Al_yGa_{1-y}N$ Bragg reflectors were demonstrated with a reflectivity of 60 % for unoptimized structures and peak reflectivity wavelengths ranging from 330 to 456 nm [16].

High quality ternary $Ga_{1-x}In_xN$ alloys as bulk films or quantum well were grown on sapphire substrates for x up to 30 % In. The In concentrations in the alloys were determined by x-ray diffraction. By correlating these with the photoluminescence bandedge emission energy, a bowing parameter of ~1.5 eV was estimated. High quality $Ga_{1-x}In_xN$/GaN superlattices were achieved with clear open detector x-ray diffraction satellite peaks and intense photoluminescence.

The origin of the yellow photoluminescence in GaN on sapphire substrates was investigated and attributed to Ga vacancies [18]. Trimethyl- and triethyl-gallium were compared as the chemical precursors for the growth of GaN. Although the films grown using either precursor had similar x-ray diffraction curves, those grown using the triethyl precursor had higher carrier mobilities, less yellow luminescence and a lower etch pit density in the growth conditions employed.

Capitalizing on the optimization work on sapphire substrates, the MOCVD growth of AlGaInN wide bandgap semiconductors was investigated on silicon substrates. The motivation was to take advantage of the wide availability, high quality and low cost of silicon substrates. (111) oriented silicon substrates were chosen because of the three fold in-plane symmetry. About 1.2 μm thick GaN films were grown and characterized on (111) silicon substrates. Typical x-ray diffraction and 300 K PL spectra exhibited linewidths of ~10.5 arcmins and 30 meV respectively, showing that the GaN was quasi-single crystalline and had optical quality, close to some of the early GaN epilayers on sapphire [19]. The characteristics of these GaN films depended on the quality of the substrates used. In particular, the GaN x-ray diffraction linewidths increased as the miscut of the (111) Si substrates.

III. GAN SCHOTTKY MSM AND GAN P-I-N PHOTODETECTORS

GaN Schottky MSM photodetectors were fabricated on ~1.2 μm-thick GaN and GaN:Mg films. Low resistivity p-type GaN was achieved in the Mg doped sample after exposure to rapid thermal annealing in an N_2 ambient environment. Interdigitated Pt/Au Schottky contacts were deposited by electron-beam evaporation with the geometry shown in Figure 1. The high quality of these Schottky contacts was assessed by measuring the current-voltage (I-V) characteristics between the Schottky contacts and an indium ohmic contact deposited near the edge of the wafer, as shown in the inset of Figure 2. They show an ideality factor of ~1.5 and ~4, for n.i.d. GaN and GaN:Mg respectively, with leakage resistances >10 GΩ. The dark currents are only ~2 nA at 5 V for the GaN MSM and ~12 nA at 5 V for the GaN:Mg MSM detector.

A Xe arc lamp was used as the optical source for the spectral responsivity studies and a standard synchronous detection scheme was employed to measure the front-side-illuminated detector signal. The system was calibrated with a UV-enhanced Si detector. The responsivity dependence on optical power was determined by excitation with a cw He-Cd laser (325 nm) [4]. The response time of the detectors was measured using a pulsed nitrogen laser (337 nm) as the optical source. Noise characterization was performed using a FFT spectrum analyzer with the devices connected to a current amplifier, so that the background noise power density of the system

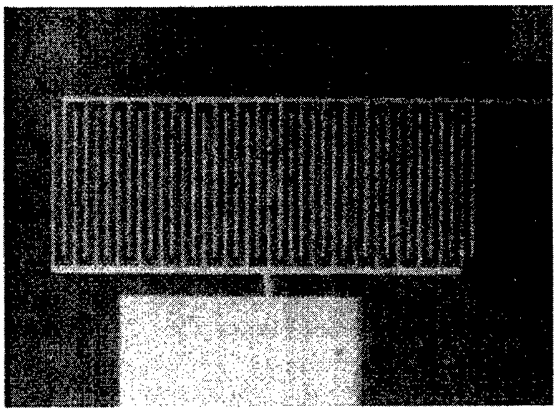

Fig. 1. MSM device with interdigitated contacts. Finger width is 2 μm, length is 150 μm, and pitch is 10 μm.

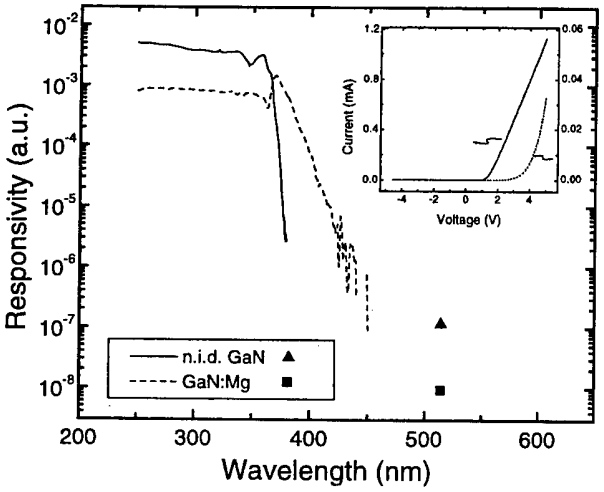

Fig. 2. Spectral response of the *n.i.d.* GaN and GaN:Mg MSM photodetectors. In the inset, the I-V characterization of the Schottky contacts.

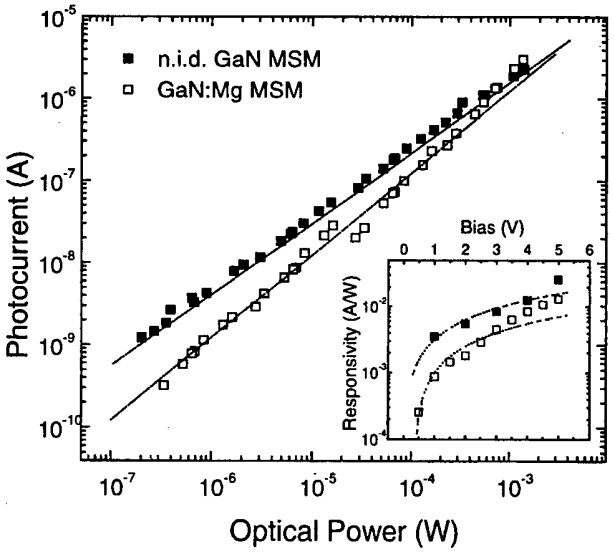

Fig. 3. Photocurrent dependence on optical power for n.i.d. GaN and GaN:Mg MSM photodetectors, measured with a He-Cd laser (325 nm). In the inset, the scaling of the responses with increasing bias voltage is shown.

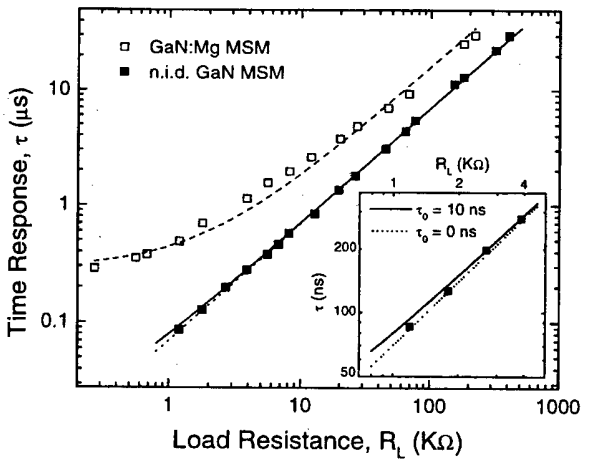

Fig. 4. Photocurrent decays measured with a pulsed nitrogen laser for different load resistances. In the inset, the magnification of low load data, showing the divergence of the 10 ns and 0 ns linear fits.

is about 10^{-24} A^2/Hz.

The spectral response for the front-side illuminated n.i.d GaN and GaN:Mg MSM detectors are shown in Figure 2. The response of the GaN MSM detector shows a very abrupt cutoff. By contrast, the GaN:Mg MSM has a more gradual decline at longer wavelengths, which is due to the presence of Mg related levels in the material. Using the measurement setup described above, it was not possible to detect any photogenerated signal for wavelengths longer than 400 nm. An Ar laser at 514 nm (green) was used to obtain a detectable photoresponse in the visible spectral region, as also shown in Figure 2. The response curves from both devices exhibit high visible rejection, with an ultraviolet/green contrast of about five orders of magnitude.

The photocurrent increases linearly with the optical power for the GaN:Mg device and shows no saturation at higher power levels over 4 decades of power, as shown in Figure 3. The n.i.d. GaN device, however, follows a P^k fit, where P is the optical power and k=0.9, which is a much better result than the k=0.1 behavior reported for n.i.d. GaN photoconductors [3]. Both MSM devices exhibited increase of responsivity with voltage bias, indicating the presence of an internal gain mechanism such as hole trapping. The shape of the spectral response was found to be independent of bias up to 5 V.

The temporal response of these devices shows no persistent photoconductivity. The photocurrent decays are measured using different load resistances. The decays are exponential for the n.i.d. GaN MSM device. By contrast, the GaN:Mg device shows exponential decays for high load resistances (>50 kΩ), but they become non-exponential for lower load resistances and tends towards a response time of 200 ns (Figure 4). In the exponential regimes the time response is limited by the RC time constant of the system. In order to estimate the minimum time response of the n.i.d. GaN MSM detector, the decay time constants are plotted as a function of the load resistance. In order to find the real speed limitation of the device, this data is fitted to linear functions with zero-load time constants of 10 ns and 0 ns (straight and dotted lines in Figure 4). From the magnified view of the low load data, shown in the insert, it is clear that this measurement provides the precision only to attest that the time response lies below 10 ns.

The noise analysis for the detectors was performed at biases up to 5 V using a SR760 FFT spectrum analyzer with the devices connected to a Keithley 428 current am-

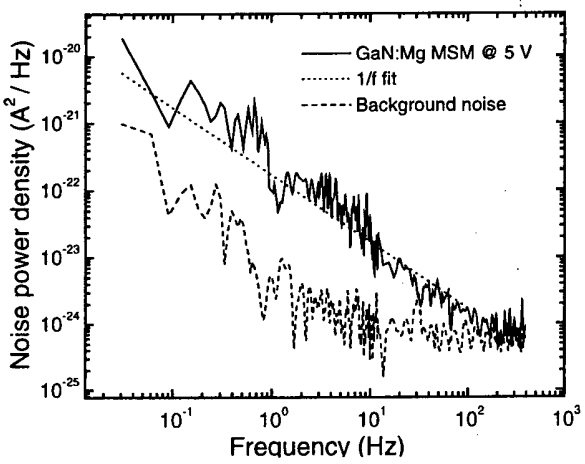

Fig. 5. Noise power density spectrum of GaN:Mg MSM photodetector and the background noise level.

plifier (the background noise power density of the system is about 10^{-24} A^2/Hz). The noise power density of the n.i.d. GaN MSM remained below the background level, even when biased at 5 V. For the GaN:Mg MSM, only at 5 V could any level be detected above the background noise of the system. In this case, the noise power density exhibited a 1/f dependence, which is expected for this wide bandgap material, as shown in Figure 5.

The GaN p-i-n photodiodes consisted of first a 1 μm n-type Si-doped GaN layer, followed by a 1000 Å undoped GaN layer, and terminated by a 2000 Å Mg-doped GaN layer, as shown in Figure 6(a). After epitaxial growth, the samples were annealed using a rapid thermal annealer (RTA) to achieve low-resistivity p-type GaN:Mg. The surface of the sample was partially removed using ECR-RF dry etching until the n-type GaN was exposed to form 400 μm×400 μm square mesa structures. Ti/Au and Ni/Au metals were evaporated onto the p-type and n-type GaN respectively, using an electron-beam evaporator. Gold wires were used to contact the mesas. The final device is shown in Figure 6(b). The measurement setup was similar to the one described above.

The absolute spectral responsivity of the GaN p-i-n photodiode without bias is plotted in Figure 7 (solid line). The responsivity was nearly constant below ~365 nm. A peak responsivity of 0.15 A/W at 363 nm was achieved, which is the best value ever reported in the literature for a GaN p-i-n device. The theoretical current responsivity for a p-i-n photodiode is given by

$$R_I(\lambda) = \frac{q\lambda}{hc}\eta$$

where λ is the photon wavelength and η is the external quantum efficiency. This external quantum efficiency includes the internal quantum efficiency and reflectivity losses. Using the value obtained for the responsivity at 363 nm, an external quantum efficiency of η~0.51 is estimated for these p-i-n photodiodes.

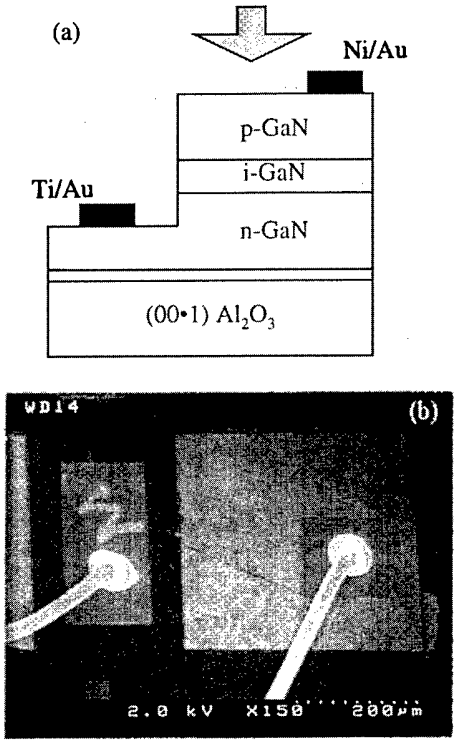

Fig. 6. (a) Schematic and (b) scanning electron micrograph of a typical photodiode mesa structure.

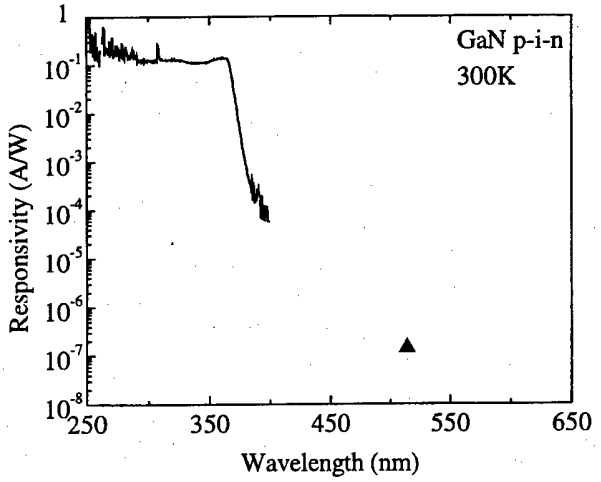

Fig. 7. Room temperature spectral response of a typical GaN p-i-n photodiode.

Using the measurement setup described above, it was not possible to detect any photogenerated signal for wavelengths longer than about 390 nm. A high power argon laser (514 nm) was then used to obtain a photoresponse in the visible spectral region and the value of the responsivity is shown in Figure 7 as a triangle. By dividing the values of the responsivity at 363 nm and at 514 nm, a value of 10^6 was obtained for the visible-to-UV rejection ratio, which is about three orders of magnitude

higher than other reports on III-Nitride based ultraviolet photodetectors. Because GaN has a wide bandgap, crystal defects or impurities in the material may easily create energy levels within the gap. These levels form recombination centers which harm the performance of UV photodetectors, in particular their solar blindness. The improvement of the solar blindness for the present GaN based UV detectors can be partly attributed to a better control of the material growth technology (reduction of impurity and defect densities).

Frequency dependent photoresponse measurements were conducted as a function of load resistance and reverse bias. The photoresponse curves were fitted to the theoretical equation for the frequency dependent responsivity. The results suggested that the speed of these GaN p-i-n photodiodes was limited by the RC time constant of the detection circuit, where R is the total resistance, including the load resistor and the internal resistance of the diode, and C is mainly the capacitance of the depletion layer in the diode [14].

IV. $AL_XGA_{1-X}N$ (0< X <1) PHOTOCONDUCTORS AND $AL_XGA_{1-X}N$ (0.05< X <0.15) P-I-N PHOTODIODES

The $Al_xGa_{1-x}N$ photoconductors consisted of two indium stripe contacts with a separation of 1 mm and a length of 4 mm on 1 μm thick $Al_xGa_{1-x}N$ films grown on (00.1) sapphire substrates in the same conditions as discussed earlier in this paper. The contacts were blocked from illumination so that the influence of any possible photoelectric effect would be minimized. The measurement setup was similar to the one discussed above.

The normalized spectral response in shown in Figure 8. A cut-off wavelength from 200 to 365 nm was achieved by controlling the $Al_xGa_{1-x}N$ alloy composition. The responsivity linearly increased with bias voltage and saturated at high voltages due to the sweep out effect [5].

The $Al_xGa_{1-x}N$ p-i-n structures consisted of first a 1.4 μm undoped GaN layer, followed by a 1 μm Si-doped $Al_xGa_{1-x}N$, a 1000 Å undoped $Al_xGa_{1-x}N$, and a 2000 Å Mg-doped $Al_xGa_{1-x}N$ layer on basal plane sapphire, as shown in Figure 9 [13,14]. Two Al concentrations were used in these experiments as determined by calibrated growth conditions: 5 % and 15 %. The processing steps included rapid thermal annealing, fabrication of 400 μm×400 μm mesas by ECR-RF dry etching, and deposition of metal contact (Ni/Au and Ti/Au). Figure 9 also shows the device current-voltage (I-V) characteristics with a series resistance of 50 Ω. The photodetector characterizations were performed using the same measurement techniques as reported earlier [4].

Figure 10 shows typical spectral response of $Al_xGa_{1-x}N$ p-i-n photodiodes with different Al contents.

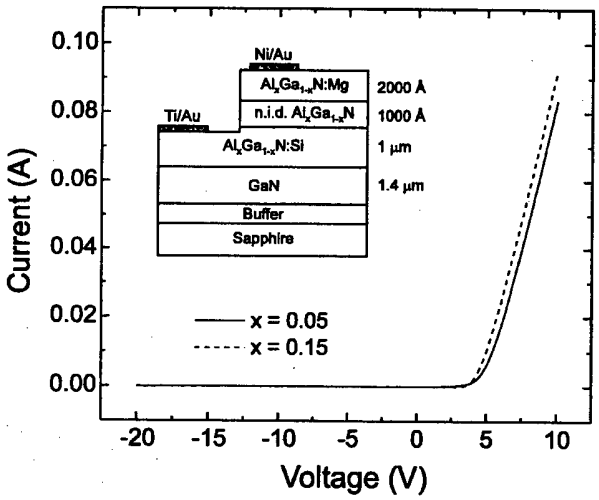

Fig. 9. Current-voltage (I-V) characteristic of $Al_xGa_{1-x}N$ p-i-n photodiodes. Schematic structure of the devices.

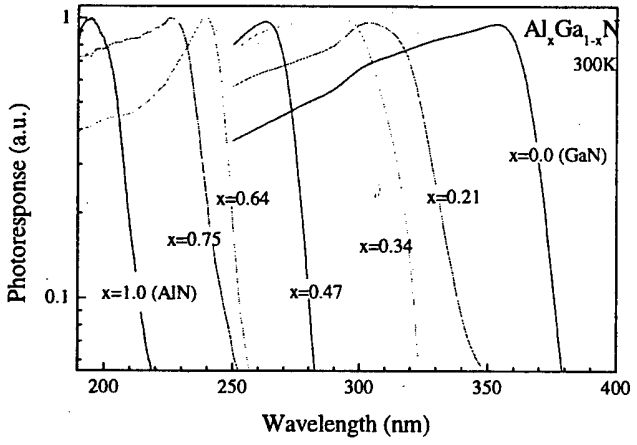

Fig. 8. Room temperature spectral response of $Al_xGa_{1-x}N$ photoconductors.

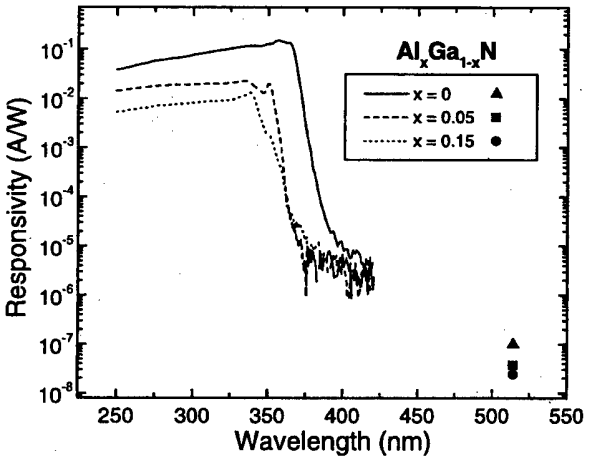

Fig. 10. Zero-bias spectral response of $Al_xGa_{1-x}N$ p-i-n photodiodes.

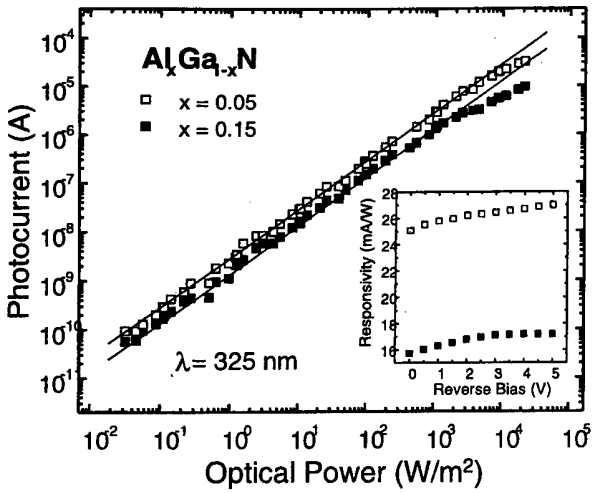

Fig. 11. Photocurrent dependence on optical power in $Al_xGa_{1-x}N$ p-i-n photodiodes, measured with a He-Cd laser. The inset shows the responsivity dependence on reverse bias.

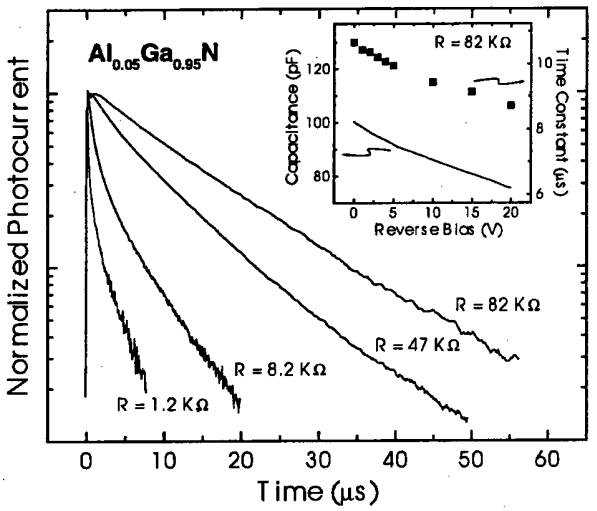

Fig. 12. hotocurrent decays measured with a pulsed nitrogen laser for different load resistances. In the inset, time constant and capacitance dependence on reverse bias.

The cutoff wavelength shifts from 365 to 338 nm with increasing Al content but the cutoff then becomes less sharp due to ternary disorder. A visible rejection of about six orders of magnitude is observed in all the samples. The photocurrent increases linearly with optical power for five decades (30 mW/m^2 up to 3 KW/m^2), as shown in Figure 11, and saturates for high power levels, likely due to the heating of the detectors. The responsivity has been observed to increase with reverse bias.

The dependence of the photocurrent decay time on the load resistance has been analyzed (Figure 12). The photocurrent decays are exponential for high load resistances (>50 kΩ). In this regime, the device time response is limited by the RC constant of the system, where R is the load resistance and C is the sum of the load capacitance

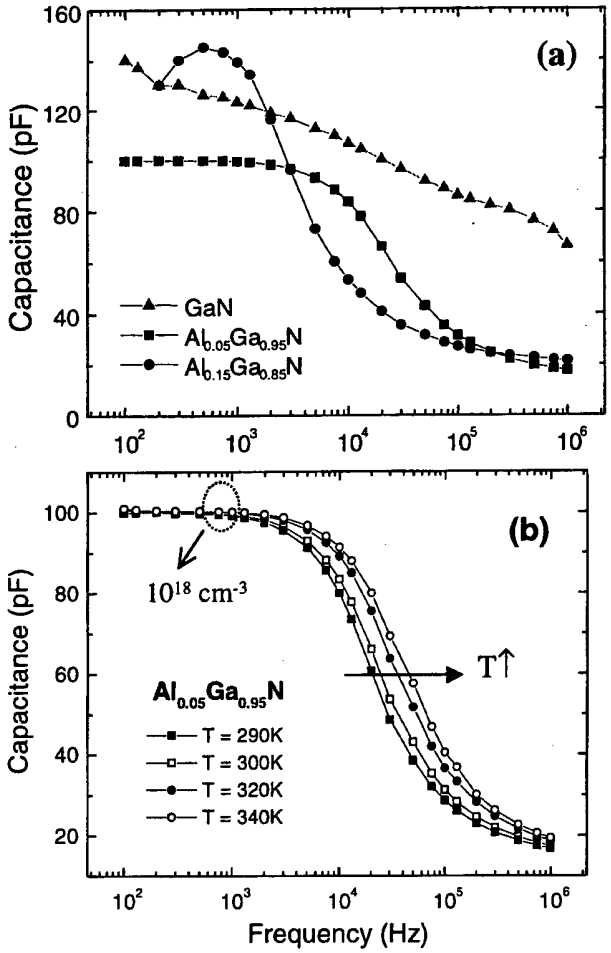

Fig. 13. (a) Capacitance-frequency (C-f) characteristics of $Al_xGa_{1-x}N$ photodiodes with different Al concentrations. (b) Evolution of the C-f curve with temperature.

(approximately 30 pF in our measurement system) and the internal capacitance of the device at low frequencies (100 pF). The time constant decreases with reverse bias as shown in the inset of Figure 12, due to the decrease of the device capacitance. For lower load, the photocurrent decays become non-exponential. The decay time is longer than the RC constant, and tends to about 500 ns for very low load resistances (~50 Ω).

The temporal behavior of the photodiodes can be explained by the dependence of their capacitance on frequency, C-f curve in Figure 13(a), measured using an impedance analyzer. A difference between the capacitance at low and high frequencies was observed and indicated the presence of an impurity in the semiconductor which responds up to higher frequencies for increasing temperature, as expected (Figure 13(b)). No bias dependence has been detected in the shape of this curve. Capacitance vs. voltage (C-V) measurements were performed both at low and high frequencies, to estimate the content of the defect. From the plots of $1/C^2$ vs. bias, concentrations of 1.5×10^{18} cm^{-3} and 8.1×10^{16} cm^{-3} are

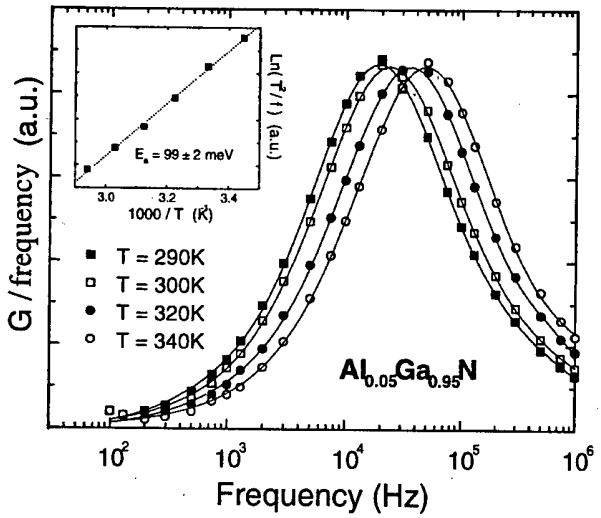

Fig. 14. Conductance divided by frequency vs. frequency measured at different temperatures. In the inset, Arrhenius plot obtained from the evolution of the peaks with temperature.

obtained at 1 kHz and 1 MHz respectively. In order to estimate the activation energy of the impurity, admittance spectroscopy measurements have been performed [20]. From the Arrhenius plot obtained from the variation of the conductance divided by frequency vs. frequency with temperature (Figure 14) an activation energy of 99 ± 2 meV was calculated.

Taking into account the capacitance of the device and the dielectric constant of GaN, the intrinsic region is completely depleted of carriers, and the value obtained from the C-V curve should correspond to the acceptor concentration in the p-type region (the n-type region is more heavily doped). The large difference in the C-V measurement at high and low frequencies imply that the impurity concentration is about 10^{18} cm^{-3}. Due to this high value and its low activation energy, we conclude that this impurity is not related to deep levels, but most probably substitutional Mg, which is not completely activated at room temperature. However, the value of 99 meV is low in comparison with the 150 meV thermal activation energy of Mg found by Hall measurements [21]. For high frequencies, when Mg cannot react, the residual capacitance should be due to the intrinsic donor, which appears in our non-intentionally-doped layers in concentrations similar to the values measured by C-V at 1 MHz.

V. LATERAL EPITAXIAL OVERGROWTH OF GAN ON SAPPHIRE AND SILICON SUBSTRATES

Lateral epitaxial overgrowth (LEO) is a promising growth method to achieve quasi defect free GaN-based materials, a goal which has thus far eluded the research community, on potentially any type of substrate [22]. Achieving quasi defect free GaN materials would lead to an immense step forward in GaN-based device performances. The two most important substrates to be investigated are (00.1) sapphire and (111) silicon substrates for obvious reasons.

Prior to conducting LEO growth, it is necessary to achieve a high quality "*template*" film, which is generally of the same nature as the LEO material, *e.g.* GaN. The GaN *template* layers on sapphire were 1~2 μm thick, whereas those on silicon were only 0.2 μm thick. The growth conditions and properties of these template films have been discussed earlier in this paper. Next, a 2000 Å thick SiO_2 film was deposited by electron beam evaporation. Standard photolithography and etching were used to define a 15 μm period pattern consisting of 3~4 μm-wide stripe openings. The samples were then loaded back into the reactor for regrowth of GaN. The films were characterized through x-ray diffraction, photoluminescence, scanning electron microscopy (SEM) and atomic force microscopy (AFM).

Several parameters need to be optimized in order to achieve high quality LEO GaN. First is the orientation of the stripes with respect to the crystallographic directions of the underlying GaN *template.* In our earlier work on the LEO of GaN, we showed that for stripes parallel to <10.0> of GaN a rectangular cross section is obtained, whereas for stripes parallel to <11.0> of GaN a truncated- or complete pyramidal shape is obtained [23]. In the former case, a higher lateral-to-vertical (L/V) growth rate ratio than in the later case is observed. The origin of this behavior is attributed to the slow growth rate of the $\{1\bar{1}1\}$ planes of GaN [24]. It is generally desired to achieve as high a L/V growth rate as possible to minimize the amount of time needed to cover the entire wafer surface. In our experiments here, the stripes were then oriented parallel to the <10.0> direction of GaN. In the literature, there has been some confusion on the labeling of crystallographic directions for hexagonal symmetry crystals such as GaN and Al_2O_3 [24,11]. In the text of the present paper, we chose to use a four digit notation for crystallographic directions. The conversion between a three digit and a four digit notation was given earlier [25]. In the early stages of GaN regrowth, it is necessary to avoid nucleation on the masked areas in order to confine the growth in the open windows. For this reason and to achieve a high L/V growth rate, one needs to enhance the surface diffusion of adatoms. One method to do so is by decreasing the growth rate, however it must not be so low that growth durations become impractical. Another method is to increase the growth temperature.

Under optimized growth conditions for our experiments, an SEM micrograph of the LEO grown GaN as shown in Figure 15 is obtained, which exhibited a rectangular cross section. The duration of the growth was only 10 minutes. The GaN grew ~2600 nm laterally and ~475 nm vertically above the SiO_2 mask, which corre-

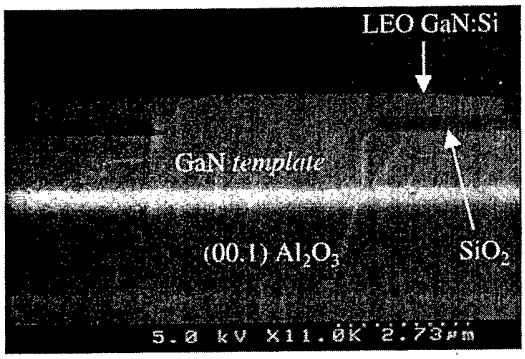

Fig. 15. Cross section SEM micrograph of an uncoalesced LEO grown GaN on (00.1) sapphire.

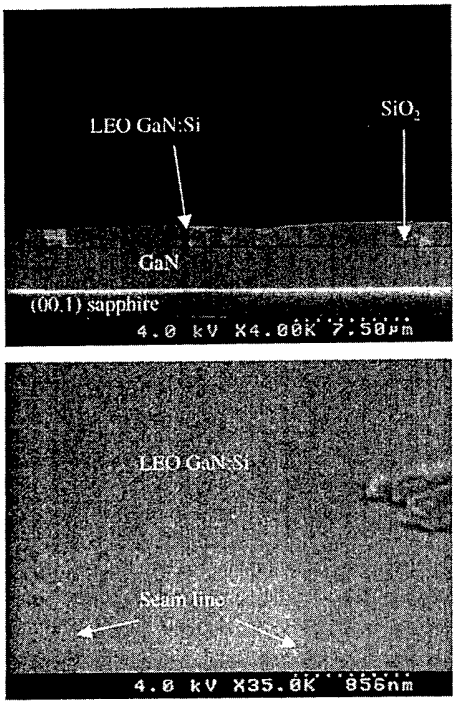

Fig. 16. SEM micrographs of coalesced LEO grown GaN on (00.1) sapphire substrate.

sponds to a L/V growth rate ratio close to 5.5, which is the highest value reported to date. The surface of the overgrown GaN is not perfectly flat and is slightly curved. The origin of this curvature is under investigation.

By further conducting the growth, the LEO film coalesced as show in the SEM cross section and surface micrographs in Figure 16. Small void areas can be observed in the cross section at the junction between two lateral growth fronts, and seamlines can be seen on the surface at that location. The x-ray diffraction and 300 K photoluminescence (PL) spectra from these coalesced films exhibited linewidths of 7 arcmins and ~95 meV, respectively. The x-ray linewidth is on the same order as the *template* layer used in these present experiments. The PL peak is broader than for a same thickness GaN grown under similar conditions on plain sapphire and doped with the same amount of Si. This suggests that there are additional impurities incorporated during LEO growth which enhance and broaden the PL, which most probably originated from the SiO_2 mask slightly decomposing during growth at such high temperatures.

These results were then applied to the LEO of GaN on silicon substrates. This was made possible after achieving high crystalline quality GaN template films on silicon substrates, as discussed earlier in this paper. Under optimized growth conditions for our experiments, a quasi rectangular cross section is obtained for LEO grown GaN on (111) Si, as shown in Figure 17. The duration of the growth was 25 minutes. The GaN grew ~4900 nm laterally and ~950 nm vertically above the SiO_2 mask, which corresponds to a L/V growth rate ratio close to 5.2, which is as high as for the LEO on Al_2O_3 substrates. The surface of the overgrown GaN is also not perfectly flat and is slightly curved, as for the LEO on Al_2O_3.

Figure 17 also shows an AFM image of the surface of the regrown GaN on Si substrates in relation with the SEM cross section. The side of the AFM image corresponds to 10 μm and the vertical scale is 74.4 nm. It can be clearly seen that the GaN grown in the open window has a significant number of pinholes and dislocation terminations. However none of these are seen in the LEO grown regions above the SiO_2 mask, which suggests that

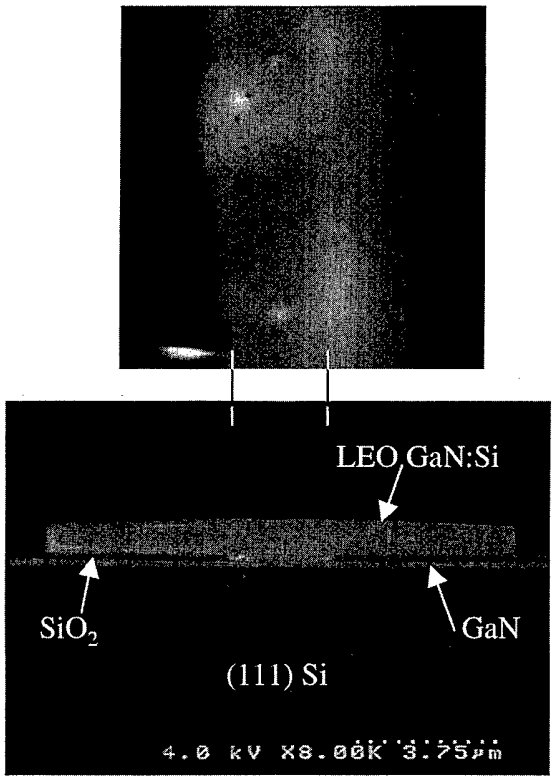

Fig. 17. FM image of the surface (top) and corresponding cross section SEM micrograph (bottom) of an uncoalesced LEO GaN grown on (111) silicon substrate.

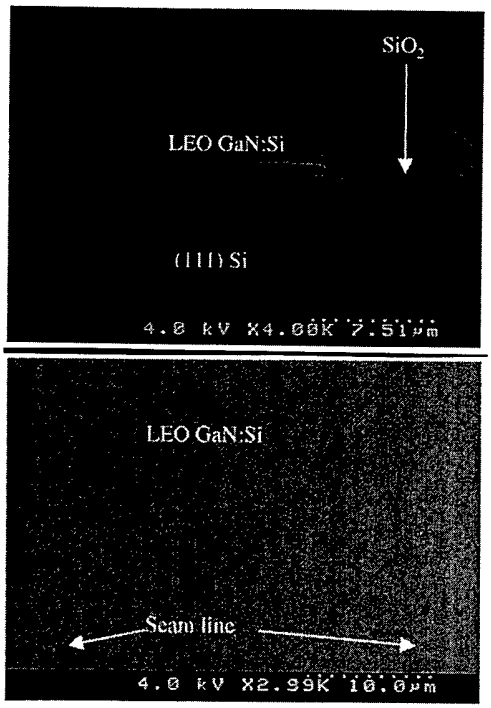

Fig. 18. SEM micrographs of coalesced LEO grown GaN on (111) silicon substrate.

these regions are less defective, confirming that LEO can be successfully used to reduce defects in GaN on silicon substrates.

By further conducting the growth, the LEO film coalesced as show in the SEM cross section and surface micrographs in Figure 18. Inverted "V" shaped voids can be observed in the cross section at the junction between two adjacent lateral growth fronts and seamlines can be seen on the surface at that location. Figure 19(a) and (b) show the x-ray diffraction from these coalesced films measured with the x-ray beam perpendicular and parallel to the stripes, respectively. In the "perpendicular beam" or (a) case, two distinct peaks for the GaN are observed. The linewidths of these peaks were on the order of 14 arcmins. By contrast, in the "parallel beam" or (b) case, there is only one peak for GaN but both this peak and the Si substrate peak are significantly broader, which is likely due to residual strain in the epilayer/substrate system in the direction parallel to the stripes. The presence of two distinct GaN peaks in the (a) case was due to a misalignment in the (00.1) GaN planes between the LEO crystals grown above the left and the right sides of the mask opening. The 300 K photoluminescence spectrum from these films exhibited a linewidth of 90 meV.

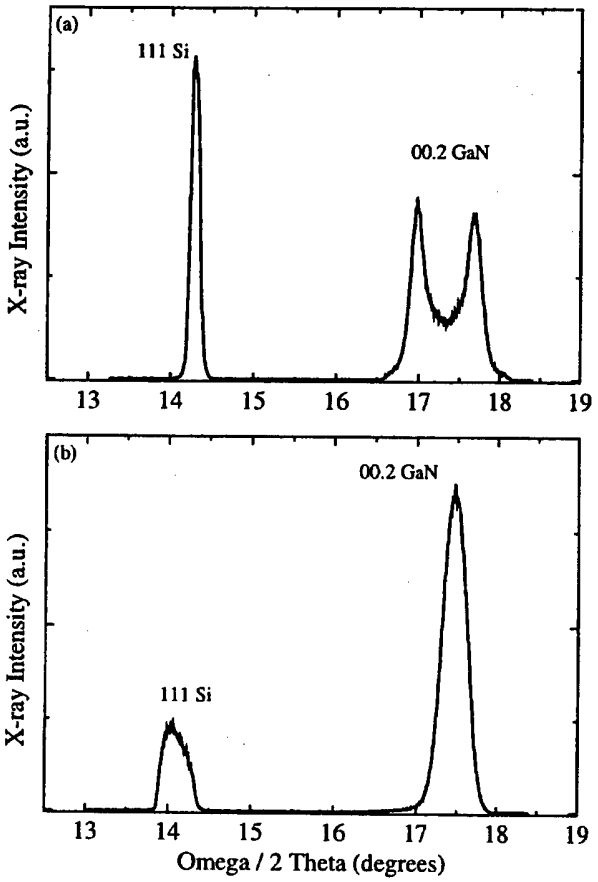

Fig. 19. X-ray diffraction spectra from a coalesced LEO grown GaN film on (111) Si substrate measured with an incident x-ray beam (a) perpendicular to the stripes, (b) parallel to the stripes.

VI. CONCLUSIONS

The growth and characterization results of AlGaInN thin films on sapphire and silicon substrates have been presented. Using high quality AlGaInN materials, high performance devices were fabricated and characterized. High speed low noise GaN based Schottky MSM photodetectors with a visible light to UV light rejection ratio higher than 105 and a response time shorter than 10 ns have been achieved. GaN p-i-n photodiodes with a visible to UV light rejection ratio higher than 10^6 have been demonstrated. $Al_xGa_{1-x}N$ photoconductors in the entire Al compositional range exhibited a cut-off wavelength continuously tunable from 200 to 365 nm. The first $Al_xGa_{1-x}N$ p-i-n photodiodes ($0 \leq x \leq 0.15$) ever reported yielded a 6 orders of magnitude visible to UV light rejection. Finally, the LEO growth and characterization of high quality GaN films on both (00.1) sapphire and (111) silicon substrates showed lateral growth rates more than 5 times as high as vertical growth rates and resulted in lower defect density GaN materials.

ACKNOWLEDGMENTS

The authors would like to acknowledge the permanent support and encouragement of M. Yoder, Y. S. Park, and C. Wood from the Office of Naval Research. This work

was supported by BMDO under ONR grant No. N00014-93-1-0235 and by ONR under grant No. N00014-98-1-0403.

REFERENCES

[1] M. Razeghi and A. Rogalski, J. Appl. Phys. **79**, 7433 (1996).

[2] D. Walker, X. Zhang, A. Saxler, P. Kung, J. Xu and M. Razeghi, Appl. Phys. Lett. **70**, 949 (1997).

[3] E. Munoz, E. Monroy, J. A. Garrido, I. Izpura, F. J. Sanchez, M. A. Sanchez-Garcia and E. Calleja, Appl. Phys. Lett. **71**, 870 (1997).

[4] D. Walker, A. Saxler, P. Kung, X. Zhang, M. Hamilton, J. Diaz and M. Razeghi, Appl. Phys. Lett. **72**, 3303 (1998).

[5] M. Razeghi and A. Rogalski, J. Appl. Phys. **79**, 7433 (1996).

[6] E. Monroy, E. Munoz, F. J. Sanchez, F. Calle, E. Calleja, B. Beaumont, P. Gibart, J. A. Munoz, F. Cusso, Semicond. Sci. Technol. **13**, 1042 (1998).

[7] P. Kung, X. Zhang, D. Walker, A. Saxler, J. Piotrowski, A. Rogalski and M. Razeghi, Appl. Phys. Lett. **67**, 3792 (1995).

[8] X. Huang, D. Mott, P. Shu, J. Chen and D. Wickenden, J. Elec. Mat. **26**, 330 (1997).

[9] Q. Chen, J. W. Yang, A. Osinsky, S. Gangopadhyay, B. Lim, M. Z. Anwar, M. A. Khan, D. Kuksenkov and H. Temkin, Appl. Phys. Lett. **70**, 2277 (1997).

[10] J. C. Carrano, T. Li, P. A. Grudowski, C. J. Eiting, R. D. Dup uis and J. C. Campbell, J. Appl. Phys. **83**, 6148 (1998).

[11] O. H. Nam, M. D. Bremser, T. S. Zheleva and R. F. Davis, Appl. Phys. Lett. **71**, 2638 (1997).

[12] S. Nakamura, M. Senoh, S. Nagahama, N. Iwasa, T. Yamada, T. Matsushita, H. Kiyoku, Y. Sugimoto, T. Kozaki, H. Umemoto, M. Sano and K. Chocho, Appl. Phys. Lett. **72**, 211 (1998).

[13] X. Zhang, P. Kung, A. Saxler, D. Walker, T. C. Wang and M. Razeghi, Appl. Phys. Lett. **67**, 1745 (1995).

[14] P. Kung, X. Zhang, D. Walker, A. Saxler and M. Razeghi, *Photodetectors: Materials and Devices III*, edited by G. J. Brown and M. Razeghi (SPIE Optical Engineering, Bellingham, 1998), SPIE Proc. Vol. 3287.

[15] P. Kung, A. Saxler, X. Zhang, D. Walker, T. C. Wang, I. Ferguson and M. Razeghi, Appl. Phys. Lett. **66**, 2958 (1995).

[16] P. Kung, A. Saxler, D. Walker, X. Zhang, R. Lavado, K. S. Kim and M. Razeghi, *III-V Nitrides*, ed. by F.A. Ponce, T.D. Moustakas, I. Akasaki and B. A. Monemar, *Materials Research Society Symposium Proceedings* (Materials Research Society, Pittsburgh, 1997), Vol. 449, p. 79.

[17] P. Kung, A. Saxler, D. Walker, A. Rybaltowski, X. Zhang, J. Diaz and M. Razeghi, MRS Internet Journal Nitride Semiconductor Research **3**, 1 (1998).

[18] X. Zhang, P. Kung, A. Saxler, D. Walker, T. Wang and M. Razeghi, Acta Physica Polanica **A88**, 601 (1995).

[19] M. E. Lin, B. Sverdlov, G. L. Zhou and H. Morko, Appl. Phys. Lett. **62**, 3879 (1993).

[20] P. Blood and J. W. Orton, *The Electrical Characterization of Semiconductors: Majority Carriers and Electron States* (Academic Press, London, 1992).

[21] I. Akasaki, H. Amano, M. Mito and K. Hiramatsu, J. Lumin. **48/49**, 666 (1991).

[22] O. H. Nam, M. D. Bremser, T. S. Zheleva and R. F. Davis, Appl. Phys. Lett. **71**, 2638 (1997).

[23] A. Saxler, Ph. D. dissertation, Northwestern University, 1998.

[24] D. Kapolnek, S. Keller, R. Vetury, R. D. Underwood, P. Kozodoy, S. P. DenBaars and U. K. Mishra, Appl. Phys. Lett. **71**, 1204 (1997).

[25] P. Kung, C. J. Sun, A. Saxler, H. Ohsato and M. Razeghi, J. Appl. Phys. **75**, 4515 (1994).

Journal of the Korean Physical Society, Vol. 34, June 1999, pp. S244~S252

Electron Transport Properties of GaN Epilayers Grown by Metal-Organic Chemical Vapor Deposition

M. G. CHEONG, K. S. KIM, K. J. LEE, G. M. YANG, K. Y. LIM, C.-H. HONG, E.-K. SUH and H. J. LEE*

Department of Semiconductor Science and Technology (Graduate School) and Semiconductor Physics Research Center, Chonbuk National University, Chonju 561-756

A. YOSHIKAWA

Department of Electronics and Mechanical Engineering, Chiba University, Chiba 263-8522, Japan

N-type GaN epilayers were grown on sapphire using the metalorganic chemical vapor deposition (MOCVD). Unintentionally doped GaN epilayers were grown as a functions of GaN buffer layer growth rate. The growth rate was found to be crucially related with the edge-type threading dislocations, and the dislocation density of $\sim 2\times10^8$ cm^{-2} was obtained at the optimum condition. The thin epilayers with higher dislocation density require a two-band model including the Γ and the impurity bands in analysing the temperature-dependent Hall effects measured in a wide range 20~800 K. But the two-band model was necessary only for temperatures lower than 300 K for doped epilayers. The thickness-dependent characteristics indicates that the impurity-band effects are ascribed to the near-interface region in unintentionally doped GaN layers.

I. INTRODUCTION

Due to the lattice and thermal mismatches, the GaN epilayers grown on sapphire substrate are known to contain high density of defects and residual levels in the band gap. In addition, the depth inhomogeneity [1], the impurity-band conduction [2] and GaN/sapphire interface [3] make it difficult to analyze the Hall effect measurements. The Hall effects have been routinely measured to evaluate the GaN epilayer quality in terms of the mobility and electron density [4–7] as in the conventional semiconductors. When the impurity-band (and/or GaN/sapphire interface) conduction and inhomogeneities of characteristics are existed in the sample, however, the as-measured data may be misleading in the epilayer evaluation.

The GaN epilayers grown on sapphire are characterized by high density edge-type threading dislocations (ETD) [8], and the low mobility of undoped layers as well as the temperature-dependency of the Hall mobility at low temperature range have been ascribed to the scattering due to the ETD [5,7]. Meanwhile, the impurity-band conduction has been also adopted to explain the low temperature electrical properties [2,10,11].

In this work, the GaN epilayers were grown on sapphire substrates as a function of GaN buffer layer growth rate using the metal-organic chemical vapor deposition (MOCVD). Samples were investigated by high resolution x-ray duffraction (HRXRD), atomic force microscopy (AFM), photoluminescence (PL), and temperature dependent Hall-effect (TDHE) measurements. The electron transport parameters in the Γ band were calculated by solving the Boltzmann transport equation (BTE) with various scattering mechanism. The iteration technique [12] was used to solve the BTE, not relying on the relaxation time approximation. To fit the experimental data, a two-band model including the Γ band and an impurity band had to be adopted. The temperature range for the two-band model depends upon the sample.

II. EXPERIMENTAL

The samples were grown on basal plane sapphire substrates by the horizontal MOCVD operating at low pressure. The substrates were cleaned in organic solvents and then etched in hot solution of $3H_2SO_4$:$1H_3PO_4$. In the reactor, the substrates were heated for 10 minutes under H_2 flowing at 1100 °C. The temperature was then reduced to 560 °C for the growth of GaN buffer layer with nominal thickness of 250 Å.

The flow rate of trimethylgallium (TMGa), f_{TMG}, was varied from 20 μmol to 90 μmol per minute in an effort to see how the buffer layer growth rate affects the epilayer property. After the buffer layer growth, the temperature

*E-mail: leehj@phy0.chonbuk.ac.kr, Fax: +82-652-270-3585
To whom correspondence should be addressed.

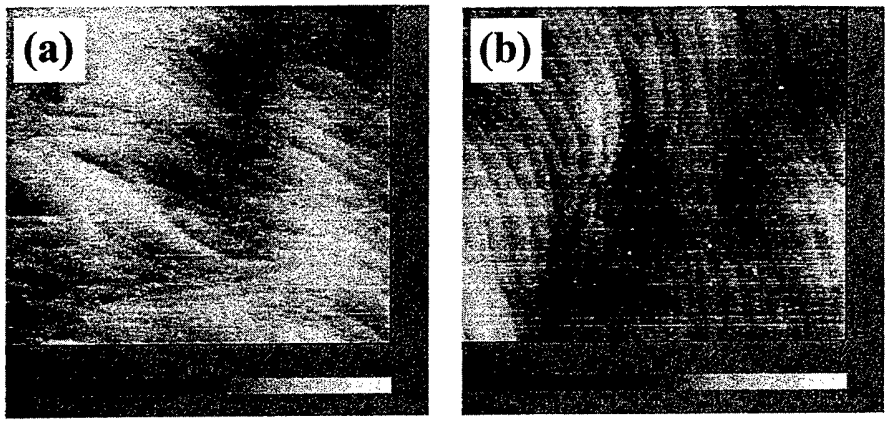

Fig. 1. The AFM surface image incorporated with capacitance image for the samples grown at f_{TMG}=20 μmol/min (a) and f_{TMG}=80 μmol/min, (b). The black points represent the terminations of pure edge and mixed treading dislocations at the surface. The dislocation densities are 9×10^9 cm^{-2} (a) and 2×10^8 cm^{-2} (b).

was increased to 1080 °C to grow the GaN epilayers, and the f_{TMG} was kept constant at 112 μmol/min for all the epilayer growths. The flow rate of NH_3 was kept constant at 156 μmol/min during the whole growing process.

The f_{TMG} was found to be crucial to the epilayer growth. The epilayer thickness grown for an hour varied from 2.8 to 1.4 μm with the f_{TMG} variation from 20 to 80 μmol/min. Figure 1 shows the AFM image of two samples grown with different f_{TMG}. The RMS dislocation density is $\sim2\times10^8$ cm^{-2} at the optimum condition and the largest value was 9×10^9 cm^{-2}. Some other experimental data related with the f_{TMG} such as the Hall mobility, Hall concentration, photoluminescence, TEM are discussed in detail elsewhere [13].

The Hall effects were measured on all the samples, and Figs. 2, 3 and 4 show some of the results. Some of the room temperature characteristics and results of the anal-

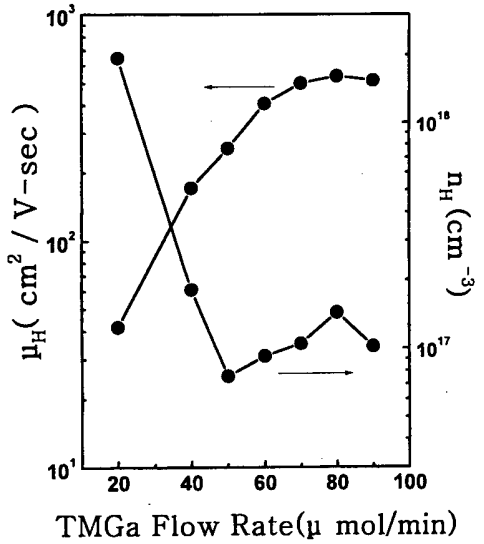

Fig. 2. The Hall mobility μ_H and concentration n_H variations with the GaN buffer growth rate.

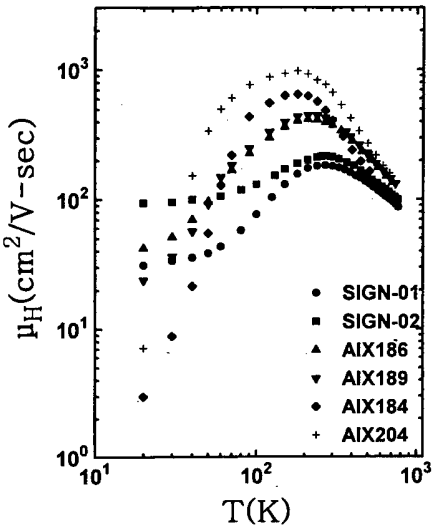

Fig. 3. The Hall mobility variations with temperature.

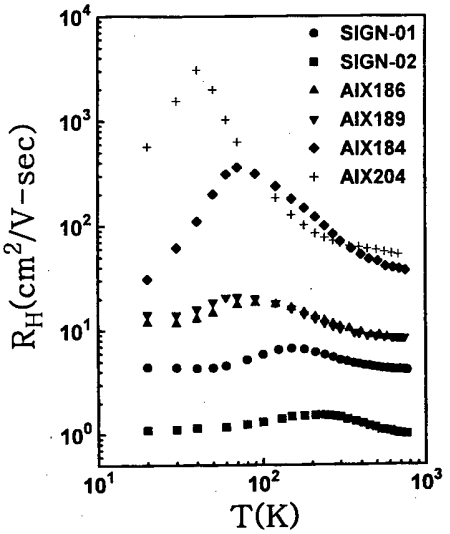

Fig. 4. The Hall coefficient variations with temperature.

Table 1. Sample characteristics.

Sample	n_H (cm^{-3})	n_Γ (cm^{-3})	μ_H (cm^2/V-sec)	Thick. (μm)	Activation Energy (meV)	N_D (cm^{-3})	N_A (cm^{-3})	NsQs (cm^{-1})
AIX184	8.81 E16	4.08 E16	406	2	22	2.60 E17	6.50 E16	5 E4
AIX191	9.52 E16	4.64 E16	500	1.7	22	2.00 E17	3.00 E16	3 E4
AIX204	1.11 E17	1.39 E17	670	5	18	2.40 E17	7.00 E16	5 E4
AIX193	1.39 E17	9.10 E16	538	1.4	17	3.30 E17	6.00 E16	3 E4
DB-01	1.48 E17	1.72 E17	580	1.2	16	2.30 E17	5.70 E16	5 E4
APL-01	2.24 E17	2.74 E17	508	2.5	13	5.50 E17	1.68 E17	5 E4
AIX187	3.11 E17	3.78 E17	352	4	14	1.10 E18	6.50 E17	5 E3
SIDB-01	3.20 E17	3.78 E17	155	1.2	12	2.90 E18	2.30 E18	4 E4
APL-02	4.91 E17	5.74 E17	372	2.5	13	1.50 E18	3.40 E17	3 E4
AIX186	5.82 E17	6.80 E17	374	2	12	1.50 E18	5.50 E17	5 E3
AIX189	6.13 E17	6.90 E17	406	8	13	1.30 E18	4.00 E17	5 E3
SiGN-01	1.22 E18	1.39 E18	180	3	10	3.60 E18	2.00 E18	–
CQD	1.59 E18	1.71 E18	123	2	8	7.20 E18	5.20 E18	–
SiGN-02	4.33 E17	4.59 E18	194	4.5	10	6.80 E18	1.00 E18	–

yses are summarized in Table 1. Figures 3 and 4 illustrate variations of the typical Hall mobility μ_H and Hall coefficient R_H variations with temperature, respectively, for three different groups; unintentionally doped, medium doped, and rather heavily doped epilayers.

III. ANALYSES

To our knowledge, subsidiary conduction band edges are high enough above the Γ edge and thus electrons in the Γ band may be assumed to be dominant in transport up to the highest temperature 800 K in the present work. The Γ band parameters such as the band-gap variation with temperature and effective mass, along with other material parameters necessary for calculations of transport parameters, seem rather well established as collected in Table 2.

Table 2. Material parameters.

Parameters	Values	Reference
γ	-8.32×10^{-4} eV/K	[14]
β	835.6 K	[14]
m_0^* (electron effective mass)	0.22	[15]
E_D (deformation potential)	13 eV	[16]
P_E (piezoelectric coefficient)	0.135	[17]
ϵ_s (low-frequency dielectric constant)	10.0	[18]
ϵ_∞ (high-frequency dielectricconstant)	5.2	*
ρ (crystal density)	6.0895 g/cm^3	**
a (lattice constant)	3.189 Å	[19]
c (lattice constant)	5.185 Å	[19]
C_l (longitudinal elastic constant)	2.65×10^{11} N/m^2	[17]
$\hbar\omega_0$ (optical phonon energy)	91.2 meV	[14,18]

*determined in this work, **estimated from a and c

As an approximation of the Γ band structure, the non-parabolic Kane form and the bottom-of-the-band effective mass may be written as [20]

$$E = \frac{\hbar^2k^2}{2m_e} + \frac{E_0^*}{2}\times\left[\left\{1+\frac{\hbar^2k^2}{m_eE_0^*}\left(\frac{m_e}{m_0}-1\right)\right\}^{1/2}-1\right] \quad (1)$$

$$\frac{m_e}{m_0} = 1+\frac{P^2}{3}\left(\frac{2}{E_0^*}+\frac{1}{E_0^*+\Delta_0}\right), \quad (2)$$

with the band gap E_0 and the effective mass band gap E_0^* variations with temperature given by [21,22]

$$E_0^*(T) = E_0(0)+\gamma T^2/(\beta+T), \quad (3)$$

$$E_0^*(T) = E_0(0)-[E_0(0)-E_0(T)]/A, \quad (4)$$

where A is assumed to be 1.5 [23].

In the presence of a vanishingly small electric field $\boldsymbol{F}$ and an arbitrary magnetic field $\boldsymbol{B}$, the perturbed electron distribution function may be written as [12]

$$f(\boldsymbol{B},\boldsymbol{k}) = f_0(E)-\frac{df_0(E)}{dE}\phi(\boldsymbol{B},\boldsymbol{k})\boldsymbol{F} \quad (5)$$

where the vector $\phi(\boldsymbol{B},\boldsymbol{k})$ is determined by solving the linearized Boltzmann equation

$$\boldsymbol{F}\cdot\left\{-e\boldsymbol{v}(\boldsymbol{k})\frac{df_0(E)}{dE}-\frac{e}{\hbar}\frac{df_0(E)}{dE}[\boldsymbol{B}\cdot\boldsymbol{v}(\boldsymbol{k})\times\nabla_k]\phi(\boldsymbol{B},\boldsymbol{k})\right\} = \left(\frac{df}{dt}\right)_{co}. \quad (6)$$

Taking the z-axis along B, $\phi(\boldsymbol{B},\boldsymbol{k})$ is given by

$$\phi(\boldsymbol{B},\boldsymbol{k}) = P_1\boldsymbol{k}_t+P_2(\boldsymbol{z}\times\boldsymbol{k}_t)+P_3k_z\boldsymbol{z} \quad (7)$$

where $\boldsymbol{k}_t=(k_x,k_y,0)$, $\boldsymbol{z}=(0,0,1)$ and the P_i are scalar functions of k alone.

The element of the conductivity tensor is given by

$$\sigma_i j = \frac{e}{4\pi^3}\int v_i(\boldsymbol{k})\phi_j(\boldsymbol{B},\boldsymbol{k})\frac{df_0(E)}{dE}d^3k, \tag{8}$$

and the only nonzero elements of σ_{ij} are written as

$$\begin{aligned}\sigma_{xx} &= \sigma_{yy} =< P_1 >\\ \sigma_{xy} &= \sigma_{yx} =< P_2 >\\ \sigma_{zz} &= < P_3 >= ne\mu\end{aligned} \tag{9}$$

where

$$< P_i >= \frac{e}{3\pi^2 E}\int_0^\infty P_i k^3\left(-\frac{\partial f_0}{\partial E}\right)dE$$

The longitudinal conductivity is just σ_{zz} in zero magnetic field, and the Hall coefficient and Hall scattering factor are given as

$$R_H = -\frac{\sigma_{yx}}{B(\sigma_{xx}^2+\sigma_{yx}^2)} \tag{10}$$

$$r_H = -neR_H \tag{11}$$

with

$$n = \frac{1}{3\pi^2}\int_0^\infty k^3\left(\frac{\partial f_0}{\partial E}\right)dE.$$

In this analysis, seven different scattering mechanisms due to polar optical phonon, acoustic-mode deformation and piezoelectric potentials, ionized and neutral impurities, space charge, and dislocation are taken into account.

Due to the possible impurity-band conduction at low temperature [2,3,10,11], the theoretical fits to the experimental data began at high temperature range. The compensating acceptor density N_A, the effective space charge cross-section N_sQ_s, and the dislocation density N_d is were assumed as unknowns in the fits. Except for unintentionally doped epilayers with low μ_H value, reasonable fits were made near and above the room temperature for all the samples in the work, as shown in Fig. 5. The difference between theory and experiment increases with decreasing temperature. This indicates the second band, *i.e.*, the impurity band, is involved in the transport only at low temperature. In this case, a two-band model may be written as [24]

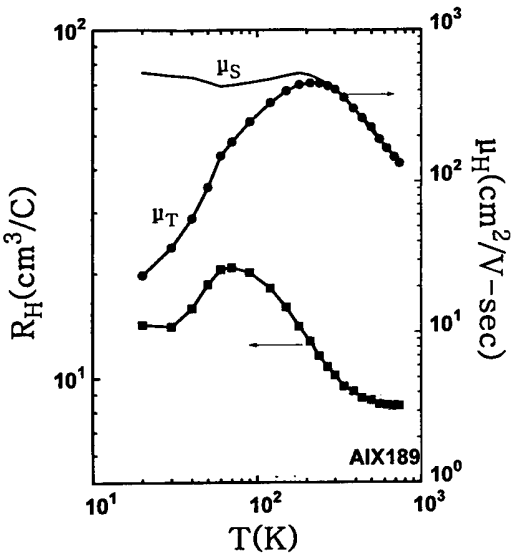

Fig. 5. The R_H and μ_H variations fitted by theoretical calculations of one-band (μ_s) and two-band models (μ_T), respectively.

$$R_H = \frac{\sum_j R_j\sigma_j^2/(1+\sigma_j^2R_j^2B^2)}{\left\{\sum_j \sigma_j/(1+\sigma_j^2R_j^2B^2)\right\}^2+\left\{\sum_j R_j\sigma_j^2B/(1+\sigma_j^2R_j^2B^2)\right\}^2} \tag{12}$$

$$\mu_H = R_H\sum_j \sigma_j \tag{13}$$

with

$$\begin{aligned}R_j &= r_j/en_j\\ \sigma_j &= en_j\mu_j\\ r_{eff} &= R_He\Sigma n_j.\end{aligned} \tag{14}$$

In the two-band analyses, the Γ band values were extrapolated to low temperatures, and the mobility μ_d and the carrier density n_d (unionized impurity density) in the impurity band were adjusted to fit the experimental data as shown in Fig. 5. Here the total concentration $n_t = N_D - N_A = n_\Gamma + n_d$ should be constant throughout the temperature variation.

IV. RESULTS AND DISCUSSION

Theoretical fits to the experimental data were made within ±7 % over the whole temperature range; obtained values are listed in Table 1. The high-frequency dielectric constant ϵ_∞ was also adjusted to obtain the best fits for all the samples, and the value is 5.2 which is in good agreement with a previously reported value, 5.5 [18].

1. Doped Samples

The Si doped samples are divided into two groups according to the carrier density; one is with $3\sim6\times10^{17}$ cm^{-3} and the other is with $1\sim5\times10^{18}$ cm^{-3} at room temperature. In these samples we ignored the scattering due to dislocation, and thus N_A and N_sQ_s values determined here may have some uncertainties. However, their resultant values do not appear unreasonable and this will be further discussed below. The space-charge scattering is, anyway, negligible in heavily doped samples [25]. In Fig.

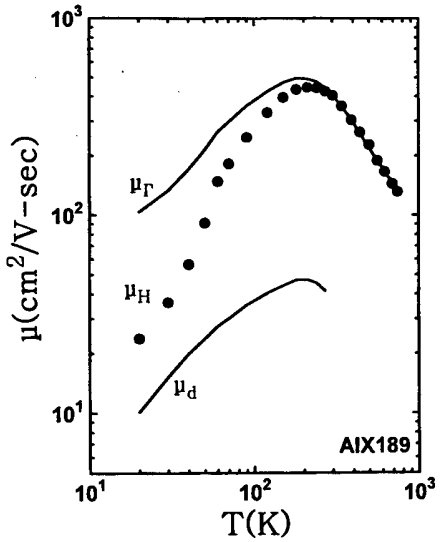

Fig. 6. The calculated μ_Γ and μ_d fitted to the μ_H variation with temperature.

6, the calculated μ_Γ and μ_d values fitted to the experimental data are shown with the μ_H data. Molnar *et al.* [2] have reported the two-band analysis without detailed transport calculation, but obtained very similar results to ours. Their results show a two-band effects even at room temperature, but far lower value of μ_H than ours is noticed. Look and Molnar [3] have reported a two-layer Hall model, proving a degenerate GaN/Al_2O_3 interface layer. But the possibility of this interface layer effects may be obviated in our doped samples. Figure 7 shows the measured Hall concentration n_H $(=1/R_He)$ along with the electron densities in the Γ band, n_Γ, and impurity band or levels, n_d, determined in this analysis. The n_Γ vs $1/T$ relation gives 13 meV of activation energy.

As will be discussed below, unintentionally doped epi-

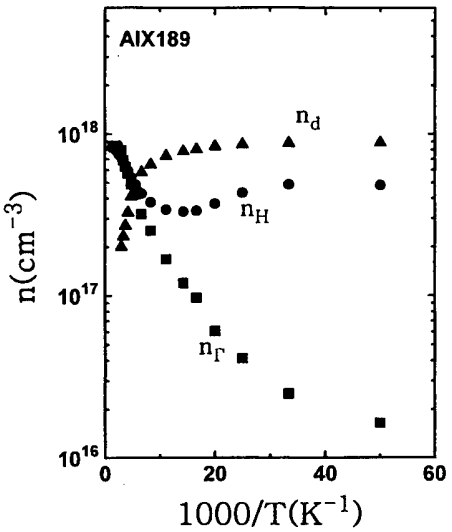

Fig. 7. The calculated n_Γ and n_d values are compared with the Hall concentration variation.

layers show thickness-dependent characteristics. In medium doped samples, meanwhile, the thickness was varied from 2 to 8 μm to validate the thickness-dependency, but no such phenomenon was observed.

2. Unintentionally Doped Samples

As shown in Fig. 2, the n_H and μ_H values vary significantly with the growth rate of the buffer layer. Furthermore, the thickness-dependency is also significant. For example, the samples AIX 193 and AIX 204 were grown with the same conditions, except the thickness. Thickness change from 1.4 to 5 μm increased the μ_H value from 538 to 670 $cm^2/V{\cdot}sec$. The μ_H variations with temperature for these two samples and the other grown at different condition are shown in Fig. 8. Drift mobility calculated for each scattering mechanism to fit the sample AIX 204 are also shown in the figure.

It is noticed that the three samples show parallel variation with temperature above ~250 K. The lattice scattering (μ_{OP+D+P} in the figure) is dominant over the high temperature range and thus it is not possible to make fits for the two other samples with lower mobility by adjusting the other four scattering mechanisms, as can be seen in Fig. 8. The only way out of this difficulty is to use a two-band model even at the high temperatures. Figure 9 illustrates a typical result of the analysis, and three different carrier density values with inverse temperature are shown in Fig. 10. At room temperature, n_H and μ_H values are 8.8×10^{16} cm^{-3} and 407 $cm^2/V{\cdot}sec$, respectively. In the Γ band, the values of n_Γ, μ_Γ and $\mu_{H\Gamma}$ turned out to be 4.1×10^{16} cm^{-3}, and 602 $cm^2/V{\cdot}sec$, respectively. The n_D and μ_D values are 1.5×10^{17} cm^{-3}

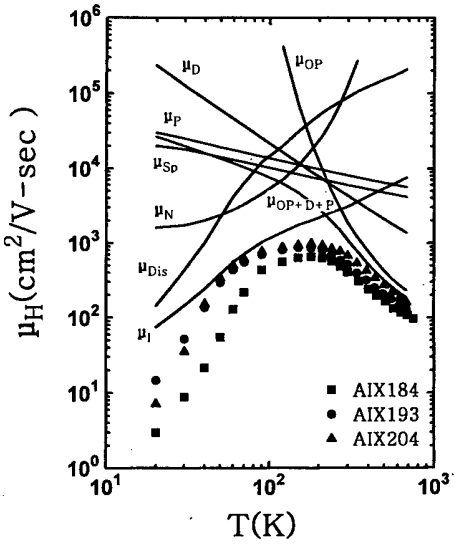

Fig. 8. The μ_H values of unintentionally doped samples. The mobility values for various scattering mechanisms are those for sample AIX 184.

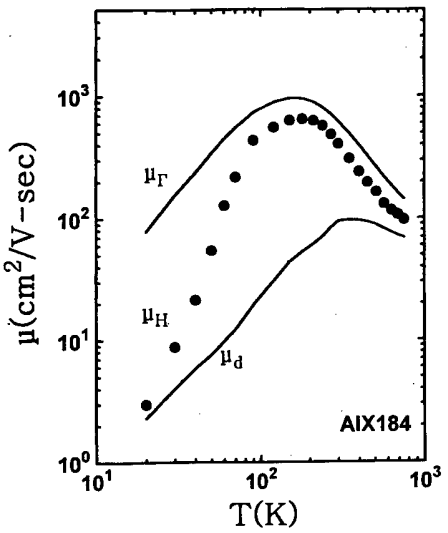

Fig. 9. The calculated μ_Γ and μ_d values to fit the μ_H variation for low-mobility unintentionally doped samples.

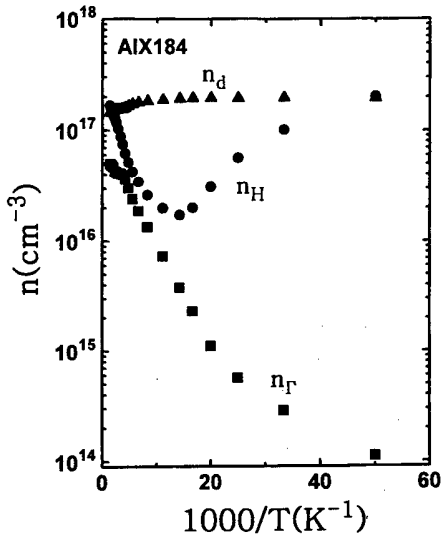

Fig. 10. The calculated n_Γ and n_d variations to fit the n_H data for the sample in Fig. 9.

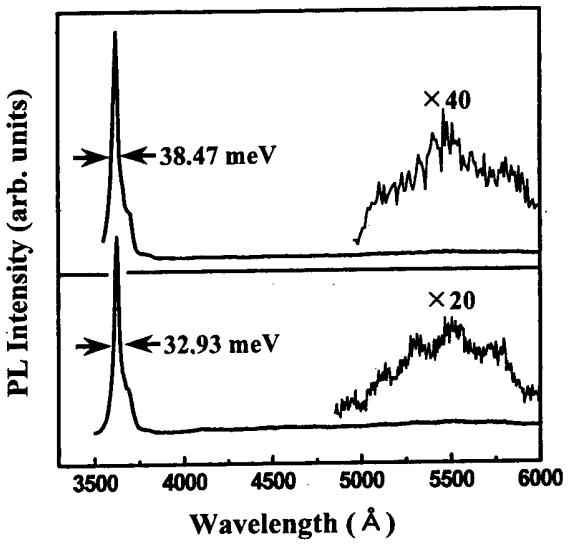

Fig. 11. Photoluminescence measurements at 300 K for two different buffer growth rate; 80 μmol/min (above): 20 μmol/min (below).

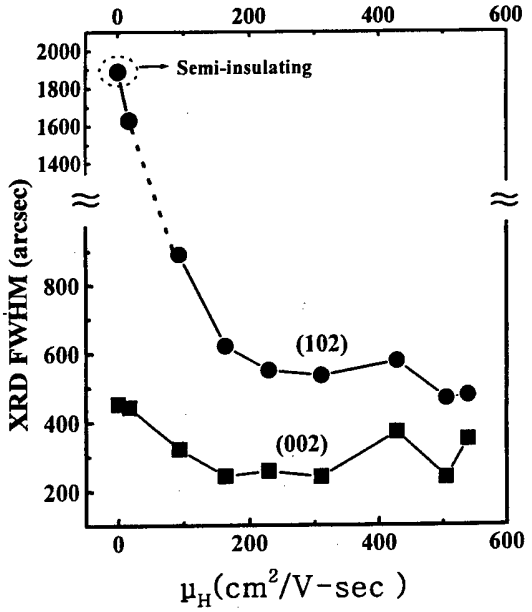

Fig. 12. High-resolution XRD measurements plotted as a function of the Hall mobility for unintentionally doped samples.

and 100 cm^2/V·sec, respectively. Considering many unknowns adopted in this analyses, the determined values may have considerable errors up to 10 %. But this analyses are regarded as a good evidence of the impurity-band involvement even at high temperatures, unlike the doped samples. This result indicates that the samples with low μ_H may have higher μ_Γ and lower n_Γ than the sample with highest μ_H grown at optimum condition in Fig. 2. Furthermore, the photoluminescence spectra at room temperature in Fig. 11 seem to support the result obtained above. That is, the sample with lowest μ_H shows narrower full-width at half maximum (FWHM) of the near band edge PL than that of the sample with highest μ_H, but exhibits much higher yellow-band intensity.

Figure 12 shows the FWHM of HRXRD peaks plotted as functions of the Hall mobility. The difference between two curves is regarded to be related with the edge threading dislocations [26]. The dislocations of screw and mixed characters are relatively unaffected by the buffer layer growth rate. Figure 12 illustrates that the edge dislocations seem to limit the electron mobility. In facts, Tansley and Eagan [5], and Weimann *et al.* [9] have explained the low-mobility in terms of scattering due to the edge dislocation. To certify this, we made a fit again for

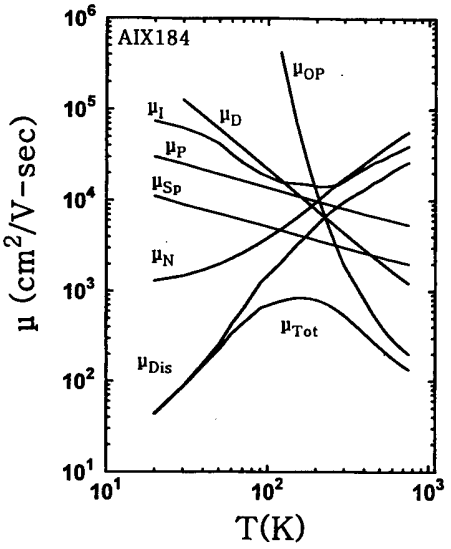

Fig. 13. Calculated mobility values for various scattering mechanisms to fit the experimental data with $N_A = 0$.

the sample AIX 184 by setting N_A=0, and the result is given in Fig. 13. The same fit was recovered, but the scattering due to the dislocation is not enough to explain the μ_H data, especially at room temperature where the scatterings by lattice and space-charge are more important. And thus the dislocation scattering cannot explain the temperature-dependent μ_H along with the room temperature value. Rather, the impurity-band conduction is the sole origin of the low mobility as illustrated in Fig. 9.

3. Impurity-Band Conduction

Impurity-band conductions and/or near-interface effects are blurring the understanding of pure electron properties in the Γ band. The impurities, especially oxygen, emerging from sapphire substrate contaminate the GaN epilayers during the growth [27]. The defective near-interfacial region [8] allows the impurities to incorporate more readily as compared to the more perfect region (epilayer). This may cause a conductive layer near the substrate, and the two-layer model has been proposed [3].

In the GaN films grown by hydride vapor phase epitaxy, Götz *et al.* [1] have measured the thickness-dependent n_H and μ_H. They explained the experimental results in terms of highly conductive near-interface layer and continuous reduction of the defect density with increasing film thickness for GaCl-pretreated and ZnO-pretreated sapphires. More interestingly, their μ_H variation with temperature above ~300 K shows the similar slope for all the samples regardless of the thickness variation, which is the case in our unintentionally doped samples.

Even though the experimental data of unintentionally doped samples except AIX 204, the 5 μm thick sample with highest μ_H, are satisfactorily analyzed over the whole temperature range using a two-band model including the impurity-band, there is no firm evidence from which we can draw a conclusion on what is the impurity-band. Furthermore, equations of R_H and σ have the same forms for both two-layer and two-band models [3]. Figure 12, however, indicates that the edge dislocation induces the reduction of the Hall mobility and the increase of the yellow luminescence as shown in Fig. 11. Many suggestions regarding gallium vacancies [28] and edge dislocation lines [29] have been made to explain the yellow luminescence, but no conclusive proof is yet available. Deep levels may be due to the dislocations and affect the characteristics of optoelectonic devices such as leakage current, lifetime, *etc.* [30]. Our results seem to support that the dislocation induces the impurity-band conduction and yellow luminescence.

Figure 14 exhibites μ_d vs $1/T$ for five different samples. As the impurity density increases, the transition from thermally-activated-to-metallic conduction is conspicuous. The critical impurity concentration for metallic conduction estimated from $N_c = 1/\{12\pi(\epsilon_s a_H m_o/m_e)^3\}$ is about 2×10^{18} cm^{-3} in GaN. The two samples SiGN-02 and SiGN-01 belong to metallic-conduction in Fig. 14. Except the unintentionally doped and low μH samples, AIX184, the impurity conduction is exhibited only temperatures lower than around 300 K. The apparent conduction between impurity states may involve the near-interface effects in unintentionally doped samples. Differential Hall effect measurements [31] should be made to depict the respective contribution of the two possible mechanisms.

The edge dislocation has two dangling bonds and thus may act as compensating acceptor centers in pure n-type samples, meanwhile, as compensating donors in p-type

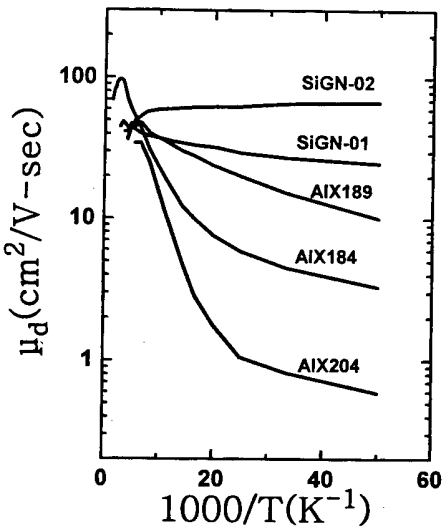

Fig. 14. The impurity-band mobility variations with temperatures.

samples. When compensating the acceptors, the charged dislocation states would be reduced, and thus ionized impurity and dislocation scatterings will be reduced in p-type samples with dislocations. Furthermore, the yellow luminescence related with dislocation would be reduced in p-type GaN.

4. Hall Scattering Factor

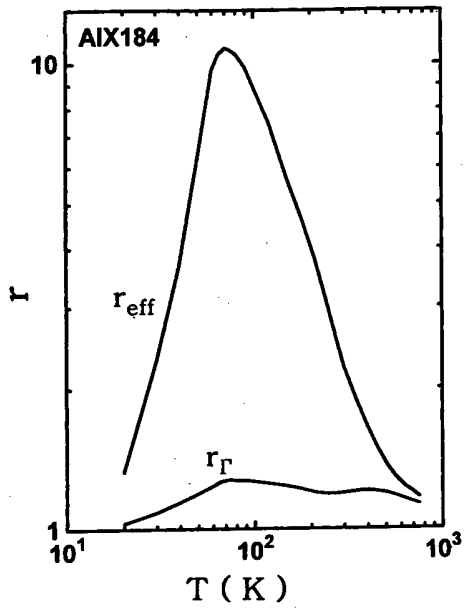

Fig. 15. The Hall scattering factor variations with temperature.

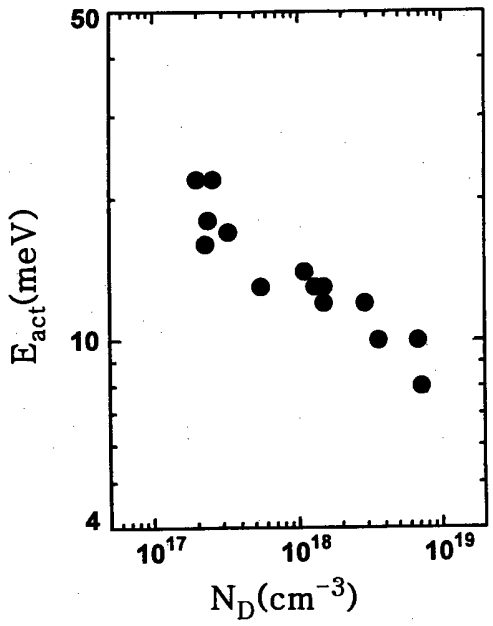

Fig. 16. The shallow level activation energyvalues plotted as a function of donor density.

Hall scattering factor r is usually assumed to be unity to estimate the carrier density from $n = r/R_H e$. Actually this estimation gives the Hall carrier density, n_H, rather than carrier density and the n_H vs T curves may be misleading especially when more than one band is involved as in the present case of GaN samples. Look *et al.* [32] have calculated the r_Γ value to obtain the n_Γ vs $1/T$ relation for GaN and showed it varies from 1.22 to 1.42 in a temperature range of 77~300 K.

Figure 15 shows typical variations of r with temperature for two different values, which were used in calculating n_Γ and $n_\Gamma + n_d$ in Fig. 10. Thus obtained n_Γ vs $1/T$ relation gives the activation energy of shallow donors, as collected in Fig. 16. The large value of r_{eff} is due to the two-band conduction.

V. SUMMARY

The growth rate of GaN buffer layer turned out to be one of the crucial parameters to control the GaN epilayer quality. The edge dislocation density decreases with increasing buffer growth rate up to the optimum value in unintentionally doped samples. The Hall mobility decreases with increasing dislocation density. This is not due to the scattering by dislocation, but due to the impurity-band conduction involvement induced by the dislocations in those samples. Details of impurity-band (and/or -state) are not clear and remain to further study. However, the near-interface may be ascribed, at least in part, to the impurity-band conduction in unintentionally doped samples. The thickness-dependency of epilayer properties is not observed in doped samples, supporting negligible near-interface effects in this case.

ACKNOWLEDGMENTS

This work was supported by the Korean Science and Engineering Foundation through Semiconductor Physics Research Center, Chonbuk National University, and by the Korean Ministry of Science and Technology for the Korea-Japan joint research. Prof. S.P. DenBaars provided the data of the samples DB-01 and SIDB-01 before publication and Prof. M. Razeghi grew the sample CQD.

REFERENCES

[1] W. Götz, L. T. Romano, J. Walker, N. M. Johnson and R. J. Molnar, Appl. Phys. Lett. **72**, 1214 (1998).
[2] R. J. Molnar, T. Lei and T. D. Moustakas, Appl. Phys. Lett. **62**, 72 (1993).
[3] D. C. Look and R. J. Molnar, Appl. Phys. Lett. **70**, 3377 (1997).
[4] S. Keller, B. P. Keller, Y.-F. Wu, B. Heying, D. Kaponek, J. S. Spede, U. K. Mishra and S. P. DenBaars, Appl.

Phys. Lett. **68**, 1525 (1996).
[5] T. L. Tansley and R. J. Egan, Phyica **B185**, 190 (1993).
[6] S. Nakamura, T. Mukai and M. Sendy, J. Appl. Phys. **71**, 5543 (1992).
[7] W. Götz, N. M. Johnson, C. Chen, H. Liu, C. Kuo and W. Imler, Appl. Phys. Lett., 3144 (1996).
[8] X. H. Wu, L. M. Brown, D. Kapolnek, S. Keller, B. Keller, S. P. DenBaars and J. S. Speck, J. Appl. Phys. **80**, 3228 (1996).
[9] N. G. Weimann, L. F. Eastman, D. Doppalapudi, H. M. Ng and T. D. Moustakas, J. Appl. Phys. **83**, 3656 (1998).
[10] M. G. Cheong, K. S. Oh, E.-K. Suh and H. J. Lee, *Silicon Carbide, III-Nitrides and Related Materials*, ed. By G. Pensl *et al.* (Trans. Tech. Pubilcations LTD, USA, 1997), p. 1385.
[11] H. J. Lee, M. G. Cheong, E-.K. Suh and M. Razeghi, Proc. of SPIE **3287**, 321 (1998).
[12] K. Fletcher and P. N. Butcher, J. Phys. **C5**, 212 (1972).
[13] K. S. Kim, G. M. Yang, J.-H. Kim, K. J. Lee, C. S. Oh, D. H. Lim, C.-H. Hong, K. Y. Lim, D. H. Byun, A. Yoshikawa and H. J. Lee, J. Korean Phys. Soc. in this volume.
[14] W. Shan, T. J. Schmidt, X. H. Yang, S. J. Hwang, J. J. Song and B. Goldenberg, Appl. Phys. Lett. **66**, 985 (1995).
[15] P. Perlin, E. Litwin-Stasaewska, B. Suchanek, W. Knap, J. Camassel, T. Suski, R. Piotrzkowski, I. Grzegory, S. Porovski, E. Kaminska and J. C. Chervin, Appl. Phys. Lett. **68**, 1114 (1996).
[16] Y. T. Hwang, S. C. Cha, B. C. Lee, Y. H. Lee, K. Y. Lim, E.-K. Suh, C. T. Choi and H. J. Lee, Jpn. J. Appl. Phys. **33**, 2459 (1994).
[17] D. L. Rode, *Semiconductors and Semimetals*, edited by R. K. Willardson and A. C. Beer (Academic, New York, 1975), Vol. 10, pp. 1-90.
[18] V. W. L. Chin, T. L. Tansley and T. Osotchan, J. Appl. Phys. **75**, 7365 (1994).
[19] H. P. Maruska and J. J. Jietjen, Appl. Phys. Lett. **15**, 327 (1969).
[20] J. Basinski, S. D. Rosenbaum, S. L. Basinski and J. C. Wooley, J. Phys. **C6**, 422 (1973).
[21] Y. P. Varshni, Physica(Utrecht), J. Phys. **34**, 149 (1967).
[22] J. Basinski and J. C. Wooley, J. Phys. **C8**, 1841 (1975).
[23] H.-J. Lee, J. Basinski, L. Y. Juravel and J. C. Wooley, J. Can. Phys. **57**, 233 (1979).
[24] R. A. Smith, *Semiconductors* (Cambridge Univ. Press, Cambridge, England, 1961).
[25] E. M. Conwell and M. O. Vassel, Phys. Rev. **166**, 797 (1968).
[26] S. Keller, D. Kapolnek, B. P. Keller, Y. Wu, B. Heying, J. S. Speck, U. K. Mishra and S. P. DenBaars, J. Appl. Phys. **35**, L285 (1996).
[27] G. Popovici, W. Kim, A. Botchkarev, H. Tang, H. Morkoc and J. Solomon, Appl. Phys. Lett. **71**, 3385 (1997).
[28] J. Neugebauer and C. G. Walle, Appl. Phys. Lett. **69**, 503 (1996).
[29] F. A. Ponce, D. P. Bour, W. Götz and P. J. Wright, Appl. Phys. Lett. **68**, 57 (1996).
[30] S. Nakamura, M. Senoh, S.-I. Nagahama, N. Iwasa, T. Matsushita and T. Mukai, Proc. 2nd Intern. Symp. on Blue Laser and Light Emitting Diodes, Chiba, Japan, 371 (1998).
[31] D. C. Look, *Electrical Characterization of GaAs Materials and Devices* (John Wiley & Sons, New York, 1989), Chap. 1.
[32] D. C. Look, J. R. Sizelove, S. Keller, Y. F. Wu, U. K. Mishra and S. P. DenBaars, Solid State Comm. **4**, 297 (1997).

Journal of the Korean Physical Society, Vol. 34, June 1999, pp. S253~S257

Electronic Structures of GaN Nanotubes

Seung Mi LEE[1] and Young Hee LEE[1,2*]

[1]*Department of Semiconductor Science and Technology,* [2]*Department of Physics, and Semiconductor Physics Research Center, Jeonbuk National University, Jeonju 561-756*

Yong Gyoo HWANG

Department of Physics, Wonkwang University, Iksan 570-749

Cheol Jin LEE

Department of Electrical Engineering, Kunsan National University, Kunsan 573-701

Density functional calculations are used to predict the electronic structures of GaN nanotubes. The graphitic GaN is an indirect band gap material with valence band maximum at K edge. Zigzag nanotube is a semiconductor with direct band gap, whereas armchair nanotube has an indirect band gap along the tube axis. The band gaps decrease with the decreasing diameter, contrary to the case of carbon nanotubes.

I. INTRODUCTION

Carbon nanotubes have been synthesized during the formation of fullerenes using arc discharge of graphite rods [1]. Recently single-wall carbon nanotubes have been produced with high yields by the laser vaporization of graphite powders mixed with small amount of transition metals [2–4]. Since then, researches on carbon nanotubes have been activated. The physical properties of carbon nanotubes as denoted by (n, m) are correlated with their diverse phases. Armchair (n, n) carbon nanotubes are metallic [5,6], while zigzag (n, 0) carbon nanotubes are semiconductors with a finite band gap except the case of $n - m = 3k$ (k: integer) which is a small band gap semiconductor [7]. Energy gap can be controlled by varying the diameter, thus allowing band gap engineering [5,8]. Strong electron field emission from carbon nanotubes have been observed, suggesting the applicability to flat panel displays [9,10]. Despite such efforts, applications of carbon nanotubes to memory devices and quantum transport devices are still challenging.

Efficient blue light-emitting diodes have been realized with GaN materials, making its application to full color displays promising [11]. In addition, GaN exhibits considerable hardness, high thermal conductivity, and little radiation damage, suggesting the applicability to high power and high temperature microelectronic devices. Although $In_xGa_{1-x}N$ has been tried for band gap engineering by varying In composition, it is still difficult to grow and control high In compositions due to the strain between InGaN and substrate [12]. Therefore, a new form of GaN structure is always desirable if possible.

In this report, we propose a new phase of GaN, a nanotube, using a density functional (DF) calculations. We will show that GaN nanotubes are as stable as carbon nanotubes and can be synthesized under some extreme conditions. Pure boron-nitride and boron-carbon-nitride nanotubes have been successfully produced by arc-discharge [13,14]. The existence of BN-nanotubes suggests the possibility of other nitride nanotube synthesis such as CN and GaN. The present calculations show that the strain energy costs to wrap up graphitic GaN sheets into nanotubes are comparable with those of carbon nanotubes, ensuring again the possibility of GaN nanotube formation. Yet, the initial nucleation seeds for GaN nanotube formation will play a crucial role. The idea of using carbon nanotubes as a nucleation seed will be discussed in conjunction with edge energies in this report. Band structures reveal that GaN zigzag nanotubes is a semiconductor with a direct band gap, whereas armchair nanotubes have an indirect band gap. The energy gap of GaN zigzag nanotubes decreases with the decreasing tube diameter, whereas that of GaN armchair nanotubes is almost constant over a wide range of the diameter, which is contrary to the case of carbon nanotubes.

II. THEORETICAL APPROACHES

Here we investigate the stability and electronic structures of GaN nanotubes and further discuss possible ways of synthesis. For our calculations we use a plane-

*To whom correspondence should be addressed

wave basis DF calculations within the local-density-approximation (LDA) [15] and the SCC-DFTB code (a self-consistent charge density-functional-based tight binding method). In the LDA calculations, the ionic potentials are described by a norm-conserving nonlocal pseudopotential generated by Troullier-Martins [16] in a separable form of Kleinman and Bylander [17]. Exchange-correlation functions parameterized by the Perdew-Zunger scheme [18] are used. The energy was converged to 0.2×10^{-4} eV/atom.

The SCC-DFTB method uses a basis of numerically obtained s, p, and d atomic orbitals. Hamiltonian overlap matrix elements are evaluated by two-center approach. Charge transfer is taken into account through the incorporation of a self-consistency scheme for Mulliken charges based on the second-order expansion of the Kohn-Sham energy in terms of charge density fluctuations. The diagonal elements of the Hamiltonian matrix employed are then modified by the charge-dependent contributions in order to describe the change in the atomic potentials due to the charge transfer. The off-diagonal elements have additional charge-dependent terms due to the Coulomb potential of ions. They decay as $1/r$ and thus account for the Madelung energy of the system. The s, p, and d orbitals in the Ga atoms and s and p in the N atoms are included in the calculations. Further details of the SCC-DFTB method have been published elsewhere [19].

III. RESULTS AND DISCUSSION

Various GaN crystal phases exist under different experimental growth conditions [12]. The Wurtzite phase is the thermodynamically stable structure at ambient conditions, whereas the zincblende (ZB) phase (Fig. 1(a)) can be stabilized on various cubic substrates [20,21]. The rocksalt phase can be induced at high pressures [22]. We first calculate the total binding energies of ZB and graphitic phases using SCC–DFTB in order to study the relative stabilities. We choose a cubic supercell of 216 atoms for ZB GaN and 200 atoms for the graphitic GaN (Fig. 1(b)). Periodic boundary conditions are applied along the x-, y-, and z-directions. For the graphitic phase, a large vacuum region above the graphitic sheets is included.

Figure 2 shows total binding-energy curves obtained by the SCC-DFTB calculations. The binding energy of the ZB GaN is -5.91 eV/atom with the nearest neighbor distance of 1.950 Å, or equivalently the cubic lattice constant of 4.503 Å. The calculated bulk modulus is 195 GPa, in good agreement with the reported LDA result [23]. A considerable amount of electron charge (0.56 e) is transferred from Ga to N, resulting in an ionic bonding nature. N loses some s electrons and gains more p electrons, whereas Ga loses more p electrons than s electrons. The binding energy of the graphitic GaN is -5.55 eV/atom with the nearest neighbor distance of 1.775 Å,

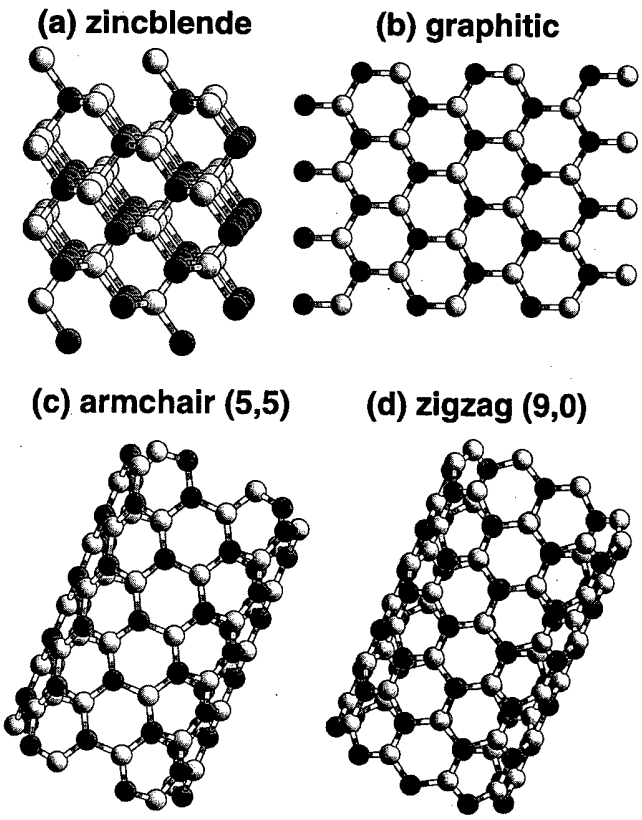

Fig. 1. Typical types of GaN nanotubes; Various phases of GaN: (a) Zincblende, (b) graphitic sheet, (c) (5,5) armchair nanotube, and (d) (9,0) zigzag nanotube. Dark-grey and light-grey spheres indicate Ga atom and N atom, respectively.

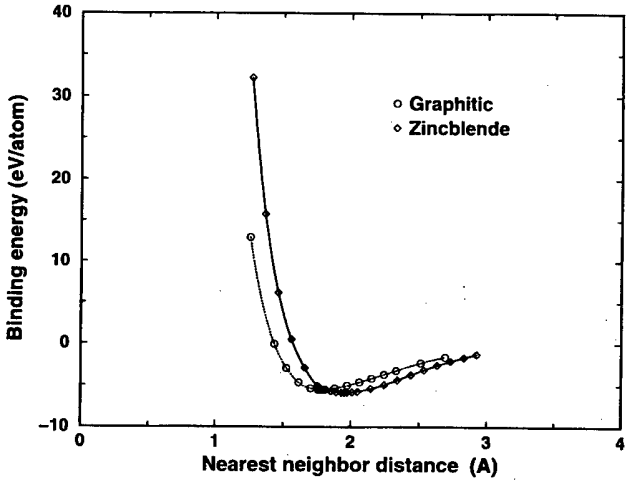

Fig. 2. Total energy curves of cubic and graphitic GaNs as a function of nearest neighbor distance, calculated by the SCC-DFTB method. The equilibrium distance is 1.95 Å for ZB and 1.775 Å in graphitic sheet. The curves are fitted by the cubic-spline method.

smaller than that of the ZB GaN. The charge transfer in graphitic GaN from Ga atom to N atom is 0.46 e, a little smaller than that of the ZB GaN. The Ga atom loses

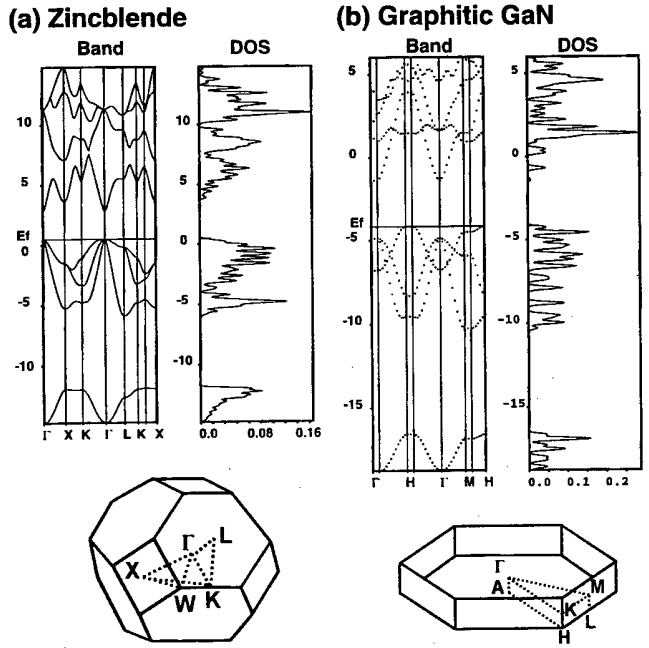

Fig. 3. Band structures and the density of states of (a) zincblende and (b) graphitic GaN. Brillouin zones with symmetric points are shown together.

more p_z in the case of graphitic GaN than that in the case of the ZB GaN, whereas N gains more p_z electrons, enhancing π bonds above the plane. This difference in the binding energy suggests the graphitic GaN to be energetically unfavorable over the ZB GaN or wurtzite GaN. Yet this small magnitude opens the possibility of forming graphitic sheets as a metastable phase. The calculated strain energies of GaN nanotubes are comparable to those of carbon nanotubes [24], again ensuring the possibility of GaN nanotubes formation.

Figure 3 shows the band structures and density of states (DOS) of cubic GaN and graphitic GaN calculated by the DFT-LDA method. We used 28 special k-points for cubic GaN and for graphitic GaN in the irreducible Brillouin zone as implemented by Monkhorst and Pack [25]. The kinetic energy cutoff for the plane-wave expansion of wavefunctions is 18 Ry. The band structure for cubic GaN shows a direct band gap, in good agreement with the previous first principles calculations [23]. Heavy hole and light hole bands are degenerate at Γ point in zincblende phase. Strong s, p hybridization occurs in Ga atoms, whereas large s, p splitting occurs in N atoms, *i.e.*, p contributes mostly to the top valence band from 0 to 6 eV and s mostly contributes to the deep band below 12 eV, in excellent agreements with previous calculations [26]. We tested the convergence for the kinetic energy cutoff and k-point samplings. The changes in the band structure with more k-point samplings were negligible. The band gap of cubic phase is 2.35 eV. With larger kinetic energy cutoff of 29 Ry, the energy gap of cubic GaN saturated to 2.6 eV but no significant changes in the shape of the band structure were found. It is well known that the LDA underestimates the band gap. Better calculations using the GW approximation will simply enlarge the band gap for most wide band gap materials [27]. Graphitic GaN is also a semiconductor with an indirect band gap where the valence band maximum is located at H edge, as shown in Fig. 3(b). The indirect band gap is 2.78 eV, slightly larger than that of the cubic phase, and the direct band gap is 3.49 eV. This can be understood by the Coulomb repulsion between the increased π electrons at N sites above the plane.

Wrapping the graphitic sheet into nanotube will require an extra strain energy. The previous calculations show that this strain energy in forming GaN nanotubes is comparable to that of carbon nanotubes, suggesting the existence of the GaN as a form of nanotubes [24,28]. Figure 1(c)-(d) shows armchair (5,5) and zigzag (9,0) GaN nanotubes. Shown in Fig. 4 are the respective band structures along the tube axis. Here we follow the notation of GaN nanotubes similar to the notation employed for carbon nanotubes. There are two inequivalent atoms in the primitive cell of GaN system. We choose (5,5) armchair nanotube with two layers (20 atoms) and (9,0) zigzag nanotube with four layers (36 atoms). The respective diameters are 8.47 and 8.81 Å. The intertube distance is 4.5 Å. The band dispersion at this vacuum separation arising from tube interactions was found to be negligible. It is very interesting to see the differences in the band structures of armchair and zigzag nanotubes. Zigzag nanotubes have a direct band gap, whereas armchair nanotubes have an indirect band gap. The respective band gaps of (5,5) and (9,0) nanotubes are 2.15 and 2.16 eV. The changes in the band structures with more k-point samplings (16 k-points) were negligible. The va-

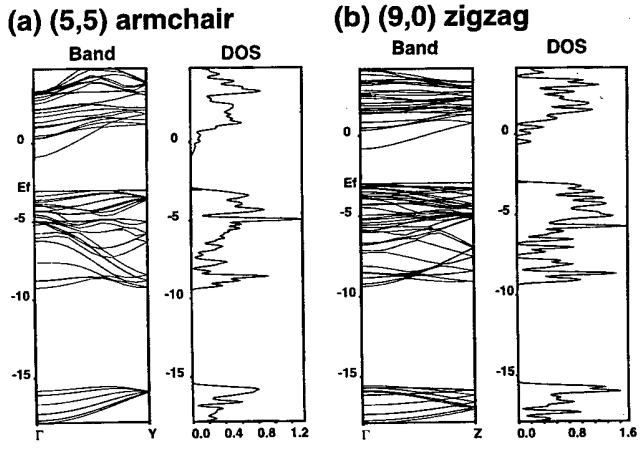

Fig. 4. Band structures along the tube axis and the corresponding density of states of (a) (5,5) GaN armchair nanotube and (b) (9,0) GaN zigzag nanotube. Y(Z) band edge corresponds to the symmetric point (0 0 1/2) $2\pi/a$ in the armchair nanotube (zigzag nanotube). The lattice constants along tube axis are a = 3.075 and 5.325 Å for armchair and zigzag nanotubes, respectively.

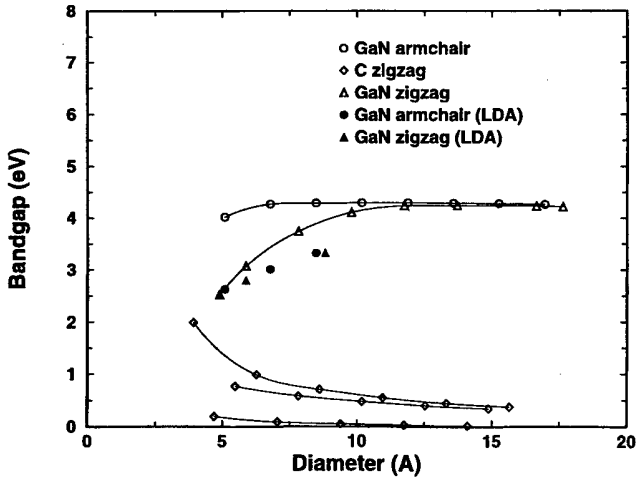

Fig. 5. Band gaps of GaN armchair and zigzag nanotubes as a function of the diameter using the SCC-DFTB and the LDA method. The open circles and open triangles are from the SCC-DFTB. The LDA results (filled circles and filled triangles) after scissor's operation by comparing the band gap of cubic phase from the LDA with that of experimental value are shown. The energy gap of carbon zigzag nanotubes (open diamonds) are also shown for comparison. The bottom curve shows the energy gap in the case of $n-m=3k$, where k is an integer. Two characteristic energy gaps are shown in carbon nanotubes as shown in the next curves.

Table 1. The values of effective mass for several GaN phases; zincblende, graphitic, and tube. The values in parentheses in zincblende are from Ref. 12. The terms, m_e^*, m_{hh}^*, m_{lh}^*, and m_{split}^* denote the electron, heavy hole, light hole, and (spin-orbit) split-off hole masses, respectively.

Structure	direction	m_e^*/m_0	m_{hh}^*/m_0	m_{lh}^*/m_0	m_{split}^*/m_0
Zincblende	Γ-X	0.17	1.09	1.09	0.17
		(0.17)	(0.86)	(0.86)	(0.17)
	Γ-K	0.33	9.54	1.06	0.15
		(0.17)	(≥ 2)	(0.84)	(0.15)
	Γ-L	0.18	3.53	3.53	0.18
		(0.18)	(1.74)	(1.74)	(0.15)
Graphitic	Γ-M	0.08	0.43	0.05	
	Γ-K	0.45	1.13	0.17	
Tube					
(3,3)	Γ-Y	0.29	0.91 (Y)		
			1.27 (Γ)		
(4,4)	Γ-Y	0.27	0.97 (Y)		
			1.72 (Γ)		
(5,5)	Γ-Y	0.16	0.98 (Y)		
			2.01 (Γ)		
(5,0)	Γ-Z	0.31	3.07		
(6,0)	Γ-Z	0.40	1.60		
(9,0)	Γ-Z	0.43	1.10		

lence band maximum of the armchair nanotube is located in the middle of the Γ-Y. The electronic density of states of both nanotubes are similar to each other.

In order to investigate the diameter dependence of the band gap, we performed the SCC-DFTB calculations for GaN nanotubes of different diameters. The relaxational changes in the atomic configurations were negligible and no buckling was observed, in contrast to BN-nanotubes [29]. The band gap changes slightly with the nanotube length. Therefore we fix the length of the nanotubes to 22 layers. We estimate the convergence of the energy gap dependence on the length of the nanotubes to be within 0.05 eV. Figure 5 shows the band gap for armchair and zigzag nanotubes. Unlike the alternating energy gap of carbon zigzag nanotubes (diamond shape) [24], the band gaps of GaN nanotubes decrease monotonically with the decreasing diameter. The energy gap of (n, n) GaN nanotubes decrease slightly with decreasing the diameter, whereas that of (n, 0) GaN nanotubes decreases significantly with the decreasing diameter. The energy gap converges to the value of the graphitic sheet at large diameter. This decrease of the band gap simply reflects the ionic bonding character, *i.e.* s and p bands localized to Ga and N respectively are well separated [26]. Wrapping of the graphitic sheet to tubes enhances the rehybridization more seriously in zigzag nanotubes than in armchair nanotubes as the diameter decreases. More p states near the valence band edge and more s states near the conduction band edge are developed at smaller diameter of zigzag nanotubes, as can be seen from the density of states of tubes in different diameters [24].

Our plane-wave DFT-LDA calculations give a energy gap of 2.35 eV for the cubic phase [30], underestimating the experimental value of 3.52 eV [21] by 1.17 eV. The energy gap of the cubic GaN from the LDA in our calculations is 2.35 eV [31], underestimating the experimental value of 3.52 eV [21] by 1.17 eV. It is well known that the LDA approach underestimates the band gap. More sophisticated calculations using GW approximation reproduces the experimental band gap more correctly. For most semiconductors, the scissors operation, simply shifting the band gap, can be applied to predict correct band gap [32,33]. One may estimate approximate band gap in the GaN nanotubes at infinite diameter. Values of the band gap with correction from the LDA calculations are also shown in Fig. 5. The band gap of graphitic sheet is 2.78 eV. The scissors operation [32,33] gives the corrected band gap of nanotubes at infinite diameter (or equivalently graphitic sheet) of approximately 3.95 eV. We note that energy gaps can be tailored by varying the diameter. This suggests that ultimate nanoscale full color displays can be realized using GaN nanotubes.

We also calculate effective masses of several GaN phases, as shown in Table 1. Our calculations for zincblende phase show good agreement with the previous first principles calculations except electron effective mass at K edge and hole effective mass at L edge [12]. Relatively large errors exist in evaluating the heavy-hole effective masses due to the ambiguity of determining the range of wave vectors which are valid within the effective mass ap-

proximation. The electron effective masses decrease with increasing diameter in armchair tubes, whereas they increase with increasing diameters in zigzag tubes. On the other hand, the hole effective masses behave completely in opposite way, *i.e.*, the hole effective masses increase with increasing diameters in armchair tubes, whereas they decrease with increasing diameters in zigzag tubes.

IV. SUMMARY

We have performed density-functional calculations to investigate electronic structures of GaN nanotubes. The calculations for the total energy reveal that GaN nanotubes are stable and may be formed under some extreme conditions. The energy gap decreases with the decreasing diameter, enabling band gap engineering. The estimated band gap of the GaN nanotubes at infinite diameter is approximately 3.95 eV, which is 0.43 eV larger than that of cubic GaN phase. This strongly suggests that ultimate nanoscale optoelectronic devices for full color displays may be realized with sophisticated modern synthesis techniques. The effective masses of several GaN phases are also calculated.

We acknowledge the financial support by the Korea Science and Engineering Foundation through the Semiconductor Physics Research Center at Jeonbuk National University. We thank J. H. Yoon at TMSI Korea for technical support.

REFERENCES

[1] S. Iijima and T. Ichihashi, Nature **363**, 603 (1993).
[2] A. Thess, R. Lee, P. Nikolaev, H. Dai, P. Petit, J. Robert, C. Xu, Y. H. Lee, S. G. Kim, D. T. Colbert, G. Scuseria, D. Tománek, J. E. Fisher and R. E. Smalley, Science **273**, 483 (1996).
[3] T. Guo, P. Nikolaev, A. Thess, D. T. Colbert and R. E. Smalley, Chem. Phys. Lett. **243**, 49 (1995).
[4] M. Terrones, N. Grobert, J. Olivares, J. P. Zhang, H. Terrones, K. Kordatos, W. K. Hsu, J. P. Hare, P. D. Townsend, K. Prassides, A. K. Cheetham, H. W. Kroto and D. R. M. Walton, Nature **388**, 52 (1997).
[5] N. Hamada, S. Sawada and A. Oshiyama, Phys. Rev. Lett. **68**, 1579 (1992).
[6] J. W. Mintmire *et al.*, Phys. Rev. Lett. **68**, 631 (1992).
[7] We follow the notation by M. S. Dresselhaus, G. Dresselhaus and P. C. Eklund, *Science of Fullerenes and Carbon Nanotubes* (Academic Press Inc., San Diego, 1996), Chap. 19.
[8] D.-H. Oh and Y. H. Lee, Phys. Rev. **B58** (1998).
[9] W. A. de Heer, A. Chatelain and D. Ugarte, Science **270**, 1179 (1995).
[10] A. G. Rinzler, J. H. Hafner, P. Nikolaev, L. Lou, S. G. Kim, D. Tománek, P. Nordlander, D. T. Colbert and R. E. Smalley, Science **269**, 1550 (1995).
[11] S. Nakamura, T. Mukai and M. Senoh, Appl. Phys. Lett. **64**, 1687 (1994).
[12] For a general review, see, for instance, *Semiconductors and Semimetals*, Eds. J. I. Pankove and T. Moutakas (Academic Press, New York, 1998), Vol. 50.
[13] A. Loiseau, F. Willaime, N. Demoncy, G. Hug and H. Pascard, Phys. Rev. Lett. **76**, 4737 (1996).
[14] K. Suenaga, C. Colliex, N. Demoncy, A. Loiseau, H. Pascard and F. Willaime, Science **278**, 653 (1997).
[15] This method is implemented in the CASTEP code which is a registered software product of Molecular Simulations Inc.
[16] N. Troullier and J. L. Martins, Phys. Rev. **B43**, 1993 (1991).
[17] L. Kleinman and D. M. Bylander, Phys. Rev. Lett. **48**, 1425 (1982).
[18] J. P. Perdew and A. Zunger, Phys. Rev. **B23**, 5048 (1981).
[19] M. Elstner, D. Porezag, M. Haugk, J. Elsner, G. Jungnickel, G. Seifert and S. Suhai, Phys. Rev. **B58**, 7260 (1998).
[20] T. Lei, T. D. Moustakas, R. J. Graham, Y. He and S. J. Berkowitz, J. Appl. Phys. **71**, 4933 (1992); R. C. Powell *et al.*, J. Appl. Phys. **73**, 189 (1993).
[21] S. Strite, J. Ruan, Z. Li, A. Salvador, H. Chen, D. J. Smith, W. J. Choyke and H. Morkoc, J. Vac. Sci. Technol. **B9**, 192 (1991).
[22] J. W. Trainor and K. Rose, J. Electron. Mater. **3**, 821 (1974).
[23] K. Miwa and A. Fukumoto, Phys. Rev. **B48**, 7897 (1993).
[24] S. M. Lee and Y. H. Lee, unpublished.
[25] H. J. Monkhorst and J. D. Pack, Phys. Rev. **B13**, 5188 (1976).
[26] T. Yamamoto and H. K. Yoshida, Jpn. J. Appl. Phys. **36**, L180 (1997).
[27] M. Rohlfing, P. Krüger and J. Pollmann, Phys. Rev. **B48**, 17791 (1993).
[28] S. M. Lee, Y. H. Lee, Y. G. Hwang, J. Elsner, D. Porezag and T. Frauenheim, Mater. Res. Soc. Proc. (1998).
[29] A. Rubio, J. L. Corkill and M. L. Cohen, Phys. Rev. **B49**, 508 (1994).
[30] We tested the convergence for kinetic energy cutoff and k-point samplings. With larger kinetic energy of 29 Ry, the E_g of cubic GaN saturates to 2.60 eV. The changes with more k-point samplings (16 k-points) were negligible.
[31] The band gap of cubic phase becomes wider with larger energy cutoff. For instance, the band gap is enlarged by 0.25 eV with the energy cutoff of 26 Ry.
[32] M. Palummo, L. Reining, R. W. Godby and C. M. Bertoni, *Proc. 21st Conference on the Physics of Semiconductors*, Beijing, Aug. 1992, Eds. Ping Jiang and Hou-Zhi Zheng (World Scientific, Singapore, 1993), p. 89.
[33] X. Blase, A. Rubio, S. G. Louie and M. L. Cohen, Phys. Rev. Lett. **51**, 6868 (1995).

Journal of the Korean Physical Society, Vol. 34, June 1999, pp. S258~S260

Polytypism in Silicon Carbide

S. I. VLASKINA
Institute of Semiconductor Physics, Ukrainian Academy of Science
45 Prospect Nauki, Kiev-28, 252650, Ukraine

D. H. SHIN
Department of Physics, Dongguk University, Seoul 100-715

The process of polytype formation in silicon carbide has been studied under identical conditions excluding the influence of temperature, impurity and pressure. Fundamental research of SiC film growth by modified Lely process, by CVD, by PECVD and phase transformation show that the stoichiometric violation influences considerably on the formation of polytypes. The prevalence or availability of Si always promotes the formation and growth of cubic SiC.

I. INTRODUCTION

Silicon carbide is an excellent semiconductor material for high power, high frequency, and high temperature devices. However, the reason for the occurrence of many different polytypes and the process of formation of each polytype as well as the conditions for the transformation between them have not been understood yet. More than 250 polytypes is known to exist. The only one cubic structure is known as β-SiC or 3C-SiC. The hexagonal wurtzite bonding in combination with the cubic zinc blende forms the hexagonal and rhombohedral silicon carbide structures known as α-SiC (6H-SiC is most well known). How can we control polytype growth? What is the reason for polytype formation? Some authors think that the presence of impurity influences the polytype formation. Others think that pressure, speed of growth, or temperature influence the polytype formation [1–3].

We have made the experiments in order to study the process of polytype formation under identical conditions after excluding the influence of temperature, impurity and pressure.

II. EXPERIMENT

The sublimation Lely [4] method and Tairov [5] method are used for manufacturing large bulk silicon carbide single crystals today. As the first step, we studied epilayers because it is not necessary to have thick bulk crystal for SiC based devices and epilayers with thickness about 20~30 μm are more than enough for this research. Two main conditions are necessary for the growth of SiC films with quality very close to that of single crystal. The first is the presence of temperature gradient for mass transportation. The second is the presence of SiC vapor.

In order to realize these conditions, a high temperature vacuum apparatus has been designed. The temperature range of 1870~2270 K needed for the epitaxial growth could be achieved by a resistively heated furnace. The growth crucible was made from vacuum-tight graphite (Fig. 1(a), part 6) and consists of susceptors made from graphite (part 4) coated with SiC, polycrystalline SiC shelves (part 2), and polycrystalline SiC powder (part 1) obtained by Achesson's method (source material). At high temperature the source material diffused through the crucible to the surface of SiC substrate (part 5) which has lower temperature in comparison with the source material. Films were grown at temperatures of 1870~2270

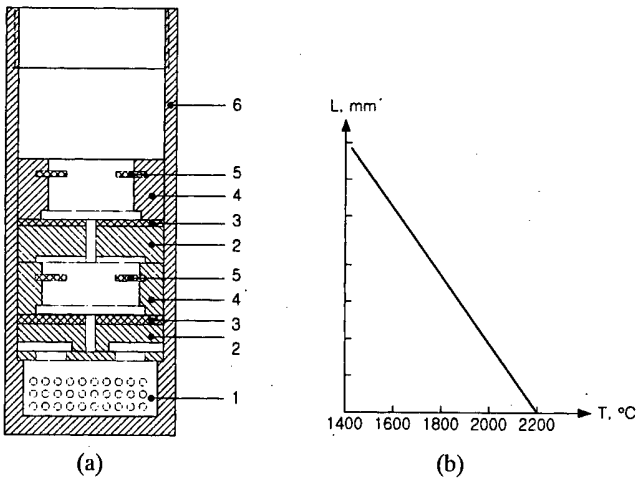

Fig. 1. Schematic design of the growth crucible. (a) 1. SiC powder, 2. SiC shelves, 3. SiC cover, 4. Graphite coating, 5. SiC substrate, 6. Vacuum-tight graphite, (b) Distribution of temperature along the crucible.

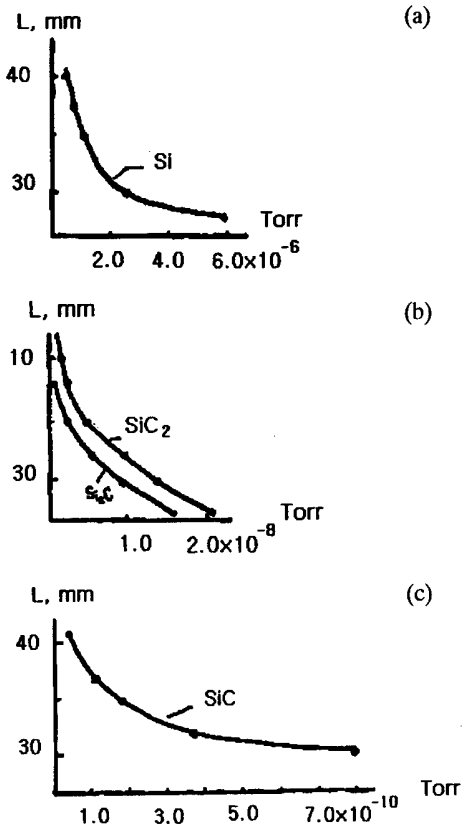

Fig. 2. Distribution of Si_2C, SiC_2, Si and SiC partial pressures along the crucible.

K at pressure of about 1.13×10^{-3} Pa. Shelves have a shape that allows obtaining temperature gradient along substrates surface. Different temperatures on the same substrate in the same conditions allowed investigation of the process of crystal growth on one substrate beginning from the initial stage of the film formation. Film structure was examined by electron diffraction on the initial growth surface. Electron diffraction analysis shows that if conditions are suitable for film growth, SiC films are single crystalline.

Film structure strongly depends on the Si vapor. On Fig. 2(a), (b), and (c), the dependence of vapor pressures along the length of the crucible are shown for 3C-SiC epilayers. Presence of Si stimulated formation and growth of cubic phase of SiC.

Defects had been studied by transmission electron microscopy after thinning using Ar ion beam. For a more precise thinning of specified spots of the samples, a foil edge thinning technique was used. On Fig. 3(a), a typical interface defect is shown—thin layer of two different polytypes parallel to the surface, which are 6H-SiC and 3C-SiC, respectively. Thickness of these layers range from a few hundred angstroms to several micrometers depending on the condition of growth. Two types of dislocation are found on the film-substrate boundary—dislocations that are parallel to the interface and dislocations that are perpendicular to the interface. Density of these dislocations near the substrate is about 10^8 cm^{-2} and decreases when thickness is increased. Investigation of the intermediate layer between 6H substrate and the 3C film shows that there exist many multi-layer structures. So, we investigated film growth very carefully and discovered that Si presence is responsible for 3C-SiC single crystalline film growth.

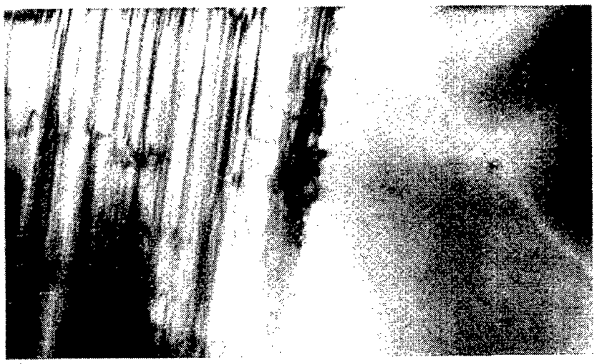

Fig. 3. Micrograph of the foil from SiC-SiC interface interface with 6H- and 3C-SiC epitaxial layers at 5000X.

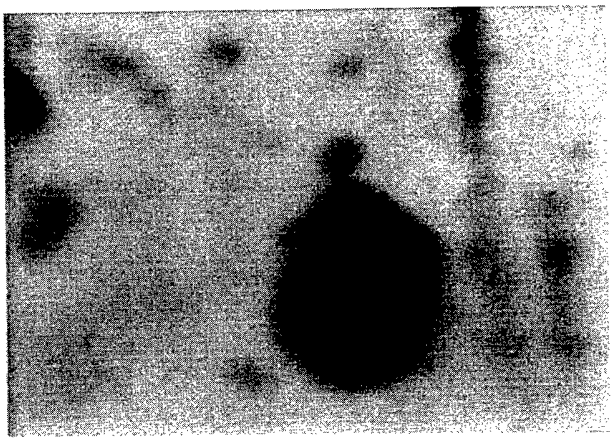

Fig. 4. Surface of etched 6H-SiC crystal with traces of evaporation X300.

For more experiments, we etched 6H-SiC crystal and deposited SiC films on this surface. Fig. 4 shows the surface SEM micrograph of 6H-SIC crystal with traces of evaporation. Optical micrograph of the nucleus formation is shown in Fig. 5. The advantage of color optical micrographs permits clear demonstration and easy identification of SiC polytypes-green for the hexagonal structure and yellow for the cubic structure. The ratio of Si to C is broken inside the etched holes because of Si evaporation. Only α-SiC crystallites are formed inside the etched holes where the supply of Si atoms is insufficient. The growth of the 3C-SiC crystallites are observed only on the edges and boundaries of the etched holes, where liquid phase Si is present in the initial stage of growth.

For better understanding of this process, special cru-

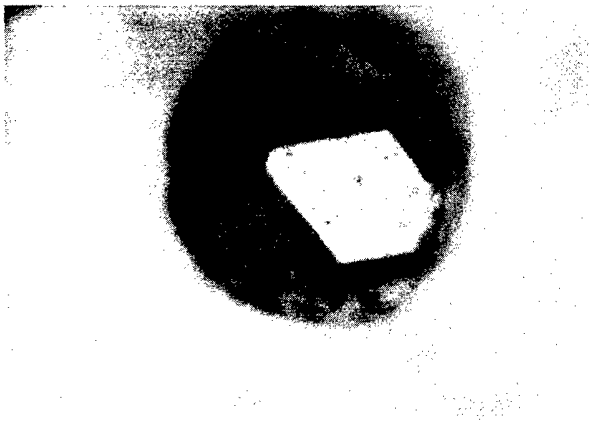

Fig. 5. Optical micrograph of nucleus formation; (a) 3C-SiC grown at the edge of the etched hole (b) 6H-SiC grown inside the etched hole.

cible has been built. Heavily nitrogen doped green 6H-SiC crystals were annealed at 1500~2500 K temperature in the presence of Si vapor in vacuum crucible. X-ray diffraction analysis of annealed crystal shows that new polytypes different from 6H-SiC appear. Together with 6H-SiC reflections, reflections from polytypes with n_c larger than 30 (n_c is the number of bilayers along c-axis) and from 3C-SiC appear. Crystal structure of samples after 60 min annealing at 2180 K was completely 3C-SiC. Photoluminescence spectra of 6H-SiC crystal before and after annealing are shown in Fig. 6. Curve 1 is typical of 6H-SiC photoluminescence. Curve 3 is typical of 3C-SiC photoluminescence. Photoluminescence at 2.3~2.5 eV in curve 2 is an evidence of the intermediate phases with some stacking defects.

This result indicates that transformation from 6H- to 3C-SiC takes place and is going on with the appearance of multylayer structures. This result confirms previous results that Si has significant influence on the stabilization of 3C-SiC not only in the case of film growth but also in the transformation between polytypes.

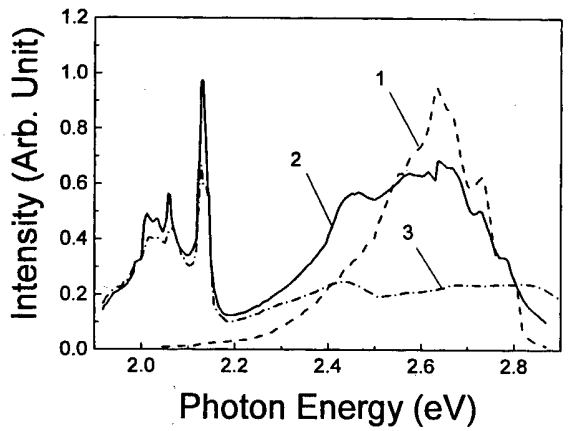

Fig. 6. Photoluminescence spectra of 6H-SiC before and after annealing.

As the next step, heavily doped 6H-SiC crystals were annealed in the presence of carbon and without Si in vapor phase. After annealing, the crystals changed color from dark green to colorless. As is well known, the green color of SiC is due to nitrogen in the crystal volume. The colorlessness of the annealed crystals shows the possibility of cleaning process in the crystals. Hall effect measurement was made at 77~1000 K. After annealing, the crystals were n-type, but free carrier concentration has decreased from 10^{18}~10^{19} cm^{-3} to 10^{15}~10^{16} cm^{-3} and free carrier mobility was increased from 40~60 to 100~200 $cm^2/V{\cdot}s$.

At this condition Si atoms sublimate from surface. This causes Si atoms to diffuse from volume to the surface resulting in Si vacancies in the bulk. Some 6H-SiC was transformed to 4H-SiC and even to 2H-SiC after annealing in the absence of Si and SiC vapor. This result is consistent with the result from the investigation of the initial stage of SiC crystal growth. Fundamental research of SiC on Si grown by CVD and PECVD methods show that only 3C-SiC polytipes are grown on Si substrate [6].

III. CONCLUSIONS

The set of received results show that stoichiometry has a considerable influence on the formation of SiC polytypes. The prevalence or availability of Si vapor always promotes the formation of 3C-SiC while the absence of Si vapor promotes the formation of 6H-SiC. The change of vacancy concentration in the underlattice of Si or C causes the change of lattice parameters. Thus, the phase transformation in SiC happens through infringement of stoichiometry. The process of 3C-SiC film growth on Si substrate by different methods is an indirect confirmation of this result.

REFERENCES

[1] A. J. Verma and P. Krishna, *Polymorphism and Polytypism in Crystals* (Wiley, New York, 1966).

[2] A. Y. Hayashi, Min. Soc. Japan **4**, 363 (1960).

[3] W. F. Knippenberg and G. Verspui, "The influence of impurities on silicon carbide crystals grown by gas-phase reaction", Proc. Int. Conf. on Silicon Carbide, Univ. Park, Materials. Res. Bull., 4, pp. 33-44 (1968, 1969).

[4] A. Lely, Ber. Disch. Keram. Ges. **32**, 229 (1995).

[5] Yu M. Tairov, "Crystal Growth of Bulk SiC", in *Silicon Carbide and Related Materials 1995* (Institute of Physics Publishing, London, 1996), p. 11.

[6] H. Matsunami, "Recent progress in epitaxial growth of SiC", in *Amorphous and Crystalline Silicon Carbide IV*, C. Y. Tang, M. M. Rahman and G. L. Harris, eds. (Springer-Verlah, Berlin, 1992).

Journal of the Korean Physical Society, Vol. 34, June 1999, pp. S261~S264

Admittance Spectroscopy of Mg-doped GaN Grown by Molecular Beam Epitaxy Using RF Nitrogen Sources

D. J. KIM, D. Y. RYU and K. H. KIM

School of Materials Engineering, Chungnam National University, Taejon 305-764

N. A. BOJARCZUK, J. KARASINSKI and S. GUHA

IBM Research Division, Yorktown Heights, New York 10598, U.S.A.

H. G. LEE

School of Electronic and Electrical Engineering, Chungbuk National University, Chungjoo 360-763

Thermal activation energies of Mg in GaN grown using RF nitrogen source with varying Mg flux were examined using an admittance spectroscopy technique. There was no noticeable difference or trend in the activation energy with varying Mg flux. The thermal activation energy for GaN:Mg was ~115 meV under the investigated Mg flux range. Negligible persistent photo-conductivity and yellow luminescence peak in PL observed in the samples suggest possible reduction of the thermal activation energies compared to the values in the literature.

I. INTRODUCTION

Magnesium has been the commonly used p-type dopant for GaN growth by molecular beam epitaxy (MBE) and metal-organic chemical vapor deposition (MOCVD). While the control of p-doping in GaN has been one of the key issues in the growth of GaN based devices, the thermal activation energy of Mg becomes an important parameter in evaluating the performance of the doping process. Many of the investigations of the thermal activation energy for Mg have determined it as 150~160 meV for both MOCVD and MBE grown GaN:Mg structures [1–5]. Tanaka *et al.* [5] particularly observed different thermal activation energies on differently doped GaN:Mg grown by MOCVD technique. Investigation of dopant activation in MBE grown Mg-doped GaN structures, however, have been limited to a few cases [3,4] with the measurement technique being limited only to the Hall effect measurement. Furthermore, as far as the authors know, any examination of GaN:Mg grown using RF nitrogen source has not been reported.

Li *et al.* [6] observed persistent photo-conductivity (PPC) phenomena for GaN:Mg structures grown by MBE and by MOCVD. They suggested that the PPC phenomenon is related with a lattice relaxation or metastability [6,7] associated with Mg impurities. The phenomenon, however, may be related to an intrinsic deep level impurity which also causes the yellow luminescence [8]. The explanation for the origin of the PPC seems scattering in the literature as such and that indicates possible process dependence of the signature of the impurities and/or defects in GaN. We report thermal activation energies measured by an admittance spectroscopy technique on a series of differently doped GaN:Mg layers grown via MBE using a RF nitrogen source.

II. EXPERIMENTAL

A series of GaN:Mg film was grown with varying Mg flux. Samples were grown using a RF nitrogen source at a fixed substrate temperature of ~750 °C on sapphire (0001) substrate. Details for the growth procedure is described in Ref. 9. The employed Mg cell temperatures and measured hole concentrations at room temperature are summarized in Table 1. For the GaN:Mg samples examined in this study, the Mg concentration (measured by SIMS) [9] was limited to $\sim 2\times10^{19}$ cm^{-3} regardless of the Mg flux under the investigated range.

Admittance [10,11] of a junction is expressed by an equivalent circuit of a parallel connection of conductance and capacitance components, $Y(\omega,T) = G(\omega,T) + j\omega C(\omega,T)$, where G is conductance and C is capacitance. The values of C and G depend on the angular frequency (ω) of the test ac-signal and the sample temperature (T). It has been routinely accepted [11,12] that the trap emission kinetics, for the acceptor doping case, is described

Table 1. Summary of the experiments and results. Free hole concentrations due to Hall effect measurements are for the room temperature. Thermal activation energies and the capture cross-section parameters are from the best fit of the admittance spectroscopy measurements assuming temperature independence of σ. The acceptor concentrations were estimated from the high temperature capacitance value at frequency 10 kHz.

Sample	Mg cell Temp. (°C)	SIMS Conc. (10^{19} cm^{-3}).	Hole Conc. (10^{17} cm^{-3})	ΔE_T (meV)	σ (10^{-20} cm^{-2})	N_A (10^{18} cm^{-3})
72	280		0.5	119 (±5)	2.6	~0.8
74	280		0.8	111 (±2)	4.4	~1.7
54	345	~2	1.2	118 (±3)	18	~1.5
55	390		0.9	113 (±4)	30	~0.7

by

$$e_h = \sigma v_{th} N_v \exp(-\Delta E_T/kT), \quad (1)$$

where e_h is the hole emission rate, σ is the capture cross-section that may or may not depend on temperature, v_{th} is the thermal velocity of holes, N_v is the valence band effective density of states, ΔE_T is the free energy change for ionization or $|E_v - E_T|$, k is the Boltzmann constant, and T is the absolute temperature. At high enough temperatures (or low frequencies) the trap responds to the test signal and thus $C(\omega, T)$ comprises the contribution from the emitted trap carriers. However, at low enough temperatures (or high frequencies) the trap cannot respond to the test signal and thus cannot contribute to $C(\omega, T)$. As a consequence, the over-all feature of the capacitance curve measured at a given frequency (say $\omega_1 = 2\pi f_1$) with varying temperature shows a transition going from the high temperature plateau down to the low temperature one as will be shown in Fig. 1. Since the transition occurs when the characteristic angular frequency coincides with the trap emission rate ($\omega_1 = e_{\eta 1}$), a pair of the transition temperature T_1 and the emission rate $e_{\eta 1}$ can be uniquely determined. For the conductance, an opposite trend shows and the curve normalized to the test frequency (G/ω) shows a peak at the transition temperature (Fig. 1). Thus by measuring the transition temperatures at various test frequencies, a series of transition temperatures can be obtained for a given sample. Now by noting that $v_{th} N_v \sim T^2$ in Eq. (1), one obtains ΔE_T from the slope in the plot of $\ln(e_h/T^2)$ vs. $1/T$ when a temperature independent σ is assumed, as will be shown in Fig. 2.

Admittance spectroscopy measurements were carried out using Ti/Au for Schottky contacts [13] and Ni/Au for ohmic contacts [14]. Square Schottky diodes were patterned in a square dot-and-ring geometry with an area of 260×260 μm^2. Capacitance and conductance are measured on selected devices showing low reverse-bias leakage currents through current-voltage measurements. HP4284A precision LCR meter was used for the measurements under zero gate bias voltage with 20 mV rms value for the small-signal. The small signal frequencies and the substrate temperatures were varied in the ranges of 100 Hz ~ 1 MHz and 100~450 K, respectively. The hole concentrations were measured by Hall effect measurement technique using In or Ni/Au ohmic contacts on Van der Pauw geometry. Photoluminescence was measured using

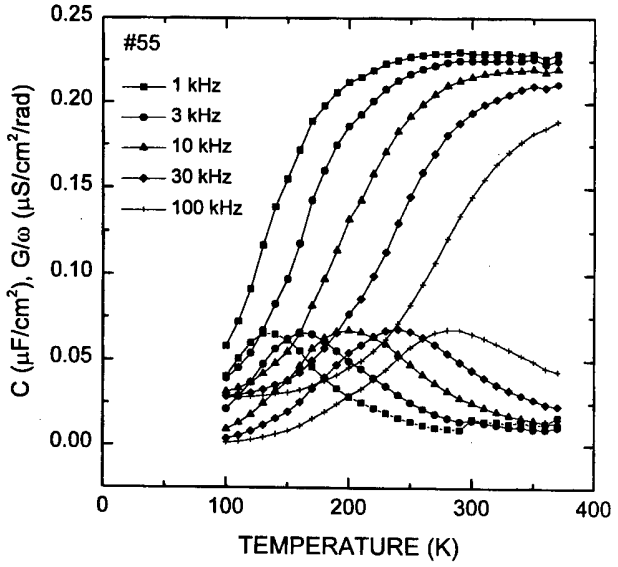

Fig. 1. Admittance spectroscopy measurement result for sample 55.

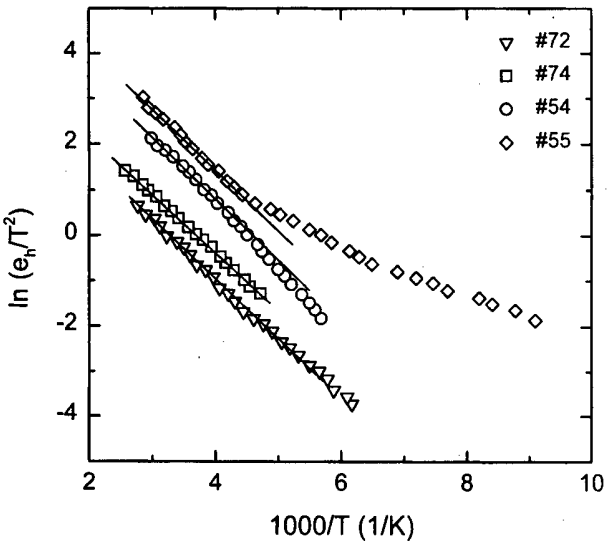

Fig. 2. $\ln(e_h/T^2)$ vs. $1/T$ plot.

He-Cd laser at 14.2 K.

III. RESULTS AND DISCUSSION

The hole concentrations measured by Hall effect were limited to $\sim 10^{17}$ cm^{-3} at room temperature. As summarized in Table 1, it was not observed a clear trend in the free carrier concentrations with varying Mg flux. Since the atomic concentration of Mg in GaN is $\sim 2\times 10^{19}$ cm^{-2} as measured by SIMS [9], less than $\sim$0.5 % of the incorporated Mg atoms have been activated. This kind of very small hole concentration ratio with respect to the chemical concentration was also observed in MBE grown structures employing ammonia [4].

Fig. 1 shows an example of the measured admittance spectroscopy curves for sample 55. Only a part of the curves, measured at 1, 3, 10, 30, and 100 kHz, were plotted for clarity. The capacitance values are normalized to the junction area and the conductance values are normalized both to the junction area and to the angular frequencies. For all the samples, well-defined smooth curves were obtained and only one energy level was detected. The transition temperature at each small-signal frequency was read from the peaks of the conductance curves.

A plot of $\ln(e_h/T^2)$ vs. $1/T$ to obtain the thermal activation energy is shown in Fig. 2. It is not clear at present for the smaller slope observed at low frequencies for sample 55. The thermal activation energies obtained through best linear fit at above $\sim$200 K are 111$\sim$119 meV for the samples as summarized in Table 1. The capture cross-sections are determined to be $3\sim 30\times 10^{-20}$ cm^{-2}. The very small capture cross-section values manifest that the acceptor level is very repulsive [15]. There was no definite trend in the change of the activation energies with Mg flux variation. The average activation energy is $\sim$115 meV for the samples grown with a RF nitrogen source in MBE system. The obtained thermal activation energies are rather smaller than what has been observed by earlier workers. Thus far, as far as the authors know, the smallest activation energies were $\sim$125 meV in MBE [16] and MOCVD [17] grown GaN:Mg structures. However, the measurement techniques may result in different ionization energies and need to be explored.

We observed a couple of distinguished aspects in all the samples. First, no remarkable PPC effect, which has been observed in MBE and MOCVD grown GaN:Mg structures [6], was observed. Second, the samples did not show noticeable yellow luminescence peak near 560 nm as exemplified in Fig. 3. It was reported that the impurities causing the yellow luminescence also induce the PPC effect in GaN [8]. This observation was, however, on undoped GaN structure, and thus is not related with Mg doping. Our observation, negligible PPC effect and yellow luminescence then may mean that the samples have negligible donor-related impurities relevant to

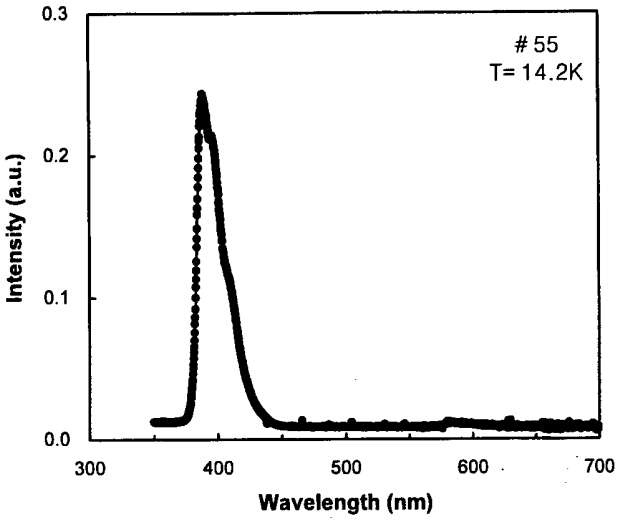

Fig. 3. Photoluminescence measurement for sample 55.

the phenomena. This result suggests that the configuration of the impurities in the lattice, including donors and acceptors, strongly depend on the growth method and the detail processes. Using RF source for activation of nitrogen may create the difference. It is clear that, whatever the origin of the phenomena, our samples will show nil activation energy for capture process and accordingly smaller activation energy for the emission process. This unique aspect of the RF source grown samples may results in the observation of smaller activation energies in the admittance spectroscopy measurements.

The carrier concentrations measured by the Hall effect is the equilibrium value, but those inducing the capacitance depends on the emission-and-capture kinetics. At high temperatures and at low frequencies the acceptors fully respond to the test signal, thus the modulated carrier concentration approach to the acceptor concentration. Thus estimated acceptor concentrations from the measured capacitance values at 350 K at 10 kHz are summarized in Table 1. They are $\sim 10^{18}$ cm^{-3}. This calculation indicates that less than 10 % of the atomic Mg acts as acceptors. Kim *et al.* [4] suggested that the remaining Mg segregate to crystalline defects such as threading dislocations.

IV. CONCLUSIONS

We grew a series of GaN:Mg structures in a MBE system using RF nitrogen source with varying Mg flux. The thermal activation energies are measured by admittance spectroscopy technique and determined to be $\sim$115 meV. This is a value smaller than that measured in other MBE and MOCVD grown GaN:Mg structures. This may be due to nil capture barrier energy, as evidenced by negligible persistent photo-conductivity effect, in the particular samples grown using RF source. There was not clear

trend in the activation energies with varying Mg flux in the investigated flux range.

ACKNOWLEDGMENTS

One of the authors (D.J.K) acknowledges support from the University Research Program of MIC and from the Academic Research Fund for Semiconductors (ISRC 96-E-1057)

REFERENCES

[1] H. Nakayama, P. Hacke and M. R. H. Khan, Jpn. J. Appl. Phys. **35**, L282 (1996).
[2] W. Gotz, N. M. Johnson, D. P. Bour, C. Chen, H. Liu, C. Kuo and W. Imler, Mat. Res. Soc. Symp. Proc. **395**, 443 (1996).
[3] T. D. Moustakas and R. J. Molnar, Mat. Res. Soc. Symp. Proc. **281**, 753 (1993).
[4] W. Kim, A. Salvador, A. E. Botchkarev, O. Atkas, S. N. Mohammad and H. Morcoc, Appl. Phys. Lett. **69**, 559 (1996).
[5] T. Tanaka, A. Watanabe, H. Amano, Y. Kobayashi, I. Akasaki, S. Yamazaki and M. Koike, Appl. Phys. Lett. **65**, 593 (1994).
[6] J. Z. Li, J. Y. Lin, H. X. Jiang, A. Salvador, A. Botchkarev and H. Morkoc, Appl. Phys. Lett. **69**, 1474 (1996).
[7] C. Johnson, J. Y. Lin, H. X. Jiang, M. Asif Khan and C. J. Sun, Appl. Phys. Lett. **68**, 1808 (1996).
[8] C.V. Reddy, K. Balakrishnan, H. Okumura and S. Yoshida, Appl. Phys. Lett. **73**, 244 (1998).
[9] S. Guha, N. A. Bojarczuk and F. Cardone, Appl. Phys. Lett. **71**, 1685 (1997).
[10] D. L. Losee, J. Appl. Phys. **46**, 2204 (1975).
[11] J. W. Huang, T. F. Kuech, H. Lu and I. Bhat, Appl. Phys. Lett. **68**, 2392 (1996).
[12] P. Blood and J. W. Orton, *The Electrical Characterization of Semiconductors: Majority Carriers and Electron States* (Academic Press, London, 1992), p. 339.
[13] M. Asif Khan, J. N. Kuznia, D. T. Olson, M. Blasingame and A. R. Bhattarai, Appl. Phys. Lett. **63**, 2455 (1993).
[14] S. Guha and N. A. Bojarczuk, Appl. Phys. Lett. **72**, 415 (1998).
[15] M. Lax, Phys. Rev. **119**, 1502 (1960).
[16] T. W. Kang, S. H. Park, H. Song, T. W. Kim, G. S. Yoon and C. O. Kim, J. Appl. Phys. **84**, 2082 (1998).
[17] J. W. Huang, T. F. Kuech, H. Lu and I. Bhat, Appl. Phys. Lett. **68**, 2392 (1996).

Journal of the Korean Physical Society, Vol. 34, June 1999, pp. S265~S267

A New Annealing Technique for Semiconductor Layers in Si MOS Transistors

Takashi NOGUCHI

Research Center, Sony Corporation, Yokohama-shi, Japan

A new technique for annealing semiconductor layers in Si MOS transistors is reported. Thermal annealing using a furnace reactor, a lamp, and a UV (Ultra Violet) pulse beam has been studied in order to form a source and drain with shallow junction in MOS transistors, to activate a poly-SiGe gate in low voltage MOS driving, and to improve the silicon channel in poly-Si TFTs (Thin Film Transistors). The ELA (Excimer Laser Annealing) with high absorption for silicon layers in the UV (Ultra-Violet) region is a promising new RTA (Rapid Thermal Annealing) process and should be developed for use with next generation Si LSIs.

I. THE STATE-OF-THE-ART PROCESS FOR ANNEALING SI LAYERS IN MOS TRANSISTORS

0.1 μm transistors have been studied extensively as they will play a leading role in ULSI's in the next century [1]. To realize ultra-small devices, ultra-shallow junctions for source and drain (S/D) are essential in order to suppress short channel effects. RTA using a lamp and conventional Furnace Annealing (FA) are common procedures but they cannot sufficiently activate impurities with little diffusion. Single shot of ELA is a candidate for overcoming this difficulty [2]. Multiple excimer-laser pulses used in gas immersion laser doping (GILD) [3] or with a pre-deposited dopant [4] is also a promising procedure when optimization of the pulse energy and shot number can be used to control the junction depth.

For an MOS gate under low-voltage driving, precise control of the thereshold voltage is important for CMOS transistors. In order to maintain current drivability without modifying the channel concentration, new gate materials with an adjustable work function within the bandgap of poly-Si are required to replace poly-Si gate for CMOS and SOI (Silicon On Insulator) transistors with a channel length less than 0.18 μm. Poly-SiGe film of narrow band-gap activated efficiently in p-type is a candidate for the new gate materials, as the films should be compatible with the conventional Si process. There have been several reports of these films being applied to MOS gates [5,6].

Research on TFTs (Thin Film Transistors) has been undertaken for application to to LCDs (Liquid Crystal Displays) and to SRAM (Static Random Access Memory) [7,8]. It has been reported that grains smaller than the channel size allow for uniform TFT characteristics [9], although carrier mobility is reduced. While high temperature annealing can improve the electronic properties of poly-Si films, ELA heating Si films up to melting point of Si is considered to be an advanced RTA process for an improvement of poly-Si [10] as it has no thermal effect on the underlying substrate and devices [11].

Furthermore, in order to realize the system on glass or SOI, such as a high-performance LSI on an arbitral substrate, some promising results have been reported adopting SPC (Solid Phase Crystallization) and ELA [12–16].

II. A NEW ANNEALING PROCESS FOR SI MOS TRANSISTORS

1. Shallow-junction Annealing for Short-channel Transistors

The absorption coefficient in amorphous and crystalline Si in the UV region is high and its absorption depth is about 7 nm [11]. Therefore, the pulse beam energy of an XeCl excimer laser (308 nm) is absorbed in a shallow region in Si and only the surface is heated to a temperature near the melting point for a very short time.

As^+ or BF_2^+ ions are implanted on Si wafers at 5 keV and $3\times10^{15}/cm^2$ before ELA. For a Si layer capped with SiO_2 for anti-reflection, a pulsed beam of an excimer laser, its shape controlled by an optical homogenizer or lamp with RTA less than 900 °C, was irradiated. There is an distinct difference in sheet resistance between ELA and RTA. For ELA with a pulse energy of less than 0.95 J/cm^2, sheet resistance less than 200 ohm/sq. was obtained while keeping the junction depth shallower than 50 nm [17].

A transistor process for a 0.1 μm channel was developed by adopting single-shot ELA. Excellent transistor characteristics with a gate voltage swing of less than 90

mV/dec, a low leakage current (about 10^{-12} A/μm) and a high on/off ratio of more than 10^7 were obtained [18].

2. Gate Activation for Low Voltage Driving

Sintered solid SiGe target were prepared from Si and Ge powder. SiGe films 80 nm thick were deposited by *r.f.* sputtering on thermally oxidized Si substrates. After B^+ ions were implanted at a dose of $2\times10^{15}/cm^2$, conventional furnace annealing below 940 °C was performed. In order to confirm the V_{fb} shift, which is related to the threshold-voltage shift for MOS transistors, MOS capacitors of SiGe gates were fabricated and compared with those of p^+, and n^+ poly-Si gates.

TEM (Transparent Electron Microscopy) micrographs show all films have the small grains peculiar to typical boron-doped poly-Si films. The higher the annealing temperature and the Ge content, the better the crystallinity. The grain size was about 30 nm for the films of Ge content x about 0.5. Spectroscopic ellipsometry showed that refractive index n and absorption index k increase as the Ge content increases, and photon energy values at the effective absorption threshold decrease. The related bandgap of SiGe narrows with the increase in Ge content and depends on the annealing temperature. Therefore, by optimizing the Ge content and the annealing conditions, the energy level at the valence band edge can be controlled. As a result of C-V measurement of MOS capacitors, the flat band voltage (V_{fb}) for p^+ poly-SiGe with a Ge ratio of 0.5 has been adjusted almost to the middle point between both types of poly-Si gate [19]. The threshold voltage (V_{th}) for MOS and SOI transistors in low-voltage driving can be controlled by adopting the single gate of p-type SiGe. Furthermore, a more advanced and lower temperature process should be possible by adopting sputtering and ELA to SiGe films [20].

3. Improvement in Semiconductor Channel in TFTs

RTA and ELA effects for small grained poly-Si TFTs were investigated. In general, although uniform characteristics can be expected for small grained TFTs, they degrade due to the existing high trap states density related to the existence of grain boundaries. For RTA, as the annealing temperature increases, the electronic properties of poly-Si films improve. Furthermore, as a result of ELA with a controlled single pulse, TFT characteristics improved remarkably, maintaining small grains and a flat surface [21].

In order to increase the grain size and improve the crystallinity in silicon films by ELA, the solidification velocity must be controlled. Effective results using substrate heating have been reported [22]. By adopting substrate heating during ELA for crystallizing amorphous silicon films 45 nm thick, uniform TFT characteristics with saving energy of 100 mJ/cm^2 was attained [23]. Lumped shot ELA with a uniform beam also makes TFT characteristics uniform within a large shot area [24]. Advanced ELA processing for poly-Si is expected to be applied for not only LCDs but also for SRAMs and for LSIs of System-on-Insulator operating at a lower voltage.

In order to form high performance TFTs in each large grain, a new crystallizing technique of compulsive localized nucleation of grains by ELA was proposed. An UV pulse was irradiated thorough small patterned holes regularly arrayed in masked amorphous silicon films on insulators. After subsequent SPC, dendritic or disk-shaped grains as large as 5 μm were grown from the selected pre-annealed location. In a disk shaped grain, preferred orientation of single-crystalline {111} face were confirmed [13]. To realize uniform and superior TFTs such as SOI on arbitral substrates, research on the positioning of large grains in required locations as well as control of the crystal-orientation in each grain using the ELA technique is necessary.

III. SUMMARY

Using current annealing techniques, improvements in the semiconductor layers with shallow junctions, for gates and in thin film channels in Si MOS transistors have been investigated.

As a result, ELA is considered to be a promising process to improve transistor performance. Controlling the heating of the semiconductor layers as well as developing a shot technique for application to the LSI structure requires further study.

ACKNOWLEDGMENTS

The author would like to thank many co-researchers, process assistants, and managers in Sony, and research collegues for discussions. Also, I would like to thank Dr. S. Usui, Dr. Y. Mori, and Dr. S. Watanabe in Sony Research Center for their encouragement.

REFERENCES

[1] G. Sai-Halasz, M. Wordeman, D. Kern, E. Ganin, S. Rishton, H. Ng, D. Zicherman, D. Moy, T. Chang and R. Dennard, Technical Digest of IEDM **87**, 397 (1987).

[2] H. Tsukamoto, H. Yamamoto, T. Noguchi and T. Suzuki, Jpn. J. Appl. Phys. **31**, 659 (1992).

[3] K-J. Kramer, S. Talwar, A. M. MaCarthy and K. H. Weiner, IEEE Trans. Electron Device Lett. **17**, 461 (1996).

[4] S. Usui, T. Sameshima and M. Hara, Optoelectronics-Devices and Technologies **4**, 235 (1989).

[5] T.-J. King *et al.*, IEDM 90 (1990).

[6] N. Kistler and J. Woo, IEDM 93 (1993).
[7] S. Morozumi *et al.*, SID 83 Digest 156 (1983).
[8] T. Katoh, IEEE Trans. Elec. Dev. **35**, 923 (1988).
[9] Satwinder D. S. Malhi *et al.*, IEEE Trans. Elec. Dev. **ED-32**, 258 (1985).
[10] T. Noguchi, K. Tajima and Y. Morita, Proc. of Mat. Res. Soc. **146**, 35 (1989).
[11] H. R. Philipp and E. A. Taft, Phys. Rev. **120**, 37 (1960).
[12] H. Kumomi and T. Yonehara, Extended abstracts of IC SSDM 26 (1993).
[13] T. Noguchi and Y. Ikeda, Proc. of Sony Research Forum 200 (1992).
[14] N. Yamauchi, J-J. Hajar and R. Reif, IEEE Trans. Electron. Devices **38**, 55 (1991).
[15] T. Noguchi, Jpn. J. Appl. Phys. **32**, 1586 (1993).
[16] M. A. Crowder, P. G. Carey, P. M. Smith, R. S. Sposili, H. S. Cho and J. S. Im, IEEE Ele. Dev. Lett. **19**, 306 (1998).
[17] K. Matsumoto, T. Noguchi, T. Hirano, M. Kubota and M. Yamagishi, Jpn. J. Appl. Meeting, 641 (Spring 1994).
[18] H. Yamamoto, T. Noguchi, M. Yamagishi, M. Kubota and K. Matsumoto, Jpn. J. Appl. Meeting, 641 (Spring 1994).
[19] T. Noguchi, Jpn. J. Appl. Meeting, 758 (Spring 1998).
[20] T. Noguchi, D.-P. Gosain and S. Usui, Mat. Res. Soc. (Fall) A.6.12, Abstracts p. 19 (1998).
[21] T. Noguchi, Technical Report of IEICE (SHIN-GAKU-GIHOU) **SDM92-171**, 23 (1992).
[22] H. Kuriyama, T. Nohda, S. Ishida, T. Kuwahara, S. Noguchi, S. Kiyama, S. Tsuda and S. Nakano, Jpn. J. Appl. Phys. **32**, 6190 (1993).
[23] T. Noguchi, J. Tsai, A. J. Tang and R. Reif, Proc. of Mat. Res. Soc. **403**, 357 (1996).
[24] T.Noguchi, J. Tsai, A. J. Tang and R. Reif, IEEE Trans Ele. Dev. **43**, 1454 (1996).

Journal of the Korean Physical Society, Vol. 34, June 1999, pp. S268~S272

Gigantic Crystal Grain by Excimer Laser with a Pulse Duration of 200 ns and Its Application to TFT

K. H. LEE, J. T. HWANG, C. Y. JUNG, T. H. IHN, S. J. YI, H. I. JEON, W. G. LEE and D. H. CHOI

TFT Process Development Department, LCD Division, Hyundai Electronics Industries, Icheon 467-701

J. JANG

Department of Physics, Kyung Hee University, Seoul 130-701

D. ZAHORSKI

SOPRA, 26 rue Pierre Joigneaux, 92270 Bois Colombes, France

C. H. LEE

Division of Physics & Semiconductor Science, WonKwang University, Iksan 570-749

The large grain growth by excimer laser annealing was observed at multi-shots with a long laser pulse duration of 200 ns. The grain size of the polycrystalline Si increases up to ~1.5 μm with 20 shots at a laser energy density of 650 mJ/cm^2, and (111) orientation is dominant. The dark conductivity and conductivity activation energy of the poly-Si were 1.47×10^{-4} S/cm and 0.54 eV, respectively. The TFT with the poly-Si exhibited a field effect mobility of 215 cm^2/Vs, a threshold voltage of -0.5 V and a subthreshold slope of 0.9 V/dec.

I. INTRODUCTION

Polycrystalline silicon (poly-Si) is a potential material for use in solar cells, thin film transistors (TFT's), and integrated drivers for active matrix liquid crystal displays (AMLCD's) [1]. The peripheral circuits and TFT switching devices can be fabricated simultaneously on the same glass substrate [2]. The excimer laser annealing (ELA) is a promising method to obtain low temperature poly-Si for high performance TFTs [3,4].

To enlarge the grain size several approaches have been carried out [5–10]. In general, the maximum grain size and process area of the laser crystallized polycrystalline silicon (poly-Si) were limited by non-equilibrium of thermal transfer, mechanical stress during phase transition from amorphous to crystal and short laser duration (30 ns). Kim *et al.* tried a multiple pulse irradiation [5,6]. A super lateral grain growth appears at nearly completely melting regime. Choi *et al.* increased the grain size using a bridge structure [7]. Kuriyama *et al.* enlarged the grain size by a large number of 128 shots [8].

In the present work we have studied the grain enlargement of ELA poly-Si and its application to TFT. A multi-shot annealing using excimer laser with a pulse duration of 200 ns was carried out after dehydrogenation. The beam size for annealing was 27 mm×68 mm. The Ni silicide source/drain/gate contacts were employed for the TFT [11]. The n-channel poly-Si TFTs exhibited a field effect mobility of ~215 cm^2/Vs and a threshold voltage of -0.5 V.

II. EXPERIMENTAL

We used the a-Si:H films prepared by plasma enhanced chemical vapor deposition (PECVD) as a starting material for laser annealing using a XeCl excimer laser (308 nm, SOPRA system). The pulse width of a square beam was 200 nsec (Full-Width at Half-Maximum, FWHM), the laser energy per shot was 14 Joule, and the pulse to pulse stability was ±2 %. The square beam size and its uniformity are 27 mm×68 mm and ±3 %, respectively. The 50 nm thick PECVD a-Si:H was deposited on glass at 350 °C, and then dehydrogenated at 450 °C for 30 min. The a-Si:H film was irradiated by a single shot at an energy density of 175~750 mJ/cm^2 at room temperature. The laser shot number was increased up to 20.

After forming the poly-Si islands, 350 nm thick SiN_X and 30 nm thick a-Si:H layers were deposited and patterned in order to define the channel. This step was

followed by ion doping to make n-type poly-Si for source/drain contacts. Flow rates of SiH_4, He and NH_3 were fixed at 0.1, 100 and 30 sccm, respectively, to deposit the SiN_X layer at 280 °C [11]. The PECVD SiN_X exhibited a breakdown field strength of 6 MV/cm and a leakage current density of $\sim 10^{-10}$ A/cm^2. Then 20 nm thick Ni was deposited, and annealed at 250 °C for 2 hr to form Ni silicide in the source/drain/gate regions. Finally, the unreacted Ni was removed away using a Ni etchant to form the Ni silicide source/drain/gate contacts. The conventional coplanar TFTs with Ni silicide contacts were fabricated. The ratio of channel width to length of the TFT was 80 μm/28 μm.

III. RESULTS AND DISCUSSION

Figure 1 shows the grain size versus shot number at the laser energy density of 550, 600 and 650 mJ/cm^2. According to Kim *et al.*, complete melting regime is thought to appear at 650 mJ/cm^2 as shown in Fig. 1. Grain size does not change with shot number at 650 mJ/cm^2 [5,6]. It is noted that a lateral grain growth can be seen at 550 and 600 mJ/cm^2, near complete melting regime [6–10]. The grain size at 600 mJ/cm^2 increases up to $\sim$1.5 μm.

Figure 2 show the SEM images of the poly-Si films crystallized at various shot numbers with a laser intensity of 600 mW/cm^2. Grain size increases up to $\sim$1.5 μm at 10 shots.

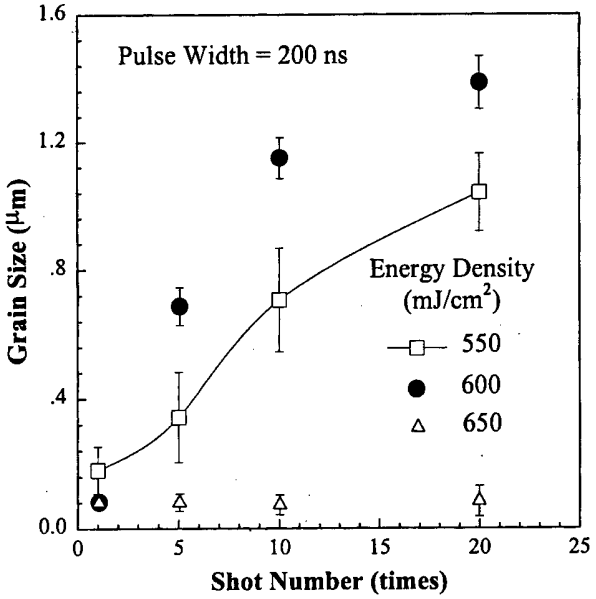

Fig. 1. The grain size versus shot number at the laser energy density of 550, 600 and 650 mJ/cm^2.

Figure 3 shows the TEM bright-field images for the poly-Si films at 600 mJ/cm^2. The grain size increases with shot number and is 1.5 μm at 20 shots (Fig. 3(d)) that is larger than that of ELA poly-Si at a 30 ns duration

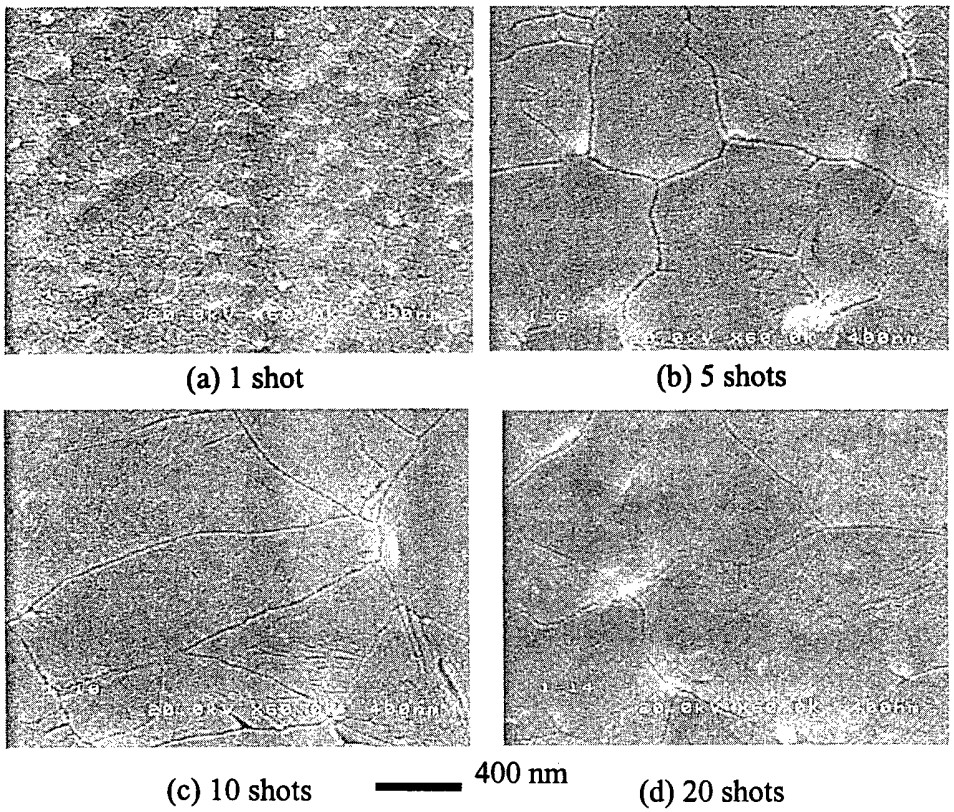

Fig. 2. SEM images of the poly-Si films at the energy density of 600 mJ/cm^2.

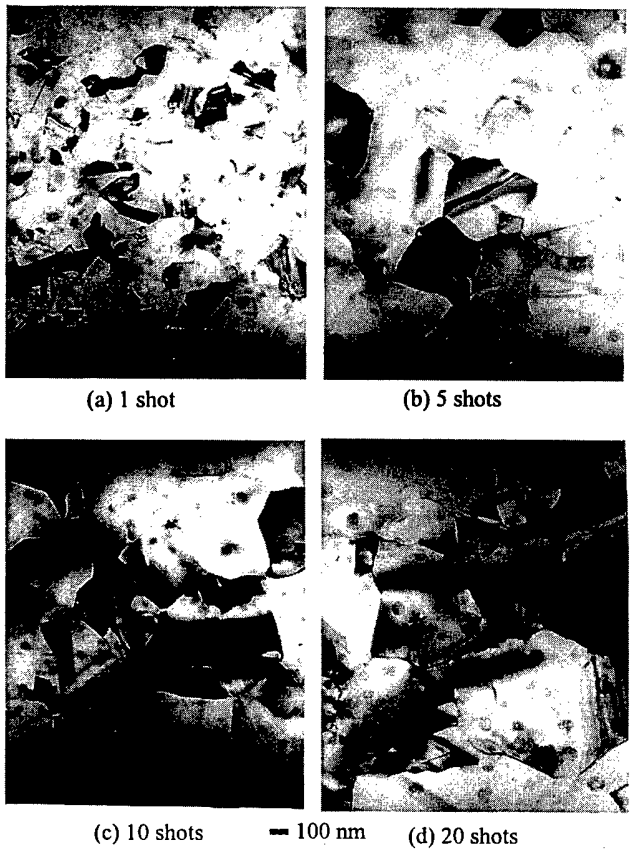

Fig. 3. TEM bright-field images for the poly-Si films crystallized at 600 mJ/cm^2.

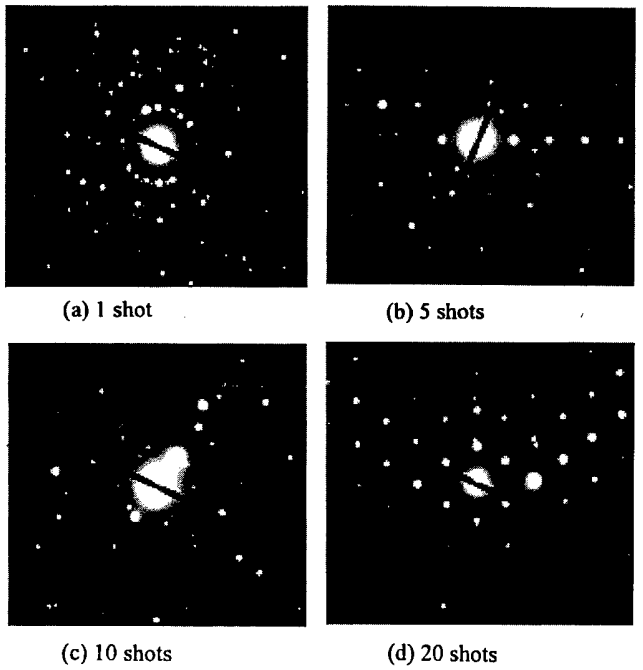

Fig. 4. Electron diffraction patterns for the poly-Si films at the energy density of 600 mJ/cm^2.

[6–10]. Note that the grain size is less than 1 μm for 30 ns case.

Figure 4 shows the electron diffraction patterns for the poly-Si films. The (111) orientation is dominant. The best crystalline quality can be seen at 20 shots.

Figure 5 shows the dark conductivity and conductivity activation energy for the poly-Si film (20 shots). The hopping transport does not appear. The dark conductivity and conductivity activation energy were 1.47×10^{-4} S/cm and 0.54 eV, respectively.

Figure 6 shows the transfer characteristics of the poly-Si TFT. The subthreshold slope and on/off current ratio

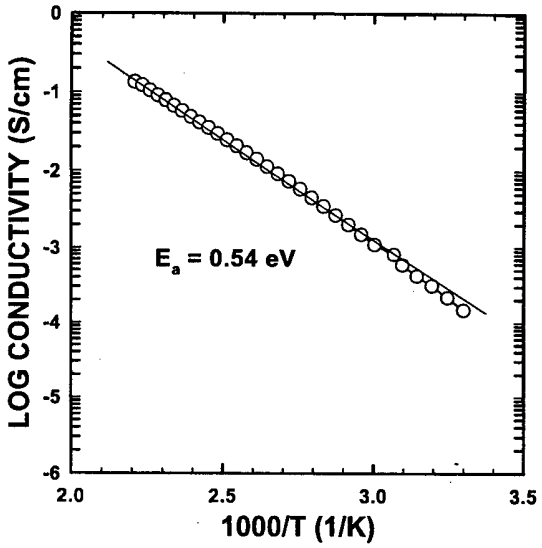

Fig. 5. The dark conductivity and conductivity activation energy for the poly-Si film at 20 shots.

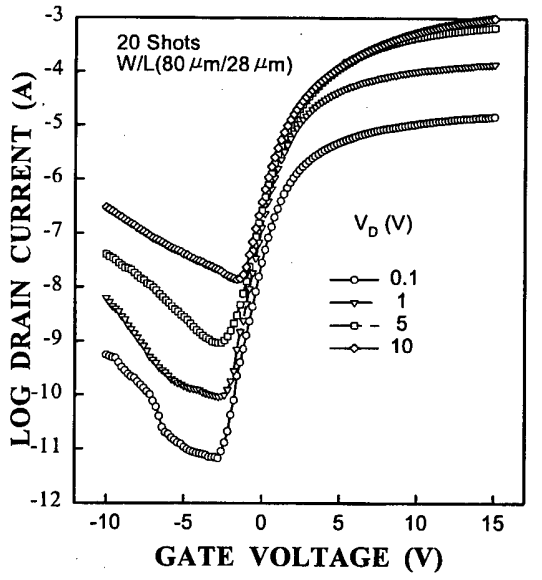

Fig. 6. Transfer characteristics of the poly-Si TFT.

at drain voltage $V_D = 5$ V are 0.9 V/dec. and $\sim 10^6$, respectively. The off-state leakage current is $\sim 10^{-11}$ A/μm at $V_D = 5$ V and gate voltage $V_G = -0.5$ V. Note that the off-state leakage currents increase with decreasing gate voltage ($V_G < 0$ V) because of the increased electron tunneling through the potential barrier [12,13].

Figure 7 shows the output characteristics of the poly-Si TFT. The current crowding effect appears at low V_D because of the resistive ohmic layer. The sheet resistance of the Ni silicide on the poly-Si was found to be ~ 2 ω/square, but n^+ poly-Si seems to be damaged by ion doping.

Figure 8 shows the transconductance and the transfer characteristics at $V_D = 0.1$ V for the poly-Si TFT.

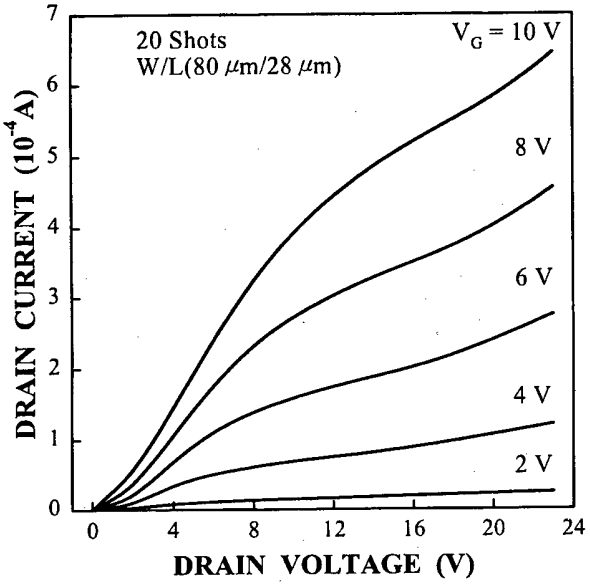

Fig. 7. Output characteristics of the poly-Si TFT.

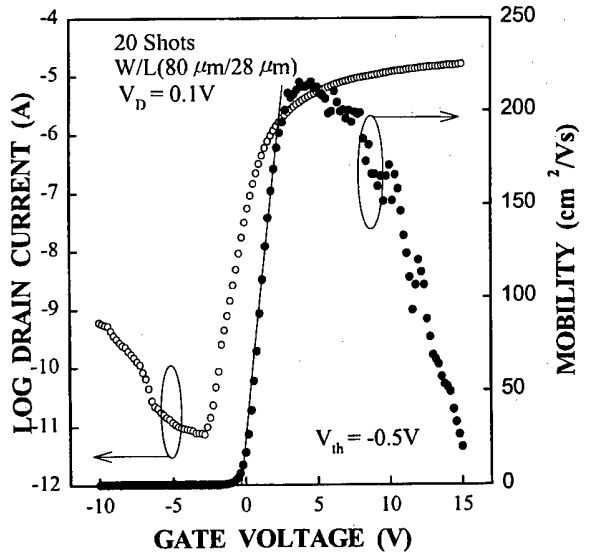

Fig. 8. Transconductance and the transfer characteristics of a poly-Si TFT at $V_D = 0.1$ V.

The poly-Si TFT exhibited a field effect mobility of 215 cm^2/Vs and a threshold voltage of -0.5 V. The field effect mobility was obtained from the transconductance (g_m) in the linear region at $V_D = 0.1$ V, *i.e.*, $g_m = \partial I_D/\partial V_G = C_i V_D \mu_n W/L$, where W/L is the ratio of channel width to length, C_i is the capacitance of gate insulator and μ_n is the field effect mobility of electrons [14]. The threshold voltage was obtained from the extrapolation of the transconductance curve versus gate voltage [14].

With increasing laser energy density, grain size increases exponentially until near complete melting regime and then decreases rapidly [5–10]. Within a long pulse duration time, thermal energy stored in the molten-Si layer is transferred into the substrate, and thus the temperature gradient in the film near interface is moderated and thus the solidification velocity decreases. The movement of the grain boundary is thermodynamically driven and proceeds in order to lower the total free energy of the closed system. According to Kim *et al.*, relocation of the original grain boundary (and therefore the apparent "growth of the grain") occurs upon impingement of the re-solidifying interfaces [5,6]. This explains the enlargement of grains by multi-shots.

IV. CONCLUSIONS

The grain size increases in the range of "near complete melting", until complete melting regime is reached. The grain size is 1.5 μm when the laser energy and shot number are 600 mW/cm^2 and 20, respectively. The dark conductivity and conductivity activation energy were 1.47×10^{-4} S/cm and 0.54 eV, respectively. The fabricated n-channel poly-Si TFT exhibited a field effect mobility ~ 215 cm^2/Vs, a threshold voltage of ~ -0.5 V and a subthreshold slope of ~ 0.9 V/dec. Therefore, the ELA with a pulse duration of 200 ns seems to be very promising for high performance TFT-LCDs.

ACKNOWLEDGMENTS

The work was supported in part by the Basic Science Institute Program (1998-015-D00112) of the Ministry of Education.

REFERENCES

[1] T. Serikawa, S. Shirai, A. Okamoto and S. Suyama, IEEE Trans. Electron Devices, **36**, 1929 (1989).

[2] T. Hashizume, S. Inoue, T. Inami, T. Nakazawa, I. Yudasaka and H. Ohshima, Ext. Abs. of SSDM '91, 638 (1991).

[3] K. Sera, F. Okumura, H. Uchida, S. Itoh, S. Kaneko and K. Hotta, IEEE Trans. Electron Devices **ED-36**, 2868 (1989).

[4] Y. Matsueda, S. Inoue, S. Takenaka, T. Ozawa, S. Fujikawa, T. Nakazawa and H. Ohshima, SID '96 Digest, 21 (1996).
[5] H. J. Kim and J. S. Im, Appl. Phys. Lett. **68**, 1513 (1996).
[6] H. J. Kim and J. S. Im, Mat. Res. Soc. Symp. Proc. **321**, 665 (1994).
[7] D.H. Choi, E. Sadayuki, O. Sugiura and M. Matsumura, Jpn. J. of Appl. Phys. **33**, 70 (1994).
[8] H. Kuriyama, S. Kiyama, S. Noguchi and Y. Kuwano, Jpn. J. Appl. Phys. **30**, 3700 (1991).
[9] T. Sameshima, M. Hara and S. Usui, Jpn. J. Appl. Phys. **28**, 1789 (1989).
[10] R. Ishihara, W. C. Yeh, T. Hattori and M. Matsumura, Jpn. J. Appl. Phys. **34**, 1759 (1995).
[11] J. I. Ryu, H. C. Kim, S. K. Kim and J. Jang, IEEE Electron Device. Lett. **18**, 272 (1997).
[12] M. Yazaki, S. Takenaka and H. Oshima, Jpn. J. Appl. Phys. **31**, 206 (1992).
[13] J.G . Fossum, A. O. Conde, H. Shichijo and S. K. Nanerjee, IEEE Trans. Electron Devices **ED-32**, 1878 (1985).
[14] S. M. Sze, *Physics of Semiconductor Devices* (John Wiley & Sons, 1981), Chap. 8.

Journal of the Korean Physical Society, Vol. 34, June 1999, pp. S273~S276

Pd/Si/Pd/Ti/Au Ohmic Contacts to N-type InGaAs for High Temperature Operation of AlGaAs/GaAs HBTs

S. H. PARK, T.-W. LEE, J. M. LEE, B.-G. MIN and M.-P. PARK
ETRI-Microelectronics Technology Laboratory, Taejon 305-350

J. Y. KIM
Department of Materials Engineering, Hoseo University, Asan 336-795

I.-H. KIM
Department of Materials Science and Engineering, Chungju National University, Chungju 380-702

Pd/Si/Pd/Ti/Au ohmic contact to n-InGaAs was investigated by various measurement techniques. In spite of the lower barrier height of metals-InGaAs junction, the ohmic system showed the non-ohmic behavior due to the presence of insulating Si layer before annealing. But the ohmic performance was enhanced by rapid thermal annealing (RTA) over 300 °C. The minimum specific contact resistance of 4.3×10^{-7} Ωcm^2 was obtained for sample annealed at 400 °C for 10 s. As the result of microstructural analyses, it was found that the ohmic performances were improved due to the generation of Pd_2Si phase at annealing temperature under 400 °C, but were slightly degraded with the increment of Pd_2Ga_5 phase over 425 °C. Up to 450 °C, the relatively good resistivities (low 10^{-6} Ωcm^2) and planar interfaces were maintained.

I. INTRODUCTION

AlGaAs/GaAs heterojunction bipolar transistors (HBTs) have been widely applied as the power devices for mobile and satellite communications, because of their advantages such as high frequency, high breakdown voltage and large current drivability. As the device sizes scale down to obtain higher speed, reducing the parasitic resistance due to ohmic contact become more important [1]. Therefore, it is very critical to achieve the reliable ohmic contact of the low-resistance and the planar metal-to-semiconductor interface even at high temperature of about 450 °C.

Refractory metal systems, including Pd-based metals, have been extensively investigated as the ohmic contact materials to n-type GaAs superior to the conventional AuGe-based systems which have photolithography limit due to the severe "ball-up" metallization [2–5]. The Pd/Si ohmic contact is similar to Pd/Ge system, including a moderately good specific contact resistance (low 10^{-6} Ωcm^2) for same doping levels and solid phase regrowth mechanisms [6–9]. Si enhances the doping level of the GaAs surface, besides acting as a barrier against Ga and As out-diffusion [1]. As an ohmic contact mechanism of this system, it was known that Pd and GaAs develop a metastable Pd_4GaAs compound on the GaAs surface at about 100 °C, and Si and Pd react and produce Pd_2Si at 200~275 °C [1,10]. And at 300 °C or above, a thin layer of n^+-GaAs is formed between Pd and GaAs substrate. Yu *et al.* [10] reported that there was no detectable epitaxial Si on GaAs after annealing at 375 °C where the ohmic behavior was observed, and that a Pd_2Si layer was in contact with the n-GaAs with the excess amorphous Si located on top of the Pd_2Si layer. It is expected that a similar phenomenon occurs on n-InGaAs, which is used as a material for HBTs [5] due to low barrier height to metals as well as high electron mobility and high electron saturation velocity. Shantharama *et al.* [11] have presented several non-alloyed ohmic contacts on n^+- and p^+-InGaAs, and authors [12] have recently reported some results on AuGe/Ni/Au, AuGe/Pd/Au, Ti/Pt/Au and WSi/Ti/Pt/Au contacts to n-InGaAs. Up to now, however, there are few detailed studies on Pd/Si-based ohmic contacts to n-InGaAs and their thermal behaviors. In this study, Pd/Si/Pd/Ti/Au ohmic contacts to n-InGaAs were comprehensively investigated using various electrical and microstructural measurements.

II. SAMPLE PREPARATION

Table 1 shows an epi-structure of AlGaAs/GaAs HBTs grown by MOCVD (metal organic chemical vapor deposition) on 3-inch semi-insulating GaAs (100) wafer. As

Table 1. AlGaAs/GaAs HBT epi-layer structures for the experiment.

Layer		Thickness (Å)	Doping (cm^{-3})	Al (In) Fraction
Cap	n^+-InGaAs	400	1×10^{19}	0.5
	n^+-InGaAs	400	1×10^{19}	$0 \rightarrow 0.5$
	n^+-GaAs	1000	3.7×10^{18}	
Emitter	n-AlGaAs	500	5×10^{17}	$0.3 \rightarrow 0$
	n-AlGaAs	1500	2×10^{17}	0.3
Base	p^+-GaAs	700	3×10^{19}	
Collector	n^--GaAs	4000	2×10^{16}	
Subcollector	n^+-GaAs	5000	4×10^{18}	

the cap layers for emitter ohmic contact, an n-GaAs layer (1000 Å, 3.7×10^{18} Si/cm^3), and a compositionally graded n-$In_xGa_{1-x}As$ ($x = 0 \rightarrow 0.5$) layer (400 Å, 1×10^{19} Si/cm^3), and an $In_{0.5}Ga_{0.5}As$ layer (400 Å, 1×10^{19} Si/cm^3) were grown sequentially on the AlGaAs emitter. Prior to contact deposition, the samples were cleaned in the HCl:H_2O (1:1) solution for 30 seconds. As shown in Figure 1, composite ohmic metals were deposited in order of Pd (500 Å), Si (750 Å), Pd (500 Å), Ti (350 Å) and Au (900 Å) on n-InGaAs by an electron beam evaporator with a base pressure below 5×10^{-7} Torr. The ohmic contact patterns are made by a lift-off technique using the photolithography process, in which metal pads have size of 100×100 μm^2 and spacing of 5, 10, 15, 20 and 30 μm among the pads. The ohmic contact area was isolated by chemical mesa etching. The final size of each smaple was about 1.5×1.5 cm^2.

The heat treatment for the ohmic contact was performed by the rapid thermal annealing (RTA) at temperatures ranging from 300 °C to 450 °C for 10 seconds. Samples were surrounded by a SiC suceptor under forming gas (N_2/H_2) atmosphere. The specific contact resistances of the ohmic system were extracted using the standard transmission line method (TLM). Phase transition was analyzed by the wide angle (2θ, 0~80°) X-ray diffraction (XRD). Auger electron spectroscopy (AES) was performed for the elemental depth profile of the samples. Ohmic metal layers were sputtered by Ar^+ (10 keV, 48 nA) ions. The kinetic energy levels for analyzing elements were In^{MNN} (397~415 eV), Ga^{LMM} (1059~1077 eV), As^{LMM} (1219~1237 eV), Pd^{MNN} (317~340 eV), Si^{KLL} (1590~1630 eV), Ti^{LMM} (368~395 eV), and Au^{NVV} (2000~2035 eV), respectively. The interfacial microstructure of metals/n-InGaAs was observed by a Philips CM20T cross-sectional transmission electron microscopy (XTEM), and (110) projection centered beam image method was used with the accelerating voltage of 200 keV.

III. RESULTS AND DISCUSSION

Figure 2 shows the specific contact resistance (ρ_c) of the Pd/Si/Pd/Ti/Au contact with RTA temperature. Before RTA treatment, the contacts did not show ohmic behavior due to the presence of insulating Si layer. Moderate specific contact resistance of 2×10^{-5} Ωcm^2 was obtained for sample annealed at 300 °C, which is believed to be due to the unreacted insulating Si layer remaining in the ohmic layers. As the annealing temperature was increased up to 400 °C, the specific contact resistance of the sample showed the minimum value of 4.3×10^{-7} Ωcm^2 as a result of the optimum phase transformation. Ohmic contact characteristics became slightly degraded for samples annealed at temperatures above 425 °C, but relatively good resistivities (~low 10^{-6} Ωcm^2) applicable to HBTs were maintained up to 450 °C.

Figure 3 shows the phase transitions between elements composing the ohmic system with RTA temperatures, which is measured by XRD. There were no detectable

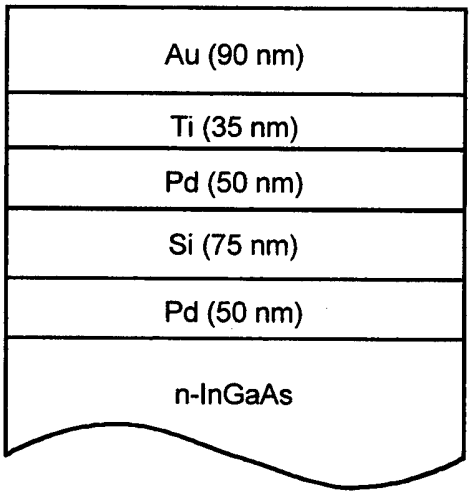

Fig. 1. Schematic cross-sectional view of the Pd/Si/Pd/Ti/Au ohmic contact to n-InGaAs.

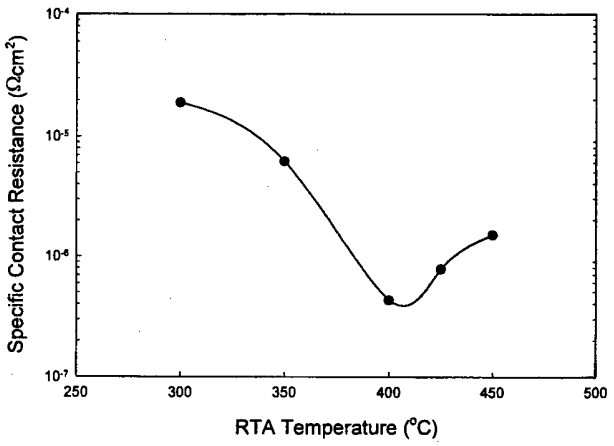

Fig. 2. Variation of the specific contact resistance of the Pd/Si/Pd/Ti/Au contact to n-InGaAs with RTA temperature.

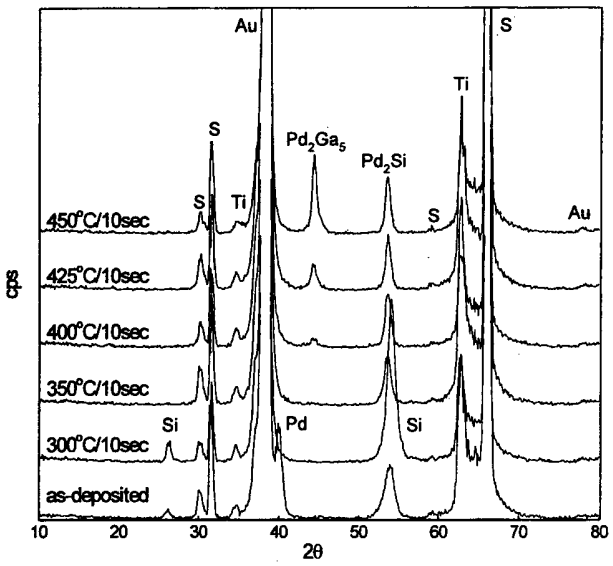

Fig. 3. XRD patterns of the Pd/Si/Pd/Ti/Au contact to n-InGaAs.

phase changes for samples annealed up to 300 °C so that original stoichiometry of each ohmic layer was maintained. By annealing at 350 °C for 10 sec, the Pd and Si layers reacted and formed Pd_2Si phase. Pd_2Si phase, which is known as a metallic compound beneficial to the reduction of ohmic resistance, began to grow with increasing RTA temperature up to 450 °C. The remarkable increase in specific contact resistance after RTA above 425 °C is attributed to the formation of Pd_2Ga_5 compound. Therefore, it is believed that the minimum specific contact resistance was obtained at 400 °C as the results of opposing effects of Pd_2Si and Pd_2Ga_5 phases. Pd_4GaAs phase, however, which had been reported by Yu *et al.* [10] for Pd/Si ohmic contact to n-GaAs, was not detected for all the samples. In addition, $AuIn_2$ and AuGa phases were not observed up to 450 °C. Thus, it is proved that the upper Pd and Ti layers act as a good barrier against Au diffusion at very high process temperature.

Figure 4 shows the AES depth profiles of the Pd/Si/Pd/Ti/Au contact annealed at typical temperatures. For as-deposited sample, each ohmic layer kept its original status and any atomic displacement did not occur. The Pd and Si atoms were moderately intermixed by RTA at 300 °C, and their interactions were more remarkable with increasing RTA temperature. Up to 450 °C, the out-diffusions of the In, Ga and As atoms were not found as well as the in-diffusion of the Au atoms. Therefore, this phenomenon well agrees with the XRD results, in which the Au-based compounds such as $AuIn_2$ and AuGa were not identified.

Figure 5 illustrates the interfacial microstructures of the Pd/Si/Pd/Ti/Au contact to n-InGaAs observed by XTEM for the samples as-deposited and annealed at 400 °C, respectively. Planar and uniform interfaces without

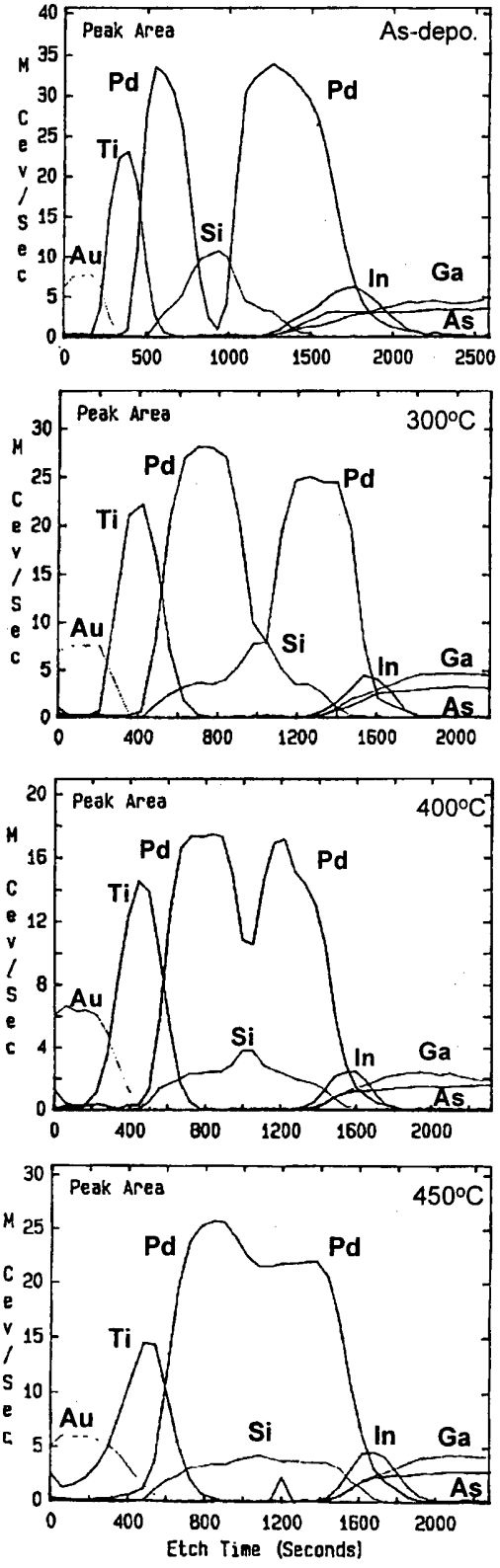

Fig. 4. AES depth profiles of the Pd/Si/Pd/Ti/Au contact to n-InGaAs.

any spiking were observed and maintained after RTA at 400 °C. The Pd-Si compound layer was also observed due

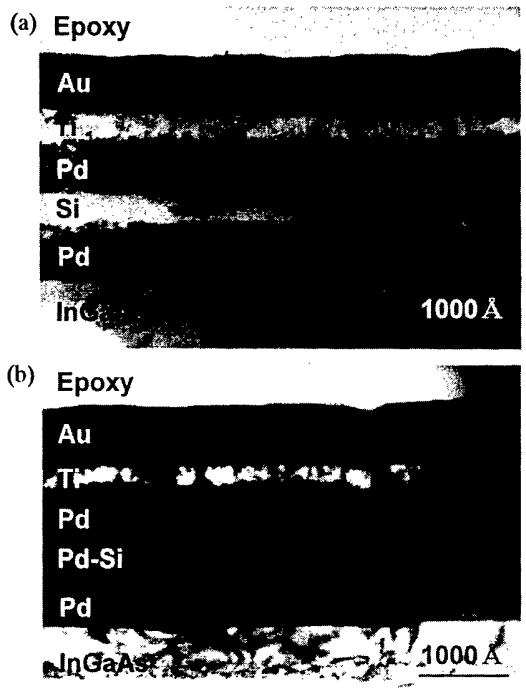

Fig. 5. Cross-sectional view of the Pd/Si/Pd/Ti/Au contact to n-InGaAs (a) as-deposited (b) annealed at 400 °C/10 sec.

to the intermixing of Pd and Si. Accurate phase analysis of each layer will be presented in the future work.

IV. CONCLUSIONS

The ohmic characteristics of the Pd/Si/Pd/Ti/Au contact system to n-InGaAs according to the annealing temperatures were investigated, and the correlation of its electrical properties with microstructures was analyzed using TLM, XRD, AES and XTEM measurements. Non-ohmic behavior was observed for as-deposited sample. Relatively good specific contact resistances due to the formation of Pd_2Si phase were obtained by RTA above 350 °C. For sample annealed at 400 °C, especially, the minimum resistance of 4.3×10^{-7} Ωcm^2 was measured. At the temperature above 425 °C, ohmic performances of samples were slightly degraded with increasing Pd_2Ga_5 phase. Nevertheless, this contact system showed such thermally stable ohmic properties as the planar and non-spiking interfaces besides moderately good resistivity (~low 10^{-6} Ωcm^2) up to 450 °C. It is believed that the Pd/Si/Pd/Ti/Au ohmic contact to n-InGaAs is very applicable for AlGaAs/GaAs HBTs operating at high temperature.

REFERENCES

[1] T. C. Shen, G. B. Gao and H. J. Morkoc, J. Vac. Sci. Technol. **B10**, 2113 (1992).
[2] E. D. Marshall, W. X. Chen, C. S. Wu, S. S. Lau and T. F. Keuch, Appl. Phys. Lett. **48**, 535 (1985).
[3] J. Tsuchimoto, S. Shikata and H. Hayashi, J. Appl. Phys. **69**, 6556 (1991).
[4] L. C. Wang, S. S. Lau, E. K. Hsieh and J. R. Velebir, Appl. Phys. Lett. **54**, 2677 (1989).
[5] A. Katz, C. R. Abermathy, S. J. Pearton, B. E. Weir and W. Savin, J. Appl. Phys. **69**, 2276 (1991).
[6] M. W. Cole, W. Y. Han, L. M. Casas, D. W. Eckart and K. A. Jones, J. Vac. Sci. Technol. **A12**, 1904 (1994).
[7] I.-H. Kim, S. H. Park, T.-W. Lee and M. P. Park, Appl. Phys. Lett. **71**, 1854 (1997).
[8] J. T. Lai and J. Y. Lee, Appl. Phys. Lett. **64**, 229 (1994).
[9] J. S. Kwak, H. N. Kim, H. K. Baek, J.-L. Lee, H. Kim, H. M. Park and S. K. Noh, Appl. Phys. Lett. **67**, 2465 (1995).
[10] L. S. Yu, L. C. Wang, E. D. Marshall, S. S. Lau and T. F. Kuech, J. Appl. Phys. **65**, 1621 (1989).
[11] L. G. Shantharama, H. Schumacher, H. P. Leblanc, R. Esagui, R. Bhat and M. Koza, Electron. Lett. **26**, 1127 (1990).
[12] S. H. Park, M. P. Park, T. W. Lee, K. M. Song, K. E. Pyun and H. M. Park, Inst. Phys. Conf. Ser. **145**, 295 (1996).

Journal of the Korean Physical Society, Vol. 34, June 1999, pp. S277~S280

Spot Size Converter Integrated Polarization Insensitive Semiconductor Optical Amplifiers

J. S. LEE, J. R. KIM, S. S. PARK, M. W. PARK,
J. S. YU, S. D. LEE, A. G. CHOO and T. I. KIM

Photonics Laboratory, Material and Device Sector,
Samsung Advanced Institute of Technology, Suwon 440-600

Spot-size converter (SSC) integrated polarization-insensitive semiconductor optical amplifiers (SOAs) with angled window structure has been designed and fabricated using both selective area growth and successive lateral tapering. A narrow beam divergence of 8°×15°, 0.2 dB amplified spontaneous emission ripple, and 0.8 dB polarization sensitivity at 1.55 μm wavelength were obtained at 29.7 dB chip gain. This gain is the highest value ever reported for SSC-SOAs grown by selective area growth techniques.

I. INTRODUCTION

Semiconductor optical amplifiers (SOAs) are now firmly established as key components for optical networks and telecommunications systems. In addition to their usefulness as a optical amplifier, they can perform a variety of other signal processing and control functions including wavelength conversion, optical demultiplexer, dispersion compensation, optical switch, and 3R (2R) signal regenerator. Polarization insensitive gain, high saturation output power, and short gain recovery time are desirable features for most of system applications. Polarization independent SOA structures based on tensile strained multiple quantum wells and tensile strained bulks have been reported [1,2]. The use of spot-size converters (SSC) at both ends of gain medium is very promising because it can improve the coupling efficiency and consequently reduce the effective reflectivity [3,4]. Three main classes of SSC have been developed to deconfine and thus to expand the optical mode in the waveguide. The first one is the vertical SSC [5,6] in which the waveguide thickness is varied from the active waveguide to the output facet. In the second class [7,8], the taper is formed by decreasing the waveguide width. In these classes, the taper is either passive or active. In the third class [9,10], the so-called double-core taper, the active waveguide is laterally tapered and combined with underlying passive waveguide. Such a combination allows to easily control the beam divergence at the output facet.

In this letter, SSC has been realized by combination of thickness variation by selective area growth (SAG) and width variation by lateral tapering. We report the fabrication and evaluation of the 1.55 μm polarization insensitive SSC integrated SOA with angled window structure for the first time.

II. SOA STRUCTURE AND FABRICATION

The growth conditions for the SAG were similar to those of the non-SAG [11], all the growth were performed in a vertical reactor in metal organic chemical vapor deposition (MOCVD), at 60 torr and 600 °C. The growth rate *i.e.*, the flow rates of the III group sources, was only reduced by one fourth of the growth rate for non-SAG, which confirms that there is no growth on the SiO_2 mask by the nucleation process. The rectangular SiO_2 mask for SAG was tilted by 7° from the crystal axis to fabricate the tilted waveguide after structure growth. The open area width between two SiO_2 masks was fixed to 15 μm. The quality of the epilayer by SAG with the tilted mask was comparable to that of the normal SAG. Figure 1 shows the thickness enhancement factors against the SiO_2 mask widths for InP, InGaAsP (λ=1.3 μm), and InGaAsP (λ=1.55 μm). The thickness enhancement factor is defined by the ratio between the growth rate at the open area placed between masks and the growth rate at the region without mask. The thickness enhancement factor was increased with mask area width and was saturated at 250 μm, which implied the diffusion length of the III group sources were about 125 μm in our growth conditions. In our SAG scheme, the increase the growth rate at open area results from the gas phase diffusion of the III-group source from mask area. The material with high Ga composition has a small thickness enhancement factor, which was explained by the different diffusion length of In and Ga radicals in gas phase. The thickness enhancement factor was greater than 3 at 150 μm wide masks.

The spatial uniformities of the photoluminescence (PL) wavelength and PL intensity for the InGaAsP (λ=1.55 μm) to the lateral direction are shown in Fig.

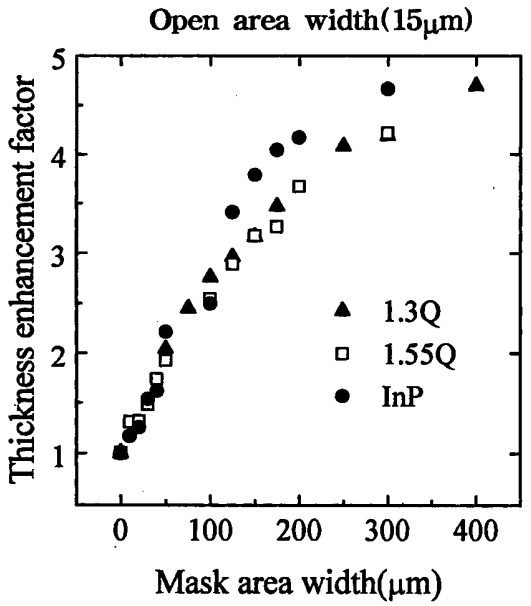

Fig. 1. Mask area width dependence of the thickness enhancement factor of InP and InGaAsP for the 15 μm open area width.

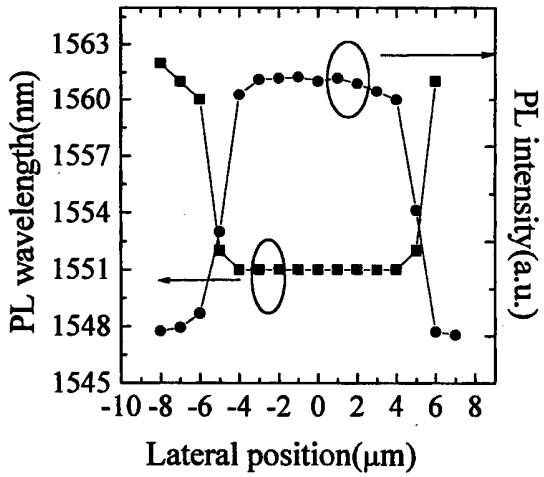

Fig. 2. The PL wavelength and intensity distribution of the InGaAsP (λ=1.55 μm) to the lateral direction for the 15 mm open region and 150 mm mask width.

2. The uniform region was about 8 μm at the center of the 15 μm open area. This uniform region is sufficient to fabricate the p-n buried hetero-structure by using the conventional photo-lithography process.

The schematic diagram of the SSC-SOA is shown in Fig. 3. The active stripe of this device is tilted by 7° from the crystal axis. The SSC is located at the end of gain region consists of a vertically and laterally tapered passive region followed by a window region. To obtain SSC, the thickness of waveguide in the taper region was reduced one third by SAG technique and the width was reduced linearly from 1 μm (wide region end) to 0.2 μm (narrow region end) by conventional lithography and wet

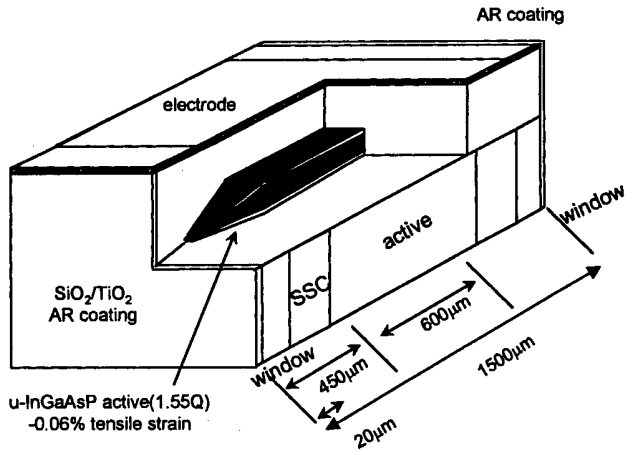

Fig. 3. Schematic diagram of polarization insensitive SSC-SOA with angled window structure.

etching. Lengths for the passive and active sections are 450 μm and 600 μm, respectively. The total length of the device is 1500 μm. The active region of device consists of 0.2 μm thick slightly tensile strained bulk InGaAsP (λ=1.55 μm) active layer and 0.1 μm thick InGaAsP (λ=1.3 μm) waveguides, which were grown by SAG technique using MOCVD to implement SSC regions simultaneously. The polarization insensitivity of slightly tensile bulk SOA have been obtained when $\Delta a/a$=−0.065 % in the active medium [12]. For SSC-SOA by SAG, polarization sensitivity of gain could be obtained by controlling the strain amount of the non-SAG region because there is a fixed strain relation between SAG and non-SAG regions. The amount of tensile strain in the SAG region could be estimated by performing double crystal x-ray diffraction measurement on the non-SAG region. After growth, the SiO_2 masks for SAG were removed and narrow mesa stripes were formed along the SAG regions. The width of the active wave-guide is 1 μm in the central gain section and reduced down to less than 0.2 μm at the taper end. For linear tapering in lateral direction, special wave-guide design is needed to reduce the loss in the transition region between SAG and non-SAG region. InP p-n current blocking layers were selectively grown at the special conditions and 8 μm thick p-InP cladding layers were grown successively to complete the BH structure. After fabrication, both facets were AR coated by SiO_2/TiO_2 to minimize the reflection from the cleaved facet.

III. RESULTS AND DISCUSSIONS

Figure 4 shows a typical far-field of the SSC-SOA at a bias current of 150 mA. The FWHM was found to be 8° in the horizontal and 15° in the vertical directions respectively. The coupling loss was less than 4 dB by using tapered lensed single mode fiber. The gain measurement

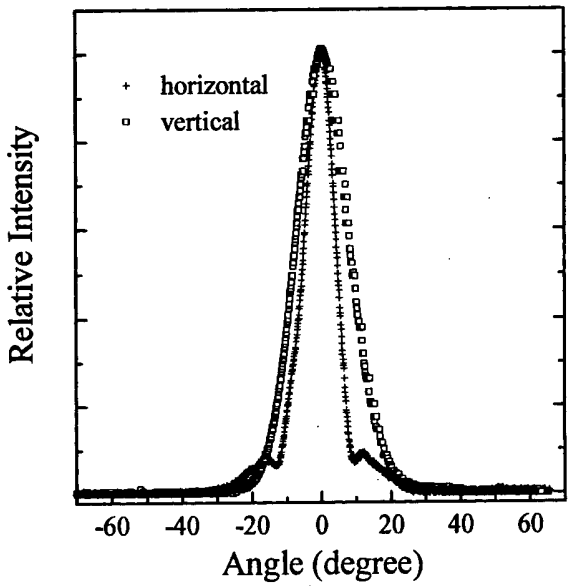

Fig. 4. Horizontal and vertical far-field patterns of SSC-SOA at 150 mA Cross: horizontal far-field, Square: vertical far-field.

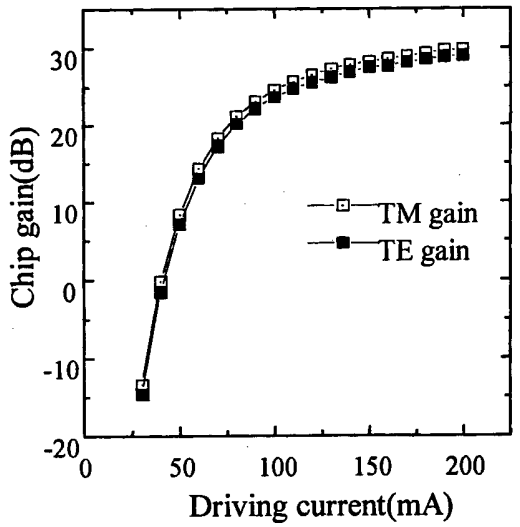

Fig. 5. SOA gain characteristics vs. current at Pin=−20 dBm and λ=1.55 μm.

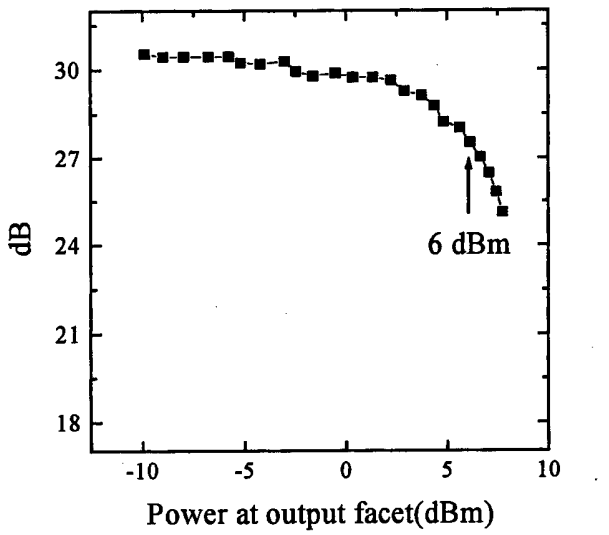

Fig. 6. SOA gain as a function of output power at I=200 mA and λ=1.55 μm.

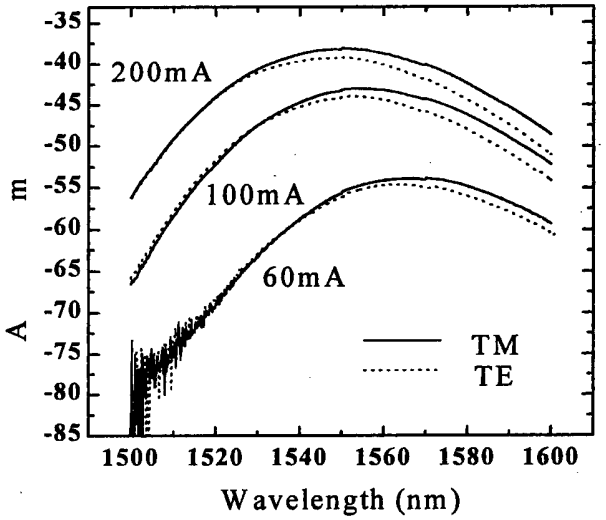

Fig. 7. Polarization resolved ASE spectra of SSC-SOA at 60, 100, 200 mA.

was performed by coupling tapered lensed fibers to both facets. The gain characteristics vs. driving currents for both TE and TM modes at wavelength of 1.55 μm for a −20 dBm input power are shown in Fig. 5. The SOA chip gain was as large as 29.7 dB at 200 mA. The polarization sensitivity is remained less than 0.8 dB over the entire range of driving current. The gain as a function of output power at 200 mA and wavelength of 1.55 μm is shown in Fig. 6. The 3 dB saturation output power was 6.1 dBm at the output facet. The saturation output power of 9.5 dBm have been reported [2]. Saturation output power depends on the saturation gain, length of the gain medium, and facet reflectivity. Low saturation output power of our device is originated from the short active medium length compare to reported data [2]. Figure 7 shows the polarization resolved amplified spontaneous emission (ASE) spectra measured at 60, 100, and 200 mA. At 100 mA, the 3 dB optical bandwidth of the ASE spectrum was 40 nm and polarization sensitivity was 1.5 dB at 1.55 μm wavelength. The amplitude of the gain ripple was less than 0.2 dB even at 200 mA. This fairly small gain ripple corresponds to the reflectivity of less than 10^{-5} on both facets [13]. This value is normally obtainable with the help of angled stripe, window structure, and proper AR coating.

IV. CONCLUSIONS

We have developed novel SSC integrated polarization-insensitive SOAs with angled window structures using both angled SAG and successive lateral tapering for the first time. A very narrow beam divergence of $8° \times 15°$ was obtained by vertical and lateral tapering of wave-guide. The ASE ripple was 0.2 dB by angled window structure and proper AR coating. The polarization sensitivity of 0.8 dB was obtained at 29.7 dB chip gain by controlling the amount of tensile strain. This gain is the highest value ever reported for SSC-SOAs grown by SAG techniques.

REFERENCES

[1] K. Magari, M. Okamoto, Y. Suzuki, K. Sato, Y. Noguchi and O. Mikami, IEEE J. Quantum Electron. **30**, 695 (1994).

[2] J.-Y. Emery, T. Ducellier, M. Bachmann, P. Doussiere, F. Pommereau, R. Ngo, F. Gaborit, L. Goldstein, G. Laube and J. Barrau, Electron. Lett. **33**, 1083 (1997).

[3] N. Yoshimoto, T. Ito, K. Magari, Y. Kawaguchi, K. Kishi, Y. Kondo, Y. Kadata, O. Mitomi, Y. Yoshikumi, Y. Hasumi, Y. Tohmori and O. Nakajima, Electron. Lett. **33**, 2045 (1997).

[4] M. Yamaguchi and M. Itoh, Proc. of OECC'98, Chiba, Japan. July, 1998. Paper 14B2-1.

[5] T. L. Koch, U. Koren, G. Eisenstein, M. G. Young, M. Oren, C. R. Giles and B. I. Miller, IEEE Photon. Technol. Lett. **2**, 88 (1990).

[6] O. Mitormi, K. Kasaya and H. Miyazawa, IEEE J. Quantum Electron. **30**, 1787 (1994).

[7] P. Dussiere, P. Garabedian, C. Graver, E. Derouin, E. Gaumont-Goarin, G. Michaud and R. Meilleur, Appl. Phys. Lett. **64**, 539 (1994).

[8] H. Sato, M. Aoki, M. Takahashi, M. Komori, K. Uomi and S. Tsuji, Electron. Lett. **31**, 1241 (1995).

[9] I. F. Lealman, L. J. Rivers, M. J. Harlow, S. D. Perrin and M. J. Robertson, Electron. Lett. **30**, 857 (1994).

[10] A. E. Kelly, I. F. Lealman, L. J. Rivers, S. D. Perrin and M. Siver, Electron. Lett. **32**, 1835 (1996).

[11] S. H. Kim, O. Laboutine, J. K. Ji, Y. C. Keh, H. S. Kim, Y. K. Oh, A. G. Choo and T. I. Kim, OECC'97, 9C2-4 (1997).

[12] J. R. Kim, J. S. Lee, S. S. Park, M. W. Park, J. S. Yu, A. G. Choo, T. I. Kim and Y. H. Lee, ISPSA'98 and J. of Korean Phys. Soc. (accepted).

[13] P. Doussière, Proc. of OAA'96, July 1996, p. 170.

Journal of the Korean Physical Society, Vol. 34, June 1999, pp. S281~S283

1550 nm Polarization Insensitive Laterally Tapered Travelling-Wave Semiconductor Laser Amplifiers with a Narrow Circular Beam Divergence

J. R. KIM*, J. S. LEE, S. S. PARK, M. W. PARK, J. S. YU,
S. D. LEE, A. G. CHOO and T. I. KIM

Photonics Laboratory, Material and Device Sector, Samsung Advanced Institute of Technology, Suwon 440-600

Y. H. LEE

Department of Physics, Korea Advanced Institute of Science and Technology, Taejon 305-701

A polarization-insensitive laterally tapered travelling-wave semiconductor laser amplifiers (TWSLAs) with a narrow circular beam divergence have been fabricated using metal-organic vapor phase epitaxy (MOVPE) technique. A narrow circular beam divergence of 20°×20°, an amplified spontaneous emission (ASE) ripple of 1.0 dB, and a polarization sensitivity of 1.5 dB were obtained at 27.8 dB chip gain.

I. INTRODUCTION

TWSLAs will be key components in future optical networks as they are able to perform a wide range of functions including linear amplification, dispersion compensation, signal processing and wavelength conversion. For enhancing fiber coupling efficiencies, narrow beam divergences *i.e.*, integration of spot-size converter is quite an efficient tool. Several approaches had been tried for this purpose [1–3]. The use of single lateral taper in TWSLAs with an angled window structures is very simple and promising because the device can be easily realized but shows a relatively good performance [3]. In this letter, we report the fabrication and evaluation of 1.55 μm single lateral tapered polarization insensitive TWSLAs.

II. TWSLA DESIGN AND FABRICATION

The device has a lateral taper at each facet for expanding the mode size. The stripe is oriented at 7° to the crystal axis. The respective lengths are 600 μm for the active section, 180 μm for the taper section and 20 μm for the window section. The total length of the device is 1.0 mm. Fig. 1 shows the schematic diagram for our device with single laterally-tapered core. The device consists of a 0.2 μm thick slightly tensile strained bulk InGaAsP (λ=1.55 μm) active layer, which is sandwiched between 0.1 μm thick InGaAsP (λ=1.3 μm) waveguides. The polarization insensitive condition was obtained at

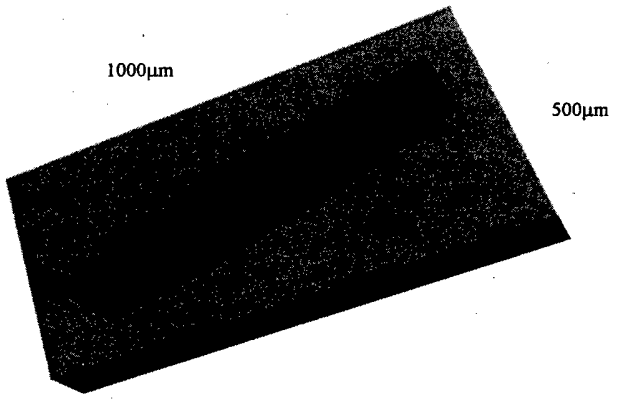

Fig. 1. Schematic diagram of TWSLA.

$\Delta a/a$=−0.065 % in the active medium [4]. By applying tensile strain in the bulk quaternary active layer, we can easily get polarization insensitive condition without going into sub-micron mesa width. A tensile strain in the active layer enhance TM gain by raising the position of the light-hole band *i.e.* by controlling both the amount of tensile strain and the width of the mesa stripe, we can get polarization insensitive conditions [3]. All the growth were performed by MOVPE at 60 torr and 600 °C. The width of the active waveguide is tightly controlled to 1 μm in the central gain section and less than 0.2 μm in the tapered regions. For achieving adiabatic mode size expansion and low loss in the angled stripe, a special mask design and fabrication are needed to reduce the step height in the angled tapered stripe photomask. The slope of the tapered region was maintained less than 6 mRad

*E-mail: acme@saitgw.sait.samsung.co.kr

to achieve adiabatic mode size expansion process. The stripe formation was performed by wet chemical etching by HBr-containing solutions. After the stripe formation, InP p-n current blocking layers were selectively regrown and after removing dielectric mask, a 2 μm thick p-InP cladding layer and a 0.2 μm p^+-InGaAs capping layer were overgrown over it. After fabrication, both facets were Anti-Reflection (AR) coated using a single pair of TiO_2/SiO_2 multi-layer films. The thickness of each coating material was calculated assuming plane waves at normal incidence so that the minimum reflectivity occurred at 1550 nm. Then they were modified slightly to account for the angled effect and the waveguide structure. The films were RF sputter-deposited sequentially with a base vacuum better than 1×10^{-6} mbar. The deposition pressure was around 1×10^{-3} mbar.

III. RESULTS AND DISCUSSIONS

Fig. 2 shows the SEM images of etched mesa stripe profiles. Along reverse-mesa direction, we can get nearly vertically etched profile but along forward-mesa direction, the etched angle is around 45°. For realizing vertically etched mesa profile, a special layer was inserted between InP and mask layers. Fig. 3 shows the typical L-I-V characteristics of TWSLAs at the room temperature pulsed operation condition. The threshold current was 50 mA and the slope efficiency was ~0.1 W/A. The slope efficiency is quite low comparing with that of conventional laser diode. It is because of the angle and window effect. The linearity was quite good up to 150 mA. It confirms that p-n current blocking layer works properly. Without AR coating, the center wavelength was ~1550 nm, but after AR coating, it moved down to 1530 nm.

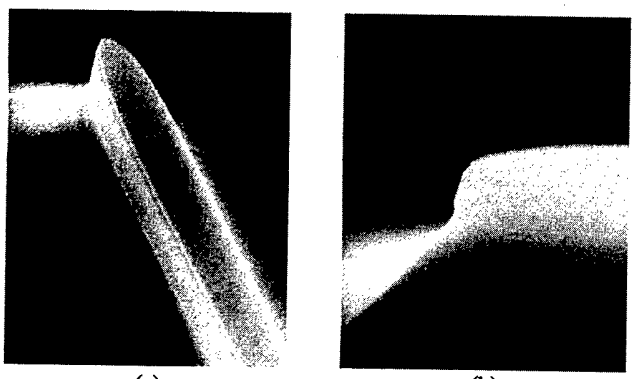

(a) (b)

Fig. 2. SEM view of mesa-etched stripe (a) Reverse mesa direction [1,−1,0] (b) Forward mesa direction [1,1,0].

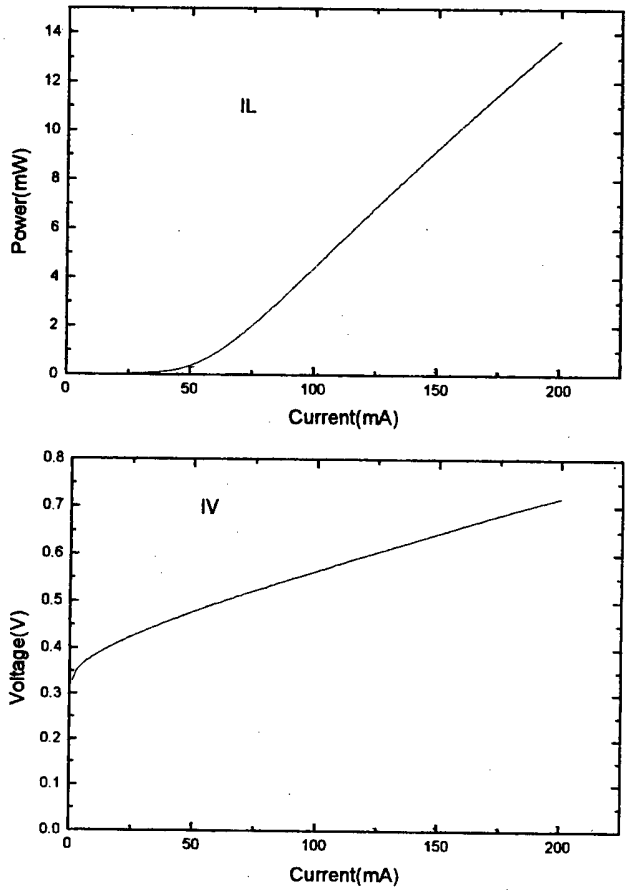

Fig. 3. Typical L-I-V characteristics of TWSLA.

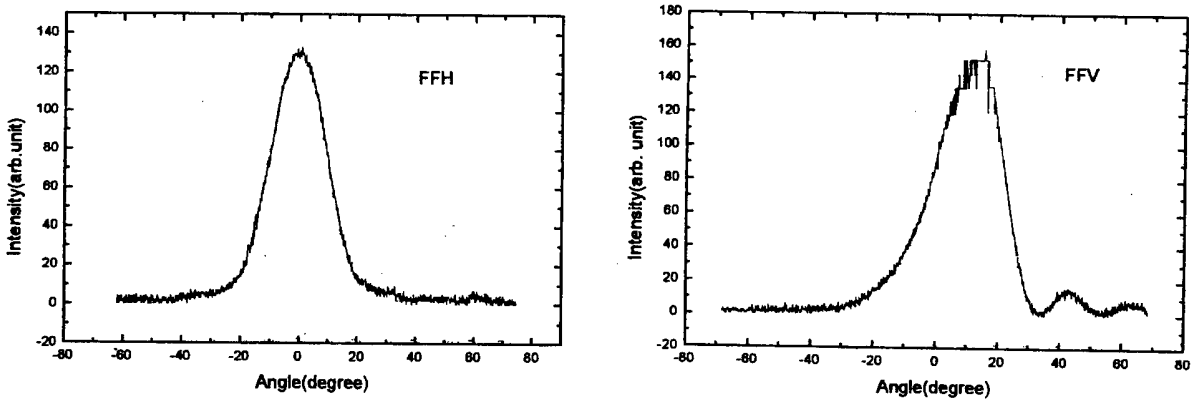

Fig. 4. Far-field patterns of TWSLA (a) and (b) represent the FFP for lateral and horizontal direction, respectively.

Fig. 4 shows a typical far-field pattern of the TWSLA at a bias current of 150 mA. The FWHM was 20° in both horizontal and vertical directions. The far-field angles of SOA are typically 50°×50°without lateral tapering. But, with lateral tapering, routinely we can get circular beam divergence of 20°×20°. The gain measurement was performed by coupling tapered lensed fibers to both facets. By the tunable laser, input optical signal was launched into SOA and the amplified output signal was monitored by optical spectrum analyzer. The gain vs. fiber input power characteristics at 1.55 μm is shown in Fig. 5. The signal gain as large as 27.8 dB was obtained at 200 mA. Fig. 6 shows the polarization resolved ASE spectra measured at 60, 100 and 150 mA. At 100 mA, the 3 dB optical bandwidth of the ASE spectrum was 40 nm. The ASE ripple amplitude of less than 1.0 dB is observed at 150 mA. This small ASE ripple corresponds to the reflectivity of $\sim 1.0\times10^{-4}$ at both facets. This value is normally obtainable with the angled, window structure and AR coating. The polarization sensitivity was 1.5 dB at 200 mA, which was made possible by controlling precisely the tensile strain amount of the active layer. More than 20 dB fiber-to-fiber gain was measured at 200 mA and the fiber coupling efficiencies per facet were ~50 % using AR-coated tapered fibers with 15 μm lenzed core.

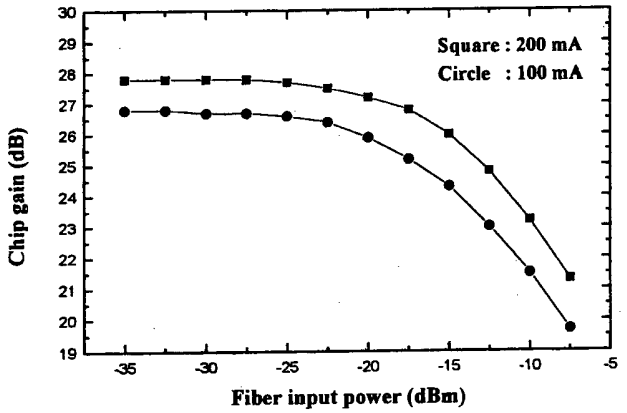

Fig. 5. Chip gain vs. fiber input power at λ=1.55 μm. Circles and squares represent the injection current of 100 mA and 200 mA, respectively.

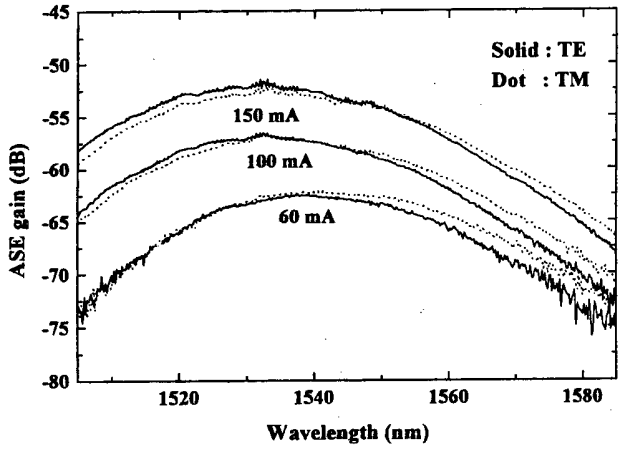

Fig. 6. Polarization resolved ASE spectra of TWSLA at 60, 100, and 150 mA. Solids and dots represent the TE and TM polarization, respectively.

IV. CONCLUSIONS

We have developed polarization-insensitive laterally tapered TWSLAs with angled window structures using MOVPE technique. A narrow circular beam divergence of 20°×20° was obtained by well defined single lateral tapering. The ASE ripple was 1.0 dB. The polarization sensitivity of 1.5 dB was obtained at 27.8 dB chip gain by controlling the amount of tensile strain in the active layer.

REFERENCES

[1] M. Yamaguchi and M. Itoh, *Proc. of OECC'98*, Chiba, Japan. July, 1998. Paper 14B2-1.

[2] N. Yoshimoto, T. Ito, K. Magari, Y. Kawaguchi, K. Kishi, Y. Kondo, Y. Kadata, O. Mitomi, Y. Yoshikumi, Y. Hasumi, Y. Tohmori and O. Nakajima, Electron. Lett. **33**, 2045 (1997).

[3] P. Doussière, *Proc. of OAA'96*, July, 1996. pp. 170-189.

[4] J. S. Lee, J. R. Kim, S. S. Park, M. W. Park, J. S. Yu, S. D. Lee, A. G. Choo and T. I. Kim, ISPSA'98 and J. Korean Phys. Soc. (accepted).

Journal of the Korean Physical Society, Vol. 34, June 1999, pp. S284~S289

Model Study of Internal Field Emission from a Nitrogen-Doped Diamond

Moon Sung CHUNG* and Byung-Gook YOON

University of Ulsan, Ulsan 680-749

Haeik LEE

Woosuk University, Wanju, Chonbuk 565-701

The field emission from the nitrogen-doped diamond is theoretically calculated. To investigate the effects of the geometry of the metal-diamond interface, we model the metal protrusion as either a sphere or a hyperboloid. The potential profiles in the depletion layer are calculated as a function of the tip geometry, the charge concentration, and the Schottky barrier. Then the field emission current densities are evaluated as the three parameters. The emission current is assumed to be identical to the internal field emission current through the metal-diamond barrier. The comparison between the theoretical and the experimental emission current leads to finding the values of the radius of curvature of the protrusion, the charge concentration in the depletion layer, and the Schottky barrier height. It is also found that, in describing both the potential profile and the depletion layer width, the hyperboloidal model is more appropriate than the spherical one.

I. INTRODUCTION

Diamond has recently received great interest as an ideal material for cold cathode field emitters. There has been much activity in developing composite thin film diamond devices for use as high-current, low-power field emission electron sources [1–3]. Difficulties associated with n-doping of diamond still persist and non-substitutional doping may be impossible [4].

Recently, protypes of diamond field emission devices have been fabricated by Geis *et al.* [5,6] and Okanao *et al.* [7]. Geis *et al.* made a vacuum device of a N-doped diamond with a roughened metal cathode [see Fig. 1] and obtained very low turn-on voltages for electron emission (~8 V). Such low onset voltages are explained to be due to the easy injection process at the back-contact. In the region near the metal, even the substitutionally doped nitrogens can be ionized by electron tunneling from N to the metal [8,9]. Due to the roughening process, there exist cone-like tips, which protrude into the diamond. Thus electrons are easily injected by tunneling through a sharp potential formed due to both a large charge concentration and a small radius of curvature of the metal tip. Once an electron is in the conduction band, it has Quasi-ballistically traversed the width of the diamond film [10]. Then it can slip into vacuum, without further acceleration by the field, because of the negative electron affinity (NEA) surface of the diamond crystal [11–13].

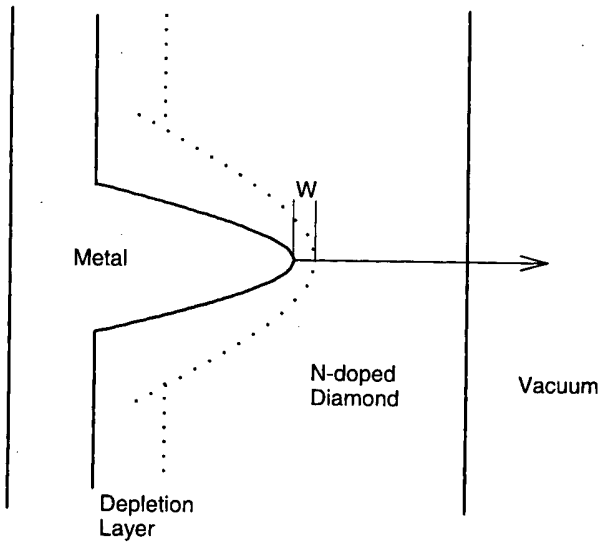

Fig. 1. Field emission from a sharp metallic emitter embedded in nitrogen-doped diamond. A depletion layer is formed due to only charge transfer from the diamond to the metal by tunneling. Unlike conventional n-doping, substitutional nitrogen-doping does not produce carriers directly in the conduction band.

The experimental work of Geis *et al.* has been theoretically explained by Lerner *et al.* [14]. They used the spherical tip model to find the properties of the potential profile in the depletion layer and calculated the field emission current j. However, they used the parametrized

*E-mail: mschung@uou.ulsan.ac.kr

Fowler-Nordheim equation to get j in agreement with experiment. Thus the full calculation is necessary to understand both the properties of Schottky barrier and the injection mechanism. The metal tip protruded into diamond can be model as either a sphere or a hyperboloid. In comparison with the spherical model, the hyperboloidal model is more complex but more exact in evaluation of the geometrical effects.

In the paper we first discuss a full calculation of j using a more exact spherical tip model. Next, we formulate a hyperboloidal model and calculate the field emission currents by assuming that the injection current is identical to the field emission current. The calculations are made exactly in principle. The current work is similar to the previous work [15] but includes the exact treatment of the spherical model.

II. SPERICAL MODEL OF A METAL-DIAMOND JUNCTION

In developing a spherical model, we follow Geis *et al.* [5] and Lerner *et al.* [14] to describe protrusions on the metal surface as spheres. Because of the strong dependence of the current on the field, the electron emission starts from the sharpest tips, *i.e.* those with the highest curvature. Emission from a protrusion is the internal tunneling through the potential barrier from the metal into the diamond. The potential $V(r)$ due to space charges in the depletion layer is the solution of the spherically symmetric part of the three-dimensional Poisson equation

$$\frac{1}{r^2}\frac{\partial}{\partial r}\left(r\frac{\partial V(r)}{\partial r}\right) - 4\pi\frac{\rho(r)}{\epsilon}, \tag{1}$$

with boundary conditions

$$V(R) = -\Phi_{Bn}, \tag{2}$$

$$\partial V(r)/\partial|_{r=R+W} = 0. \tag{3}$$

Here, ϵ is the dielectric constant of diamond (=5.7), W is the width of a depletion layer and Φ_{Bn} is the height of a Schottky barrier between metal and the n-type semiconductor. We assume that the charge density for $\rho = eN_d$ for $R < r < R + W$ (in the depletion layer) and $\rho = 0$ for $r > R + W$ (outside the depletion layer), where N_d is the concentration of the charged nitrogens. The solution of Eq. (1) satisfying the boundary conditions of Eqs. (2) and (3) is given by

$$V(r) = -\Phi_{Bn} + \frac{4\pi eN_d}{3\epsilon}[(R^2 - r^2)/2 \tag{4}$$

$$+(R+W)^3(1/R - 1/r)], \quad R < r < R + W$$

As shown in Eq. (4), $V(r)$ is given a function of R, N_d, and Φ_{Bn}.

We set V_B to be the potential drop over the depletion layer, *i.e.* the difference between the peak of a Schottky barrier and the bottom of the diamond conduction band in the absence of a field. Then we have $V(r = R+W) = -\Phi_{Bn} + V_B$, which leads to an equation

$$W^3 + \frac{3}{2}RW^3 - \frac{3\epsilon V_B R}{4\pi eN_d} = 0. \tag{5}$$

The solution of the cubic equation is

$$W = \begin{cases} \frac{R}{2}[(t+\sqrt{t^2-1})^{1/3} + (t-\sqrt{t^2-1})^{1/3} - 1], & t \geq 1 \\ \frac{R}{2}(2\cos\theta/3 - 1), & t \leq 1 \end{cases} \tag{6}$$

where

$$t = \frac{3\epsilon V_B}{\pi eN_d R^2} - 1, \tag{7}$$

$$\theta = \cos^{-1} t. \tag{8}$$

Similar to $V(r)$, W is given a function of R, N_d, and Φ_{Bn} (*i.e.* V_B).

III. HYPERBOLOIDAL MODEL OF METAL-DIAMOND JUNCTION

Protrusions on the metal look like a cone. Thus the field emission phenomena may be well described by a hyperboloidal tip model [15]. A hyperboloid is given by the coordinate surface of $\beta = \beta_o$ in prolate spheroidal coordinates (α, β, φ). The transformations are $x = a\sin h\alpha \sin\beta\cos\varphi$, $y = a\sin h\alpha\sin\beta\sin\varphi$, and $z = a\cos h\alpha\cos\beta$, where a is the focal length (see Fig. 2).

Similarly to the spherical model, the electric potential V satisfies the axially symmetric part of the 3-dimensional Poisson equation

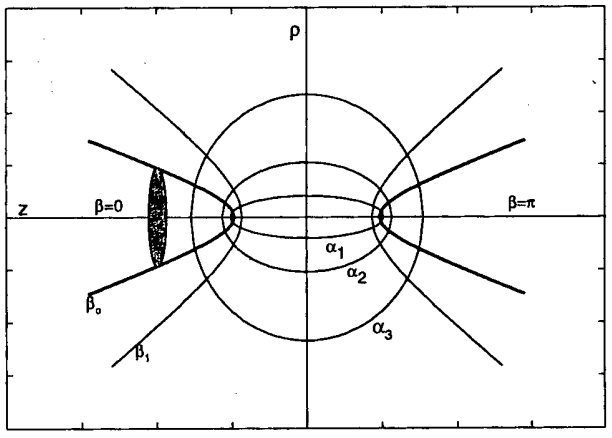

Fig. 2. Prolate spheroidal coordinates (α, β, φ). A hyperboloid is given by β=constant and is used as a shape of the cathode. The transformations are $x = a\sin h\alpha\sin\beta\cos\varphi$, $y = a\sin h\alpha\sin\beta\sin\varphi$, $z = a\cos h\alpha\cos\beta$, where a is the focal length.

$$\frac{1}{a^2(\sin h^2\alpha+\sin^2\beta)}\left[\frac{1}{\sin h\alpha}\frac{\partial}{\partial\alpha}\left(\sin h\alpha\frac{\partial V}{\partial\alpha}\right)+\frac{1}{\sin\beta}\frac{\partial}{\partial\beta}\left(\sin\beta\frac{\partial V}{\partial\beta}\right)\right]=-\frac{4\pi\rho}{\epsilon} \tag{9}$$

with the boundary conditions are $V(\beta_o)=-\Phi_{Bn}$ and $\left.\frac{dV}{d\beta}\right|_{\beta_1}=0$ [15]. The charge density is assumed to be $\rho=eN_d$ for $\beta_o\le\beta\le\beta_1$ (in the depletion region) and $\rho=0$ for $\beta\ge\beta_1$ (outside the depletion region).

For description of field emission, we do not need the solution of the Poisson equation in the whole region but only in the emission region, *i.e.* along the z-axis. In the region of interest ($\alpha=0$), the solution of Eq. (9) satisfying the required boundary conditions is [15]

$$v(\beta)=\frac{4\pi N_d a^2}{3\epsilon}\left[2\ln\frac{\sin\beta}{\sin\beta_o}+\frac{1}{2}(\sin^2\beta-\sin^2\beta_o)-\cos\beta_1(2+\sin^2\beta_1)\ln\frac{\tan\beta/2}{\tan\beta_o/2}\right]-\Phi_{Bn} \tag{10}$$

The geometrical parameters a and β_o are related to the radius, R, of curvature of the emitter. If the surface is given by $\beta=\beta_o$, then R is given by

$$R=a\sin\beta_o\tan\beta_o. \tag{11}$$

The coordinate β_1 is determined by the potential drop V_B over the depletion layer. At the same time, the width W of the depletion layer along the z-axis is obtained:

$$W=a(\cos\beta_o-\cos\beta_1), \tag{12}$$

where is given from Eq. (11).

The use of Eqs. (11) and (12) make it possible to replace β_o and β_1 by more apparent quantities R and W in Eq. (10). We had also better change the position variables from β to z , where z is the distance from the surface of $\beta=\beta_o$. By argument analogous to Eq. (12) for W, we easily have $z=a(\cos\beta_o-\cos\beta)$. Now we can obtain the electric potential as a function of z for given R, W, and Φ_{Bn}. The obtained potential energy is used in evaluation of transmission coefficients, which are also used in calculation of emission currents.

IV. INTERNAL FIELD EMISSION

The internal field emission from the metal into the diamond is the same process as the tunneling from the material to vacuum. The difference is that a space charge exists in diamond, while no space charge exists in vacuum. The current density of the internal emission is then given by the following equation [16]

$$j=\frac{4\pi me}{h^3}\int f(E)D(E-E_t)dE_tdE \tag{13}$$

where e is the electronic charge, E the total energy, E_t the transverse component of E, $f(E)$ the Fermi distribution function, and $D(E_n)$ the transmission coefficient with normal energy $E_n=E-E_t$.

To investigate the effects of the tip geometry and the ion concentration more exactly, we employed the scheme of Lui and Fukuma [17] for $D(E_n)$. The basic idea of that scheme is the use of the Airy function which is the exact solution of the Schrodinger equation in the linear potential region. By dividing the whole domain into very many subdivisions and matching each solution at the boundary, we find $D(E_n)$ for the Schottky barrier. An electron injected into the conduction band propagates quasi-ballistically through the diamond thin film. The NEA of diamond's surface allows the electron to escape into vacuum with minimal or zero potential drop. Therefore, the internal field emission from the metal into the diamond at the back contact can be identified with the field emission through the whole device.

V. CALCULATIONS AND RESULTS

We calculate the electric potential energies $-eV(z)$ for several R's and N_d's. In the calculation, we use $eV_B=E_F+e\Phi_{Bn}$, where $E_F=6.0$ eV, the Fermi energy of Ni. For comparison with the work of Geis *et al.*, we use a Ni metal tip. These potential energies with respect to the Fermi energy of diamond are shown in Fig. 3(a) for a spherical model and in Fig. 3(b) for a hyperboloidal model. As expected, sharp drops are seen near the junction. The larger the curvature of the emitter surface, the larger the barrier reduction and the thinning. When $N_d=10^{19}/\text{cm}^3$, $R\to\infty$ (a flat surface), and $\Phi_{Bn}=4.0$ eV [7,18,19], we obtained $W=250$ Å for both a spherical and a hyperboloidal tip. Figure 4(a) and (b) also show that the depletion layer width W depends on the curvature for several values of N_d. It can be seen that a large reduction of W is made as R decreases or N_d increases. The effect of high nitrogen- doping is twofold. Firstly, the field creates a space charge near the metal, producing a sharp drop in the field strength. Secondly, the depletion layer is thin enough to facilitate field-emission transport through the resulting Schottky barrier. The effect of the ion concentration is more effective than the curvature in producing a barrier reduction and thinning. This also implies that the depletion layer is most important for the injection process.

Now we find the electric potential energy $U(z)$, which will be used, for the calculation of the transmission co-

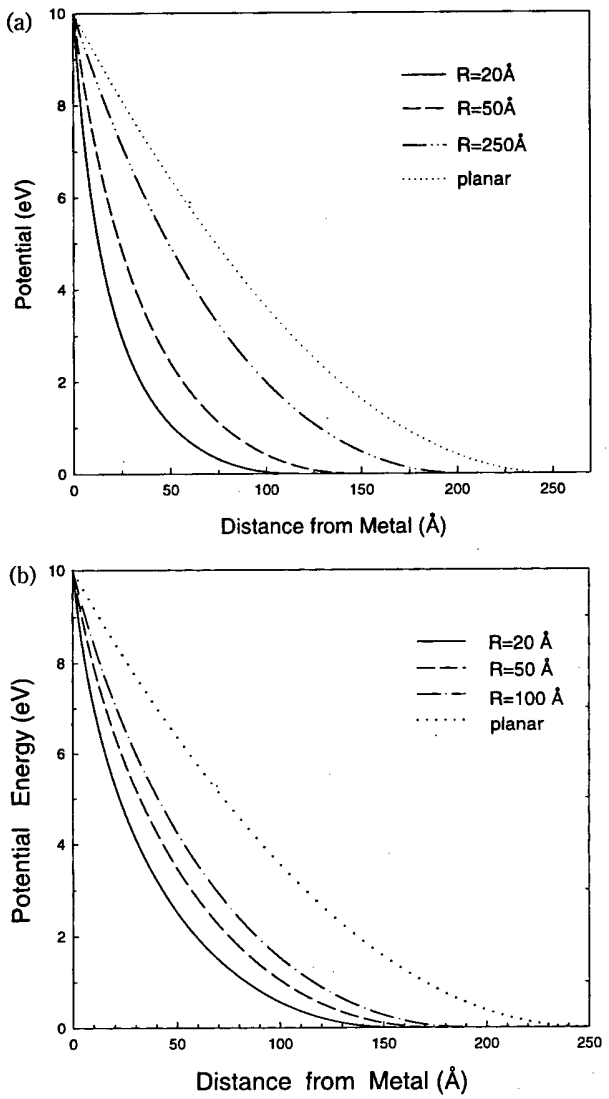

Fig. 3. Potential in the depletion layer for a spherical emitter (a) and for a hyperboloidal emitter (b). These are plotted with respect to the Fermi energy of diamond, where the Fermi energy of the metal (Ni) is 6 eV. We choose the ionized nitrogen concentration $N_d = 10^{19}/\text{cm}^3$, the Schottky barrier height $\Phi_{Bn} = 4.0$ eV, and the radius of curvature $R = 20$, 50, 100 (or 250) Å, ∞).

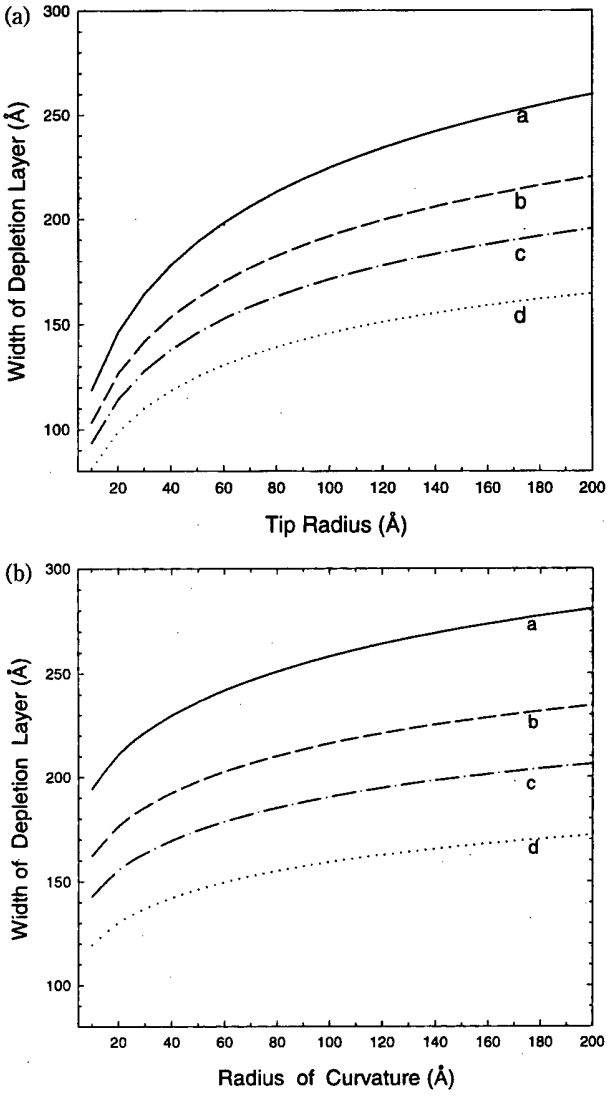

Fig. 4. Plot of the width of depletion layer vs. the radius of curvature for a spherical emitter (a) and for a hyperboloidal emitter (b). We choose $\Phi_{Bn} = 4.0$ eV and $N_d = 0.50$ (a), 0.75 (b), 1.00 (c), 1.50 (d) $\times 10^{19}$/cm. It is shown that W depends strongly on N_d as well as on R.

efficient $D(E)$. With respect to the Fermi energy of diamond, $U(z)$ is a sum of the electric potential $-eV(z)$ due to space charge, the image interaction U_{im}, and the field energy $-eFz/\epsilon$:

$$U(z) = E_F - eV(z) + U_{im} - eFz/\epsilon. \tag{14}$$

It is clear that U_{im} has curvature dependence. Approximating the curved surface as a sphere, we have [20]

$$U_{im}(z) = \frac{-e^2}{4\epsilon}\left(\frac{1}{z+z_i} - \frac{1}{z+z_i+2R}\right) \tag{15}$$

where z is the distance measured from the curved surface and represents the image plane. In the limiting case of $R \to \infty$, U_{im} becomes $-e^2/(4\epsilon(z+z_i))$, the image interaction for a flat surface. This implies that the image potential for a curved surface is less than that for a flat surface. Then we evaluate the total potential energy $U(z)$ as a function of both R, N_d, and Φ_{Bn}.

The obtained $U(z)$ is used to calculate the transmission coefficient $D(E)$. Instead of the WKB method, we use the Lui and Fukuma [17] scheme to calculate $D(E)$ which is exact in principle. We divide the depletion layer into about 400 subdivisions so that the potential may be linear. Then we calculated $D(E)$ using the scheme explained in the previous section. Difference of one or two orders in magnitude were found between values of $D(E)$ calculated by the WKB and current methods.

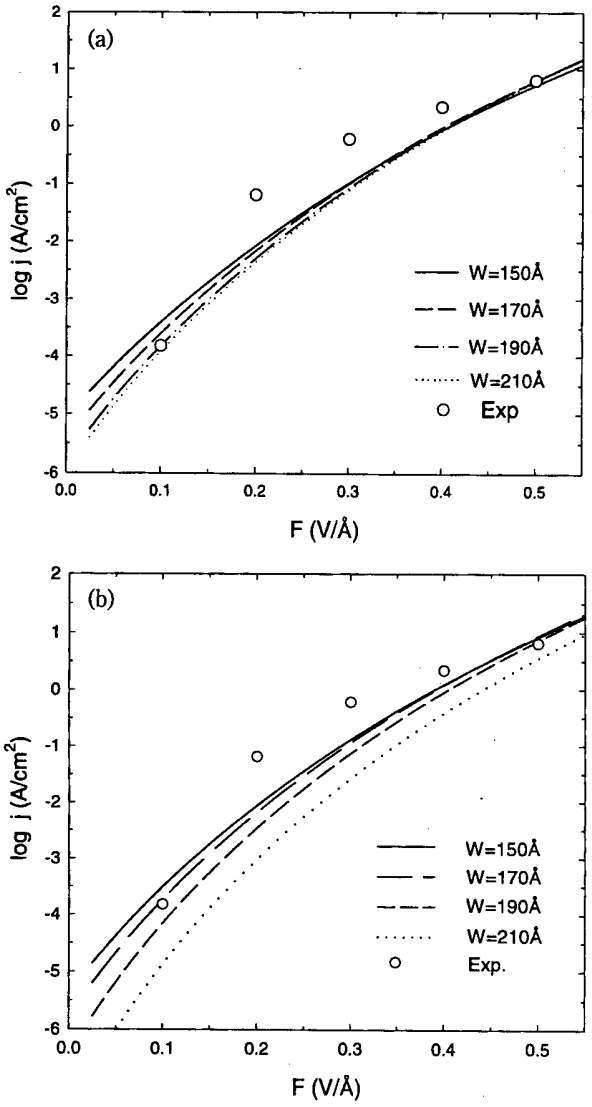

Fig. 5. Field emission current density vs. the external field for a spherical model (a) and a hyperboloidal model (b). The emission current density j's are plotted for several values of W which were determined from the values of Φ_{Bn}, N_d, and R (see Table 1). The theoretical values are in reasonable agreement with the data of Geis *et al.* [5] (circles).

Once $D(E)$ is obtained, evaluation of Eq. (13) is straightforward because the integral does not depend on the band structure. For given values of Φ_{Bn}, N_d, and R, we calculate the internal emission current densities j. These results are shown in Fig. 5(a) for a spherical model and in Fig. 5(b) for a hyperboloidal model. The plots are labeled with W instead of the given set (Φ_{Bn}, N_d, R). The reason is because all the sets of (Φ_{Bn}, N_d, R) associated with a specific value of W yield almost the same j (see Table 1). As far as only j are concerned, both seem to be in reasonable agreement with the experimental values [5].

Among the theoretical calculations using the hyperboloidal model, the j-curves of $W = 170$ and 190 Å look

Table 1. Set (Φ_{Bn}, N_d, R) associated with depletion layer width W. Here, Φ_{Bn} is the Schottky barrier height, N_d the doping concentration, and R the radius of curvature. These values are chosen so that the calculated emission currents can be best fitted with the measured values.

Tip	Sphere				Hyperboloid			
W (Å)	150	170	190	210	150	170	190	210
$e\Phi_{Bn}$ (eV)	4.5	4.3	4.2	4.2	4.2	4.1	4.0	4.0
N_d (10^{19}/cm^3)	1.40	1.00	0.73	0.53	1.75	1.25	0.95	0.75
R (Å)	91	91	88	80	99	85	82	79

to be in best agreement with experiment. This choice is based on the agreements in both j and (Φ_{Bn}, N_d, R). As shown in Table 1, the value of $W = 170$ Å corresponds to the set ($\Phi_{Bn} = 4.1$ eV, $N_d = 1.25\times10^{19}$/cm^3, $R = 85$ Å). The $W = 170$ Å corresponds to the set ($\Phi_{Bn} = 4.0$ eV, $N_d = 0.95\times10^{19}$/cm^3, $R = 82$ Å). The experimental values of Geis *et al.* are $\Phi_{Bn} = 4.0$ eV, $N_d = 1.0\times10^{19}$/cm^3, and $r \leq 100$ Å. However, this good agreement is found to not expected for a spherical model. We try to obtain set (Φ_{Bn}, N_d, R) in such agreement with values of Geis *et al.* As shown in Table 1, the Schottky barrier height corresponding the values of $W = 170$ and 190 Å for spherical model are 4.5 and 4.3 eV which seems to be too large in comparison to the measured ones.

It is also argued that the hyperboloidal shape is the more realistic shape. In the above analysis, a given hyperboloid is assumed to have the same radius of curvature of the sphere at the tip apex. Thus, we have similar results in j for two models. However, the tip apex is taper-like and then may better be described by a curvature-changing shape. In addition, the hyperboloidal model can take into account the enhancement of the due to the protrusion at the tip apex. In regard to this argument, it is also noted that the field intensities used in the Fig. 5 are local fields. The local fields are much different from the macroscopic fields which are measured in experiments. The difference in two values may ranges over factors of from 100 to 10000, depending on the geometry. Such a geometry effect can be better considered using the hyperboloidal model that the spherical model. When the potential difference V_o is applied between a hyperbolic cathode of $\beta = \beta_o (< \pi/2)$ and the planar counter electrode with distance $z_o (= a\cos\beta_o)$, the field at the tip apex is given by $F = V_o/[a\sin^2\beta_o \ln\tan(\beta_o/2)]$ or $F = V_o/[R\cos\beta_o \ln\tan(\beta_o/2)]$, where R is given by Eq. (11). Instead, the field at the spherical surface is given by $F = V_o/R$ for a sphere of radius r. This implies that the hyperboloidal model can describe the field at the tip more appropriately than the spherical model. Finally, the width of the depletion layer changes with the curvature of the tip surface, which can be explained only by the hyperboloidal model.

The comparison between theoretical and experimental values, at some fields, reveals one or two orders of

magnitude difference, which is not considerable in the emission current. There is also a difference in shape of the I-V characteristic curve between theory and experiment. This seems to be significant to the property of the Schottky barrier, which may be due to several reasons. One is that the theoretical j is the emission current from one tip, while the experimental j is the result of those from many tips. This difference changes with the field intensity, as shown in Fig. 5. Another is due to the different quantities used as abscissa. The abscissa of the I-V curve is the field in theory, while it is the voltage in experiment. Combining the first reason and the second reason gives rise to a different relation between the field and the voltage, depending on the number of tips (*i.e.* the shape of the emission area). The third reason is that the theoretical j is the emission current through the back contact while the measured j is that through the whole device. That is, the reason is partly due to our assumption of ballistic transport in diamond and a negative electron affinity at the diamond-vacuum interface. The other reason is the fact that internal injection through the Schottky barrier is not the only possibility for the presence of nitrogen in the diamond lattice [21,22]. It has been conjectured that high concentrations of these non-stoichiometric atoms can produce defect subbands as sources of tunneling states in the energy gap.

VI. CONCLUSIONS

The internal field emission is believed to be an important process which makes the field emission from a substitutionally nitrogen-doped diamond possible. The structual and the compositional dependences of the Schottky barrier can be understood using the two models, a spherical and a hyperboloidal tip model. Since negative electron affinity surfaces are involved in the electron emission into vacuum, the internal emission from the metal into the diamond is approximately equal to the field emission from the whole device. A reasonable agreement exists between the theoretical and the experimental emission currents. This leads to finding of material parameters, the curvature of the metal protrusion, the charge concentration, and the Schottky barrier height. It is finally concluded that the hyperboloidal model is good for describing the Schottky barrier of a roughened junction.

ACKNOWLEDGMENTS

This work is supported by the academic research fund of the Ministry of Education, Republic of Korea (project No. ISRC 98-E-4417).

REFERENCES

[1] T. Yamada, H. Ishihara, K. Okano, S. Koizumi and J. Itoh, J. Vac. Sci. Technol. **B15**, 1678 (1997)

[2] W. I. Milne, *Proceeding of the 2nd Int. Vac. Electron Sources Conf.*, Tsukuba, Japan, July 7-10, 1998, p. 67.

[3] G. A. J. Amaratunga, M. Baxendale, N. Rupasinghe, D. A. I. Munindrasada, M. Chhowalla and T. Butler, *Proceeding of the 11th Int. Vac. Microelectronics Conf.*, Ashevill, NC, USA, July 19-24, 1998, p. 184.

[4] G. Popovici and M. Prelas, *Wide Band Gap Electronic Materials*, edited by M. Prelas, P. Gielisse, G. Povovici, B. V. Spitsyn and T. Stacy (Kluwer, Dordrecht, 1995), p. 1.

[5] M. W. Geis, J. W. Twichell and T. M. Lyszcczarz, J. Vac. Sci. Technol. **B14**, 2060 (1996).

[6] M. W. Geis, J. W. Twichell, N. N. Efremow, K. Krohn and T. M. Lyszcczarz, Appl. Phys. Lett. **68**, 2294 (1996).

[7] K. Okano, S. Komizumi, S. Ravi, P. Silva and G. A. J. Amaratunga, Nature **381**, 140 (1996).

[8] Y. Miyamoto and M. Saito, Phys. Rev. **B57**, 6527 (1998).

[9] P. H. Cutler, N. M. Miskovsky, P. Lerner and M. Chung, submitted to Appl. Surf. Sci.

[10] P. H. Cutler, Z.-H. Huang, N. M. Miskovsky, P. D'Ambrosio and M. Chung, J. Vac. Sci. Technol. **B14**, 2020 (1996).

[11] R. J. Nemanich, P. K. Baumann and J. van der Weide, Proceeding of Appl. Diamond Films and Related Mat. 3rd Int. Conf., 1995, edited by A. Felderman, Y. Tzeng, Y. Yoshigawa and M. Murakawa, p. 17.

[12] J. van der Weide and R. J. Nemanich, J. Vac. Sci. Technol. **B10**, 1940 (1992).

[13] C. Bandis and B. B. Pate, Phys. Rev. Lett. **74**, 777 (1995).

[14] P. Lerner, P. H. Cutler and N. M. Miskovsky, J. Vac. Sci. Technol. **B15**, 337 (1997).

[15] M. S. Chung, Chai Pyo Lim and Byung-Gook Yoon, J. Korean Phys. Soc. **33**, 730 (1998).

[16] A. Modinos, *Field, Thermionic, and Secondary Emission Spectroscopy* (Plenum, New York, 1984).

[17] W. W. Liu and M. Fukuma, J. Appl. Phys. **60**, 1555 (1986).

[18] F. J. Himpsel, P. Heimann and D. E. Eastman, Solid. State Comm. **36**, 631 (1980).

[19] T. Tachibana, B. E. Williams and J. T. Glass, Phys. Rev. **B45**, 11975 (1992).

[20] J. D. Jackson, *Classical Electrodynamics*, 2nd edition (John Wiley and Sons, NY, 1974).

[21] M. S. Chung, I. W. Kim and J. M. Park, J. Korean Phys. Soc. **30**, S198 (1997).

[22] Z.-H. Huang, P. H. Cutler, N. M. Miskovsky and T. E. Sullivan, Appl. Phys. Lett. **65**, 2562 (1994).

Journal of the Korean Physical Society, Vol. 34, June 1999, pp. S290~S294

First-principles Calculations for the Vibrational Frequencies of H_2 and H_2^* Complexes in Si

Yong-Sung KIM, Young-Gu JIN, Ji-Wook JEONG and K. J. CHANG

Department of Physics, Korea Advanced Institute of Science and Technology, Taejon 305-701

We present the results of first-principles pseudopotential calculations for the local vibrational frequencies of H_2 and H_2^* complexes in crystalline Si within the local-density-functional approximation. The vibrational modes and frequencies are determined by the full dynamical matrix which is constructed using a supercell geometry. Including gradient corrections for the exchange-correlation potential, we find the vibrational frequencies of 2071 and 1784 cm^{-1} for the stretch modes of the H_2^* complex, while 784 and 598 cm^{-1} for the wagging modes, consistent with experimentally measured values. For the H_2 molecule at a tetrahedral site, we examine the [100], [110], and [111] orientations, and find the stretch modes in the range of 3556~3643 cm^{-1}, in good agreement with previous calculations and experiments.

There have been extensive studies for the behavior of hydrogen impurities in semiconductors. Hydrogen incorporated in semiconductors exhibits a number of different configurations such as isolated interstitials or hydrogen-associated complexes bound to defects or impurities. There have many indications that hydrogen also forms a dimer configuration. Many theoretical calculations predicted that the most stable formation is a H_2 molecule at a tetrahedral site [1–3]. Because of the strong interaction between the two H atoms, the binding energy of the H_2 molecule is much higher than that of interstitial H atoms. Direct experimental evidence for the existence of H_2 molecules has been failed until recently, which is attributed to the presumed infrared inactivity due to no dipole moment. Very recently, Murakami and his coworkers obtained a direct evidence for the presence of H_2 molecules in hydrogenated Si by measuring a broad Raman line at 4158 cm^{-1} [4], close to that of a free molecule (4160 cm^{-1}) in the gas phase. They assigned the Raman line to the stretch mode of the isolated H_2 molecule at or near a T_d site. Two subsequent Raman and infrared spectroscopy studies also confirmed the molecular formation, however, the measured vibrational frequency is 3618 cm^{-1} [5,6], well below the free-molecule value. Thus, it is now believed that the measured line at 4158 cm^{-1} results from H_2 molecules trapped within the voids formed by the hydrogen plasma-induced platelets which are generated during the hydrogen plasma treatment [7]. A number of theoretical calculations showed that the vibrational frequency of the H_2 molecule exhibits a substantial downward shift, compared with that of a free molecule [8–10]. It was argued that the weakening of the H-H bond is correlated with the semiconductor host charge density near the interstitial site. Because the H_2 molecule is positioned at the tetrahedral site, the anharmonic effects were shown to be significant, lowering the harmonic vibrational frequency [9]. In previous studies which are based on the local-density-functional approximation, the vibrational frequency is generally underestimated by several hundreds of cm^{-1}, as compared to experiments. The other stable form of hydrogen dimers was predicted to be the H_2^* complex, in which one H atom is in the bond-centered position, while the other is in the antibonding position [11]. Although the energy difference between the H_2 and H_2^* dimers is few tens of eV, most theoretical calculations indicated that the H_2 molecule is more stable than the H_2^* complex [3,11,12]. The experimental evidence for the presence of H_2^* was first given by Holbech *et al.*, who measured infrared modes in proton-implanted Si [13].

In this paper, we report the results of first-principles pseudopotential calculations for the local vibrational frequencies of the H_2 and H_2^* complexes in crystalline Si within the local-density-functional approximation (LDA). We also test the generalized-gradient approximation (GGA), and find that the H-associated bond lengths are smaller than those obtained from the LDA, raising the vibrational frequencies. We set up the full dynamical matrix using a supercell geometry, and determine the normal vibrational modes for each complex. For the H_2 molecule, we consider three different orientations along the [100], [110], and [111] directions. With the generalized-gradient approximation for the exchange and correlation potential, the stretch modes of the H_2 molecule in these orientations lie in the range of 3556~3643 cm^{-1}, in good agreement with recent experimental results. If the anharmonic effects are considered, we expect that the vibrational frequencies calculated by the GGA are still lower by about 200 cm^{-1} than the measured value. In addition to the stretch mode, we

find that the H_2 molecule exhibits a localized mode at 650~700 cm^{-1} above the bulk phonon band, which is experimentally observable. For the H_2^* complex, the GGA also gives slightly higher vibrational frequencies for both the stretch and wagging modes, compared with the LDA results.

The total energies are calculated using the first-principles pseudopotential method within the local-density-functional approximation [14]. Norm-conserving nonlocal pseudopotentials are generated by the scheme of Troullier and Martins [15], and then transformed into a separable form of Kleinman and Bylander [16]. The wave functions are expanded in a plane-wave basis set with a kinetic energy cutoff up to 64 Ry. The vibrational frequency of a stretch mode strongly depends on the corresponding bond length, because a stronger bond causes a smaller bond length and thus increases the vibrational frequency. Therefore, it is important that the calculated bond lengths of H-related bonds are fully converged. The bond lengths of the Si-H bonds in the H_2^* complex are plotted as a function of the kinetic energy cutoff in Fig. 1(a). In the LDA calculations, the Ceperley-Alder expression [17] for the LDA exchange-correlation potential gives shorter Si-H bond lengths, compared with the Wigner interpolation formula. These bond lengths are further reduced when the PW91 form is employed for the GGA exchange-correlation energy [18]. Similarly, the H-H bond length of the H_2 molecule is also decreased in the GGA calculations, as shown in Fig. 1(b). We ensure from Fig. 1 that the bond lengths and the total energies are well converged with the kinetic energy cutoff of 64 Ry.

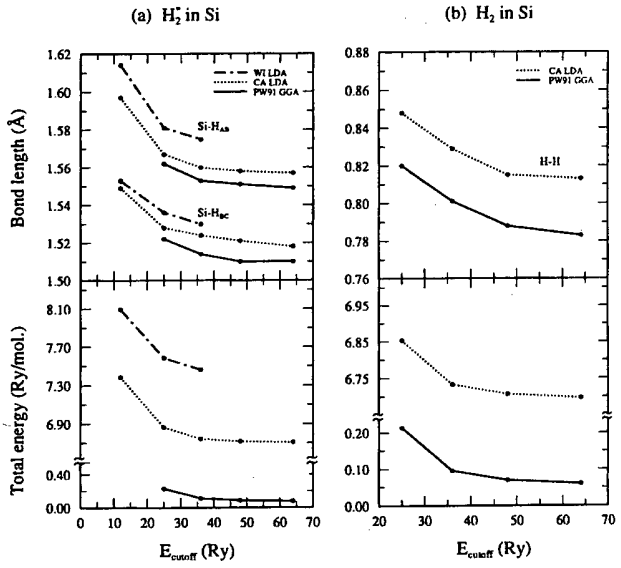

Fig. 1. The bond lengths and the total energies for (a) the H_2^* complex and (b) the H_2 molecule are plotted as a function of the kinetic energy cutoff. The LDA results using the Wigner (WI) interpolation formula and the Ceperley-Alder (CA) expression for the exchange-correlation potential are compared with the GGA results.

We employ a supercell containing 32 host atoms throughout this work, which was also shown to be sufficient in obtaining numerical convergence [8,9]. We optimize the atomic geometries of the H_2^* and H_2 complexes until the Hellman-Feynman forces [19] acting on the atoms are less than 0.001 Ry/(a.u.)^2. Testing a larger 64-atom supercell, we find no changes in the energetics and vibrational frequencies of the H_2^* and H_2 complexes. To perform the Brillouin zone summation of the charge density, we use a special **k**-point set of uniform grids in the 32-atom supercell, while only the Γ point in the 64-atom supercell.

In modern first-principles electronic structure calculations, the atomic model of a defect in a solid mostly relies on the energetics of various defect configurations. Although this theoretical approach enables us to calculate the vibrational frequencies of defects, the calculations are usually performed for known normal modes with the use of a frozen-phonon approximation. As an alternative method, if the dynamical matrix approach is used, all the vibrational modes associated with a defect as well as the corresponding vibrational frequencies can be determined once the force constants between atoms are calculated. Nevertheless, the calculations of the dynamical property of a defect provides rich information on identifying the defect model, in conjunction with Raman and infrared spectroscopy studies. Here we set up the dynamical matrix using a supercell geometry, which contains either a H_2 molecule or a H_2^* complex. The dynamical matrix elements are obtained by first calculating the Hellman-Feynman forces acting on all the atoms, when a given atom is displaced. For each direction, we choose both forward and backward displacements to eliminate the third-order anharmonic effect, with displacements of 2~10 % of the bond length. To reduce the computational effort, we replace the matrix elements associated with atoms very far from a defect by those calculated for a supercell geometry of perfect bulk Si. We find that this approach gives very accurate estimates for the localized vibrational frequencies of defects, although it may cause some errors for the bulk phonon band of the host material. Testing two different sets of the displaced atoms in the neighborhood of each hydrogen complex, we find almost no change in the defect vibrational frequencies. The resulting dynamical matrix is diagonalized for zero wave vector. To produce the degeneracy of vibrational modes for each complex, the matrix elements are calculated for atoms within the supercell, which preserve the defect symmetry. The H_2 molecule at a tetrahedral site has D_{2d}, C_{2v}, and C_{3v} symmetries for the [100], [110], and [111] orientations, respectively, while the H_2^* complex with two Si-H bonds aligned along the [111] direction has C_{3v} symmetry. We test the 32- and 64-atom supercells and estimate the vibrational frequencies to be accurate to within 5 %.

For the H_2 molecule at or near a tetrahedral site, two localized vibrational modes exist for all the orientations considered here, as shown in Fig. 2, while the oth-

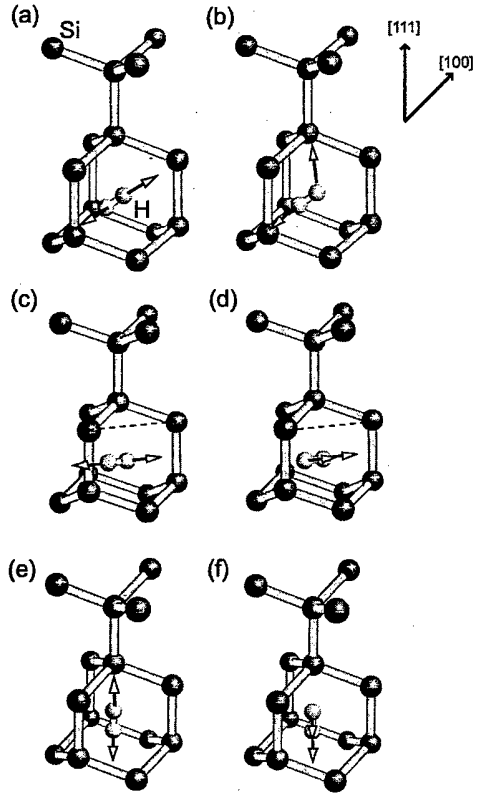

Fig. 2. Atomic displacements are drawn schematically for (a) the stretch and (b) twist modes of the H_2 molecule in the [100] orientation. For the [110] orientation, the localized modes correspond to (c) the stretch and (d) longitudinal displacement modes, while the same modes for the [111] orientation are given in (e) and (f).

er modes are resonant in the bulk phonon band. In this case, the stretch mode has the highest vibrational frequency with the out-of-phase displacements of the H atoms along the orientation of the molecule. For the H_2 molecule in the [100] orientation, our LDA calculations show that the vibrational frequency of the stretch mode is 3260 cm^{-1} (see Table 1), similar to other LDA results of 3000~3400 cm^{-1} [8,9]. In the GGA calculations, this vibrational frequency is increased to 3556 cm^{-1}. For the [110] and [111] orientations, we estimate the GGA vibrational frequencies to be 3603 and 3643 cm^{-1}, respectively. Thus, the LDA generally underestimates the vibrational frequencies of the H_2 molecule, while the GGA results are close to the measured value of 3618 cm^{-1} [5,6]. The better agreement of the GGA calculations with experiments is attributed to the reduced bond length of the H-H bond, as illustrated in Table 1. However, we point out that if anharmonic effects are included, the harmonic frequencies of the stretch mode by the GGA are expected to be reduced. For a free H_2 molecule in the gas phase, we find that although the GGA gives a vibrational frequency of 4124 cm^{-1}, close to the measured value of 4160 cm^{-1}, the lowering of the harmonic frequency due to anharmonic effects is as much as 160 cm^{-1}. Compared with the [100] orientation, the vibrational frequencies of the H_2 molecules with the [110] and [111] orientations are closer to the experimental value. However, the analysis of the energetics can not give a definite decision for the orientation because the energy differences between the different orientations are about 0.01 eV, less than the accuracy of our calculations. Nevertheless, both the LDA and GGA calculations indicate that the vibrational frequency of the H_2 molecule in the Si lattice is substantially downward shifted from that of the free molecule, correlated with other theoretical calculations. Thus, our results are consistent with previous suggestions that the Raman line observed at 4158 cm^{-1} results from H_2 molecules trapped in voids, which may be created during the hydrogen plasma treatment. The vibrational frequency of the other localized mode is found to lie just above the bulk phonon band, suggesting that this new mode is experimentally observable. The atomic displacements of the new localized mode are drawn in Fig. 2. For the [100] orientation, the new normal mode called as a twist mode has a vibrational frequen-

Table 1. The relative energies (ΔE), bond lengths (d_{H-H}), and local vibrational frequencies (ω) for the H_2 molecules in the [100], [110], and [111] orientations are listed. The LDA and GGA results are compared with other calculations and experiments.

	Mode	[100]		[110]		[111]		Other	Expt.
		LDA	GGA	LDA	GGA	LDA	GGA	Calc.	
ΔE (eV/mol)		0	0	0.008	0.008	0.012	0.011		
d_{H-H} (Å)		0.813	0.783	0.810	0.780	0.808	0.779		
ω (cm^{-1})	stretch	3260	3556		3603		3643	3363[a]	3618[b,c]
								3396[d]	
								3708[e]	
	twist	605	651						
	long. displ.				688		699		

[a]Reference [8].
[b]Reference [5].
[c]Reference [6].
[d]Reference [9].
[e]Reference [10].

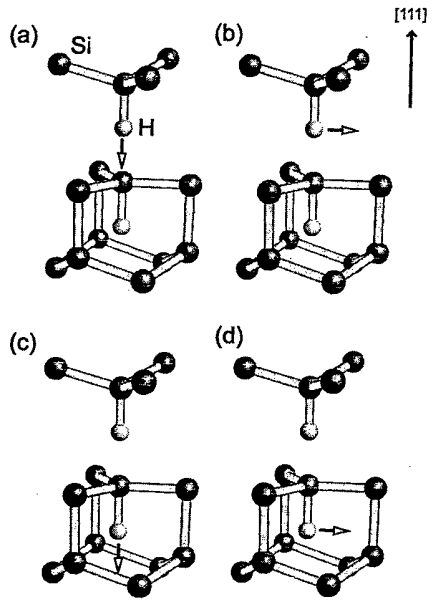

Fig. 3. Atomic displacements are drawn schematically for the stretch and wagging modes of the H_2^* complex: (a) the BC stretch, (b) BC wagging, (c) AB stretch, and (d) AB wagging modes.

cy of 605 cm^{-1} in the LDA calculation, while 651 cm^{-1} in the GGA. When the H_2 molecule is oriented either along the [110] or [111] direction, the new localized mode looks like a longitudinal displacement along the bond direction, with in-phase displacements, as shown in Fig. 2. The GGA calculated frequencies of the longitudinal displacement mode are 688 and 699 cm^{-1} for the [110] and [111] orientations, respectively, similar to the twist mode in the [100] orientation.

The normal modes of the H_2^* complex are illustrated in Fig. 3. Because of the C_{3v} symmetry, the wagging modes for both the H atoms positioned at the bond-centered and antibonding sites are degenerate. Since the Si atom adjacent to the H_{BC} atom has a sp^3-like bonding configuration, the H_{BC} atom is more strongly bonded to the Si atom, as compared to the H_{AB} atom bonded to the neighboring Si atom with a sp^2-like hydridization. In fact, our LDA calculations show that the equilibrium bond length of the Si-H_{BC} bond is 1.518 Å, whereas it is 1.557 Å for the Si-H_{AB} bond, as shown in Table 2. Thus, the vibrational frequency of 1945 cm^{-1} for the stretch mode of the Si-H_{BC} bond is much higher than the value of 1677 cm^{-1} for the Si-H_{AB} bond. In the wagging mode, we find the LDA vibrational frequency of 553 cm^{-1} for the Si-H_{BC} bond, while a higher value of 711 cm^{-1} for the Si-H_{AB} bond. The higher wagging frequency of the Si-H_{AB} bond results from the fact that the H_{AB} atom experiences stronger restoring forces during the vibration, because more charges are accumulated on the plane which is formed by the sp^2-bonded Si atom and the three neighboring Si atoms. We note that the LDA vibrational frequencies for both the stretch and wagging modes are underestimated by about 6~13 %, compared with infrared absorption spectroscopy measurements [13]. In the GGA, the bond lengths of the Si-H_{BC} and Si-H_{AB} bonds are reduced by about 0.5 %, raising the vibrational frequencies, as shown in Table 2. Thus, the GGA values for both the stretch and wagging modes are in better agreement with experiments. It is known that the LDA usually overestimates the bind energies, which may be attributed to the underestimation of the transfer energy from *s*-orbital to *p*-orbital [20]. Since there is almost no *sp* hybridization in the H atom, the correlation energies for the H-related bonds may be different from that of the Si-Si bond, thus, the LDA weakens the H-H and Si-H bonds. Including gradient corrections for the exchange-correlation potential, the GGA appears to increase the strength of the H-associated bonds.

Table 2. The bond lengths (d_{Si-H}) and local vibrational frequencies (ω) for the H_2^* complex are listed. The LDA and GGA results are compared with other calculations and infrared measurements.

	Bond	Mode	LDA	GGA	Other Calc.[a]	Expt.[a]
d_{Si-H} (Å)	Si-H_{BC}		1.518	1.510		
	Si-H_{AB}		1.557	1.549		
ω (cm^{-1})		stretch(BC)	1945	2071	2165	2062
		stretch(AB)	1677	1784	1844	1838
		wagging(AB)	711	784	1002	817
		wagging(BC)	553	598	612	

[a]Reference [13].

In summary, we have calculated the local vibrational frequencies of the H_2 and H_2^* complexes in Si using the first-principles pseudopotential method within the local-density-functional approximation and also performed the GGA calculations. Using the dynamical matrix approach, we have determined the normal modes and corresponding vibrational frequencies. We find that the LDA generally underestimates the vibrational frequencies, compared with experiments. When the GGA is employed, the bond distances of the H-H and Si-H bonds are slightly reduced, raising the vibrational frequencies. Thus, the GGA harmonic frequencies of the stretch and wagging modes for the H_2^* complex are in good agreement with experiments. For the H_2 molecule at or near the tetrahedral site, we have considered the [100], [110], and [111] orientations, and find the GGA frequencies for the stretch modes to lie in the range of 3556~3643 cm^{-1}, close to the measured value of 3618 cm^{-1}. We predict that the H_2 molecule exhibits a localized mode just above the bulk phonon band, with a frequency of 651~699 cm^{-1}. Finally, we address that although the GGA gives the vibrational frequencies in better agreement with experiments, the harmonic frequencies are expected to be decreased by including the anharmonic effects.

We would like to thank Dr. Y.-J. Ko and Dr. T.-Y.

Chung for helpful discussions. This work is supported by the MOST-FOTD and the CMS at KAIST.

REFERENCES

[1] J. W. Corbett, S. N. Sahu, T. S. Shi and L. C. Snyder, Phys. Lett. **93A**, 303 (1983).

[2] C. G. Van de Walle, Y. Bar-Yam and S. T. Pantelides, Phys. Rev. Lett. **60**, 2761 (1988).

[3] K. J. Chang and D. J. Chadi, Phys. Rev. **B40**, 11644 (1989).

[4] K. Murakami, N. Fukata, S. Sasaki, K. Ishioka, M. Kitajima, S. Fujimura, J. Kikuchi and H. Haneda, Phys. Rev. Lett. **77**, 3161 (1996).

[5] R. E. Pritchard, M. J. Ashwin, J. H. Tucker and R. C. Newman, Phys. Rev. **B57**, R15048 (1998).

[6] A. W. R. Leitch, V. Alex and J. Weber, Phys. Rev. Lett. **81**, 421 (1998).

[7] A. W. R. Leitch, V. Alex and J. Weber, Solid State Commun. **105**, 215 (1998).

[8] Y. Okamoto, M. Saito and A. Oshiyama, Phys. Rev. **B56**, R10016 (1997).

[9] C. G. Van de Walle, Phys. Rev. Lett. **80**, 2177 (1998).

[10] B. Hourahine, R. Jones, S. Öberg, R. C. Newman, P. R. Briddon and E. Roduner, Phys. Rev. **B57**, R12666 (1998).

[11] K. J. Chang and D. J. Chadi, Phys. Rev. Lett. **62**, 937 (1989).

[12] C. G. Van de Walle, Phys. Rev. **B49**, 4579 (1994).

[13] J. D. Holbech, B. Bech Nielsen, R. Jones, P. Sitch and S. Öberg, Phys. Rev. Lett. **71**, 875 (1993).

[14] M. L. Cohen, Phys. Scr. **T1**, 5 (1982).

[15] N. Troullier and J. L. Martins, Phys. Rev. **B43**, 1993 (1991).

[16] L. Kleinman and D. M. Bylander, Phys. Rev. Lett. **48**, 1425 (1982).

[17] D. M. Ceperley and B. J. Alder, Phys. Rev. Lett. **45**, 566 (1980).

[18] J. P. Perdew, *Electronic Structure of Solids '91*, edited by P. Zeische and M. Eschrig (Akademie Verlag, Berlin, 1991).

[19] H. Hellmann, *Einführung in die Quantenchemie* (Deuticke, Leipzig, 1937), p. 285; R. P. Feynman, Phys. Rev. **B56**, 340 (1939).

[20] P. Fulde, *Electron Correlations in Molecules and Solids* (Springer, Berlin, 1995), p. 49.

Journal of the Korean Physical Society, Vol. 34, June 1999, pp. S295~S298

Photoluminescence Study of 1018 meV Defect Lines from Ion-implanted Silicon

Hosun LEE*, Suk-Ho CHOI, Euze SEONG and S. M. KIM

Department of Physics and Institute for Natural Sciences, Kyung Hee University, Suwon 449-701

H. J. LIM

Department of Physics, Ajou University, Suwon 442-749

We investigated the defects of ion-implanted silicon with boron and argon ions using photoluminescence method. The 1018 meV line, so called I_1 line, and its phonon side bands were observed in both boron- and argon-implanted silicon crystals. In argon-implanted silicon crystals, we observed 1009 meV line ($I_1 - Ar$) and its phonon side bands which arose from argon-I_1 complex in addition to the splitting of the I_1 line. Annealing temperature dependence of the intensities of the I_1 and $I_1 - Ar$ lines in argon-implanted silicon was very similar for both Czochralski and float zone silicon crystals whereas that of boron-implanted silicon was very different between the two growing methods. We discussed on the origin of the defects responsible for the I_1 and $I_1 - Ar$ lines.

I. INTRODUCTION

With ever decreasing electronic device size, small concentration of defects may affect device performance significantly and the understanding of defects is essential to optimize device performance. Ion implantation method is a standard processing step in silicon devices. Ion bombardment generates defects in silicon and subsequent thermal annealing does not remove defects completely. There may be remaining defect centers associated with ion-implantation.

The 1018 meV line, so called I_1 or W line, was observed using photoluminescence from silicon crystals which were ion implanted or neutron irradiated [1–4]. With electron irradiation, no I_1 line was reported so far. And yet the origin behind the 1018 meV is controversial [5]. The I_1 line is independent of the impurity content of the crystal or of the species being implanted. Therefore it may be caused by an intrinsic defect. The line has C_{3v} symmetry and may arise from the electron paramagnetic resonance A3 center (a tetragonal vacancy or a trigonal di-interstitialcy) or the trigonal di-interstitialcy [6,7]. Recently, Estreicher *et al.* suggested using Hartree-Fock calculations that divacancies may be the origin for I_1 line [8]. However, they did not investigated other defects, *e.g.* Si self-interstitials, as a candidate.

Here, using photoluminescence method, we investigated the I_1 and $I_1 - Ar$ lines in detail and studied the annealing temperature dependence of the lines. Based on the experiments, we discuss the nature of defects which are responsible for the I_1 and $I_1 - Ar$ lines.

*E-mail: hlee@nms.kyunghee.ac.kr, Fax: 82-331-204-8114

II. EXPERIMENTS

Ions such as boron and argon were implanted at room temperature on Czochralski (CZ) and Float Zone (FZ) silicon wafers which were lightly doped with n-type dopant (phosphorous) or p-type dopant (boron). The resistivities of CZ and FZ n-Si were $16 \sim 23$ ohm-cm and 50 ohm-cm, respectively. The kinetic energy of the ions was 90 keV and the ion dose was 10^{13} cm^{-2}. Thermal annealing was performed in ultra high vacuum chamber up to 750 °C for 30 minutes. The photoluminescence system was composed of 1 m focal length monochromator with 8 K low temperature cryostat. The excitation source was argon ion laser with wavelength 4880 Å. The power density was varied between 25 Wcm^{-2} and 50 Wcm^{-2}.

III. RESULTS

Figure 1(a) and 1(b) are the photoluminescence spectra of n-type silicon substrates ((a) CZ-grown and (b) FZ-grown) implanted with boron and argon ions which were subsequently annealed at 580 °C and 750 °C, respectively. In Figure 1(a), we observed 1018 meV line (I_1 line) and its phonon side band. In Figure 1(b), in addition to the I_1 line, we observed 1009 meV line ($I_1 - Ar$) which arose from the complex of I_1 defect center and ar-

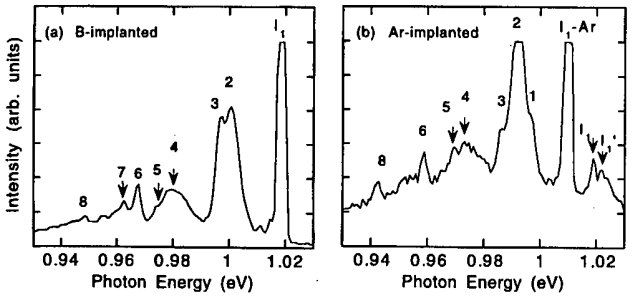

Fig. 1. Plot of 8-K photoluminescence spectra of (a) boron-implanted n-type CZ Si and (b) argon-implanted n-type FZ Si which were isochronally annealed at 580 °C and 750 °C, respectively. The numbers designate the phonon side bands of I_1 (1018 meV) and $I_1 - Ar$ lines (1009 meV).

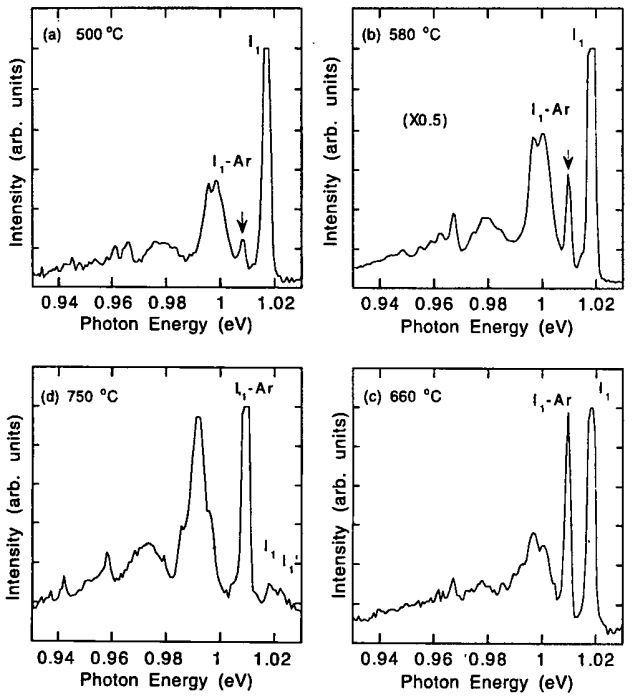

Fig. 2. Plot of 8-K photoluminescence spectra of argon-implanted n-type CZ Si which were isochronally annealed at (a) 500 °C, (b) 580 °C, (c) 660 °C, and (d) 750 °C.

gon ion.

Figure 2 is the plot of CZ n-type silicon which were ion-implanted with argon and annealed isochronally between 500 °C and 750 °C. Almost identical PL spectra were also observed in Ar-implanted FZ n-Si. The 1009 meV feature began to appear at 500 °C and dominated the I_1 line at 750 °C. For 750 °C annealed Ar-implanted Si of both CZ and FZ, we observed new 1022 meV line (I_1') in addition to 1018 meV line. The 1022 meV line could be the splitting of 1018 meV line.

Figure 3(a) and 3(b) are plots of the temperature dependence of the I_1 and $I_1 - Ar$ lines which arose from ion-implanted Si crystals with boron and argon, respec-

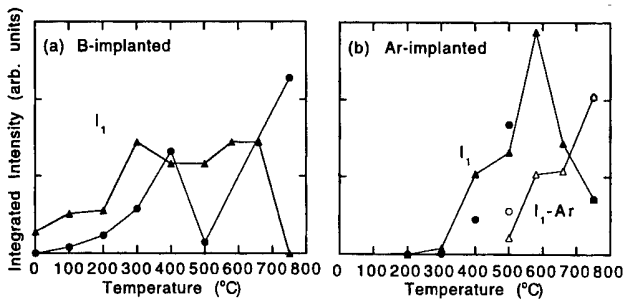

Fig. 3. Temperature dependence of the intensities of I_1 line (1018 meV) and $I_1 - Ar$ line (1009 meV) from (a) boron-implanted and (b) argon-implanted n-type Si. Full triangles and circles designate the integrated intensities of I_1 line from CZ and FZ n-Si and unfilled triangles and circles designate the same for $I_1 - Ar$ line.

tively. It shows clearly that the I_1 oscillator strength began to be transferred to the $I_1 - Ar$ complex at about 500 °C.

IV. DISCUSSION

In Figure 1(a) and 1(b), we observed the zero-phonon luminescence, 1018 meV (Fig. 1(a)) and 1009 meV line (Fig. 1(b)), and their phonon sidebands. The coupling between electronic transitions and localized phonons near defect centers were studied theoretically in detail by Maradudin and Davies *et al.* [4,9]. Electronic transitions associated with defect centers can be coupled either to delocalized phonons to conserve momentum or localized phonons because the equilibrium position of defects in ground and excited states is different. The sharp zero-phonon line was explained in analogy with Mössbauer effect. It has been reported that the I_1 defect center can couple to the noble gas atoms (He, Ne, Ar, Kr, or Xe) and thus I_1-noble gas atom complexes show very similar phonon sideband to those of bare I_1 defect centers [3]. The relative energies of phonon sidebands with respect to zero-phonon energy were the same for both of I_1 and $I_1 - Ar$. In Fig. 1(a) and 1(b), 2 is associated with TA phonon (18 meV) and 4 is associated with 2TA line (38 meV), respectively, and others are associated with localized phonons near the defect centers. They showed characteristic features such as mass-dependent systematic line shift of zero phonon line and common trigonal defect symmetry [10–12]. In Fig. 1(b), the $I_1 - Ar$ line dominated the I_1 defect center at 750 °C. The splitting of I_1 line in 750 °C annealed argon-implanted Si may be due to local strain around the I_1 defect center caused by nearby Ar ions [12]. In contrast, $I_1 - Ar$ line may be a chemical bonding between I_1 defect center and Ar ion. According to Bürger *et al.*, uniaxial stress applied on ion implanted Si crystals along [110] or [111] direction caused similar splittings of the I_1 line [10]. Depending

on the site of Ar ion in unit cell, I_1 defect and Ar ion could form $I_1 - Ar$ complex or the charge distribution near the I_1 defect center may be simply distorted due to local strain near Ar ion when the Ar atom is near the defect center with some distance.

In Fig. 2 and 3(b), only the I_1 line and its phonon sideband were observed up to 400 °C in Ar-implanted Si. And the oscillator strength of the I_1 line began to be transferred to the $I_1 - Ar$ complex at 500 °C suggesting the formation of the bonding between the I_1 defect center and Ar ions. This may suggest that the barrier height for the Ar atom to form bonding with the I_1 defect center is about 67 meV. Near 750 °C, the $I_1 - Ar$ complex dominated the whole spectra. Similar temperature dependence was also reported by Bürger *et al.* [3]. They reported that the intensity of I_1 line reached maximum at 200 °C and transformed to $I_1 - Ar$ line near 450 °C. This discrepancy of annealing temperature for the I_1 and $I_1 - Ar$ lines may arise from difference in ion energy, ion dose, or residual impurities. We note that we observed similar temperature dependence of the intensities of the I_1 and $I_1 - Ar$ lines for Ar implanted Si, whether CZ or FZ Si.

The defect center responsible for the I_1 line is under controversy. Possible defect centers are intrinsic vacancies or interstitials, independent of implanted ions and residual impurities. Recently, Estreicher *et al.* studied the implantation of noble-gas ions in Si using Hartree-Fock calculations [8]. According to their study, noble-gas-divacancy complexes are very stable and may be the origin for the 1009 meV line and its phonon side band. According to their study, the $I_1 - Ar$ complex has the minimum energy when an Ar atom occupy the divacancy. And they suggested that the 1018 meV line is due to the neutral divacancy.

In Fig. 3(b), the I_1 line in boron-implanted CZ and FZ Si crystals show very different temperature dependence. The I_1 line intensity in CZ Si increased up to 300 °C and began to decrease abruptly at 660 °C and disappered at 750 °C. whereas the I_1 line intensity in FZ Si almost disappeared at 500 °C and began to increase rapidly above 500 °C. However, in Fig 3(a), the I_1 and $I_1 - Ar$ line showed very similar temperature dependence for both CZ and FZ argon-implanted Si. The different temperature dependence between B-implanted CZ and FZ Si should arise from interactions of boron atoms with residual oxygens or carbons. We note that CZ Si have much higher oxygen content than FZ Si. The I_1 line is observed without annealing for boron-implanted Si whereas $I_1 - Ar$ line is only observed after annealing for Ar-implanted Si. The interactions between borons and impurities may be responsible for the difference. Boron-impurity interactions have been studied by several groups [13–15].

In Fig. 3(a), the intensity of I_1 line reached maximum at [300, 660] degrees and decreased abruptly near 700 degrees in B-implanted CZ Si. This may support that divacancies are the origin of I_1 line as was suggested by Estreicher *et al.* Recently, Eichler *et al.* studied divacancies in B-implanted Si using infrared absorption method and found that the divacancy concentration disappeared near 475 °C for B-implanted CZ Si [16]. Considering unknown residual defects or impurities of the Si crystals, the temperature dependence of the intensities is roughly similar to ours. However, Libertino *et al.* used deep level transient spectroscopy (DLTS) measurement to study defects in B-implanted Si thin films which were grown epitaxially. They noted that a balance of concentration of divacancies and interstitials was maintained up to 350 °C of annealing temperature and only interstials rather than divacancies remained above 350 °C [17,18].

The dominance of the concentration of interstitials over that of divacancies at high annealing temperature could be due to extra ion effect. In electron-irradiated Si, however, the concentration of vacancies and interstitials was the same for any annealing temperature [17]. One notable point is the extra ion effect; the Frenkel pair generation of an equal number of vacancies and interstitials is unbalanced by the incorporated extra ions which displace Si atoms from equilibrium points in the lattice. This is the basis for +1 model [18,19]. Surprisingly, we note that the I_1 line has not been observed yet from electron-irradiated Si which is free from the extra ions although divacancies and interstitials are abundant in electron-irradiated Si crystals [4]. Based on this we suggest that the I_1 line may arise from other defects, *e.g.* self interstitials, rather than divacancies. More detailed study is under progress using DLTS and electron paramagnetic resonance.

V. CONCLUSIONS

The photoluminescence of boron- and argon-implanted silicon crystals was studied experimentally. We observed the I_1 line (1018 meV) and the $I_1 - Ar$ line (1009 meV). The annealing temperature dependence of the I_1 and $I_1 - Ar$ lines was measured. For Ar-implanted CZ and FZ Si, the intensity of the I_1 line decreased and that of $I_1 - Ar$ line increased as temperature increased between 400 °C and 750 °C. This is explained that the bare I_1 defect center began to form a complex with an Ar ion near 500 °C. Furthermore, we observed the splitting of the I_1 line for Ar-implanted, 750 °C-annealed Si. We attribute the splitting to the local strain near the I_1 defect center caused by nearby Ar ion. We compared to literature the temperature dependence of the I_1 line in boron-implanted CZ and FZ Si.

ACKNOWLEDGMENTS

This work was supported in part through Basic Science Research Program, Ministry of Education, BSRI-97-2443.

REFERENCES

[1] J. R. Noonan, C. G. Kirkpatrick and B. G. Streetman, Rad. Eff. **21**, 225 (1974).

[2] C. G. Kirkpatrick, J. R. Noonan and B. G. Streetman, Radiation Effects **30**, 97 (1976).

[3] N. Bürger, K. Thonke, R. Sauer and G. Pensl, Phys. Rev. Lett. **52**, 1645 (1984).

[4] G. Davies, E. C. Lightowlers and Z. E. Ciechanowska, J. Phys. **C20**, 191 (1987).

[5] G. Davies, Phys. Rep. **176**, 83 (1989).

[6] Y. H. Lee and J. W. Corbett, Phys. Rev. **B9**, 4351 (1974).

[7] J. W. Corbett, J. C. Bourgoin and C. Weigel, IOP Conf. Ser. **16**, 1 (1973)

[8] S. K. Estreicher, J. Weber, A. Derecskei-Kovacs and D. S. Marynick, Phys. Rev. **B55**, 5037 (1997).

[9] A. A. Maradudin, *Solid State Physics*, edited by F. Seitz and D. Turnbull (Academic, New York, 1966), Vol. 18, p. 273.

[10] N. Bürger, E. Irion, A. Teschner, K. Thonke and R. Sauer, Phys. Rev. **B35**, 3804 (1987).

[11] N. S. Minaev, A. V. Mudrii and V. D. Tkachev, Phys. Stat. Sol. (b) **108**, K89 (1981).

[12] V. D. Tkachev, A. V. Mudry and N. S. Minaev, Phys. Stat. Sol. (a) **81**, 313 (1984).

[13] M. T. Asom, J. L. Benton, R. Sauer and L. C. Kimmerling, Appl. Phys. Lett. **51**, 256 (1987).

[14] T. E. Haynes, D. J. Eaglesham, P. A. Stalk, H.-J. Gossman, D. C. Jacobson and J. M. Poate, Appl. Phys. Lett. **69**, 1376 (1996).

[15] P. B. Rasband, P. Clancy and M. O. Thompson, J. Appl. Phys. **79**, 8998 (1996).

[16] S. Eichler, J. Gebauer, F. Börner, A. Polity, R. Krausr-Rehberg, E. Wendler, B. Weber, W. Wesch and H. Börner, Phys. Rev. **B56**, 1393 (1997).

[17] S. Libertino, J. L. Benton, D. C. Jacobson, D. J. Eaglesham, J. M. Poate, S. Coffa, P. Kringhoj, P. G. Fuochi and M. Lavalle, Appl. Phys. Lett. **71**, 389 (1997).

[18] J.L. Benton, S. Libertino, P. Klinghoj, D. J. Eaglesham, J. M. Poate and S. Coffa, J. Appl. Phys. **82**, 120 (1997).

[19] M. D. Giles, J. Electrochem. Soc. **138**, 1160 (1991).

Journal of the Korean Physical Society, Vol. 34, June 1999, pp. S299~S304

Si/Ge Intermixing Phenomena on Ge/Si(100) Surface

Xiao Yan ZHU[1] and Young Hee LEE[1,2*]

Department of Semiconductor Science and Technology[1,2], Department of Physics[2], and Semiconductor Physics Research Center[1,2], Jeonbuk National University, Jeonju 561-756

Nam-kyun Kim

Department of Bionics and Biomedical Engineering, Jeonbuk National University, Jeonju 561-756

Si/Ge interfacial intermixing phenomena have often been observed in epitaxial Ge overlayer growth on Si surfaces. Yet, it is not clear if this Si/Ge intermixing originates from an energetically favorable configuration or from nonequilibrium growth conditions. Using the first principles calculations we propose a model of defect-induced Si/Ge intermixing that is both energetically and kinetically favorable. Dimer-exchange and monomer-exchange processes are evaluated, and found to be energetically stable. The respective energy barriers in our calculations are 0.6 eV and 1.9 eV, and the estimated annealing temperatures are close to the experimental values.

I. INTRODUCTION

Despite well-known fabrication processes for Si-based electronic devices, its application to optoelectronic devices is still limited by the indirect band gap of Si. Si/Ge quantum wells and superlattices have been suggested to convert the bandgap into the direct bandgap by the zone-folding effect. The difficulty of fabricating such quantum structures arises from the atomistic control of Si/Ge abrupt interfaces during the heteroepitaxial crystal growth, let alone the realization of the zone-folding effect.

Controlling one monolayer (ML) of Ge atoms on Si surface is thus fundamentally important. The Ge atoms can easily float to the growing surface due to the surface free energy difference between the Si and the Ge layers when alternating Si/Ge layers are fabricated. The interface of the Ge atoms on Si surface is believed to be smoother than those of the Si atoms on Ge surface, supporting the concept of surface free energy difference [1–4]. Contrary to these observations, recent experiments suggest that the interfacial Si/Ge intermixing occurs even in the case of Ge overlayer depositions on Si surface followed by typical annealing temperatures [5–11]. The intermixing phenomena are observed in a wide range of Ge overlayer coverage up to seven MLs [8,10] and in a temperature range from 650 to 900 K.

It is generally believed that the surface free energy is lowered when the Ge atoms are deposited on Si surfaces, since Ge bulk has weaker binding energy than Si bulk. Therefore it is difficult to imagine how the Ge atoms can be able to intermix with subsurface Si atoms, which seems to violate the energetics. One may conjecture that this intermixing is associated with nonequilibrium processes. Yet, one monolayer deposition of Ge atoms at low temperature subsequently followed by high temperature annealing clearly suggests that both energetically and kinetically stable intermixed Si/Ge configuration may exist [11].

In this paper, we explore energetically and kinetically favorable configurations of Si/Ge intermixed layers. We note that one full monolayer of the Ge atoms on Si surface is always energetically favorable over one monolayer of the Si atoms on Ge surface. This suggests that under normal circumstances the intermixing is unlikely to be observed. Therefore, in this study we introduce a defect, for instance, a dimer vacancy in the dimerized Ge monolayer on Si surface. A monomer-exchange process and a dimer-exchange process are investigated in this work. We first search for the energetically stable configurations of intermixed Si/Ge geometries near the Ge dimer vacancy. We will also endeavor to find appropriate kinetic pathways that may occur at reasonable growth temperatures.

II. THEORETICAL APPROACHES

Our calculations have been carried out using Car-Parrinello molecular dynamics (MD) approach [12]. The interaction between ionic cores and valence electrons is described by a fully nonlocal norm-conserving pseudopotential [13] with a separable form of s (s, p) nonlocality for Si (Si and Ge) introduced by Kleinman and Bylander [14] and similarly the H atom is treated locally [15,16].

*E-mail: leeyh@sprc2.chonbuk.ac.kr

The electronic wavefunctions are expanded with a kinetic energy cutoff of 12 Ry for the Si/Ge system, and the Γ point is used as the single special sampling point for the zone summation [17,18].

The convergence of the kinetic energy cutoff was evaluated with a silane molecule, which provides the Si-H bond length of 1.51 Å, slightly overestimating the experimental value of 1.48 Å, and reproduces the reasonable vibrational frequencies of silane molecules. The test was also done for the Si-Ge dimer, reproducing the correct ratio of the Si-Ge bond length of the Si-Ge alloys [19]. We estimate the energy difference between different configurations with larger cutoff to be approximately 0.1 eV. We searched for the electron energy minimization using a steepest decent approach for a given geometry. Ions were then moved by the fast relaxation scheme [20]. Remaining forces on surface atoms were less than 1.5×10^{-3} Ry/Å in equilibrium. The energy was converged to 1.0×10^{-5} Ry through calculations.

The surface is simulated by a periodically repeated slab of Si atoms in which six atomic layers (each layer with (4×2) surface unit cell) are included, with the bottom surface terminated by hydrogens to saturate dangling bonds. One ML of Ge atoms are placed on the top of the Si surface with p(2×2) asymmetric structure, being followed by a vacuum region of 6 Å. Two bottom Si layers and an additional H layer are fixed to prevent any spurious forces by the H atoms. The periodic boundary conditions are applied to the x ([110]), y ([1$\bar{1}$0]) and z ([001]) directions. The surface is exposed along the z direction.

III. RESULTS AND DISCUSSION

We first study one full ML of Ge atoms on Si (001) surface. Figure 1 shows fully relaxed Ge p(2×1), Ge p(2×2), and Si p(2×2) phases. The fully relaxed Ge ML prefers to reconstruct with an asymmetric p(2×2) phase, since the total energy of the p(2×1) structure is higher than that of the p(2×2) by 0.24 eV/dimer. The energy difference is almost twice as that of Si/Si(001) surface [21], suggesting stonger dehybridization to sp^2+p for Ge/Si(001) surface. The asymmetry of the p(2×2) phase is larger than that of the p(2×1) phase. The bond lengths of the top Ge-Ge dimers of these two structures are and similar and elongated to 2.53 Å, compared to those of the bulk Ge of 2.45 Å. This agrees well with the experimental results [8,22]. In the p(2×2) configuration, the Ge-Si bond lengths between the top Ge and the subsurface Si layers are about 2.39 Å in average, following Vegard's rule. The asymmetry and the tilt angle of Ge dimers are 0.87 Å and 20.1°, respectively, larger than those of Si dimer surface [23,24]. Some results are compared with experimental and theoretical values as shown in Table 1. One can see from the table that larger k-points sampling in the LDA calculations will give smaller asymmetries and smaller tilt angles, whereas larger kinetic energy cutoff will give larger Ge-Ge bond lengths. We note that larger kinetic energy cutoff is necessary in order to reproduce correct Si-Ge dimer bond lengths, following the Vegard's law, as described in previous works [19].

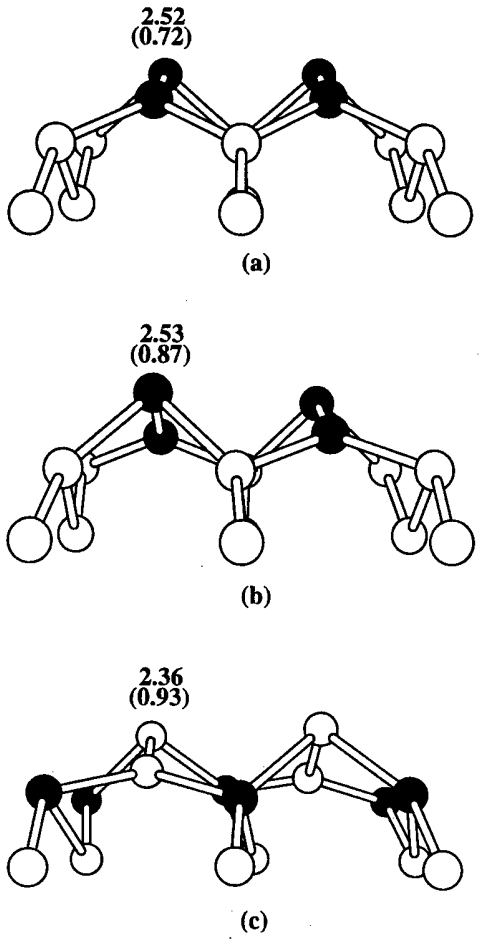

Fig. 1. The fully relaxed surface structures in a single p(2×2) unit cell together with the top three layers for (a) p(2×1)Ge/Si/Si(001) (b) p(2×2)Ge/Si/Si(001) and (c) p(2×2)Si/Ge/Si(001).

In order to see the relative energetics, we next study the configuration of the Ge layer exchanged with the subsurface Si layer, *i.e.*, the Ge layer is sandwiched between Si layers, as shown in Fig. 1(c). The fully relaxed top Si layer prefers to reconstruct with asymmetric p(2×2) phase. One finds that the top Si dimer bond length is 2.36 Å, close to an ideal Si bulk bond length. The total energy of this Si/Ge/Si(001) surface is higher by 0.61 eV/dimer than the previous Ge/Si/Si(001) surface (Fig. 1(b)). This energetics clearly shows that the Ge atoms prefer to stay on top surface. The energy difference is comparable to 0.38 eV/dimer between Si/Ge/Ge(001) (2×1) surface and Ge/Si/Ge(001) (2×1) surface [28]. Under normal experimental conditions, the Ge atoms float to the front growing surface via some exchange processes when the Si atoms are deposited on the Ge surface.

Table 1. Structural values of 1 ML of Ge on Si(001) surface. E_{cutoff} indicates the kinetic energy cutoff in Ry. The number of K-points sampling in the irreducible Brillouin zone is indicated by n_K. d_{Ge-Ge} is the bond length of top Ge-Ge dimer. The bond length between top Ge and the sublayer Si (d_{Ge-Si}) is averaged over several different bonds for comparison with other experimental results. Δz is the buckling of Ge-Ge dimer.

	E_{cutoff} (Ry)	n_K	Symmetry	d_{Ge-Ge} (Å)	d_{Ge-Si} (Å)	Δz (Å)	tilt angle (degree)
This work	8	1	p(2×2) asy	2.49	2.38	0.81	18.9
	12	1	p(2×2) asy	2.53	2.39	0.87	20.1
	12	1	p(2×1) asy	2.52	2.45	0.72	16.6
LDA-JL[a]	8	1	p(2×2) asy	2.44		0.79	19
LDA-CK[b]	10	32	p(2×1) asy	2.39		0.67	16.3
LDA-JS[c]	8	32	p(2×1) asy	2.38		0.76	18.5
XAFS[d]			p(2×1) sym	2.51	2.40		
XSW[e]			p(2×1) asy	2.60±0.04		0.55	12.1
bulk Ge				2.45			

[a] [25] Plane wave basis by Jin and Lewis.
[b] [26] Plane wave basis by Cho and Kang.
[c] [27] Plane wave basis by Jenkins and Srivastava.
[d] [8] X-ray absorption fine structure measurements.
[e] [22] X-ray standing wave measurements.

Based on the energetics of the previous calculations, it is very unlikely for the Ge atoms at top layer to intermix with the Si atoms in the subsurface. Yet, experimental observations show the Ge atoms at top layer to intermix with the subsurface Si atoms [5–11,29]. Although the intermixing may be attributed to nonequilibrium growth processes, a possibility for stable local configuration to exist cannot be excluded. In this report, it is our purpose to search for a stable intermixed configuration. Furthermore we like to find out an appropriate pathway that reaches such a stable configuration.

Recent high resolution scanning tunneling microscopy (STM) images of the Si(001) surface have shown that single missing dimers or dimer vacancies are the dominant defect structures at the surface [30–32]. Situations are similar even on the Ge-covered Si(001) surface [33,34]. Since the energetics of full monolayer of the Ge atoms on Si(001) surface are always favorable over Si/Ge/Si(001) surface as shown in the previous calculations, we here introduce a dimer vacancy on Ge/Si(001) surface and search for an intermixed stable configuration. Figure 2(a) shows the fully relaxed geometry of the dimer vacancy. Once a Ge dimer is removed, the sublayer Si atoms are stabilized by rebonding themselves with bond lengths of 2.40 and 2.56 Å. The rebonding is usually observed at the stepped surfaces [35]. The rebondings stretch down the top Ge dimers near the vacancy and decrease the buckling. We note that reduction of the buckling occurs asymmetrically, *i.e.*, one Ge dimer becomes nearly symmetric. Figure 2(b) shows the fully relaxed geometry of two Ge atoms being in the sublayer by exchanging their positions with Si atoms in the sublayer. The total energy of Fig. 2(b) is 0.1 eV higher than that of the original one in Fig. 2(a). This energy difference is small within the accuracy and it's difficult to understand intuitively how this energy gain is achieved by the exchange process.

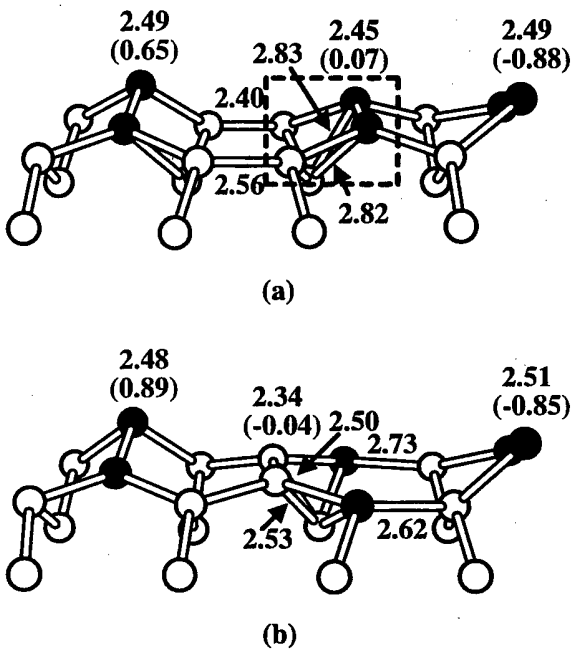

Fig. 2. The surface structures for the fully relaxed geometries of (a) dimer vacancy on p(2×2)Ge/Si/Si(001) surface and (b) two Ge atoms in the sublayer being exchanged with Si atoms. The atoms in the dashed box are chosen for bond-counting.

A simple way to estimate the energetics is to do bond-counting near the dashed box, as shown in Fig. 2(a). The number of bonds within the dashed box is 1 Ge-Ge + 6 Si-Ge + 6 Si-Si, whereas that of Fig. 2(b) is 8 Si-Ge + 5 Si-Si. The difference of the bond-counting is 2 Si-Ge - 1 Ge-Ge - 1 Si-Si. If we assume the Vegard's rule, the energy difference of these two configurations will be negligible. We note from Fig. 2(a) that the Ge atoms at

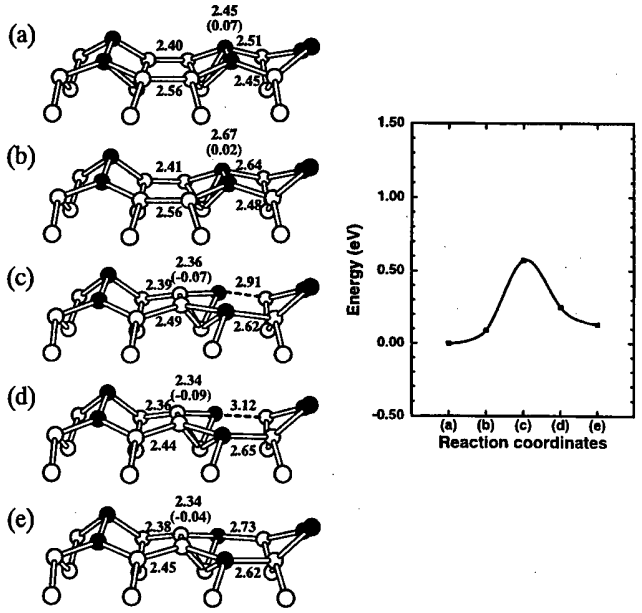

Fig. 3. The dimer-exchange process. The inset shows the total energy changes over the corresponding pathway. The energy of step (a) is chosen for the reference.

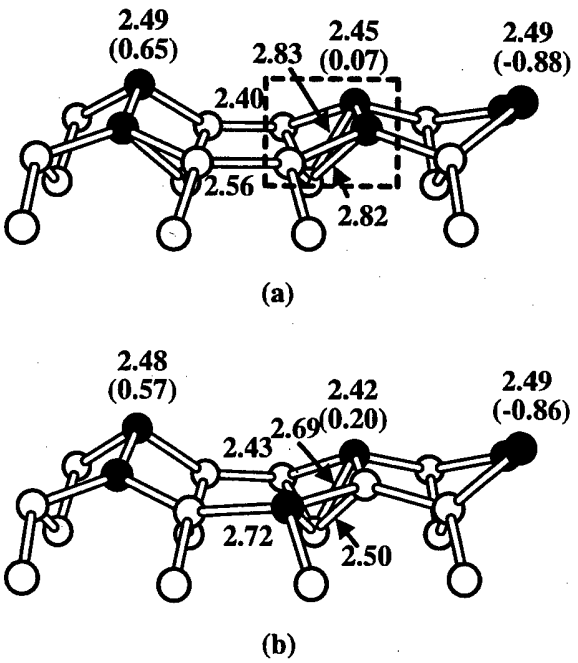

Fig. 4. The surface structures for the fully relaxed geometries of (a) dimer vacancy on p(2×2)Ge/Si/Si(001) surface and (b) one Ge atom on the sublayer being exchanged with a Si atom. The atoms in the dashed box are chosen for bond counting.

the top dimer inside the box rehybridize with Si atoms in the sublayer. The bond lengths are 2.83 and 2.82 Å as shown in the figure indicated by the arrows. Similar rehybridizations of top Si dimer with the subsurface Si atoms occur in Fig. 2(b), where rehybridizations occur more strongly with Si-Si bond lengths of 2.5 and 2.53 Å in this configuration.

Since these two configurations are energetically stable, the next step is to evaluate an energy barrier to see if the intermixing is kinetically favorable under some reasonable experimental temperatures. One way to achieve the intermixing is to push the top Ge dimer to the left (y direction) and let two Si atoms in the sublayer move upward at the same time, as shown in Fig. 3(b)-3(e). In each step we fix the y axis of the Ge dimer and relax all other coordinates including the full relaxation of other atoms. In step (c) the sublayer Si atoms in the adjacent vacancy form a bond while the Ge dimer breaks the bond and tries to rebond to the adjacent Si sublayer atoms, where one of them forms a weak bond. The energy of this step is 0.6 eV higher than that of the step (a). Since new Si dimer breaks bonds with the sublayer Si atoms, the energy cost is large, forming a barrier. Further moving to the left will reduce the bond angle distortions around the Si dimer, lowering the total energy. The step (e) is the final configuration where the intermixing of Ge atoms with sublayer Si atoms is achieved. The buckling of the Si dimer almost disappears and the positions of the Si dimer are lower than those of the adjacent Ge dimers. The Ge atoms in the sublayer form again rebondings with the adjacent Si atoms. The potential barrier is 0.6 eV, suggesting that this process is kinetically favorable, *i.e.*, can be occurred at relatively low annealing temperature. One may try different pathways which might give a lower activation barrier. However, the previous calculation [35] shows that the current pushing-out process gives relatively lower activation barrier than other dimer-exchange processes.

The previous studies for the adsorption of Ge atoms at the step edge suggest that the energy is lowered by having two Ge atoms in separate sites [36], not as a form of a dimer which are shown in the previous paragraph. We find in this work a new stable geometry where two Ge atoms are located in different sites, as shown in Fig. 4(b). One Ge atom is placed in the vacancy site, whereas another Ge atom is located in the dimer site. The total energy of this monomer-intermixed geometry is 0.02 eV lower than the original one. Again the energy gain can be rationalized by the bond-counting, similar to the previous case. The top Si and Ge atoms in the dimer rehybridize with the Si atoms in the sublayer, as shown in Fig. 4(b), lowering the total energy.

We next consider the monomer-exchange process near the dimer vacancy. In this process we move one Ge atom of the surface dimer near the dimer vacancy to the left and and one Si atom in the subsurface to the right, as shown in Fig. 5. In each step, the y coordinates of the chosen Ge atom and Si atom are fixed and all other coordinates are fully relaxed similar to the previous case. In step (b) the Si-Si weak bond is broken by moving the Si atom to the right, which costs 0.6 eV in the total en-

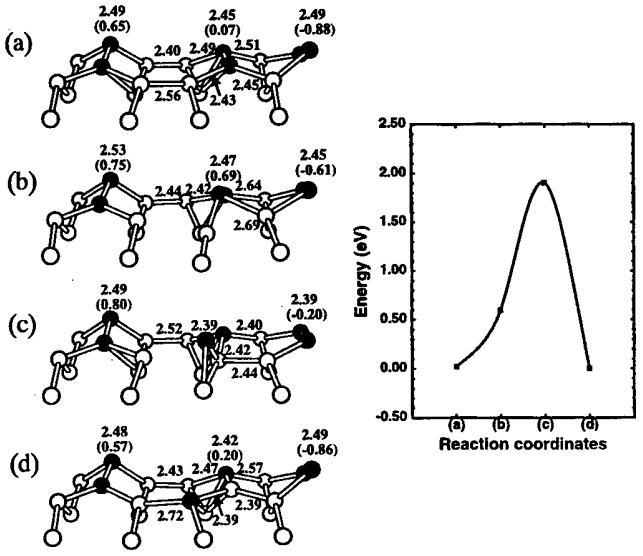

Fig. 5. The monomer-exchange process. The inset shows the total energy changes over the corresponding pathway. The energy of step (a) is chosen for the reference. The shaded and open balls indicate Ge and Si atoms, respectively. All the bond lengths and asymmetries shown in parentheses are in unit of Å.

ergy. Moving the Si atom further to the right and at the same time moving the Ge atom to the left involve several bond-breakings and rebondings, as shown in step (c), resulting in a large potential barrier of 1.9 eV. The step (d) shows the finally reached equilibrium configuration. Although the energy barrier of monomer-exchange process is higher than that of the dimer-exchange process, the intermixing may occur at high temperature since the exchanged configuration is as stable as the unmixed one. One may simply estimate the annealing temperature for the above process to occur, using the Redhead's relationship [37], $T_P = E_A/(0.06$ Kcal/Mol K)=730±146 K, close to the observed annealing temperatures of 650~900 K [5–11,22].

One may consider some other types of defect-induced intermixing. For instance, energetically favorable intermixing can occur near the steps. The previous calculations [36] show that a single Ge atom can reside stably in the sublayer near the D_B step, supporting our monomer-exchange process. In order to predict the intermixing effect in a comprehensive way, the energetics as well as the kinetics are crucial factors. Based on our calculations, we can say that at low annealing temperatures, the intermixing can be achieved via the dimer-exchange process. At relatively high temperature, the intermixing can occur via both dimer-exchange process and monomer-exchange process. Once the Ge atoms reside in the sublayer, the Ge atoms may be enhanced further to diffuse into deeper layers due to the strains involved in the sublayer [11]. At very high annealing temperature, the intermixing phenomena will be governed by the entropy of mixing since the relative energy difference between different configurations is not so large.

Experimental observations [7,8,10] suggest that the intermixing effect is more obvious for the deposition of two or three monolayers of Ge atoms than for the deposition of one ML of Ge atoms. In the case of a few ML of Ge atoms, the Ge atoms at the interface have no dangling bonds. In such a case, the surface energy is not an appropriate quantity to consider. The energetics will be governed by the bond-counting. The kinetics will be more important than the energetics since the energy is not much different. The intermixing at the interface will be dominated by the entropy of mixing.

IV. CONCLUDING REMARKS

In summary, the defect-induced intermixing phenomena of the Si/Ge interface have been studied as the possible solution to understand the mysterious Si/Ge intermixing by using the first principles calculations. We have searched for energetically stable and kinetically possible configurations. We have found two intermixed configurations which are energetically favorable, where the energy gain is achieved by the rehybridization of dimer atoms with the sublayer atoms. Dimer-exchange and monomer-exchange processes are evaluated. The respective potential barriers are 0.6 eV and 1.9 eV.

We thank H. W. Yeom for helpful discussions. We acknowledge financial support by the Korea Science and Engineering Foundation (KOSEF) through the Semiconductor Physics Research Center at Jeonbuk National University, and in part by the Korea Research Foundation made in the program year of 1998.

REFERENCES

[1] D. E. Jesson, S. J. Pennycook and J.- M. Baribeau, Phys. Rev. Lett. **66**, 750 (1991).
[2] N. Ikarashi, K. Akimoto, T. Tatsumi and K. Ishida, Phys. Rev. Lett. **72**, 3198 (1994).
[3] D. E. Jesson, S. J. Pennycook, J.-M. Baribeau and D. C. Houghton, Phys. Rev. Lett. **68**, 2062 (1992).
[4] D. E. Jesson, S. J. Pennycook, J. Z. Tischler, J. O. Budai, J.-M. Baribeau and D. C. Houghton, Phys. Rev. Lett. **70**, 2293 (1993).
[5] J. C. Tsang, S. S. Iyer and S. L. Delage, Appl. Phys. Lett. **51**, 1732 (1987).
[6] S. S. Iyer, J. C. Tsang, M. W. Copel, P. R. Pukite and R. M. Tromp, Appl. Phys. Lett. **54**, 219 (1989).
[7] M. Copel, M. C. Reuter, M. Horn von Hoegen and R. M. Tromp, Phys. Rev. **B42**, 11682 (1990).
[8] H. Oyanagi, K. Sakamoto, R. Shioda and T. Sakamoto, Jpn. J. Appl. Phys. **33**, 3545 (1994).
[9] M. Sasaki, T. Abukawa, H. W. Yeom, M. Yamada, S. Suzuki, S. Sato and S. Kono, Appl. Surf. Sci. **82/83**, 387 (1994).

[10] H. Oyanagi, K. Sakamoto, R. Shioda, Y. Kuwahara and K. Haga, Phys. Rev. **B52**, 5824 (1995).
[11] H. W. Yeom, M. Sasaki, S. Suzuki and S. Kono, Surf. Sci. **381**, L533 (1997).
[12] R. Car and M. Parrinello, Phys. Rev. Lett. **55**, 2471 (1985).
[13] G. B. Bachelet, D. R. Hamann and M. Schlüter, Phys. Rev. **B26**, 4199 (1982).
[14] L. Kleinman and D. M. Bylander, Phys. Rev. Lett. **48**, 1425 (1982).
[15] F. Buda, G. L. Chiarotti, R. Car and M. Parrinello, Phys. Rev. Lett. **63**, 294 (1989).
[16] S. Jeong and A. Oshiyama, Phys. Rev. Lett. **79**, 4425 (1997).
[17] For k-point sampling dependence, for instance, see the paper by T. Yamasaki, T. Uda and K. Terakura, Phys. Rev. Lett. **76**, 2949 (1996).
[18] C. W. Oh, E. Kim and Y. H. Lee, Phys. Rev. Lett. **76**, 776 (1996).
[19] E. Kim and Y. H. Lee, J. Korean Phys. Soc. **28**, S172 (1995).
[20] C. Wang, Q.-M. Zhang and J. Bernholc, Phys. Rev. Lett. **69**, 3789 (1992).
[21] S. M. Lee and Y. H. Lee, Surf. Sci. **347**, 329 (1996).
[22] E. Fontes, J. R. Patel and F. Comin, Phys. Rev. Lett. **70**, 2790 (1993).
[23] John E. Northrup, Phys. Rev. **B47**, 10032 (1993).
[24] M. S. Jeong, Y. H. Lee and Y. G. Hwang, Phys. Rev. **B51**, 17156 (1995).
[25] J. -M. Jin and L. Lewis, Phys. Rev. **B49**, 2201 (1994).
[26] J. H. Cho and M. H. Kang, Phys. Rev. **B49**, 13670 (1994).
[27] S. J. Jenkins and G. P. Srivastava, J. Phys.: Condens. Matter **8**, 6641 (1996).
[28] S. J. Jenkins and G. P. Srivastava, Phys. Rev. **B57**, 8794 (1998).
[29] X. Chen, D. K. Saldin, E. L. Bullock, L. Patthey, L. S. O. Johansson, J. Tani, T. Abukawa and S. Kono, Phys. Rev. **B55**, R7319 (1997).
[30] N. Kitamura, M. G. Lagally and M. B. Webb, Phys. Rev. Lett. **71**, 2082 (1993).
[31] R. J. Hamers and U. K. Koehler, J. Vac. Sci. Technol. **A7**, 2854 (1989).
[32] J. Wang, T. A. Arias and J. D. Joannopoulos, Phys. Rev. **B47**, 10497 (1993).
[33] X. Chen, F. Wu, Z. Zhang and M. G. Lagally, Phys. Rev. Lett. **73**, 850 (1994).
[34] F. Wu, X. Chen, Z. Zhang and M. G. Lagally, Phys. Rev. Lett. **74**, 574 (1995).
[35] E. Kim, C. W. Oh and Y. H. Lee, Phys. Rev. Lett. **79**, 4621 (1997).
[36] S. M. Lee, E. Kim, Y. H. Lee and N.-K. Kim, J. Korean Phys. Soc. **33**, 684 (1998).
[37] R. I. Masel, *Principles of Adsorption and Reaction on Solid Surfaces* (John Wiley & Sons, INC, New York, 1996), p. 513.

Journal of the Korean Physical Society, Vol. 34, June 1999, pp. S305~S309

Angle-Resolved XPS Investigation of the Fluorine-related Passivation Layer on Etched Al (Cu 1 %) Surface After SF_6 Treatment

Yong-Sun YOON*, Kyu-Ha BAEK and Jong-Moon PARK

Electronics and Telecommunications Research Institute, Taejon 305-600

Kwang-Ho KWON

Department of Electronic Engineering, Hanseo University, Asan 356-820

Chang-Il KIM

School of Electrical & Electronic Engineering, Chungang University, Seoul 156-756

In-Gab HWANG

School of Electrical & Electronics Engineering, Jeonju University, Jeonju 560-240

A fluorine-related passivation layer on etched Al-Cu alloy films was investigated by transmission electron microscope (TEM) and angle-resolved X-ray photoelectron spectroscopy (XPS). The passivation layer was produced during SF_6 plasma treatments after $SiCl_4/Cl_2/He/CHF_3$ mixed gas plasma etching. The passivation layer is composed of fluorine-aluminum compounds on the etched Al-Cu surface. It was found that this layer suppresses effectively the corrosion on the etched surface by preventing moisture penetration from air even if the residual chlorine atoms exist on the etched surface. The existence of the passivation layer was verified by TEM analysis. To investigate characteristics of the passivation layer, angle-resolved XPS was carried out for heat-treated samples. The heat treatments of the samples were *in-situ* carried out in the XPS analysis chamber for the temperatures of 150, 300, and 400 °C, respectively. The binding energy of the composed elements of the passivation layer shifted to the higher binding energy position as the heat treatment temperature was increased.

I. INTRODUCTION

As the device geometry becomes smaller, the interconnection metal line becomes finer. Aluminum and its alloys are widely used as the interconnection material for the VLSI circuits because of their good characteristics such as low resistivity, low cost, and good adhesion, *etc.* For a high performance and reliability of the metallizations, Cu addition to Al are utilized because the Cu atoms in Al alloy system improve the resistance to electromigration, stress migration failures, and hillock formation [1–3]. Plasma etching technique using gas chemistries containing chlorine is commonly used for patterning Al and Al-alloy films. However, Cu addition to Al promotes corrosion seriously in plasma etching processes by the residual chlorine atoms on the etched metal surface [4–6]. The corrosion on the etched surface occurs rapidly upon atmospheric exposure and degrades the performance and reliability of the devices. There has been intensive research to prevent or to avoid the corrosion phenomena [4–10]. It was well known that the corrosion might be prevented by substitution of fluorine atoms for the residual chlorine atoms with the SF_6 treatment [11,12]. Recently, fresh reports for the corrosion mechanism were published [13–15]. They suggest that corrosion is suppressed by the passivation layer composed of the fluorine-related compounds on the etched surface.

In this study, corrosion phenomenon on the etched Al-Cu film surfaces has been investigated by scanning electron microscope (SEM). An existence of the passivation layer produced on the SF_6-treated surface was demonstrated by transmission electron microscope (TEM) analysis. The characteristics of the passivation layer were also investigated by angle-resolved X-ray photoelectron spec-

*E-mail: ysyoon@etri.re.kr, Phone: +82-42-860-5342, Fax: +82-42-860-6108

troscopy (XPS).

II. EXPERIMENTAL

The samples were prepared using (100) boron doped, 125 mm Si wafers in the resistivity ranges of 0.85~1.15 Ωcm. After diluted HF cleaning, an oxide layer was deposited in the thickness range of 6000 Å by low pressure chemical vapor deposition (LPCVD). The Al-Cu (1 wt.% Cu) films were deposited successively in the thickness range of 8000 Å by the sputtering system. Plasma etch of the Al-Cu alloy films was carried out at a pressure of 600 mTorr using $SiCl_4/Cl_2/He/CHF_3$ mixed gas. The helium gas was used as the carrier gas and the flow rate of the $SiCl_4$, Cl_2, and CHF_3 were 210, 16, and 9 sccm, respectively. The Al-Cu films were etched partially to a thickness of 6000 Å, and the corrosion was investigated on the remaining Al-Cu surfaces after exposure to air for 10 minutes. In Al-Cu alloy system, corrosion occurs rapidly on the etched surface by residual chlorine atoms, and it occurs dominantly at the grain boundaries rather than the crystalline surfaces. For some samples, SF_6-plasma treatments subsequent to etching were carried out immediately in the same reaction chamber. The treatments were carried out at the total pressure of 100, 200 and 300 mTorr, respectively. After the SF_6 plasma treatments, the samples had been exposed also to the atmospheric environment. The corrosion could be suppressed successfully with the SF_6 treatment at a total pressure of 300 mTorr. The etched metal surfaces with or without SF_6 treatment were compared with those of as-deposited ones by SEM. To demonstrate the existence of the passivation layer, TEM analysis was carried out on SF_6-treated sample surface at 300 mTorr. Angle-resolved XPS narrow scan analyses were also carried out to investigate the composition and the chemical bonding states on the passivation layer surfaces.

III. RESULTS AND DISCUSSION

1. Anti-corrosion and Passivation Layer

The surface of Al-Cu alloy was investigated by SEM. Fig. 1(a) shows the SEM image of the as-deposited surface. Fig. 1(b) shows etched Al-Cu surface with the SF_6 treatment at a pressure of 300 mTorr and air exposure. This shows that the grain boundaries are clearer than that shown in Fig. 1(a) but the corrosion on the surface is not observed. Fig. 1(c) shows the typically corroded surface, which was exposed to air subsequent to etching without a SF_6 plasma treatment. An arrow shown in the Fig. 1(c) indicates the corroded position. Fig. 1(c) shows that the corrosion occurs rapidly on the etched surface by residual chlorine atoms, and it occurs

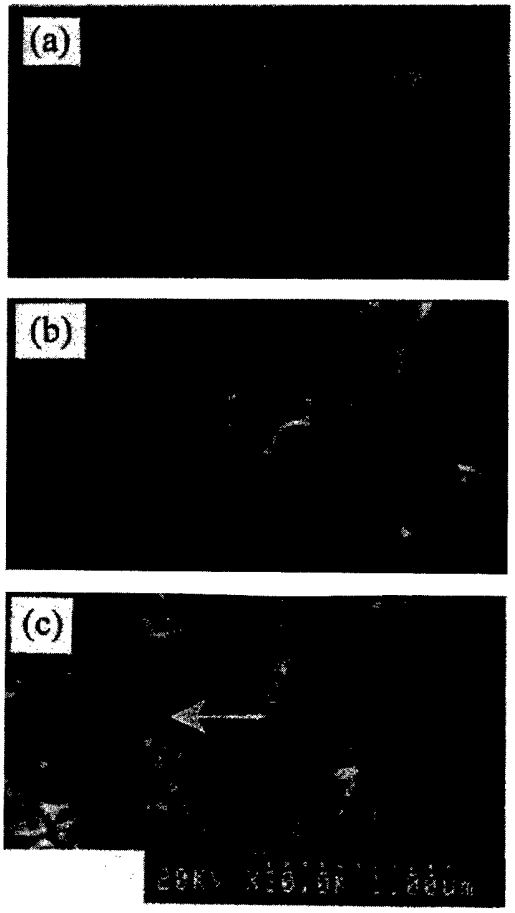

Fig. 1. SEM photographs of the Al-Cu alloy film surface: (a) as-deposited surface, (b) etched surface with the SF_6 plasma treatment in the pressure of 300 mTorr, and (c) etched surface without the SF_6 treatment.

dominantly at the grain boundaries rather than the crystalline surfaces. The corrosion is due to HCl, which is produced by reaction of residual chlorines with moisture in air. However, the SF_6 treatment subsequent to etching successfully suppresses the corrosion on the etched surface as shown in Fig. 1(b).

Fig. 2 shows the cross sectional TEM image of the passivation layer on the etched Al-Cu surface. The samples were treated with the SF_6 plasma at a pressure of 300 mTorr subsequent to etching. It shows that the passivation layer exists on the etched Al-Cu surface in the thickness range of several 100 Å. The passivation layer during the SF_6-plasma treatment would be formed on the etched surface. The passivation layer prevents moisture penetration from air, and corrosion is successfully suppressed by this passivation layer as shown in Fig. 1(b).

2. Characteristics of the Passivation Layer

To investigate the characteristics of the passivation lay-

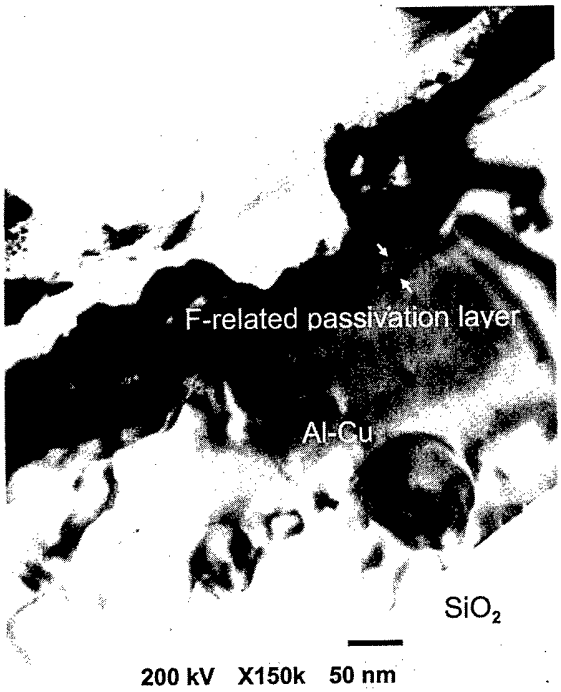

Fig. 2. TEM image of the fluorine-related passivation layer on the etch Al-Cu alloy surface.

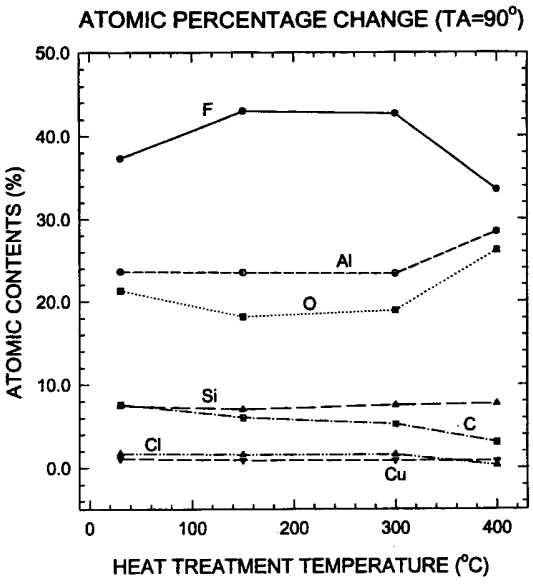

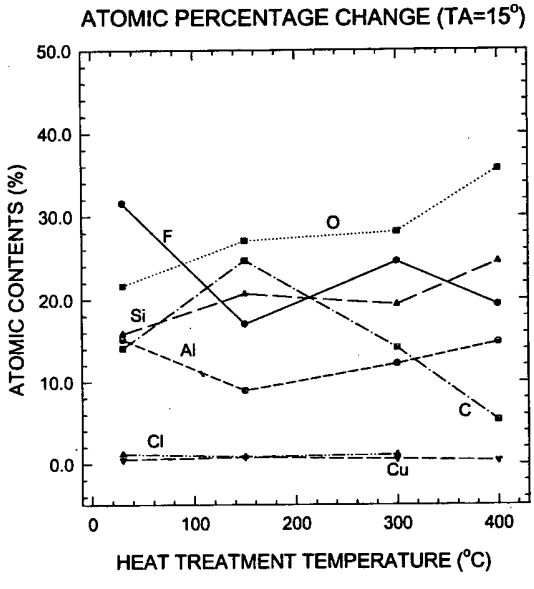

Fig. 3. Atomic species and their contents obtained at various take-off angle : (a) take-off angle=90°, (b) take-off angle=15° (more surface sensitive).

er, atomic contents were measured at various take-off angles. All the samples were treated with SF_6 plasma at a pressure of 300 mTorr subsequent to etching, at which pressure corrosion was not occurred on the samples after exposure to air. The samples were *in-situ* annealed in the XPS analysis chamber with the temperatures of 150, 300, and 400 °C, respectively. Fig. 3 shows the atomic species and their relative contents on the passivation layer obtained at take-off angles of 90 and 15°, respectively. In the deep position of the passivation layer, that is, at large take-off angle, atomic content distributions are nearly constant with annealing temperatures but 400 °C as shown in Fig. 3(a). However, they are all scattered except chlorine and copper on the surface of the passivation layer as shown in Fig. 3(b). At the take-off angle of 90°, the amount of fluorine atoms is decreased and that of oxygen atoms is increased at the temperature of 400 °C. In the case of near the surface of the passivation layer, the amount of oxygen atoms is increased as the annealing temperature is increased, while that of fluorine atoms is generally decreased as shown in Fig. 3(b). These indicate that the oxygen atoms may come from air exposure, and they move toward the surface of the passivation layer as the annealing temperature increases. In the case of chlorine, however, the total amount is not affected by the annealing temperature both in the deep position and on the surface of the passivation layer. This may imply some interesting fact that chlorine atoms are distributed entire regions of the passivation layer and on the etched metal surface. If the passivation layer is formed thinner, that is, when the SF_6-plasma treatments subsequent to etching are carried out below 300 mTorr, corrosion occurs [13–15]. This indicates the chlorine atoms also exist on the etched metal surfaces. At the annealing temperature of 400 °C shown in Fig. 3(b), the amount of chlorine atoms in not observed. This means that chlorine-related compounds vaporize from the passivation layer at the temperature of 400 °C. The amount of fluorine atoms is relatively smaller on the surface rather than in the deep position of the passivation layer. On the contrary, in

the case of oxygen, the amount on the surface is larger than that in the deep position of the passivation layer. As the annealing temperature is increased, these phenomena tend to be more apparent. These explain that the passivation layer prevents oxygen and moisture penetration from air and corrosion is significantly suppressed. This indicates the passivation layer might be formed with water-related structure.

To confirm the validity of the above assumptions, an XPS narrow scan analysis for fluorine was carried out. The chemical bonding states with the annealing temperature were investigated. Fig. 4(a) shows the narrow scan spectra of F 1s states for non-annealed samples on the passivation layer with take-off angles of 90, 60, 30, and 15°, respectively. In the case of take-off angle of 90°, the peak position is located at 686.2 eV, which might be related with hydrated AlF_3, that is, $AlF_3 \cdot 3H_2O$ [16]. On the surface of the passivation layer, that is, when the take-off angle is 15°, it is located at 686.8 eV. It shows that the peak position moves toward higher binding energy as the take-off angles are lowered. This indicates bonding states on the surface are different from that in the deep position of the passivation layer because the concentration of oxygen and moisture on the surface is larger than that in the deep positions of the passivation layer. The boding states are tighter on the surface than that in the deep position of the passivation layer. Fig. 4(b) represents F 1s spectra for annealed samples at 400 °C. It shows the peak position with take-off angle of 90 and 15° are located at 687.7 and 688.0 eV, respectively. The bonding state also grows tighter as the annealing temperature is higher as shown in Fig. 4(b). The shapes of the peak do not change but the peak positions move toward higher energy.

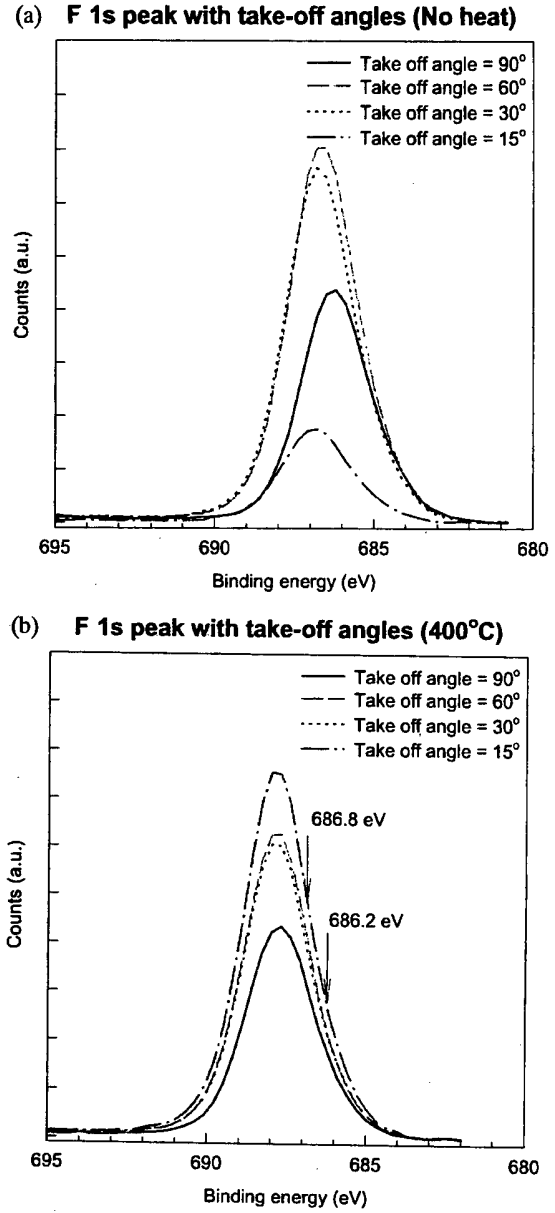

Fig. 4. F 1s narrow scan spectra for samples with take-off angles of 90, 60, 30, and 15°. All the samples are treated with SF_6 treatment at a pressure of 300 mTorr subsequent to etching. (a) non-annealed sample, (b) annealed at 400 °C.

In order to investigate the annealing effect of the hydrated AlF_3 layer, narrow scan analysis for annealed samples with take-off angle of 90° was carried out. Fig. 5 represents the spectra for samples with the annealing temperatures of 150, 300, and 400 °C, respectively. It shows that the peak position move toward higher binding energy as the annealing temperature increases. And the peak height becomes higher up to annealing temperature of 300 °C, but not at 400 °C. The chemical bonding state moves to higher energy distinctively as the annealing temperature increases but the peak shape does not

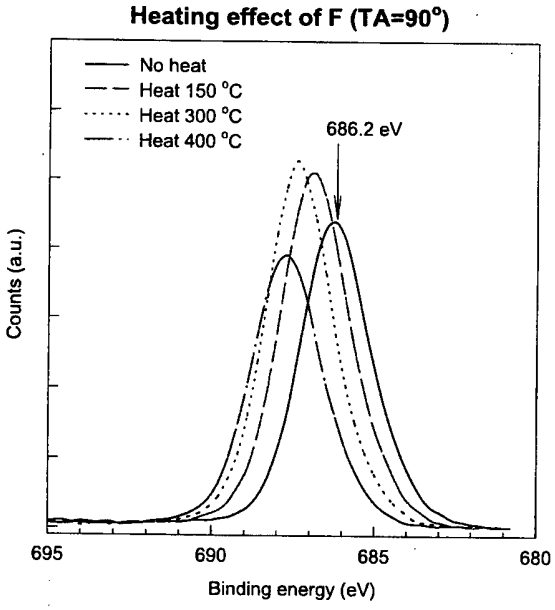

Fig. 5. Annealing effects of fluorine peak in the passivation layer with various annealing temperatures.

change. This phenomenon is same for all take-off angles. This might be caused from redistribution of the elements in the passivation layer by annealing.

IV. CONCLUSIONS

Corrosion phenomenon on the etched Al-Cu film surfaces using $SiCl_4/Cl_2/He/CHF_3$ gas plasma has been investigated by SEM. An existence of a passivation layer on the etched Al-Cu alloy surfaces was demonstrated after SF_6-plasma treatment by TEM. The characteristics of the passivation layer was studied with angle-resolved XPS analysis. The passivation layer is composed of $AlF_3 \cdot 3H_2O$, and the residual chlorine atoms are embedded in it. The passivation layer prevents moisture penetration from air and suppresses the corrosion effectively. The characteristics of the passivation layer on its surface somewhat different from ones in the deep position. The binding energy on the surface is larger than that in the deep position of the layer due to moisture in air. When the passivation layer is annealed, surface binding energy is increased with increasing of the annealing temperature.

REFERENCES

[1] W. Y. Lee, J. M. Eldridge and G. C. Schwartz, J. Appl. Phys. **52**, 2994 (1981).

[2] A. R. Sethuraman, J.-F. Wang and L. M. Cook, J. Electronic. Materials **25**, 1617 (1996).

[3] T. Nogami and T. Nemoto, Proceedings of AIP conference, 198 (1996).

[4] Y. Horiike, T. Yamazaki, M. Shibagaki and T. Kurisaki, Jpn. J. Appl. Phys. **21**, 1412 (1982).

[5] T. Suzuki, H. Kitagawa, K. Yamada and M. Nagoshi, J. Vac. Sci. Technol. **B10**, 596 (1992).

[6] D. A. Danner, M. Dalvie and D. W. Hess, J. Electrochem. Soc. **134**, 669 (1987).

[7] N. Hayasaka, Y. Koga, K. Shimomura, Y. Yoshida and H. Okano, Jpn. J. Appl. Phys. **30**, 1571 (1991).

[8] T. Ishida, N. Fujiwara, M. Yoneda, K. Nakamoto and K. Horie, Jpn. J. Appl. Phys. **31**, 2045 (1992).

[9] J-S. Maa, H. Gossenberger and R. J. Paff, J. Vac. Sci. Technol. **B8**, 1052 (1990).

[10] K-I. Siozawa, N. Fujiwara, H. Miyatake and M. Yoneda, Jpn. J. Appl. Phys. **36**, 2496 (1997).

[11] D. M. Manos and D. L. Flamm, *Plasma Etching* (Academic Press, 1989).

[12] M. A. Lieberman and A. J. Lichtenberg, *Principles of Plasma Discharges and Materials Processing* (John Wiley & Sons, 1994).

[13] K. H. Baek, Y. S. Yoon, J. M. Park, K.-H. Kwon, C. I. Kim and K. S. Nam, . Materials Letters. **35**, 183 (1998).

[14] K.-H. Kwon, S. J. Yun, C. I. Kim, J. M. Park, K. H. Baek, Y. S. Yoon, S. G. Kim and K. S. Nam, J. Electrochemical Soc. **45**, 1044 (1998).

[15] K. H. Baek, C. I. Kim, K.-H. Kwon, T. H. Kim, E. G. Chang, S. J. Yun, Y. S. Yoon, S. G. Kim and K. S. Nam, J. Vacuum Sci. and Tech. **A16**, Part II, 1469 (1998).

[16] John F. Moulder, William F. Stickle, Peter E. Sobol and Kenneth D. Bomben, *Handbook of X-ray Photoelectron Spectroscopy* (Perkin-Elmer Corporation, 1992).

Journal of the Korean Physical Society, Vol. 34, June 1999, pp. S310~S314

Nonlinear Electrical Transport in Semiconductors : a Nonequilibrium Thermodynamics Approach

Deug Yong KIM and Chang Sub KIM*

Department of Physics, Chonnam National University, Kwangju 500-757

We present a transport theory of semiconductors in the high-field regime where the usual linear-response theory breaks down. We start from the Boltzmann-Peierls equation for the coupled electron-phonon system to generate the macroscopic transport equations. We use the idea of the extended irreversible hydrodynamics in selecting the relevant nonequilibrium state variables and also incorporate the nonequilibrium ensemble method that introduces the phenomenological ansatz imposing the second law of thermodynamics by hands. In order to manifest the utility of the theory constructed, we sketch how to calculate the nonlinear drift velocity.

The electrical transport problems in semiconductors are nonequilibrium phenomena and most conveniently described by the hydrodynamic equations (or balance equations) that involve the directly measurable, macroscopic variables of the system [1–8]. Such nonequilibrium state-variables are the carrier density, drift velocity, and temperature in the conventional hydrodynamic description [1–4] and also momentum and heat fluxes are included in the generalized hydrodynamic equations approach [5–8]. Due to the many-particle nature, the observables are defined microscopically as the statistical average of the relevant operators over the nonequilibrium occupancy, the single-particle distribution function. In the linear response regime (or near equilibrium) where the external perturbation is weak, there exists the firm foundation between the desired macroscopic quantities and the underlying microscopic physics. For instance, the Ohmic conductivity can be calculated by either solution to the Boltzmann equation or the Kubo formula, equivalently [9]. However, in the high-field regime there remain the fundamental difficulties in understanding the nonlinear transport properties. First of all, it is not a priori obvious what are the relevant quantities to be specified, since physics depends on space and time scales under consideration. Also, it is not known how to comply with the macroscopic law of thermodynamics under general nonequilibrium situation, in particular the second law of thermodynamics. On the other hand, the modern miniaturization trend of semiconductor devices demands a better understanding of this long-standing problems ever since. In this paper, we attempt to tackle this nonlinear transport problem in semiconductors while giving much effort to constructing thermodynamic consistencies in the theory.

*E-mail: cskim@boltzmann.chonnam.ac.kr

In solids, the electrical current density $\boldsymbol{j}$ is most microscopically described by the statistical average of the group velocity $\boldsymbol{v}_g^{(\alpha)}(\boldsymbol{k})$ of the electron wave $\psi_{\alpha\mathbf{k}}$ over the nonequilibrium distribution function $f_e(\boldsymbol{k})$ as

$$\boldsymbol{j} = 2\sum_{\alpha}\int \frac{d\boldsymbol{k}}{(2\pi)^3}(-e)\boldsymbol{v}_g^{(\alpha)}(\boldsymbol{k})f_e(\mathcal{E}_\alpha(\boldsymbol{k})) = n(-e)\boldsymbol{u} \quad (1)$$

where $\boldsymbol{u}$ is the drift velocity and the carrier density n is defined through the normalization condition for f_e as

$$n = 2\sum_{\alpha}\int \frac{d\boldsymbol{k}}{(2\pi)^3} f_e(\mathcal{E}_\alpha(\boldsymbol{k})) \quad (2)$$

where the summation is over all filled bands and the integration is to be carried out in the full first Brillouin zone. The group velocity is given by the Hellmann-Feynman theorem as

$$\boldsymbol{v}_g^{(\alpha)}(\boldsymbol{k}) = \frac{1}{\hbar}\frac{\partial \mathcal{E}_\alpha(\boldsymbol{k})}{\partial \boldsymbol{k}} \quad (3)$$

where $\mathcal{E}_\alpha(\boldsymbol{k})$ is the band structure of the material under consideration. For a single parabolic band with constant spherical energy surface,

$$\mathcal{E}(\boldsymbol{k}) = \frac{\hbar^2 k^2}{2m_e^*}, \quad (4)$$

characterized by an isotropic effective mass m_e^*, the group velocity is given as

$$\boldsymbol{v}_g(\boldsymbol{k}) = \frac{\hbar \boldsymbol{k}}{m_e^*}. \quad (5)$$

In this simple band model the drift velocity $\boldsymbol{u}$ is reduced to

$$\boldsymbol{u} = n^{-1}\frac{1}{4\pi^3}\int d\boldsymbol{k}\boldsymbol{v}_g(\boldsymbol{k})f_e(\boldsymbol{k}). \quad (6)$$

Given a band structure, knowing the distribution function f_e is the essential part in evaluating Eq. (6). For the coupled electron-phonon system in the external DC-field $\boldsymbol{E}$, the distribution function is determined from the Boltzmann-Peierls equation [10]

$$\left(\frac{\partial}{\partial t}+\boldsymbol{v}_g(\boldsymbol{k})\cdot\frac{\partial}{\partial \boldsymbol{r}}-\frac{e\boldsymbol{E}}{\hbar}\cdot\frac{\partial}{\partial \boldsymbol{k}}\right) f_e(\boldsymbol{r},\boldsymbol{k},t) = R_e[f_e,f^0_{ph}], \tag{7}$$

and

$$R_{ph}[f_e,f^0_{ph}]=0, \tag{8}$$

where the phonon equation is simply given by the condition of vanishing the collision operator because phonons are assumed to be in equilibrium, f^0_{ph}. The collision operator in the right side of Eq. (7) is given as [10]

$$\begin{aligned} R_e[f_e,f^0_{ph}] &= V\int\frac{d\boldsymbol{q}}{(2\pi)^3}\,A(\boldsymbol{q})\left\{\left[1+f^0_{ph}(\boldsymbol{q})\right]f_e(\boldsymbol{r},\boldsymbol{k}+\boldsymbol{q},t)\left[1-f_e(\boldsymbol{r},\boldsymbol{k},t)\right]\right.\\ &\left.-f^0_{ph}(\boldsymbol{q})f_e(\boldsymbol{r},\boldsymbol{k},t)\left[1-f_e(\boldsymbol{r},\boldsymbol{k}+\boldsymbol{q},t)\right]\right\}\delta\left[E(\boldsymbol{k}+\boldsymbol{q})-E(\boldsymbol{k})-\hbar\omega_{\mathbf{q}}\right]\\ &+V\int\frac{d\boldsymbol{q}}{(2\pi)^3}\,A(\boldsymbol{q})\left\{f^0_{ph}(\boldsymbol{q})f_e(\boldsymbol{r},\boldsymbol{k}-\boldsymbol{q},t)\left[1-f_e(\boldsymbol{r},\boldsymbol{k},t)\right]\right.\\ &\left.-\left[1+f^0_{ph}(\boldsymbol{q})\right]f_e(\boldsymbol{r},\boldsymbol{k},t)\left[1-f_e(\boldsymbol{r},\boldsymbol{k}-\boldsymbol{q},t)\right]\right\}\delta\left[E(\boldsymbol{k}-\boldsymbol{q})-E(\boldsymbol{k})+\hbar\omega_{\mathbf{q}}\right] \end{aligned} \tag{9}$$

and the phonon collision operator in Eq. (8) is given as

$$\begin{aligned} R_{ph}[f_e,f^0_{ph}] &= V\int\frac{d\boldsymbol{k}}{(2\pi)^3}A(q)\left\{\left[1+f^0_{ph}(\boldsymbol{q})\right]f_e(\boldsymbol{r},\boldsymbol{k}+\boldsymbol{q},t)\left[1-f_e(\boldsymbol{r},\boldsymbol{k},t)\right]\right.\\ &\left.-f^0_{ph}(\boldsymbol{q})\,f_e(\boldsymbol{r},\boldsymbol{k},t)\left[1-f_e(\boldsymbol{r},\boldsymbol{k}+\boldsymbol{q},t)\right]\right\}\delta\left[E(\boldsymbol{k}+\boldsymbol{q})-E(\boldsymbol{k})-\hbar\omega_{\mathbf{q}}\right],\\ &+V\int\frac{d\boldsymbol{k}}{(2\pi)^3}A(q)\left\{\left[1+f^0_{ph}(\boldsymbol{q})\right]f_e(\boldsymbol{r},\boldsymbol{k},t)\left[1-f_e(\boldsymbol{r},\boldsymbol{k}-\boldsymbol{q},t)\right]\right.\\ &\left.-f^0_{ph}(\boldsymbol{q})\,f_e(\boldsymbol{r},\boldsymbol{k}-\boldsymbol{q},t)\left[1-f_e(\boldsymbol{r},\boldsymbol{k},t)\right]\right\}\delta\left[E(\boldsymbol{k}-\boldsymbol{q})-E(\boldsymbol{k})+\hbar\omega_{\mathbf{q}}\right], \end{aligned} \tag{10}$$

where V is the volume of the sample. There exists an important restriction that any solutions to Eqs. (7) and (8) must meet. Namely, when the Boltzmann entropy is defined through [11]

$$S(t) = -k_B\int d\boldsymbol{r}\frac{2}{(2\pi)^3}\int d\boldsymbol{k}\left[f_e\ln f_e+(1-f_e)\ln(1-f_e)\right], \tag{11}$$

it must hold that

$$\frac{dS(t)}{dt}\geq 0,$$

where we have neglected the contribution from the phonon part since the phonons are in equilibrium. We find it convenient to define the local entropy density, $\mathcal{S}(\boldsymbol{r},t)$, through

$$S(t)=\int_V d\boldsymbol{r}\,\rho\mathcal{S}(\boldsymbol{r},t), \tag{12}$$

where the electron mass density $\rho=m^*_e n$ has been inserted in the definition for later convenience. Then, by taking time-derivative of Eq. (12) and also with use of Eq. (7), one can obtain the balance equation for the entropy as

$$\rho\frac{d\mathcal{S}}{dt}=-\boldsymbol{\nabla}\cdot J_s+\sigma_{ent}, \tag{13}$$

where use has been made of

$$\frac{d}{dt}=\frac{\partial}{\partial t}+\boldsymbol{u}\cdot\boldsymbol{\nabla},\quad \boldsymbol{C}=\frac{\hbar\boldsymbol{k}}{m^*_e}-\boldsymbol{u}$$

In the above the entropy flux $\boldsymbol{J}_s$ is given by

$$\boldsymbol{J}_s = -k_B\frac{2}{(2\pi)^3}\int d\boldsymbol{k}\boldsymbol{C}\left\{f_e(\boldsymbol{r},\boldsymbol{k},t)\ln f_e+(1-f_e)\ln(1-f_e)\right\} \tag{14}$$

and the entropy production σ_{ent} is given by

$$\sigma_{ent}=k_B\frac{2}{(2\pi)^3}\int d\boldsymbol{k}\ln(f_e^{-1}-1)R_e[f_e,f^0_{ph}]. \tag{15}$$

After some manipulation, one can prove the famous H-theorem in the local form

$$\sigma_{ent}\geq 0. \tag{16}$$

The equality holds at equilibrium where the distribution functions are specified by

$$f^0_e=\frac{1}{\exp\left[\left(\mathcal{E}(\boldsymbol{k})-\mu^0\right)/k_BT_0\right]+1}, \tag{17}$$

and

$$f^0_{ph}=\frac{1}{\exp\left[\hbar\omega_q/k_BT_0\right]-1}, \tag{18}$$

where T_0 an μ_0 are the equilibrium temperature and

chemical potential, respectively.

Next, we derive the evolution equation for the drift velocity $\boldsymbol{u}$, that is directly related with the electric current, as

$$\rho\frac{d\boldsymbol{u}}{dt} = -\boldsymbol{\nabla}\cdot\boldsymbol{P} - \rho\frac{e}{m_e^*}\boldsymbol{E} + \boldsymbol{\Lambda}^{(v)}, \tag{19}$$

where $\boldsymbol{P}$ is the pressure tensor that is defined to be

$$\boldsymbol{P} = \frac{2}{(2\pi)^3}\int d\boldsymbol{k}\; m_e^*\boldsymbol{C}\boldsymbol{C}f_e(\boldsymbol{r},\boldsymbol{k},t) \tag{20}$$

and the dissipation term $\boldsymbol{\Lambda}^{(v)}$ is defined by

$$\boldsymbol{\Lambda}^{(v)} = \left\langle \hbar\boldsymbol{k}R_e[f_e, f_{ph}^0]\right\rangle. \tag{21}$$

Here, it is important to notice that Eq. (19) is not closed for the chosen macroscopic variable $\boldsymbol{u}$ in the sense that it requires the information on the higher order moment $\boldsymbol{P}$. Furthermore, it still depends on the microscopic distribution function through Eq. (21). Thus, in the conventional theory such as the Chapman-Enskog method [12], in order to resolve this closure problem a *normal* solution is sought for by imposing the functional dependence,

$$f(\boldsymbol{r},\boldsymbol{k},t) = \mathcal{F}[\rho,\boldsymbol{u},T;t]$$

where T is the local temperature. Namely, the space- and time-dependence of the distribution function is assumed be occurred only through the conserved macroscopic variables. In this theory, the higher order fluxes are also expressed as functionals of the conserved first five moments.

In the present work, we adopt the idea of the generalized hydrodynamics where the higher order moments are also included in the theory as the relevant macroscopic variables [13]. In this spirit, we further generate the evolution equation for the pressure tensor as

$$\rho\frac{d\hat{\boldsymbol{P}}}{dt} = -\boldsymbol{\nabla}\cdot\boldsymbol{\psi}^{(s)} - \left[\boldsymbol{P}\cdot\boldsymbol{\nabla}u + (\boldsymbol{\nabla}u)^t\cdot P\right] + \boldsymbol{\Lambda}^{(s)}, \tag{22}$$

where superscript t means the transpose and $\hat{\boldsymbol{P}} = \boldsymbol{P}/\rho$, and other functions are defined to be

$$\boldsymbol{\Lambda}^{(s)} = \frac{2}{(2\pi)^3}\int d\boldsymbol{k}\; m_e^*\boldsymbol{C}\boldsymbol{C}R_e[f_e, f_{ph}^0], \tag{23}$$

$$\boldsymbol{\psi}^{(s)} = \frac{2}{(2\pi)^3}\int d\boldsymbol{k}\; m_e^*\boldsymbol{C}\boldsymbol{C}\boldsymbol{C}f_e. \tag{24}$$

In addition, we utilize the nonequilibrium ensemble method where the nonequilibrium canonical distribution function is introduced as a phenomenological ansatz [14],

$$f_e^c = \frac{1}{\exp\left[\beta\left(E(\boldsymbol{C}) + H_1 - \mu\right)\right] + 1}, \tag{25}$$

where β and μ are to be fixed, and H_1 is the nonequilibrium thermodynamic potential. In nonequilibrium ensemble method, the nonequilibrium thermodynamic entropy Ψ,

$$\Psi(t) = \int_V d\boldsymbol{r}\;\rho\hat{\Psi}, \tag{26}$$

is distinguished from the Boltzmann entropy S, Eq. (11), as a generalized Clausius entropy. The theory is devised to extend the equilibrium thermodynamics to nonequilibrium states as

$$d_t\hat{\Psi} = T^{-1}\left(d_tU + pd_tv + \sum_{k\geq 1}X_k d_t\hat{\Phi}_k\right) \tag{27}$$

where U and v are the internal energy density and the specific volume, respectively, and X_k and $\hat{\Phi}_k$ are the nonequilibrium state-variables and their nonequilibrium thermodynamic conjugates. The function $\hat{\Psi}$, which is reminiscent of the Clausius entropy, is defined through

$$\begin{aligned}\rho\hat{\Psi}(\boldsymbol{r},t) &= -k_B\frac{2}{(2\pi)^3}\int d\boldsymbol{k}\left[f_e(\boldsymbol{r},\boldsymbol{k},t)\ln f_e^c\right.\\ &\quad\left.+(1-f_e)\ln(1-f_e^c)\right].\end{aligned} \tag{28}$$

The differential form Eq. (27) can be derived from Eq. (28) after a tedious algebra. The entropy production σ_c obtained using f_e^c is different from the one σ_{ent} obtained from the solution f_e to the Boltzmann equation. In general, it holds that

$$\begin{aligned}\sigma_{ent} &= \sigma_c + k_B\frac{2}{(2\pi)^3}\int d\boldsymbol{k}\;\ln\left(\frac{f_e^{-1}-1}{f_e^{c-1}-1}\right)\\ &\quad\times R_e[f_e, f_{ph}^0].\end{aligned} \tag{29}$$

The difference goes to zero as the fluctuation $\delta f_e = f_e - f_e^c$ vanishes and then it is reduced to

$$\sigma_{ent} = \sigma_c = T^{-1}\sum_{k\geq -1}X_k\Lambda^{(k)} \geq 0 \tag{30}$$

where the dissipation terms are now specified as

$$\Lambda^{(k)} = (\beta g)^{-1}\sum_{l\geq -1}R^{(kl)}X_l\frac{\sinh\kappa}{\kappa} \tag{31}$$

where g is a constant and κ is to be determined. Here, we provide a few of $\Lambda^{(k)}$ as an illustration:

$$\Lambda^{(-1)} = -(\beta g)^{-1}R^{(-1-1)}\cdot\boldsymbol{u}\frac{\sinh\kappa}{\kappa} = \Lambda^{(v)}, \tag{32}$$

$$\Lambda^{(0)} = (\beta g)^{-1}R^{(00)}\left(\beta^{-1}\Delta\beta\right)\frac{\sinh\kappa}{\kappa} \tag{33}$$

where $\Delta\beta \equiv \beta - \beta_0$. And, to the same order we have

$$\kappa^2 = R^{(00)}\left(\beta^{-1}\Delta\beta\right)^2 + \tfrac{1}{3}R^{(-1-1)}\boldsymbol{u}\cdot\boldsymbol{u} \tag{34}$$

where the collision bracket integrals $R^{(00)}$ and $R^{(-1-1)}$ are to be evaluated through

$$R^{(-1-1)} = \frac{g\beta^2 V\hbar^2}{(2\pi)^6}\int d\boldsymbol{k}\int d\boldsymbol{k}'(\boldsymbol{k}-\boldsymbol{k}')^2 f_e^o(\boldsymbol{k}')A(\boldsymbol{q})\{f_{ph}^o\delta[E(\boldsymbol{k})-E(\boldsymbol{k}')-\hbar\omega_q] + (f_{ph}^o+1)\delta[E(\boldsymbol{k})-E(\boldsymbol{k}')+\hbar\omega_q]\} \quad (35)$$

$$R^{(00)} = \frac{g\beta^2 V}{(2\pi)^6}\int d\boldsymbol{k}\int d\boldsymbol{k}'(E(\boldsymbol{k})-E(\boldsymbol{k}'))^2 f_e^o(\boldsymbol{k}')A(\boldsymbol{q})\{f_{ph}^o\delta[E(\boldsymbol{k})-E(\boldsymbol{k}')-\hbar\omega_q] + (f_{ph}^o+1)\delta[E(\boldsymbol{k})-E(\boldsymbol{k}')+\hbar\omega_q]\}. \quad (36)$$

Finally, we present briefly how to calculate the hot electron drift velocity, utilizing the formulated nonequilibrium thermodynamics method, as a function of the electric field. The underlying idea is the usual recognition that the nonconserved flux $\boldsymbol{P}$ is the fast changing variables in space/time compared to the slowly varying $\boldsymbol{u}$. Accordingly, by dropping out higher order terms in Eq. (22) we get

$$-\boldsymbol{P}\nabla\cdot\boldsymbol{u} - \Big[\boldsymbol{P}\cdot\boldsymbol{\nabla}u + (\boldsymbol{\nabla}u)^t\cdot P\Big] + \Lambda^{(s)} = 0. \quad (37)$$

This is the closed equation for the pressure tensor, and thus its solution provides the desired closure ansatz for the drift velocity, Eq. (19). Then, to the lowest order in the gradients the drift velocity equation becomes

$$\rho\frac{d\boldsymbol{u}}{dt} = -\boldsymbol{\nabla}p - e\rho\boldsymbol{E} - (\beta g)^{-1}R^{(-1-1)}\frac{\sinh\kappa}{\kappa}\boldsymbol{u}. \quad (38)$$

In the steady state for a homogeneous semiconductors, it gives

$$e\rho\boldsymbol{E} + (\beta g)^{-1}R^{(-1-1)}\frac{\sinh\kappa}{\kappa}\boldsymbol{u} = 0 \quad (39)$$

where κ was determined in Eq. (34). Although Eq. (39) has been written as a closed form for $\boldsymbol{u}$, it is not the case as far as the field-dependence is concerned. This is because the temperature β appearing in it is the hot electron temperature through which additional $\boldsymbol{E}$ dependence occurs. In fact, in order to treat the problem exactly, one has to generate the energy balance equation that couples to Eq. (38). Obviously, it constitutes a demanding job, although possible, and it is out of the scope of the present work. Here, we shall assume that the temperature remains in equilibrium and will set aside the full calculation as a separate project [16]. Then, one can readily obtain, for an isotropic semiconductors, that

$$u = \frac{1}{\sqrt{R^{(-1-1)}/3}}\sinh^{-1}\left[\frac{e\rho\beta_0 g}{\sqrt{R^{(-1-1)}/3}}E\right]. \quad (40)$$

In the linear response regime, Eq. (40) tends to $u = \mu_0 E$ where the linear mobility is given by

$$\mu_0 = \frac{3e\rho\beta_0 g}{R^{(-1-1)}}. \quad (41)$$

Equation (40) does not properly account for the velocity saturation or the interesting negative differential conductivity because of its over simplified nature and also of the neglect of the intervalley scattering. Thus, we do not intend to compare it with the existing experimental data [15].

In conclusion, we have used essentially two steps in reducing the formally exact transport equation, Eq. (19), to the desired macroscopic level, Eq. (38). The usual closure problem is one ingredient and the other one is to incorporate the irreversibility properly. We have taken care of the closure problem using the concept of the generalized hydrodynamics. Eu's nonequilibrium ensemble method was adopted in monitoring the second law of thermodynamics. In this brief report we have presented only a simple application of the theory, while reserving the full report elsewhere [16].

ACKNOWLEDGMENTS

We thank Prof. B. C. Eu for bringing up the idea of nonequilibrium thermodynamics to us. This work was supported by KOSEF Grant No. 971-0202-011-2 and also in part by the Ministry of Education through Grant No. BSRI-97-2431.

REFERENCES

[1] E. Bringuier, Phys. Rev. **B58**, 4543 (1998).
[2] X. L. Lei, J. Korean Phys. Soc. **30**, S191 (1997).
[3] A. K. Ghorai and D. P. Bhattacharya, Phys. Sat. Sol. (b) **197**, 125 (1996).
[4] D. Y. Kim and C. S. Kim, Phys. Rev. **B51**, 14207 (1995).
[5] C. S. Kim, J. C. Nahm and O. Olnedski, J. Korean Phys. Soc. **30**, S321 (1997).
[6] R. Thoma, A. Emunds, B. Meinerzhagen and H.-J. Peifer, IEEE Trans. Electron Devices **38**, 1343 (1991).
[7] D. Chen, E. C. Kan and K. Hess, J. Appl. Phys. **68**, 5360 (1990).
[8] E. E. Kunhardt, M. Cheng and C. Wu, J. Appl. Phys. **64**, 1220 (1988).
[9] R. Kubo, J. Phys. Soc. Japan **12**, 570 (1957); D. A. Greenwood, Proc. Phys. Soc. London **71**, 585 (1958).
[10] P. B. Allen, Phys. Rev. Lett. **59**, 1460 (1987).
[11] K. M. Vliet, Phys. stat. sol. (b) **78**, 667 (1976).
[12] Y. J. Park and C. S. Kim, J. Korean Phys. Soc. **29**, 466

(1996).

[13] See, for a review, D. Jou, J. Casas-Vázquez and G. Lebon, *Extended Irreversible Thermodynamics* (Springer-Verlag, Berlin, 1993).

[14] B. C. Eu, *Kinetic Theory and Irreversible Thermodynamics* (Wiley, New York, 1992).

[15] C. Canali, G. Ottaviani and A. A. Quaranta, J. Phys. Chem. Solids **32**, 1707 (1971); P. M. Smith, M. Inoue and J. Frey, Appl. Phys. Lett. **37**, 797 (1980).

[16] D. Y. Kim, C. S. Kim and B. C. Eu, *Theory of High-field Transport of Hot Electrons in Semiconductors*, to be published.

Journal of the Korean Physical Society, Vol. 34, June 1999, pp. S315~S317

Fabrication of 1.3 μm Strained InGaAsP/InGaAsP MQW SSC-LD by Selective Area MOCVD Growth

T. J. KIM*, J. K. JI, Y. C. KEH, H. S. KIM, S. D. LEE,
A. G. CHOO and T. I. KIM

Photonics Laboratory, Material & Device Sector, Samsung Advanced Institute of Technology, Suwon 440-600

High performance 1.3 μm spot-size converter integrated laser diodes (SSC-LD) were developed by using selective area metal organic chemical vapor deposition (MOCVD) growth. InP and InGaAsP single layers were investigated in terms of the growth rate enhancement and material quality by adjusting the growth rate and SiO_2 mask width. Lasing characteristics, such as a low threshold current and high slope efficiency, were achieved by using a high-quality 0.8 % compressively strained multiple quantum well (MQW) structure. A narrow radiation angle of $11^\circ \times 14^\circ$ was obtained by optimizing the vertically tapered-waveguide profile. And a high coupling efficiency of 47 % was achieved between SSC-LD chip and single-mode fiber. This SSC-LD is very appropriate as a light source for access network systems, which require a low- cost LD module.

I. INTRODUCTION

Laser diodes with a narrow radiation beam, which could be highly coupled into the optical fiber with a large alignment tolerance, is one of the key device for subscriber laser module. However, it is difficult to get a narrow beam by a conventional laser diode with low threshold current and high efficiency because the expansion of the mode profile to get a narrow beam makes optical confinement low and threshold current high. To meet these requirements, spot size converted laser diodes (SSC-LD) integrated with tapered-thickness waveguide, which is fabricated using a selective area metal organic chemical vapor deposition (MOCVD) growth are proposed by many groups [1–3]. SSC-LD can provide low loss direct coupling to the optical fiber without the need for a lens and offer expanded tolerance for optical alignment. These features reduce the number of components needed for the module assembly and make possible the passive alignment between the LD's and fiber.

Selective area MOCVD growth is an attractive device fabrication method for expanding the use of a variety of optical devices. Selective area growth (SAG) makes possible the control of the band-gap energy of the multiple quantum well (MQW) structure and of the thickness of the epitaxial layer by merely changing the width of opening window and SiO_2 mask patterned on the InP substrate. These features of selective area MOCVD growth are very useful in the fabrication of vertical taper SSC-LD's.

*E-mail: tjkim@sait.samsung.co.kr, Tel: +82-331-280-9360, Fax : +82-331-280-9357

II. SELECTIVE AREA MOCVD GROWTH

The thickness of the selective growth region (opening window region used as gain region) is thicker than that of the planar region (used as tapered region) by growth enhancement. The widths of mask (w_m) and opening window (w_o) were changed to obtain optimum thickness enhancement factor to make optical mode transition in vertically tapered waveguide region. Fig. 1 is a graph

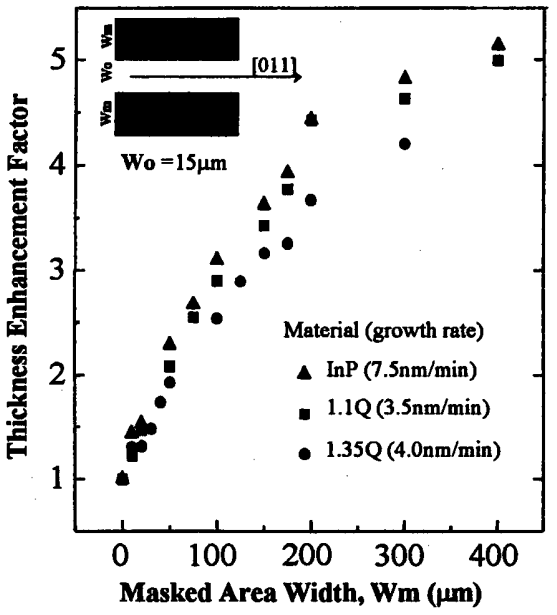

Fig. 1. Mask width dependence of thickness enhancement factor.

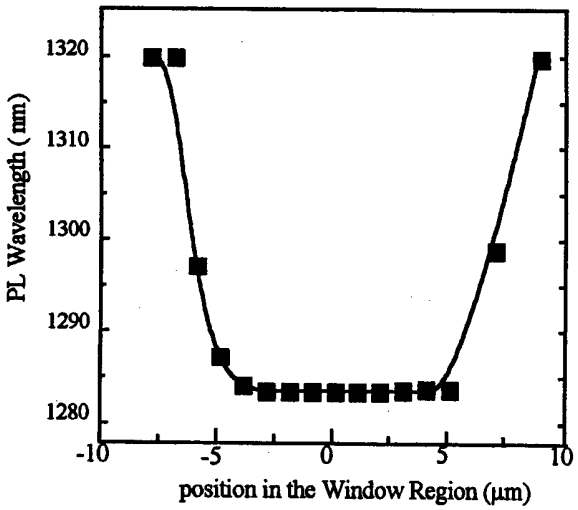

Fig. 2. PL wavelength uniformity in opening window region.

showing mask width dependence of the growth rate when opening window width is 15 μm. As mask width increased, thickness enhancement factor increased up to five when mask width is 400 μm. With the mask width of 150 μm, thickness enhancement factor of three was obtained inside the opening region of 15 μm, and the growth rate of 35 Å/min is used to obtain high quality of material by employing micro-PL technique.

Uniform and high-quality 0.8 % compressive strained MQW structures were obtained by selective area MOCVD growth and confirmed by the fact that the intensity and full width at half maximum of PL spectra were the same as those for the MQW grown by conventional MOCVD. The uniformity of PL wavelength in opening window region was shown in Fig. 2. Uniform region of PL wavelength deviation of $\pm$1 nm is obtained within 10 μm width inside the opening region of 15 μm.

III. DEVICE FABRICATION AND ITS CHARACTERISTICS

Fig. 3 shows the schematic structure of the 1.3 μm strained MQW SSC-LD. The vertically tapered waveguide was integrated as a spot size-converter on the front side of the laser, in order to expand the beam spot size. The multiple quantum well active layer consists of 0.8 % compressive strained well layers composed of InGaAsP (6 nm thick, 7 periods) and lattice matched barrier layers composed of 1.10 μm wavelength InGaAsP (10 nm thick). The MQW active layers are surrounded by 100 nm thick separate-confinement heterostructure (SCH) layers composed of 1.10 μm wavelength InGaAsP on both sides. The active layer and the vertically tapered wavguide were grown continuously on SiO_2 mask patterned S-doped n-InP substrate by selective area MOCVD growth. Stripe of mesa profile was obtained by photolithography and wet etching. To complete buried hetero (BH) structure, p/n-InP blocking layers and p-InP/P^+-InGaAs contact layers were successively regrown by MOCVD.

The light output power versus injection current (L-I) characteristics at various temperature and divergence angle for a HR coated laser with L_{gain}=350 μm and L_{wg}=150 μm is shown in Fig. 4. It has a low threshold

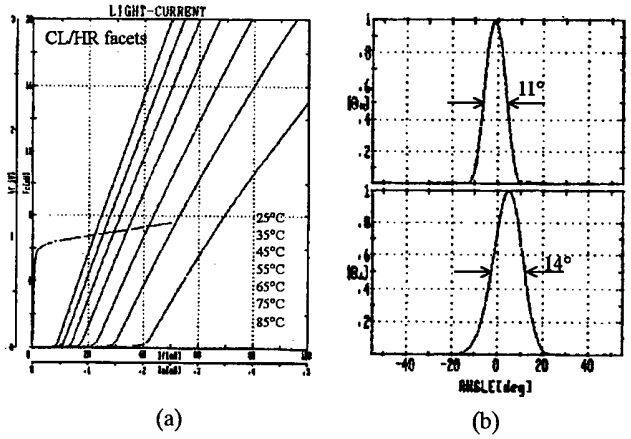

Fig. 4. (A) L-I characteristics at various temperature (B) FFP of SSC-LD.

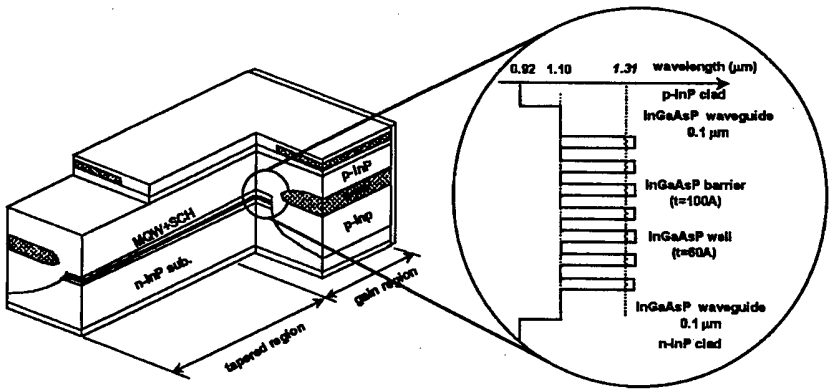

Fig. 3. Schematic diagram of an SSC-LD fabricated by use of selective area growth.

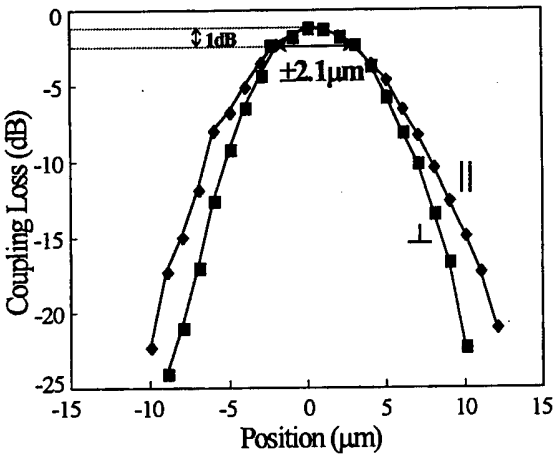

Fig. 5. −1 dB alignment tolerance between SSC-LD and SMF.

current of 7 mA and slope efficiency of more than 0.45 mW/mA at RT. The parallel and perpendicular far field pattern to the junction plane is 11° and 14°, respectively.

IV. COUPLING CHARACTERISTICS

The measurement of the coupling characteristics (coupling efficiency and coupling tolerance) between a laser and a single mode fiber is very important for the performance evaluation of a laser module packaged by a passive alignment method. The characteristics of direct coupling to a cleaved 9 μm/125 μm single mode fiber were investigated for the SSC-LD, as shown in Fig. 5. The maximum coupling efficiency was 47 % and the −1 dB alignment tolerance was ±2.1 μm for both horizontal and vertical alignment. This coupling tolerance enables us to align the laser beam to a SMF in a passive alignment scheme with high coupling efficiency.

V. CONCLUSIONS

1.3 μm strained MQW SSC-LD of narrow beam was fabricated by the use of selective area MOCVD growth. The waveguide profile of the SSC section was controlled using SiO_2 mask and opening window, and optimum profile was determined. Superior lasing characteristics were achieved as low threshold current of 7 mA and high slope efficiency of more than 0.45 mW/mA at RT. We obtained a narrow divergence angle of 11°×14°, resulting in coupling efficiency of 47 % to a cleaved 9 μm/125 μm single mode fiber with the −1 dB alignment tolerance of −2.1 μm.

REFERENCES

[1] H. Kobayashi, M. Ekawa, N. Okazaki, O. Aoki, S. Ogita and H. Soda, IEEE Photonics Technol. Lett. **6**, 1080 (1994).

[2] G. Muller, B. Stegmuller, H. Westermeier and G. Wenger, Electron. Lett. **27**, 1836 (1991).

[3] R. N. Thurston, E. Kapon and A. Shahar, Opt. Lett. **16**, 306 (1991).

Journal of the Korean Physical Society, Vol. 34, June 1999, pp. S318~S321

Lifetime Projection Model of Semiconductor Laser Diodes by Thermal Degradation

Nam HWANG, Seung-Goo KANG, Hee-Tae LEE, Sang-Hwan LEE,
Gwan-Chong JOO and Min-Kyu SONG

*Compound Semiconductor Research Department, Electronics and Telecommunications Research Institute, Taejon 305-350**

A lifetime projection model of semiconductor laser diodes (LD) is presented. By correlating initial thermal characteristics and long-term degradation, a relationship between LD degradation and ambient temperature has been investigated. The proposed model is found to be efficient for the lifetime projection of LDs, which requires a thermal characterization only at $t = 0$.

I. INTRODUCTION

The reliability of a laser diode (LD) in a high speed optical transmission module (OTx) is of great importance for the development of an optical communication system (OCS) due to its large capacity and long-haul transmission capability are major advantages of OCS. The reliability test results of LDs are required to ensure the long-term performance of OTx in the field. Prior to the fabrication of OTx, reliability tests of LDs in bare chips or sub-assembled structures are required to screen weak LDs, and to burn-in the selected LDs to stabilize their characteristics. Then, the LDs to be used in OTx are evaluated for their life expectancy by an accelerated lifetime test. However, the accelerated lifetime test is costly and time consuming, requiring hundreds or thousands of hours. Also, it does not provide real-time information on the fabrication processes of LD as well as OTx. Hence, a reliability test has to be developed to predict reliability accurately and within reasonable test time.

The rate of LD degradation is a function of both current density and temperature. Reliability projection of LD has been characterized by monitoring an increase in threshold current (I_{th}) or operating current (I_{op}) [1–9]. Conventionally, the LD lifetime is defined at the 50 % increase of I_{th} or I_{op} [8,9]. In order to limit the reliability evaluation time for a slowly degrading device such as LDs, both temperature and time extrapolations are possible in principle. It is that reliability assurance is to be determined by extrapolation in temperature rather than time. Either one or the other is inevitable when the desired system lifetimes are tens of years, and clearly it is unacceptable to wait for 25 years to determine whether a device operating field conditions will actually live 25 years [9].

The common pattern of the LD degradation by long-term stressing is found to be similar to that of the thermal degradation measured before stressing. That is, the change of optical characteristic after the aging test is found a strong close correlation with that monitored during the initial thermal characteristics measurements. Hence, the purpose of this paper is to propose a novel reliability projection model of LDs by correlating the initial thermal characteristics as a means of predicting and/or screening for LD degradation. In this paper, the proposed empirical method will explore the potential use of initial voltage characteristics as a means of predicting and/or screening for LD degradation for high-speed optical communication systems.

II. EXPERIMENT

The SEM photograph of the cross section of LD used in this study is shown in Fig. 1, where the LD was fabricated for a high speed OSC (>2.5 Gbps) [10,11]. The LD was fabricated by a stable fabrication process employing metal organic vapor phase epitaxy (MOVPE) and reactive ion etching (RIE). The p-InP/n-InP/p-InP layers were grown with current blocking layers. The active layer is 0.15 μm thick, 1.5 μm wide, and 400 μm long. The I_{th} and slope efficiency of LD were typically measured to be 20 mA and 0.04 mW/mA, respectively. To avoid any infant failure mechanism, a purge test was performed under a constant injection current of 100 mA at 100 °C. The initial thermal characteristics (L-I measured at 23 °C~70 °C) are shown in Fig. 2(a) where the characteristic temperature (T_o) of the LD is measured to be 34.6 °K as shown in Fig. 2(b).

The accelerated lifetime test was performed at the ag-

*E-mail: nhwang@etri.re.kr, Tel: +82-42-860-5244, Fax: +82-42-860-6183

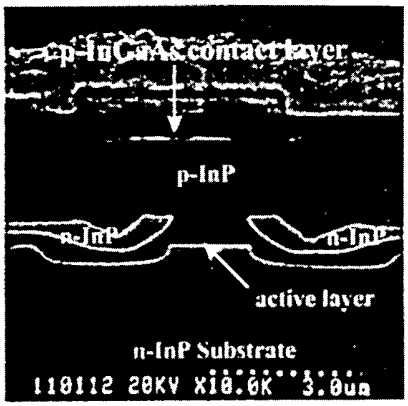

Fig. 1. A SEM photograph of the cross section of LD used in this study. The LD was designed for a high speed application (>2.5 Gbps).

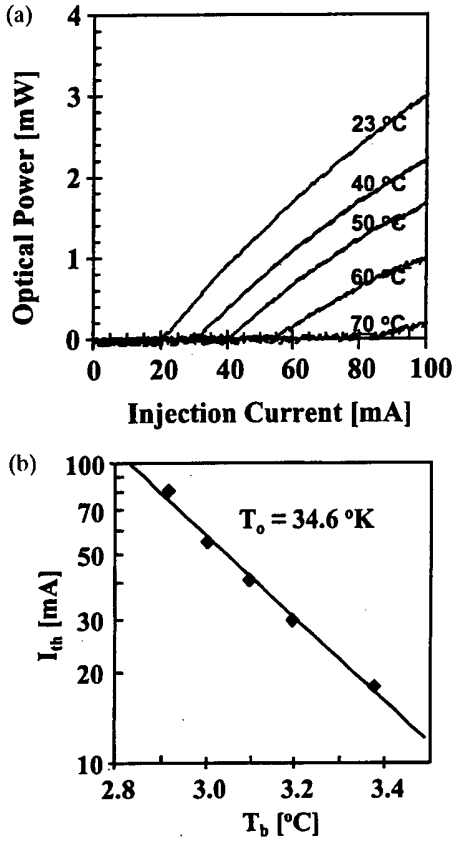

Fig. 2. Initial thermal characterization of LD; (a) optical characteristics (L-I) of LD were measured as varying the base temperatures (T_b) from 23 °C to 70 °C, and (b) the characteristic temperature (T_o) of the LD was calculated to be 34.6 °K.

ing temperature (T_a) of 50 °C under a constant current of 100 mA in a dry-nitrogen ambient in order to investigate the long-term degradation of LDs. During accelerated lifetime testing, the optical characteristics were measured in every 20 hours at the ambient temperature of 50 °C

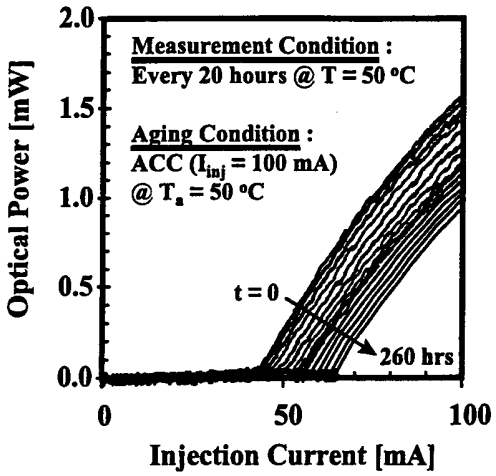

Fig. 3. The L-I curves measured in every 20 hours during the accelerated lifetime test at the ambient temperature of 50 °C with a constant current injection of 100 mA.

as shown in Fig. 3. It should be pointed out that the L-I curves of long-term degradation as shown in Fig. 3 are quite similar to those of the thermal degradation as shown in Fig. 2(a). For example, the L-I curve measured at 50 °C prior to the aging test in Fig. 2(a) is the same as that measured at $t = 0$ in Fig. 3 while the L-I curve measured at 60 °C prior to the aging test in Fig. 2(a) is quite similar to that measured after 220 hours of the aging test in Fig. 3.

This result shows that the long-term degradation of LD is related with the thermal degradation such as an increase of the junction temperature of LD. The LD degradation is resulted from both optical (*i.e.*, quantum efficiency, facet coating index and/or thickness, *etc.*) and electrical (*i.e.*, ohmic contact, interfacial defects, *etc.*) characteristics degradation. Once the optical and electrical characteristics of LD are degraded, then the increase of I_{th} and I_{op} of LD causes the internal temperature of LD to increase. Hence it is clear that the LD degradation has a same mechanism in the thermal degradation.

Then, the proposed LD reliability projection model of I_{th} shift has been developed by adapting the Arrhenius relationship described as

$$I_{th}(T_1) = I_{th} \cdot \exp\left(\frac{T_1 - T_2}{T_o}\right) \tag{1}$$

where T_1 is a test temperature for thermal characterization, T_2 is an ambient temperature under an operating condition, and T_o is the characteristic temperature [12]. The Arrhenius relationship is simple but efficient for developing the thermal degradation of LD in terms of I_{th}. From Eq. (1), once T_o is determined, then it is possible to determine I_{th} at an elevated temperature as well as ΔI_{th} defined as

$$\Delta I_{th}(T) = \frac{I_{th}(T_1) - I_{th}(T_2)}{I_{th}(T_2)} \tag{2}$$

By using $\Delta I_{th}(T)$ definition in Eq. (2), Eq. (1) can be expressed as

$$\Delta I_{th}(T_1) = \exp\left(\frac{T_1 - T_2}{T_o}\right) - 1 \quad (3)$$

In order to develop a long-term degradation model of LD, the model has to be accurate and simple enough to be conveniently applied for the extrapolation of LD lifetime. The conventional methods for predicting degradation of I_{th} are by means of the power-law model [13,14] described as

$$\Delta I_{th}(t) = A \cdot t^m \exp\left(\frac{E_a}{k \cdot T_a}\right) \quad (4)$$

where E_a is the activation energy, k is Boltzmann's constant (8.62×10^{-5} eV/°K), T_a is the aging temperature, m is an exponent, and A is the empirical constant. Then, the lifetime model is developed by equating $\Delta I_{th}(T) = \Delta I_{th}(t)$ from Eqs. (3) and (4):

$$t = C \cdot \left[\exp\left(\frac{E_a}{k \cdot T_a}\right) \cdot \left\{\exp\left(\frac{T_b - T_c}{T_o}\right) - 1\right\}\right]^{\frac{1}{m}} \quad (5)$$

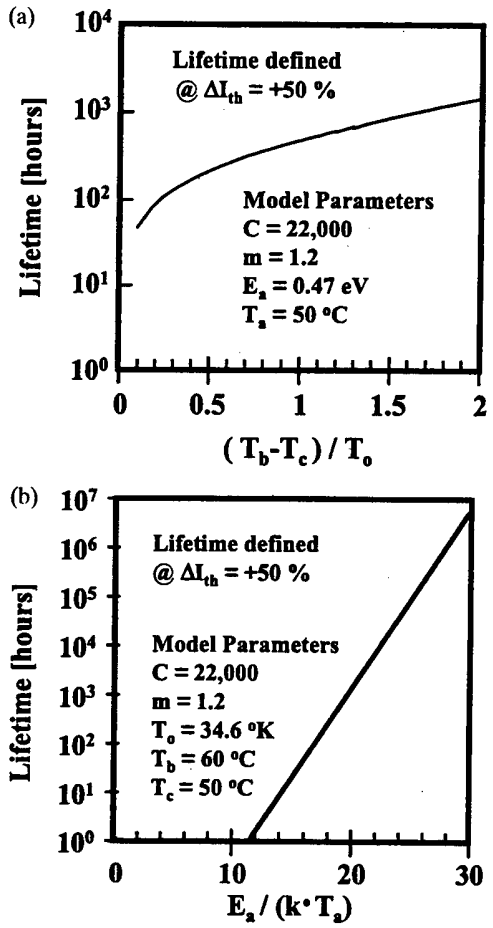

Fig. 4. The effect of parameter variations of the proposed lifetime projection model in Eq. (5): (a) the initial thermal parameters and (b) the lifetime projection parameters.

where T_b is the base temperature during thermal characterization, T_c is the critical temperature of thermal degradation of I_{th} shift, and C is the empirical constant.

In order to apply the proposed model for lifetime projections, T_b has to be correlated with ΔI_{th} from the initial thermal characterization measurement as shown in Fig. 2(b).Then, T_c is chosen according to the failure criterion (*i.e.*, $T_c = T_b@\Delta I_{th} = +50$ %). As shown in Fig. 4, the variations of proposed model parameters have revealed that the lifetime projection is mainly affected by the accuracy of E_a.

The accelerated life test results are shown in Fig. 5. We have monitored the rate of LD degradation in a conventional method with I_{th} shift as shown in Fig. 5(a), and the activation energy of LD is found to be 0.47 eV by determining lifetimes at $\Delta I_{th} = +50$ % as shown in Fig. 5(b). The LD degradation rate in terms of I_{th} shift as a function of ambient temperatures is 0.3 %/hours, 0.4 %/hours, and 0.5 %/hours at 50 °C, 60 °C, and 70 °C,

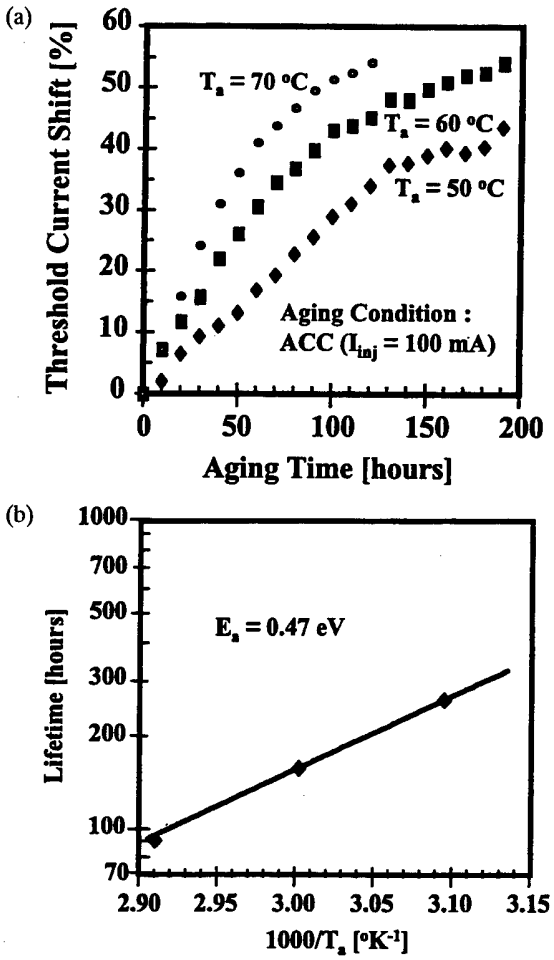

Fig. 5. The conventional life test of LD monitoring I_{th} shift during the accelerated lifetime test: (a) I_{th} shift measured at 50 °C, 60 °C, and 70 °C under the constant current injection of 100 mA and (b) the activation energy of LD degradation was calculated to be 0.47 eV.

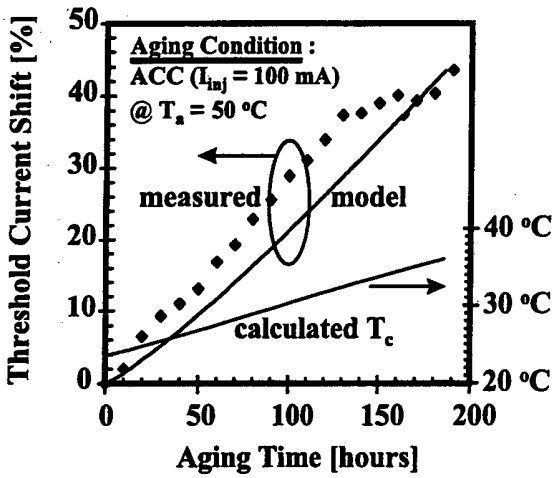

Fig. 6. The lifetime comparison of experimental measurements and simulated results of the proposed lifetime model projections.

respectively. This linear relationship of the thermal acceleration life test reveals that the LD degradation mechanism is constant under the temperature range.

The simulated results of proposed lifetime projection model at 50 °C have been compared with the experimental measurements of the LD degradation as shown in Fig. 6, where the LD lifetime at $\Delta I_{th} = +50$ % is measured and calculated to be 220 hours at the aging temperature of 50 °C. In order to apply the model to a lifetime projection, Eq. (5) can be simplified by using a series expansion and $m \approx 1$;

$$t \approx Q \cdot \left(\frac{T_b - T_c}{T_o} \right) \tag{6}$$

where $Q = C \cdot \exp\{E_a/(k \cdot T_a)\}$ in Eq. (5). Eq. (6) shows a linear relationship of LD lifetimes in terms of T_b, meaning that the long-term LD degradation is linear with thermal degradation. From the preliminary life test result, T_c was calculated with the LD degradation as shown in Fig. 6 where T_c for $\Delta I_{th} = +50$ % was found to be about 38 °C at $T_a = T_b = 50$ °C. The lifetime rate of thermal degradation was determined to be 16.9 hours/°C at the operating temperature of 50 °C. For the application of proposed model to screen LDs, T_c and T_o have to be determined from the initial thermal characterization where small T_c and large T_o are desirable for the guarantee of LD reliability.

III. SUMMARY

In conclusion, we have developed a lifetime projection model of LD degradation. The LD degradation mechanism of long-term aging test was observed as same as that monitored in the thermal characterization. By correlating initial thermal characteristics and long-term degradation, a relationship between LD degradation and ambient temperature has been investigated. The proposed model is found to be efficient for the lifetime projection of LDs, which requires a thermal characterization result measured at $t = 0$.

Further experimental results are required at various temperature ranges and operating conditions to enhance the accuracy of the proposed lifetime projection model. Also, researches on failure mechanism analysis of the LD degradation are necessary to support the physical mechanism of the proposed lifetime projection model.

REFERENCES

[1] N. Hwang, S.-G. Kang, H.-T. Lee, S.-S. Park, M.-K. Song and K.-E. Pyun, 1997 IEEE International Reliability Phys. Proc., Denver, CO, Apr. 8-10, p. 272, 1997.

[2] N. Hwang, S.-G. Kang, H.-T. Lee, M.-K. Song and K.-E. Pyun, 1996 IEEE International Reliability Phys. Proc., Dallas, TX, Apr. 30-May. 2, p. 195, 1996.

[3] N. Hwang, M.-K. Song, S.-G. Kang, H.-T. Lee, K.-H. Park, D.-H. Jang, S.-S. Park, H.-S. Han, D.-G. Kim and H.-M. Park, Proceedings of the 45th Electronic Components & Technology Conference, Las Vegas, NV, May 1-4, p. 318, 1995.

[4] D. P. Wilt, Proc. 6th International Conf. on Indium Phosphire and Related Materials, Santa Barbara, CA., p. 296, 1994.

[5] N. Hwang, H.-S. Cho, M.-K. Song, H.-M. Kim and K.-E. Pyun, J. Korean Phys. Soc. **30**, S151 (1997).

[6] S.-S. Park M.-K. Song, N. Hwang, S.-G. Kang, H.-T. Lee, H.-R. Choo, H.-M. Kim and K.-E. Pyun, J. Korean Phys. Soc. **30**, S163 (1997).

[7] S.-H. Lee, G.-C. Joo, H.-S. Cho, K.-S. Park, M.-K. Song and Y.-H. Lee, J. Korean Phys. Soc. **33**, S444 (1998).

[8] C. C. Shen, J. J. Hsieh and T. A. Lind, Appl. Phys. Lett. **30**, 353 (1977).

[9] F. R. Nash, W. J. Sundburg, R. L. Hartman, J. R. Pawlik, D. A. Ackerman, N. K. Dutta and R. W. Dixon, AT&T Tech. Journal **64**, 809 (1985).

[10] K.-H. Park, D.-H. Jang, J.-K. Lee, H.-S. Cho, J.-S. Kim, J.-H. Han, H.-T. Lee, N. Hwang, H.-M. Kim, H.-M. Park and S.-C. Park, Optical and Quantum Electronics **27**, 547 (1995).

[11] H.-M. Kim, J.-S. Kim, C.-D. Park, D.-K. Oh, H.-R. Kim, H.-R. Choo, H.-M. Kim, S.-S. Park, M.-K. Song and K.-E. Pyun, Conference Proceedings of LEOS'96 9th Annual Meeting, Boston, MA, **2**, ThU5, 421 (1996).

[12] P. A. Davis and D. C. Trindade, *Applied Reliability*, 2nd Ed. (Van Nostrand Reinhold, N.Y., 1995), pp. 334-371.

[13] O. Ueda, *Reliability and Degradation of III-V Optical Devices* (Norwood, MA: Artech House, 1996).

[14] *Optoelectronic Packaging*, A. R. Mickelson, N. R. Basavanhally, Eds. Y.-C. Lee (Wiley, New York, 1997), p. 70.

Journal of the Korean Physical Society, Vol. 34, June 1999, pp. S322~S325

High Speed and Short Channel Transport Characteristics of Scaled Sub-100 nm Gate High Eelection Mobility Transistors

Jaeheon HAN*

Department of Electronic Engineering, Kangnam University, Yongin 449-702

Ultra-short channel AlGaAs/GaAs High electron Mobility Transistors have been fabricated with gate lengths ranging from 35 nm to 115 nm, in order to examine the characteristics of sub-100 nm HEMT scaling. Measurements of the transconductance and extraction of the effective electron velocity show a initial decrease in these quantities near 50 nm of gate length due to the dominance of short-channel effect. The rise in transconductance below this gate length is attributed to the onset of velocity overshoot in the channel region. We have investigated this behavior by comparison between the effective average electron velocities obtained analytically from the measured transconductance and those calculated numerically from the transient transport model. The results yield qualitative agreement with both the measurements and the interpretation given above.

I. INTRODUCTION

Recent progress in electron beam lithography and molecular beam epitaxial growth technology has brought critical dimensions of a field-effect transistor down to 100 nm. The enhanced dc and microwave characteristics of GaAs based, subquarter-micron channel High Electron Mobility Transistors (HEMTs) are direct consequences of efforts to decrease the gate length [1–3]. Reducing the gate length results in a smaller gate aspect ratio, however, deteriorating device parameters such as transconductance and threshold voltage [4]. On the other hand, velocity overshoot occurs, which improve the device performance [5,6].

In this study, we describe how the device characteristics of sub-100 nm gate AlGaAs/GaAs HEMTs are affected by the carrier transport properties governed by velocity overshoot due to near-ballistic electrons and by short-channel effect due to very low gate aspect ratio.

II. DEVICE FABRICATION

AlGaAs/GaAs HEMTs were fabricated on Molecular Beam Epitaxy (MBE) grown wafers. The wafers had a 5 nm Si-doped 2×10^{18} cm^{-3} n^+-GaAs cap layer, 35 nm Si-doped 4×10^{18} cm^{-3} n^+-AlGaAs layer, 300 nm undoped GaAs layer, and a semi-insulating GaAs substrate heterostructures. High doping concentration in the n^+-AlGaAs active layer and the absence of an undoped AlGaAs spacer layer maximizes the carrier density in the channel.

The fabrication requires four mask levels to define mesa, source-drain contacts, pads, and gate. All exposures were accomplished using electron-beam lithography. The active mesa area is first defined by using Shipley SAL 601-ER7 negative electron-beam resist and wet etching in a 1:1:150 mixture of H_2O_2:H_2SO_4:H_2O solution. The resist is spun to obtain a thickness of 500 nm, and developed in Shipley SAL MF-622 developer for 2.5 minutes. All three subsequent mask levels are defined using positive e-beam resist developed in a 3:7 solution of cellosolve:methanol. The second step is ohmic contact formation. AuGeNi ohmic contacts are formed by using e-beam evaporation and a lift-off process followed by a forming gas annealing step. The third step is the formation of the probing pads, which consist of a 5 nm layer of Cr topped by a 200 nm layer of Au. Before the wafer is patterned for the gate line, the thin highly doped n^+-GaAs cap layer is removed completely by wet chemical etching. To write the gate line, positive electron-beam resist is spun on to a thickness of 70 to 90 nm. A thinner resist would make smaller lines possible. However, for successful lift-off, the resist thickness must generally be at least twice the thickness of the deposited metal. The resist thickness is chosen to obtain a gate thickness of 30 nm, sufficient to assure step coverage of the gate at the edge of the mesa area. The gate lines are 35 nm to 115 nm long and 20 μm wide. These are exposed at a pixel-to-pixel spacing of 21.7 nm at 40 kV. The gates are deposited Au metals defined by lift-off. Figure 1 is an optical micrograph of a completed AlGaAs/GaAs HEMT.

*E-mail: jhan@kns.kangnam.ac.kr, Tel: 0331-280-3806, Fax: 0331-280-3750

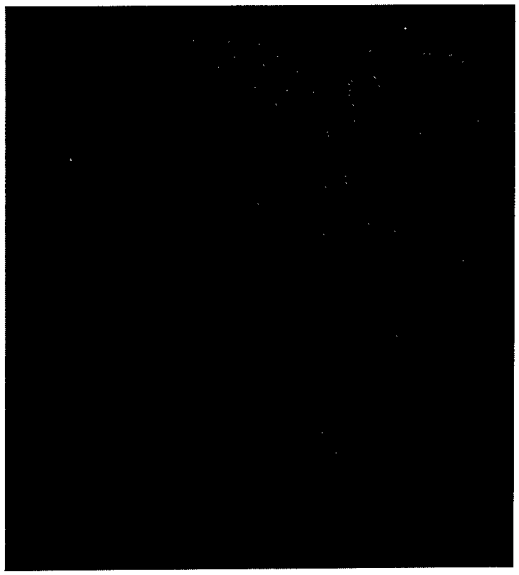

Fig. 1. SEM micrograph showing the active device area of a completed AlGaAs/GaAs HEMT.

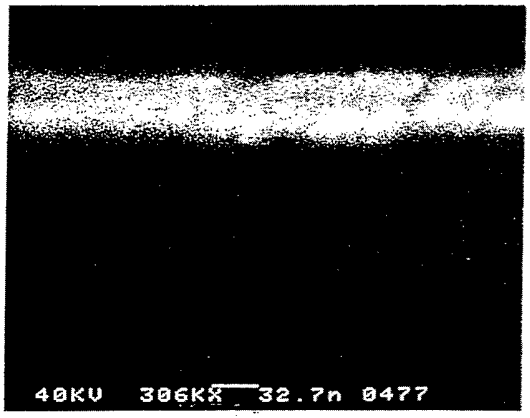

Fig. 2. SEM micrograph showing 40 nm gate line of the fabricated HEMT.

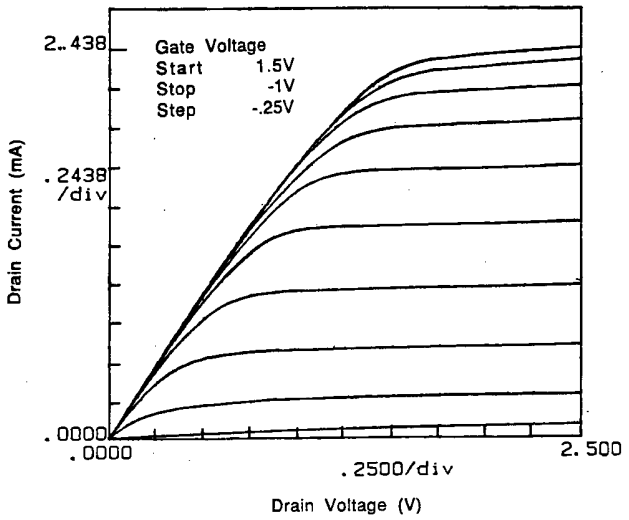

Fig. 3. I_{DS} vs. V_{DS} curves for 40 nm gate length HEMT.

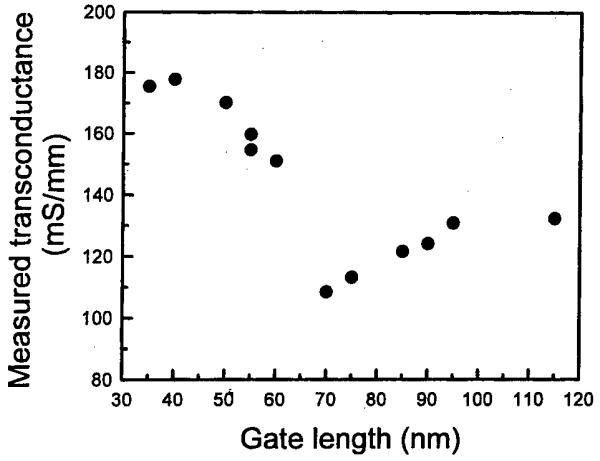

Fig. 4. Measured transconductance vs. gate length for HEMTs.

III. EXPERIMENTAL RESULTS AND DISCUSSION

The fabricated devices are tested using a HP 4145B semiconductor parameter analyzer followed by gate length measurement with a SEM, usually at 300,000×. Figure 2 is a SEM micrograph showing a 40 nm gate line of the fabricated AlGaAs/GaAs HEMT.

Figure 3 displays I_{DS} vs. V_{DS} curves for a 40 nm gate length AlGaAs/GaAs HEMT with the maximum measured transconductance of 178 mS/mm. The device exhibits good pinch-off characteristics and no evidence of breakdown up to $V_{DS} = 2.5$ V. The measured transconductance is plotted as a function of gate length in Fig. 4. The transconductance decreases with gate length to 70 nm. Below this, the transconductance starts to increase again for gates shorter than 70 nm. The initial degradation of transconductance with the gate length occurs until the gate length reaches to 70 nm, mainly due to the short-channel effect. While the gate aspect ratio, defined here by gate length-to-active layer thickness ratio, becomes smaller, the short-channel effect is induced by a non-planar depletion layer under the gate, which is dominated more by the edge fringing regions than by the flat regions and acts less like a parallel plate capacitor and more like a circular capacitor. The transconductance keeps decreasing until the gate length becomes of the order of the inelastic mean free path of electrons. At this point, for gate length below 70 nm, velocity overshoot starts to occur. Here, the gate lengths are sufficiently short that electrons transit the entire channel region without ever stabilizing to the saturation velocity, thus increasing transconductance.

The range of intrinsic transconductance obtained for the HEMTs is from 140 mS/mm to 275 mS/mm. Al-

though these intrinsic transconductances are lower than published results [1,7], they are precisely what is to be expected from the size of these devices, where the aspect ratio is less than 2. By an approximate calculation, the intrinsic transconductance can be theoretically obtained from its definition for a long-gate HEMT with the saturated electron velocity,

$$g_{m,max} = \frac{dI_{ds}}{dV_{gs}} = C_{gs} \cdot v_{sat} = \epsilon \cdot v_{sat}(d + \Delta d) \approx 233 \text{ mS/mm} \quad (1)$$

where C_{gs} is the gate-source capacitance, ϵ is the permitivity of the AlGaAs layer ($\sim 1 \times 10^{-10}$ F/m), d is the active layer thickness of 35 nm, and Δd is the average set-back distance of the two-dimensional electron gas (2DEG) from the heterointerface in the GaAs layer due to the quantized wave function, ~8 nm [8]. The calculated intrinsic transconductance is about 30 to 40 % higher than the measured one of a 70 nm gate length HEMT. This deterioration of transconductance is the direct result of short-channel effect. Generally, the electron saturation velocity of very short gate length FETs having a gate aspect ratio less than 5 or gate length shorter than about 100 nm should take into consideration the short channel effect. The effective average electron velocity of a HEMT, $v_{eff,(MOD)}$ can be obtained by compensating with a short-channel effect due to the non-flat geometry of the gate depletion region. Figure 5 shows the schematic of an effective gate length geometry at pinch-off in a HEMT. As the gate length decreases, the effective gate length will be increasingly dominated by the extended gate length of the lateral depletion width due to the short-channel effect. When the length of the gate depletion region becomes equal to the thickness of the active region including the average set-back distance of the two-dimensional electron gas (2DEG), the HEMT operates at channel pinch-off condition and drain current starts to saturate. In general, the drain-source bias V_{DS} is much higher than the gate-source bias V_{GS} at pinch-off, and the lateral depletion region beyond the physical gate length is extended mainly toward the drain region, especially when the drain voltage is increased beyond $V_{D,sat}$. In this condition, the contribution of the laterally extended depletion region to the effective gate length is mainly determined by the magnitude of the gate-drain lateral depletion region. Also, the shape of the depletion region may be assumed to be a rectangle, which represents the complete pinch-off condition to have maximum effective gate length (assuming the worst case). Then, the effective gate length of a HEMT, $L_{g,eff,(MOD)}$ can be approximated by

$$L_{g,eff(MOD)} = L_g + (d + \Delta d). \quad (2)$$

Here, $(d + \Delta d)$ is the extended gate length due to the gate-drain lateral depletion region. The gate aspect ratio compensation factor for a HEMT, M, is given by

$$M = \frac{A_{eff(MOD)}}{A_o} = \frac{L_{g,eff(MOD)} \cdot W}{L_g \cdot W} = 1 + \frac{(d + \Delta d)}{L_g}, \quad (3)$$

where $A_{eff,(MOD)}$ and A_o are the effective HEMT and normal FET (larger gate HEMT) gate areas of the gate capacitance, L_g is the normal gate length, and W is the gate width. Then, the effective average electron velocity for a HEMT, $v_{eff,(MOD)}$ is

$$v_{eff,(MOD)} = v \cdot M = \frac{g_m(d + \Delta d)}{g} \cdot \left[l + \frac{(d + \Delta d)}{L - g} \right]. \quad (4)$$

By using the above estimates, the effective average electron velocity of the HEMTs is plotted as a function of gate length in Fig. 6. The effective average electron velocities for HEMTs having gate lengths larger than 70 nm (those which do not show overshoot), are between 0.95×10^7 cm/sec and 1.12×10^7 cm/sec, and these are approximately equal to the saturated electron velocity,

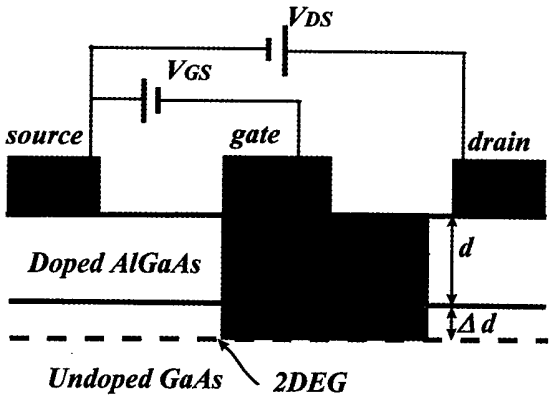

Fig. 5. Schematic representation showing the effective gate length of a HEMT.

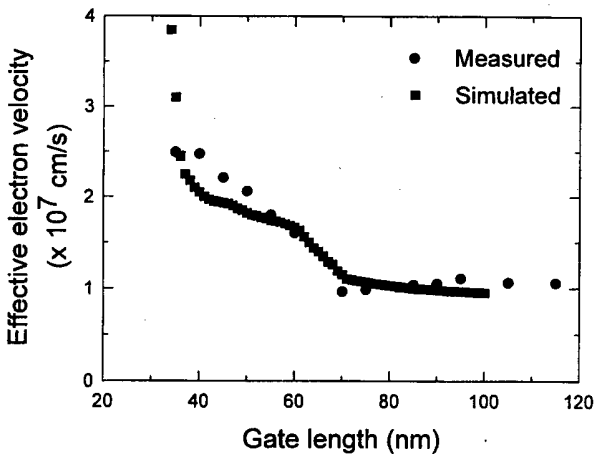

Fig. 6. Effective average electron velocity of the HEMTs as a function of gate length.

$\sim 1\times10^7$ cm/sec. This indicates that, while this might be an overly simple correction, direct fit of the effective average electron velocity by compensating the short-channel effect confirms Eq. (4) to within 10 to 15 %. As the gate length decreases below 70 nm, the effective average electron velocity increases and reaches a maximum of 2.55×10^7 cm/sec for a gate length of 40 nm. Velocity overshoot is responsible for this drastic increase in effective average electron velocity.

To investigate the velocity overshoot, a transport model based on the Retarded Langevin equation (RLE) was used. The time scales for transport under the gate here are comparable to the memory time within the RLE kernel. That is, the field seen by an individual electron changes significantly in a time comparable to the relaxation times. Thus, retardation and memory effects must be considered with respect to the ordinary Langevin equation. Start by considering an ensemble of carriers initially at equilibrium with the lattice, and characterized by a Maxwellian distribution function with $< v^2 >= 3$ kBT/m*, with T being the lattice temperature. At a certain time, $t = 0$, apply a macroscopic and homogeneous electric field whose amplitude is sufficiently large to generate a hot carrier distribution. These conditions give rise to a transient dynamic response (TDR) of the carriers, velocity overshoot and retarded relaxation, all of which arise from the retarded Langevin equation [9]. This leads to the time response of velocity equation after inverse Laplace transforming of $X(t)$

$$v(t) = v(0)\cdot X(t) + \frac{eE}{m^*}\int_0^t X(u)du + \frac{1}{m^*}\int_0^t R(t-u)\cdot X(u)du, \quad (5)$$

which is a general expression of the evolution of the velocity of each carrier, with a random force of $R(t)$. The random force is the non-regular (non-averaging) part of the interaction of the carriers with the lattice. Equation (5) is the Retarded Langevin equation, since the rate of change of the average velocity depends upon past values of the velocity. The function $X(t)$ is obtained by averaging over the ensemble (assuming that R is uncorrelated to the velocity, which in essence means noninteracting carriers). This yields

$$X(t) = \frac{1}{s+\gamma(s)} = \frac{m^*}{eE}\cdot\frac{dv_d}{dt}, \quad (6)$$

where v_d is the drift velocity and approaches the saturation velocity. Thus, $X(t)$ represents the macroscopic acceleration of the ensemble, but can also be shown to be the non-stationary function for the velocity. Equation (6) is solved in a parameterization fitting routine for the initial condition $< v(0) >= 0$. The results are plotted in Fig. 6 in comparison with the effective average electron velocity obtained analytically from the measured data. The simulated result matches the measured data reasonably well, and confirms the velocity overshoot becomes significant below the gate length of about 70 nm in our devices.

IV. CONCLUSIONS

Sub-100 nm AlGaAs/GaAs HEMTs, with gate lengths from 35 nm to 115 nm, were fabricated and have been demonstrated successfully with electron-beam lithographic techniques on MBE grown epitaxial wafers. These devices indicate that short-channel effect and velocity overshoot are occurring. As the gate length decreases from 105 nm and reaches to 70 nm, the decrease in transconductance is the result of low gate aspect ratio induced short-channel effect. Then, the overshoot can be observed once the gate length is approximately the inelastic mean free path of the carriers with further reduction in gate length. The measured transconductance and the effective electron velocity increase to a maximum of 178 mS/mm and 2.55×10^7 cm/sec for a 40 nm and a 35 nm HEMT, respectively. Simple modeling of the effective electron velocity by an analytical approximation and the average transient velocity by a Retarded Langevin equation yield qualitative agreement with the experimental results.

ACKNOWLEDGMENTS

The author would like to thank professor David K. Ferry from Arizona State University to allow to use his facilities.

REFERENCES

[1] P. C. Chao, *et al.*, IEEE Trans. Electron Devices **36**, 461 (1989).
[2] S-J. Meang, *et al.*, J. Korean Phys. Soc. **30**, S117 (1997).
[3] B-S. Park, *et al.*, J. Korean Phys. Soc. **30**, S140 (1997).
[4] J. R. Hauser, Solid-State Electron. **10**, 577 (1967).
[5] J. Han and D. K. Ferry, Japanese J. Appl. Physics **37**, 4672 (1998).
[6] J. Han and D. K. Ferry, Solid-State Electron. **43**, 335 (1998).
[7] D. R. Allee, *et al.*, J. Vacuum Science and Technol. **B6**, 328 (1988).
[8] T. J. Drummond, H. Morkoc, K. Lee and M. Shur, IEEE Electron Device Lett. **3**, 338 (1981).
[9] J. R. Baker, D. K. Ferry and H. L. Grubin, IEEE Elec. Dev. Lett. **EDL-1**, 209 (1980).

Journal of the Korean Physical Society, Vol. 34, June 1999, pp. S326~S329

20 GHz Bandwidth Electro-Absorption Modulator Integrated Distributed Feedback Laser Diode Module

Seong-Su PARK*, Seung Won LEE, Myung-Gyoo KIM and Min Kyu SONG

Compound Semiconductor Technology Department, Micro-Electronics Laboratory, Electronics and Telecommunications Research Institute, Taejon 305-350

Package design and electrical performance of electro-absorption modulator integrated distributed feedback laser diode (MIDFB-LD) modules which are based on InGaAsP/InGaAsP strained multiple quantum well (MQW) DFB laser diodes were discussed. Among the many aspects of packaging the laser diodes, we emphasize the electrical characteristics, such as frequency response and return loss of the laser diode modules considering the structure of the module. Besides the MIDFB-LD, module consists of a butterfly package with a K-connector, a thermo-electric cooler, a thermistor, and a monitor photodiode. For the electrical signal path, the components are a K-connector, a microstrip line, a MIDFB-LD, an impedance matching resistor, and 2 wire bondings. From the model and the measured data, as in the case of the laser diode module, the most important component affecting the electrical characteristics is wire bonding, considered as inductors at high frequency range. As a result, we could propose optimum wire bonding geometry and selection of bonding wires.

I. INTRODUCTION

In building information super-highway, the use of high-bit-rate optical communication systems is inevitable. As a modulated light source, laser diode (LD) module for direct modulation or a combination of laser diode and external modulator such as $LiNbO_3$ Mach-Zender modulator and electro-absorption modulator will be a core component. While directly modulated LD module has inherent chirping at the wavelength of 1550 nm to transmit using single mode fiber, externally modulated light sources could control the amount of chirping even into negative. This makes externally modulated light source very promising one for high-bit-rate optical communication system. Also, The fact that MIDFB-LDs are very small in size and are not much sensitive to temperature variation likelihood in $LiNbO_3$ Mach-Zender modulator shows that MIDFB-LD has inevitable reason for choosing as a modulated light source.

For high-bit-rate transmission, the modulation bandwidth must exceed required bit-rate. For use at the bit rate of 10 Gbps, the 3 dB small signal modulation bandwidth must reach 10 GHz. In this paper, effect of packaging parasitics, especially wire bonding, on bandwidth and return loss will be discussed.

II. MIDFB-LD STRUCTURE

*E-mail: sspark@etri.re.kr, Tel: +82-42-860-4870, Fax: +82-42-861-6183

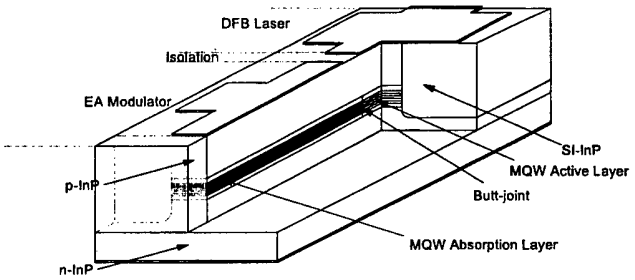

Fig. 1. Structure of modulator integrated distributed feedback laser diode.

The structure of the electro-absorption (EA) modulator integrated with a gain coupled distributed feedback (GC-DFB) laser is schematically shown in Fig. 1. This integrated device consists of an EA modulator and a GC-DFB laser. We utilized butt-coupling technology to integrate the EA modulator and the DFB laser, in a simple process requiring only two epitaxial steps. An electrical isolation region was formed between the DFB laser and the modulator to eliminate electrical crosstalk. In order to decrease excess chirping effects caused by the optical feedback reflected from modulator facet, the modulator facet was coated with an antireflection (AR) film and a window structure was introduced into the modulator facet. We fabricated the planar buried heterostructure MQW modulator with a semi-insulating (SI) InP:Fe current blocking layer in favor of the parasitic capacitance minimization of optical modulator. Also, we used polyimide to minimize pad capacitance.

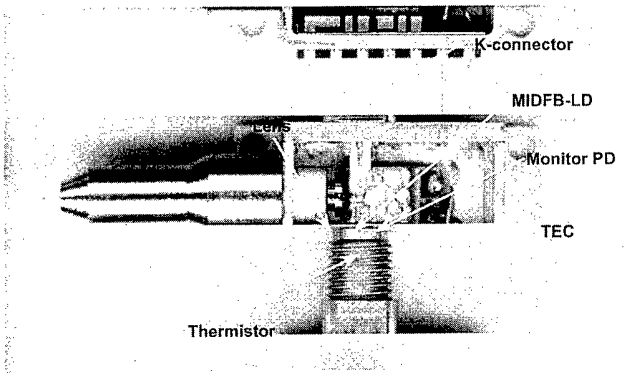

Fig. 2. Photograph of the MIDFB module.

III. MODULE DESCRIPTION AND MEASUREMENT SETUP

In high-speed optical module, high-frequency and broad-band characteristics are required. These requirements have led to adaption of many advanced electronic packaging technologies. In the interconnection of high speed device, minimization of parasitic effects is one of the key problems. The flip-chip bonding technique which reduces interconnection parasitics drastically is the alternative method which substitutes wire bonding. However, flip-chip bonding has another problems such as placement of both p, n-metal on the top side of the laser diode, difficulty of forming solder bumps, removal of residual flux, and lack of heat dissipation paths if the device chip is small and has few bumps. These difficulties retard the development of flip-chip application to high-speed laser diodes. There are few investigators reporting the application of flip-chip bonding to high-speed laser diodes [1–3]. Thus, we used conventional wire bonding as an interconnection method in this study.

The module, shown in Fig. 2, consists of a Wiltron K-connector, a 50 Ω microstrip transmission line, wire bondings, EA modulator, wire bonding to an impedance matching resistor. The K-connector is soldered to the microstrip line and the microstrip line is wire-bonded to EA modulator, and another bonding wire is placed to connect to the 50 Ω matching thin film resistor, and the n-side (bottom side) of MIDBF-LD is die-bonded on ground block. Third wire bonding is used to connect the p-side of the laser diode to the package pin through which LD bias will be appled. All the above electrical parts are mounted on a small copper alloy sub-mount. Below the sub-mount, to pump out the heat generated by the device chip, thermoelectric cooler (TEC) is bonded to the butterfly package. Meanwhile, to control the thermoelectric cooler the temperature sensor, *i.e.*, thermistor, is located near the device chip on the copper alloy sub-mount.

The measurement setup of modulation bandwidth and return loss, as shown in Fig. 3, consists of a lightwave component analyzer, a power meter, a thermoelectric

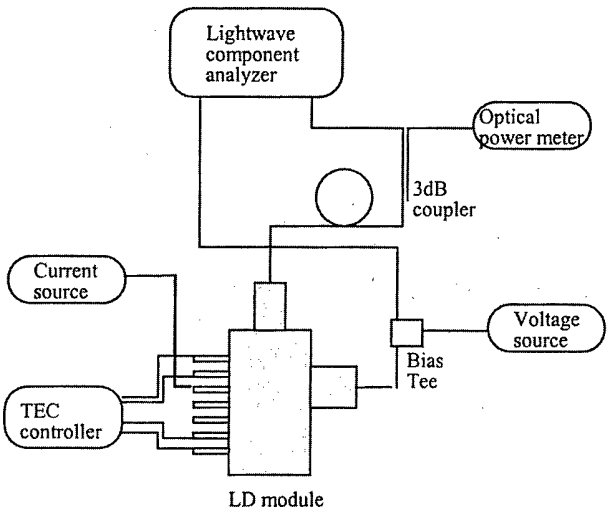

Fig. 3. Small signal modulation measurement setup.

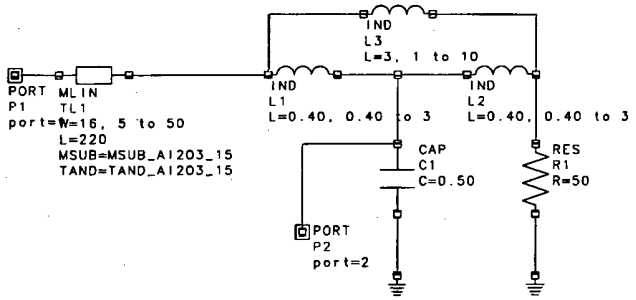

Fig. 4. Equivalent circuit model of MIDFB-LD module.

cooler controller, a current source, a voltage source, a bias Tee, and a 3 dB optical coupler. The thermoelectric cooler controller was used to maintain a constant temperature, 21 °C, of the module. The optical coupler splitted the optical power generated from the module into halves. One of them was connected to the optical power meter, and the other was connected to the lightwave component analyzer. In this case, we were able to monitor the optical power *in situ*.

IV. SMALL SIGNAL CIRCUIT MODEL AND SIMULATION RESULTS

The equivalent circuit model of the packaged module is shown in Fig. 4. There are a connector, TL_1, a transmission line having characteristic impedance of 50 Ω, L_1, a bonding wire to EA modulator, C_1, EA modulator, L_2, a bonding wire to matching resistor, R_1, and L_3, a bonding wire between TL_1 and R_1. By optimizing the bonding wire values, optimized L_1, L_2, L_3, values are $L_1 < 0.4$ nH, $0.4 < L_2 < 2$ nH, L_2 =open. The simulated results of $L_1 = 0.4$ nH, $L_2 = 0.4$ nH, and L_3 =open, are shown in Fig. 5. The measured results with L_3, being wire bonded with 5 mil width ribbon wire of 2 times, and L_3

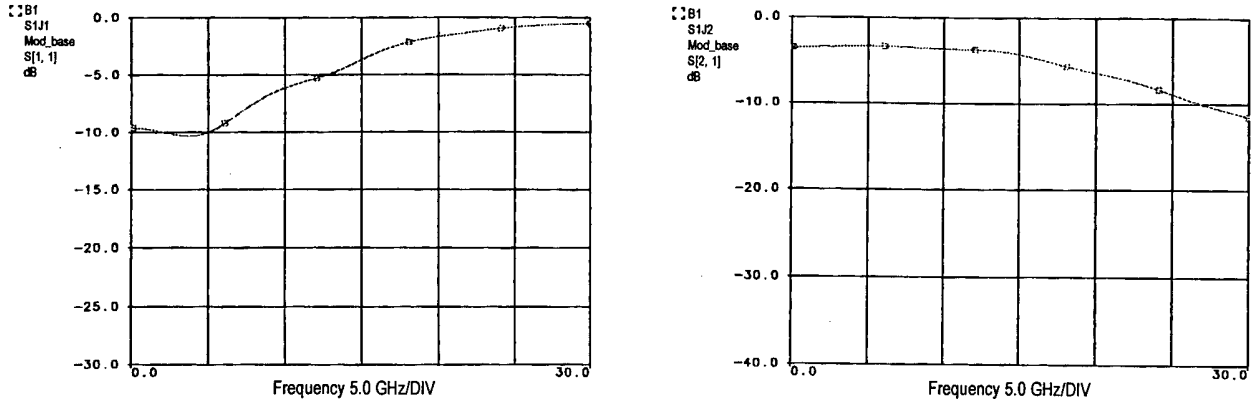

(a) (b)

Fig. 5. Small signal simulation results of return loss (a), and frequency response (b).

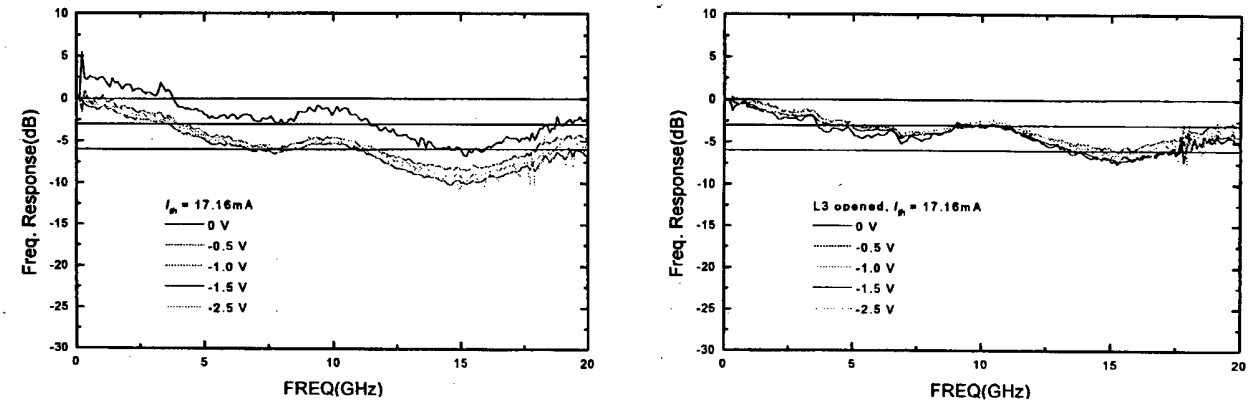

(a) (b)

Fig. 6. Measured frequency response of L_3 wire bonded (a), and L_3 opened (b) for the same chip.

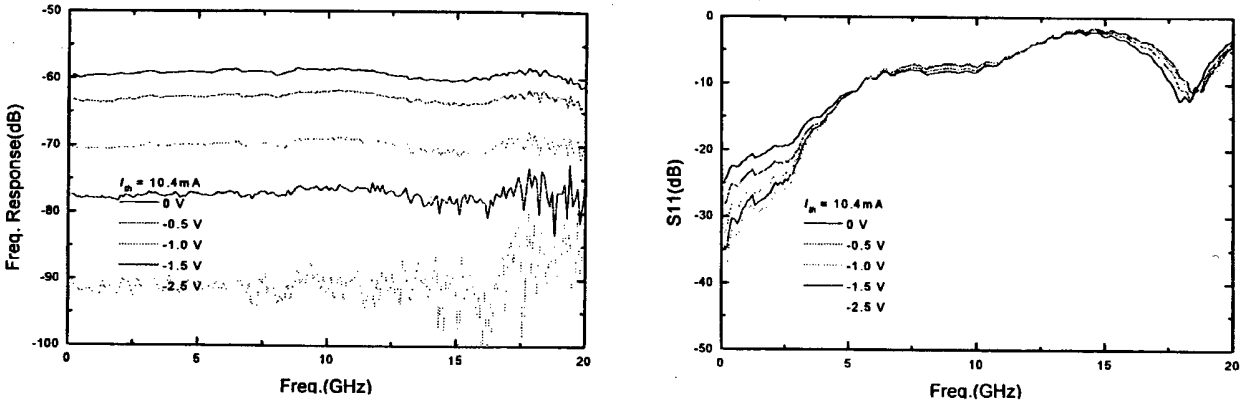

(a) (b)

Fig. 7. Measured frequency response (a) and return loss (b).

opened after removing the bondig wires are shown in Fig. 6 for the same chip.

From the wire bonding condition above mentioned, 5 mil width wire bonded L_1, normal 1 mil diameter wire bonded L_2, and opened L_3, we could obtain 20 GHz bandwidth and -8 dB return loss at 10 GHz. L_1 shows similar behavior for the case of laser diode module wire bonding fully explained in the former work [4].

V. CONCLUSIONS

Method of making a fully packaged 1.55 μm MIDFB laser diode module showing bandwidth of 20 GHz was proposed. The bandwidth of electro-aborption modulator was sensitively affected by wire bonding condition for 3 wire bonding sites. To reach to maximum frequency response, the first wire bonding inductance, wire bond-

ing between transmission line and the modulator's upper p-side, should be as small as it can be realized, and the second wire bonding, between the modulator's upper side p-side and 50 Ω matching resistor, would have rather variational margin up to 2 nH, and the third wire bonding, wire bonding between transmission line and 50 Ω matching resistor, is not necessary. From the previous work [4], the geometry of the minimum inductance of the first wire bonding will be as wide as could be realized and be as short as could be done. From the electromagnetic calculation of various size and length of bonding wire, the suitable and realistic dimension of the first wire bonding would be 5 mil (1 mil = 1/1000 inch) width and below 20 mil length, which inductance calculated was 0.4 nH.

REFERENCES

[1] K. D. Pedrotti, C. W. Seabury, N. H. Sheng, C. P. Lee, R. Agarwal, A. D. M. Chen and D. Renner, Proc. OFC'92, 241 (1992).

[2] D. G. Kim, H. Han, S. -S. Park, G. C. Joo, M. K. Song, N. Hwang, S. G. Kang, H. T. Lee and H. M. Park, 45th Electronics Components & Technology Conference, Las Vegas, 872 (1995).

[3] S. Lindgren, H. Ahlfeldt, L. Baecklin, L. Forssen, C. Vieider, H. Elderstig, M. Svensson, l. Granlund, B. Kerzar and B. Broberg, 22nd European Conference on Optical Commun., 1.103 (1996).

[4] S.-S. Park, M. K. Song, N. Hwang, S. G. Kang, H. T. Lee and H. R. Choo, J. Korean Phys. Soc. **30**, S163 (1997).

Journal of the Korean Physical Society, Vol. 34, June 1999, pp. S330~S333

Low Voltage Coefficient Double Polysilicon Capacitors Using Thin Dielectrics for Analog Circuit Applications

Jae Sung LEE*

Department of Computer & Communication Engineering, Uiduk University, Kyongju 780-713

Hoon Soo PARK

Department of Semiconductor Engineering, Uiduk University, Kyongju 780-713

In this paper, a self-aligned double-polysilicon capacitor was developed to obtain extremely low voltage coefficient of capacitance (VCC). Depending on the dielectric preparation methods, the electrical properties including VCC, breakdown field, leakage current, bias polarity and time-to-breakdown were investigated. Among the electrical parameters, especially VCC and leakage current were highly sensitive to the process conditions. From the results, tetraethyl orthosilicate (TEOS) dielectric films which were deposited at 670 °C exhibited excellent properties such as VCC, field strength, and time-to-breakdown compared to other films.

I. INTRODUCTION

In recent years, the double-polysilicon capacitors have been widely used for an analog-digital CMOS (Complementary Metal-Oxide-Semiconductor Field-Effect Transistor) technology. The advantages of double-polysilicon capacitors are the low parasitic capacitance and excellent dielectric isolation properties of both capacitor plates from the substrate [1]. The metal-oxide-semiconductor (MOS) capacitor circuits generally perform an analog/digital (A/D) conversion, analog attenuation, and filtering. The performance and cost effectiveness of MOS capacitors depend on the accuracy of the capacitor matching and layout effect [2]. In accordance with a rapid scaling down the mixed analog/digital large-scaled integrations (LSI's), the area of analog capacitor must be scaled with transistor fabrication technology [3]. Therefore, the scaling down of insulator thickness is indispensable for reducing the capacitor area. However, it increases the voltage coefficient of capacitance (VCC), which inversely proportional to the square of the insulator thickness. The high VCC of capacitor directly deteriorates the accuracy of analog circuits [4]. For the precise and reliable operation of analog circuits, the VCC of capacitor should be kept as a low value over the wide range of applied voltages. Moreover, thermal budget due to the additional process for the analog modules should be minimized to keep the device characteristics of the core logic cell unchanged [1]. Thus, special manufacturing techniques are required to build polysilicon capacitor, which exhibits specifically desired electrical behavior.

*E-mail: jaesung@viro.uiduk.ac.kr, Tel: +82-561-760-1643

In this paper, we fabricated a double-polysilicon capacitor with an extremely low VCC manufactured using 0.35 μm mixed analog/digital CMOS technology. The dielectrics of capacitors were prepared at low temperature less than 800 °C in order to suppress the parametric shifts of CMOS transistors. In addition to the VCC characteristics, the dielectric properties including breakdown field, leakage current, bias polarity and time-to-breakdown depending on the various dielectric preparation methods were investigated in detail.

II. EXPERIMENTAL PROCEDURE

The layout pattern and schematic cross-section of double polysilicon capacitor in this study were shown in Fig. 1(a) and (b), respectively. To fabricate the double-polysilicon capacitors, a 350 nm thick field oxide was grown on the n-well region. After gate oxidation of MOS transistors of digital parts of wafer, a 250 nm thick bottom polysilicon electrode was deposited by the low-pressure chemical vapor deposition (LPCVD) at the temperature of 560 °C and doped by the phosphorous ion implantation. The bottom electrode of capacitor also serves as the gate electrodes of MOS transistors. Subsequently, thin dielectrics were prepared by different methods : one is thermal oxide grown either by wet or dry oxidation at 800 °C, and another is TEOS film deposited at 710 °C (TEOS1) or 670 °C (TEOS2). For the case of TEOS films, annealing was performed at the temperature of 800 °C for 20 min under the nitrogen ambient. The resultant oxide thickness of TEOS and polysilicon dry oxide films are same as 20 nm, while that of polysilicon wet oxide film

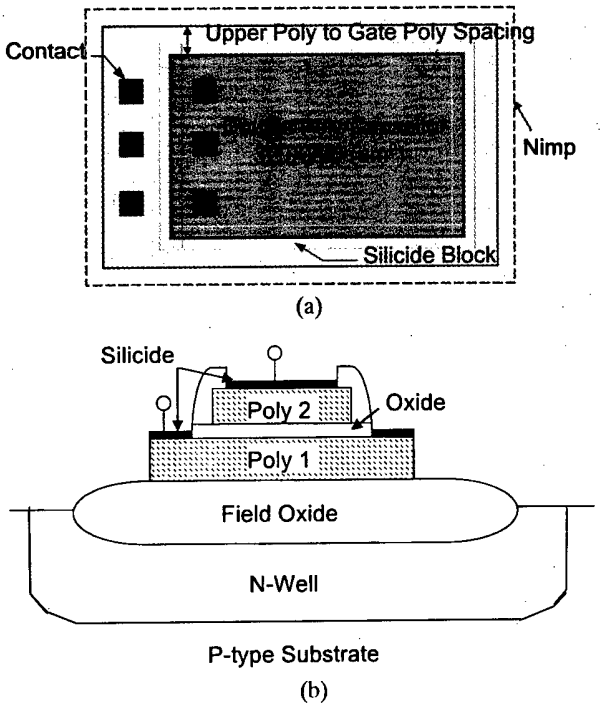

Fig. 1. The feature of double-polysilicon analog capacitor; (a) top view, (b) cross-sectional view.

is about 18 nm. Then, the top polysilicon electrode was deposited and doped by the phosphorous impurity. The sheet resistance of polysilicon electrodes is approximately 38~40 ohm/sq. Then, the capacitor electrodes were formed by titanium sputtering and silicidation. After interconnection process, final annealing was performed at 400 °C in nitrogen ambient for 30 min. The capacitor area is 320×220 μm^2, as shown in Fig. 1(a).

III. RESULTS AND DISCUSSION

Fig. 2 demonstrates the normalized capacitance characteristics of each dielectric depending on the applied voltages. The capacitance of capacitor fabricated by a conventional process usually decreased monotonically with applied voltage [1]. On the contrary, in this work, the capacitance variation depending on the applied voltage is very small and shows a peak at zero applied voltage. However, the capacitance variations in the negative applied voltage were somewhat larger than the positive voltage due to the impurity depletion of bottom electrode.

Considering the series combination of oxide and space-charge capacitance of both polysilicon electrodes, the linear VCC is calculated by the following equation [2].

$$VCC(V_{fb}) = Cox^2/(3q\epsilon_{si}N_d). \quad (1)$$

where, Cox, q, ϵ_{si}, and N_d is the oxide capacitance, electronic charge, relative dielectric constant of silicon, and doping concentration of polysilicon electrodes, respectively. From the above equation, VCC property can be improved by increasing the doping concentration and oxide thickness.

In Fig. 3, the measured VCC of each dielectric was shown. The quadratic VCC represents the curvature. It is obvious that the voltage coefficients of capacitors highly depend on the dielectric growing methods and temperature. For the case of thermal oxides, wet oxide showed superior linear VCC property (about 140 ppm/V) to wet oxide (less than 50 ppm/V). This result may be considered that the amount of impurity depletion or redistribution in the bottom polysilicon electrode was much large for the dry oxide due to the comparatively longer oxidation time (1 hr and 20 min.) than that of wet oxide (30 min.). However, investigating the linear and quadratic VCC properties of TEOS dielectrics, the low temperature deposited TEOS (TEOS2) shows much improved VCC characteristics. In particular, the linear VCC of capacitor with TEOS2 dielectric is extremely low value of 12 ppm/V. Despite of a thin dielectric thickness (~20 nm),

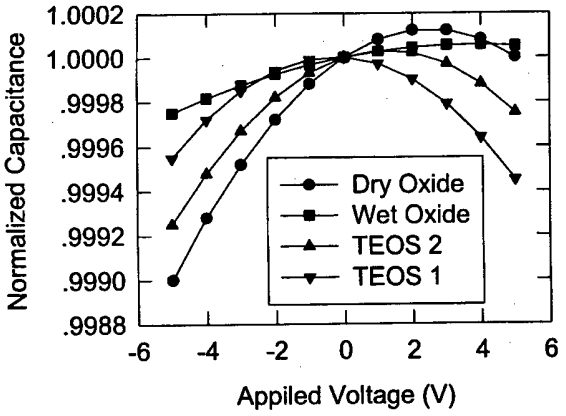

Fig. 2. Variation of capacitance as a function of applied voltage for various dielectrics. TEOS1 and TEOS2 represent the TEOS films prepared at 710 °C and 670 °C, respectively.

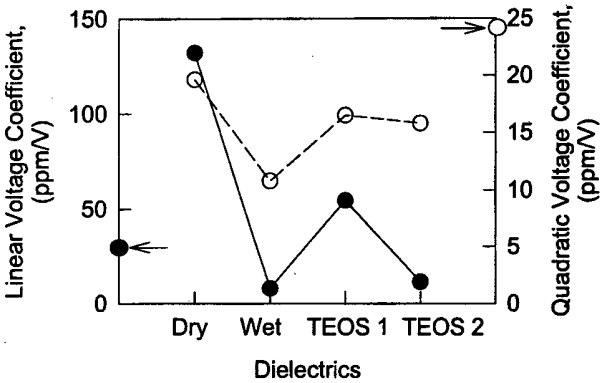

Fig. 3. Linear and quadratic voltage coefficient for various dielectrics. The data for capacitors without salicide contacts are also shown as arrows. Solid and open circles represent linear and quadratic VCC's, respectively.

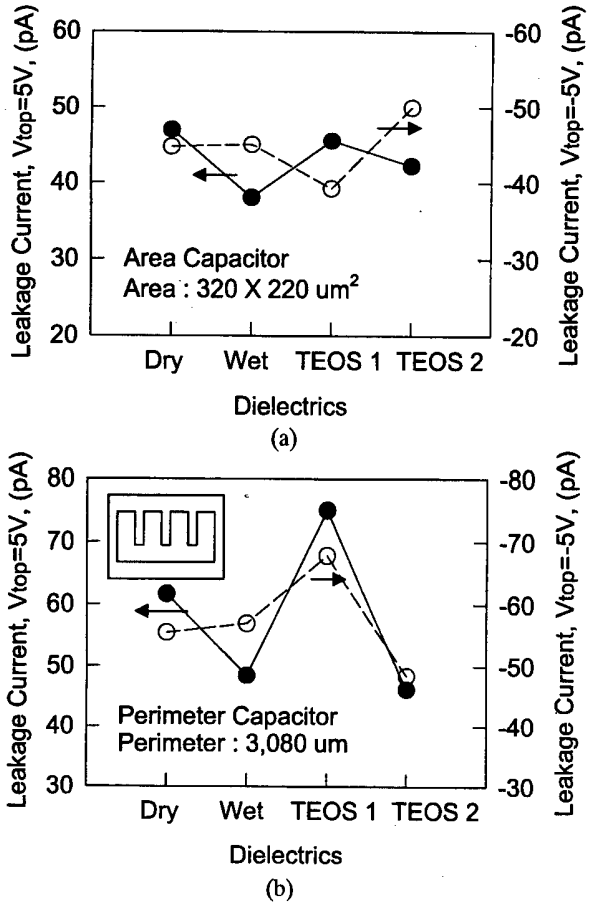

Fig. 4. Leakage current for various dielectrics measured at ±5 V with (a) area capacitor and (b) perimeter capacitor. The insert in Fig. 4(b) represents the top view of perimeter capacitor.

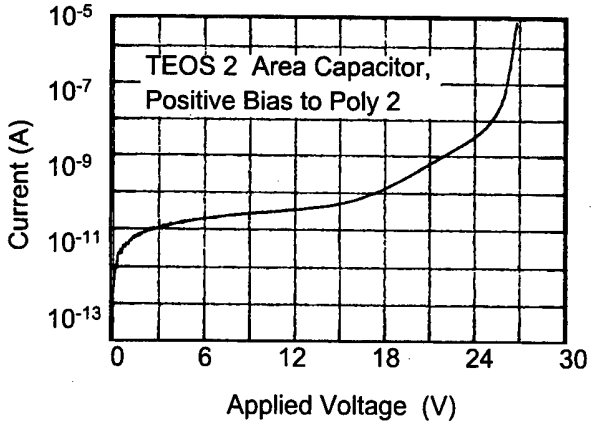

Fig. 5. Typical Fowler-Nordheim tunneling current curve of a 200 Å TEOS2 capacitor oxide. Positive voltage was applied at top polysilicon electrode.

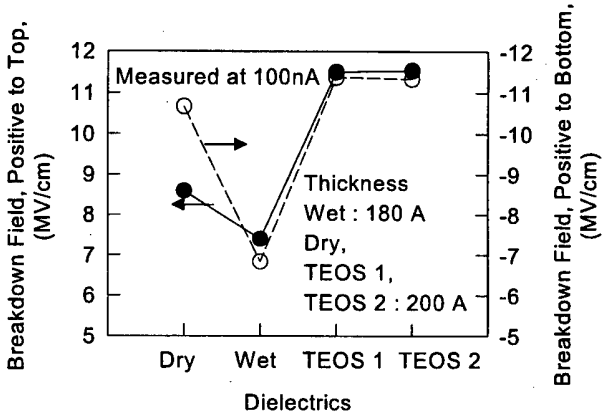

Fig. 6. Variation of breakdown voltage measured at ±100 nA for various dielectrics.

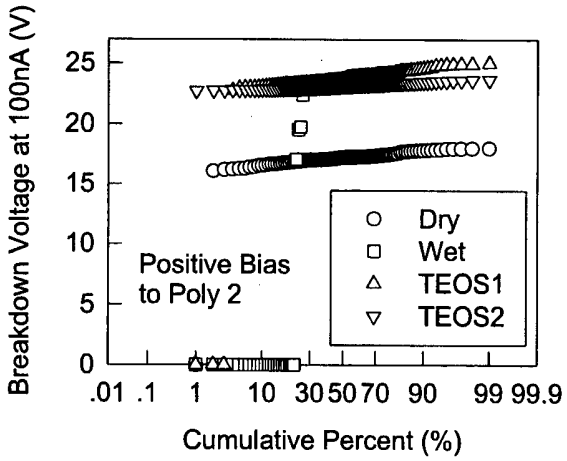

Fig. 7. Time-dependent dielectric breakdown (TDDB) voltage distributions for each film measured at 100 nA. Positive voltage was applied at top polysilicon electrode.

VCC characteristics of this work were greatly improved results compared to the previous studies [2,4,5], due to the minimization of phosphorous depletion or redistribution during TEOS deposition. To compare the salicide effects, non-salicided capacitors were also fabricated. As shown in Fig. 3, the quadratic VCC of salicided capacitor was improved.

Figure 4(a) and 4(b) show the leakage current measurements for the area and the perimeter capacitors, respectively. The insert in Fig. 4(b) represents the top view of perimeter capacitor. Leakage current was defined as a measured current at the applied voltage of ±5 V. From the leakage current measurements in 320×220 μm^2 area capacitor, capacitor with dry oxide revealed fairly large leakage current. During the high temperature oxidation, the surface roughness of bottom polysilicon was increased, which also enhanced the local electric field and then increased leakage current. The dielectric films that were grown by wet oxidation or deposited by 670 °C CVD (TEOS2) show lower leakage currents than the other films. In contrast, the capacitor with a wet oxide exhibited a little large bias polarity. This asymmetrical bias polarity is also the consequence of unequal charge injection between the two electrodes.

Figure 5 shows a typical Fowler-Nordheim current-voltage (I-V) curve through the 20 nm TEOS 2 capacitor oxide. Positive voltage was applied at top polysilicon electrode. The typical distribution of breakdown voltages is between 24 and 30 V.

Figure 6 shows that the breakdown field property of each film measured at ±100 nA, respectively. The wet oxide had an excellent leakage current property but showed a poor breakdown field property.

Figure 7 shows time-dependent dielectric breakdown (TDDB) voltage distributions for each film measured at the current of 100 nA. Both TEOS oxides have shown better reliability than the thermal oxides. For the wet oxide, initial failure rate is high, that is closely related with lower breakdown field in Fig. 6.

IV. CONCLUSIONS

We investigated the electrical properties of polysilicon capacitors depending on the dielectric materials and process conditions and fabricated double polysilicon capacitors featuring the excellent VCC properties compared to the previous works. From the results, TEOS film deposited at the temperature of 670 °C, exhibited excellent properties such as VCC, field strength, and time-to-breakdown compared to the thermal oxides. Despite of a very thin dielectric thickness (~20 nm) of TEOS film, the improvement of the VCC characteristics was due to the minimization of phosphorous depletion or redistribution during the film deposition. Such a low process temperature may also improve the breakdown field charateristic of capacitor and also minimize the variations of electrical parameters of CMOS transistors. Therefore, the optimized process of an analog capacitor proposed in this paper can be applied for precise deep submicron mixed analog/digital circuit design.

REFERENCES

[1] E. Laes, H. J. Casier, E. Schutz and M. Alcatel, "Analog-Digital Technologies for Mixed-Signal Processing", IEEE Micro, p. 34 (1992).

[2] R. Singh and A. B. Bhattacharyya, Solid-State Electronics **32**, 299 (1989).

[3] M. Miyamoto, T. Ishii, R. Nagai, T. Nishida and K. Seki, "0.3 um Mixed Analog/Digital CMOS Technology for Low-Voltage Operation", Proceeding of Custom Integrated Circuits Conference, p. 24.4.1 (1993).

[4] D. B. Slater. JR and J. J. Paulous, IEEE J. of Solid-State Circuits **24**, 165 (1989).

[5] C. B. Oh, G. J. Jung, J. H. Kim, Y. S. Kim, Y. W. Kim and H. K. Park, "The Study of Voltage Characteristics of CMOS Analog Capacitor", Proceeding of ICVC, p. 604 (1997).

Journal of the Korean Physical Society, Vol. 34, June 1999, pp. S334~S338

Longitudinal Spin-Charge Responses and Collective Modes in Spin-Polarized Quantum Devices

K. S. YI*, S. P. HONG and Y. N. BAE

Department of Physics, Pusan National University, Pusan 609-735

J. J. QUINN

Department of Physics and Astronomy, University of Tennessee, Knoxville, Tennessee 37996 and Oak Ridge National Laboratory, Oak Ridge, Tennessee 37831, U.S.A.

The generalized longitudinal charge-spin susceptibility functions and the collective excitations of spin-polarized quantum structures are investigated within the framework of spin-dependent linear response theory. We evaluate the charge response and the longitudinal spin response to a general external disturbance. Exchange-correlation effects between electrons of spin σ and σ' are included by using spin-polarization dependent generalized local field factors. Both the collective charge-density and spin-density excitations are examined. The present results are compared with the case of a spin-unpolarized system. In contrast to the result for an unpolarized system, the mixing of charge and spin responses results in coupled charge-spin excitations in the spin polarized system.

I. INTRODUCTION

A spin-polarized quantum structure can be fabricated in a semiconductor quantum well (QW) by applying an *effective* dc magnetic field B perpendicular to the QW [1,2]. The spin-polarized quantum well (SPQW) of n-electrons per unit area consists of n_σ electrons of majority spin σ and $n_{\bar{\sigma}}$ electrons of minority spin $\bar{\sigma}$ embedded in a uniform positive charge background. The spin polarization ζ is defined by $\zeta = (n_\sigma - n_{\bar{\sigma}})/(n_\sigma + n_{\bar{\sigma}})$. Previous investigations of the linear response and collective excitations of a SPEG were either limited to the case of infinitesimal spin polarization, or they used the Hartree-Fock approximation (HFA) or the local spin-density approximation (LSDA) [3–5]. In this work we include the spin correlations effects by introducing spin-dependent local field factors $G_\sigma{}^{\pm}$. In this paper we present the linear response of a SPQW to an electromagnetic perturbation with arbitrary space and time dependence. The dispersion relations of charge-density wave (CDW) and spin-density wave (SDW) excitations are derived and compared with the existing theories of spin-unpolarized or infinitesimally spin-polarized QW.

II. FORMULATION

The SPQW is described in terms of two different spin subband ladders with eigenvalues $\varepsilon_{n\sigma}(\boldsymbol{k})$ and eigenfunctions $|n\sigma\boldsymbol{k}>$. Here n is the subband level index, σ the spin index, and $\boldsymbol{k}$ the wavevector parallel to the layer. These spin subbands are eigenstates of an unperturbed Hamiltonian H_0. The exchange-correlation interactions between electrons of the same spin (ss) or of opposite spins ($s\bar{s}$) are included by employing spin-dependent local-field factors $G_s{}^{\pm}$ and $G_{\bar{s}}{}^{\pm}$ [6,7]. We assume the SPQW is disturbed by an infinitesimal external electric potential $v_0(\boldsymbol{r},t)$ and magnetic field $\boldsymbol{b}_0(\boldsymbol{r},t)$. In response to these external disturbances, charge and spin fluctuations are set up in the system, and the Hamiltonian for an electron with spin $\boldsymbol{s}$ can be approximated as $H = H_0 + H_1{}^{\boldsymbol{s}}$. Here H_0 is the Hamiltonian of a single quasiparticle of the SPQW in the absence of the external disturbance, and $H_1{}^{\boldsymbol{s}}$ is the *spin-dependent self-consistent* effective perturbation. In this work we assume the spin-splitting is much greater than the Landau level splitting and ignore any degree of orbital quantization. The effective magnetic field B is taken to be in the z direction. Since the most general disturbance can be decomposed into its Fourier components, we choose the disturbances [$v_0, \boldsymbol{b}_0$ and $H_1{}^{\boldsymbol{s}}$] to vary as $[v_0(q,\omega,z), \boldsymbol{b}_0(q,\omega,z)$, and $H_1{}^{\boldsymbol{s}}(q,\omega,z)]e^{i\omega t - i\boldsymbol{q}\cdot\boldsymbol{r}}$ where $\boldsymbol{q}$ and $\boldsymbol{r}$ are the 2D vectors corresponding to the wavevector of the disturbance and the position parallel to the QW. The self-consistent magnetic disturbance $\boldsymbol{b}$ is the sum of $\boldsymbol{b}_0$ and $4\pi\boldsymbol{m}$, where $\boldsymbol{m}$ is the induced spin magnetization. The Fourier component of the most general $H_1{}^{\boldsymbol{s}}(\boldsymbol{r},t)$ can be written as [2,7,8]

*E-mail: ksyi@hyowon.pusan.ac.kr, Fax: +82-51-513-7664

$$H_1{}^s(q,\omega,z) = \gamma_0 \boldsymbol{s}\cdot\boldsymbol{b}(q,\omega,z) + v_0(q,\omega,z) + v_q\int_{-\infty}^{\infty} dz' e^{-q|z-z'|}[\delta n(q,\omega,z')\,(1-G_s^+(q,\omega)) - \delta\boldsymbol{m}(q,\omega,z')\cdot\boldsymbol{s}\,G_s^-(q,\omega)]. \quad (1)$$

Here γ_0 is the effective Bohr magneton defined by $\gamma_0 = \frac{1}{2}g^*\mu_B$ with g^*, μ_B, $\boldsymbol{s}$, and v_q being the effective g-factor, the Bohr magneton, Pauli spin operator, and the 2D Fourier transform of the bare Coulombic potential, respectively. Equation (1) is the generalization of the effective interaction Hamiltonian of an electron with spin s in the SPQW in the presence of infinitesimal magnetic and electric disturbances. The local fields $G_s{}^+$ and $G_s{}^-$ are responsible for charge- and spin-induced correlation effects on an electron of spin s [2,7]. For the sake of brevity, the explicit $\boldsymbol{q}$ and ω dependence of the local fields, fluctuations, and disturbances is frequently not displayed in the remainder of this paper.

In response to the external disturbance, a charge-density and spin-density fluctuation will be induced in the system. We evaluate, using the self-consistent field prescription within a standard density-matrix technique [9], the charge-density fluctuation δn and longitudinal spin-density fluctuation δm_z

$$\delta n(q,\omega,z') = \sum_{nn'}\begin{pmatrix} \Pi_{n'\sigma n\sigma}(q,\omega) < n\sigma|H_1{}^s(q,\omega,z)|n'\sigma > \xi_{n'\sigma}(z')\xi_{n\sigma}(z') \\ +\Pi_{n'\bar\sigma n\bar\sigma}(q,\omega) < n\bar\sigma|H_1{}^s(q,\omega,z)|n'\bar\sigma > \xi_{n'\bar\sigma}(z')\xi_{n\bar\sigma}(z') \end{pmatrix}, \quad (2)$$

$$\delta m_z(q,\omega,z') = \sum_{nn'}\begin{pmatrix} \Pi_{n'\sigma n\sigma}(q,\omega,z) < n\sigma|H_1{}^s(q,\omega,z)|n'\sigma > \xi_{n'\sigma}(z')\xi_{n\sigma}(z') \\ -\Pi_{n'\bar\sigma n\bar\sigma}(q,\omega) < n\bar\sigma|H_1{}^s(q,\omega,z)|n\bar\sigma > \xi_{n'\bar\sigma}(z')\xi_{n\bar\sigma}(z') \end{pmatrix}. \quad (3)$$

We note that these fluctuations are related to the self-consistent disturbance $H_1{}^s$ and that δm_z vanishes in the case of spin-unpolarized electron gas. In Eqs. (2) - (3), $\Pi_{n's_1ns_2}$ is the 2D Lindhard-type electric ($s_1 = s_2$) or spin ($s_1 \neq s_2$) susceptibility.

$$\Pi_{n's'ns}(q,\omega) = \sum_{\boldsymbol{k}} \frac{f_0(\varepsilon_{n's'}(\boldsymbol{k}+\boldsymbol{q})) - f_0(\varepsilon_{ns}(\boldsymbol{k}))}{\varepsilon_{n's'}(\boldsymbol{k}+\boldsymbol{q}) - \varepsilon_{ns}(\boldsymbol{k}) - \hbar\omega + i\eta}, \quad (4)$$

where $f_0(\varepsilon_{ns}(\boldsymbol{k}))$ denotes the equilibrium distribution of quasiparticles in the (n,s) subband. We take the matrix element of the effective perturbation, Eq. (1), with respect to the unperturbed eigenstates $|nks> = e^{i\boldsymbol{k}\cdot\boldsymbol{r}}|ns>$ where $|ns> = \xi_n(z)\chi_s$ is the product of an envelope function $\xi_n(z)$ and a spin eigenfunction χ_s. Then taking a 2D Fourier transform of the resulting expressions in the plane parallel to the QW and combining the results with Eqs. (2) - (3) yields the coupled equations for $< nks|H_1{}^s(\boldsymbol{q},\omega,z)|n'\boldsymbol{k}'s' >$ in terms of the external charge and spin disturbances. We solve the coupled equations for $< ns_1|H_1{}^s|n's_2 >$ and substitute the corresponding matrix elements back into the expressions of the fluctuations given by Eqs. (2) - (3). The fluctuations in charge and spin density δn, δm_z can then be expressed, formally, in terms of a generalized susceptibility matrix $\underline{\chi}$ as [2,7]

$$\begin{pmatrix} -e\delta n \\ \gamma_0\delta m_z \end{pmatrix} = \begin{pmatrix} \chi^{ee} & \chi^{em} \\ \chi^{me} & \chi_\parallel{}^{mm} \end{pmatrix}\begin{pmatrix} \varphi_0 \\ b_{0z} \end{pmatrix}. \quad (5)$$

Here φ_0 denotes the external electric potential corresponding to the external disturbance $v_0(= -e\varphi_0)$. The superscripts e and m on $\underline{\chi}$ designate charge and spin response (or electric and magnetic disturbance), respectively. Because the condition for the collective modes of the system is that self-sustaining oscillations in the charge and spin densities occur when φ_0 and b_0 vanish, these modes are related to the divergence of the susceptibility matrix in Eq. (5). We now substitute the fluctuations given by Eqs. (2) - (3) into the right hand side of $H_1{}^s(q,\omega,z)$ and then take the matrix element $< n\sigma|H_1{}^s(q,\omega,z)|m\sigma' >$ to obtain the coupled equations for $< n\sigma|H_1{}^{ext}|m\sigma >$ and $< n\bar\sigma|H_1{}^{ext}|m\bar\sigma >$. It is extremely difficult to obtain exact dispersion relations in the general case. We consider a simple case by taking the electric quantum limit, in which all of the occupied states are confined to the lowest subband of each spin. In the electric quantum limit, the coupled equations reduce to

$$< n\sigma|H_1{}^{ext}|1\sigma > = \sum_{n'} < n'\sigma|H_1{}^s|1\sigma > \{\,\delta_{nn'} - \chi_{n'\sigma 1\sigma}(q,\omega)\,[\,v_q F^{n'\sigma 1\sigma}_{n\sigma 1\sigma}(q)(1-G_\sigma^+-G_\sigma^-) + 4\pi\gamma_0^2\Phi^{n'\sigma 1\sigma}_{n\sigma 1\sigma}\,]\,\} - \sum_{n'} < n'\bar\sigma|H_1{}^s|1\bar\sigma >\ \chi_{n'\bar\sigma 1\bar\sigma}(q,\omega)\,[\,v_q F^{n'\bar\sigma 1\bar\sigma}_{n\sigma 1\sigma}(q)(1-G_\sigma^++G_\sigma^-) - 4\pi\gamma_0^2\Phi^{n'\bar\sigma 1\bar\sigma}_{n\sigma 1\sigma}\,], \quad (6)$$

$$< n\bar\sigma|H_1{}^{ext}|1\bar\sigma > = \sum_{n'} < n'\bar\sigma|H_1{}^s|1\bar\sigma > \{\,\delta_{nn'} - \chi_{n'\bar\sigma 1\bar\sigma}(q,\omega)\,[\,v_q F^{n'\bar\sigma 1\bar\sigma}_{n\bar\sigma 1\bar\sigma}(q)(1-G_{\bar\sigma}^+-G_{\bar\sigma}^-) + 4\pi\gamma_0^2\Phi^{n'\bar\sigma 1\bar\sigma}_{n\bar\sigma 1\bar\sigma}\,]\,\} - \sum_{n'} < n'\sigma|H_1{}^s|1\sigma >\ \chi_{n'\sigma 1\sigma}(q,\omega)\,[\,v_q F^{n'\sigma 1\sigma}_{n\bar\sigma 1\bar\sigma}(q)(1-G_{\bar\sigma}^++G_{\bar\sigma}^-) - 4\pi\gamma_0^2\Phi^{n'\sigma 1\sigma}_{n\bar\sigma 1\bar\sigma}\,], \quad (7)$$

where $\chi_{n\sigma 1\sigma} = \Pi_{n\sigma 1\sigma} + \Pi_{1\sigma n\sigma}$. Here H_1^{ext} denotes $H_1^{ext} = \gamma_0 b_0^z + v_0^{ext}$. Longitudinal collective modes are given by solving the coupled equations for the matrix elements $< n\sigma|{H_1}^{ext}|1\sigma >$ and $< n\bar{\sigma}|{H_1}^{ext}|1\bar{\sigma} >$ given by Eqs. (6) and (7). The structure factor $F^{n'\sigma_1' m'\sigma_2'}_{n\sigma_1 m\sigma_2}(q)$ and the overlap integral $\Phi^{n'\sigma_1' m'\sigma_2'}_{n\sigma_1 m\sigma_2}$ are defined, respectively, as

$$F^{n'\sigma_1' m'\sigma_2'}_{n\sigma_1 m\sigma_2}(q) = \int_{-\infty}^{\infty} dz \int_{-\infty}^{\infty} dz' \xi_{n\sigma_1}(z)\xi_{m\sigma_2}(z)e^{-q|z-z'|} \times \xi_{n'\sigma_1'}(z')\xi_{m'\sigma_2'}(z')$$

$$\Phi^{n'\sigma_1' m'\sigma_2'}_{n\sigma_1 m\sigma_2} = \int_{-\infty}^{\infty} dz\, \xi_{n\sigma_1}(z)\xi_{m\sigma_2}(z)\xi_{n'\sigma_1'}(z)\xi_{m'\sigma_2'}(z)$$

Equations (6) and (7) are still too involved to be solved as they stand. Hence, we make a further simplification by assuming that only $n = n'$ terms contribute in the sum. This means that we neglect mixing between different intersubband excitations for a given spin orientation. With this assumption we obtain a simple relation between matrix elements of the external perturbation H_1^{ext} and matrix elements of the self-consistent perturbation H_1^s:

$$\begin{pmatrix} < n\sigma|{H_1}^{ext}|1\sigma > \\ < n\bar{\sigma}|{H_1}^{ext}|1\bar{\sigma} > \end{pmatrix} = \underline{D}_L(q,\omega) \begin{pmatrix} < n\sigma|{H_1}^{s}|1\sigma > \\ < n\bar{\sigma}|{H_1}^{s}|1\bar{\sigma} > \end{pmatrix}. \quad (8)$$

Here the matrix $\underline{D}_L(q,\omega)$ is defined by

$$\underline{D}_L(q,\omega) = \begin{pmatrix} 1-\chi_{n\sigma 1\sigma}A^{n\sigma}_{n\sigma} & -\chi_{n\bar{\sigma}1\bar{\sigma}}B^{n\bar{\sigma}}_{n\sigma} \\ -\chi_{n\sigma 1\sigma}B^{n\sigma}_{n\bar{\sigma}} & 1-\chi_{n\bar{\sigma}1\bar{\sigma}}A^{n\bar{\sigma}}_{n\bar{\sigma}} \end{pmatrix}, \quad (9)$$

and $A^{m\sigma}_{n\sigma}$ and $B^{m\sigma'}_{n\sigma}$ are given by $A^{m\sigma}_{n\sigma} = v_q F^{m\sigma 1\sigma}_{n\sigma 1\sigma}(q)(1 - G^+_\sigma - G^-_\sigma) + 4\pi\gamma_0^2 \Phi^{m\sigma 1\sigma}_{n\sigma 1\sigma}$ and $B^{m\sigma'}_{n\sigma} = v_q F^{m\sigma' 1\sigma'}_{n\sigma 1\sigma}(q)(1 - G^+_\sigma + G^-_\sigma) - 4\pi\gamma_0^2 \Phi^{m\sigma' 1\sigma'}_{n\sigma 1\sigma}$.

The condition of the longitudinal charge density and spin density modes is given by the zeros of the determinant of $\underline{D}_L(q,\omega)$, [10] that isœ

$$(1-\chi_{n\sigma 1\sigma}A^{n\sigma}_{n\sigma})(1-\chi_{n\bar{\sigma}1\bar{\sigma}}A^{n\bar{\sigma}}_{n\bar{\sigma}}) - \chi_{n\sigma 1\sigma}\chi_{n\bar{\sigma}1\bar{\sigma}}B^{n\sigma}_{n\bar{\sigma}}B^{n\bar{\sigma}}_{n\sigma} = 0. \quad (10)$$

In this equation the last term indicates the *coupling* between the intersubband excitations belonging to two different spin orientations.

III. RESULTS AND DISCUSSION

For a purely 2D system, the electron-density profile in the z direction is a δ function, and only the $n = 1$ element contributes. In this case $\chi_{1\sigma 1\sigma}$ equals $\Pi_{1\sigma 1\sigma} = \Pi_{\sigma\sigma}$, and we have $F^{m\sigma' 1\sigma'}_{n\sigma 1\sigma} = \delta_{n1}\delta_{m1}$ and $\Phi^{n\sigma' 1\sigma'}_{n\sigma 1\sigma} = \delta_{n1}$. Thus, Eq. (10) becomes

$$1 = \Pi_{\sigma\sigma}\left(v_q(1-2G^{xc}_\sigma) + 4\pi\gamma_0^2\right) + \Pi_{\bar{\sigma}\bar{\sigma}}\left(v_q(1-2G^{xc}_{\bar{\sigma}}) + 4\pi\gamma_0^2\right) - 2\Pi_{\sigma\sigma}\Pi_{\bar{\sigma}\bar{\sigma}}[v_q(1-G^+_\sigma)(4\pi\gamma_0^2 - v_q G^-_{\bar{\sigma}}) + v_q(1-G^+_{\bar{\sigma}})(4\pi\gamma_0^2 - v_q G^-_\sigma)]. \quad (11)$$

For the case of spin-unpolarized system, $\Pi_{\sigma\sigma} = \Pi_{\bar{\sigma}\bar{\sigma}} = \frac{1}{2}\Pi_{2D}$ and $G^\pm_\sigma = G^\pm_{\bar{\sigma}} = G^\pm$, and thus Eq. (11) reduces to $[1 - \Pi_{2D}v_q(1-G^+)][1 - \Pi_{2D}(4\pi\gamma_0^2 - v_q G^-)] = 0$. This is just a simple product of the dispersion relations of charge-density and spin-density modes in a spin-unpolarized system. The two modes are completely decoupled in this case [2,7]. On the other hand, in RPA where $G^\pm_\sigma = G^\pm_{\bar{\sigma}} = 0$, Eq. (11) becomes

$$1 - (\Pi_{\sigma\sigma} + \Pi_{\bar{\sigma}\bar{\sigma}})(v_q + 4\pi\gamma_0^2) + 16\pi\gamma_0^2 v_q \Pi_{\sigma\sigma}\Pi_{\bar{\sigma}\bar{\sigma}} = 0, \quad (12)$$

where $\Pi_{\sigma\sigma} \neq \Pi_{\bar{\sigma}\bar{\sigma}}$ in the system of finite spin polarization. Even in RPA, it is clearly seen that, from Eq. (12), charge-density and spin-density wave excitations are coupled.

For the case of spin-polarized quantum wells, the dispersion relation of intra-spinsubband excitations ($n\sigma \leftrightarrow n\sigma$ or $n\bar{\sigma} \leftrightarrow n\bar{\sigma}$) is given by

$$(1-\Pi_{1\sigma 1\sigma}A^{1\sigma}_{1\sigma})(1-\Pi_{1\bar{\sigma}1\bar{\sigma}}A^{1\bar{\sigma}}_{1\bar{\sigma}}) - \Pi_{1\sigma 1\sigma}\Pi_{1\bar{\sigma}1\bar{\sigma}}B^{1\sigma}_{1\bar{\sigma}}B^{1\bar{\sigma}}_{1\sigma} = 0. \quad (13)$$

Here, in the long-wavelength limit, one can replace $\Pi_{1\sigma 1\sigma}$ and $\Pi_{1\bar{\sigma}1\bar{\sigma}}$ by their limiting values, $\Pi_{\sigma\sigma} \simeq \frac{n_\sigma q^2}{m\omega^2}$; $\Pi_{\bar{\sigma}\bar{\sigma}} \simeq \frac{n_{\bar{\sigma}} q^2}{m\omega^2}$. Using the long-wavelength forms of the noninteracting susceptibilities, we find two solutions of Eq. (13)

$$\omega^2_{CD} = (\omega^2_{P\sigma} + \omega^2_{P\bar{\sigma}})[1 - \alpha_{CD}(\zeta)q + O(q^2)], \quad (14)$$

and

$$\omega^2_{SD} = (\omega^2_{P\sigma} + \omega^2_{P\bar{\sigma}})\frac{n_\sigma n_{\bar{\sigma}}}{n_0^2}\alpha_{SD}(\zeta)q, \quad (15)$$

where α_{CD} and α_{SD} are functions of spin polarization ζ, but independent of q in the long wavelength limit,

$$\alpha_{CD}(\zeta) = \left(\tfrac{n_\sigma}{n_0}\right)^2[(1-2G^{xc}_{\sigma\sigma})S_1(\sigma\sigma;\sigma\sigma) - \tfrac{2\gamma_0^2}{e^2/\epsilon_s}\Phi^{\sigma\sigma}_{\sigma\sigma}] + \left(\tfrac{n_{\bar{\sigma}}}{n_0}\right)^2[(1-2G^{xc}_{\bar{\sigma}\bar{\sigma}})S_1(\bar{\sigma}\bar{\sigma};\bar{\sigma}\bar{\sigma}) - \tfrac{2\gamma_0^2}{e^2/\epsilon_s}\Phi^{\bar{\sigma}\bar{\sigma}}_{\bar{\sigma}\bar{\sigma}}] + 2\tfrac{n_\sigma n_{\bar{\sigma}}}{n_0^2}[(1-G^c_{\sigma\bar{\sigma}} - G^c_{\bar{\sigma}\sigma})S_1(\sigma\sigma;\bar{\sigma}\bar{\sigma}) + \tfrac{2\gamma_0^2}{e^2/\epsilon_s}\Phi^{\bar{\sigma}\bar{\sigma}}_{\sigma\sigma}],$$

and

$$\alpha_{SD}(\zeta) = 2(1-G^c_{\sigma\bar{\sigma}} - G^c_{\bar{\sigma}\sigma})S_1(\sigma\sigma;\bar{\sigma}\bar{\sigma}) - (1-2G^c_{\sigma\bar{\sigma}})S_1(\sigma\sigma;\sigma\sigma) - (1-2G^c_{\bar{\sigma}\sigma})S_1(\bar{\sigma}\bar{\sigma};\bar{\sigma}\bar{\sigma}) + \frac{2\gamma_0^2}{e^2/\epsilon_s}(\Phi^{\sigma\sigma}_{\sigma\sigma} + \Phi^{\bar{\sigma}\bar{\sigma}}_{\bar{\sigma}\bar{\sigma}} + 2\Phi^{\sigma\sigma}_{\bar{\sigma}\bar{\sigma}}).$$

In these expressions $n_0 = n_\sigma + n_{\bar\sigma}$, and $\omega_{P\sigma}(\omega_{P\bar\sigma})$ is the 2D plasma frequency of majority(minority)-spin electron gas, $\omega_{P\sigma}^2 = \frac{2\pi n_\sigma e^2}{\epsilon_s m} q$ ($\omega_{P\bar\sigma}^2 = \frac{2\pi n_{\bar\sigma} e^2}{\epsilon_s m} q$). In obtaining the above expressions, we expanded the structure factor $F_{1\sigma 1\sigma}^{1\bar\sigma 1\bar\sigma}(q)$ in powers of q,

$$F_{n\sigma n\sigma}^{n\sigma' n\sigma'}(q) \simeq 1 - S_1(\sigma\sigma;\sigma'\sigma')q + \frac{1}{2}S_2(\sigma\sigma;\sigma'\sigma')q^2 - \frac{1}{6}S_3(\sigma\sigma;\sigma'\sigma')q^3 + O(q^4),$$

and defined $S_m(\sigma\sigma;\sigma'\sigma')$ as $S_m(\sigma\sigma;\sigma'\sigma') = \int\int_{-\infty}^{\infty} dz\, dz' \xi_{n\sigma}(z)\xi_{n'\sigma}(z)|z - z'|^m \xi_{n\sigma'}(z')\xi_{n'\sigma'}(z')$. The expressions in Eqs. (14) and (15) are valid up to terms linear in q and should be read with the long-wavelength forms of the local fields, $G_{\sigma\sigma'}$. We observe that the two distinct modes of $\omega_{CD}(q)$ and $\omega_{SD}(q)$ originate, respectively, from the charge-density and spin-density fluctuations of the system, and that the latter mode $\omega_{SD}(q)$ softens rapidly in the long wavelength limit.

The inter-spinsubband excitations are related with the transitions $m \leftrightarrow m'$ and $\bar m \leftrightarrow \bar m'$ where m and $\bar m$ denote the subbands $m\sigma$and $m\bar\sigma$, respectively. In this case the susceptibilities $\chi_{m\sigma m'\sigma}$ and $\chi_{m\bar\sigma m'\bar\sigma}$ are approximated, in the long-wavelength limit, by [10–12] $\chi_{m\sigma m'\sigma}(\boldsymbol{q},\omega) \simeq \frac{2(n_{m'}-n_m)}{\hbar}\frac{\omega_{mm'}}{\omega^2-\omega_{mm'}^2}$ ($\chi_{m\bar\sigma m'\bar\sigma}(\boldsymbol{q},\omega) \simeq \frac{2(n_{\bar m'}-n_{\bar m})}{\hbar}\frac{\omega_{\bar m\bar m'}}{\omega^2-\omega_{\bar m\bar m'}^2}$) where n_m is the number of electrons per unit area in subband $m\sigma$, and $\omega_{mm'}$ and $\omega_{\bar m\bar m'}$ are the frequencies corresponding to spinsubband separations, $\omega_{mm'} = (\varepsilon_{m\sigma} - \varepsilon_{m'\sigma})/\hbar$ for the majority spin electrons and $\omega_{\bar m\bar m'} = (\varepsilon_{m\bar\sigma} - \varepsilon_{m'\bar\sigma})/\hbar$ for the minority spin electrons. The structure factor $F_{n\sigma m\sigma}^{n\sigma' m\sigma'}$ is expanded in powers of q by

$$F_{n\sigma m\sigma}^{n\sigma' m\sigma'}(q) \simeq -qS_1(nm;n'm') + \frac{1}{2}q^2 S_2(nm;n'm') + O(q^3),$$

where again the composite notation $n = n\sigma$ and $n' = n'\sigma$ is used, and $S_2(nm;\bar n\bar m) = -2 < z >_{nm} < z >_{\bar n\bar m}$ for symmetric quantum wells. Substituting these long-wavelength forms into Eq. (10) gives

$$\omega^2 = \frac{1}{2}\left[\tilde\omega_{n1n1}^2(q) + \tilde\omega_{\bar n\bar 1\bar n\bar 1}^2(q)\right] \pm \frac{1}{2}\left\{\left[\tilde\omega_{n1n1}^2(q) - \tilde\omega_{\bar n\bar 1\bar n\bar 1}^2(q)\right]^2 + v4\tilde\omega_{n1\bar n\bar 1}^2(q)\tilde\omega_{\bar n\bar 1 n1}^2(q)\right\}^{1/2}, \tag{16}$$

where $\tilde\omega_{n'1'n'1'}$ and $\tilde\omega_{n1n'1'}$ are defined, in terms of various components of the structure factors and local fields, as $\tilde\omega_{n1n1}^2(q) = \omega_{n1}^2\left[1 + (\alpha_{n1}^{n1} - \mu_{n1}^{n1}q)(1 - 2G_{\sigma\sigma}^{xc}) + \gamma_{n1}^{n1}\right]$, $\tilde\omega_{\bar n\bar 1\bar n\bar 1}^2(q) = \omega_{\bar n\bar 1}^2\left[1 + (\alpha_{\bar n\bar 1}^{\bar n\bar 1} - \mu_{\bar n\bar 1}^{\bar n\bar 1}q)(1 - 2G_{\bar\sigma\bar\sigma}^{xc}) + \gamma_{\bar n\bar 1}^{\bar n\bar 1}\right]$, $\tilde\omega_{n1\bar n\bar 1}^2(q) = \omega_{n1}^2\left[(\alpha_{n1}^{\bar n\bar 1} - \mu_{n1}^{\bar n\bar 1}q)(1 - 2G_{\sigma\bar\sigma}^{c}) - \gamma_{n1}^{\bar n\bar 1}\right]$, and $\tilde\omega_{\bar n\bar 1 n1}^2(q) = \omega_{\bar n\bar 1}^2\left[(\alpha_{\bar n\bar 1}^{n1} - \mu_{\bar n\bar 1}^{n1}q)(1 - 2G_{\bar\sigma\sigma}^{c}) - \gamma_{\bar n\bar 1}^{n1}\right]$. The symbols $\alpha_{n1}^{n'1'}$, $\mu_{n1}^{n'1'}$, and $\gamma_{n1}^{n'1'}$ are given by $\alpha_{n1}^{n'1'} = -\frac{2n_\sigma}{\hbar\omega_{n1}}\frac{2\pi e^2}{\epsilon_s}S_1(n1;n'1')$, $\mu_{n1}^{n'1'} = -\frac{n_\sigma}{2\hbar\omega_{n1}}\frac{2\pi e^2}{\epsilon_s}S_2(n1;n'1')$, and $\gamma_{n1}^{n'1'} = \frac{2n_\sigma}{\hbar\omega_{n1}}4\pi\gamma_0^2\Phi_{n1}^{n'1'}$. For the case of a spin-unpolarized system the general dispersion relation given by Eq. (10) decouples into the well-known intersubband charge-density excitation, ω_{CD} and of intersubband spin-density excitation, ω_{SD} [11,13,14]: $\omega_{CD}^2(q) = \omega_{n1}^2\left[1 + (1 - G^+)(\alpha_{n1}^{n1} - \mu_{n1}^{n1}q)\right]$ and $\omega_{SD}^2(q) = \omega_{n1}^2\left[1 + \gamma_{n1}^{n1} - G^-(\alpha_{n1}^{n1} - \mu_{n1}^{n1}q)\right]$. However, in this case, the latter modes $\omega_{SD}(q)$ appear only in the single-particle continuum region of frequency-wavenumber space and, hence, it is not possible to observe the modes. On the other hand, in the SPQW the mode corresponding to ω_{SD} of the unpolarized system($\zeta = 0$) is well defined to be observed experimentally. The two parts in ω_{CD}, one independent of G^+ but linear in α_{n1}^{n1} and the G^+-dependent one are, respectively, the terms giving rise to so-called depolarization and excitonic shifts. They are well known in cases of quantum wells with zero or infinitesimal spin polarization [11,13,14]. The contribution of the term proportional to γ_{n1}^{n1} in ω_{SD} is magnetic in origin, and it appears in the spin-density excitations only. This term has its origin in the use of the self-consistent magnetic disturbance, $\boldsymbol{b}$ in our effective perturbation given by Eq. (1). The latter contribution disappears, if we take the external magnetic disturbance $\boldsymbol{b}_0$, instead of $\boldsymbol{b}$, as our effective magnetic disturbance in Eq. (1). The dipole oscillation term, μ_{n1}^{n1}, comes into the dispersion relation only at finite q modifying its slope; it has opposite effect in the charge-density and spin-density excitations. One example of the dispersion relation of the longitudinal modes of a SPQW in an electric quantum limit is shown in figure 1. The inter-spin-subband modes(upper panel) and the intra-spin-subband modes (lower panel) are displayed as a function of wavenumbers. Two pairs of thin solid lines starting from the same points of the vertical axis in the upper panel denote the boundaries of single-particle inter-spin-subband transition continuum(the hatched area) in the case of finite spin polarization. In the spin-polarized system we clearly observe well-defined two modes which are related to two distinct inter-spin-subband transitions. When the spin polarization vanishes the lower modes lie in the region of the single particle continuum, the boundary of which is also indicated with a pair of thin dotted lines in the figure. Intra-spin-subband modes of the cases with finite spin polarization are overlapped and are indistinguishable in this figure with the modes of spin-unpolarized case.

In this paper, we presented a self-consistent theory of the longitudinal charge and spin density responses of spin-polarized quasi-two dimensional quantum devices, and applied the results to spin-polarized quantum wells.

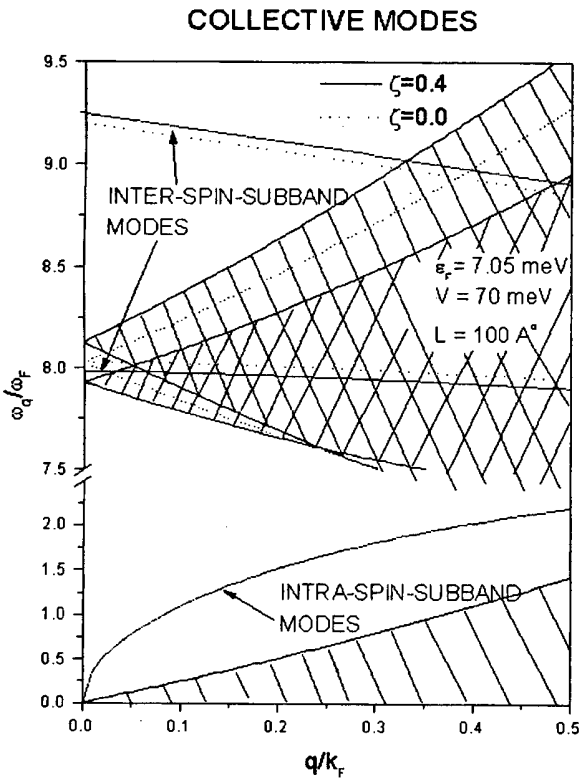

Fig. 1. Dispersion relations of the longitudinal collective excitations in a spin-polarized semiconductor quantum well. The inter-spin-subband modes (upper panel) and the intra-spin-subband modes (lower panel) are displayed as a function of wavenumbers. The hatched area denotes the single-particle inter-spin-subband transition continuum in the case of finite spin polarization. In the spin-polarized system we clearly observe well-defined two modes which are related to two distinct inter-spin-subband transitions. When the spin polarization vanishes the lower modes lie in the region of the single-particle continuum, the boundary of which is also indicated with a pair of thin dotted lines in the figure. Intra-spin-subband modes of the cases with finite spin polarization are overlapped and are indistinguishable in this figure with the modes of spin-unpolarized case.

We discussed the conditions of the longitudinal collective modes and examined the dispersion relations of the longitudinal spin-charge collective excitations. The coupling of charge-density and spin-density wave excitations is apparant even in the RPA. The spin polarization is seen to introduce new features to the collective excitation spectrum. We suppose that the spin-polarized quantum structure would be realized in a spin-polarized semiconductor quantum well and the spin-charge coupled modes could be observed in its light scattering experiments. One example of the possible candidates of the spin-polarized quantum structures is magnetic quantum wells fabricated in a modulation doped dilute magnetic semiconductor in which the large effective g-value leads to a spin splitting that is very large compared to the cyclotron energy.

This work was supported in part by the Korea Research Foundation (Project number 1997-001-D00131) and in part by the Matching Fund Program of RIBS, Pusan National University, Korea (Project No. RIBS-PNU-98-201).

REFERENCES

[1] A. B. Oparin and J. J. Quinn, Solid St. Commun. **98**, 791 (1996).
[2] D. C. Marinescu, J. J. Quinn and K. S. Yi, Physica **B249**, 727 (1998).
[3] M. S-C. Luo, S. L. Chuang, S. Schmitt-Rink and A. Pinczuk, Phys. Rev. **B48**, 11086 (1993).
[4] D. Gammon, B. V. Shanabrook, J. C. Ryan and D. S. Katzer, Phys. Rev. **B41**, 12311 (1990).
[5] J. C. Ryan, Phys. Rev. **B43**, 4499 (1991).
[6] C. A. Kukkonen and A. W. Overhauser, Phys. Rev. **B20**, 550 (1979).
[7] K. S. Yi and J. J. Quinn, Phys. Rev. **B54**, 13398 (1996).
[8] X. Zhu and A. W. Overhauser, Phys. Rev. **B33**, 925 (1986).
[9] H. Ehrenreich and M. Cohen, Phys. Rev. **115**, 786 (1959).
[10] K. S. Yi , J. Korean Phys. Soc. **21**, 295 (1988).
[11] A. C. Tselis and J. J. Quinn, Phys. Rev. **B29**, 3318 (1984).
[12] J. K. Jain and S. Das Sarma, Phys. Rev. **B36**, 5949 (1987).
[13] K. S. Yi and J. J. Quinn, Phys. Rev. **B27**, 2396 (1983).
[14] J. C. Ryan, Phys. Rev. **B43**, 12406 (1991).

Journal of the Korean Physical Society, Vol. 34, June 1999, pp. S339~S342

The Self-Heating Effect on SOI LIGBTs under the Steady-State Condition

Young-Dong Koo and Oh-Kyong Kwon*

Department of Electronic Engineering, Hanyang University, Seoul 133-791

We investigate the self-heating effect of 300 V SOI Lateral Insulated Gate Bipolar Transistors (LIGBTs) and propose the new structure in order to reduce the silicon temperature increased by high supply voltage and driving current through the LIGBT. Conventional LIGBTs are simulated using the device simulator of MEDICI with the lattice temperature model considering heat generation in the SOI layer. Simulation results indicate that their forward biased safe-operation area (FBSOA) performance and current driving capability are degraded under the steady-state condition compared with the device simulation results ignoring the self-heating effect. The proposed SOI LIGBTs have the 5 μm thick metal layer on the passivation layer for sinking the generated heat in the SOI layer. The second breakdown voltage is enhanced from 50 V in the conventional SOI LIGBT to 220 V in the proposed structure at the gate voltage of 10 V and the current driving capability of the proposed structure is improved by 35 % than that of the conventional LIGBT.

I. INTRODUCTION

Lateral Double diffused MOSFETs (LDMOSFETs) have been used as high voltage devices in high voltage integrated circuits (HVICs) because of the compatability with low voltage CMOS device processes. They have high-speed switching characteristics due to the operation without minority carrier and simple gate drive circuitry. These features are particularly attractive in high voltage integrated circuits (HVICs) at high frequencies where switching losses are dominant. But in order to drive high current, the relatively low current driving capability of LDMOSFETs enlarges the chip size of HVICs. Therefore, Insulated Gate Bipolar Transistor (IGBT) were developed in 1980s to improve the current driving capability due to conductivity modulation by injected minority carrier in drift region and to take advantages of LDMOSFETs [1]. In some HVIC applications requiring the high driving current, lateral IGBTs (LIGBTs) are used as output buffers of high voltage devices, and then this leads to decrease the chip size of HVICs [2]. Dielectric isolation (DI) technology has been the best choice of HVIC technologies due to smaller isolation area and less parasitic effect such as parasitic latch-up and leakage current than those of junction isolation (JI) and self-isolation [2,3]. But it has a disadvantage of low thermal conductivity due to the buried oxide and small heat capacitance of the SOI layer. The heat generated by high supply voltage and driving current in HVICs cannot be efficiently transferred to external environment because of thick buried oxide under the SOI layer and the passivation layer over metal interconnects, and then increases the temperature in SOI layer. Anold *et. al.* studied the self-heating effect of LDMOSFETs using both bulk-silicon technology and SOI technology. They show that the temperature rise of SOI devices is more rapid than that of bulk-silicon devices in a initial stage of power pulse and it is dependent on the buried oxide thickness. In addition, in [7] the FBSOA performance of a vertical IGBT is investigated as a function of pulse duration. In the initial stage of gate pulse duration, the device is operated properly. As the pulse duration increases, the current is reduced becuase of the reduction of the field effect carrier mobilities due to generated heat. Further increasing the pulse duration, the driving current is rapidly increased due to turn-on of the parasitic thyristor. This results in the destruction of IGBTs. In this paper, we optimize the 300 V class LIGBT on a SOI wafer, analyze the self-heating effect by device simulations including lattice temperature model and propose the new structure of a LIGBT suppressing the self-heating effect. The process flow of LIGBT on a SOI wafer and the LIGBT structure is described in II and III, respectively and the results of simulation and experiment follows in IV.

II. FABRICATION PROCESS FLOW

The main fabrication sequence of 300 V lateral IGBTs on a SOI wafer is shown in Fig. 1. The starting wafer is

*E-mail: okwon7@chollian.net, Phone: +82-2-447-4522, Fax: +82-2-3436-0133

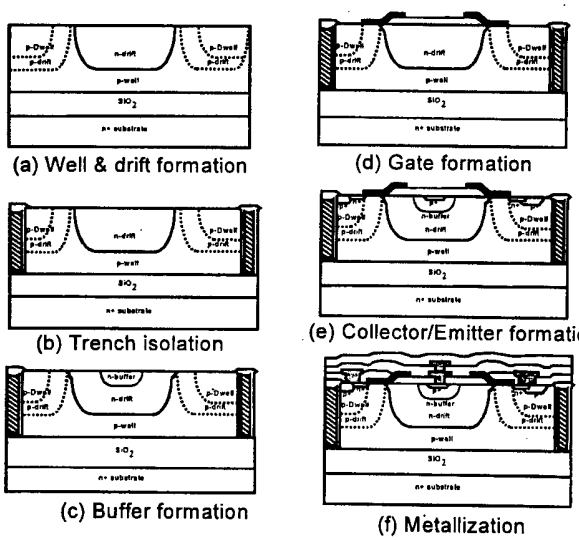

Fig. 1. The process flow of a conventional SOI LIGBT.

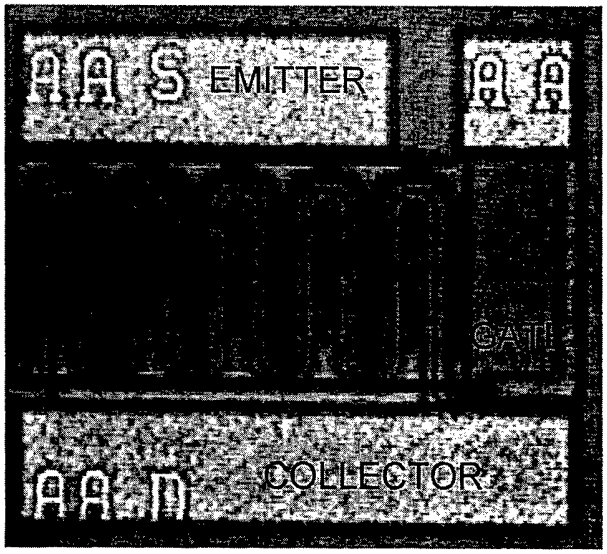

Fig. 2. The photograph of a fabricated SOI LIGBT.

the bonded SOI wafer with the SOI layer thickness of 5.5 μm and the buried oxide thickness of 3 μm. The p-well is implanted by Bf2 ion at 100 KeV and diffused at 1200 °C for 510 min to reach the p-well junction to the top of the buried oxide layer. And n-drift and p-drift regions are formed implanting phosphorus ion at 150 KeV and boron ion at 90 KeV, respectively, and drive-in at 1200 °C for 420 min. The ion implantation dose of p-well and n-drift are determined to meet the reduced surface field (RESURF) condition. The doses of p-well and n-drift are 3.0E12 and 4.8E12 cm^{-2}, respectively. The p-Dwell is formed for suppressing latch-up of the parasitic thyristor by lowering body resistance. For the trench isolation structure, 2 μm wide silicon trench is etched surrounding active regions. After 4000 Å thickness thermal oxide on the trench sidewall is grown, the trench is refilled by poly-Si and LOCOS is formed on the top of trenches as shown in Fig. 1(b). The buffer region formation in the collector area for preventing the punch-through is performed as shown in Fig. 1(c). The 1.3 μm thick oxide is deposited for field oxide in the drift region and etched the oxide with the taper angle of 40° as shown in Fig. 1(d). The n^+ poly-Si gate and source/collector are formed as the same as low voltage CMOS processes. Fig. 2 shows the photograph of a fabricated LIGBT.

III. THE PROPOSED STRUCTURE OF A LIGBT

The cross-sectional view of the conventional SOI LIGBT is shown in Fig. 3(a). The high voltage is applied to the collector electrode, the high current flows through the drift region and the channel region and there are buried oxide under SOI layer and passivation layer over metal layer, which have low thermal conductivity. Because

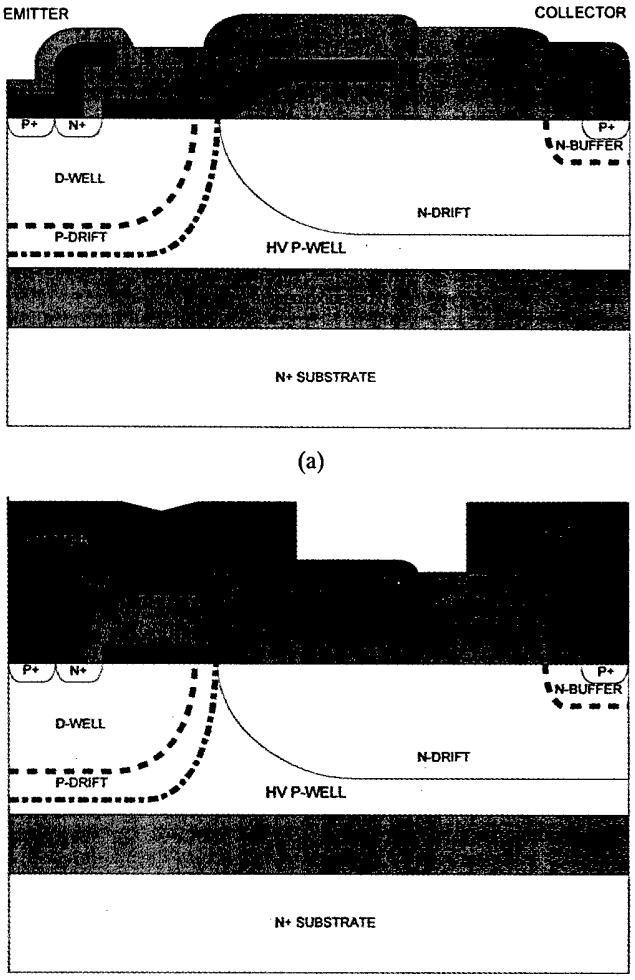

Fig. 3. The Schematic cross-sectional view of (a) the conventional SOI LIGBT and (b) the proposed SOI LIGBT.

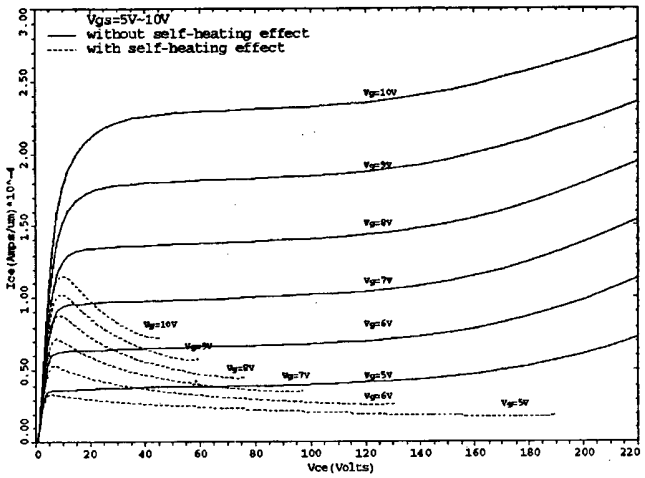

Fig. 4. Simulated I-V characteristics of a conventional LIGBT with self-heating effect (dotted lines) and without self-heating effect (solid lines).

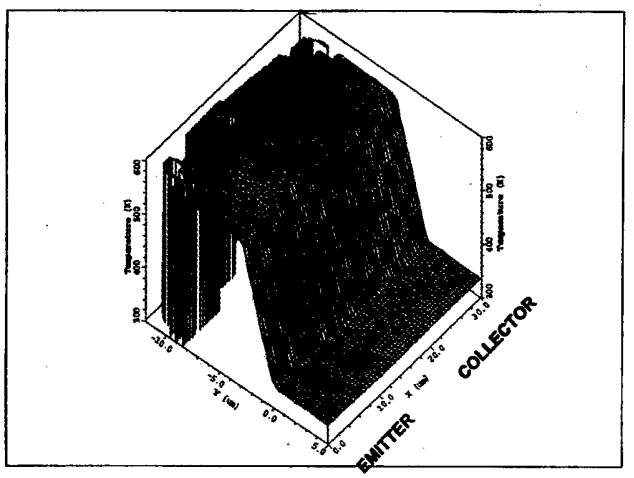

Fig. 5. Simulated temperature profile of a conventional LIGBT at Vg=5 V and Vce=50 V.

the generated heat in SOI layer is dissipated through only thin metal line in conventional LIGBTs, the increased silicon temperature degrades the performance of the high voltage device. The proposed structure of a LIGBT has an additional metal layer on the passivation layer in order to sink the heat from the SOI layer efficiently as shwon in Fig. 3(b). The additional metal layer is 5 μm-thick electroplated copper layer on the passivation layer.

IV. RESULTS OF SIMULATION AND EXPERIMENT

Fig. 4 shows I-V characteristic curves of the conventional LIGBT obtained from device simulation using Medici [8] with and without self-heating effect. The solid line in Fig. 4 represents the electrical characteristics of the conventional LIGBT ignoring the heat generation in the SOI layer. When the self-heating effect is ignored, a conventional LIGBT can operate free from device destruction and the degradation of the current driving capability for collector voltages up to 220 V at even gate voltage of 10 V. But when a conventional LIGBT is simulated with lattice temperature advanced application module (AAM) of Medici at the environment of room temperature, the heat is generated in silicon layer by high potential drop between source and collector and current flow through drift region and the channel. This results in the temperature elevation in the SOI layer. Under steady state condition, the heat generated in SOI layer cannot be dissipated to the etrernal environmet because of low thermal conductivity of buried oxide and passivation layer as shown in Table 1. This leads to increase silicon temperature up to 600 K at collector voltage of 50 V and gate voltage of 5 V as shown in Fig. 5. And the temperature of bottom bureid oxide is nearly equal to the room temperature. This means that the generated heat is not transferred through the buried oxide. Therefore, the high silicon temperature degrades the field effect carrier mobility then decreases the current driving capability of the LIGBT as shown dotted lines in Fig. 4. In addition, the lowered built-in potential at p-n junction by high silicon temperature turns on the parasitic thyristor at low collector voltage. This leads to thermal runway and device destruction.

Fig. 6 shows that measured I-V characteristic curves

Table 1. Thermal conductivity of various matetials.

Material	Thermal conductivity
Silicon	1.5 W/cmK
Oxide	0.014 W/cmK
Aluminum	2.35 W/cmK

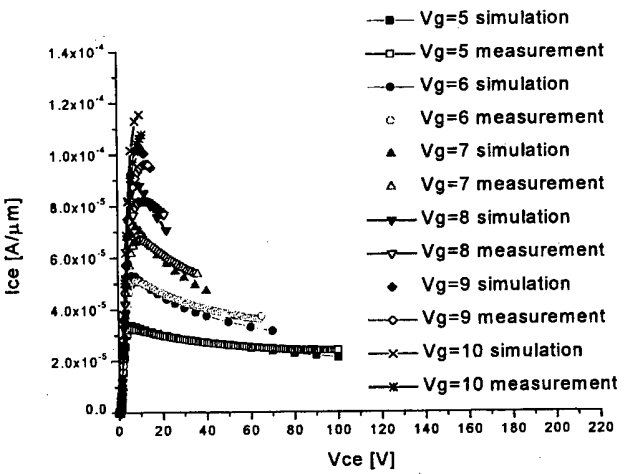

Fig. 6. Simulated and measured I-V characteristic curves of a conventional LIGBT.

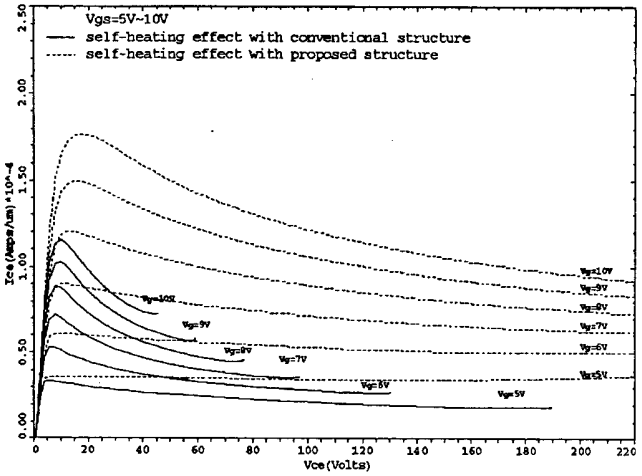

Fig. 7. Simulated I-V characteristics of the proposed LIGBT structure (dotted lines) and the conventional LIGBT structure (solid lines) with self-heating effect.

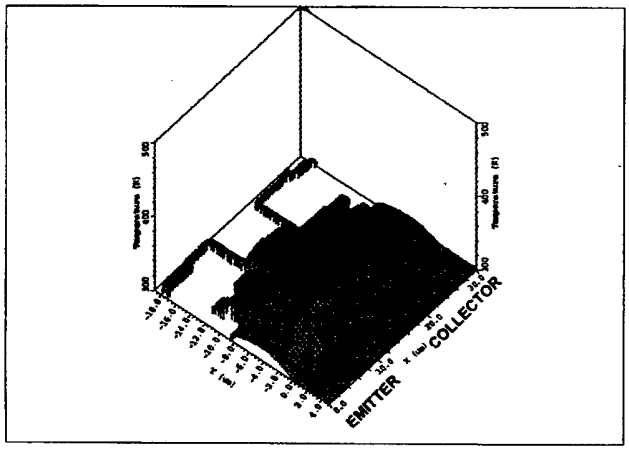

Fig. 8. Simulated temperature profile of the proposed LIGBT at Vg=5 V and Vce=50 V.

of a conventional LIGBT agree well with the simulation results of a SOI LIGBT using the lattice temperature model for the self-heating effect. The measured I-V characterisitcs at gate voltages of 8, 9 and 10V are appeared in low collector voltage ranges because of the power limitation of the measurement instrument. Fig. 7 shows simulation results of I-V characteristics of the conventional and the proposed LIGBTs considering the self-heating effect. In Fig. 7, the solid curves and dotted curves are for the conventional and the proposed LIGBTs, respectively. As shown in Fig. 7, the second breakdown voltage of the proposed LIGBT structure is extended to collector voltage of over 220 V at gate voltage of 10 V, which is equal to the electrical characteristic without self-heating effect but the current driving capability is still degraded, which is improved by 35 % at gate voltage of 10 V than that of a conventional LIGBT. Although the generated heat in silicon is transferred through the thick metal layer, the silicon temperature is increased still by small amount as shown in Fig. 8. The temperature of top silicon surface near to thick metal interconnect is almost equal to room temperature of 300 K but other silicon temperature is increasing toward buried oxide. The temperature profile in the SOI layer of the proposed device structure (Fig. 8) is much lower than that of the conventional LIGBT (Fig. 5).

V. CONCLUSIONS

The current driving capability and FBSOA of a conventional SOI LIGBT is degraded under steady state condition by self-heating effect because of low thermal conductivity of buried oxide and passivation layer. We analyzed the self-heating effect on a conventional SOI LIGBT using Medici with lattice temperature model and confirmed the analysis results by measured I-V characteristics of a conventional one. We propose the new structure of a SOI LIGBT with 5 μm-thick electroplated copper layer on the passivation layer in order to dissipate the heat generated in silicon layer. Analysis results indicate that the second breakdown voltage of a proposed SOI LIGBT is enhanced from 50 V to 220 V and the current driving capability is improved by 35 % at gate voltage of 10 V than that of a conventional LIGBT.

ACKNOWLEDGMENTS

This work is partially supported by the power semiconductor technology development project #ps-02-A-01 of the Science and Technology Policy Institute.

REFERENCES

[1] B. J. Baliga, M. S. Adler, R. P. Love, P. V. Gray and N. D. Zommer, IEEE Tran. Electron Device **31**, 821 (1984).
[2] H. Sumida, A. Hirabayashi, H. Shimabukuro, Y. Takazawa and Y. Shigeta, Proceedings of 10th ISPSD 137 (1998).
[3] K. Kobayashi, H. Yanagigawa, K. Mori, S. Yamanaka and Akira Fujiwara, Proceedings of 10th ISPSD 141 (1998).
[4] Y. K. Leung, Y. S. Suzuki, K. E. Goodson and S. S. Wong, Proceedings of 7th ISPSD 136 (1995).
[5] E. Aonold, H. Pein and S. P. Herko, Technical Digest of IEDM 813 (1994).
[6] L. T. Su, J. E. Chung, D. A. Antoniadis, K. E. Goodsom and M. I. Flik, IEEE Tran. Electron Device **41**, 69 (1994).
[7] H. Hagino, J. Yamashita, A. Uenishi and H. Haruguchi, IEEE Tran. Electron Device **43**, 490 (1996).
[8] *TMA* (MEDICI User's Manual, Technology Modeling Association, 1997).

Journal of the Korean Physical Society, Vol. 34, June 1999, pp. S343~S346

Textured ZnO Thin Films by RF Magnetron Sputtering

Masno GINTING*, Jeong Chul LEE, Ki-Hwan KANG, Seok-Ki KIM,
Kyung Hoon YOON, I-Jun PARK and Jinsoo SONG

R&D Center for Applied Physics, Indonesian Institute of Sciences, Serpong-Indonesia
**Korea Institute of Energy Research, Taejon 305-343*

Textured thin films ZnO has been successfully grown by rf magnetron sputtering method using a special technique of introducing a small amount of water and methanol on the deposition chamber. The grain size of the textured surface is highly dependent on the argon pressure during the deposition. The pressure in this experiment was varied from 50 mTorr down to 5 mTorr and the highest grain size of the film is obtained at 5 mTorr. The total transmittane of the films are more than 85 % in the wavelength of 400 to 800 nm, and haze ratio of about 14 % is obtained at 400 nm wavelength. Beside the textured surface, these films also have very low resistivity, which is lower than 1.4×10^{-3} Ω·cm. X-ray analysis shows that the films with textured surface have four diffraction peaks on the direction of (110), (002), (101) and (112), while the non-textured films have only (110) and (002) peaks. Due to the excellent characteristics of this film, it will make the film very good TCO alternatives for the thin film silicon solar cells.

I. INTRODUCTION

Many publications have been reported in the growing of ZnO thin films using different techniques, such as MOCVD [1], reactive evaporation [2], spray pyrolysis [3,4], DC and RF sputtering [5,6]. It has been known that the textured surface of the TCO film is very important in the fabrication of the solar cell, especially for the thin film amorphous or polycrystalline silicon cells, in order to increase its efficiency. T. Nakada *et al.* [7] had reported that by applying the textured ZnO film into their $CuInSe_2$ thin film solar cells, they have shown that the efficiency increases from 8.85 % (flat ZnO film) to 10.3 % (textured ZnO film). It is well known that sputtering technique is suitable for low cost and large-scale production of thin film. It has been also long known that the textured ZnO films can be easily obtained using MOCVD technique as has been reported by Wilson *et al.* [8]. However most of the films prepared by sputtering technique have been reported to have flat surface morphology and columnar structure, while only a few groups have reported for the textured ZnO thin film by employing their own techniques. J. A. Anna *et al.* have used rf sputtering at 150 °C substrate temperature by using argon gas mixed with H_2O [9], Tokio Nakada *et al.* by dc magnetron sputtering in B_2H_6-Ar mixtures [10] and also in the H_2O partial pressure [11] at the substrate temperatures equal to or higher than 200 °C.

In this paper we report on the result of the ZnO thin film grown by rf magnetron sputtering with special technique of introducing water and methanol in the deposition chamber. The substrate temperature for the textured ZnO thin film is around 100 °C, which is the lowest substrate temperature that ever reported. The preliminary result of low resistivity, high transparency, textured surface and the effect of the deposition pressure on the grain size of the film are also reported.

II. EXPERIMENTAL

The target used in this work is a 4 inch disk type ZnO (99.99 % purity) doped with Al_2O_3 (2.5 wt%). The substrates were 5 cm×5 cm 7059 glass. A few drops of water or methanol were introduced to the deposition chamber, and after inserting the substrate, the system was pumped down until the pressure is reaching about 1×10^{-6} Torr. Then high purity Ar gas is introduced to adjust the deposition pressure during experiment. After the required rf power, substrate temperature and chamber pressure are ready, the deposition started by opening the shutter. The deposition time for this experiment is fixed to be about 2 hours long. Thickness of the prepared ZnO films was estimated by utilizing a conventional surface roughness detector with a stylus (Tencor 2000). Electrical resistivity, Hall mobility, and carrier concentrations were measured at room temperature by the van der pauw method. The optical transmission of the films was measured in the wavelength range of 300~800 nm by spectrophotometer (Shimadzu UV-3101PC). X-ray diffraction measurements were carried out to examine the crystalline structure of the films.

III. RESULTS AND DISCUSSION

1. Surface and Structural Properties

Figure 1 shows the SEM photographs of the three ZnO films. The deposition conditions of these three films were fixed to be same; 100 °C substrate temperature, 250 W rf power and 2 hours deposition, while argon pressure varied from 5 to 50 mTorr. It must be noted that all the prepared ZnO films have pyramid like surface structure and the degree of the texture strongly depends on the pressure during the deposition. The largest texture is obtained at the investigated lowest pressure. This is believed due to the effect of the deposition rate that is higher at lower pressure. According to our knowledge, this large grain size is believed to be the first result ever reported using rf magnetron sputtering technique at substrate temperature as low as 100 °C.

In Figure 2 are shown the SEM photographs of the side view of the sample depicted in Fig. 1(a). It seems that the ZnO films have columnar structure at the beginning of the film growth. But as the growth progresses, the columnar growth is changing into granular growth. This growth change can be clearly seen for the film grown at 5 mTorr pressure, while for films grown at 25 and 50 mTorr

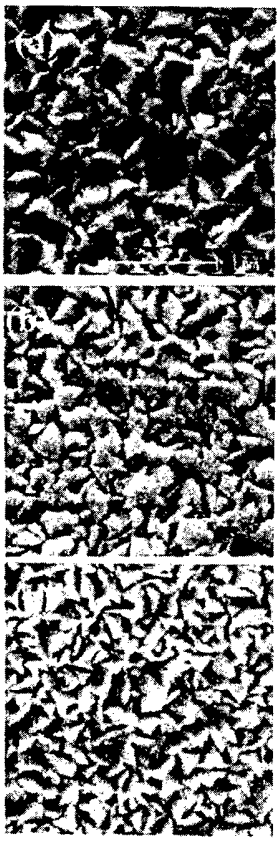

Fig. 1. The SEM surface morphology of the textured ZnO films deposited at; (a) 5, (b) 25, and (c) 50 mTorr.

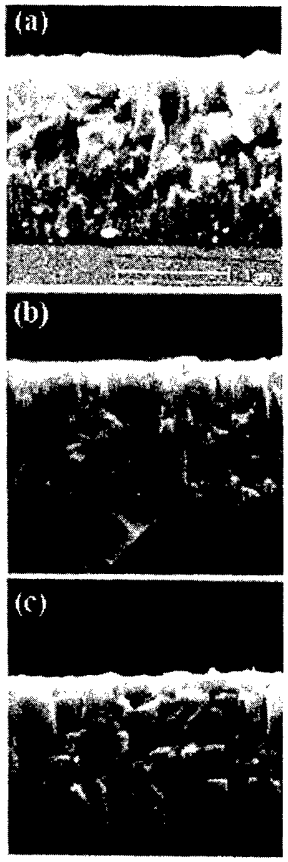

Fig. 2. SEM side view of the textured ZnO films with different pressure; (a) 5, (b) 25, and (c) 50 mTorr.

the growth change is not seen clearly. At the moment, we are not able to explain clearly the mechanism of this growth change in our films. However, we are suspected that this growth change might be due to the special technique of introducing water or methanol to our deposition chamber, since the amount of OH molecules is changing from the beginning to the end of the growth. We will investigate this phenomenon in more deeply, and if our assumption for the mechanism of the growth change is true, it may be a new growth process of ZnO thin films by rf magnetron sputtering. What had been done in reference [9], [10] and [11] in obtaining the textured ZnO films are by introducing constant OH molecules during the deposition time, which is completely different with what we have done in our experiment. The grain size as big as about 0.75 μm could be obtained for the best samples deposited at 5 mTorr pressure.

While all the films that are grown without introducing water or methanol into the deposition chamber are showing flat surface as shown in Figure 3. As one can see from Figure 2 and 3, the structure of the textured films is quite different with the flat films. It is clearly seen from Figure 3 that the flat film has a columnar growth from the beginning to the end of the deposition.

Although it is not shown in this paper, we found

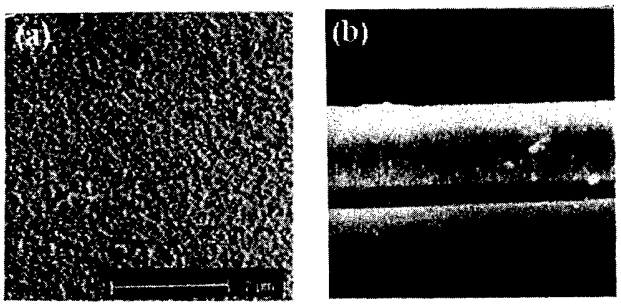

Fig. 3. SEM photographs of the flat surface film. (a) top view and (b) side view.

out that the ZnO films grown by introducing Methanol showed slightly different texture properties with the one using water as catalyst. Tokio *et al.* [11] have explained that the main species responsible for their textured surface film is the molecules of OH. By their explanation, we also believed, although we have no proof in this paper, that methanol seems to introduce more OH molecules than water in the deposition chamber during the deposition process. More discussion about the results between the films grown by using water and methanol is planing to be done in the separate publication.

In Figure 4 is shown the X-ray diffraction patterns of the textured surface (Fig. 4(a)) and flat surface (Fig. 4(b)). For the textured surface there are present four peaks which are (002), (101), and two weak peaks in the direction of (100) and (112). The only (100) and (002) peaks are present for ZnO with the flat surface. The strong (002) peak indicates that ZnO films have hexagonal wurtzite structure, which means the film highly *c*-axis oriented. The textured film however has the (101) peak besides (100) and (002), which is corresponding to granular structure of the film as shown in Fig. 1.

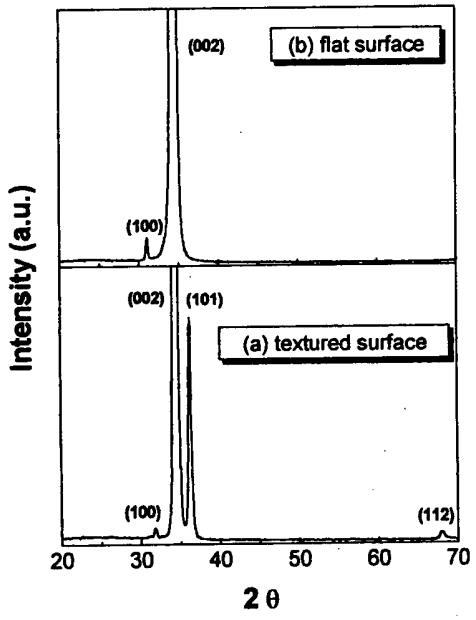

Fig. 4. The XRD patterns of ZnO films; (a) textured surface and (b) flat surface.

2. Optical Properties

Figure 5 shows the transmission spectra of the textured ZnO films with different working pressure. The total transmittance is shown in figure 5(a), compared with diffused. Enlarged diffused transmittance is redrawn in figure 5(b). It must be noted by comparing Figure 1 and 5 that the effect of both grain size and the degree of texturing on refraction of incident light occurs; the higher grain size or texture is the larger diffused transmittanc and vice versa. This is consistent with the nature of the reflection and refraction of light on the surface of the textured films. The higher the texture quality is (Figure 5(a)), then the more the light can be diffused. Moreover, the diffusion of the light may be also affected by the thickness of the film. However, if we compare the thickness of these three films as it can be seen at Table 1, they are not significantly different. So we believe that the most effect of the higher percentage of diffused light is mainly due to the textured surface quality.

The average total transmittance of our films varies from 86 to 92 % on the range of 400 to 800 nm wavelength, which also make the films more attractive for the use of TCO on silicon solar cell application. The haze

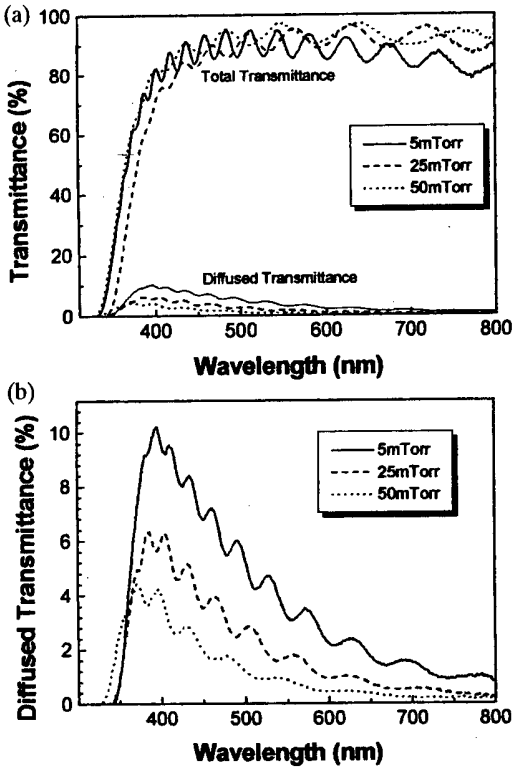

Fig. 5. The transmission spectra of the textured ZnO films; (a) Diffused, (b) Total transmittance.

Table 1. The characteristics of the textured ZnO films.

S.N. / Porp.	Mzno-06	Mzno-31	Mzno-30
Pressure (mtorr)	5	25	50
Thickness (mm)	1.6	1.3	1.0
Resistivity $\times 10^{-4}$ W·cm	11.2	14.0	10.8
Mobility $cm^2/V{\cdot}s$	28.7	15.4	14.0
n 10^{20} cm^{-3}	3.16	2.89	4.11
Haze (%) at 400 nm	14.1	8.6	5.4

factor, which is the ratio of refracted light to total transmitted one, is also given in Table 1. The highest haze factor is about 14.1 % at about 400 nm wavelength for the film, which has a highest textured quality as shown in Fig. 1.

3. Electrical Properties

The electrical properties of the ZnO films that had been grown is measured using Vander Paw method, and for the three films is given in Table 1.

The resistivity of the films does not vary too much, which is around 1×10^{-3} to 1.4×10^{-3} Ω·cm. Also the carrier concentration on the films is between 2.89×10^{20} cm^{-3} to 4.11×10^{20} cm^{-3}. However the mobility of the carrier for the different films very dependent on the grain size of the films. As it can bee seen from Table 1, sample MZNO-06 that had the largest grain size has the mobility twice of the mobility for the sample MZNO-30 which has the smallest grain size.

IV. CONCLUSIONS

Textured thin films ZnO has been grown by rf magnetron sputtering using a special technique of introducing a small amount of water and methanol on the deposition chamber. The grain size of the textured surface is highly dependent on the pressure during the deposition. The largest grain size was obtained at pressure of 5 mTorr. The film thickness varies from 1 μm to 2 μm, and having an average total transmittance of 86∼92 % on the range of 400 to 800 nm wavelength, and the highest haze factor obtained is about 14.1 % around 400 nm wavelength. The highest carrier mobility is found for best textured film which value is 28.7 $cm^2/V{\cdot}s$ and the carrier concentration of 3.16 cm^{-3} and with resistivity value of 1.4×10^{-3} Ω·cm. From XRD measurements, it shows that the textured surface showing four peaks on the direction of (110), (002), (101) and (112), while the non-textured films only show on direction of the (110) and (002). Due to the excellent characteristics of this film, it should make the film very good TCO alternatives for the thin film silicon solar cell.

REFERENCES

[1] M. Yoshino, W. W. Wenas, A. Yamada, M. Konagai and K. Takahasi, Jpn. J. Appl. Phys. **32**, 726 (1993).

[2] D. E. Brodie, R. Singh, J. Morgan, J. D. Leslie, C. J. More and E. E. Dixon, *Proceeding of the 12th IEEE Photovoltaic Specialists Conference* (New York, 1980), p. 468.

[3] J. Song, I.-J. Park, K.-H. Yoon, W.-Y. Cho and K.-S. Lim, J. Korean Phys. Soc. **29**, 219 (1996).

[4] C. H. Lee, K. S. Lim and Jinsoo Song, Jpn. J. Appl. Phys. **36**, 4418 (1997).

[5] L.-J. Meng and M. P. dos Santos, Thin Solid Films **250**, 26 (1994).

[6] T. Minami, H. Sato, H. Imamoto and S. Takata, Jpn. J. Appl. Phys. **321**, L257 (1992).

[7] N. N. Murakami and A. Kunioka, Mat. Res. Soc. Symp. Proc. **426**, 411 (1996).

[8] W. W. Wenas, A. Yamada, M. Konagai and K. Takahashi, Jpn. J. Appl. Phys. **30**, L441 (1991).

[9] Anna Selvan, H. Keppner and A. Shah, Mat. Res. Soc. Symp. Proc. **426**, 497 (1996).

[10] Tokio Nakada, Yukiyasu Ohkubu, Naoki Murakami and Akio Kunioka, Jpn. J. Appl. Phys. **34**, 3623 (1995).

[11] Tokio Nakada, Yukinobu Ohkubo and Akio Kunioka, Jpn. J. Appl. Phys. **30**, 3344 (1991).

Journal of the Korean Physical Society, Vol. 34, June 1999, pp. S347~S349

Effect of Probe Contact Resistance on Precision Measurements of Sheet Resistance of Metallized Thin Films

Kwang Min YU, Kook Jin KIM, Ryu Je CHEON and Jeon Hong KANG

Korea Research Institute of Standards and Science, Taejon 305-600

We have developed a method to measure sheet resistances and contact resistances of metallized thin films simultaneously and investigated the effect of probe contact resistance on precision measurements of sheet resistances of the films because it is essential to make precision measurements of sheet resistance in order to determine dose and thickness uniformity of the films. We found there being a linear relation between them, so that contact properties directly effects on precision measurements of sheet resistance, that is, uniformity of the films. This results also have physical meaning that have similiar trends to spreading resistance method to determine sheet resistances from contact resistance measurements

I. INTRODUCTION

Dual configuration method [1–3] of four-point probe technique in sheet resistance measurements is applied to dose uniformity and thickness uniformity monitoring of metallized thin films and semiconducting layers because of its higher precision and reproducibility than single configuration. Sheet resistances by these two methods is defined as electrical resistivity divided by sample thickness and the equations to obtain sheet resistance by the two configurations are as followings.

$$\text{In single configuration, } R_S = K_a \cdot R_a \quad (1)$$

(K_a : geometrically dependent − correction factor)

$$\text{In dual configuration, } R_S = K_a \cdot R_a, \quad (2)$$

$$(K_a = -14.696 + 25.173(R_a/R_b) - 7.872(R_a/Rb)^2)$$

(Here R_a and R_b is resistance values)

In single configuration, K_a is directly related to probe spacing, thickness, and diameter, but in dual configuration it is only related to resistance values to be measured and it can be known that dual configuration method is more precise than single configuration method. And also, while it is known that the characteristics of probe head is related to the reproducibility of the two configuration method, it is little known about probe contact effect on the reproducibility. From the last decades to the present, spreading resistance probe technique [4] which measure sum of mechanical contact resistance and current-spreading resistance have been studied to obtain electrical resistivity and electrical resistivity is used in analysing impurity concentrations of semiconductors and materials to have high resistance values, and now the method is applied to electrical characterization for semiconducting devices of very small scale. In the method spreading resistance means probe contact resistance described here and the spreading resistance is electrical resistivity divided by contact area and linearly-dependent on electrical resistivity. In the method, sheet resistance, electrical resistivity divided by thickness of sample, is obtained by measuring contact resistance and so it is interesting to verify the relation between the contact resistance and sheet resistance and also their dependence on the measurement reproducibility of sheet resistance. Therefore, we intend to describe the effect of probe contact resistance on precision measurements of sheet resistance of metallized thin films by simultaneously measuring method of sheet resistances and probe contact resistances to sample surfaces.

II. SIMULTANEOUS MEASUREMENT METHOD OF PROBE CONTACT RESISTANCE AND SHEET RESISTANCE

Here the arrow means each pin of a four-point probe and total 12 resistance measurements are carried out by switch selections through configuration (a) and (b).

$$C1+C4=b,\ C2+C3=a,\ C2+C4=c,$$
$$C1+C3=d,\ C1+C2=f, C3+C4=e, \quad (3)$$
$$a=R(8)-R(1),\ b=R(7)-R(2),\ c=R(10)-R(3),$$

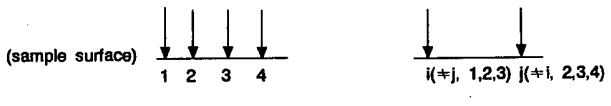

Fig. 1. Contact shape to measure probe contact resistance and sheet resistance simultaneously.

$$d=R(9)-R(4),\ e=R(12)-R(5),\ f=R(11)-R(6), \quad (4)$$

$$C1=(b+d-e)/2, C2=(2f-b+e-d)/2,$$

$$C3=(d-b+e)/2, C4=(b+e-d)/2 \quad (5)$$

Here Ci means each probe contact resistance, $R(A)$ (A=1~6), resistance values from 6 switch selections of configuration (a), and $R(B)$ (B=7~12), resistance values from 6 switch selections of configuration (b). Each $R(A)$ is obtained by current supply through outer two probes and voltage measurements between inner two probes and also $R(B)$ is resistance values between two positions i and j, each position being the superposition of one current probe and one voltage probe. From the 12 switch selections we can measure sheet resistance and probe contact resistance against sample surface simultaneously.

III. EXPERIMENTAL APPARATUS

As shown in figure 2 we used probe station of Napson RT-8A-8 (Japan-made) and high insulation-constant current source of Burster 6426 (Germany-made) with 0.1 % accuracy, digital voltmeter of Datron 1281 (U.S.A-made) with 0.001 % accuracy, and four-point probe head (Jandel of U.K, tip material:tungsten carbide, tip radius : 100 μm, tip pressure : 100 g, probe spacing : 1.596 mm) to measure sheet resistance and probe contact resistance simultaneously. Total systematic uncertainty of sheet resistance measurements by dual configuration method is 0.1 % and by single configuration is 0.5 % from rot-sum-square (RSS) estimation of geometrical correction accuracy and instrument accuracy.

IV. RESULTS AND DISCUSSIONS

As samples we used TiN film of 0.11 μm thickness on silicon oxide layer of 0.1 μm, tungsten-silicide film of 0.2 μm thickness on the same layer and $POCl_3$ gas-diffused polysilicon of 0.22 μm thickness. For each of these sample we measured sheet resistance 10 times by single and dual configuration method and probe contact resistance

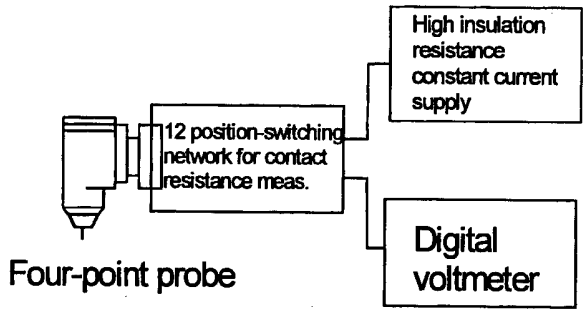

Fig. 2. Block diagram of sheet resistance and probe contact resistance measurement system.

Table 1. Sheet resistance and probe contact resistance values of metallized thin films.

Sample	r_1 (ohm)	r_2 (ohm)	r_3 (ohm)	r_4 (ohm)	sheet resistance (ohm/sq)	
					single conf.	dual conf.
WSi_X	70.4	37.8	47.8	49.3	52.22	52.49
	0.9 %	1.9 %	3.8 %	2.9 %	0.12 %	0.04 %
TiN	162.9	90.4	103.6	111.1	132.21	132.30
	0.25 %	0.26 %	0.31 %	0.39 %	0.04 %	0.005 %
$POCl_3$	92.7	52.0	60.6	64.6	72.71	72.86
	1.0 %	1.2 %	1.4 %	1.3 %	0.08 %	0.02 %

Table 2. Ratios of probe contact resistance to sheet resistance.

Sample	r_1/R_S	r_2/R_S	r_3/R_S	r_4/R_S
WSiX	1.3	0.7	0.9	0.9
TiN	1.2	0.7	0.8	0.8
$POCl_3$	1.3	0.7	0.8	0.9

of each 4 probe using the method mentioned above and measurement results are as followings.

Here, r_1, r_2, r_3, r_4 means probe contact resistance and lower values of each number are estimated standard deviation of each 10 measurements and R_S means sheet resistance values

As shown in Table 1, when measurement precision of probe contact resistance is increasing, that of sheet resistance is also increasing and the ratios of probe contact resistance to sheet resistance have linear relation as shown in Table 2. This result is similar to linear relation of spreading resistance to sheet resistance.

V. 5. CONCLUSIONS

we have developed a method to measure sheet resistance and probe contact resistance simultaneously and investigated the effect of probe contact resistance on precise sheet resistance measurements of metallized thin films and semiconducting layers. We found that sheet resistance values by dual configuration method have a linear dependence on probe contact resistances, and which is similar to the results of spreading resistance method and we also found resistance measurement precision by dual configuration have nearly the same change rate as that of probe contact resistance. Based on these results we intend to compare and analyse the results by the above four-point probe method and that by spreading resistance method in the near future.

REFERENCES

[1] J. R. Ehrstein and M. C. Croarkin, The Certificate of

100 mm Diameter Silicon Resistivity SRMs 2541 through 2547 Using Dual-Configuration Four-Point Probe Measurements, NIST (formerly NBS) SP 260-131 (1997).

[2] ASTM F 1529-94, Standard Test Method for Sheet Resistance Uniformity Evaluation by In-Line Four-Point Probe with the Dual-Configuration Procedure (1994).

[3] D. S. Perloff, *etc.*, Dose Accuracy and Doping Uniformity of Ion Implantation Equipment, Solid state Tech. **24**, 112 (1981).

[4] ASTM F 525-88, Standard Test Method for Measuring Resistivity of Silicon Wafers Using a Spreading Resistance Probe (1994).

Journal of the Korean Physical Society, Vol. 34, June 1999, pp. S350~S354

Effects of RF Plasma Parameters on the Growth of InGaN/GaN Heterostructures Using Plasma-Assisted Molecular Beam Epitaxy

K. H. SHIM, M. C. PAEK, K. H. KIM, S. U. HONG and K. I. CHO

Wide Bandgap Semiconductors Team, Microelectronics Technology Laboratory, Electronics and Telecommunications Research Institute, Taejon 305-350

H. G. LEE

School of Electrical and Electronic Engineering, Chungbuk National University, Chongju 361-763

J. KIM

Department of Materials Engineering, Hoseo University, Asan 336-795

The effects of rf plasma power on the structural/optical properties of GaN-based nitride epilayers grown by plasma-assisted molecular beam epitaxy have been investigated. Atomic force microscopy and high-resolution x-ray diffraction analyses revealed that the sharp interface of $In_{0.2}Ga_{0.8}N$/GaN heterostructures could be obtained by suppressing the surface roughening at high rf power. Photoluminescence data suggested that the formation of damaged subsurface due to energetic particles was alleviated in the InGaN growth in comparison with the GaN growth. In our experimental set-up, the rf power of 400 W appeared to properly suppress the 3D island formation without causing defects at the subsurface of $In_{0.2}Ga_{0.8}N$. The phenomena associated with the indium incorporation could be explained by an inequality with two kinetic processes of the surface diffusion and the plasma stimulated desorption.

I. INTRODUCTION

Recently, lots of achievements have been accomplished in the field of GaN-based nitride semiconductors by remarkable breakthroughs in epitaxial growth technology, especially in metallic organic chemical vapor deposition [1]. Similarly, plasma assisted molecular beam epitaxy (PAMBE) has demonstrated useful results along with its advantageous features such as plasma-assisted processes and atomic layer growth. However, the development of GaN-based epilayers using PAMBE has been hindered by uncertainty about the effect of the plasma parameters on film quality and inadequate control of the energetic species in the nitrogen plasma. Meanwhile, the application of very low energy ion beams of a few tens of eV have focused on the modulation of surface reaction kinetics, strain relaxation, and island formation [2–4]. Despite the relevant role of plasma parameters, relatively few articles have focused on the study of plasma parameters in GaN epilayers using PAMBE [5–7]. A fundamental understanding of the interactions of low-energy ions with semiconductor surfaces would enable the tradeoff between damage production and surface enhancement.

The objective of this study is to understand the effect of the rf power on the growth of GaN-based epilayers by exploring correlations between the structural/optical properties and the rf plasma parameters. Our experimental results on $In_{0.2}Ga_{0.8}N$/GaN superlattice (SL) structures provide a framework for understanding the complicated role of plasma parameters on the growth of GaN-based heterostructures.

II. EXPERIMENT

Shown Fig. 1 is the schematic of a PAMBE system modified for the growth of GaN-based wide bandgap semiconductors including SiC. Nitrogen plasma was generated using an inductively coupled rf plasma source (SVT). After the conventional solvent cleaning and etching processes, 20-nm-thick AlN buffer layers were grown on sapphire (0001) at 500 °C. Then GaN epilayers were grown at 720 °C and followed by the growth of ten periods of $In_{0.2}Ga_{0.8}N$/GaN (25/50 Å) at 670 °C. The growth chamber maintained 7×10^{-5} torr for whole growth process. The surface structure of epilayer was monitored by in-situ reflection high energy diffraction (RHEED) and the quality of obtained epilayers was characterized by

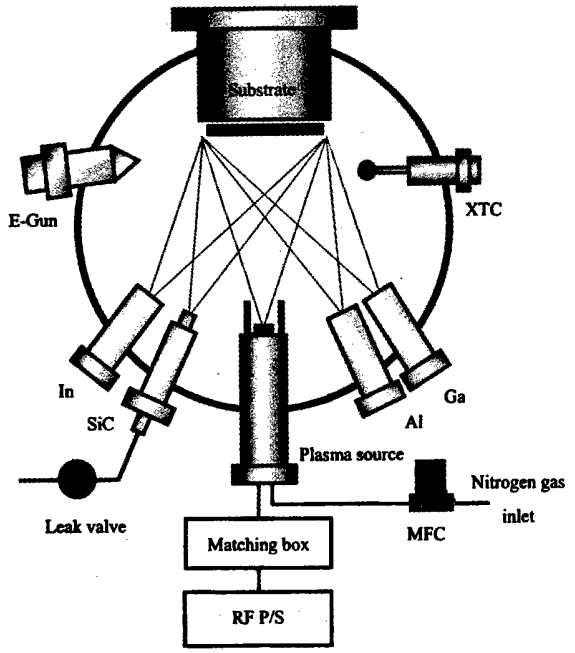

Fig. 1. Schematic diagram of the PAMBE system equipped with a nitrogen plasma source, an electron gun, and several effusion cells. The rf plasma source is designed to deflect the charged particles ejecting from a PBN nozzle, to prohibit ions from arriving at the surface of epilayers.

atomic force microscopy (AFM), high resolution x-ray diffraction (HR-XRD), and low-temperature (LT) photoluminescence (PL). HR-XRDs using a triple axis diffraction (TAD) method were measured in the θ-2θ mode as well as ω-rocking curve mode using CuK_α radiation at voltage 50 kV and current 140 mA. Other experimental details can be found elsewhere [8].

III. RESULTS AND DISCUSSION

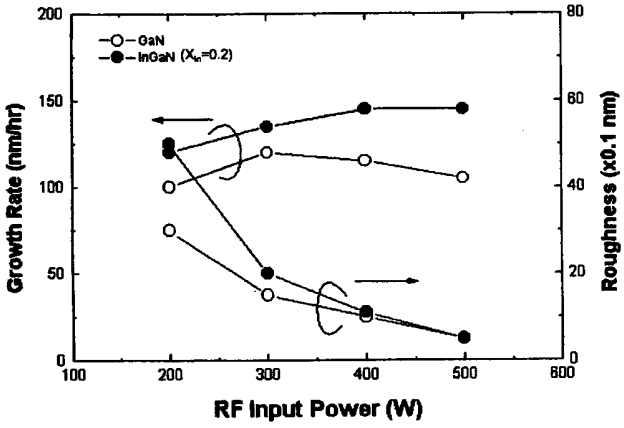

Fig. 2. Growth rate and roughness data plotted as a function of rf input powers for GaN [9] (open circles), and $In_{0.2}Ga_{0.8}N$ (closed circles).

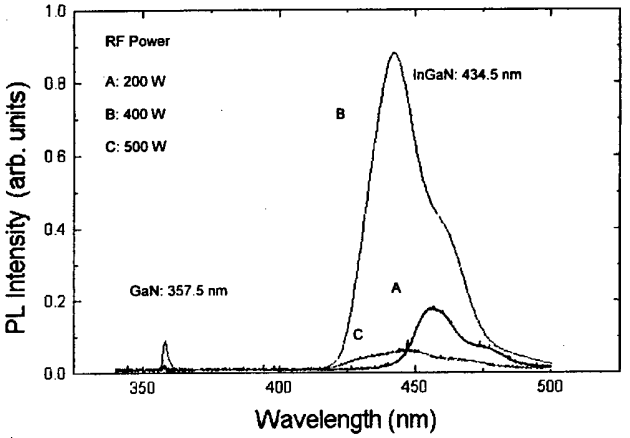

Fig. 3. LT-PL spectra measured at 13 K from InGaN/GaN superlattice samples grown with the rf input powers of 200, 400, and 500 W.

Growth rates and root mean square (rms) roughness data are plotted in Fig. 2 as a function of the input rf power. The typical, panoramic features of PAMBE are well identified from the data on GaN. The flux of reactive nitrogen looks sufficient at around 300 W and the plasma stimulated desorption reduces the growth rate at higher rf power levels. The surface roughness shows a significant fall at low rf power and decreases monotonously above 300 W. The characteristic behaviors are closely related to the energy and flux of energetic particles being governed by the rf power level. Two distinctive features are found in InGaN growth: the growth rate above 400 W saturates to 145 nm/hr and the roughness of InGaN at 200 W is roughly two folds of GaN. These differences are discussed below in conjunction with a kinetic process in PAMBE, the plasma-stimulated desorption.

InGaN/GaN SLs were prepared to investigate the effect of rf powers on the optical transitions in InGaN quantum wells. Shown Fig. 3 represents the PL spectra for the samples grown with 200, 400, and 500 W. Among the spectra, the sample B grown with 400 W reveals much better optical properties than the other spectra in terms of high emission efficiency and peak positions as well. It was previously observed that the PL emission in GaN epilayers was substantially degraded above 300 W [9]. The strong light emission at 400 W indicates that the critical ion energy producing defects in InGaN was slightly higher than that in GaN. These differences are presumably attributed to the indium incorporation, which is to modify reactions at growth fronts and crystal quality as well.

From the separation between InGaN peaks of A and B, ~90 meV, the carrier concentration in the sample A was calculated as high as 8×10^{19} cm^{-3} [10]. Instead, the carrier concentration in the sample B was in the range of low 10^{18} cm^{-3}, which is comparable to the level of carrier concentration excited by laser illumination. The data indicate that plenty of donor and acceptor centers were

Table 1. Lattice constants (a, c); binding energy between group III and nitrogen atom, E_{III-N}; threshold ion energy causing defects at subsurface, E_c; surface energy, γ; surface diffusion coefficient of group III adatoms, D_s; decomposition temperature, T_d; and nitrogen flux, ϕ_{N2}, decomposing from surfaces of AlN, GaN, and InN [9,14,16].

	AlN	GaN	InN
a_{epi} (Å)	3.112	3.189	3.544
c_{epi} (Å)	4.982	5.185	5.718
E_{III-N} (eV)	2.88	2.2	1.93
E_c (eV)	16.5	15	17
γ (erg cm^{-2})	2,747	2,098	1,416
D_s (cm^2 s^{-1})	–	0.007exp(-2.48/k_BT) on (0001) plane	–
ϕ_{N2} (cm^{-2} s^{-1})	3.6×10^{31} exp(-4.29/k_BT)	1.2×10^{31} exp(-3.93/k_BT)	3.7×10^{31} exp(-3.48/k_BT)
T_d (°C)	1040	850	630

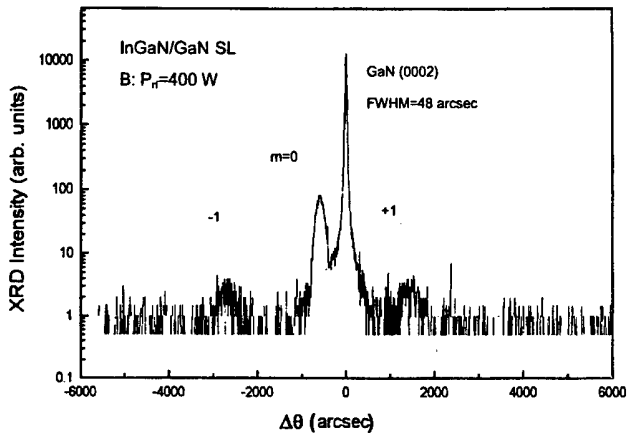

Fig. 4. HR-XRD spectra from InGaN/GaN superlattice structures, measured using the TAD method. The FWHM 48 arcsec is much smaller than 720 arcsec measured from a rocking curve obtained using a double axis diffraction method, in which the peaks were not separable. The angular separation of adjacent satellite peaks (m=−1, 0, +1) is related to the period of the superlattice structures.

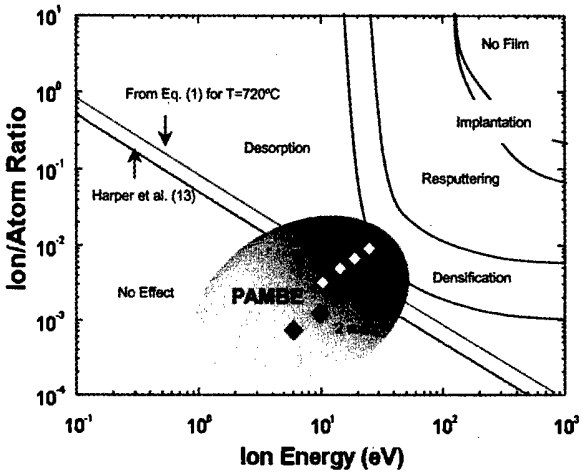

Fig. 5. Schematic of various kinetic processes occurring by the ion bombardment as a function of ion energy and the ion/atom flux ratio [9]. The low limit of ion effects, a solid line was obtained by Harper et al. in experiments for various metallic films [13]. The shaded area indicates the typical growth conditions of PAMBE, where the open and closed diamonds are the specific points for 1 and 2 sccm nitrogen gas flow, respectively, with the increase of rf input powers from 200 to 500 W with the interval of 100 W. The dotted line for GaN is the inequality crossovers of thermal and kinetic processes, approximated from Eq. (1) for T=720 °C.

produced in the sample A due to its nitrogen deficiency condition. Meanwhile, the peak position of InGaN in the sample C remains at the same energy level as in the sample B regardless substantial degradation in transition efficiency.

HR-XRD measurements were performed in order to investigate the crystalline quality of the samples. The lattice constants of GaN were measured to be very close to that of bulk GaN listed in Table 1, c=5.183 Å. We also observed that the increased energy and flux of nitrogen ions led to a preferred orientation structure and that the 2D planar growth enhanced at high rf power. The sharp and strong diffraction peaks were obtained from highly crystalline GaN epilayers grown with 300∼400 W. The HR-XRD spectrum in Fig. 4 shows GaN (0002) peak with the full-width at half maximum (FWHM) as small as 48 arcsec and three diffraction peaks due to the InGaN/GaN superlattice, noted as m=−1, 0, and +1. The measured period of SLs from the separation between satellite peaks was same as designed, 75 Å. In addition, the peak position of InGaN, θ_{InGaN}=17.184°, gives its lattice constant 5.212 Å from an equation, $c_{InGaN}=\lambda/\cos\theta_{InGaN}$. The lattice constant of $In_{0.2}Ga_{0.8}N$ is estimated as 5.292 Å and, then, the compressive strain in InGaN epilayer is obtained as 1.5 %. This residual strain less than the original strain 2 % between InGaN and GaN, indicates that the InGaN epilayers were partially relaxed. Meanwhile, from transmission electron microscopy observations, we found that dislocations were not newly initiated at the interface of InGaN and GaN. This confirms that the thickness of InGaN was less than the critical thickness, 7.6 nm, calculated from a theoretical estimation using a Matthew and Blakeslee model, so that the relaxation occurred in elastic deformation.

Various process regimes due to ion bombardments are distinguished in Fig. 5 as a function of ion energy and

ion/atom flux ratio [11–13]. According to our previous work, the operational conditions of PAMBE, the shaded area is placed at a broad range near to the surface desorption. The solid line in Fig. 5, determined by Harper *et al.* from experimental results on various metallic films, divides the lowest limit of ion bombardment [13]. A few works regarding the effect of ion beam bombardment on the epilayer growth support our experimental results. Their data involving energetic particles often reveal discrepancies, which are particularly subject to the substrate materials, reactive particles, and plasma parameters affecting the energy and flux of ions. The stress accumulated by the lattice mismatch between adjacent epilayers is known to cause 2D-to-3D transitions. This surface roughening must be either promoted by surface diffusion or relieved by plasma stimulated-desorption.

The nucleation behavior of 3D islands is described using kinetic rate equations consisting of forward and reverse reactions. The effects of ion-induced displacement on the nucleation rate can be estimated by adding a term for the breakup of the critical size nuclei. The forward reaction of nucleation which occurs by the direct impingement of Ga and the diffusion of single adatoms with surface density n_1 to critical-sized clusters with surface density n_{cr} is rate limited by thermal and plasma-stimulated desorption, using an ion beam with energy E_i and flux J_i. The desorption rate is given by $r = n_a(1/\tau_{th} + BE_iJ_i)$, in which na is the number density of adsorbed atoms, τ_{th} is the average residence time of the adatoms influenced by the thermal energy, and a constant B ($=4.4\times10^{-15}$ cm^2/V for GaN) is the plasma stimulated desorption yield per ion [9,14–16]. Then the reaction rate can be expressed as;

$$\frac{\partial n}{\partial t} = [F_iA + \sigma D n_1]n_{cr} - \left[\frac{1}{\tau_{th}} + BE_iJ_i\right] N_sAn_{cr+1}, \quad (1)$$

where F_i is the flux of incoming Ga atoms, N_s is the surface atomic density, A is the average surface area covered by a stable nucleus ($\sim10^{-14}$ cm^{-2}), and σ is a geometrical factor describing adatom diffusion to critical islands, typically 2~4.

After abbreviation by fixing the flux and the substrate temperature same, the inequality to suppress 3D nucleation is $\sigma D/A<BE_iJ_i$. Using $D_s=0.007\exp(-2.48/k_BT)$ for Ga in Table 1 and $\sigma=2$, the inequality is satisfied when $E_iJ_i > 3\times10^{13}$ eV cm^{-2} sec^{-1} for the substrate temperature of 720 °C.

The dotted line in Fig. 5 represents the inequality line for the GaN growth at 720 °C. The inequality crossover exists apparently near to the solid line. As discussed above, *in-situ* RHEED patterns showed streaky lines at high rf power level and the morphology of resulting epilayers turned out to be smooth with small roughness values. For InGaN, the diffusion term in Eq. (1) looks predominant at the low rf power regime and resulted in very rough surface morphology as shown in Fig. 2. Currently, the same consideration as GaN may be applied to the InN growth. Nevertheless it is believed that the inequality line for InGaN would exist above the dotted line because of high diffusivity and large mass of indium.

Unlike the structural properties, the optical properties of epilayers would be more likely depending on the ion energy than its flux. The displacement energy of bulk atoms, $E_b \sim 24$ eV, is approximated as three times of the cohesive energy for GaN. Since the surface atoms are less tightly bound by a factor of two than atoms in the bulk, *i.e.*, lower coordination numbers, the displacement energy of surface atoms is approximated as $E_s \sim 12$ eV. The threshold energy E_{th} for displacement is given by $E_{th} = E/\gamma$, where the ratio, γ, indicates the recoil energy transfer efficiency, and given by $\gamma = 4M_1M_2/(M_1+M_2)^2$, where M_1 and M_2 are the mass of the projectile and the target atom. That is, γ=1.0, 0.82, and 0.63 for AlN, GaN, and InN, respectively. By employing critical energies for the displacement of atoms at subsurface, the threshold energy of particles for defect formation at the subsurface are estimated as 16.5, 15, and 17 eV for AlN, GaN and InN, respectively.

Above considerations show that ions with energy <15 eV alter surface kinetics without causing bulk damage. The rf powers corresponding to 15 eV are 300 and 400 W for 1 and 2 sccm nitrogen gas flow, respectively. Considering the Boltzman distribution of ion energy, the average ion energy less than 15 eV looks safe for the high quality, defect free film growth. Consequently, the strong PL emission in Fig. 3 could be achieved from the InGaN/GaN grown with 400 W. The influence of ion bombardment may be excluded by raising the growth temperature. However, the thermal generation of nitrogen vacancy due to surface decomposition appears as a limiting factor again, as noted T_d in Table 1. In reality, the PAMBE system in Fig. 1 is equipped with a pair of electrodes, which is designed to deflect charged particles ejecting through a PBN nozzle. The electrical bias above 300 V prohibits charged particles from arriving at the surface of epilayers. Our observations suggest that the growth with high rf power is beneficial for the growth of flat buffer layer and that the removal of energetic particles for the growth of active layer requiring high optical properties. Experimental results about the growth with the removal of energetic particles will be discussed in a separate issue.

IV. CONCLUSIONS

We have investigated the effect of the rf plasma power on kinetic processes and the structural/optical properties of $In_{0.2}Ga_{0.8}N$/GaN superlattice grown by PAMBE. AFM and HR-XRD data demonstrated that the interface of $In_{0.2}Ga_{0.8}N$/GaN heterostructures was significantly improved by the bombardment of energetic particles sup-

pressing 3D island formation. PL data revealed that the influence of energetic particles on $In_{0.2}Ga_{0.8}N$ growth was substantially alleviated in comparison with GaN. In our experimental set-up, the rf power of 400 W appeared to properly suppress the 3D island formation without causing defects at the subsurface of $In_{0.2}Ga_{0.8}N$ epilayers. The phenomena associated with the indium incorporation could be properly explained by the inequality consisting of the surface diffusion and the plasma stimulated desorption.

ACKNOWLEDGMENTS

The support of the Ministry of Information and Communications of Korea in this work is gratefully acknowledged. The authors thank J. B. Park at KMAC for his TEM analysis and Dr. C. S. Lee at KRISS for HR-XRD measurements.

REFERENCES

[1] S. Nakamura, M. Senoh, S. Nagahama, N. Iwasa, T. Yamada, T. Matsushita, H. Kiyoku, Y. Sugimoto, T. Kozaki, H. Umemoto, M. Sano and K. Chocho, Appl. Phys. Lett. **72**, 211 (1998).

[2] C. J. Tsai, H. A. Atwater and T. Vreeland, Appl. Phys. Lett. **57**, 2305 (1990).

[3] C. H. Choi and S. A. Barnett, Appl. Phys. Lett. **55**, 2319 (1989).

[4] S. A. Barnett, C. H. Choi and R. Kaspi, Mat. Res. Soc. Symp. Proc., 201 (1991).

[5] M. S. H. Leung, R. Klockenbrink, C. Kisielowski, H. Fujii, J. Kruger, Sudkier G. S., A. Anders, Z. Liliental-Weber, M. Rudin and E. R. Weber, Mater. Res. Soc. Symp. Proc. **449**, 221 (1997).

[6] H. Fujii, C. Kisielowski, J. Krueger, M. S. Leung, R. Klockenbrink, M. Rubin and E. R. Weber, Mat. Res. Soc. Symp. Proc. **449**, 227 (1997).

[7] M. Yeadon, F. Hamdani, G. Y. Xu, A. Salvador, A. E. Botchkarev, J. M. Gibson and H. Morkoc, Appl. Phys. Lett. **70**, 3023 (1997).

[8] K. H. Shim, J. M. Myoung, O. Gluschenkov, K. Kim, C. Kim and I. Robinson, Jap. J. of Appl. Phys. Lett. **37**, 313 (1998).

[9] K. H. Shim, Ph.D. Thesis, The University of Illinois at Urbana-Champaign, 1997.

[10] Donor energy level in semiconductor is expressed as $E_D = E_{DA} - E_{eA} - kT/2 + \alpha n^{1/3}$, where α=2.1×10^{-8} eV cm, $\Delta E_{DA} = E_{DA}(B) - E_{DA}(A) \sim 90$ meV $\Delta n = n(B) - n(A) \sim 8 \times 10^{19}$ cm^{-3}.

[11] W. J. Varhue, J. L. Rogers, P. S. Andry and E. Edams, Appl. Phys. Lett. **68**, 349 (1966).

[12] M. V. R. Murty, H. A. Atwater, A. J. Kellock and J. E. E. Baglin, Appl. Phys. Lett. **62**, 2566 (1993).

[13] J. M. E. Harper, J. J. Cuomo and H. T. G. Hentzell, Appl. Phys. Lett. **43**, 547 (1983).

[14] R. C. Powell, N. E. Lee, Y. W. Kim and J. E. Greene, J. Appl. Phys. **73**, 189 (1993).

[15] J. A. Venables, G. D. T. Spiller and M. Hanbucken, Rep. Prog. Phys. **47**, 399 (1984).

[16] O. Ambacher, M. S. Brandt, R. Dimitrov, T. Metzger, M. Stutzmann, R. A. Fischer, A. Miehr, A. Bergmaier and G. Dollinger, J. Vac. Sci. Technol. **B14**, 3532 (1996).

Journal of the Korean Physical Society, Vol. 34, June 1999, pp. S355~S358

Growth of Polycrystalline GaN and InGaN on Various Substrates

Doo-Cheol PARK, Shizuo FUJITA and Shigeo FUJITA

Department of Electronic Science & Engineering, Kyoto University, Kyoto 606-8501, Japan

Hyun-Chul KO

Venture Business Laboratory, Kyoto University, Kyoto 606-8501, Japan

On the various substrates of silicon (001), fused-silica glass and indium tin oxide (ITO)/glass, polycrystalline GaN thin films have been grown by RF plasma enhanced chemical vapor deposition (PECVD). X-ray diffraction (XRD) measurements revealed that introduction of low temperature GaN buffer layer made the main GaN layer to be sticky and stable, and the main GaN layers were oriented in (0002) planes. Polycrystalline $In_xGa_{1-x}N$ thin films on ITO/glass substrates were also grown by RF PECVD. XRD measurement revealed that the (0002) and ($10\bar{1}1$) planes were detected and the 2θ angles of the planes shifted to the lower angles with increasing the In vapor ratios. Optical absorption measurements indicated that the absorption band edges of the films shifted to the lower energy with increasing of In solid compositions.

I. INTRODUCTION

GaN-based heteroepitaxial structures grown on sapphire substrates by metalorganic vapor phase epitaxy (MOVPE) method have become the most promising material for the blue/ultraviolet light emitters [1]. Although a sapphire substrate is highly lattice mismatched with the GaN epitaxial layer and this gives rise to high density of dislocations, the GaN based structures have shown the high quantum efficiency. Recently, Iwata *et al.* successfully fabricated polycrystalline GaN thin films on fused-silica quartz substrates by molecular beam epitaxy (MBE). The samples grown at 750 °C showed a strong photoluminescence (PL) emission peak without deep level emission at room temperature (RT) [2]. Other group has attempted the use of conventional silicate glass substrates, where the growth temperature should be lower than the strain points of the glass (*e.g.*, 600~670 °C). Radio-frequency (RF) reactive evaporation was applied for the growth of polycrystalline GaN, and the result showed that the GaN films grown on the glass substrate at low temperatures have the possibility of large-area device applications [3].

RF plasma enhanced chemical vapor deposition (PECVD) is one of the suitable methods for growing polycrystalline GaN thin films on the non-crystalline substrates such as glass because the growth temperature can be lowered owing to the decomposition of N_2 by RF plasma [4]. This technique also has been suitable for the fabrication of large area samples. Furthermore, this technique offers easy composition control of InGaN and other alloys and introduction of various impurities is possible by flow rate of source gases.

In this work, we report about growth of polycrystalline GaN and InGaN on the various substrates, *e.g.*, silicon for a crystalline substrate, fused-silica quartz glass and indium tin oxide (ITO) deposited on silicate glass for the non-crystalline substrates, by RF PECVD.

II. EXPERIMENTAL DETAILS

Silicon (001), fused-silica quartz glass, and silicate glass substrates (Corning code 1737) deposited with ITO thin films were used for growth of polycrystalline GaN and ITO/glass was also used for $In_xGa_{1-x}N$ thin films by RF PECVD. The growth equipment is schematically shown in Fig. 1. Trimethlyindium (TMIn) and triethlygallium (TEGa) with N_2 carrier gas were introduced close to the substrates and used for the In and Ga sources, respectively. Mass flow controllers (MFC) were used to control the flow rate of the sources with using N_2 bubbling gas. Inductively coupled plasma of N_2 generated at 13.56 MHz was utilized for the nitrogen source. The size of silicon and fused-silica quartz substrates was 10×10 mm^2. An ITO/glass substrate was 15×15 mm^2 in size and the thickness of the ITO film was about 1400 Å. The substrates were cleaned in organic solvents using conventional processes before introduction to the growth chamber. The typical sample structure consisted of the low temperature grown GaN buffer layer and the main GaN or $In_xGa_{1-x}N$ layer. The growth temperature of the buffer layer and main layers varied, depending on the different substrates, to obtain better quality of the main

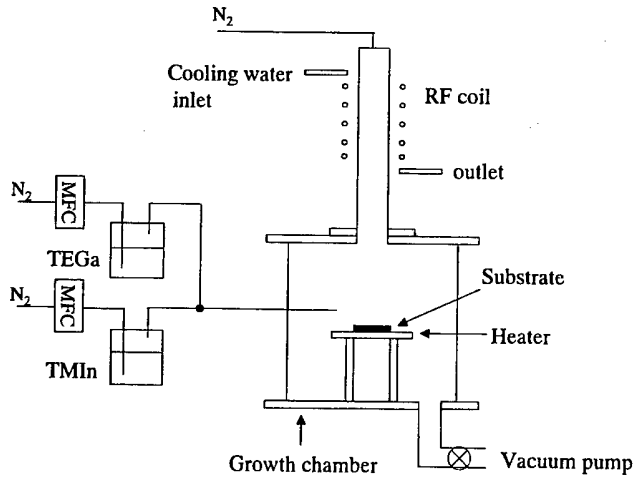

Fig. 1. Schematic diagram of RF plasma enhanced chemical vapor deposition (PECVD) equipment.

layers. However, we should have noted that the growth on an ITO/glass substrates must be done at the temperature sufficiently lower than the strain point (667 °C) of the silicate glass. The growth experiments of $In_xGa_{1-x}N$ were done on the ITO/glass substrates. The main layer was grown by varying the TMIn and TEGa vapor ratios at the growth temperature of 500 °C.

The thickness of the buffer layer was typically 250 Å and that of the main GaN or $In_xGa_{1-x}N$ layer was about 1.0 μm. The structural characterization of the samples was carried out by X-ray diffraction (XRD), and their optical properties were characterized by absorption using a deuterium lamp. Surface morphologies were observed by Nomarski interference microscopy.

III. RESULTS AND DISCUSSIONS

1. Growth of Polycrystalline GaN

a. Structural Characteristics

Figure 2 shows the XRD measurements of GaN thin films grown on (a) silicon, (b) fused-silica quartz glass, and (c) ITO/glass substrates. In Fig. 2(a), the buffer GaN layer and the main layer were grown on silicon at 400 °C and 650 °C, respectively. The sample without buffer GaN layer does not show any XRD peaks of the crystal planes comparing with that having the buffer layer showing highly oriented (0002) planes. Fig. 2(b) indicates the results on fused-silica quartz glass substrates, which show the XRD peaks originating from (0002) and $(10\bar{1}1)$ planes in the sample that has the buffer layer. Here, the growth temperatures were 250 °C and 650 °C for the buffer and main GaN layers, respectively. Fig. 2(c) shows the results on the ITO/glass substrates, which reveal the similar tendency with other substrates. Only

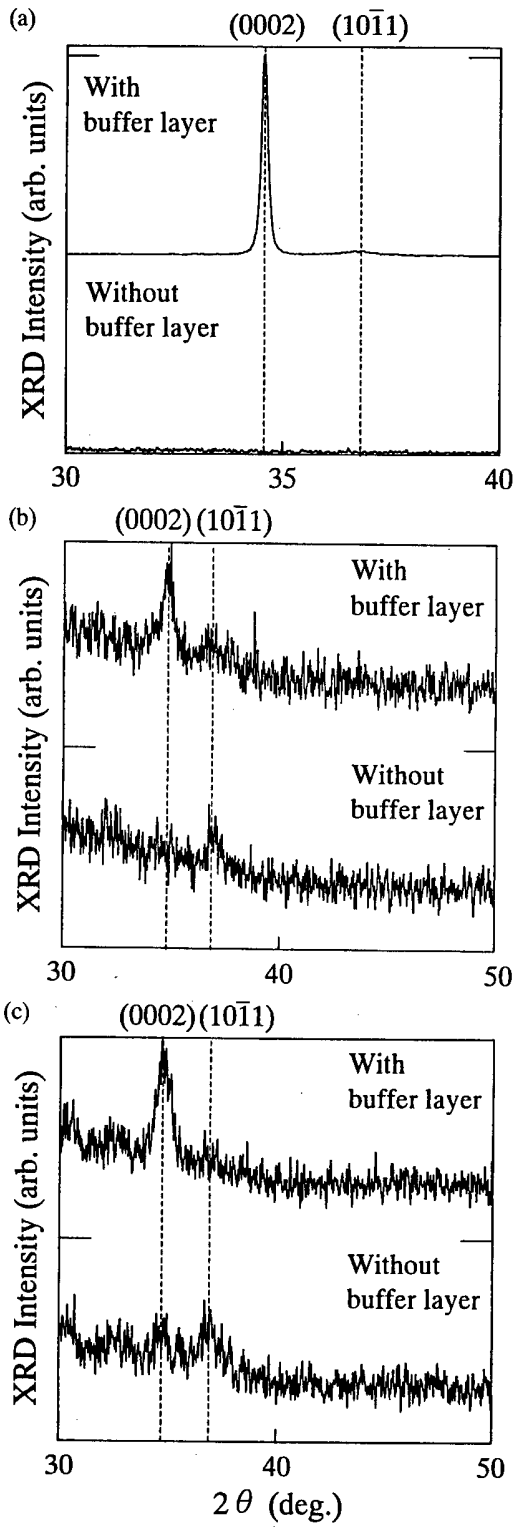

Fig. 2. XRD patterns of the GaN thin films grown on (a) silicon, (b) fused-silica quartz glass, and (c) ITO/glass substrates with and without the GaN buffer layer.

but the growth temperatures (buffer layer; 200 °C, main layer; 500 °C) were lower than those on silicon and fused-silica glass substrates.

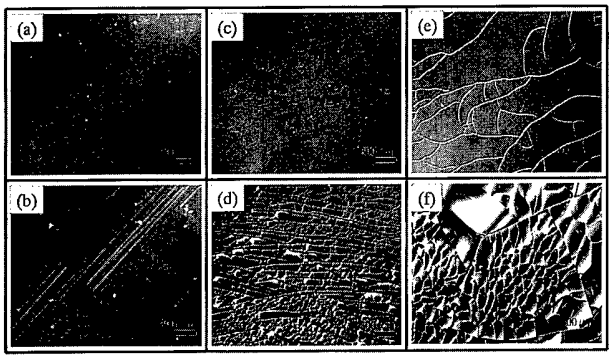

Fig. 3. Surface morphologies of the GaN thin films (a) with and (b) without buffer layer on silicon, (c) with and (d) without buffer layer on fused-silica quartz glass, and (e) with and (f) without buffer layer on the ITO/glass substrates observed by Nomarski interference microscopy.

As a result, in the growth of polycrystalline GaN thin film, introduction of GaN buffer layer was helpful for making crystallinity of main GaN layer better. Especially, the full width at half maximum (FWHM) in the crystalline substrate was much smaller than those in the non-crystalline substrates. Consequently, it is well consistent with that the buffer layer in the conventional growth of epitaxial GaN has been reported to play a role in producing a high quality sample with a flat and smooth surface [5,6].

b. Surface Morphology

Surface morphologies of GaN thin films grown on the various substrates with and without buffer layer observed by Nomarski interference microscopy are indicated in Fig. 3. The morphology of GaN grown on a silicon substrate without the buffer layer (Fig. 3(b)) shows many cracks oblique on the surface. Growth with the buffer layer (Fig. 3(a)) did not give any cracks on it. Figs. 3(c) and (d) show the morphologies of GaN grown on fused-silica quartz glass substrates with and without the buffer layer, respectively. In Fig. 3(d), many irregular strips are observed, on the contrary, only a few circle-like cracks are left in Fig. 3(d). In the case of GaN grown on ITO/glass substrates, Figs. 3(e) and (f) show the morphologies with and without the buffer layer. Many irregular cracks are observed in (f), however the cracks decrease extremely as being observed in (e). Consequently, the growth of the buffer layer was very helpful to make the surface to be sticky flat. The quality of the samples with growing the buffer layer was different with the substrates, *e.g.*, the one on a crystalline silicon substrate does not have so many cracks comparing with those on the non-crystalline substrates.

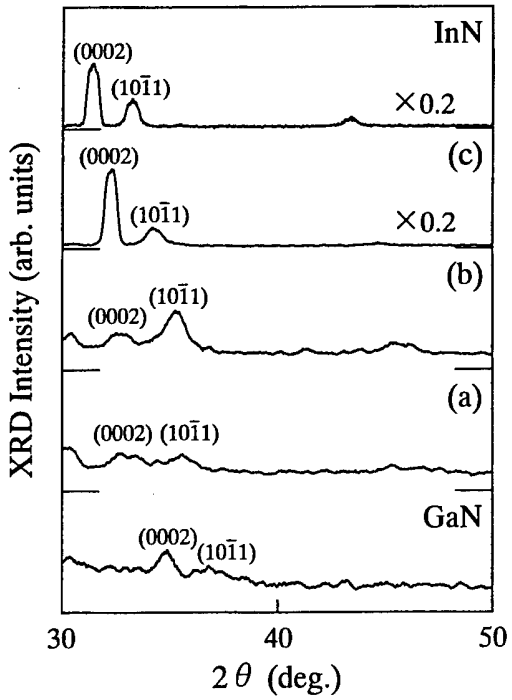

Fig. 4. XRD patterns of InN, GaN and $In_xGa_{1-x}N$ grown on ITO/glass with the indium vapor ratios of (a) 27 %, (b) 32 %, and (c) 52 %.

2. Growth of Polycrystalline InGaN

a. Structural Characterization by XRD Measurements

In Fig. 4, the results of XRD measurements of GaN, InN, and $In_xGa_{1-x}N$ thin films are shown. The growth conditions were that the RF plasma power of 200 W, N_2 flow rate of 40 sccm, and the growth temperature of 500 °C. For the growth GaN and InN, the flow rates of TEGa and TMIn were 0.43 μmol/min and 0.47 μmol/min, respectively. For the $In_xGa_{1-x}N$ thin films, the flow rates of TEGa and TMIn were controlled with MFCs and adjusted [TMIn]/([TEGa]+[TMIn]) to be between 0 and 1. The XRD result of GaN shows a peak at 2θ=34.54° which originates from (0002) planes, indicating *c*-axis orientation, and another peak at 2θ=36.9° originating from (10$\bar{1}$1) plane. The result of InN shows strong peaks at 2θ=31.4° and 33.2° which originate from (0002) and (10$\bar{1}$1) planes, respectively. With increasing of vapor ratios of TMIn from (a) 27 %, (b) 32 %, to (c) 52 %, the XRD peaks from (0002) and (10$\bar{1}$1) planes of $In_xGa_{1-x}N$ shifts to the lower 2θ angles. These results are explained by the well-defined correlation between Ga and In solid compositions in the films.

In solid composition in the film was calculated using Vegard's law from the lattice constants. In Fig. 5, the obtained In solid compositions x are shown against TMIn vapor ratios of [TMIn]/([TEGa]+[TMIn]) and lat-

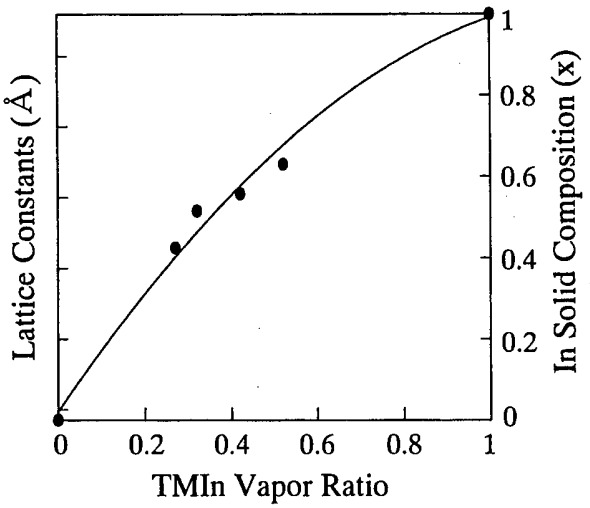

Fig. 5. Variations between TMIn vapor ratio, lattice constants and In solid composition.

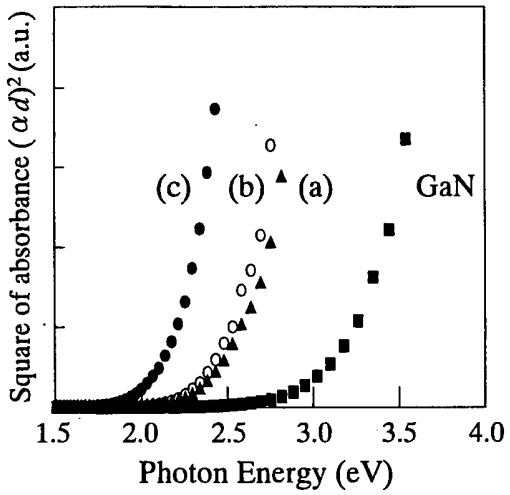

Fig. 6. Optical absorption measurements of $In_xGa_{1-x}N$ thin films of In solid compositions (x) (a) 42 % (solid triangles), (b) 52 % (hallow circles), (c) 63 % (solid circles) and GaN (solid rectangles) on the ITO/glass substrates grown at 500 °C.

tice constants. As increasing the TMIn vapor ratio, In solid composition increases with some bowing effects, which is similar to those often holds in many III-V compound structures [7].

b. Optical Absorption Measurements

In optical absorption measurements at RT, relations between the photon energy $h\nu$ and $(\alpha d)^2$, square of the product of absorption coefficient α and d of film thickness, are shown in Fig. 6. This plot is given assuming that the absorbance αd is proportional to $(h\nu - E_{edge})^{1/2}$ in direct transition, where E_{edge} is the absorption band-edge energy. Fig. 6 shows that the absorption band edge of GaN is about 3.25 eV and those of $In_xGa_{1-x}N$ are shifted to the lower energies as increasing the In solid compositions, *i.e.*, (a) 2.7 eV for x=42 % and (c) 2.23 eV for x=63 %. The calculated energy band gaps of single crystalline $In_xGa_{1-x}N$ are 2.76 eV and 2.45 eV for x=42 % and x=63 %, respectively, showing that the measured absorption band edges in this experiment are smaller than the energy bandgap. That is probably because of band tailings in polycrystalline InGaN films.

IV. CONCLUSIONS

Polycrystalline GaN thin films have been grown on the various substrates of silicon, fused-silica quartz glass and ITO/glass by RF PECVD. Growth of low temperature GaN buffer layer made the main GaN layer to be sticky and stable. XRD measurements revealed that GaN grown on non-crystalline substrates was oriented in the (0002) planes.

Polycrystalline $In_xGa_{1-x}N$ thin films on ITO/glass substrates were also grown by RF PECVD. The results of XRD measurement indicated that the (0002) and ($10\bar{1}1$) planes were oriented on the $In_xGa_{1-x}N$ films and the 2θ angles of the planes shifted to the lower angles with increasing the In vapor ratios. Results of optical absorption measurements showed that the absorption band edges of the samples shifted to the lower energy with increasing of In solid compositions. These results consistently indicate well-defined correlation between Ga and In solid compositions in the films.

ACKNOWLEDGMENTS

We wish to thank that D.-C. Park is partly supported by the grant from the International Communications Foundation (ICF).

REFERENCES

[1] S. Nakamura, IEEE J. Sel. Top. Quantum Electron. **3**, 435 (1997).
[2] K. Iwata, H. Asahi, K. Asami, R. Kuroiwa and S. Gonda, Jpn. J. Appl. Phys. **36**, L661 (1997).
[3] Y. Sato, A. Kurosaki and S. Sato, J. Crystal Growth **189/190**, 42 (1998).
[4] D. C. Park, H. C. Ko, Sz. Fujita and Sg. Fujita, Jpn. J. Appl. Phys. **37**, L294 (1998).
[5] H. Amano, I. Akasaki, K. Hiramatsu, N. Koide and N. Sawaki, Thin Solid Films **163**, 415 (1988).
[6] S. Nakamura, Jpn. J. Appl. Phys. **30**, L1705 (1991).
[7] S. Yoshida, S. Misawa and S. Gonda, J. Appl. Phys. **53**, 6844 (1982).

Journal of the Korean Physical Society, Vol. 34, June 1999, pp. S359~S363

GaN Epitaxial Growth on a Si(111) Substrate Using γ-Al_2O_3 as an Intermediate Layer

N. OHSHIMA*, A. WAKAHARA, M. ISHIDA, H. YONEZU, A. YOSHIDA,
Y. C. JUNG and H. MIURA

Department of Electrical and Electronic Engineering, Toyohashi University of Technology, Toyohashi 441-8580, Japan

An epitaxial growth process of GaN on gamma(γ)-Al_2O_3/Si(111) substrate was investigated by *in-situ* reflection high-energy electron diffraction (RHEED) and atomic force microscopy (AFM) observations. The γ-Al_2O_3 layer was epitaxially grown on a Si(111) substrate by molecular beam epitaxy (MBE) method and used as an intermediate layer. The thickness of γ-Al_2O_3 is about 2 nm and the surface morphology is almost flat structure. The GaN epilayer was regrown on the γ-Al_2O_3/Si(111) structure by radio frequency MBE. It is found that the GaN layer is epitaxially grown on γ-Al_2O_3/Si(111) substrate under the epitaxial relationship with $[11\bar{2}0]_{GaN}//[1\bar{1}0]_{\gamma-Al_2O_3/Si}$. It is considered that γ-Al_2O_3 layer is effective as the intermediate layer and hexagonal GaN layer succesfully grown on the γ-Al_2O_3/Si(111) structure.

I. INTRODUCTION

The III-V nitride semiconductors are promising materials for blue and ultra violetwavelength optoelectronic applications [1–3]. Many GaN-based applications of optoelectronic and electronic devices are demonstrated on sapphire and SiC substrates [4–8]. It is, however, difficult to obtain the large size and high quality GaN epilayer on a silicon (Si) substrate [9]. Devices formed on Si substrates have not yet been performed regardless of many advantages of Si such as high quality, large size, low cost and controllability of the conductivity [10,11]. The Si substrate is mismatched with GaN in the lattice constant and thermal expansion coefficient as same as sapphire. Therefore, it has been expected to grow a high quality GaN epilayer on Si using an appropriate buffer layer [12–18].

The lattice mismatch between Si and γ-Al_2O_3 is about 4 %. It was reported that a single γ-Al_2O_3 layer was epitaxially grown on Si(100) with mirror-like surface by low-pressure chemical vapor deposition (CVD) using $Al(CH_3)_3$ and N_2O gas sources [19,20]. T. Kimura *et al.* [21–23] reported that a single 90-nm-thick γ-Al_2O_3 layer with flat surface is obtained on the Si(100) by ultrahigh vacuum CVD using O_2 as the oxidation source gas [24–26]. In addition, it was reported previously that the single 2 nm-thick γ-Al_2O_3 layer is grown on Si(111) substrates by Al-N_2O mixed source molecular beam epitaxy (MBE) [26].

*E-mail: nohshima@eee.tut.ac.jp, Tel: +81-532-44-6746, Fax: +81-532-44-6757

In recent, it was reported that a thin GaN epilayer with the flat surface is successfully grown on a sapphire (0001) substrate using a-GaN buffer layer deposited at room temperature [27]. Therefore, it has been expected to grow a high quality h-GaN layer on Si substrate using the γ-Al_2O_3 epilayer as an intermediate layer. It is considered that the γ-Al_2O_3/Si(100) substrate is effective for an application combined with Si-ULSI technology. On the other hand, the surface of the γ-Al_2O_3/Si(100) substrate has a tetragonal symmetry because the crystal phase of γ-Al_2O_3 is a cubic one. Therefore, the γ-Al_2O_3/Si(111) substrate is more useful for the investigation of the growth process of h-GaN. However, the initial growth processes of h-GaN on γ-Al_2O_3/Si substrates have not been clarified [21,22]. In the present work, we have investigated the growth of GaN epilayer on the γ-Al_2O_3/Si(111) substrate by radio frequency (RF) MBE with *in-situ* reflection high-energy electron diffraction (RHEED) system.

II. EXPERIMENT

A growth apparatus for RF-MBE equipment with a RHEED system was used for *in-situ* observation of the growth process of GaN epilayers. Since details of the apparatus have been reported previously [27], only a brief outline is described here. A chamber was evacuated by an oil diffusion pump with a liquid N_2 trap, and the base pressure was 2×10^{-10} Torr.

The single γ-Al_2O_3 intermediate layers were epitaxially grown on Si(111) substrate by mixed source MBE

[25]. Thickness of γ-Al_2O_3 epilayer was about 2 nm. GaN layer was regrown on the γ-Al_2O_3/Si(111) structures by RF-MBE mentioned above. They were chemically cleaned with etching by dipping in a solution of HF:H_2O=1:50 before being set in the preparation chamber. After thermal cleaning of the surface for 10 min at 800 °C, the amorphous GaN buffer layer was deposited on the substrate at room temperature for 4 min under the condition of a N_2 flow rate of 0.5 sccm and a Ga flux of 3×10^{-8} Torr. The substrate temperature was measured by an optical pyrometer corrected using the Al melting point. The amorphous GaN buffer layer changes to the single crystal by thermal annealing at 700 °C and then the GaN epilayer was grown at 700 °C under the Ga flux of 3×10^{-7} Torr and N_2 flow rate of 0.5 sccm. The pressure during growth was 2×10^{-4} Torr. The substrate surface and growth process in the initial stage were in-situ observed by RHEED system operated at an acceleration voltage of 15 kV. The morphology of the substrate and the growing surfaces was proved by AFM system.

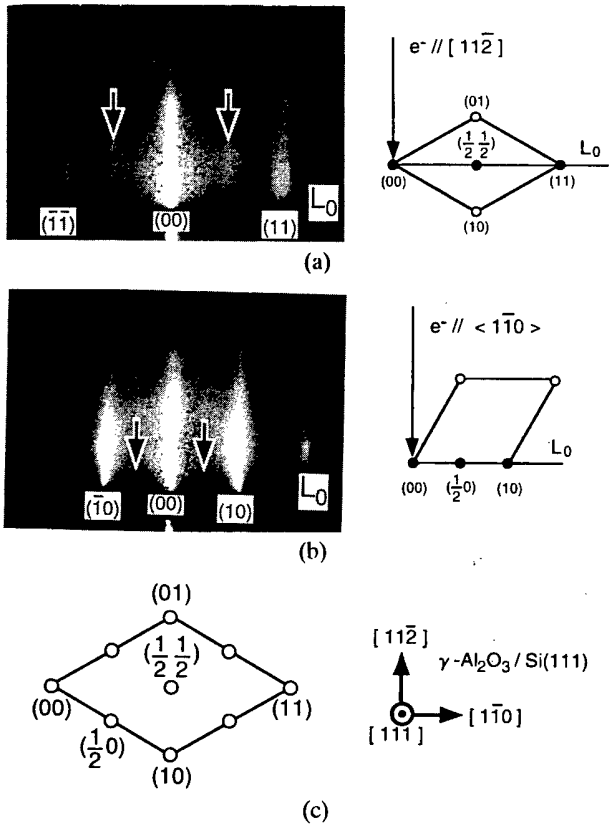

Fig. 1. In situ RHEED patterns from γ-Al_2O_3/Si(111) substrate after thermal cleaning and corresponding schematic diagrams of the two-dimensional (2D) reciprocal lattice explaining the RHEED patterns. The incident electron beam is parallel to the (a) [11$\bar{2}$] and (b) [1$\bar{1}$0] directions. The solid circles represent the diffraction streaks observed in the zeroth Laue (L0) zone of the RHEED patterns. (c) is a unit cell in the 2D reciprocal lattice derived from (a) and (b).

III. RESULT S AND DISCUSSIONS

We first investigated the surface structure of the γ-Al_2O_3/Si(111) substrate after thermal cleaning at 800 °C for 10 min. Figure 1 shows RHEED patterns from the thermally cleaned surface of the substrate and schematic diagrams of the reciprocal lattice space. The incident electron beam is parallel to the (a) [11$\bar{2}$] and (b) [1$\bar{1}$0] direction. In Fig. 1, fractional diffraction streaks (indicated by allows) in the zeroth order Laue (L_0) zone are observed among fundamental streaks which two-dimensional (2D) miller indices are (11), (00) and ($\bar{1}\bar{1}$). The distance between (00) rod and a fractional rod is just half one between fundamental rods. Therefore, it is considered that 2D miller indices of these fractional rods are (1/2 1/2) and ($\frac{\bar{1}}{2}\frac{\bar{1}}{2}$). Furthermore, another half order streaks are also observed in the L_0 zone as indicating by arrows in Fig. 1(b). 2D reciprocal unit cell derived from these results is shown in Fig. 1(c). Therefore, it is found that a (2×2) surface reconstructed structure was formed on the γ-Al_2O_3/Si(111) substrate.

In order to investigate the growth process of GaN epilayer and the epitaxial relationship between the epilayer and substrate, the GaN epilayer is grown by a two-step

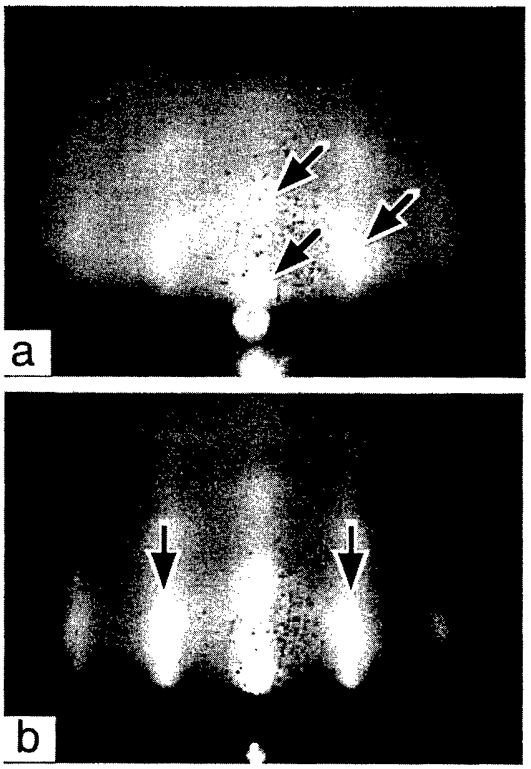

Fig. 2. RHEED patterns taken in situ from (a) the amorphous GaN buffer layer deposited on the γ-Al_2O_3/Si(111) substrate at room temperature and (b) the annealed GaN buffer layer at 700°C after the deposition. The thickness of the buffer layer is about 2 nm. The incident electron beam is parallel to the [11$\bar{2}$0] direction.

growth method using an amorphous GaN buffer layer deposited at room temperature (RT). Fig. 2 shows RHEED patterns taken from (a) the 2 nm-thick GaN deposited at RT and (b) the GaN layer after thermal annealing at 700 °C. The sample was always exposed to RF plasma-enhanced nitrogen gas irradiation through the deposition and annealing processes. It is noticed that very weak and diffraction spots indicated by arrows are observed on the halo pattern as shown in Fig. 2(a). Appearance of the diffraction intensity in Fig. 1(c) suggests that crystallization of the amorphous GaN layer partly occurred during the deposition. These diffraction spots become streaky as raising of the substrate temperature up to 700 °C in Fig. 2(b). The lattice spacings parallel to the growing surface of Figs. 2(a) and 2(b) agree with the one of GaN, which are determined by the distance between the diffraction rods. It is found that the amorphous GaN buffer layer crystallizes to single hexagonal (h) GaN layer in solid phase epitaxy mode by thermal annealing. Therefore, it is considered that the lattice mismatch between γ-Al_2O_3/Si(111) substrate and GaN layer is relaxed during the crystallization of the amorphous GaN buffer layer.

Figure 3 shows the changes of RHEED patterns during the growth of GaN epilayer on the annealed buffer layer at a substrate temperature of 700 °C. The incident electron beam is parallel to the $[11\bar{2}0]_{GaN}$ direction.

At the first stage of the initial growth of GaN epilayer, RHEED pattern changes a spot pattern with prominent streaks from some diffraction spots. This means that a faceting islands are grown on the surface [28,29]. These diffraction spots become weaker and, on the other hand, two-dimensional diffraction streaks appear as shown in Fig. 3(b). Finally, the sharp and strong streaks are only observed as proceeding of the growth of GaN layer, as shown in Fig. 3(c). These changes of the RHEED pattern mean that the islanding growth mode in the initial growth stage becomes a two-dimensional like growth mode. This agrees with an AFM observation of the sur-

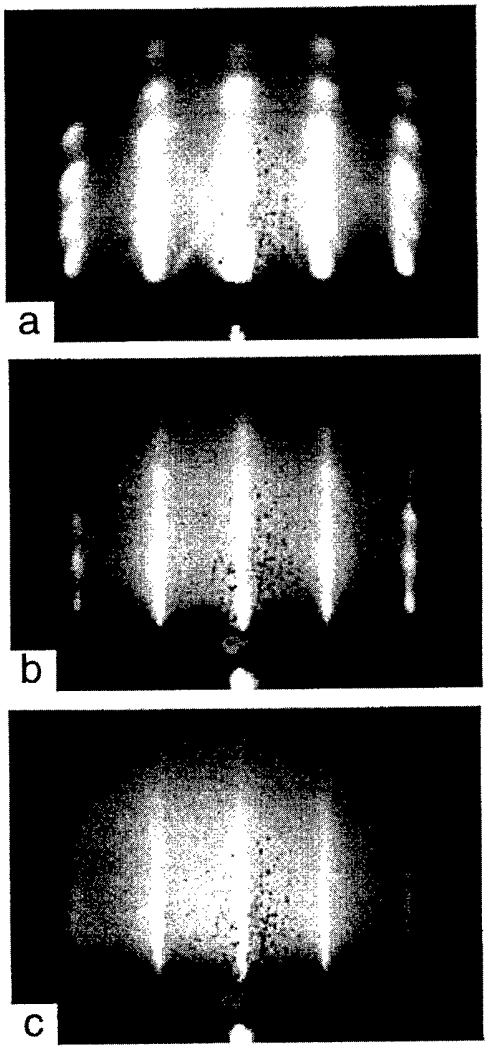

Fig. 3. RHEED patterns taken in situ from several growth steps of GaN epilayers on the annealed buffer layer. The growth thicknesses of the GaN epilayers are (a) 2 nm, (b) 10 nm and (c) 40 nm, respectively.

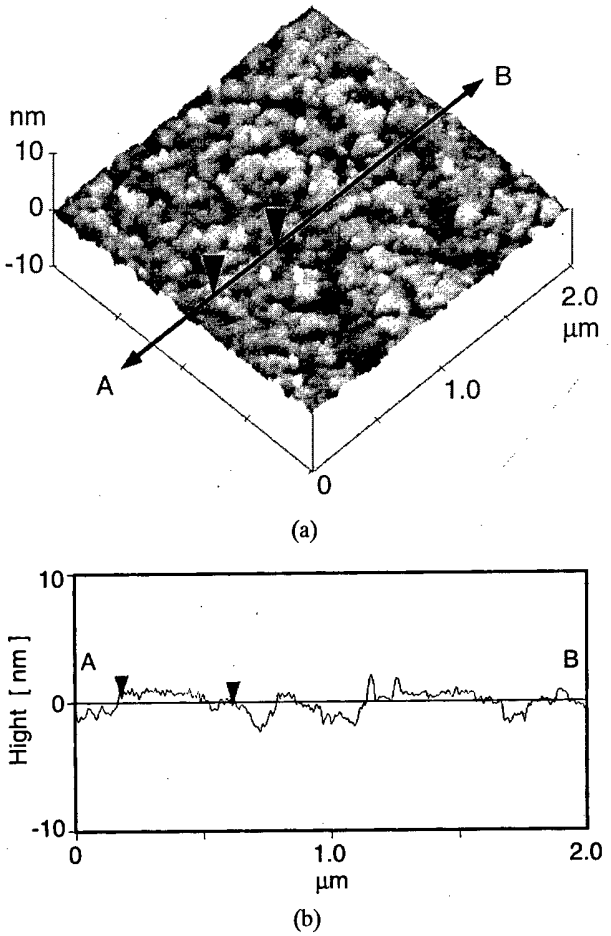

Fig. 4. (a) An AFM image of the surface of the 45 nm-thick GaN epilayer on the γ-Al_2O_3/Si(111). (b) a cross sectional image along the line between 'A' and 'B' marked in the Fig. 4(a).

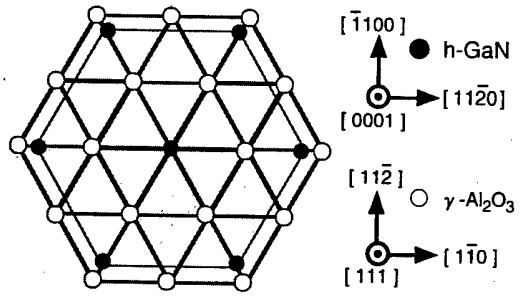

Fig. 5. A schematic diagram of the epitaxial relationship between the γ-Al_2O_3/Si(111) substrate and the h-GaN epilayer.

face morphology of the growing GaN epilayer, as showing in Fig. 4(a). It is found that there are many islands having flat top surfaces. Fig. 4(b) shows the cross sectional image of the AFM image along the line between the marks of "A" and "B" in Fig. 4(a). The RMS value of the top surface between the solid triangles in Fig. 4 is about 0.4 nm. This supports the RHEED pattern of Fig. 3(c).

Fig. 5 shows a schematic diagram explaining the epitaxial relationship between the γ-Al_2O_3/Si(111) substrate and GaN epilayer. In Fig. 1(b) and Fig. 2, the incident direction of the electron beam was the same azimuth before and after the growth of GaN epilayer on the γ-Al_2O_3/Si(111) substrate. Therefore, it is found that h-GaN(0001) was epitaxialy grown on the γ-Al_2O_3(111)/Si(111) with the relationship of $[11\bar{2}0]_{GaN}//[1\bar{1}0]_{\gamma-Al_2O_3}$. In this case, the lattice mismatch is about 13.5 %.

From these results, it is considered that the epitaxial γ-Al_2O_3 layer is the appropriate intermediate layer for the GaN growth on Si substrates and the two-step growth method using room-temperature-deposited buffer layer is effective for the GaN epilayer growth on the γ-Al_2O_3/Si(111) as well as for sapphire substrates. However, in order to obtain the GaN epilayer with the atomically flat surface, a further study on the growth mechanism of the GaN epilayer is necessary.

IV. CONCLUSIONS

The growth process of GaN epilayer on a γ-Al_2O_3/Si(111) substrate by two-step growth method using amorphous GaN buffer layer deposited at room temperature has been investigated by in situ RHEED and ex situ AFM observations. It has been found that a (2×2) reconstructed structure is formed on the γ-Al_2O_3/Si(111) substrate after thermal cleaning. A h-GaN epilayer was grown on the γ-Al_2O_3/Si(111) substrate with the relationship of $[11\bar{2}0]_{GaN}//[1\bar{1}0]_{\gamma-Al_2O_3}$. The detailed analysis of the mechanism of GaN heteroepitaxy is in progress.

ACKNOWLEDGMENTS

This works has been partly supported by a Grant-in-Aid for Scientific Research from Ministry of Education, Science, Sports and Culture of Japan, No. 0845503.

REFERENCES

[1] S. Nakumura, M. Senoh, S. Nagahama, N. Iwasa, T. Yamada, T. Matsushita, H. Kiyoku, H. Umemoto, M. Sano and K. Chocho, J. Cryst. Growth **189-190**, 820 (1998).
[2] S. Nakumura, M. Senoh, S. Nagahama, N. Iwasa, T. Yamada, T. Matsushita, H. Kiyoku, H. Umemoto, M. Sano and K. Chocho, Jpn. J. Appl. Phys. **37**, L.627 (1998).
[3] T. Kobayashi, F. Nakamura, T. Tojyo, H. Nakajima, T. Asatsuma, H. Kawai and M. Ikade, Electron. Lett. **34**, 1494 (1998).
[4] S. Nakamura, M. Senoh, S. Nagahama, N. Iwasa, T. Yamada, T. Matsushita, Y. Sugimoto and H. Kiyoku, Appl. Ohys. Lett. **70**, 2753 (1997).
[5] I. Akasaki, S. Sota, H. Sakai, T. Tanaka, M. Koike and Amano, Elctron. Lett. **32**, 1105 (1996).
[6] A. Kuramata, K. Domen, R. Soejima, K. Horino, S. Kubota and T. Tanahashi, *Proc. Int. Conf. Nitride Semiconductors* (Tokushima, Japan, 1997), p. 450.
[7] S. Nakamura, M. Senoh, N. Iwasa, S. Nagahama, T. Yamada and T. Mukai, Jpn. J. Appl. Phys. **34**, L1332 (1995).
[8] S. Nakamura, M. Senoh, N. Iwasa and S. Nagahama, Appl. Phys. Lett. **67**, 1868 (1995).
[9] S. Guha and N. A. Bojarczuk, Electron. Lett. **33**, 1986 (1997); J. W. Yang, C. J. Sun, Q. Chen, M. Z. Anwar and M. A. Khan, Appl. Lett. Phys. **69**, 3566 (1996).
[10] M. A. Sanchez-Garcia, E. Calleja, E. Monroy, F. J. Sanchez, F. Calle, E. Munoz and R. Beresford, J. Cryst. Growth **183**, 23 (1998).
[11] I. Berishev, A. Bensaoula, I. Rusakova, A. Karabutov, M. Ugarov and V. P. Ageev, Appl. Phys. Lett. **73**, 1808 (1998).
[12] N.Ohshima, H. Yonezu, S. Uesugi, K. Gotoh and S. Yamahira, Mat. Res. Soc. Sympo. Proc. **512**, 405 (1998).
[13] L. Wang, X. Liu, Y. Zan, J. Wang, D. Wang, D. Lu and Z. Wang, Appl. Phys. Lett. **72**, 109 (1998).
[14] X. Zhang, P. Kung, A. Saxler, D. Walker, T. C. Wang and M. Razeghi, Appl. Phys. Lett. **67**, 1745 (1995).
[15] M. Kondow, K. Uomi, K. Hosomi and T. Mozue, Jpn. J. Appl. Phys. **33**, L.1056 (1994).
[16] W. J. Meng and T. A. Perry, J. Appl. Phys. **76**, 7824 (1994).
[17] T. D. Moustakas, T. Lei and R. J. Molnar, Physica **B185**, 36 (1993).
[18] T. Lei, T. D. Moustalas, R. J. Graham, Y. He and S. J. Berkowitz, J. Appl. Phys. **71**, 4933 (1992).
[19] M. Ishida, I. Katakabe, T. Nakamura and N. Ohtake, Appl. Phys. Lett. **52**, 1326 (1988).
[20] K. Sawada, M. Ishida and T. Nakamura, Appl. Phys. Lett. **52**, 1672 (1988).
[21] T. Kimura, A. Sengoku and M. Ishida, Jpn. J. Appl. Phys. **35**, 1001 (1996).
[22] T. K imura, A. Sengoku, H. Yaginuma, Y. Moritasu and

M. Ishida, Jpn. J. Appl. Phys., 7126 (1997).
[23] T. Kimura, H. Yaginuma, A. Sengoku, Y. Moritasu and M. Ishida, Jpn. J. Appl. Phys. **37**, 1285 (1998).
[24] H. Wado, T. Shimizu and M. Ishida, Appl. Phys. Lett. **67**, 2200 (1995).
[25] Y. C. Jung, H. Wado, K. Ohtani and M. Ishida, Appl. Phys. Lett. **68**, 3001 (1996).
[26] Y. C. Jung, H. Miura, K. Ohtani and M. Ishida, J. Cryst. Growth, to be published (1998).
[27] N. Ohshima, H. Yonezu, S. Yamahira and K. Pak, J. Cryst. Growth 189/190 (1998).
[28] Y. koide, S. Zaima, N. Ohshima and Y. Yasuda, Jpn. J. Appl. Phys. **28**, L690 (1989).
[29] Y. Koide, S. Zaima, N. Ohshima and Y. Yasuda, J. Cryst. Growth **99**, 254 (1990).

Journal of the Korean Physical Society, Vol. 34, June 1999, pp. S364~S369

Growth and Characterization of GaN Thin Films on β-SiC/Si Substrate Using Rapid Thermal Chemical Vapor Deposition

Y. H. Mo and K. S. Nahm*

Also School of Chemical Engineering and Technology, Semiconductor Physics Research Center, Chonbuk National University, Chonju 561-756

S. H. Yang, K. C. Kim and W. H. Lee

Also Department of Semiconductor Science and Technology, Semiconductor Physics Research Center, Chonbuk National University, Chonju 561-756

E-K. Suh and K. Y. Lim

Also School of Science and Technology, Semiconductor Physics Research Center, Chonbuk National University, Chonju 561-756

GaN films were grown on β-SiC/Si and the structural and optical properties of the GaN were examined with XRD and PL measurements. GaN was grown on SiC films which were deposited on Si at temperatures of 900~1000 °C, but no growth occurred on SiC films deposited at temperatures of 500~800 °C and 1100 °C. The structural and optical properties of the GaN significantly varied depending on the growth condition of SiC on Si. A deep level yellow emission was observed at 2.23 eV of PL spectra for GaN films grown predominantly along $(10\bar{1}0)$ orientation, while near band edge blue emission at 3.4 eV from GaN films grown along the *c*-plane. GaN film grown on β-SiC/Si substrate at the best condition produced a strong UV emission with FWHM of 152 meV at room temperature and suppressed completely the deep level yellow emission. XRD spectrum for the GaN exhibited the growth of highly oriented wurtzite GaN with FWHM of ~424 arcsec.

I. INTRODUCTION

GaN has attracted much attention in last few years as a promising material for high-power optoelectronic devices in the blue-ultraviolet wavelength region. However, the growth of high quality GaN epilayer for the device applications has been impeded because bulk GaN crystals available so far are too small in size to be used a substrate [1]. At present, sapphire is the most commonly used substrate for the growth of GaN epilayer because of its merits such as the commercial availability with relatively low cost, and excellent surface preparation [2]. However, sapphire has a very large lattice mismatch (~16 %) with wurtzite GaN, which inevitably leads to a formation of a large defect density in GaN epilayers. Recently, there have been several attempts to grow high quality GaN on various substrates such as Si, GaAs, GaP, spinel ($MgAl_2O_4$), MnO, SiC, *etc.* [3]. Among these materials, hexagonal silicon carbides (6H and 4H polytypes) have been extensively investigated as a substrate for the growth of high quality GaN epilayer because of relatively low lattice mismatch (~3 %) with GaN [4]. However, the limited availability of hexagonal silicon carbides due to their high cost and small size (<5 cm) becomes significant obstacles for the practical use as substrates for the GaN growth [5]. Meanwhile, some investigators have attempted to use β-SiC (3C-SiC or zinc-blende silicon carbide) as a substrate for the growth of GaN because large area β-SiC wafers have been supplied at low cost by the epitaxial growth on Si in the conventional CVD reactor [6,7]. The average lattice constant and thermal expansion coefficient for β-SiC are 4.38 Å and 4.7×10^{-6}/K, respectively, which match quite well with those for GaN.

In this paper, we have deposited β-SiC on Si by pyrolyzing tetramethylsilane, followed by the *in-situ* growth of GaN on β-SiC/Si to study the possible application of β-SiC for a substrate of GaN growth. The growth was carried out under various conditions and the structural and optical properties of the grown films were characterized with XRD and PL measurements.

II. EXPERIMENT

To employ β-SiC/Si as a substrate for the growth

*E-mail: nahmks@che.chonbuk.ac.kr, Fax: +82-652-270-2306

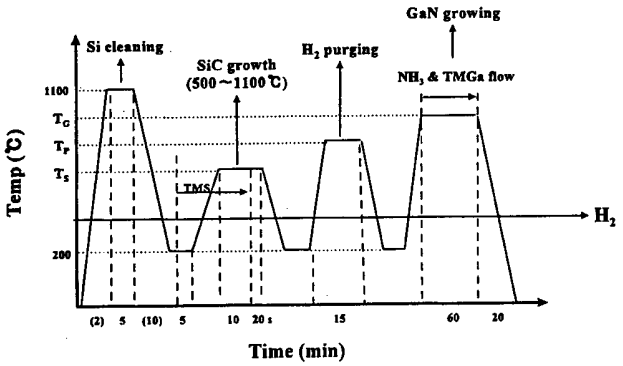

Fig. 1. Growth sequences for SiC and GaN thin films.

of GaN films, single crystal 3C-SiC(111) was deposited by pyrolyzing tetramethylsilane (TMS, $Si(CH_3)_4$) in a low-pressure rapid thermal chemical vapor deposition (RTCVD). The detailed growth system can be found elsewhere [8]. The growth sequences of SiC and GaN films are shown in Fig. 1. Prior to the growth of SiC on Si, Si wafers were mounted on a substrate holder after pretreated in acetone, dipped in HF, and rinsed in DI water. The reactor was evacuated to 10^{-4} Torr for 30 minutes and then purged with hydrogen gas at a flow rate of 20 sccm. The substrate was heated to the growth temperature after TMS was supplied to the reactor. When the growth was completed, TMS flow was first stopped and then the temperature of the reactor was cooled down to about 200 °C under the flow of hydrogen gas. The SiC growth was carried out as functions of substrate temperature, TMS flow rate, H_2 flow rate, and gas pressure. The TMS and trimethylgallium (TMGa, $(CH_3)_3Ga$) reservoirs were immersed in icy water baths. In-situ growth of GaN films were performed on β-SiC films in the same growth system using TMGa and ammonia (NH_3) for Ga and N sources, respectively. GaN was grown for 60 min with TMGa flow rates of 16 and 24 μmol/min at 1050 °C, 2000 sccm NH_3, and 500 sccm H_2, along with the growth sequence shown in Fig. 1.

The crystal structure of β-SiC and GaN films grown under various conditions was analyzed with a X-ray diffraction (XRD) using a CuKα_1. Photoluminescence (PL) was used to characterize optical properties of GaN films. The PL was excited with a 325 nm line of a He-Cd laser at room temperature and detected with a standard photon counting electronics. The excitation power was 30 mW. The surface morphology of grown films was examined with an atomic force microscope (AFM). Raman spectroscopy was also used to characterize the structural property of the GaN films; Raman spectra were recorded in the near back scattering configuration with the incident photon wavevector nearly parallel to the surface of the epilayer which is perpendicular to the c-axis of the GaN. In order to observe all phonon modes, the polarization of the scattered light was not analyzed.

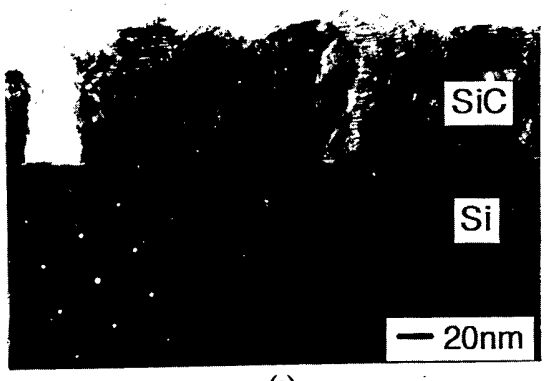

(a)

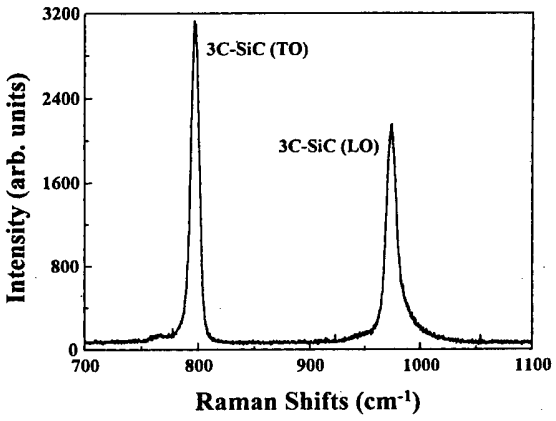

(b)

Fig. 2. A typical cross-sectional TEM with TED pattern and Raman spectrum for β-SiC grown for 30 min at an optimum growth condition of 1100 °C, 1.7 Torr, 0.3 sccm TMS, and 200 sccm H_2.

III. RESULTS AND DISCUSSION

1. Growth of SiC on Si

To determine the optimum growth condition of β-SiC(111), SiC films were grown on Si(111) at various temperatures (800~1200 °C), TMS flow rates (0.3~10 sccm), H_2 flow rates (100~200 sccm), and gas pressures (1.7~12 Torr), and the crystal quality of grown SiC films were evaluated. The detailed discussion for the growth of high quality β-SiC on Si and the optimum growth condition can be found elsewhere [8,9]. Figure 2 contains a typical cross sectional TEM photograph and Raman spectrum for 3C-SiC grown for 30 min at the optimum growth condition of 1100 °C, 1.7 Torr, 0.3 sccm TMS, and 200 sccm H_2. TED image (Fig. 2(a)) manifests that the grown films are oriented along the (111) plane of 3C-SiC. The Raman spectrum, as shown in Fig. 2(b), exhibits TO and LO modes of β-SiC at 795 and 972 cm^{-1}, respectively.

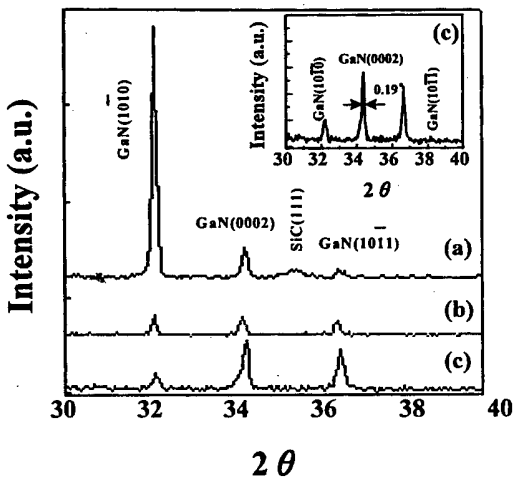

Fig. 3. XRD spectra for GaN films grown on SiC/Si grown at 900 °C in 200 sccm H_2. (a) β-SiC growth : 0.3 sccm TMS for 10 min, GaN growth : 16 μmol/min TMGa, (b) β-SiC growth : 0.5 sccm TMS for 20 min, GaN growth : 16 μmol/min TMGa, (c) β-SiC growth : 0.5 sccm TMS for 20 min, GaN growth : 24 μmol/min TMGa. GaN was grown for 60 min at 1050 °C with 2000 sccm NH_3 and 500 sccm H_2.

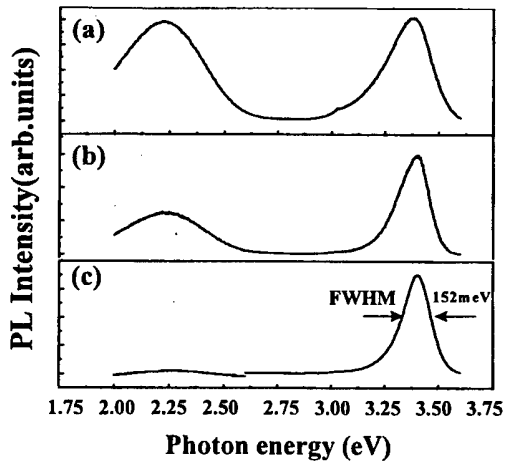

Fig. 4. PL spectra measured at room temperature for GaN film on SiC grown at 900 °C in 200 sccm H_2. (a) β-SiC growth : 0.3 sccm TMS for 10 min, GaN growth : 16 μmol/min TMGa, (b) β- SiC growth : 0.5 sccm TMS for 20 min, GaN growth : 16 μmol/min TMGa, (c) β-SiC growth : 0.5 sccm TMS for 20 min, GaN growth : 24 μmol/min TMGa. GaN was grown for 60 min at 1050 °C with 2000 sccm NH_3 and 500 sccm H_2.

2. Growth of GaN on SiC

GaN films were grown for 60 min at 1050 °C and 4.2 Torr with 16 μmol/min TMGa and 200 sccm NH_3 flow rates on SiC films grown at the optimum condition mentioned earlier except growth temperature. To investigate the effect of SiC growing condition on the GaN growth, the growth temperature of SiC films were varied in the range from 500 to 1100 °C. GaN was observed to grow only on SiC films which were grown at temperatures between 900 and 1000 °C; but no growth occurred on SiC films grown at other temperatures, even at 1100 °C. Figure 3(a) shows a XRD spectrum for the GaN film grown on SiC that was grown at 900 °C. We observe the most intense peak at a powder diffraction value of 2θ=32.4° corresponding to (10$\bar{1}$0) GaN and other two weak peaks at 2θ=34.4° and 36.7° corresponding to the (0002) and (10$\bar{1}$1) reflections, respectively. This indicates the growth of a wurtzite GaN film with dominant growth orientation along the (10$\bar{1}$0) plane. Meanwhile, PL spectrum measured at room temperature for the GaN film (Fig. 4(a)) exhibits both yellow and blue band emissions at peak energies of 2.23 and 3.38 eV, respectively, with comparable intensities. Similar XRD and PL spectra were observed from GaN film on SiC grown at 1000 °C.

To clarify the role of SiC for the growth of GaN, SiC films deposited at the temperatures of 500~1100 °C were characterized by XRD measurements. As shown in Fig. 5, XRD spectra display that amorphous SiC films are grown in the temperature range of 500~900 °C and crystal 3C-SiC(111) films begin to grow from 950 °C. This result elucidates that GaN films are deposited on SiC grown at transition temperatures where the crystallinity of SiC changes from amorphous phase to crystalline. We speculate that the growth of GaN on SiC grown at this temperature range is closely related to the solid crystallization time of amorphous SiC layer during the GaN growth. Recently, the growth of GaN using GaN buffer layer showed the amorphous GaN buffer layer deposited at low temperatures effectively releases strains existing at GaN/sapphire interface to grow high quality GaN film [10]. In addition, it was observed in situ by TEM that solid phase crystallization of the amorphous buffer lay-

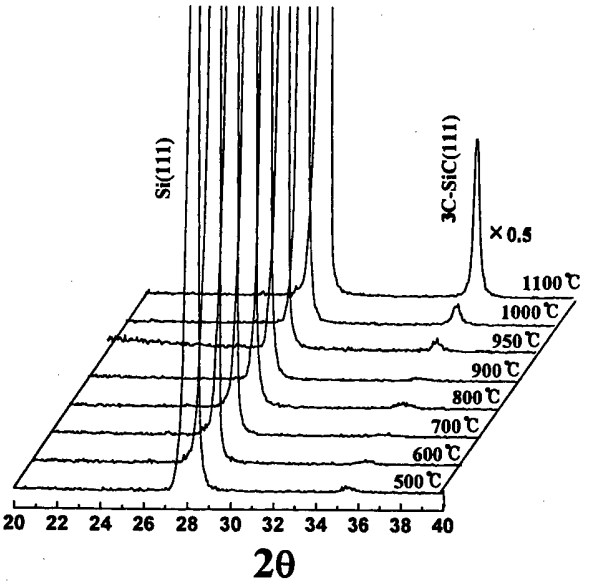

Fig. 5. XRD spectra for SiC films grown at growth temperatures of 500~1100 °C.

ers on the sapphire substrate occurs during the growth of GaN film [11]. GaN growth was attempted on SiC formed at 500 °C with an increased TMGa flow rate of 24 μmol/min to scrutinize whether the growth of GaN was impeded by a low TMGa flow rate. The XRD and PL analyses showed that no GaN layers were grown on SiC deposited at this temperature. This indicates that the growth of GaN is significantly influenced by the property of the SiC film rather than TMGa flow rate.

Figure 3(b) and 4(b) show XRD and PL spectra for GaN film grown on SiC which is deposited for 20 min at an increased TMS flow rate of 0.5 sccm. The XRD spectrum shows that three peaks appear at different values of 2θ for the film. They arise at 2θ=32.4°, 34.4°, and 36.7° corresponding to $(10\bar{1}0)$, (0002), and $(10\bar{1}1)$, respectively. It is worthwhile to note that the intensity of $(10\bar{1}0)$ peak decreases, while those of (0002) and $(10\bar{1}1)$ peaks increase with respect to Fig. 3(a). On the other hand, the PL spectrum exhibits a much stronger UV emission appeared at 3.4 eV in comparison to the yellow emission at 2.24 eV as shown in Fig. 4(b). To examine the influence of the surface morphology of SiC on the GaN growth, we observed surface morphologies of SiC films grown for 10 min at 0.3 sccm TMS and for 20 min at 0.5 sccm, respectively, using an AFM. Figure 6 shows that there was no significant difference in the roughness of the two samples and the average surface roughness was about 50 Å. This suggests that different structural and

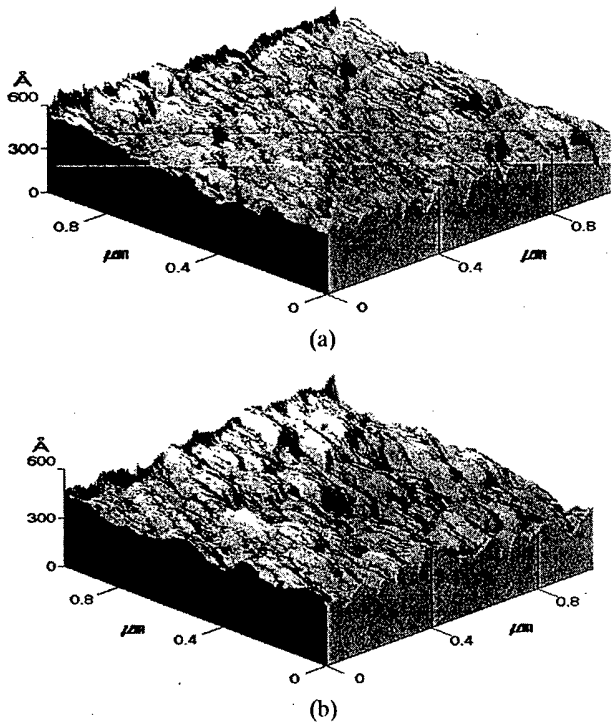

Fig. 6. AFM images for the surface morphologies of SiC films grown (a) for 10 min at 0.3 sccm TMS and (b) for 20 min at 0.5 sccm 20 min, respectively.

optical properties of GaN films shown in Fig. 3 and 4 are not stemmed from the surface roughness of the SiC substrates, but more from the thickness and crystallinity of the SiC layers. To see the effect of SiC thickness on the GaN growth, SiC films were deposited on Si for 10~60 min, respectively, and then GaN was grown on them. SiC and GaN films were grown at the same condition given in Fig. 3(b) and 4(b). Although not shown in this paper, PL spectra for the GaN films showed that the intensity of yellow emission with respect to blue emission decreases as the growth time of SiC films increases from 10 to 20 min, but grows from 30 min with increasing the time. Similar trends for the intensity of the $(10\bar{1}0)$ peak at 2θ=32.4° were observed from XRD spectra for the films. This indicates that the optical and structural properties of GaN film are significantly influenced by the thickness of SiC films.

GaN films were grown for 60 min with an increased TMGa flow rate of 24 μmol/min at 1050 °C, 2000 sccm NH_3, and 500 sccm H_2. SiC film used for the growth was grown for 20 min at 900 °C with the TMS flow rate of 0.5 sccm. Figure 3(c) and 4(c) show XRD and PL spectra for the GaN film. The PL spectrum shows that the GaN film produces a strong band edge blue emission (FWHM: 152 meV) at 3.4 eV and completely suppressed deep level yellow emission as can be seen in Fig. 4(c). The XRD spectrum for the GaN film, shown in the inset of Fig. 3(c), exhibits highly oriented wurtzite GaN with dominant growth orientation along the *c*-axis. The uncorrected FWHM of the (0002) peak is about 0.19° or 684 arcsec. FWHM corrected for the system broadening was about 424 arcsec, which is comparable to the value reported previously [12].

The Raman spectra of GaN/3C-SiC/Si grown in this work exhibit phonons of wurtizte GaN crystal, *i.e.*, the high frequency E_2 mode at 568 cm^{-1}, A_1 (TO) and E_1 (TO) modes at 532 cm^{-1}, and 560 cm^{-1}, respectively, and unresolved weak E_1 (LO) and A_1 (LO) modes around 739 cm^{-1}, in the near backscattering configuration explained earlier. No clear indication of the inclusion of cubic GaN was obtained even in the sample showing a strong $(10\bar{1}0)$ XRD peak, as can be seen from the Raman spectrum in Fig. 7.

Throughout the experiments, we have observed the evolution of a strong yellow luminescence from GaN films whose XRD spectra revealed that the GaN films dominantly grew along the $(10\bar{1}0)$ plane. But the deep level yellow emission was significantly suppressed when GaN was grown along the *c*-axis. This suggests that the optical properties of our samples are greatly influenced by the growth direction of SiC films. When we consider a schematic diagram of the possible atomic arrangements in the interface region between GaN epilayer and cubic SiC substrate, it is common that the SiC(111) surface induces the growth of wurtzite GaN because of the close match of structural symmetry of 3C-SiC(111) with

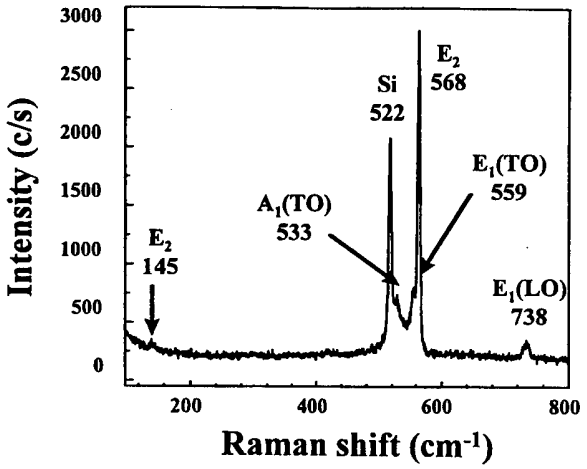

Fig. 7. A typical Raman spectrum of GaN grown on SiC/Si.

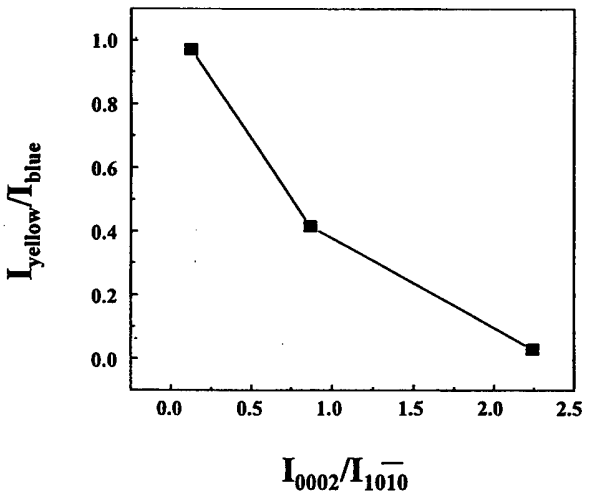

Fig. 8. A plot of the intensity ratio of the PL peaks at 2.23 eV and 3.4 eV, I_{yellow}/I_{blue}, as a function of that of (0002) and (10$\bar{1}$0) peaks of XRD, $I_{(0002)}/I_{(10\bar{1}0)}$.

GaN(0001) [13]. Wurtzite GaN and zinc-blende SiC take the stacking sequences of ABAB.... and ABCABC...., respectively. Thus, the (0001) axis of wurtzite GaN is almost parallel to the (111) axis of zinc-blende SiC. When the atoms are bonded according to the mode of ABAB on the (111) plane of zinc-blende SiC, wurtzite GaN can be grown on the zinc-blende SiC substrate. In Fig. 3(c), for example, it is considered that the surface of SiC substrate might be reconstructed along (111) direction during the GaN growth at higher temperature so that wurtizte GaN grow with dominant growth orientation of (0001) plane. However, wurtzite GaN(10$\bar{1}$0) may predominantly grow on SiC film which has a surface plane other than (111) orientation. Since the (10$\bar{1}$0) plane of hexagonal GaN is perpendicular to the close-packed basal plane of (0001) GaN, the growth along (10$\bar{1}$0) direction in the wurtzite GaN might generate high density of defects or dangling bonds at the boundaries between GaN structures of different orientations. This high defect density in the GaN epilayer seems to be related with the yellow luminescence at 2.23 eV. The intensity ratio of the PL peaks observed at 2.23 eV and 3.4 eV, I_{yellow}/I_{blue}, was extracted from Fig. 4 for each sample and depicted as a function of that of (0002) and (10$\bar{1}$0) peaks appeared in XRD spectra of Fig. 3, $I_{(0002)}/I_{(10\bar{1}0)}$, to correlate the results of XRD and PL spectra quantitatively. Figure 8 shows that the ratio of I_{yellow}/I_{blue} decreases with increasing $I_{(0002)}/I_{(10\bar{1}0)}$, indicating that the yellow emission is greatly suppressed when the wurtzite GaN film grows along the (0001) plane. Noguez *et al.* [14] studied the optical properties of the GaN (10$\bar{1}$0) surface using a tight-binding formalism based on a sp^{3}s* orbital basis. They reported the wurtizte GaN grown along with (10$\bar{1}$0) orientation has a bandgap of 2.7 eV, which partly support our experimental observation. On the other hand, it is not clear why the growth of GaN layer was not detectable on high quality SiC crystal film grown at the optimum growth condition. The highly crystallized solid surface usually produces isolated islands on it to impede the formation of thin film, especially at high temperature. Most of the researches have reported the growth of GaN on β-SiC at temperatures under 900 °C [13,15]. Hashimoto *et al.* [13] reported that no growth occurred at 800 °C when they grew GaN on 3C-SiC(100). We believe that further experiments are necessary to clarify the reason why no growth occurred on the highly crystallized SiC surface.

IV. CONCLUSIONS

We have grown GaN on β-SiC/Si and characterized the structural and optical properties of the GaN. GaN was observed to grow only on SiC films which were grown at temperatures between 900 and 1000 °C; but no growth occurred on SiC films grown at other temperatures, even at 1100 °C. When SiC is deposited for 20 min at 0.5 sccm TMS, 200 sccm H_2, and 900 °C, followed by the in-situ growth of GaN for 60 min with 24 μmol/min at 1050 °C, 2000 sccm NH_3, and 500 sccm H_2, highly oriented wurtzite GaN was grown along the (0002) plane with FWHM of ~424 arcsec. A strong yellow luminescence was observed from GaN films whose XRD spectra revealed that the GaN films dominantly grew along the (10$\bar{1}$0) plane, while the deep level yellow emission was significantly suppressed when GaN were grown along the *c*-axis. It was considered that the optical properties of our grown GaN films are influenced by the growth direction of SiC films.

ACKNOWLEDGMENTS

The authors wish to acknowledge the financial support of the Korea Research Foundation made in the program

year of 1998 (1998-016-D00004).

REFERENCES

[1] S. Oorowski, J. Jun, P. Perlin, I. Grzegory, H. Teissere and T. Suski, Inst. Phys. Conf. Ser. **137**, 369 (1994).
[2] S. Najamura, M. Senoh, N. Iwasa and S. Nagahma, Jpn. J. Appl. Phys. **34**, L797 (1995)
[3] T. Sasaki and T. Matsuoka, J. Appl. Phys. **64**, 4531 (1988)
[4] J. H. Edgar, J. Mater. Res. **7**, 235 (1992).
[5] J. Devrajan, A. J. Steckl, C. Tran and R. A. Stall, Mat. Sci. Forum **264-268**, 1149 (1998).
[6] S. Nishino, H. Suhara, H. Ono and H. Matsunami, J. Appl. Phys. **61**, 4889 (1987).
[7] Y. H. Seo, K. C. Kim, H. W. Shim, K. S. Nahm, E.-K. Suh and H. J. Lee, J. Korean Phys. Soc. **33**, S324 (1998).
[8] K. C. Kim, H. W. Shim. E.-K. Suh, H. J. Lee and K. S. Nahm, J. Korean Phys. Soc. **32**, 588 (1998).
[9] Y. H. Seo, K. C. Kim, H. W. Shim, K. S. Nahm, E.-K. Suh, H. J. Lee, D. K. Kim and B. T. Lee, J. Electrochem. Soc. **145**, 292 (1998).
[10] S. Nakamura, Jpn. J. Appl. Phys. **304L**, 1705 (1991).
[11] H. Amano, T. Takeuchi, H. Sakai, S. Y amaguchi, C. Wetzel and I. Akasaki, Materials Science Forum **264-268**, 1115 (1998).
[12] A. J. Steckl, J. Devrajan, C. Tran and R. A. Stall, J. Electronic Materials **26**, 217 (1997)
[13] T. Hashimoto, O. Imafuji, M. Ishida, Y. Terakoshi, T. Sugino, A. Yoshikawa, K. Itoh and J. Shirafuji, J. Cryst. Growth **169**, 185 (1996)
[14] C. Noguetz, R. Esquivel-Sirvent, D. R. Alfonso, S. E. Ulloa and D. A. Drabold, Mat. Res. Soc. Symp. Proc. **449**, 911 (1997)
[15] J. Wu, H. Yaguchi, H. Nagasawa, Y. Yamaguchi, K. Onabe, Y. Shiraki and R. Ito, Jpn. J. Appl. Phys. **36**, 4241 (1997).

Journal of the Korean Physical Society, Vol. 34, June 1999, pp. S370~S373

Dependence of Optical Property on the Defects in Si-doped GaN Grown by Metal Organic Chemical Vapor Deposition

Chinkyo KIM*, Sungwoo KIM, Jaehyung YI, Yoonho CHOI and Tae-Kyung YOO

Optoelectronics Group, LG Corporate Institute of Technology, Seoul 137-724

Chang-Hee HONG

Semiconductor Physics Research Center, Chonbuk National University, Chonju 561-756

We investigated dependence of optical property on the microstructures and defects for Si-doped GaN grown by metal organic chemical vapor deposition using photoluminescence and x-ray diffraction measurements. Radiative transitions at different wavelengths were observed to be related to the different type of microstructures which can be characterized by x-ray diffraction measurements. Attempts were made to explain the relation between optical property and microstructures.

Wide band gap compound semiconductors have drawn much interest as candidate materials for high power electronic devices and short wavelength optical devices [1–6]. In particular, GaN-based optical devices have been rapidly developed during past few years [7,8]. Unlike other compound semiconductor devices, GaN-based optical devices show relatively high performance in spite of enormous amount of crystalline disorder, in which typical values of dislocation density range from 10^7 to 10^{11} (cm^{-2}) [9,10]. This fact has led many researchers to investigate the various properties of GaN in conjunction with crystalline disorder and defects. Since it was essential to realize p-type GaN for optical devices, which seemed to be impossible until several years ago, it was true that far more attention had been drawn toward realization of p-type GaN than n-type GaN [8]. With success of p-type doping, it became possible to fabricate short wavelength optical devices. However, to improve the optical characteristics, it was pursued to improve and understand the characteristic of n-type layer for more efficient carrier injection. Therefore, it became more important to obtain the detailed understanding of the properties of Si-doped GaN for better device performance.

Recently, much work has been done on the optical and structural properties of Si-doped GaN [11–13]. It has been typically observed that there exists near-band edge emission and yellow luminescence in Si-doped n-type GaN [14–16]. Defects induced by different dopants in GaN film have been studied by Ruvimov *et al.* [13]. Ponce *et al.* suggested that yellow luminescence originate from extended defects inside the grains and at low-angle grain boundaries [14]. And Schubert *et al.* theoretically showed that broadening of band edge emission can be explained by potential fluctuations due to random distribution of donor impurities [16]. However, not many attempts have been made to understand the correlation between the specific radiative transitions, such as band edge emission or yellow emission, and structural disorders including extended defects.

In this letter, we report the correlation between the radiative transitions and direction dependent crystallinity of Si-doped GaN epitaxial films with different carrier concentrations. And its physical meaning will be discussed.

X-ray rocking curve measurements provide information about the orientational coherence of an epitaxial film so that full width at half maximum (FWHM) of out-of-plane peak have been used as a figure of merit for crystalline quality of epitaxial films [17]. Considering that growth of GaN on sapphire substrate involves huge mismatch of lattice constants and thermal expansion coefficients, it is generally believed that epitaxial GaN seems to grow in columnar forms with many extended defects propagating along film growth direction [18,19]. In particular, for GaN epitaxial films, it was reported that pure edge type dislocations are dominant and (0002) Bragg peak is insensitive to that type of extended defects [9,20]. Therefore, the rocking curve measurement of out-of-plane peak is insensitive to rotational mosaic spreading in azimuthal angle and does not necessarily provide accurate assessment of crystalline disorder in general [21,22]. On the other hand, since $(10\bar{1}2)$ rocking scan of ϕ angle reflects in-plane direction mosaic spreading, it is more appropriate for evaluating crystalline quality of GaN epitaxial films.

Si-doped hexagonal (wurtzite) GaN epitaxial films were grown on sapphire (0001) substrate by metal organic chemical vapor deposition (MOCVD). Substrates were degreased with trichloroethylene, acetone and methanol.

*E-mail: chnkkim@mail.lgcit.com

Table 1. A list of Si-doped samples with different carrier concentrations, n, and corresponding mobility, μ, by controlling silane (SiH_4) flow rate.

Samples	n (cm^{-3})	μ ($cm^2/V{\cdot}s$)
S1	2.00×10^{17}	417
S2	2.73×10^{17}	284
S3	2.55×10^{17}	262
S4	3.45×10^{17}	228
S5	2.40×10^{18}	206
S6	5.22×10^{18}	196
S7	5.50×10^{18}	192
S8	6.00×10^{18}	142

Then, the cleansed substrates were etched in 3:1 mixture of H_2SO_4 and H_3PO_4. Upon etching, the substrates were rinsed with deionized water. The substrates loaded in MOCVD reactor were preheated at 1100 °C for 10 minutes in H_2 atmosphere prior to growth. Low temperature GaN buffer layer was then grown at 550 °C and 2 μm of Si-doped GaN layers were grown. Different carrier concentrations ranging from 2.00×10^{17} to 6.00×10^{18} were obtained by controlling silane (SiH_4) flow rate. Carrier concentrations and mobilities of these samples were measured using Van der Pauw method and are listed in Table 1. A He-Cd laser (325 nm) was used as an excitation source for photoluminescence (PL) and the excitation power was maintained constant during the measurements. X-ray rocking curve measurements of (0002) and $(10\bar{1}2)$ were done employing a four circle diffractometer with a double axis geometry [23]. For (0002) and $(10\bar{1}2)$ rocking scans, θ and ϕ scans were made, respectively. Cu $K\alpha_1$ was used for diffraction and the use of a double axis geometry provided $\Delta\lambda/\lambda=1.3\times10^{-4}$ and 13 arcsec of beam divergence.

In Fig. 1, FWHM values of (0002) and $(10\bar{1}2)$ rocking curves for Si-doped GaN films are plotted as a function of carrier mobility. For FWHM values of $(10\bar{1}2)$, there is a

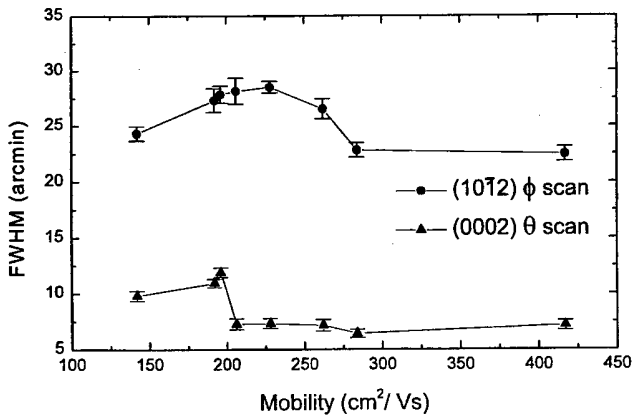

Fig. 1. The FWHM values of (0002) θ scan and $(10\bar{1}2)$ ϕ scan as a function of carrier mobility for GaN:Si epitaxial films.

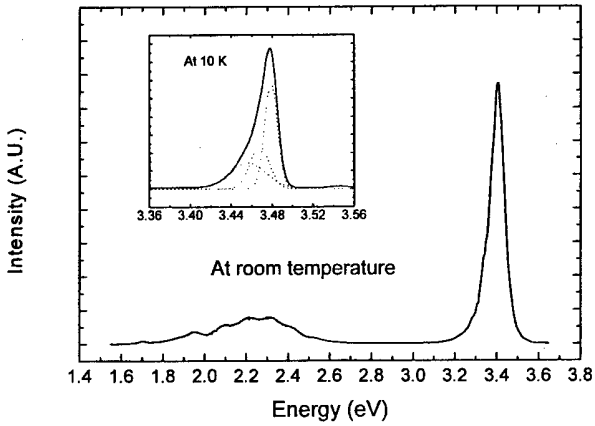

Fig. 2. Typical PL spectra of our samples measured at room temperature and 10 K, respectively. 3.47 eV peak shown at 10 K PL spectrum is related to donor bound excition and three Gaussian fits are shown as dotted lines. Broad yellow emission centered at 2.25 eV is observed in room temperature PL spectrum.

maximum around the mobility of 225 ($cm^2/V{\cdot}s$), but the curve of (0002) FWHM values does not show that feature. Lee *et al.* reported a similar result on the trend of FWHM values of $(10\bar{1}5)$ peak for Si-doped GaN samples with a wider range of carrier concentrations [24]. They, however, observed monotonic increase of FWHM of $(10\bar{1}5)$ values as a function of carrier concentration and explained that the Si doping induced overall defects and gave rise to strain relaxation of GaN, which resulted in broadening of FWHM of $(10\bar{1}5)$ [24].

In Fig. 2, room temperature PL spectrum of the sample with mobility of 192 ($cm^2/V{\cdot}s$) is shown and the inset is for PL spectrum measured at 10 K, which are typically observed in our samples investigated. A peak observed at 3.479±0.005 eV in low temperature spectrum is attributed to donor bound exciton (DBE) transition and the peak position is consistent with previously reported value [12]. Two more peaks, not clearly resolved from DBE, are observed at 3.467±0.005 eV and 3.455±0.005 eV. Those are related to acceptor bound excitons (ABE). It is generally known that the acceptor binding energies in GaN vary considerably depending on the nature of acceptors involved [25]. In the PL spectrum at room temperature, a dominant peak was observed at 3.415±0.005 eV and the energy shift from the peak position of the donor bound exciton at 10 K was 64 meV. This amount of energy shift is consistent with the temperature dependence of GaN band gap [12,26,27]. Therefore, the peak observed at 3.415±0.005 eV must be donor bound exciton which ought to follow the temperature dependence of GaN band gap. Typical yellow emission observed in Si-doped GaN samples is also seen in our samples centered at 2.25 eV. Yellow emission is generally believed to originate from crystalline disorder [11,14]. In Fig. 3, FWHM of band edge emission and the peak intensity of yellow

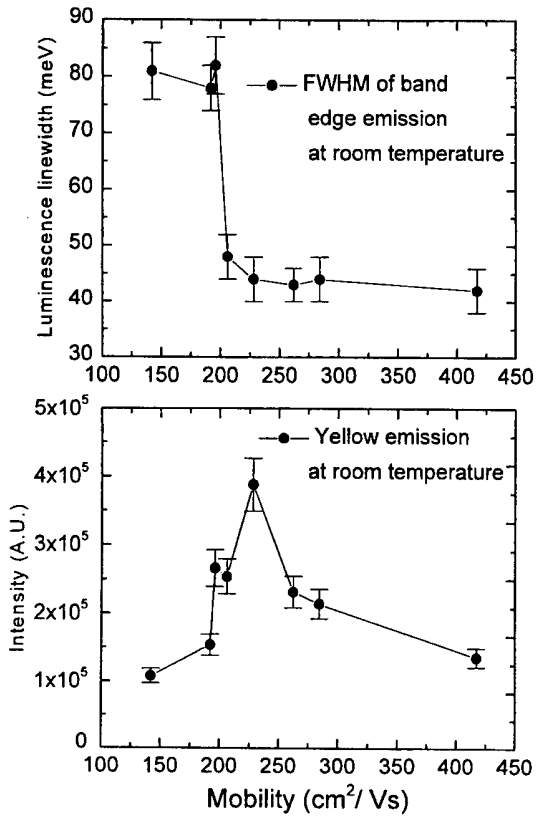

Fig. 3. The FWHM's of band edge emission and the peak height of yellow emission are shown as a function of carrier mobility for GaN:Si epitaxial films in the upper and lower panel, respectively. The data were obtained at room temperature PL measurements.

emission are shown as a function of carrier mobility in the upper and lower panel, respectively. Since the FWHM's of yellow emission do not vary much among the samples, the peak intensities of yellow emission are proportional to the integrated intensities of yellow emission. Note that FWHM's of band edge emission are almost constant in low-doped samples.

As clearly seen in Fig. 1 and Fig. 3, there exists a certain relationship between PL spectrum and FWHM values of Bragg peaks. For a series of samples with different carrier concentrations, the FWHM values of (0002) Bragg peak and band edge emission showed the same behavior as a function of carrier mobility. In the meanwhile, the FWHM values of $(10\bar{1}2)$ Bragg peak exhibit a similar trend to the peak intensities of yellow emission. From these results, it can be inferred that for Si-doped GaN the FWHM of (0002) Bragg peak is more closely related to the characteristic of radiative transition involving near band edge states than that of off-axis Bragg peak such as $(10\bar{1}2)$. And the FWHM of (0002) Bragg peak is not sensitive to the defects generated by Si doping over a certain range of the carrier concentration. On the other hand, the FWHM of $(10\bar{1}2)$ Bragg peak can be used in conjunction with yellow emission intensity as a figure of merit for appropriate estimation of the extent of crystalline disorder like extended defects caused by Si doping. This interpretation is also consistent with the previous report that the band edge luminescence originates from the bulk of the columnar grains and the yellow emission is associated with the presence of defects such as dislocations at low-angle grain boundaries [14].

In summary, Si-doped GaN samples with carrier mobility ranging from 142 ($cm^2/V{\cdot}s$) to 417 ($cm^2/V{\cdot}s$) were investigated using PL and x-ray diffraction. The FWHM values of (0002) and $(10\bar{1}2)$ Bragg peaks were measured and it was found that they varied in different manners as a function of mobility. The FWHM values of (0002) Bragg peak and band edge emission showed a similar trend as a function of carrier mobility. On the other hand, the FWHM values of $(10\bar{1}2)$ Bragg peak exhibit the same trend as the peak intensity of yellow emission. Therefore, it can be inferred from this observation that mosaic spreadings in in-plane and out-of-plane directions are relevant to the yellow emission associated with the extended defects and band edge emission originated from columnar grains of GaN, respectively.

We would like to thank Dr. Sangsig Kim for useful discussions.

REFERENCES

[1] H. Morkoç, S. Strite, G. B. Gao, M. E. Lin, B. Sverdlov and M. Burns, J. Appl. Phys. **76**, 1363 (1994).
[2] M. A. Khan, M. S. Shur, J. N. Kuzunia, Q. Chen, J. Burm and W. Schaff, Appl. Phys. Lett. **66**, 1083 (1995).
[3] O. Aktas, Z. F. Fan, S. N. Mohammad, A. E. Botchkarev and H. Morkoç, Appl. Phys. Lett. **69**, 3872 (1996).
[4] S. C. Binari, L. B. Rowland, W. Kruppa, G. Kelner, K. Doverspike and D. K. Gaskill, Electron. Lett. **30**, 1248 (1994).
[5] S. Nakamura, MRS Bull. **22**, 29 (1997).
[6] M. S. Shur and M. A. Khan, MRS Bull. **22**, 44 (1997).
[7] S. Nakamura, M. Senoh, S. Nagahama, N. Iwasa, T. Yamada, T. Matsushita, H. Kiyoku, Y. Sugimoto, T. Kozaki, H. Umemoto, M. Sano and K. Chocho, Appl. Phys. Lett. **72**, 211 (1998).
[8] S. Nakamura and G. Fasol, *The Blue Laser Diode* (Springer, Berlin, 1997).
[9] D. Kapolnek, X. H. Wu, B. Heying, S. Keller, B. P. Keller, S. P. DenBaars and J. S. Speck, Appl. Phys. Lett. **67**, 1541 (1995).
[10] F. A. Ponce, B. S. Krusor, J. S. M. Jr., W. E. Plano and D. F. Welch, J. Appl. Phys. **67**, 410 (1995).
[11] M. H. Zaldivar, P. Fernández and J. Piqueras, J. Appl. Phys. **83**, 462 (1998).
[12] A. V. Andrianov, D. E. Lacklison, J. W. Orton, D. J. Dewsnip, S. E. Hooper and C. T. Foxon, Semicond. Sci. Technol. **11**, 366 (1996).
[13] S. Ruvimov, Z. Liliental-Weber, C. Dieker, J. Washburn, M. Koike, H. Amano and I. Akasaki, Mat. Res. Soc. Symp. Proc. **468**, 287 (1997).
[14] F. A. Ponce, D. P. Bour, W. Götz and P. J. Wright, Appl.

Phys. Lett. **68**, 57 (1996).
[15] W. Grieshaber, E. F. Schubert, I. D. Goepfert, R. F. Karlicek, Jr., M. J. Schurman and C. Tran, J. Appl. Phys. **80**, 4615 (1996).
[16] E. F. Schubert, I. D. Goepfert, W. Grieshaber and J. M. Redwing, Appl. Phys. Lett. **71**, 921 (1997).
[17] K. G. Fertitta, A. L. Holmes, J. G. Neff, F. J. Ciuba and R. D. Dupuis, Appl. Phys. Lett. **65**, 1823 (1994).
[18] W. T. Read, Philos. Mag. **45**, 775 (1954).
[19] F. A. Ponce, MRS Bull. **22**, 51 (1997).
[20] T. Lei, K. F. Ludwig, Jr. and T. D. Moustakas, J. Appl. Phys. **74**, 4430 (1993).
[21] Q. Zhu, A. Botchkarev, W. Kim, O. Aktas, A. Salvador, B. Sverdlov, H. Morkoç, S. -C. Y. Tsen and D. Smith, Appl. Phys. Lett. **68**, 1141 (1996).
[22] S. Keller, B. P. Keller, Y. -F. Wu, B. Heying, D. Kapolnek, J. S. Speck, U. K. Mishra and S. P. DenBaars, Appl. Phys. Lett. **68**, 1525 (1996).
[23] P. F. Fewster, Semicond. Sci. Technol. **8**, 1915 (1993).
[24] I. -H. Lee, I. -H. Choi, C. R. Lee and S. K. Noh, Appl. Phys. Lett. **71**, 1359 (1997)).
[25] J. W. Orton, Semicond. Sci. Technol. **10**, 101 (1995).
[26] J. Cao, D. Pavlidis, A. Eisenbach, A. Philippe, C. Bru-Chevallier and G. Guillot, Appl. Phys. Lett. **71**, 3880 (1997).
[27] B. Monemar, Phys. Rev. **B10**, 676 (1974).

Journal of the Korean Physical Society, Vol. 34, June 1999, pp. S374~S377

Time-resolved Photoluminescence Measurements in InGaN/GaN Quantum Wells Grown by MOCVD

Eun-joo SHIN, N. W. SONG, J. I. LEE and D. KIM

Spectroscopy Group, Korea Research Institute of Standards and Science, Taejon 305-600

M. Y. RYU and P. W. YU

Department of Information & Communications, K-JIST, Kwangju 506-712

D. LEE

Department of Physics, Chungnam National University, Taejon 305-764

Y.-H. CHOI

Optoelectronics Group, L. G. CIT, Seoul 137-140

C. -H. HONG

SPRC, Chonbuk National University, Chonju 560-756

We report the results of time-resolved studies on InGaN/GaN multiple quantum well. The sample was grown by vertical rotating disk metalorganic chemical vapor deposition. Time- resolved photoluminescence (PL) measurements were investigated at various emission- photon energies and in different time domains. The behavior of laser excitation intensity dependent PL and decay profiles of the emission-photon energy dependence has revealed that the main peak is due to the recombination of localized excitons. Longer recombination lifetime component which has the decay time of several hundred ns was also observed for the first time with a ns pulsed laser. The properties of these optical transitions was discussed.

I. INTRODUCTION

III-nitrides have attracted much attention recently because of their potential for many applications such as blue light-emitting diodes (LEDs), laser diodes (LDs), high temperature and high-power electronic devices. The demonstration of high-brightness LEDs and LDs with InGaN active region has established the III-nitrides as an important material system for optoelectronics operating in the green-UV range [1]. But there remains much to be investigated. Better understanding of optical emission in InGaN quantum well is needed for the improvements of optoelectronic devices based on these materials. In this study we carried out time-resolved measurements at various emission-photon energies and in different time domains to study the mechanisms of optical transitions in InGaN/GaN multiple quantum wells. We observed a long decay component which has a lifetime of several hundred ns in InGaN/GaN multiple quantum wells for the first time.

II. EXPERIMENT

InGaN/GaN multiple quantum well (MQW) sample used in this study was grown by a metalorganic chemical vapor deposition (MOCVD) system. Prior to the deposition of the MQW structure with 5QWs, Si-doped n-type GaN (3×10^{18} cm^{-3}) of 2 μm thickness was grown on a thin 300 Å GaN buffer layer on a (0001) sapphire substrate. The thickness of the active $In_xGa_{1-x}N$ ($x\sim0.18$) well is estimated to be about 75 Å with the 60 Å-thick GaN:Si barrier.

The steady-state PL was measured by using a cw He-Cd laser as an excitation source. The laser intensity dependence was controlled by using a set of UV neutral density filters. The sample was mounted in a closed-cycle liquid-helium cryostat (Janis C-210) for low temperature measurements. We have employed two kinds of time-resolved PL (TRPL) measurements. The one was measured by time-correlated single photon counting (TCSPC) system. The excitation source is a picosecond dual-jet dye laser (Coherent 702) synchronously pumped by a mode-locked argon ion laser (Coherent Innova 200). The output beam with a cavity dumper (Coherent 7220) has about 2 ps pulse width at 3.8 MHz dumping rate. The collected emission was detected with a microchannel

plate photomultiplier tube (Hamamatsu, R2809U). The TCSPC system gives about 10 ps time resolution through deconvolution technique [2]. For longer TRPL measurements, a Q-switched Nd:YAG laser (Spectron SL803G) pumped dye laser (Spectron SL400 G/B) output (5 ns pulse width) was used as an excitation source. The laser beam intensity was reduced by neutral density filters to reduce the high density excitation effect as small as possible. The beam diameter was reduced to be 1 mm by using a pin-hole. Luminescence spectra were detected by using a photomultiplier tube (Hamamatsu, R955). The temporal profiles of PL were monitored by a 500 MHz digital storage oscilloscope (HP 54503A). The instrumentation can resolve decays down to about 10 ns [3].

III. RESULTS AND DISCUSSION

Fig. 1 is the PL spectrum of InGaN/GaN quantum wells measured at 10 K which shows two emission lines. The main PL peak around 3.00 eV results from the InGaN active region and is predominantly due to the recombination of localized excitons. The FWHM is about 70 meV which indicates that the sample under investigation is of high crystalline quality. The additional line around 3.48 eV with lower emission intensity results from the optical recombination in GaN barriers. The inset in Fig. 1 shows the laser excitation intensity dependence of PL peak energy. It is clear that the PL peak position is shifted toward higher energies as laser excitation intensity increases. This observation is expected for a localized exciton recombination. In semiconductor alloys, excitons are localized in random potential wells induced by alloy disorder. At higher excitation intensities lower energy states are more likely to be occupied and consequently

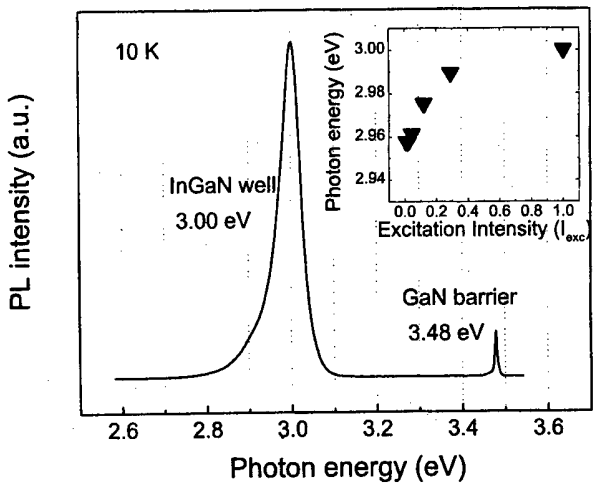

Fig. 1. PL spectrum of InGaN/GaN multiple quantum well measured at 10 K. The inset shows the laser excitation intensity dependence of PL peak position.

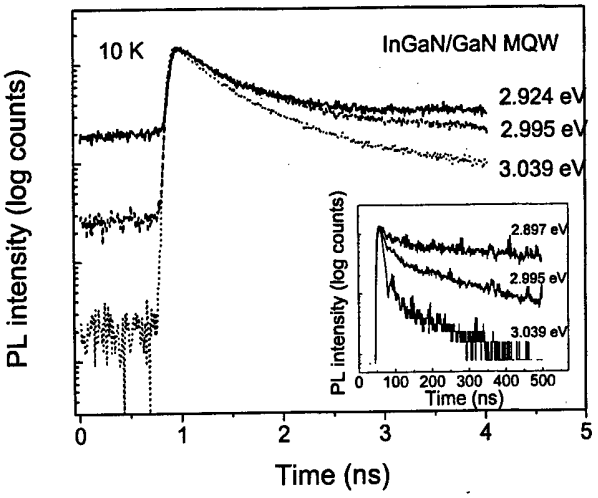

Fig. 2. PL decay profiles with various emission-photon energies at 10 K. As the emission-photon energy decreases the decay time (τ_1 & τ_2 in Fig. 3(a)) becomes slower and the background component (τ_3 in Fig. 3(b)) increases. The inset shows the PL decay profiles with various emission-photon energies measured by ns pulsed laser. It was measured that the background component has the decay time of several hundred ns.

more excitons have to fill in higher energy states which causes the shift of emission peak toward higher energies like state filling effect by the photo-injected electron-hole pairs [4–6].

In order to understand the nature of PL spectrum in InGaN/GaN MQW, we have employed the TRPL measurements using TCSPC system to study its dynamic behavior. The PL temporal responses at various emission-photon energies are shown in Fig. 2. As the emission-photon energy increases, the PL decay becomes faster. The PL decay profiles was well described by a two-exponential function which is composed of fast (τ_1) and slow (τ_2) decay component. And we can see from this figure that the background component (τ_3) increases as the emission-photon energy decreases. This phenomenon means that there exists a much slower recombination decay component of which the lifetime increases as the emission-photon energy decreases. The main PL peak can be clearly resolved from the results of PL decay profiles. We can consider that the PL peak from InGaN active well consists of three different peaks of the first (τ_1), the second (τ_2) and the third (τ_3) PL emission. The first PL emission corresponds to the main peak 3.00 eV, and the second and third PL emissions are located lower than main peak in energy. For the decay measurement of a much slower recombination component, ns pulsed laser was used. The PL decay profiles of background component or third PL emission which has much slower recombination lifetime were shown in the inset of Fig. 2. The PL temporal responses become faster as the emission-photon energy increases. The decay time is in the range of several hundred ns. And we observed that the ampli-

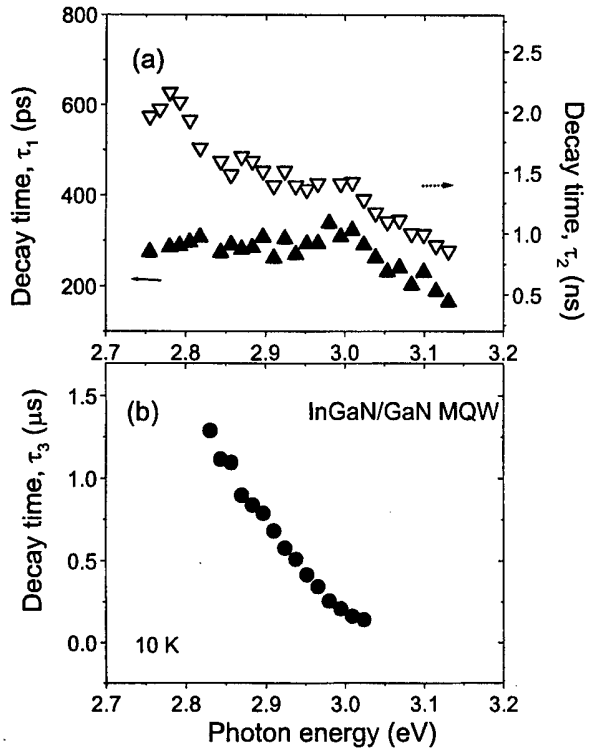

Fig. 3. The emission-photon energy dependence of PL decay times.

tude of faster decay component becomes larger for the higher emission-photon energy. These facts indicate that the faster component represents the decays of the first and second PL emission.

As a result we plot the recombination lifetimes τ_1, τ_2 and τ_3 of the PL emission from InGaN active well as a function of emission-photon energy in Figs. 3(a) and (b). Across the entire fitting of decay profiles in Fig. 2, the amplitude of the decay component of the first PL emission is always greater than that of the second PL. The decay time τ_1 of the first PL emission is almost constant in the energy range from 2.75 to 3.00 eV, and decreases from 300 to 150 ps as the emission-photon energy increases from 3.00 to 3.13 eV as shown in Fig. 3(a). From this experimental results we interpreted that the first PL emission was due to localized excitons. Localized excitons can transfer from higher energy sites to lower energy sites through a relaxation whose rate increases with the increase of emission energy in semiconductor alloys. The decay rate of localized excitons is expressed by radiative recombination decay rate plus relaxation rate to the lower-lying energy states. Thus the decay time decreases with the increase of emission-photon energy. There is second PL emission component τ_2 which has a recombination lifetime ranging from 1 to 2.3 ns in Fig. 3(a). As the emission-photon energy increases the decay rate of the second PL decreases. This component may be an impurity related peak. This dependence on emission energy suggests that the energy level of impurity involved in this transition may have a distribution together with alloy disorder in InGaN quantum wells. The overlap of much slower background component and weak amplitude of the second PL decay in temporal response makes it difficult to analyze this recombination component at this stage.

In Fig. 3(b) we have plotted the emission-photon energy dependence of the third PL emission or the background component showing that the lifetime is of the order of hundred ns. The decay time decreases monotonously as the emission-photon energy increases. This slower decay component is suggested as due to the band-to-impurity transitions. The impurity may be related to the Si donor which exists in GaN barrier layer together with alloy disorder or the interface roughness. The properties of the band-to-impurity transition have been observed previously in GaN epilayer [7] and p-type GaN [8]. These results in emission-photon energy dependence of recombination lifetime τ_3 indicate that the binding energy of impurity involved in this transition has a distribution. It was shown that the radiative recombination lifetime of a band-to-impurity transition depends on impurity binding energy E_D [7]. It is described by $\tau \propto E_D^{3/2} \propto (E_g - h\nu)^{3/2}$, with emission-photon energy, $h\nu$. Experimentally observed emission-photon energy dependence of the decay time τ_3 can be described by $\tau = A(E_0 - E)^{3/2}$, $(E \leq E_0)$ where A is constant and E is emission-photon energy. The fitted value E_0 of 3.06 eV is in agreement with the bandgap energy E_g of 3.04 eV. In addition, based on a theoretical model [9], the asymptotic decay of the band-to-impurity transition at longer time follows a power law, $I(t) \propto t^{-\alpha}$. We have plotted PL decay profiles in double logarithmic scale and found that the decay at longer time follows a power law. This further supports the nature of the band-to-impurity recombination.

IV. SUMMARY

Time-resolved PL measurements in InGaN/GaN multiple quantum well grown by MOCVD was studied in different time domain. From the results of TRPL, the PL peak from InGaN active well was considered as a convolution of three different peaks of the first, second and third PL emission. The laser excitation intensity dependent PL and the emission-photon energy dependence of decay time show that the main PL emission or first PL emission in InGaN well is due to the recombinations of localized excitons. The properties of emission- photon energy dependence on decay time of the second and third PL emission are suggested to be impurity related transitions. We observed for the first time that there is the recombination lifetime component which has the decay

time of several hundred ns in third PL emission.

REFERENCES

[1] M. S. Minsky, S. B. Fleischer, A. C. Abare, J. E. Bowers, E. L. Hu, S. Keller and S. P. Denbaars, Appl. Phys. Lett. **72**, 1066 (1998).

[2] E. -j. Shin, J. I. Lee, N. Q. Liem, D. Kim, J. Y. Leem, J. -S. Son, S. K. Noh and D. Lee, Solid State Commun. **102**, 855 (1997).

[3] E. -j. Shin, N. W. Song, J. I. Lee, D. Kim, Y. Choi and C. -H. Hong, J. Korean Phys. Soc. (1998) in press.

[4] K. C. Zeng, M. Smith, J. Y. Lin, H. X. Jiang, J. C. Robert, E. L. Piner, F. G. Mclntosh, S. M. Bedair and J. Zavada, J. Vac. Sci. Technol. **B15**, 1139 (1997).

[5] A. Satake and Y. Masumoto, Phys. Rew. **B57**, R2041 (1998).

[6] E. S. Jeon, V. Kozlov, Y. -K. Song, A. Vertikov, M. Kuball, A. V. Nurmikko, H. Liu, C. Chen, R. S. Kern, C. P. Kuo and M. G. Craford, Appl. Phys. Lett. **69**, 4149 (1996).

[7] J. D. Chen, M. Smith, J. Y. Lin, H. X. Jiang, A. Salvador, B. N. Sverdlov, A. Botchkarev and H. Morkoc, J. Appl. Phys. **79**, 2675 (1996).

[8] M. Smith, G. D. Chen, J. Y. Lin, H. X. Jiang, A. Salvador, B. N. Sverdlov, A. Botchkarev, H. Morkoc and B. Goldenberg, Appl. Phys. Lett. **68**, 1883 (1996).

[9] P. Avouris and T. N. Morgan, J. Chem. Phys. **74**, 4347 (1981).

Journal of the Korean Physical Society, Vol. 34, June 1999, pp. S378~S381

Surface Morphology and Optical Properties of Epitaxial $Al_XGa_{1-X}N$

Je Won KIM and In-Hoon CHOI
Department of Materials Science, Korea University, Seoul 132-701

Young K. PARK and Yong Tae KIM
Semiconductor Materials Laboratory, Korea Institute of Science and Technology, Seoul 130-650

The surface morphology and absorption edges of epitaxial $Al_XGa_{1-X}N$ layers grown on (0001) sapphire substrate by molecular beam epitaxy are investigated with the change of AlN mole fractions. Transmission and photothermal deflection spectroscopy determine the absorption coefficient at room temperature. Photothermal deflection spectroscopy can be applied to determine the low absorbance values. The uniform depth profile and linear dependence of average atomic concentration of epitaxial $Al_XGa_{1-X}N$ layers on AlN mole fraction imply that the epitaxial growth of $Al_XGa_{1-X}N$ layers with variation of AlN mole fraction is well controlled without the compositional fluctuation in depth of the epilayer. It is observed by atomic force microscopy that the surface grain shape and roughness of epitaxial $Al_XGa_{1-X}N$ layers change at a middle of AlN mole fraction, and also observed that the effective bandgaps increase with increasing AlN mole fraction.

I. INTRODUCTION

Wide band gap III-V nitride systems have been received much attention as promising materials for optoelectronic device applications [1], such as high-power amplifiers, ultraviolet (UV), blue, green, and yellow light-emitting diodes (LEDs), and short-wavelength laser diodes [2–4]. Observation of optically pumped stimulated emission in GaN epilayers has led to increased interest in the development of efficient nitride UV-visible light emitters [5]. In fact, superbright high efficiency blue LEDs have been commercialized and current injection laser diodes based on nitride heterostructures have been reported [6–8]. Among them, the AlGaN alloy system is particularly important because its direct band gap covers a wide spectral range from UV to blue, and it is also suitable for high power and high temperature electronic device applications [9–13]. So far, the research activities have concentrated on the optimization of structural properties. However, it is rare to study the optical properties of AlGaN alloy system with the change of structural properties of hexagonal $Al_XGa_{1-X}N$ epilayers covering the wide range of AlN mole fraction.

The structural properties of epitaxial $Al_XGa_{1-X}N$ layers grown on (0001) sapphire by molecular beam epitaxy (MBE) with variation of AlN mole fraction is characterized by various characterization systems. Depth uniformity and surface morphology are characterized using Auger electron microscopy (AES) and atomic force microscopy (AFM). The dependence of the absorption edges of $Al_XGa_{1-X}N$ layers on AlN mole fraction was determined from transmission spectra and photothermal deflection spectroscopy (PDS) measurements. By absorption coefficient data, we can estimate the effective bandgap of $Al_XGa_{1-X}N$ layers at room temperature.

II. EXPERIMENT

The epitaxial $Al_XGa_{1-X}N$ layers were grown using a plasma-induced molecular beam epitaxy (PIMBE) using conventional effusion cells for the metallic components and radio frequency *rf* plasma atomic radical source for the nitrogen. This nitrogen source has advantages of high contents of nitrogen radicals compared with ionic species, and low ion-induced damage during growth. The inductively coupled plasma power and pressure in the MBE chamber during growth were 400 W and 4×10^{-5} mbar, respectively. The deposition temperature was varied from 840 °C to 1000 °C. AlN mole fraction of epitaxial $Al_XGa_{1-X}N$ layers for characterizing the structure and surface morphology was varied from 0.16 to 0.76. The epitaxial $Al_XGa_{1-X}N$ layers were imaged with contact mode AFM (SFM-BD2, Park Scientific Instruments) under ambient conditions which is based on the optical lever deflection mechanism, and a pyramidal Si_3N_4 cantilever whose length is 200 μm. Auger electron microscopy (Physical Electronics PHI 680) depth profil-

ing was carried out to characterize uniformity of constituents of $Al_XGa_{1-X}N$ layers, and variation of Al and Ga as a function of AlN mole fraction [14].

Transmission spectroscopy and PDS determined the relative absorption edges of AlGaN alloys. AlN mole fraction of epitaxial $Al_XGa_{1-X}N$ layers for determining the relative absorption edges was varied from 0 to 1 [15,16]. The transmission measurement was carried out by Perkin-Elmer Lambda 900 double beam spectrometer with a resolution of 1 nm in the spectral range from 195 to 2000 nm [17,18]. PDS was applied to determine the low absorbance values. The useful features of the PDS are the extremely high sensitivity. Absorbance values of III-V nitrides as low as $\alpha d=10^{-5}$ can be measured by this technique.

III. RESULTS AND DISCUSSION

AES depth profiles of $Al_{0.29}Ga_{0.71}N$ as a function of sputter time are shown in Fig. 1. Solid, dashed, and dotted lines represent the peak of Al, Ga, and N, respectively. The atomic concentrations of all the constituents of the epitaxial $Al_XGa_{1-X}N$ layers show a linear dependence on the sputter time, which explains that all the constituents of epilayer have good uniformity throughout the sputter time until the lines reach the interface between $Al_XGa_{1-X}N$ layers and sapphire substrate. The concentration of carbon and oxygen as impurities in the epilayer is negligible in the given sputter time range. The abrupt increase in oxygen peak at the interface is attributed to oxygen constituent of sapphire (α-Al_2O_3) substrate. All the $Al_XGa_{1-X}N$ samples studied in this work show a good AES depth profile uniformity of all the constituents throughout the sputter time. The uniform

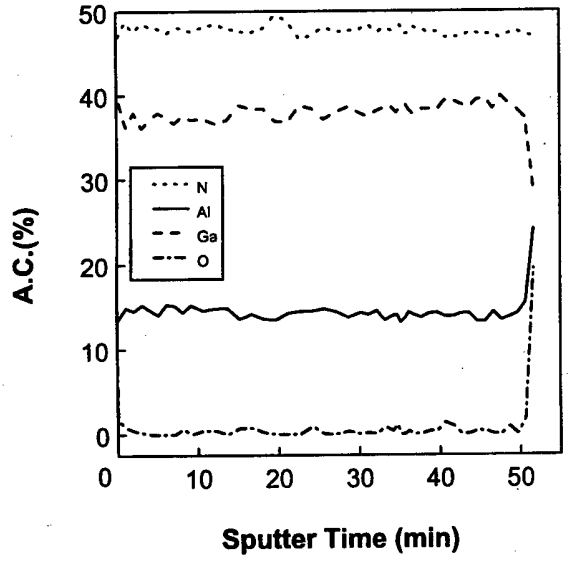

Fig. 1. AES depth profile of $Al_{0.29}Ga_{0.71}N$ as a function of sputter time.

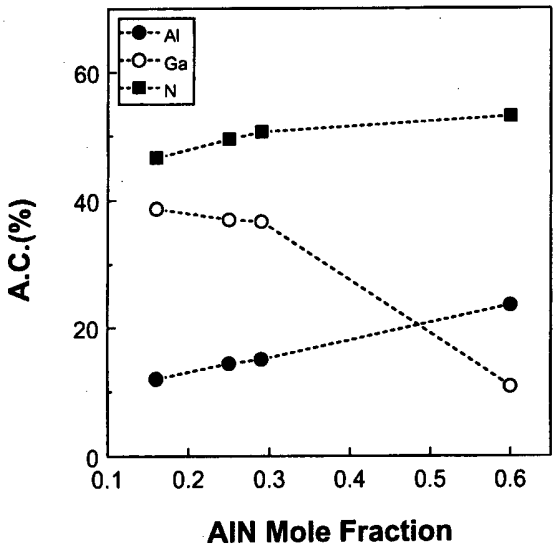

Fig. 2. Atomic concentrations of Al, Ga, and N in $Al_XGa_{1-X}N$ epilayers as a function of AlN mole fraction.

depth profile implies that there is not the compositional fluctuation of constituents in AlGaN epilayer.

The atomic concentration of Al, Ga, and N in the $Al_XGa_{1-X}N$ epilayer as a function of AlN mole fraction is shown in Fig. 2. The atomic concentration of N remains nearly the same amount with variation of AlN mole fraction within 10 % error range of AES. Both Al and Ga atomic concentrations show good linearity. The linear dependence of atomic concentration of constituents on AlN mole fraction and uniform depth profile as shown in Fig. 2 support that the composition of AlGaN epilayer is well controlled without compositional fluctuation of any constituents during the growth of $Al_XGa_{1-X}N$ epilayers.

Atomic force microscopy characterization is performed to investigate the surface of $Al_XGa_{1-X}N$ epilayers with higher lateral resolution below 1 μm. With increasing AlN mole fraction up to 0.29, the grain shape changes from roundish to coalesced one and the grain size of AlGaN becomes larger. While, at higher AlN mole fraction with increasing AlN mole fraction from 0.29 to 0.76, the grain shape changes more faceted and rougher one. The surface morphology of $Al_XGa_{1-X}N$ layers consists of homogeneous grains at low AlN mole fraction. The variation of surface roughness can be analyzed by the root mean square (RMS) and average roughness.

The RMS and average roughness of the surface of $Al_XGa_{1-X}N$ layers obtained from AFM images are shown as a function of AlN mole fraction in Fig. 3. The RMS and average roughness of the AlGaN epilayers increase with increasing AlN mole fraction up to 0.6. On the other hand, the RMS and average roughness of the $Al_{0.76}Ga_{0.24}N$ are smaller than those of $Al_{0.6}Ga_{0.4}N$. It seems that the trend is caused from the grain shape of the AlGaN epilayers. The grain shape of the AlGaN epilayer changes from homogeneous roundish to faceted

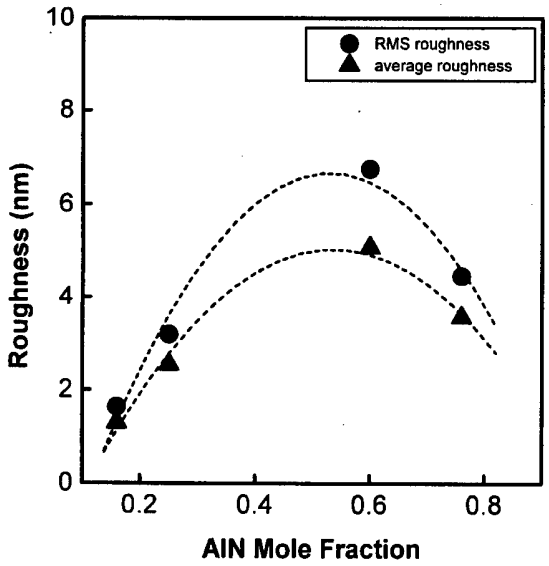

Fig. 3. RMS and average roughness estimated by AFM images as a function of AlN mole fraction.

grain as increasing AlN mole fraction up to 0.6 and then at $Al_{0.76}Ga_{0.24}N$ the grain shape becomes more homogeneous than that of $Al_{0.6}Ga_{0.4}N$. From the observation of change in grain shape and the analysis of roughness, there would be the transition point of the change of grain shape at a middle of AlN mole fraction.

The absorption coefficient of AlGaN alloys is obtained from transmission and PDS measurements. The absorption coefficients of epitaxial $Al_XGa_{1-X}N$ layers as a function of photon energy for various AlN mole fractions are shown in the inset of Fig. 4. AlN mole fraction is varied from 0 toward 0.2, 0.5, 0.86, and 1, respectively. With increasing AlN mole fraction, dependence of absorption coefficient of $Al_XGa_{1-X}N$ as a function of photon energy shifts to higher energy. With these absorption coefficient data, the effective bandgap of the AlGaN alloys is deduced. The effective bandgap of the AlGaN alloys was determined by comparison of the photon energies $E_{4.8}$ at which $\alpha_{AlGaN}=10^{4.8}$ cm^{-1}. The physical justification for this definition is given by the determining the bandgap of GaN, showing that $E_{4.8}$ lies at the bandgap of GaN, 3.4 eV. In Fig. 4, the effective bandgaps of $Al_XGa_{1-X}N$ layers as a function of AlN mole fraction are shown. The effective bandgaps of AlGaN alloys for the AlN mole fractions of 0, 0.2, 0.5, 0.86 and 1 are 3.42, 3.89, 4.43, 5.5 and 6.13 eV, respectively. From the energy position of the absorption edge versus AlN mole fraction, a bowing parameter of 1.3 eV can be determined.

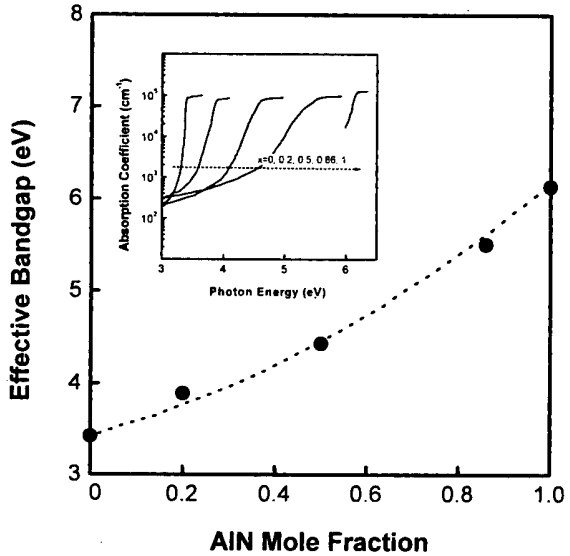

Fig. 4. Effective bandgaps for various AlN mole fractions. Solid circles and dotted line represent the effective bandgaps of $Al_XGa_{1-X}N$ layers as a function of AlN mole fraction and the determined bowing parameter, respectively. Inset shows that absorption coefficients of epitaxial $Al_XGa_{1-X}N$ layers were measured by transmission and PDS at room temperature. AlN mole fraction was varied from 0 to 1.

As can be seen in Fig. 4, the effective bandgaps increase with increasing AlN mole fraction. But the surface and structural properties are changed with increasing AlN mole fraction. There is a transition point in the change of grain shape in the middle AlN mole fraction region. With the results of the absorption properties and structural change in epitaxial AlGaN layer, it is concluded that the effective bandgaps of AlGaN is increased with increasing AlN mole fraction and the RMS and average roughness of the surface of epitaxial $Al_XGa_{1-X}N$ layers are changed in the middle AlN mole fraction.

IV. SUMMARY

The absorption edges and structural properties of epitaxial $Al_XGa_{1-X}N$ layers have been investigated. With increasing AlN mole fraction, it is observed that the surface grain shape of the epitaxial layers changes from roundish to coalesced one. There is a transition point of the change of grain shape at a middle AlN mole fraction, which corresponds to a peak value of RMS roughness. The highly sensitive PDS measurements allow us to determine the absorption coefficients explicitly for the AlGaN alloy samples within the wide compositional range of AlGaN alloy. The absorption coefficient of epitaxial $Al_XGa_{1-X}N$ layers as a function of photon energy shifts towards higher photon energies with increasing the AlN mole fraction. The effective bandgap of the AlGaN alloys was deduced from the absorption coefficient that the photon energy lies at $E_{4.8}$. We found that the effective bandgaps of AlGaN alloys were varied from 3.42 to 6.13 eV. From the absorption properties and structural investigations. The absorption properties are deduced and the change of structural properties of epitaxial $Al_XGa_{1-X}N$ layers are observed.

ACKNOWLEDGMENTS

This work was supported by the Ministry of Trade, Industry and Energy (Contract No. 2M08380 and 2M08790) and by the Korea Institute of Science and Technology (Contract No. 2E15940). Je Won Kim thanks the Korea Science and Engineering Foundation for financial support to visit Walter Schottky Institut, Technische Universität, München.

REFERENCES

[1] H. Morkoç, S. Strite, G. B. Gao, M. E. Lin, B. Sverdlov and M. Burns, J. Appl. Phys. **76**, 1363 (1994).

[2] J. I. Pankove, Mater. Res. Soc. Symp. Proc. **162**, 515 (1990).

[3] S. Strite and H. Morkoç, J. Vac. Sci. Technol. **B10**, 1237 (1992).

[4] K. Domen, A. Kuramata and T. Tanahashi, Appl. Phys. Lett. **72**, 1359 (1998).

[5] X. H. Yang, T. Schmidt, W. Shan, J. J. Song and B. Goldenberg, Appl. Phys. Lett. **66**, 1 (1995).

[6] S. Nakamura, M. Senoh, S. Nagahama, N. Iwasa, T. Yamada, T. Matsushita, H. Kiyoku and Y. Sugimoto, Jpn. J. Appl. Phys. **35**, L74 (1996).

[7] S. Nakamura, M. Senoh, S. Nagahama, N. Iwasa, T. Yamada, T. Matsushita, H. Kiyoku and Y. Sugimoto, Appl. Phys. Lett. **68**, 2105 (1996).

[8] S. Nakamura, T. Mukai and M. Senoh, J. Appl. Phys. **76**, 8189 (1994).

[9] M. A. Khan, J. N. Kuznia, D. T. Olson, W. J. Schaff, J. W. Burm and M. S. Shur, Appl. Phys. Lett. **65**, 1121 (1994).

[10] D. Walker, X. Zhang, P. Kung, A. Saxler, J. Xu and M. Razeghi, Appl. Phys. Lett. **68**, 2100 (1996).

[11] S. Imanaga and H. Kawai, J. Appl. Phys. **82**, 5843 (1997).

[12] G. Y. Xu, A. Salvador, W. Kim, Z. Fan, C. Lu, H. Tang, H. Morkoç, G. Smith, M. Estes, B. Goldenberg, W. Yang and S. Krishnankutty, Appl. Phys. Lett. **71**, 2154 (1997).

[13] A. Osinsky, S. Gangopadhyay, B. W. Lim, M. Z. Anwar, M. A. Khan, D. V. Kuksenkov and H. Temkin, Appl. Phys. Lett. **72**, 742 (1998).

[14] J. W. Kim, C. S. Son, I. H. Choi, Y. K. Park, Y. T. Kim, O. Ambacher and M. Stutzmann, J. Cryst. Growth, to be published.

[15] J. W. Kim, C. S. Son, I. H. Choi, Y. K. Park and Y. T. Kim, J. Korean. Vac. Soc., to be published.

[16] J. W. Kim, C. S. Son, I. H. Choi, Y. K. Park and Y. T. Kim, *Abstracts of the 9th International Symposium on the Physics of Semiconductors and Applications* (Seoul, Korea, 1998), p. 95.

[17] J. W. Kim, C. S. Son, Y. G. Jang, I. H. Choi, Y. K. Park, Y. T. Kim, O. Ambacher and M. Stutzmann, Korean J. Mat. Res. **9**, 42 (1999).

[18] J. W. Kim, C. S. Son, I. H. Choi, Y. K. Park, Y. T. Kim, O. Ambacher and M. Stutzmann, *Abstracts of the 4th International Conference on Electronic Materials* (Cheju, Korea, 1998), p. 94.

Journal of the Korean Physical Society, Vol. 34, June 1999, pp. S382~S385

Evolution of Crystalline Orientations of Polycrystalline GaN on Indium Tin Oxide/Glass Substrates by Nitridation

Doo-Cheol PARK, Shizuo FUJITA and Shigeo FUJITA

Department of Electronic Science & Engineering, Kyoto University, Kyoto 606-8501, Japan

Hyun-Chul Ko

Venture Business Laboratory, Kyoto University, Kyoto 606-8501, Japan

Polycrystalline GaN on the nitrided indium tin oxide (ITO)/glass substrates with nitrogen plasma was grown by radio frequency plasma enhanced chemical vapor deposition (PECVD). X-ray photoelectron spectroscopy (XPS) study revealed that the nitridation of ITO surface proceeded with higher temperature, longer time, and higher flow rate of N_2 gas. X-ray diffraction (XRD) measurements showed that the crystallinity of GaN on nitrided ITO/glass was improved comparing to that on ITO/glass without the nitridation, and the preferred orientations of $(10\bar{1}0)$ and $(10\bar{1}1)$ planes of GaN were controllable with the nitridation conditions.

I. INTRODUCTION

Polycrystalline GaN is promising for the applications to large area display panel devices [1]. Our group has intensively studied on the growth of polycrystalline GaN on various substrates [2]. The indium tin oxide (ITO)/silicate glass substrate has been considered as one of the most attractive substrates, since many display panel devices need transparent electrodes on inexpensive large area transparent substrates. However, due to the low strain point of silicate glass (600 °C~670 °C), the growth of GaN on ITO/glass should be performed below 600 °C, where generally the crystallinity of GaN tends to be worse compared to that of GaN grown at the higher temperatures (*e.g.*, 800 °C).

For the epitaxial growth of GaN layer on the sapphire substrates, pretreatment such as introduction of buffer layer or nitridation of the sapphire substrate surface prior to the growth has been reported to be very important to improve the structural, optical, and electrical properties of the grown GaN films [3–5]. From this point of view, in this work, attempts have been made for the control of crystal orientation in polycrystalline GaN on ITO/glass substrates by nitridation of the ITO surface prior to the growth of GaN.

We report that the crystallinity of polycrystalline GaN on ITO/glass substrates grown by radio frequency (RF) plasma enhanced chemical vapor deposition (PECVD) at 600 °C is improved and the crystal orientations can be controlled by the nitridation of the ITO surface.

II. EXPERIMENTAL DETAILS

The substrate used in the experiment was ITO/glass (Corning 1737) with the dimension of 15×15 mm^2 and the ITO film thickness about 1400 Å. The substrates were cleaned in organic solvents using a conventional process before introduction to the growth chamber. Surface nitridation was performed by the inductively coupled plasma of N_2 generated at 13.56 MHz at 200 °C, 300 °C, and 400 °C with different nitridation time in the growth chamber. The nitridation was followed by the growth of polycrystalline GaN using RF PECVD. Triethlygallium (TEGa) with N_2 carrier gas was introduced close to the substrate. The N_2 gas plasma was utilized for the nitrogen source. The typical sample structure consisted of the buffer layer and the main layer. The buffer GaN layer was grown at 400 °C with its thickness about 250 Å. The growth of buffer layer has been found to be effective to improve the crystallinity of the main layer [2]. Growth of the main layer was performed at the growth temperature of 600 °C which was sufficiently lower than the strain

Table 1. Summary of nitridation and growth conditions.

	Nitridation	Buffer layer	Main layer
N_2	40, 80	40	40
RF plasma (W)	200	200	200
TEGa (μmol/min)	–	0.43	0.43
Substrate temp. (°C)	200, 300, 400	400	600
Gas pressure (mTorr)	130	170	170

point (667 °C) of the glass substrate. The thickness of the main layer was about 1.5 μm. The nitridation and growth conditions are summarized in Table 1.

X-ray photoelectron spectroscopy (XPS) measurements were carried out to examine the occurrence and proceeding of nitridation of the ITO surface. The structural characterization of polycrystalline GaN was done by X-ray diffraction (XRD) measurements.

III. RESULTS AND DISCUSSIONS

1. Nitrided Substrate Composition Analysis

Figure 1 shows XPS spectrum peaks of nitrogen on the nitrided ITO surface at the different nitridation temperatures and time. The nitridation conditions were 40 sccm of N_2 gas flow rate, 200 W of RF power at 200 °C, 300 °C, and 400 °C. Reference binding energy of indium $3d$ photoemission (445 eV) was utilized. The intensities of nitrogen $1s$ core-level photoemission (399 eV) were normalized by those of indium. No XPS spectrum peak of nitrogen is seen for the sample with no nitridation. By the way, the nitrogen peak intensities are increased with the increase of temperatures at all the three nitridation time as shown in Figs. 1(a) (10 min), (b) (30 min), and (c) (60 min). As a result, the nitridation is significantly effected by the nitridation temperature, *i.e.*, the higher temperature effectively enhances the nitridation.

Figure 2 exhibits XPS spectrum peaks of nitrogen and oxygen on the ITO surface nitrided under the N_2 gas flow rates of (a) 40 sccm and (b) 80 sccm at 400 °C with increasing the nitridation time. The intensities of oxygen $1s$ core-level photoemission (531 eV) were also normalized by those of indium. Both of Figs. 2(a) and (b) show that nitrogen peak intensity increases with time while that of oxygen decreases. Those results imply that the nitridation proceeds with time. For the N_2 gas flow rate, there seems no big difference between the results of (a) 40 sccm and (b) 80 sccm. However, the careful investigations of peak signal intensities, including the data for other nitridation conditions, have revealed the tendency that the more nitridation is proceeded under 80 sccm

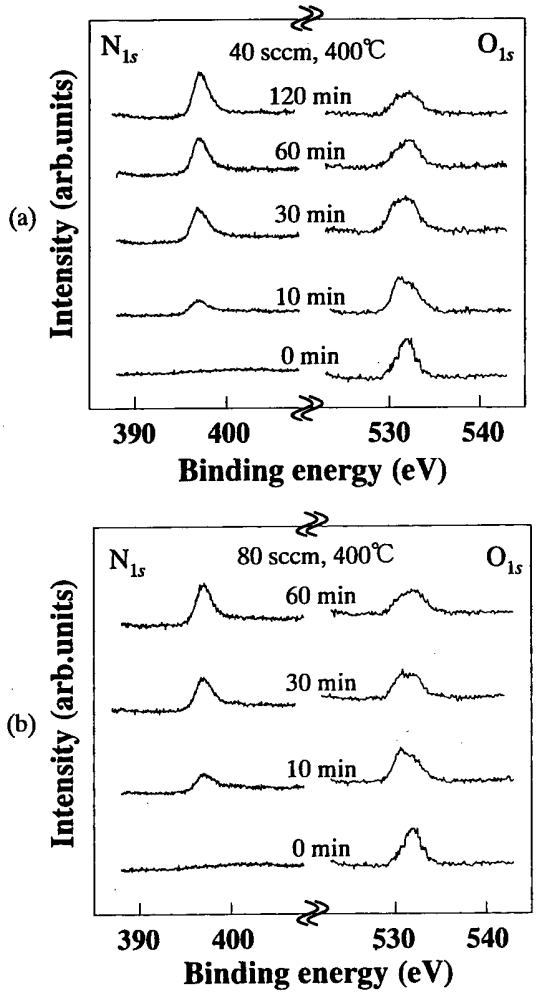

Fig. 2. XPS intensities of nitrogen and oxygen of $1s$ core-level photoemissions of ITO surface nitrided under (a) 40 sccm and (b) 80 sccm nitrogen flow rates at 200 °C, 300 °C, and 400 °C.

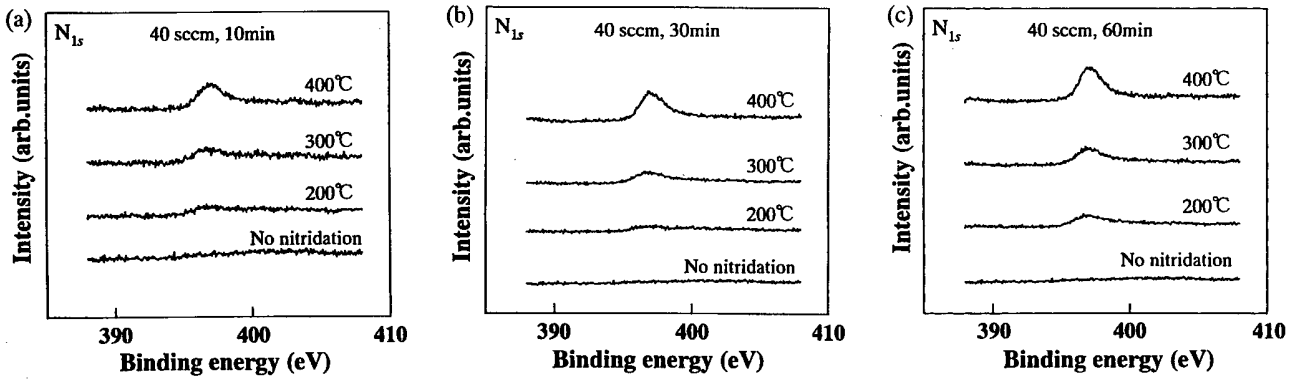

Fig. 1. XPS intensities of nitrogen $1s$ core-level photoemission of ITO surface nitrided during (a) 10 min, (b) 30 min, and (c) 60 min nitridation time at 400 °C.

than 40 sccm. For example, the nitrogen peak intensity of the sample (60 min) in Fig. 2(b) is rather close to that of the sample (120 min) in Fig. 2(a). Further, with the nitridation, oxygen desorption occurs and tends to be enhanced with the increase of nitridation time. Considering the results in Fig. 2, showing the increase of nitrogen with the decrease of oxygen, it is suggested as a plausible model that oxygen sites of the ITO film are substituted with nitrogen atoms, although some nitrogen atoms may be at interstitial sites.

2. Structural Characterization by XRD Measurements

First, XRD measurements were carried out to investigate the orientation change of the ITO surface with respect to the XPS results. However, the results indicated no orientations of it and no difference between before and after the nitridation in the experimental range. This is because the nitrided layer formed on ITO is so thin (estimated to be less than a hundred Å) that any change of its orientations, even if it occurs, cannot be detected by the XRD measurements. Therefore we cannot deny a possibility of the orientation change of ITO surface which may influence on the orientations of GaN grown on it. The discussions will be given later.

Then, we investigated how the nitrided ITO surface made effects on the orientation of the polycrystalline GaN thin films. Figure 3 shows the results of XRD measurements of GaN on the ITO/glass substrate nitrided under the different conditions, *i.e.*, (a) 40 sccm and (b) 80 sccm of nitrogen flow rates, 200 W of RF power and at 400 °C of nitridation temperature. The sample without nitridation (0 min) which consists of the low temperature buffer layer and the main GaN layer is weakly-oriented along $(10\bar{1}0)$ and $(10\bar{1}1)$ planes. In the Figs. 3(a) and (b), note that the intensity of XRD peaks becomes larger by the nitridation, which means that the crystallinity of GaN is improved.

Figure 3(a) clearly demonstrates that two peaks change with increasing the nitridation time. After the 10 minutes nitridation, the $(10\bar{1}0)$ peak becomes larger drastically, while the $(10\bar{1}1)$ peak does not change. With longer the nitridation time, the intensity ratio, $(10\bar{1}0)/(10\bar{1}1)$, becomes smaller slowly, *i.e.*, the $(10\bar{1}0)$ peak becomes smaller and the $(10\bar{1}1)$ peak larger. For the sample nitrided during 120 minutes, the $(10\bar{1}1)$ peak becomes the largest and dominant.

Figure 3(b) indicates the results of XRD measurements of GaN, where the ITO surface was nitrided under 80 sccm. The variation of patterns of the two XRD peaks is similar with that of Fig. 3(a). By 10 minutes, the peak from the $(10\bar{1}0)$ planes becomes large. As time increases, it becomes smaller while the $(10\bar{1}1)$ peak gets larger. Finally, the $(10\bar{1}1)$ peak becomes large drastically and dominant at 60 minutes nitridation. The XRD pattern of 60 minutes in Fig. 3(b) is quite similar to that of 120 minutes in Fig. 3(a). That is, the orientations of GaN on ITO nitrided under 40 sccm with 120 minutes are similar with those on ITO nitrided under 80 sccm with 60 minutes.

Here it is worth noting that the optical properties of polycrystalline GaN will be significantly influenced by the crystallinity and orientation. At the present stage we have not achieved the high optical functions of polycrystalline GaN and further improvement of its qualities is necessary, nevertheless the results shown in this paper offer a promising technique in the future to control the orientation of polycrystalline GaN so that its optical

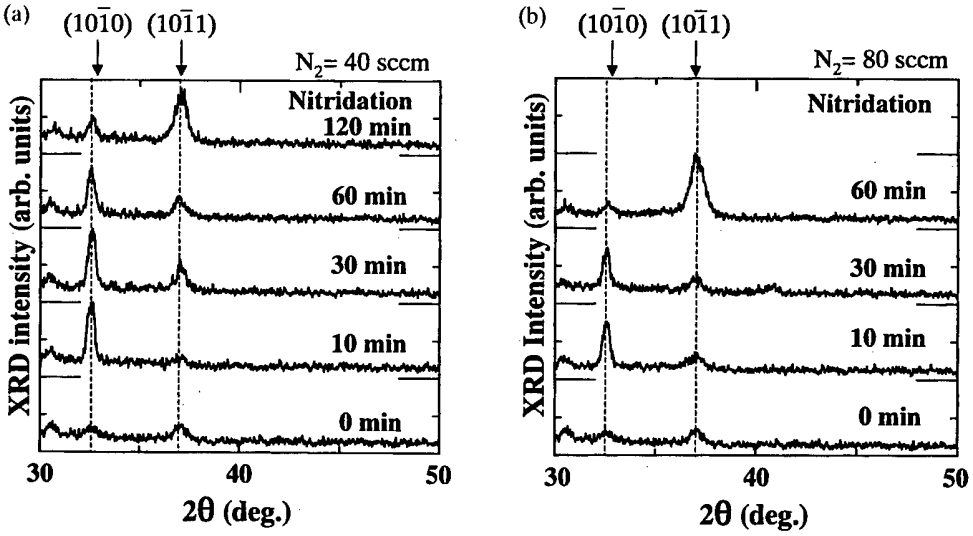

Fig. 3. XRD patterns of GaN thin films on ITO/glass substrates whose ITO surfaces were nitrided at 400 °C under (a) 40 sccm and (b) 80 sccm of N_2 gas flow rates.

functions are fully employed.

The mechanism for the change of preferred orientation due to the nitridation of ITO surface is not clearly explained at present, but as possible reasons we considered the change of orientation, composition, and roughness of ITO surface by the nitridation. The driving force for these phenomena may be not only reaction with nitrogen on the ITO surface but also bombardment by energetic species including nitrogen atoms, ions, and electrons in the N_2 gas plasma during the nitridation process. It has been well recognized that the properties of ITO films are greatly influenced by their growth and annealing conditions [6,7]. Slight increase of the surface roughness by the nitridation was detected by atomic force microscopy. It seems reasonable to assume that the very thin surface layer of ITO was modified by the nitridation process, although it was so thin that its crystallinity, even if somewhat oriented, could not be detected by the sensitivity of the XRD measurements, and it, for example, modified the surface stress to change the preferred orientation of GaN on it. Since the phenomena occurred during the nitridation are very complicated, the surface structure of the ITO after the nitridation cannot be discussed only in terms of the XPS measurements and more systematic investigations with various surface analysis techniques are necessary to reveal the surface structure. However, it is expected that the nitridation process occurs more effectively for longer time and higher N_2 gas flow rate; this seems to be a reason for the similar XRD pattern of GaN between the nitridation time for ITO surface of 120 min at 40 sccm and of 60 min at 80 sccm, discussed above.

IV. CONCLUSIONS

Effects of nitridation of ITO surface on the orientations of polycrystalline GaN grown by PECVD on it were investigated. The nitridation was performed using the N_2 gas plasma. The XPS measurements revealed that the nitridation proceeds more at higher nitridation temperature, longer time, and higher flow rate of N_2 gas. Crystallinity of polycrystalline GaN grown on the nitrided ITO/glass substrates was characterized by the XRD measurement. As a result, crystallinity of GaN was improved by the nitridation. Further, the crystal orientations of $(10\bar{1}0)$ and $(10\bar{1}1)$ planes were controllable by changing the nitridation conditions, suggesting that the nitridation can be a promising technique in the future to effectively utilize the optical functions of polycrystalline GaN films on ITO/glass substrates.

ACKNOWLEDGMENTS

We wish to thank that D.-C. Park is partly supported by the grant from the International Communications Foundation (ICF).

REFERENCES

[1] K. Iwata, H. Asahi, K. Asami, R. Kuroiwa and S. Gonda, Jpn. J. Appl. Phys. **36**, L661 (1997).
[2] D. C. Park, H. C. Ko, Sz. Fujita and Sg. Fujita, Jpn. J. Appl. Phys. **37**, L294 (1998).
[3] H. Amano, N. Sawaki, I. Akasaki and Y. Toyoda, Appl. Phys. Lett. **48**, 353 (1986).
[4] S. Nakamura, Jpn. J. Appl. Phys. **30**, L1705 (1991).
[5] K. Uchida, A. Watanabe, F. Yano, M. Kouguchi, T. Tanaka and S. Minagawa, J. Appl. Phys. **79**, 3487 (1996).
[6] Y. Shigesato, S. Takaki and T. Haranoh, J. Appl. Phys. **71**, 3356 (1992).
[7] P. Thilakan and J. Kumar, Phys. Stat. Sol. **A160**, 97 (1997).

Journal of the Korean Physical Society, Vol. 34, June 1999, pp. S386~S392

Tensile Strain Effects on GaN-based Quantum Well Lasers

Sean J. YOON* and Insook LEE

LG Corporate Institute of Technology, Seoul 137-724

The strain effects on optical gain and threshold current density in cubic GaN-based quantum well (QW) lasers are studied theoretically using the $k \cdot p$ method with 6×6 Luttinger-Kohn Hamiltonian and the density matrix formalism with intraband relaxation. Compared with compressive strained GaN-based QW lasers, tensile strained QW lasers show improvements in optical gain, differential gain, and threshold current density. This is mainly because tensile strain in GaN-base QW laser increases dipole matrix element due to the very narrow spin-orbit (SO) split-off energy. In this study, tensile strained GaN-based QWs are realized by introducing $In_x(Ga_{1-y}Al_y)_{1-x}N$ for barrier layers. Therefore, we can achieve cubic GaN-based QW lasers with better performance by using tensile strain rather than compressive strain.

I. INTRODUCTION

Recently, group III nitride-based semiconductors have drawn a lot of attention for short wavelength optoelectronic devices. After Nakamura *et al.* reported their pioneering work on high-brightness blue-green light emitting diodes (LEDs) based on wurtzite III-nitride semiconductors [1], many authors have made efforts to obtain blue-green or ultraviolet LED [2] and laser diodes (LDs) [3] using these materials. In spite of these efforts, the laser characteristics such as optical gains and threshold current densities are still unsatisfactory compared with those of typical GaAs lasers. This is not only because III-nitride materials have difficulties in finding suitable substrates but also because their large density of states due to large effective electron and hole masses at the zone center lead to high transperant carrier densities and high threshold current densities.

Even though most experimental studies have concentrated on the hexagonal (wurtzite) crystals, some of the recent studies [4] on cubic (zinc-blend) GaN crystals show that cubic III-nitride epilayers may offer superior thermal, electronic, and optical properties due to the smaller electron and hole masses and the possibility of reduced phonon scattering in cubic crystal structure. A cubic crystal structure can be obtained by suitable choice of substrate and growth condition. Recently, along with the experimental study for cubic III-nitride materials, theoretical studies such as band structures for the bulk materials [5–7] and optical gains for the GaN-based QWs [8–10] have been performed.

In this paper, we theoretically studied strain effects on optical gain and threshold current density in cubic GaN-based QW lasers to obtain better lasing performance using cubic III-nitride materials. Due to the lack of experimental data for band structure parameters, we used theoretically estimated values in references [5–8]. Compared with the conventional III-V materials, III-nitride materials have very narrow SO split-off energies, which lead to different strain effects. To clarify strain effects on GaN-based QW laser characteristic, we consider a 60 Å $GaN/Al_{0.26}Ga_{0.74}N$ QW system by varying strain strength of the well, fixing other material parameters and well thickness. We have found that tensile strains enhance QW laser characteristics more effectively. By introducing $In_x(Ga_{1-y}Al_y)_{1-x}N$ for barrier layers, the tensile strained GaN-based QW laser was realized and its results were also compared with those of the compressive strained QW laser. In section II, we explain the numerical method for the band structure, the optical gain, and the threshold current density for QW lasers. The theoretical calculations and numerical results for the strain effects on optical gain, differential gain, and threshold current density in GaN-based QW lasers are then discussed in section III. Finally, section IV presents the conclusion.

II. THEORY AND FORMALISM

In this section, we describe our numerical method to obtain band structure, optical gain for strained QWs, and threshold current density for the QW lasers. The QW is considered to be grown along the z axis. The band structure for QWs are calculated by using the $\boldsymbol{k} \cdot \boldsymbol{p}$ method. The conduction band is assumed to be decoupled from the valence bands and to be parabolic, for simplicity, which is a good approximation for large bandgap

*E-mail: yoonsj@mail.lgcit.com

semiconductors such as GaN. The valence band structure is calculated by using the 6 × 6 Luttinger-Kohn Hamiltonian [11] with the spin-orbit (SO) coupling effects considered, since III-nitride materials have very narrow SO split-off energy. First of all, we make a unitary transformation of the 6 × 6 Luttinger-Kohn Hamiltonian

$$\begin{aligned}\bar{H} &= \bar{U}H\bar{U}^{\dagger} \\ &= \begin{bmatrix} H^U & 0 \\ 0 & H^L \end{bmatrix}\end{aligned} \tag{1}$$

to decouple the upper and lower blocks, H^U and H^L [12].

The upper and lower block solutions are given by [13]

$$\Psi^{\sigma}_{m\mathbf{k}_{||}}(\boldsymbol{r}) = \sum_{\nu} g^{(\nu)}_m(\boldsymbol{k}_{||}, z)e^{i\mathbf{k}_{||}\cdot\mathbf{r}_{||}}|\nu> \quad \begin{cases} \nu = 1,2,3 \ \text{ for } \sigma = U \\ \nu = 4,5,6 \ \text{ for } \sigma = L, \end{cases} \tag{2}$$

where $g^{(\nu)}_m(\boldsymbol{k}_{||}, z)$ is the envelope function, $\{|\nu>\}$ denotes the transformed Bloch basis at the zone center, m is the QW subband index, $\boldsymbol{k}_{||} = k_x\hat{x} + k_y\hat{y}$, $\boldsymbol{r}_{||} = r_x\hat{x} + r_y\hat{y}$, and $\sigma = U$ (or L) refers to the upper (or lower) block. Then, the block-diagonalized envelope functions $\{g^{(\nu)}_m(\boldsymbol{k}_{||}, z)\}$ satisfy the coupled differential equations [12]

$$-\sum_{\nu'}\left[H^{\sigma}_{\nu\nu'}\left(\boldsymbol{k}_{||}, -i\frac{\partial}{\partial z}\right) + V_h(z)\delta_{\nu\nu'} + H^{\sigma}_{\epsilon\nu\nu'}\right] \times g^{(\nu')}_m(\boldsymbol{k}_{||}, z) = E^{\sigma}_m(\boldsymbol{k}_{||})g^{(\nu)}_m(\boldsymbol{k}_{||}, z), \tag{3}$$

where H^{σ}_{ϵ} is the block-diagonalized Hamiltonian for strain (shear) potential and $V_h(z)$ is the valence band offset, which is related to ΔE_v.

For a strained quantum well of lattice constant a, a barrier region with a lattice constant a_0, the strain ϵ is expressed as

$$\epsilon = \frac{a_0 - a}{a}. \tag{4}$$

And the hydrostatic and shear components of the strain are given by

$$\delta E_{hy} = -2a_v\frac{C_{11} - C_{12}}{C_{11}}\epsilon \tag{5}$$

and

$$\delta E_{sh} = -2b\frac{C_{11} + 2C_{12}}{C_{11}}\epsilon, \tag{6}$$

respectively, where a_v and b are the deformation potentials and C_{11} and C_{12} are the elastic constants. Since the hydrostatic components raise or lower the whole bands uniformly, they are considered in estimating the band offsets. Then, the strain potential H^{σ}_{ϵ} in Eq. (3) is given by

$$H^U_{\epsilon} = \begin{bmatrix} \zeta & 0 & 0 \\ 0 & -\zeta & \sqrt{2}\zeta \\ 0 & \sqrt{2}\zeta & 0 \end{bmatrix}$$

and

$$H^L_{\epsilon} = \begin{bmatrix} 0 & \sqrt{2}\zeta & 0 \\ \sqrt{2}\zeta & -\zeta & 0 \\ 0 & 0 & \zeta \end{bmatrix}, \tag{7}$$

where

$$\zeta = \frac{1}{2}\delta E_{sh}. \tag{8}$$

After the matrix elements in Eq. (3) are determined, the equations (3) are solved numerically using the finite difference method. The differences in the Luttinger-Kohn parameters of the H^{σ} for the well and the barrier materials are considered by following the approach of Chao and Chuang [14].

Once the subband levels are obtained, in the multiband effective mass approximation, the optical dipole matrix element is given by

$$\hat{\epsilon}\cdot\boldsymbol{M}^{\eta\sigma}_{lm}(\boldsymbol{k}_{||}) = \begin{cases} \sum_{\nu=1,2,3} < g^{(\nu)}_m|\phi_l >< \nu|\hat{\epsilon}\cdot e\boldsymbol{r}|S,\eta > & \text{for } \sigma = U \\ \sum_{\nu=4,5,6} < g^{(\nu)}_m|\phi_l >< \nu|\hat{\epsilon}\cdot e\boldsymbol{r}|S,\eta > & \text{for } \sigma = L, \end{cases} \tag{9}$$

where $\hat{\epsilon}$ is the polarization vector of the optical field, $\boldsymbol{M}^{\eta\sigma}_{lm}(\boldsymbol{k}_{||})$ is the optical dipole matrix element between the lth conduction band with a spin state η and the mth valence band of a σ block, ϕ_l is the envelope function for the lth conduction band, and S denotes the spherical Bloch function for the conduction band at the zone center. The $|\hat{\epsilon}\cdot\boldsymbol{M}^{\eta\sigma}_{lm}|^2$ for the TE mode (the optical electric field is polarized in the $x-y$ plane) and the TM mode (the optical electric field is polarized in the z plane) is obtained as follows [12],

$$\begin{aligned}
|\hat{\epsilon}\cdot\mathbf{M}^{\eta U}_{lm}(\boldsymbol{k}_{||})|^2 &= \frac{1}{4} < S|ex|X >^2 \left(< \phi_l|g^{(1)}_m >^2 + \frac{1}{3} < \phi_l|g^{(2)}_m >^2 + \frac{\sqrt{8}}{3} < \phi_l|g^{(2)}_m >< \phi_l|g^{(3)}_m > \right), \\
|\hat{\epsilon}\cdot\mathbf{M}^{\eta L}_{lm}(\boldsymbol{k}_{||})|^2 &= \frac{1}{4} < S|ex|X >^2 \left(< \phi_l|g^{(6)}_m >^2 + \frac{1}{3} < \phi_l|g^{(5)}_m >^2 + \frac{\sqrt{8}}{3} < \phi_l|g^{(5)}_m >< \phi_l|g^{(4)}_m > \right), \quad \text{for TE mode,} \\
|\hat{\epsilon}\cdot\mathbf{M}^{\eta U}_{lm}(\boldsymbol{k}_{||})|^2 &= \frac{1}{3} < S|ez|Z >^2 \left(< \phi_l|g^{(2)}_m > - \frac{1}{\sqrt{2}} < \phi_l|g^{(3)}_m > \right)^2,
\end{aligned} \tag{10}$$

$$|\hat{\epsilon}\cdot\mathbf{M}_{lm}^{\eta L}(\boldsymbol{k}_{||})|^2=\frac{1}{3}<S|ez|Z>^2\left(<\phi_l|g_m^{(5)}>-\frac{1}{\sqrt{2}}<\phi_l|g_m^{(4)}>\right)^2,\quad\text{for TM mode.}\tag{11}$$

The value of $<S|ez|Z>^2$ is given by

$$\begin{aligned}<S|ez|Z>^2&=<S|ex|X>^2\\&=\frac{(e\hbar)^2}{2}\left(\frac{E_G+\Delta}{E_G(E_G+2\Delta/3)}\left(\frac{1}{m_c^*}-\frac{1}{m_0}\right)\right),\end{aligned}\tag{12}$$

where E_G is the bandgap energy, Δ is the SO split-off energy, m_c^* is the effective mass of electron in the conduction band, and m_0 is the mass of electron. The linear optical susceptibility $\chi(\omega)$ of QWs can be calculated using the density matrix formalism [12]

$$\epsilon_0\chi(\omega)=\frac{1}{V}\sum_{\sigma\eta lmk_{||}}|\hat{\epsilon}\cdot\mathbf{M}_{lm}^{\eta\sigma}(\boldsymbol{k}_{||})|^2\times\frac{f_c^l-f_{h\sigma}^m}{E_l^c(\boldsymbol{k}_{||})-E_m^{h\sigma}(\boldsymbol{k}_{||})+E_G-\hbar\omega-i\hbar/\tau_{in}},\tag{13}$$

where ϵ_0 is the permittivity of free space. f_c^l and $f_{h\sigma}^m$ are the Fermi functions and $E_l^c(\boldsymbol{k}_{||})$ and $E_m^{h\sigma}(\boldsymbol{k}_{||})$ are the energies for the lth conduction band and mth valence band at $k_{||}$, respectively. ω is the angular frequency of the photon, V is the volume of the active layer, and τ_{in} is the intraband relaxation time. The linear material gain $g(\omega)$ of the QWs is defined as

$$g(\omega)=\frac{\omega\mu c}{n_r}\,\mathrm{Im}\,\epsilon_0\chi(\omega),\tag{14}$$

where μ is the permeability, n_r is the refractive index, and c is the speed of light in free space.

For QW lasers, the modal gain g_m is obtained by multiplying the material gain with the optical confinement factor Γ, *i.e.*, $g_m=\Gamma g$. The threshold current density is achieved when the peak modal gain is large enough to compensate the intrinsic loss α_{int} and the loss at the mirrors α_m,

$$\Gamma g(n_{th})=\alpha_{int}+\alpha_m,\tag{15}$$

where n_{th} is the threshold carrier density. After determining the threshold carrier density, the threshold current density J_{th} can be found by

$$J_{th}=eL_z n_{th}/\tau_{tot},\tag{16}$$

where L_z is the QW thickness and τ_{tot} is the carrier life time.

III. NUMERICAL RESULTS AND DISCUSSION

In this section, we show our numerical results for strain effects on optical gains and threshold current densities for cubic GaN-based QW lasers. Due to the lack of experimental data for band structure parameters and band offsets, we use theoretically estimated values in references [5–8] and they are listed in Table 1. And we assume that ΔE_v is 0.4 times of ΔE_G. To clarify strain effects on GaN-based QW laser characteristic, we consider a 60 Å GaN/$Al_{0.26}Ga_{0.74}N$ QW system by varying strain strenth of the well, fixing other material parameters and well thickness. We analyze the strain-induced changes in the valence band structure and laser performance by examining characterization parameters such as density of states and squared dipole matrix elements.

The valence band structures for a QW consisting of a 60 Å GaN QW surrounded by $Al_{0.26}Ga_{0.74}N$ barriers with various strain strength, ranging from −1.5 % compressive strain to 1.5 % tensile strain, are shown in Fig. 1. We labeled valence subbands as HH (heavy hole), LH (light hole), or SO (spin-orbit) band according to the characteristics of the wave function at the zone center. Due to the small SO split-off energy as 0.017 eV, GaN QW shows different behavior of valence bands from that of conventional III-As or III-P QW. For large compressive strains such as the cases of Figs. 1(a)-(c), the first excited subband is SO band rather than LH band and the separations between the first two subbands at the zone center are almost the same. This can be understood from the behavior of valence bands in bulk GaN with strain. HH, LH, and SO bands of bulk lie at $-\zeta$ and $(\zeta-\Delta\pm\sqrt{\Delta^2+2\Delta\zeta+9\zeta^2})/2$ from the band edge at the zone center, respectively, which is obtained form Eqs. (1) and (7). When Δ becomes small compared with the strain energy ζ, the LH and the SO bands are located at $2\zeta-\Delta/3$ and $-\zeta-2\Delta/3$, respectively, and first excted subband for compressive strain is SO band. While the energy separation between the HH and the LH bands varies as the amount of $3\zeta-\Delta/3$, the energy separation between the HH and the SO bands is constant as $2\Delta/3$.

Table 1. Material parameters for cubic III-nitrides used in this work

parameters	AlN	GaN	InN
a_0 (Å) [8]	4.38	4.53	4.98
E_G (eV) (T=300 K) [5,8]	6.0:direct, 5.11:indirect	3.2	2.2
m_c^*/m_0 [8]	0.21	0.15	0.14
Δ (eV) [8]	0.017	0.017	0.017
γ_1 [8]	2.42	3.06	3.24
γ_2 [8]	0.58	0.91	1.00
γ_3 [8]	0.71	1.03	1.12
C_{11} (Mbar) [7]		2.61	2.14*
C_{12} (Mbar) [7]		1.27	1.18
b (eV) [6]	−1.443	−1.61	−1.33
a_g (eV) ($a_v=a_g\times0.4$) [6]		−6.8	−3.5
n_r [8]		2.9	2.9

*marked value is an assumed one for the experimental trend of C_{12} for conventional Ga-V and In-V materials.

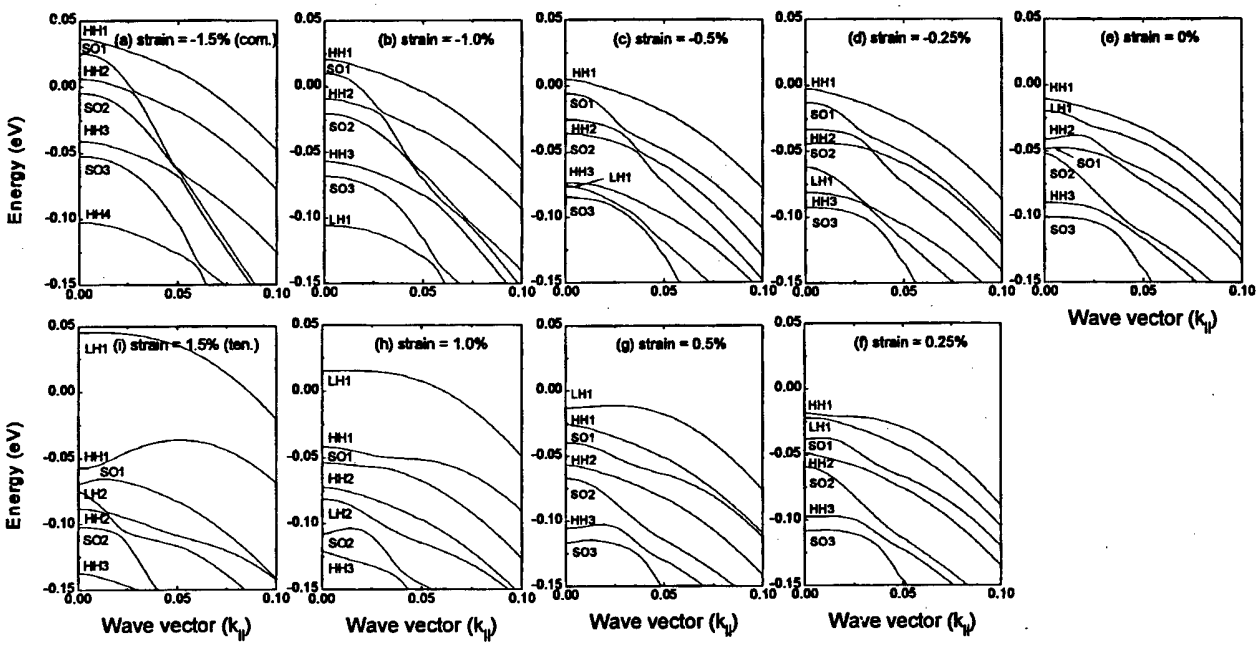

Fig. 1. Valence band structures of a 60 Å GaN/ $Al_{0.26}Ga_{0.74}N$ QW versus in-plain wave vector $k_{||}$ (in units of $2\pi/a_0$) at various strains ranging from ϵ=−1.5 % (compressive) to ϵ=1.5 % (tensile).

From the bulk analysis, it is obvious that the separation between the HH1 and the SO1 at $k_{||}$=0 for large strains in Figs. 1(a)-(c) and (g)-(i) is constant and the separation energy is about 0.011 eV ($2\Delta/3$). The shapes of first few bands under large compression can be easily seen to saturate with increasing compressive strain due to the above reason. Note that while the SO band moves in the same direction to the HH band with the increasing strain in Fig. 1, the LH band moves in opposite direction to the HH band with the increasing strain, which is also examined from tha locations of corresponding valence band in bulk GaN. With increasing compressive strain, the energy level of the LH1 band goes down rapidly, while it goes up, become the top of the valence band, and moves away from the HH1 band significantly with increasing tensile strain.

In Fig. 1, we also see the strain changes the curvatures of the subbands, which is inversely proportional to the effective mass of the subband and the density of states (DOS) in the QW layer. Because the DOS near the band edge plays an important role in determining the transparent carrier density, the gain, and the threshold current density for the QW laser, it is important to examine the strain-induced changes of the curvatures in Fig. 1. In Figs. 1(a)-(e), it is observed that increasing compressive strain tends to reduce the effective masses for the first few subbands, and under large compressive strains (especially in the cases of Fig. 1(a) and (b)), the effective masses saturate, as already-mentioned. Among the cases where HH1 band is the ground state, at ϵ=0.25 %, the most DOS is expected, since the effective masses are the largest and the energy separations between the first few bands are the nearest with each other. In addition to curvatures of the subbands, energy separation between the first few bands is one of important factors for determining the DOS near the band edge because the decrease of the subband energy separation result in a increase in DOS due to the rapid accumulation of DOS for each band. From Fig. 1(g)-(i), it is noticed that increase of tensile strain more than ϵ=0.25 % leads to small DOS, mainly due to increase of the energy separation between the ground state and the first excited state. When we compare the DOS for the tensile strained QW with ϵ=1.0 % with that for the compressive strained QW with the same amount of strain, ϵ=−1.0 %, it is conjectured that there is little difference between them despite of larger effective mass of the ground state near zone center for the tensile strained one since the energy separation between the ground state and the excited states for the tensile strained one is larger than the compressive strained one.

Next, we consider the squared dipole matrix element between conduction band and valence band. Because of the Fermi function difference in Eq. (13), $f_c^l - f_h^m$, the transitions only between l=1 and m=1, 2 states are important. The dipole matrix element varies slowly with the wave vector near the zone center in most of the cases. Therefore, we focus on the values at the zone center. Table 2 shows the squared dipole matrix element between l=1 (C1) and m=1,2 (V1 and V2) states at the zone center for both TE and TM modes for the QW band structures shown in Fig. 1. We also include the squared dipole matrix element at nonzero $k_{||}$ if the ground state changes its characteristic with the first excited state near zone center due to the strong valence band mixing. The TM mode for tensile strained layer and the TE mode for compressive strained and unstrained

Table 2. The calculated squared dipole matrix element between l=1 and m=1,2 states at the zone center for both TE and TM modes for various cases of Fig. 1. C1 is the first subband of the conduction band and V1 and V2 are the first and the second subbands of the valence band, respectively.

	|dipole matrix element|^2/e^2 (m^2)			
	C1-V1 (TE mode)	C1-V2 (TE mode)	C1-V1 (TM mode)	C1-V2 (TM mode)
(a) ϵ=-1.5 %	1.61×10^{-20}	1.60×10^{-20}	0	0.01×10^{-20}
(b) ϵ=-1.0 %	1.63×10^{-20}	1.62×10^{-20}	0	0.01×10^{-20}
(c) ϵ=-0.5 %	1.65×10^{-20}	1.63×10^{-20}	0	0.04×10^{-20}
(d) ϵ=-0.25 %	1.66×10^{-20}	1.61×10^{-20}	0	0.08×10^{-20}
(e) ϵ= 0 %	1.67×10^{-20}	1.53×10^{-20}	0	0.28×10^{-20}
(f) ϵ= 0.25 %	1.68×10^{-20} (0.51×10^{-20} at $k_{\|\|}=0.024$)	0.09×10^{-20} (1.25×10^{-20} at $k_{\|\|}=0.024$)	0 (1.97×10^{-20} at $k_{\|\|}=0.024$)	1.58×10^{-20} (0.64×10^{-20} at $k_{\|\|}=0.024$)
(g) ϵ= 0.5 %	0.16×10^{-20}	1.69×10^{-20}	3.09×10^{-20}	0
(h) ϵ= 1.0 %	0.02×10^{-20}	1.71×10^{-20}	3.41×10^{-20}	0
(i) ϵ= 1.5 %	0	1.73×10^{-20}	3.48×10^{-20}	0

layer are dominant mode due to the light-hole and the heavy-hole characters of the ground states in those wells, respectively, from Table 1. For all the strained QWs, the squared dipole matrix elements of C1-HH1 transition for TE mode are almost the same, ranging between 1.61×10^{-20} e^{2}m^2 and 1.73×10^{-20} e^{2}m^2. TM dipole matrix elements of the ground states are greatly increased under tensile strain. The squared dipole matrix elements of the transition between C1 and LH1 states for TM mode for tensile strained layers are almost two times as large as those of the transition between C1 and HH1 states for TE mode for compressive strained layers. This is because of the very strong coupling between the SO component ($g^{(3)}$) and the light-hole component ($g^{(2)}$) of the LH1 band due to the very narrow spin-orbit (SO) split-off energy in GaN material. Large dipole matrix element will result in the large optical gain and the differential gain for a tensile strained GaN-based QW compared with a compressive strained one.

In Fig. 2, we plot the peak linear gains for (a) the TE modes for the cases of Fig. 1(a)-(f) and for (b) the TM modes for the cases of Fig. 1(f)-(i) as a function of injected carrier density at T=300 K. And we can simply read differential gain as the slopes of the peak gain in Fig. 2. In addition to the gain and the differential gain, threshold current densities J_{th} is one of the important parameters to determine the laser performance. Table 3 shows J_{th} for the cases of Fig. 1(a)-(f). For the calculation of the optical gain, we assume that τ_{in} is the same for all subbands as 1×10^{-13} s. And device parameters we used in calculation of J_{th} are as follows: τ_{tot} is 1×10^{-9} s, α_{int} is 30/cm, facet power reflectivity is 0.32, cavity length is 400 μm, and the optical confinement factor Γ is 0.03. It is found from Fig. 2(a) that with increasing compressive strain, the transparent carrier density n_{cr}, where the optical gains occur, decreases due to the decrease of the DOS. And the decrease of the DOS leads not only small n_{cr} but also large differential gain because small DOS results in more quick increase of $f_c^l - f_h^m$ with increase of injected carrier density. The

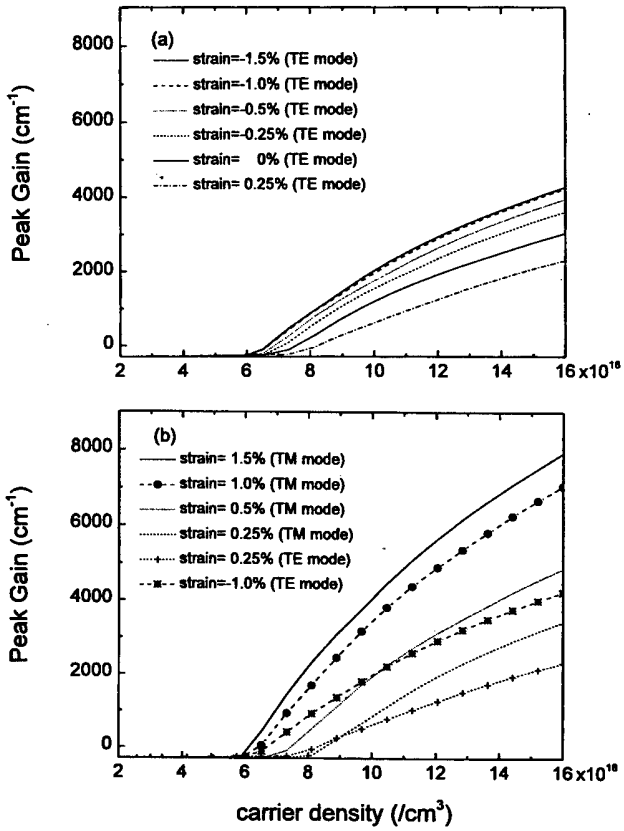

Fig. 2. The peak linear gains of (a) the TE modes for the cases of Fig. 1(a)-(f) and of (b) the TM modes for the cases of Fig. 1(f)-(i) as a function of injected carrier density.

largest compressive strain (ϵ=−1.5 %) among Fig. 2(a) shows the smallest J_{th}, but the J_{th} difference with the ϵ=−1.0 % case is small due to the saturation of the band structure. As expected, the largest n_{cr}, the smallest optical gain in all carrier density regions and smallest differential gain are obtained at ϵ=0.25 % for TE mode due to the largest DOS which is from the fact that the first few valence bands are very flat and they are very close

Table 3. Calculated threshold current density J_{th} for various strained QW lasers of Fig. 1.

Strain	J_{th} (A/cm^2)
(a) ϵ=−1.5 %	947 for TE mode
(b) ϵ=−1.0 %	958 for TE mode
(c) ϵ=−0.5 %	1003 for TE mode
(d) ϵ=−0.25 %	1057 for TE mode
(e) ϵ= 0 %	1162 for TE mode
(f) ϵ= 0.25 %	1160 for TM mode
	1394 for TE mode
(g) ϵ= 0.5 %	964 for TM mode
(h) ϵ= 1.0 %	807 for TM mode
(i) ϵ= 1.5 %	745 for TM mode

to each other. However, from Fig. 2(b), it is found that the differential gain of TM mode for ϵ=0.25 % strained QW is much larger than that of TE mode in spite of the larger n_{cr}, which is from the change of characteristics between HH1 and LH1 band near the zone center (at about $k_{||}$=0.02), and thus increase of dipole matrix element of TM mode. From this reason, at ϵ=0.25 %, J_{th} of TM mode is smaller than that of TE mode. With increasing tensile strain, n_{cr} decreases, the optical gain and the differential gain increase, and J_{th} decreases rapidly owing to increased dipole matrix element as well as the decreased DOS. Compared with the compressive strained QW, the tensile strained one shows dramatical improvements in differential gain. Especially, the 1.0 % strained QW has the larger optical gain and differential gain and smaller J_{th} than the −1.0 % strained QW in spite of almost the same n_{cr}. This improvement for the tensile strained QW mainly comes from much larger dipole matrix elements as listed in Table 2.

Upto this point, we have dealt with the virtual system to examine strain effect on GaN-based QW lasers by

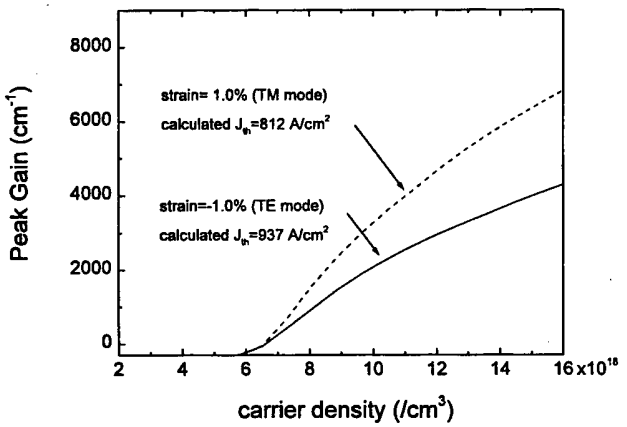

Fig. 3. The peak linear gains for TM modes for a 60 Å GaN/$In_{0.2}(Ga_{0.6}Al_{0.4})_{0.8}N$ QW (dashed curve) and for TE modes for a 60 Å $In_{0.1}Ga_{0.9}N/In_{0.1}(Ga_{0.67}Al_{0.33})_{0.9}N$ QW (solid curve) as a function of injected carrier density. The two structures have almost the same absolute strain of ∼1.0 %. Calculated J_{th} for two cases are also included.

varying the strain strength, fixing the other material parameters. Here, we consider an example of real QW systems and compare a tensile strained GaN-based QW laser with compressive one. Tensile strain in GaN-base QW is realized by introducing $In_x(Ga_{1-y}Al_y)_{1-x}N$ for barrier layers. We take a 60 Å GaN/$In_{0.2}(Ga_{0.6}Al_{0.4})_{0.8}N$ QW and a 60 Å $In_{0.1}Ga_{0.9}N/In_{0.1}(Ga_{0.67}Al_{0.33})_{0.9}N$ QW as examples of the tensile and compressive strained QWs, respectively. These two structures are designed so that the ΔE_G and the lasing wavelength of the QWs are almost the same and that the absolute strain strength are almost equal to 1.0 %, in order to see the strain effect clearly. Figure 3 shows maximum gain versus injected carrier density and threshold current densities for two structure. The tensile strained QW laser shows to have better laser performance than the compressive one. Therefore, operation at lower current can be achieved by using of proper tensile strain in GaN-based QW lasers.

IV. CONCLUSION

In this paper, we have investigated strain effects on optical gain and threshold current density in cubic GaN-based QW lasers by considering valence band mixing effects. The calculation of valence band structures at various strains from −1.5 % compressive to 1.5 % tensile strain for a 60 Å GaN/$Al_{0.26}Ga_{0.74}N$ QW shows that the increase of compressive strain saturates the energy separation between the ground state (HH1) and the first excited state (SO1) as small value of $2\Delta/3$ due to the small SO split-off energy of GaN, reducing the effective masses of the first few subbands and DOS near band edge slowly, and changing the TE dipole matrix element very little, which leads slowly decreasing transparent carrier density and increasing differential gain. On the other hand, increasing tensile strain, the LH1 band moves up significantly above HH1 band, the TM dipole matrix elements are increased, and the DOS near band edge is reduced, which result in significant enhancement of lasting performance. Compared with the −1.0 % compressive strained QW, the 1.0 % tensile strained QW has the larger effective mass for the ground state, but has the larger energy separation between the first two states. The two have almost the same DOS near band edge and transparent carrier density. And TM dipole matrix element for the tensile strained QW is much larger than TE dipole matrix element for the compressive one due to the very narrow SO split-off energy. Because of these reasons, the tensile strained QW laser was found to have larger optical gain at all the injected carrier densities, larger differential gain, and lower threshold current density. We also provide an example of real QW systems with tensile strain by introducing $In_x(Ga_{1-y}Al_y)_{1-x}N$ for barrier layers. Our results suggest that we can improve the performance of cubic GaN-based QW lasers by using tensile strain rather than compressive strain.

ACKNOWLEDGMENTS

The authors are grateful to Dr. C. S. Kim for his consistent encouragement of this work.

REFERENCES

[1] S. Nakamura, T. Mukai and M. Senoh, Jpn. J. Appl. Phys. **30**, Part2, L1998 (1991).

[2] M. G. Craford, Circuits & Devices, September, 24 (1992); S. Nakamura, T. Mukai and M. Senoh, Appl. Phys. Lett. **64**, 1687 (1994); S. Nakamura, IEEE J. Sel. Top. Quanutm Electron. **3**, 712 (1997).

[3] A. Khan, M. Olson, J. M. Van Hove and J. N. Kuznia, Appl. Phys. Lett. **65**, 520 (1994); I. Akasaki and H. Amano, Electron. Lett. **32**, 1105 (1996); S. Nakamura, M. Senoh, S. Nagahama, N. Iwasa, T. Yamada, T. Matsushita, H. Kiyoku and Y. Sugiimoto, Jpn. J. Appl. Phys. Lett. **35**, L74 (1996).

[4] S. Miyoshi, K. Onabe, N, Ohkouchi, H. Yaguchi, R. Ito, S. Fukatsu and Y. shiraki, J. Cryst. Growth **124**, 439 (1992); H. Okumura, S. Yoshida and Okahisa, Appl. Phys. Lett. **64**, 2997 (1994).

[5] A. Rubio, J. L. Corkill, M. L. Cohen, E. L. Shirley and S. G. Louie, Phys. Rev. **B48**, 11810 (1993).

[6] K. Kim, W. R. L. Lambrecht and B. Segall, Phys. Rev. **B53**, 16310 (1996).

[7] M. B. Nardelli, K. Rapcewicz and J. Bernholk, Phys. Rev. **B55**, R7323 (1997).

[8] A. T. Meney, E. P. O'Reilly and A. R. Adams, Semicond. Sci. Techncl. **11**, 897 (1996).

[9] W. W. Chow, A. F. Wright and J. S. Nelson, Appl. Phys. Lett. **68**, 296 (1996).

[10] D. Ahn, J. Appl. Phys. **79**, 7731 (1996).

[11] J. M. Luttinger and W. Kohn, Phys. Rev. **97**, 869 (1955).

[12] D. Ahn and S. J. Yoon, J. Korean Phys. Soc. **28**, 145 (1995); D. Ahn, S. J. Yoon, S. L. Chuang and C. S. Chang, J. Appl. Phys. **78**, 2489 (1995); S. J. Yoon and D. Ahn, J. Korean Phys. Soc. **29**, 88 (1996); C. S. Chuang and S. L. Chuang, IEEE J. Sel. Top. Quanutm Electron. **1**, 218 (1995).

[13] G. D. Sanders and Y.-C. Chang, Phys. Rev. **B35**, 1300 (1987).

[14] C. Y. P. Chao and S. L. Chuang, Phys. Rev. **B46**, 4110 (1992).

Journal of the Korean Physical Society, Vol. 34, June 1999, pp. S393~S396

Donor-acceptor Pair and Free-to-bound Recombinations in Undoped Thick GaN Grown by HVPE

C. S. PARK and P. W. YU*

Department of Information & Communications, Kwang-Ju Institute of Science and Technology, Kwangju 506-303

S. T. KIM

Department of Material Engineering, Taejon National University of Technology, Taejon 300-717

The radiative recombination in undoped thick GaN of 870 um freestanding and other 10~300 um GaN on Si has been studied by photoluminescence spectroscopy. The emission consists of dominant donor bound exciton line, donor or acceptor related band at 3.41~3.42 eV and the donor acceptor pair transition at 3.269 eV. We analyze the donor-acceptor pair transition at 3.269 eV with change of excitation intensity and temperature. The donor and acceptor binding energies are obtained from the dependence of the peak energy on excitation intensity. The donor binding energy is obtained from the limiting photon energy of the excitation-dependent band and the obtained donor binding energy is 21±3 meV. The acceptor binding energy is obtained from an obtained fit explaining the excitation dependent energy of the transition and the obtained binding energy is 224±5 meV. The donor-acceptor pair transitions are present in all samples, which have different thickness. Finally, Peaks at 3.41~3.42 eV are attributed to the free-to-bound (FB) recombination on the basis of the temperature and excitation dependence of photoluminescence characteristics of the line.

I. INTRODUCTION

Recently, GaN attracts the interests for its possible short-wavelength light emitting diodes and current injection laser diodes [1]. There has been a lot of research on the material and devices [2,3]. However, there still remains some problems unsolved yet. The lack of suitable substrate is one of them. Due to the large lattice mismatch between GaN and substrate such as sapphire, there is very high density of misfit dislocation, which have a detrimental effect on the operation of optoelectronic devices. Growth of the bulk crystals, which could be used as substrate for homoepitaxy, can be candidate for solving such misfit dislocation. But the growing of GaN bulk crystal is difficult for the decomposition of GaN at about 1000 °C at normal pressure. Another way of making quasi-bulk crystal is to use hydride vapor phase epitaxy (HVPE) method. Since HVPE allows large growth rates, this can be a promising alternative. For bulk material the unintentional n-type background doping of nominally undoped GaN layers is also one of the problems. Therefore we choose the samples grown by HVPE method in this study. Our study focused on the donor acceptor pair of 3.269 eV line of the 870 um thick freestanding sample. And from the excitation dependence of this line, we determined binding energy of donor and acceptor. In addition, we also studied on the 3.41~3.42 eV line, which we designated as a free-to-bound transition on the basis of the dependence of the photoluminescence characteristics with change of temperature and excitation intensity.

*E-mail: pwyu@eunhasu.kjist.ac.kr, Fax: +82-62-970-2204

II. EXPERIMENT

The samples used were grown on AlN/Si by HVPE without an intentional doping. The thickness ranges from 100~870 μm. The 870 μm thick sample is freestanding without substrate. The typical background level is estimated to be in order of 10^{17} cm^{-3}. The sample was mounted on a copper sample holder in a variable-temperature cryostat, allowing temperature to vary from 10 up to 300 K. Photoluminescence (PL) was excited with the 325 nm line of He-Cd UV laser. The power was changed by using neutral density filters over four orders of magnitude. The luminescence light was dispersed by a 0.75 m Spex single monochromator and detected by a cooled GaAs photomultiplier.

III. RESULTS

Figure 1 shows a typical spectrum from the freestanding sample of 870 um thickness. The spectrum consists of a strong excitonic line near 3.472 eV, the transition at

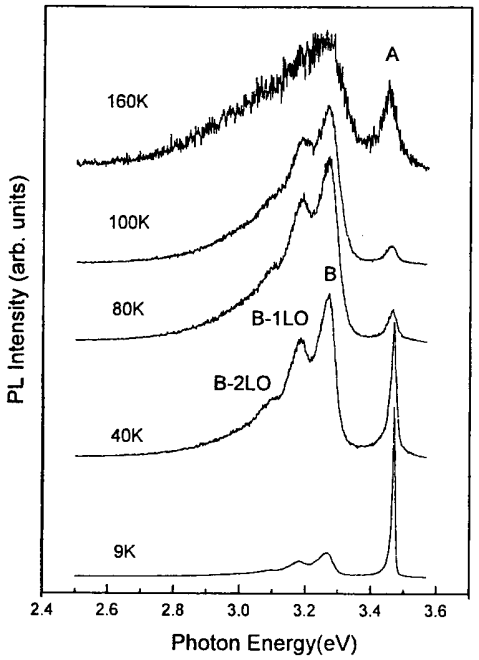

Fig. 1. PL spectra of 870um thick freestanding sample at different temperature.

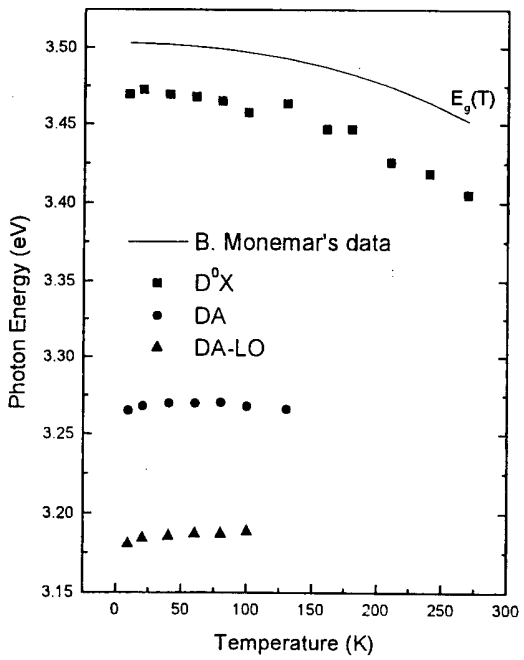

Fig. 2. Temperature dependence of the photoluminescence lines. Freestanding sample.

3.269 eV, which was attributed to the no phonon of the donor-acceptor pair line based on the dependence of the transition on temperature and excitation intensity, and its phonon side bands. From the n-type conduction of these layers and the closeness of the free exciton reference energy we attribute the 3.472 eV line to an exciton bound to a neutral donor (D^0X). The donor is usually considered to be the N vacancy [4]. The D^0X line was reported to be changeable depending on the magnitude of stress. Our samples show the peak position near 3.47 eV. The samples we study also have a strong line above the 40 °K at 3.269 eV as shown in Figure 1. This was previously known as donor-acceptor pair [5]. This was observed from both doped and undoped samples. No-phonon line initially shifts to a higher energy with the increase of temperature and then shifts to a lower energy with the more increase of temperature, as shown in Figure 2. This behavior doesn't follows that of the band edge. It's a behavior of DAP line. This initial shift with increasing temperature is believed to be caused by the enhancement of more closely spaced pairs by a higher thermal ionization rate for the donor [6]. For a distant DAP, the energy of the emitted photon can be expressed as [7]:

$$E_{DA} = E_g - (E_D + E_A) + \frac{e^2}{\epsilon R} \qquad (1)$$

E_g is the band gap of GaN, E_D and E_A are the donor and acceptor binding energies respectively and R is the distance between the involved donor and acceptor. ϵ is the dielectric constant. The last term represents the coulomb energy due to the attraction between the ionized donor

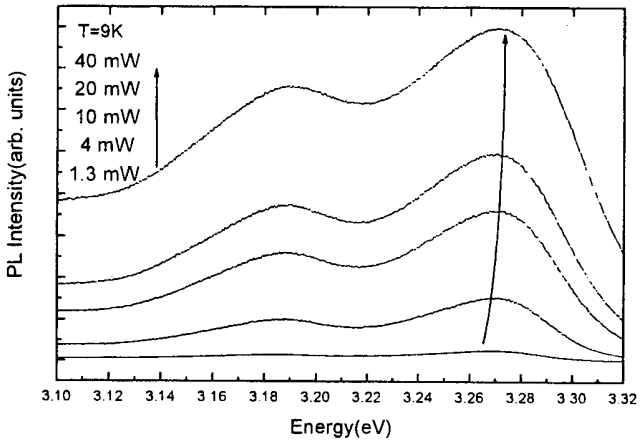

Fig. 3. Excitation dependence of the D-A emission peak.

and acceptor. Under continuous wavelength PL measurement, the DA pair peak shifts to higher energy with increasing excitation intensity [8,9], following equation (2). In figure 3 we shows this excitation dependence of the DA pair line. The excitation intensity J vs. the D-A emission peak energy $h\nu_p$ relation is described by Zacks and Halperin [9]:

$$J = D\frac{(h\nu_p - h\nu_\infty)^3}{(h\nu_B + h\nu_\infty - 2h\nu_p)} \exp\left(\frac{2(h\nu_B - h\nu_\infty)}{h\nu_p - h\nu_\infty}\right) \qquad (2)$$

with $E_B = h\nu_B - h\nu_\infty = e^2/\epsilon R_B = 2E_D$, $E_p = h\nu_m - h\nu_\infty$, and $h\nu_\infty = E_g - (E_D + E_A)$. and D is a constant. The dependence of the peak energy on excitation intensity was used to calculate the parameters, $h\nu_B$, $h\nu_\infty$, and D. and the observed emission peak energy will be between

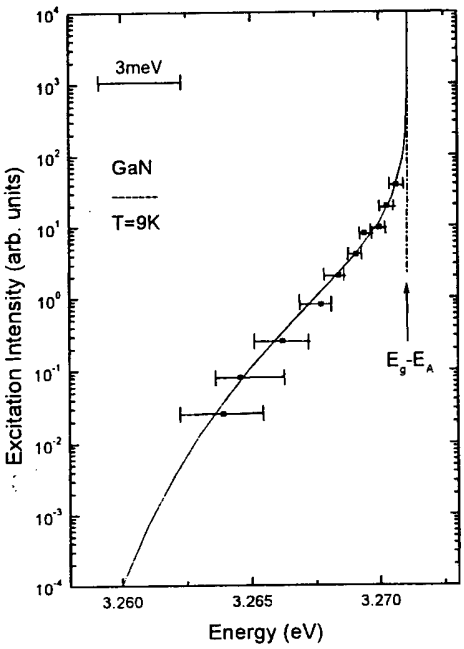

Fig. 4. Excitation dependence of the emission peak of the 3.269 eV D-A transition. The solid line is fitted to experimental data by equation (2).

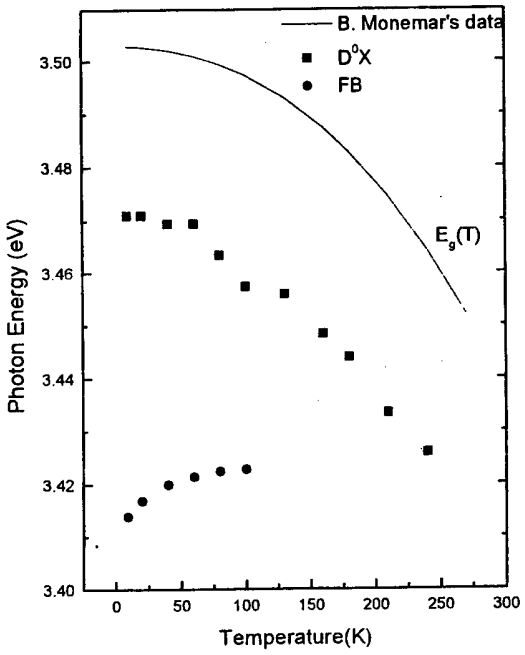

Fig. 5. Temperature dependence of the Photoluminescence line.

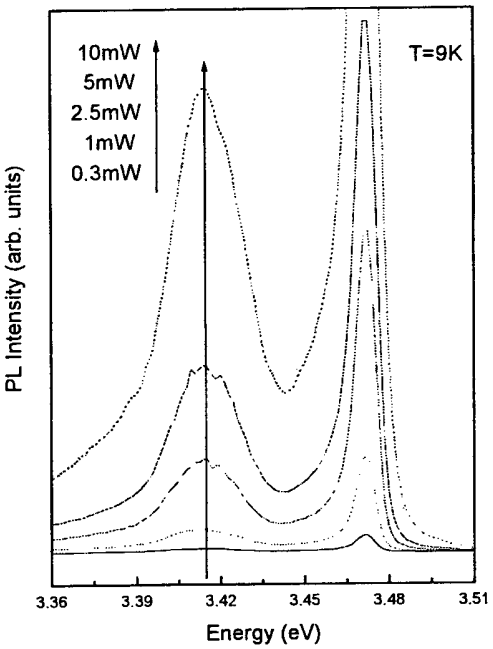

Fig. 6. Excitation intensity dependence of 3.41~3.42 eV FB line.

$E_g - E_D - E_A$ and $E_g - E_A$ corresponding to excitation intensities approaching the lowest and highest limits respectively. Figure 4 gives best-fit curves using the experimental points. We determined that the binding energy for donor and acceptor is 21±3 meV and 224±5 meV, respectively. The obtained acceptor binding energy is similar to previously reported data [6,10]. The same binding energy is reported for the Zn, Cd, Mg, and Be doped samples, but these species are not identical and consequently it has been proposed that the acceptor is actually Ga vacancy [11,12]. Dominant donor is believed to be the N vacancy [13,14]. And the binding energy of the shallow donor is ranges from 17 meV [15] to 42 meV [5]. The fitted donor binding energy is significantly smaller than that determined for the effective mass theory ($E_{D,EMT}$~32 meV [16]). This shallow donor was previously reported from a donor bound exciton [15,17] and also from Hall measurement. This shallow donor was attributed to an intrinsic defect. We also suggest that this donor state comes from the intrinsic defect on the basis of the undoped status of sample.

There are many studies on the line 3.40~3.43 eV. Andrianov *et al.* [18] attributed a peak at 3.42~3.43 eV of sample grown on sapphire to a free-to-bound transition. On the contrary, Ren *et al.* [19] found the evidence of D-A recombination for a peak at 3.404~3.413 eV. Also Celle *et al.* [20] attributed a peak at 3.41~3.42 eV (GaN/Si) to a D-A recombination. Godlewski *et al.* [21] found a long decay time of a peak at 3.414 eV and attributed to shallow D-A recombination or free-to-bound recombination. In all samples studied, the peak energy varies from sample to sample. S. T. Kim previously observed that these energy variations are dependent on the crystal quality [22] and its emission energy is affected by crystallographic orientation. Our present study supports the attribution to a free-to-bound recombination. As shown in Figure 5 the 3.414 eV line does not follow the temperature dependent variation of the band gap, but the peak position gradually increase to higher energy as tem-

perature increases. There's no shift to a higher energy with increasing excitation intensity as seen from the case of the D-A transition (see Figure 6). This is consistent with expectation for a free to bound transition, which is characterized by the equation:

$$E_{peak} = E_g - E_i + nkT \quad (3)$$

where E_i is the binding energy of the localized carrier on the impurity and the last term arises from the thermal energy of the free carrier in the appropriate band. n=1/2 [23] or 3/2 [24]. Our sample can be fit with n=3/2 well.

In addition, we do not observe the sharp lines that are typical of D-A pair recombination [20]. From the all evidences, we conclude that this emission is the free-to-bound transition.

IV. CONCLUSIONS

We report low temperature photoluminescence characteristics of thick GaN free-standing sample and thick GaN grown on AlN/Si. Both are grown by HVPE method. We attribute the 3.269 eV line to the D-A pair recombination, and obtained values of binding energy of both donor and acceptor from the dependence of the peak energy of the pair photoluminescence band on excitation intensity. These are 21±3 meV and 224±5 meV for donor and acceptor, respectively. Though donor binding energies are shallower than effective mass theory limit. The acceptor binding energies are also similar to that of Ga vacancy. The 3.41~3.42 eV line can be ascribed to a free to bound transition considering the photoluminescence characteristics depending on excitation intensity and temperature.

REFERENCES

[1] S. Nakamura and G. Fasol, *The Blue Laser Diodes* (Spring-Verlag, Heidelberg, 1997).

[2] H. Morkoc, S. Strite, G. B. Gao *et al.*, J. Appl. Phys. **76**, 1369 (1994).

[3] W. Nakamura, M. Senoh, N. Iwasa *et al.*, Jpn. J. Appl. Phys. **34**, L1332 (1995).

[4] H. P. Maruska and J. J. Tietjen, Appl. Phys. Lett. **15**, 327 (1969).

[5] R. Dingle and M. Ilegems, Solid State Commun. **9**, 175 (1971).

[6] O. Lagerstedt and B. Monemar, J. Appl. Phys. **45**, 2266 (1974).

[7] D. G. Thomas, J. J. Hopfield and W. M. Augustyniak, Phys. Rev. **A140**, 202 (1965).

[8] B. G. Ren Orton, J. W. Orton, T. S. Cheng, D. J. Dewsnip, S. E. D. E. Lacklison, C. T. Foxon, C. H. Malloy and X. Chen, Mater. Res. Soc. Internet J. Nitride Semicon. Res. 1 article 22 1996 (http://nrs.mij.mrs.org).

[9] E. Zacks and A. Halperin, Phys. Rev. **B6**, 3072 (1972).

[10] B. Monemar, H. P. Gislason and O. Lagerstedt, J. Appl. Phys. **51**, 640 (1980).

[11] B. Monemar, O. Lagerstedt and H. P. Gislason, J. Appl. Phys. **51**, 625 (1980).

[12] J. Neugebauer and C. G. Van de Walle, Phys. Rev. **B50**, 8067 (1994).

[13] J. I. Pankove, S. Bloom and G. Harbeke, RCA Rev. **36**, 163 (1975).

[14] P. Boguslawski, E. L. Briggs and J. Bernholc, Phys. Rev. **B51**, 17255 (1995).

[15] V. S. Vavilov, S. I. Makarov, M. V. Chukichev and I. F. Chtverikoa, Sov. Phys. Semicond. **13**, 1259 (1979).

[16] D. Volm, K. Oettinger, T. Streibl, D. Kovalev, M. Ben-Chorin, J. Diener, B. K. meyer, J. Majewski, L. Eckey, A. Hoffmann, H. Amano, I. Akasaki, K. Hiramatsu and T. Detchprohm, Phys. Rev. **B53** (1996).

[17] S. Fischer, D. Volm, D. Kovalev, B. Averboukh, A. Graber, H. C. Alt, B. K. Meyer, Material Science and Enguneering **B43**, 192 (1997).

[18] A. V. Andrianov, D. E. Lacklison, J. W. Orton, D. J. Dewsnip, S. E. Hooper and C. T. Foxon, Semicond. Sci. Technol. **11**, 366 (1996).

[19] G. B. Ren, D. J. Dewsnip, D. E. Lacklison, J. W. Orton, T. S. Cheng and C. T. Foxon, Mat. Sci. Eng. **B43**, 242 (1997).

[20] F. Calle, F. J. Sanchez, J. M. G. Tijero, M. A. Sanchez-Garcia, E. Calleja and R. Beresford, Semicond. Sci. Technol. **12**, 1396 (1997).

[21] M. Godlewski, J. P. Bergman, B. Monemar, U. Rossner and A. Barski, Appl. Phys. Lettt. **69**, 2089 (1996).

[22] F. Fisher, Wetzel, W. Walukiewicz and E. E. Haller, Mat. Res. Soc. Symp. Proc. **395**, 571 (1996).

[23] D. M. Eagles, J. Phys. Chem. Solids **16**, 76 (1960).

[24] K. Colbow, Phys. Rev. **141**, 742 (1966).

Journal of the Korean Physical Society, Vol. 34, June 1999, pp. S397~S400

Ti/Ag Ohmic Contacts to n-type GaN

D. J. LEE, S. H. LEE and H. C. PARK

Department of Electronic Engineering, Dongguk University, Seoul 100-715

We report on a study of Ti/Ag ohmic contacts to n-type GaN. Ti/Ag contacts on relatively low-doped ($7\times10^{17}/cm^3$) n-type GaN, annealed in N_2 gas at 850 °C, reached a specific contact resistance of 9.5×10^{-4} Ωcm^2 without special surface treatments. This value is similar to that of Ti/Al ohmic contacts fabricated side-by-side. Unlike Ti/Al contacts, however, Ti/Ag contacts showed smooth surface morphology and excellent long-term stability, as the specific contact resistance increased only by 25 % in three months. I-V and SIMS analysis suggest that, in achieving ohmic behavior in our Ti/Ag contacts, the formation of a low-barrier Ti-Ag intermetallic phase at the GaN surface may be more important than the formation of TiN and/or N vacancies near the interface.

I. INTRODUCTION

Gallium nitride (GaN) is promising not only for blue light emitting devices, but also for high power transistors able to operate at high temperatures and in other harsh environments. Making reliable ohmic contacts is one of the key ingredients in realizing such devices.

Currently, titanium/aluminum (Ti/Al) metalization, usually annealed at 600 °C to 900 °C, is the most popular choice for ohmic contacts to n-type GaN. However, this system often requires special surface treatments before the metal evaporation, such as reactive ion etching (RIE) [1], pre-annealing [2], or ion implantation [3], to achieve low specific contact resistance ρ_c. Moreover, after annealing at high temperatures, Al tends to ball-up severely resulting in a rough surface, and the rapid oxidation of Al makes reliable electrical contact difficult, not alone degraded specific contact resistance over time.

Compared with Al, silver (Ag) has lower resistivity, higher melting temperature, and does not oxidize much. We have investigated Ti/Ag ohmic contacts to relatively low-doped ($7\times10^{17}/cm^3$) n-type GaN without special surface treatments, other than the usual oxide etch before the metal evaporation. The previous report on Ti/Ag contacts was on very high-doped ($1.7\times10^{19}/cm^3$) GaN [4], which may not be reproducible, or compatible with practical device applications such as diodes or field effect transistors.

II. EXPERIMENTS

The GaN wafer used in this work, with 3.1 μm-thick n-type GaN grown on sapphire substrate by MOCVD, was purchased from EMCORE Corporation. The charge density and the electron mobility by Hall measurement were 7×10^{17} /cm^3 and 380 cm^2/Vs, respectively. Ti/Ag (300 Å/1200 Å) layers were deposited by e-gun evaporation at less than 1×10^{-6} Torr. Ti/Al (300 Å/1200 Å) contacts were also fabricated side by side for comparison. GaN samples were briefly etched in dilute NH_4OH before the metal evaporation to remove the native oxide on the surface. No other surface treatment was performed.

Circular TLM patterns, which do not require isolation etch, were defined by lift-off. If both r_1 and r_2 are much larger than four times L_T, which is the case in this work, the total resistance between the inner and the outer contacts is given by

$$R_{tot} = \frac{\rho_s}{2\pi}\ln\frac{r_2}{r_1} + \frac{\rho_{sc}}{2\pi}\cdot L_T\left(\frac{1}{r_1}+\frac{1}{r_2}\right),$$
$$\text{with } L_T = \sqrt{\frac{\rho_c}{\rho_{sc}}}, \quad (1)$$

where r_1 is the radius of the inner contact, r_2 is the radius of the outer contact, ρ_s is the sheet resistance of the GaN, ρ_{sc} is the sheet resistance of the GaN under the metal contact, ρ_c is the specific contact resistance, and L_T is the transfer length [5]. ρ_s and ρ_{sc} are generally not equal, and one can determine both values with additional end-resistance measurement [6]. However, since the accuracy of the end-resistance value may be questionable as the calculation involves taking the difference between large resistance values, ρ_s and ρ_{sc} are assumed to be identical in this work. In this case, equation (1) reduces to

$$R_{tot} = \frac{\rho_s}{2\pi}\left[\ln\frac{r_2}{r_1} + L_T\left(\frac{1}{r_1}+\frac{1}{r_2}\right)\right],$$
$$\text{with } L_T = \sqrt{\frac{\rho_c}{\rho_s}}, \quad (2)$$

and one can calculate ρ_c by a non-linear fit to the measured TLM data. If both r_1 and r_2 are much larger than

d, the gap distance between the outer and the inner contacts ($r_2 - r_1$), one can divide R_{tot} by a correction factor given by

$$cf = \frac{r_2 \ln \frac{r_2}{r_1}}{d}, \quad (3)$$

to compensate for the geometric differences between the circular TLM patterns and the usual rectangular TLM patterns, and use a linear fit to the measured TLM data instead of the non-linear fit to calculate ρ_c, with little additional error [2,5].

$$\frac{R_{tot}}{cf} \approx \frac{\rho_s}{2\pi r_2}(d + 2L_T), \quad (4)$$

In this work, r_2 was fixed at 200 μm, with d of 5, 10, 15, 20, 25, 30, 40 and 50 μm. The corresponding cf is 1.013, 1.026, 1.040, 1.054, 1.068, 1.084, 1.116 and 1.151, respectively.

Samples were annealed at 620 °C and 850 °C for 30 sec in a flowing N_2 ambient using rapid thermal annealing (RTA). The annealing conditions were not optimized. Current-voltage (I-V) characteristics were measured using an HP4155A Semiconductor Parameter Analyzer with the current compliance set at 100 mA, and ρ_c was obtained using equation (4). Ti/Ag samples were further analyzed by secondary ion mass spectrometry (SIMS) using CAMECA ims-4f. The primary ion was O_2^+, with the ion energy, the beam current, and the spot size of 5.5 keV, 5×10^{-8} A, and 150 μm, respectively.

III. RESULTS AND DISCUSSION

Fig. 1 shows the I-V characteristics of Ti/Al and Ti/Ag contacts. Both contacts were rectifying as deposited. After annealing at 620 °C, Ti/Al contacts became ohmic with ρ_c of 8.8×10^{-4} Ωcm^2, showing some balling-up. Ti/Ag contacts showed non-linear characteristics at this temperature. Ti/Al contacts annealed at 850 °C showed severe balling-up, with degraded ρ_c of 2×10^{-3} Ωcm^2. Ti/Ag contacts were ohmic with ρ_c of 9.5×10^{-4} Ωcm^2, and the surface morphology was very smooth. Probing Ti/Al contacts, especially after annealing, was very difficult due to Al oxidation. The probe tips had to be forced down quite hard to penetrate the oxidized surface for any consistent measurement.

Long-term stability of these contacts was investigated. ρ_c of the Ti/Al contacts annealed at 620 °C degraded from 8.8×10^{-4} Ωcm^2 to 1.5×10^{-2} Ωcm^2 in three months, a 17-fold increase (1700 %). In the same three month period, ρ_c of the Ti/Ag contacts annealed at 850 °C degraded from 9.5×10^{-4} Ωcm^2 to 1.2×10^{-3} Ωcm^2, only a 25 % increase. The surface was still very clean and smooth, without any sign of tarnish.

Fig. 2 shows the results of SIMS analysis on Ti/Ag contacts. All analyses were performed on the same day.

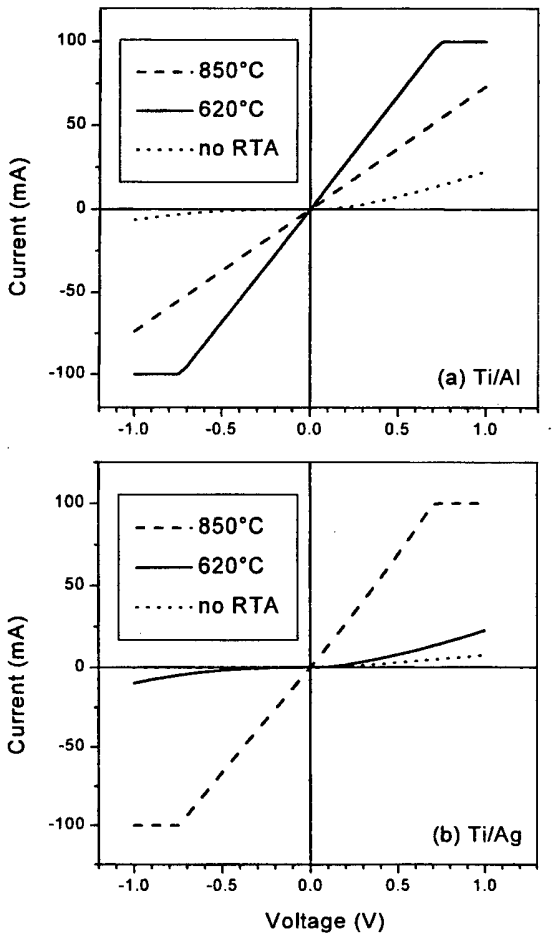

Fig. 1. I-V characteristics of (a) Ti/Al contacts and (b) Ti/Ag contacts.

From the as-deposited sample, distinct peaks of Ti and Ag counts are observed, showing no sign of mixing of the metal layers. After annealing at 620 °C, some mixing of Ti and Ag took place, but the two peaks are still separated. The observed Ti diffusion into GaN and the reduction of N count near the interface suggest the formation of TiN interfacial layer and N vacancies near the interface. This would be contrary to previous reports [7,8] that TiN formation requires high annealing temperatures above 900 °C. Since the I-V characteristics were not ohmic at this annealing temperature as shown in Fig. 1(b), it would be also contrary to the reports [7–9] that the formation of TiN and N vacancies is the key for ohmic contact behavior when Ti is the contacting metal to n-type GaN. Complete mixing of Ti and Ag took place on the sample annealed at 850 °C, with large amount of Ag at the GaN surface. This coincides with good ohmic characteristics as shown in Fig. 1(b). Luther *et al.* [10] observed AlN formation at the interface of their Ti/Al ohmic contacts, and suggested that this thin AlN layer is responsible for the ohmic behavior. Obviously, this is not the case in our Ti/Ag contacts since there is no Al to form AlN. Anoth-

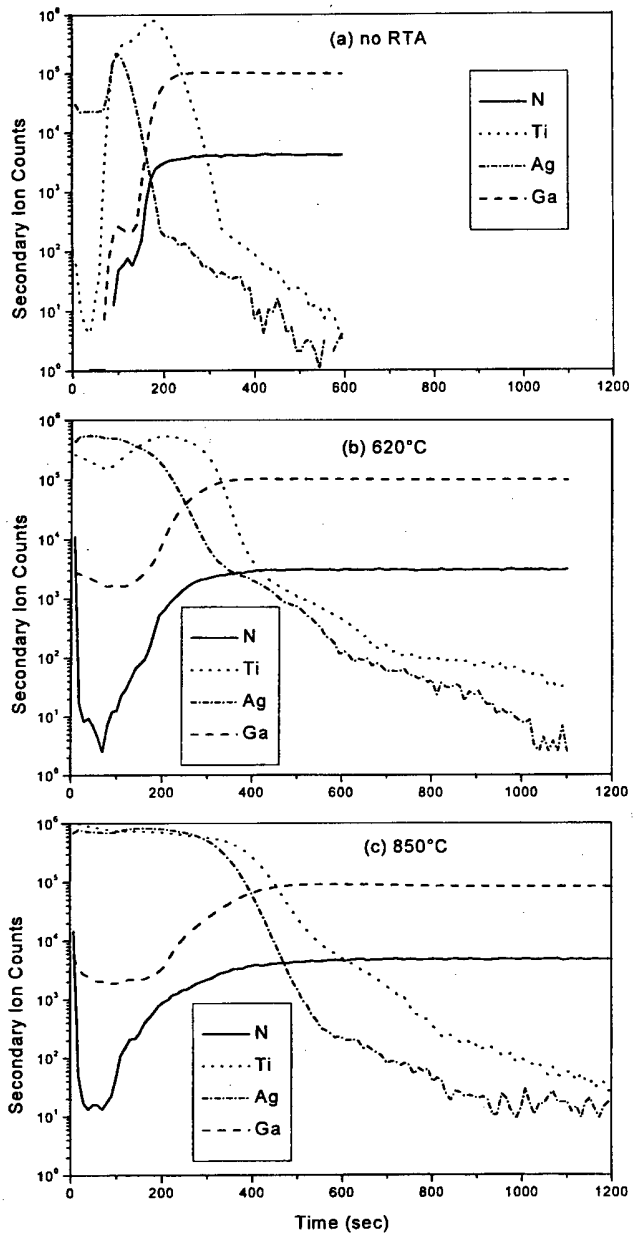

Fig. 2. SIMS analysis of Ti/Ag contacts (a) as deposited, (b) after 620 °C annealing, and (c) after 850 °C annealing.

er proposed mechanism of Ti/Al ohmic contacts is that Ti reduces the native oxide on the GaN surface and Al diffuses through the Ti layer to make contact with GaN in the form of an Al-Ti intermetallic phase that has a low work function [11]. The resulting low barrier would allow current flow by thermionic or thermionic-field emission. This mechanism can explain our Ti/Ag contacts when Al is replaced with Ag. Ohmic behavior was observed only after Ag reached the GaN surface after annealing at 850 °C. In fact, the Schottky barrier height of Ag on GaN is even lower than that of Ti or Al [12]. The formation of N vacancies would also aid the ohmic contact formation by enhancing the thermionic-field emission.

IV. SUMMARY

We have fabricated and characterized Ti/Ag and Ti/Al ohmic contacts, side-by-side, to relatively low-doped (7×10^{17} /cm^3) n-type GaN. No surface treatments, other than the oxide etch in NH_4OH, were performed before the metal evaporation and RTA annealing. Ti/Ag contacts reached a specific contact resistance of 9.5×10^{-4} Ωcm^2 after annealing at 850 °C. Ti/Al contacts reached a similar value after annealing at 620 °C, and the value degraded after higher temperature annealing. Unlike Ti/Al contacts, Ti/Ag contacts showed very smooth surface morphology and excellent reliability. The specific contact resistance of Ti/Ag contacts increased only by 25 % in three months, while that of Ti/Al contacts showed 17-fold increase in the same period. Ti/Ag ohmic contacts should be very useful in devices requiring long-term stability. I-V and SIMS analysis suggest that the formation of a low-barrier Ti-Ag intermetallic phase at the GaN surface may be more important than the formation of TiN and/or N vacancies near the interface in achieving ohmic behavior in this contact system.

ACKNOWLEDGMENTS

This study was supported by the academic research fund of Ministry of Education, Republic of Korea, through Inter-University Semiconductor Research Center (ISRC 97-E-5007) in Seoul National University.

REFERENCES

[1] Z. Fan, S. N. Mohammad, W. Kim, O. Aktas, A. E. Botchkarev and H. Morkoc, Appl. Phys. Lett. **68**, 1672 (1996).

[2] L. F. Lester, J. M. Brown, N. C. Ramer, L. Zhang, S. D. Hersee and J. C. Zolper, Appl. Phys. Lett. **69**, 2737 (1996).

[3] J. Burm, K. Chu, W. A. Davis, W. J. Schaff and L. F. Eastman, Appl. Phys. Lett. **70**, 464 (1997).

[4] J. D. Guo, C. I. Lin, M. S. Feng, F. M. Pan, G. C. Chi and C. T. Lee, Appl. Phys. Lett. **68**, 235 (1996).

[5] G. S. Marlow and M. B. Das, Solid-State Electron. **25**, 91 (1982).

[6] G. K. Reeves and H. B. Harrison, IEEE Electron Dev. Lett. **3**, 111 (1982).

[7] M. E. Lin, Z. Ma, F. Y. Huang, Z. Fan, L. H. Allen and H. Morkoc, Appl. Phys. Lett. **64**, 1003 (1994).

[8] Y. F. Wu, W. N. Jiang, B. P. Keller, S. Keller, D. Kapolnek, S. P. Denbaars, U. K. Mishra and B. Wilson, Solid-State Electron. **41**, 165 (1997).

[9] S. Ruvimov, Z. Liliental-Weber, J. Washburn, K. J. Duxstad, E. E. Haller, Z-F. Fan, S. N. Mohammad, W.

Kim, A. E. Botchkarev and H. Morkoc, Appl. Phys. Lett. **69**, 1556 (1996).

[10] B. P. Luther, J. M. DeLucca, S. E. Mohney and R. F. Karlicek, Jr., Appl. Phys. Lett. **71**, 3859 (1997).

[11] B. P. Luther, S. E. Mohney, T. N. Jackson, M. A. Khan, Q. Chen and J. W. Yang, Appl. Phys. Lett. **70**, 57 (1997).

[12] J. S. Foresi and T. D. Moustakas, Appl. Phys. Lett. **62**, 2859 (1993).

Journal of the Korean Physical Society, Vol. 34, June 1999, pp. S401~S404

Investigations of Mg-doped GaN grown by Metalorganic Chemical Vapor Deposition

C. S. OH, K. S. KIM, K. J. LEE, J. Y. CHOI, H. K. CHO, O. H. CHA,
G. M. YANG, C.-H. HONG, E.-K. SUH, K. Y. LIM* and H. J. LEE

Department of Semiconductor Science and Technology and Semiconductor Physics Research Center, Chonbuk National University, Chonju 561-756

Electrical and optical properties of Mg-doped GaN films grown by metalorganic chemical vapor deposition are investigated as a function of the Cp_2Mg flow rates through the Hall effect and photoluminescence measurements. It is found that there is a critical flow rate of Cp_2Mg at which the hole concentration is maximum and the resistivity is minimum, simultaneously. The activation energy of shallow Mg acceptor is obtained about 160 meV from the temperature dependent Hall effect measurement. In case of high Mg incorporation, we found that Mg-related deep donors (E_d=540 meV) compensate the shallow acceptors. The strong blue emission around 2.72 eV of as-grown Mg-doped p-type GaN is sharply decreased after thermal annealing. This result indicates that the thermal annealing activates hydrogen passivated deep levels as well as Mg-H complexes.

I. INTRODUCTION

The group III nitrides are strong candidates for blue light emitting diodes (LEDs) and laser diodes (LDs) [1]. In order to realize these devices, it is important that high quality films and doping control in both n- and p-type should be achieved. Because of the absence of lattice matched substrate, GaN thin film on sapphire substrate using heteroepitaxy includes many structural defects such as high density of threading dislocations that act as scattering centers of mobile carriers [2]. In addition to this, high background electron concentrations coming from nitrogen vacancy of undoped GaN, hydrogen passivation of Mg acceptor and donor compensation induced Mg-related complexes make it more difficult to grow a p-type GaN with high hole concentration [3-5]. Nevertheless, high efficient blue LEDs and LDs were fabricated on sapphire substrate using Mg-doped GaN as a p-contact electrode [6,7]. But it is still necessary to enhance hole concentration for the improvement of LEDs and LDs performance. Until now, to our knowledge, using MOCVD only a few groups obtain the hole concentration of -10^{18} cm^{-3} [8]. Therefore, in order to obtain Mg-doped GaN films of the high hole concentration and low resistivity, the physical properties of Mg-doped GaN must be understood more profoundly.

In this study, the electrical and optical properties of Mg-doped GaN with different Cp_2Mg flow rates during the growth were investigated, which are grown on sapphire substrate by metalorganic chemical vapor deposition.

*E-mail: kylim@phyo.chonbuk.ac.kr

II. EXPERIMENT

Mg-doped GaN epitaxial layers were grown on (0001) oriented sapphire substrates by a horizontal rotating MOCVD equipment. We used bis-cyclopentadienylmagnesium (Cp_2Mg), trimethylgallium and ammonia, as Mg, Ga and N sources, respectively. Before loaded into the reactor, sapphire substrates were rinsed in organic solvents and etched in H_2SO_4:H_3PO_4=3:1 hot solution for 3 min. After loaded, high temperature thermal cleaning was conducted in H_2 ambient for 10 min at 1150 °C. A 25 nm thick GaN buffer layer was deposited at 560 °C. After then, Mg-doped GaN layers were deposited under different Cp_2Mg flow rates at 1080 °C for 1 hour using hydrogen carrier gas. Cp_2Mg flow rate was varied from 0.6 to 4.2 μmol/min. Layers thickness were estimated to 1~2 μm by scanning electron microscope (SEM). All as-grown Mg-doped GaN showed a p-type conduction, but the hole concentrations were low and resistivities were high. Therefore, all samples were activated by rapid thermal annealing (RTA) for dissociation of Mg-H bonding. RTA treatment was conducted in a N_2 ambient at 800 °C for 40 sec.

The electrical properties of the grown samples were evaluated by van der Pauw Hall measurement. The optical characteristics were measured by photoluminescence (PL) using 325 nm He-Cd laser at room temperature.

III. RESULTS AND DISCUSSIONS

We have examined the effects of Cp_2Mg flow rate

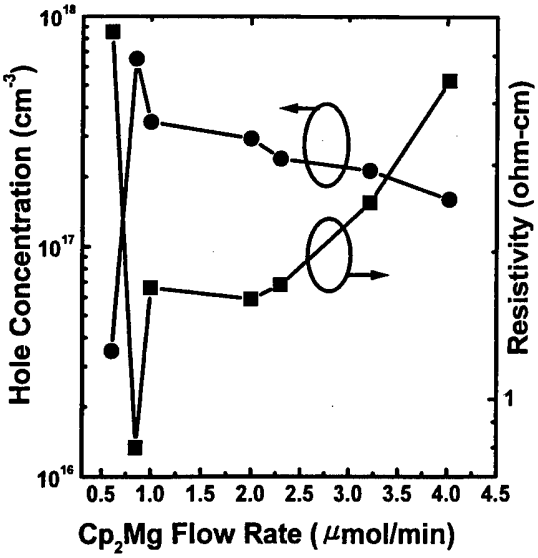

Fig. 1. Hole concentration and resistivity depending on the Cp_2Mg flow rate from 0.6 to 4.2 μmol/min after RTA thermal annealing.

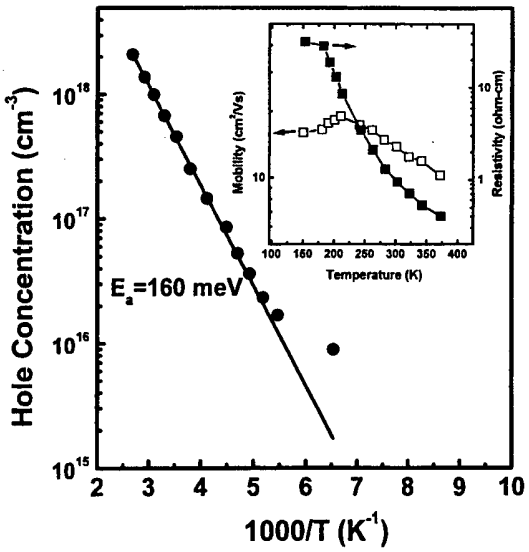

Fig. 2. Arrhenius plot of hole concentration of Mg-doped GaN film with f_{Cp_2Mg}=0.85 μmol/min. Solid circles and solid line indicate experimental values and fitted curve, respectively. Inset shows resistivity and mobility as a funtion of temperature.

(f_{Cp_2Mg}) dependence on hole concentration and resistivity. Cp_2Mg flow rates are varied from 0.6 to 4.2 μmol/min. As-grown Mg-doped GaN films show the p-type conduction of middle 10^{16} cm^{-3}. After RTA treatment, hole concentration was increased by approximately one order. These results are plotted in Fig. 1. As shown in Fig. 1, we know that there is a critical point in Cp_2Mg flow rate to obtain a maximum hole concentration and a minimum resistivity. At f_{Cp_2Mg}=0.85 μmol/min, the maximum hole concentration of 6.4×10^{17} cm^{-3} and the minimum resistivity of 0.8 Ω-cm. is obtained. Below this flow rate (f_{Cp_2Mg}<0.85 μmol/min), as the Cp_2Mg flow rate is increased hole concentration (resistivity) is increased (decreased). Above this flow rate (f_{Cp_2Mg}>0.85 μmol/min) as the Cp_2Mg flow rate is increased hole concentration (resistivity) is decreased (increased). This behavior is considered that in the region of f_{Cp_2Mg}<0.85 μmol/min, the incorporated Mg contribute to raise hole concentration, in other words, most of incorporated Mg are substituted for Ga site. But in the region of f_{Cp_2Mg}>0.85 μmol/min, two possibilities are considered. One is the hydrogen passivation of shallow Mg acceptor [4], the other is the compensation of Mg-related donor [5]. In case of the former, the more Mg is incorporated, the less Mg-H bonding is broken as compared to that of f_{Cp_2Mg}=0.85 μmol/min when as-grown Mg-doped GaN is activated at the same RTA conditions. As a consequence, though Mg is more incorporated, hole concentration is not increased. However, such Mg-H complex alone does not well explain the decrease of the hole concentration with the increase of Mg concentration. In case of the latter, all of incorporated Mg do not contribute to raise the hole concentration, that is, as the Mg is more incorporated, other sites (Mg-interstitial *etc.*) rather than Ga-substitutional sites augment more and more. Recently, its possibility was reported that Mg-interstitials and N-vacancies could be formed as compensating donor complexes [9]. These deep donors decrease the hole concentration and increase the resistivity. Introduction to deep donor formation is well consistent with PL spectra discussed later.

Figure 2 shows the Arrhenius plot of temperature dependent Hall characterization of the sample with f_{Cp_2Mg}=0.85 μmol/min. From the Fig. 2, it is estimated that a shallow Mg acceptor ionization energy is about 160 meV. This value shows a good agreement with that reported elsewhere [10]. Inset in Fig. 2 represents the resistivity and mobility as a function of temperature. Mobility increases with increasing temperature up to 200 K. Above 200 K, mobility gradually decreases. The behavior is interpreted that ionized impurity scattering dominates below 200 K and lattice scattering dominates above 200 K. However, if it is assumed that the temperature dependence of mobility is nearly constant in the temperature range 150 K to 350 K, resistivity (or conductivity) is determined by hole concentration not mobility as shown Fig. 2. Therefore, in order to obtain p-type GaN with low resistivity, high hole concentration is necessary.

Figure 3 shows room temperature PL spectra of as-grown Mg-doped GaN with different Cp_2Mg flow rates. In case of f_{Cp_2Mg}<0.85 μmol/min, two dominant peaks are observed. One is the transition from a conduction band to valence band (e-h) at 3.415 eV. (this peak position corresponds to band-edge peak of our undoped GaN at room temperature PL.) and the other is a conduction band to shallow acceptor (e-A^0) at 3.241 eV. On

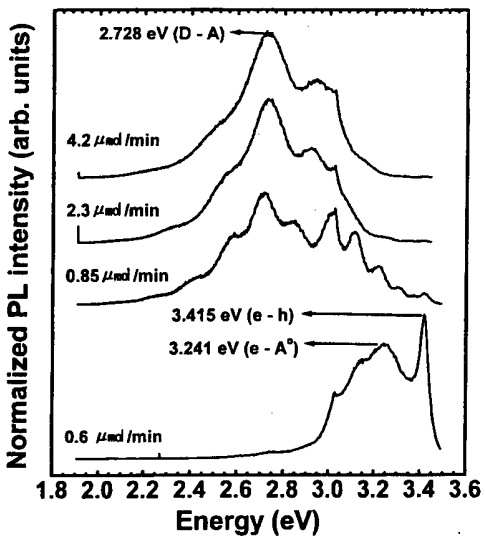

Fig. 3. Room temperature PL spectra of Mg-doped GaN films with different Cp_2Mg flow rate.

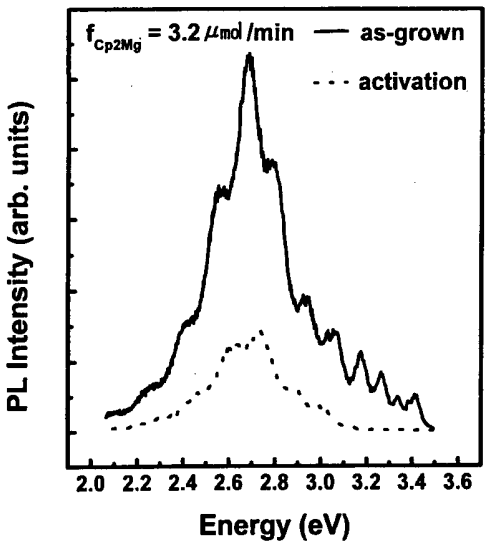

Fig. 4. Room temperature PL spectra of Mg-doped GaN film with. f_{Cp2Mg}=3.2 μmol/min before and after RTA treatment.

the other hand, $f_{Cp_2Mg} \geq 0.85$ μmol/min, a blue emission peak is observed at 2.728 eV. The blue emission indicates that Mg concentration was incorporated above 10^{19} cm^{-3} [11]. The blue emission is attributed to donor acceptor pair (DAP) transition [12]. Mg-interstitial and N-vacancy complex are possible candidate for deep donors as mentioned previously [9]. From the equation of $h\nu = E_g - (E_a + E_d) + E_c$ [13], deep donor activation energy (E_d) is estimated about 540 meV by electrically measured acceptor binding energy (E_a) of 160 meV, Coulomb interaction energy (E_c) of 15 meV [14] and bandgap energy (E_g) of 3.415 eV. From Fig. 3 and Fig. 1, whenever as-grown Mg-doped GaN shows blue emission at room temperature, its hole concentration exhibit at least over 10^{17} cm^{-3} after RTA treatment. However, Tokunaga *et al.* [15] reported that p-type conduction is obtained after thermal activation when as-grown Mg-doped GaN shows only the band to band transition. However, this difference is not clearly understood yet.

Figure 4 shows the room temperature PL spectra of Mg-doped GaN with f_{Cp_2Mg}=3.2 μmol/min before and after RTA treatment. Nakamura *et al.* reported that the blue emission intensity of Mg-doped GaN was increased after thermal annealing [16]. The increase of blue emission intensity after thermal annealing was blamed for the increase of number of the active Mg acceptor related with the blue emission, which is originated from the activation of hydrogen passivated Mg. However, in our case, the blue emission intensity of the thermally annealed sample is steeply decreased compared with as-grown sample, as shown in Fig. 4. As mentioned in Fig. 1, hole concentration of our Mg-doped GaN is increased by one order compared with as-grown one after RTA treatment. Therefore, it is necessary to compensate the annealing effect for PL intensity. It can be inferred from the fact that the RTA treatment activates the hydrogen passivated Mg as well as non-radiative defect centers, as reported by Li *et al.* [17]. We consider that dislocation induced defects might be responsible for such behavior. A transmission electron microscopy revealed that our Mg-doped GaN film has the dislocation density of $\sim 10^{11}$ cm^{-2}. Before the RTA treatment, these defects are passivated by hydrogen resulting in charge neutralization, which are not acted as non-radiative centers. However, after the RTA treatment, these passivated defect centers are also activated and charged, which are acted as non-radiative centers causing PL intensity reduction.

IV. SUMMARY

The electrical and optical properties of Mg-doped GaN films have been investigated as a function of Cp_2Mg flow rates. A shallow Mg acceptor activation energy is obtained about 160 meV from the temperature dependent Hall effect measurement. At f_{Cp_2Mg}=0.85 μmol/min, the maximum hole density is 6.4×10^{17} cm^{-3} and the minimum resistivity is 0.8 Ω-cm. Mg-related deep donor (E_d=540 meV) compensation plays an important role in heavily Mg-incorporated GaN in terms of electrical and optical properties. The RTA treatment activates hydrogen-passivated deep levels as well as Mg-H complexes.

ACKNOWLEDGMENTS

This work has been supported by MSTK and by

KOSEF through the Semiconductor Physics Research Center at Chonbuk National University, and by the Project of ISRC 97-E-3037 of the Ministry of Education of Korea.

REFERENCES

[1] S. Strite and H. Morkoc, J. Vac. Sci. Technol. **B10**, 1237 (1992).

[2] N. G. Weimann and L. F. Eastman, J. Appl. Phys. **83**, 3656 (1998).

[3] H. P. Maruska and J. J. Tietjen, Appl. Phys. Lett. **15**, 327 (1969).

[4] S. Nakamura, N. Iwasa, M. Senoh and Mukai, Jpn. J. Appl. Phys. **31**, 1258 (1992).

[5] M. Smith, G. D. Chen, J. Y. Lin, H. K. Jiang, A. Salvador, B. N. Sverdlov, A. Botchkarev, H. Morkoc and B. Goldenberg, Appl. Phys. Lett. **68**, 1883 (1996).

[6] S. Nakamura, M. Senoh, S. Nagahama, N. Iwasa, T. Yamada, T. Matsushita, H. Kiyoku, Y. Sugimoto and H. Kiyoku, Appl. Phys. Lett. **68**, 2105 (1996).

[7] S. Nakamura, M. Senoh, S. Nagahama, N. Iwasa, T. Yamada, T. Matsushita, H. Kiyoku, Y. Sugimoto and H. Kiyoku, Appl. Phys. Lett. **69**, 1477 (1996).

[8] L. Sugiura, H. Suzuki and J. Nishio, Appl. Phys. Lett. **72**, 1748 (1998).

[9] K. J. Chang and S.-G. Lee, '98 Korea-Japan Joint Workshop, p. 86 (1998).

[10] H. Nakayma, P. Hacke, M. R. H. Khan, T. Detchprohm, K. Hiramatsu and N. Sawaki, Jpn. J. Appl. Phys. **35**, L282 (1996).

[11] U. Kaufmann, M. Kunzer, M. Maier, H. Obloh, A. Ramakrishnan, B. Santic and P. Schlotter, Appl. Phys. Lett. **72**, 1326 (1998).

[12] E. S. Oh, H. S. Park and Y. J. Park, Appl. Phys. Lett. **72**, 70 (1998).

[13] J. I. Pankove, *Optical Processes in Semiconductors* (Dover Publications, Inc., NY., 1971), p. 66.

[14] O. Lagerstedt and B. Monemar, J. Appl. Phys. **45**, 2266 (1994).

[15] H. Tokunaga, I. Waki, A. Yamaguchi, N. Akutsu and K. Matsumoto, Proc. 2nd Int. Conf. Nitride Semiconductors, p. 60 (1997).

[16] S. Nakamura and G. Fasol, *The Blue Laser Diode* (Springer-Verlag, 1997), p. 107.

[17] Y. Li, Y. Lu, H. Shen, M. Wraback, M. Schurman, W. Mayo, T. Salagaj and R. A. Stall, Mat. Res. Soc. Symp. Proc. **395**, 369 (1996).

Journal of the Korean Physical Society, Vol. 34, June 1999, pp. S405~S408

Structural and Optical Characteristics of Si Doped and Si-Zn Codoped InGaN Films Grown by Metalorganic Chemical Vapor Deposition

K. J. LEE, K. S. KIM, C. S. OH, S. C. CHOI, G. M. YANG,
C.-H. HONG, K. Y. LIM* and H. J. LEE

Department of Semiconductor Science and Technology, Semiconductor Physics Research Center, Chonbuk National University, Chonju 561-756

Si doped and Si-Zn codoped InGaN films were grown by low pressure metalorganic chemical vapor deposition. The InGaN surface is characterized by hexagonal spiral growth around threading dislocation that Si dopant act on core of InGaN island with screw component. In solid solubility is related dopant flow. Zn related donor-acceptor emission was observed at photoluminescence spectra. The 2-dimensional high resolution x-ray reciprocal space mapping reveals InGaN/GaN pseudomorphic compressive strained structures, indicating coherency of InGaN/GaN heterostructures.

I. INTRODUCTION

InGaN and AlGaN ternary alloys attract a lot of attention recently due to their interesting physical properties making them promising materials for short wavelength light emitters. InGaN alloys have been attracting much attention as active layers for the fabrication of blue light emitting diodes (LEDs) and laser diodes (LDs). In spite of the fact that the growth process occurs in the presence of a large number of the threading dislocations, blue LEDs using of Si-Zn codoped InGaN active layer have been already fabricated [1]. Epilayers and quantum wells based on InGaN/GaN have proved to exceptionally efficient photoemmitters at room temperature. However, the relationships of optical emission efficiency and flow rates of dopant materials was not elucidated clearly. In this work, we report the optimal growth conditions of InGaN layers with Si-Zn codoping and the relationship between structural and optical properties and dopant gas flow rates.

II. EXPERIMENT

All films were grown by low pressure metalorganic chemical vapor deposition using trimethylgalium (TMGa), trimethylindium (TMIn) and ammonia as precusors on *c*-plane sapphire substrates. Silane (SiH_4) and diethylzinc (DEZn) was used as Si and Zn dopant, respectively. The sapphire substrate was degreased in boiling organic solvents, etched in $3H_2SO_4$: H_3PO_4 acid chemical solution and rinsed deionized water. In order to relieve the lattice mismatch between GaN and sapphire substrate, the conventional GaN buffer layers were deposited at 560 °C, followed by the growth of a 2 μm thick GaN films at 1120 °C and H_2 ambient. The InGaN growth was initiated after cooling the GaN film to 750~850 °C and changing N_2 carrier gas ambient. Afterwards the InGaN films were grown at the different temperatures and flow rate of source and dopant materials. First, we grew InGaN films at different growth parameters and the characteristics of the grown samples were analyzed by photoluminescence (PL), high resolution x-ray diffraction (HXRD), atomic force microscope (AFM). The optimized growth temperature of high quality InGaN films was 880 °C and [TMIn]/[TMIn+TMGa] is 0.8. The 200 nm InGaN films for above growth conditions were obtained. PL peak wavelength of band edge emission and double crystal x-ray rocking curve FWHM of (002) plane is 3895 Å and 676 arcsec, respectively. For the purpose of blue emission, we grew the Si and Zn codoped InGaN/GaN heteroepitaxial layers.

III. RESULTS AND DISCUSSIONS

Figure 1 shows the AFM images of the Si doped InGaN films with a SiH_4 flow of (a) 1.05 nmol/min, (b) 2.06 nmol/min. The InGaN surface is characterized by spiral growth around threading dislocations with screw component [2]. The spiral height and diameter decreased with increasing SiH_4 flow. Thereby, spiral mono layer step on islands relax to lateral direction, randomly. And the valley depth between islands decreased. This result indicates InGaN smooth surface mode which Si act on

*E-mail: kylim@phyo.chonbuk.ac.kr

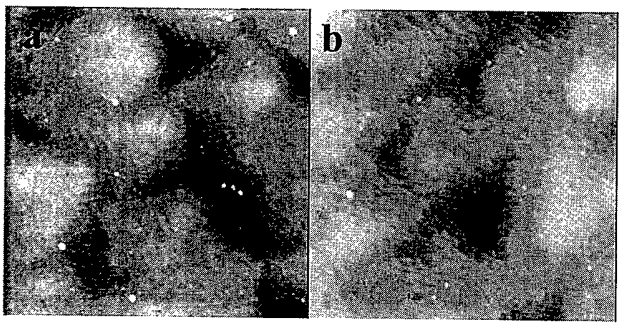

Fig. 1. Atomic force microscope images of the surface of Si doped InGaN films with (a) SiH_4 flow 1.05 nmol/min and (b) SiH_4 flow 2.06 nmol/min. Total vertical scale is 3 μm.

core of InGaN spiral islands. Comparing the sample (a) 1.05 nmol/min SiH_4 flow with (b) 2.06 nmol/min SiH_4 flow, we found that the splitting of the 2θ-ω scan for (002) plane diffraction between GaN and InGaN is not changed by SiH_4 flow. Therefore, in this Si doping range, the peak position of 3830 Å of room temperature photoluminescence band edge emission is almost the same value. But PL intensity was reduced and FWHM increase with increasing SiH_4 flow. These results indicate that In solid composition was not changed by SiH_4 flow. However, in the heavily Si doped InGaN films, the grain size becomes small and grain boundary larger as shown in figure 1.

The effect of DEZn flow on Si-Zn codoped InGaN film was showed in figures 2, 3. Figure 2 is HXRD 2θ-ω rocking curves of (002) plane. The splitting between GaN and InGaN increase up to the DEZn flow rate of 6.08 nmol/min and then decrease with increasing the flow

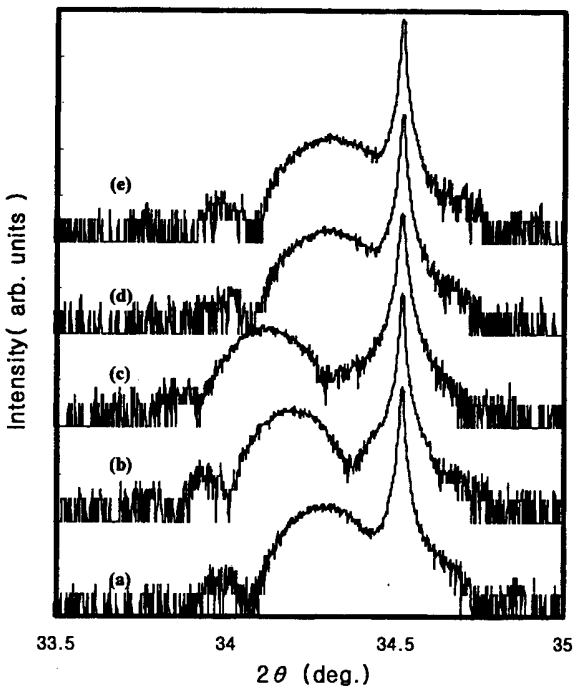

Fig. 2. High resolution x-ray diffraction 2θ-ω rocking curves of Si-Zn codoped InGaN films under the same SiH_4 flow 1.05 nmol/min. DEZn flow is (a) 0 nmol/min, (b) 4.05 nmol/min, (c) 6.08 nmol/min, (d) 8.11 nmol/min, (e) 9.46 nmol/min.

rate of DEZn. Figure 3 shows the room temperature PL spectroscopy (a) and the PL peak position of InGaN band edge emission and FWHM of them (b). The band edge emission peaks increase up DEZn flow rate of 6.08

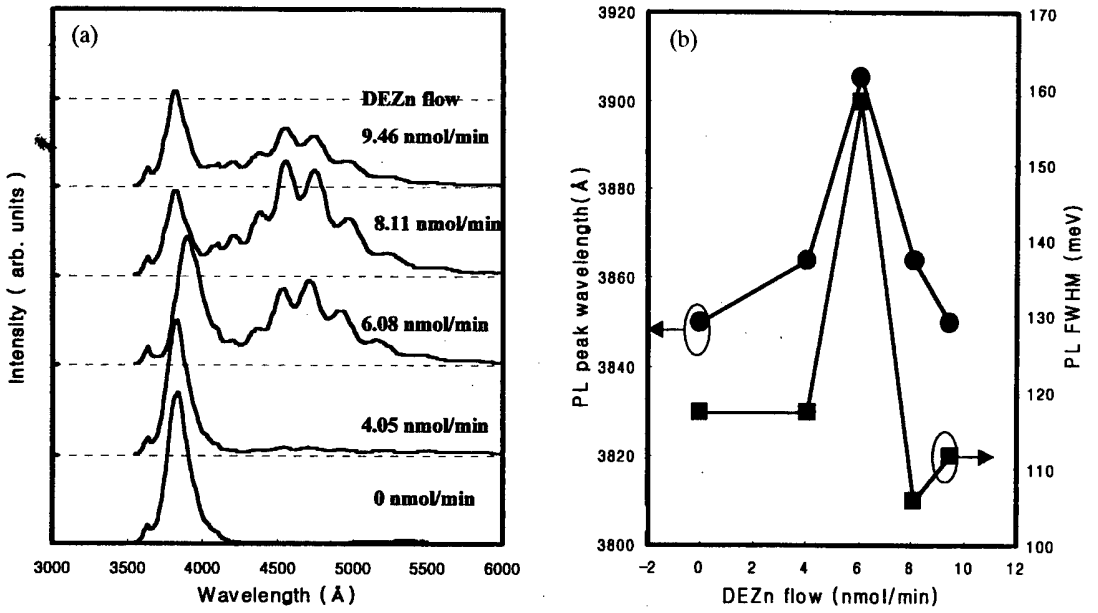

Fig. 3. Room temperature photoluminescence spectra (a) and the PL peak position and FWHM of band edge eission (b) of Si-Zn codoped InGaN films under the same SiH_4 flow 1.05 nmol/min.

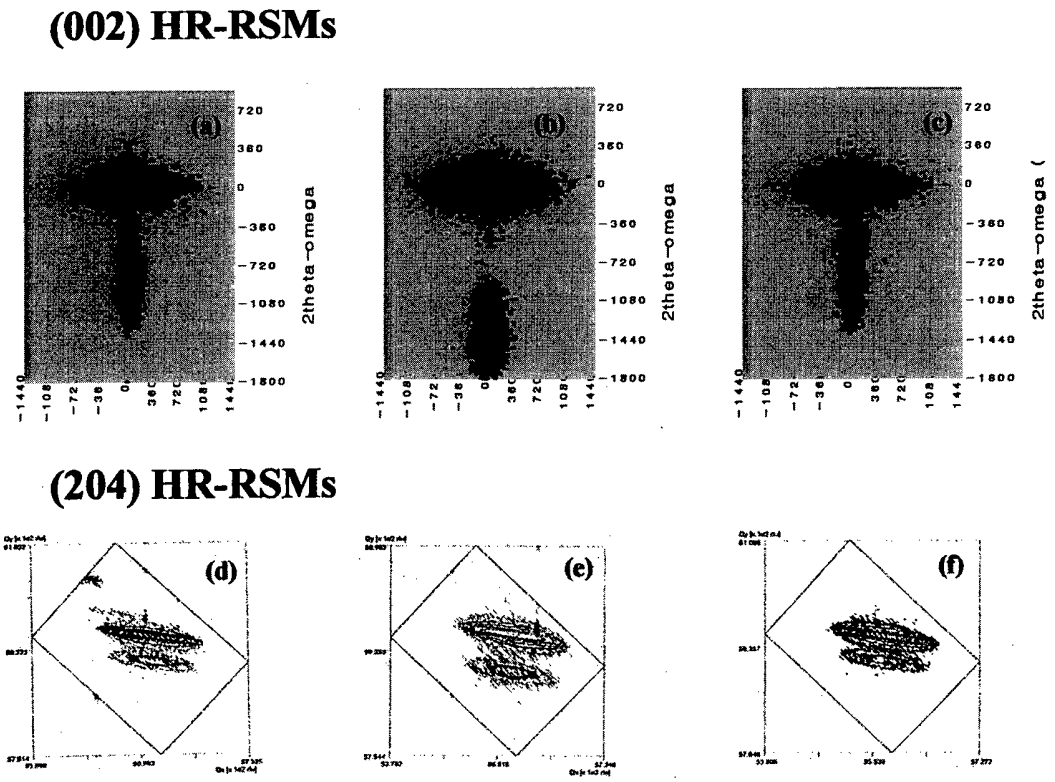

Fig. 4. The (002) symmetry plane HR-RSMs and the (204) asymmetry plan HR-RSMs of Si-Zn codoped InGaN films under the same SiH_4 flow 1.05 nmol/min. DEZn flow is (a), (d) 0 nmol/min, (b), (e) 6.08 nmol/min, (c), (f) 9.46 nmol/min.

nmol/min and then decrease more DEZn flow, However Zn related deep emission PL intensity increase with DEZn flow. Under the low DEZn flow on InGaN growth, We consider that Zn act on surfactant and increase In solid solubility efficiency. But excess DEZn flows disturb to diffuse In radicals to surface at gas flow boundary layer, and In solid compositions are decreased.

The lattice coherence of InGaN/GaN heterostructure was showed figure 4 which are high resolution x-ray reciprocal space mapping (HR-RSM) of (002) symmetry planes and (204) asymmetry planes of Si-Zn codoped InGaN film. It is well showed that GaN and InGaN diffraction. InGaN diffraction is elongated along the 2θ-ω scan axis. The diffraction intensity is related to the lattice relaxation and density of various dislocations [3,4]. The spreading of HR-RSM indicate GaN and InGaN features aligned along the surface normal direction. According to Bragg's law

$$2d\sin\theta = m\lambda,$$

lattice thickness variation (d) and tilt variation (θ) of reflection plane is displayed 2θ-ω scan and ω scan, respectively [5]. The ω scan provides information on the mosaic structure of the films and the peak width of the 2θ-ω scan provides more direct information on the crystal coherence which can be directly related to defects caused by the spiral growth component of InGaN films and pseudomorphic compressive strained InGaN/GaN heteroepitaxial films [6,7]. In figure 4, (002) symmetry plane HRRSM is showed well the splitting of between GaN and InGaN. The dispersion of InGaN x-ray diffraction intensity elongate along 2θ-ω scan axis and ω-scan width of InGaN film is smaller than one of GaN. The closure failure of a screw dislocation of InGaN film leads to a Burgers vector parallel to the dislocation line. In this case, lattice fluctuations of c-axis are increased and displayed 2θ-ω scan broadening. These results indicate InGaN film is spiral growth and relaxed mosaic structure.

In order to investigate the more information related dislocations and structural defects, we measure the (204) asymmetry plane HR-RSM and showed figure 4(d), (e), (f). This figure is marked reciprocal lattice unit (RLU) and inner square is showed real space axis unit of 2θ-ω and ω scan. According to this result, we can also conclude the strained state of InGaN/GaN heterostructure film and all films are grown coherently on GaN layer.

IV. SUMMARY

The doped InGaN heteroepitaxial thin films were grown by low pressure metalorganic chemical vapor deposition. The growth of Si doped and Si-Zn codoped InGaN films relate to various growth conditions and dopant

flows. We found the origin of InGaN spiral growth mode was result that Si dopant act as core of spiral growth with screw components. Under the low DEZn flow, Si-Zn codoped InGaN films increase HXRD splitting between GaN and InGaN and Zn related PL emission efficiency with increasing DEZn flow. Also, pseudomorphic compressive strain exists on InGaN/GaN heterostructure.

ACKNOWLEDGMENTS

This work has been supported by MSTK and by KOSEF through the Semiconductor Physics Research Center at Chonbuk National University and by the Project of ISRC-97-E-3037 of the Ministry of Education of Korea. The authors specially would like to thank Prof. Yosikawa of Chiba University at Japan for HXRD measurements.

REFERENCES

[1] S. Nakamura and G. Fasol, *The Blue Laser Diode* (Springer, Berlin, Heidelberg, New York, 1997).
[2] S. Keller, U. K. Mishra, S. P. DenBaars and W. Seifert, Jpn. J. Appl. Phys. **37**, L431 (1988).
[3] D. Kapolnek, X. H. Wu, B. Heying, S. Keller, B. P. Keller, U. K. Mishra, S. P. DenBaars and J. S. Speck, Appl. Phys. Lett. **67**, 1541 (1996).
[4] B. Heying, X. H. Wu, S. Keller, Y. Li, D. Kapolnek, B. P. Keller, S. P. DenBaars and J. S. Speck, Appl. Phys. Lett. **68**, 643 (1996).
[5] M. A. G. Halliwell, J. Cryst. Growth. **170**, 47 (1997).
[6] W. Li, P. Bergman, I. Ivanov, W.-X. Ni, H. Amano and I. Akasaki, Appl. Phys. Lett. **69**, 3390 (1996).
[7] T. Takeuchi, H. Takeuchi, S. Sota, H. Sakai, H. Amano and I. Akasaki, Jpn. J. Appl. Phys. **36**, L177 (1997).

Journal of the Korean Physical Society, Vol. 34, June 1999, pp. S409~S414

The Effects of the Threading Dislocations on the Qualities in Undoped GaN

K. S. KIM, G. M. YANG*, J.-H. KIM, K. J. LEE, C. S. OH, D. H. LIM, C.-H. HONG, K. Y. LIM and H. J. LEE

Department of Semiconductor Science & Technology and Semiconductor Physics Research Center, Chonbuk National University, Chonju 561-756

D. J. BYUN

Department of Material Science & Engineering, Korea University, Seoul 136-701

A. YOSHIKAWA

Department of Electrical and Electronics Engineering, Chiba University, 1-33 Yoyoi-cho, Inage-ku, Chiba 263, Japan

We investigated the effects of growth rate during the growth of GaN buffer layer on the GaN epilayer. It was found that the growth rate of the GaN buffer layer plays a key role in improving the quality of GaN film on a sapphire and optimum growth rate is in existence to show best crystal quality. The improvements obtained from changing buffer growth rate are explained by the promotion of lateral growth mode under optimum buffer growth rate. Besides, We have observed edge dislocations among several threading dislocation components existing in GaN epilayer are related with the reduction of electron Hall mobility and optical luminescence efficiency.

I. INTRODUCTION

The crystal growth of GaN and its related alloy materials has been widely investigated because of their potential applications of optoelectronic devices [1]. A major obstacle to growing high quality GaN epilayer and manufacturing optoelectronic devices on a sapphire substrate is the mismatch in lattice constant and thermal expansion coefficient between GaN and the sapphire substrate. This commonly results in a large amount of misfit and threading dislocations to the GaN epilayer. For the direct growth of GaN on sapphire, the growth of the GaN layer with high compensation mobility and low optical efficiency is inevitable [2]. Therefore, two step growth with a low temperature grown buffer layer, which is believed to provide a number of nucleation sites for the subsequent GaN growth, is imperative in the growth of the GaN film with a flat surface and device quality on the sapphire substrate [3]. It is therefore essential to understand how this buffer layer grows and how buffer layer growth parameters affect on the GaN epilayer. Besides, it is important know the mechanism of the compensation of electron mobility and the abatement of optical efficiency in GaN films, which is elusive up to now.

*E-mail: gyemo@moak.chonbuk.ac.kr

In this study, we demonstrate that the GaN buffer growth rate plays a deterministic role to enhance the crystal qualities of GaN epilayer. In addition, it is discussed that the edge dislocations among several dislocation components play a role to reduce the electron Hall mobility and optical luminescence intensity.

II. EXPERIMENT

The samples were grown in a horizontal metalorganic chemical vapor deposition reactor operating at a low pressure. The source materials of GaN are trimethylgallium (TMGa) and ammonia (NH_3) for Ga and N precursors, respectively. Basal c-plane sapphire substrates were used after degreased in organic solvents and etched in a hot solution of $3H_2SO_4 : 1H_3PO_4$. After loaded into the reactor, the substrates were thermally-cleaned in H_2 ambient for 10 minutes at 1100 °C. Nominal 25 nm-thick GaN buffer layers with different growth rates from 4.56 to 20.58 nm/min were deposited at 560 °C by varying TMGa flow rates. Afterwards, undoped GaN overlayers were grown on the buffer layers at a high temperature of 1080 °C for 1 hour, where the flow rate of TMGa was 112 μmol/min. The growth rates of the GaN buffer layers were determined by optical reflectivity method after

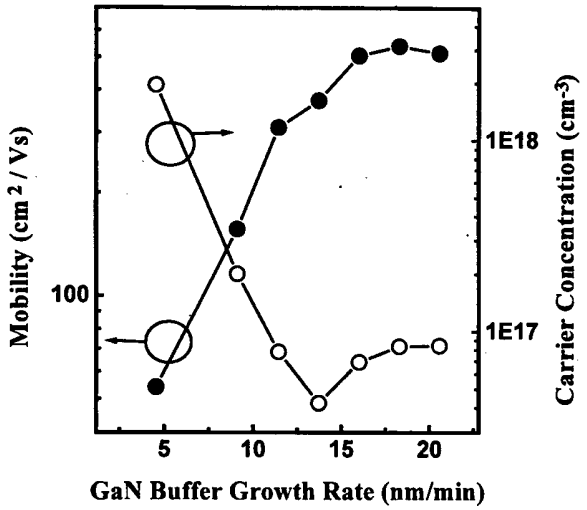

Fig. 1. Dependence of electron Hall mobility (solid circle) and carrier concentration (open circle) at room temperature on the growth rate during the growth of the GaN buffer layer.

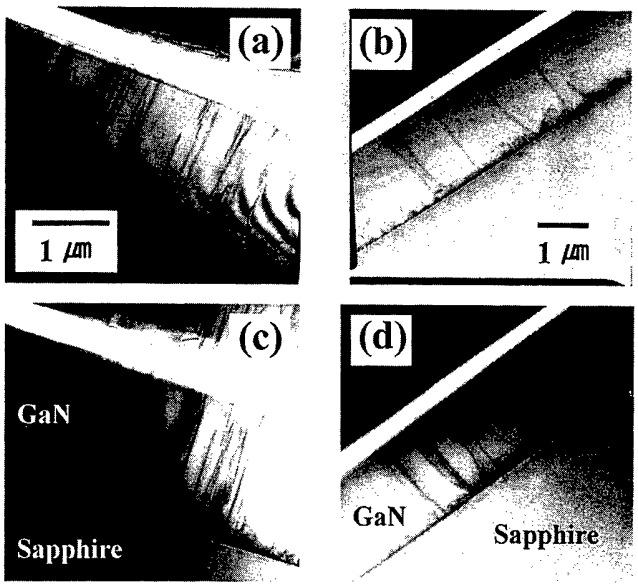

Fig. 2. Bright field TEM images taken in cross section of GaN films with buffer growth rate of 4.56 [(a) and (c)] and 18.30 nm/min [(b) and (d)] when the active beam direction is (a) [002], (b) [002], (c) [110], and (d) [110].

growing only buffer layers for 2 hours. The flow rate of NH_3 during the growth of the GaN buffer and overlayers was kept constant to 156 mmol/min.

III. RESULTS AND DISCUSSION

1. The Effects of GaN Buffer Growth Rate

Figure 1 shows the variation of the electron Hall mobility and carrier concentration at room temperature of GaN overlayers with different growth rates for the GaN buffer layers. The conventional van der Pauw Hall measurement was used for the electrical characterization. The mobility abruptly increases from 54 to 539 cm^2/Vs while the growth rate varies from 4.56 to 18.3 nm/min. A further increase of the growth rate to 20.58 nm/min makes the mobility decrease to a value of 514 cm^2/Vs. There is also a significant change in the carrier concentration. As the growth rate increases from 4.56 to 13.74 nm/min, the carrier concentration rapidly decreases and has minimum value of 4.2×10^{16} cm^{-3} at a growth rate of 13.74 nm/min. If the growth rate is larger than 13.74 nm/min, the carrier concentration undergoes small increase and then saturates to approximately 9×10^{16} cm^{-3}.

Figure 2 shows the conventional cross-sectional TEM images obtained in bright field using two-beam diffraction conditions. For buffer growth rates of 4.56 and 18.3 nm/min, the TEM images of GaN overlayer under **g**=[002] are shown in Fig. 2(a) and (b), respectively. Under active beam of **g**=[002], screw (**b**=±[001]) and mixed type dislocations (**b**=±[101], ±[011], or [111]) can be visible by applying **g**·**b** criteria [4]. However, the pure edge dislocations (**b**=±[100], ±[110], or ±[010]) are invisible. Therefore, the TEM images of GaN films with buffer growth rates of 4.56 and 18.3 nm/min under **g**=[110] are simultaneously provided in Fig. 2(c) and (d), respectively. In this diffraction beam condition, the dislocations with pure edge character as well as mixed-type dislocations are visible. Total threading dislocation densities of GaN epilayers with buffer growth rates of 4.56 and 18.3 nm/min are approximately 6×10^9 cm^{-2} and 2×10^8 cm^{-2}, respectively. The GaN film grown with a relatively high buffer growth rate has a low dislocation density.

In order to clarify the effects of the embedded buffer layer on the epilayer quality as a function of growth rate, the GaN buffer layers with different growth rates were prepared and then the surfaces of them were evaluated by atomic force microscopy (AFM). The AFM images of as-grown GaN buffer layers with growth rates of 4.56, 11.46, and 18.3 nm/min are displayed in Fig. 3(a), (b), and (c), where the surface rms roughness are 1.2, 0.48, and 0.3 nm, respectively. The surface roughness is increased as the buffer growth rate decreases. The surface roughness and the structure of GaN buffer layer might be related with the migration velocity of Ga species under constant N pressure when GaN grows in a facet growth mode during the coalescence of GaN islands. Ramer *et al.* [5] reported that the high mismatch strain between GaN and sapphire drives the buffer layer, which is initially deposited uniformly, to form three dimensional polycrystalline islands where the free energy is minimized. At low growth rate of the buffer layer Ga species are effectively more mobile on the sapphire surface allowing the growth of polycrystalline islands. However, at high growth rate the surface species are less mobile and the buffer material is not able to fully recognize to achieve minimum free

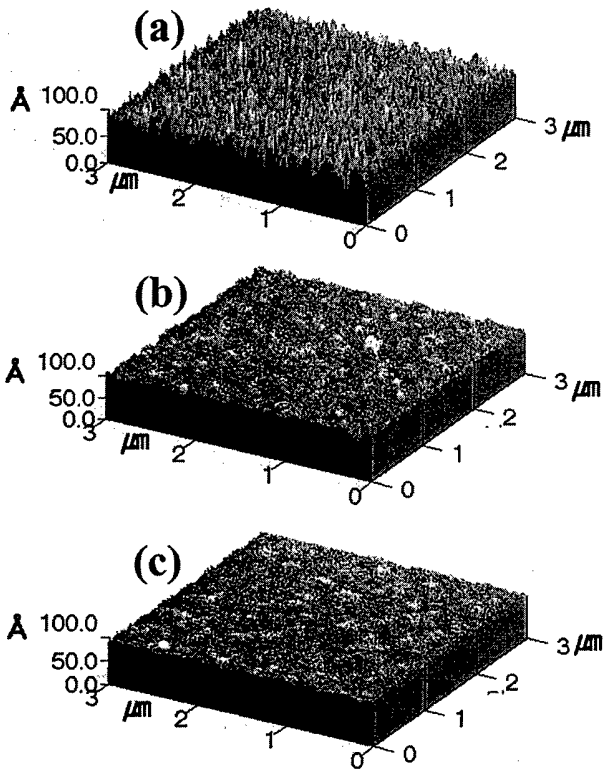

Fig. 3. AFM images of GaN buffer surfaces with growth rates of (a) 4.56, (b) 11.46, and (c) 18.30 nm/min.

energy. Consequently lateral growth mode is more dominant for the GaN buffer layer with a high growth rate than that with a low growth rate.

Figure 4(a), (b), and (c) denote the cross-sectional scanning electron microscope (SEM) images of the GaN films grown for 1 hour with different buffer growth rates of 4.56, 11.46, and 18.30 nm/min, respectively. The film thicknesses of the GaN overlayers are 2.8, 1.9, and 1.4 μm, respectively. One can easily see that the GaN overlayer thickness apparently is decreased as the buffer growth rate increases. The TEM images in Fig. 2 also show the same trend. This implies that the surface structure of GaN buffer layer (or buffer growth rate) exerts enormous influence on the growth mode of GaN overlayer. At high growth rate of the GaN buffer layer, the lateral growth mode along a direction is promoted and columnar growth mode along c direction is suppressed. This result can obviously explain the reduction of dislocation density at the buffer growth rate of 18.30 nm/min because the low growth rate of GaN overlayer generally leads to lower probabilities of generating internal defects, namely point defects, threading dislocations, and so on. It also coincides with the results of Li *et al.* [6]. They said the fine columnar growth, grain merge, and lateral growth zones are affected strongly by surface diffusion process. When the V/III ratio of the buffer layer increases (correspond to low growth rate of the buffer layer), the thickness of the nucleation zone increases and the columnar mosaicity also increases. Therefore, there is a balance between diffusion process and interfacial energy, which might be affected by V/III ratio in the films.

Figure 5(a) shows the variation of (002) and (102) full width at half maximum (FWHM) values for ω-2θ scan using high resolution x-ray diffraction measurement (HRXRD). With increasing the buffer growth rate, (002) FWHM value increases while (102) FWHM value decreases. From the FWHM of ω-2θ scan, coherent

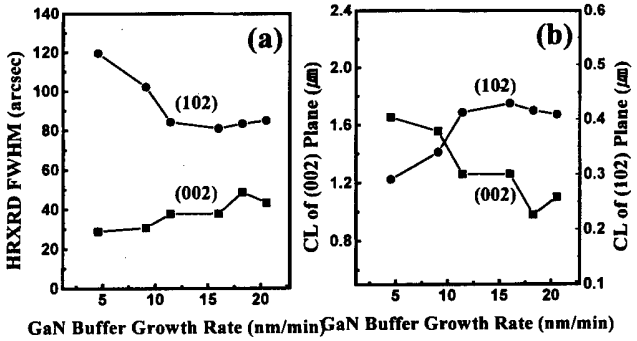

Fig. 5. Measured HRXRD FWHM and calculated coherent length for (002) and (102) reflections of ω-2θ scan as a function of buffer growth rate.

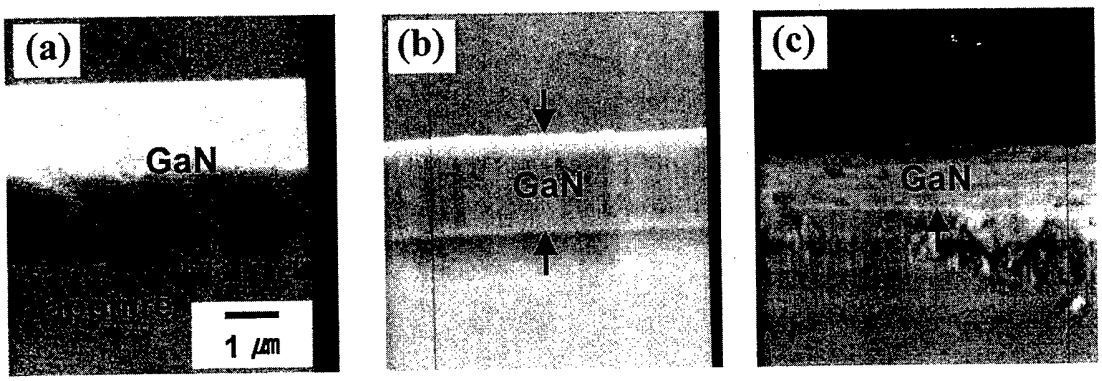

Fig. 4. SEM photographs indicating thickness variation of the GaN overlayers grown for 1 hour with different buffer growth rates of (a) 4.56, (b) 11.46, and (c) 18.30 nm/min.

length (CL) can be estimated by the Scherer formula: $CL=[0.89\lambda]/[2\Delta\omega\sin\theta_B]$ [7], where λ is the x-ray wavelength, $\Delta\omega$ is the FWHM of the HRXRD rocking curve, and θ_B is the Bragg angle corresponding to the reflecting plane. The estimated CLs are shown in Fig. 5(b), using the values of λ=1.541 Å for Cuα_1 line, θ_B (002)=17.278°, and θ_B (102)=24.044°. As the buffer growth rate is increased, the CL of (002) plane is decreased while the CL of (102) plane is increased. In the case of a fully relaxed film, the CL of (002) plane could be related with the film thickness. Thus, the decrement of CL for (002) plane can directly indicate the reduction of GaN film thickness as buffer growth rate increases, previously examined in Fig. 4. Here we should also take note of the variation of in-plane (102) CL, which is related with the mean spacing of randomly distributed threading dislocations. In other words, the large value of (102) CL means the low threading dislocation density in GaN epilayer. This result is also well matched with the observation of dislocations by TEM measurement in Fig. 2. The more information of in-plane (102) plane can be obtained from the ω scan of HRXRD measurement, which will be examined in next section.

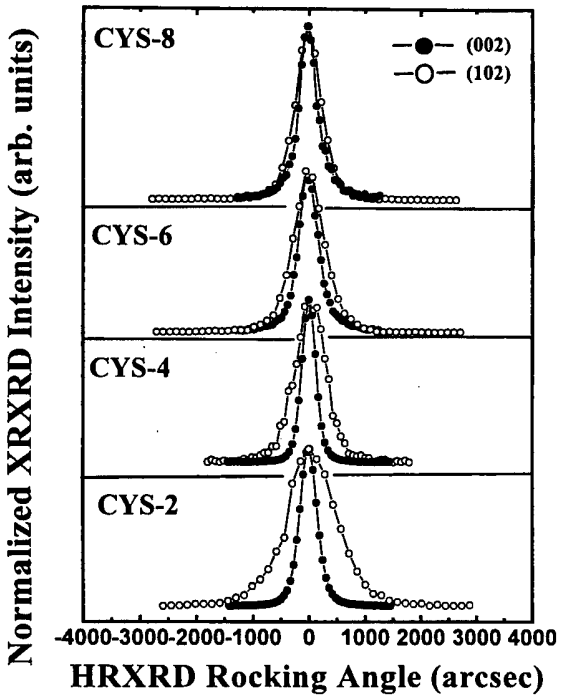

Fig. 6. HRXRD rocking curves for symmetric (002) and asymmetric (102) reflecting planes corresponding to the samples of CYS-2, CYS-4, CYS-6, and CYS-8.

2. The Relationship Between Electrical, Structural, and Optical Properties

Especially, in order to investigate the origin of electron mobility compensation and optical efficiency abatement, several kinds of samples with different electron Hall mobility values from 17 to 539 cm^2/Vs under nearly same carrier concentrations from 6.2×10^{16} to 9.6×10^{16} cm^{-3} are prepared. The detailed electrical data of all films evaluated by van der Pauw Hall measurement are shown in Table 1. All samples had specular and smooth surfaces, which were corroborated by Normarski optical microscope.

In order to investigate the structural properties of the grown GaN films, HRXRD measurements of symmetric (002) and asymmetric (102) planes were conducted for all samples. Fig. 6 represents the obtained HRXRD rocking curves for (002) and (102) reflecting planes corresponding to the samples of CYS-2, CYS-4, CYS-6, and CYS-8. The Gaussian fitted [8] FWHM for each rocking curve is shown in Table 1. The information of structural quality of the highly dislocated GaN layer can be directly obtained from the linewidth broadening of the HRXRD due to the distortion of asymmetric (102) plane, not symmetric (002) plane [9]. That is why HRXRD rocking curve for (102) plane responds to all threading dislocations including pure edge dislocations, whereas that for (002) plane is only broadened by screw and mixed type dislocations.

The relationship between the FWHMs of the (002) and (102) HRXRD rocking curves and the electron Hall mobilities is shown in Fig. 7. As the mobility increases from 17 (CYS-1) to 163 cm^2/Vs (CYS-3), the FWHM of (002)

Table 1. Summary of experimental values of mobility, carrier concentration, (002) HRXRD FWHM, (102) HRXRD FWHM, PL intensity, and PL FWHM at 300 K.

Sample #	Electrical properties at 300 K		Structural properties		Optical properties at 300 K	
	Mobility (cm^2/Vs)	Carrier Density ($\times10^{16}$ cm^{-3})	(002) FWHM (arcsec)	(102) FWHM (arcsec)	PL Intensity (arb. units)	PL FWHM (meV)
CYS-1	17	9.6	440	1620	84	35.37
CYS-2	93	8.9	322	890	1356	34.00
CYS-3	163	6.2	243	621	2256	35.57
CYS-4	229	9.4	257	550	3863	36.38
CYS-5	310	7.8	241	534	7080	36.92
CYS-6	428	8.6	371	576	13730	38.79
CYS-7	505	6.9	239	468	15946	38
CYS-8	539	7.9	349	477	15632	38.47

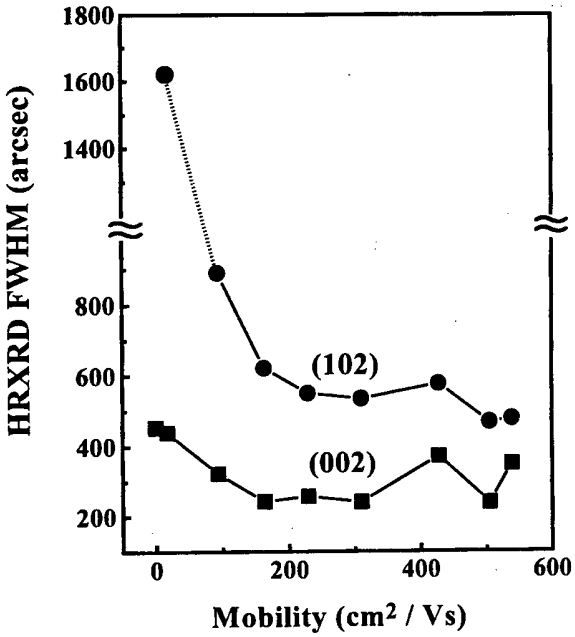

Fig. 7. The variation of the FWHMs of (002) and (102) HRXRD rocking curves for scan as a function of the electron Hall mobility.

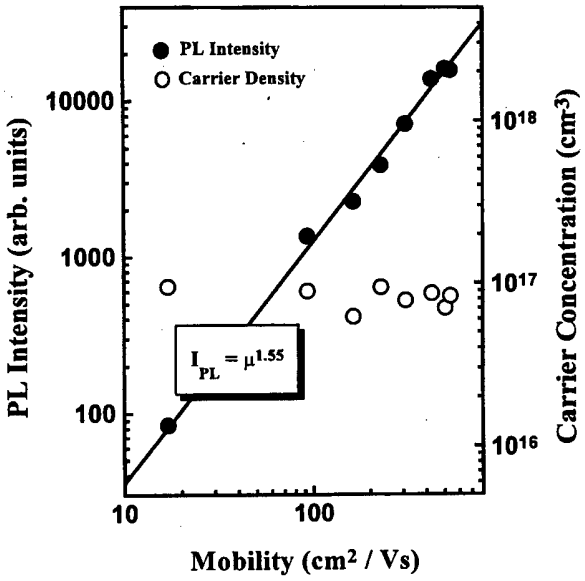

Fig. 8. The experimental data of PL intensity (solid circles) of band edge emission at 300 K and carrier concentration (open circles) vs. electron Hall mobility. The linear line indicates the least squares fit of the experimental data.

HRXRD rocking curve decreases monotonously. Above that, the (002) FWHM does not further decrease and even fluctuates. On the other hand, the FWHM of (102) HRXRD rocking curve decreases inversely as the mobility increases (The some increase in the (102) FWHM of CYS-6 is due to the increase of the FWHM of (002) HRXRD rocking curve, we suppose). This means the threading dislocations, especially pure edge dislocations, have something to do with the reduction of electron Hall mobility, of which detailed study is reported in another paper in this volume.

The optical properties of samples were characterized by photoluminescence (PL) measurement at room temperature. The excitation power density of He-Cd laser operating at 325 nm line was kept constant at 3.8 W/cm^2. The measured PL Intensity (I_{PL}) and FWHM of band edge emission for all samples are shown in Table 1. The peak positions are identical to 362 nm. The I_{PL} is superlinearly increased as a function of mobility, as depicted in Fig. 8. The effect due to the difference of carrier concentration can be excluded in the increase of the I_{PL} because the deviation of carrier density is as low as 13.7 % in our prepared samples. It accordingly suggests that the defects centers around near surface responsible for the decrease of electron Hall mobility directly behave as optical non-radiative recombination centers because photogenerated carrier density is same for all samples and the penetration depth of He-Cd laser of 325 nm line is very shallow (~56 nm). The linear line in Fig. 8 represents the least-squares fit of data and the fitted exponent is 1.55.

IV. SUMMARY

The electrical, structural, and optical properties of GaN epitaxial layers grown on (0001) sapphire strongly depend on the growth rate during the growth of the GaN buffer layer. The results show an optimum growth rate of the GaN buffer layer exists in order to obtain high quality GaN epitaxial layers with high electron Hall mobility and low threading dislocation density. Besides, electron Hall mobility is in inverse proportion to the FWHM of (102) HRXRD rocking curve and PL intensity has the dependence with superlinear exponent of 1.55 on the mobility.

ACKNOWLEDGMENTS

This work has been supported by MSTK and by KOSEF through the Semiconductor Physics Research Center at Chonbuk National University.

REFERENCES

[1] S. Strite and H. Morkoc, J. Vac. Sci. Technol. **B10**, 1237 (1992).
[2] A. E. Wickenden, D. K. Wickenden and T. J. Kistenmacher, J. Appl. Phys. **75**, 5367 (1994).
[3] S. Nakamura, Jpn. J. Appl. Phys. **30**, L1705 (1991).
[4] F. A. Ponce, D. Cherns, W. T. Young and J. W. Steeds, Appl. Phys. Lett. **69**, 770 (1996).
[5] J. C. Ramer, K. Zheng, C. F. Kranenberg, M. Banas and S. D. Hersee, Mat. Res. Soc. Symp. Proc. **395**, 225 (1996).
[6] Y.-X. Li, L. S. Riba, K. Wongchotigul, P. Zhou, M. G.

Spencer and V. K. Jones, Mat. Res. Soc. Symp. Proc. **482**, 137 (1998).

[7] A. Saxler, M. A. Capano, W. C. Mitchel, P. Kung, X. Zhang, D. Walker and M. Razeghi, Mat. Res. Soc. Symp. Proc. **449**, 477 (1997).

[8] A. Pelzmann, M. Mayer, C. Kirchner, D. Sowada, T. Rotter, M. Kamp, K. J. Ebeling, S. Christiansen, M. Albrecht, H. P. Strunk, B. Hollder, S. Mantl, MRS Internet J. Nitride Semicon. Res. **1**, 40 (1996).

[9] B. Heying, X. H. Wu, S. Keller, Y. Li, D. Kapolnek, B. P. Keller, S. P. DenBaars and J. S. Speck, Appl. Phys. Lett. **68**, 643 (1996).

Journal of the Korean Physical Society, Vol. 34, June 1999, pp. S415~S419

Influence of Epilayer Thickness on Optical Properties in GaN Films Grown by MOCVD

M. S. JEONG, W. H. LEE, K. Y. LIM, E.-K. SUH* and H. J. LEE

Semiconductor Physics Research Center and Department of Semicoductor Science and Technology, Chonbuk National University, Chonju 561-756

H. Y. AN

State Key Laboratory On Integrated Optoelectronics, Jilin University, Changchun, 130023, P. R. China.

We studied the thickness dependence of optical properties of 2~8 μm thick GaN epilayers grown on sapphire by MOCVD, by using PL, Raman scattering, and X-ray diffraction (XRD) measurements. The PL data show that the peak intensity of yellow band (YB) luminescence normalized to that of exciton band (EB) recombination is weaker than that of donor-acceptor pair (DAP) line for the thin GaN epilayers, but becomes stronger in the case of thick layers. However, the integrated intensity of YB luminescence is stronger than that of DAP line for all the samples. The intensity YB line normalized to that of EB line competes with the normalized intensity of DAP line suggesting that defects involved in those recombination is common. The intensity ratio of acceptor bound exciton to donor bound exciton transition in EB decreases with the epilayer thickness indicating the acceptor density decreases with the growth direction. From the Raman scattering data, the relaxation of the compressive strain and the microstructural reorientation for samples with the increasing thickness have been shown. The XRD measurement results exhibit that the intensity ratio of YB luminescence to EB line has a close relationship with the XRD $(10\bar{1}0)$ peak intensity. Based on these results, the origins of the YB luminescence have been discussed.

I. INTRODUCTION

Besides the near band edge emission due to free and bound excitons and donor-acceptor pair (DAP) recombination, a broad yellow band (YB) luminescence is usually present in the photoluminescence (PL) spectra of nominally undoped and intentionally doped n-type GaN epilayers. Since this broad YB luminescence will seriously influence the efficiencies of GaN optoelectronic devices, there are many experimental and theoretical researches on the origin of the deep level states related with the YB luminescence. The candidates can be summarized as residual impurities [1–6], native defects such as vacancies, anti-sites, or interstitials, native defect-impurity complex [7–13], and extended defects such as dislocation or grain boundaries [14,15]. This is a subject of much discussion, and there are still some contradictory results reported in the literature. It has been known that the crystal quality of GaN epilayer was improved with increasing thickness [16]. E. R. Glaser *et al.* [17] have observed intensities of donor-acceptor pair (DAP) recombination and yellow band (YB) luminescence in photoluminescence (PL) spectra changed with the epilayer thickness. For the electrical properties, Gotz *et al.* [18] have performed Hall effect measurements with various epilayer thickness. Their experimental results demonstrate that the dependence of electron concentration and Hall mobility on film thickness is indicative of a nonuniform distribution of electrically active defects. The studies of dependence of optical and electrical properties on the thickness of GaN epilayers grown up to 10 μm by MOCVD have some practical use, because most of the GaN LED and LD structures possess GaN epilayer thickness less than a few μm.

In this investigation, the thickness dependence of optical and electrical properties of 2~8 μm thick GaN epilayers grown on sapphire by MOCVD is studied with PL, Raman scattering, Hall measurements and X-ray diffraction (XRD). The origins of the YB luminescence are discussed.

II. EXPERIMENTS

PL experiments were performed on a set of GaN epilayers with different thickness grown on (0001) oriented sapphire substrates by MOCVD. A 20 nm GaN buffer layer was grown at 550 °C on the substrates prior to the

*E-mail: eksuh@phy0.chonbuk.ac.kr

Table 1. Parameters of GaN epilayers investigated in this work.

Sample No.	Thicknesses	Carrier concentration (RT)	Mobility (RT)
No. 1	8 μm	6.7×10^{17} cm^{-3}	406 cm^{2}V^{-1}s^{-1}
No. 2	6 μm	6.4×10^{17} cm^{-3}	337 cm^{2}V^{-1}s^{-1}
No. 3	4 μm	3.1×10^{17} cm^{-3}	352 cm^{2}V^{-1}s^{-1}
No. 4	2 μm	5.8×10^{17} cm^{-3}	374 cm^{2}V^{-1}s^{-1}
No. 5	2 μm	1.5×10^{16} cm^{-3}	10 cm^{2}V^{-1}s^{-1}
No. 6	2 μm	6.0×10^{16} cm^{-3}	97 cm^{2}V^{-1}s^{-1}
No. 7	2 μm	7.0×10^{16} cm^{-3}	505 cm^{2}V^{-1}s^{-1}
No. 8	2 μm	8.0×10^{16} cm^{-3}	539 cm^{2}V^{-1}s^{-1}
No. 9	2 μm	8.8×10^{16} cm^{-3}	406 cm^{2}V^{-1}s^{-1}
No. 10	2 μm	5.8×10^{17} cm^{-3}	374 cm^{2}V^{-1}s^{-1}
No. 11	2 μm	1.3×10^{18} cm^{-3}	267.5 cm^{2}V^{-1}s^{-1}

growth of GaN layers at 1125 °C. The carrier concentrations and mobilities determined from the room temperature (RT) Hall effect measurements for various samples are summarized in Table 1. The PL from GaN layers excited by 325 nm line of a He-Cd laser is detected and analyzed by a photomultiplier tube, 1 m double-grating monochromator and photon counting system. The sample temperature was controlled from 4.2 K to RT by using optical cryostat. The RT Raman spectra were taken in the near backscattering $x(yu)\bar{x}$ and $z(yu)\bar{z}$ geometry in which the wavevectors of incident and scattered photons almost lie in the planes of the layers perpendicular and parallel to the c-axis, respectively, by using 514.5 nm line of an argon-ion (Ar^+) laser. The polarization of the scattered light was not analyzed.

III. RESULTS AND DISCUSSION

A typical PL spectrum at 5 K is shown in Fig. 1. Near the band gap the strong excitonic recombinations of free, donor bound exciton (D^0X) and acceptor bound exciton (A^0X) with their phonon replicas are detected. These bands are called exciton band (EB). The next PL emissions observed in Fig. 1 are characterized by a DAP line and a series of well resolved LO phonon replicas at lower energies. The lowest energy band observed in Fig. 1 is a broad emission of YB luminescence. Fig. 2 shows the peak intensity and integrated intensity of DAP and YB luminescence normalized to that of EB line as functions of epilayer thickness, respectively. From Fig. 2, we

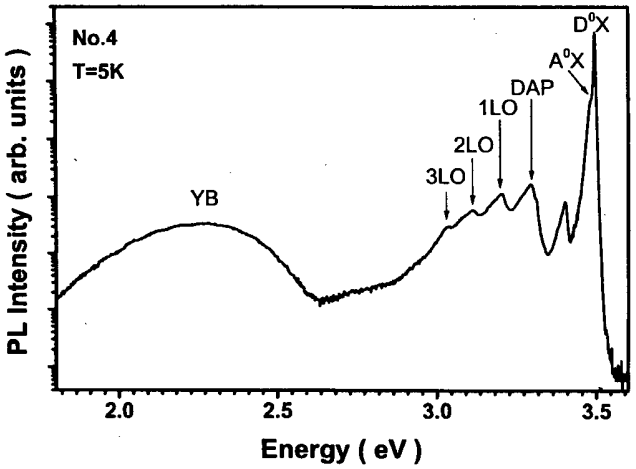

Fig. 1. Fig. 1. PL spectrum at 5 K for sample No. 4.

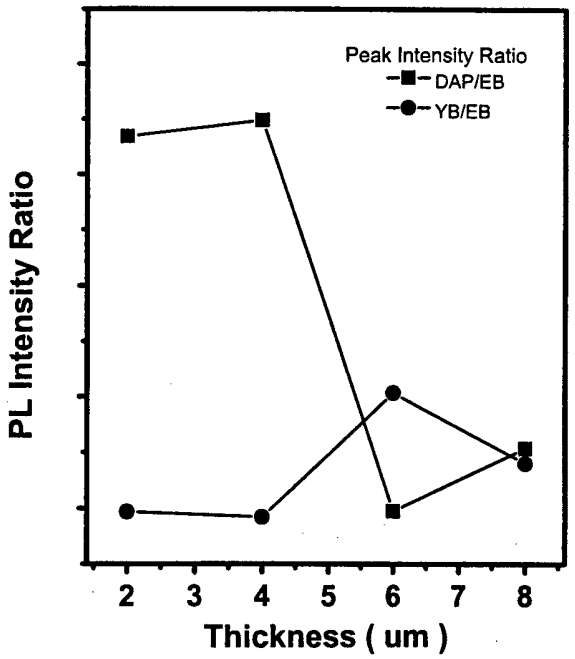

Fig. 2. The peak intensity of YB luminescence normalized to that of EB line as a function of epilayer thickness.

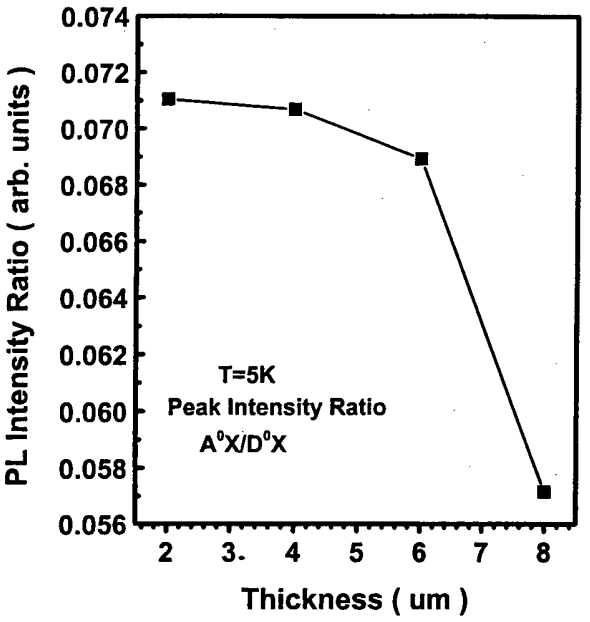

Fig. 3. The intensity ratio of acceptor bound exciton peak to that of donor bound exciton peak as a function of epilayer thickness.

can see that the peak intensity of YB luminescence normalized to that of EB line is weaker than that of DAP recombination for thin GaN epilayers, but, it becomes stronger in the case of thick layers. The ratio of the intensity of YB line to that of EB line increases, whereas that of DAP line decreases with increasing epilayer thickness it indicates that the DAP recombination competes with the YB recombination suggesting the defect or impurity center are commonly involved in those recombination.

Fig. 3 shows the intensity ratio of acceptor bound exciton line to donor bound exciton line as a function of epilayer thickness. It shows that the ratio decrease with increasing epilayer thickness. It has been reported that the dislocation density within the first 0.5 μm of the GaN films grown on 100 nm AlN buffer layer was found to be about 1×10^9 cm^{-2} from plan-view transmission electron microscopy [19] and to decrease rapidly by two orders of magnitude with increasing film thickness. Thus, the decrease of the acceptor density with the dislocation is very film thickness suggests that the residual acceptors might be related with the dislocation.

Fig. 4(a) shows Raman spectrum for sample No. 3 measured at room temperature (RT) in the near back scattering, $x(yu)\bar{x}$ geometry; in this geometry, A_1(TO), E_1(TO), and E_2 modes can be observed. In addition to peaks located at 419 cm^{-1} and 753 cm^{-1} originated from sapphire substrate, A_1(TO), E_1(TO) and high-frequency E_2 modes are observed at 534 cm^{-1}, 562 cm^{-1} and 571 cm^{-1}, respectively. Fig. 4(b) shows the comparison of Raman spectra for sample Nos. 1, 2, 3 and 4 measured at RT in near $x(yu)\bar{x}$ geometry. In addition to small frequency shift due to the strain change, it is interesting to note the change in scattering intensity of the different phonon modes. As Fig. 4(c) illustrates, the intensity ratio of A_1(TO) mode to that of E_2 mode decreases with increasing the epilayer thickness from 4 to 8 μm. The scattering intensity ratio of E_1(TO) mode to that of E_2 mode show similar trend with the epilayer thickness. Since the incident polarization of the exciting laser remained constant throughout the experiment, these results indicate the microstructural orientation of GaN epilayer changes slightly with its thickness. Figure 5 shows the RT Raman spectra taken in $z(yu)\bar{z}$ configuration with the z-direction along the c-axis of GaN, for sample Nos. 1, 2, 3 and 4, respectively. All spectra are dominated by E_2 mode as we expected from the selection rule for the scattering configuration employed. It has been reported that the wurtzite GaN E_2 mode is caused by the deformation potential scattering [20]. The non-polar E_2 mode with lattice displacements perpendicular to the GaN [0001] growth direction is very sensitive to the change of the elastic constants with strain [21]. The Raman peak will shift toward higher energies and be broaded with increasing the biaxial compressive strain as a consequence of the change in elastic constant with strain. As Fig. 5 shows, the peak of the high frequency E_2 mode is strongly enhanced and narrowed with

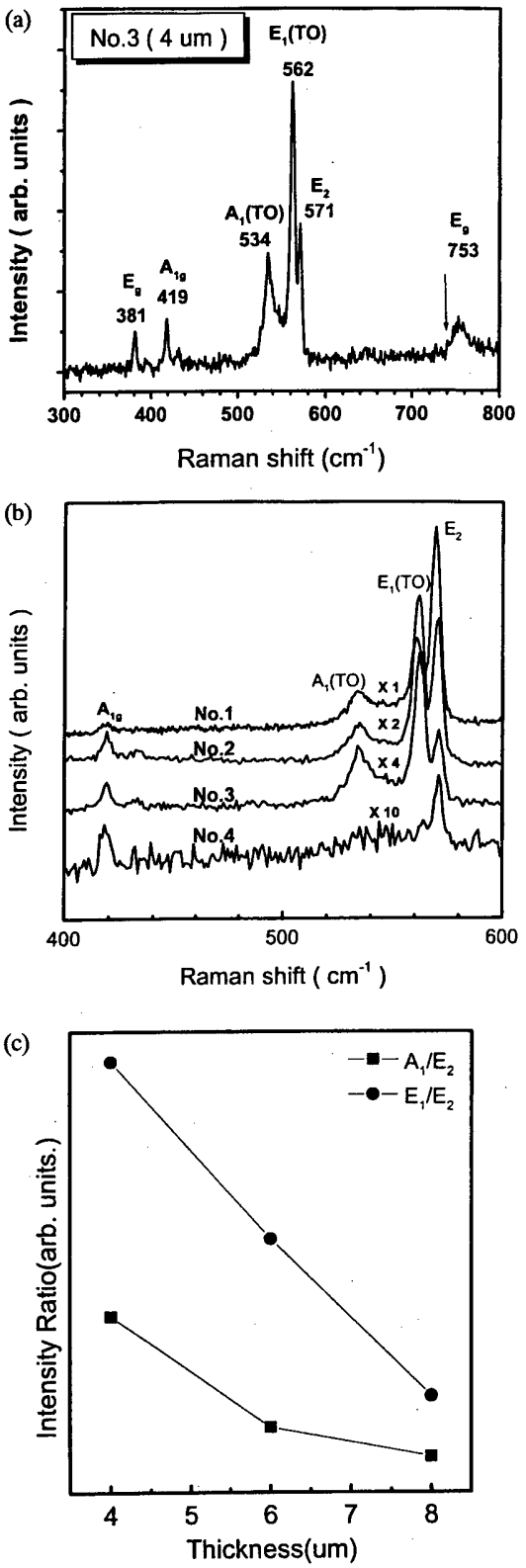

Fig. 4. (a). Raman spectrum for sample No. 3 recorded at room temperature (RT) in the near back scattering $x(yu)\bar{x}$ geometry. (b). The Raman spectra for samples No. 1, No. 2, No. 3 and No. 4 recorded at RT in the near back scattering $x(yu)\bar{x}$ geometry. (c). The intensity ratio of mode to the E_2 (high) mode and E_1(TO) mode to the E_2 (high) mode of samples No. 2, No. 3 and No. 4, respectively.

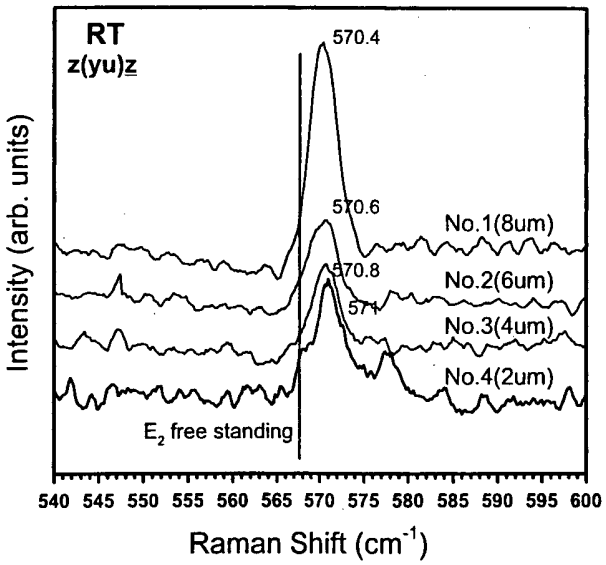

Fig. 5. The Raman spectra for samples No. 1, No. 2, No. 3 and No. 4 taken at RT in the near back scattering $z(yu)\bar{z}$ geometry.

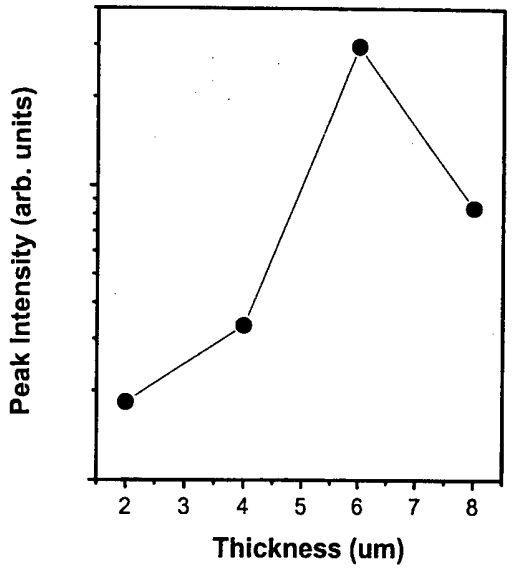

Fig. 6. The intensity variation of $(10\bar{1}0)$ peak in the X-ray diffraction variation as a function of the epilayer thickness.

increasing epilayer thickness. The E_2 (high) mode peaks is observed at 570.4 cm^{-1} for sample No. 1, shifts toward higher energies of 570.6 cm^{-1}, 570.8 cm^{-1} and 571 cm^{-1} for the amples No. 2, No. 3 and No. 4, respectively. T. Kozawa *et al.* [21] have reported that the relation between the compressive strained GaN and the frequency shift $\Delta\omega$ (in cm^{-1}) of E_2 mode is $\Delta\omega$=6.2σ, where σ denotes the stress in GPa. With Hooke's law, $\sigma = \varepsilon_c E/\nu$, where ε_c is the strain; E and ν is the bulk modulus and Poisson ratio, respectively, the relation between $\Delta\omega$ and ε_c can be written as $\Delta\omega$=(6.2 E/ν)ε_c. We took the value of E_2 mode for free-standing GaN as 568 cm^{-1} [22], and estimated the residual compressive stress for sample Nos. 1, 2, 3 and 4 to be 0.39, 0.42, 0.45 and 0.48 GPa, respectively; it shows a linear dependence with the layer thickness.

Finally, the XRD spectra of these four samples show $(10\bar{1}0)$ peak whose intensity changes with the epilayer thickness. Figure 6 shows the $(10\bar{1}0)$ peak intensity variation as a function of the epilayer thickness. It is very interesting to note that the variation of $(10\bar{1}0)$ peak intensity show almost similar trends with the intensity change of YB luminescence shown in Fig. 2. Mo *et al.* [23] also observed the same phenomena. This suggests that the relative intensity of YB luminescence has direct relation with the defects associated with the microstructural orientation. S. Christiansen *et al.* [14] proposed that YB luminescence is related to the screw dislocations with b=[0001]. On the other hand, F. A. Ponce *et al.* [15] suggested that the dislocations necessary to maintain crystalline coherence at low angle boundaries are the source of the YB luminescence. However, Neugebauer *et al.* [13] carried out first-principle calculation and showed that deep levels related to the origin of YB luminescence are due to native defects, such as Ga vacancy, and native defect-impurity complex, while extended defects may just act as traps of native defects and impurities. The relation of the YB luminescence with the microstructural orientation and defects associated with the grain boundary should be studied further in detail.

IV. CONCLUSIONS

We have studied the thickness dependence of optical properties in 2~8 μm thick GaN epilayers grown on sapphire by MOCVD using PL, Raman scattering, and XRD measurements. The PL experimental results show that the intensity of YB luminescence and the intensity of DAP emission normalized to that of band edge recombination varied with the epilayer thickness. The relative intensity of YB line increases, whereas that of DAP line decreases with increasing epilayer thickness. The intensity ratio of acceptor bound exciton to donor bound exciton transition decreases with the thickness suggesting that the dislocations may be very efficient at trapping residual shallow acceptors near the epilayer/buffer layer interface. From the Raman scattering data, the relaxation of the compressive strain and the microstructural reorientation for samples with increasing thickness have been observed. The XRD measurement show that the intensity ratio of YB luminescence to EB line has a close relation with the $(10\bar{1}0)$ peak intensity in the XRD sprecra. Based on these results, the origins of the YB luminescence can be attributed to the defects associated with the microstructural orientation and grain boundary, which should be studied further in detail.

ACKNOWLEDGMENTS

This work was supported in part by the Korea Science and Engineering Foundation through the Semiconductor Physics Research Center at Chonbuk National University and by the academic research fund of the Ministry of Education, Republic of Korea, through the Inter-University Semiconductor Research Center (ISRC 97-E-3036) in Seoul National University.

REFERENCES

[1] T. Ogino and M. Aoki, Jpn. J. Appl. Phys. **19**, 2395 (1980).

[2] E. R. Glaser, T. A. Kennedy, K. Doverspike, L. B. Rowland, D. K. Gaskill, J. A. Freitas, Jr., M. Asif Khan, D. T. Olson, J. N. Kuznia and D. K. Wickenden, Phys. Rev. **B51**, 13326 (1995).

[3] A. Y. Polyakov, M. Shin, J. A. Freitas, M. Skowronski, D. W. Greve and R. G. Wilson, J. Appl. Phys. **80**, 6349 (1996).

[4] R. Niebuhr, K. Bachem, K. Bombrowski, M. Maier, W. Pletschen and U. Kaufmann, J. Electron. Mater. **24**, 1531 (1995).

[5] R. Zhang and T. F. Kuech, Appl. Phys. Lett. **72**, 1611 (1998).

[6] R. J. Molnar and T. D. Moustakas, J. Appl. Phys. **76**, 4587 (1994).

[7] T. Suski, P. Perlin, H. Teisseyre, M. Leszczynski, I. Grzegory, J. Jun, M. Bockowski, S. Porowski and T. D. Moustakas, Appl. Phys. Lett. **67**, 2188 (1995).

[8] M. Ramsteiner, J. Menniger, O. Brandt, H. Yang and K. H. Ploog, Appl. Phys. Lett. **69**, 1276 (1996).

[9] E. Calleja, F. J. Sanchez, D. Basak, M. A. Sanchez-Garcia, E. Munoz, I. Izpura, F. Calle, J. M. G. Tijero, J. L. Sanchez-Rojas, B. Beaumont, P. Lorenzini and P. Gibart, Phys. Rev. **B55**, 4689 (1997).

[10] D. M. Hofmann, D. Kovalev, G. Stevde, B. K. Meyer, A. Hoffmann, L. Eckey, R. Heitz, T. Detchprom, H. Amano and I. Akasaki, Phys. Rev. **B52**, 16702 (1995).

[11] E. R. Glaser, T. A. Kennedy, H. C. Crookham, J. A. Freitas, Jr., M. Asif Khan, D. T. Olson and J. N. Kuznia, Appl. Phys. Lett. **63**, 2673 (1993).

[12] P. Boguslawski, E. L. Briggs and J. Bernholc, Phys. Rev. **B51**, 17225 (1995).

[13] Jorg Neugebauer and Chris G. Vande Walle, Appl. Phys. Lett. **69**, 503 (1996).

[14] S. Christiansen, M. Albrecht, W. Dorsch, H. P. Strunk, C. Zanotti-Fregonara, G. Salviati, A. Pelzmann, M. Mayer, P. Kamp and K. J. Ebeling, in MRS Internet Journal, Nitride Semiconductor Research **1**, 19 (1996).

[15] F. A. Ponce, D. P. Bour, W. Gotz and P. J. Wright, Appl. Phys. Lett. **68**, 57 (1996).

[16] S. D. Hersee, J. C. Ramer and K. J. Malloy, MRS Bulletin, July 1997, p. 45.

[17] E. R. Glaser, T. A. Kennedy, S. W. Brown, J. A. Freitas Jr., W. G. Perry, M. D. Bremser, T. W. Weeks and R. F. Davis, Mat. Res. Soc. Symp. Proc. **395**, 667 (1996).

[18] W. Götz, L. T. Romano, J. Walker, N. M. Johnson and R. J. Molnar, Appl. Phys. Lett. **72**, 1214 (1998).

[19] T. W. Weeks Jr., M. D. Bremster, K. S. Ailey, E. Carlson, W. G. Perry and R. F. Davis, Appl. Phys. Lett. **67**, 401 (1995).

[20] D. Behr, R. Niebuhr, J. Wagner, K. -H. Bachem and U. Kaufmann, Appl. Phys. Lett. **70**, 363 (1997).

[21] T. Kozawa, T. Kachi, H. Kano, H. Nagase, N. Koide and K. Manabe, J. Appl. Phys. **77**, 4389 (1995).

[22] W. Rieger, T. Metzger, H. Angerer, R. Dimitrov, O. Ambacher and M. Stuzmann, Appl. Phys. Lett. **68**, 970 (1996).

[23] Y. H. Mo, K. C. Kim, W. H. Lee, K. S. Nahm, E.-K. Suh and K. Y. Lim, accepted at. J. Korean Phys. Soc.

Journal of the Korean Physical Society, Vol. 34, June 1999, pp. S420~S421

Degradation Processes Occur on the CdTe Thin Films Solar Elements

S. A. MIRSAGATOV, S. K. SHAMIRZAEV, M. MAKHMUDOV and S. A. MUZAPHAROVA

**Physical-technical Institute of Uzbekistan Academy of Sciences, G. Mavlyanova 2-b, 700084, Tashkent*

It is shown the Cu in CdTe polycristalline films is diffusing on the complex mechanism. By bringing of W atoms in thin CdTe layers it is possible to operate diffusion's speed of Cu atoms. Initiation of the $(Cu^{+}W^{-}_{Cd})$ complexes under the conditions $N(W^{-}_{Cd}) \geq N(Cu^{+}_{i})$ hardly reduce the diffusion velocity of Cu atoms.

Occur on both Cu_2Te-CdTe and Cu_2S-CdS (Zn CdS) thin films Solar Elements degradation processes are dictated by Cu atoms' diffusion in thin layers of CdTe. Initiation of the complexes hardly reduce the diffusion velocity of Cu atoms [1]. Within CdTe crystals W atoms localized at the bands of Cd sublattice. As a result they become ionized acceptor centers and form the stable complexes. W atoms belong the Mo support were bringing in the act of growing CdTe film [2]. Concentration (N_W) of W atoms depends of the support's temperature (T_{sup}). We find out-for T_{sup}=550 °C; $N_W \leq 10^{18}$ cm^{-3} and for T_{sup}=680 °C; N_W=10^{20} cm^{-3}. So we get the way to change the N_W. The solubility of W atoms in CdTe sized up by neutron-activation analysis are 10^{-1}~10^{-3} % by weight.

Using the label atoms method we find out the effective diffusion coefficients of Cu^{64} atom equal $D_{Cu}(T)$=2.7×10^{-13}-1.8×10^{-12} cm^2/s in the temperature range of T=573~723 K. Figure shows the concentration (N_{Cu}) distribution of Cu atom's inside of CdTe layers for various temperature (T):

$$N_{Cu}(T) = 7.2 \times 10^{-20} \times \exp(-0.32/kT) \quad \text{cm}^{-3} \quad (1)$$

$$D_{Cu}(T) = 6.7 \times 10^{-9} \times \exp(-0.49/kT) \quad \text{cm}^2/\text{s} \quad (2)$$

It is shown also, that Cu in CdTe polycristalline films is diffusing on the complex mechanism. Most probable is diffusion with association [1]. The calculated value of association's entalpy $(Cu^{+}W^{-}_{Cd})\times H$=0.50 eV well coincides with found from diffusion curves by value of Cu atoms' energy of activation Q=0.49 eV in CdTe layers. For the formula

$$D(T) = D_0 \times \exp(-Q/kT) \quad (3)$$

as follow from [3], there is the next relation between D_0 and Q:

$$Q = 2.1 \times 10^{-4} \times [10 + lg(D_0, \text{cm}^2/\text{s})] \times T_{ml} \quad (4)$$

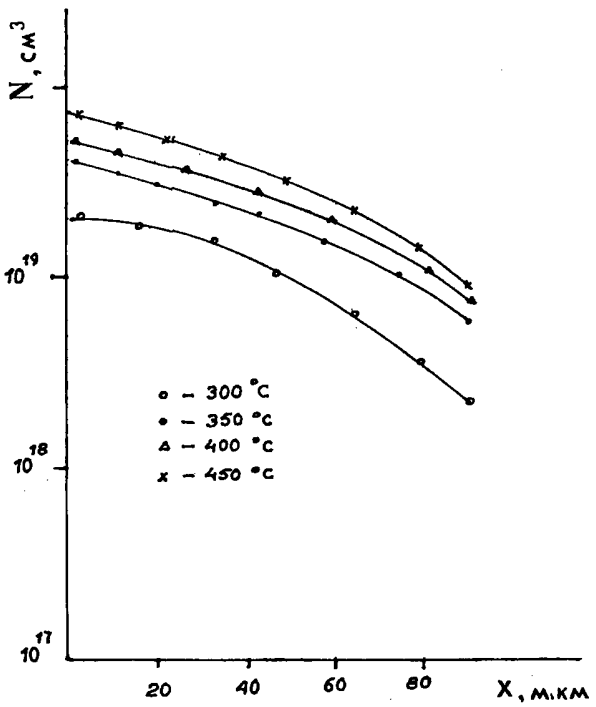

Fig. 1. Conentration (N cm^{-3}) of label Cu^{64} atoms inside of CdTe layers for various temperature (T) of diffusion processes took 4 hours.

There T_{ml} is the melting point.

For CdTe T_{ml}=1315 K and from (2) one find D_0=6.7×10^{-9} cm^2/s. Using (4) we find once more Q=0.5 eV.

As thus $N(W^{-}_{Cd}) \geq N(Cu^{+}_{i})$ this result is satisfied condition shows, that all diffusing Cu atoms are completely connected in complexes with ionized $(W^{-}_{Cd}\cdot)$ acceptors centre.

Thus is shown, that by bringing of W atoms in thin CdTe layers it is possible to operate diffusion's speed of Cu atoms. It is important for wide use thin film elements with structures Cu_2Te-CdTe and Cu_2S-CdS (Zn CdS).

*E-mail: shamir@physic.uzsci.net

REFERENCES

[1] M. A. Kovalec, E. S. Nikonyuk and V. P. Zayachkivsky, *The Drift and Diffusion of Cu in p-CdTe Crystalline* (Ukraine physical journal, 1986), Vol. 31, No. 7, p. 1088.

[2] Sh Mirsagatov, S. Shamirzaev, M. Makhmudov and S. Muzapharova, *The Possibility to Operate of Degradation and Kinetic Processes in Thin Film Based on p-CdTe Solar Elements* (Geliotechnica, 1998), No. 5

[3] V. A. Kasilishin, *The Correlation Between Diffusion Parameters of Semiconductor Materials* (Izvestiya Academii Nauk SSSR. Nonorganic materials, 1991), Vol. 27, No. 4, p. 680.

Journal of the Korean Physical Society, Vol. 34, June 1999, pp. S422~S426

A New Switching Characteristics of Highly Doped Multi-Quantum Well

Chung-Kun SONG* and Do-Hyun KIM

School of Electrical and Electronics and Computer Engineering, Dong-A University, Pusan 604-714

A new type of hysteretic current-voltage characteristics, which switched from a low conductance off-state into a high conductance on-state at a threshold voltage and the high conductance state was sustained even when the bias voltage reduced below the threshold voltage, was experimentally observed for the highly doped multi-quantum well structure. The characteristics were attributed to confinement of electrons and impact ionization of the confined electrons out of the quantum wells. The test devices employing 10 periods of quantum wells were fabricated by using AlGaAs/GaAs semiconductor heterostructure and I-V characteristics were examined.

I. INTRODUCTION

The quantum well structures have been considerably employed to implement the special functions such as resonant tunneling for RTD (Resonant Tunneling Diode) [1–4] and band-to-band impact ionization for APD (Avalanche Photo Diode) [5]. For the photodetection purpose APD uses multi-quantum well structure to reduce the dark current for the reverse bias and enhance the ratio of electron to hole band-to-band impact ionization rate [6–8].

In this paper the multi-quantum well structure whose quantum wells are highly doped is employed to produce a new type of hysteretic forward current-voltage characteristics. Below the threshold voltage it shows the low conductance off-state and switches to the high conductance on-state above the threshold. Especially it should be noted that the on-state is sustained even when the applied voltage reduces below the threshold once it turns on. The characteristic is identified to be attributed to confinement of the thermally ionized electrons within the quantum wells and ejection of the confined electrons out of the quantum wells through impact ionization.

The similar quantum well structures have been used to detect IR radiation [9]. However it is different from IR detector that the quantum wells in this paper do not have contact for themselves to supply the ejected electrons compensating the ionized donors while for the IR detector the quantum wells have the contacts to keep compensating the ionized donors when IR is detected. The operation of device employing the quantum wells in the paper will be discussed later.

The test devices were fabricated with AlGaAs/GaAs semiconductor and the current-voltage characteristics were examined. And the theoretical model is proposed and verified by the experiment.

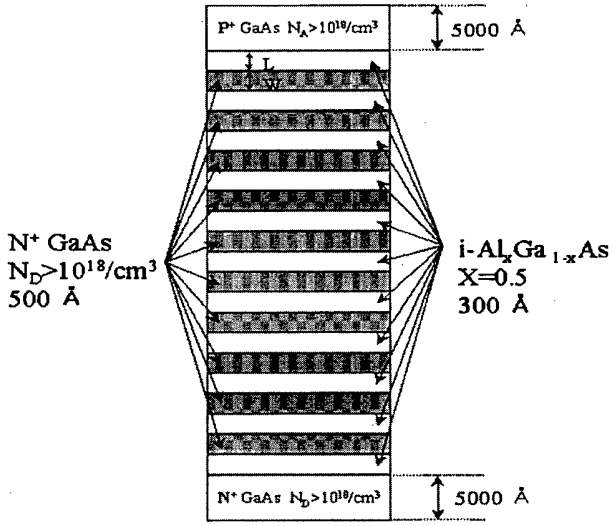

Fig. 1. The structure of device using 10 periods of AlGaAs/GaAs quantum wells.

II. DEVICE STRUCTURE AND FABRICATION

The test devices consist of 10 periods of AlGaAs/GaAs multi-quantum well (MQW) structures inserted between p^+-GaAs anode and n^+-GaAs cathode as shown in Fig. 1. The barriers are made of $Al_xGa_{1-x}As$ with Al mole fraction of $x = 0.5$ which produces the barrier energy of $\Delta E_c = 0.38$ eV to GaAs, and the width of 300 Å. The GaAs quantum wells are highly doped with silicon of 10^{18}

*E-mail: cksong@daunet.donga.ac.kr, Tex: 82-51-200-7711, Fax: 82-51-200-7712

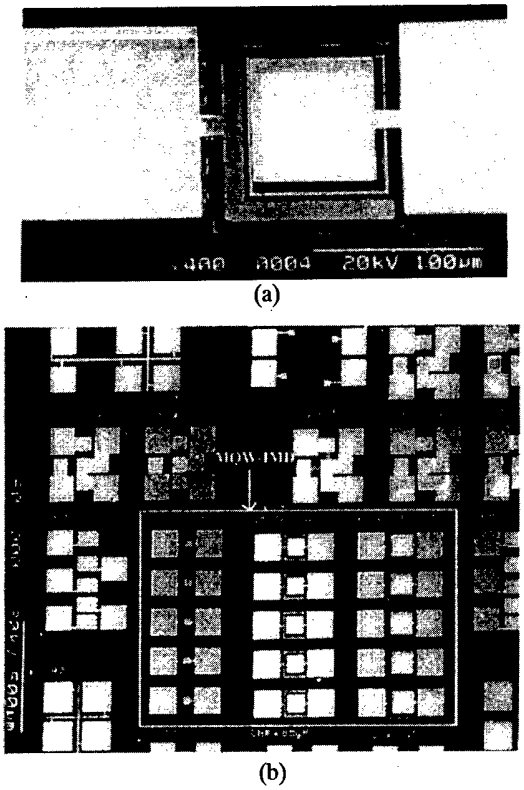

Fig. 2. (a) SEM picture of the fabricated device and (b) the test chip.

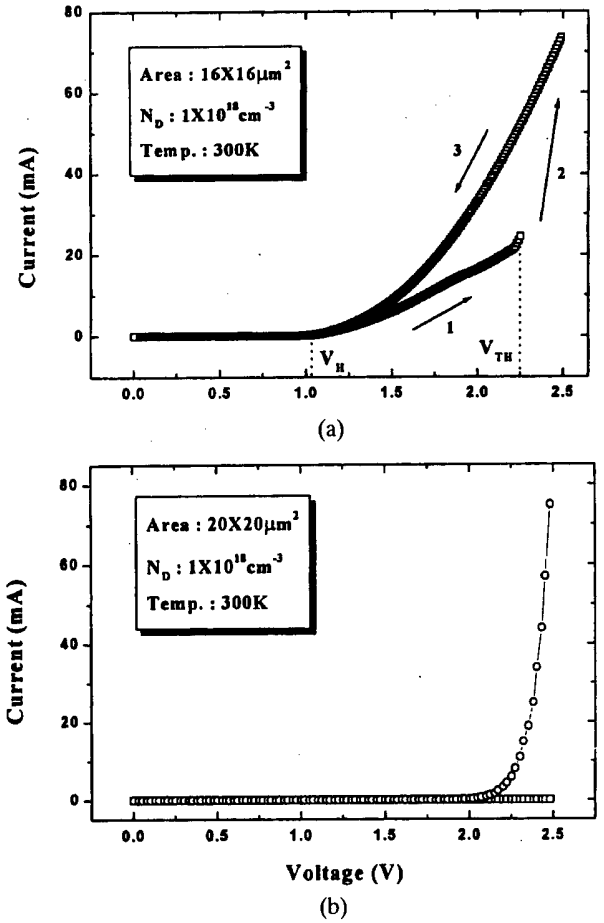

Fig. 3. (a) The measured and (b) The theoretical current-voltage characteristic of device.

cm^{-3} and the width is 500 Å. The epitaxial layers were grown by MBE.

For the fabrication p^+-GaAs anode and MQW layer are first mesa-etched down to n^+-GaAs cathode by RIE. And AuBe/Pt/Au metal is deposited and lifted-off for the ohmic contact to p^+-GaAs anode. Subsequently n^+-GaAs cathode layer is also etched. AuGe/Ni/Au metal is deposited and lifted-off for the ohimic contact to n^+-GaAs cathode. SiN of about 3000 Å is deposited for passivation. Both ohmic contacts are sintered for 30 sec at 500 °C in 4 % forming gas. Finally the contact windows are opened and interconnection Au metal is deposited and lifted-off. The final fabricated device is seen in Fig. 2(a). In addition the various test structures are included such as Kelvin, van der Pauw and TLS as shown in Fig. 2(b).

III. A NEW SWITCHING CHARACTERISTICS

Hysteretic current-voltage characteristics were observed by HP4155A as shown in Fig. 3(a). The I-V characteristics can be divided into two states; a low conductance off-state and a high conductance on-state. The switching from the off-state to on-state occurs at about 2.25 V which is the threshold voltage. For each state of I-V characteristic the energy band diagrams of device are shown in Fig. 4. In the low conductance off-state the device exhibited the small current limited by the barrier at the cathode to electron injection and thermally assisted transport across the barriers as shown in Fig. 4(a). In the quantum wells the thermally ionized electrons from the donor states are confined so that the voltage drop across the well is negligible and the field across the MQW layer is uniform. At about threshold voltage the device was abruptly switched into the high conductance on-state where the injected electrons have enough energy to eject the confined electrons from the quantum wells through the impact ionization process. As the confined electrons escape from the wells, the positively ionized donor impurities are left behind to form the positive space charge region inducing the large field across the barrier at the cathode and then enhancing the electron injection from cathode as shown in Fig. 4(b). Especially, the high conductance on-state remains even when the bias voltage sweeps back to a small holding voltage of about 1 V less than the threshold voltage because the positive space charge region is sustained until the injected electrons are trapped in the quantum wells and neutralize the space charge region. The space charge is not completely neutralized even below the threshold since the induced

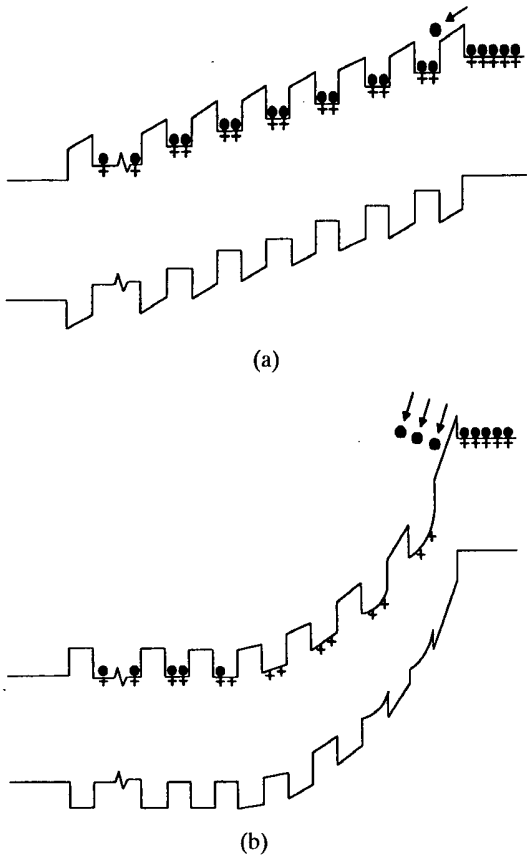

Fig. 4. Energy band diagram of device (a) in low conductance off-state and (b) in high conductance on-state.

electric field below the threshold is still large enough to prevent the injected electrons being trapped in the wells. This behavior gives the hysteretic current-voltage characteristic.

IV. THEORY

The hysteretic I-V characteristics are resulted from the confinement of the thermally ionized electrons within the wells, the escape of the confined electrons from the wells and the incomplete neutralization of the space charge below the threshold. In this section the theoretical model for the confinement and impact ionization as well as I-V characteristics will be described. Since the quantum wells are highly doped by donors, the electrons are thermally ionized from the donor states and confined within the wells. The discrete energy levels in the wells are given by

$$E_{Qn} = \frac{\hbar^2}{2m^*}\left(\frac{n\pi}{L_{wn}}\right)^2 \tag{1}$$

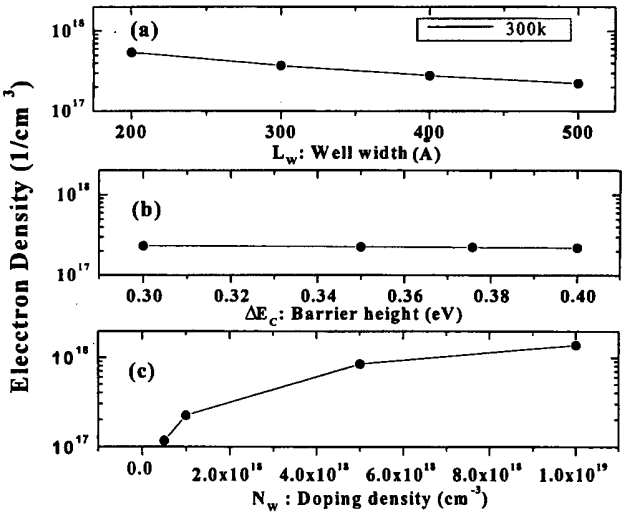

Fig. 5. The confined electron density in the quantum well vs the parameters of quantum wells such as (a) the well width, (b) the barrier height and (c) the doping density.

where L_{wn} is the effective well width of n-th energy level taking account of the penetration of the wave function on n-th energy level into the barrier.

The density of confined electrons in the wells n_s is expressed by [10]

$$n_s = \int_{E_{Q1}}^{\infty} f(E)\cdot g(E)dE$$

$$\sum_n \frac{m^* kT}{\pi\hbar^2 L_{wn}} \cdot \ln(1+e^{(E_F-E_{Qn})/kT}) \tag{2}$$

The density of confined electrons is varied along with the quantum well parameters such as the well width L_W and the doping density of donors N_W as well as the barrier energy height ΔE_C. In Fig. 5 the dependence of the confined electron density on the quantum well parameters is shown. The electron density is found to be a strong function of the donor doping density.

The impact ionization of quantum well is developed based on the model as shown in Fig. 6(a). The particle denoted by 1 is the incident electron from the barrier and the particle 2 is the confined electron. The confined electron 2 collides with the incident electron 1 and when the energy of the incident electron is large, both electrons escape from the quantum well as denoted by 1' and 2' respectively. The impact ionization rate is derived based on Fermi Golden rule and expressed by [11]

$$\frac{1}{\tau(E_0)} = \sum_n \frac{4\pi e^4}{\hbar^2\epsilon^2}\left(\frac{L_{wn}}{L}\right)^2 \frac{k_{2t}^{(n)^2}}{(4\pi)L_{wn}}\left[S\left(z^*k_{1z}, z^*\frac{n\pi}{L_{wn}}\right) + S\left(z^*k_{1z}, -z^*\frac{n\pi}{L_{wn}}\right)\right] \tag{3}$$

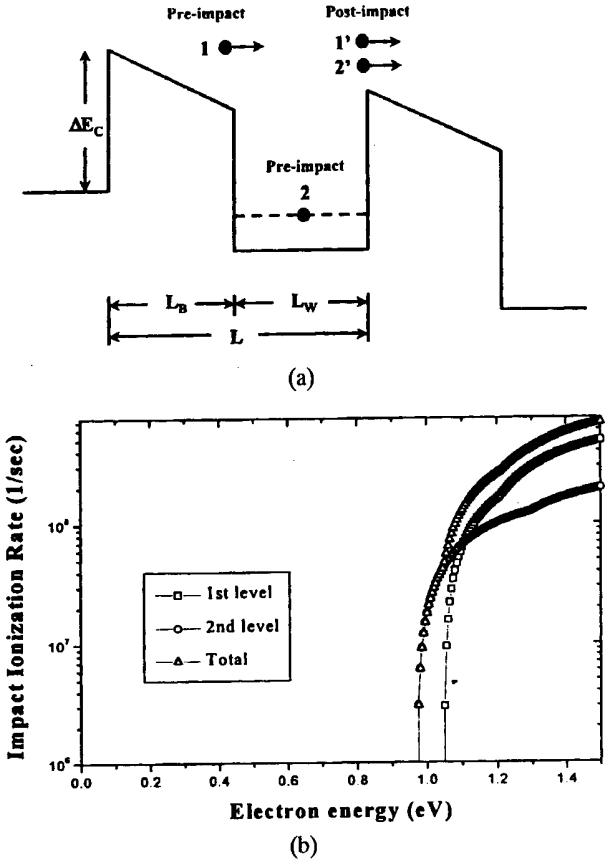

Fig. 6. (a) The model of impact ionization and (b) The typical impact ionization rate vs the energy of incident electron : $\Delta E_C = 0.37$ eV, N_D=1×10^{18} cm^{-3}, T=300 K.

where L is the sum of the well width L_W and the barrier width L_B, and $k_{2t}(n)$ is the transverse wave number of the confined electron in the n-th energy level. $S\left(z^*k_{1z}, z^*\frac{n\pi}{L_{wn}}\right)$ and $S\left(z^*k_{1z}, -z^*\frac{n\pi}{L_{wn}}\right)$ are the interaction integral between the wave function of the injected electron and the wave function travelling $+z$ as well as $-z$ direction of the confined electron respectively.

The typical impact ionization rate along with the energy of incident electron is shown in Fig. 6(b) for $L_W = 500$ Å, $L_B = 300$ Å, $\Delta E_C = 0.38$ eV associated with Al mole fraction of x=0.5, and $N_W = 10^{18}$ cm^{-3}. There is a threshold energy above which the rate abruptly increases and corresponds to about 3 times ΔE_C and this produces the threshold voltage in I-V characteristic. In this case there exist two energy levels under Fermi energy level on which the most of electrons are distributed. The first level ($E_1 = 0.0001$ eV) has the larger impact ionization rate than the second level ($E_2 = 0.0004$ eV) since the concentration of the confined electrons on the first level is larger and also the threshold energy (1.05 eV) for first level is larger than the second (0.96 eV) since the first level is more deeply located than the second.

The average impact ionization rate over the energy of incident electron is given by assuming the Maxwellian

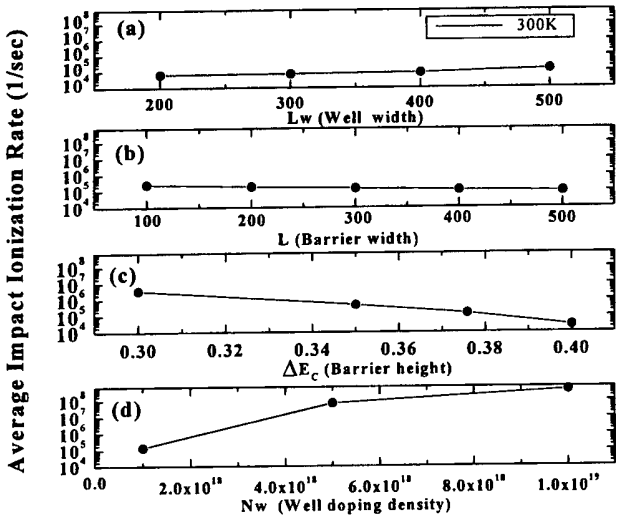

Fig. 7. The average impact ionization rate vs the parameters of quantum well such as (a) the well width, (b) the barrier width, (c) the barrier height and (d) the doping density.

distribution of incident electrons in the energy states and written by

$$\left\langle \frac{1}{\tau} \right\rangle \approx \int \frac{dk_0}{2\pi} 4 \left(\frac{\pi\hbar^2}{2m_a^* kT_e}\right)^{\frac{1}{2}} \exp\left(\frac{-\hbar^2 k_{0z}^2}{2m_a^* kT_e}\right) \frac{1}{\tau(E_{0z})} \quad (4)$$

where T_e is electron temperature and m_a^* is the electron effective mass in the barrier. According to the variation of parameters such as the well width L_W, the barrier width L_B, the doping density N_W and the barrier height ΔE_C the variation of the average ionization rate is depicted in Fig. 7. As shown in the figure the average impact ionization rate is strongly dependent on the doping density.

The equation for I-V characteristic can be derived based on the model. At the low voltage the current is limited by the thermionic emission of carriers (electrons at cathode and holes at anode) so that the current level is small and given by

$$J = A^*T^2 \exp[-(\Delta E_C - qdF_C/kT)] \quad (5)$$

where F_C is the cathode field given by $(V - V_{bi})/L_T$, V_{bi} is the built-in voltage of the pn junction associated with the anode and cathode and L_T is the total width of MQW, and d is the cathode interface parameter. At the high voltage above threshold the induced space charge due to the impact ionization enlarges the cathode field given by

$$F_C = \frac{(V - V_{bi})}{L_T} + \frac{1}{L_T \epsilon} \int_{L_T - W}^{L_T} x\rho(x)dx \quad (6)$$

where $\rho(x)$ is the induced space charge density and W is the width of space charge region. The enlarged cath-

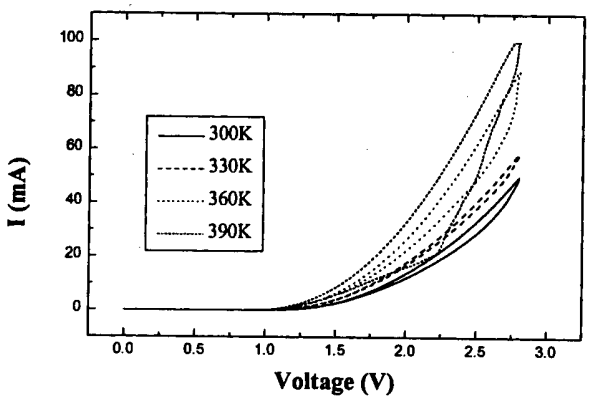

Fig. 8. I-V Characteristics at the various temperatures.

ode field produces the large current resulting in the high conductance on-state. The theoretical I-V curve is calculated and presented in Fig. 3(b), using the effective mass of GaAs 0.067 m_0, which exhibits the similar characteristic to the measured.

In order to confirm validity of the model, which insists that the hysteretic I-V characteristic is due to the electron confinement and the impact ionization of the electrons, the I-V characteristics were measured with the various temperatures as shown in Fig. 8. As the temperature increases, the hysteretic characteristic enhances and the ratio of the current in on-state to off-state becomes large. This characteristic can be explained by the model. Since at low temperature the effective mass of electron is small, the impact ionization rate between the single electron to the single electron is large comparing with at high temperature. However, since the concentration of the confined electrons at high temperature is larger and then the probability of interaction between the incident single electron and the confined electrons becomes large, the number of ionized electrons at high temperature is much larger. The ratio of the number of the ionized electrons per unit volume and unit time at high to at low temperature is given by

$$R_I = \frac{\left\langle \frac{1}{\tau} \right\rangle_{high} \cdot [n_s \cdot \sigma_n \cdot \nu_{th} \cdot t]_{high}}{\left\langle \frac{1}{\tau} \right\rangle_{low} \cdot [n_s \cdot \sigma_n \cdot \nu_{th} \cdot t]_{low}} \cong \frac{\left\langle \frac{1}{\tau} \right\rangle_{high}}{\left\langle \frac{1}{\tau} \right\rangle_{low}} \cdot \frac{n_{S\ high}}{n_{S\ low}} \quad (7)$$

where σ_n is the cross section of impact ionization and [ ] term represents the probability of collision between the incident single electron and the confined electrons in the well. The ratio is approximately proportional to the ratio of the average ionization rate and the ratio of the electron concentration at the temperature. For example the average ionization rate at $T = 77$ K is 1.2 times larger than $T = 300$ K but the concentration of electrons at $T = 300$ K is 5 times larger than $T = 77$ K. Thus the number of the ionized electrons at $T = 300$ K is larger than $T = 77$ K, resulting in the larger current ratio at high than low temperature.

V. CONCLUSIONS

The highly doped multi-quantum well structure inserted between p^+ anode and n^+ cathode produced the hysteretic current-voltage characteristic exhibiting the low conductance off-state and the high conductance on-state which was sustained when the bias voltage swept back below the threshold voltage. It was found that the characteristics were attributed to the confinement of the thermally ionized electrons from donors and the ejection of the confined electrons from the wells through the impact ionization which induced the positive space charge regions and the incomplete neutralization of the induced space charge. The theoretical model was developed and verified by the experiment.

The I-V characteristics can be applied to IR detector and to develop a novel device mimicking the functions of biological neuron which requires the hysteretic I-V characteristics.

ACKNOWLEDGMENTS

This paper is supported by the 1998 grant of IITA in Republic of Korea.

REFERENCES

[1] P. Mounaix, J. M. Libberecht and D. Lippens, Solid-State Electronics **38**, 1899 (1995).
[2] HanYu Sheng, Modern Physics Letters **BP**, 849 (1995).
[3] F. Capasso, *Physics of Quantum Electron Devices*, ed. Springer Series in Electronics and Photonics (Springer-Verlag Berlin Heidelberg, Germany, 1990).
[4] C. Lee, J. Korean Phys. Soc. **31**, 112 (1997).
[5] S. Adachi, *GaAs and Related Materials : Bulk Semiconducting and Superlattice Properties* (World Scientific, 1994).
[6] I. H. Oguzman, J. Kolnik and K. F. Brennan, IEEE Transactions on Electron Devices **44**, 535 (1997).
[7] K. S. Lee, O. K. Kwon, B. S. Jeong, W. S. Han, B. Lee and E. H. Lee, J. Korean Phys. Soc. **31**, 693 (1997).
[8] S.-H. Park, J. Korean Phys. Soc. **32**, 713 (1998).
[9] S. Datta, *Quantum Phenomena in Modern Semiconductor Devices*, Modular Series on Solid State Devices (Addison-Wesley Pub., 1989), Vol. VIII.
[10] F. Capasso, J. Allam, A. Y. Cho, K. Mohammed, R. J. Malik, A. L. Hutchinson and D. Sivco, Appl. Phys. Lett. **48**(19), 1294 (1986).
[11] S. L. Chuang and K. Hess, J. Appl. Phys. **59** (1987).

Journal of the Korean Physical Society, Vol. 34, June 1999, pp. S427~S431

Comparison of the Pd/Ge/Au/Ni/Au and Pd/Ge/Pd/Ti/Au Ohmic Contacts to N-type InGaAs

S. H. PARK, J. M. LEE, T.-W. LEE, M.-P. PARK and C. S. PARK

ETRI-Microelectronics Technology Laboratory, Taejon 305-350

I.-H. KIM

Department of Materials Science and Engineering, Chungju National University, Chungju 380-702

J. Y. KIM

Department of Materials Engineering, Hoseo University, Asan 336-795

The Pd/Ge/Au/Ni/Au and Pd/Ge/Pd/Ti/Au ohmic contact systems on n-InGaAs were investigated and compared. In both contacts, a good ohmic behavior was obtained even without annealing. This is due to their lower barrier height. The contact resistivity was further decreased by rapid thermal annealing. The Pd/Ge/Au/Ni/Au contact was degraded by intermixing of the ohmic metals with InGaAs above 425 °C. This indicates that the Ni layer could not act as a diffusion barrier in this contact system. The out-diffusion of the In and As atoms also deteriorated the ohmic contact due to both an increase in barrier height and charge compensation. The Pd/Ge/Pd/Ti/Au contact showed better ohmic behavior compared with the Pd/Ge/Au/Ni/Au contact, especially at high temperature. The Ti layer acted as the diffusion barrier. Non-spiking and planar interfaces were observed even at 450 °C.

I. INTRODUCTION

The parasitic resistance and capacitance are dominant factors to degrade the intrinsic performance of the semiconductor devices. The higher the device operation frequency, the larger their effects. It is critical that the parasitic components should be reduced for the high-speed device application. One of the substantial parasitic resistances is induced from ohmic contact. Therefore, it is necessary to make reliable, planar and low-resistance ohmic contacts to the active layers for high frequency operation of devices.

The Pd/Ge-based system has been investigated as an ohmic contact on n-GaAs [1–6]. The ohmic contact mechanism of this system is known that Pd decomposes Ga and As oxides, and Ge atoms diffuse into GaAs and act as dopant. Its diffusion length after annealing is as short as several hundreds of Å, and it has a planar interface and a good surface morphology. It is expected that a similar phenomenon occurs on n-InGaAs, which is used as a material for high speed devices such as a heterojunction bipolar transistor (HBT) [7] and a high electron mobility transistor (HEMT) [8] due to its high electron mobility and high electron saturation velocity. Shantharama *et al.* [9] have briefly discussed some non-alloyed ohmic contacts (Ti/Pt/Au, SnAu/Au, Pd/AuGe and AuBe/Pt/Au system) on heavily doped n- and p-InGaAs, and Park *et al.* [10] have reported the work on AuGe/Pd/Au and other refractory metal contacts to n-InGaAs. There is, however, little information on Pd/Ge-based ohmic contacts to n-InGaAs and their alloying temperature effect. In this study, Pd/Ge/Au/Ni/Au and Pd/Ge/Pd/Ti/Au ohmic contacts to n-InGaAs were studied through electrical and microstructural analyses.

II. EXPERIMENTS

N-type $In_{0.5}Ga_{0.5}As$ epitaxial layer doped with 1×10^{-19} Si/cm^3 was grown by metal organic chemical vapor deposition (MOCVD) on 3-inch semi-insulating GaAs (100) wafer. Figure 1 shows the schematic cross-sectional diagram of the ohmic contact layers on n-InGaAs. Ohmic contact materials of Pd(400 Å)/Ge (300 Å)/Au(600 Å)/Ni(500 Å)/Au(900 Å) and Pd(500 Å)/Ge(1200 Å)/Pd(500 Å)/Ti(350 Å)/Au(900 Å) were deposited sequentially on n-InGaAs by the electron beam evaporation, and ohmic contact patterns were made by the conventional lift-off technique.

The ohmic alloying was carried out by the rapid thermal annealing (RTA) process in a forming gas (N_2/H_2) atmosphere at various temperatures up to 450 °C for

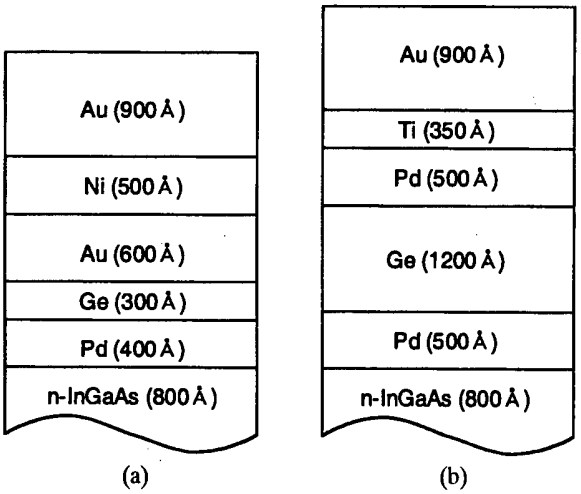

Fig. 1. Schematic cross-sectional diagram of the ohmic contact layers on n-InGaAs. (a) Pd/Ge/Au/Ni/Au contact, (b) Pd/Ge/Pd/Ti/Au contact.

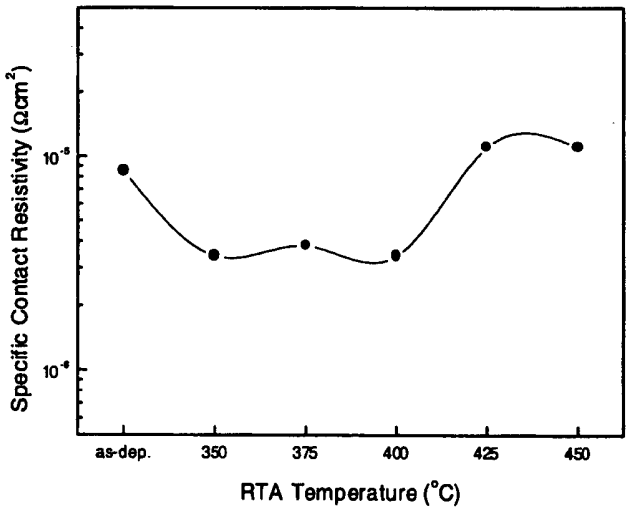

Fig. 2. Variation of the specific contact resistance of the Pd/Ge/Au/Ni/Au contacts to n-InGaAs with RTA temperature.

10 seconds. The standard transmission line method was used to measure the specific contact resistance. Photolithography was employed to make 100×100 μm^2 pads for the measurement of the contact resistivity, which were arranged linearly spacing 5, 10, 15, 20 and 30 μm. Phase transition was analyzed by the X-ray diffraction (XRD). The X-ray source was the Cu K_α target (30 kV, 40 mA) and the scanning speed was 3°/min. Atomic redistribution was examined by the Auger electron spectroscopy (AES) depth profiling. Ohmic contact layers were sputtered by Ar^+ (5 keV, 5 mA) ions at the speed of 60 Å/sec. The kinetic energy levels for element analysis were Pd^{MNN} (317~340 eV), Ti^{LMM} (368~395 eV), In^{MNN} (397~415 eV), Ni^{LMM} (835~860 eV), Ga^{LMM} (1059~1077 eV), Ge^{LMM} (1130~1158 eV), As^{LMM} (1219~1237 eV), and Au^{NVV} (2000~2035 eV). The interface of the ohmic contact materials/n-InGaAs was observed by the cross-sectional transmission electron microscopy (XTEM), and (110) projection centered beam image method was adopted with the accelerating voltage of 200 keV.

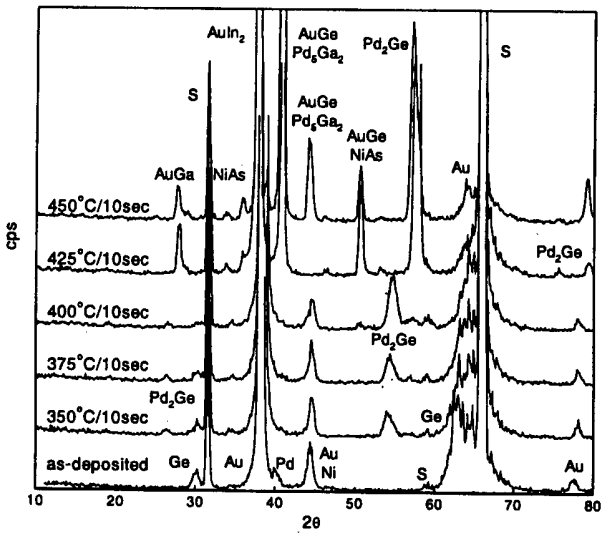

Fig. 3. XRD patterns of the Pd/Ge/Au/Ni/Au contacts to n-InGaAs.

III. RESULTS AND DISCUSSION

1. Pd/Ge/Au/Ni/Au Ohmic Contacts

The specific contact resistance variation with the RTA temperature is shown in Fig. 2. It shows a relatively low value (high-10^{-6} Ωcm^2) even without annealing. This is due to the reduction of Schottky barrier height (~0.2 eV) at the interface of metal/n-InGaAs. As the annealing temperature was increased up to 400 °C, the specific contact resistance was reduced to 3.7×10^{-6} Ωcm^2. However, the ohmic contact characteristics was degraded considerably above 425 °C.

Figure 3 shows the X-ray diffraction pattern with annealing temperature. No remarkable phase change was observed below 350 °C. The phase changes were observed at 375 °C, resulting from the reaction of ohmic metals with InGaAs. At 425 °C, various compounds such as Pd_2Ge, AuGe, Pd_5Ga_2, AuGa, NiAs, and $AuIn_2$ were identified. Comparing the results in Fig. 3 with those, the increase in specific contact resistance above 425 °C is attributed to the considerable reaction between ohmic metals and InGaAs, especially the formation of $AuIn_2$ and Pd_5Ga_2 compounds. This suggests that the composition of InGaAs becomes nonstoichiometric, resulting in both the corresponding increase in barrier height of the metal/n-InGaAs contact, and the deterioration of ohmic behavior.

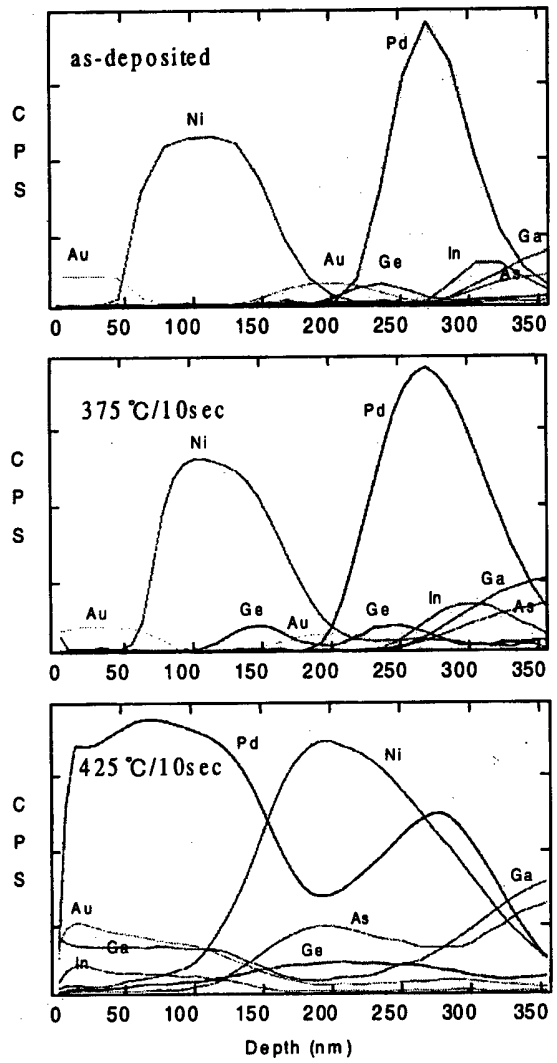

Fig. 4. AES depth profiles of the Pd/Ge/Au/Ni/Au contacts to n-InGaAs.

Figure 4 indicates the AES depth profiles of the Pd/Ge/Au/Ni/Au contacts on n-InGaAs. A slight in-diffusion of Ge was observed at 375 °C. This suggests that the doping concentration below the contact increases. No other significant diffusion was detected except a little interdiffusion of Au and Ge. However, considerable intermixing was found at 425 °C. The out-diffusion of In deteriorates the ohmic contact due to an increase in barrier height, as shown in Fig. 4. The out-diffusion of As is also responsible for the degraded ohmic contact at 425 °C because it encourages the Ge atoms to occupy the As sites where they behave as acceptors. The results show that the reaction of the ohmic metals with InGaAs causes the reduction of electron concentration, resulting in the formation of a highly resistive interface.

The ohmic materials/n-InGaAs interface observed by XTEM was illustrated in Fig. 5. Non-spiking and planar interface was found even for the contact annealed at 425 °C for 10 sec. After RTA, the ohmic contact layers appeared to be composed of two different layers, but further microscopic analysis was required.

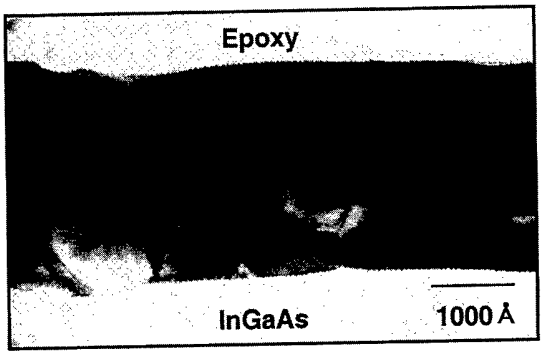

Fig. 5. Cross-sectional diagram of the Pd/Ge/Au/Ni/Au contacts to n-InGaAs annealed at 425 °C for 10 sec.

2. Pd/Ge/Pd/Ti/Au Ohmic Contacts

Figure 6 shows the RTA temperature effect on the specific contact resistance of the Pd/Ge/Pd/Ti/Au contact. It shows a low resistance before RTA like the Pd/Ge/Au/Ni/Au contact as seen in Fig. 2, and also indicates much better ohmic characteristics compared with the Pd/Ge/Au/Ni/Au contact, especially at high temperature. As the annealing temperature was increased up to 400 °C, the specific contact resistance was reduced to 1.1×10^{-6} Ωcm^2, and good ohmic behavior was maintained. However, the ohmic contact characteristics was degraded above 450 °C.

Phase transformations due to RTA were investigated by XRD and the results are shown in Fig. 7. The Pd and Ge layers reacted so that PdGe phase was formed when annealed at 300 °C for 10 sec. This PdGe phase

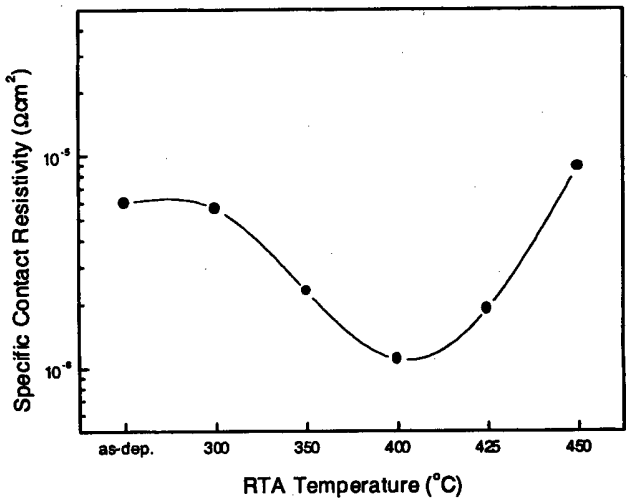

Fig. 6. Variation of the specific contact resistance of the Pd/Ge/Pd/Ti/Au contacts to n-InGaAs with RTA temperature.

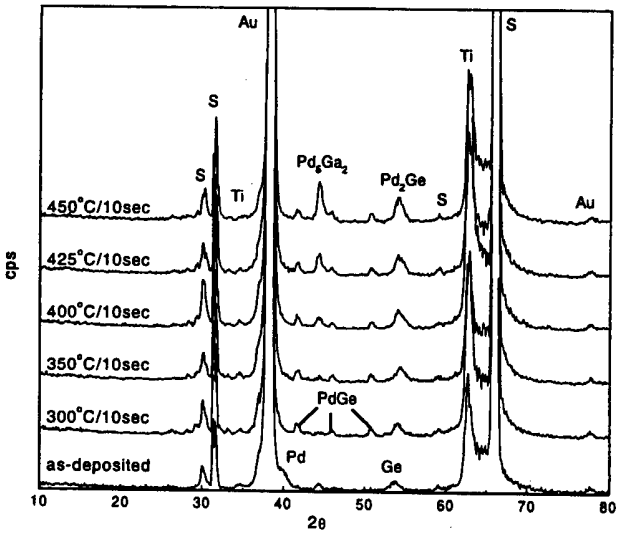

Fig. 7. XRD patterns of the Pd/Ge/Pd/Ti/Au contacts to n-InGaAs.

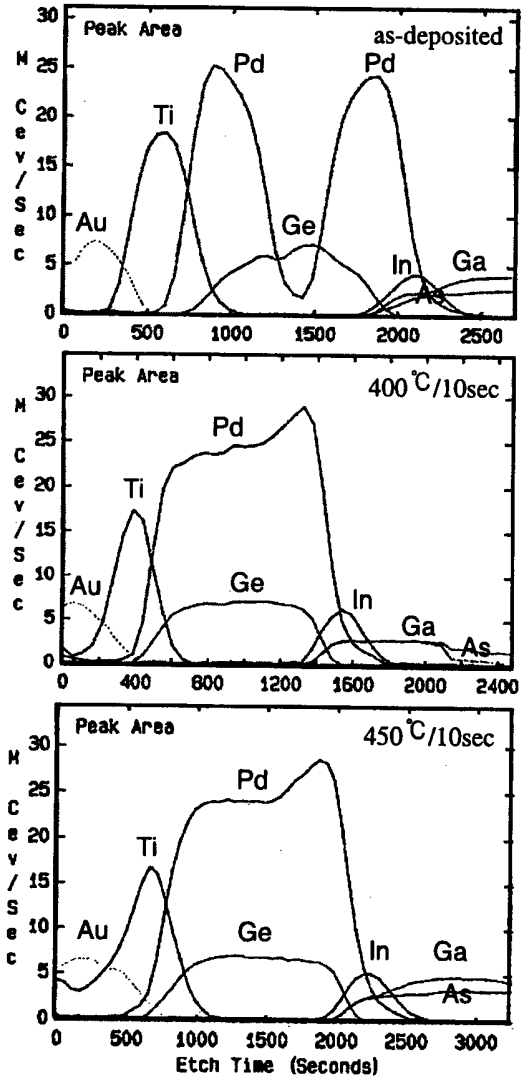

Fig. 8. AES depth profiles of the Pd/Ge/Pd/Ti/Au contacts to n-InGaAs.

was changed to Pd_2Ge phase by higher temperature annealing and this phase transition was related to lower specific contact resistance. The increase in specific contact resistance above 450 °C is attributed to the Pd_5Ga_2 compound formation. $AuIn_2$, AuGe and AuGa phases were not identified unlike the Pd/Ge/Au/Ni/Au contact as shown in Fig. 3. It is, therefore, expected that the Ti layer acts as a superior diffusion barrier.

Figure 8 illustrates the AES depth profiles of the Pd/Ge/Pd/Ti/Au contact on n-InGaAs. The Pd and Ge atoms were intermixed by RTA and it is in good agreement with the XRD results. The out-diffusions of the In, Ga and As atoms were not found and neither was the in-diffusion of the Au atoms. Therefore, the Au-based compounds such as $AuIn_2$, AuGe and AuGa were not identified in XRD analysis. Thus it was reconfirmed that the Ti layer was an excellent diffusion barrier in this contact system

The interface of the Pd/Ge/Pd/Ti/Au contact to n-InGaAs observed by XTEM is shown in Fig. 9. Non-

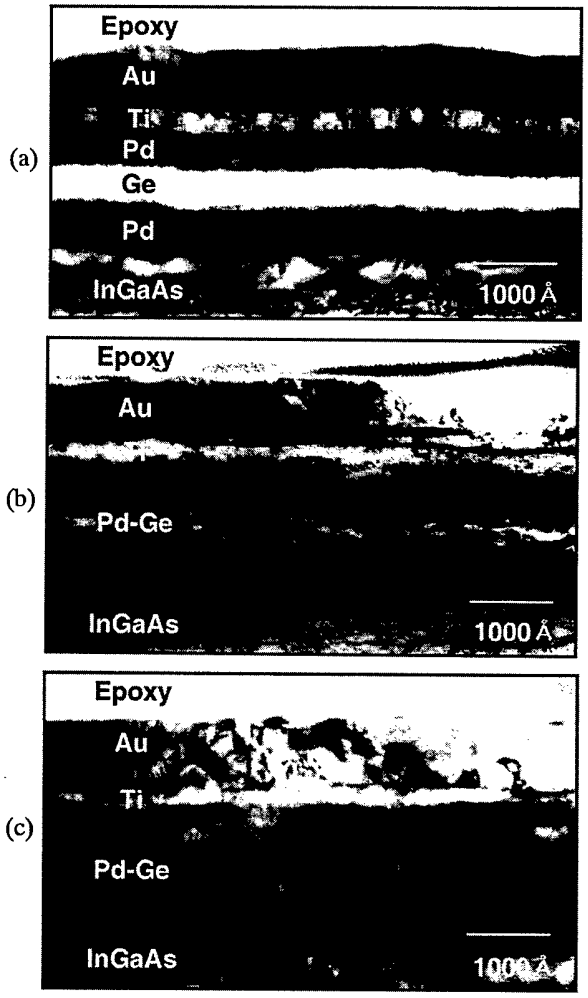

Fig. 9. Cross-sectional view of the Pd/Ge/Pd/Ti/Au contacts to n-InGaAs. (a) as-deposited, (b) 425 °C/10 sec, (c) 450 °C/10 sec.

spiking and planar interface was also found and maintained after RTA. The Pd-Ge compound layer was also observed due to the intermixing of Pd and Ge.

IV. CONCLUSIONS

The ohmic characteristics of the Pd/Ge/Au/Ni/Au and Pd/Ge/Pd/Ti/Au contact systems on n-InGaAs were studied, and the correlation of their electrical properties with microstructures was examined. In both contacts, relatively good ohmic behavior was found even without annealing due to their lower barrier height, and better ohmic contacts were obtained after RTA. In the case of the Pd/Ge/Au/Ni/Au contact, it was deteriorated by intermixing and phase reaction of the ohmic metals with InGaAs substrate above 425 °C, especially by the formation of $AuIn_2$ and Pd_5Ga_2 phases. The Ni layer could not act as a diffusion barrier. The outdiffusion of the In and As atoms makes degradation of the ohmic contact through an increase in barrier height and charge compensation. The Pd/Ge/Pd/Ti/Au contact showed better ohmic behavior than that of the Pd/Ge/Au/Ni/Au contact, especially at high temperature, because of excellent diffusion barrier of the Ti layer. Non-spiking and planar interfaces were observed after annealing in both contacts, and thus it is confirmed that the Pd is a good material as a contact layer to n-InGaAs. It is suggested that the Pd/Ge/Pd/Ti/Au ohmic contact system is promising for semiconductor device applications.

REFERENCES

[1] E. D. Marshall, W. X. Chen, C. S. Wu, S. S. Lau and T. F. Keuch, Appl. Phys. Lett. **48**, 535 (1985).

[2] J. Tsuchimoto, S. Shikata and H. Hayashi, J. Appl. Phys. **69**, 6556 (1991).

[3] L. C. Wang, S. S. Lau, E. K. Hsieh and J. R. Velebir, Appl. Phys. Lett. **54**, 2677 (1989).

[4] M. W. Cole, W. Y. Han, L. M. Casas, D. W. Eckart and K. A. Jones, J. Vac. Sci. Technol. **A12**, 1904 (1994).

[5] I.-H. Kim, S. H. Park, T.-W. Lee, M. P. Park, B. R. Ryum, K. E. Pyun and H.-M. Park, IEEE International Symposium on Compound Semiconductors **97TH8272**, 455 (1998).

[6] J.-W. Lim, J.-K. Mun and J.-J. Lee, J. Korean Phys. Soc. **34**, 275 (1999).

[7] I.-H. Kim, S. H. Park, T.-W. Lee and M. P. Park, Appl. Phys. Lett. **71**, 1854 (1997).

[8] J. H. Lee, H. S. Yoon, B. S. Park, C. S. Park, S. S. Choi and K. E. Pyun, ETRI Journal **18**, 171 (1996).

[9] L. G. Shantharama, H. Schumacher, H. P. Leblanc, R. Esagui, R. Bhat and M. Koza, Electron. Lett. **26**, 1127 (1990).

[10] S. H. Park, M. P. Park, T. W. Lee, K. M. Song, K. E. Pyun and H. M. Park, the 22nd Int. Symp. Compound Semiconductors, 295 (1995).

Journal of the Korean Physical Society, Vol. 34, June 1999, pp. S432~S434

Etching Effect of Carbon Tetrabromide in the Vertical Growth of GaAs during Metalorganic Chemical Vapor Deposition

Young K. PARK and Seong-Il KIM

Semiconductor Materials Laboratory, Korea Institute of Science and Technology, Seoul 130-650

Chang-Sik SON

Department of Materials Science, Korea University, Seoul 136-701

In order to explain the etching effect of the carbon tetrabromide in the vertical growth of GaAs during metalorganic chemical vapor deposition, the dependence of the vertical growth rate of GaAs epilayer on the growth temperature and on the carbon tetrabromide mole fraction has been investigated. The vertical growth rate decreases with increasing growth temperature in the range of 600~700 °C, whereas it increases with increasing growth temperature in the range of 700~800 °C. The vertical growth rate, thus, shows the minimum value at the growth temperature of 700 °C. The high mole fraction of carbon tetrabromide causes a significant diminution of the vertical growth rate of GaAs epilayer. The decrement of the vertical growth rate is attributed to the increment of bromine atoms in the reactor with increasing the carbon tetrabromide mole fraction. The increment of bromine atoms causes the etching effect of carbon tetrabromide.

I. INTRODUCTION

Metalorganic chemical vapor deposition (MOCVD) of III-V group semiconductor is now being extensively studied for the realization of quantum confinement structures such as quantum wires and quantum dots by controlling the lateral dimension of the structure [1–4]. Selective epitaxy (SE) has been emerging as a promising technique for fabricating the quantum confinement structures because it is a direct approach to achieve arbitrary lateral structures using a traditional planar deposition. Conventional SE refers to the spatially controlled growth of an epitaxial layer on partially masked substrates with growth in the opening part of the mask and no growth on the mask [5–10]. The masking material is usually a dielectric material such as SiO_2 or Si_3N_4 [11]. There are some drawbacks in using dielectric materials. In particular, deposition and etching processes are necessary to make the mask before SE and an additional etching process is required to remove the mask after SE. The etching process causes damage and contamination at the regrowth interface and surface of the sample, which can strongly affect the quality of devices. On the other hand, maskless SE by one-step growth [12–14] does not require the etching processes. The maskless SE was achieved using a dramatic lateral growth enhancement by supplying carbon tetrabromide (CBr_4) in our previous works [12–16]. The dependence of the growth rate on the growth parameters is very important to realize the SE [17,18] or to achieve a huge ratio of the lateral over the vertical growth rate. However, it is still not clearly explained the detail role of CBr_4 on the huge lateral growth enhancement. In this work, the dependence of the vertical growth rate of GaAs epilayer on the growth temperature and on the CBr_4 mole fraction has been investigated to explain the etching effect of the CBr_4 in the vertical growth of GaAs by metalorganic chemical deposition. We believe that the information is useful to explain how the maskless SE could be achieved.

II. EXPERIMENT

First, the exact (100) oriented semi-insulating GaAs substrates were patterned in stripes aligned along the $[0\bar{1}1]$ direction using standard photolithography and wet chemical etching. A photomask with a center stripe separation of 2 μm was used. The width and depth of the stripes were 2 μm and 1 μm, respectively. After the pattern was transferred, the mesa was generated by wet chemical etching using a solution of H_2SO_4 : H_2O_2 : H_2O (1:8:40 by volume ratio). After removal of the photoresist, samples were flushed in de-ionized water and blown with filtered nitrogen before being loaded into MOCVD reactor.

CBr_4-doped GaAs epilayers were then grown on single mesa patterned GaAs substrates by atmospheric pressure MOCVD in a vertical quartz reactor [19,20]. Pri-

or to loading into the reactor, the substrates were degreased. Reactor was flushed by H_2 gas to maintain the constant oxygen free condition. Trimethylgallium (TMG, $(CH_3)_3Ga$) and arsine (AsH_3) of 10 % diluted in pure hydrogen were used as the source materials. CBr_4 was used as an extrinsic C doping source which could bring out the lateral growth enhancement of GaAs epilayers. AsH_3 was introduced at the V/III ratio of 60. In order to investigate the dependence of the vertical growth rate of GaAs on the growth temperature and on the CBr_4 mole fraction, the growth temperature was varied from 600 to 800 °C and the mole fraction of CBr_4 was varied in the range of $2\sim6\times10^{-6}$. Pd-diffused H_2 gas was used as a carrier gas. The total reactor flow rate was kept at 5,000 sccm. The as-grown samples were stain-etched by a solution of KOH : $K_3Fe(CN)_6$: H_2O (12 g : 9 g : 75 cc), and then their cross-sectional micrographs were observed by field emission scanning electron microscopy (SEM) to measure the thickness of the epilayers.

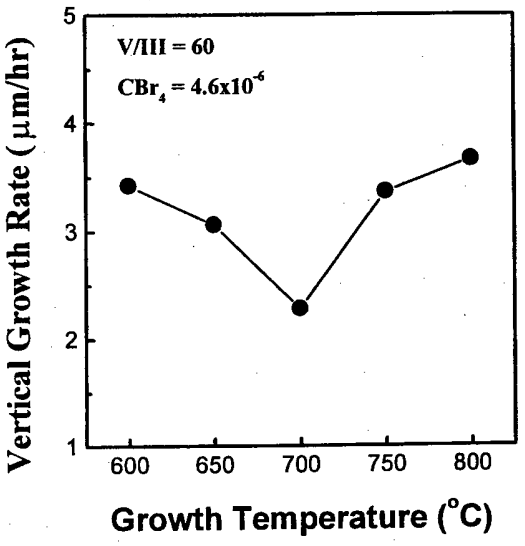

Fig. 2. The vertical growth rate of GaAs on the mesa as a function of CBr_4 mole fraction. V/III ratio and growth temperature are 60 and 700 °C, respectively.

III. RESULTS AND DISCUSSION

In the GaAs epitaxial growth by MOCVD, the use of TMG and AsH_3 is one of the most useful reactant combinations. In general, the growth rate is directly proportional to the partial pressures of the source materials. However, in the GaAs epitaxial growth, because of the relatively inefficient decomposition of AsH_3 compared to TMG, the partial pressure of the Ga atoms is the critical factor in determining the growth rate of GaAs in MOCVD [21]. The Ga atoms are produced by pyrolysis of TMG on the GaAs surface. Then, the GaAs epitaxial layer is grown in vertical direction of the As-rich GaAs surface by diffusion of the Ga atoms together with As from the boundary layer [21].

When CBr_4 is introduced into the reactor for the carbon doping into the GaAs epilayer, where TMG and arsine are supplied into the reactor simultaneously, arsenic is not the only atom to combine with Ga atom. Arsenic atoms compete with bromine atoms, which are produced from the thermal decomposition of CBr_4, for the available gallium atoms. The Br atoms, which combine with Ga, form Ga-Br complexes such as GaBr or $GaBr_2$. The amount of Ga atoms which are bonding to the crystal surface, therefore, is reduced and we call it an etching effect of the CBr_4 in this work.

First, the dependence of the growth temperature on the etching effect of the CBr_4 in the GaAs epilayer has been investigated. The vertical growth rate of the single epitaxial layer on the mesa pattern as a function of growth temperature is shown in Fig. 1. The vertical growth rate decreases with increasing growth temperature at the temperature in the range of 600~700 °C, whereas it increases with increasing growth temperature in the range of 700~800 °C. The vertical growth rate, thus, shows the minimum value at the growth temperature of 700 °C. This minimum vertical growth rate can be applied to a selective area growth and the work has been presented elsewhere [12].

At the growth temperature below 700 °C, the vertical growth rate decreases with increasing growth temperature because the etching effect of CBr_4 increases with increasing growth temperature up to 700 °C. It is known that the presence of bromine atoms leads to the etching of the GaAs and the only detected product of the etching is GaBr [22]. Since higher thermal energy at a higher growth temperature enhances the decomposition of CBr_4 into C and Br_x, the number of bromine atoms in the reactor increases and the etching effect of CBr_4 increases with increasing growth temperature up to 700 °C.

However, because of high thermal energy at the growth temperature of higher than 700 °C, bromine atoms do not act as an efficient etching species anymore. At the temperature beyond 700 °C, the bromine atoms do not efficiently combine with gallium atoms because of high thermal energy, so the etching effect is reduced. Thus more gallium atoms are available to arsenic atoms and, therefore, growth rate increases with increasing growth temperature.

In Fig. 2, a vertical growth rate of the single epitaxial layer on the mesa as a function of CBr_4 flow rate is shown. The growth temperature was fixed at 700 °C. As can be seen in Fig. 2, the high mole fraction of CBr_4 causes a significant diminution of the vertical growth rate of GaAs epilayer. The decrement of the vertical growth rate is attributed to the increment of bromine atoms in the reactor with increasing the CBr_4 mole fraction and the bromine atoms presumably forms $GaBr_x$ (x=1, 2, 3) which leads the increment of the etching effect of CBr_4. The satu-

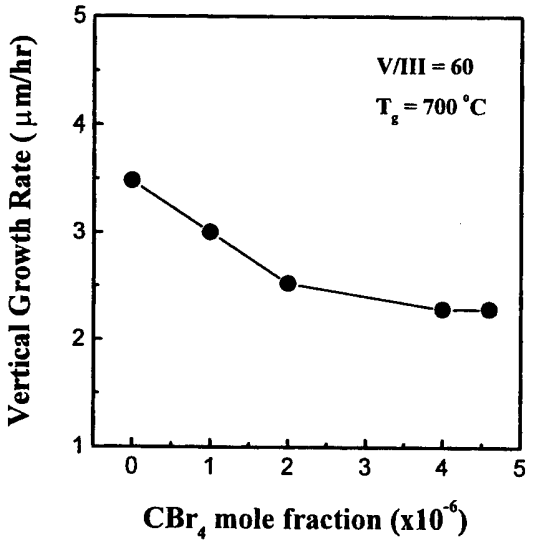

Fig. 1. The vertical growth rate of GaAs on the mesa as a function of growth temperature. V/III ratio and CBr_4 mole fraction are 60 and 4.6×10^{-6}, respectively.

ration of the decrement rate of the vertical growth rate may indicate that the decomposition efficiency of CBr_4 is reduced with increasing the mole fraction of CBr_4.

IV. SUMMARY

In this work we have studied the etching effect of carbon tetrabromide in the vertical growth of GaAs epilayers on mesa patterned GaAs substrates during metalorganic chemical vapor deposition. We found that the vertical growth rate of GaAs has a strong dependence on the growth temperature and on the mole fraction of the carbon tetrabromide. We can summarize our results as the following. First, a vertical growth rate of the GaAs epilayer decreased as an increment of growth temperature up to 700 °C because of the etching effect. Whereas the vertical growth rate increased with increasing growth temperature beyond 700 °C, because the etching effect is weakened by the decomposition of $GaBr_x$. As a result, the curve of the vertical growth rate as a function of the growth temperature shows a valley at the growth temperature of 700 °C. Second, the vertical growth rate decreases as increasing carbon tetrabromide mole fraction in the range of 2×10^{-6}-4.6×10^{-6}. The decrement of the vertical growth rate is attributed to the increment of bromine atoms in the reactor with increasing the carbon tetrabromide mole fraction. The increment of bromine atoms causes the etching effect of carbon tetrabromide. These results are useful in understanding the detail role of CBr_4 on the huge lateral over the vertical growth enhancement and how the maskless SE could be achieved.

ACKNOWLEDGMENTS

This work was supported by the Ministry of Trade, Industry and Energy and the Ministry of Science and Technology (Contract No. 2M08790, 2M08380, and 2E15940).

REFERENCES

[1] M. Grundmann, N. N. Ledentsov, O. Stier, D. Biberg, V. M. Ustinov, P. S. Kopev and Zh. I. Alferov, Appl. Phys. Lett. **68**, 979 (1996).
[2] D. Leonard, M. Krishnamurty, C. M. Reaves, S. P. DenBaar and P. M. Petroff, Appl. Phys. Lett. **63**, 3203 (1993).
[3] W. Seifert, N. Carlsson, J. Johansson, M. E. Pistol and L. Samuelson, J. Cryst. Growth **170**, 39 (1997).
[4] K. Komori and M. Arakawa, Jpn. J. Appl. Phys. **36**, 1927 (1997).
[5] T. G. Kim, J. H. Park, S. I. Kim, C. S. Son, M. S. Kim, E. K. Kim and S. K. Min, in *Proc. of SPIEs Int. Sym. on Microlithography* (the Soc. of Photo-Optical Instrumentation Engineers, Santa Clara, California, 1996), Vol. 2723, p. 63.
[6] M. López, N. Tanaka, I. Matsuyama and T. Ishikawa, Appl. Phys. Lett. **68**, 658 (1996).
[7] M. Araki, Y. Hanada, H. Fujikura and H. Hasegawa, Jpn. J. Appl. Phys. **36**, 1763 (1997).
[8] P. Finnie, M. Buchanan, C. Lacelle and A. P. Roth, J. Cryst. Growth **160**, 220 (1996).
[9] S. Tsukamoto, Y. Nagamune, M. Nishioka and Y. Arakawa, J. Appl. Phys. **71**, 533 (1992).
[10] K. Shimoyama, S. Nagao, Y. Inoue, K. Kiyomi, N. Hosoi, K. Fujii and H. Gotoh, J. Cryst. Growth **145**, 734 (1994).
[11] L. Korte, Chr. Thanner, M. Huber and Ch. Hoyler, J. Cryst. Growth **124**, 220 (1992).
[12] Y. K. Park, S. I. Kim, Y. Kim, E. K. Kim, S. K. Min, C. S. Son and I. H. Choi, J. Korean Phys. Soc. **32**, 704 (1998).
[13] C. S. Son, Y. K. Park, S. I. Kim, Y. Kim, E. K. Kim, S. K. Min and I. H. Choi, Jpn. J. Appl. Phys. **37**, 1701 (1998).
[14] E. K. Kim, T. G. Kim, C. S. Son, S. M. Hwang, Y. Kim, Y. K. Park and S. K. Min, J. Korean Phys. Soc. **33**, S338 (1998).
[15] Y. Kim, Y. K. Park, M. S. Kim, J. M. Kang, S. I. Kim, S. M. Hwang and S. K. Min, Appl. Phys. Lett. **67**, 1871 (1995).
[16] S. I. Kim, M. S. Kim, Y. Kim, C. S. Son, S. M. Hwang, B. D. Min, E. K. Kim and S. K. Min, Appl. Phys. Lett. **69**, 815 (1996).
[17] M. J. Anders, M. M. G. Bongers, P. L. Bastos and L. J. Giling, J. Cryst. Growth **154**, 240 (1995).
[18] S. D. Hersee, E. Barbier and R. Blondeau, J. Cryst. Growth **77**, 310 (1986).
[19] C. S. Son, S. I. Kim, Y. Kim, Y. K. Park, E. K. Kim, S. K. Min and I. H. Choi, J. Appl. Phys. **82**, 1205 (1997).
[20] Y. K. Park, C. S. Son, S. I. Kim, Y. Kim, E. K. Kim, S. K. Min and I. H. Choi, J. Appl. Phys. **83**, (1998).
[21] M. Razeghi, *The MOCVD Challenge* (Institute of Physics Publishing, Bristol and Philadelphia, 1995), Vol. 2,.
[22] M. McEllistrem and J. M. White, J. Vac. Sci. Technol. **A13**, 1448 (1995).

Journal of the Korean Physical Society, Vol. 34, June 1999, pp. S435~S438

Fabrication of AlGaAs/GaAs Heteroface Solar Cells

Hyo-Jin KIM*, Young K. PARK, Seong-Il KIM and Eun Kyu KIM

Semiconductor Materials Laboratory, Korea Institute of Science and Technology, Seoul 130-650

Tae-Whan KIM

**Department of Physics, Kwangwoon University, Seoul 139-701*

Optimal conditions of the thickness and doping concentration for AlGaAs/GaAs heteroface solar cell were calculated. Our result shows that the dependence of efficiency on the thickness and doping concentration of emitter is higher than that of base. The optimum conditions of the thickness and doping concentration of the emitter are 600 nm and 4.0×10^{17} cm^{-3}, respectively. Using the calculated optimum conditions, the solar cells were fabricated by atmospheric pressure metalorganic chemical vapor deposition. The size of the solar cell was 1 cm × 1 cm. When the power of the incident light was 86 mW/cm^2, the measured open-circuit voltage, short-circuit current, and fill factor were 0.79 V, 23.1 mA/cm^2, and 0.64, respectively, and the measured efficiency was 13.7 %.

I. INTRODUCTION

Solar cell is a basic component of modern satellites. Experts estimate that more than 50 % of all of the commercial satellites now under construction will be equipped with GaAs solar cells [1]. GaAs solar cells will never be as cheap as Si based solar cells. However, satellite manufacturers are willing to pay a premium for GaAs solar cells because it shows higher efficiency, superior radiation hardness, and less degradation in extreme temperature [2–4].

Incident photons with energies greater than the band gap of the semiconductor create electron-hole pairs which are separated by the junction. Some photogenerated minority carriers move to the surface and recombine with surface states which are arise from dangling bonds, chemical residues, metal precipitates, and native oxides [2–4]. In order to prevent the surface recombination, a thin AlGaAs layer is usually grown on the GaAs junction and it is called an AlGaAs/GaAs heterface solar cell [2–4].

In order to determine the optimum conditions of the AlGaAs/GaAs heteroface solar cell, computer simulations have been done. The problem of minimizing cell resistance has taken on somewhat of a different nature with the advent of the extremely shallow diffused cells. The older deeper-diffused cell resistances were limited mainly by contact resistance at the electrodes. The present-day cells with grid lines, however, are usually limited by the resistance in the diffused sheet due to the very small cross-sectional area which the carriers in this region traverse, while the contact resistance has been made negligible, for the most part, by the technology of the contact fabrication. Using the results of the optimized parameters, p-AlGaAs/p-GaAs/n-GaAs heteroface solar cells have been fabricated by atmospheric pressure metalorganic chemical vapor deposition (MOCVD) on n-type GaAs substrate and the solar cell characteristics were investigated.

II. SIMULATIONS

Computer simulations have been performed to investigate the optimum conditions of a p-AlGaAs/p-GaAs/n-GaAs heteroface solar cell. Quantum efficiency has been calculated as functions of physical parameters such as the film thickness and the doping concentrations of a window layer, a p-GaAs, and an n-GaAs. To allow more light in the underlying GaAs layer, the Al mole fraction of AlGaAs should be increased and the thickness of the AlGaAs layer must be reduced. When the external voltage is zero, the current of flowing into solar cell is short-circuit current (I_{sc}) which is equal to the light-generated current (I_{ph}) in ideal case. The total current of solar cell is given by [4]

$$I_{tot} = J_0 \cdot A_{tot}\left(\exp\left(\frac{q(V - I_{tot}R_s)}{KT}\right) - 1\right) - J_{ph} \cdot A_{act} \quad (1)$$

where A_{act} is an effective area, A_{tot} is total area on the front surface, and J_0 is saturation current density in finite cell dimension [5]. When the current flowing into solar cell is zero, voltage is open-circuit voltage. According to

Eq. (1), open-circuit voltage (V_{oc}) is given by

$$V_{oc} = \frac{kT}{q} \ln \left(\frac{J_{ph} A_{act}}{J_o A_{tot}} + 1 \right) \tag{2}$$

The V_{oc} is determined by the relation between saturation current density (J_0) and light-generated current density (J_{sc}). For I-V curve of solar cell, when the output power for any operating point in the fourth quadrant is maximum, the voltage is V_m, and the current is I_m. The conversion efficiency (η) and fill factor (FF) of solar cell are given by

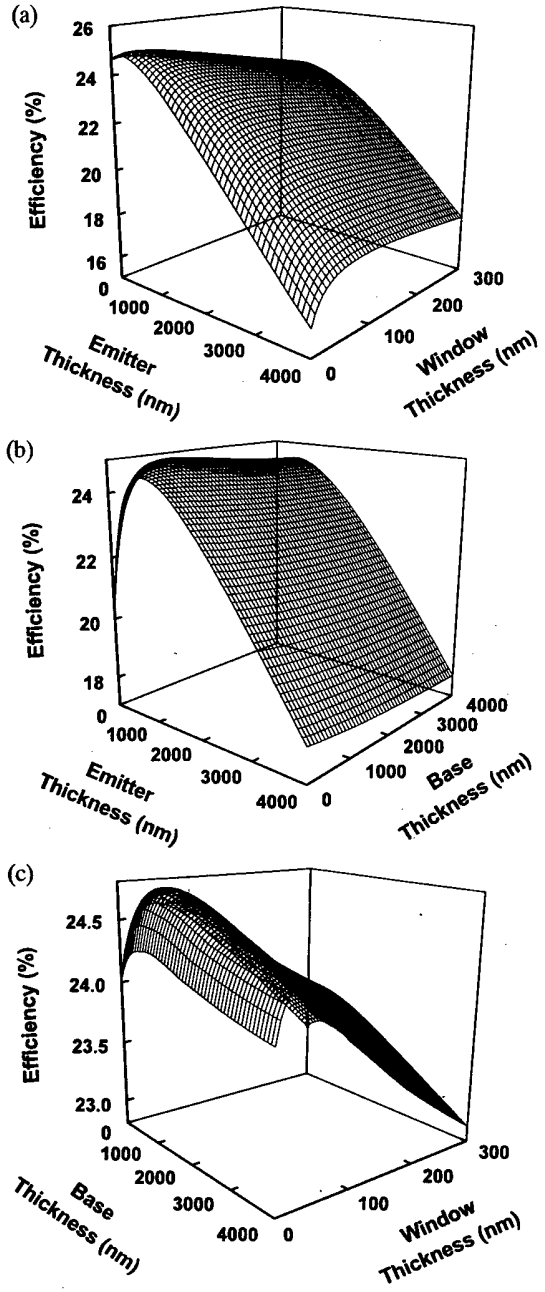

Fig. 1. Calculated efficiencies of p-AlGaAs/p-GaAs/n-GaAs solar cells as functions of thicknesses of (a) emitter and window, (b) emitter and base, and (c) window and base.

$$\eta = \frac{|IV|_{\max}}{P_{in}} = \frac{FF \cdot I_{sc} \cdot V_{oc}}{P_{in}}, \tag{3}$$

$$FF = \frac{I_m V_m}{I_{sc} V_{oc}}. \tag{4}$$

The efficiency of AlGaAs/GaAs solar cell increases as Al mole fraction x increases. In Fig. 1, the calculated efficiencies of p-AlGaAs/p-GaAs/n-GaAs solar cells as functions of thicknesses of two different layers are shown. Figure 1(a) shows the efficiencies as functions of thicknesses of emitter and window. The dependence of the efficiency on the thickness of emitter is stronger than that of window as can be seen in Fig. 1(a). The current generated in a solar cell is related with a semiconductor absorption coefficient, a recombination velocity of interface layer, and a saturation current. The optimum thickness of p-AlGaAs window layer is in the range of 20~60 nm. In that thickness range, both the carrier absorption at the window layer and the recombination velocity at the p-AlGaAs/p-GaAs interface are small. Therefore, theoretically, the thickness of the AlGaAs could be reduced to around 20~60 nm. Compromising the benefits of reducing the thickness and minimizing series resistance, the thickness of 300 nm is appropriate [6]. The optimum thicknesses of p-GaAs emitter and n-GaAs base are in the range of 200~600 nm and 500~1000 nm, respectively. The calculated efficiency of the heteroface solar cell was dramatically changed by small variation of the doping concentration and the thickness of the emitter. When the effective area on the front surface of solar cell is 90~92 % with the optimum condition, the efficiency of solar cell is 24.9 %. In Figs. 1(b) and (c), the calculated efficiencies of p-AlGaAs/p-GaAs/n-GaAs solar cells as functions of the thicknesses of emitter and base and those of base and window layer, respectively. The dependence of the efficiency on the thickness of emitter is stronger than that of base as can be seen in Fig. 1(b). On the other hand, the dependence of the efficiency on the thickness of window layer is stronger than that of base as shown in Fig. 1(c). Therefore, the thicknesses of the window and emitter are more important than that of base. The thickness of n^+-GaAs substrate layer does not affect largely on the recombination velocity of n-GaAs/n^+-GaAs interface because the energy gap difference between the n-GaAs base and the n^+-GaAs substrate is very small.

In Fig. 2, the calculated conversion efficiencies of the p-AlGaAs/p-GaAs/n-GaAs solar cells as functions of the doping concentrations of the emitter and base are shown. The dependence of the efficiency on the doping concentration of the emitter is stronger than that of the base as shown in Fig. 2. The calculated conversion efficiency of the heteroface solar cell is high when the doping concentration of p-GaAs emitter is smaller than that of p-AlGaAs window layer. The doping level of the window layer is high enough to help in reducing the series resistance, allowing the p-GaAs emitter to be doped more

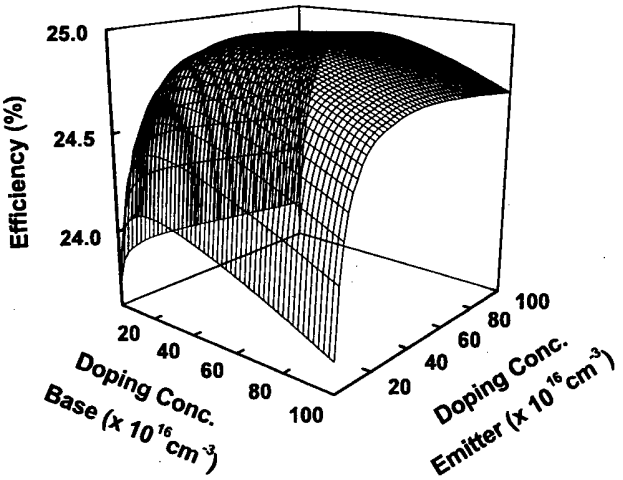

Fig. 2. Calculated efficiencies of p-AlGaAs/p-GaAs/n-GaAs solar cells as functions of the doping concentrations of emitter and base layer.

lightly for a higher lifetime and better collection efficiency. However, the open-circuit voltage decreases as an increment of the doping concentration of p-GaAs emitter. The optimum doping concentrations of p-AlGaAs window and p-GaAs emitter are 5×10^{17} cm^{-3} and 1.5-4.0×10^{17} cm^{-3}, respectively. The relation of doping concentration between n-GaAs base and n^+-GaAs substrate is similar to the relation between p-AlGaAs window and p-GaAs emitter. The optimum doping concentration of n-GaAs base is $3.0 - 8.0 \times 10^{17}$ cm^{-3}.

III. EXPERIMENT

The heteroface solar cells consisting of an n^+-GaAs substrate, an n-GaAs base, a p-GaAs emitter, a p-type $Al_xGa_{1-x}As$ window layer on the p-GaAs emitter, with composition of x=0.9 were fabricated. Epilayers of the AlGaAs/GaAs heteroface solar cell were grown on n^+-GaAs substrate by atmospheric pressure MOCVD in a vertical quartz reactor [7–11]. The substrate was degreased by boiling in organic solvents (trichloroethylene, acetone, and methanol) in ten minutes and was etched with a $5H_2SO_4 : 1H_2O_2 : 1H_2O$ solution for two minutes. The substrate was then sufficiently rinsed in deionized water, dried by pure nitrogen, and finally loaded into the reactor. The reactor was flushed by the H_2 gas to maintain the constant oxygen free condition. Prior to the epitaxial growth, the substrates were heated up to 700 °C under an arsine (AsH_3) flux to remove the native oxide. Trimethylgallium (TMG) and AsH_3 of 10 % diluted in pure hydrogen were used as the source materials. AsH_3 was introduced at the V/III ratio of 60. The carrier gas was Pd-diffused hydrogen, with the flow rates being 5,000 sccm. The growth temperature was 650 °C. Flow rates of CCl_4 was 0.023 sccm. The as-grown samples were stain-etched by a solution of KOH : $K_3Fe(CN)_6$: H_20 (12 g : 9 g : 75 cc), and then their cross-sectional micrographs were observed by field emission scanning electron microscopy (SEM) to measure the thickness of the epilayers. The electrical properties were measured by van der Pauw Hall analysis at room temperature.

The ohmic contacts of the as-grown samples were then done by thermal evaporation using a shadow mask. The Au-Zn (5 %) contact to the window layer and the Au-Ge (12 %) contact to the substrate. After metallization, the samples were thermally annealed at the temperature of 420 °C for three minutes in an N_2 atmosphere. The thermal treatment step is important to achieve negligible contact resistance. The fill factors vary from growth run to growth run, apparently due to differences in series resistance, sheet resistivity, and contact resistance. The finished solar cell characteristics were measured by HP-4156A using a tungsten light source.

IV. RESULTS AND DISCUSSION

Solar cells consisting of p-AlGaAs/p-GaAs/n-GaAs have been fabricated by atmospheric pressure MOCVD on n-type GaAs substrate. The thicknesses and doping concentrations of each layers were determined from the calculating results. The thicknesses and doping concentrations of p-AlGaAs window layer, p-GaAs emitter, and n-GaAs base were 25 nm and 5×10^{17} cm^{-3}, 600 nm and 4×10^{17} cm^{-3}, and 700~1000 nm and $5 - 6 \times 10^{17}$ cm^{-3}, respectively. In order to improve ohmic contact, highly doped p^+-GaAs capping layer was grown on the window layer. The thickness and doping concentration of p^+-GaAs layer were 12 nm and 2×10^{18} cm^{-3}, respectively. The solar cell characteristics were measured using a tungsten light source. In Fig. 3, the current-voltage be-

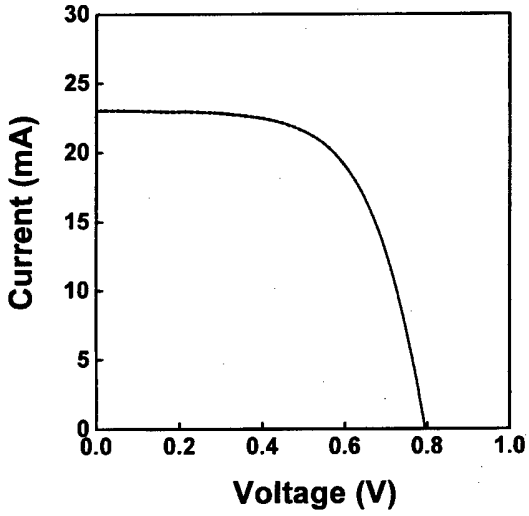

Fig. 3. Current-voltage behavior of a p-AlGaAs/p-GaAs/n-GaAs solar cell for 86 mW/cm^2 intensity.

havior of the p-AlGaAs/p-GaAs/n-GaAs solar cell for 86 mW/cm^2 intensity is shown. The measured open-circuit voltage, short-circuit current, and fill factor were 0.79 V, 23.1 mA/cm^2, 0.64, respectively, and the conversion efficiency was 13.7 % as can be seen in Fig. 3. The fill factor of 0.64 is less than general values in the range of 0.74~0.82 and it is due to large resistance [2]. In order to have better fill factor, it is necessary to improve the ohmic contact process and to optimize the metal pattern [6]. In this work, we used a single junction structure, however, to obtain higher efficiency, it is necessary to use a multijunction structure.

V. SUMMARY

For the improvement of the efficiency of p-AlGaAs/p-GaAs/n-GaAs heteroface solar cell, the efficiencies were calculated as functions of the film thicknesses and doping concentrations. The optimum thicknesses of p-AlGaAs window layer, p-GaAs emitter, and n-GaAs base were about 300 nm, 200~600 nm, and 500~1000 nm, respectively. The optimum doping concentrations of p-AlGaAs window layer, p-GaAs emitter, and n-GaAs base were about 5×10^{17} cm^{-3}, $1.5-4.0\times10^{17}$ cm^{-3}, and $3.0-8.0\times10^{17}$ cm^{-3}, respectively. Using the simulation results, the p-AlGaAs/p-GaAs/n-GaAs heteroface solar cells were fabricated by atmospheric pressure MOCVD. From the current-voltage behavior of the solar cell, we found that the measured open-circuit voltage, short-circuit current, and fill factor were 0.79 V, 23.1 mA/cm^2, 0.64, respectively, and the conversion efficiency was 13.7 % for 86 mW/cm^2 intensity. The fill factor of 0.64 is less than general values and it is due to large resistance. In order to have better fill factor, it is necessary to improve the Ohmic contact process and to optimize the metal pattern.

ACKNOWLEDGMENTS

This work was supported by the Ministry of Trade, Industry and Energy (Contract No. 2M08380 and 2M08790) and by the Korea Institute of Science and Technology (Contract No. 2E15940).

REFERENCES

[1] M. Meyer and R. A. Metzger, Compound Semiconductor **2**, 22 (1996).

[2] H. J. Hovel, *Semiconductors and Semimetals,* edited by R. K. Willardson and A. C. Beer (Academic, New York, 1975), Vol. 11.

[3] L. D. Partain, *Solar Cells and Their Applications* (Wiley, New York, 1995).

[4] S. M. Sze, *Physics of Semiconductor Devices*, 2nd Ed. (Wiley, New York, 1981).

[5] J. P. Mckelvey, *Solid State and Semiconductor Physics* (Harper & Row, New York, 1966).

[6] H. J. Kim, Y. K. Park, S. I. Kim, D. U. Lee, E. K. Kim and T. W. Kim, Ungyong Mulli **11**, 631 (1998).

[7] H. J. Kim, Y. K. Park, S. I. Kim, E. K. Kim, S. M. Hwang and T. W. Kim, Proceedings of the 9th Seoul International Symposium on the Physics of Semiconductors and Applications, 136 (1998).

[8] Y. K. Park, S. I. Kim, H. J. Kim, S. M. Hwang, E. K. Kim and Y. T. Kim, Proceedings of the 20th Anniversary Conference of KSES, 522 (1998).

[9] C. S. Son, S. I. Kim, Y. Kim, Y. K. Park, E. K. Kim, S. K. Min and I. H. Choi, J. Appl. Phys. **82**, 1205 (1997).

[10] Y. K. Park, C. S. Son, S. I. Kim, Y. Kim, E. K. Kim, S. K. Min and I. H. Choi, J. Appl. Phys. **83**, 2519 (1998).

[11] Y. K. Park, S. I. Kim, Y. Kim, E. K. Kim, S. K. Min, C. S. Son and I. H. Choi, J. Korean Phys. Soc. **32**, 704 (1998).

Journal of the Korean Physical Society, Vol. 34, June 1999, pp. S439~S442

Magnetotransport and Charge Transfer Studies on Delta-Modulation-Doped $In_xGa_{1-x}As/Al_yGa_{1-y}As$ Strained Single Quantum Wells

M. JUNG, D. U. LEE and T. W. KIM

Department of Physics, Kwangwoon University, Seoul 139-701

K. H. YOO

Department of Physics, Kyung Hee University, Seoul 130-701

M. D. KIM and H. S. PARK

Photonics Laboratory, Samsung Advanced Institute of Technology, Suwon 440-600

D. L. KIM

Joint Research Facility Division, Korea Basic Science Center, Taejon 305-333

Shubnikov-de Haas (S-dH) and Van der Pauw Hall-effect measurements on a $In_{0.18}Ga_{0.82}As/Al_{0.25}Ga_{0.75}As$ strained single quantum well grown by molecular beam epitaxy have been performed to investigate the existence of the two-dimensional electron gas (2DEG) in the $In_{0.18}Ga_{0.82}As$ single quantum well. The fast Fourier transform for the S-dH data and the observation of the quantum Hall effect clearly indicate 2DEG occupation of a subband in the $In_{0.18}Ga_{0.82}As$ single quantum well. Electronic subband energy and the corresponding wavefunction in the $In_{0.18}Ga_{0.82}As$ quantum well were calculated by a self-consistent method taking into account exchange-correlation effects together with strain and nonparabolicity effects.

I. INTRODUCTION

Recently, rapid advancements in epitaxial film growth technology have made possible the fabrication of several new types of strained quantum wells [1–5]. Among these strained quantum structures, pseudomorphic $In_xGa_{1-x}As/Al_yGa_{1-y}As$ quantum well structures have been attractive due to their large conduction band discontinuities and due to the increase in the electron saturation velocities in the $In_xGa_{1-x}As/Al_yGa_{1-y}As$ quantum well compared to those in $GaAs/Al_xGa_{1-x}As$ quantum wells [6–10]. Although the mobility of an $In_xGa_{1-x}As/Al_yGa_{1-y}As$ modulation-doped structure is smaller than that of a conventional $Al_xGa_{1-x}As/GaAs$ modulation-doped structure at low temperatures due to the poor interface quality and the alloy scattering, its room temperature mobility is higher than that of the $Al_xGa_{1-x}As/GaAs$ structure. In addition, a two-dimensional electron gas (2DEG) with a density up to 10^{12} cm^{-2} can be achieved in an $In_xGa_{1-x}As/Al_yGa_{1-y}As$ system. Such properties have allowed a variety of device applications such as high electron mobility transistors [11] and double barrier resonant tunneling structures [12,13]. Although some studies concerning the electrical and optical properties in $In_xGa_{1-x}As/Al_yGa_{1-y}As$ quantum well structures have been studied [14,15], both detailed charge transfer and electronic subband studies are still very important.

II. EXPERIMENTAL DETAILS

The sample used in this work were grown on a semi-insulating (100)-oriented GaAs substrate by molecular beam epitaxy (MBE) and consisted of the following structures: a 100-Å Si-doped (2×10^{18} cm^{-3}) GaAs capping layer for ohmic contacts, a 330-Å undoped $Al_{0.25}Ga_{0.75}As$ layer, a delta Si-doped (2.0×10^{12} cm^{-2}) $Al_{0.25}Ga_{0.75}As$ modulation layer, a 40-Å undoped $Al_{0.25}Ga_{0.75}As$ spacer layer, a 80-Å undoped $In_{0.18}Ga_{0.82}As$ quantum well layer and 5600-Å GaAs buffer layer. The compositions of the layers were measured by using photoluminescence (PL) and double-crystal X-ray diffraction (DCXD), and the thicknesses of the layers were determined from the transmission electron microscopy (TEM) measurements. Even though there are potential errors in the determination of the indium and aluminum mole fractions by the PL measurements, such as the uncertainties of the recombination mechanisms, the band gap energies and the exciton ef-

fects, the indium and aluminum concentrations obtained from the PL measurements were confirmed by the DCXD measurements.

Ohmic contacts to the samples for the S-dH and Hall effect measurements were made by diffusing a small amount of indium through several layers at 450 °C in a hydrogen atmosphere for approximately 10 min. After ohmic contacts were performed, the GaAs cap layer was removed to get rid of parallel conductance for measurements. The S-dH and Hall-effect measurements were carried out at 1.5 K in a magnetic field up to 18 T in an Oxford superconducting magnet system using a Keithely 181 nanovoltmeter.

III. RESULTS AND DISCUSSION

The bright-field TEM image shows that there are no defects due to dislocations or stacking faults. The electron diffraction pattern from the sample shows that there are no misfit dislocations at the $Al_{0.25}Ga_{0.75}As$/$In_{0.18}Ga_{0.82}As$ and the $In_{0.18}Ga_{0.82}As$/GaAs heterointerfaces. A high-resolution cross-sectional TEM image of the $In_{0.18}Ga_{0.82}As$/$Al_{0.25}Ga_{0.75}As$ structure shows that the lattice structures on both sides of the heteroepitaxial interface have no dislocations, stacking faults, and twins and that they have a very smooth interface on the atomic scale. Therefore, the $In_{0.18}Ga_{0.82}As$ active quantum well is pseudomorphically grown on the GaAs buffer layer.

The existence of mobile electrons in an $In_{0.18}Ga_{0.82}As$ /$Al_{0.25}Ga_{0.75}As$ single quantum well was demonstrated by the Van der Pauw Hall effect measurements. The Hall-effect measurements at 300, 77 and 1.5 K in a magnetic field of 0.5 T showed that the mobilities and carrier concentrations were 6.18×10^3, 2.56×10^4 and 1.52×10^5 cm^2/V-sec, and 2.21×10^{12}, 2.12×10^{12} and 2.07×10^{12} cm^{-2}, respectively. The magnitude of mobility at 1.5 K is almost comparable with that obtained from the $In_{0.17}Ga_{0.83}As$/$In_{0.15}Ga_{0.85}As$ strained quantum well [8], and the mobility at low temperatures is saturated by the increased remote ionized impurity scattering. The increase in the carrier density with increasing temperature is attributed to the thermal generation of carriers in the $Al_{0.25}Ga_{0.75}As$ modulation layer.

S-dH measurements were carried out in order to investigate the nature of the free electron providing the high conductivity at 1.5 K. The results of the S-dH is shown in Fig. 1. The period of the oscillation changes with the angle θ between the magnetic field and the surface normal, indicative of a 2DEG occupying the $In_{0.18}Ga_{0.82}As$ quantum well. Additionally, the observed quantum Hall-steps in the Hall resistance as shown in Fig. 2 confirms the existence of a 2DEG in the $In_{0.18}Ga_{0.82}As$ quantum well. The presence of the plateaus also confirms the existence of localized states, which are expected to exist in real two-dimensional systems [16].

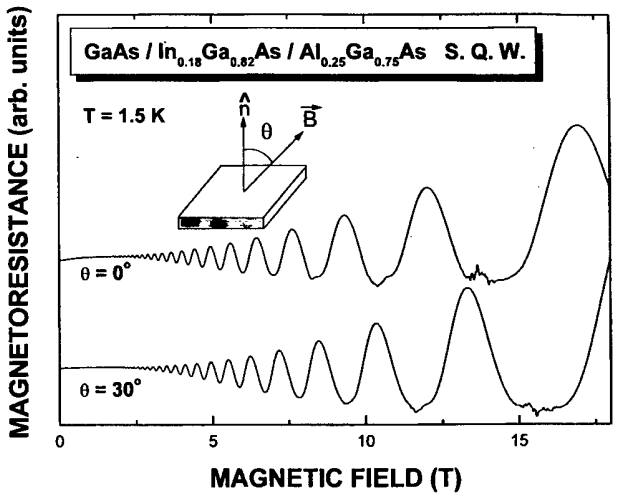

Fig. 1. Results of Shubnikov-de Haas measurements on a GaAs/$In_{0.18}Ga_{0.82}As$/$Al_{0.25}Ga_{0.75}As$ strained single quantum well at 1.5 K. θ represents an angle between the magnetic field and to the heterointerface normal.

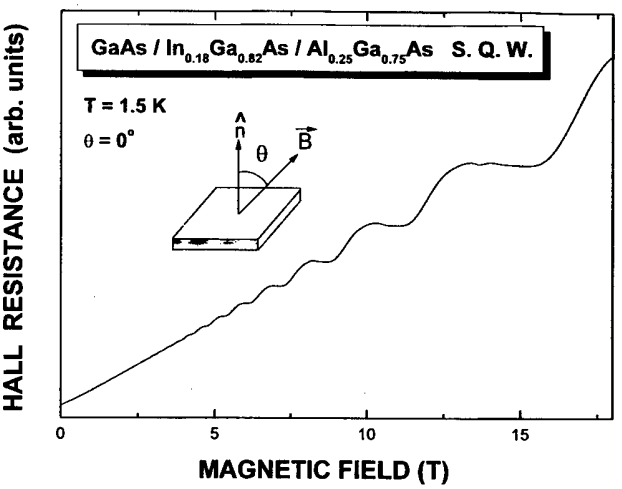

Fig. 2. Results of Hall effect measurements on a GaAs/ $In_{0.18}Ga_{0.82}As$/$Al_{0.25}Ga_{0.75}As$ strained single quantum well at 1.5 K.

After high-pass filtering was performed in order to get rid of the background magnetoresistance, the S-dH data were digitized linearly in terms of the inverse of the magnetic field [17]. The result of a fast Fourier transform (FFT) is shown in Fig. 3. A peak is observed at 41.7 T, with its second harmonic at 83 T. The corresponding electron density is $(2.016\pm0.3)\times10^{12}$ cm^{-2}. The agreement of the carrier density determined from the S-dH and Hall effect measurements at the same temperature is reasonable. When the magnetic field is oriented at 30° with respect to the surface normal, the peak postion is shifted to 47.3 T which is (41.7 T/cos 30°).

To determine the subband energy and the corresponding wavefunction the experimental results and a self-

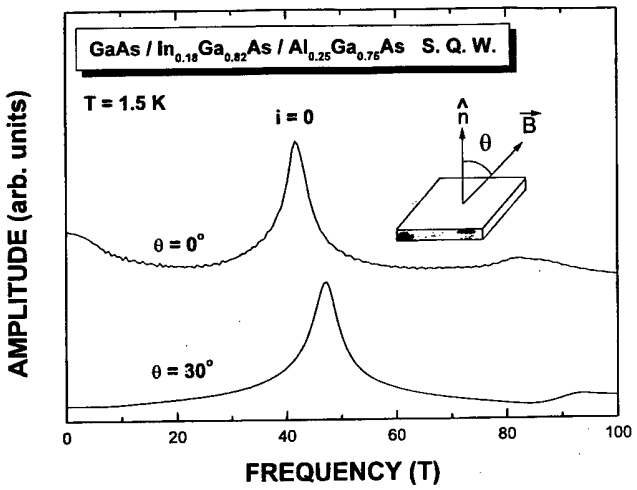

Fig. 3. Fast Fourier analyses of Subnikov-de Haas data for a $GaAs/In_{0.18}Ga_{0.82}As/Al_{0.25}Ga_{0.75}As$ strained single quantum well.

consistent numerical calculation taking into account the exchange-correlation effects together with strain and nonparabolicity effects were used [18]. The detailed studies on the strain, the nonparabolicity, the exchange-correlation effects were discussed in the literature [19]. The dielectric constant of 13.5 is chosen to be the same in both the barriers and the well [20], while the conduction band edges and the electron effective masses were assumed to change abruptly at the heterointerface. The conduction band offsets at the $In_{0.18}Ga_{0.82}As/Al_{0.25}Ga_{0.75}As$ and $In_{0.18}Ga_{0.82}As/GaAs$ heterointerfaces taking into account strain effects were taken to be 345 meV and 44 meV, respectively [20]. The effective masses of the $Al_{0.25}Ga_{0.75}As$, $In_{0.18}Ga_{0.82}As$, and GaAs were taken to be 0.082 me, 0.059 me and 0.067 me, respectively [21]. The results of the numerical calculation for the electronic subbands in an $GaAs/In_{0.18}Ga_{0.82}As/Al_{0.25}Ga_{0.75}As$ single quantum well are shown in Fig. 4. The solid and the dotted lines represent the ground state subband energy and the corresponding wavefunction, respectively, and EF represented by the dashed line indicates the Fermi energy level.

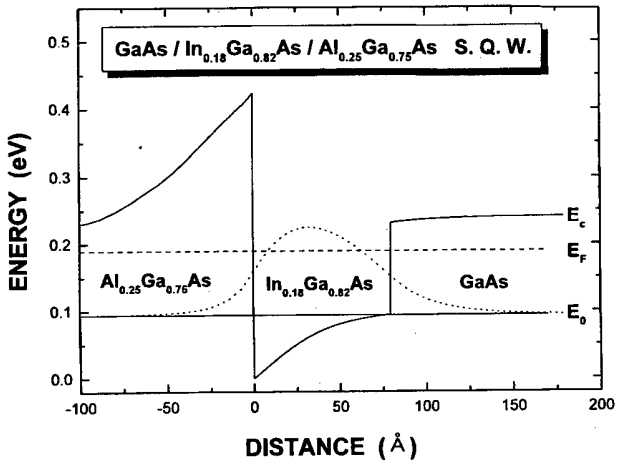

Fig. 4. An electronic subband structure of a $GaAs/In_{0.18}Ga_{0.82}As/Al_{0.25}Ga_{0.75}As$ quantum well calculated by taking into account the strain and nonparabolicity effects.

IV. SUMMARY AND CONCLUSIONS

S-dH measurements and the Hall measurement were performed on an $GaAs/In_{0.18}Ga_{0.82}As/Al_{0.25}Ga_{0.75}As$ single quantum well grown by MBE. The angular dependence of the S-dH measurements and the clear observation of the quantum Hall plateaus at 1.5 K demonstrated the existence of 2DEG in the system. The FFT results for the S-dH data indicate that a 2DEG was occupied at one subband in the asymmetric $In_{0.18}Ga_{0.82}As$ quantum well. Self-consistent numerical calculations taking into account exchange-correlation effects together with strain and nonparabolicity effects were carried out in order to determine the subband level and the corresponding wavefunction in the $In_{0.18}Ga_{0.82}As$ quantum well.

ACKNOWLEDGMENTS

This work was supported by the Korea Science and Engineering Foundation (Contract No. 971-0209-038-1).

REFERENCES

[1] F. Capasso, *Physics of Quantum Electron Devices* (Springer-Verlag, Heidelberg, 1990).
[2] C. Weisbuch and B. Vinter, *Quantum Semiconductor Structures* (Academic Press, Boston, 1991).
[3] L. Q. Qian and B. W. Wessels, Appl. Phys. Lett. **63**, 628 (1993).
[4] O. Buchinsky, M. Blumin and D. Fekete, Appl. Phys. Lett. **72**, 1484 (1998).
[5] A. Y. Lew, S. L. Zuo, E. T. Yu and R. H. Miles, Phys. Rev. **B57**, 6534 (1998).
[6] N. Moll, M. R. Hueschen and A. Fisher-Colbrie, IEEE Trans. Electron Devices **ED-35**, 879 (1988).
[7] T. Schweizer, K. K hler and P. Gauser, Appl. Phys. Lett. **60**, 469 (1992).
[8] P. W. Yu, B. Jogai, T. J. Rogers, P. A. Martin and J. M. Ballingall, Appl. Phys. Lett. **65**, 3263 (1994).
[9] M. L. F. Abbade, F. Iikawa, J. A. Brum, Th. Tr ster, A. A. Bernussi and R. G. Pereira, J. Appl. Phys. **80**, 1925 (1996).
[10] R. B. Dunford, D. Popovic, F. H. Pollak and T. F. Noble, J. Appl. Phys. **83**, 3144 (1998).
[11] T. Henderson, J. Klem, C. K. Peng, J. S. Gedymin, W. Kopp and H. Morkoc, Appl. Phys. Lett. **45**, 1080 (1990).
[12] H. Riechert, D. Bernklass, J. P. Reithmaier and R. D. Schnell, Electron. Lett. **26**, 341 (1990).
[13] R. Kapre, A. Madhukar, K. Kariami, S. Guha and K. C. Rajkumar, Appl. Phys. Lett. **56**, 922 (1990).

[14] Y. Yin, H. Qiang, F. H. Pollak, D. C. Streit and M. Wojtowicz, Appl. Phys. Lett. **61**, 1579 (1992).
[15] A. Dimoulas, K. Zekentes, M. Androulidaki, N. Kornelios, C. Michelakis and Z. Hatzopoulos, Appl. Phys. Lett. **63**, 1417 (1993).
[16] K. V. Klitzing, Rev. Mod. Phys. **58**, 519 (1986).
[17] D. G. Seiler, G. B. Ward, R. J. Justice, R. J. Koestner, M. W. Goodwin, M. A. Kinch and J. R. Meyer, J. Appl. Phys. **66**, 303 (1989).
[18] G. Ji, U. K. Reddy, D. Haung, T. S. Henderson and H. Morkoc, Superlattices and Microstruct. **3**, 539 (1987).
[19] T. W. Kim, M. Jung, D. U. Lee, J. H. Kim, K. H. Yoo, J. Y. Lee and S. Y. Ryu, J. Appl. Phys. **82**, 4388 (1997).
[20] S. Niki, C. L. Lin, W. S. C. Chang and H. H. Wieder, Appl. Phys. Lett. **55**, 1339 (1989).
[21] W. Chen, M. Fritze, W. Walecki, A. V. Nurmikko, D. Ackley, J. M. Hong and L. L. Chang, Phys. Rev. **B45**, 8464 (1992).

Journal of the Korean Physical Society, Vol. 34, June 1999, pp. S443~S446

The Effect of Structural-Phase Transitions in Metalization Layers on Radiation Stability of NbN_X-GaAs Contacts

A. A. BELYAEV, R. V. KONAKOVA and V. V. MILENIN
Institute of Semiconductor Physics, Kiev, Ukraine

I. HOTOVY
Slovak Technical University, Bratislava, Slovakia

G. PIACZENSKI
Osnabrueck University, Osnabrueck, Germany

The problem of of structural-phase transitions in the metalization layers of NbN_X-GaAs Schottky contacts is considered. The results of scanning electron microscopy (SEM), energy dispersion X-rays (EDX) analysis and γ-irradiation effect on the electro-physical parameters of diodes are presented. It has been found that the radiation stability of NbN_X-GaAs contacts could be improved by varying the structural-phase content of NbN_X films.

I. INTRODUCTION

The problem related with the fabrication of metal-semiconductor (S) contact structures subjected to extreme effects remains unsolved till now. It is connected to the unsufficient understanding of the role of the various physical-chemical factors in mechanisms of formation and degradation of MS transitions subjected to various active effects that does not allow to predict intensity and directions of interactions of metals with semiconductor and, consequently, to determine a degree of their influence on electro-physical parameters of the contact. To the number of such not enough investigated factors, defining structure and properties of the interphase boundaries (IPB) of MS contacts, it is possible to refer the structural-phase transitions in the metalization layers influencing not only on sizes of transitional area of contact, but also on its structural-chemical homogeneity.

The NbN_X-GaAs structures subjected to the γ-irradiation from ^{60}Co were studied. The choice of niobium nitride as a barrier material was stipulated by that varying conditions of sputtering and annealing acceptable to obtain a film as in amorphous and crystalline conditions [1].

II. EXPERIMENTAL DETAILS

The layers of NbN_X were produced by magnetron sputtering of Nb (99.95 %) with various concentration of nitrogen in a gas mixture with an argon. GaAs of a n-type ($n \cong 5 \cdot 10^{16}$ cm^{-3}) with the (100) surface orientation was used as substrate. The fabricated contacts were annealed at T=850 °C for 10 s for the modification of the structural state of sputtered metal films.

The chemical content data of NbN_X layers was taken using the EDX microanalysis. The scanning electron microscopy (SEM) in a mode of secondary electrons was used to study the morphology of coated films.

To determinate of electrophysical parameters of contacts and their modifications subjected to γ-irradiation $I(V)$ dependences were measured. The used set of experiments yields the barrier height (φ_b), ideality factor (n), density of surface states (N_{ss}) and sizes of transitional area (δ/ϵ) [2].

III. RESULTS AND DISCUSSION

The study of coated film structure with the use of SEM (Fig. 1) has shown that sputtered layers consist of tiny particles or crystals whose dispersibility depends on the film fabrication conditions. Most homogeneous low-dispersive films were obtained with the gas mixture of low nitrogen content. In a case of mixture gas with high nitrogen concentration the formation of microclusters is observed. The annealing promotes the improvment of a structural homogeneity of films but one should note the formation of separate large-scale clusters.

The results of EDX analysis of NbN_X films before and after annealing are shown in Fig. 2. According to EDX spectra as-deposited layers which were obtained in different modes of sputtering do not contain contaminations. The annealing which promotes a modification of struc-

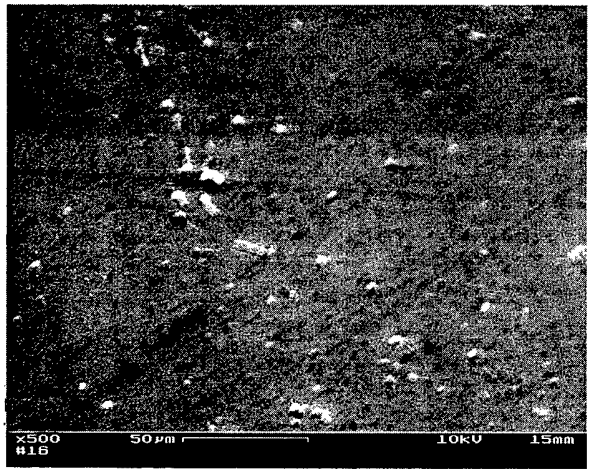

Fig. 1. The tipical SEM image of NbN_X films' surface.

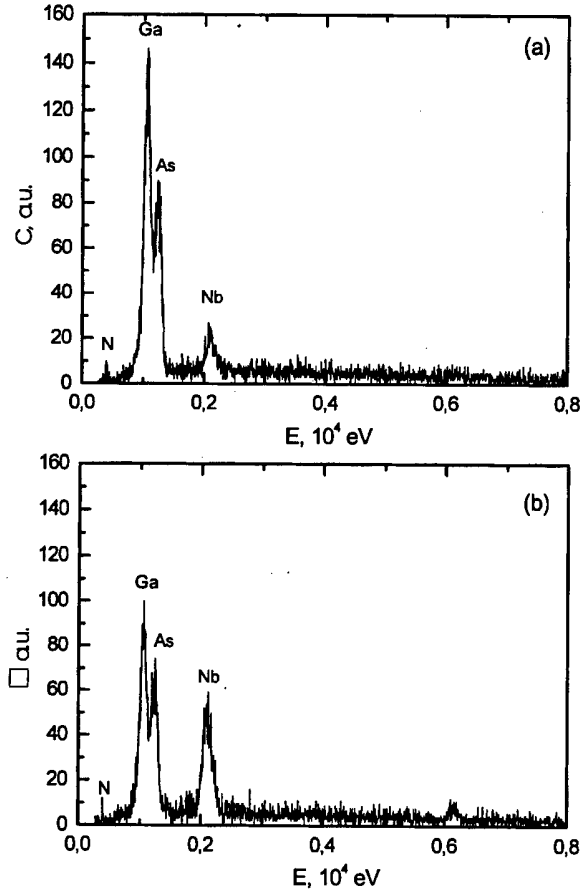

Fig. 2. The result of EDX analysis of NbN_X films before (a) and after annealing (b). The fabrication condition for the examined sample is clarified in text.

tural condition and morphology of sputtered layers [1] results to more uniform distribution of components in NbN_X layers.

The appearing of Ga, As peaks in the energy range from 1.1 KeV to 1.3 KeV is connected to scanning of semiconducting substrate. One can explain that the depth of generation of X-rays of Ga and As R_α lines whose critical potential on the order is more than an excitation energy of electrons from L shells considerably exceeds a thickness of NbN_X sputtered layer (0.5 μm). Taking into account an absorption of generated X-radiation it is possible to suppose that the observable modifications of spectral lines' intensities describe the modifications of nuclear structure of GaAs contact layers which define electrophysical parameters of heterojunctions.

One of the reasons of observable modifications in chemical structure of NbN_X layers before and after annealing could be the transformation of their nuclear structure accompanying with diffusion redistribution of components in sputtered films and their possible partial diffusion into semiconducting substrate. Actually, as it was marked in [1], due to modification of concentration of nitrogen in a working mixture and annealing the following structural phase transitions take place:

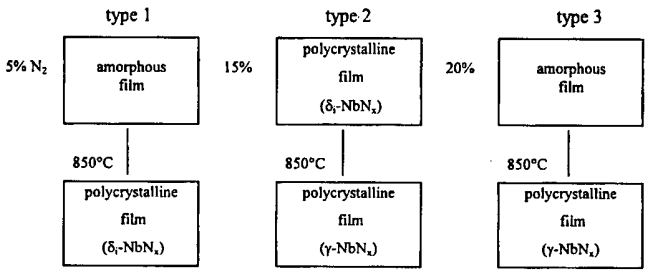

Amorphous layers of niobium nitride, obtained with low ($\leq$5 %) and high ($\geq$20 %) concentration of nitrogen, are in various structural modifications which define the type of a lattice after consequent crystallization due to temperature annealing [1].

Thus, conditions of film sputtering and their heat treatment influence on a chemical homogeneity, nuclear structure and morphology of metalization layers. This fact should be taken into account in a case of analysis of electrophysical parameters' stability of contact structures obtained in different technological modes subjected to the external extreme factors, in particular, ionizing radiation.

The modifications of the Schottky NbN_X-GaAs contats'parameters caused by 煆^{60} γ-irradiation dose are represented in Table 1, 2 and 3. One can observe that the γ-irradiation has pronounced influence to the ideality factor n, weakly changing barrier height φ_b, and practically does not affect on the magnitude of a reverse current Irev. In the last case any correlation between I_{rev} modifications versus γ-irradiation and conditions of contact structure's fabrication was not observed, *i.e.* there are no structural modifications of metalization layers. The recent study of the influence of 煆^{60} γ-irradiation on properties of metal-GaAs contacts the with monocomponent metallization has shown that in the investigated range of γ-irradiation dozes took place the sharp decrease of I_{rev}

Table 1. Set of clectrophysical parameters of NbN_X-GaAs Schottky contacts (type 1) versus γ-radiation dose.

(a) before annealing

	φ_B, eV	n	I_{rev}, μA	N_{ss}, 10^{-12} cm^{-2}	δ/ϵ_i, nm
as deposited	0.68	1.18	0.80	6.96	9.00
10^5 Rad	0.61	1.09	0.67	8.37	8.32
10^6 Rad	0.60	1.28	0.50	6.96	8.21
10^7 Rad	0.58	1.10	0.52	8.58	8.00

(b) after annealing T=850 °C

	φ_B, eV	n	I_{rev}, μA	N_{ss}, 10^{-12} cm^{-2}	δ/ϵ_i, nm
as deposited	0.54	1.41	31.65	5.95	7.58
10^5 Rad	0.55	1.80	20.80	1.98	7.68
10^6 Rad	0.55	1.70	13.15	2.98	7.68
10^7 Rad	0.51	1.62	20.40	4.01	7.23

Table 2. Set of clectrophysical parameters of NbN_X-GaAs Schottky contacts (type 2) versus γ-radiation dose.

(a) before annealing

	φ_B, eV	n	I_{rev}, μA	N_{ss}, 10^{-12} cm^{-2}	δ/ϵ_i, nm
as deposited	0.58	1.06	21.65	8.96	8.00
10^5 Rad	0.57	1.02	10.50	9.47	7.90
10^6 Rad	0.59	1.04	11.75	9.03	8.11
10^7 Rad	0.57	1.10	10.40	8.69	7.90

(b) after annealing T=850 °C

	φ_B, eV	n	I_{rev}, μA	N_{ss}, 10^{-12} cm^{-2}	δ/ϵ_i, nm
as deposited	0.58	1.53	0.18	4.48	8.00
10^5 Rad	0.58	1.51	0.20	4.67	8.00
10^6 Rad	0.71	1.50	0.42	4.11	9.27
10^7 Rad	0.65	1.50	0.13	4.38	8.71

Table 3. Set of clectrophysical parameters of NbN_X-GaAs Schottky contacts (type 3) versus γ-radiation dose.

(a) before annealing

	φ_B, eV	n	I_{rev}, μA	N_{ss}, 10^{-12} cm^{-2}	δ/ϵ_i, nm
as deposited	0.60	1.58	30.50	3.90	8.21
10^5 Rad	0.55	1.12	31.15	8.74	7.68
10^6 Rad	0.59	1.12	20.35	8.28	8.11
10^7 Rad	0.57	1.18	23.50	7.92	7.90

(b) after annealing T=850 °C

	φ_B, eV	n	I_{rev}, μA	N_{ss}, 10^{-12} cm^{-2}	δ/ϵ_i, nm
as deposited	0.64	2.04	1.10	0.93	8.61
10^5 Rad	0.63	1.79	1.15	1.83	8.51
10^6 Rad	0.70	1.70	1.50	2.49	9.18
10^7 Rad	0.64	1.74	0.95	2.30	8.61

(on the orders of magnitudes) [3,4]. This phenomenon is stipulated by processes of annihilation of initial structural defects that causes to magnification of effective life time of minority carriers and, therefore, Irev decrease. The absence of γ-irradiation influence on excess redundant reverse currents of NbN_X-GaAs diodes can be led to destruction of GaAs surface layers due to magnetron sputtering of NbN_X, *i.e.* the process of NbN_X film diffusion to GaAs is accompanied by destruction of a semiconducting lattice and capturing of Ga and As atoms by a growing film. The spectra of defects and their concentration depend on conditions of a film sputtering and determine reference values of diodes' reverse currents. At the same time the magnitudes of φ_b and n versus a doze of γ-irradiation depend on a structural condition of a metal film and have, as a rule, nonmonotonous character. Let us mark that the observable φ_b and n modifications are not connected only to nuclear structure of covered film, but also to type of structural-phase transition: "disorder-order" or "order-order" of the NbN_X film. Taking into account both φ_b and n dependence on concentration of surface electron states (SES) [2] it would be possible to explain the observed doze modification due to their mutual modifications by introducing SES. However, as follows from Tables 1, 2, 3 there is no precise correlation in doze dependencies φ_b and n. The calculations specify a nonmonotonous Nss modification with a doze of γ-irradiation and modification of a thickness of the transitional layer. The extrema of theese magnitudes do not coincide and corespond to different dozes of γ-irradiation. In this case it is necessary to assume that the correlation of sputtered metal films' structure and the degree of modification of electro-physical parameters of SB for fixed dozes of γ-irradiation will be reduced because of structural-chemical heterogeneities of MS contacts. The role of structural-chemical heterogeneities of contacts in mechanisms of formation and degradation of SB based on GaAs were specified in [5].

Thus, the results of our experiments allow to conclude that modification of the structural-phase content of metalization layers results to an increasing of MS contacts radiation stability. However, the choice of optimum technology modes of contacts' fabrication for these purposes is closely connected to a solution of a problem of maintenance of structural-chemical homogeneity of the MS transition. The work was supported by STCU under the project 464. A. A. Belyaev would like to thank DAAD for given grant.

REFERENCES

[1] J. Brcka and I. Hotovy, Vacuum. **64**, 1407 (1995).

[2] V. I. Strikha, E. V. Buzaneva and I. A. Radzievsky, *Semiconductor Schottky Barrier Devices*, Moscow., Sov. Ra-

dio., 248 (1974) (in Russian).

[3] J. Breza, R. A. Ismailov, R. V. Konakova, S. Liday, V. G. Lyapin, V. V. Milenin, A. A. Naumovets, I. V. Prokopenko, V. A. Statov and Yu. A. Tkhorik, Functional Materials **2**, 282 (1995).

[4] *Radiation Effects in Layered Structures Based on* A_3B_5, O. Yu. Borkovskaya, N. L. Dmitruk, R. V. Konakova *et al.* (Institute of Physics of Academy of Sciences of USSR, Kiev, 1986), p. 68 (in Russian).

[5] O. Yu. Borkovskaya, N. L. Dmitruk, R. V. Konakova, V. G. Lyapin, V .V. Milenin, V. A. Statov, Yu. A. Tkhorik and J. Liday, J. of Electr. Eng. **46**, 402 (1995).

Journal of the Korean Physical Society, Vol. 34, June 1999, pp. S447~S450

Reactions Between Phases and Electronic Processes at the TiB_x (TiN_x)-GaAs Heterostructures Interfaces

V. V. MILENIN, I. B. ERMOLOVICH, R. V. KONAKOVA, V. G. LYAPIN,
A. A. BELYAEV and D. I. VOITSIKHOVSKIY

Institute of Semiconductor Physics of the National Academy of Sciences of Ukraine, 45 Prospect Nauki, 252650 Kiev-28, Ukraine

O. D. SMIJAN

E. O. Paton Electric Welding Institute of the National Academy of Sciences of Ukraine, 11 Bozhenko Str., 252650 Kiev-5, Ukraine

V. N. IVANOV and N. S. BOLTOVETS

SRI "Orion", 8a Eugene Pottier Str., 252057, Kiev-57, Ukraine

Using structural, electrophysical and photoluminescence methods, we investigated the effect of rapid thermal annealing (RTA) on the properties of TiB_x (TiN_x)-n-n^+-GaAs structures. It was shown that the changes in the spectra of point defects in the near-contact regions resulting from RTA at T=400, 600 and 800 °C are due to the interactions between phases in the metallization materials and the substrate. Judging from the heat stability of the electrophysical parameters of Schottky barriers, the TiN_x-n-n^+-GaAs surface-barrier structures have higher heat tolerance.

I. INTRODUCTION

During the last years it has been found that the use of conventional metal materials (such as titanium, platinum, chromium, *etc.*) for formation of highly reliable barrier contacts to gallium arsenide is limited by the interactions between phases at the interfaces-from the sides of both a metal (phase formation) and gallium arsenide (mass transport of a metal into semiconductor, appearance of the recombination-generation centers) [1,2]. That is why the contacts made of the alloys of refractory metals nitrides and borides (that practically do not chemically interact with semiconductor) are proposed as an alternative to the barriers made of pure metals [3,4]. However, there are practically no direct experimental evidences of the absence of such contacts interaction with gallium arsenide.

Here we present some results of our investigations of the effect of rapid thermal annealing (RTA) at temperatures from 400 to 800 °C on the properties of TiB_x (TiN_x)-n-n^+-GaAs interfaces. The studies have been performed using structural, electrophysical and photoluminescence methods.

II. EXPERIMENTAL

We have studied the TiB_x (TiN_x)-n-n^+-GaAs surface-barrier structures. The Te-doped epitaxial layers of n-GaAs were VPE-grown on the heavily Te-doped Czochralski-grown GaAs (100). The epitaxial structures were industrially manufactured in accordance with the ETO.035.026 standard. The dopant concentration in the n-regions of different samples varied from 3 to 4×10^{16} cm^{-3}, while that in the n^+-regions was $\geq 2\times10^{18}$ cm^{-3}. The n-region (substrate) thickness was $\sim 5\div 6$ μ (300 μ).

The TiN_x and TiB_x layers, 50 nm thick, were deposited onto the n-n^+-GaAs structures (previously exposed to photon cleaning) using magnetron sputtering. The deposition rate was $5\div 10$ A/s for both metallization systems, the discharge current being 0.2~0.4 Å. The electron-diffraction patterns taken for the initial metal layers demonstrated only the substantially blurred diffraction lines (see Fig. 1(a) for TiB_x films and Fig. 1(b) for TiN_x films). This fact indicates that the deposited films were quasiamorphous.

III. RESULTS AND DISCUSSION

Shown in Fig. 2 are the Schottky barrier height φ_B and the ideality factor n vs the annealing (for 60 s) temperature curves. They were calculated from the forward branches of the $I-V$ curves for the TiB_x-n-n^+-GaAs (curves 1, 3) and TiN_x-n-n^+-GaAs (curves 2, 4) surface-barrier structures. One can see that the TiN_x-n-n^+-

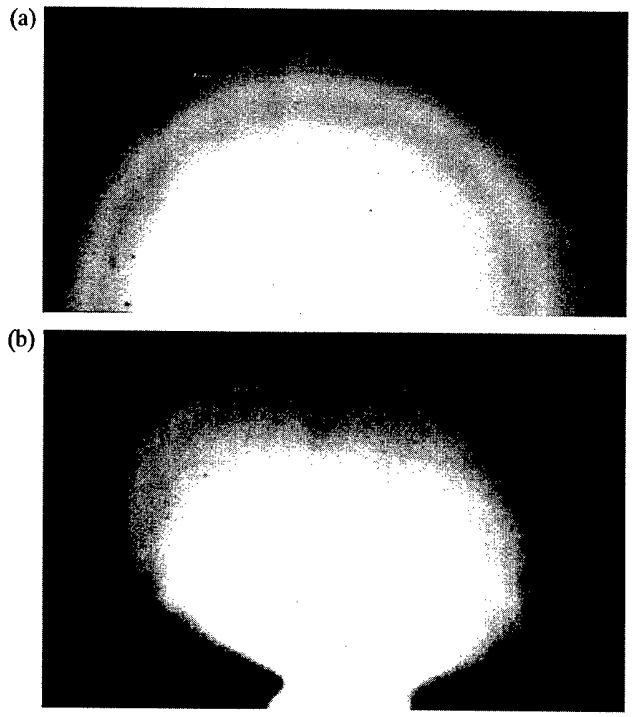

Fig. 1. Electronography pattern of TiB_x (a) and TiN_x (b) layers.

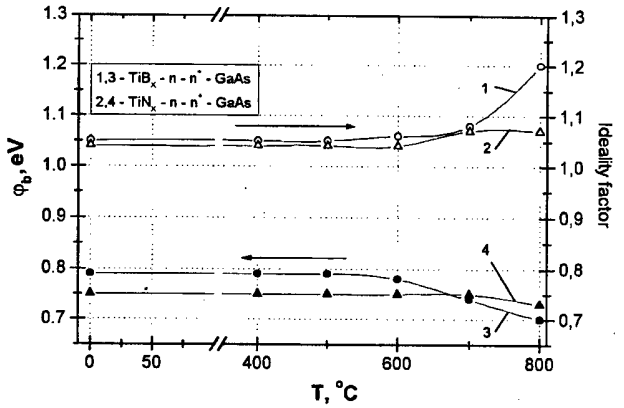

Fig. 2. Barrier height φ_B and ideality factor n vs annealing temperature curves.

GaAs diode structures demonstrate higher heat stability: their Schottky barrier height and ideality factor practically do not change under thermal annealing at temperatures up to 700 °C.

These results are supported with the Auger concentration depth profiles for the components of both type contacts taken for the initial and annealed test structures (Fig. 3(a), b-TiB_x-n-n^+-GaAs structures, Fig. 4(a), b-TiN_x-n-n^+-GaAs structures). An analysis of these profiles has shown that both initial and annealed (at T=400 and 600 °C) test structures have practically the same interfaces whose spreading due to heat annealing is but slight; the layered structure of contacts is stable. Howev-

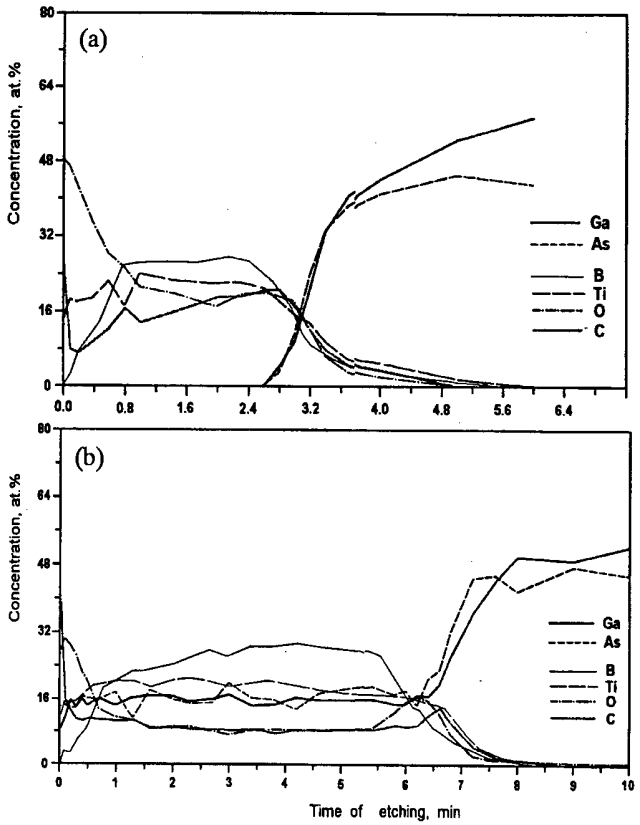

Fig. 3. Element concentration depth profiles for the TiB_x-n-n^+-GaAs Schottky contacts: (a)-initial samples; (b)-after annealing at T=800 °C.

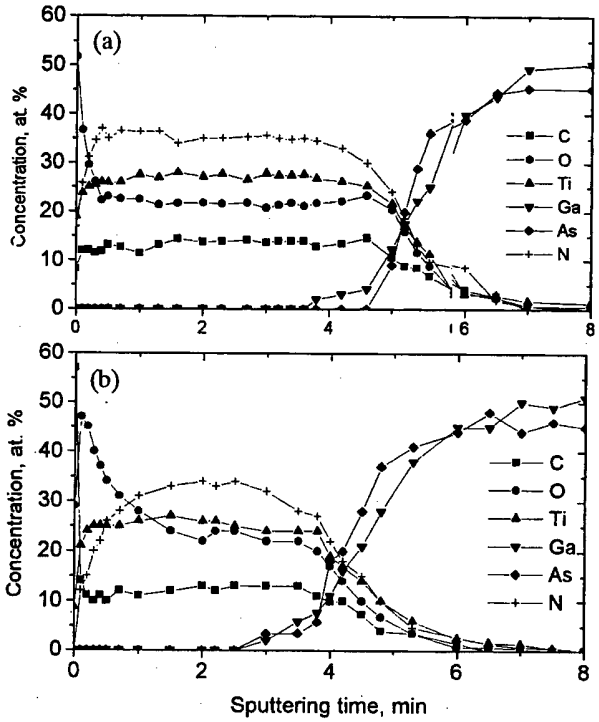

Fig. 4. Element concentration depth profiles for the TiN_x-n-n^+-GaAs Schottky contacts: (a)-initial samples; (b)-after annealing at T=800 °C.

er, the titanium nitride and boride layers are chemically nonuniform. In addition to Ti, N and B, they contain also large quantities of carbon and oxygen. Presence of oxygen in the reaction area is accompanied with the titanium oxidation that is competitive with the titanium interaction with nitrogen. As a result, the titanium oxides, oxinitrides and oxiborides are formed. Presence of carbon prevents the reaction in the film to end. Thus the resulting film coatings are not in the state of thermodynamic equilibrium.

When the annealing temperature is increased up to 800 °C, then further changes of phase composition take place in the TiB_x and TiN_x films. For TiB_x-n-n^+-GaAs structures intermixing of components occurs (see Fig. 3(b)), while in the TiN_x-n-n^+-GaAs structures the transition layer spreading grows (see Fig. 4(b)). The latter fact provides higher heat stability of the TiN_x-n-n^+-GaAs contact as compared with the TiB_x-n-n^+-GaAs one. This agrees with the electrophysical parameters of the surface-barrier diode structures (Fig. 2).

Another factor affecting the physical properties of the barrier contacts of both types is the physico-chemical structure of the contact transition layer. One can expect that during the nitride and boride layers deposition at the initial stages of their formation there exists a high probability for the formation, in the GaAs surface region, of the $GaAs_xB_{1-x}$ ($GaAs_xN_{1-x}$) solid solutions in the case of TiB_x (TiN_x) metallization.

Formation of solid solutions based on GaAs and titanium and boron nitrides was confirmed by both mass spectrometry and photoluminescence studies-see Table 1 and Fig. 5. From the analysis of the photoluminescence spectra shown in Fig. 5 one can conclude that:
– more photoluminescence bands are observed in the GaAs near-contact region as compared to the GaAs substrate; this fact indicates at a production of structural and impurity defects in a thin near-contact layer of GaAs during contact formation and annealing;
– all the observed photoluminescence bands increase their intensity after heat annealing at T=400 and 600 °C, while heat annealing at T=800 °C leads to the intensity decrease, or even to the disappearance of the bands;
– there are excitonic bands in the photoluminescence spectra taken from the contact side: they are located at 1.54 eV for the initial TiB_x-n-n^+-GaAs sample and

Table 1. Mass spectrometry of the TiB_x (TiN_x)-n-n^+-GaAs structures.

Structure	Atomic units mass	Element/ compound	Ion current in the transition layer, arb. unit.
TiB_x-n-n^+ -GaAs	75	As	$\leq 10^4$
	155	GaBAs	10^2
	192	GaAsTi	2×10^2
TiN_x-n-n^+ -GaAs	75	As	$\leq 10^2$
	172	$GaAsN_2$	5
	192	GaAsTi	3

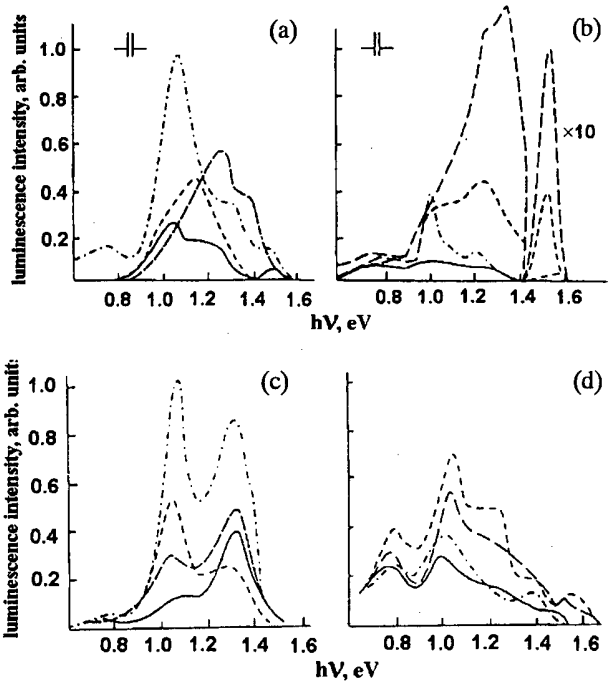

Fig. 5. Photoluminescence spectra of the TiB_x-n-n^+-GaAs (a), (b) and TiN_x-n-n^+-GaAs (c), (d) struc- tures taken at T = 77 K from the substrate side (a), (c) and from the metallization layer side (b), (d): initial (——) and after annealing at 400 (- - - - -), 600 (– – –) and 800 °C (·····).

at 1.52 eV for the TiB_x-n-n^+-GaAs samples annealed at T=400 and 600 °C, while there was no excitonic band in the samples exposed to heat annealing at T=800 °C; for the TiN_x-n-n^+-GaAs samples this band lies at ~1.50 eV (initial sample and after annealing at T=800 °C), while after annealing at T=400 and 600 °C it is at ~1.54 eV;
– the photoluminescence spectra of the TiN_x-n-n^+-GaAs structure taken from the contact side are more stable against heat action than those of the TiB_x-n-n^+-GaAs contacts;

The shown photoluminescence spectra of the contacts of both types-and, especially, presence in them of the excitonic bands (whose peaks lie at higher energies than that of GaAs) indicating at the fact that in the GaAs near-contact region thin and perfect interlayers of the compounds whose gaps exceed that of GaAs are formed-support the results of mass spectrometry. They are also in a good agreement with the results of the electrophysical parameters measurements for the surface-barrier structures studied.

IV. CONCLUSIONS

Thus our investigations of structural, photoluminescence and electrophysical properties of the TiB_x (TiN_x)-n-n^+-GaAs surface-barrier structures enabled us to fol-

low the changes in the spectra of the point defects in the near-contact regions resulting from RTA at T=400, 600 and 800 °C. We have shown also that such changes are due to the interactions between phases in the metallization materials and the substrate and found that the TiN_x-n-n^+-GaAs surface-barrier structures are more stable against heat action (judging from the heat stability of the electrophysical parameters of Schottky barriers).

ACKNOWLEDGMENTS

This work was partially supported by the Science and Technology Center in Ukraine grant no. 464.

REFERENCES

[1] VLSI Electronics, *Microstructure Science* (Eds. N. G. Einspruch and W. R. Wisseman), Vol. 11 (GaAs Microelectronics). Academic Press, Orlando-San Diego-New York-London-Toronto-Montreal-Sydney-Tokyo, 1985.

[2] J. Breza, E. F. Venger, R. V. Konakova, V. G. Lyapin, V. V. Milenin, V. A. Statov and Yu. A. Tkhorik, Poverkhnost. No. 5, pp. 110-127 (1998).

[3] N. V. Talalikhin, B. V. Markin and V. V. Chikun. Elektronnaya Technika, Ser. 1. Elektronika SVCh. No. 4, p. 38 (1994).

[4] A. A. Belyaev, I. Hotovy, E. F. Venger, R. V. Konakova, V. V. Lyapin, V. V. Milenin, Yu. A. Tkhorik and G. N. Kashin, Zhurn. Tekhn. Fiz. **68**, 63 (1998).

Journal of the Korean Physical Society, Vol. 34, June 1999, pp. S451~S454

Asymmetric Double Quantum Well Structure as a Tunable Detector in the Far-Infrared Range

Uk SHIN

Department of Material Science, Advanced Institute of Military Science and Technology, Seoul 139-799

Naeho SHIN, Myoung-jin PARK, Seung-joo LEE

Department of Physics, Korea Military Academy, Seoul 139-799

The eigenvalues and the wave functions of GaAs/$Al_xGa_{1-x}As$ asymmetric double quantum well structure have been calculated by using of complex energy method. Based on theoretical calculations, tuning ranges from 9 to 14 μm are predicted for the proposed asymmetric coupled-quantum-well structure. In addition we calculated the energy eigenvalues and the wave functions of an electron in GaAs/$Al_xGa_{1-x}As$ single quantum well structure (including δ-perturbation). The variation in E_1, the ground state energy eingenvalue of the electron, depends on the strength and position of the perturbation within the well.

I. INTRODUCTION

Long-Wavelength Infrared (LWIR) imaging in the wavelength range from 8 to 14 μm has been attractive to many researchers, especially military scientists, owing to its own physical properties such as propagation stability in atmosphere due to very small absorption of photon waves by water molecules or CO_2 and the maximum emission energy of the block body radiation at room temperature [1,2]. Thus LWIR imaging by using HgCdTe (MCT) has been widely used in both military and civil applications like low-light night surveillance TV, missile target detect and guide, and building security. However, despite its own advantage in good gain and detection rate, MCT has its characteristic problems, that is, such as material unstability, difficulties in crystal growth, high cost, and nonuniform pixel. Thanks to the recent state-of-art technology in multi quantum-well structures, the III-V semiconductor compounds such as GaAs/AlGaAs have been introduced as the next-generation of the LWIR imaging detectors, so called Quantum Well Infrared Photodetector (QWIP), replacing for the MCT [3]. Technical advantage of QWIP over MCT relies on the fact that detection wavelength depends on the width of the quantum well and the barrier height and thus a variety of tunable detectors can be fabricated corresponding to required capabilities of them [4–6].

In this paper, the asymmetric coupled-quantum-well structure consisted of a pair of quantum wells separated by a barrier (about 30 Å) narrow enough that considerable interaction occurs between electronic states in these two adjacent wells. The coupled quantum well structures were designed to have only two confined states, the ground state E_1 and the first excited state E_2. The infrared radiation is absorbed via the intersubband resonance absorption (for the incident photoenergy $\hbar\omega = E_2 - E_1$), and the photoexcited electrons can tunnel out of the well to produce photoelectrons. Both symmetric coupled-quantum-well and the asymmetric coupled-quantum-well structures do give good tunability. However, the former cannot be used for fabricating a $\lambda = 8 \sim 12$ μm photodetector because of the insufficiency resonant absorption energy and the lower absorption coefficient. In contrast, the asymmetric coupled quantum well photodetectors do give a large enough eigenenergy difference $\Delta E = E_2 - E_1$ to detect $\lambda = 8 \sim 12$ μm atmospheric window spectral region. Based on theoretical calculations, tuning ranges from 9 to 14 μm are predicted for the asymmetric coupled-quantum-well structure. This tuning capability is achieved by the applied electric field in the 0~100 kV/cm range.

II. CALCULATIONS OF ENERGY AND LIFETIME BY COMPLEX ENERGY METHOD

For the sake of simplicity, the real potential energy of the conduction electrons in the multi quantum wells is approximated to an array of rectangular shape potential energy as shown in Fig. 1(a). Thus the energy eigenvalues in every well can be obtained by solving the time-

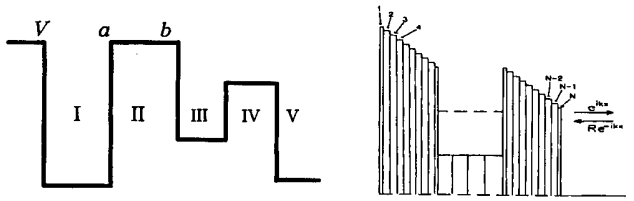

(a) (b)

Fig. 1. (a) Schematic description of an array of rectangular potential, (b) A simplified potential model of a dc biased superlattice.

independent Schrödinger equation which is given by

$$-\frac{\hbar^2}{2m_n}\frac{d^2\psi_n}{dx^2} + V_n\psi_n = E\psi_n \tag{1}$$

where m_n is the effective mass and V_n is the effective potential energy in region n which is assumed to be constant.

Typical solutions of the above equation are

$$\psi_{\rm II}(x) = A_n e^{k_n(x-a)} + B_n e^{-k_n(x-a)}, \tag{2}$$

$$\psi_{\rm III}(x) = A_{n+1} e^{k_{n+1}(x-b)} + B_{n+1} e^{-k_{n+1}(x-b)}, \tag{3}$$

where both A_n and B_n are the coefficients of the right- and left-propagating plane waves of the nth region, respectively, with the wave number $k_n = \left[-\frac{2m_n}{\hbar^2}(E - V_n)\right]^{\frac{1}{2}}$. Application of the boundary conditions, *i.e.*, the continuities of both ψ and $\frac{1}{m}\frac{d\psi}{dx}$ at the boundary ($x = b$) gives rise to the following equation in matrix form [6].

$$\begin{pmatrix} A_{n+1} \\ B_{n+1} \end{pmatrix} = \frac{1}{2}\begin{pmatrix} 1 & 1 \\ 1 & -1 \end{pmatrix} \times \begin{pmatrix} e^{k_n d_n} & e^{-k_n d_n} \\ \frac{m_{n+1}k_n}{m_n k_{n+1}} e^{k_n d_n} & -\frac{m_{n+1}k_n}{m_n k_{n+1}} e^{-k_n d_n} \end{pmatrix} \begin{pmatrix} A_n \\ B_n \end{pmatrix} \tag{4}$$

Under the external biased electric field induced from left to right as shown in Fig. 1(b), the localized electrons in a dc biased superlattice can only propagate into the righthand side (collector side) due to the potential barrier which is increasing gradually toward the left side. Thus we put an additional boundary condition,

$$A_l = 1, \quad B_l = 0, \quad and \quad B_r = 0 \tag{5}$$

where both l and r refer to the left- and rightmost regions, respectively, that is, there exist only the right-propagating waves in the left- and rightmost regions. Since the electrons in the dc biased superlattice can not stay permanently in an energy level (rather stay in a metastable state), the corresponding energy levels are expressed by [7]

$$E = E_0 - i\frac{\Gamma}{2} \tag{6}$$

where E_0 is the energy level in the metastable state and Γ represents the energy instability which is related to the electronic lifetime given by

$$\Delta t = \frac{\hbar}{\Gamma} \tag{7}$$

The approximated solutions are obtained numerically using the subroutine ZANLYT in program IMSL.

III. NUMERICAL RESULTS AND DISCUSSION

1. Asymmetric Double Quantum Well Structure

The model device consists of two GaAs/$Al_{0.32}Ga_{0.68}As$ asymmetric quantum wells connected next to each other by a barrier (a barrier-well-barrier-well-barrier structure with the corresponding widths, 50-60-30-12-50 Å) as shown in Fig. 2. With application of a dc biased external field ranged from 0 to 100 kV/cm to the device, the complete model QWIP having tuneable IR detecting range in wavelengths can be established (See Fig. 3). The resultant calculations show both the schematic description of the electron wavefunctions and the probability of finding the electron in the device given by Fig. 2 and 4, respectively. As shown in from Fig. 2 to Fig. 5, quantum confinement results in energy level increase in the narrow well so that the ground state energy in the narrow well is equivalent to the first excited state in the wide well. Since the probability of finding an electron in E_2 state (the first excited state in the first well and the ground state in the second well, respectively) in the

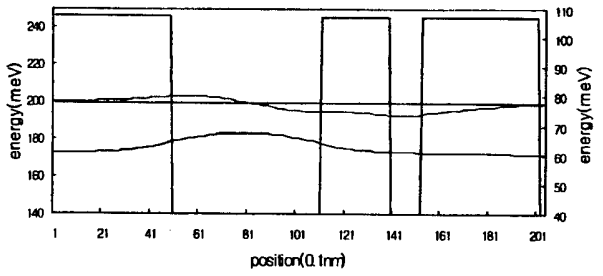

Fig. 2. Asymmetric double quantum well (0 kV/cm).

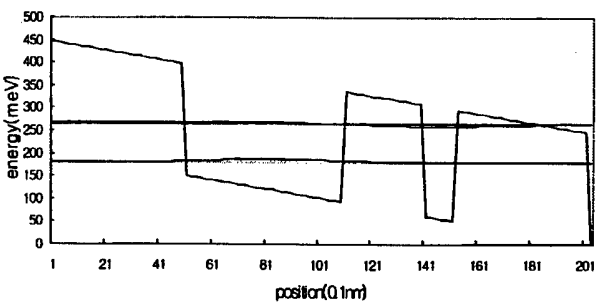

Fig. 3. Asymmetric double quantum well (100 kV/cm).

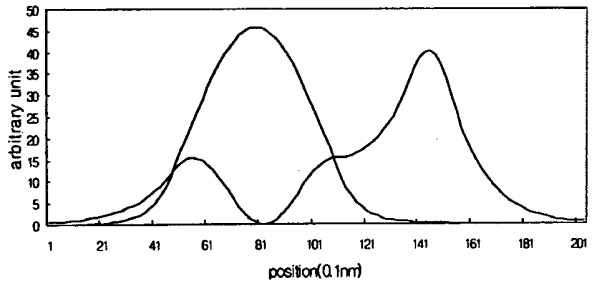

Fig. 4. Initially located wave packet (0 kV/cm).

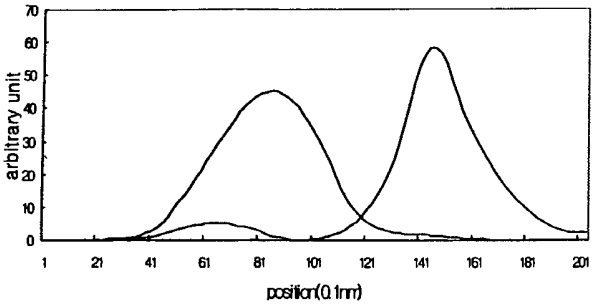

Fig. 5. Initially located wave packet (100 kV/cm).

narrow well is more than twice in the zero biased case and even ten times in the 100 kV biased case than that in the wide well, we expect that the detecting mechanism is more likely to be governed by electron tunnelling from the first wide well to the second narrow well after transition from the E_1 state to the E_2 state in the wide well. From the Table 1 and 2, we see that the tuneable detecting range varies from 9 to 14 μm dependent of the bias voltages and the very small lifetime of the E_2 state clearly shows the metastable characteristics of transition electrons.

Table 1. Energy levels and detection wavelength of asymmetric double quantum well.

bias (kV/cm)	E_1 (meV)	E_2	E_3	$E_2 - E_1$	detection wave length (μm)
0	61	199	244	138	8.85
20	84	214	268	130	9.40
40	109	229	291	120	10.18
60	133	242	314	109	11.20
80	156	255	337	99	12.34
100	180	267	360	87	14.04

Table 2. Energy levels and life time of asymmetric double quantum well.

	E_1		E_2		E_3	
bias (kV/cm)	energy level (meV)	life time (ps)	energy level (meV)	life time (ps)	energy level (meV)	life time (ps)
0	61	0.584E3	199	0.310	244	0.222
20	84	0.278E3	214	0.206	268	0.164
40	109	0.144E3	229	0.154	291	0.151
60	133	0.753E2	242	0.113	314	0.135
80	156	0.39E2	255	0.102	337	0.115
100	180	0.199E2	267	0.0087	360	0.094

2. Single Quantum Well (Including δ-perturbation) Structure

The single quantum well structure, which has a δ-perturbation within 40 Å GaAs well, sandwiched by 500 Å $Al_{0.26}Ga_{0.74}As$ barriers.

In the case of positive perturbation (from Fig. 6 to Fig. 10 and Table 3 and Table 4) E_1, the ground state energy of an electron, is proportional to the strength of the perturbation and is getting lower as the position of the perturbation is getting closer to the barrier. For the negative perturbation, it is vice versa (Table 5, 6).

As seen from Figure 2 and Figure 10, the variation of

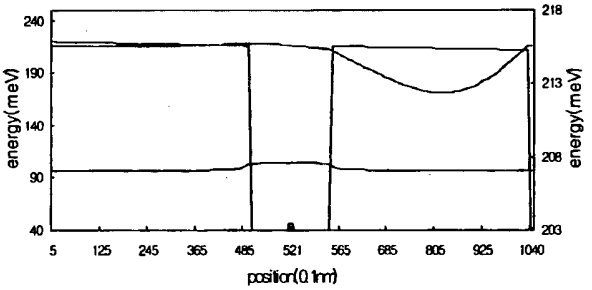

Fig. 6. δ-perturbation (42.4 meV) in square well.

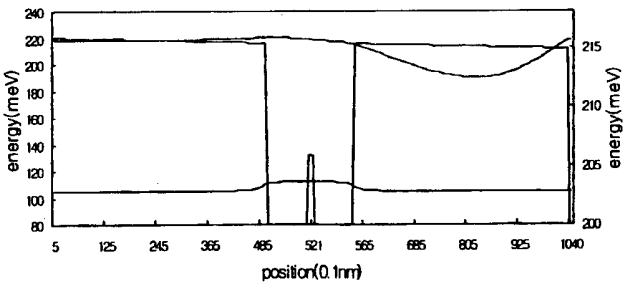

Fig. 7. δ-perturbation (127.2 meV) in square well.

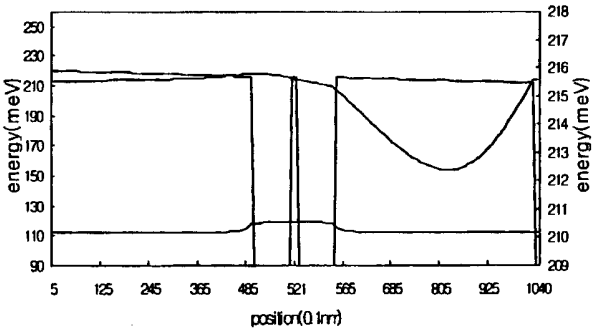

Fig. 8. δ-perturbation (212 meV) in square well.

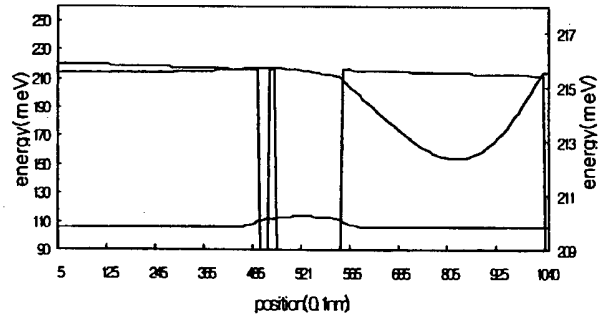

Fig. 9. Left located δ-perturbation.

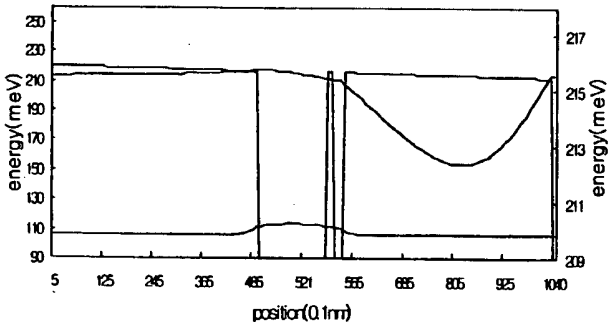

Fig. 10. Right located δ-perturbation.

Table 3. Energy levels and life time of due to the δ-perturbation in square well.

strength of δ-perturbation (+meV)	E_1 energy level (meV)	E_1 life time (ps)	E_2 energy level (meV)	E_2 life time (ps)
0	93.5	0.26E14	215.5	0.24E1
42.4	97.5	0.65E14	215.5	0.24E1
84.8	101.4	0.3E14	215.5	0.24E1
127.2	105.2	0.16E14	215.5	0.24E1
169.6	108.9	5.7E14	215.5	0.24E1
212	112.5	0.10E14	215.5	0.24E1

Table 4. Energy levels and life time of due to the position of δ-perturbation.

position of δ-perturbation (+212 meV) from left barrier (Å)	E_1 energy level (meV)	E_1 life time (ps)
4	105.9	0.77E13
12	110.1	0.28E16
20	112.5	0.26E14
28	110.1	0.15E11
36	105.9	0.13E14

the ground state energy of an electron due to the barrier or δ-perturbation, which is changing location within the well, is similar each to each. This result is in good agreement with expectations.

IV. CONCLUSIONS

Table 5. Energy levels and life time of due to the δ-perturbation in square well.

strength of δ-perturbation (−meV)	E_1 energy level (meV)	E_1 life time (ps)
0	93.5	0.26E14
20	91.6	0.86E13
40	89.7	0.13E14
60	87.7	0.52E14

Table 6. Energy levels and life time of due to the position of δ-perturbation.

position of δ-perturbation (−60 meV) from left barrier (Å)	E_1 energy level (meV)	E_1 life time (ps)
4	88.9	0.76E10
12	88.3	0.11E11
20	87.7	0.52E14
28	88.3	0.24E15
36	89.3	0.19E14

At temperatures above absolute zero, all bodies emit infrared radiation. A large fraction of total IR radiation emitted naturally from objects at ambient temperatures falls within the LWIR band. By using the complex energy method, we calculate energy levels and life times of the metastable state of an electron in the various GaAs/$Al_xGa_{1-x}As$ quantum well structures, which absorb LWIR photons. Under the presence of the external dc biased field varying from 0 to 100 kV/cm which is gradually increasing from the right (emitter) to the left (collector), the numerical results show the tuneable detecting range covering from 9 to 14 μm as a function of the bias voltages, the metastable characteristics of transition electrons due to the very small lifetime of the E_2 state, and the main detecting mechanism, *i.e.*, a transition-tunnelling mechanism. Consequently, the obtained results in this paper can be used as theoretical background for future fabrication of various IR detectors having detecting capability of wide range of photon frequencies.

REFERENCES

[1] B. F. Levin, J. Appl. Phys. **74**, R1 (1993).
[2] T. Whitaker, Compound Semiconductor, Spring II, (1998).
[3] Y. Huang and C. Lien, J. Appl. Phys. **74**, 2598 (1993).
[4] S. V. Bandara, S. D. Gunapala, J. K. Liu, E. M. Luong, J. M. Mumolo, W. Hong, D. K. Sengupta and M. J. McKelvey, Appl. Phys. Lett. **72**, 2427 (1998).
[5] C. J. Chen, K. K. Choi, W. H. Chang and D. C. Tsui, Appl. Phys. Lett. **72**, 7 (1998).
[6] J. W. Choe, H. J. Hwang, A. G. Perera, S. G. Matsik and M. H. Francombe, J. Appl. Phys. **79**, 7510 (1996).
[7] L. D. Landau and E. M. Lifshitz, Quantum Mechanics : Non Relativistic Theory, Pergamon, 555 (1997).

Journal of the Korean Physical Society, Vol. 34, June 1999, pp. S455~S457

Determination of Empirical Relationship between Vapor and Solid Phase Composition of GaInAsP in MOVPE

Dae Kon OH, Kwang Eui PYUN, Hyun Soo KIM* and In-Hoon CHOI*

ETRI Telecommunication Basic Research Laboratory, Taejon 305-350
**Department of Materials Science and Engineering, Korea University, Seoul 136-701*

GaInAsP ($\lambda = 1.05 \sim 1.55$ μm) lattice matched to InP were successfully grown by using a LP-MOVPE. The As solid composition with the AsH_3 gas composition shows the non-linear relation, and the As distribution coefficient is severely affected by the amount of Ga while Ga distribution coefficient is not affected by group V. From the analytical fitting between wavelength and gas composition, input gas composition in MOVPE can be exactly estimated for designed wavelength of GaInAsP.

I. INTRODUCTION

Because of its large wavelength coverage in the infrared region, InP-based quaternary system is very important for optoelectronic applications in the fiber communication. Empirical determination of the exact relationship between the vapor and solid phase composition in metal organic vapor phase epitaxy (MOVPE) is indispensable not only for the precise composition control but also for the deep understanding of growth mechanism in multiple composite, *i.e.* $Ga_xIn_{1-x}As_yP_{1-y}$. Several groups have studied the complicated sticking behaviors between them [1–4].

In general, the relationship between gas composition in group III might be influenced by the gas composition of group V and vice versa, group III might influence the relationship between gas composition in group V. However, the dependencies of solid compositions for the group III and group V species on the vapor phase compositions have been reported that the solid composition of each group is independent of another group vapor phase composition [5–7].

In this paper, we are to consider the composition relationship for GaInAsP quaternary system (1.05~1.55 μm) which is lattice matched to the InP substrate. The general solution for the growth function in MOVPE has not been sufficiently developed yet, in spite of the numerous studies on the growth model [8,9], because there are so many input parameters to be considered and their complexities during the growth. For the practical point of view, the exact relationships between the wavelength of the bulk quaternary film and mole fraction of input gas sources were obtained in our reactor system with the strain-free film condition. The relative incorporation behaviors in group III and V were also observed by means of intra, and inter-group variation effect. And, the above phenomena will be discussed in detail by means of the words of relative distribution coefficients.

II. EXPERIMENTAL

The MOVPE growth was performed in an AIX 200/4 system with a horizontal gas flow. Epitaxial layers of $Ga_xIn_{1-x}As_yP_{1-y}$ quaternary alloys were grown on S doped InP(001) substrate. The growth conditions were fixed at 650 °C and 100 mbar. The growth rate was varied on composition from 2.0 to 3.6 μm/hour, which was measured by cross-section scanning electron microscopy (SEM). The compositions of quaternary layers were determined by the measurements of X-ray rocking curve and photoluminescence.

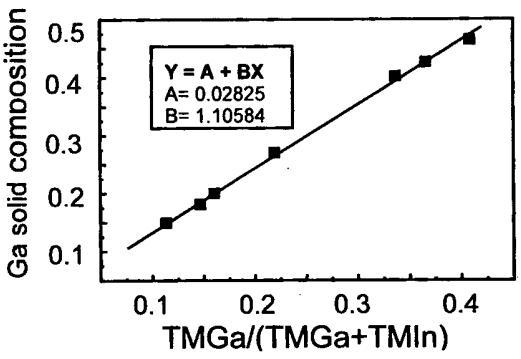

Fig. 1. The plot of group III solid composition vs. gas phase mole fraction for GaInAsP lattice matched to InP.

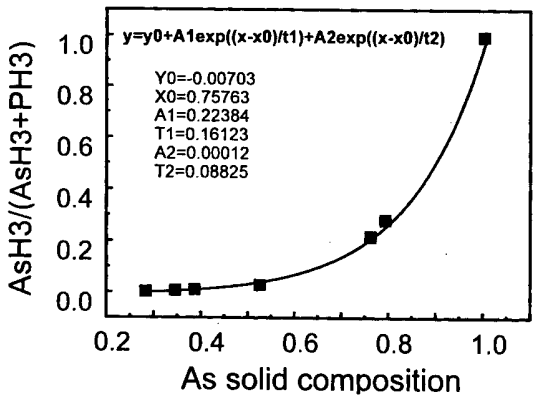

Fig. 2. The relationship between As solid composition and AsH_3 mole fraction in GaInAsP.

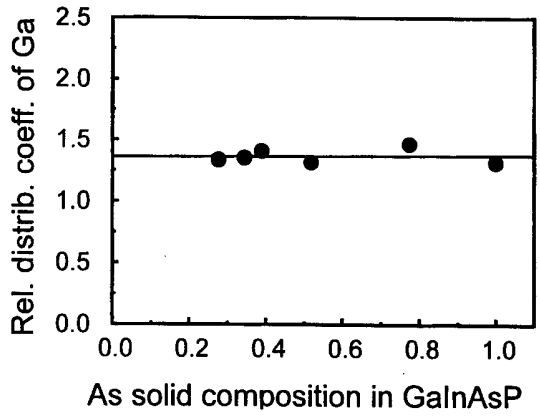

Fig. 3. The relation between relative distribution coefficient of Ga and As solid composition of GaInAsP lattice matched to InP.

III. RESULTS AND DISCUSSIONS

Fig. 1 shows the plot of group III solid composition with the gas phase mole fraction for GaInAsP, which is lattice, matched to InP substrate. The relationship between them shows the good linear fit for experimental points. The value of incorporation coefficient for Ga atom is 1.1, which means that the Ga is more easily incorporated into the solid surface than the In. Therefore, we can control the group III solid composition of quaternary epitaxial layer only by varying the gas composition of group III.

The relation between AsH_3 gas composition and the As solid composition is not linear but looks like an exponential shape as shown in Fig. 2. Some analytical models were proposed to fit the empirical data in group V by MBE groups [5,9]. However, the fitting of our MOVPE data to those formula did not so successful even though we had some trial and errors. These results might be caused from the complexities of reactor design and growth conditions in MOVPE. Therefore, through the direct analytical fitting procedure, we observed that the series sum of two exponential functions could be well fitted for empirical data. The general formula for statistical fitting is as follows; $y = y_0 + a\exp((x - x_0)/t_1) + b\exp((x - x_0)/t_2)$. From the fitting of empirical data, we obtained the analytical function of $y = 0.22\exp((x - 0.76)/0.16)$ in approximation, where y is AsH_3 mole fraction and x is As solid composition in GaInAsP. This relation means that one species, here As atom, has the absolutely larger value of incorporation coefficient than the other one, P atom, in group V. The constants of above analytical function strongly depend on the reactor design and growth parameters, so we can justify those values as reactor characteristic constants.

Figure 3 shows the relation between relative distribution coefficient of Ga atom and As solid composition of GaInAsP lattice matched to InP. Here, the relative distribution coefficient of Ga atom was defined by the ratio

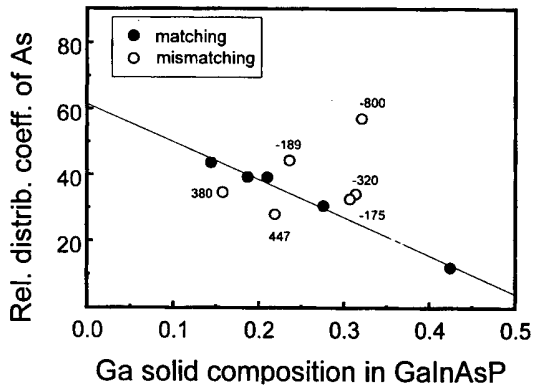

Fig. 4. The relation between relative distribution coefficient of As and Ga solid composition of GaInAsP lattice matched to InP.

of solid Ga mole fraction to gas TMGa mole fraction divided by the ratio of solid In mole fraction to gas TMIn mole fraction. This result indicates that group V does not affect the relative incorporation behavior of group III. However, the relative incorporation of group V is severely affected by the composition of group III as shown in Figure 4. As the Ga composition in lattice matched GaInAsP increases, the incorporation coefficient of As atom is drastically decreased compare to the P atom. From the extra-polation for the Ga free composition in GaInAsP, the maximum relative distribution coefficient of As atom is above 60. The open circles represent the GaInAsP lattice mis-matched to InP, where the values are two-theta angles of double crystal x-ray diffraction in arcsec. Compressive strained GaInAsP, which means the minus symbol in front of the value, indicate that it shows the trend of higher value in relative distribution coefficient of As, while the tensile strain affects lowering that value.

The relationship between bandgap wavelength of lattice matched GaInAsP and input gas phase mole fraction

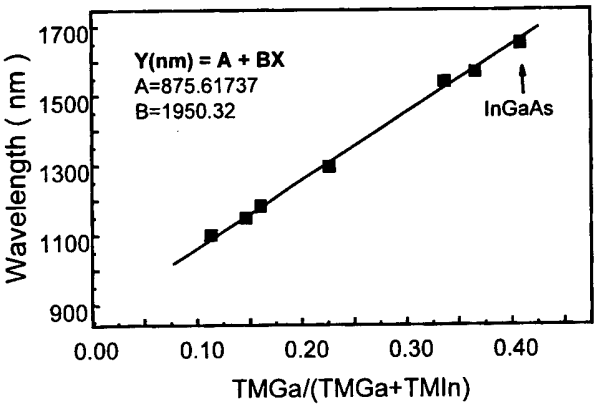

Fig. 5. The band-gap wavelength of GaInAsP lattice matched to InP with the gas phase group III mole fraction.

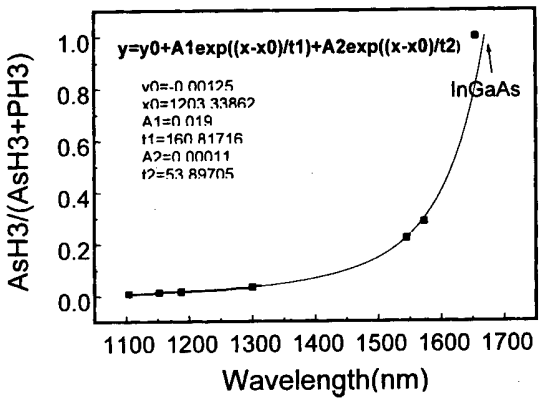

Fig. 6. The band-gap wavelength of GaInAsP lattice matched to InP with the gas phase group V mole fraction.

indicates the conclusive reactor characteristics in a practical point of view. The Figure 5 shows the bandgap wavelength increases linearly with the TMGa gas mole fraction, where the Ga free composite means InP. From the fitting of empirical data, we obtained the analytical function of $y(\text{nm}) = 876 + 1950x$, where x means TMGa mole fraction and y means bandgap wavelength of lattice matched GaInAsP. Figure 6 shows the relationship between bandgap wavelength and mole fraction of group V precursor. While the group III precursor shows the linear relationship to the bandgap wavelength, the group V shows the good coincidence between them by merging of two different exponential functions in the analytical fitting. From the result of analytical fitting, we obtained the function of exponential, $y = 0.019\exp((x - 1203)/160.8)$ in approximation. The analytical functions between bandgap wavelength and gas phase mole fraction in our MOVPE make it easy to achieve the designed bandgap of GaInAsP by controlling the input gas mole fraction which is obtained from above analytical function.

IV. CONCLUSIONS

GaInAsP ($\lambda = 1.05 \sim 1.55$ μm) lattice matched to InP were successfully grown by using a LP-MOVPE. A Ga solid composition is linearly proportional to the gas composition with the relative distribution coefficient value of 1.1 which means the preferred incorporation probability compare to the In. The As solid composition with the AsH_3 gas composition shows the non-linear relation, and the As distribution coefficient is severely affected by the amount of Ga while Ga distribution coefficient is not affected by group V. From the analytical fitting between wavelength and gas composition, input gas composition in MOVPE can be exactly estimated for designed wavelength of GaInAsP.

REFERENCES

[1] T. Nomura, H. Ogasawara, M. Miyao and M. Hagino, J. Crystal Growth **111**, 61 (1991).
[2] J. F. Carlin, A. Rudra and M. Ilegems, J. Crystal Growth **131**, 387 (1993).
[3] C. T. Foxon, B. A. Joyce and M. T. Norris, J. Crystal Growth **49**, 132 (1980).
[4] Y. Matsushima and S. I. Gonda, J. J. A. P. **15**, 2093 (1986).
[5] L. Samuelson, P. Omling and H. G. Grimmeiss, J. Cryst. Growth **61**, 425 (1983).
[6] T. Iwamoto, K. Mori, M. Mizuta and H. Kukimoto, Jpn. J. Appl. Phys. **22**, 191 (1983).
[7] M. Ogura, Y. Ban, M. Morisaki and N. Hase, J. Cryst. Growth **68**, 32 (1984).
[8] B. W. Liang and C. W. Tu, J. Appl. Phys. **74**, 255 (1993).
[9] T. L. Lee, J. S. Liu and H. H. Lin, '95 IPRM, WP26 (1995).

Journal of the Korean Physical Society, Vol. 34, June 1999, pp. S458~S460

The Splitting of Heavy and Light Holes due to the Indium-Induced Strain in 3-Inch Indium-Alloyed Semi-Insulating GaAs Substrates

J. S. KIM, S. W. PARK and P. W. YU*

Department of Information & Communications, Kwang-Ju Institute of Science & Technology (K-JIST), Kwang-Ju 500-712

Room temperature photoreflectance (PR) was used to determine the splitting of the heavy and light holes in the edge region of 3-inch diameter semi-insulating (SI) bulk indium-alloyed GaAs materials grown by the liquid-encapsulated Czochralski (LEC) method. The shift of heavy hole energy is larger in the edge region of wafer compared to the central region. This non-uniformity is attributed to the radial distribution of indium; Indium content being higher and lower, respectively, around the edge region and at the central area. In addition, when the indium content reaches a critical point, we find the splitting of the heavy and light holes near the edge of the GaAs wafer due to the indium-content variation induced strain in the process of growing GaAs substrate. The variation of heavy hole energy indicates that of the indium content in the wafer and the separation between the heavy and light holes is attributed to the different indium content in adjacent regions where indium content varies rapidly.

I. INTORDUCTION

The bulk substrates of GaAs are the basic materials widely used for the electronic and optoelectronic devices. The performance of these devices depends on the quality of the substrate materials. Particularly, the quality is influenced in varying degrees by dislocation effects. Indium incorporation was reported [1] as an efficient way to reduce the dislocation density. That is, 3-inch diameter of GaAs ingot which contains only a few hundred of dislocations per unit area (cm^2) can successfully be grown with the indium incorporation, while standard undoped SI LEC GaAs wafers usually exhibit about 10^4~10^6 dislocation per unit area. GaAs:In ($In_xGa_{1-x}As$) crystals grown this way typically incorporate ~mole fraction 0.1~2 % of indium. Thus, it is desirable to have a simple nondestructive method to measure the indium content and its distribution in the ingot [2]. Unfortunately, many analytical techniques are destructive. Nondestructive photoluminescence (PL) measurements have been used [3] to determine indium content from the PL transition energy shift of indium-alloyed $In_xGa_{1-x}As$. However, low temperatures are usually needed for accurate PL measurements in order to obtain sharp transitions. It is difficult to cool such a large sample as a 3-inch wafer due to limited Dewar space. In the present work, room-temperature PR was used to measure the band-gap shift due to indium in the indium-alloyed SI LEC GaAs and to determine the inhomogeneity of indium distribution present in the GaAs wafer. PR measurements also showed the splitting of the heavy and light holes due to the stress arising from the regions of high and low indium content.

*E-mail: pwyu@eunhasu.kjist.ac.kr

II. EXPERIMENTS

The modulation in the reflectivity was produced by mechanically chopping the laser beam which created the electron-hole pairs. A 5-mW He-Ne laser chopped at 100 HZ was used for this purpose. The probe light from a quartz tungsten halogen lamp passing through the monochromator was irradiated on the surface of the indium-alloyed GaAs substrate. The reflected light signal was detected with a silicon photodiode using a lock-in amplifier. A lock-in amplifier provided the differential reflectance (ΔR) and the absolute reflectance (R) was given by the detector output. The diagram for the experimental setup is given in Fig. 1. To observe the radial distribution of the band edge energy due to the indium content in 3-inch indium-alloyed GaAs ($In_xGa_{1-x}As$) wafer, we used two samples from Westinghouse, No. 292 and No. GY423-2, and chose 19 points and 24 points, respectively, for sample No. 292 and No. GY423-2 along the <011> of the diameter of a wafer. The heavy and light holes energies were obtained with PR line shape analysis.

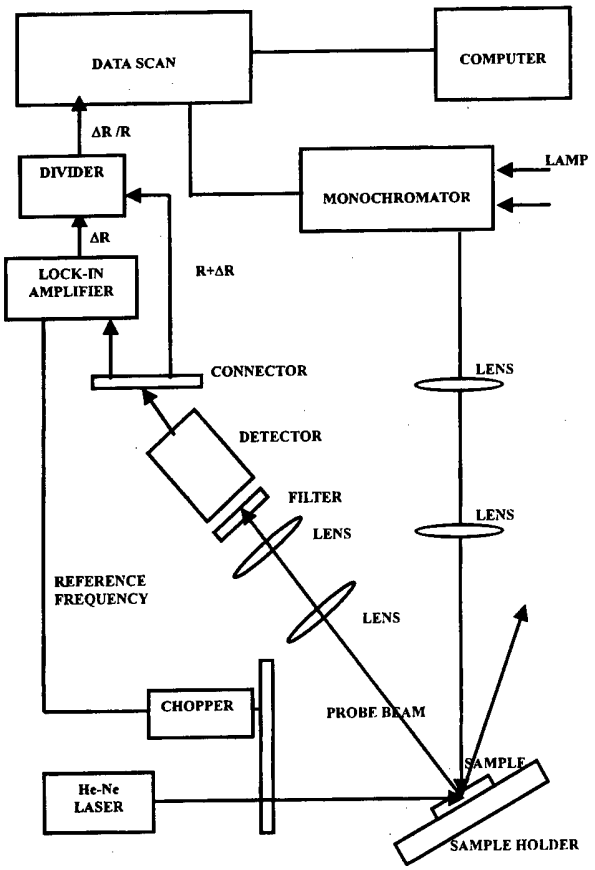

Fig. 1. The schematic representation of PR experimental configuration.

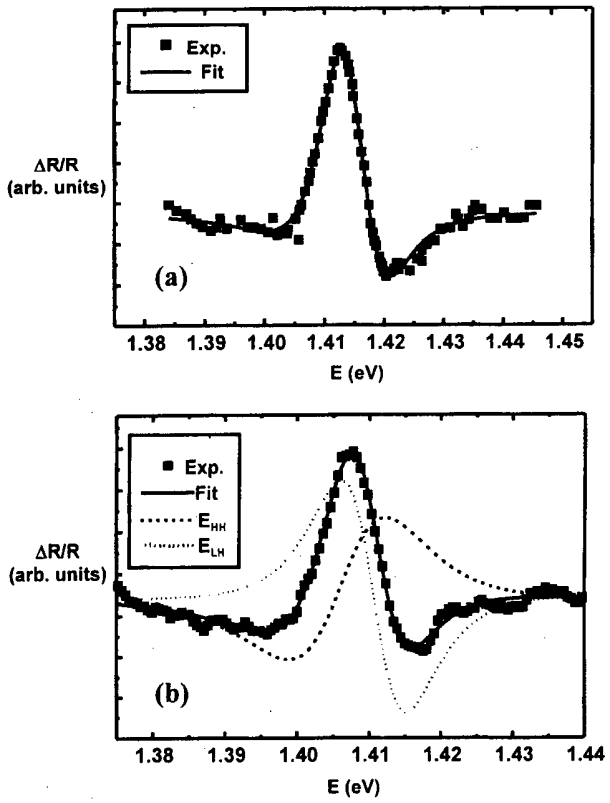

Fig. 2. 300-K PR spectra obtained (a) from sample No. 292 (b) from sample No. GY423-2.

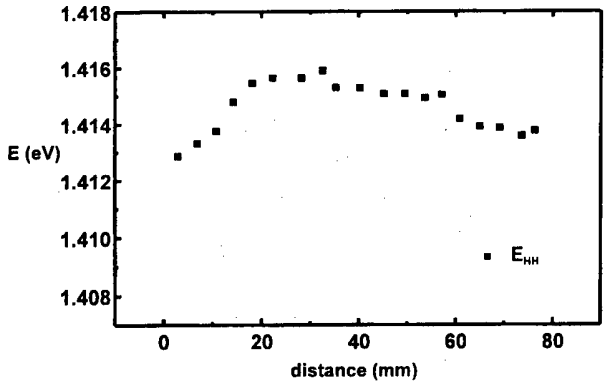

Fig. 3. One-dimensional position-dependent variation of the transition energies of E_{HH} along the radial direction across the diameter of a 3 inch wafer No. 292.

III. RESULTS

The Fig. 2(a) and (b) show the PR spectra (squared) from indium-alloyed samples at 300 K. The solid line is a least-square fit of the experimental data to the Aspnes third-derivative functional form line-shape expression

$$\frac{\Delta R}{R} = Re\left\{\sum_{j=1}^{p} C_j e^{i\theta_j}(E - E_{gi} + i\Gamma_j)^{-m_j}\right\}$$

where p is the number of the spectral function to be fitted, E is the photon energy and C_j, θ_j, E_{gj}, and Γ_j are the amplitude, phase, energy, and broadening parameter of the jth feature, respectively. The parameter m is related to the type of the critical point. The values of m are 5/2 and 2.0, respectively, for the three-dimensional interband and excitonic transition [4].

The fit to the experimental data is quite good for crystals of a wide range of x. We do not observe any other PR features such as Franz-Kelldysh oscillations [5] beside the band-edge transition mode.

The Fig. 2(a) and (b) show the PR spectra obtained from sample No. 292 and No. GY423-2 respectively at 300 K. The Fig. 2(a) only shows the heavy hole (E_{HH}) spectrum whereas Fig. 2(b) shows the contribution from both heavy hole (E_{HH}) and light hole (E_{LH}). The spectrum of the Fig. 2(a) is fitted very well with the heavy hole transition only. However, Fig. 2(b) can be fitted with both heavy and light holes contribution.

The Fig. 3 shows the position-dependent variation of the band gap for moderately indium-alloyed sample No.292. The band gap energy of the indium-alloyed GaAs substrate is lower than that of GaAs and the energy varies almost symmetrically from the center to the

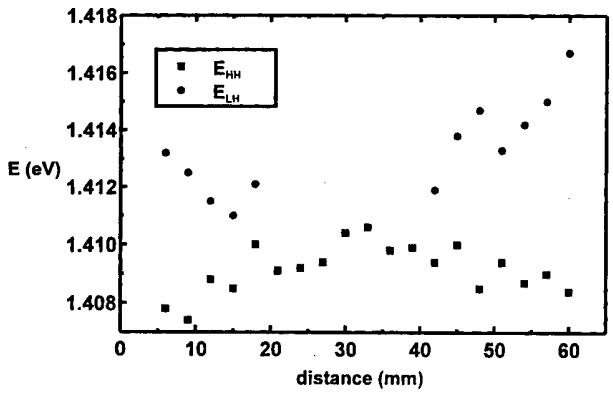

Fig. 4. One-dimensional position-dependent variation of the transition energies of both E_{HH} and E_{LH} along the radial direction across the diameter of a 3-inch wafer No. GY423-2.

edge of the wafer. It also shows that indium-rich region occurs around the edge of GaAs substrate [2].

The Fig. 4 shows the position-dependent variation of the band gap for sample No. GY423-2. It shows the variation of band gap energy with the heavy hole band energy and splitting the heavy and light holes degeneracy. Above the critical point of indium content, indium induced-strain lifts the degeneracy of the valence band. Above this critical point of the indium content, we note the larger splitting of the heavy and light holes energies.

The radial distribution of the indium content which was obtained from the heavy hole energy across the diameter can be understood by considering the LEC crystal growth process. The growth of a bulk crystal is a solidification process where the solid-liquid advances. The shape of growth interface between the solid and liquid can become (a) concave to the melt, (b) almost flat, and (c) convex to the melt depending on the thermal gradient [5]. With case (c), one can expect that the indium content in a wafer is higher at the outer part compared to the central part.

We propose the possible mechanism to describe splitting caused by the indium-induced strain; this is similar to the case of the epitaxial growth InGaAs on the GaAs substrate, that is, epitaxial growth of $In_{x'}Ga_{1-x'}As$ on $In_xGa_{1-x}As$ substrate where x' is larger than x. The size of two regions of $In_xGa_{1-x}As$ and $In_{x'}Ga_{1-x'}As$ may vary. Thus, one of these regions could be stressed differently due to the difference of indium content. Indium content is larger along the edge of the wafer as noted by the heavy hole energy and separation between the heavy and light holes can be ascribed to the different indium content in adjacent regions where indium content varies rapidly.

IV. CONCLUSIONS

The room-temperature PR technique was used to quantitatively measure the changes of the band gap due to the indium alloying in commercially available 3-inch GaAs wafers. The inhomogeneity of the indium in the radial directions was determined. The radial distribution of indium content makes the band gap lower from the central area to the edge of the wafer, in particular, indium higher region occurs around the edge of the substrate and indium lower region occurs at the central area. Indium-induced strain lifts the degeneracy of the valence band above the critical point of the indium content within the wafer. This is the first observation of lifting the degeneracy of the heavy and light holes band due to the indium induced-strain in the 3-inch GaAs substrates.

ACKNOWLEDGMENTS

This work was supported in part by the Korean Science Engineering Foundation (KOSEF) through Ultra-Fast Fiber-Optic Networks (UFON) Research Center at Kwang-Ju Institute of Science and Technology (K-JIST).

REFERENCES

[1] H. Kohda, K. Yamada, H. Wakanishi, T. Kobayashi, J. Osaka and K. Hoshikawa, J. Cry. Growth **91**, 813 (1985).

[2] P. W. Yu, S. Ravipati, B. E. Taylor and W. C. Mitchel, J. Appl. Phys. **67**, 1471 (1990).

[3] K. Kitahara, K. Kodama and M. Oxeki, Jpn. J. Appl. Phys. **24**, 1503 (1985).

[4] D. E. Aspnes, *Handbook on Semiconductors*, edited by T. S. Moss, Vol. 2, edited by M. Balkanski (North-Holland Publishing Company, 1980), Chap. 4.

[5] P. Y. Yu and M. Cardona; *Fundamentals of Semiconductors Physics and Materials Properties* (Springer-Verlag, 1996), Chap. 6.

[6] P. W. Yu, D. C. Walters and W. C. Mitchel, J. Appl. Phys. **60**, 3864 (1986).

Journal of the Korean Physical Society, Vol. 34, June 1999, pp. S461~S463

Adsorption and Desorption of P on (001) InP Surface in Metalorganic Chemical Vapor Deposition by Surface Photoabsorption

Tae-Wan LEE, Heedon HWANG, Youngboo MOON and Euijoon YOON

School of Materials Science & Engineering and ISRC, Seoul National University, Seoul 151-742

Young Dong KIM

Department of Physics, Kyung Hee University, Seoul 130-701

We studied the surface structure of (001) InP in metalorganic chemical vapor deposition (MOCVD) ambient by surface photoabsorption (SPA). A P-dimer peak at 430 nm and an In-dimer peak at 600 nm were observed from the SPA subtraction spectra. A maximum SPA reflectivity change of 8 % between the P-stabilized and the In-stabilized surfaces was obtained at 470 nm. A first-order desorption kinetics was assumed to curve-fit the SPA signal and an activation energy of 3.36 eV was obtained.

I. INTRODUCTION

Because of their increasing technological importance as high-speed electronic and photonic devices for optical communication, III-V compound semiconductors have attracted much attention. For the successful fabrication of such devices, it is indispensable to grow high-quality epitaxial layers. Molecular beam epitaxy (MBE) and metalorganic chemical vapor deposition (MOCVD) and other techniques have been successfully used to grow ultra-thin, high-quality heterostructures for such devices. Knowledge about the surface structure and the surface kinetics on growth surfaces is crucial for the precise control of composition and thickness with atomic resolution.

Adsorption and desorption processes of group V in MOCVD are elementary surface kinetic processes occurring on growth surfaces of III-V compound semiconductors. Especially, during the growth of mixed group V alloys, adsorption and desorption processes of several group V elements occur simultaneously, leading to the determination of the composition of the alloys. Thus, the *in situ*, real-time monitoring of the surface process of group V elements will be beneficial to control the composition of III-V compound semiconductors. Surface photoabsorption (SPA) is an optical *in situ* monitoring technique appropriate for MOCVD, based on the reflectivity measurement of p-polarized light incident at the Brewster angle on the substrate [1,2]. It can sensitively detect small changes in reflectivity caused by surface chemical processes such as desorption or adsorption of P from InP surfaces [3,4]. In this paper, we studied the adsorption and desorption processes of P from (001) InP surface in MOCVD by *in situ*, real time SPA.

II. EXPERIMENTAL DETAILS

A schematic diagram of the MOCVD system with a SPA setup is shown in Fig. 1. A monochromatic, p-polarized light irradiated a (001) InP surface at an incident angle of 75°. The reflected light was detected by a photomultiplier tube (PMT) and a lock-in amplifier was used to obtain high signal-to-noise (S/N) ratios. The time constant of the SPA system was 0.1 sec. The power density of the optical probe was below 0.1 mW/cm^2, so the probe did not affect the reaction processes on the InP substrate. The fast stream of H_2 along the quartz wall maintained an optical path clean during the experiment.

After a conventional *ex situ* cleaning sequence to re-

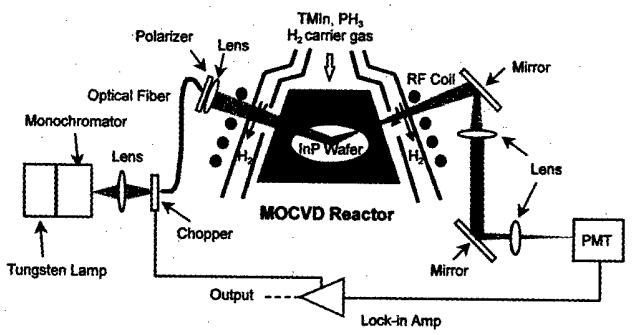

Fig. 1. The horizontal MOCVD reactor with the SPA system used in this study.

move surface contaminants, (001) InP substrates were loaded in our horizontal MOCVD reactor. Then, the substrates were thermally cleaned *in situ* at 600 °C for 5 min in PH_3 ambient, subsequently and a 1000 Å InP buffer layer was grown using trimethylindium (TMIn) and PH_3 at 10^4 Pa. After the buffer layer growth, P adsorption and desorption experiments were performed by switching PH_3 flow on and off at various temperatures. The azimuthal direction for the SPA measurement was $[1\bar{1}0]$.

III. RESULTS AND DISCUSSIONS

In order to study the P adsorption and desorption kinetics from InP surfaces, it is necessary to understand the surface structure of P-stabilized InP surfaces. Thus, we studied the InP surface by SPA subtraction spectra [4,5] at various substrate temperatures and PH_3 partial pressures as shown in Fig. 2. The subtraction spectra were defined as follows [4,5];

$$\begin{aligned} R[1\bar{1}0]-R[110] &= (R_P[1\bar{1}0]-R_{In}[1\bar{1}0])/R_{In}[1\bar{1}0] \\ &\quad -(R_P[110]-R_{In}[110])/R_{In}[110] \\ &= R_P[1\bar{1}0]/R_{In}[1\bar{1}0] \\ &\quad -R_P[110]/R_{In}[110], \end{aligned} \tag{1}$$

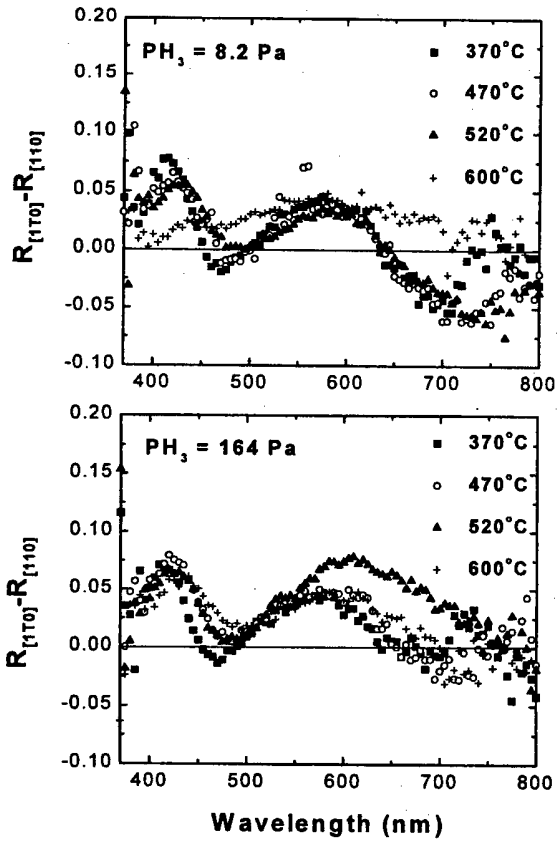

Fig. 2. SPA subtraction spectra for (001) InP at various substrate temperatures: (a) PH_3 partial pressure 8.2 Pa, and (b) PH_3 partial pressure 164 Pa.

where R_P and R_{In} represent the reflectivity of a P-stabilized surface when PH_3 was introduced, and the reflectivity of an In-stabilized surface after the P desorption, respectively. $[1\bar{1}0]$ and [110] represent the azimuthal directions of the SPA probe beam. By taking the difference between $[1\bar{1}0]$ and [110] spectra, isotropic information from both spectra are cancelled out, resulting in only information on surface anisotropy due to surface dimers. If the surface dimer direction is parallel to the electric filed of the polarized probe beam, an electronic transition by surface dimer bonds is allowed, resulting in increased reflectivity. However, this transition by surface dimer bonds is prohibited when the dimer direction is perpendicular to the electric field [4,6]. The positive peaks observed at Fig. 2 implies that the directions of the P- and the In-dimers are $[1\bar{1}0]$ and [110], respectively. The red shifts of the spectra with increasing temperature were also observed, presumably due to the band gap narrowing effect at high temperatures [7].

In the subtraction spectra, two positive peaks were observed near 430 nm and 600 nm at most conditions. However, at 600 °C and PH_3 8.2 Pa, a P-stabilized surface was not obtained during PH_3 injection since the P overpressure was not enough. The peak near 430 nm was very low and the peak near 600 nm was not discernable. Aspnes *et al.* [6,8,9] assigned the two anisotropic peaks at 2.6 eV and at 1.8 eV to As-dimer and Ga-dimer peaks on GaAs respectively from their reflectance difference spectroscopy (RDS) experiments and theoretical calculation. Johal *et al.* [10] and Ozanyan *et al.* [11] independently observed the optical anisotropy near 1.9 eV and 2.9 eV in their RDS studies of (001) InP and assigned the peaks to In and P dimers, respectively. Therefore, considering the higher bond strength of P-P than As-As [5], the peak at 430 nm can be assigned to P-dimer, whereas the other peak near 600 nm can be assigned to In-dimer peak.

The P adsorption kinetics was studied by monitoring

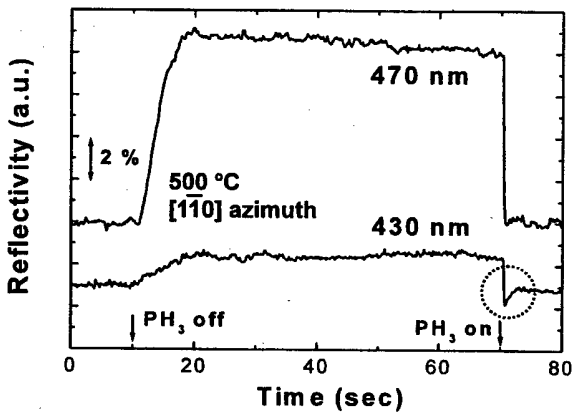

Fig. 3. Changes in SPA reflectivity at 430 nm and 470 nm during P desorption and adsorption (Rapid drop and successive slow recovery of SPA signal are shown by dotted circle at 430 nm).

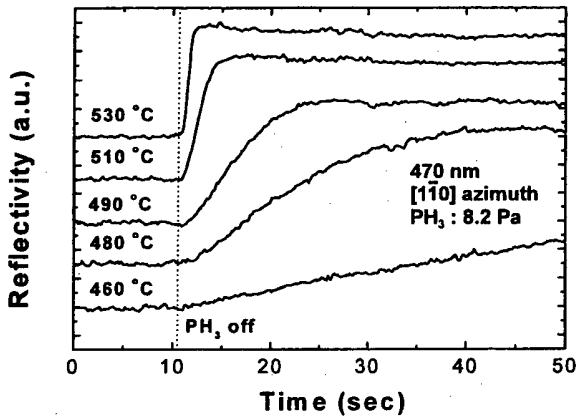

Fig. 4. Changes in SPA reflectivity during P desorption at various substrate temperatures.

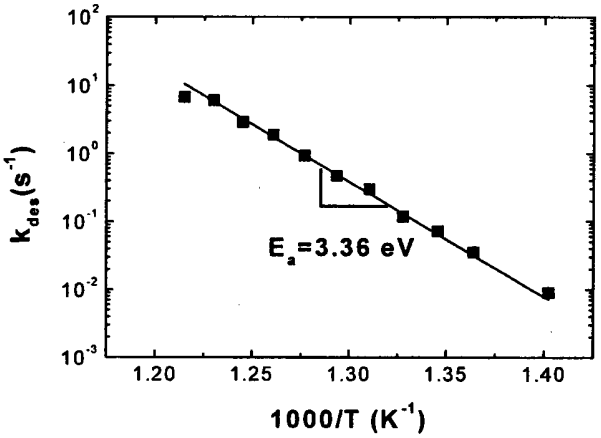

Fig. 5. Arrhenius plot of P desorption rate constants (k_{des}).

SPA signals at 430 and 470 nm along [1$\bar{1}$0] azimuth, as shown in Fig. 3. During the P adsorption by PH_3 injection, we first observed that the SPA signal at 430 nm decreased abruptly even below its P-stabilized value and then slowly recovered. The two-step P adsorption, however, was not observed at 470 nm. The reason for the drop below the level of In-stabilized surface is not known at the moment. The changes in SPA signal between In-stabilized and P-stabilized surfaces were larger for 470 nm [5], therefore, we monitored the P desorption process after PH_3 interruption at 470 nm. The signal difference was about 8 % between the P-stabilized surface and the In-stabilized surface.

The SPA signal changed when P desorbed at various substrate temperatures, as shown in Fig. 4. Notice that the P desorption rate increased with substrate temperature. The SPA curves at various substrate temperatures were fitted assuming a first-order desorption kinetics [3,4], where the SPA reflectivity, R, during P desorption can be expressed as follows;

$$R = R_{\mathrm{In}} - (R_{\mathrm{In}} - R_{\mathrm{P}})\exp(-k_{des}(t - t_0)) \qquad (2)$$

Here, k_{des} is the desorption rate constant and t_0 is the time when PH_3 was switched off. From the curve fitting, the desorption rate constants could be obtained. An Arrhenius plot of the desorption rate constants give an activation energy of 3.36 eV as shown in Fig. 5. The SPA signals at the initial stage of P desorption in Fig. 4 was slightly deviated from the exponential shape. This deviation at initial stage may result from excess P [5] on [1$\bar{1}$0] P-dimer during PH_3 injection. However, the effect of excess P on desorption process must be examined for the clear understanding of a desorption mechanism.

IV. CONCLUSIONS

We studied the surface structure of (001) InP in metalorganic chemical vapor deposition (MOCVD) ambient by SPA. The SPA subtraction spectra at various temperatures and phosphine pressure resulted in a P-dimer peak at 430 nm and an In-dimer peak at 600 nm. A maximum SPA reflectivity change of 8 % was obtained at 470 nm between the P-stabilized and the In-stabilized surfaces. A first-order desorption kinetics was assumed to curve-fit the SPA signals, and an activation energy of 3.36 eV was obtained.

ACKNOWLEDGMENTS

This work is supported by Korea Science and Engineering Foundation under contract No. 98-0200-05-01-3.

REFERENCES

[1] N. Kobayashi and Y. Horikoshi, Jpn. J. Appl. Phys. **28**, L1880 (1989).
[2] N. Kobayashi and Y. Horikoshi, Jpn. J. Appl. Phys. **29**, L702 (1990).
[3] N. Kobayashi and Y. Kobayashi, Jpn. J. Appl. Phys. **30**, L1699 (1991).
[4] N. Kobayashi, J. Cryst. Growth **145**, 1 (1994).
[5] Y. Kobayashi and N. Kobayashi, J. Electron. Mater. **25**, 691 (1996).
[6] Y. C. Chang and D. E. Aspnes, Phys. Rev. **B41**, 12002 (1990).
[7] Y. P. Varshni, Physica **34**, 149 (1967).
[8] D. E. Aspnes, Y. C. Chang, A. A. Studna, L. T. Florez, H. H. Farrell and J. P. Harbison, Phys. Rev. Lett. **64**, 192 (1990).
[9] I. Kamiya, D. E. Aspnes, L. T. Florez and J. P. Harbison, Phys. Rev. **B46**, 15894 (1992).
[10] T. K. Johal, S. D. Barrett, M. Hopkinson, P. Weightman and J. R. Power, J. Appl. Phys. **83**, 480 (1998).
[11] K. B. Ozanyan, P. J. Parbrook, M. Hopkinson, C. R. Whitehouse, Z. Sobiesierski and D. I. Westwood, J. Appl. Phys. **82**, 474 (1997).

Journal of the Korean Physical Society, Vol. 34, June 1999, pp. S464~S467

X-ray Scattering Studies on the Strained InGaAs/InP and InGaAsP/InP Multi-quantum Wells

M. S. OH, D. H. WOO, E. H. KOH, J. S. YAHNG and S. H. KIM

Photonics Research Center, Korea Institute of Science and Technology, Seoul 130-650

Y. D. KIM

Department of Physics, KyungHee University, Seoul 130-701

We have carried out an X-ray study on ternary $In_{1-x}Ga_xAs/InP$ and quaternary $In_{1-x}Ga_xAs_yP_{1-y}/InP$ strained multi-quantum well (MQW) structures on (001) InP substrates grown by chemical beam epitaxy. The presence of well-defined higher order harmonics in the double crystal X-ray diffraction (DCXRD) measurement showed the high quality of our MQW structures. By comparing the DCXRD measurements with X-ray simulation results, we could obtain layer thicknesses and amounts of perpendicular strains relative to the InP barrier.

I. INTRODUCTION

Much attention has been given to strained layer superlattices and multi-quantum well (MQW) structures, in which multilayer structures are grown lattice mismatched to the substrate but with the layer thickness small enough to accommodate the mismatch strain coherently rather than to create misfit dislocations [1]. This elastic layer strain gives rise to a number of interesting properties and MQWs can also be conveniently used to study strain effects.

X-ray rocking curve measurement is a powerful method to study these strained layers, providing informations on depth profiles of the strain, layer thickness, compositions, and diffussion profiles, so that it has proven to be useful for the structural assessment of MQW layers [2–5]. In the double-crystal geometry the sample is rocked through the Bragg angle using an open end detector. This arrangement results in good resolution around the substrate peak.

The technique of chemical beam epitaxy (CBE) has been recently applied in the growth of InGaAs(P)/InP MQWs [6–8]. In order to achieve well-controlled beams of phosphorus and phosphorus plus arsenic, elemental sources in molecular beam epitaxy (MBE) were replaced with sources that permit the required element to be obtained from the decomposition of simple chemicals [9].

In this study, we have carried out a double crystal X-ray diffraction (DCXRD) study of ternary $In_{1-x}Ga_xAs/InP$ and quaternary $In_{1-x}Ga_xAs_yP_{1-y}/InP$ strained MQW structures grown on (001) InP substrates by CBE. The DCXRD is a proper method to study their structure, since it allow to obtain a well-resolved X-ray satellite pattern over a wide range. We note that conventional DCXRD has been used in studies of MQW mostly with a large number of periods producing X-ray satellite intensities strong enough to allow a detailed analysis [10,11]. The MQWs in this study have been grown for device applications, so they have relatively small number of periods. However, even if the intensities of the satellites are small, they are better separated from the substrate peak to be able to study small strain shift. We used dynamical diffraction theory to simulate the measured X-ray rocking curve. By comparing the simulation results and the DCXRD data, we could obtain structure factors and perpendicular strains relative to the InP barrier.

II. EXPERIMENTALS

MQW layers were grown at 500 °C on (100) oriented n-InP substrates. We use arsine (AsH_3) and phosphine (PH_3) as group V element precursors, and triethylgallium (TEGa) and trimethylindium (TMIn) as group III element precursors [9,12–14]. The CBE is highly sensitive to the growth temperature, T_g, so it must be controlled within a few degrees precision. The T_g was monitored by an infrared pyrometer (Minolta 630), having its measurement wavelength shorter than 1.1 μm. Photons of this wavelength is absorbed by the InP substrate above 480 °C so that the pyrometer truly measures the surface temperature.

A 0.05-μm-thick InP buffer layer was grown prior to the MQW growth. Two sets of MQW samples with opposite strains were prepared, *i.e.* $In_{1-x}Ga_xAs$ and $In_{1-x}Ga_xAs_yP_{1-y}$ well layers with tensile and compres-

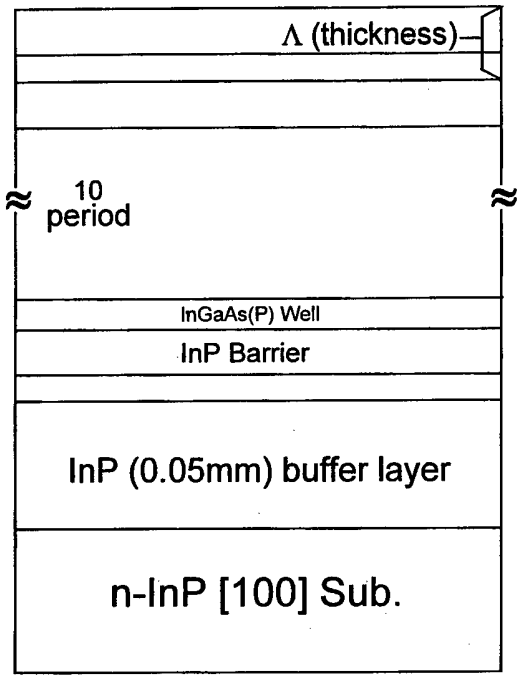

Fig. 1. Schematic of InGaAs(P)/InP multi-quantum well structure.

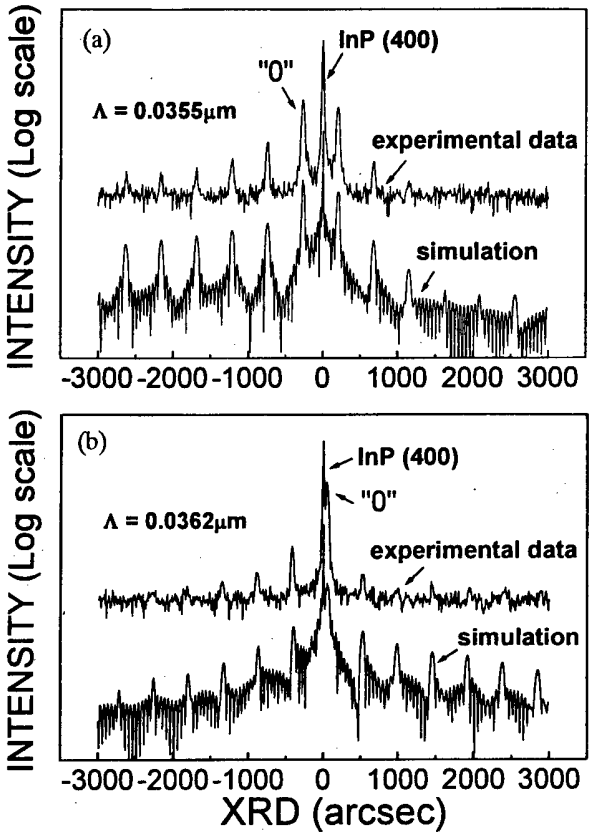

Fig. 2. Double-crystal X-ray scans of the (400) reflection of strained 10-well InGaAs/InP ternary MQWs (upper curves) with the results of simulation (lower curves); (a) compressive strain 0.6 %. (b) tensile strain 0.3 %.

sive strains between InP barrier layers. Each set consisted of ten identical single quantum wells (about 30 Å) separated by 300-Å-thick barriers as shown in Fig. 1 (Strains are confined in well layers). For $In_{1-x}Ga_xAs/InP$ MQWs, the well compositions were kept at x=0.40 and 0.54 for samples with tensile and compressive strains, respectively. For $In_{1-x}Ga_xAs_yP_{1-y}/InP$, the well strains were kept at −0.8 % and +0.4 % for samples with tensile and compressive strains, respectively. The numbers of wells and the thicknesses of layers for all MQWs were chosen to assure that the total thicknesses of the entire MQWs were below the critical thickness limit.

To assess the uniformity of $In_{1-x}Ga_xAs$ and $In_{1-x}Ga_xAs_yP_{1-y}$, we performed DCXRD measurement. This technique provides a rapid and nondestructive means of characterizing an epitaxial crystalline structure, and it is particularly useful for the semiconductor alloys $In_{1-x}Ga_xAs_yP_{1-y}$, since the lattice parameter of this material is strongly dependent on x and y. To extract information of epilayers, the measured X-ray rocking curve was analyzed using a dynamical diffraction theory. Generally, the X-ray rocking curve is analyzed using a kinematical or dynamical diffraction theory. The kinematical theory (which is an approximation to the dynamical theory) neglects the extinction (*i.e.*, multiple scattering), so it serves as an adequate model when the maximum reflecting power is less than about 6 %. When the reflecting power exceeds 6 %, the dynamical theory should be used in the rocking curve analysis [15,16]. This dynamical model is widely applied to the analysis of rocking curves to get detailed strains and damage depth distributions. In the dynamical theory, rocking curves are calculated by solving the typical Takagi-Taupin equations [17,18]. For a single homogeneous layer the equation can be solved analytically, giving the amplitude ratio at one surface relative to that at another. In order to apply for heteroepitaxial structures we considered each sample as subdivided into layers of constant lattice parameter and structure factor. Ramdom polarization is assumed in the incident beam. The reflectivity of the sample is convoluted with the reflectivity curve for the first crystal used in the double crystal diffractometer to give the rocking curve.

III. RESULTS AND DISCUSSIONS

The upper curve of Fig. 2(a) shows a measured X-ray rocking curve of the (400) reflection of InGaAs MQWs with compressive strain. Clear observation of zeroth peak from InGaAs multilayer tells that these multilayer structures are mismatched with respect to the InP[100] substrate. The satellite peaks located asymmetrically on each side of the multilayer main peak confirm the high quality growth of well-defined InGaAs/InP MQWs.

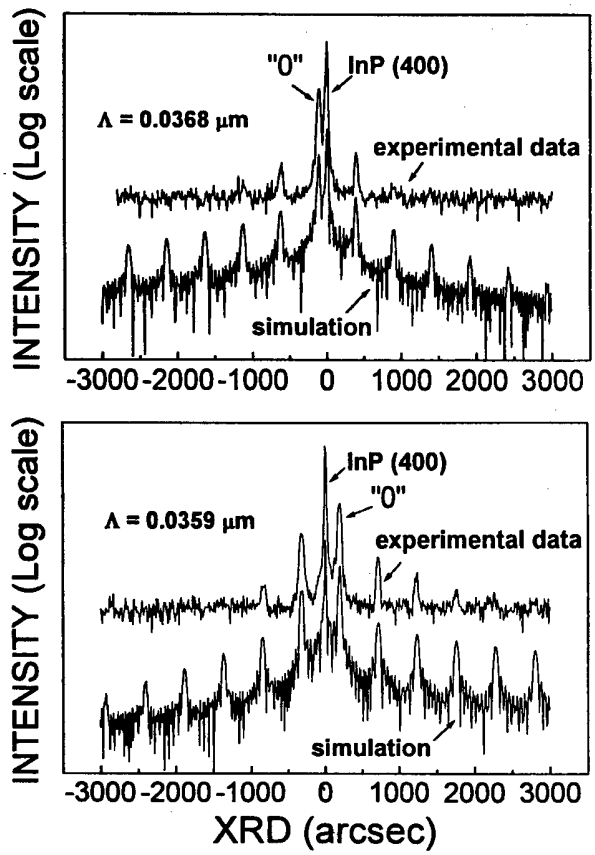

Fig. 3. Double-crystal X-ray scans of the (400) reflection of strained 10-well InGaAsP/InP quaternary MQWs (upper curves) with the results of simulation (lower curves); (a) compressive strain 0.4 %. (b) tensile strain 0.8 %.

This was also confirmed by the observation of narrow linewidth of the photoluminescence (PL) spectrum on this sample, which is explained elsewhere in detail [19]. The upper curve of Fig. 2(b) shows the same InGaAs MQWs data but with tensile strain, showing again clear peaks from multilayers. The quaternary InGaAsP/InP grown on lattice mismatched to the InP [100] substrate also exhibits a well-defined MQWs structure with the distinct satellite peaks for both tensile and compressive strained MQWs as shown in Fig. 3 by upper curves.

To extract information, the X-ray rocking curve was analyzed using a dynamical diffraction theory mentioned above. First, the MQWs period (Λ) has been obtained by averaging over the positions of satellite peaks of order n according to the equation [3,4],

$$\frac{2\sin\theta_n - 2\sin\theta_{SL}}{\lambda_{\mathrm{CuK}\alpha_1}} = \pm\frac{n}{\Lambda}. \quad (1)$$

Here, θ_{SL} and θ_n are the zeroth order peak and the n-th order peak of MQWs, respectively, while $\lambda_{\mathrm{CuK}\alpha_1}$ (=1.540562 Å) is the wavelength of the incident X-ray beam. Next, the basic equation used for all rocking curve calculations gives the rate of change of the ratio of diffracted to incident beam amplitudes, X, as a function of depth Z below the surface of the crystal. It is derived from the Takagi-Taupin theory of diffraction for distorted crystals [17,18,20],

$$\frac{dX}{dZ} = \frac{i\pi}{\lambda\sin\theta_0}(cY_H X^2 + [2Y_0 - \alpha_H(Z)]X + cY_H) \quad (2)$$

where θ_0 is the Bragg angle; Y is related to the structure factor F by the formula

$$Y = -(\lambda^2/\pi V)r_e F \quad (3)$$

where V is the unit cell volume, λ is the wavelength, and r_e is the classical electron radius. The $\alpha_H(Z)$ is defined as,

$$\alpha_H(Z) = -2\lambda(\theta - \theta_0)\cos\theta_0/d \quad (4)$$

with θ the angle of incidence, where subscript H refers to the 004 reflection and subscript 0 refers to the 000 reflection; c is the polarization factor, which is 1 and $\cos\theta$ for σ and π polarization, respectively. Eq. (2) can be written in the simpler form

$$\frac{dX}{dZ} = iC[A(X^2+1) + 2BX] \quad (5)$$

to have a solution

$$X(Z) = \frac{x_0 S + i(A + x_0 B)\tan[CS(Z - z_0)]}{S - i(B + Ax_0)\tan[CS(Z - z_0)]} \quad (6)$$

where $S = (B^2 - A^2)^{0.5}$ and $Z = z_0$ at $X = x_0$. Hence the value of X at the top surface of the layer can be calculated if the value at the bottom surface is known.

Using above Eq. (6) as lineshape of X-ray measurement and assuming less than two molecular layer thick interfacial layers with obtained value of Λ, the X-ray satellite patterns of the (h00) scans were computer simulated to have fit determined structural parameters. The results are also shown in Figs. 2 and 3 together as lower curves. The structural parameters obtained from the simulation are listed in Table 1. This result implies that the MQWs grown by our CBE technique have well defined interfaces. For the ternary materials, well thicknesses obtained are 37 Å (compressive strain) and 35 Å (tensile strain). For the quaternaries, the values are 35 Å (compressive strain) and 31 Å (tensile strain). We note that recent DCXRD studies [3,21,22] have demonstrated that MQWs can be analyzed with one molecular

Table 1. Results of X-ray curve simulations on period, lattice mismatch, and well thickness of 10-well quaternary and ternary multilayers.

	Period (Λ,Å)	strain	well thickness (Å)
Compressive InGaAs/InP MQWs	355	+0.6 %	37
Tensile InGaAs/InP MQWs	362	−0.3 %	35
Compressive InGaAsP/InP MQWs	368	+0.4 %	35
Tensile InGaAsP/InP MQWs	359	−0.8 %	31

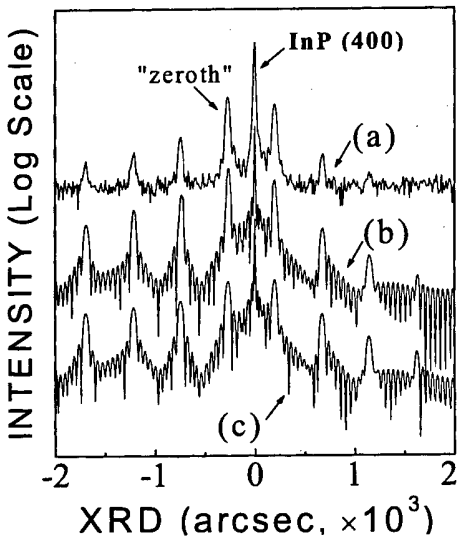

Fig. 4. (a) DCXRD plot of a ten-period $In_{0.62}Ga_{0.38}As$/InP MQWs with a period of 355 Å and well width of 37 Å. (b) Computed DCXRD plot assuming biatomic strained interfacial layers. (c) Computed DCXRD plot with ideally sharp interfaces.

layer (~3 Å) precision in periodicity by using dynamic diffraction theory, where ideally sharp interfaces are assumed. The excellent agreement between the observed and the simulated curves in current work thus demonstrated the high quality of interfacial sharpness along the growth direction in multilayers grown by CBE for this study. These results would not have been obtained if interfacial roughness had exceeded more than about 2 molecular layers.

Figure 4 shows the effect of non-interfacial layers (*i.e.* ideally sharp interfaces) in case of compressive InGaAs/InP MQWs as an example. The peak intensities and positions did not change significantly without these thin interfacial layers. Careful look at the zeroth and the 1st satellite peaks shows that the insertion of interfacial layers fits the experimental line shape only slightly better. We found that in these lattice-mismatched MQWs the elastic strain inside the well is the major contributing factor in achieving computer simulated fit, and the presence of thin strained interfacial regions of one molecular layer thick has a negligible effect on the simulation.

We also performed PL, scanning electron microscope (SEM), and transmission electron microscope (TEM) measurements. Those results confirmed our above analysis on X-ray data, which will be discussed in detail elsewhere [19].

IV. CONCLUSIONS

We have carried out a DCXRD study on ternary $In_{1-x}Ga_xAs$/InP and quaternary $In_{1-x}Ga_xAs_yP_{1-y}$/InP strained MQW structures grown on (001) InP substrates by CBE. The DCXRD scans were analyzed by dynamical diffraction model of alternating wells and barriers. This dynamical model resulted in exellent fits to measured lineshapes of MQWs. Structural parameters such as the thicknesses of the layers and the amounts of perpendicular strain were obtained. We also showed that assuming the interfacial layer of about biatomic thickness improved the simulation of lineshape slightly better but has negligible effect on our current analysis.

ACKNOWLEDGMENTS

This work is supported by Korea Science and Engineering Foundation (KOSEF) under contract No. 98-0200-05-01-3.

REFERENCES

[1] M. B. Panish, H. Temkin and S. Sumski, J. Vac. Sci. Technol. **3**, 657 (1985).
[2] M. d. Naurois, J. Stagl, W. Faschinger and G. Bauer, J. Appl. Phys. **81**, 6120 (1997).
[3] J. M. Vandenberg, A. T. Macrander, R. A. Hamm and M. B. Panish, Phys. Rev. **B44**, 3991 (1991).
[4] Y. T. Hwang, H. J. Lee, K. H. Lee, J.-K. Lee, S. C. Lee and J. J. Lee, J. Korean Phys. Soc. **29**, 614 (1996).
[5] H. Temkin, D. G. Gershoni, S. N. G. Chu, J. M. Vandenberg, R. A. Hamm and M. B. Panish, Appl. Phys. Lett. **55**, 1668 (1989).
[6] D. Gershoni, J. M. Vandenberg, R. A. Hamm, H. Temkin and M. B. Panish, Phys. Rev. **B36**, 1320 (1987).
[7] I. C. Bassignana, C. J. Miner and N. Puetz, J. Appl. Phys. **65**, 4299 (1989).
[8] X. R. Wang, X. Y. Chi, H. Zheng, Z. L. Miao and J. Wang, J. Vac. Sci. Technol. **6**, 34 (1988).
[9] A. Rudra, J. F. Carlin, P. Ruterana, M. Gaihanou, J. L. Staehli and M. Ilegems, J. Crystal Growth. **120**, 338 (1992).
[10] C. C. Coman, R. B. Tassius, A. S. Brown and N. M. Jokerst, Appl. Phys. Lett. **70**, 1754 (1997).
[11] W. Li, P. Bergman, I. Ivanov and W. X. Ni, Appl. Phys. Lett. **69**, 3390 (1996).
[12] V. J. Mifsud, P. W. Sullivan and D. Williams, J. Crystal Growth. **105**, 289 (1990).
[13] S. D. Hersee and J. M. Ballingall, J. Crystal Growth. **105**, 282 (1990).
[14] M. Kampf, F. Konig, G. Morsch and H. Luth, J. Crystal Growth. **120**, 124 (1992).
[15] B. E. Warren, *X-Ray Diffraction* (Addison-Wesley Publishing Company, 1969).
[16] C. R. Wie, T. A. Tombrello and T. Vreeland, J. Appl. Phys. **59**, 3743 (1986).
[17] S. Tagaki, Acta Cryst. **15**, 1311 (1962).
[18] D. Taupin, Bull. Soc. Franc. Mineral. Crist. **87**, 469 (1964).
[19] M. S. Oh, Y. D. Kim, D. H. Woo, E. H. Koh and S. H. Kim, unpublished.
[20] M. A. G. Halliwell and M. H. Lyons, J. Crystal Growth. **68**, 523 (1984).
[21] J. M. Vandenberg, M. B. Panish, H. Temkin and R. A. Hamm, Appl. Phys. Lett. **53**, 1920 (1988).
[22] J. M. Vandenberg, M. B. Panish, R. A. Hamm and H. Temkin, Appl. Phys. Lett. **56**, 910 (1990).

Journal of the Korean Physical Society, Vol. 34, June 1999, pp. S468~S473

A New Control Method of Lattice Constant and Bandgap Energy for InGaAsP/InP Liquid Phase Epitaxy

Su Hwan OH, Sang Ku HWANG, Jeong Ho KIM and Tchanghee HONG

Department of Electronics and Communications Engineering, Korea Maritime University, Pusan 606-791

Ho Sung CHO†

Compound Semiconductor Research Department, ETRI-Micro-Electronics Technology Laboratory, Taejon 305-600

We proposed the new method in order to control the lattice mismatch and bandgap energy for the growth of independently lattice-matched InGaAsP layers on InP with LPE (Liquid Phase Epitaxy) system. This method is controlling the lattice mismatch and bandgap energy using the differential distribution coefficient of Ga and As. We had varied the wavelength and lattice constant at each growth temperature of 590 °C and 630 °C for InGaAsP epilayer with the new method. It was confirmed that experimental data and estimated data of proposed method was coincide. It has been confirmed from the results that the proposed method is useful to control not only the lattice mismatch but also the bandgap energy exactly.

I. INTRODUCTION

InGaAsP layer is grown in thermodynamic equilibrium tate between solid and liquid phases in LPE system. Therefore, the quality of the grown layer would be expected better than that of the other growth method such as MBE (Molecular Beam Epitaxy) and MOCVD (Metal Organic Chemical Vapor Deposition). It is very important to calculate the liquid composition exactly, since the solid composition is decided by the distribution coefficient of the liquid composition. But it has been well known that this is hard work. In case of quaternary compound the calculation is very complicated comparing with binary and ternary compounds particularly, because it is grown by combination of the interaction coefficient of ternary compound as well as binary compound. Therefore the accurate calculation of the phase diagram has been very difficult. Calculations of the phase diagram of quaternary compound have been studied by many researchers [1–8]. The liquid composition of quaternary compound calculated from thermodynamic phase diagram using these interaction coefficients was very different from the experiment results, because the interaction coefficient between binary compounds is different from the interaction coefficient between ternary compounds.

In case of LPE, lattice mismatch and band gap energy must be different in each systems, because the system depends on the form of furnace, the structure of graphite boat, and the flow of an ambient gas. For solving these problems, the schematic phase diagram was determined by J. J. Hsieh [9], but even in this case the results were a little different from the experimental results too. Through this similar method, the schematic phase diagram was estabilished with making reference to many experimental data by K. Nakajima [10,11]. Especially, E. Kuphal established InGaAsP/InP empirical phase diagram in the growth temperature between 570 °C and 660 °C by curve fitting to about 330 published experimental data [12]. Even though we have made efforts a lot of times to control the lattice matching condition and the bandgap energy separately using the above mentioned method, the results were not so sufficient ones.

We propose a new method to control the lattice mismatch and bandgap energy independently, using the concept of differential distribution coefficient in experimental phase diagram of Ga and As. In this paper it has been shown that the experimental results obtained from the 1.3 μm InGaAsP/InP epitaxial wafer at 590 °C and 630 °C using the proposed method were good agreement with the theoretical calculation values.

II. AN INDEPENDENT CONTROL METHOD OF LATTICE CONSTANT AND BANDGAP ENERGY

We must weight each amount of liquid components In,

*E-mail: k951402g @hanbada.kmaritime.ac.kr
†E-mail: hoscho @etri.re.kr

Ga, As and P exactly in order to grow the high quality $In_{1-x}Ga_xAs_{1-y}P_y$ epilayer. Many calculations for the model which describes thermodynamic equilibrium state between solid and liquid of the groups III-III-V-V quaternary compounds semiconductors has been done from the phase diagram of binary and ternary compounds [13–15]. The III-III-V-V phase diagram derived from them have been shown as being unequal with the experimental results because of inexact interaction coefficients of binary and ternary compounds. In case of quaternary compound, the phase diagram is derived from curve fitting of the experimental data of binary one and ternary one. Since most of these data was determined by observing gold furnace at high temperature, the accuracy of these data was decreased in lower temperature range of 570 °C to 670 °C for InP system. Therefore, we need to adjust the interaction coefficient in order to get the data approximated to the experimental value. In that case, the thermodynamic characteristic of III-III-V-V system may be deviated from the general case. Generally in the case of In-Ga-As-P system, several researchers made data for experiment using the liquid equations of solid-liquid equilibria for quaternary system proposed by A. S. Jordan *et al.* [15], but the results differ from our experiment data. The other experimental method was the seed dissolution method that was performed to obtain liquid composition. But in case of quaternary compound, the liquid composition of one component can be determined from three kinds of the determined liquid composition, so that it is difficult to get epilayer to satisfy both of lattice matched condition and band gap energy at the same time. In order to compensate these problems, the method of graphic display was made with various published data. Especially E. Kuphal made the empirical equation using the published data and it is a well known method up to now [12]. However, in case of applying InGaAsP epilayer to the devices such as laser diode, we must be able to change the lattice matching condition and wavelength at the same time.

When we control the lattice mismatch or the band gap energy deviation, the lattice matching condition is obtained by the liquid composition of Ga in the base of GaAs and the band gap energy deviation is controlled by the liquid composition of As in the base of InAs. But the lattice constant is changed by the liquid composition of In. It cannot control the liquid composition of Ga and As, respectively. Till now in LPE growth technique, nobody proposed the method of independently controlling the lattice constant and the bandgap energy of quaternary InGaAsP layer. Therefore, we introduced a new method, the differential distribution coefficients method, to find out the rate of solid to liquid composition variation. Using this new method we can control lattice constant and bandgap energy independently. The lattice mismatch and the wavelength deviation to liquid composition deviation can be expressed as follow.

$$\Delta\bar{a} = \sum_i \frac{\partial\bar{a}}{\partial X_i^l}\Delta X_i^l \qquad \left(\bar{a} \equiv \frac{\Delta a}{a}\right) \tag{1}$$

$$\Delta\lambda = \sum_i \frac{\partial\lambda}{\partial X_i^l}\Delta X_i^l \tag{2}$$

In the equation (1) and (2), X_l^i is the liquid composition of i component and in case of InGaAsP the lattice constant, a, and wavelength, λ, are affected by the liquid compositions of Ga and As. Since the supersaturation is mainly occured by Phosphorus, the variation of phosphorus component is neglected.

Especially when we grow epilayer by InP two phase solution, the component of phosphorus is fed automatically, therefore equation (1) and (2) is given

$$\begin{aligned}\Delta\bar{a} &= \frac{\partial\bar{a}}{\partial X_{\mathrm{Ga}}^l}\Delta X_{\mathrm{Ga}}^l + \frac{\partial\bar{a}}{\partial X_{\mathrm{As}}^l}\Delta X_{\mathrm{As}}^l \\ &= A\Delta X_{\mathrm{Ga}}^l + B\Delta X_{\mathrm{As}}^l \end{aligned} \tag{3}$$

$$\begin{aligned}\Delta\lambda &= \frac{\partial\lambda}{\partial X_{\mathrm{Ga}}^l}\Delta X_{\mathrm{Ga}}^l + \frac{\partial\lambda}{\partial X_{\mathrm{As}}^l}\Delta X_{\mathrm{As}}^l \\ &= C\Delta X_{\mathrm{Ga}}^l + D\Delta X_{\mathrm{As}}^l \end{aligned} \tag{4}$$

where A, B, C, and D is given by

$$A = \frac{\partial\bar{a}}{\partial X_{\mathrm{Ga}}^l} = \frac{\partial\bar{a}}{\partial x}\frac{\partial x}{\partial X_{\mathrm{Ga}}^l} \tag{5}$$

$$B = \frac{\partial\bar{a}}{\partial X_{\mathrm{As}}^l} = \frac{\partial\bar{a}}{\partial y}\frac{\partial y}{\partial X_{\mathrm{As}}^l} \tag{6}$$

where x and y are solid composition of Ga and of As, respectively.

$$C = \frac{\partial\lambda}{\partial X_{\mathrm{Ga}}^l} = \frac{\partial\lambda}{\partial E_g}\frac{\partial E_g}{\partial X_{\mathrm{Ga}}^l} = -\frac{\lambda^2}{1.2398}\frac{\partial E_g}{\partial x}\frac{\partial x}{\partial X_{\mathrm{Ga}}^l} \tag{7}$$

$$D = \frac{\partial\lambda}{\partial X_{\mathrm{As}}^l} = -\frac{\lambda^2}{1.2398}\frac{\partial E_g}{\partial y}\frac{\partial y}{\partial X_{\mathrm{As}}^l} \tag{8}$$

where $\bar{a}$ and E_g are given by $\bar{a} = 0.03227y - 0.007128x + 0.002214xy$

$$\begin{aligned}E_g &= 1.35 + 0.668 - 1.068y + 0.758x^2 + 0.078y^2 \\ &\quad -0.069xy - 0.322x^2y + 0.03xy^2\end{aligned}$$

In these equation (5) to (8), $\partial\bar{a}/\partial x$, $\partial\bar{a}/\partial y$, $\partial E_g/\partial x$, and $\partial E_g/\partial y$ mean the differential value of each solid compositions. We refer to the differential distribution coefficient as $\partial x/\partial X_{\mathrm{Ga}}^l$ and $\partial y/\partial X_{\mathrm{As}}^l$ and can control the lattice mismatch and wavelength deviation with liquidus compositions of Ga and As according to these coefficients.

These coefficients can be got from the empirical equations in reference [12] and are shown in Fig. 1. We show the deviation of the differential distribution coefficient due to wavelength of InGaAsP epilayer in Fig. 1. If wavelength becomes longer, $\partial x/\partial X_{\mathrm{Ga}}^l$ decreases gradually but $\partial y/\partial X_{\mathrm{As}}^l$ increases. It means that moving from InP of the shortest wavelength to InGaAs of the longest wavelength

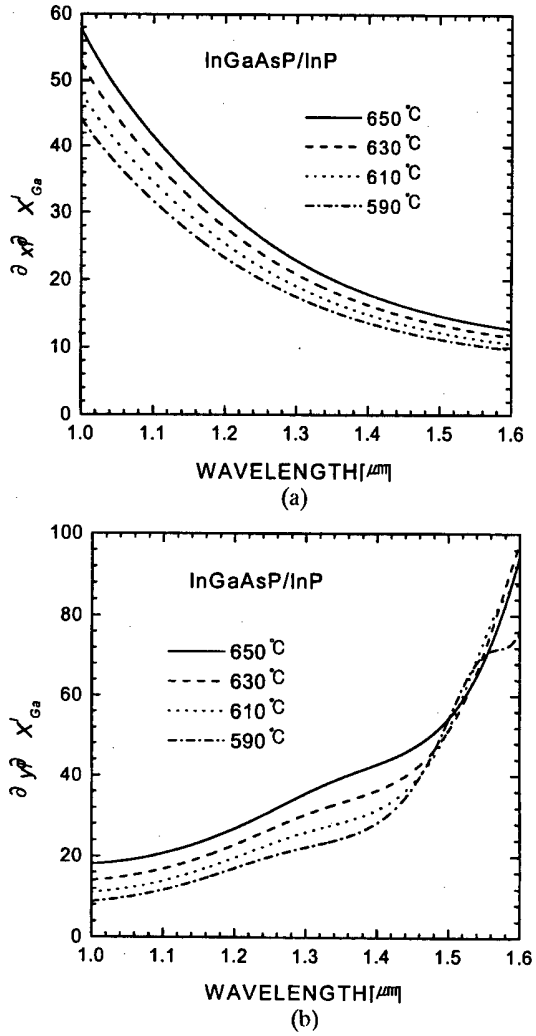

Fig. 1. Differential distribution coefficient of Ga and As with the wavelength (a) Variation of differential distribution coefficient Ga with the growth temperature, (b) Variation of differential distribution coefficient As with the growth temperature.

makes the wavelength deviation sensitive according to liquidus composition of As. That is the reason why the method of changing InAs to control wavelength is useful. In the short wavelength range $\partial x/\partial X^l_{\mathrm{Ga}}$ and $\partial y/\partial X^l_{\mathrm{As}}$ are increased according to increase of growth temperature. It is difficult to control wavelength in short range because of the influence of supersaturation of growth solution. In other words it means that the exact control of the liquid component of Ga and As in order to control wavelength is very difficult in case of high growth temperature.

Therefore in order to get desirous lattice constant and wavelength, we can obtain ΔX^l_{Ga} and ΔX^l_{As}, the deviation of the liquidus composition of Ga and As, from equation (9) and (10) derived equation (3) and (4).

$$\Delta X^l_{\mathrm{Ga}} = \frac{B\Delta\lambda - D\Delta\bar{a}}{BC - AD} \tag{9}$$

$$\Delta X^l_{\mathrm{As}} = \frac{C\Delta\bar{a} - A\Delta\lambda}{BC - AD} \tag{10}$$

We can obtain ΔX^l_{Ga} and ΔX^l_{As} if the amount of lattice mismatch measured experimentally at some growth temperature, the desirous wavelength deviation and the coefficient A, B, C and D are substituted into Eq. (9) and (10), wavelength and coefficient A, B, C, D in the equation (9), (10), we can get ΔX^l_{Ga} and ΔX^l_{As}, the deviations of liquid component of Ga and As. We dare to say that the method using the distribution coefficient proposed above methods regards as very effective method to control the lattice constant and the variations of wavelength in the InGaAsP layer. Because this method can control the lattice constant and the wavelength more exactly and easily than that of empirical methods. In the following section, this will be proved as an useful method in growing the InGaAsP.

III. EXPERIMENT AND DISCUSSION

The growth of 1.3 μm InGaAsP was done at the growth temperature 590 °C and 630 °C in order to confirm whether the wavelength and lattice constant is controlled independently or not. In our experiments a vertical LPE system with a cylindrical rotary crucible of high purity graphite boat was used. InGaAsP growth was performed in a hydrogen ambient using two-phase solution technique. After loading the boat with the substrate and the InGaAsP solution, the melt was homogenized for 1 hrs at above saturation temperature more than 20 °C and cooled at a rate of 0.4 °C/min.

At first, 1.3 μm InGaAsP epilayers were grown during 10 seconds with supersaturated temperature of 3 °C and its result was measured by DXRD (double-crystal x-ray diffraction) and room temperature PL (photoluminescence). The wavelength of the grown epilayers was 13244.9 Å, the lattice mismatch was present -1.0×10^{-3}. The wavelength and the lattice constant were adjusted under these results by using equation (9) and (10). The result of experiment under the fixed wavelength is shown in Fig. 2 and the lattice mismatch changed at the rate of 3.0×10^{-4}. The result of DXRD measurement and PL measurement are shown in Fig. 2(a) and (b), respectively. As you know from figure, lattice mismatch changes linearly in the direction of positive and the wavelength changes maximum 126 Å. It can be controlled exactly within 57 Å compared with the wavelength of InGaAsP layer just before adjustment. Fig. 3 shows that variation amounts and experiment values of ΔX^l_{Ga} and ΔX^l_{As} from reported method are compared with those of ΔX^l_{Ga} and ΔX^l_{As} with standard experiment 5. The solid line and dashed line represent the variation of the liquid composition in Ga and As. The symbol □ and • represent the measurement of liquid composition for Ga and As respectively according to the lattice mismatch. As you know

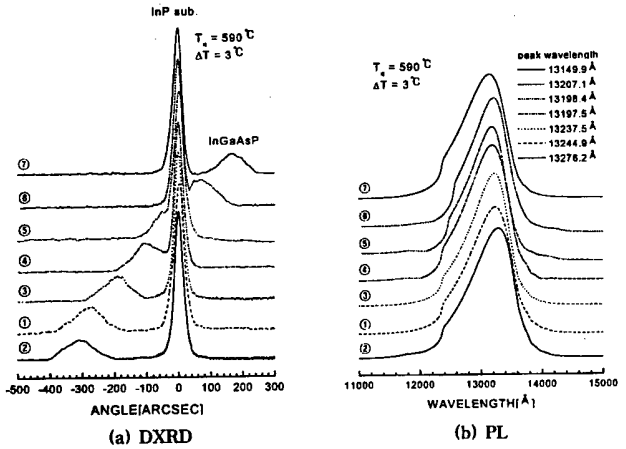

Fig. 2. The measurement result of the DXRD and PL with the lattice mismatch correction at 590 °C.

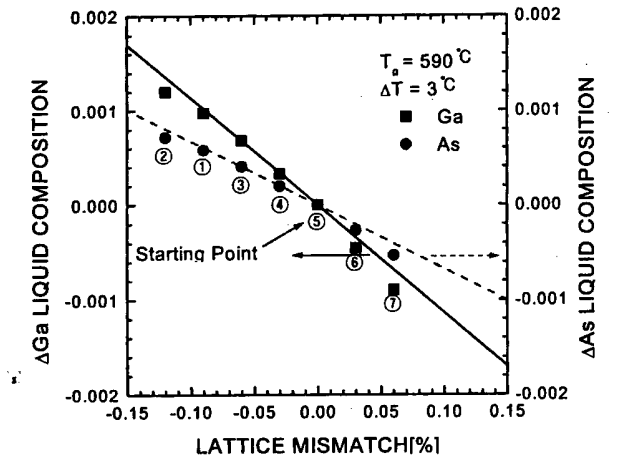

Fig. 3. Analysis of an experimental and calculated result with the lattice mismatch correction.

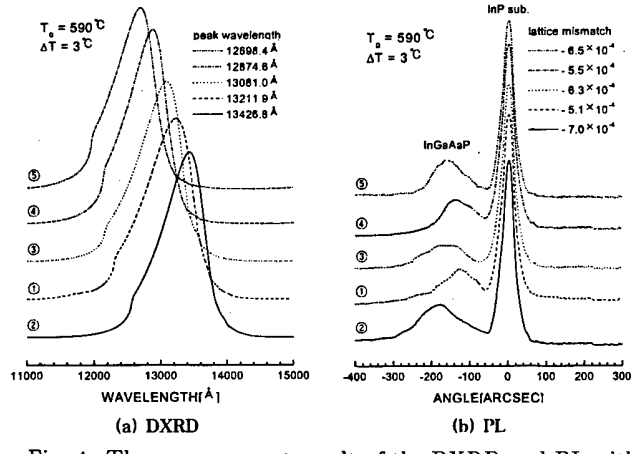

Fig. 4. The measurement result of the DXRD and PL with the wavelength correction at 590 °C.

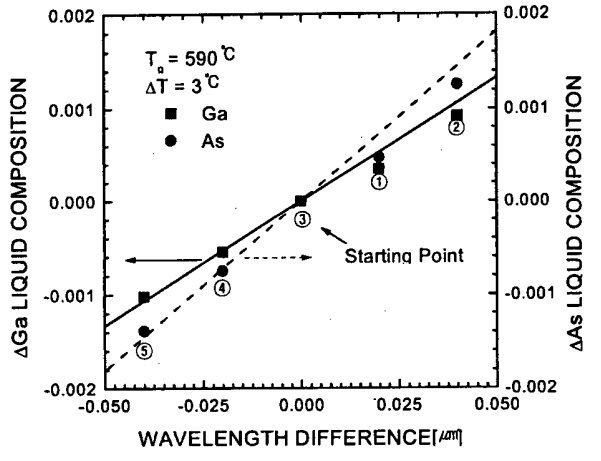

Fig. 5. Analysis of an experimental and calculated result with the wavelength correction.

from Fig. 3 measurements and calculated value were almost equal. Although it is not represented in the figure, the lattice pulling phenomenon happens, if the lattice mismatch was larger than 0.05 %, that is because we used two-phase solution technique. We confirmed that the lattice mismatch can be adjusted freely without varying the wavelength.

In the contrast of previous experiment, the next experiment was done contrary to the previous experiment fixed under the lattice mismatch and the wavelength variation. The lattice mismatch of start point is -5.1×10^{-4}, and the wavelength is 13211.9 Å. In this case, we shifted the wavelength with fixed lattice mismatch toward short wavelength range by 200 Å each. And these results are shown in Fig. 4. Fig. 4(a) shows results of controlling the lattice constant with various wavelength in Fig. 4(b) In spite of varied wavelength this method exactly controlled the lattice mismatch variation less than 0.002 % as shown in the Fig. 4(a). The experimental results of adjusting wavelength are compared with the theoretical data obtained by the proposed method in Fig. 5.

Although we varied wavelength by the 0.8 μm, we can get the wanted wavelength conversion by this method. In the range of short wavelength, the supersaturation could be increased generally as the solubility of P component is increased by decreasing the As component of InGaAsP solution. However, this experiment, we could neglect the effect of the P component because the supersaturation almost do not happen.

We grew the 1.3 μm InGaAsP in the growth temperature 630 °C, and we varied the wavelength and lattice mismatch according to the proposed method. We first used epilayer which had lattice mismatch of -7.8×10^{-4} and wavelength of 13388.3 Å. We have varied the lattice mismatch with fixing wavelength by 3.0×10^{-4} each. The results are shown in Fig. 6. It can be seen from Fig. 6. that the lattice mismatch is varied linearly. From Fig. 6(b) the wavelength change is as small as 87 Å, and the maximum of deviation between pre-correction and post-correction was larger than that in Fig. 2(b). It's reason

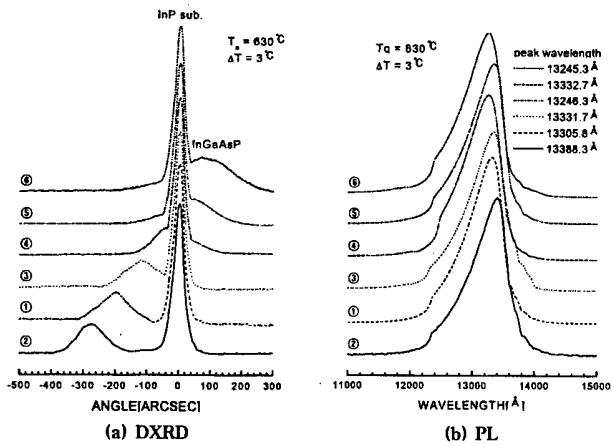

(a) DXRD (b) PL

Fig. 6. The measurement result of the DXRD and PL with the lattice mismatch correction at 630 °C.

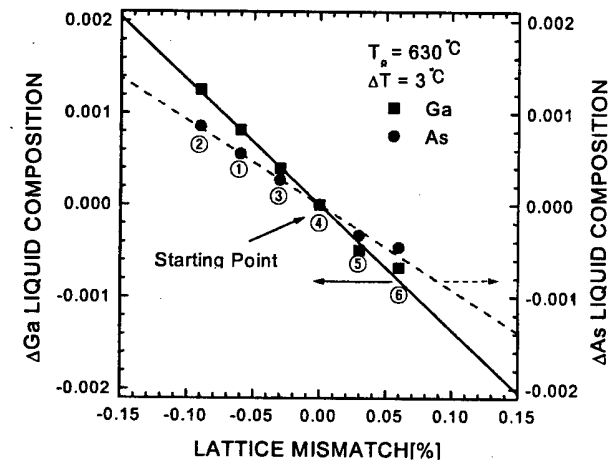

Fig. 7. Analysis of an experimental and calculated result with the wavelength correction.

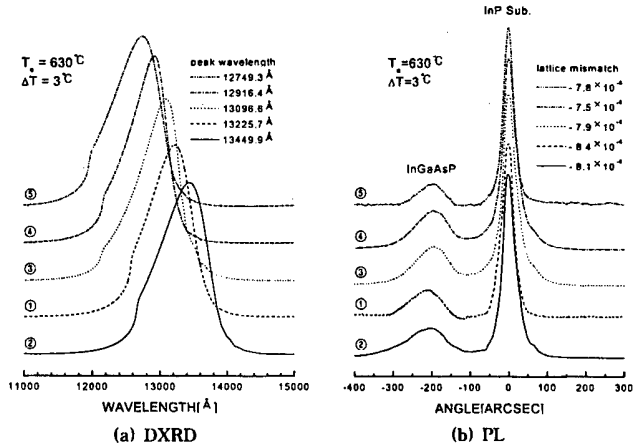

(a) DXRD (b) PL

Fig. 8. The measurement result of the DXRD and PL by the wavelength correction at 630 °C.

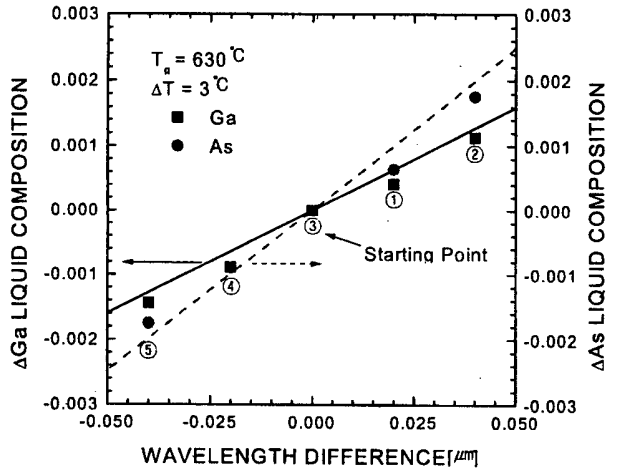

Fig. 9. Analysis of an experimental and calculated result by the wavelength correction.

may be that the differential distribution coefficient of As component at 630 °C had increased over about 1/3 more than at 590 °C. The estimated data and experimental data for liquid compositions of Ga and As with the proposed method are shown in Fig. 7. It can be found that the experimental results coincide with the estimated data well. And above 5.0×10^{-4}, the lattice pulling phenomenon was occurred just as Fig. 3.

Finally, we fixed the lattice mismatch and varied the wavelength. InGaAsP epilayer at the starting point had the mismatch of -8.4×10^{-4} and the wavelength of 13225.7 Å we began varying the wavelength at the interval of about 200 Å. The experimental result is shown in Fig. 8(a). Fig. 8(b) gives the lattice mismatch of each experiment, Even the maximum variation of 0.019 %, the influence of lattice mismatch hardly appeared. The comparison of experimental results and estimated results by proposed method is given in Fig. 9. The same phenomenon has also appeared as shown in Fig. 5.

As the above-mentioned, the epilayer where initial lattice mismatch and wavelength shift were occurred was controlled independently by introducing new concept of differential distribution coefficient for Ga and As therefore we confirmed that it was possible to control wavelength and lattice constant independently.

IV. CONCLUSIONS

It was a problem that the independent control of lattice match and wavelength variation was impossible in case of InGaAsP epilayer growth by using conventional phase diagrams. In order to overcome it, we first introduced the new concept of "differential distribution coefficient" in this research. Then we proposed the method by which it's possible to control the wavelength and lattice constant independently. We had varied the wavelength and lattice constant at each growth temperature of 590 °C and 690 °C for InGaAsP epilayer with the method. It

was confirmed that experimental data and estimated data of proposed method was coincide in the measurement of lattice mismatch with fixing wavelength and varying lattice mismatch at the interval of 3.0×10^{-4} each. At this time, the wavelength shifts of 57 Å and 87 Å only were observed at the growth temperature 570 °C and 630 °C respectively. And it can be concluded that the experimental data coincides with estimated data by fixing the lattice mismatch and varying the wavelength. At this time, it was confirmed that lattice mismatch was varied only by 0.02 % and 0.0019 % only at the growth temperature of 590 °C and 630 °C, respectively. From these results, we could confirm it was so useful to control wavelength and lattice constant independently by using differential distribution coefficient.

ACKNOWLEDGMENTS

This work was supported in part by the KOSEF and the ISRC in Seoul National University.

REFERENCES

[1] A. J. Jordan and M. Ilegems, J. Phys. Chem. Solids **36**, 329 (1975).
[2] K. Nakajima, T. Kusunoki, K. Akita and T. Kotani, J. Electrochem. Soc. **125**, 123 (1978).
[3] M. A. Pollack, R. E. Nahory, J. C. DeWinter and A. A. Ballman, Appl. Phys. Lett. **33**, 314 (1978).
[4] K. Nakajima, A. Yamaguchi, K. Akita and T. Kotani, J. Appl. Phys. **49**, 5944 (1979).
[5] E. H. Perea and C. G. Fonstad, J. Appl. Phys. **51**, 331 (1980).
[6] N. A. Bert, A. T. Gorelenok, A. G. Dzigasov, S. G. Konnikov, T. B. Popova, I. S. Tarasov and V. K. Tibilov, J. Crystal Growth **52**, 716 (1981).
[7] B. De Cremoux, IEEE J. Quantum Electron. **QE-17**, 123 (1981).
[8] K. Nakajima and T. Tanhashi, J. Crystal Growth **17**, 463 (1985).
[9] K. Nakajima, S. Yamazaki and K. Akita **56**, 547 (1982).
[10] K. Nakajima and T. Tanahashi, J. Crystal Growth **71**, 463 (1985).
[11] J. J. Hsieh, IEEE J. Quantum Electron **QE-17**, 118 (1981).
[12] E. Kuphal, J. Crystal Growth **67**, 441 (1984).
[13] M. Ilegems and M. B. Panish, J. Phys. Chem. Solids **35**, 409 (1974).
[14] G. B. Stingfellow, J. Cryst. Growth **27**, 21 (1974).
[15] A. S. Jordan and M. Ilegems, J. Phys. Chem. Solid **36**, 329 (1975).

Journal of the Korean Physical Society, Vol. 34, June 1999, pp. S474~S477

The Growth of InGaAsP/InP MQW Layers Using a Modified Vertical LPE System

Su Hwan OH, Sang Ku HWANG and TchangHee HONG

Department of Electronics and Communication Engineering, Korea Maritime University, Pusan 606-791

A conventional vertical LPE (Liquid Phase Epitaxy) system was modified in order to grow thin MQW (Multiple Quantum Well) layers below 100 Å reproducibly. Although MQW layers were grown by using the modified system, it was difficult to get a reproducible thin layer because of the unstability of solution during growth. To solve this problem, we made a new structure of graphite boat. After growth using it the uniformity of each layer was improved, and also more than 1/2 of growth thickness and 1/3 of thickness deviation could be reduced. Moreover, minimum growth thickness of 60 Å (InGaAsP QW layer) was achieved. It could be concluded that the unstability of solution affected a reproducible growth of MQW layers.

I. INTRODUCTION

The typical methods for growing III-V compound semiconductor are LPE, MOVPE, MBE *etc.* In case of LPE although the performance controlling the thickness of growth a little inferior to the other methods, a good quality of epitaxial layer can be achieved from the ideal thermal equilibrium state and the structure is simple. For this reason the chemical growth mechanism and method have been researched with LPE system for over 30 years [1,2] since tunneling diode and GaAs semiconductor laser was made with LPE method by Nelson in 1963 [3]. There are two kinds of LPE system such as a vertical type and a horizontal type according to direction of a reaction tube. The vertical system has several advantages such as low maintenance cost and the size etc. In this research a conventional vertical LPE system was modified, and its characteristics was evaluated.

In case of a vertical LPE system growth is proceeded in rotation of solution holder as upper part of a graphite boat. It was seen that there happened a problem in equilibrium condition due to rolling of solution by the abovementioned structural effect. Therefore we designed and made a new structure of graphite boat capable of solving this problem. The influence of solution unstability on grown layers has been investigated by research of the characteristics of a graphite boat.

In section II improvement of a vertical LPE system was described, the influence of solution unstability on growth of MQW layers was discussed in section III, and a conclusion was given finally in section IV.

*E-mail: k951402g@hanbada.kmaritime.ac.kr

II. THE IMPROVEMENT OF A VERTICAL LPE SYSTEM

In order to control the thickness of a grown layer precisely and reproducibly, the temperature of growth solution must be maintained uniformly and the temperature difference in the growth solution must be reduced. This temperature characteristic is affected mainly by the temperature characteristic of a furnace, besides by the structure of reaction tube and a graphite boat.

Heat was supplied in parallel to a graphite boat in a horizontal LPE system, while it was supplied converging from outside of a graphite boat in a vertical system so that the temperature in the center of the graphite boat is lower than the outside. Thereby it is difficult to get the uniform thickness of a growth layer because the inside of a substrate is grown thicker due to higher supersaturation than the outside. Therefore the system was modified to solve the problem as Fig. 1.

The new furnace used in the modified LPE system is as follows: 1) reduces the temperature difference between the inside and the outside of a graphite boat because it is able to supply heat from bottom. 2) the zirconium tube of a high thermal capacity was inserted between KANTAL wire and reation tube in order to decrease thermal nonuniformity in azimuth direction. But the vertical difference of temperature between the substrate and growth solution could be increased by supplying of heat from the bottom of the furnace, so that there can be happened an abnormal growth. Therefore we determined the optimum condition of the distance between the graphite boat and the bottom of the furnace. Fig. 2 shows the measured result of the azimuth directional temperature characteristic of the furnace shown in Fig. 1.

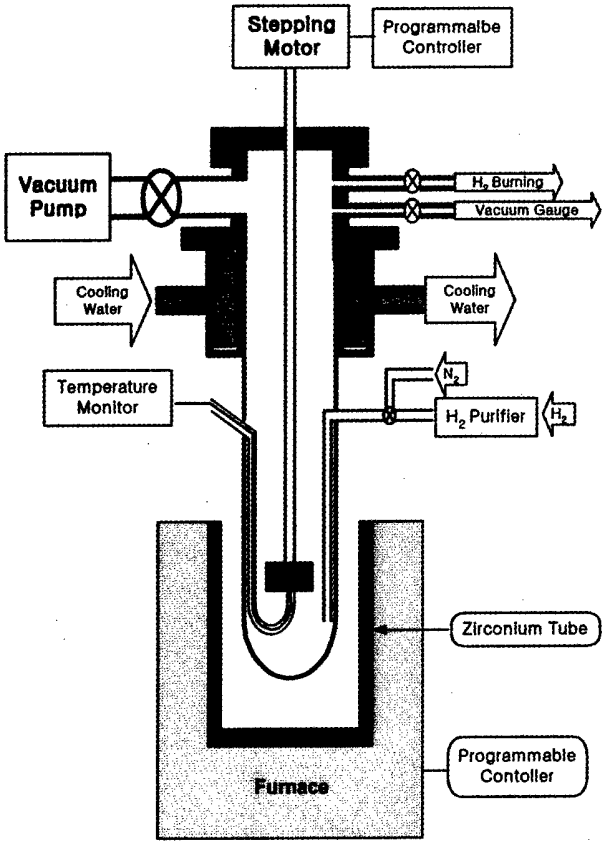

Fig. 1. A schematic diagram of the modified LPE system.

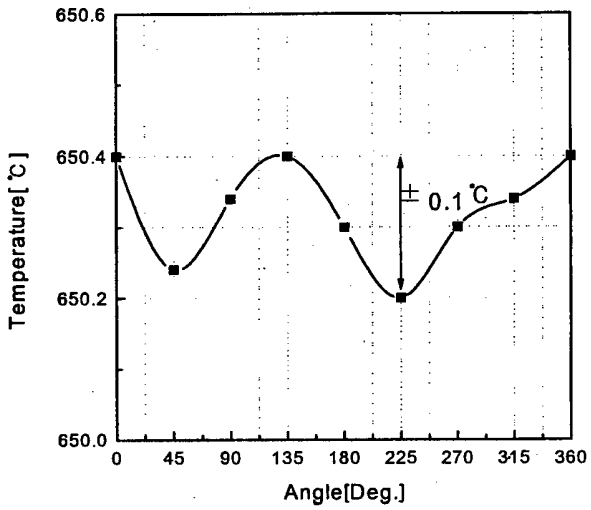

Fig. 2. Temperature characteristics of a graphite boat shown in Fig. 1 in azimuth direction.

It is seen from Fig. 2 that the temperature difference of azimuth direction is about ±0.1 °C, while the temperature difference of the commercial LPE system is about ±1 °C. Therefore the performance of the modified furnace of our system is about ten times better than the commercial one. Because the quality of an epitaxial layer depends on vacuum of LPE system, a flange was made as all-in-one part to prevent leakage and its coupling had a good structure capable of being joined to a reation tube by an o-ring. Moreover, a small water tube inside the flange was replaced efficiently with any additional cooling pipe for protecting thermal damage of an o-ring from heat. The vacuum of the modified system could be 10^{-5} Torr as the maximum vacuum of a mechanical pump.

III. INFLUENCE ON GROWTH OF MQW LAYER DUE TO SOLUTION INSTABILITY

When we grew an epitaxial layer with the modified LPE system to make MQW-LD, it was a big problem that thickness of the layer was not uniform and reproducible. It was considered that epitaxial layer was grown on a substrate by rotation of solution in a vertical system, while moving of a substrate in a horizontal system. Fig. 3 shows a photograph of a graphite boat in a conventional vertical LPE system [4].

Left side of Fig. 3 is a holder of solution and right side is a holder of substrates. It shows the structure of

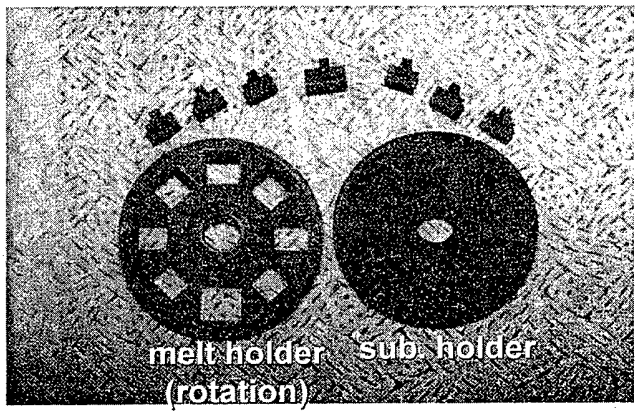

Fig. 3. A graphite boat of rotating solution.

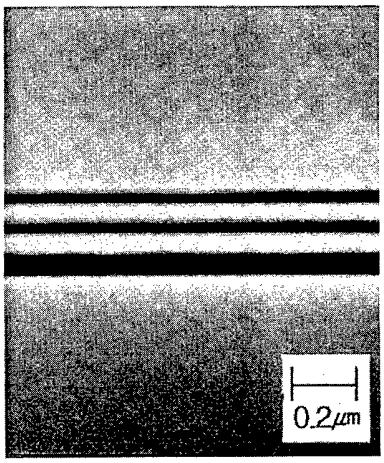

Fig. 4. MQW layers grown by using the graphite boat shown in Fig. 3.

rotating solution during growth. Fig. 4 shows the most typical result of MQW-DH wafer which was grown in 630 °C and cooling speed of 0.4 °C/min by using the graphite boat shown in Fig. 4.

As shown in Fig. 4, there is problems in uniformity on the grown layers, and it can be seen that the thickness of the grown layers was more decreased than the previous grown layer. A conclusion was deduced from the growth result as follows: When InP layers and InGaAsP layers were grown alternately with rotation of a solution holder in growth of MQW layers, the equilibrium condition could be broken due to disturbance of solution. In case of InP two phase solution method used in growth of InGaAsP/InP MQW layers, InP seed maintains thermal equilibrium condition of growth solution layer until growth. It was thought that initial growth rate was increased by broken thermal equilibrium due to disturbance of solution, and growth rate was decreased due to lack of V-group elements because of continuous diffusion-limited growth by V-group elements of big distribution coefficient. It was concluded that the most important thing is to get stability of solution to decrease initial growth rate and to get a uniform MQW layer. Therefore a new graphite boat of the structure shown in Fig. 5 was designed and made to get stability of solution.

A graphite boat of left side shown in Fig. 5 fixes solution holder of left side by using two quartz pins in front, and also fixes a reaction tube. A center graphite boat is connected to the rotation axis as a substrate holder, and has the structure of rotating substrates with being inserted between the left side and the right side as comparing to the graphite boat shown in Fig. 3. In case of a vertical system in Fig. 3 a graphite boat is easy to rotate unstably by bending of rotation stick or deviation of rotation axis, but a graphite boat of Fig. 5 prevent from unstable rotation by the structure of 3-step. Fig. 6 shows a cross-sectional photograph of the result grown on the same condition as Fig. 2 by using a graphite boat of Fig. 5.

It can be seen from Fig. 6 that deviation of thickness between growth layers was decreased, and also uniformity and quality of interface was improved. It can be concluded from the above-mentioned fact that rotating substrates scheme gives more stable condition of solution than rotating solution scheme. InGaAsP layers as QW layers were grown by three layers per one second in 0.4 °C/min of cooling rate and 630 °C of temperature. Table 1 shows average thickness and deviation of each grown layer in center and edge. The experiment with a graphite boat of Fig. 3 had been done more than 200 times, and that of Fig. 5 had been done more than 80 times.

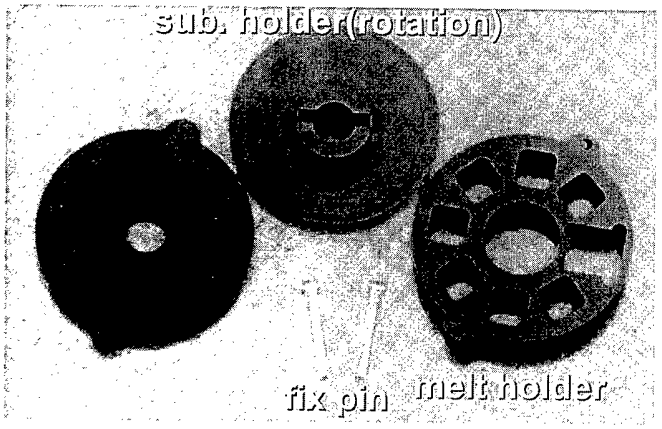

Fig. 5. A photograph of a modified graphite boat.

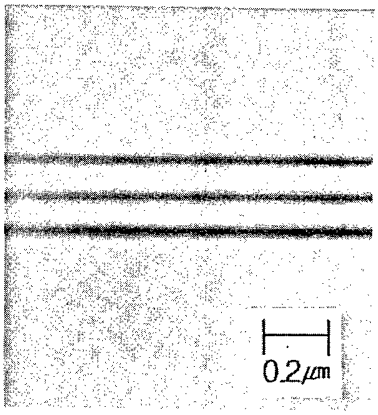

Fig. 6. MQW layers using the graphite boat of Fig. 5.

It can be seen from Table 1 that edge overgrowth have happened on the result taken by using a graphite boat of Fig. 3 more severely than the case of Fig. 5. Its cause seems to be that supersaturation in solution was different by rolling of solution during rotation of solution holder. In case of Fig. 3 average thickness and thickness deviation between grown layers is very big. The more a layer was grown later, the more its average thickness was decreased because initial supersaturation become big due to broken equilibrium by rolling of solution. But in

Table 1. Average thickness and standard deviation of MQW layers.

(a) using the graphite boat of Fig. 3

point	edge		center	
growth layer	average (Å)	standard deviation (Å)	average (Å)	standard deviation (Å)
first layer	455	155	348	110
second layer	354	120	343	113
third layer	284	98	282	82

(b) using the graphite boat of Fig. 4

point	edge		center	
growth layer	average (Å)	standard deviation (Å)	average (Å)	standard deviation (Å)
first layer	189	44	180	39
second layer	159	28	153	27
third layer	143	27	141	27

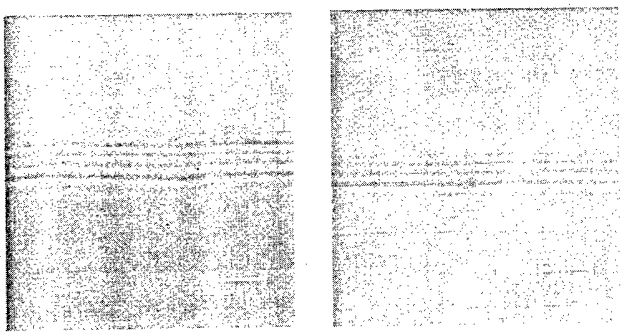

(a) (b)

Fig. 7. SEM photograph of MQW layers (growth temperature: 590 °C) (a) 1.3 μm InGaAsP/InP MQW layers and (b) 1.1 μm InGaAsP/InP MQW layers.

case of Fig. 5 uniformity of each layer and also average thickness of grown layers were increased considerably so that average thickness was decreased more than 1/2 and thickness deviation was decreased more than 1/3.

Moreover, Fig. 7 shows the result grown at temperature of 590 °C in order to know what is the limit to be grown with LPE system. (a) and (b) represent the grown layers of 1.3 μm-InGaAsP/InP and 1.1 μm-InGaAsP/InP respectively, and each thickness is about 60 Å. This is the result beyond the report that uncertainty of interface between grown layers is about 100 Å [5] in case of LPE. Therefore it means that high quality of optical devices having MQW layers can be made also by using LPE system. From the above results it can be seen that the modified graphite boat is excellent. It can be deduced that thickness deviation between grown layers appeared big in unstable solution due to increase of initial supersaturation. Therefore it can be concluded that the stability of solution is very important in reproducibility and thickness control of growth layers.

IV. CONCLUSIONS

The conventional LPE system has been modified to improve the reproducibility in grown QW layers and to get high qualities of epitaxial layers. Especially the temperature characteristics of a furnace and the stability of the system has been improved. The temperature characteristics of a graphite boat in azimuth direction were measured after modification and the result was ± 0.1 °C. Vacuum of the system was also improved to be 10^{-5} Torr by replacing with a new reaction tube and flange. The important problem was that the MQW epitaxial layers grown with the modified LPE system was not reproducible and also was not controlled their thickness. It is because growth was achieved on substrates in rotation of solution generally in a vertical LPE system. In order to solve the unstability occurred by rotation of solution, a new graphite boat was designed and made to move substrate holder without rotation of solution. From the growth result with the modified graphite boat uniformity of each layer was improved, thickness deviation between the grown layers was decreased, and growth thickness and thickness deviation could be decreased more than 1/2 and 1/3 respectively. Moreover, minimum growth thickness of 60 Å was achieved and it is an excellent result considering the uncertainty between interfaces grown by LPE. Therefore it could be concluded that LPE system could be used also in fabrication of optical devices having MQW layers.

ACKNOWLEDGMENTS

We would like to thank professor Ko Jung Dae of Cheju University for helpful support. This work was supported by the Korea Research Foundation

REFERENCES

[1] K. Oe and K. Sugiyama, Jpn. J. Appl. Phys. **15**, 1740 (1976).
[2] S. Arai, Y. Suematsu and Y. Itaya, Jpn. J. Appl. Phys. **18**, 709 (1979)
[3] H. Nelson, RCA Rev **24**, 603 (1963).
[4] Ho Sung Cho, Sang Ku Hwang, Jeong Cheol Bae, TchangHee Hong, Jae Chang Kim and Jong Hwang Oh, Ungyong Mulli (Korean J. of Appl. Phys.) **6**, 151 (1993).
[5] L. W. Cook, M. Feng, M. M. Tashima, R. J. Blatter and G. E. Stillman, J. Crystal Growth. **65**, 588 (1983)

Journal of the Korean Physical Society, Vol. 34, June 1999, pp. S478~S481

High Breakdown Voltage P-HEMT Using Single Gate Lithography and Two-Step Gate Recess Process

Hyung-Sup YOON, Jin-Hee LEE, Byung-Sun PARK, Chul-Wook LEE and Chul-Soon PARK

*Compound Semiconductor Research Department, ETRI-Microelectronics Technology Laboratory, Electronics and Telecommunications Research Institute, Taejon 305-350**

In this paper, we report a two-step gate recess process that uses the single step gate patterning and the sequentially selective dry and wet etchings to improve the breakdown voltage of low noise P-HEMT device. The current-voltage (I-V) and gate-to-drain reverse diode characteristics of P-HEMT fabricated by using two-step gate recess are compared with those by using the conventional single gate recess. The high gate-to-drain breakdown voltage (−11.7 V), low output conductance (19 mS/mm), and low leakage current (0.4 μA) in pinch-off region of I-V characteristics are obtained for the low noise P-HEMT fabricated with two-step gate recess process.

I. INTRODUCTION

At present, the low noise high electron mobility transistors(HEMTs) are widely used in the front end of satellite communications, radio astronomy, and satellite direct broadcasting receiver systems [1,2]. The pseudomorphic AlGaAs/InGaAs/GaAs HEMT (P-HEMT) has demonstrated high frequency and low noise performance at millimeter and microwave frequency [3,4]. However, the low noise P-HEMT has the limiting factor for power applications due to the relatively low gate-to-drain breakdown voltage. Although the breakdown mechanism in field effect transistors including MESFET and P-HEMT is still not totally understood, it is generally known that breakdown occurs at the gate edge nearest the drain where the electric field is highest or along the surface between the gate and the drain [5,6]. To improve the gate to drain breakdown voltage of P-HEMT device, the gate recess process is the most critical. For low noise applications, it is important to have a narrow recess that is slightly larger than the gate footprint. But a gate recess larger than the gate footprint is necessary for power applications.

In this study, we report the low noise P-HEMT devices with a high reverse gate-to-drain breakdown voltage in which a two-step gate recess uses the single step gate patterning and the sequentially selective dry and wet etchings. The P-HEMT fabricated using two-step gate recess exhibited the improved gate reverse breakdown and output conductance characteristics compared with those fabricated using the conventional single gate recess.

*E-mail: hsyoon@cadvax.etri.re.kr, Fax: 042-860-6183

II. HEMT STRUCTURE AND FABRICATION

The low noise P-HEMT epitaxial structure has been grown by using molecular beam epitaxy (MBE). The cross-section of P-HEMT structure is shown in Figure 1. An 80 nm thick undoped GaAs buffer and 10 period AlAs-GaAs superlattices are grown on a 3-inch diameter semi-insulating GaAs substrate, followed by a 600 nm thick undoped GaAs layer. We used 12 nm $In_{0.15}Ga_{0.85}As$ as the channel layer. The Si-planar doping layer with a doping density of 5×10^{12} cm^{-2} is separated from the active layer by 3 nm thin undoped $Al_{0.24}Ga_{0.76}As$ spacer. The undoped $Al_{0.24}Ga_{0.76}As$ Schottky layer was 30 nm. Then, the 50 nm thick GaAs

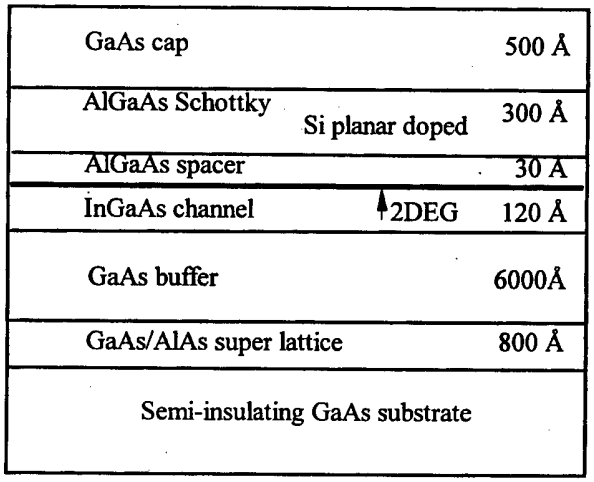

Fig. 1. Schematic cross-section of AlGaAs/InGaAs/GaAs pseudomorphic HEMT epitaxial layers.

cap layer was highly doped with Si of 5×10^{18} cm^{-3} to reduce parasitic resistance. Hall measurements of P-HEMT structure yielded an electron density of n_s= 2.1×10^{12} cm^{-2} with mobility of μ_H=6,000 $cm^2/V\cdot s$ at 300 K.

P-HEMT devices consisting of 0.2 μm gate length and 100 μm gate width were fabricated using mix-and-match of *i*-line optical stepper and electron-beam lithography. The ohmic drain-to-source distance of 2.6 μm with gate-to-source spacing of 0.7 μm was used. The sequence for device fabrication is as follows. After mesa isolation by wet chemical etching in H_3PO_4:H_2O_2:H_2O=4:1:90, ohmic contacts were formed by evaporating AuGe/Ni/Au metallic layers and then alloyed at 410 °C using a rapid thermal annealing. The PMMA/P (MAA-MAA) bi-layer resists system was used to form the T-shaped gate with 0.2 μm gate length. After these resists were exposed by using the electron beam direct-writing lithography, the top and bottom resists were developed by the mixed solution of MIBK and IPA. After patterning the T-shaped gate, the selective dry gate recess was firstly performed by using BCl_3/SF_6 to precisely control the recess depth. Secondly, selective wet gate recess etching was performed by using the mixed solution of citric acid and hydrogen peroxide to obtain lateral gate recess larger than the gate length. Then, Ti/Pt/Au (0.6 μm thick) metal layers were deposited with electron-beam evaporator and lifted-off with acetone.

III. RESULTS AND DISCUSSION

Figure 2 and 3 show the cross section of P-HEMT devices fabricated by using the conventional single-step gate recess and two-step gate recess, respectively. As shown in Fig. 2, the etch profile obtained by single-step gate recess has the side-etched separation (Lgo) of 35 nm between the gate and the edge of etched n^+ ohmic layer. But the etch profile performed by two-step gate recess has the side-etched separation (Lgo) of 95 nm between

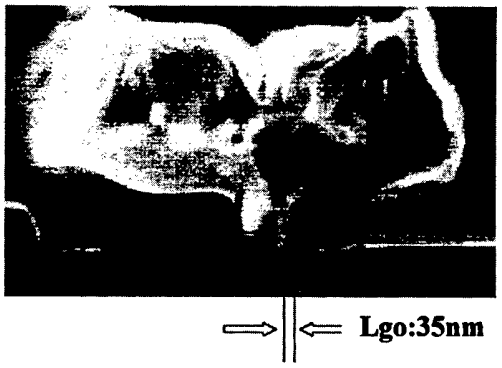

Fig. 2. The cross section of P-HEMT device fabricated by using the conventional single-step gate recess of BCl_3/SF_6 dry etching.

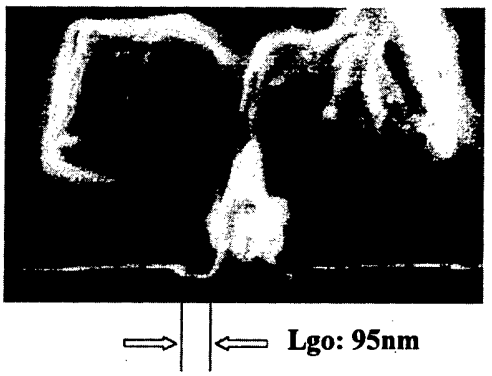

Fig. 3. The cross section of P-HEMT device fabricated by using the two-step gate recess of the BCl_3/SF_6 dry etching and citric acid/H_2O_2 wet etching.

the gate and the edge of the n^+ ohmic layer as shown in Fig. 3. Therefore, the two-step gate recess provides the lateral gate recess larger than the gate length that is effective for improving the gate to drain breakdown voltage of P-HEMT device.

Figure 4 shows the gate-to-drain reverse I-V characteristics of P-HEMT devices fabricated by using the two-step and conventional single-step gate recesses for 0.2 μm×100 μm P-HEMT device. The gate to drain breakdown voltage is defined as the voltage at which the gate current reaches 1 mA/mm. It is clear that the gate-to-drain breakdown voltage (−11.7 V) obtained with the two-step gate recess is higher than that (−8 V) with conventional single-step gate recess. The studies for P-HEMT devices with the conventional gate recess reported breakdown voltage in the range of −6 to −8 V [7,8]. The improvement of breakdown voltage in case of the two-step gate recess is attributed to the large side-etched separation (Lgo) of 95 nm between the gate and the edge of the n^+ ohmic layer by applying selective wet etching of citric acid/H_2O_2 as shown in Fig. 3. In contrast to convention-

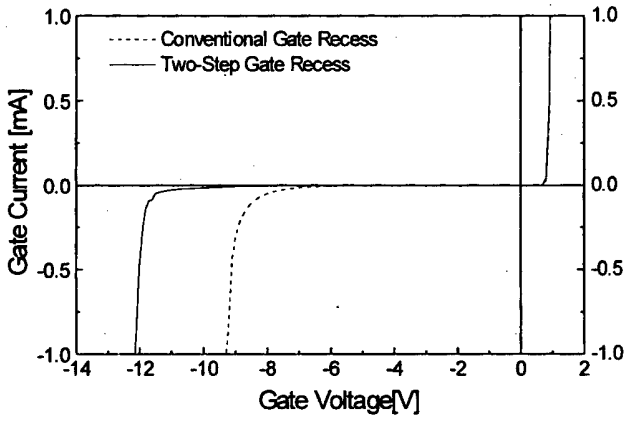

Fig. 4. The gate-to-drain reverse I-V characteristics of P-HEMT devices fabricated by using the two-step and conventional single-step gate recess.

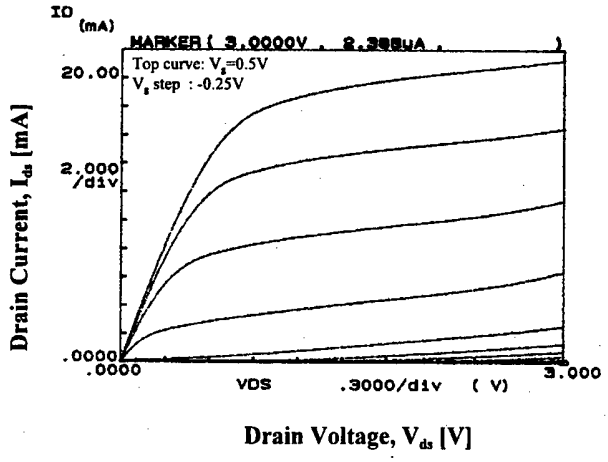

Fig. 5. Drain current, I_{ds}, as a function of source-to-drain voltage, V_{ds}, for 0.2 μm×100 μm P-HEMT devices fabricated by using the conventional single-step gate recess.

al double recess process that requires two gate lithography steps [8], the current two-step recess eliminated a lithography step and the critical alignment by using only a single gate lithography step, thereby effectively improving gate recess process to increase the breakdown voltage in low noise P-HEMT devices.

Figure 5 shows drain current as a function of source-to-drain voltage (V_{ds}) for 0.2 μm×100 μm P-HEMT devices fabricated by using the conventional single-step gate recess. As shown in Fig. 5, P-HEMT devices exhibit a leakage current (2.4 μA) in pinch-off region for drain voltage of 3 V and gate voltage of −2.5 V. For P-HEMT devices fabricated by using the two-step gate recess, the typical I-V characteristics are shown in Fig. 6. It exhibits a very small leakage current (0.4 μA) in pinch-off region for drain voltage of 3 V and gate voltage of −2.5 V. This very small leakage characteristics result from the large separation (Lgo) of 95 nm between the gate and the edge of the etched n^+ ohmic layer formed by using two-step gate recess as shown in Fig. 3. Also, the output conductance (g_{mo}) for the P-HEMT recessed with the two-step gate recess is 19 mS/mm while the P-HEMT fabricated with the conventional gate recess exhibited a g_{mo} of 30 mS/mm as calculated from Fig. 5 and 6. It is noticed that the improvement in g_{mo} is achieved with only slight degradation in drain current when comparing the two-step gate recessed P-HEMT to the conventional gate recess. For 0.2 μm×100 μm P-HEMT recessed by using the conventional single-step dry etching, the extrinsic transconductance (g_m) and drain current (I_{ds}) as a function of source-to-gate voltage (V_{gs}) are shown in Fig. 7. The threshold voltage (V_{th}) is defined by a linear extrapolation of the square root of drain current versus gate voltage to zero current. V_{th} was measured as −0.72 V at V_{ds}=2 V. And the maximum g_m was measured as 470 mS/mm at V_{gs}= 0.1 V and V_{ds}=2 V. Figure 8 shows the extrinsic g_m and drain I_{ds} as a function of V_{gs} for 0.2 μm×100 μm P-HEMT recessed by using the two-step dry

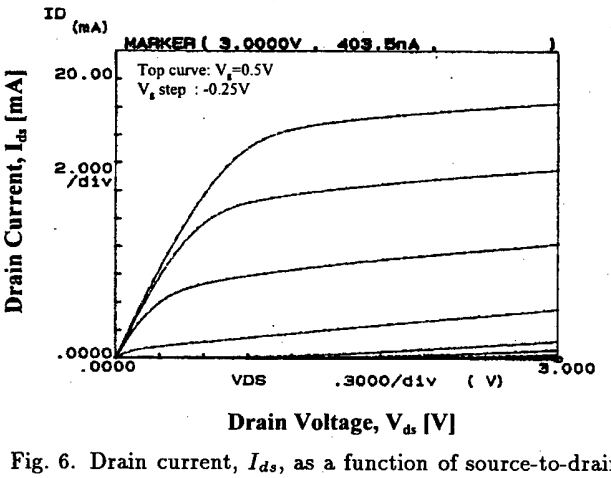

Fig. 6. Drain current, I_{ds}, as a function of source-to-drain voltage, V_{ds}, for 0.2 μm×100 μm P-HEMT devices fabricated by using the two-step gate recess.

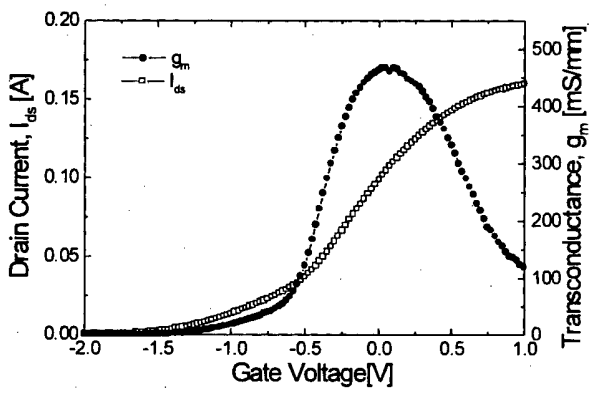

Fig. 7. The extrinsic transconductance (g_m) and drain current (I_{ds}) as a function of source-to-gate voltage (V_{gs}) for 0.2 μm×100 μm P-HEMT fabricated by using the conventional single-step dry etching.

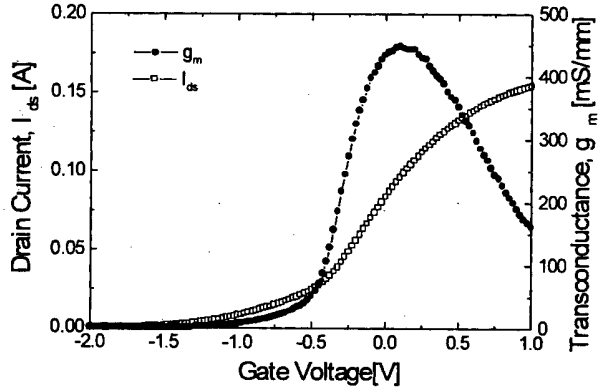

Fig. 8. The extrinsic transconductance (g_m) and drain current (I_{ds}) as a function of source-to-gate voltage (V_{gs}) for 0.2 μm×100 μm P-HEMT fabricated by using the two-step gate recess.

etching. It exhibits that the V_{th} and maximum g_m are is -0.67 V and 460 mS/mm, respectively. The value of g_m obtained in the two-step dry etching is a little less than that in the case of single-step gate recess. The slight reduction in g_m shown in the two-step recessed P-HEMT is attributed to the increased source resistance that was caused by the large side-etching of ohmic layer on the source side of the gate using the two-step gate recess etching.

IV. CONCLUSIONS

We report a two-step gate recess process, which uses the single step gate patterning and the sequentially selective dry and wet etchings to improve the breakdown voltage of low noise P-HEMT device. The gate-to-drain reverse I-V characteristics of P-HEMT fabricated by using two-step gate recess are compared with those by using the conventional single gate recess. The high gate-to-drain breakdown voltage (-11.7 V), low output conductance (19 mS/mm) of I-V characteristics, and the low leakage characteristics (0.4 μA) in pinch-off region are obtained for the low noise P-HEMT fabricated using two-step gate recess process. The improvement of breakdown voltage and leakage characteristics in case of the two-step gate recess is attributed to large side-etched separation of 95 nm between the gate and the edge of the etched n^+ ohmic layer in P-HEMT devices. The two-step gate recess process developed in this study eliminated a lithography step and the critical alignment by using only a single gate lithography step, thereby effectively improving gate recess process to increase the breakdown voltage in low noise P-HEMT devices.

ACKNOWLEDGMENTS

This work was financially supported by the Korea Telecom.

REFERENCES

[1] J. J. Berenz, K. Nakano and K. P. Weller, IEEE Monolithic Circuits Symp. Dig., 83 (1984).

[2] M. Abe, T. Mimura, N. Kobayashi, M. Suzuki, M. Kosugi and M. Nakayama, IEEE Trans. Electron Devices **36**, 2021 (1989).

[3] N. Moll, M. R. Hueschen and A. Fischer-Colbrie, IEEE Trans. Electron Devices **35**, 879 (1988).

[4] Hyung-Sup Yoon, Jin-Hee Lee, Sang-Soo Choi, Chul-Soon Park, Pyun-Kwang Eui and Hyung-Moo Park, J. Korean Phys. Soc. **29**, 234 (1996).

[5] T. M. Barton and P. H. Ladbrooke, Solid State Electron Devices **29**, 807 (1986).

[6] Y. Wada and M. Tomizawa, IEEE Trans. Electron Devices **35**, 1765 (1988).

[7] K. L. Tan, R. M. Dia, Dwight C. Streit, Tzuenshyan Lin, Tien Q. Trinh, A. C. Han, P. H. Liu, Pei-Min D. Chow and H. C Yen, IEEE Electron Device Letters **11**, 585 (1990).

[8] J. C. Huang, P. Saledas, J. Wendler, A. Platzker, W. Boulais, S. Shanley, W. Hoke, P. Ltman, L. Aucoin, A. Miquelarena, C. Bedard and D. Atwood, IEEE Electron Device Letters **14**, 456 (1993).

Journal of the Korean Physical Society, Vol. 34, June 1999, pp. S482~S487

The Photoluminescence Study on Thermally Annealed ZnTe/CdTe Heterostructure Interface

I. J. KIM, Y. H. KIM, J. K. HONG, K. N. OH, D. Y. SHIN, E. S. KIM,
I. S. CHOI, G. J. CHANG, S. U. KIM and M. J. PARK

Department of Physics, Korea University, Seoul 136-701

The electrical characteristics of semiconductor devices are largely governed by the properties of the semiconductor surface. ZnTe is proposed as the passivation material for the surface of CdTe which is widely used for the solar cells, the substrates of the $Hg_{1-x}Cd_xTe$, and the high-energy detectors. By the method of e-beam evaporation, ZnTe has been deposited onto the CdTe surface which is treated by suitable etching solution to prepare the better surface state for the deposition. Because of 6.2 % lattice mismatch between ZnTe and CdTe, the interface structure of ZnTe/CdTe heterostructure should be of inferior quality, thus thermal annealing process is required to reduce the imperfection of the interfacial structure. The change of ZnTe/CdTe interface has been analyzed by the photoluminescence and X-ray diffraction. In this study, the suitable thermal annealing condition is accomplished to obtain better interface state of ZnTe/CdTe structure. Also this results have been estimated by the photoluminescence study.

I. INTRODUCTION

The surface preparation of the semiconductor is one of the most important processes for the device fabrication. In general the surface plays a major role in device performance. After the surface treatments, *i.e.*, polishing and chemical etching, for example, the surface passivation of the semiconductor plays an important role of minimizing the leakage current [1,2]. It is needed also to prevent indeterminate and progressive chemical changes to the surface structure. ZnS and $Cd_{1-x}Zn_xTe$ have been studied as materials used for CdTe surface passivation. Recently ZnTe has been proposed as the alternative candidate for the passivant of the CdTe surface, since CdTe is the wide bandgap materials, which have been widely used for the optical fibers, the solar cells, and the high-energy detectors. Some researchers are interested in the study of ZnTe/CdTe superlattice and ZnTe/CdTe structure as a back-contact interface layer for thin film CdS/CdTe solar cells. But ZnTe/CdTe heterostructures have been hardly researched for the optical characteristics, *e.g.*, photoluminescence, optical absorption, *etc.* In this study we will propose the process to improve the property of the interface state of ZnTe/CdTe heterostructure. Because of the large difference of the lattice constants between ZnTe (6.1037 Å) [3] and CdTe (6.481 Å) [4], the interface state of ZnTe/CdTe heterostructure should be of inferior quality. The surface of CdTe prior to passivation has been etched by different etching solutions. Then the differences of the etched surfaces are compared with each others by atomic force microscopy (AFM) and photoluminescence (PL) methods. The thermal annealing processes have been performed to improve the inferior interface qualities caused by the large lattice mismatch between ZnTe and CdTe. The changes of ZnTe/CdTe interface states are compared with each others by photoluminescence and x-ray diffraction methods.

II. EXPERIMENTAL

Single crystal of CdTe has been grown by the vertical Bridgman method. The purity of cadmium and tellurium used in this study is 99.9999 %. ZnTe source material to be deposited onto the surface of CdTe has been synthesized by the vertical Bridgman method and then it has been zone-refined several times. The surface of CdTe is treated as the followings; mechanical polishing with Al_2O_3 powder-D.I. water and then the chemical polishing with 1 % bromine-ethylene glycol solution [5]. After chemical polishing, the surface of CdTe is chemically etched by two different etching solutions during 30 sec. One is 2 % Br-methanol (BM) solution and the other is 2 % Br-ethylene glycol solution containing 20 % Lactic acid (BLE). After these etching processes, the data of the PL and AFM for the surface states of CdTe are compared. ZnTe has been deposited on the p-CdTe (111) plane by the e-beam evaporator. The thicknesses of the deposited ZnTe layers are in the range of 1000 to 4000 Å. The deposition rates are 0.2 Å/sec from the initial to 500 Å, and 1 Å/sec from 500 Å to the final. The thermal annealing of the ZnTe/CdTe structures are performed in the

range between 500 and 600 °C in vacuum state about 10^{-6} Torr. After these treatments, the optical properties of the interface of ZnTe/CdTe heterostructures are compared with the results of the photoluminescence measurements. The instruments used to measure the PL spectra are composed of the JANIS cryostat (cooling temperatures: 77 K, 4 K), INNOVA 300 Ar^+-ion laser (514.5 nm light source), Da-781-IR PMT (the detection range: 300 to 1100 nm), and AM 506 ARC spectrophotometer (600 groove/mm grating). The power intensity of laser source is 250 mW/cm^2. The surface morphology was analyzed by the AFM (AFM BFD-B2, Park scientific Inc). The scanning range is 3×3 μm^2 and the spectroscopy scan rate is 0.2 Hz. The crystallinity and crystal structure of the interface of ZnTe/CdTe structure have been measured by X-ray diffraction (Rigaku Co.).

III. RESULTS

1. CdTe Surface Preparation

In the figure 1, the changes of the relative peak intensities by the different etching conditions are shown. The ratio of the intensity of defect emission to the intensity of edge emission in the PL spectra depend on the surface states of the etched CdTe. The intensities of the DAP band in the etched surfaces are lower than those in unetched surface. The PL spectra at 4 K were measured to examine the changes of the DAP bands in detail (Fig. 2). When the values of the FWHM of the neutral acceptor bound exciton peak (A^o, X) in 1.583 eV are compared with each others, the case of BLE solution has more smaller value than others, *i.e.*, the values of the FWHM are 13.1 meV for the case of no-etched, 8.8 meV for the case of BM etching, and 8.1 meV for the case of BLE etching (Fig. 2(a) and Table 1). And the intensity of DAP band dominantly decreases in the case of BLE solution among the others (Fig. 2(b)). Bromine in the etching solution can selectively remove the cadmium in the CdTe surface. Thus this removal makes Te^{4+} ions rich in the CdTe surface after the chemical etching. This is the origin of being more Cd vacancies, which act as the surface trap states, in the CdTe surface than in the CdTe bulk [6,7]. It can be predicted that the CdTe surface etched by BLE solution contains the smaller acceptor centers in the bandgap rather than those by other etching solution.

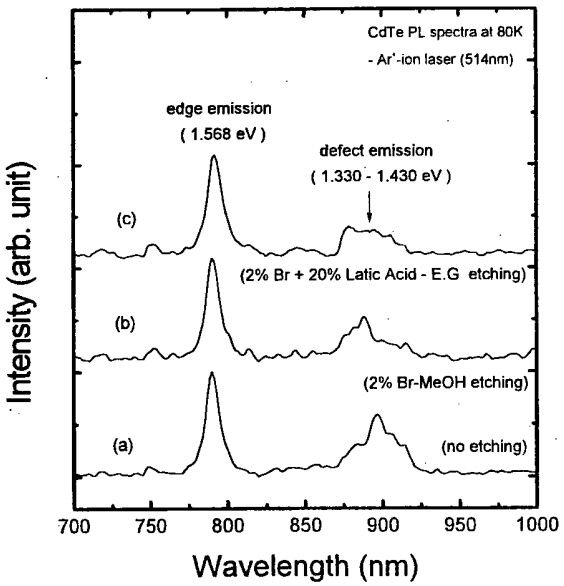

Fig. 1. The PL spectra at 80 K of the CdTe etched by two different etching solutions, (a) chemical polishing and no-etching, (b) 2 % Br-methanol (BM) solution, (c) 2 % Br-ethylene glycol solution containing 20 % latic acid (BLE).

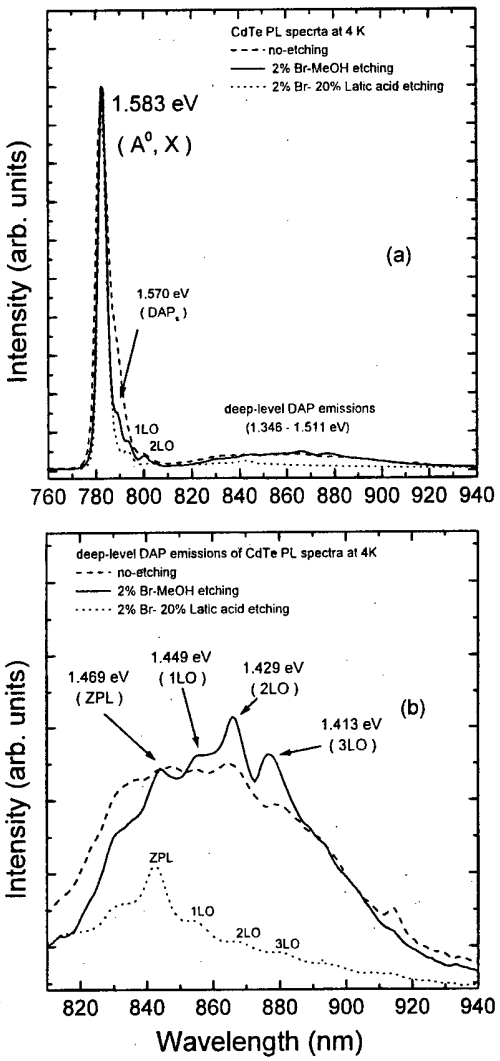

Fig. 2. The PL spectra at 4 K of the CdTe etched by two different etching solutions, (a) shows bound exciton and DAP emissions, (b) shows that deep level DAP emissions of CdTe in the case of BLE etchant decreases dominantly.

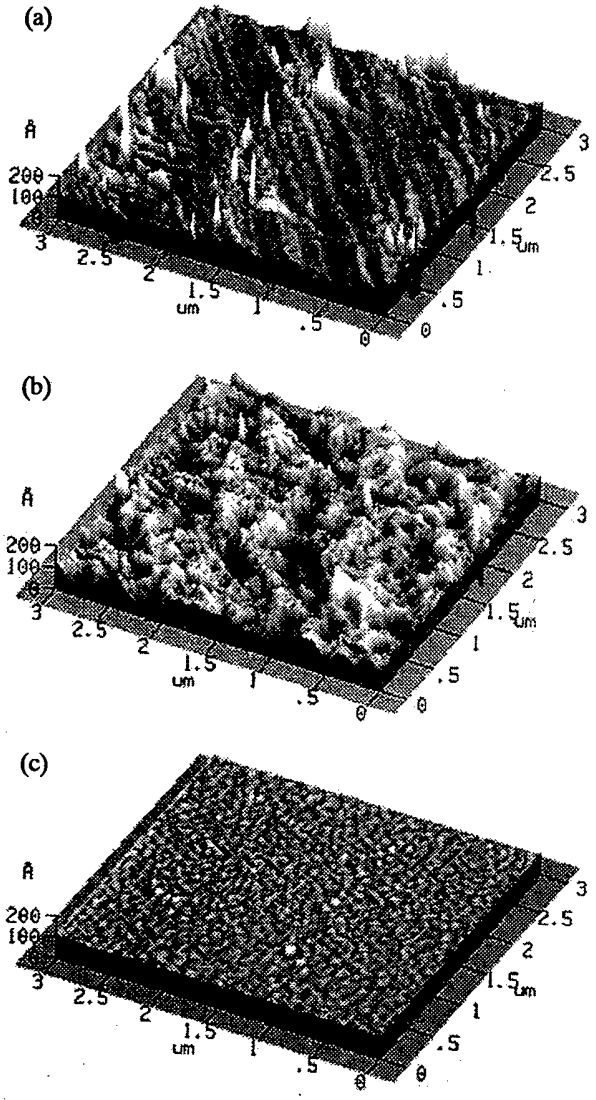

Fig. 3. AFM results about the surface morphology of CdTe. The surface roughnesses are 3.483 nm in the case of no-etching in (a), 3.719 nm in the case of 2 % Br-methanol solution in (b), and 0.278 nm in the case of 2 % Br-ethylene glycol solution containg 20 % latic acid in (c).

This is confirmed by examining the surface morphology through the AFM measurement as shown in the figure 3. It can be seen in the figure that the CdTe surface roughness is much smaller in the case of BLE etching than in the other cases, *i.e.*, the surface roughness are 0.278 nm in the case of BLE etched, 3.719 nm in the case of BM etched, and 3.483 nm in the case of no-etched.

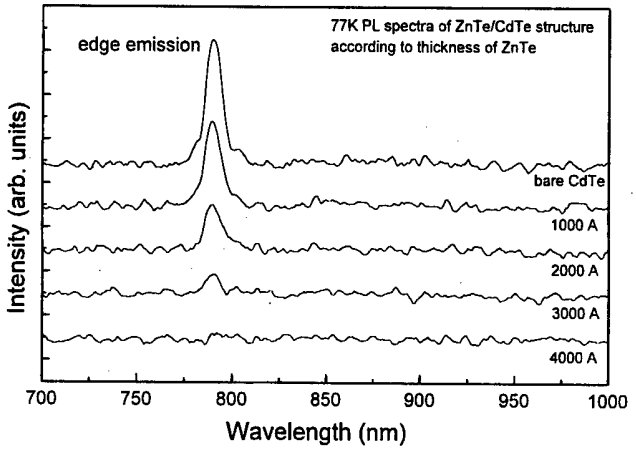

Fig. 4. The PL spectra at 77 K of ZnTe/CdTe structure according to thickness of ZnTe.

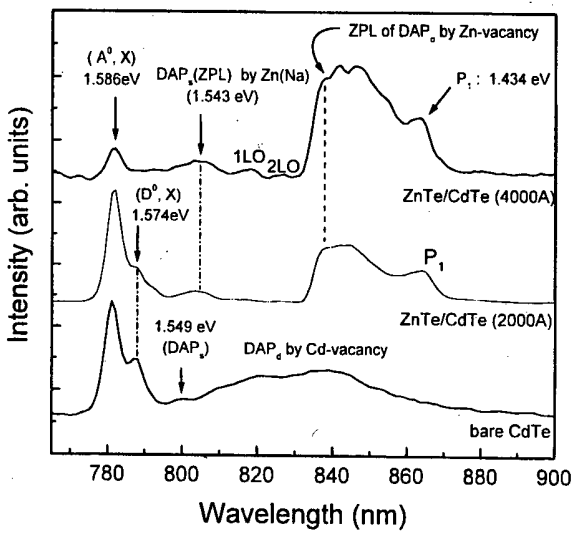

Fig. 5. The PL spectra at 4 K of ZnTe/CdTe heterostructure according to the thickness of ZnTe.

Table 1 displays the PL and AFM results according to the surface treatment of CdTe.

2. The PL characteristics of ZnTe/CdTe heterostructure

Figure 4 shows the PL spectra at 77 K in the cases of different thickness of ZnTe layer deposited onto the

Table 1. The results of PL and AFM of CdTe etched by two different etching solutions.

Etchant	(A^o, X) (eV)	DAP$_S$ (ZPL) (eV)	DAP$_D$ (ZPL) (eV)	I (DAP$_S$) /I (A^o, X)	I (DAP$_D$) /I (A^o, X)	FWHM (A^o, X) (meV)	Surface roughness (nm)
No etching	1.583	1.570	1.467	0.346	0.041	13.1	3.483
BM sol.	1.583	1.570	1.469	0.151	0.040	8.8	3.719
BLE sol.	1.583	1.570	1.470	0.069	0.025	8.1	0.278

surface of CdTe. As the ZnTe layer is thicker, the peak intensity of band edge emission of CdTe (1.576 eV) decreases. This informs the change of the crystallinity of the ZnTe layer deposited on the surface of CdTe and the formation of the interface of ZnTe/CdTe. To analyze this effect, the PL spectra at 4 K have been measured in the cases of 2000 and 4000 Å thickness of ZnTe layer (Fig. 5). The peak of the neutral acceptor bound exciton (A^o, X) which has a high intensity is observed in 1.586 eV and the peak of the neutral donor bound exciton (D^o, X) which has a low intensity is observed in 1.574 eV with bare CdTe (ZnTe undeposited). This means that CdTe has p-type conductivity. The deep level DAP emission occurs in the range between 1.424 and 1.543 eV. This is originated by the acceptor centers formed by the Cd vacancy (V_{Cd}) [6,7]. In the case of ZnTe deposited CdTe, PL spectra give the shallow level DAP emission at 1.543 eV, meaning that sodium (Na) acceptors from the zinc and shallow donors make the shallow level DAP emission [8]. The zero phonon line (ZPL) of deep level DAP emission is intensively shown at 1.478 eV, formed by many Zn vacancies (V_{Zn}). This indicates that the ZnTe layer formed on the surface of CdTe should have very incomplete composition because of Zn vacancy. This incomplete ZnTe layer may be formed in process of the e-beam deposition. In the evaporation of ZnTe by the e-beam, the high energy of e-beam broke the bond of ZnTe and then the difference of the partial pressure between Zn and Te made the non-stoichiometry of ZnTe layer [9,10]. But the intensity of deep level DAP emission formed by Cd vacancy (V_{Cd}) dominantly decreased because Zn filled the site of Cd vacancy during the deposition process of ZnTe layer onto the surface of CdTe.

From the PL spectra at 77 K in the case of 2000 Å thick ZnTe/CdTe, the effects about the thermal annealing at various temperatures are revealed (Fig. 6). In the PL spectra, P1 peak (1.570 eV) and E1 band indicate the edge emission of CdTe and the defect emission, respectively. In the as-deposited ZnTe/CdTe PL spectra, E1 band disappears and E2 band is formed because Zn of ZnTe layer fills Cd vacancy of CdTe surface. Thus the crystal defects by Cd vacancy are decreased and, therefore, E1 band is disappeared. However, the occurrence of Zn vacancy of ZnTe layer in process of evaporation makes the increase of deep level acceptor center, forming E2 band by the DAP emission from ZnTe layer.

To improve the quality of the ZnTe/CdTe interface, ZnTe/CdTe structures have been thermally annealed at each different temperatures. The changes of the ZnTe/CdTe structures have been investigated by measuring the PL and XRD. From the PL measurements, it is found that the intensity of E2 band is dominantly increased after the thermal annealing at 500 °C for 1 hour. In the case of heavily doped semiconductors, deep level DAP emission band is largely increased. As the impurity concentration is increased, the spectral components begin to merge into a single broader emission line. At this annealing condition, Cd were largely diffused into surface through the interface. And then Cd impurities in the interface and ZnTe layer were increased, so that the E2 band might be largely grown in intensity [11]. In the case of the thermal annealing at 550 °C for 1 hour, E2 band is abruptly decreased and E3 band begins to be formed. ZnTe/CdTe structure might be in the transition process of significantly changing in the interfacial structure, as confirmed by the XRD results shown in figure 8. CdZnTe polycrystalline region is appeared obviously from the XRD results. Thus it can be inferred that at this thermal annealing condition, CdZnTe polycrystal having more various Zn composition is to be spread from the interface to the surface. At the other annealing condition of 600 °C for 1 hour, the new interfacial compound is

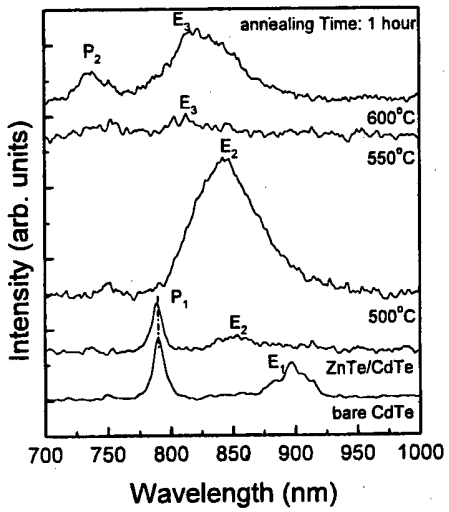

Fig. 6. The PL spectra at 77 K of ZnTe/CdTe structure thermally annealed with different temperatures (the thickness of ZnTe is 2000 Å).

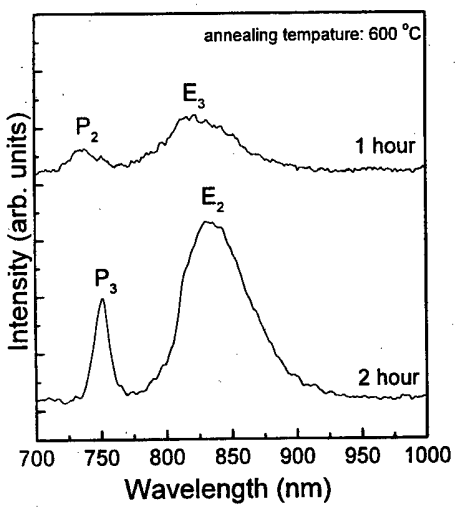

Fig. 7. The PL spectra at 77 K of ZnTe/CdTe structure thermally annealed at 600°C according to two different annealing times, *i.e.*, 1 hour and 2 hours.

cleanly formed at the interface of ZnTe/CdTe structure. Thus E2 band is dominantly increased and P2 peak is appeared. Because of the interdiffusion of Zn and Cd through the suitable thermal fluctuation, CdZnTe could be almost recrystallized. To improve the crystallinity, it makes ZnTe/CdTe structure annealed for 2 hours. In the figure 7, it can be seen that the crystallinity of the interfacial compound, CdZnTe, is surely improved. It is known that the P2 peak is concerned with the band edge emission of $Cd_{1-x}Zn_xTe$ and that the composition of zinc in the interface structure is approximately 0.25.

The band shift from E3 to E2 in the figure 7 can be explained by the equation (1). The recombination energy of pair band luminescence is given by the equation

$$h\nu = E_g - (E_A + E_D) + \frac{e^2}{Kr} \quad (1)$$

where E_g is the bandgap energy, r is the separation between the impurities, and K is the dielectric constant. This equation tells that if r is increased, luminescence shifts to higher energy and vice verse. In the case of E3 band, Cd diffused from CdTe bulk to interface may be easily located at interstitial sites, and if the annealing temperature is increased, the interstitial Cd will be re-organized to be located in the Zn vacancy or Te substitution. As r is decreased, luminescence shifts to lower energy. this is the origin of the shift in luminescence from E3 band to E2 band [11].

3. X-ray Diffraction of ZnTe/CdTe Heterostructure

In order to confirm the results of PL spectra of the ZnTe/CdTe structure, the X-ray diffraction patterns have been measured at the different annealing temperatures. As shown in figure 8 and figure 9, as-deposited

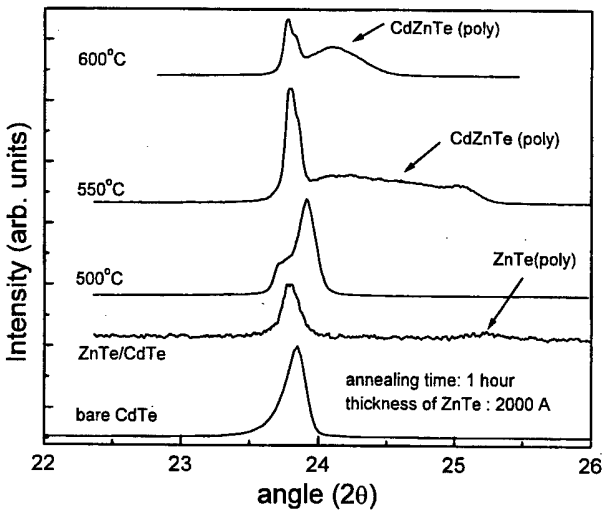

Fig. 8. The XRD results of the ZnTe/CdTe structure from (111) plane according to different annealing temperature.

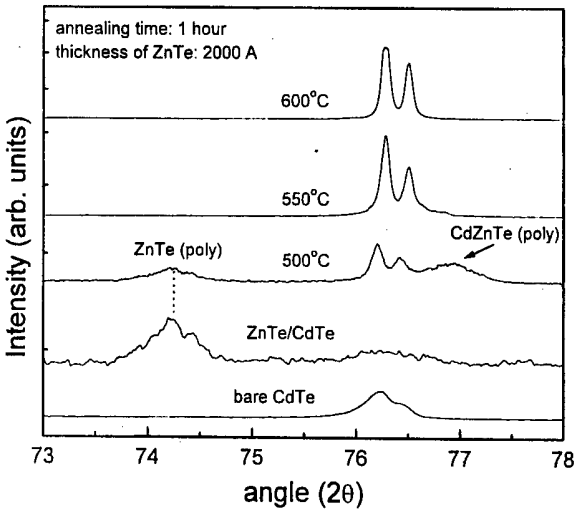

Fig. 9. The XRD results of the ZnTe/CdTe structure from (333) plane according to different annealing temperatures.

ZnTe layer is formed in polycrystal onto the surface of CdTe. The structure of ZnTe/CdTe interface is being gradually transformed into new interfacial compound of CdZnTe polycrystal with increasing the annealing temperature. Figure 9 shows the results of XRD from (333) plane of ZnTe/CdTe. As shown in the figure 9, in the case of 500 °C annealing condition, the borad peak appears about 77 arcsec by CdZnTe polycrystalline layer, meaning that the CdZnTe polycrystal is newly formed in the ZnTe/CdTe interface. In the case of 550 °C annealing condition, the XRD peak of CdZnTe polycrystalline layer becomes widely spread as shown in figure 8. These results can be seen that the interfacial compound is not completely recrystallized, thus, in the CdZnTe polycrystalline layer, there might be gradual distribution in Zn component. In the case of 600 °C annealing condition, however, the peaks of CdZnTe layer in the figure 8 and figure 9 indicates that CdZnTe polycrystalline layer is to be nearly recrystallized. It is, therefore, concluded that the interfacial compound of ZnTe/CdTe structure could be recrystallized to nearby composition by the thermal annealing condition.

IV. CONCLUSIONS

Fixed charges Te^{4+}, which act as surface trap states in the surface of CdTe, have been occurred by the etching the CdTe surface. This is the reason for appearing many Cd vacancies (V_{Cd}) in the surface which acts deep level acceptor center in the bandgap. Cd vacancy makes the zero phonon line of deep level DAP emission at 1.469 eV in the PL spectra. These Te^{4+} are dominantly decreased by etching the CdTe surface with the BLE solution rather than the BM solution, thus the phonon replica of this ZPL by the interaction between the lattice defects in the CdTe surface can be decreased. These can

be confirmed by the surface morphology through AFM measurements. It is concluded that the interfacial compound of ZnTe/CdTe heterostructure can be the more stable structure being less spread in Zn composition by the suitable thermal annealing condition. By the thermal annealing at 600 °C for 1 hour, the $Cd_{1-x}Zn_xTe$ polycrystalline structure is to be more stable Zn composition, x=0.25, in the interface of ZnTe and CdTe. It is found, in this study, that the photoluminescence analysis gives an information on the structural variation of ZnTe/CdTe heterostructure by the thermal annealing.

ACKNOWLEDGMENTS

This study is supported by the academic research fund of Ministry of Education (N-97-28), Republic of Korea.

REFERENCES

[1] M. B. Reine, A. K. Sood and T. J. Tredwell, *Semiconductors and Semimetals*, edited by R. K. Willardson and A. C. Beer (Academic press, New York, 1981), Vol. 18, p. 220.

[2] Y. Nemirovsky and G. Bahir, J. Vac. Sci. Technol. **A7**, 450 (1989).

[3] M. Aven and J. S. Prener, *Physics and Chemistry of II-VI Compounds* (North-Holland, Amsterdam, 1967), Chap. 3, p. 127.

[4] M. G. Williams, R. D. Tomlinson and M. J. Hampshire, Solid State Commun. **7**, 1831 (1969).

[5] I. J. Kim *et al.*, Korean J. of Appl. Phys. **11**, 594 (1998).

[6] D. E. Aspnes and H. Arwin, J. Vac. Sci. Technol. **A2**, 1309 (1984).

[7] M. S. Eggebert and H. J. Richter, J. Vac. Sci. Technol. **A6**, 2699 (1988).

[8] E. Molva, J. P. Chamonal and J. L. Pautrat, Phys. Status Solid **B109**, 635 (1982).

[9] R. F. Brebrick and A. J. Strauss, J. Phys. Chem. Solids, **25**, 1441 (1964).

[10] R. F. Brebrick, J. Electrochem. Soc. **116**, 1274 (1969).

[11] E. H. Bogardus and H. B. Bebb, Phys. Rev. **176**, 993 (1968).

Journal of the Korean Physical Society, Vol. 34, June 1999, pp. S488~S491

CdSe/$Zn_{1-x}Cd_xSe$ Quantum Wire Aarray Structures Fabricated by Self-Organization Technique

Hyun-Chul Ko*

Kansai Electronics Research Laboratory, NEC Corporation, Japan

Doo-Cheol PARK and Shigeo FUJITA

Depatment of Electronic Science and Engineering, Kyoto University, Kyoto 606-8501, Japan

Moderately strained $Zn_{1-x}Cd_xSe$ layers grown by molecular beam epitaxy (MBE) on the GaAs(110) surfaces obtained by cleaving in ultrahigh vacuum (UHV) produced Δ-shaped ridge structures parallel to the [1$\bar{1}$0] direction together with pyramidal-shaped islands as a result of the inhomogeneous in-plane strain relaxation. CdSe/$Zn_{1-x}Cd_xSe$ quantum wire (QWR) array structures were fabricated on the GaAs(110) surface utilizing such ridges. Regularly corrugated CdSe active layer grown on the $Zn_{1-x}Cd_xSe$ ridges of the lower cladding layer caused quasi-one-dimensional structures. The photoluminescence (PL) peak at 2.44 eV from the samples showed strong polarization characteristics of $(I_{//[110]}/I_{\perp[110]}) = 3.6$ due to the quasi-one-dimensional quantum confinement effect. Sharp PL peak (FWHM of 10 meV) of QWRs was observed when the active layer was selectively excited. Moreover, sharp photoluminescence excitation (PLE) spectra also reveals that the broadness of PL is due to the inhomogeneous effect as a result of size fluctuation of QWR structures.

I. INTRODUCTION

In recent years, there has been great interest in the research of the one-dimensional semiconductor nanostructures because of their novel physical properties and promising potential applications for optoelectronic devices [1–4]. The optoelectronic devices such as laser diodes and high speed detectors are expected to have much enhanced operation characteristics when active layers composed of quantum wells (QWs) are replaced by quantum wires (QWRs) [2]. These advantages are primarily related to the narrow density-of-states of the one-dimensional structures, where the quantized energy levels of electrons and holes occur in two transverse directions. This leads extremely low threshold current and high temperature stability in laser diode [3]. Furthermore, the narrowing of the density of state will yield potentially enhanced non-linear optical effect due to the phase-space filling of carriers and the polarization property [4]. Such non-linear optical properties are applicable in optical communications that involve switching, amplification, and signal processing.

For the realization of high quality quantum structures, various techniques including the self-formation during the growth and the patterning of two-dimensional quantum well structures have been suggested and demonstrated [5–7]. However, since the II-VI compound semiconductors have small exciton volumes and brittle natures, conventional lithographic methods are not appropriate for the materials to obtain sufficient quantum confinement effects and low interface defects of the quantum structures. Therefore, in-situ fabrication methods are promising for the formation of II-VI compound semiconductor quantum structures because the self-formed quantum structures have low density of interface defects, good optical- and electrical-properties.

In this study, we propose a new fabrication methods of CdSe/$Zn_{1-x}Cd_xSe$ QWR array structures as an original and simple method using the self-organization technique. QWR structures were naturally formed onto the GaAs(110) cleaved surface during the molecular beam epitaxy (MBE). By utilizing the unique self-organization phenomena of $Zn_{1-x}Cd_xSe$ strained layer on GaAs(110) surface, *i.e.* Δ-shaped ridge structures oriented to the [1$\bar{1}$0] direction were formed in the moderately strained $Zn_{1-x}Cd_xSe$ layers, QWRs were produced without any minute process.

II. SAMPLE STRUCTURE AND PREPARATION

QWR structures were formed on the GaAs(110) crys-

*E-mail: ko@kel.cl.nec.co.jp, Tel: +81-77-537-7686
Fax: +81-77-537-7689

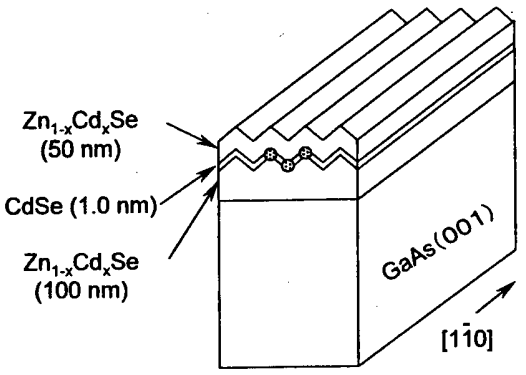

Fig. 1. Schematic diagram of CdSe/$Zn_{1-x}Cd_xSe$ QWR structures fabricated on the GaAs(110) surface. The corrugated active layer produces the quasi-one-dimensional quantum waveguides on the top and troughs of the ridges. Circles in the figure represent the position of QWRs.

tal surface cleaved in ultra high vacuum (UHV). As discussed in our previous study, Δ-shaped ridge structures are naturally formed on GaAs(110) surface along the [1$\bar{1}$0] direction during the growth of $Zn_{1-x}Cd_xSe$ layers due to the strong anisotropic in-plane strain relaxation [8]. The QWR structures were fabricated utilizing such ridges. Figure 1 illustrates the schematic diagram of the fabricated CdSe/$Zn_{1-x}Cd_xSe$ QWR structures. It is expected that the regularly corrugated well layer in QW result in a regular modulation of well thickness of QW [9]. As a result, the corrugated active layer produces the quasi-one-dimensional quantum wave-guide, *i.e.* the formation of QWR structures, on the top and troughs of the ridges.

$Zn_{0.91}Cd_{0.09}Se$ lower cladding layer of 120 nm in thickness was used for the formation of QWRs. CdSe active layer of 1.0 nm in thick (5 monolayers; MLs) and $Zn_{0.91}Cd_{0.09}Se$ capping layer were successively grown on the surface of the $Zn_{0.91}Cd_{0.09}Se$ lower cladding layer. Typical growth conditions were as follows: the growth temperature of 250 °C, the equivalent beam pressure ratio p(VI)/p(II) of 1.0 which was measured by an ion gauge at the position of substrate, and the growth rate of 0.1 μm/hr. The thickness of the layers was estimated by the growth rate. The details of the experimental apparatus and cleaved edge overgrowth process has been described in elsewhere [10,11]. Ridge structures were observed by atomic force microscopy (AFM). AFM measurements were performed in air within 30 minutes after the growth, using Si_3N_4 cantilever with a spring constant of 0.1 N/m and a resonant frequency of 10 kHz. The spatial resolution of the AFM (Seiko SPI 300) is 0.01 nm in z-axis. Constant force mode was used in AFM observation. No phase contrast and filtering of spatial image were used.

III. RESULTS AND DISCUSSION

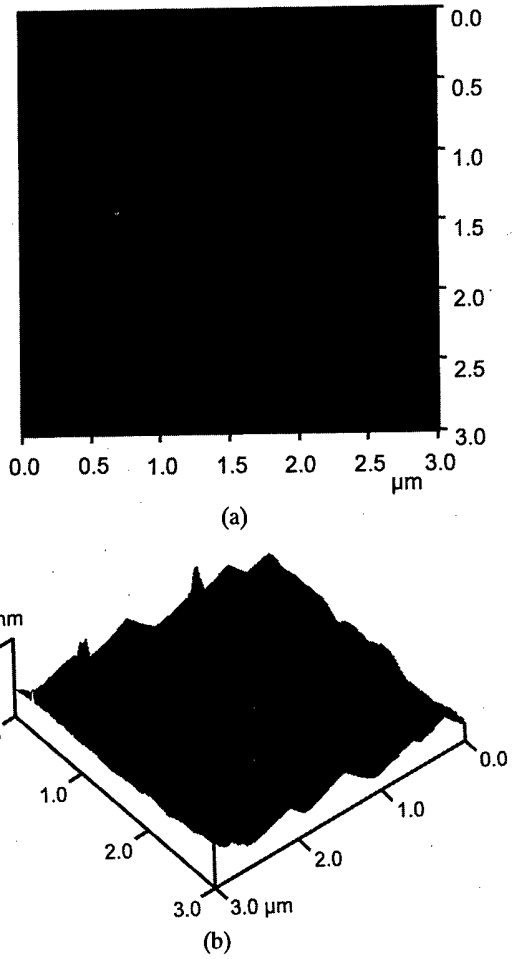

Fig. 2. AFM observation of $Zn_{0.70}Cd_{0.30}Se$ grown on the GaAs(110) surface obtained by cleaving in UHV. Top and side view images of 120 nm thick $Zn_{1-x}Cd_xSe$ layer. The observed area is 3 μm×3 μm. Average width and height of the ridge structures are 600 nm and 40 nm, respectively.

The surface feature of lower cladding layer was investigated by AFM observation. Figure 2 shows the AFM images of $Zn_{0.91}Cd_{0.09}Se$ lower cladding layer without CdSe active and $Zn_{0.91}Cd_{0.09}Se$ capping layers. As shown in the figure, Δ-shaped ridges directed toward [1$\bar{1}$0]-direction were covered whole surface with good uniformity together with island structures with low density of $\sim 10^8$ cm^{-2}. The ridges have average width of 600 nm and height of 40 nm. Those ridges are extremely long to be formed across from the one end to the another end of the substrate.

Figure 3 represents the dependence of ridge shape on the Cd compositions of $Zn_{1-x}Cd_xSe$ layer. Solid and dotted lines represent the ridge width and height with various Cd compositions, respectively. When Cd composition is larger than 40 %, the ridge structures did not formed at all and no QWRs were observed but produced Stranski-Krastanow type island structures. In particular, when Cd composition is less than 20 %, clear ridge

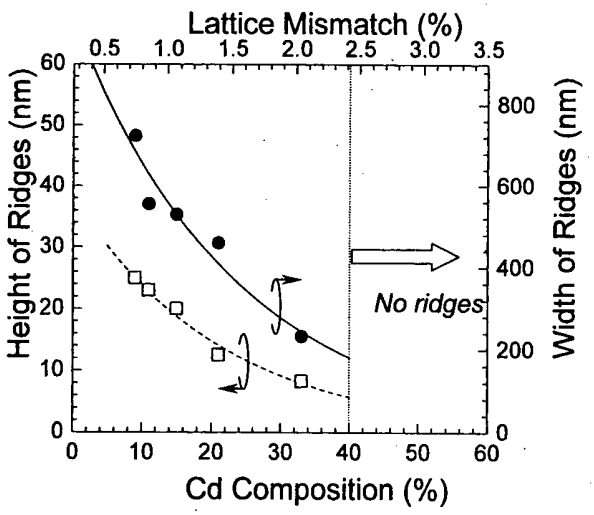

Fig. 3. The evolution of ridge structures of the $Zn_{1-x}Cd_xSe$ layers with the various Cd compositions. The nominal thickness of the layers is 120 nm. No ridge structures except the islands were observed when the layer had larger Cd composition than 40 %.

structures were appeared on the surface. As the Cd composition decreased the density of ridges decreased. These properties imply that size and density of QWRs can be controlled by the Cd concentration of the lower cladding layer.

Figure 4 shows optical properties of the fabricated QWR samples. For the selectively excited photoluminescence (PL) and in-plane polarization dependent measurements, the emission spectra were detected with a cooled charge coupled device (CCD) in conjunction with 50 cm-monochrometer. Figure 3(a) shows the selectively excited PL spectra. Xe lamp with monochrometer was used for the excitation light source. When the $Zn_{0.91}Cd_{0.09}Se$ cladding layer was selectively excited, quite broad peak (100 meV of FWHM value) was observed around 2.4 eV. On the contrary, when the active layer was selectively excited by the light energy of 2.465 eV, sharp peak (at 2.445 eV) with 30 meV of FWHM value was observed at the lower energy side of 20 meV from the excitation energy. This narrowing phenomena of the PL spectra indicates that the broadness of the PL spectrum obtained by the excitation of cladding layer is composed of the sharp peaks from individual QWRs implicating carriers or excitons transfer to some extent from the QWRs to QWRs with different sizes. Moreover, the Stoke's shift of 20 meV seemed to be originated from the size fluctuations in each QWR.

Since the QWRs structures have one-dimensional confinement of the carriers, the PL spectra have in-plane polarization properties. The polarized PL measurement was performed to evaluate the QWR sample. In this measurement, the non-polarized HeCd laser (325 nm line) laser light with power density of 1.5 W/cm^2 was irradiated with an angle of 45° to the sample surfaces, and

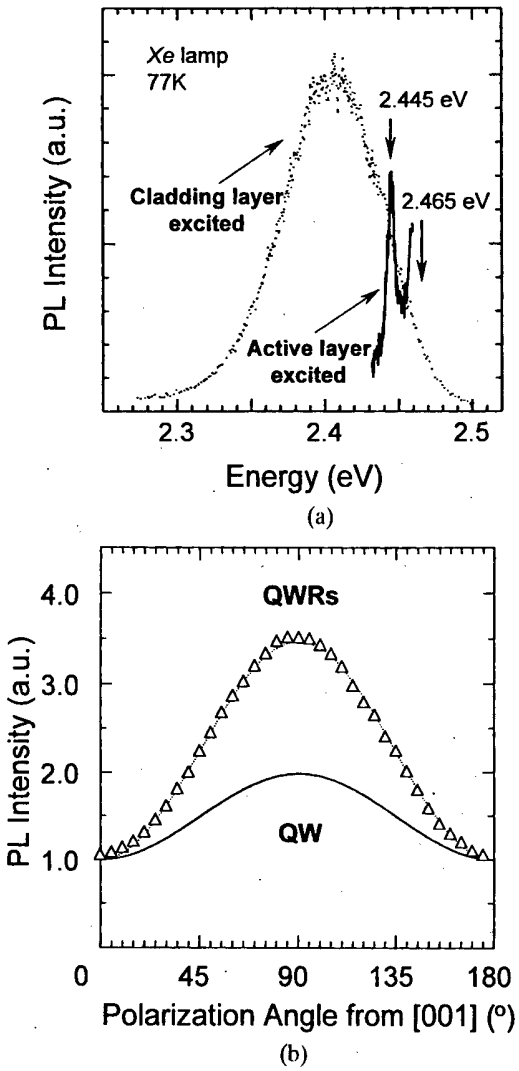

Fig. 4. PL spectra from the QWRs. (a) Selectively excited PL spectra. Dotted lines represents the PL spectra when the $Zn_{0.91}Cd_{0.09}Se$ cladding layer was selectively excited by excitation energy of 2.68 eV. Solid line represents the PL spectra when the active layer was selectively excited by excitation energy of 2.465 eV. Monochromatic light of Xe lamp was used as an excitation source. (b) Polarization angle dependence of PL intensities of QWRs Dotted line is fitted curve by assuming sinusoidal function. Solid line is calculated value for the $CdSe/Zn_{0.91}Cd_{0.09}Se(110)$ QW. Polarization angle denoted the measured angle between the electric field vector of the emitted light and [001] direction.

the PL was collected from the vertical direction to the sample surface. Polarization direction was controlled by the rotation of Gran-Tompson linear polarizer, which was placed in front of the optical fiber. Figure 4(b) shows a polarization angle dependence of PL intensity from the sample. The fabricated QWRs show a clear anisotropic in-plane polarization properties. Strong polarization parallel to the $[1\bar{1}0]$ direction, *i.e.*, the direction of ridges, was observed. The ratio of peak intensity parallel to the

QWRs of [1$\bar{1}$0] direction to that perpendicular to the QWRs of [1$\bar{1}$0] direction is as large as 3.6. On the other hand, the (110)-oriented QWs also have similar polarization properties due to the strong valence-band anisotropy caused by the low crystal symmetry of (110) plane. As a result, the oscillator strength of interband optical transitions is sensitive to the crystallographic direction even in the same planes of the epitaxial growth. Moreover, such anisotropy is multiplied by the strain. The ratio of maximum to minimum values of the polarized PL intensity can be calculated. Details about the linear polarization properties of (110)-oriented QWs were discussed in elsewhere [12]. The obtained relative optical matrix elements ratio for the CdSe (3 MLs)/$Zn_{0.91}Cd_{0.09}Se$ QW was about 2.0 which was consistent with the experimental value of 1.8, considering the rough estimation of the material parameters. The polarization behaviors of QWR sample can not be explained by this crystallographic low-symmetry of (110)-oriented surface together with the strain-induced anisotropy. Therefore, the enhanced polarization is considered as a result of one-dimensional carrier confinement to the QWRs.

IV. CONCLUSIONS

In conclusion, the natural formation of CdSe/$Zn_{1-x}Cd_xSe$ QWR structures on the GaAs(110) crystal surface by cleaved edge over growth technique was investigated. By utilizing the unique self-organization phenomena, *i.e.* Δ-shaped ridge structures oriented to the [1$\bar{1}$0] direction were formed in the moderately strained $Zn_{1-x}Cd_xSe$ layers, regularly corrugated CdSe well layer was formed. In the corrugated QW structures, QWRs were obtained due to the regular modulation of well thickness. Strong quantum confinement effects were observed from the fabricated QWR structures. The PL peak at 2.44 eV from QWRs showed strong polarization of $(I_{//[110]}/I_{\perp[110]}) = 3.6$. In contrast the PL peak was broad (FWHM of 100 meV) when the cladding layer was excited, sharp peak (FWHM of 10 meV) was observed when the active layer was selectively excited. These results suggest the present self-formed QWR structure fabrication technique have great potential as new nanostructures technology.

ACKNOWLEDGMENTS

The authors would also like thanking Dr. T. K. Yoo of the LG Corporate Institute of Technology for his encouragement. This work was supported in part by the Kyoto University-Venture Business Laboratory (KU-VBL) project and also by LG CIT in Korea.

REFERENCES

[1] Y. Arakawa and H. Sasaki, Appl. Phys. Lett. **40**, 938 (1982).
[2] J. L. Merz and P. M. Petroff, Mater. Sci. Eng. **B9**, 275 (1991).
[3] E. Kapon, Proc. IEEE **80**, 398 (1992).
[4] V. D. Kulakovskii, E. Lach and A. Forchel, Phys. Rev. **B40**, 8087 (1989).
[5] S. Hara, J. Motohisa, T. Fukui and H. Hasegawa, Jpn. J. Appl. Phys. Lett. **34**, 4401 (1995).
[6] M. Takeuchi, K. Shiba, K. Sato, H. K. Huang, K. Inoue and H. Nakashima, Jpn. J. Appl. Phys. Lett. **34**, 4411 (1995).
[7] K. Inoue, K. Kimura, K. Maehashi, S. Hasegawa, H. Nakashima, M. Iwane, O. Matsuda and K. Murase, J. Crystal Growth **127**, 1041 (1993).
[8] H. C. Ko, D. C. Park, Y. Kawakami, Sz. Fujita and Sg. Fujita, Appl. Surf. Sci. **117/118**, 484 (1997).
[9] K. Vacek, A. Sawada and T. Usagawa, Appl. Phys. Lett. **65**, 3096 (1994).
[10] H. C. Ko, S. Yamaguchi, H. Kurusu, Y. Kawakami, Sz. Fujita and Sg. Fujita, Jpn. J. Appl. Phys. **35**, L366 (1996).
[11] H. C. Ko, D. C. Park, Y. Kawakami, Sz. Fujita and Sg. Fujita, J. of Crystal Growth **178**, 246 (1997).
[12] H. C. Ko, D. C. Park, Y. Kawakami, Sz. Fujita and Sg. Fujita, Semicond. Sci. & Tech. **11**, 1873 (1996).

Journal of the Korean Physical Society, Vol. 34, June 1999, pp. S492~S495

Fabrication and Optical Properties of ZnCdSe/ZnSe Quantum Wires with Strain-Induced Lateral Confinement

Hyun-Chul Ko*

Kansai Electronics Research Laboratory, NEC Corporation, Japan

Doo-Cheol PARK and Shigeo FUJITA

Depatment of Electronic Science and Engineering, Kyoto University, Kyoto 606-8501, Japan

Fabrication and optical investigation of strain-induced quantum wires (QWRs) for ZnCdSe/ZnSe heterostructures were investigated. To produce an in-plane lattice modulation on (110) cleaved surface, 20 periods of AlGaInP/GaInP strained layer superlattice was grown on GaAs(001) substrate. Then, the wafer was cleaved in ultrahigh vacuum (UHV) chamber, and $Zn_{0.85}Cd_{0.15}Se$/ZnSe single quantum well (SQW) was successively grown on the cleaved surface of (110) plane. As a result, the [001]-oriented AlGaInP/GaInP strained layer superlattice achieved in-plane strain confinement effect on (110)-oriented $Zn_{0.85}Cd_{0.15}Se$/ZnSe SQW. The fabricated sample showed a large red shift (about 300 meV) with respect to the $Zn_{0.85}Cd_{0.15}Se$/ZnSe single quantum well grown on the cleaved plane without strained layer superlattice on [001] direction. The ratio of polarized photoluminescence peak intensity parallel to the QWRs to that perpendicular to the QWRs was 2.5. Such a strong in-plane polarization dependence of photoluminescence from the sample gives a clear evidence for the carrier confinement to the QWRs.

I. INTRODUCTION

During the last years, much attention has been devoted to the fabrication of low-dimensional quantum structures of compound semiconductors such as quantum wires (QWRs) and quantum dots (QDs), which are quite important for optoelectronic device applications and for basic physical interests [1,2]. To obtain a quantum confinement effect, size of those structures should be compare to the exciton volumes. The exciton Bohr radius and Vicker's hardness of ZnSe-based materials is about 3.5 nm and 138 kg/mm^2, respectively. Therefore, it is very difficult to obtain high quality quantum structures of ZnSe-based materials using dry/wet-etching methods together with electron beam lithography [3]. In this point of view, in-situ fabrication methods with molecular beam epitaxy (MBE) without any minute process are very preferred to obtain high quality structures of wide bandgap II-VI materials. Recently, Gershoni *et al.* suggested and demonstrated the strain-induced quantum wires (QWRs) of AlGaAs/GaAs system with InGaAs/GaAs strained-layer superlattice (SLS) [4].

In this study, we described the fabrication and optical investigation of strain-induced QWRs for ZnCdSe/ZnSe heterostructures. QWRs were formed in the single quantum well (SQW) structure grown by MBE using cleaved edge overgrowth technique. The fabricated QWRs showed quasi-one-dimensional optical properties.

II. SAMPLE CONFIGURATION

Samples were fabricated by two step epitaxial growth. Figure 1 shows the schematic diagram of the fabricated QWR sample. The [001]-oriented $(Al_{0.70}Ga_{0.30})_{0.05}In_{0.50}P/Ga_{0.58}In_{0.42}P$ SLS achieved in-plane strain-induced confinement effect on (110)-oriented $Zn_{0.85}Cd_{0.15}Se$/ZnSe SQW. In the first step, a 20 periods $(Al_{0.70}Ga_{0.30})_{0.50}In_{0.05}P/Ga_{0.58}In_{0.42}P$ SLS which have 0.8 % of strain was grown on a GaAs(001) substrate which is 7°-off toward [011] direction by low-pressure metal-organic vapor phase epitaxy (MOCVD). SLS was composed of 10 nm thick $(Al_{0.70}Ga_{0.30})_{0.050}In_{0.50}P$ and 7 nm thick $Ga_{0.42}InP$ layers. The SLS was grown on the 20 nm thick GaAs buffer layer. GaAs of 100 nm in thickness was grown on the SLS as a capping layer. Then, the wafer was cleaved in ultrahigh vacuum (UHV) chamber, and $Zn_{0.85}Cd_{0.15}Se$/ZnSe SQW was successively grown on the cleaved surface of (110) plane. The SQW was having of 5 nm thick active and 40 nm thick cladding layers. Two-chamber MBE system, one for the cleaving of the substrate in UHV and the other for the epitaxial growth of $Zn_{1-x}Cd_xSe$, was used for cleaved edge overgrowth of

*E-mail: ko@kel.cl.nec.co.jp, Tel: +81-77-537-7686, Fax: +81-77-537-7689

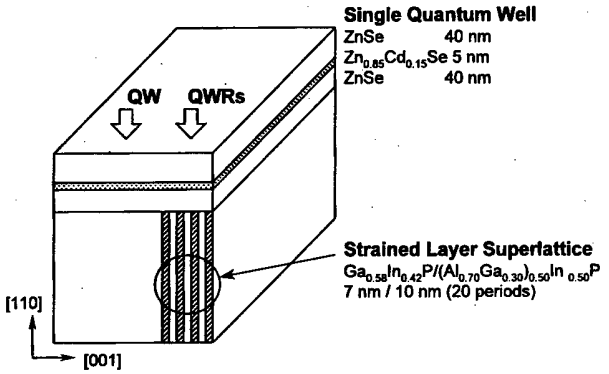

Fig. 1. Schematic illustration of the fabricated quantum wires utilizing the strain-induced lateral confinement.

ZnCdSe/ZnSe SQW. After the growth of SLS, the wafer was mounted vertically on the substrate holder and introduced into the preparation chamber. Details of the experimental apparatus and process has been described elsewhere [5]. Typical growth conditions were as follows: growth temperature of 250 °C, beam equivalent pressure ratio p(Se)/p(Zn) of 1.0. As a result, the ZnCdSe active layer have periodic strain modulation on the top of SLS cleaved plane.

III. RESULTS AND DISCUSSIONS

To investigate optical properties of the sample, microphotoluminescence (PL) measurement were performed. Typical PL spectra measured at 20 K is presented in Fig. 2. These PL spectra were obtained from two different region of the sample, as indicated by arrows in Fig. 1 and insets of Fig. 2. The PL spectrum of QW region shows single peak at 2.80 eV with 21 meV of full width at half maximum (FWHM). On the contrary, the PL spectrum of QWRs region exhibits two peaks. These peaks of 2.80 and 2.54 eV can be considered to originate from the recombination of $n = 1$ intrinsic heavy hole excitons of QW and the localized excitonic recombination at QWRs, respectively. Note that the excitation laser spot size (~1 μm in diameter) is much larger than the QWR region one, *i.e.* SLS area (~340 nm in width), PL spectra from QWRs are contributed from both QW and QWRs emission. Although the excited area is lager than that QWR region, QWR emission intensity is stronger than that of QW indicating the carrier diffusion from QW to QWR is quite efficient.

In order to make a conformation of the peak origin, polarized PL measurements were performed. Figure 3 shows the polarization angle dependence of the PL spectra from the sample. In the measurement, the lumi-

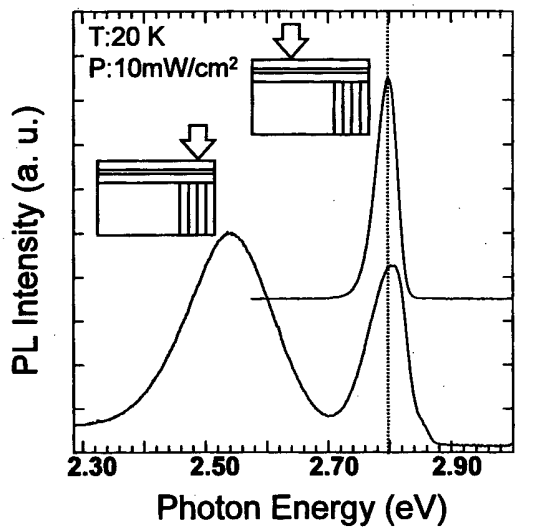

Fig. 2. PL spectra of the QWR sample measured at two different positions indicated in Fig. 1. (a) [110]-oriented $Zn_{0.85}Cd_{0.15}Se/ZnSe$ SQW region. (b) Strained-induced $Zn_{0.85}Cd_{0.15}Se/ZnSe$ QWR region grown on top of the $(Al_{0.70}Ga_{0.30})_{0.50}In_{0.50}P/Ga_{0.58}In_{0.42}P$ strained superlattice. The PL spectra were measured at 20 K.

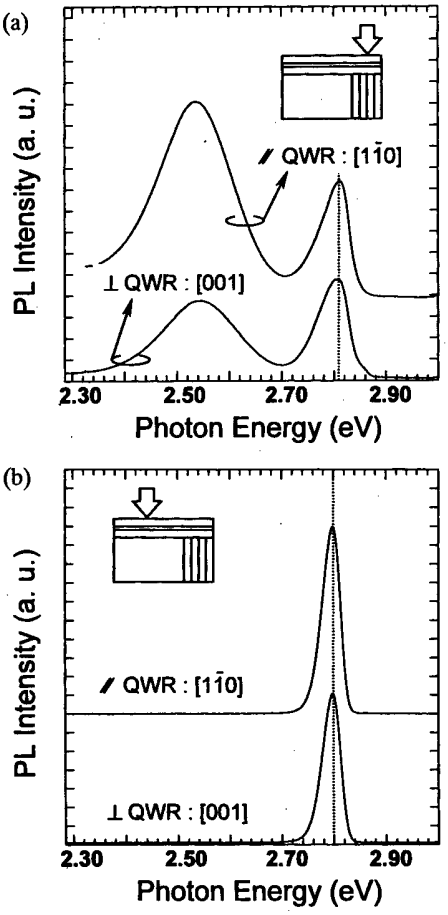

Fig. 3. Polarization angle dependence of the PL spectra from the QWRs at position (a). The ratio of peak intensity parallel to the QWRs to that perpendicular to the QWRs was 2.5.

nescence was polarized by Gran-Tompson linear polarizer and then introduced into spectrometer through the optical fiber. The polarized PL spectra show strong anisotropic polarization properties. PL intensity of the QW and QWR peaks have maximum and minimum value when the polarization is parallel to the [110] and [001] direction, respectively. The ratio of maximum to minimum values of QW peak is about 1.27. On the contrary, QWR peak shows the ratio of 2.5, which was much larger than that of QW peak.

On the other hand, the hole wave functions and optical properties of quantum confined systems (*e.g.* QWs, QWRs, or quantum dots) should be sensitive to the crystallographic direction of epitaxial growth. This is mainly due to the valence-band anisotropy of the zincblend type compounds. As a result, both the energies and the oscillator strength of interband optical transitions are sensitive to the crystallographic direction of the epitaxial growth. As for the (110)-oriented QWs, the valence-subband structures are highly anisotropic. It is well known that the valence-subband along the $[1\bar{1}0]$ direction is flat, while that along the [001] direction is very steep [6]. This may be due to different degrees of coupling between light- and heavy-hole states along these two in-plane directions. The large intrinsic anisotropy would substantially affect the transport of holes. The relative optical matrix elements for the (110)-oriented strained QW expressed as follows:

$$|M|^2/|Mb|^2(e \rightarrow HH) = 1 + \alpha \cos^2\theta + \beta \sin^2\theta \qquad (1)$$

$$\alpha = 1 + \frac{1}{2}\frac{\varsigma}{\sqrt{\varsigma^2+\xi^2}} + \frac{\sqrt{3}}{2}\frac{\xi}{\sqrt{\varsigma^2+\xi^2}},$$

$$\beta = 1 + \frac{1}{2}\frac{\varsigma}{\sqrt{\varsigma^2+\xi^2}} + \frac{\sqrt{3}}{2}\frac{\xi}{\sqrt{\varsigma^2+\xi^2}}, \qquad (2)$$

$$\varsigma = \frac{1}{4m_0}\left(\frac{hk_z}{2\pi}\right)^2(\gamma_2+3\gamma_3) + \left(\frac{1}{4}b - \frac{\sqrt{3}}{4}d\right)\Delta\epsilon \qquad (3)$$

$$\varsigma = \frac{1}{4m_0}\left(\frac{hk_z}{2\pi}\right)^2(\gamma_2+3\gamma_3) + \left(\frac{1}{4}d - \frac{\sqrt{3}}{4}b\right)\Delta\epsilon \qquad (4)$$

$$\Delta\epsilon = \frac{2(C_{11}+2C_{12})}{C_{11}+C_{12}+2C_{44}}\cdot\epsilon_{//}, \quad \epsilon_{//} = \frac{a_s - a_f}{a_f} \qquad (5)$$

where γ_2 and γ_3 are the Luttinger parameters of the well layer [7]. b and d are deformation potentials, and C_{11}, C_{12}, and C_{44} are elastic constants. as and af are the lattice constants of the substrate and the well layer, respectively. k_z is a wave number along the growth direction in the QW. The relevant parameters for the $Zn_{0.85}Cd_{0.15}Se$ are obtained by linear interpolation from those of ZnSe and CdSe [8–10]. Luttinger parameters (especially for γ_3) for $Zn_{0.85}Cd_{0.15}Se$ are not available, we use $\gamma_2 = 1.24$ and $\gamma_3 = 1.67$, which are the values of ZnSe. The calculated ratio of relative optical matrix elements for the structures of the fabricated SQW on GaAs(110) cleaved plane is 1.47, the which is fairly agrees with the experimentally obtained intensity ratio with considering the rough estimation of the material parameters.

In other words, such a strong polarization behavior of QWR emission could hardly be explained by the anisotropic optical matrix element. The enhanced polarization is considered to result of one-dimensional carrier confinement at strain-induced QWR structures, which is one of the well-known evidence of QWRs [11].

IV. CONCLUSIONS

In this conclusion, we described the fabrication and optical investigation of strain-induced QWRs for ZnCdSe/ZnSe heterostructures using cleaved edge overgrowth technique. $Zn_{0.85}Cd_{0.15}Se$/ZnSe SQW was grown on the top of cleaved surface of $(Al_{0.70}Ga_{0.30})_{0.50}In_{0.50}P$/$Ga_{0.58}In_{0.42}P$ SLS grown on the (001) plane. Due to the in-plane lattice modulation on (110) cleaved surface, QWR structures were formed. The fabricated sample showed a large red shift (about 300 meV) with respect to the $Zn_{0.85}Cd_{0.15}Se$/ZnSe single quantum well grown on the cleaved plane without strained layer superlattice on [001] direction. The ratio of polarized photoluminescence peak intensity parallel to the QWRs to that perpendicular to the QWRs was 2.5. Such a strong in-plane polarization dependence of photoluminescence from the sample gives a clear evidence for the carrier confinement to the QWRs.

ACKNOWLEDGMENTS

The authors would also like thanking Dr. T. K. Yoo of the LG Corporate Institute of Technology for his encouragement. This work was supported in part by the Kyoto University-Venture Business Laboratory (KU-VBL) project and also by LG CIT in Korea.

REFERENCES

[1] J. L. Merz and P. M. Petroff, Mater. Sci. Eng. **B9**, 275 (1991).
[2] E. Kapon, Proc. IEEE **80**, 398 (1992).
[3] G. Bachel, M. Illing, A. Forchel, D. Hommel, B. Jobst and G. Landwehr, Phys. Sta. Sol. **B187**, 371 (1995).
[4] D. Gershoni, J. S. Weiner, S. N. G. Chu, G. A. Baraff, J. M. Vandenberg, L. N. Peiffer, K. West, R. A. Logan and T. Tabun-Ek, Phys. Rev. Lett. **65**, 1631 (1990).
[5] H. C. Ko, D. C. Park, Y. Kawakami, Sz. Fujita and Sg. Fujita, J. of Crystal Growth **178**, 246 (1997).
[6] F. H. Pollak, *Strained-Layer Supperlattices: Physics*, Ed. Thomas P. Pearsall (Academic, San Diego, 1990), p. 17.
[7] R. H. Henderson and E. Towe, J. Appl. Phys. **78**, 2447 (1995).
[8] R. M. Martin, Phys. Rev. **B6**, 4546 (1972).
[9] D. W. Langer, R. N. Euwara, K. Era and T. Koda, Phys. Rev. **B2**, 4005 (1970).

[10] B. A. Weinstine, R. Zallen, M. L. Slade and A. De-Lozanne, Phys. Rev. **B24**, 4562 (1981).
[11] M. Tsuchiya, J. M. Geines, R. H. Yan, R. J. Simes, P. O. Holtz, L. A. Coldren and P. M. Petroff, Phys. Rev. Lett. **62**, 466 (1989).

Journal of the Korean Physical Society, Vol. 34, June 1999, pp. S496~S498

Dielectric Function of $Cd_{0.57}Mg_{0.43}Te$ Alloy Film Studied by Ellipsometry

T. J. KIM and Y. D. KIM
Department of Physics, Kyung Hee University, Seoul 130-701

S. D. YOO and D. E. ASPNES
Department of Physics, North Carolina State University, U.S.A.

J. KOSSUT
Institute of Physics, Polish Academy of Sciences, Warsaw, Poland

We report new measurement of the above-bandgap optical properties of zincblend $Cd_{0.57}Mg_{0.43}Te$ ternary alloy film. These differ from previous data on bulk alloys, in that the present $<\epsilon_2>$ values are much lower and higher near E_0 fundamental edge and E_2-peak, respectively, indicating that the present spectra are closer to the true bulk dielectric function of this alloy. Energy derivative spectrum calculated numerically from this data also show better-resolved structure in the E_2-peak region.

I. INTRODUCTION

$Cd_{1-x}Mg_xTe$ is an especially promising barrier material for optoelectronic devices because the whole visible band-gap range can be covered with Mg compositions (x) between 0.30 and 0.75. Furthermore, the lattice mismatch between either MgTe or CdTe can be as small as 1.0 % [1]. Even though the properties of the binary endpoint CdTe of these alloys are well known [2,3], only a few studies of the critical point energies of CdMgTe alloys have been reported [4]. Recently we reported the results of a systematic study on the dielectric functions of bulk CdMgTe alloys [5]. However our spectra had nonzero $<\epsilon_2>$ values below the E_0 band gap, which we attributed to surface roughness of the bulk samples. Here, we report spectroscopic ellipsometric (SE) measurements on $Cd_{0.57}Mg_{0.43}Te$ film grown on GaAs substrate. Since the surface of this film is much smoother, we expect that the result from the film is closer to the true dielectric function of $Cd_{0.57}Mg_{0.43}Te$ alloy.

II. EXPERIMENTALS

Four layers of nominal magnesium concentration, $x =$ 0.0, 0.23, 0.32, and 0.43 were grown epitaxially by MBE on [001]-oriented GaAs substrates. The layers were typically 1 μm thick and have no surface cap layers. In this work we concentrate on the result from $x = 0.43$ film to compare with those from bulk samples. Room temperature pseudodielectric spectra $<\epsilon(\omega)>=<\epsilon_1(\omega)>+i<\epsilon_2(\omega)>$ were obtained from 1.5 to 6.0 eV by a rotating analyzer ellipsometer as described elsewhere [6,7]. The system uses a 75 W Xenon arc lamp, a Cary 14 monochromator, quartz Rochon prisms, and a photomultiplier detector. The angle of incident was 67.08°.

III. RESULTS AND DISCUSSION

The sample was mounted in a windowless cell, optically aligned with a He-Ne laser, and maintained in flowing purified N_2 to minimize surface contamination. It is well known that the existence of overlayers on the surface complicates efforts to obtain the intrinsic response of samples by ellipsometry because of its surface sensitivity [8]. Therefore, we removed oxide overlayers in situ immediately before measurement. We followed the wet chemical etching procedure described in Refs. 9, 10, where the successful removal of oxide overlayers on ZnTe with $NaBH_4$ was reported. The chemical treatment was repeated until real-time ellipsometric data showed no further changes. This also corresponded to the highest values of $<\epsilon_2>$ at the E_2-peak.

Since dielectric function of $Cd_{0.57}Mg_{0.43}Te$ has not known yet, to compare our performance of chemical etching procedure we show the effect of chemical treatments on $<\epsilon_2>$ for a CdTe film grown epitaxially on GaAs in Fig. 1. We obtained a maximum $<\epsilon_2>$ value of 11.92 with $NaBH_4$ in deionized water, which is comparable to the best reported value on bulk CdTe, 12.12 [2].

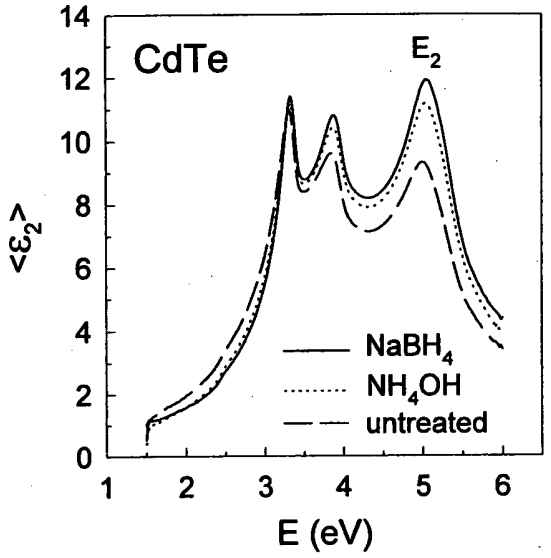

Fig. 1. Effects of chemical treatments on $<\epsilon_2>$ spectrum of CdTe film epitaxially grown on GaAs.

$Cd_{0.57}Mg_{0.43}Te$ sample was treated in the same way and showed similar optimum $<\epsilon_2>$ values with the $NaBH_4$ treatment.

Figure 2(a) shows our best spectrum of epitaxial $Cd_{0.57}Mg_{0.43}Te$ after chemical etching. Previous bulk data from Ref. 5 are shown in Fig. 2(b). The present data from film exhibit a higher $<\epsilon_2>$ value at the E_2-peak, even though the film has a higher Mg content. According to this standard measure of quality by SE, the film has a better surface than that of the bulk material. In addition, the spectrum of Fig. 2(a) shows clear interference oscillations below the E_0 threshold as expected in the region of transparency (We did not perform the multilayer calculation necessary to remove this interference pattern, because the thickness of the film is not known to sufficient accuracy). The value of $<\epsilon_2>$ just above the E_0 threshold is also lower than that shown in Fig. 2(b), which is another measure of higher quality. On the basis of these two improved $<\epsilon_2>$ values, we believe that our current result is the closest to the true bulk dielectric function of $Cd_{0.57}Mg_{0.43}Te$ alloy that has been reported so far. These data are listed from 2.2 eV up to 5.9 eV in Table 1 on a scale that should be sufficiently detailed to allow ϵ values to be obtained at intermediate energies by general interpolation techniques.

To obtain the critical point (CP) energies, we calculated second energy derivative spectra numerically and fit them to the standard analytic CP expression [11–13]:

$$\frac{d^2\epsilon}{d\omega^2} = n(n-1)Ae^{i\phi}(\hbar\omega - E + i\Gamma)^{n-2} \quad n \neq 0,$$
$$= Ae^{i\phi}(\hbar\omega - E + i\Gamma)^{-2} \quad n = 0, \quad (1)$$

where the critical point is described by the amplitude A, the threshold energy E, the broadening Γ, and the phase ϕ. Both real and imaginary parts were fit simul-

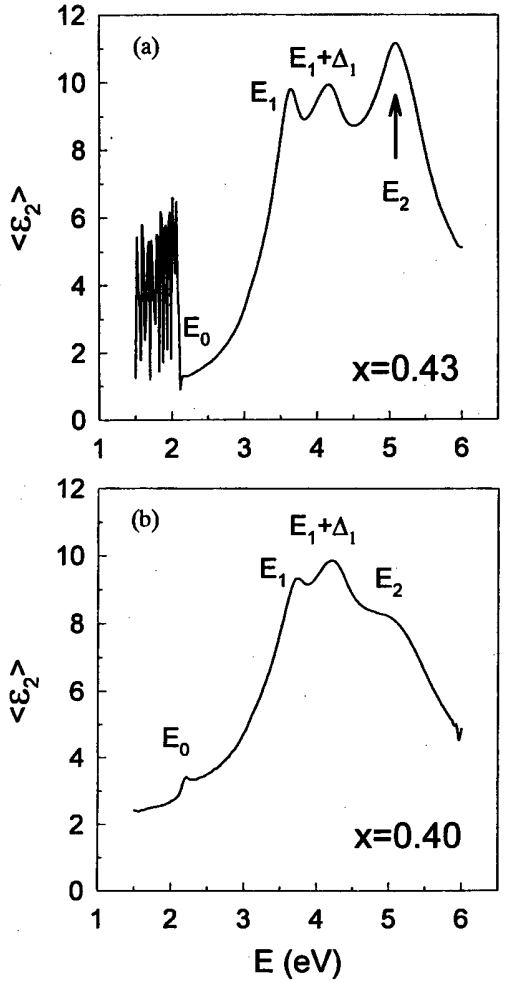

Fig. 2. (a) $<\epsilon_2>$ spectrum of $Cd_{0.57}Mg_{0.43}Te$ film epitaxially grown on GaAs. (b) $<\epsilon_2>$ spectrum of bulk $Cd_{0.60}Mg_{0.40}Te$ from Ref. 5.

Table 1. Pseudodielectric function of $Cd_{0.57}Mg_{0.43}Te$ determined in this work.

E (eV)	ϵ_1	ϵ_2	E (eV)	ϵ_1	ϵ_2
2.2	8.96	1.29	4.1	5.82	9.84
2.3	8.95	1.39	4.2	4.84	9.88
2.4	9.06	1.51	4.3	4.06	9.38
2.5	9.21	1.67	4.4	3.89	8.85
2.6	9.42	1.85	4.5	3.93	8.70
2.7	9.65	2.09	4.6	3.96	8.79
2.8	9.94	2.38	4.7	3.91	9.07
2.9	10.27	2.76	4.8	3.75	9.53
3.0	10.63	3.30	4.9	3.34	10.17
3.1	10.87	4.01	5.0	2.44	10.87
3.2	11.06	4.74	5.1	0.99	11.14
3.3	11.23	5.66	5.2	-0.35	10.66
3.4	11.23	6.87	5.3	-1.37	9.92
3.5	10.75	8.35	5.4	-2.13	8.96
3.6	9.32	9.65	5.5	-2.46	7.92
3.7	7.54	9.53	5.6	-2.49	7.03
3.8	7.07	8.92	5.7	-2.37	6.30
3.9	6.94	9.03	5.8	-2.17	5.78
4.0	6.55	9.44	5.9	-1.95	5.33

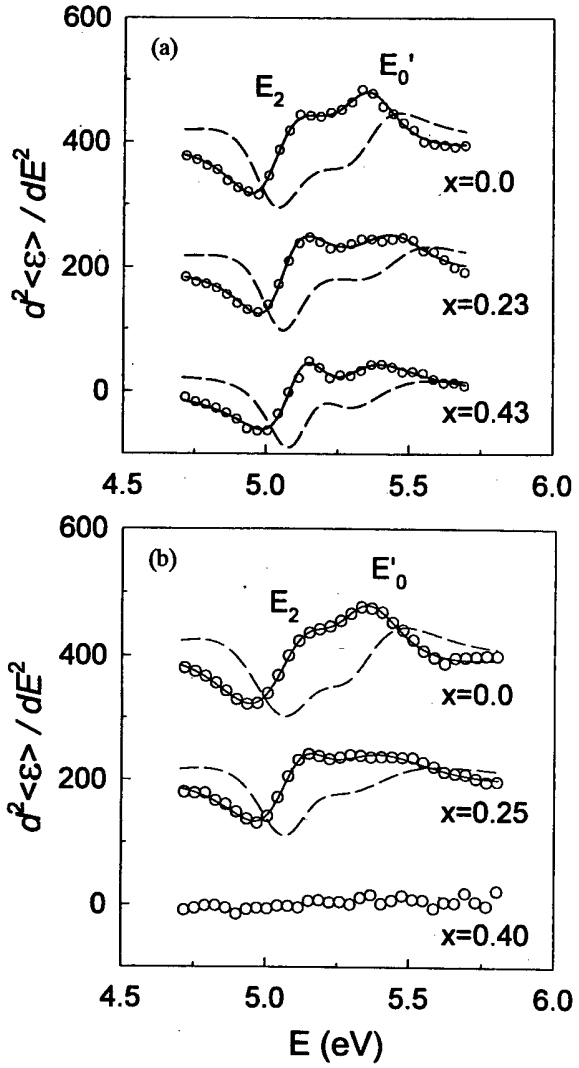

Fig. 3. Second energy derivative spectra of $<\epsilon_1>$ (circles) calculated from (a) current results reported on epitaxial $Cd_{1-x}Mg_xTe$ films and (b) previous result obtained on bulk material as reported in Ref. 5. For clarity, only half the data are shown. The solid and dashed curves represent the best fits to $<\epsilon_1>$ and $<\epsilon_2>$, respectively.

taneously, assuming an exciton CP line shape $n = -1$ as discussed previously [5,14,15]. In Fig. 3(a) we show these numerically calculated second derivative spectra by open circles in the E_2 and E_0' region together with the best fits to $d^2<\epsilon_1>/dE^2$ (solid lines) and $d^2<\epsilon_2>/dE^2$ (dashed lines). For clarity the $d^2<\epsilon_2>/dE^2$ data are not shown, but the quality of the fits is similar. To clearly prove the improvement of current data, we show the results of CdTe and $Cd_{0.77}Mg_{0.23}Te$ together. Similar results from Ref. 5 on bulk samples are shown in Fig. 3(b). These spectra show that the E_2 structure is well resolved in the present data up to $x = 0.43$, while that in the bulk spectra are poorly defined even at $x = 0.25$ and cnanot be resolved at all at x =0.40. The resulting CP energies $E_0 + \Delta_0$, E_1, $E_1 + \Delta_1$, E_2, and E_0' structures are 3.016 eV, 3.650 eV, 4.248 eV, 5.088 eV, and 5.315 eV.

IV. CONCLUSIONS

We report the above band gap pseudodielectric function values of $Cd_{0.57}Mg_{0.43}Te$ film at room temperature from 2.2 eV up to 5.9 eV. By proper chemical etching procedure, we obtained accurate approximations to the true dielectric response of $Cd_{0.57}Mg_{0.43}Te$. The dielectric function below the fundamental gap requires additional analysis, which will be reported elsewhere. Well resolved structures are observed, which allows us to obtain accurate values of the $E_0 + \Delta_0$, E_1, $E_1 + \Delta_1$, E_2, and E_0' critical point energies.

ACKNOWLEDGMENTS

This work was supported by KOSEF Grant No. 98-0200-05-01-3. The work done at North Carolina State University was supported by the Office of Naval Research under contract no. N00014-93-1-0255. The work in Poland was supported by State Committee for Scientific Research under grant PBZ28.11.

REFERENCES

[1] A. Waag, H. Heinke, S. Scholl, C. R. Becker and G. Landwehr, J. Cryst. Growth **131**, 607 (1993).
[2] H. Arwin and D. E. Aspnes, J. Vac. Sci. Technol. **A2**, 1316 (1984).
[3] L. Viña, C. Umbach, M. Cardona and L. Vodopyanov, Phys. Rev. **B29**, 6752 (1984).
[4] M. Luttmann, F. Bertin and A. Chabil, J. Appl. Phys. **78**, 3387 (1995).
[5] S. G. Choi, Y. D. Kim, S. D. Yoo, D. E. Aspnes, I. Miotkowski and A. K. Ramdas, Appl. Phys. Lett. **71**, 249 (1997).
[6] D. E. Aspnes, Opt. Commun. **8**, 222 (1973).
[7] D. E. Aspnes and A. A. Studna, Appl. Opt. **14**, 220 (1975).
[8] D. E. Aspnes and A. A. Studna, Phys. Rev. **B27**, 985 (1983).
[9] Y. D. Kim, S. G. Choi, M. V. Klein, S. D. Yoo, D. E. Aspnes, S. H. Xin and J. K. Furdyna, Appl. Phys. Lett. **70**, 610 (1997).
[10] S. G. Choi, Y. D. Kim, M. V. Klein, S. D. Yoo, D. E. Aspnes, S. H. Xin and J. K. Furdyna, J. Korean Phys. Soc. **31**, 202 (1997).
[11] M. Cardona, in *Modulation Spectroscopy*, Suppl. vol. 11 of *Solid State Physics*, edited by F. Seitz, D. Turnbull and H. Ehrenreich (Academic, New York, 1969).
[12] D. E. Aspnes, in *Handbook on Semiconductors*, edited by M. Balkanski (North-Holland, Amsterdam, 1980), Vol. 2, p. 109.
[13] Y. D. Kim, S. L. Cooper, M. V. Klein and B. T. Jonker, Appl. Phys. Lett. **62**, 2387 (1993).
[14] Y. D. Ko, Y. D. Kim, S. L. Cooper, M. V. Klein, J. -H. Park and B. T. Jonker, J. Korean Phys. Soc. **31**, 108 (1997).
[15] P. Lautenschlager, M. Garriga, L. Viña and M. Cardona, Phys. Rev. **B36**, 4821 (1987).

Journal of the Korean Physical Society, Vol. 34, June 1999, pp. S499~S503

Silicidation of Co/Ti, Co/Nb, and Co/Hf Bilayers on the Si (100) Substrate

Youngjae KWON and Chongmu LEE

Department of Metallurgical Engineering, Inha University, Inchun 402-751

Ho-Kyu KANG and Dae-Lok BAE

LS Process Development Semiconductor R&D Center, Samsung Electronics, Yongin 449-900

The formation mechanism of epitaxial cobalt silicide from Co/Ti, Co/Hf, and Co/ Nb/(100) Si structures has been investigated. The crystallographic orientations of the silicide films formed after annealing these bilayer metals on (100)Si at 800 °C are found to strongly depend upon the thin metal layer used as an epitaxy promoter. Epitaxial cobalt silicide was grown from Co/Ti/(100)Si. Epitaxial and non-epitaxial $CoSi_2$ formed simultaneously in Co/Hf/(100)Si, while only non-epitaxial $CoSi_2$ formed in Co/Nb/(100)Si system. The reason why the crystallographic orientation of $CoSi_2$ differs for these systems seems to be related to the formation and decomposition of stable reaction barriers at high temperatures. Stable reaction barriers formed at high temperatures make the uniform diffusion of Co atoms possible, resulting in the growth of epitaxial $CoSi_2$.

I. INTRODUCTION

Titanium silicide and cobalt silicide are the two most widely used silicides for the self-aligned silicide (salicide) technology [1–3]. When a silicidation annealing is carried out at a single titanium or cobalt layer on the Si substrate, the Si-silicide interface easily becomes rough due to non-uniform silicidation, which, in turn would produce increased junction leakage current and high contact resistance [4]. In general thermal grooving occurs at the grain boundaries of thin films upon high temperature annealing owing to local energy equilibrium. The grooving can lead to the formation of an "island" structure at higher temperatures. This phenomenon is known as agglomeration [5]. Groove formation occurs both at the silicide surface and at the silicide-Si interface. Therefore, it is the best idea to grow an epitaxial silicide film on the Si substrate in preventing agglomeration of the silicide film [6,7]. The epitaxial silicide layer can be realized by rapid thermal annealing of a Co/metal bilayer on the Si substrate [8]. Metals appropriate for the Co/metal bilayer are refractory metals like Ti, Zr, V, Hf, Nb, and Ta. Rapid thermal annealing of Co/metal/(100)Si in a N_2 ambient induces inversion in position between the Co layer and the metal layer, because of the following three reasons;

(1) The silicidation temperature of these metals are higher than that of Co

(2) Co is a main diffuser in $CoSi_2$ formation process

(3) The diffusion coefficient of Co is higher than those of refractory metals and that of Si

The refractory metals listed above get rid of the native oxide, because they have stronger tendency of oxidation than that of Si. Co atoms arrive at the metal/Si interface after moving through the metal layer and then react with Si atoms in the Si substrate to form $CoSi_2$. Therefore, the $CoSi_2$ layer can grow epitaxially, because the lattice mismateh between $CoSi_2$ and Si is nothing but 1.2 % [9] and also because the refractory metal removes the native oxides on the Si substrate by reducing them into Si.

Byun *et al.* [10] reported to obtain an epitaxial silicide using a Co/Ta/Si system. They also tried Co/Zr/Si, Co/V/Si system, although the qualities of the final structures were not so satisfactory. Most of the refractory metals except W and Mo may be used as an epitaxy promoter like Ti in the Co/Ti/Si system. In this work the final structures and the silicide formation mechanisms of Co/Ti, Co/Nb, and Co/Hf bilayers on (100)Si have been investigated.

II. EXPERIMENTAL

P-type Si wafers with (100) orientation were cleaned in a 10 % HF solution and rinsing in diluted water. Then Co/Ti, Co/Nb and Co/Hf layers were deposited on the substrates by dual target sputtering to form a Co(15 nm)/metal(10 nm)/(100)Si structure. The base pressure of the deposition system was 5×10^{-7} Torr. Silicidation annealing treatments were performed using a rapid thermal annealing system in a vacuum of 2×10^{-5} Torr at various temperatures for 30 sec. Glancing angle X-ray diffraction was used to identify the phases. AES depth

profile was used to investigate the layer structures. The sheet resistances of the films were measured with a four-point probe technique.

III. RESULTS AND DISCUSSION

The reactions of the Co/metal bilayers with Si during rapid thermal processing have been studied. Figure 1 shows the sheet resistance after a sequential deposition of refractory metal interlayer and Co films on the Si substrate and annealing at various temperatures for 30 sec. Ti, Hf, and Nb were used for the interlayer. The thicknesses of the interlayer and the top Co layer were 10 nm and 15 nm, respectively. The sheet resistance increases as the annealing temperature increases from 330 °C to 420 °C, where the resistance is maximized. As the annealing temperature increases further, the sheet resistance rapidly decreases and then holds constant above 500 °C regardless of the kind of interlayer metal. The change in sheet resistance can be directly related to the phase transition. The peak of the resistance between 380 and 500 °C is due to the formation of CoSi and Co_2Si phases with high resistivities.

X-ray diffraction spectra of the Co/Ti bilayer silicide using glancing angle XRD show the presence of these phases at lower temperatures in figure 2(a). The CoSi phase grows and the Co layer is completely converted into CoSi at 420 °C. The phase evolution simultaneously leads to the formation of $CoSi_2$ at 420 °C annealing. With increasing the annealing temperature, other low temperature phases disappear and only $CoSi_2$ is observed above 600 °C. The phase sequence with respect to the annealing temperature obtained from XRD agrees well with the

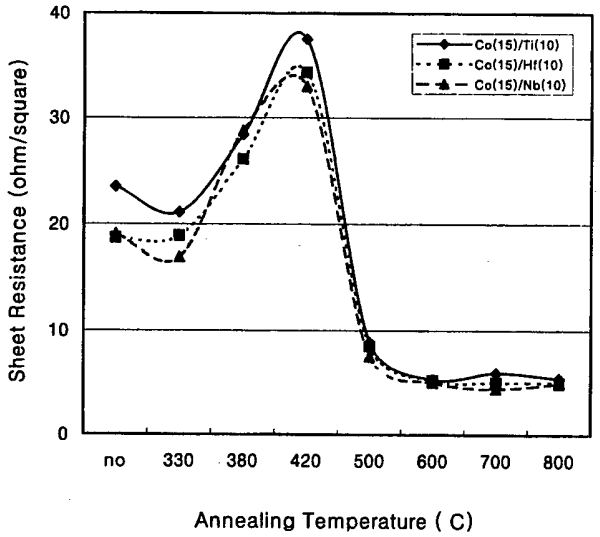

Fig. 1. The sheet resistances of the Co/refractory metal bilayer silicides on Si(100) substrate as a function of annealing temperature.

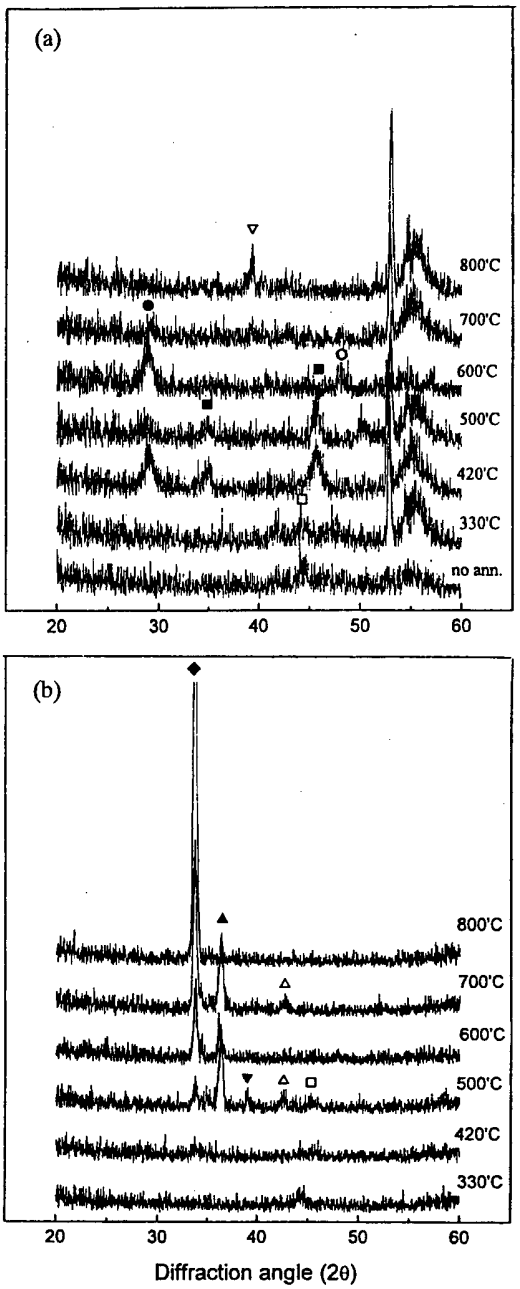

Fig. 2. Glancing angle XRD spectra of the Co/Ti bilayer silicide on the Si(100) substrate as a function of RTA annealing temperature for 30 sec.; (● : $CoSi_2$(111), o : $CoSi_2$(220), ◆ : $CoSi_2$(200), ■ : CoSi, □ : Co, ▲ : Co_2TiO_4, △ : $CoTiO_3$, ▽ : $TiSi_2$ ▼ : TiO_2). (a) X-ray incident angle : 1° and (b) X-ray incident angle : 16.7°.

sheet resistance data (≈70 $\mu\Omega$cm for Co_2Si, ≈100~150 $\mu\Omega$cm for CoSi, and ≈15~25 $\mu\Omega$cm for $CoSi_2$) [11]. It is interesting to note that $CoSi_2$ is not observed above 700 °C in figure 2(a). We obtained the glancing angle XRD spectra of figure 2(a) at a fixed incident angle of 1°. To investigate the epitaxial silicide formation better, we obtained a glancing angle XRD spectra at an incident angle of 16.7° which is the incident angle for $CoSi_2$ (200)

diffraction and the results are shown in figure 2(b). The appearance of the diffraction peak of $CoSi_2$ (200) suggests an epitaxial growth of $CoSi_2$ on the Si (100) substrate. The diffraction peak of $CoSi_2$ (200) begins to be appeared at 500 °C, which is somewhat higher than that for $CoSi_2$ (111) or (220). This peak is further grown with increasing the temperature and no other cobalt silicide peaks are found above 700 °C in figure 2(b). These results imply that the $CoSi_2$ layer has a polycrystalline structure below 600 °C, but grows epitaxially on the Si (100) substrate above 700 °C. After annealing at 500 °C, an XRD peak corresponding to a ternary compound of Co-Ti-O is also detected as shown in figure 2(b). The studies by Vantomme *et al.* [12] and Kim *et al.* [13] suggested that the formation and decomposition of a ternary compound like Co-Ti-Si play an important role in epitaxial growth of $CoSi_2$ during thermal processing. Also, other ternary compounds, for example a Co-Ti-O spinel phase, were presented as epitaxy promoters [14]. In the study, these

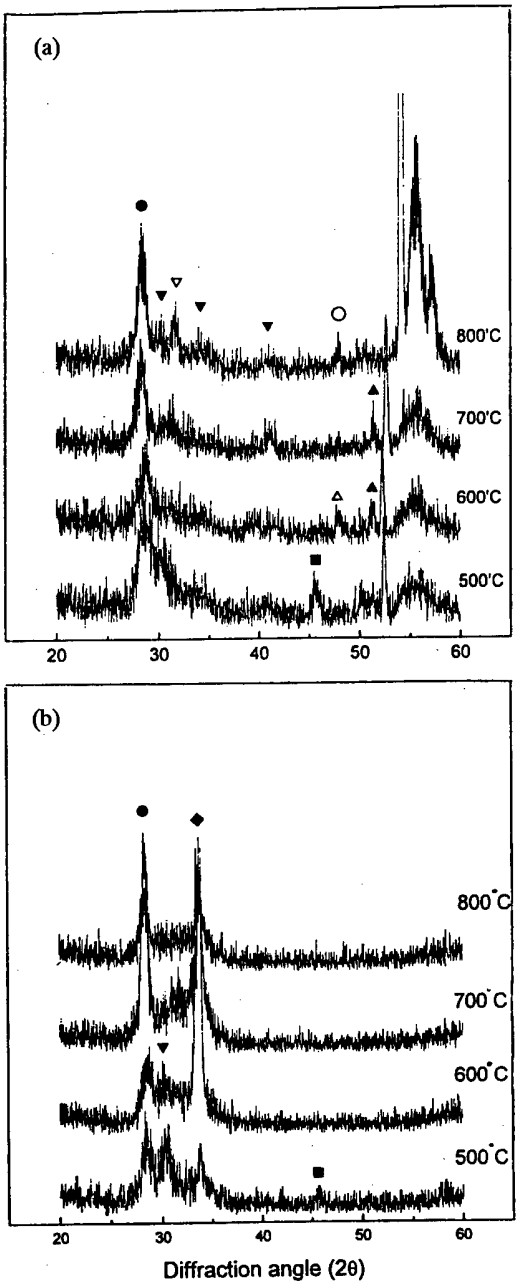

Fig. 3. Glancing angle XRD spectra of the Co/Hf bilayer silicide on the Si(100) substrate as a function of RTA annealing temperature for 30 sec.; (● : $CoSi_2$(111), ○ : $CoSi_2$(220), ◆ : $CoSi_2$(200), ■ : CoSi, □ : Co, ▽ : HfSi, ▼ : HfO_2, ▲ : β-Co_2SiO_4, △ : $HfSiO_4$). (a) X-ray incident angle : 1° and (b) X-ray incident angle : 16.7°.

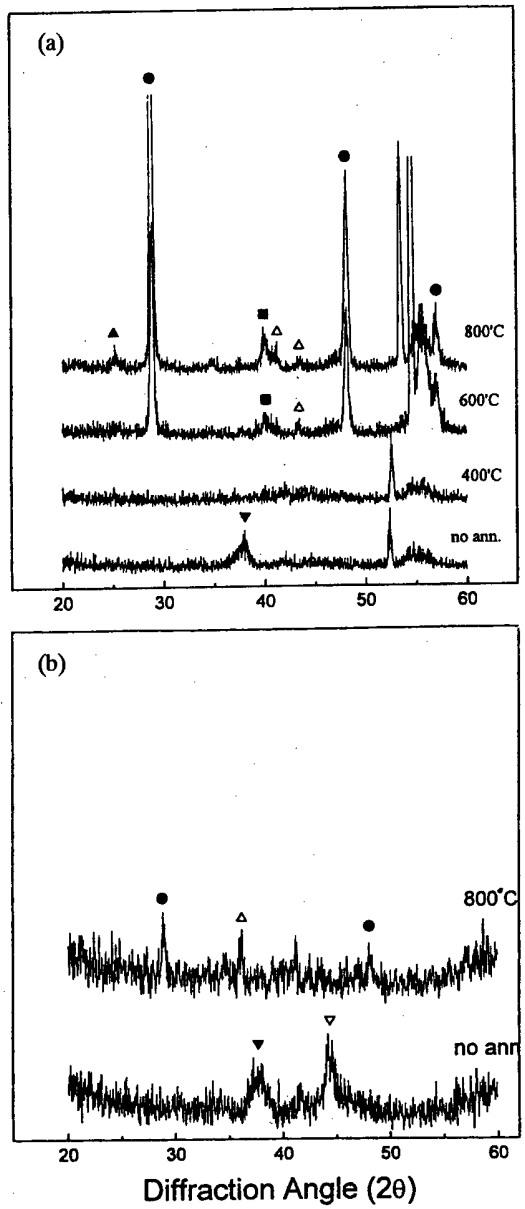

Fig. 4. Glancing angle XRD spectra of the Co/Nb bilayer silicide on the Si(100) substrate as a function of RTA annealing temperature for 30 sec.; (● : $CoSi_2$, ▲ : β-Nb_2O_5, △ : Nb_2O_5, ■ : Nb_6Co_7, ▼ : Nb, ▽ : Co). (a) X-ray incident angle : 1° and (b) X-ray incident angle : 16.7°.

spinel phases may contribute to reducing the native oxide on the underlying Si substrate and to controlling the inter-diffusion between Si and Co during the reaction, thereby promoting epitaxial growth of $CoSi_2$. From the appearance and disappearance of the Co-Ti-O peak (indexed as Co_2TiO_4 and $CoTiO_3$) at 500, 600, and 700 °C, it may be said that the Co-Ti-O ternary compound is decomposed into TiO_2 and Co-Ti-Si during annealing and controls the inter-diffusion of Co and Si moderately, which may help $CoSi_2$ grow epitaxially. The evolution of the layer structure will be represented later.

The XRD spectra of Co(15 nm)/Hf(10 nm)/(100)Si and Co(15 nm)/Nb(10 nm)/(100)Si after rapid thermal annealing for 30 sec at various temperatures are also shown in figure 3 and 4. At 500 °C, both $CoSi_2$ and CoSi reflection peaks appeared. These silicide peaks of Co/Hf are basically the same as that of Co/Ti. The CoSi reflection intensity is much weaker than that of $CoSi_2$ at 500 °C, which implies that $CoSi_2$ is a cobalt silicide phase dominant at this temperature. These results agree well with the sheet resistance curve of figure 1. HfO_2 peaks are also found at this temperature. It is worth noting that Hf does not form ternary compounds such as Co-Hf-O or Co-Hf-Si. The native oxide at the interface with the Si substrate is changed to HfO_2 by reacting with Hf, not to Co-Hf-O. It appears that CoSi completely transforms into $CoSi_2$ or a silicate phase like β-Co_2SiO_4 and $HfSiO_4$ are newly formed during annealing at 600 °C (figure 3(a)). Further reactions occurred and the silicate phases sequentially disappear as the annealing temperature increases to 700 and 800 °C. The temperatures at which β-Co_2SiO_4 and $HfSiO_4$ are not found are 700 and 800 °C, respectively. The XRD spectra of the Co/Hf/(100)Si after annealing are shown in figure 3(b). The $CoSi_2$ layer has textured structures, not epitaxial structures. I(200)/I(111) which represent the degree of epitaxy is the highest at the annealing temperature of 600 °C.

For Co/Nb/(100)Si, $CoSi_2$ begins to form at 500 °C (figure 4(a)). Co-Nb alloys and Nb oxides also form above 500 °C, but no ternary compound is observed. As shown in figure 4(b), epitaxial growth is also not achieved even at temperatures above 800 °C. The non-epitaxial growth and no ternary compound formation seem to be the most saliant features in Co/Nb bilayer silicidation. To investigate the redistribution of each element, AES depth profiles were performed. Figure 5 shows the AES depth profiles for Co/Ti/(100)Si. In the as-deposited specimens, oxygen contamination is detected in the Ti interlayer and at the surface of the specimen. The oxygen in the interlayer seems to be due to the native oxide. The oxygen a the specimen surface may be contaminated during deposition. Figure 2(b) and 5(b) show that, during annealing at 500 °C, a part of the cobalt and silicon inter-diffused through the Ti interlayer and reacted to form CoSi and $CoSi_2$. The layer structure after annealing at 500 °C consists of three layers : the upper layer of a mixture

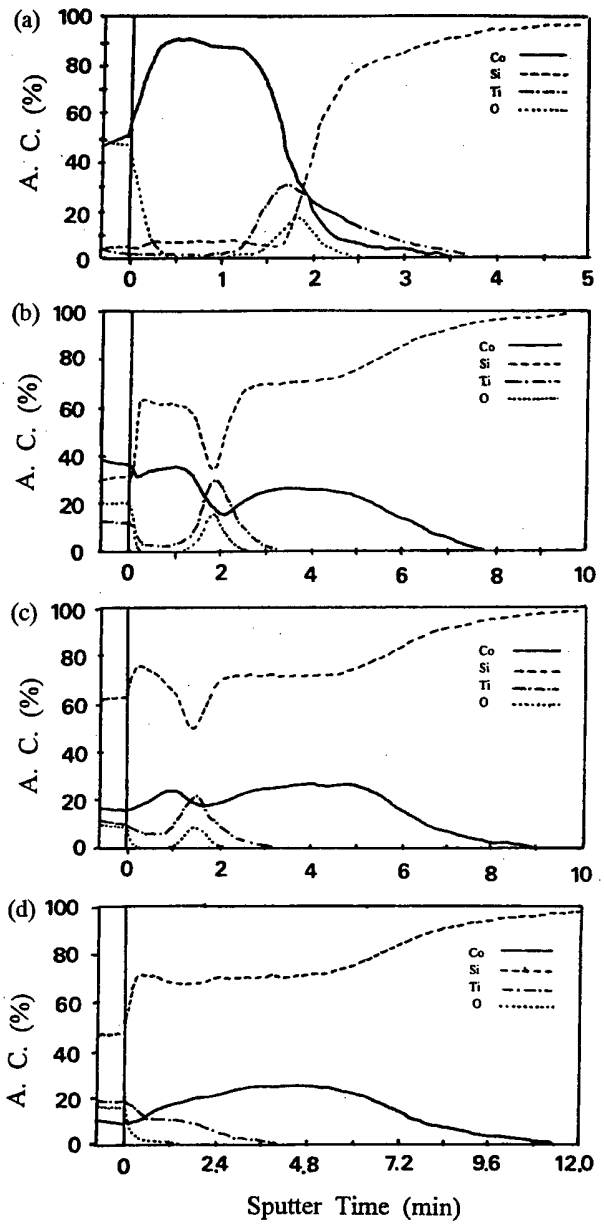

Fig. 5. The AES depth profiles of the Co(15 nm)/Ti(10 nm)/Si(100) sample after RTA annealing for 30 sec; (a) as-deposited, annealed at (b) 500 °C, (c) 600 °C, and (d) 700 °C.

of CoSi and $CoSi_2$, the interlayer of Co-Ti-O compounds and the lower layer of epitaxial $CoSi_2$. This layer structure is maintained up to 600 °C, the epitaxial $CoSi_2$ layer grows further at the $CoSi_2$-Si interface and the Co-Ti-O compounds in the interlayer are decomposed as the annealing temperature increases up to 700 °C (figures 2(b) and 5). A complete layer inversion between Co and Ti occurs at 700 °C. Figure 6 shows the AES depth profiles of Co/Hf/(100)Si after annealing. It can be seen from figure 6(c) that the final structure of Co/Hf/(100)Si after annealing differs from that of Co/Ti/(100)Si. It seemed that these Co and Hf silicate phases coexist in the same interlayer as a solid solution at 600 °C. After decompo-

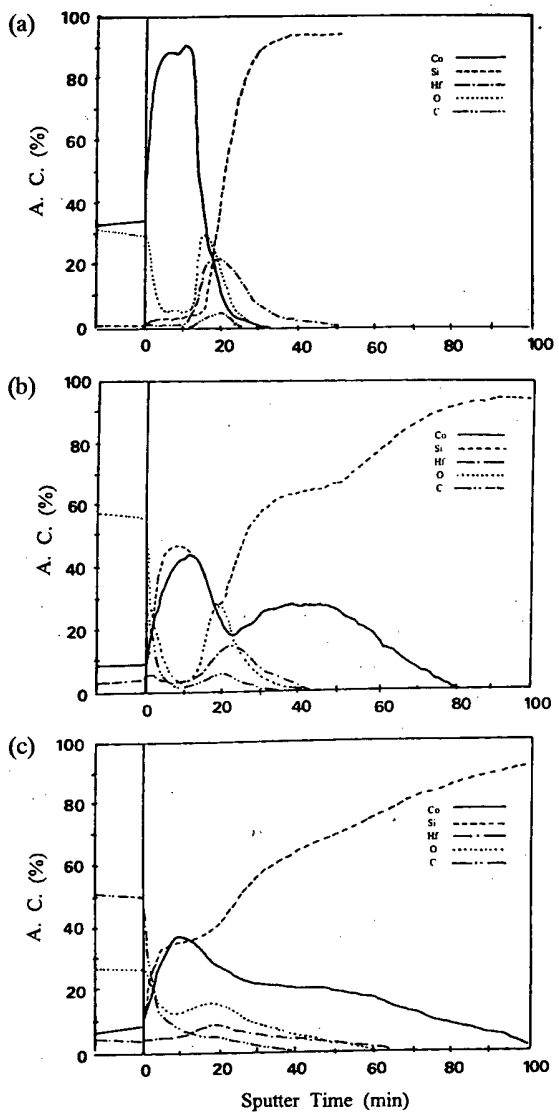

Fig. 6. The AES depth profiles of the Co(15 nm)/Hf(10 nm)/Si(100) sample after RTA annealing for 30 sec; (a) as-deposited, annealed at (b) 600 °C, and (c) 700 °C.

sition of $HfSiO_4$ above 600 °C, β-Co_2SiO_4 which formed at 500 °C remains at the top of the sample even at temperatures higher than 700 °C. Diffusion of Co into the Si substrate is considerably suppressed up to 700 °C. Due to the unstable thermal decomposition of $HfSiO_4$ at higher temperatures the epitaxial growth of $CoSi_2$ is imperfect, in other words, a textured structure is obtained.

IV. CONCLUSIONS

Various ternary compounds formed during the initial stage of the reaction seem to play a role of the reaction barrier for the formation of epitaxial $CoSi_2$ in the Co/metal/(100)Si system. They control diffusion of Co into the Si substrate, resulting in the formation of an epitaxial $CoSi_2$. For Co/Ti/Si(100), the Co-Ti-O ternary compound formed at the metal/Si interface and the Hf-Si-O formed during silicidation of Co/Hf bilayer act as reaction barriers. No ternary compound forms in Co/Nb/(100)Si during annealing. The final layer structure obtained after a rapid thermal annealing of Co/Ti/(100)Si bilayer turned out to be Ti oxide/Co-Ti-Si/epi-$CoSi_2$/ (100)Si. The crystallographic orientations of the cobalt silicide formed at 500 °C seems to strongly depend on the metal used as an epitaxy promoter in Co/metal/(100)Si. Epitaxial and non-epitaxial $CoSi_2$ simultaneously formed in Co/Hf/(100)Si, while only non-epitaxial $CoSi_2$ form in Co/Nb/(100)Si. The reason why the crystallographic orientation of $CoSi_2$ differs between these two systems seems to be related to the formation and decomposition of stable reaction barriers at high temperatures. The stable reaction barriers formed at high temperatures may control the diffusion of Co atoms into the Si substrate which enables epitaxial growth of $CoSi_2$.

ACKNOWLEDGMENTS

This work was supported by Samsung Electronics Co. Ltd.

REFERENCES

[1] C. K. Lau, Y. C. See, D. B. Scott, J. M Bridges, S. M. Perna and R. D Davis, '98 IEDM Tech. Dig., 714 (1982).
[2] G. J. van Gurp and C. Langereis, J. Appl. Phys. **46**, 4301 (1975).
[3] A. E. Morgan, E. K. Broadbent, M. Delfino, B. Coulman and D. K. Sadana, J. Electrochem. Soc. **134**, 925 (1987).
[4] Q. F. Wang, C. M. Osburn, P. L. Smith, C. A. Canovai and G. E. McGuire, J. Electrochem. Soc. **140**, 200 (1993).
[5] S. L. Hsi and T. Y. Tan *et al.*, J. Appl. Phys **72**, 1864 (1992).
[6] R. T. Tung, J. C. Bean, J. M. Gibbson, J. M. Poate and D. C. Jacobson, Appl. Phys. Lett **40**, 684 (1982)
[7] K. N. Tu, E. I. Allessandrini, W. K. Chu, H. Krutle and J. W. Mayer, Jpn. J. Appl. Phys. Suppl. **2**, 669 (1974).
[8] M. L. A. Dass, D. B. Fraser and C.-S. Wei, Appl. Phts. Lett. **58**, 1308 (1991).
[9] M.-A. Nicolet and S. S. Lau, *VLSI Electronics : Microstructre Science*, edited by N. G. Einspruch and G. B. Larrabee (Academic, New York, 1983), Vol. 6, p. 402.
[10] J. S. Byun, Ph. D. Thesis, Seoul National University, (1993).
[11] K. Maex, Mater. Sci. and Eng. **R11**, Nos. 2-3 (1993).
[12] A. Vantomme, M. -A. Nicolet and N. D. Theodore, J. Appl. Phys **75**, 3882 (1994).
[13] G. B. Kim, H. K. Baik and S. M. Lee, Appl. Phys. Lett **69**, 3498 (1996).
[14] T. I. Selinder, T. A. Roberts, D. J. Miller, M. A. Beno, G. S. Knapp, K. E. Gray, S. Ogawa, J. A. Fair and D. B. Fraser, J. Appl. Phys. **77**, 6730 (1995).

Journal of the Korean Physical Society, Vol. 34, June 1999, pp. S504~S509

Thermal Stability of Nb-Si-N and Ta-Si-N as Diffusion Barriers between Cu and Si

Hyung-Jin BAE, Young-Hoon SHIN and Chongmu LEE

Department of Metallurgical Engineering, Inha University, Incheon 402-751

Jong-choul KIM

Anam Industrial Co. Ltd., Buchon 420-130

In this study, Nb-Si-N and Ta-Si-N films were deposited on (100)Si wafers using a reactive sputtering technique and their thermal stability indispensable for a barrier metal against Cu was investigated using sheet resistance measurement, X-ray diffraction, and Auger electron spectroscopy depth profiling. The N_2/Ar gas flow ratio for the sputter deposition of the Nb-Si-N and Ta-Si-N films with the highest thermal stability were found to be 5 % and 15 %, respectively. The Nb-Si-N film failed at 700 °C, while the Ta-Si-N film failed at 900 °C. The failure mechanism of the Nb-Si-N was found to be as follows : Cu atoms move to the Nb-Si-N/Si interface through the Nb-Si-N film and react with Si atoms in the Si substrate resulting in the formation of Cu3Si at the Nb-Si-N/Si interface. Also the failure mechanism of Ta-Si-N was found to be nearly the same as that of Nb-Si-N.

I. INTRODUCTION

The integration density of large scale integrated circuits has doubled every two years for the past twenty-five years. The trend curve of the integration level predicts that the fabrication technique for 0.1 μm width interconnections will realize the 4 Gbit dynamic random access memory (DRAM) within ten years. Aluminum and its alloys have been extensively used for interconnection materials in very large scale integrated circuits (VLSI). However, time delay and electromigration will become serious problems in the application of aluminum interconnections to ultralarge scale integrated circuit (ULSI). Copper has an electrical bulk resistivity of 1.7 $\mu\Omega$cm and fewer electromigration problems than aluminum alloys [1]. However, Cu metallization also has several drawbacks such as diffusion of Cu into the Si substrate through the SiO_2 layer. Cu can become a recombination-generation center, a cause of leakage current near a p-n junction, and a cause of threshold voltage shift of the MOS capacitor [2,3] by being precipitated as a form of a silicide [4]. Cu also forms Cu_3Si by reacting with the substrate Si at the lower temperatures than 200 °C [5]. After the formation of the Cu_3Si phase, the underlying Si in the Cu_3Si/Si structure is readily oxidized even at room temperature [6,7]. Hence a diffusion barrier is strongly needed between Cu and SiO_2. The various barrier materials for Cu metallization have been reported. Among these, the ones with the highest thermal stability are ternary compounds such as Ta-Si-N [8,9], Ti-Si-N [10], Mo-Si-N [11], and W-Si-N [11]. Kolawa *et al.* [8] reported that $Ta_{36}Si_{14}N_{50}$ does not fail up to 950 °C. Ti-Si-N, Mo-Si-N, and W-Si-N were reported not to fail up to 850, 800, and 700 °C, respectively [8–11]. The barrier performance of these materials were evaluated mostly by using I-V measurements of the n^+-p shallow junction diodes and Rutherford back scattering spectrometry in those works [8–11].

In this paper, we report on the barrier properties of the Nb-Si-N and Ta-Si-N by using X-ray diffraction and AES depth profiling. The focus is on the effect of N_2/Ar gas flow ratio of the reactive sputter deposition process on the barrier properties of the Nb-Si-N and Ta-Si-N.

II. EXPERIMENTAL METHODS

Substrates of 5Ω-cm n-type(100)Si were cleaned in a dilute HF solution (HF : H_2O = 1 : 20) for 2 min and rinsed in de-ionized water and subjected to N_2 blowing before loaded into the deposition chamber. The Nb-Si-N film with the thickness of approximately 100 nm were deposited on the Si substrates by reactive dc magnetron sputtering using Nb_2Si in Ar and N_2 gas mixture. The base vacuum was maintained below 1×10^{-6} Torr and the dc plasma power and the total gas pressure were fixed to be 100 W and 10 mtorr, respectively. The N_2/Ar ratio was varied to be 5, 7.5, 10, 15, 20, and 30 % for Nb-Si-N deposition. 100 nm-thick Cu films were subsequently sputter deposited on the top of Nb-based films. The samples were then annealed in a vacuum furnace at the pressure of 7×10^{-7} Torr and various temperatures ranging

from 600 to 900 °C for 30 min. The Ta-Si-N specimens were also prepared by reactive sputtering using an Ta_5Si_3 target in the same manner.

Sheet resistance of the samples were measured both before and after annealing by fourpoint probe to survey the overall reaction involving Cu. Auger electron spectroscopic (AES) depth profiling, X-ray diffraction (XRD), and transmission electron microscopy (TEM) were used for the analysis of reaction product phases and the interdiffusion of the elements across the interface, respectively.

III. RESULTS AND DISCUSSION

The most important process parameter in reactive sputtering of Nb-Si-N and Ta-Si-N which determines the composition and the barrier property of the Nb-Si-N and Ta-Si-N film is N_2/Ar gas flow ratio. Figs. 1 shows the XRD spectra for the specimen in which a Nb-Si-N film 100 nm thick and a Cu film 100 nm thick were sequentially deposited with various N_2/Ar gas flow ratios and followed by annealing at 600. In the case of the annealing at 600 °C only Cu(111) and Cu(200) peaks appeared for the N_2/Ar gas ratio of 5 and 10 %. In contrast Cu_3Si(312) and Cu_4Si peaks as well as Cu(111) and Cu(200) peaks appeared for the N_2/Ar gas ratios higher than 15 %. Some of Cu atoms in the Cu film diffused into the Si substrate through the Nb-Si-N film and reacted with the Si substrate to form silicide in the Nb-Si-N/Si interface, which implies that the Nb-Si-N barrier failed for the N_2/Ar gas ratios higher than 15 %.

The reason why the properties of the Nb-Si-N film change with the variation of the nitrogen flow rate has never been reported yet. It is the authors' opinion that

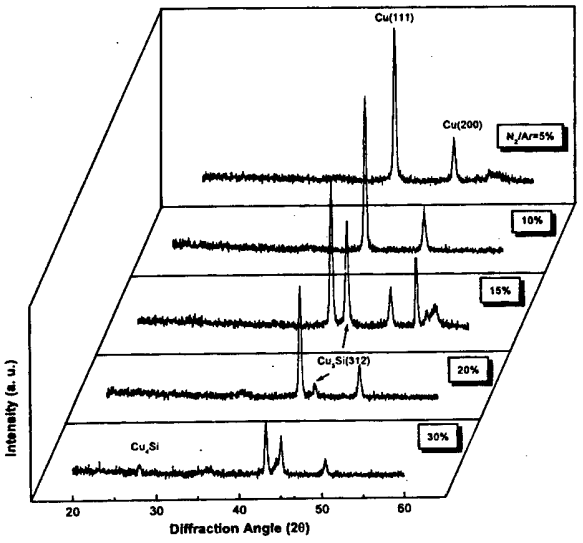

Fig. 1. XRD spectra of the Cu/Nb-Si-N/(001)Si for various N_2/Ar gas flow ratios of the sputter deposition process of Nb-Si-N at 600 °C.

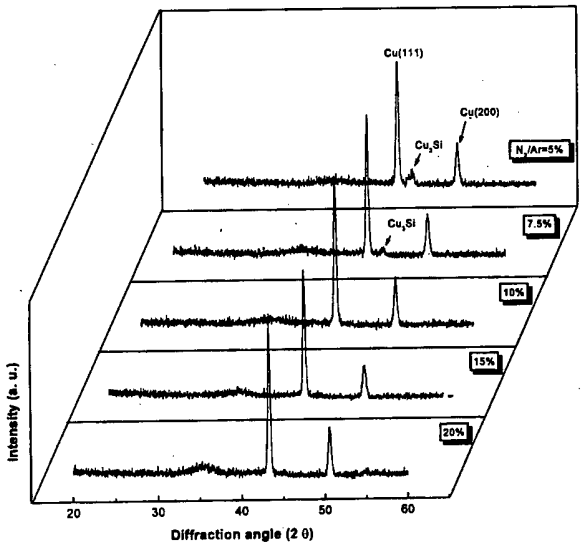

Fig. 2. XRD spectra of the Cu/Ta-Si-N/(001)Si for various N_2/Ar gas flow ratios of the sputter deposition process of Ta-Si-N at 800 °C.

the Si/N ratio changes as the nitrogen flow rate are varied. The thermal properties of Nb-Si-N also change as a result of the change in the Si/N ratio. Thus the Nb-Si-N film deposited with the N_2/Ar ratio higher than 15 % and then annealed at 600 °C is not effective as a diffusion barrier against Cu.

Next in the case of annealing at 700 °C silicides formed between Cu and Si for any N_2/Ar ratio. The Cu_3Si peak in the XRD spectra for the N_2/Ar ratio of 10 % is considerably higher than that of 5 %.

Figs. 2 shows the XRD spectra for Cu/Ta-Si-N/Si for the various N_2/Ar gas flow ratios of the sputter deposition process of Ta-Si-N and annealed at 800 °C. A Cu_3Si intensity peak is found for the N_2/Ar gas flow ratios of 5 % and 7.5 % at the annealing temperature of 800 °C. This result implies that the N_2/Ar ratios below 7.5 % does not offer good barrier properties. Ta-Si-N samples with the N_2/Ar ratio of 10, 15, and 20 % in sputtering of Ta-Si-N were annealed at 900 °C to determine the optimum N_2/Ar ratio. For the N_2/Ar ratio of 10 % some of Cu atoms in the Cu film migrates to the Ta-Si-N/Si interface through the Ta-Si-N layer and react with Si to form Cu_3Si. For the case of 20 % N_2/Ar ratio, the Cu peaks vanish completely and only Cu_3Si peaks appear. Thus, all of the Cu atoms in the Cu film migrate into the Si substrate and react with Si atoms to form Cu_3Si. On the contrary hardly any Cu_3Si peak appears for the case of 15 %. Therefore, we may conclude that the optimum N_2/Ar ratio in the sputter deposition process of Ta-Si-N is 15 %. The Ta-Si-N samples used in this study hereafter were deposited with the N_2/Ar ratio of 15 %. The optimum N_2/Ar ratios of Nb-Si-N and Ta-Si-N were 5 % and 15 %, respectively.

Fig. 3 shows XRD spectra of Cu/Nb-Si-N/Si where

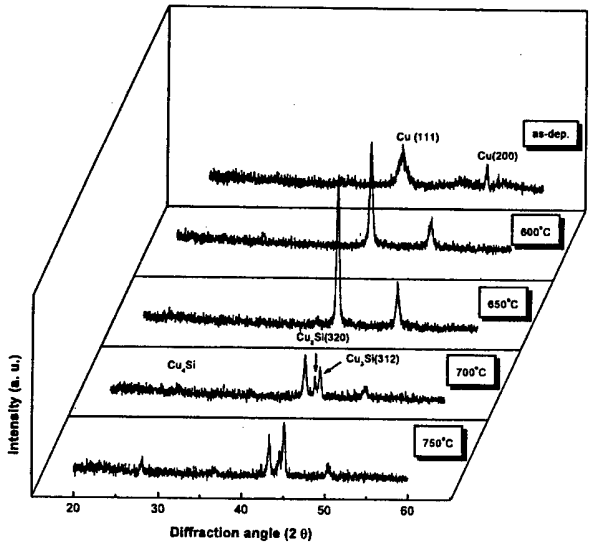

Fig. 3. XRD spectra of the Cu/Nb-Si-N/(001)Si before and after annealing at various temperatures : (a) as-deposited (b) 600 °C (c) 650 °C (d) 700 °C and (e) 750 °C.

Nb-Si-N films were deposited with the optimum N_2/Ar ratio of 5 % and then annealed in the temperature range from 600 °C to 750 °C with the increment of 50 °C. After annealing at 600 °C for 30 min, Cu crystal growth is observed, and no reaction between Cu and Si is observed. The Cu(111) and (200) peak heights for 650 °C are almost the same as those for 600 °C. It implies that Nb-Si-N film does not fail at 650 °C and works well as a diffusion barrier against Cu. The formation of Cu_3Si and Cu_4Si compounds is observed after annealing 700 °C for 30 min, which indicates that Cu diffuses to Si through the barrier layer. The XRD peaks of Cu_3Si and Cu_4Si are higher at 750 °C than at 700 °C.

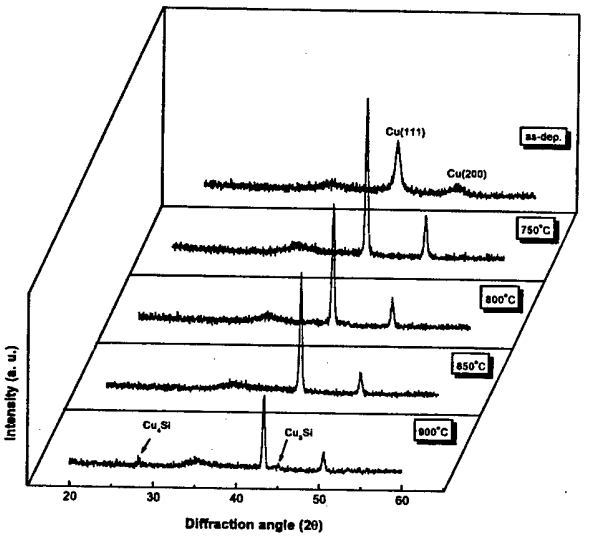

Fig. 4. XRD spectra of the Cu/Ta-Si-N/(001)Si before and after annealing at various temperatures : (a) as-deposited (b) 750 °C (c) 800 °C (d) 850 °C and (e) 900 °C.

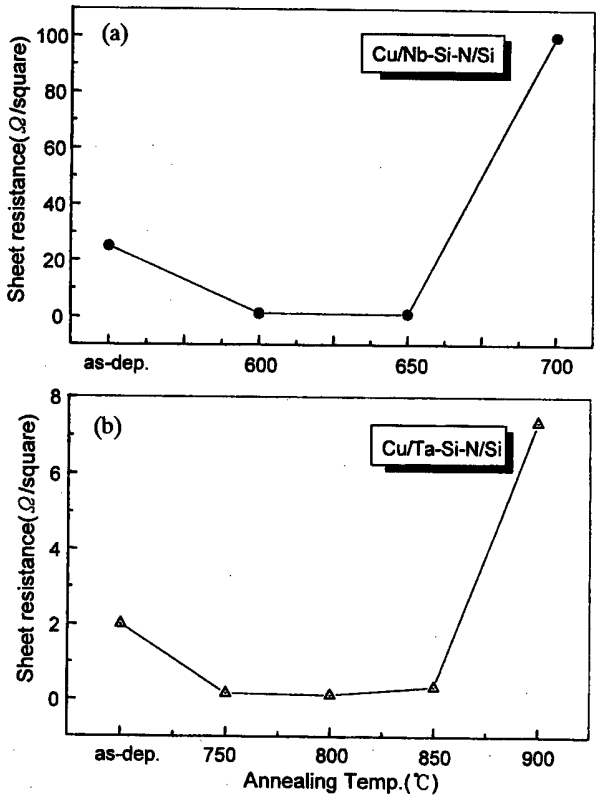

Fig. 5. Sheet resistance of Cu/Nb-Si-N/(001)Si and Cu/Ta-Si-N/(001)Si as a function of annealing temparature.

Fig. 4 shows the XRD spectra for the Cu/Ta-Si-N/Si annealed at various temperatures. There was no change in X-ray diffraction patterns for annealing at temperatures below 900 °C. After annealing at 900 °C, $Cu_3Si(312)$ and Cu_4Si diffraction peaks appeared. The formation of the Cu_3Si and Cu_4Si is confirmed from the sheet resistance measurement and TEM analysis results as shown in Fig. 5 and Fig. 6, respectively. It can be concluded that Nb-Si-N and Ta-Si-N films deposited by reactive sputtering with the N_2/Ar ratio of 5 %, and 15 %, respectively, offers the best barrier property against Cu diffusion, and that the failure temperatures of Nb-Si-N and Ta-Si-N are 700 °C and 900 °C, respectively.

The sheet resistances of Cu/Nb-Si-N/Si system and Cu/Ta-Si-N/Si system were measured on the copper surface at room temperature after annealing for 30 min at different temperatures [Fig. 5(a) and (b)]. The sheet resistances of both systems were initially decreased with increasing the annealing temperature up to 600 and 750 °C, respectively, although the sheet resistance slightly increased with increasing annealing temperature from 600 to 650 °C and from 750 to 850 °C, respectively. It is owing to the crystallization and grain growth of Cu, but the sheet resistances of the Cu/Nb-Si-N/Si system and the Cu/Ta-Si-N/Si system were abruptly increased at 700 and 900 °C, respectively. It results from the formation of copper silicide. The increase in the resistivity

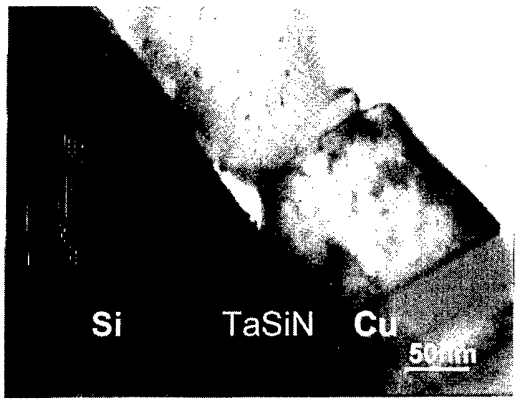

(a)

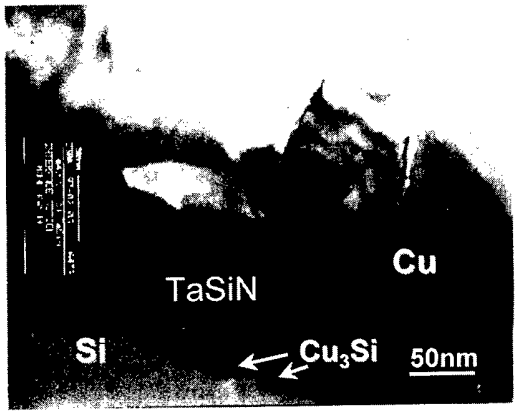

(b)

Fig. 6. TEM cross-sectional micrographs of Cu/Ta-Si-N/(100)Si : (a) annealed at 850 °C, and (b) annealed at 900 °C.

implies that a reaction occurred between Cu and Si. The highest temperature of each sample at which a barrier layer prevents Cu-Si interaction during the subsequent heat treatment can be used as a measure of diffusion barrier effectiveness [12]. Fig. 5(a) and (b) appears to suggest that the Cu/Nb-Si-N/Si system has lower thermal stability than the Cu/Ta-Si-N/Si system.

The compositional depth profiles of the Cu/Nb-Si-N/Si and Cu/Ta-Si-N/Si before and after heat treatment are shown in Figs. 7 and 8, respectively. Figs. 7(a) and 8(a) show that Nb- Si-N and Ta-Si-N layers exist as a diffusion barrier between the Cu layer and the Si substrate and that their boundaries are clearly observable. Nearly no change is found in the profiles of both barrier metals below 700 °C and 900 °C, respectively, while the profiles changed significantly after annealing at 700 °C and 900 °C, respectively. During annealing at the critical temperature of each system, Cu atoms diffused into the Si substrate through the Nb-Si-N and the Ta-Si-N layers of both systems. The Cu atoms which moved deep into the Si substrate made bonds with Si atoms in the substrate to form copper silicides such as Cu_3Si and Cu_4Si. This reaction has been already found by XRD analysis results (Figs. 3 and 4) and is confirmed by these AES depth profiles. Ta-Si-N layer moved up to the top of the sample where the Cu film was originally positioned. However, the amount of Cu was still larger than that of Ta-Si-N at the top of the sample. Some of the Ta and N atoms migrated into the Si substrate, but there was no evidence of Si migration through the Ta-Si-N layer into the Cu layer. We may conclude that copper silicide was formed by migration of Cu through the Ta-Si-N

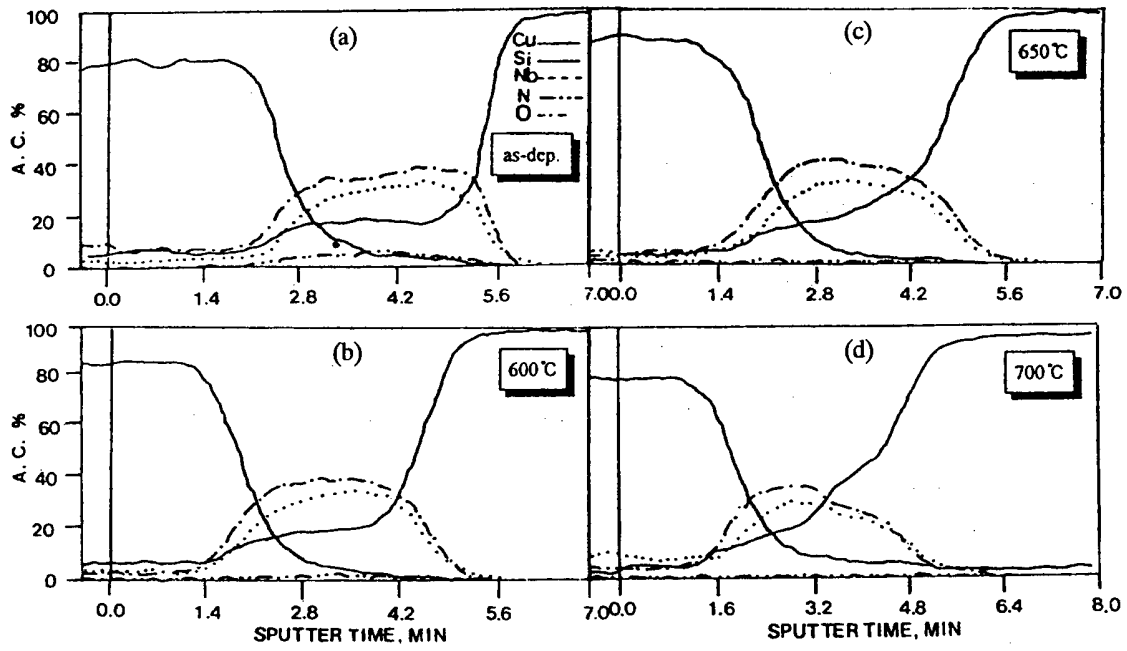

Fig. 7. AES depth profiles of Cu/Nb-Si-N/(001)Si : (a) as-deposited (b) annealed at 600 °C, (c) annealed at 650 °C, and (d) annealed at 700 °C.

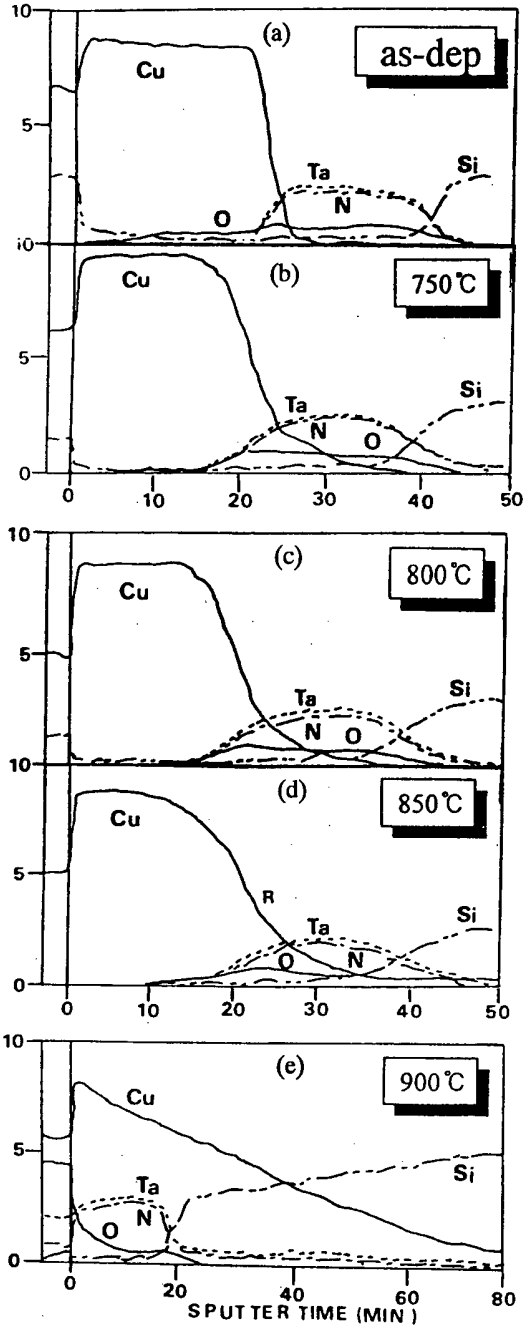

Fig. 8. AES depth profiles of Cu/Ta-Si-N/(001)Si : (a) as-deposited (b) annealed at 750 °C, (c) annealed at 800 °C, (d) annealed at 850 °C, and (e) annealed at 900 °C.

layer and reaction with Si. In other words the main diffuser in the Ta-Si-N layer is not Si but Cu, and copper silicide forms at the Ta-Si-N/Si interface instead of the Cu/Ta-Si-N interface. However, the fact that the XRD peaks of Nb-Si-N and Ta-Si-N crystals are not found at 750 °C and 900 °C, respectively, suggests that the Nb-Si-N and Ta-Si-N films have not been crystallized yet even after annealing at 750 °C and 900 °C, respectively, and that the path through which Cu atoms migrate is not the grain boundary of diffusion barriers. Generally, it is well known that a material with a higher crystallization temperature shows a better barrier property. However, the experimental results obtained in this study show that the failure temperature of a barrier does not always coincide with the crystallization temperature and that it is possible to fail at a temperature lower than the crystallization temperature.

IV. CONCLUSIONS

Barrier properties against Cu diffusion of Nb-Si-N and Ta-Si-N films deposited on the (100) Si substrates by a reactive sputtering method were investigated and the results obtained are as follows :

1) The optimum N_2/Ar flow ratios for the sputter deposition of Nb-Si-N and Ta-Si-N which offer the best barrier property is 5 %, and 15 %, respectively.

2) Nb-Si-N and Ta-Si-N barriers fail by migration of Cu through the barrier metal layer to the Nb-Si-N/Si and Ta-Si-N/Si interfaces, respectively, and reaction of Cu with Si to form copper silicides such as Cu_3Si and Cu_4Si.

3) The crystallization temperature of Nb-Si-N for the Cu/Nb-Si-N/Si system is higher than 750 °C while its failure temperature is 700 °C. Also, the crystallization temperature of Ta-Si-N for the Cu/Ta-Si-N/Si system is higher than 900 °C while its failure temperature is 900 °C. Therefore, the failures of Nb-Si-N and Ta-Si-N are not directly related to the crystallization of Nb-Si-N and Ta-Si-N.

4) Ta-Si-N offers better barrier properties and is more stable at high temperatures than Nb-Si-N, because the failure temperature of Ta-Si-N is higher than that of Nb-Si-N.

ACKNOWLEDGMENTS

This work was supported by Korea Science and Engineering Foundation through Research Center for Thin Film Fabrication and Crystal Growing of Advanced Materials.

REFERENCES

[1] J. D. McBrayer, R. M. Swanson and T. W. Sigmon, J. Electrochem. Soc. **133**, 1242 (1986).
[2] G. C. Schwartz and P. M. Schaible, J. Electrochem. Soc., **130**, 1777 (1983).
[3] P. L. Pai and C. H. Ting, IEEE VMIC Proc., 258 (1989).
[4] S. Sacamitsu, S. Sumita, N. Fujino and T. Shirarwa, Japanese, J. Appl. Phys. **27**, L1819 (1988).
[5] S. Q. Hong, C. Comrie, S. W. Russell and J. W. Mayer, J. Apply. Phys. **70**, 3655 (1991).
[6] J. M. E. Harper, A. Charai, L. Stolt, F. M. d'Heurle and

P. M. Fryer, Appl. Phys. Lett. **56**, 2519 (1990).

[7] J. Li, J. W. Mayer, L. J. Matienzo and F. Emmi, Mater. Chem. Phys. **32**, 390 (1992).

[8] E. Kolawa, J. S. Chen, J. S. Reid, P. J. Pokela and M-A. Nicolet, J. Appl. Phys. **70**, 1369 (1991).

[9] E. Kolawa, J. S. Reid and J. S. Chen, *Sbmicron Metallization* (SPIE, Belligham, W. A., 1992), Vol. 1805, p. 11.

[10] J. S. Reid, X. Sun, E. Kolawa and M-A. Nicolet, *Ti-Si-N Diffusion Barriers between Silicion and Copper*, IEEE Electron Device Letters, submitted.

[11] J. S. Reid, E. Kolawa and M-A. Nicolet, Thin Solid Films **236**, 319 (1993).

[12] K. Holloway, P. M. Fryer, C. Cabral, Jr. J. M. E. Harper, P. J. Bailey and K. H. Kelleher, J. Appl. Phys. **71**, 5433 (1992).

Journal of the Korean Physical Society, Vol. 34, June 1999, pp. S510~S515

Effects of Microwave Power on the Deposition and the Properties of ECR-CVD Oxides

Moonsang KANG*

Department of Mechatronics, Induk Institute of Technology, Seoul 139-749

Yongseo KOO

Department of Electronic Engineering, Seokyeong Universiyy, Seoul 136-704

Chul AN

Department of Electronic Engineering, Sogang University, Seoul 121-742

The electrical and structural properties of SiO_2 films were investigated as a function of microwave power using electron cyclotron resonance (ECR) plasma chemical vapor deposition (CVD) method. The refractive index ranging from 1.45 to 1.48 was obtained. The presence of a stretching mode (1065 cm^{-1}), bending mode (812 cm^{-1}) and rocking mode (450 cm^{-1}) of Si-O bonds were observed. The oxygen to Si ratio was 1.88~2.12 throughout the films. Interface trap density (D_{it}) and flat-band voltage increased with increasing microwave power. From the capacitance-voltage characteristics, we may assume that the positive ions (O_2^+ or O^+) exist in the SiO_2 films and these positive ions increase with increasing microwave power. The interface trap density was 10^{10}~10^{11} $eV^{-1}cm^{-2}$. The best breakdown field and D_{it} value achieved in this study was 11.3 MV/cm and 1×10^{10} $eV^{-1}cm^{-2}$, which sets a new record for the lowest D_{it} in ECR plasma CVD oxides fabricated to date.

I. INTRODUCTION

The deposition of insulators at low-temperatures has applications in a number of semiconductor device technologies. For example, as secondary passivation layers, inter layer isolation and lithographic mask in integrated circuits and also as primary gate dielectrics for thin film transistor applications. At high-temperatures, potential problems such as dopant diffusion and redistribution, material interaction and thermally induced stress can seriously degrade device performance. Therefore, a high-quality oxide film grown at low-temperature is extremely desirable. Recently, the interest in electron cyclotron resonance (ECR) plasma chemical vapor deposition (CVD) for microelectronic fabrications [1–5] has increased. The attractive features of the ECR plasma CVD processing are as follows [4,5]: (a) It does not involve electrodes so that contamination due to sputtering of electrodes during plasma processing does not occur. (b) It yields a large degree of electrons and ions. (c) It can be performed for a wide range of process conditions and (d) plasma processing is a low-temperature process. Therefore, the ECR plasma method is expected to operate at low-temperature and a high deposition rate.

In order to obtain SiO_2 films using ECR plasma, two methods are generally used. The first is oxygen plasma [6–10] and the other [2,11,12] is deposition method. Chau and Kao [6] studied the fabrication of SiO_2 films in microwave oxygen plasmas as a function of gas pressure. They obtained a low value of interface trap density (D_{it}=9×10^{10} $eV^{-1}cm^{-2}$). Matsuoka and Tohno [7] fabricated various oxide films, including SiO_2, in an oxygen-argon gas atmosphere. Sung and Pang [8] studied the oxidation of Si in an oxygen plasma by a multipolar ECR source. They obtained a high quality oxide films with breakdown field strength 12 MV/cm and fixed charge density 3×10^{10} cm^{-2}. Carl *et al.* [9] studied the oxidation of Si in an ECR oxygen plasma. The average breakdown strength was about 7 MV/cm and fixed charge density was about 1×10^{11} cm^{-2}. Salbert *et al.* [10] also studied the oxide growth on Si using an ECR oxygen plasma. The average breakdown field was about 7.8 MV/cm and D_{it} was about 5×10^{11} $eV^{-1}cm^{-2}$. Machida *et al.* [2] studied the water-related hot-carrier degradation as a function of SiH_4/O_2 gas flow rate using deposition method. In our previous work [11] we studied the capacitance-voltage (C-V) characteristics of SiO_2 films as a function of SiH_4/O_2 ratio and microwave power using the ECR plasma deposition method. The positive ions (O_2^+ or O^+) exist in the SiO_2 films and these positive ions increase with increasing O_2 content or microwave power. The D_{it} was 10^{10}~10^{11} $eV^{-1}cm^{-2}$. Nguyen and Albaugh [12] also

*E-mail: mskang@induk-c.ac.kr

obtained SiO_2 films deposited by ECR CVD using SiH_4 and O_2 mixed gas. They studied only the physical and chemical properties of SiO_2 films deposited at room temperature.

While many physical and electrical properties of the SiO_2 films have been reported using oxygen plasma method [6–10], deposition method [2,11,12] have not been extensively studied. In particular, the characteristics of metal-oxide semiconductor (MOS) capacitors, fabricated by deposition method using SiH_4 and O_2 mixed gas, have not been studied. In our previous study [11], we described only the C-V characteristics. In this work, the physical and electrical parameters of the ECR plasma CVD produced SiO_2 films are studied as a function of microwave power including the C-V characteristics.

II. EXPERIMENTS

The purpose of ECR plasma is to increase the path of electrons in the plasma by applying a magnetic field, thus enhancing the probability of ionization. Resonance is achieved when the frequency at which energy is fed to an electron circulating in a magnetic field is equal to the characteristic frequency at which the electron circulates. This circulating motion increases the ratio of ionized to nonionized species in ECR plasma by three orders of magnitude over that in simple radio-frequency (RF) plasmas. The high efficiency in exciting the reactants in ECR plasma enables the deposition of films at room temperature without the need for thermal activation.

An Astex-1000 ECR plasma generator, a homemade CVD reactor (Fig. 1) and a high vacuum system were employed to carry out the experiments. Microwave power was supplied to a plasma chamber through a rectangular waveguide. The magnetic field for the ECR plasma excitation was applied perpendicularly to the substrate surface. The plasma stream was introduced into the deposition chamber in the direction of the substrate by this magnetic field. The system consisted of two chambers, the plasma chamber and the deposition chamber. The reactants were introduced through two separate inlets; oxygen molecules were introduced into the plasma chamber, while silane (SiH_4) was fed into the deposition chamber. Microwave power was introduced into the plasma chamber through a rectangular waveguide at a frequency of 2.45 GHz. The cylindrical plasma chamber operated as a microwave cavity resonator. The electron cyclotron frequency was controlled by magnetic coils arranged at the periphery of the chamber. At the above microwave frequency, resonance was achieved at a magnetic strength of 875 Gauss. Highly activated plasma was then obtained at very low gas pressures. Ions were extracted from the plasma chamber into the deposition chamber and subjected to a divergent magnetic field that spread the plasma stream over the entire wafer.

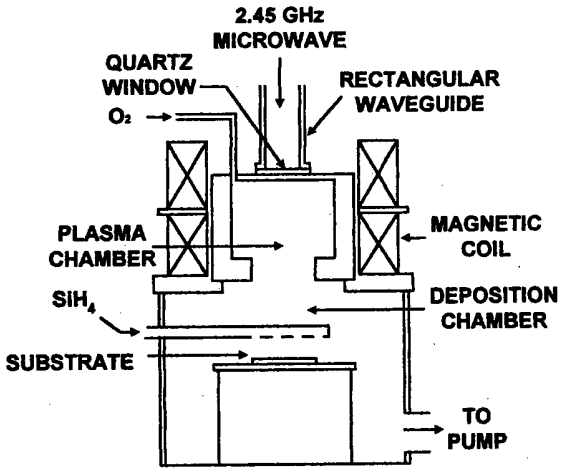

Fig. 1. Schematic diagram of ECR plasma CVD system.

The deposition conditions were as follows: the substrate temperature was 400 °C, pressure was 4.5 mTorr, distance from the substrate to the plasma chamber was 2 cm, total flow rate was 15 standard cubic centimeters per minute (sccm), O_2 content was 93 % (the ratio of SiH_4/O_2 was 1/14), and the microwave power was 200, 300, 400, 500 and 600 W. Boron doped (111) single-crystal Si wafers with a resistivity of 1-3 Ωcm were chemically cleaned. The native oxide on silicon was removed prior to deposition by dipping in dilute hydrofluoric (HF) acid, followed by de-ionized (DI) water rinse. The deposited oxide films were annealed at 600 °C in N_2 for 1 hour. The refractive index and deposition rate was measured using ellipsometry. The surface roughness was measured using atomic force microscopy (AFM). The structural properties of the SiO_2 films were studied by X-ray photoelectron spectroscopy (XPS), Auger and Fourier transform infrared (FT-IR) spectroscopy. The interface trap density was measured using the high-low frequency C-V characteristics method. The flat-band voltage, dielectric constant and current-voltage characteristics of SiO_2 films measurements were performed on MOS capacitors.

III. RESULT AND DISCUSSION

The refractive index ranging from 1.45 to 1.48 was obtained. From the FT-IR spectroscopy, the presence of a stretching mode (1065 cm^{-1}), bending mode (812 cm^{-1}) and rocking mode (450 cm^{-1}) of Si-O bonds were observed in silicon oxide films. The stoichiometry of the oxide films was studied using XPS measurements. Figure 2 shows XPS spectra of oxide film when the microwave power was 300 W. The oxygen to Si ratio was 1.99. Other samples were 1.88~2.12 throughout the films, indicating uniform SiO_2 stoichiometry identical to high-temperature thermal oxide. No impurities were detected

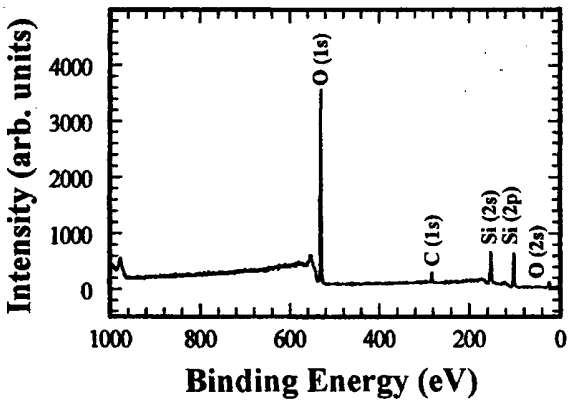

Fig. 2. XPS spectra of SiO_2 film.

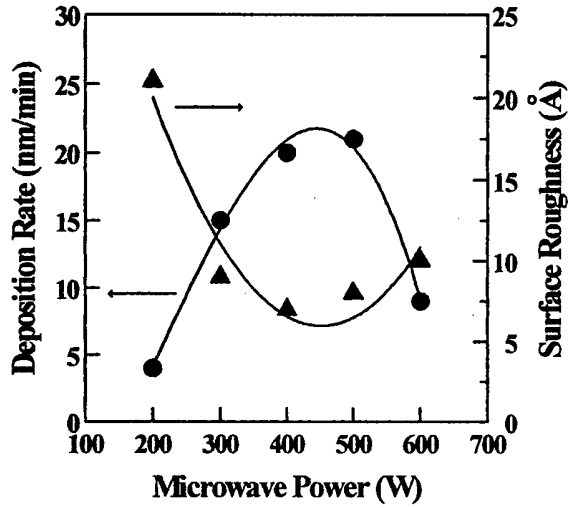

Fig. 3. Deposition rate and surface roughness as a function of microwave power.

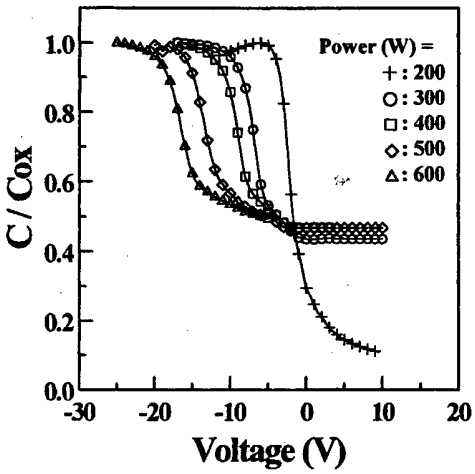

Fig. 4. Normalized capacitance as a function of gate bias with microwave power.

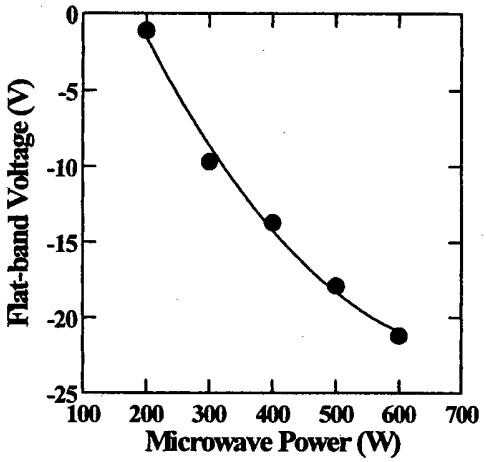

Fig. 5. Flat-band voltage as a function of microwave power.

using Auger analysis in the oxide films.

Figure 3 shows the deposition rate and surface roughness of the oxide films as a function of the microwave power. The deposition rate increase, reaches a maximum at 500 W, and then decrease. The increase in the deposition rate with microwave power depends on the increase of reactive radicals [8]. It is assumed that the reactive radicals increased with increasing microwave power. Due to these reasons, the deposition rate increased with increasing microwave powers. However, high microwave power (at 600 W) is expected to generate very many oxygen ions (O_2^+ or O^+) with high kinetic energy in the deposition chamber. Therefore, much ion flux with high kinetic energy reach the substrate and then impact the film surface. Consequently, the deposition rate was low due to surface etching at 600 W. The surface roughness decreased with increasing the microwave power (from 200 to 500 W) due to adequate surface etching. At 600 W, the surface roughness was increased a little because many positive ions did damage to the film surface. The surface roughness was low at 400 W because of the adequate surface etching.

Fig. 4 shows normalized capacitance as a function of gate bias with microwave power. The C-V curves are normalized to the maximum value of the oxide capacitance (C_{ox}). The measurement frequency was 1 MHz. The C-V curves of Fig. 4 are shifted along the voltage axis. That is, the absolute values of the flat-band voltage increase with increasing microwave power (Fig. 5). The flat-band voltage shift was large, which is not normally observed in the thermally grown oxide films. The flat-band voltage shift toward the negative gate voltage, indicating that there are positive ions accumulated in the bulk of the oxide. In order to find out the positive ions, which affect the shift of flat-band voltage, Auger analysis was used. As the result of Auger analysis, such impurities as Na^+ are not detected.

Figure 6 shows the interface trap density and dielectric constant as a function of microwave power. The D_{it}

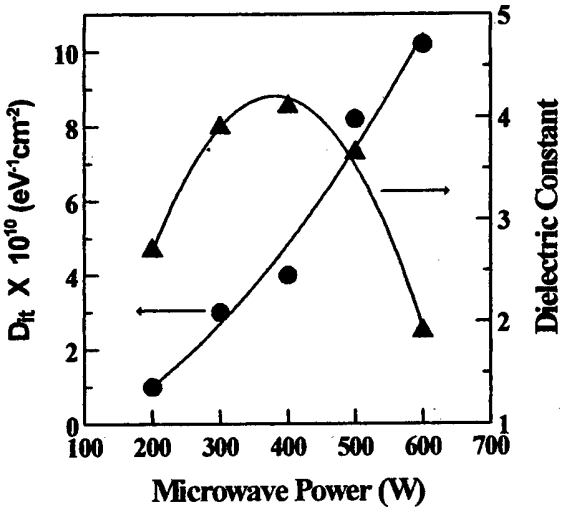

Fig. 6. Interface trap density and dielectric constant as a function of microwave power.

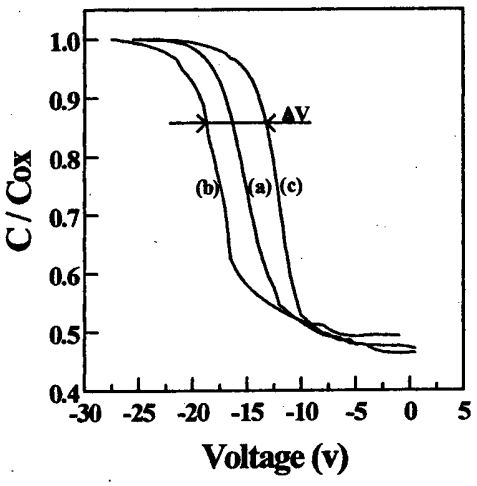

Fig. 7. C-V characteristics (a) initial (b) after 30 min, 180 °C, V_g = +5 V (c) after 30 min, 180 °C, V_g = −5 V.

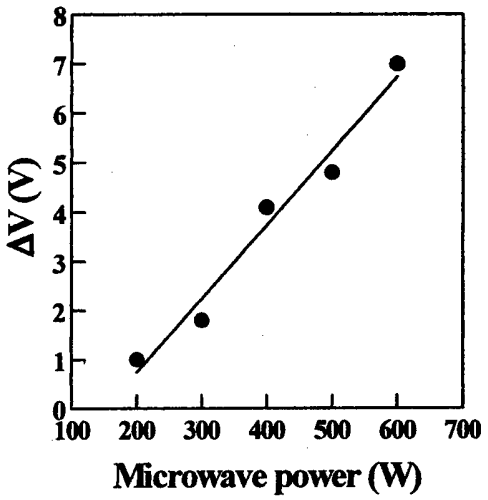

Fig. 8. ΔV versus microwave power.

was obtained high frequency (1 MHz) and low frequency (10 Hz) C-V characteristics of the MOS capacitor. The D_{it} and dielectric constant value was found to be in the range of 10^{10}~10^{11} $eV^{-1}cm^{-2}$ and 2~4. These D_{it} values are comparable to thermally grown oxides at high-temperatures. The D_{it} increased with increasing microwave power. From figures 5 and 6, the flat-band voltage shift was large, which is not observed in low value of D_{it}. From these results, we may suppose [11] the positive ions (O_2^+ or O^+) accumulated in the bulk of the oxide. These shifts are due to the migration of positive oxygen ions through the oxide layer. From these reasons, the flat-band voltages are increased with increasing microwave power due to increase positive oxygen ions in the plasma. Carl *et al.* [9] and Kimura *et al.* [13] reported that highly exited O and O_2^+ exist in the plasma. Dzioba *et al.* [14] also observed not only O and O_2^+ but also O^+. However, they did not consider the positive ions in the bulk of the oxide films. They considered only plasma region. Chau *et al.* [6] already reported that the emission intensities of the O_2^+ increase with increasing input power and the positive or negative ions existed in the bulk of the oxide. They said that these results may be caused the noncomplete bonding due to the lattice mismatching or electrons trapped at the interface. An increase in the microwave power may result in an increase in O_2^+ or O^+ ions in the deposition chamber. Therefore, the energetic ion flux reaching substrates may also be increased with increasing microwave power. Consequently, the impingement of the positive ions (O_2^+ or O^+) increased with increasing microwave power on the film surface. Due to these reasons, the D_{it} increased (Fig. 6) with increasing microwave power.

In order to find out the flat-band voltage shift, we studied the C-V characteristics before and after bias-temperature stress. Fig. 7, ΔV is defined. The C-V characteristics observed initially are marked by (a), while those observed after 30 min at 180 °C, with V_g (gate voltage) = +5 V, are marked by (b). Mark (c) denotes the C-V curve after 30 min at 180 °C with V_g = −5 V applied. We define the difference between (b) and (c) as ΔV. Fig. 8 shows plot of ΔV versus microwave power. ΔV increased with increasing microwave power. From figures 7 and 8, the positive ions are accumulated in the bulk of the oxide. Matsuo *et al.* [15] reported that the negative potential generated by the divergent magnetic field as a function of the distance from the plasma extraction window. The negative potential increases with decreasing the magnetic field intensity. The energy of the ion is about 20 eV at the position of the substrate. Friedel *et al.* [16] also reported that the positive ions create over 12 eV in an oxygen plasma. Chau *et al.* [6] reported that the emission intensities of the O_2^+ increase with increasing input power at 10 mTorr. No neutral

oxygen molecular emission has been detected at a high input power. From these reports, it is supposed that the many positive ions (O_2^+ or O^+) created in the plasma region and then the positive ions accelerated to the substrate due to the negative potential. An increasing of microwave power may result an increasing of O_2^+ or O^+ ions in the deposition chamber. Therefore the energetic ion flux reaching substrates may also be increased with increasing microwave power. Consequently, the O_2^+ or O^+ ions are injected the oxide films. From these reasons, it is supposed that the O_2^+ or O^+ ions increase with increasing microwave power in the bulk of the oxide films. The flat-band voltage shift of the dependence of microwave power is supposed to be originated from a accumulation of positive ions in the bulk of oxide films due to the O_2^+ or O^+ ions. The low ion energy is important to avoid positive ions in the oxide films so that high quality oxide can be obtained. We can not determine which effect is most dominant for flat-band voltage shift and which deposition conditions get rid of these positive ions in the bulk of oxide. Further studies are required about

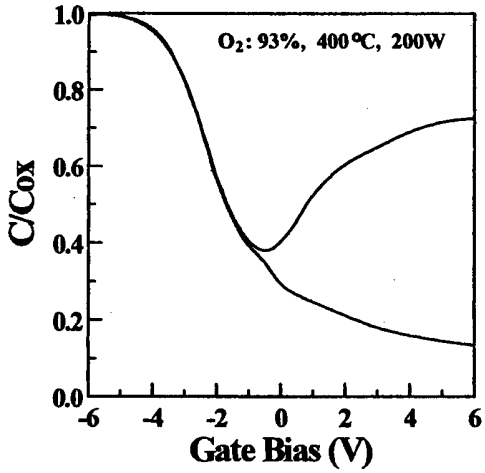

Fig. 9. The measured high/low frequency for MOS capacitor.

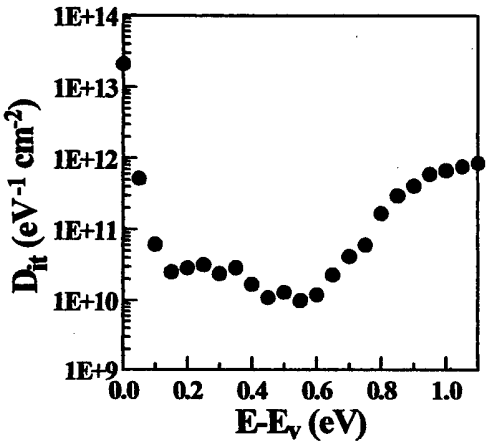

Fig. 10. D_{it} versus $E - E_v$.

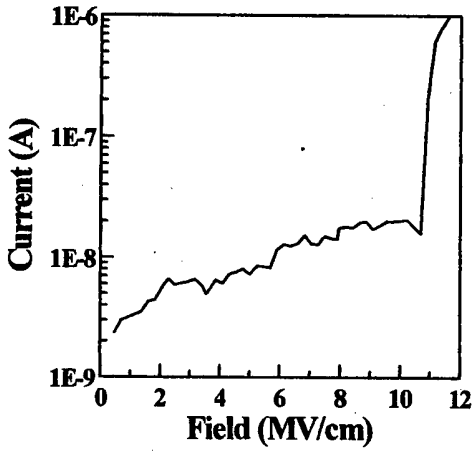

Fig. 11. Current voltage characteristics of SiO_2 film.

flat-band voltage shift and optimal deposition conditions.

Figure 9 shows the best high-frequency (1 MHz) and low-frequency (10 Hz) C-V characteristics measured in this study on a MOS capacitor. The D_{it} spectrum calculated from the high-low frequency curves of Fig. 9 is shown in Fig. 10, which shows a minimum D_{it} value of 1×10^{10} $eV^{-1}cm^{-2}$ around the midgap. This value is comparable to thermally grown oxides at high-temperatures. A low D_{it} value of 1.1×10^{10} $eV^{-1}cm^{-2}$ was reported by Chen *et al.* [17]. Their investigation, direct plasma-enhanced (PE) CVD in conjunction with a photo-assisted anneal was used to achieve low D_{it} in MOS capacitor. They used p-type (100) silicon wafers. In comparison with our study, we obtained a lower value of D_{it} than Chen *et al.* because we used (111) Si wafers in this study.

Figure 11 shows the best current-voltage characteristics of SiO_2 films deposited at 200 W. The breakdown field is defined as the electric field that will introduce 1 μA leakage current across the MOS capacitor. The breakdown field was about 11.3 MV/cm. The breakdown field for this oxide film is comparable to thermally grown oxide at high-temperature.

IV. CONCLUSIONS

The electrical and structural properties of SiO_2 films were investigated as a function of microwave power. The films were deposited by ECR plasma CVD method. The refractive index ranging from 1.45 to 1.48 was obtained. From the FT-IR spectroscopy, the presence of a stretching mode (1065 cm^{-1}), bending mode (812 cm^{-1}) and rocking mode (450 cm^{-1}) of Si-O bonds were observed in silicon oxide films. The oxygen to Si ratio was 1.88~2.12 throughout the films. Interface trap density and flat-band voltage increased with increasing microwave power. The interface trap density was 10^{10}~10^{11} $eV^{-1}cm^{-2}$. From the C-V characteristics before and af-

ter bias-temperature stress, there are positive ions accumulated in the bulk of the oxide. The existence of positive ions in the SiO_2 films is highlighted in this study. The positive ions increase with increasing microwave power and the interface trap density increase with increasing the positive ions. In the deposition chamber, many positive ions with high kinetic energy impact and damage to the film surface. And then, some of these positive ions drive in the SiO_2 films. In order to obtain high quality SiO_2 films, the kinetic energy of the positive ions is reduced. That is, the ECR plasma CVD oxide is deposited at low microwave power. The best breakdown field and D_{it} value achieved in this study was 11.3 MV/cm and 1×10^{10} $eV^{-1}cm^{-2}$. This sets a new record for the lowest D_{it} in ECR plasma CVD oxides fabricated to date.

ACKNOWLEDGMENTS

The authors wish to thank Dr. T. H. Lim, Dr. I. H. Oh and Dr. B. J. Jeon for their support during this work.

REFERENCES

[1] J. W. Lee, N. I. Lee, J. I. Han and C. H. Han, IEEE Trans. Electron Device Lett. **18**, 172 (1997).

[2] K. Machida, N. Shimoyama, J. Takahashi, Y. Takahashi, N. Yabumoto and E. Ari, IEEE Trans. Electron Devices **41**, 709 (1994).

[3] C. S. Pai, J. F. Miner and P. D. Foo, J. Appl. Phys. **73**, 3531 (1993).

[4] M. Kang, J. Kim, T. Lim, I. Oh, B. Jeon, I. Jung and C. An, Jpn. J. Appl. Phys. **36**, L986 (1997).

[5] M. Kang, J. Kim, Y. Koo, T. Lim, I. Oh, B. Jeon, I. Jung and C. An, Materials Chem. & Phys. **51**, 152 (1997).

[6] T. T. Chau and K. C. Kao, J. Vac. Sci. & Technol. **B4**, 527 (1996).

[7] M. Matsuoka and S. Tohno, J. Vac. Sci. & Technol. **A13**, 2427 (1995).

[8] K. T. Sung and S. W. Pang, J. Vac. Sci. & Technol. **B10**, 2211 (1992).

[9] D. A. Carl, D. W. Hess and M. A. Lieberman, J. Vac. Sci. & Technol. **A8**, 2924 (1990).

[10] G. T. Salbert, D. K. Reinhard and J. Asmussen, Vac. Sci. & Technol. **A8**, 2919 (1990).

[11] M. Kang, Y. Koo and C. An, Jpn. J. Appl. Phys. **37**, L1244 (1998).

[12] S. V. Nguyen and K. Albaugh, J. Electrochem. Soc. **136**, 2835 (1989).

[13] S. Kimura, E. Murakami, K. Miyoshi, T. Warabisako, H. Sunami and T. Tokuyama, J. Electrochem. Soc. **132**, 1460 (1985).

[14] S. Dzioba, G. Este and H. M. Naguib, J. Electrochem. Soc. **129**, 2537 (1982).

[15] S. Matsuo and M. Kiuchi, Jpn. J. Appl. Phys. **22**, L210 (1983).

[16] P. Friedel and S. Gourrier, J. Phys. & Chem. Solids **44**, 353 (1983).

[17] Z. Chen, K. Yasutake A. Doolittle and A. Rohatgi, Appl. Phys. Lett. **63**, 2117 (1993).

Journal of the Korean Physical Society, Vol. 34, June 1999, pp. S516~S520

Fabrication and Characterization of the Ultra Shallow Junction Diode with Cobalt Silicide Contact

Gee Keun CHANG and Ho Jung CHANG

Department of Electronics Engineering, Dankook University, Chenan 330-714

Woo Yong OHM

Department of Electronics, Inha Technical Junior College, Incheon 402-752

The Co–silicides were formed from Co(200 Å)/Ti(100 Å) bilayer on the BF_2^+ ion implanted Si substrates by the rapid thermal annealing process and evaluated in terms of the sheet resistances, the cross-sectional morphologies, the crystallinites and the atomic species distributions. The stable $CoSi_2$ crystal phases were obtained at the annealing temperature of 700 °C for 20 seconds and the sheet resistances were decreased from 48.5 Ω/□ to 4.7 Ω/□ according to the increase of the annealing temperature from 600 °C to 800 °C. In the fabrication of the p^+-n shallow junction diodes, the Co(120 Å)/Ti(40 Å) bilayer was used to reduce the silicide thickness up to 500 Å. From the SIMS analysis results, we found that the emitter junction depth including silicide layer was about 0.14 μm. The p^+-Si/silicide/Al structure exhibited the Kelvin resistance of 1.2 Ω through the contact area of 10×10 μm^2 and the specific contact resistance of 1.2×10^{-6} Ω·cm^2. The application of Co/Ti bilayer silicide contact on the p^+-n ultra shallow junction resulted in the improvement of ideality factor as well as the reduction of source-drain sheet resistance and specific contact resistance.

I. INTRODUCTION

With continued scaling to the submicron dimension in the metal-oxide-semiconductor (MOS) devices, ultra shallow junctions with junction depth of $x_j \leq 0.15$ μm have been studied tremendously [1,2]. In order to achieve the high performance device, it is necessary to develop optimum process resulting in a low ohmic contact and low sheet resistance in the source-drain region with good thermal stability.

As the design rules are becoming strict in the MOS devices, the parasitic resistance in the source-drain region, the resistance of interconnection line and the contact resistance between metal and semiconductor may interrupt with the stable operation of VLSI devices [3,4].

Salicide(self-aligned silicide) [5–7] is known to the promising technique to form ultra shallow junction by metal-silicon reaction and adopted for the shallow junction technology to reduce the sheet resistance of the source-drain region with contact reliability.

Among various metal silicides, $TiSi_2$ and $CoSi_2$ seems to be more promising materials because of their low resistivity and good thermal stability [8–12]. In addition, $CoSi_2$ has desirable properties like lattice matching with Si and suppression of metal-dopant compound formation, reducing the risk of reaction with oxide films. It is generally recognized that the silicide formation depends on the reaction conditions such as metal thickness, annealing temperature and ambient atmosphere. However, some major problems such as silicon consumption during metal/silicon reaction, dopant redistribution and evaporation in the silicide are limited to the widespread applications [13,14].

In this paper, the ultra shallow junction diodes with cobalt silicide contact were prepared by Salicide technology using Co/Ti bilayer and the crystallinities of Co-silicides, the dopant profiles and electrical properties of the diodes were investigated in view of possible applications in the semiconductor devices.

II. EXPERIMENTAL PROCEDURE

1. Formation of $CoSi_2$

Co-silicides were formed on the BF_2^+ ion-implanted substrate and evaluated the crystalline and electrical properties as well as the cross-sectional morphologies and the atomic species distributions.

Phosphorous ions were implanted with the dose of 3.4×10^{13} cm^{-2} at 150 keV on the p-type (100) Si wafers with resistivity of 1~10 Ω·cm to form n-well region. After the drive-in process at 1150 °C for 3 hours, the source-drain region was formed by implanting BF_2^+ with the dose of 5×10^{15} cm^{-2} at 30 keV. For the formation of Co-silicide, the Co/Ti (thickness:200 Å/100 Å) bilayers were

deposited by the E-beam evaporation at the base pressure of 4×10^{-6} Torr. The silicidation was accomplished by the rapid thermal annealing (RTA) in N_2 ambient at the temperatures ranging from 600 °C to 850 °C for 20 seconds. The unreacted metals on the silicidation process were removed by selective etching in the solutions of $HCl:H_2O_2$=3:1 and $NH_4OH:H_2O_2:H_2O$=1:1:5. To investigate the thermal stability for the silicides, the as-formed layers were post-annealed at 850 °C~1000 °C for 30 minutes in the furnace under N_2 ambient.

2. Formation of the Junction Diodes

The p^+-n ultra shallow junction diodes with $CoSi_2$ contact were fabricated by the implantation of BF_2^+ on the n-well and the silicidation of Co(120 Å)/Ti(40 Å) bilayer films to make the shallow junction with the depth of below 0.15 μm. After the BF_2 ion implantation on the n-well, a SiO_2 layer with the thickness of 4500 Å was formed by chemical vapor deposition (CVD). The Si mesa etching was performed to form the base contact region and oxidation was followed at 800 °C for 30 minutes under wet O_2 ambient. Subsequently, the CVD oxide layer on the emitter window was removed for the opening of the silicided area. The Co/Ti bilayer was deposited on the substrate and the silicidation was accomplished at 800 °C for 20 seconds by the RTA process. The unreacted Ti and Co were removed in the selective etching solutions as mentioned above 1. Finally, aluminum was deposited on the opened contact windows to form junction electrodes. The fabrication flow chart of the p^+-n shallow junction diode was shown in Fig. 1. Fig. 2 shows the cross-sectional view of the fabricated diode.

The sheet resistances were measured by four point probe method. The crystal phases of Co-silicides were studied by X-ray diffraction (XRD) analysis. The cross-sectional views of the silicides layers were investigated by transmission electron microscopy (TEM). Auger electron microscopy (AES) and secondary ion mass spectroscopy (SIMS) were used to measure the dopant profiles. The specific contact resistance and the current-voltage characteristics of the fabricated diode were measured by the Kelvin test resistor and the HP4145B semiconductor parameter analyzer.

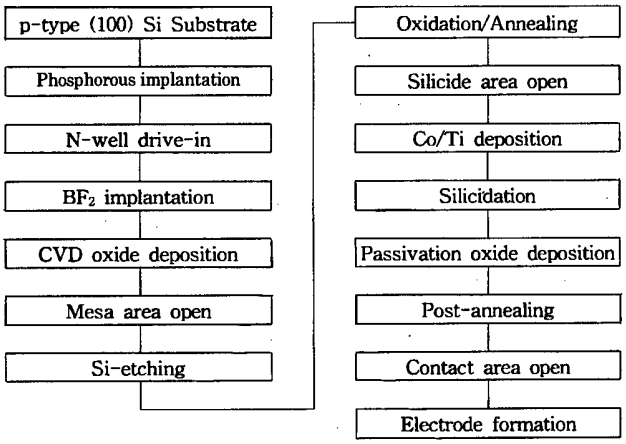

Fig. 1. Flow chart of the diode fabrication.

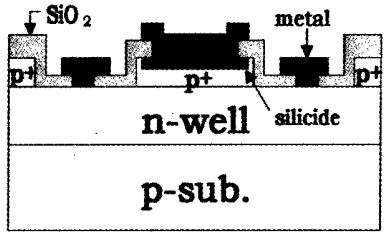

Fig. 2. Cross-sectional view of the fabricated diode.

III. RESULTS AND DISCUSSION

As the preliminary experiments before the diode fabrication, we investigted the crystalline and electrical properties of the Co-silicides obtained from Co(200 Å)/Ti(100 Å) bilayer to find out the optimum silicidation condition.

Fig. 3 shows the X-ray diffraction patterns of the Co/Ti bilayer silicides annealed at the temperatures of 600 °C, 700 °C, 800 °C and 850 °C in N_2 ambient. The XRD analysis showed that stable $CoSi_2$ crystal phases were obtained at the annealing temperatures of above 700 °C with higher peaks according to the increase of the annealing temperature. At 600 °C, there was no crystalline phases showing amorphous phase due to the low anneal-

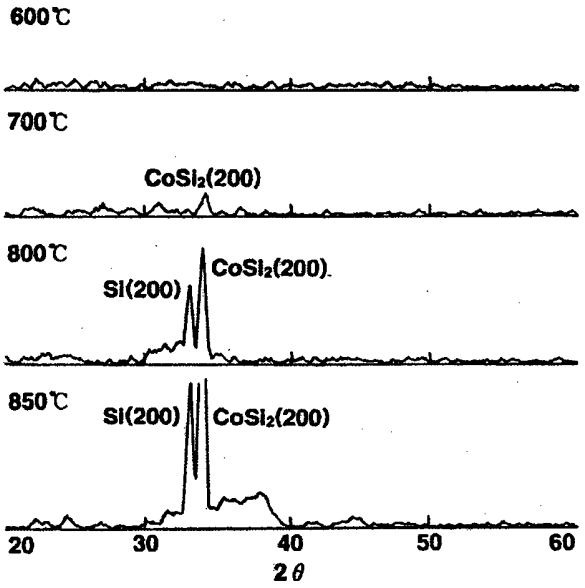

Fig. 3. XRD patterns of the Co(200 Å)/Ti(100 Å) bilayer silicides annealed at 600 °C, 700 °C, 800 °C and 850 °C for 20 seconds in N_2 ambient.

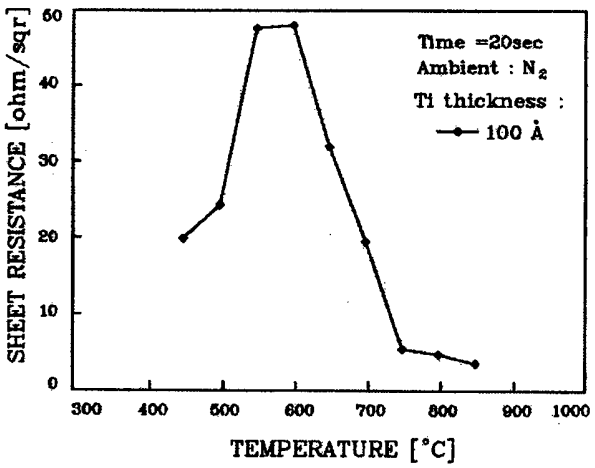

Fig. 4. The change of the sheet resistances for Co/Ti bilayer silicides as a function of the RTA annealing temperatures.

ing temperature. It has been known that Co atoms with high diffusion coefficient are reversed with Ti atoms in position during silicidation process and Ti atoms makes the Si surface clean by removing the native oxide [15,16].

Fig. 4 shows the change of the sheet resistances for the Co/Ti bilayer silicides as a function of RTA annealing temperature. The sheet resistances were decreased from 48.5 Ω/□ to 4.7 Ω/□ as the annealing temperature were increased from 600 °C to 800 °C. The large sheet resistances at the temperature below 700 °C may be ascribed to the amorphous phases as shown in Fig. 3.

Fig. 5 shows the cross-sectional TEM micrographs (a) before and (b) after the silicidation of Co/Ti bilayer at 800 °C for 20 seconds. The thickness of the silicided film was about 600 Å and the boundary of silicide/Si interface was very flat.

To investigate the atomic species of the silicided region, the AES analysis was performed. The AES depth profiles before and after the silicidation of Co/Ti bilayer

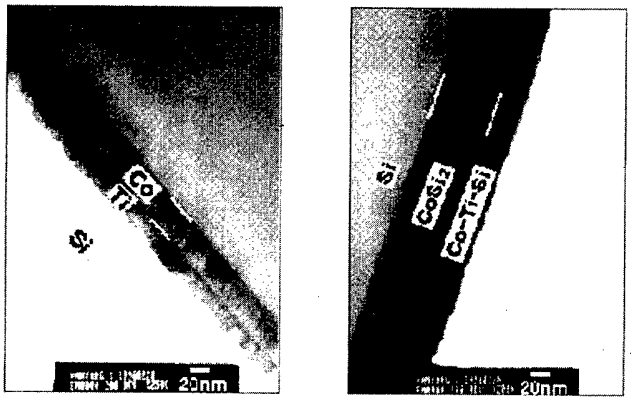

(a) (b)

Fig. 5. Cross-sectional TEM micrographs (a) before and (b) after the silicidation of Co/Ti bilayer at 800 °C for 20 seconds.

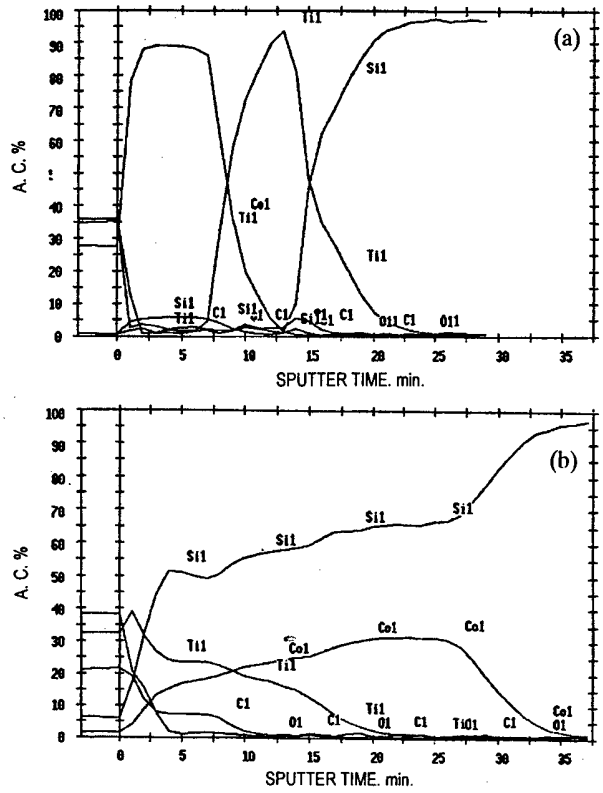

Fig. 6. AES depth profiles (a) before and (b) after the silicidation of Co/Ti bilayer at 800 °C for 20 seconds.

were shown in Fig. 6. The Co-Ti-Si compounds appeared at the surface region of the silicided film, while Co-Si atoms were only distributed between surface region and Si substrate. This explains that the silicide obtained from Co/Ti bilayer is a pure Co-silicide ($CoSi_2$) on the Si-silicide interface. In the Co/Ti bilayer before silicidation, atomic species were discriminated clearly at the interfaces without any interaction of layers as shown in Fig. 6(a). The as-formed silicide films were post-annealed at the high temperatures ranging from 850 °C to 1000 °C to investigate the thermal instabilty.

Fig. 7 shows the sheet resistances changes of the post-annealed silicide films accoring to the various annealing conditions. There was no significant change in the sheet resistances for the silicided films after the high temperature annealing at 850 °C and 900 °C for 30 minutes. On the other hand, the sheet resistance was increased within 5 % in the post-annealed sample at 1000 °C for 30 minutes. From these results, it may be concluded that the Co/Ti bilayer silicides fabricated in this process have a good thermal stability. For the application of shallow junction diodes with the junction depth below 0.15 μm, Co(120 Å)/Ti(40 Å) bilayer film was used to reduce the silicide thickness up to 500 Å.

After the silicidation and post-annealing, the silicide layers were removed off by BOE solution to mesure the junction depth and investigate the boron concentration

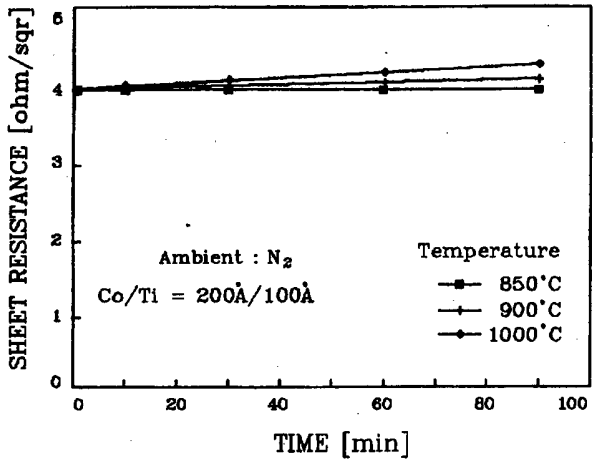

Fig. 7. The sheet resistance changes of the post-annealed silicide films accoring to the various annealing conditions.

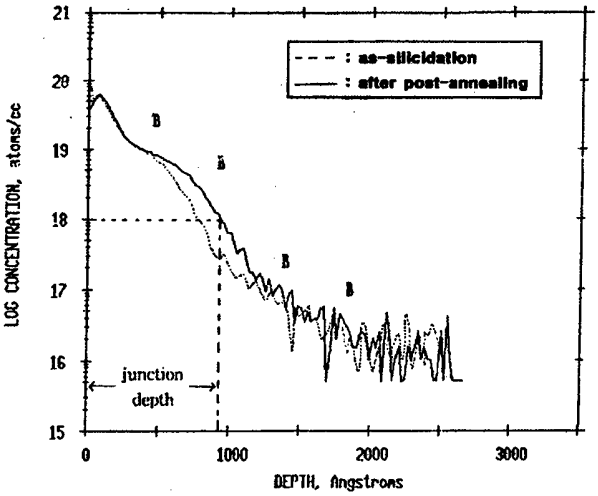

Fig. 8. SIMS boron depth profiles after removing the silicide layers.

at the silicide/silicon interface. The SIMS boron depth profiles after removing silicide layers are shown in Fig. 8. The boron concentration at the surface was about 6×10^{19} cm^{-3} and the junction depth was about 0.09 μm at the boron concentration of 1×10^{18} cm^{-3} in the n-well region. From these profiles, we found that the emitter junction depth including the silicide layer of 500 Å was about 0.14 μm.

Fig. 9 shows the cross-sectional TEM micrograph of the silicided film in the junction diode. From TEM micrograph, the thickness of silicide was about 500 Å showing the interfacial roughness of about 20 %.

Fig. 10 shows the sheet resistances measured at various process steps in the diode fabrication. The sheet resistances of the as-implanted and the pre-annealed samples were about 230 Ω/□ and 175 Ω/□, respectively. When the sample was silicided, the sheet resistance was greatly decreased to about 7.9 Ω/□. There was no distinct change in the sheet resistance after the post-annealing at 850 °C for 30 minutes. It is considered that this good thermal stability may be related to the epitaxial growth of the Co-silicide films.

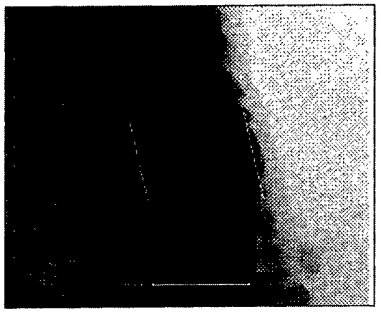

Fig. 9. Cross-sectional TEM micrographs of the silicided films in the junction diode.

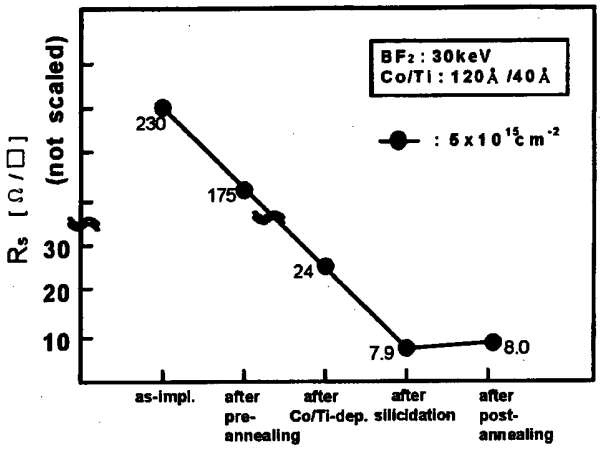

Fig. 10. The sheet resistances measured at various process steps in the diode fabrication.

Fig. 11 shows I-V characteristic curves of the fabricated diodes (a) with silicide layer and (b) without silicide layer in the conventional diode. The diode with silicide layer exhibited the ideality factor of 1.06 and the leakage current of 8.6 μA/cm^2 under the reverse bias of 3 V. In addition, p$^+$-Si/silicide/Al structure showed the Kelvin resistance of 1.2 Ω through the contact area of 10×10 μm^2 and the specific contact resistance of 1.2×10^{-6} Ω · cm^2. On the other hand, the conventional p$^+$-n diode exhibited the ideality factor of 1.23, the specific contact resistance of 1.0×10^{-5} Ω · cm^2 and the leakage current of 5.0 μA/cm^2 at the reverse bias of 3 V. The application of Co/Ti bilayer silicide resulted in the improvement of the ideality factor as well as the reduction of emitter sheet resistance and the specific contact resistance, while it led to a little increase of the leakage current.

The increase of the leakage current may be caused by the surface defects due to the mesa structure and the poor quality of protective oxide layer. It is expected that the

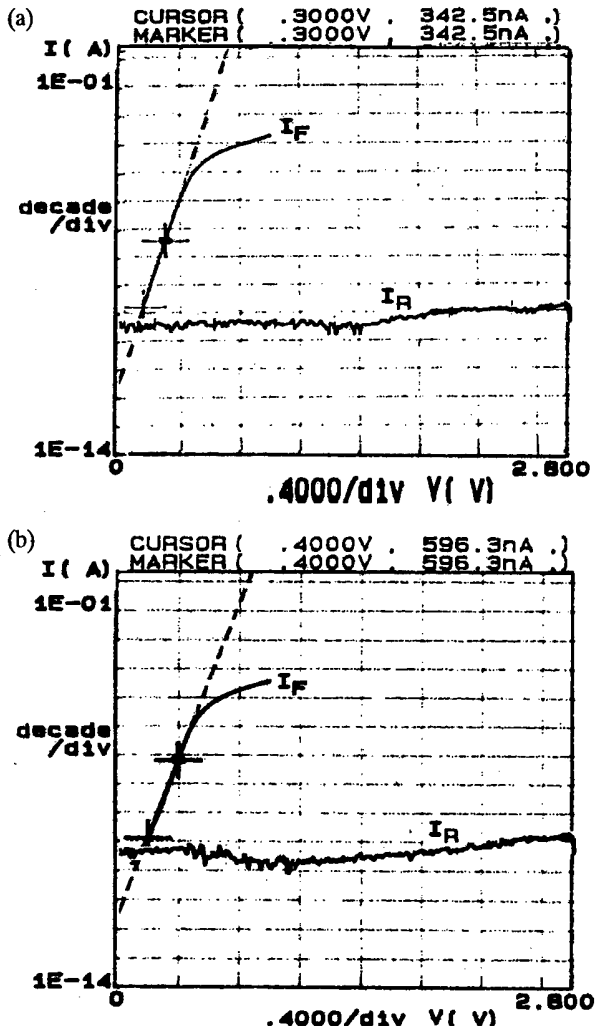

Fig. 11. I-V characteristics of the fabricated diodes (a) with silicide layer and (b) without silicide layer in the conventional diode.

leakage current of the silicided diodes can be minimized if the device has the planar structure and the thermal oxide as the passivation layer.

IV. CONCLUSIONS

Co-silicides were formed on the BF_2^+ ion-implanted substrate by RTA process and evaluated in terms of the sheet resistances, the cross-sectional morphologies, the crystallinities and the atomic species distributions. The stable $CoSi_2$ crystal phases were obtained at the RTA annealing temperature of 700 °C for 20 seconds and the sheet resistances were decreased from 48.5 Ω/□ to 4.7 Ω/□ as the annealing temperatures were increased from 600 °C to 800 °C. In the diode structure, the thickness of silicide layer was about 500 Å showing the interfacial roughness of about 20 %. From the SIMS boron profiles, we found that the emitter junction depth including silicide layer was about 0.14 μm. The diode with silicide layer exhibited the ideality factor of 1.06 and the leakage current of 8.6 $\mu A/cm^2$ under the reverse bias of 3 V. The p^+-Si/silicide/Al structure exhibited the Kelvin resistance of 1.2 Ω through the contact area of 10×10 μm^2 and the specific contact resistance of 1.2×10^{-6} $\Omega \cdot cm^2$. The application of Co/Ti bilayer silicide resulted in the improvement of the ideality factor as well as the reduction of the emitter sheet resistance and the specific contact resistance.

REFERENCES

[1] C. M. Osburn, J. Electron Materials **19**, 67 (1990).
[2] S. Wolf, Silicon Processing for the VLSI Era, V. 2-Process Integration, Lattice Press 154 (1990).
[3] J. Amano, K. Nauka, M. P. Scott, J. E. Turner and R. Tsai, Appl. Phys. Lett. **49**, 737 (1986).
[4] S. M. Sze, VLSI Technology, McGraw-Hill, 397 (1988).
[5] C. Y. Ting, S. S. Iyer, C. M. Osburn, G. J. Hu and A. M. Schweighard, Proc. Electrochem. Soc. Meeting **82-2**, 224 (1982).
[6] C. K. Lau, Y. C. See, D. B. Scott, J. M. Bridges, S. M. Perna and R. D. Davies, IEDM Tech. Dig. 714 (1982).
[7] A. E. Morgan, E. K. Broadbeut, M. Delfino, B. Coulman and D. K. Sadana, J. Electrochem. Soc. **134**, 925 (1987).
[8] M. Tabaskky, E. S. Bulat, B. M. Pitchek, M. A. Sullivan and S. C. Shatas, IEEE Trans. Electron Devices **34**, 548 (1987).
[9] S. P. Murarka, D. B. Fraser, A. K. Sinha, H. J. Levinstein, E. J. Lloyd, R. Liu, D. S. Williams and S. J. Hillenius, IEEE Trans. Electron. Devices **34**, 2108 (1987).
[10] P. Ruterana, P. Houdy and P. Boher, J. Appl. Phys. **68**, 1033 (1990).
[11] J. M. Phillips, J. L. Bastone, J. C. Hensel, I. Yu and M. Cerullo, J. Mater. Res. **5**, 1032 (1990).
[12] J. M. Gibson, J. L. Vastone and R. T. Tung, Appl. Phys. Lett. **51**, 45 (1987).
[13] C. Y. Ting, F. M. dHeurle, S. S. Lyer and P. M. Fryer, J. Electrochem. Soc.: Solid-State Science and Technology **133**, 2621 (1986).
[14] S. P. Murarka, *Silicides for VLSI Applications* (Academic Press, New York, 1983), p. 164.
[15] S. L. Hsia, T. Y. Tan, P. Smith and G. E. McGuire, J. Appl. Phys. **72**, 1864 (1992).
[16] S. L. Hsia, T. Y. Tan, P. Smith and G. E. McGuire, J. Appl. Phys. **70**, 7579 (1991).

Journal of the Korean Physical Society, Vol. 34, June 1999, pp. S521~S525

Effects of Attractive Potential between Ultra-Low Energy Boron and Silicons and Boron Diffusion in the Beginning of Annealing : Molecular Dynamics Study

Jeong-Won KANG, Eu-Suk KANG and Ho-Jung HWANG

Semiconductor Process & Device Laboratory, Department of Electronic Engineering, Chung-Ang University, Seoul 156-756

We have investigated effects of attractive potential between ultra-low energy boron and silicons using molecular dynamics simulation. For B-Si, we use the Stillinger-Weber (SW)-type interatomic potential. For strong repulsive interaction at short interatomic distance, we use the Ziegler, Biersack, and Littmark (ZBL) potential with the repulsive part of the term being splined to SW-type B-Si potential. Molecular dynamics simulation using proposed potential revealed more scattering angles than that using ZBL, since collision time using proposed potential was longer than that using ZBL. Because thin films by low energy ion beams have been important to fabricate gigantic-scale-integragted (GSI) devices, molecular dynamics study about ion beam processes should include attractive potential. At 1000 K $\sim$ 1300 K, calculated diffusivities nearly were 10^{-7} cm^2/s and *Arrhenius* relationship with temperature. In the beginning of annealing, boron diffusivities were very high, since the damages formed by ion implant were rapidly dissolved, many Si interstitials are generated, and borons are swiftly diffused.

I. INTRODUCTION

There have been a lot of studies on ion implantation which is important in semiconductor processes, because shallow junction for advanced semiconductor devices are nowadays fabricated by ion implant. It is predicted that MOS devices will have 50 nm channel length and 20 nm junction depth in 2012. Thus, the molecular dynamics (MD) method is well-suited for studying the collision cascades and the mechanisms of damage production both in bulk and close to the surface, and has been extensively applied in studies of ion-beam [1–9]. In classical MD, the quality of results obtained by simulations depends on the quality of the model potential used. For the dopant ion implant simulation, Ziegler, Biersack, and Littmark (ZBL) universal screening Coulomb repulsive potential [10] has been widely used in describing interactions between ion and target atoms.

As the device dimensions shrink, the importance of ultra-low energy ion beams is being increased. At the low range of impact energies, Hanson *et al.* investigated that a screened Coulomb potential was not necessary to describe the steep repulsive interaction at small separations [11]. Most of the simulations considering attractive potential and repulsive potential have been the cases of self atom primary kick-on atom (PKA) simulation [12–14], but the earlier works of dopant implant did not consider attractive interatomic potential energy [5,8,12]. At ultra-low energy ion beams processes, however, collision cascades can be sensitively dependent on the attractive potential.

In this paper, we propose the interatomic potential between boron and silicon and perform the molecular dynamics simulation. Differences between results of proposed potential and results of ZBL repulsive potential are compared. We also calculate boron diffusivities in the beginning of annealing.

II. INTERATOMIC POTENTIAL MODEL AND MOLECULAR DYNAMICS

For Si-Si, we use well-tested Stillinger-Weber (SW) potential [15] with spline data by Gartner *et al.* [16] We simulate ultra-low energy boron ion implantation considering B-Si attractive potential, and compared results using proposed potential with results using ZBL. Interaction between boron and silicon is approximated to two-body term. For B-Si, we use the Stillinger-Weber-type interatomic potential from Ref. 17. For strong repulsive interaction at short interatomic distance, we use the ZBL potential with the repulsive part of the term being splined to SW-type B-Si potential, since repulsive term of SW-type interatomic potential is bad at short distance. Interatomic potentials in this paper is defined as

$$f_2(r) = \begin{cases} V_{ZBL}, & r < r_1 \\ \alpha + \beta r + \gamma r^2 + \delta r^3, & r_1 \le r < r_2 \\ A(B(\frac{r}{\sigma})^p - (\frac{r}{\sigma})^q)\exp(\frac{r}{\sigma} - a)^{-1}, & r_2 \le r < \sigma a \\ 0, & r \ge \sigma a \end{cases} \quad (1)$$

Table 1. Parameters in Eq. (1) for Si-Si and Si-B, respectively.

	Si-Si	Si-B
λ	45.5075 eV	40.8000 eV
γ	1.200000	1.866938
$\cos\theta_t$	$\frac{1}{3}$	0.4212354
A	15.2764 eV	24.2407 eV
B	0.602240	0.708769
p	4.000000	5.996808
q	0	4.292831
σ	2.09510 Å	2.38703 Å
a	1.800000	1.861019
r_1	1.2107 Å	1.4009 Å
r_2	1.8454 Å	2.25057 Å
α	335.0594 eV	53.02835 eV
β	-492.3905 eV Å^{-1}	-44.9923 eV Å^{-1}
γ	244.5280 eV Å^{-2}	7.56818 eV Å^{-2}
δ	-41.2347 eV Å^{-3}	0.66877 eV Å^{-3}

where r is distance between two atoms, and V_{ZBL} is the ZBL universal screened Coulomb repulsive potential following as

$$V_{ZBL}(r) = \frac{Z_1 Z_2 e^2}{r} \sum_{i=1}^{4} c_i \exp\left(-d_i \frac{r}{a}\right) \tag{2}$$

with $c_1 = 0.2817$, $c_2 = 0.28022$, $c_3 = 0.50986$, $c_4 = 0.18175$, $d_1 = 0.20162$, $d_2 = 0.40290$, $d_3 = 0.94229$, $d_4 = 0.319980$, and the screening length $a = 0.46850$ Å$/(Z_1^{0.23} + Z_2^{0.23})$. The complete descriptions of the SW and ZBL potentials are given in Ref. 15 and Ref. 10, respectively. The other parameters in Eq. (1) are shown in Table 1.

For the electronic stopping power, we use a simple Lindhard electronics stopping power model [19]. In this model, the losses are described as a simple drag force applied as a damping of atomic velocity. Thus, the classical equations of motion are modified as

$$\boldsymbol{F} = m_i \ddot{\mathbf{x}}_i - \beta \dot{\mathbf{x}}_i \tag{3}$$

where $\boldsymbol{x}$ is atom position and β is given the Lindhard theory as

$$\beta = \frac{K N Z_1^{7/6} Z_2}{\left(Z_1^{2/3} + Z_2^{2/3}\right)^{3/2}} \tag{4}$$

where Z_1 is the atomic number of the projectile, Z_2 the atomic number of the target, $K = 0.857$ (eV$^{1/2}$Å^2), and N the target density. At the start of simulations, the bulk lattice silicon atoms are given an initial velocity corresponding to temperature. Velocity distribution is assumed Maxwell-Gaussian distribution. A constraint method is used for maintaining a set of particles at constant temperature, and the simplest method is to scale the velocities at each time step by a factor of

$$\left(\frac{T_0}{T}\right)^{1/2} \tag{5}$$

where T is the current kinetic temperature at T_0, the desired temperature [20]. In order to reduce the calculation time, we use the energetic particle approximation method [21]. Implanted ion stops when total energy of ion, which is ion kinetic energy added to ion potential energy, is below 5 eV.

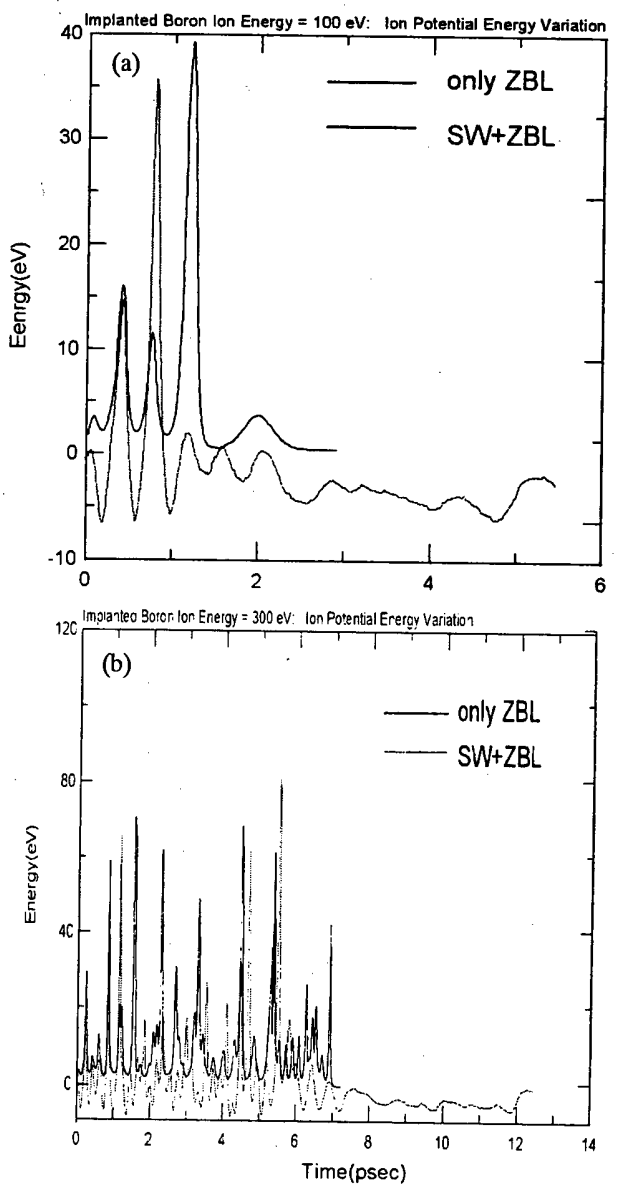

Fig. 1. Potential energy variation with time after projectile using proposed potential and ZBL. (a) in the case of 100 eV and (b) in the case of 300 eV.

III. RESULTS AND DISCUSSIONS

1. Ultra-Low Energy Boron Ion Implantations in Silicon

In the cases of boron ion implant, Si penetration threshold energy is 50 eV. Therefore, we simulate 50 eV ~ 1 keV energy boron ion implantation. We compare results using of proposed potential with that using ZBL. Figure 1 shows potential energy variation with time after projectile using proposed potential and ZBL. Figure 1(a) is the cases of 100 eV and Fig. 1(b) the cases of 300 eV. Ion movement time with proposed potential is usually longer than only with ZBL, since energy losses are less with proposed potential than only with ZBL. We have more impact energy losses and shorter period only with ZBL than with proposed model including the attractive potential.

Figures 2 and 3 show implanted profiles with implant energy. Figure 2 compares profiles only using ZBL with that using proposed potential with 50 eV, 100 eV, and 200 eV energy, respectively. Figure 3 shows profiles of 400 eV and 500 eV with the type of potential. Through the Figs. 2 and 3, tail profiles are deeper in the results using ZBL than in the results using proposed potential. The reason of above results are that attractive potential induced the dechanneling effects, although energy losses are less with proposed potential than only with ZBL. When boron collides with silicons, collision time becomes longer by attractive potential, and therefore scattering angles become larger. Interatomic interactions are usually divided into physical interaction and chemical interaction. Collisions between energetic particles are dominated by physical interaction. However the less energy

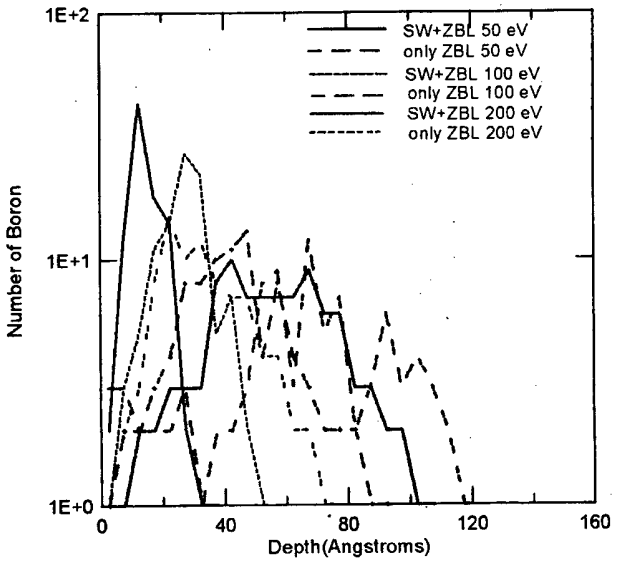

Fig. 2. Comparison profiles only using ZBL with that using proposed potential with 50 eV, 100 eV, and 200 eV, respectively.

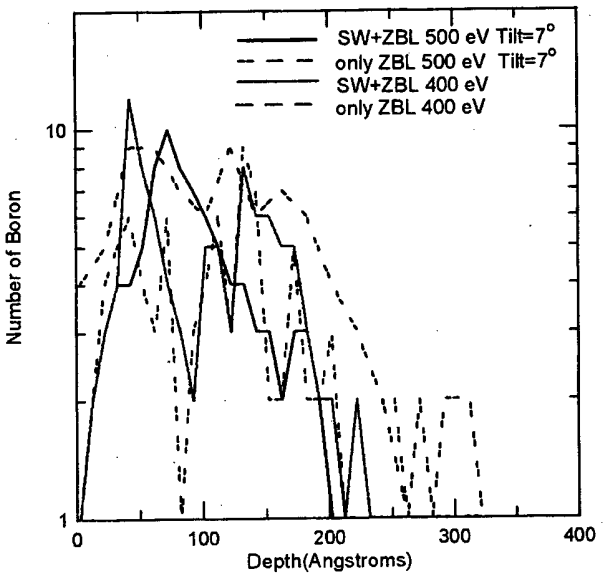

Fig. 3. Comparison profiles only using ZBL with that using proposed potential with 400 eV and 500 eV.

of particle is, the more increases the effect of chemical interaction [22]. In order to form ultra-shallow junction and thin films to fabricate future nano-structure semiconductor devices, importance of below 500 eV ion beams processes is increased. Therefore, attractive potential should be considered in molecular dynamics simulations for ultra-low energy ion beam processes, since effect of chemical interaction increases in the cases of ultra-low energy ion beam processes.

2. Ultra-Low Energy Boron Ion Implantations in Silicon

1 keV boron ion implant profile is initial condition for transient enhanced diffusion (TED) simulation. We simulate annealing during 100 ps. Diffusion coefficient is calculated by the following equation

$$D = \sum_i [r_i(t) - r_i(0)]^2/6t \qquad (6)$$

where, t is annealing time, $r_i(0)$ initial positions, and $r_i(t)$ positions after t seconds.

Figure 4 shows boron diffusion coefficient calculated by Eq. (4) from 1000 K to 1300 K. In the paper, diffusion coefficients calculated are almost 10^{-7} cm^2/s and *Arrhenius* relationships with temperature. Boron diffusivities of TED have been measured with following methods. Boron δ-layer has been formed by methods as molecular beam epitaxy (MBE) *etc.* Damages are generated by silicon self ion implantation. Then diffisivities have been measured by dopant profiles after annealing. Thus measured diffusivities are almost 10^{-14} cm^2/s [23]. Difference between measured diffusivities and calculated diffu-

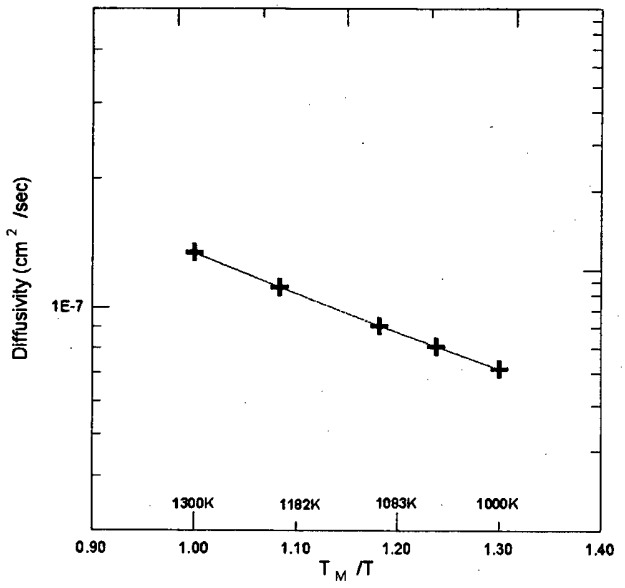

Fig. 4. In the beginning of annealing, boron transient enhanced diffusion coefficient calculated by Eq. (4) from 1000 K to 1300 K.

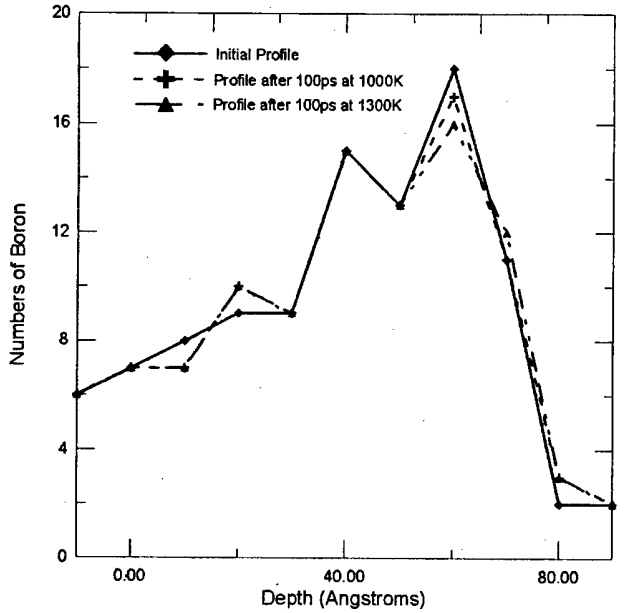

Fig. 5. At 1000 K and 1300 K, Boron profiles after annealing during 100 ps.

visities in the paper is appeared, because we simulated just in the beginning of annealing and boron trapping and clustering decreasing diffusion is not considered. Effects of Boron trapping and clustering will be investigated by long time molecular dynamics simulation. In the beginning of annealing, damages caused by ion implantations are rapidly relaxed and therefore diffusivities is larger than mean diffusivities during whole annealing duration. Because atomic mass of boron is smaller than that of silicon, silicon interstitials kick-out substitutional borons in lattice points and occupy those points. The amorphous-like pocket produced by collision cascades is dissolved in the beginning of annealing, then many silicon interstitials are generated, and that interstitials interact boron dopants. Therefore, boron diffusivities in the beginning of annealing is larger than mean-diffuvisities, because there are a lot of silicon interstitials and boron dopants are swiftly diffused by interstitialcy mechanism. Figure 5 shows boron profiles with annealing temperature. It is shown that peak value of profile decreases after annealing.

Through simulated results, we found that in the beginning of annealing at high temperature, boron transient diffusion coefficient is very high. Interstitials through relaxation and dissolution of amorphous-like pocket induce boron transient enhanced diffusion with high diffusion coefficient of almost 10^{-7} cm^2/s in the beginning of annealing. However, as annealing goes on, TED shall be disappeared because concentration of excess interstitial reduces to equilibrium concentration [23].

IV. CONCLUSIONS

We compare results using proposed potential with those using ZBL. Ion movement time with proposed potential is usually longer than only with ZBL, since energy losses are less with proposed potential than only with ZBL. We found that in the results using ZBL, energy loss more increased than in ther results using proposed potential, and it also took shorter collision period than in the results using proposed potential. When boron collides with silicons, collision time becomes longer by attractive potential, and therefore scattering angles become larger. In order to form ultra-shallow junction and thin films to fabricate future GSI semiconductor devices, importance of below 500 eV ion beams processes has been increased. Therefore, attractive potential should be considered by molecular dynamics simulations for ultra-low energy ion beam processes, since effect of chemical interaction increased in the processes.

The amorphous-like pocket produced by collision cascades is dissolved in the beginning of annealing. As the result, many silicon interstitials are generated, and than interstitials interact with boron dopants. Calculated boron diffusion coefficients are almost 10^{-7} cm^2/s, *Arrhenius* relationships with temperature, and larger than boron mean-diffuvisities, because there are a lot of silicon interstitlas and boron dopants are swiftly diffused through interstitialsy mechanism. The reason for the difference between measured diffusivities and calculated diffuvisities in the paper is that we simulate just in the beginning of annealing and boron trapping and clustering decreasing diffusion is not considered.

As era of micro-chip technologies turn into era of nanotechnologies, it is more important to understand physi-

cal mechanisms of atomic scale interactions. In nanotechnology era, more researches of ion beams processes should be investigated.

REFERENCES

[1] K. Sugio, Y. Shimomura and T. D. de la Rubia, JPSJ **67**, n3, 882 (1998).

[2] T. D. de la Rubia, N. Soneda, M. J. Caturla and E. A. Alonso, J. Nuclear Materials **251**, 13 (1997).

[3] D. J. Bacon, A. F. Calder and F. Gao, J. Nuclear Material **251**, 1 (1997).

[4] R. E. Stoller, J. Nuclear Materials **233-237**, 999 (1996).

[5] H. L. Heinisch and B. N. Singh, J. Nuclear Materials **232**, 206 (1996).

[6] T. D. de la Rubia, J. M. Perlado and M. Tobin, J. Nuclear Materials **233-237**, 1096 (1996).

[7] M. J. Caturla, T. D. de la Rubia, L. A. Marques and G. H. Gilmer, Phys. Rev. **B54**, 16683 (1996).

[8] J. W. Kang, M. S. Son, E. S. Kang and H. J. Hwang, JKPS **33**, S229 (1998).

[9] J. W. Kang and H. J. Hwang, J. Korean Phys. Soc. **34**, 477 (1999).

[10] J. F. Ziegler, J. P. Biersack and U. Littmark, *The Stopping and Range of Ions in Solids* (Pergamon Press, New York, 1985).

[11] D. E. Hanson, A. F. Voter and J. D. Kress, J. Appl. Phys. **82**(7), 3552 (1997).

[12] T. Diaz de la Rubia, Nucl. Instr and Meth. in Phys. Res. **B120**, 19 (1996).

[13] K. Nordlund, R. S. Averback, T. Diaz de la Rubia, MRS **469**, 113 (1997).

[14] K. Nordlund, M. Ghaly and R. S. Averback, J. Appl. Phys. **83**, 1238 (1998).

[15] F. H. Stillinger and T. A. Weber, Phys. Rev. **B31**, 5262 (1985).

[16] Gärtner, D. Stock, B. Weber, G. Betz, M. Hautala, G. Hobler, M. Hou, S. Sarite, W. Eckstein, J. J. Jimenea-Rodriguez, A. M. C. Perez-Martin, E. P. Andribet, V. Konoplev, A. Gras-Marti, M. Posselt, M. H. Shapiro, T. A. Tombrello, H. M. Urbassek, H. Hensil, Y. Yamamura and W. Takeuchi, Nulc. Instrum. Meth. **B102**, 183 (1995).

[17] P. B. Rasband, P. Clanc and M. O. Thompson, J. Appl. Phys. **79**, 8998 (1996).

[18] J. Lindhard and M. Scharff, Phys. Rev. **124**, 128 (1961).

[19] M. P. Allen and D. J. Tildersley, *Computer Simulation of Liquids* (Clarendon Press, Oxford, 1987).

[20] J. W. Kang, M. S. Son and H. J. Hwang, JIEEK-D **35**, 230 (1998).

[21] *Plasma Etching : An Introduction*, edited by D. M. Manos and D. L. Flamm (Academic press, INC., 1989).

[22] P. A. Stolk, H. J. Gossmann, D. J. Eaglesham and J. M. Poate, NIM **B96**, 187 (1995).

[23] P. A. Stolk, H. J. Gossmann, D. J. Eaglesham, D. C. Jacobson, C. S. Rafferty, G. H. Gilmer, M. Jaraiz, J. M. Poate, H. S. Luftman and T. E. Haynes, J. Appl. Phys. **81**(9), 6031 (1997).

Journal of the Korean Physical Society, Vol. 34, June 1999, pp. S526~S531

The Formation of $CoSi_2$ Thin Layer on Crystalline and Amorphous Si Substrates Using CoZr Alloy Layer

S. G. PARK and Hyeongtag JEON

Division of Materials Science and Engineering, CPRC, Hanyang University, Seoul 133-791

The growth of $CoSi_2$, between the CoZr alloy layer on crystalline and on amorphous Si substrates, was investigated. The Zr and Co were co-deposited with a dual e-beam evaporation system and followed by rapid thermal annealing from temperatures between 500 °C and 800 °C with 100 °C increments. The phase identification was carried out by XRD, and chemical compositions of these elements were analyzed by AES. The surface and interface morphologies of Co-silicide layer were investigated by SEM and cross sectional TEM. The sheet resistance was measured by four-point probe. The polycrystalline $CoSi_2$ film was formed both on the crystalline and the amorphous substrates at the annealing temperature of 600 °C. The phase transformation of $CoSi_2$ on amorphous Si substrate was considerably accelerated and the grain size of the silicide phases became smaller. It can be expected that the $CoSi_2$/Si interface on the amorphous Si substrate is smoother than that on the crystalline Si substrate. However, in this study, the $CoSi_2$ layer formed on the crystalline Si substrate exhibits better uniformity than the $CoSi_2$ formed on the amorphous Si substrate because of the nonuniform diffusion of Co through the amorphous Si substrate. The resistivity on the crystalline Si substrate was lower than that on the amorphous Si substrate at high temperatures.

I. INTRODUCTION

Metal silicides have received much interest over the years due to their application in microelectronic devices such as contact, gate electrode, and interconnect materials. This is mainly because of their low resistivity, high thermal stability and compatibility with current processing techniques [1,2]. Among the silicide materials, $TiSi_2$ has been of special interest because of its low resistance, high thermal stability and good ohmic contact to Si substrate [3,4]. However, the reactions between Ti and oxide may cause the formation of a bridge in the source/drain contact region, and it can lead to the electrical short of device [5]. In addition, the phase transition and surface agglomeration at high temperatures (above 650 °C) is considered to be the one of the major drawbacks in applying this material to Si-based device process [6].

As for the substitution for $TiSi_2$ among contact and interconnect materials, the $CoSi_2$ has been considered to be the most attractive one for contact and interconnect materials in next generation devices because it exhibits low resistivity among other metal silicides and shows no reaction with oxide spacers due to the low heat of the formation of Co oxide [7,8]. However, in the case of using Co single layer on the Si substrate, the formation of $CoSi_2$ has been found to have many problems, such as the inability to remove native oxide and the formation of rough interfaces due to the non-uniform reaction between Co and Si [9]. Moreover, the large amount of Si consumption in the Co/Si thin film reaction made it difficult to form shallow junction in MOS device [10]. To solve these problems, many researchers [11–13] have recently suggested the formation of Co silicide using a Co/refractory metal bilayer. Among the refractory metals used for the interlayer, Zr is one of the candidates known to have strong reactivity with oxygen [14] and little solid solubility with Co [15] implying that it will have the capability to remove native oxide and act as a barrier material for Co flux to Si. In case of co-depositing Co and Zr, both Co and Zr atoms are present on the Si surface, and the nucleation and growth of both Zr-silicide and Co-silicide phases can compete simultaneously. However, since the formation temperature of $ZrSi_2$ is much higher than that of $CoSi_2$ [16], it can be expected that the uniform and smooth $CoSi_2$ layer can be formed at relatively low temperatures and the formation of Co-silicide will be affected by the reaction of Co with Zr. The growth of $CoSi_2$ on the different Si substrate will be also affected by the microstructure of Si surface. Since the surface energy of amorphous Si substrate is higher than that of crystalline Si substrate, the formation of Co-silicide will be affected by the latent energy of the amorphous Si substrate.

In this study, the formation of Co silicide using a CoZr alloy layer on the crystalline Si (100) and on the amorphous Si substrate will be discussed to find out the dependence of surface microstructure on Co-silicide formation. And the interface morphologies of Co-silicide will be analyzed. The amorphous Si film was grown on the crystalline Si (100) by the CVD (chemical vapor deposition). The CoZr alloy layer films were deposited on both the

crystalline and the amorphous Si substrates and annealed by RTA (rapid thermal annealing) in an N_2 ambient. To examine the physical and electrical properties of Co-silicides, XRD (x-ray diffractometer), AES (auger electron spectroscopy), SEM (scanning electron microscopy), TEM (transmission electron microscope) and four-point probe were used.

II. EXPERIMENTS

The substrates used in this study were 2-inch Si(100) wafers with resistivities of 5~10 Ωcm (P-type, Boron doped). Amorphous Si films of 1000 Å were grown at the temperature of 500 °C on the crystalline Si(100) substrate by the CVD process. Prior to Zr and Co deposition, the Si substrate was cleaned by piranha cleaning (H_2SO_4+H_2O_2) to remove the organic contaminants and followed by HF solution cleaning (HF:H_2O=1:50) to remove native oxide. After cleaning, the crystalline and amorphous Si substrates were loaded into a dual ebeam evaporation system. During metal evaporation, the vacuum was maintained between 5×10^{-8} and 5×10^{-7} Torr. The 200 Å of Zr and Co were co-deposited and the atomic concentration was maintained to have $Co_{0.9}Zr_{0.1}$. The film thickness was measured by using a quartz crystal thickness monitor. After deposition, all samples were annealed by the rapid thermal process to form the $CoSi_2$ at temperatures ranging from 500 to 800 °C in an N_2 ambient for 30 sec with 100 °C increments. The phase identification of $CoSi_2$, depending on the annealing temperatures, was analyzed with using XRD. The AES depth profiles to investigate the chemical composition of Co silicides were carried out. The surface and interface morphologies were examined using SEM and cross-sectional TEM. The sheet resistance was measured by four-point probe.

III. RESULTS AND DISCUSSION

The phases formed after rapid thermal annealing at various temperatures were identified by XRD. The XRD data of the CoZr alloy layer deposited on the crystalline Si substrate at different temperatures are shown in Fig. 1. The Co_2Si peak was found in the 500 °C annealed sample. After annealing at 600 °C, Co_2Si peak disappeared and $CoSi_2$ (220) peak became much dominant with increasing annealing temperature. The $CoSi_2$ (111) peak was also observed. In the present study, Co_2Si was found to be the first crystalline silicide formed during annealing. Since the value of effective heat for formation of $CoSi_2$ is higher than that of Co_2Si in absolute value [17], the former was expected to begin to grow on the limited interface region between Co_2Si and Si substrate by Co diffusion into the Si substrate. Once the $CoSi_2$ grains were nucleated at the Co_2Si/Si interface,

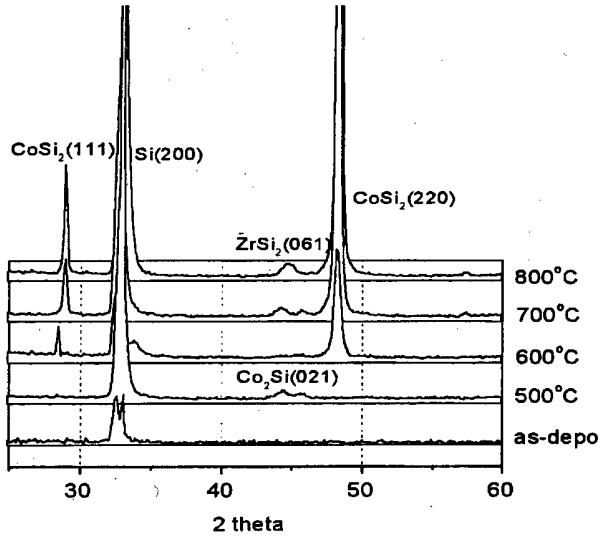

Fig. 1. XRD data of the CoZr alloy layer deposited on the crystalline Si substrate annealed at as-deposited, 500 °C, 600 °C, 700 °C and 800 °C.

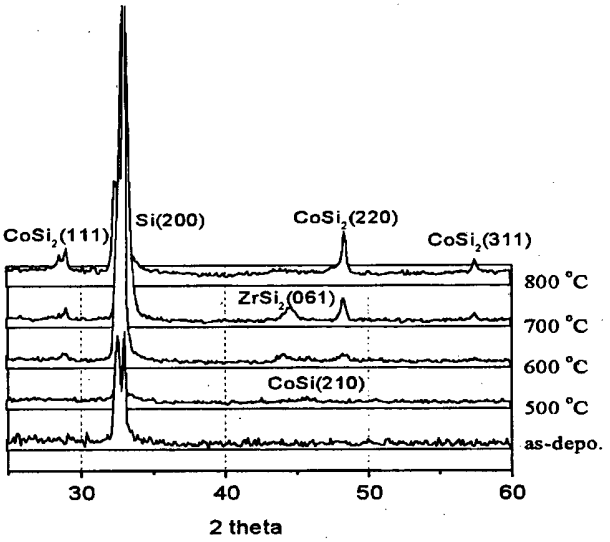

Fig. 2. XRD data of the CoZr alloy layer deposited on the amorphous Si substrate annealed at as-deposited, 500 °C, 600 °C, 700 °C and 800 °C.

further growth of the Co_2Si layer was retarded. The XRD data of Co silicide grown on the amorphous Si substrate are shown in Fig. 2. The CoSi peak was observed at 500 °C and several peaks related to $CoSi_2$ such as $CoSi_2$(111), $CoSi_2$(220), $CoSi_2$(311) were observed above 600 °C annealing. In this case, Co_2Si peak was not found. It is previously reported that the formation sequence of Co-silicide, depending on annealing temperatures, was $Co_2Si \rightarrow CoSi \rightarrow CoSi_2$ [18]. The Co_2Si is believed to be in the first phase when there is enough Co flux to form the Co-silicide phase because of the lowest effective heat of formation of Co_2Si (−26.01 kJ/mol atom) [18]. Howev-

er, in this case, Co_2Si peak was not found. According to the XRD analysis shown in Fig. 1 and 2, Co_2Si and CoSi were found to be the first phases on crystalline and amorphous Si substrates, respectively. Therefore, the CoSi phase, which has a higher formation temperature than Co_2Si, was formed on the amorphous Si substrate without forming Co_2Si. This means that the formation temperature of Co silicide grown on the amorphous substrate is lower than that grown on the crystalline substrate. This is due to the latent energy stored in amorphous Si substrate. The low temperature reaction was thought due to the heat of crystallization of the amorphous Si. The enthalpy of amorphous Si is 12 kJ/mol higher than the crystalline Si [19], so the kinetics of the reaction of Co with an amorphous Si substrate is considerably enhanced. Consequently, it can be concluded that the driving force for the formation of Co-silicide on an amorphous Si substrate is increased by the latent energy stored in amorphous Si substrate. Silicidation of the complete Co-Zr layer, resulting in the formation of $CoSi_2$ and $ZrSi_2$, is found to take place after annealing of 700 °C. The intensity of XRD signal is weaker than that of crystalline Si substrate. This is because the amorphous Si substrate was not crystallized completely for short annealing time of 30 sec.

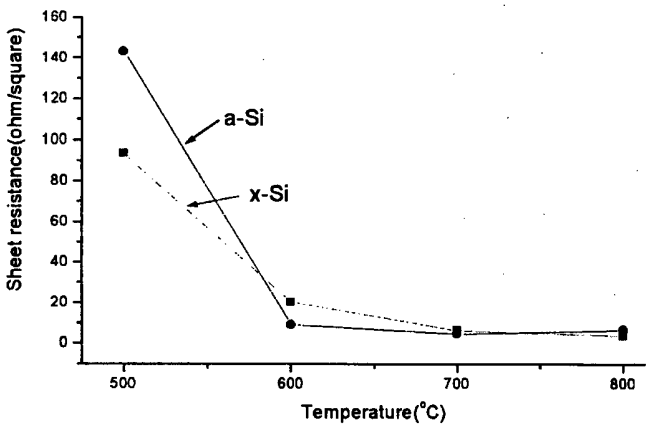

Fig. 3. Sheet resistance data of CoZr alloy layer deposited on the crystalline and amorphous Si substrate annealed from 500 °C to 800 °C.

Fig. 3 shows the sheet resistance of the Co-silicide layer at various annealing temperatures. The sheet resistance measurements were carried out using a four-point probe. The sheet resistance is suddenly dropped at 600 °C on both Si substrates due to the formation of $CoSi_2$ phase and this results are consistent with XRD data. The resistivity is decreased further by the growth of $CoSi_2$ as the annealing temperature increases and all of these silicides exhibited the lowest sheet resistance at 800 °C.

The AES depth profiles of Co-silicides on the crystalline Si substrate at various annealing temperatures are shown in Fig. 4. Fig. 4(a) shows AES depth profile of the as-deposited film without annealing. The elements of Co and Zr coexist uniformly throughout the Co-metal layer and there is no intermixing between Co and Si at this deposition temperature. After annealing at 500 °C, as shown in Fig. 4(b), there was an atomic intermixing between Co and Si. The atomic ratio of Co to Si peak exhibits approximately 2:1 in the bottom layer of the film, which contacts with Si substrate. This is consistent with the formation of Co_2Si phase on the crystalline Si substrate at annealing temperature of 500 °C by XRD data. At annealing temperature of 800 °C, as shown in Fig. 4(c), the atomic ratio of Co to Si peak exhibits approximately 1:2. Therefore, the $CoSi_2$ phase is formed on the Si substrate. The oxygen peak at the surface is due to the strong affinity of Zr with oxygen. Because the heat of the formation of zirconium oxide (ZrO_2) is much higher than that of cobalt oxide (CoO) and silicon oxide (SiO_2) [13], a native oxide (SiO_x) formed on Si substrate can be removed easily by the Zr. Therefore, the clean Si interface surface can be obtained by forming Zr oxide. This is

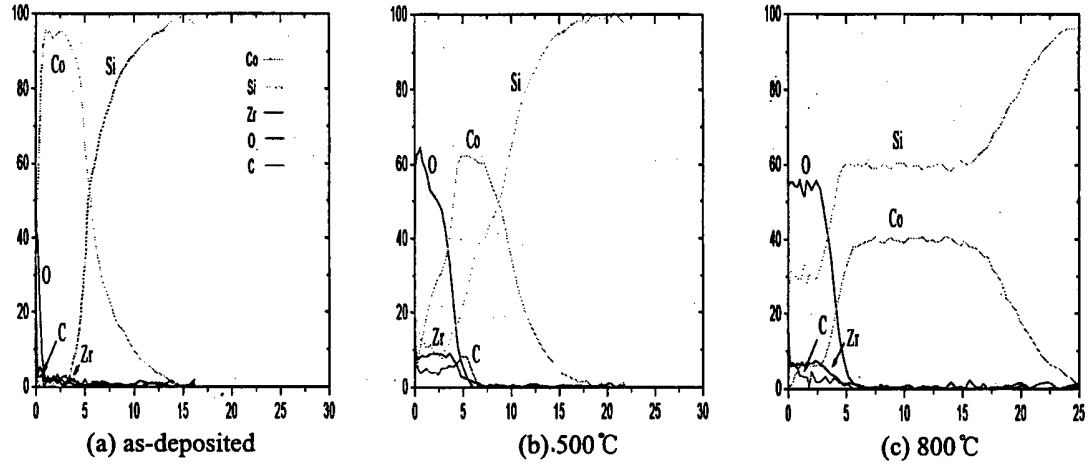

Fig. 4. AES depth profiles of CoZr alloy layer deposited on the crystalline Si substrate annealed at (a) as-deposited, (b) 500 °C and (c) 800 °C.

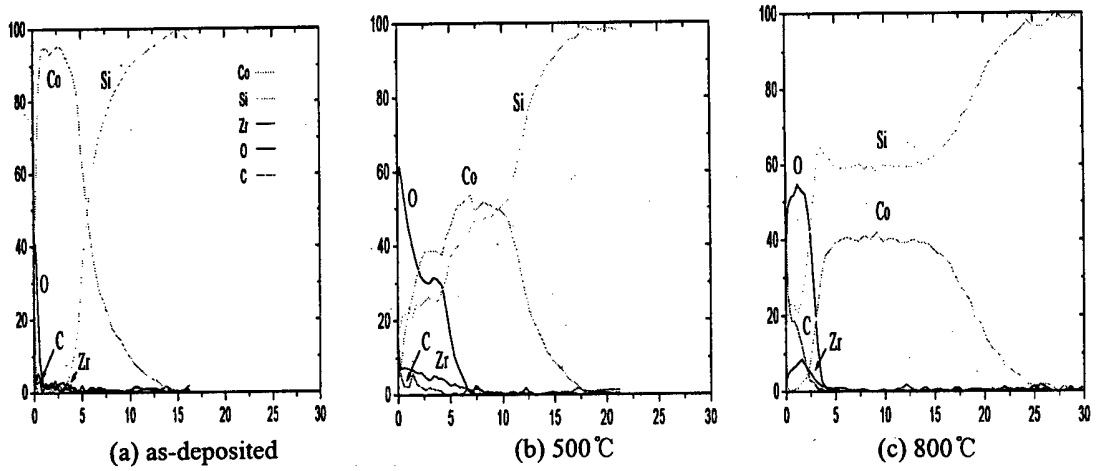

Fig. 5. AES depth profiles of CoZr alloy layer deposited on the amorphous Si substrate annealed at (a) as-deposited, (b) 500 °C and (c) 800 °C.

an important factor for the formation of Co-silicide with smooth interface on the Si substrate. The AES depth profiles of Co-silicide on the amorphous Si substrate are shown in Fig. 5. As shown in Fig. 5(b), the atomic ratio of Co to Si peak exhibits approximately 1:1. This is consistent with the formation of CoSi phase on the amorphous Si substrate at annealing temperature of 500 °C by XRD data. In this case, CoSi phase is formed instead of Co_2Si, since the energy barrier for nucleation of Co-silicide is decreased due to the latent energy stored in amorphous Si substrate. At annealing temperature of 800 °C, the same result in the case of using crystalline Si substrate is observed which is the formation of $CoSi_2$.

The surface morphologies of Co-silicide were analyzed by SEM. Fig. 6 and Fig. 7 show the SEM micrographs of Co-silicide, which is formed on the crystalline Si substrate and the amorphous Si substrate after annealing at temperatures of 500 °C and 800 °C. We could not find the difference of surface morphologies of Co-silicide between the crystalline Si substrate and the amorphous Si substrate at 500 °C. As the annealing temperatures increase, the change in surface morphologies of Co-silicide are observed between the crystalline Si substrate and the

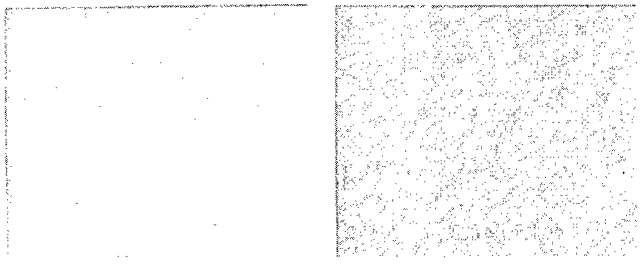

Fig. 6. SEM micrographs of CoZr alloy layer deposited on the crystalline Si substrate annealed at (a) 500 °C and (b) 800 °C.

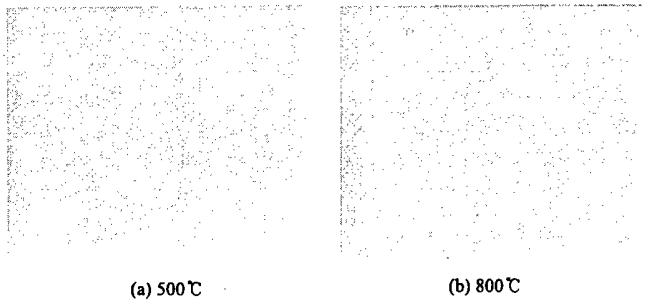

Fig. 7. SEM micrographs of CoZr alloy layer deposited on the amorphous Si substrate annealed at (a) 500 °C and (b) 800 °C.

amorphous Si substrate. At the annealing temperature of 800 °C, the surface morphology of Co-silicide formed on the crystalline Si substrate is rougher than that of Co-silicide formed on the amorphous Si substrate. This is due to the difference of the surface energy between the crystalline and the amorphous Si substrate. The energy barrier for nucleation of Co-silicide on the amorphous Si substrate is decreased by the latent energy stored in amorphous Si substrate. Therefore, the nucleation of Co-silicide on the amorphous Si substrate is faster than on the crystalline Si substrate. On the amorphous Si substrate, since the nucleation rate of Co-silicide is faster than the growth rate, smaller grain than that on the crystalline Si substrate is uniformly distributed. This is the reason why the surface morphology of Co-silicide formed on the amorphous Si substrate is better than that of Co-silicide formed on the crystalline Si substrate. The nucleation rate, as accelerated by the stored energy of amorphous Si, is not only ceased to act as the limiting process in the $CoSi_2$ formation, but also considerably improved the microstructure of the silicide films.

Fig. 8 shows the cross-sectional TEM bright field images of the samples on the crystalline Si substrate and on the amorphous Si substrate annealed at 800 °C. In this

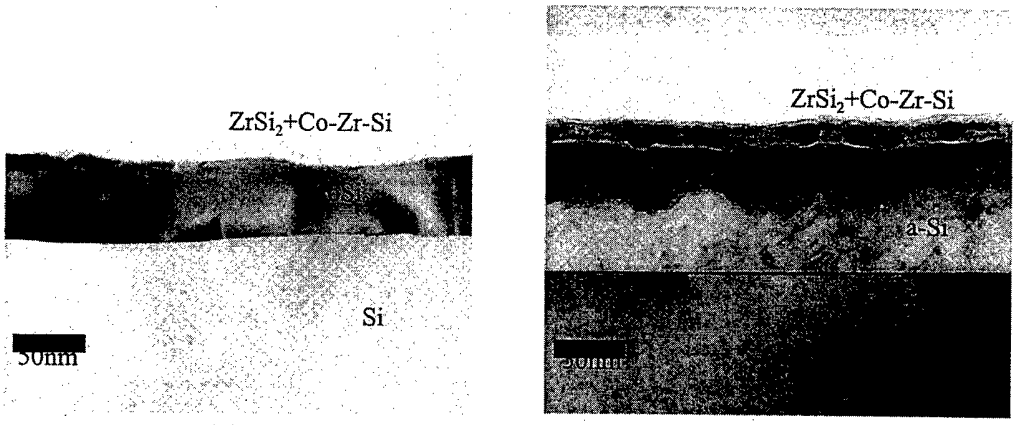

Fig. 8. Cross-sectional TEM micrographs of Co-silicide on the crystalline (a) and the amorphous (b) Si substrate annealed at 800 °C.

study, we knew that the amorphous Si substrate was not consumed completely and that the polycrystalline $CoSi_2$ phases were formed on both the crystalline Si substrate and amorphous Si substrate. Cross sectional TEM exhibits that the interface of $CoSi_2$ phase grown on the amorphous Si substrate is much rougher than that on the crystalline Si substrate. This can be explained by the grain boundary diffusion through the polycrystalline $CoSi_2$ layer and by the nonuniform diffusion of Co between the amorphous Si substrate and the polycrystalline $CoSi_2$. The Co atoms diffuse along the grain boundaries of $CoSi_2$ phase from the top layer to $CoSi_2$/Si interface and react with Si, leading to enhanced growth of $CoSi_2$ at the junctions of grain boundaries of $CoSi_2$ phase and $CoSi_2$/Si interface [20]. At these junctions, the growth of $CoSi_2$ phase will be started. Compared with the $CoSi_2$ phase on the crystalline Si substrate, the $CoSi_2$ phase on the amorphous Si substrate has a large number of these junctions because of the high density of $CoSi_2$ nuclei. Therefore, the polycrystalline Si were partially formed in the amorphous Si and this resulted in nonuniform diffusion of Co through the amorphous Si substrate. This is the reason why the $CoSi_2$/Si interface on the amorphous Si substrate is rougher than that on the crystalline Si substrate.

IV. SUMMARY

We have compared the reaction between a CoZr alloy layer on both crystalline and amorphous Si substrates. The microstructure of $CoSi_2$ exhibited polycrystalline on both the crystalline and amorphous Si substrates at annealing temperature of 600 °C. The sheet resistance of CoZr thin films on two different Si substrates abruptly decreased at 600 °C. The AES data indicated that Zr removed a native oxide on the Si substrate, which provided an atomically clean Si substrate. The thickness of the $CoSi_2$ phases formed on Si substrate are approximately 500 Å. The interface morphology of $CoSi_2$ formed on the crystalline Si substrate showed better uniformity than that formed on the amorphous Si substrate because of the nonuniform grain boundary diffusion of Co between the amorphous Si substrate and the polycrystalline $CoSi_2$. There is a close relationship among the $CoSi_2$/Si interface roughness, the silicide grain size, and the phase transformation kinetics. Both the phase transformation kinetics and the grain size of the $CoSi_2$ on an amorphous Si substrate were the results of latent energy stored in the amorphous silicon, which accelerated the nucleation rate of the $CoSi_2$ phase and resulted in the relatively wavy interface of $CoSi_2$.

ACKNOWLEDGMENTS

This study was supported by Korea Science & Engineering Foundation (KOSEF), through grant KOSEF (96-0300-21-3).

REFERENCES

[1] S. P. Murarka, *Silicides for VLSI Applications* (Academic, New York, 1983).
[2] R. J. Nemanich, R. Fiordalice and H. Jeon, IEEE J. Quantum Electron **25**, 997 (1989).
[3] R. W. Mann and L. A. Clevenger, J. Electrochem. Soc. **141**, 1347 (1994).
[4] C. Y. Ting, F. M. d'Heurle, S. S. Iyer and P. M. Fryer, J. Electrochem. Soc. **133**, 2621 (1986).
[5] J. B. Lasky, J. S. Nakos, O. J. Cain and P. J. Geiss, IEEE Trans. Electron Devices **ED-38**, 262 (1991).
[6] H. Jeon, C. A. 2Sukow, J. W. Honeycutt, G. A. Rozgonyi and R. J. Nemanich, J. Appl. Phys. **71**, 4269 (1992).
[7] S. P. Murarka, *Silicides for VLSI Applications* (Academic, New York, 1983).
[8] C. S. Wei, G. Raghan, M. Lawrence, A. Dass, M. Frost,

T. Brat and D. B. Fraser, in V-MIC Conference, Santa Clara, California, June, 241 (1989).
[9] A. E. Morgan, E. K. Broadbent, M. Delfino, B. Couldman and D. K. Sadana, J. Electrochem. Soc. **134**, 925 (1987).
[10] Q. F. Wang, C. M. Osburn, P. L. Smith, C. A. Canovai and G. E. Mcguire, J. Electrochem. Soc. **140**, 200 (1993).
[11] S. L. Hsia and T. Y. Tan, J. Appl. Phys. **70**, 7579 (1991).
[12] J. S. Byun, S. B. Kang, H. J. Kim, K. H. Park and C. Y. Kim, J. Appl. Phys. **72**, 1508 (1993).
[13] J. S. Byun, J. J. Kim, W. S. Kim and H. J. Kim, J. Electrochem. Soc. **142**, 2805 (1995).
[14] R. Pretorius, J. M. Harris and M. A. Nicolet, Solid State Electron **21**, 667 (1978).
[15] T. B. Massalski, Binary Alloy Phase Diagrams, American Society for Metals Park, OH (1986).
[16] G. Ottaviani and J. W. Mayer, *Reliability and Degradation*, Editors M. J. Howes and D. V. Morgan (John Wiley & Sons, Inc., New York, 1981), Chap. 2.
[17] R. Pretorius, Mater. Res. Soc. Symp. Proc. **25**, 15 (1984).
[18] R. Pretorius, Thin Solid Films **290**, 447 (1996).
[19] E. P. Donovan, F. Spaepen, D. Turnbull, J. M. Poate and D. C. Jacobson, J. Appl. Phys. **57**, 1795 (1985).
[20] Z. G. Xiao, J. W. Honeycutt and G. A. Rozgonyi, MRS. Symp. Proc. **202**.

Journal of the Korean Physical Society, Vol. 34, June 1999, pp. S532~S537

MOCVD of Hexagonal Boron Nitride Thin Films on Si(100) Using New Single Source Precursors

Jin-Hyo Boo* and Soon-Bo LEE

Institute of Basic Science and Department of Chemistry, Sungkyunkwan University, Suwon 400-746

Kyu-Sang YU and Yunsoo KIM

Thin Film Materials Laboratory, Korea Research Institute of Chemical Technology, Taejon 305-600

Yun-Soo KIM and Joon T. PARK

Department of Chemistry, Korea Advanced Institute of Science and Technology, Taejon 305-701

We have been carried out the growth of hexagonal boron nitride (h-BN) thin films on Si(100) substrates by low pressure metal-organic chemical vapor deposition (LPMOCVD) method using triethylborane *tert*-butylamine complex (TEBTBA), $Et_3BNH_2(^tBu)$, and triethylborane isopropylamine complex (TEBIPA), $Et_3BNH_2(^iPr)$ as a new single molecular precursors in the temperature range of 850~1000 °C. Polycrystalline, crack-free h-BN film was successfully grown on Si(100) substrate at 850 °C using TEBTBA. This growth temperature is very lower than those in previous reports. Carbon-rich polycrystalline BN was also obtained at 900 °C from TEBIPA. With increasing substrate temperatures to 1000 °C, however, BC_4N-like species are strongly formed along with h-BN and the BN films obtained from both TEBTBA and TEBIPA but almost polycrystalline. To our best knowledge, this is the first report of the growth of h-BN films formed with the new single source precursors of $Et_3BNH_2(^tBu)$ and $Et_3BNH_2(^iPr)$. High-resolution XPS and FTIR measurements were utilized as a good probes for identifying the crystal structure of BN films together with the XRD.

I. INTRODUCTION

Boron nitride (BN) films have attracted a growing interest for a variety of technological applications due to their excellent characteristics, namely hardness, chemical inertness, and dielectrical behavior, *etc.* There are two crystalline phases of BN that are analogous to phases of carbon. Hexagonal boron nitride (h-BN) has a layered structure which is sp^2-bonded structure similar to that of graphite, and is the stable ordered phase at ambient conditions [1]. Cubic boron nitride (c-BN) has a zinc blende structure with sp^3-bonding like as diamond, and is the metastable phase at ambient conditions. Also like carbon, there are amorphous and poorly crystalline forms of BN having sp^2-bonding. Among of their prototypes, especially the c-BN is an interesting material because it has almost the same hardness and thermal conductivity as diamond [2,3]. c-BN is a chemically resistant, especially insulating material and is used in applications where carbon-based materials are limited by oxidation [4]. Moreover, c-BN films may better suited than diamond for electronic device applications as high-temperature semiconductors since the wide, direct energy band gap (6.4 eV) and it can be easily doped both n-type or p-type with the silicon or beryllium to form a materials for high-temperature semiconductors whereas diamond cannot [4]. Furthermore, the 1.4 % lattice mismatch between c-BN and diamond suggests that c-BN may be the most attractive substrate for heteroepitaxial diamond film growth [5–9]. On the other hand, h-BN as well as c-BN has high thermal stability and excellent tribological properties that are not degraded in air. Due to its good physical properties, h-BN has been widely used a material for a hard and protective coating or a heat sink. Under the conditions of high pressure and temperature, however, h-BN transforms into a wurzite (w-BN) or a cubic (c-BN). Therefore, the films of both h-BN and c-BN are promising not only as a material for hard coating and heat sink, but also as a semiconductor material for electronic devices, especially masks for x-ray and low

*E-mail: jhboo@chem.skku.ac.kr, Fax: +82-331-290-7075

energy electron beam.

Conventionally, significant progress has been made in the experimental techniques for synthesizing *c*-BN film using various methods of the physical vapor deposition and chemical vapor deposition. But, the major disadvantage of *c*-BN films is that they are much more difficult to synthesize than diamond films due to its narrow stability phase region, high compression stress, and problem of boron or nitrogen source control [10,11]. Recent studies of the metal-organic chemical vapor deposition (MOCVD) of III-V compound have established that a molecular level understanding of the deposition process is mandatory in controlling the selectivity parameter [12]. This led to the concept of using a single source precursor, having the constituent elements in stoichiometric ratio, for MOCVD growth of the required binary compound [13–15]. A similar strategy is warranted in the CVD of BN to switch the balance from hexagonal to cubic phase by tailoring the organometallic precursor having boron and nitrogen in 1:1 stoichiometry.

In this study, therefore, we has been carried out the low pressure MOCVD growth of *h*-BN thin films on Si(100) substrates using a new organometallic compounds of triethylborane *tert*-butylamine complex (TEBTBA), $Et_3BNH_2(^tBu)$, and triethylborane iso-propylamine complex (TEBIPA), $Et_3BNH_2(^iPr)$ as a single source precursors.

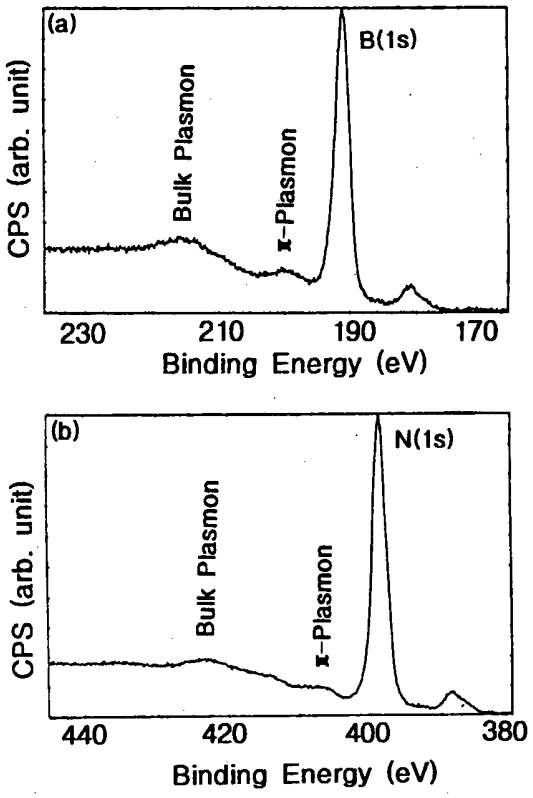

Fig. 1. High resolution x-ray photoelectron spectra of the *h*-BN film deposited on Si(100) substrate using $Et_3BNH_2(^tBu)$ at 850 °C; (a) B (1s), (b) N (1s).

II. EXPERIMENTAL

CVD is carried out in a simple vacuum chamber which is consists of quartz glass. Si(100) substrates used in the present study were cleaned and etched using standard procedure. The precleaned substrates were mounted the sample holder and then the precursors were admitted into the deposition chamber without carrier gas. The deposition was carried out for 5~6 hours after which the substrates were slowly brought to ambient temperature. Several independent experiments were carried out between 800 and 1000 °C. The temperatures of substrate/film were detected by an optical pyrometer and the deposition pressures during deposition were adjusted between 50 and 70 Pa. The details of experimental have been published elsewhere [16,17]. The films produced by CVD were characterized by x-ray photoelectron spectroscopy (XPS), x-ray diffraction (XRD), scanning electron microscopy (SEM), and Fourier transform infrared spectroscopy (FTIR).

III. RESULTS AND DISCUSSION

The CVD was carried out using triethylborane *tert*-butylamine complex (TEBTBA), and triethylborane iso-propylamine complex (TEBIPA) as a single source precursors at the temperature range of 850~1000 °C. The elemental composition and film structure of the as-grown BN films were in first analyzed by XPS and FTIR. It has been shown previously that the hexagonal and cubic of BN have discernible features in both XPS and Auger electron spectroscopy [18,19]. Both *c*-BN and *h*-BN have bulk plasmon (BP) loss peaks at approximately 27 and 25 eV respectively, away from the B (1s) and N (1s) peaks. However, due to difference the bonding between *h*-BN (sp^2) and *c*-BN (sp^3), only *h*-BN has a π plasmon loss peak at approximately 9 eV away from the B (1s) and N (1s) peaks. We use the presence of this feature as a 'fingerprint' to further confirm the presence of sp^2 bonding in the *h*-BN films. The high resolution XP spectra of typical *h*-BN film grown on Si(100) substrate at 850 °C using TEBTBA are shown in figure 1. The B (1s) peak is centered at 191 eV and the N (1s) peak is at 398 eV, in good agreement with values in the published literature [18]. The bulk plasmon and the π plasmon loss peaks are present at about 25 eV and 9 eV, respectively, away from the 1s peak in their expected positions for a *h*-BN. This result is also confirmed with a FTIR data. Because the FTIR spectroscopy can provide direct information about either the local bonding environment or the structure of the constituents of the film. For sp^2-bonded BN (crystalline or amorphous *h*-BN), there are two characteristic

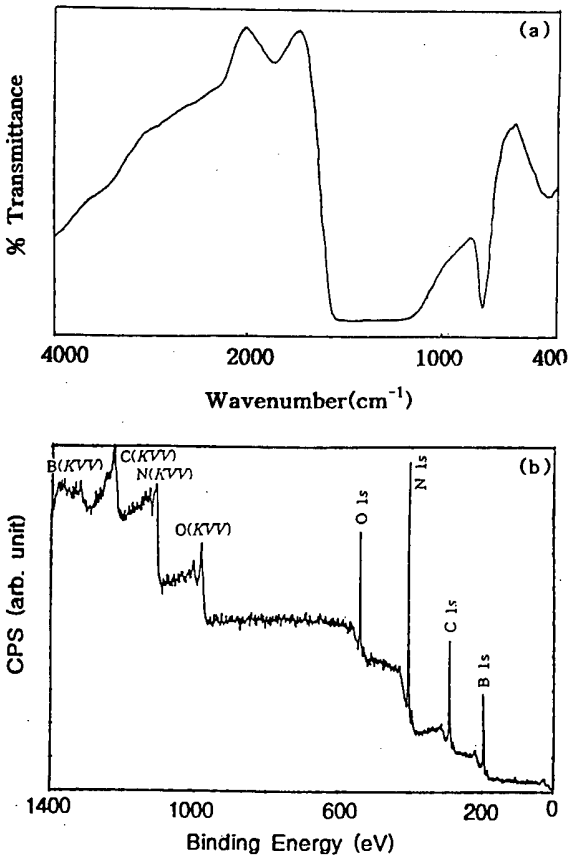

Fig. 2. FTIR and x-ray photoelectron survey spectra of the h-BN film grown on Si(100) substrate with $Et_3BNH_2(^tBu)$ at 850 °C; (a) FTIR, (b) XPS.

peaks at 1400 cm^{-1} and 770 cm^{-1}, which are associated with the in-plane (IP) B-N bond stretching vibration and the out-of-plane (OOP) B-N-B bending vibration. Cubic BN with sp^3 bonding, on the other hand, has an IR active TO mode at ca. 1100 cm^{-1}. The FTIR spectrum of a hexagonal boron nitride film grown on Si(100) at 850 °C using TEBTBA is shown in figure 2(a). A typical absorption peak due to OOP B-N-B bending vibration in the h-BN film is clearly observed at ca. 770 cm^{-1}. This result is in good agreement with that of XPS and with reported one previously [20]. However due to the thick thickness of the as-grown BN film, there is no absorption peak around 1400 cm^{-1}. Moreover, two additional absorption peaks were also appeared at about 500 cm^{-1} and 1950 cm^{-1} attributed to B-C and C-C (possibly incorporated from precursor or residual gas) vibrations. It is evident that the B-N peak was decreased and the peaks of B-C and C-C vibrations were rapidly increased with increasing growth temperatures. These results are also in good agreement with those of XPS and will be discussed later. Figure 2(b) shows the X-ray photoelectron survey spectrum of the BN film deposited on Si(100) substrate at 850 °C using TEBTBA. The survey spectra clearly shows the photoelectron peaks of Si (2s), Si (2p), B (1s), and N (1s) which are indicating formation of hexagonal boron nitride film on the Si(100) surface. Besides these relevant peaks, there also appear C (1s), O (1s) photoelectron peak and C (KVV), O (KVV) Auger peaks. Surface carbon and native oxygen can be attributed to surface contamination of the newly formed films by air and/or precursor during sample transfer and deposition, respectively. Because after Ar ion sputtering the amounts of C and O were greatly reduced. Therefore as a results of our measurements of XP survey spectrum, high resolution XP spectra, and FTIR data of BN films, we confirmed that the BN films deposited on Si(100) substrates has hexagonal structure. Because both the B (1s) and N (1s) core level spectra of BN films show loss features at ca. 9 and 25 eV higher binding energy than the core peaks which are also characteristic of h-BN. But, with increasing substrate temperatures, BC_xN-like species are strongly formed along with h-BN. Figure 3 show a survey scan spectra of the h-BN films grown on Si(100) substrates at 910 °C (Fig. 3(a)) and at 1000 °C (Fig. 3(b)) using the same single molecular precursor of $Et_3BNH_2(^tBu)$. From figure 3, we realized that the carbon concentration of the as-grown h-BN film depends on the growth temperature indicating surface carbon adsorption on BN film surface or carbon incorporation (or replacement) reaction with BN.

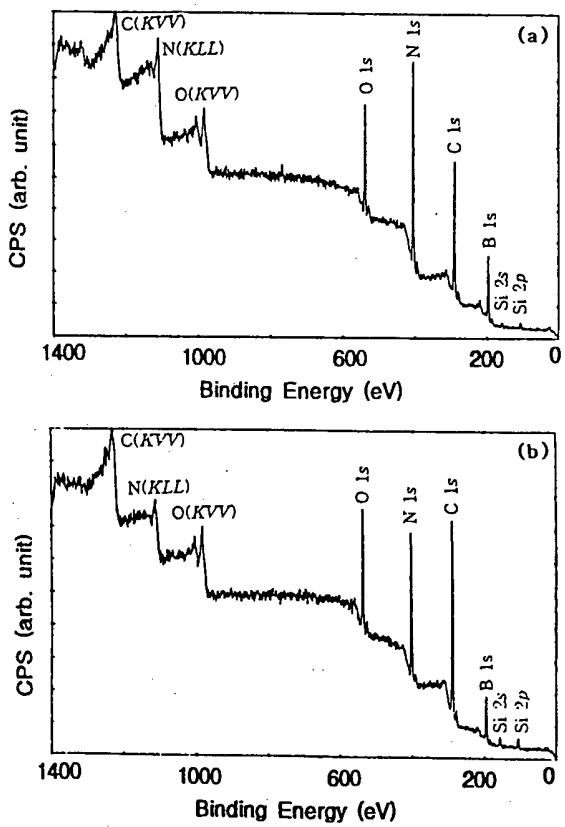

Fig. 3. X-ray photoelectron survey spectra of the h-BN films deposited using $Et_3BNH_2(^tBu)$ on Si(100) substrates at (a) 910 °C and (b) 1000 °C.

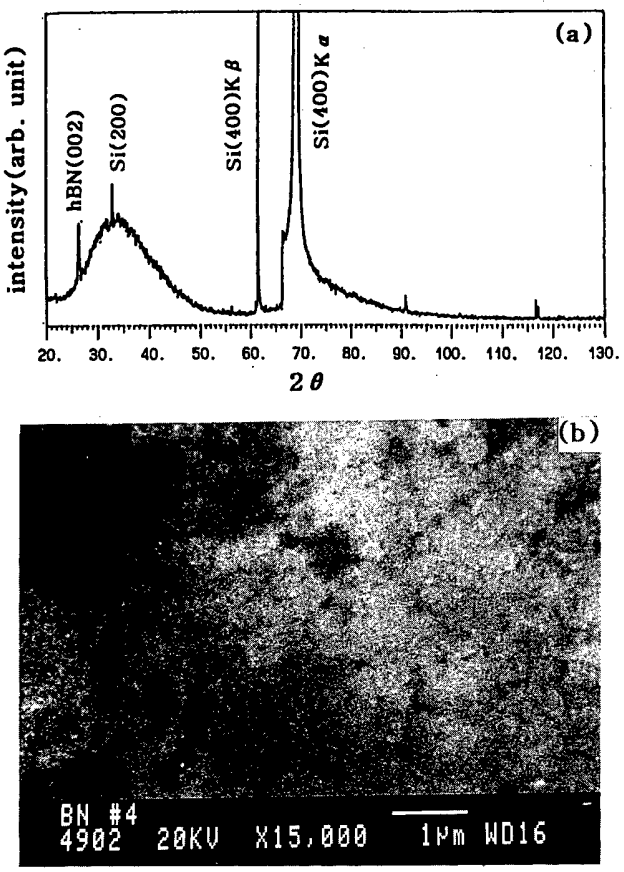

Fig. 4. X-ray diffraction pattern and SEM image of the *h*-BN film grown on Si(100) substrate using $Et_3BNH_2(^tBu)$ at 850 °C; (a) XRD, (b) SEM.

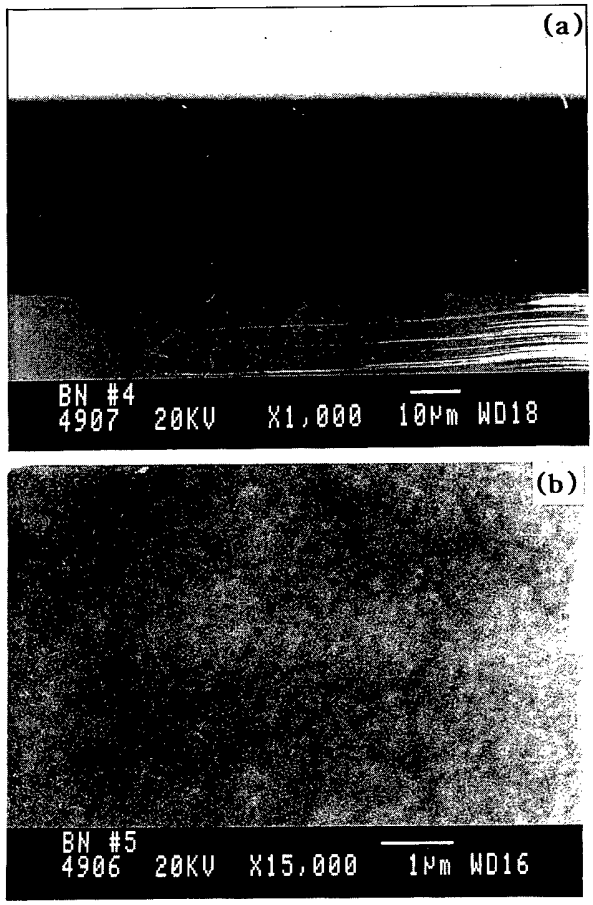

Fig. 5. Cross-sectional and plan-view SEM images of the *h*-BN film grown on Si(100) substrate using $Et_3BNH_2(^tBu)$ at (a) 850 °C and (b) 1000 °C.

The deposited BN films were also characterized by XRD and SEM. Due to the small x-ray cross-section area of boron that is one of the light element, it is very difficult to obtain the x-ray diffraction pattern of BN thin film. Therefore, in this study, we try to grow the BN films with thickness more than 10 μm for obtaining a strong XRD pattern. Figure 4 shows the x-ray diffraction pattern and SEM image of a BN film grown on Si(100) substrate with TEBTBA at 850 °C. X-ray diffraction pattern of the film which was formed at 850 °C showed a hint of hexagonal boron nitride formation, since the *h*-BN coating exhibited a relatively intense BN(002) peak which was appeared at $2\theta = 26.8°$ (see Fig. 4(a)). There is no other detectable phase in the diffraction pattern. The thickness of the as-grown film is approximately 40 μm according to cross-sectional SEM measurement. How- ever, the film's quality of the film is judged poor, and the film surface consists of some minute grains confirmed by SEM as shown in figure 4(b). The cross-sectional SEM photograph of the same BN film as figure 4 is shown in figure 5(a). The photograph of figure 5(a) shows that the thickness of BN film layer is very thick and the interface is showed very sharp indicating good adhesion between BN layer and silicon substrate. Figure 5(b) shows a plan-view SEM image of a BN film grown on Si(100) with TEBTBA at 1000 °C. Much rougher BN film's surface with more grains and hillocks than that of figure 4(b) was obtained. This suggests that the BN film quality and surface smoothness deposited at low temperature as 850 °C are more better than that grown at 1000 °C. The XRD pattern (not shown) of the same BN films grown at 1000 °C showed more higher FWHM values than those of the BN films grown at 850 and 910 °C respectively, signifying poor quality of film. The XPS data shown in figures 2(b) and 3 also shows the same trends as XRD, that is, with increasing the substrate temperature to 1000 °C from 850 °C, the stoichiometry of BN films confirmed with the analysis of the XP high resolution spectra of B1s, N1s, and C1s were drastically changed and the carbon contents were increased due possibly to a formation of BC_xN compounds such as BC_2N or BC_4N-like species along with *h*-BN at 910 and 1000 °C, respectively. According to the previous reports [21,22], a series of BC_xN compounds with x of 0.9, 2, 2.5, 3, 4, and 7 can be synthesized as an intermediate between graphite and *h*-BN. The BC_xN compounds where carbon atoms of graphite are partially substituted by boron and nitrogen at high

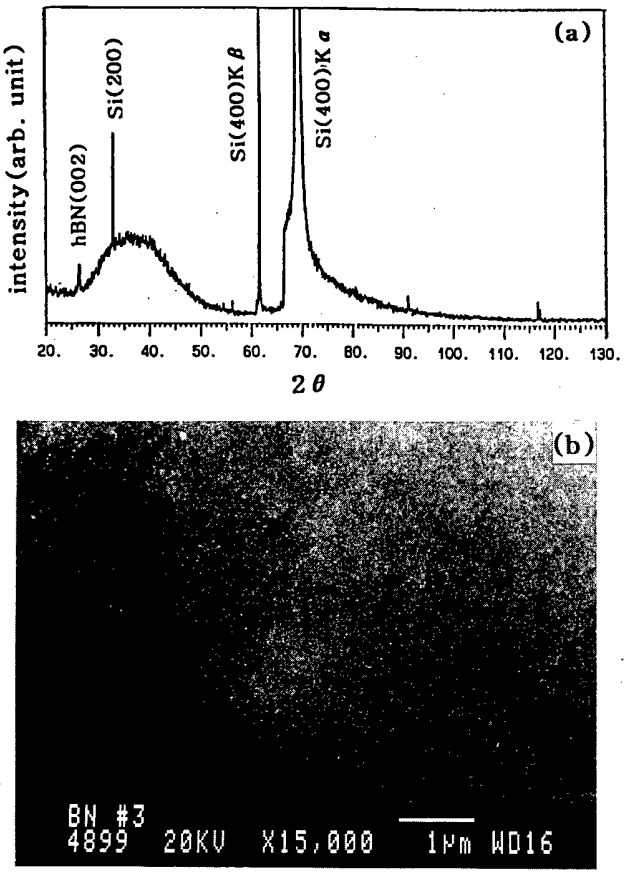

Fig. 6. X-ray diffraction pattern and SEM image of the h-BN film deposited using $Et_3BNH_2(^tPr)$ on Si(100) substrates at 900 °C: (a) XRD, (b) SEM.

temperature are attractive as electronic materials and as superhard materials [23,24].

Typical x-ray diffraction pattern and SEM image of a BN film deposited using TEBIPA at 900 °C are shown in figure 6. The XRD data of figure 6(a) indicates that the film is also hexagonal BN because the characteristic peak due to h-BN is appeared at a 2θ value of ca. 27°. But the figure 6(a) shows that the BN films are more amorphous-like polycrystalline than the film of figure 4(a). At below 900 °C, moreover, only amorphous BN films (not shown) were obtained on Si(100) substrate using the same precursor of TEBIPA, signifying carbon-rich film due to the high growth temperature and more higher bond dissociation of precursor itself compared to that of TEBTBA. The possible explanation of these results can be based on the difference of a functional group attached to the nitrogen atom. Even though the *tert*-butyl group has large size, the bond dissociation energy between N and C of *tert*-butyl group is much lower than that of iso-propyl group. That's why using TEBTBA it is possible to make more good BN film with stoichiometry at lower temperature rather than TEBIPA. But the mechanism of CVD of the single molecular precursors of either $Et_3BNH_2(^tBu)$ or $Et_3BNH_2(^iPr)$ is not yet known, so whatever happens on the substrate surfaces in the initial deposition stage still remains to be investigated. The SEM image of figure 6(b) shows that there was some hillocks on the whole surface of BN film.

IV. CONCLUSIONS

Hexagonal boron nitride (h-BN) thin films have been grown on Si(100) substrates by LPMOCVD method using triethylborane *tert*-butylamine complex (TEBTBA), and triethylborane iso-propylamine complex (TEBIPA) as a new single molecular precursors in the temperature range of 850~1000 °C. Polycrystalline, crack-free h-BN film was successfully grown on Si(100) with both TEBTBA and TEBIPA at temperature as low as 850 °C. At above 900 °C, however, carbon-rich polycrystalline BN was obtained from TEBIPA. With increasing substrate temperatures to 1000 °C, moreover, a carbon-rich compounds as BC_4N-like species are also strongly formed along with h-BN. The high resolution XPS and FTIR are important probes of identifying the crystal structure of the BN films. This growth temperature is very lower than that in previous reports, and this is the first report of h-BN film growth formed from those precursors.

ACKNOWLEDGMENTS

One of authors (J.-H.B) acknowledges to the Faculty Research Fund of the Sungkyunkwan University. Support of this research by the Korea Research Foundation and the Ministry of Science and Technology, Korea is gratefully acknowledged.

REFERENCES

[1] H. Saitoh and W. A. Yarbrough, Diamond Related Mater. **1**, 137 (1992).
[2] S. P. S. Arya and A. D'Amico, Thin Solid Films **157**, 267 (1988).
[3] L. Vel, G. Demazeau and J. Etourneau, Mater. Sci. Eng. **B10**, 149 (1991).
[4] L. Vel. G. Demazeau and J. Etourneau, Diamond Related Mater. **2**, 197 (1993).
[5] L. Wang, P. Irouz, A. Argoita, J. Ma and J. C. Angus, Appl. Phys. Lett. **63**, 1336 (1993).
[6] D. H. Berns and M. A. Cappelli, Appl. Phys. Lett. **68**, 2711 (1996): see also M. Yoshikawa, H. Ishida, A. Ishitani, T. Murakamí, S. Koizumi and T. Inuzuka, J. Appl. Phys. **57**, 428 (1990).
[7] T. Ichiki, S. Amagi and T. Yoshida, J. Appl. Phys. **79**, 4381 (1996).
[8] H. Xin, Y. Chen, X. Shi, H. Xu, C. Lin, S. Zou, Thin Solid Films **266**, 173 (1995).
[9] G. L. Doll, J. A. Sell, C. A. Taylor II and R. Clarke,

Phys. Rev. **B43**, 6816 (1991).
[10] O. Mishima, K. Era, J. Tanaka and S. Yamaoka, Appl. Phys. Lett. **53**, 962 (1988).
[11] C. Comez-Aleixandre, A. Essafti, M. Feranadez, J. L. G. Fierro and J. M. Albella, J. Phys. Chem. **100**, 2148 (1996).
[12] A. H. Cowley and R. A. Jones, Angew. Chem. Int. Ed. Engl. **28**, 1208 (1989).
[13] A. R. Phani, G. S. Devi, S. Roy and V. J. Rao, J. Chem. Soc. Chem. Commun. **1993**, 684.
[14] C. Rohr, J. -H. Boo and W. Ho, Thin Solid Films **322**, 9 (1998).
[15] J. -H. Boo, C. Rohr and W. Ho, J. Crystal Growth **189-190**, 439 (1998).
[16] J. -H. Boo, K. -S. Yu, I. -N. Jung, S. -H. Yoen and Y. Kim, Chem. Mater. **7**, 694 (1995).
[17] J. -H. Boo, K. -S. Yu, M. Lee and Y. Kim, Appl. Phys. Lett. **66**, 3486 (1995).
[18] R. Trehan, Y. Liftshitz and J. W. Rabalais, J. Vac. Sci. Technol. **A6**, 4026 (1990).
[19] T. Mega, R. Morimoto, M. Morita and J. Shimomura, Surf. Interface Anal. **24**, 375 (1996).
[20] R. Geick, C. H. Perry and B. Rupprecht, Phys. Rev. **146**, 543 (1966): see also A. Lehmann, L. Schumann and K. Hubner, Phys. Status Solidi **B121**, 505 (1984).
[21] J. Kouvetakis, T. Sasaki, C. Shen, R. Hagiwara, M. Lerner, K. M. Krishnan and N. Bartlett, Synth. Met. **34**, 1 (1989): see also T. Sasaki, M. Akaishi, S. Yamaoka, Y. Fujiki and T. Oikawa, Chem. Mater. **5**, 695 (1993).
[22] J. Bill and R. Riedel, Mater. Res. Symp. Proc. **271**, 839 (1992).
[23] A. Y. Liu and M. L. Cohen, Science **245**, 841 (1989): see also A. Y. Liu, R. M. Wentzcovitch and M. L. Cohen, Phys. Rev. **B39**, 1760 (1989).
[24] M. O. Watanabe, S. Itoh, T. Sasaki and K. Mizushima, Phys. Rev. Lett. **77**, 187 (1996): see also M. O. Watanabe, S. Itoh, K. Mizushima and T. Sasaki, J. Appl. Phys. **78**, 2880 (1995).

Journal of the Korean Physical Society, Vol. 34, June 1999, pp. S538~S541

Characteristics of Ultrathin Oxide Grown by High Pressure Oxidation for ULSI Device Applications

Tae Moon ROH*, Dae Woo LEE, Jongdae KIM, Sang Gi KIM,
Jin Gun KOO, Kee Soo NAM and Dae Yong KIM

ETRI-Micro-Electronics Technology Laboratory,
Electronics and Telecommunications Research Institute (ETRI), Taejon 305-350

The characteristics of 33~94 Å thick oxides grown by high pressure oxidation (HIPOX) technique in 5 atm O_2 ambient at 700 °C have been investigated to use an insulator for ULSI devices. The oxide thickness extracted by high frequency C-V method is about 10 Å thicker than that measured by TEM. The leakage current of the HIPOX oxide is less than 1.0×10^{-9} A/cm^2 and the breakdown electric field is larger than 12.1 MV/cm. The midgap interface trap density (D_{itm}) of the 75 Å thick HIPOX oxide is about 2.0×10^{10} cm$^{-2}\cdot$eV^{-1} which is comparable to that of control oxide. The D_{itm} variation of the HIPOX oxide is not more than that of control oxide as stress time varies. The n-MOSFET with HIPOX oxide shows higher reliability than that with control oxide.

I. INTRODUCTION

The scaling of ULSI devices needs ultrathin oxide formed by low temperature process to reduce the impurity redistribution, leading to short channel and narrow width effects on MOSFETs. The low temperature methods such as pyrogenic oxidation and low pressure chemical vapor deposition (LPCVD) technologies cause hydrogen incorporated reliability problem [1]. However, a high pressure oxidation (HIPOX) technique in O_2 ambient can alleviate this problem because it reduces both oxidation temperature and time without hydrogen involved gas, resulting in maintaining sharp dopant profiles during the oxidation [2–7]. The high pressure oxidation also significantly reduces the oxidation-induced stacking faults in the silicon [2,4,5]. So far, thick field oxides grown at low temperatures under ambient pressure range up to 500 atm have been widely studied [2,6], but ultrathin oxide has not so much [7].

In this paper, we present the characteristics of 33~94 Å thick oxides grown by HIPOX method in dry O_2 ambient for ULSI device applications. The electrical characteristics of the HIPOX oxides were also compared with those of control oxides grown by conventional thermal oxidation technique. The reliability of n-MOSFETs with HIPOX oxide and control oxide was investigated.

II. EXPERIMENT

MOS capacitors and conventional n-MOSFETs with HIPOX oxide and control oxide were fabricated on p-type, 5", (100) silicon wafers using conventional LOCOS isolation and n^+ doped polysilicon as gate electrode. A 300 Å thick sacrificial oxide was grown and stripped before gate oxide was grown. The HIPOX oxides of 33~94 Å were grown in 5 atm O_2 ambient at 700 °C. To compared with the HIPOX oxide, the control oxides of 46 and 75 Å were also grown by a conventional furnace in dry O_2 ambient at 800 and 850 °C, respectively. A 3000 Å of polysilicon was deposited by LPCVD and doped in $POCl_3$ at 875 °C for 30 min. An n^+ polysilicon gate was defined by photolithography and dry etching techniques. Source/drain were formed by arsenic (As) ion implantation and annealing in N_2 ambient at 875 °C for 30 min. After aluminum metallization, the wafers were sintered in forming gas at 400 °C for 30 min.

The thickness of the oxide was evaluated by high frequency (100 kHz) capacitance-voltage (C-V) method using a HP4275A, and also confirmed by TEM. The electrical characteristics of the oxide were investigated by current-voltage (I-V), time-zero dielectric breakdown (TZDB), high frequency and quasi-static C-V measurement. The I-V and quasi-static C-V were measured by HP4140B, and TZDB measured by HP4145B and HP computer. To compare the reliability of the HIPOX oxide and the control oxide, the interface trap density (D_{it}) of the oxide was evaluated by high frequency and quasi-static C-V measurement after constant current stress. To evaluate the hot carrier effect of n-MOSFET, transconductance (g_m) and threshold voltage (V_t) were measured by HP4156A precision semiconductor parameter analyzer and HP computer.

*E-mail: tmroh@ etri.re.kr, Phone: +82-42-860-6272, Fax: +82-42-860-6108

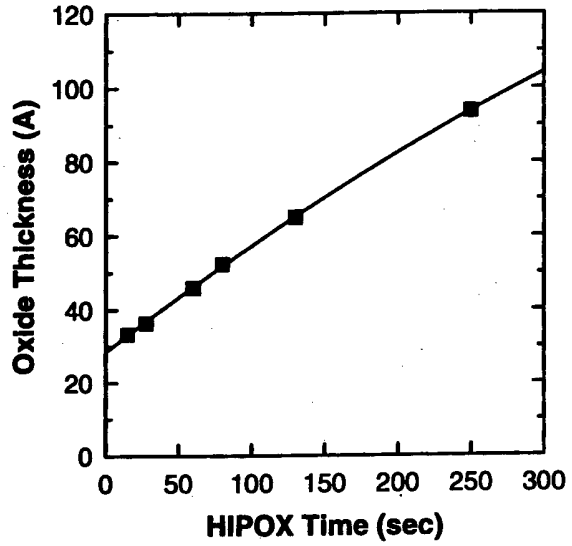

Fig. 1. Oxide thickness variation as a function of HIPOX time (HIPOX condition: 700 °C, 5 atm O_2).

III. RESULTS AND DISCUSSION

Fig. 1 shows the thickness variation of the HIPOX oxide grown at 700 °C in 5 atm O_2 ambient as oxidation time increases. The HIPOX oxide thickness was extracted from the MOS capacitors with those oxides using a high frequency C-V measurement. The MOS capacitor size was 160000 μm^2 and the dielectric constant of the HIPOX oxide was assumed to a customary nominal value of 3.9. The thickness of the HIPOX oxide increases from 33 Å to 94 Å as the oxidation time increases from 15 min to 250 min. In Fig. 1, the oxide thickness increases as the HIPOX time increases.

The physical thickness and the roughness of the interface between the oxide and the silicon (or polysilicon) for the HIPOX oxide and the control oxide and were investigated by TEM photographs (Fig. 2). In Fig. 2, the thickness of the HIPOX oxide and the control oxide are 36 and 36 Å, respectively. However, the thickness of the HIPOX oxide and the control oxide measured by high frequency C-V are 46 and 46 Å, respectively. This means that the physical thickness of the HIPOX oxide and the control oxide is about 10 Å thinner than that of the oxide calculated by high frequency C-V method. This is due to the parasitic capacitance at polysilicon gate and substrate silicon itself because the variation of the dielectric constant can not explain the same difference of the oxide for the various thickness of the oxides. In Fig. 2, the roughness of a few mono-layers in the interface between HIPOX oxide (or control oxide) and silicon substrate (or polysilicon gate) can be seen, which can affect on the electrical characteristics of the oxide.

Fig. 3 shows current-voltage characteristics of MOS capacitors with the HIPOX oxides. To reject a displacement current during the I-V measurement, a staircase

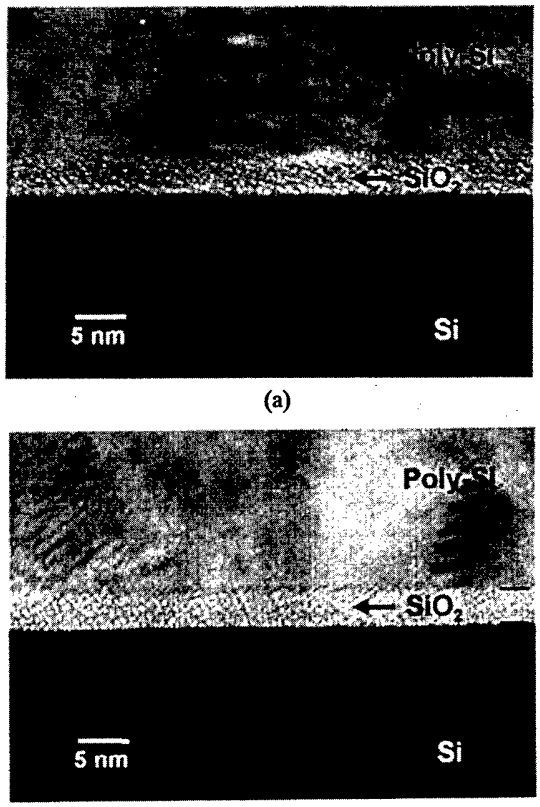

Fig. 2. TEM photographs of HIPOX oxide and control oxide. (a) HIPOX oxide: 700 °C, 5 atm O_2, (b) Control oxide: 800 °C, O_2.

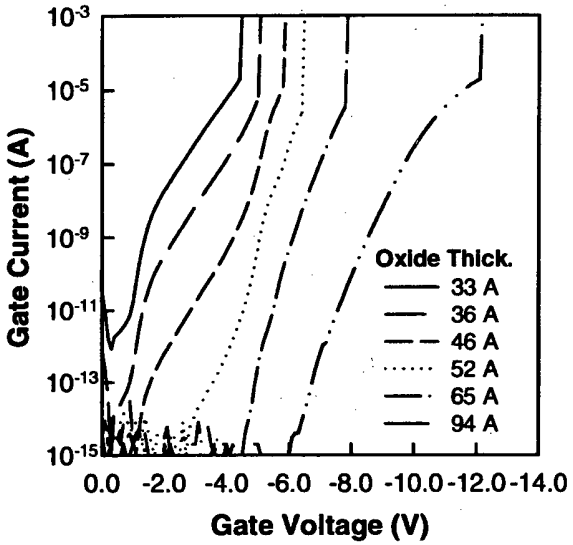

Fig. 3. Current-voltage characteristics of HIPOX oxide versus HIPOX time. The capacitor size was 10000 μm^2.

wave voltage with the step delay time of 5 sec was applied to the MOS capacitor. The leakage current prior to electron tunneling through the oxide, as shown in Fig. 3, is less than 1.0×10^{-9} A/cm^2. Fig. 4 shows the E_{Tunnel}

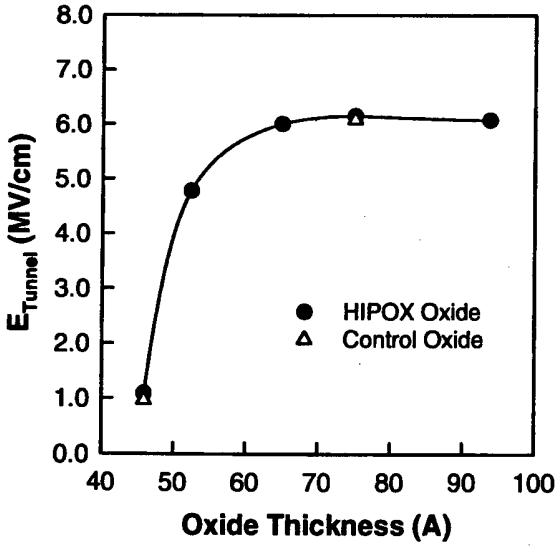

Fig. 4. E_{Tunnel} characteristics of HIPOX oxide control oxide for applied bias polarities as a function of oxide thickness.

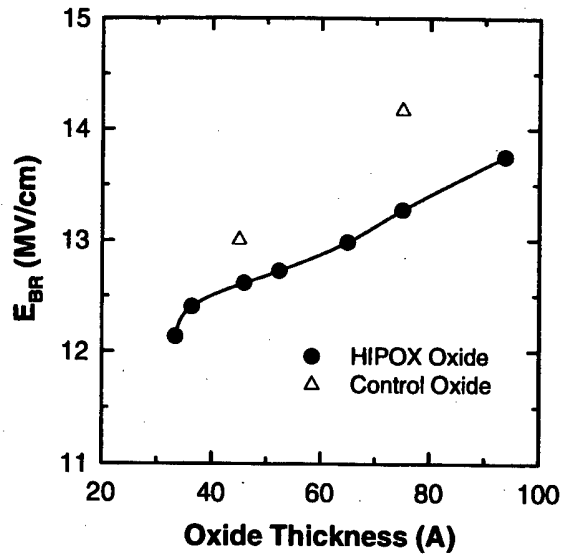

Fig. 5. Dielectric breakdown characteristics of HIPOX oxide and control oxide as a function of oxide thickness.

of the HIPOX oxide and the control oxide as a function of a oxide thickness. The E_{Tunnel}, calculated from Fig. 3, is the electric field needed for the starting electron tunneling current density of 1.0×10^{-9} A/cm^2 through the oxide, considering the flat band voltage and Fermi potential of the MOS capacitor as

$$E_{Tunnel} = (V_{Tunnel} - V_{FB} + (0.55 - \phi))/T_{ox} \qquad (1)$$

where V_{Tunnel} is voltage needed for the starting electron tunneling through the oxide, flat band voltage (V_{FB}) is -0.90 V, Fermi potential (ϕ_F) is 0.35 V, and T_{ox} is oxide thickness. The E_{Tunnel} of 6.0 MV/cm stays constant when the oxide is thicker than 65 Å, while decreases rapidly as the oxide is thinner than 65 Å. The E_{Tunnel} of 46 Å thick HIPOX oxide decreases up to 1.1 MV/cm. Typically, the E_{Tunnel} of 6.0 MV/cm is a electric field required to the electron tunneling through the oxide by Fowler-Nordheim emission [8]. In Fig. 4, one of the main reasons of the E_{Tunnel} reduction results from the interface roughness between the oxide and the silicon substrate (or polysilicon gate), leading to the reduction of local oxide thickness, as shown Fig. 2. The direct electron tunneling through the thin oxide also takes place. The E_{Tunnel} of the control oxides with 46 and 75 Å as shown in Fig. 4 are 1.0 and 6.1 MV/cm, respectively, which are nearly the same values of the HIPOX oxide. This result means that E_{Tunnel} of the oxide is not dependent on the oxidation technology but the oxide thickness.

Fig. 5 shows the dielectric breakdown electric field (E_{BR}) of HIPOX oxide and control oxide obtained by TZDB method. The E_{BR} of the oxide was defined by taking into account the silicon surface band bending using equation (1) as shown in Fig. 4. The E_{BR} of the HIPOX oxide increases from 12.1 to 13.7 MV/cm as the oxide thickness increases from 33 to 94 Å. The E_{BR} of the control oxides with 46 and 75 Å are 13.0 and 14.2 MV/cm, respectively. The E_{BR} of the HIPOX oxide is lower than that of the control oxide.

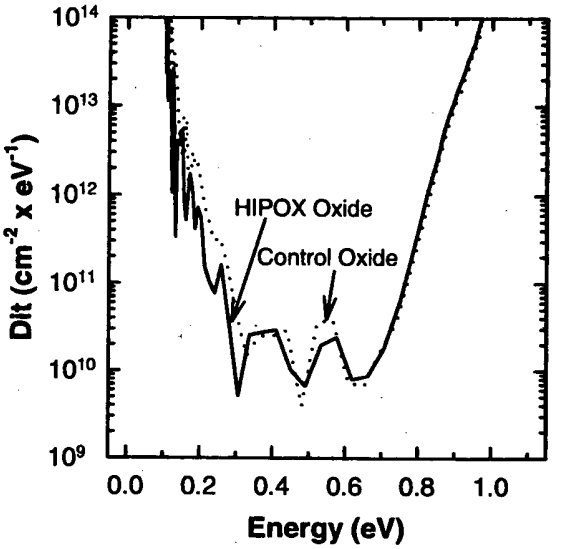

Fig. 6. Interface trap density distribution of 75 Å of HIPOX oxide and the same thickness of control oxide.

To compare the reliability of the HIPOX oxide with that of the control oxide, the D_{it} of the oxides were investigated by high frequency and quasi-static C-V measurement after constant current stress. Fig. 6 shows the D_{it} distribution of the 75 Å of the HIPOX oxide and the same thickness of the control oxide. The virgin midgap interface trap density D_{itm} of the HIPOX oxide is 2.0×10^{10} cm^{-2}·eV^{-1} that is comparable to that of the control oxide. Fig. 7 shows the D_{itm} variation of the HIPOX oxide and the control oxide. The D_{itm} variation of the oxides under the stress current density of -0.1 mA/cm^2 increase as stress time increases. The D_{itm} variation of the HIPOX oxide is nearly same to that of the control

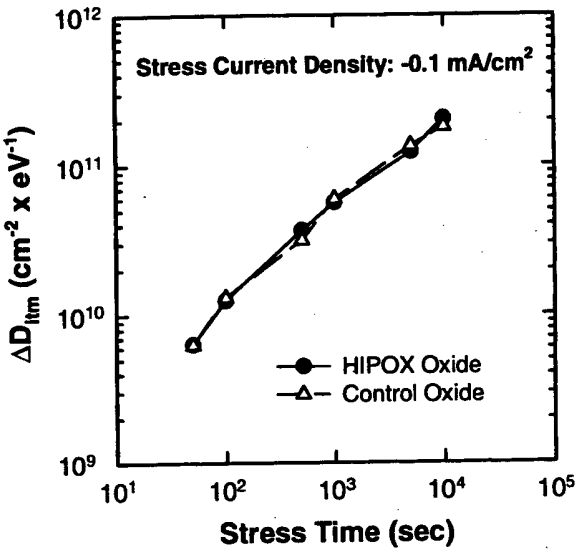

Fig. 7. Midgap interface trap density variation of HIPOX oxide and control oxide as a function of stress time.

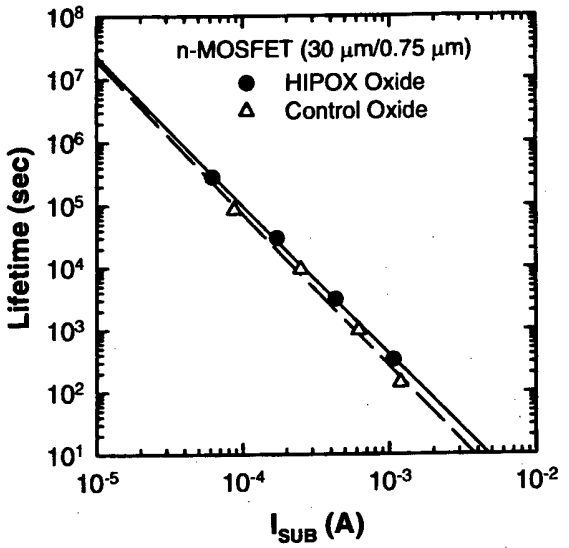

Fig. 8. Lifetime of n-MOSFET with HIPOX oxide and control oxide as a function of substrate current.

oxide as stress time varies. This result indicates that the interface characteristics of the HIPOX oxide is not worse than that of the control oxide and the HIPOX oxide will be a good insulator for ULSI devices because the D_{it} and D_{itm} variation of oxides after electrical stress are strongly dependent on the quality of Si-SiO_2 interface even if the E_{BR} of the HIPOX oxide is lower than that of the control oxide [9].

The hot carrier immunity of MOSFETs are dependent on the reliability of the Si-SiO_2 interface characteristics such as D_{itm} variation after electrical stress [10]. For the application of the ultrathin HIPOX oxide to ULSI devices, n-MOSFETs with the HIPOX oxide and the conventional oxide were fabricated and compared, especially with hot carrier effects of the n-MOSFETs. Fig. 8 shows the lifetime of the n-MOSFETs with the 75 Å of HIPOX oxide and the same thickness of control oxide as a function of substrate current. The lifetime of n-MOSFETs is defined as the time required for $\Delta g_{mmax}/\Delta g_{mmax0}$ to reach 10 % reduction [11]. In Fig. 8, the lifetime of the n-MOSFET with the HIPOX oxide is longer than that of the n-MOSFET with control oxide. These results correspond to the reliability of the oxide shown in Fig. 7 because the relative transconductance reduction of n-MOSFET is linearly proportional to the number of interface traps generated [10].

IV. CONCLUSIONS

The ultrathin HIPOX oxides were grown in 5 atm O_2 ambient at 700 °C, and compared with the control oxides grown by using conventional furnace in atmosphere O_2 ambient at 800 and 850 °C. The thickness of the oxide measured by TEM is 10 Å thinner than that of the oxide extracted by high frequency C-V technique. The HIPOX oxide shows good leakage and interface trap density characteristics, while the dielectric breakdown characteristics of the HIPOX oxide itself are not better than that of the control oxide. The reliability of n-MOSFETs with the HIPOX oxide is better than that of n-MOSFET with the control oxide. Therefore, the ultrathin oxide grown by HIPOX at low temperature can be applied to a gate insulator of ULSI devices because it has many advantages such as low temperature process, better interface characteristics between the oxide and silicon, and better reliability compared to the control oxide although the dielectric breakdown voltage at the HIPOX oxide itself are not better.

REFERENCES

[1] R. A. Gdula, J. Electrochem. Soc. **123**, 42 (1976).
[2] E. A. Irene, D. W. Dong and R. J. Zeto, J. Electrochem. Soc. **127**, 396 (1980).
[3] S. P. Tay, J. P. Ellul, J. J. White and M. I. H. King, J. Electrochem. Soc. **134**, 1484 (1987).
[4] L. N. Lie, R. R. Razouk and B. E. Deal, J. Electrochem. Soc. **129**, 2828 (1982).
[5] L. P. Trombetta, R. J. Zeto, F. J. Feigl and M. E. Zvanut, J. Electrochem. Soc. **132**, 2706 (1985).
[6] S. Marshall, R. J. Zeto and C. G. Thoronton, J. Electrochem. Soc. **122**, 1411 (1975).
[7] M. Hirayama, H. Miyoshi, N. Tsubouchi and H. Abe, IEEE Trans. Electron Devices **ED-29**, 503 (1982).
[8] M. Lenzlinger and E. H. Snow, J. Appl. Phys. **40**, 278 (1969).
[9] D. J. DiMaria, E. Cartier and D. Arnold, J. Appl. Phys. **73**, 3367 (1993).
[10] F.-C. Hsu and S. Tam, IEEE Electron Device Lett. **4**, 50 (1984).
[11] T. M. Roh, D. W. Lee, J. Kim, J. G. Koo and K.-S Nam, 5th ICVC Conference Proceedings, 593 (1997).

Journal of the Korean Physical Society, Vol. 34, June 1999, pp. S542~S545

Effects of Drain Structures on the Hot-Carrier Degradation of High-Voltage LDMOS Transistors

D. W. LEE*, T. M. ROH, J. KIM, J. G. KOO, K. S. NAM and D. Y. KIM

ETRI Micro-Electronics Technology Laboratory, Taejon 305-350

H. S. PARK

Department of Semiconductor Engineering, Uiduk University, Kyongju 780-713

A new high-voltage n-channel LDMOS (nLDMOS) transistor with a convexed drain structure is proposed that can significantly suppress hot-carrier induced device degradation. Under high-field stress condition, it was found that hot-carrier induced specific on-resistance (R_{on}) and drain saturation current (I_{Dsat}) degradations of our proposed LDMOS transistors were about 2~4 times lower than those of conventional LDMOS devices. Such a strong hot-carrier immunity of our proposed nLDMOS device is considered that the amount of hot-carrier generation in the convexed nLDMOS device is much less than the conventional one due to the current spreading at the drain junction.

I. INTRODUCTION

High-voltage lateral-double diffused MOSFET's (LDMOSFET) have been used as basic devices in power discrete devices and integrated circuits. In accordance with scaling down of the device, hot-carrier induced electrical parameter and long-term reliability degradations in high-voltage LDMOS transistors have become a major concern [1]. Generally, two long-term reliability tests were performed on the power MOS transistors: high-temperature reverse-bias (HTRB) test and high-temperature gate stress (HTGS) test [2]. For the case of power LDMOS and VDMOS (vertical-double diffused MOS) transistors with relatively thick gate oxides, both reliability tests are sufficient. However, the thickness of the gate oxide of power transistors has been reduced by the recent advances in multiple Bipolar-CMOS-DMOS (BCD) technology considering the compatibility with dense CMOS logic. From the rapid scaling down and high-current density of LDMOS transistors, hot-carrier induced device degradation and destructive snapback may significantly degrade long-term reliability and also arise another limitation in safe operating area of power devices [1,3]. Hot-carrier degradation in low-voltage nMOS transistors has been intensively investigated [4,5]. On the other hand, much less is known of the hot-carrier behavior in high-voltage transistors. Comparing to low-voltage nMOS transistors, the hot-carrier induced degradations of high-voltage LDMOS transistors are quite different because of the different drain structure and doping profile.

*E-mail: leedw@cadvax.etri.re.kr, Fax: +82-42-860-6108

In this work, we proposed a new high-voltage nLDMOS transistors with a convexed drain structure in order to reduce both current crowding and hot-carrier generation at the drain junction. The hot-carrier induced degradations depending on the different drain structures were investigated in detail.

II. EXPERIMENTAL RESULTS AND DISCUSSION

The layout patterns and schematic cross-section of nLDMOS transistors in this study are shown in Fig. 1(a) with the conventional drain structure, and (b) with the

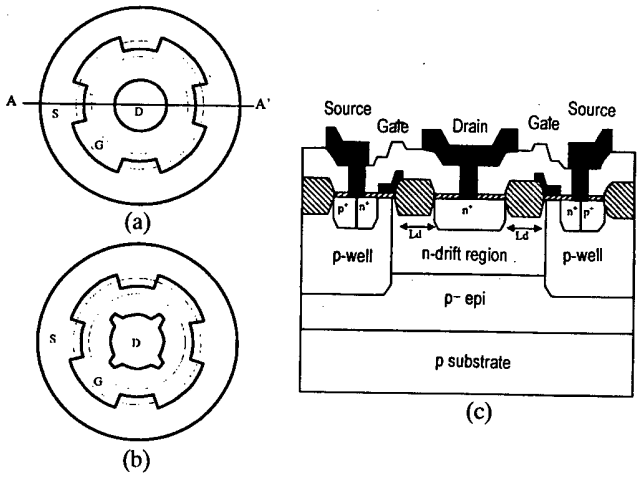

Fig. 1. nLDMOS structures with (a) non-convexed drain, (b) convexed drain and (c) device cross-section (A-A' line).

Table 1. Summary of layout and electrical parameters of the nLDMOS transistor with the convexed drain structure.

Parameter	Value
nLDMOSFET	
– Channel Width, W_c (μm)	38.5
– Channel Length, L_g (μm)	2.4
– Drift Length, L_d (μm)	8.4
– Drain Width, W_d (μm)*	59.1
– Gate Oxide Thickness (Å)	350
Electrical Parameter	
– Threshold Voltage (V)	1.56
– Transconductance, G_m (μS)	53.75
– Sat. Drain Current I_{Dsat} (mA/μm) at V_G/V_{DS} = 10 V/80 V	0.176
– Specific Resistance, R_{on} (Ω·cm^2) at V_G/V_{DS} = 10 V/1 V	5.59
– Breakdown Voltage (V)	160

*) Non-convexed drain structure; W_d=41.5 μm

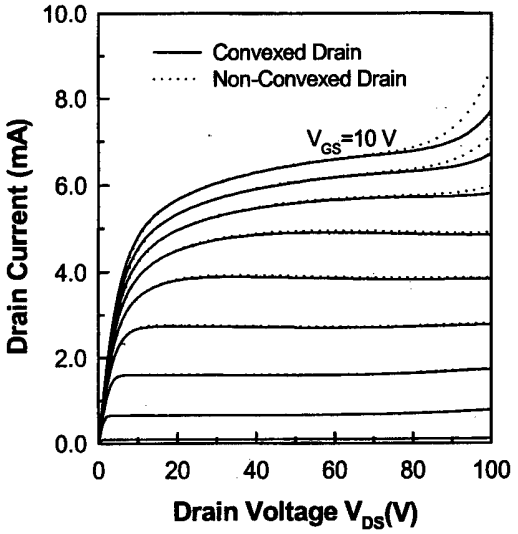

Fig. 2. $I_D - I_{DS}$ characteristics of non-convexed and convexed nLDMOS transistors (V_G: 1 V/step).

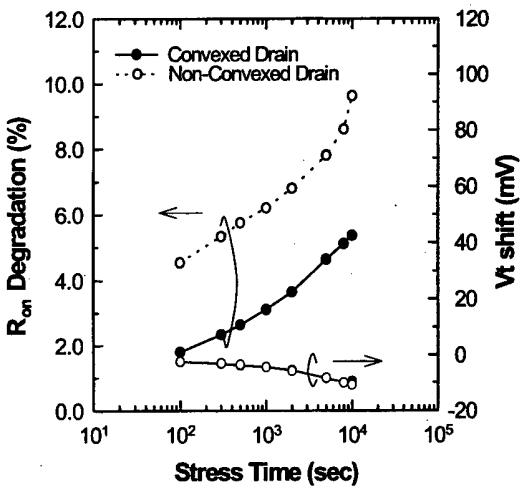

Fig. 3. R_{on} degradation and Vt shift as a function of stress time for non-convexed and convexed nLDMOS transistors (stress condition: V_G = 10 V and V_{DS} = 100 V).

proposed drain structure, respectively. Here, we call that the device shown in Fig. 1(a) is a non-convexed and the other shown in Fig. 1(b) is a convexed nLDMOS transistor for convenience. The source layout was slightly modified to improve the controllability of drain current density. The nLDMOS with a convexed drain was designed to uniformly spread the channel current and alleviate the current crowding which can cause high level of hot-carrier generation and destructive snapback at the drain junction. As shown in Table 1, channel length (L_g) and width (W_c) of the nLDMOS transistor were 2.4 and 38.5 μm, respectively. The drift length (L_d) of the device was 8.4 μm. The schematic cross-section of the nLDMOS device is similar to conventional nLDMOS transistor as shown in Fig. 1(c). To fabricate the nLDMOS transistors, 25 μm thick p-type epitaxial layer ($\rho = 5 \sim 8\ \Omega$·cm) was first grown on the boron-doped substrate. A drift region was implanted by phosphorus, 2.0×10^{12} cm^{-2} at 100 keV. A deep p-well, which acts as a channel of nLDMOS transistor, was implanted by using boron with a dose of 4.0×10^{13} cm^{-2}, and annealed at 1200 °C in N_2 ambient. After local oxidation process, a 350 Å gate oxide was grown. The process sequences such as polysilicon gate, source/drain, and double metal formation processes in this work were almost same as conventional CMOS process. After double metallization, the devices were annealed at 400 °C in N_2 ambient.

Fig. 2 demonstrates the typical $I_D - V_{DS}$ characteristics of both our proposed convexed and non-convexed nLDMOS devices. The threshold voltage of nLDMOS exhibited approximately 1.56 V. From the figure, in particular, the drain current of non-convexed nLDMOS was rapidly increased especially when the applied voltages of gate and drain terminals were simultaneously high. This rapid increase of drain current may be caused by the hot-carrier generation at the drain junction. And this phenomenon results from the more current crowding in the non-convexed nLDMOS than that in the convexed one at the drain edge. An off-state breakdown voltage was revealed approximately 160 V. Other electrical parameters were summarized in Table 1.

Fig. 3 shows the hot-carrier induced specific on-resistance (R_{on}) and threshold voltage degradations depending on the stress time. The on-state stress was done at V_G = 10 V and V_{DS} = 100 V. It is evident from the figure that the hot-carrier induced on-resistance degradation of the non-convexed nLDMOS transistor was about two times larger than that of the convexed nLDMOS device. It is presumed that the amount of hot-carrier generation in a convexed nLDMOS device is suppressed due to the current spreading at the drain junction. On the other hand, the threshold voltage shifts of the two de-

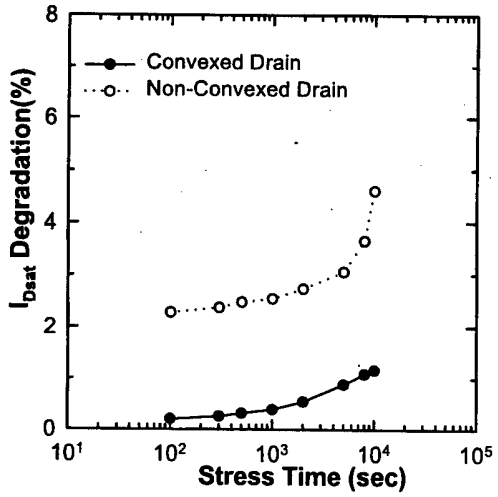

Fig. 4. I_{Dsat} degradation versus stress time of non-convexed and convexed nLDMOS transistors (stress condition: $V_G = 10$ V and $V_{DS} = 100$ V).

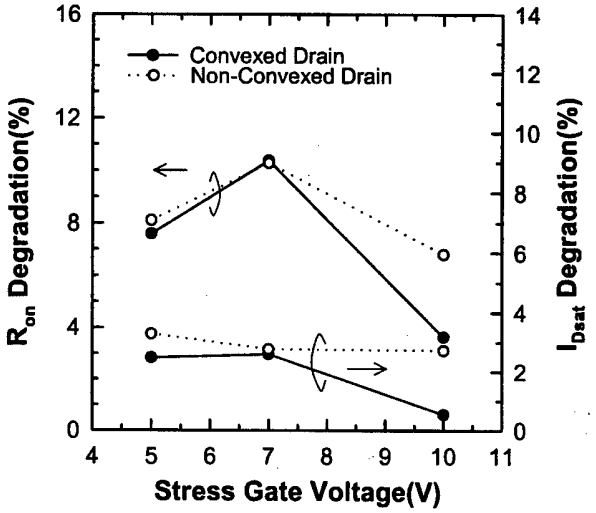

Fig. 5. R_{on} and I_{Dsat} degradation as a function of stress gate voltage for non-convexed and convexed nLDMOS transistors (stress condition: $V_{DS} = 100$ V, stress time=2×10^3 sec).

vices were similar. Up to the stress time 10,000 seconds, threshold voltage of two devices was shifted from about 10 mV. This results suggest that the maximum channel field is located at the drift region where the interface-state generation or electron trapping is mainly occurred [1,3].

We also investigated a drain saturation current (I_{Dsat}) degradation as a function of stress time. A drain saturation current was measured at $V_G = 5$ V and $V_{DS} = 80$ V. As shown in Fig. 4, the drain saturation current degradations of the non-convexed and convexed nLDMOS transistors for the stress time of 1,000 seconds were 2.5 % and 0.4 %, respectively. Comparing to specific on-resistance degradation, two devices have shown similar degradation trend. But the increment of I_{Dsat} degradation of non-convexed drain was much rapid with increasing the stress time.

Fig. 5 demonstrates the drain saturation current and specific on-resistance degradations depending on the different gate voltages while the stressed drain voltage and time are fixed at $V_{DS} = 100$ V and 2,000 seconds, respectively. It was found that the maximum degradation of specific on-resistance was monitored at the gate voltage of 7 V in both the convexed and non-convexed nLDMOS transistors. For the case of the stress gate voltage below 7 V, the difference of hot-carrier degradations between the two devices was very small. However, as the stressed gate voltage increases up to 10 V, hot-carrier induced R_{on} (6.8 %) and I_{Dsat} (2.7 %) degradations of the non-convexed nLDMOS device were much greater than those of the convexed one (R_{on} : 3.6 % and I_{Dsat} : 0.6 %). Therefore, hot-carrier degradations depending on the drain structures are dominantly monitored under the high gate and drain voltage regions. Moreover, specific on-resistance degradation was much larger than drain saturation current degradation under the same stress gate voltage. Then, the specific on-resistance was more prone to hot-carrier degradation than the drain saturation current.

III. CONCLUSIONS

We proposed a new high-voltage nLDMOS transistor with convexed drain structure, which can effectively reduce both current crowding and hot-carrier generation at the drain junction. Due to the hot-carrier induced current component, the drain current of non-convexed nLDMOS rapidly increased at the high gate and drain biased regions. Under the $V_G = 10$ V and $V_{DS} = 100$ V stressed condition, the drain saturation current and specific on-resistance degradations of non-convexed nLDMOS transistors were approximately 2 or 4 times larger than those of convexed nLDMOS devices. Moreover, as the stressing gate voltage increased up to 10 V, hot-carrier induced R_{on} (6.8 %) and I_{Dsat} (2.7 %) degradations of the non-convexed nLDMOS device were much greater than those of the convexed one (R_{on} : 3.6 % and I_{Dsat} : 0.6 %). It is evident that the hot-carrier degradation depending on the drain structure is dominantly monitored under the high gate and drain voltage regions. Therefore, our proposed high-voltage nLDMOS transistor may be applied to power IC that requires long-term hot-carrier reliability.

REFERENCES

[1] A.W. Ludikhuze, M. Slotboom, A. Nezar, N. Nowlin and R. Brock, Proceeding of ISPSD, 53 (1997).
[2] S. Manzini and C. Contiero, Proceeding of ISPSD, 65

(1996).
[3] R. Versari, A. Pieracci, S. Manzini, C. Contiero and B. Ricco, Proceeding of IEDM, 371 (1997).
[4] P. T. Lai, J. P. Xu, W. M. Wong, H. B. Lo and Y. C. Cheng, IEEE Trans. on Electron Devices **45**, 521 (1998).
[5] T. Wang, T. E. Chang, C. H. Wang, N. K. Zous and C. Huang, IEEE Trans. on Electron Devices **45**, 1511 (1998).

Journal of the Korean Physical Society, Vol. 34, June 1999, pp. S546~S550

Improved Method for Electro-optical Simulation of Liquid Crystal Displays

Sung-Min JUNG and Woo-Sang PARK*

School of Electrical and Computer Engineering, Inha University, Inchon 402-751

The deformation profile of molecule directors inside liquid crystal displays and the light propagation through a given deformation profile are discussed in this paper. A modified algorithm from Chen's method is proposed to obtain a general deformation profile. This method enables us to accomplish stable and fast calculation of various molecular orientation profiles. The analytical expression for the eigenvectors related to the light propagation through uniaxial anisotropic media is also presented, based on the set of eigenvetors described by Berreman. It is clarified that the calculation speed of this method is more than twice faster than the faster 4×4 matrix method.

I. INTRODUCTION

Recently, owing to the widespread applications of liquid crystal displays (LCDs), there has been a remarkable interest in designing LCDs with wide viewing angle, good contrast ratio and fast response time. In order to obtain good electro-optical characteristics of LCDs, a rigorous simulation for optimizing material and device parameters is essentially required. The simulations are generally classified into two physical problems; one is to describe the deformation profile of molecule directors inside the cell with an applied voltage, and the other is to solve the light propagation through a given deformation profile.

For the time-varying deformation profile, the relaxation method was suggested by Berreman [1,2]. Some methods based on a discretized expression have since been proposed to solve a general deformation profile of LCDs [3,4]. Most of these methods, however, require too much time in the numerical calculation because of their iterative procedure. Chen proposed a general method to improve the problems by applying an analytical model to the LCDs with general boundary conditions [5,6]. However, this method has some problems of both stability and convergence speed in finding the numerical solutions.

For the light propagation through an inhomogeneous cell, the 4×4 propagation matrix method introduced by Teitler and Henvis [7], was first applied to LCDs by Berreman [8]. In this method, the liquid crystal layer is divided into many thin slabs to consider each slab as homogeneous one. The whole transfer matrix given by the product of the propagation matrices for the individual slabs, describes the relation between the tangential components of the electric and magnetic fields at the entrance of the liquid crystal layer and those at the exit. For accurate approximation in this method, each slab must be taken sufficiently thin to neglect the effect of higher-order terms on the power series of the propagation matrix [9]. As the slab becomes thinner, however, it takes much time to manipulate the matrices. Wöhler derived an exact analytical expression [10,11] for the 4×4 propagation matrix by means of the Cayley and Hamilton theorem. This requires much less computation time compared with the original Berreman's 4×4 matrix method. However, it still requires rather long numerical calculation time because of the several operations of matrix product.

In this paper, we discuss a modified algorithm from Chen's method [5] for obtaining a general deformation profile. We also present an analytical expression for the eigenvectors related to the light propagation through uniaxial anisotropic media, based on the set of eigenvectors described first by Berreman. Finally, we apply this method to calculate the electro-optical characteristics of both LCDs and polarizers, and compare the accuracy and calculation speed of this method with those of the conventional methods.

II. CALCULATION OF DEFORMATION PROFILE

The equilibrium deformation profile of LCDs under a constant applied voltage is obtained by minimizing the electric Gibbs free energy, which depends not only on the director configuration but also on the electric condition. Chen presented a general method [5] to solve the deformation profile of chiral nematic liquid crystal displays with asymmetric pretilt angles for the strong anchoring. This method is based on minimizing the Gibbs free energy by using Euler-Lagrangian equations and Newton-Rhapson method for the numerical calculation.

Taking the z axis perpendicular to the cell plates with

*E-mail: wspark@inha.ac.kr, Phone: +82-32-860-7762

thickness d in cartesian coordinates and defining the molecular director as tilt angle θ and twist angle ϕ, we obtain the following equations describing the relations between the cell gap thickness d, total twist angle ϕ_s and the applied voltage V.

$$d = \pm\left(\int_{\theta_{s1}}^{\theta_m} + \int_{\theta_{s2}}^{\theta_m}\right)\left|\sqrt{N(\theta)}\right| d\theta \qquad (1)$$

$$\phi_s = \pm\left(\int_{\theta_{s1}}^{\theta_m} + \int_{\theta_{s2}}^{\theta_m}\right)\frac{B+k_{22}\frac{2\pi}{p}\cos^2\theta}{g(\theta)}\left|\sqrt{N(\theta)}\right| d\theta \qquad (2)$$

$$V = \mp\left(\int_{\theta_{s1}}^{\theta_m} + \int_{\theta_{s2}}^{\theta_m}\right)\frac{D_z}{\epsilon_p\sin^2\theta+\epsilon_v\cos^2\theta}\left|\sqrt{N(\theta)}\right| d\theta \qquad (3)$$

where,

$$N(\theta) = \frac{f(\theta)}{\left(\begin{array}{l} f(\theta_m)\left(\frac{d\theta}{dz}\right)_{\theta=\theta_m} + \frac{\left(B+k_{22}\frac{2\pi}{p}\cos^2\theta_m\right)^2}{g(\theta_m)} - \frac{\left(B+k_{22}\frac{2\pi}{p}\cos^2\theta\right)^2}{g(\theta)} \\ + \frac{D_z^2}{\epsilon_p\sin^2\theta+\epsilon_v\cos^2\theta} - \frac{D_z^2}{\epsilon_p\sin^2\theta_m+\epsilon_v\cos^2\theta_m} \end{array}\right)}$$

$$f(\theta) = k_{11}\cos^2\theta + k_{33}\sin^2\theta$$

$$g(\theta) = (k_{22}\cos^2\theta + k_{33}\sin^2\theta)\cos^2\theta. \qquad (4)$$

Here θ_{s1} and θ_{s2} are pretilt angles of z=0 and z=d, respectively; θ_m is the maximum tilt angle; $(d\theta/dz)_{\theta=\theta_m}$ is gradient of tilt angle at the maximum tilt angle; B is an integration constant of z [5]; D_z is the z-directional component of displacement vector; k_{11}, k_{22} and k_{33} are the elastic constants of liquid crystals for splay, twist and bend, respectively; p is the chiral pitch; ϵ_p and ϵ_v are the parallel and perpendicular components of the dielectric constants of liquid crystals, respectively. The unknown parameters in the equations θ_m, $(d\theta/dz)_{\theta=\theta_m}$, D_z and B can be solved by using the Newton-Rhapson method [12].

In case that θ_m is located between θ_{s1} and θ_{s2}, however, there may be some problems in choosing the initial values of the parameters, especially θ_m, for the numerical calculation. Because the function to be integrated is a complex trigonometric function of θ_m, θ_m do not converge unconditionally to the solution but diverge for an improper initial value.

In this method, taking θ_m as a known parameters to avoid divergence in finding the solution of θ_m, we input the value of θ_m and then find the two remaining parameters B and D_z by applying Newton-Rhapson method to equations (1) and (2). Finally, solving the following equations (5) and (6) with B and D_z, we obtain the deformation profile.

$$z = \pm\left(\int_{\theta_{s1}}^{\theta} + \int_{\theta_{s2}}^{\theta}\right)\left|\sqrt{N(\theta)}\right| d\theta \qquad (5)$$

$$\phi = \pm\left(\int_{\theta_{s1}}^{\theta} + \int_{\theta_{s2}}^{\theta}\right)\frac{B+k_{22}\frac{2\pi}{p}\cos^2\theta}{g(\theta)}\left|\sqrt{N(\theta)}\right| d\theta \qquad (6)$$

The relation between the applied voltage V and θ_m is also derived from equation (3).

III. CALCULATION OF LIGHT PROPAGATION

Choosing coordinates such that z-axis is normal to the interface and the plane of incidence is in xz-plane, Berreman formulated following four linear differential equations for the light propagation in stratified anisotropic media, based on Maxwell's equations [8],

$$\frac{\partial\boldsymbol{\psi}}{\partial z} = ik\Delta\boldsymbol{\psi} \qquad (7)$$

where $k = \omega/c = 2\pi/\lambda$, λ is the wavelength of the incident lights, $\boldsymbol{\psi}$=$[E_x,\ H_y,\ E_y,\ -H_x]^T$ is the wave vector, and

$$\Delta = \begin{bmatrix} \Delta_{11} & \Delta_{12} & \Delta_{13} & 0 \\ \Delta_{21} & \Delta_{11} & \Delta_{23} & 0 \\ 0 & 0 & 0 & 1 \\ \Delta_{23} & \Delta_{13} & \Delta_{43} & 0 \end{bmatrix}$$

$$\Delta_{11} = -X\epsilon_{13}/\epsilon_{33}$$
$$\Delta_{12} = 1 - X^2/\epsilon_{33}$$
$$\Delta_{13} = -X\epsilon_{23}/\epsilon_{33}$$
$$\Delta_{21} = \epsilon_{11} - \epsilon_{13}^2/\epsilon_{33}$$
$$\Delta_{23} = \epsilon_{12} - \epsilon_{13}\epsilon_{23}/\epsilon_{33}$$
$$\Delta_{43} = \epsilon_{22} - \epsilon_{23}^2/\epsilon_{33} - X^2$$
$$X = n_i\sin\theta_i. \qquad (8)$$

The eigenvalues of the matrix Δ related mainly to the dielectric tensor ϵ can be derived as

$$\lambda_{1,2} = \pm\sqrt{\epsilon_\perp - X^2}$$

$$\lambda_{3,4} = -\frac{\epsilon_{13}}{\epsilon_{33}}X \pm \frac{(\epsilon_\parallel\epsilon_\perp)^{1/2}}{\epsilon_{33}}\left\{\epsilon_{33} - \left(1 - \frac{\Delta\epsilon}{\epsilon_\parallel}\sin^2\theta\cos^2\phi\right)X^2\right\}^{1/2}, \qquad (9)$$

with $\Delta\epsilon$=$\epsilon_\parallel - \epsilon_\perp$. For each eigenvalue of equation (9), we find a corresponding eigenvector as follows :

$$\psi_j = N_j \begin{bmatrix} b_j(\Delta_{11}-\lambda_j)-\Delta_{23}a_j \\ -\Delta_{21}b_j \\ -\Delta_{21}a_j \\ \lambda_j\Delta_{21}a_j \end{bmatrix}$$
$$a_j = \Delta_{21}\Delta_{23}-\Delta_{13}(\Delta_{11}-\lambda_j)$$
$$b_j = \Delta_{13}\Delta_{23}-(\Delta_{43}-\lambda_j^2)(\Delta_{11}-\lambda_j), \quad (10)$$

where N_j stands for normalization factor. From the set of four eigenvectors, the 4×4 matrix Ψ with elements ψ_{ij} may then be obtained. The diagonal phase matrix $\boldsymbol{K}$ is also obtained from the eigenvalues of equation (9) as

$$K_{jj} = e^{iq_jh}, \quad \text{where} \quad q_j = \frac{\lambda_j\omega}{c}. \quad (11)$$

The matrices $\boldsymbol{P}$ and $\boldsymbol{F}$ are then evaluated as follows;

$$\boldsymbol{P} = \Psi^{-1}\boldsymbol{K}\Psi \quad (12)$$
$$\boldsymbol{F} = \boldsymbol{P}_N\boldsymbol{P}_{N-1}\cdots\boldsymbol{P}_1, \quad (13)$$

where $\boldsymbol{F}$ is the transfer matrix for the whole liquid crystal layer.

On the other hand, the relation between the incident and transmitted field vectors can be represented as [8]

$$\begin{bmatrix} T_x \\ T_y \end{bmatrix} \begin{bmatrix} a_{11} & a_{12} \\ a_{21} & a_{22} \end{bmatrix} \begin{bmatrix} E_x \\ E_y \end{bmatrix}, \quad (14)$$

where

$$a_{11}=(g_{32}+g_{42})/D, \quad a_{12}=-(g_{12}+g_{22})/D$$
$$a_{21}=-(g_{31}+g_{41})/D, \quad a_{22}=(g_{11}+g_{21})/D \quad (15)$$

and $D=(g_{11}+g_{21})(g_{32}+g_{42})-(g_{21}+g_{22})(g_{31}+g_{41})$. The elements g_{ij} are related to the elements of the matrix $\boldsymbol{F}$, the incident angle and the refractive index of surroundings [8]. Replacing E_x, E_y, T_x and T_y in equation (14) to E_s, E_p, T_s and T_p, respectively, the transmittance for the incident wave of random polarization is derived as

$$T = \frac{1}{2}\frac{n_t\cos\theta_t}{n_i\cos\theta_i} \quad (16)$$
$$\left\{|a_{11}|^2\frac{\cos^2\theta_i}{\cos^2\theta_t}+\frac{|a_{12}|^2}{\cos^2\theta_t}+|a_{21}|^2\cos^2\theta_i+|a_{22}|^2\right\},$$

where θ_i and θ_t stand for the incident and transmitted anlges, respectively; n_i and n_t stand for the refractive indices of the entrance and exit, respectively. This equation can be also used for calculating the transmittance of polarizers.

Polarizers are considered as thin absorbing plates of uniaxial anisotropic media with complex indices of refraction. The optic axis of polarizers is located in xy-plane, so that the dielectric tensor is described as a relatively simple form. Therefore, the eigenvalues of the matrix Δ is given as

$$\lambda_{1,2} = \pm\sqrt{\epsilon_\perp - X^2}$$
$$\lambda_{3,4} = \pm\sqrt{\left(\frac{\epsilon_\parallel\epsilon_\perp}{\epsilon_{33}}\right)\cdot\left(1-\frac{X^2}{\epsilon_{33}}\right)} \quad (17)$$

The elements of the matrix Δ is also simplified as follows;

$$\Delta = \begin{bmatrix} 0 & 1-\frac{X^2}{\epsilon_{33}} & 0 & 0 \\ \epsilon_{11} & 0 & \epsilon_{12} & 0 \\ 0 & 0 & 0 & 1 \\ \epsilon_{12} & 0 & \epsilon_{22}-X^2 & 0 \end{bmatrix} \quad (18)$$

From this matrix, the eigenvectors of polarizers are obtained as

$$\psi_j = N_j \begin{bmatrix} \left(1-\frac{X^2}{\epsilon_{33}}\right)(\epsilon_{22}-X^2+\lambda_j^2) \\ -\lambda_j(\epsilon_{22}-X^2+\lambda_j^2) \\ \epsilon_{12}\left(1-\frac{X^2}{\epsilon_{33}}\right) \\ -\lambda_j\epsilon_{12}\left(1-\frac{X^2}{\epsilon_{33}}\right) \end{bmatrix} \quad (19)$$

Following the procedure of equations (12)~(16) with these eigenvectors, we obtain the transmittance of polarizers.

IV. RESULTS AND DISCUSSION

Using the modified algorithm from Chen's method, we calculated the molecular orientation profile of liquid crystals. In this calculation, one-dimensional model is used, and strong anchoring is assumed so that the surface energy is neglected. The values of simulation parameters are listed in Table 1.

Figure 1 shows the tilt angle θ and twist angle ϕ as a function of distance z for a twisted nematic cell with pretilt angles of 2° and 10°. It is clarified that the result of the present method agrees very well with that of Chen's method as in figure 1. Figure 2 shows the deformation profile for a hybrid aligned nematic (HAN) mode with pretilt angles of 3° and 90°. As the applied voltage increases, the tilt angle varies abruptly near the substrate of pretilt angle 3° and varies slowly near the pretilt angle 90°. Fig. 3 indicates the optical transmittance calculated by the eigenvector method, as a function of applied volt-

Table 1. List of parameters used in the simulation.

Input parameter	Value
Cell thickness d	5 μm
Ordinary refractive index n_o	1.47
Extraordinary refractive index n_e	1.57
Parallel dielectric constant ϵ_p	5.61
Perpendicular dielectric constant ϵ_v	5.31
Splay elastic constant k_{11}	2.91×10^{-12} [N/m]
Twist elastic constant k_{22}	2.03×10^{-12} [N/m]
Bend elastic constant k_{33}	3.70×10^{-12} [N/m]
n_o for polarizer	1.5−j0.000025
n_e for polarizer	1.5−j0.0015
Polarizer thickness	210 μm
Input wavelength λ	550 nm

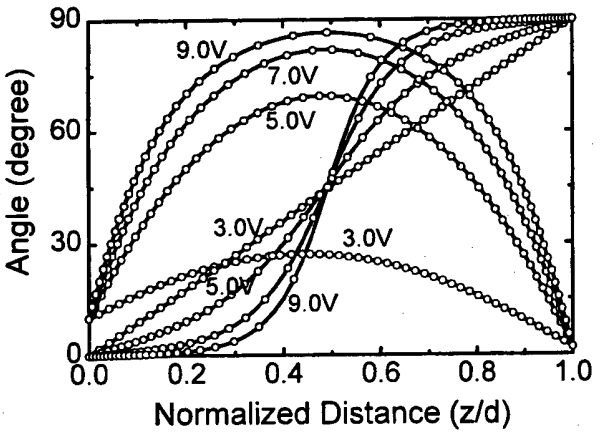

Fig. 1. Deformation profile of asymmetric twist nematic LCD with pretilt angles 2° and 10° at various applied voltages. The solid lines and circles indicate the results obtained by the modified method and Chen's method, redpectively.

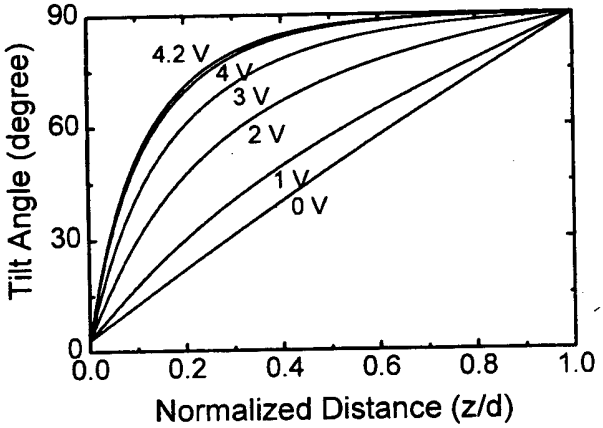

Fig. 2. Deformation profile of hybrid aligned nematic (HAN) mode at different applied voltages.

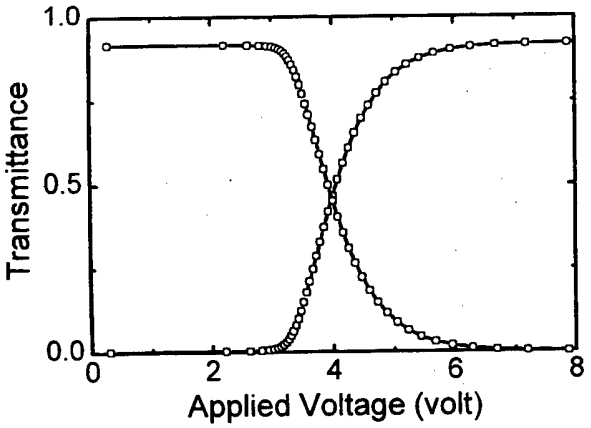

Fig. 3. Optical transmittance as a function of applied voltage for both normally black and white modes. The solid lines illustrate the results obtained by the eigenvector method. The result obtained by the faster 4×4 matrix method are also shown as circles for comparison.

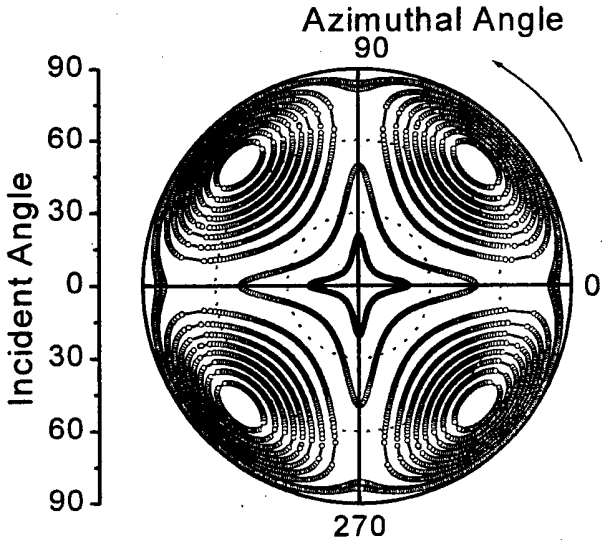

Fig. 4. Contour plot of transmittance as a function of incident and azimuthal angles for two crossed polarizers. The solid lines indicate the results obtained by the eigenvector mehtod. The results from Yeh's 4×4 method are also plotted as circles on the figure for comparison.

age for both normally black and white modes with normal incident light. For comparison, we also present the result obtained by using the faster 4×4 matrix method. The two results indicate complete agreement as shown in figure 3.

As an another example, we calculated the optical transmittance of two crossed polarizers, and showed the result in figure 4. The result agrees well with that of Yeh's 4×4 matrix method [13,14]. The transmittance of two crossed polarizers, namely leakage light, increases gradually up to the incident angle about 80°, and then decreases abruptly due to the increase of reflection. As can be seen in figure 4, a small amount of leakage is observed even for the normal incident angle. From the results shown in figure 3 and 4, the eigenvector matrix, faster 4×4 matrix and Yeh's 4×4 matrix methods are found to be all accurate for the electro-optical calculation. The computation speed, however, of the eigenvector matrix method is more than twice faster than the faster 4×4 matrix method, and as fast as Yeh's 4×4 matrix method.

V. CONCLUSIONS

We proposed a modified algorithm from Chen's method for obtaining a general deformation profile. In case that the maximum tilt angle θ_m is located between the two substrates, taking θ_m as a known parameter to avoid divergence in finding the solution of θ_m, we input the value of θ_m, and then find the solutions of the two remaining parameters B and D_z. This method enables us to accomplish stable and fast calculation of a general

molecular orientation profile. We also presented an analytical expression for the eigenvectors related to the light propagation through uniaxial anisotropic media, based on the set of eigenvetors described first by Berreman. Applying the eigenvector method to both LCDs and two crossed polarizers, we are convinced that the calculation speed of this method is more than twice faster than the faster 4×4 matrix method, and as fast as Yeh's 4×4 matrix method. Therefore, this method is considered to be effective, with Yeh's 4×4 matrix method, for the calculation in which accuracy and speed are required, such as computing both the leakage of two crossed polarizers and the viewing angle dependence of LCDs.

ACKNOWLEDGMENTS

The author would like to thank G. B. Park for the numerical calculations. This work was supported by the G-7 project of Korea.

REFERENCES

[1] D. W. Berreman, Appl. Phys. Lett. **25**, 12 (1974).
[2] D. W. Berreman, J. Appl. Phys. **46**, 3746 (1975).
[3] C. Z. van Doorn, J. Appl. Phys. **46**, 3738 (1975).
[4] I. Heynderickx, Phys. Rev. **A37**, 1725 (1988).
[5] C. J. Chen, M. I. Nathan and A. Lien, SID '95 Digest, 548 (1995).
[6] Y. Saitoh, H. Takano, C. J. Chen and A. Lien, SID '96 Digest, 662 (1996).
[7] S. Teitler and B. Henvis, J. Opt. Soc. Am. **60**, 830 (1970).
[8] D. W. Berreman, J. Opt. Soc. Am. **62**, 502 (1972).
[9] D. W. Berreman, J. Opt. Soc. Am. **63**, 1374 (1973).
[10] G. Haas, H. Wöhler, M. Fritsch and D. A. Mylnski, J. Opt. Soc. Am. **5**(9), 1554 (1988).
[11] G. Haas, H. Wöhler, M. Fritsch and D. A. Mylnski, J. Opt. Soc. Am. **5**(9), 1571 (1988).
[12] W. H. Press, S. A. Teukolsky, W. T. Vetterling and B. P. Flannery, *Numerical Recipes* (Cambridge Univ. Press, Cambridge, 1988), Chap. 9.
[13] P. Yeh, J. Opt. Soc. Am. **72**(4), 502 (1972).
[14] P. Yeh, J. Opt. Soc. Am. **69**(5), 742 (1979).

Journal of the Korean Physical Society, Vol. 34, June 1999, pp. S551~S554

Proposal on the Kickback Voltage Free TFT-LCD for Large-area Application

J. I. RYU, K. N. KIM, K. H. YOO, B. S. BAE and Jin JANG

Department of Physics, Kyung Hee University, Seoul 130-701

We proposed a kickback voltage free pixel structure for a large-area TFT-LCD. A floating with patterned common electrode, dual TFT in one pixel and opposite polarity data signal were employed. We have calculated the kickback voltage, the charging time, the voltage holding capability and drawn a conclusion that the proposed structure overcomes a problem based on a flicker and a DC level shift.

I. INTRODUCTION

In Active Matrix Liquid Crystal Display (AMLCD), Thin Film Transistors (TFTs) are widely used for the switching elements [1–4]. The applications of TFT-LCD are recently diversified because of its low production cost and high-quality visual legibility. Cathode Display Tube (CDT) is being replaced by TFT-LCD monitor and the commercial TV will be also replaced by large-area LCD in the future.

The kickback voltage (ΔV_p) is one of the key issues in the design of the large-area AMLCDs to obtain high quality image.

LCDs do not work properly under DC bias, so they are always operated in the AC mode. Due to gate voltage drop and the parasitic capacitance C_{gs} between gate and source, there is a DC voltage offset and a kickback voltage ΔV_p in the pixel voltage V_p. The ΔV_p causes undesirable effects on the performance of the LCD such as flicker, image sticking and uniformity of brightness [5].

Several driving schemes have been proposed to reduce the ΔV_p [6–8]. Takeda [6] proposed a capacitively coupled driving method to reduce the DC level shift. But, this method can be only applied to the pixel structure with a storage capacitor connected to the previous gate bus line. Jung *et al.* [7] reported a segmented counter electrode structure to reduce the ΔV_p. In order to compensate the ΔV_p, they apply the different V_{com} to the each counter electrode and thus the DC level shift can be reduced. But this method can be only applied to the pixel structure with extra segment counter electrodes that are perpendicular to the gate bus line.

The C_{gs} and ΔV_g should be reduced and C_{st} should be increased to reduce the ΔV_p. Reduction of the ΔV_g or the increase of the C_{st} leads to increase of charging and discharging time. Therefore, there are certain limitations to the reduction of the ΔV_p by controlling the ΔV_g and the C_{st}.

However, the compensation driving method and pixel structure proposed so far can not completely compensate ΔV_p.

In the present work we have designed a ΔV_p free pixel structure which is more useful for a large-area TFT-LCD. The new pixel structure overcomes a problem for a flicker associated with ΔV_p and a DC level shift. We calculated the ΔV_p, charging time and voltage holding capability and it was proved that proposed structure is useful structure for a large area TFT-LCD.

II. SIMULATION

We used a PSPICE (Professional Simulation Program with Integrated Circuit Emphasis) circuit simulator implemented with an a-Si:H TFT device. Figure 1 shows a typical pixel potential as a function of time. The gate signal changes from V_g^{low} to V_g^{high} ($V_g^{low} = -10$ V, $V_g^{high} = 20$ V) with a period of 16.6667 ms. The gate pulse width is 13.8889 μs for an UXGA (1600×3×1200) resolution. The rising and falling edges of the gate pulse are typically of the order of microseconds. Table 1 lists the parameters for the simulation.

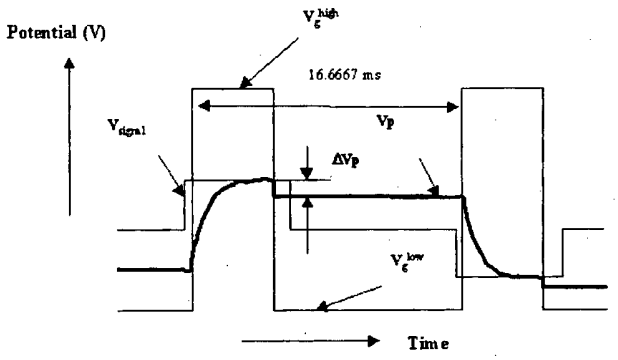

Fig. 1. A typical pixel potential for a TFT-LCD.

Table 1. Parameters used for the simulation.

Parameter	Value
Panel size	40″
Gate driving frequency	60 Hz
Gate(Data) bus-line thickness	0.2 μm
Storage capacitance	0.2 pF
Cell gap	5 μm
ϵ_{pe}, ϵ_{pa}	3.4, 10.8
LC resistivity	1.2×10^{12} Ω-cm
Resolution	UXGA(1600×3×1200)
Gate bus-line width	8 μm
Gate(Data) bus-line metal	Al
Data bus-line width	6 μm
W/L of TFT	12 μm/4 μm
Gate pulse width	13.8889 μs
Pulse rising (falling) time	1 μs

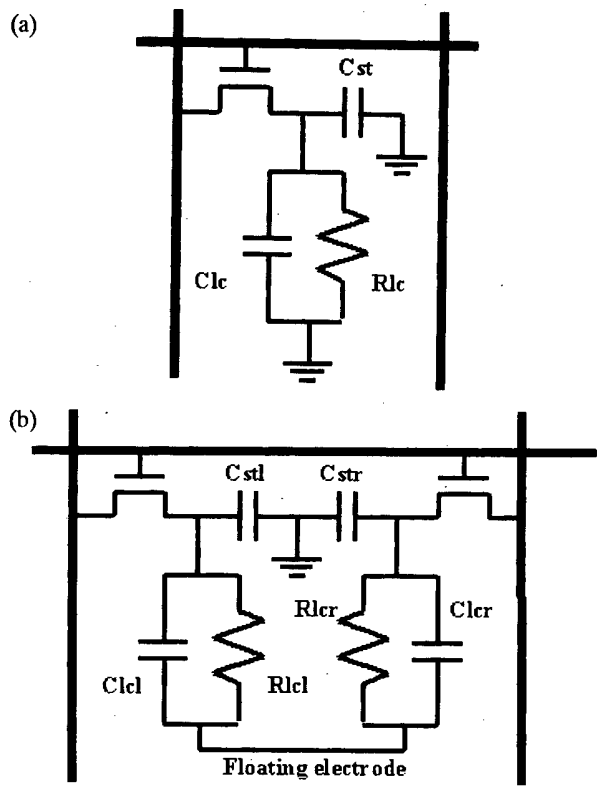

Fig. 2. Equivalent circuits of the conventional structure (a) and the proposed structure (b). A floating common electrode, dual TFTs in a pixel and opposite polarity data signal have been employed for (b).

Figure 2 shows the equivalent circuit diagrams of the conventional (a) and the proposed structure (b). A floating common electrode, dual TFTs in a pixel and opposite polarity data signal have been employed for ΔV_p free TFT-LCD.

Figure 3 shows a cross-sectional view of the proposed structure. One pixel consists of two subpixels. A floating common electrode with patterned, dual TFT in one pixel and opposite polarity data signal were employed. The shape of patterned common electrode is the same one of pixel electrode that is a TFT area except from conventional TFT-LCD.

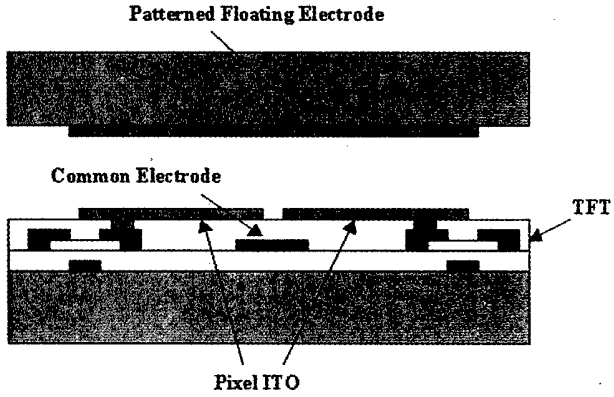

Fig. 3. A cross-sectional view of the proposed structure.

III. RESULTS AND DISCUSSION

From the charge conservation law, a ΔV_p can be expressed by

$$\Delta V_{pi} = \frac{C_{gsl}\Delta V_g + C_{lcl}\Delta V_f}{C_{gsl} + C_{lcl} + C_{stl}}$$
$$\Delta V_{pr} = \frac{C_{gsr}\Delta V_g + C_{lcr}\Delta V_f}{C_{gsr} + C_{lcr} + C_{str}} \quad (1)$$

where the subscript l and r indicate the left and right sub-pixels, respectively. The ΔV_p is the pixel electrode voltage difference $(V_p - V_p')$. The subscript f indicates the floating electrode and the superscript $'$ indicates the voltage at $V_g = V_g^{low}$. The ΔV_g is the voltage swing of gate driving pulse $(V_g^{high} - V_g^{low})$. The C_{gs}, C_{lc} and C_{st} are parasitic capacitance, capacitance of LC and capacitance of storage capacitor, respectively.

The pixels have a symmetrical structure ($C_{gsl} = C_{gsr}$, $C_{lcl} = C_{lcr}$, $C_{stl} = C_{str}$), then pixel voltage difference can be represented as:

$$\Delta V_{pl} = \Delta V_{pr} \equiv \Delta V_p \quad (2)$$

The ΔV_f, the floating electrode voltage difference $(V_f - V_f')$, is given by

$$C_{lcl}(V_f - V_{pl}) + C_{lcr}(V_f - V_{pr}) \quad (3)$$
$$= C_{lcl}(V_f' - V_{pl}') + C_{lcr}(V_f' - V_{pr}'),$$

thus,

$$\Delta V_f = \Delta V_p. \quad (4)$$

In the case of an opposite polarity data signal, left and right sub-pixels have an opposite potential.

Figure 4 shows the time dependence of a pixel poten-

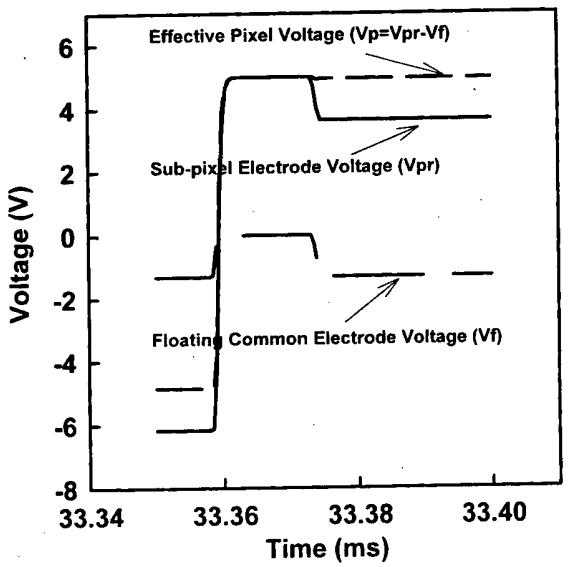

Fig. 4. Time dependence of a pixel potential (V_{signal} = 5 V).

tial. The V_p reaches V_{signal} in the charging operation. When the gate pulse goes low level V_g^{low}, V_p is shifted by ΔV_p because of the C_{gs}. The transient characteristics of V_f is similar to V_p. When the gate pulse goes V_g^{low}, V_f is shifted by ΔV_f because of the charge redistribution to be with opposite polarity V_{signal}. It thus appears that the effective pixel electrode voltage ($V_p - V_f$) does not change.

Consequently, in the proposed structure, the kickback voltage is negligible because ΔV_p has the same value as ΔV_f; therefore, the image quality degradation by the kickback voltage can be avoided.

The $RMS(V_p)$ is root mean square (rms) value of the effective pixel electrode voltage between pixel electrode voltage V_p and common electrode voltage V_{com}. $RMS(V_p)$ may be expressed as:

$$RMS(V_p) = \sqrt{\frac{1}{T}\int_0^T [V_p(t) - V_{com}(t)]^2 dt}, \qquad (5)$$

where, T is the period of an alternating voltage applied to a liquid crystal [9]. In the proposed structure, V_{com} is replaced V_f. Because transmittance of the liquid crystal T_{lc} depends on $RMS(V_p)$, variations in $RMS(V_p)$ result in the difference in T_{lc}.

Figure 5 shows a comparison of $RMS(V_p)$ between conventional and proposed structures. The proposed structure has a small variation of T_{lc} and thus an excellent display quality.

Figure 6 shows the charging times and ΔV_p's for the conventional and proposed structure, respectively. The ΔV_p of the proposed structure is almost zero. The shorter charging time is attributed to smaller capacitances of C_{st} and C_{lc}.

Figure 7 shows the pixel discharging behavior, *i.e.* the

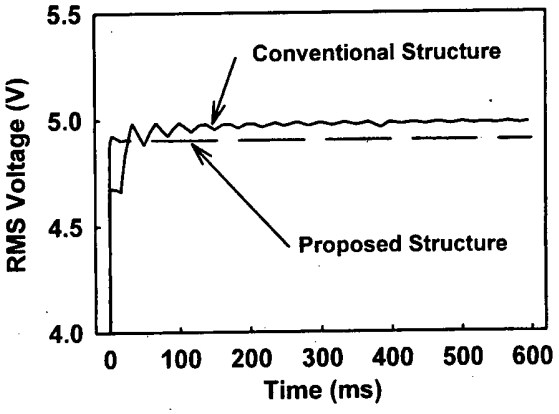

Fig. 5. A comparison of the RMS(Vp) between proposed structure and conventional TFT-LCD (V_{signal} = 5 V).

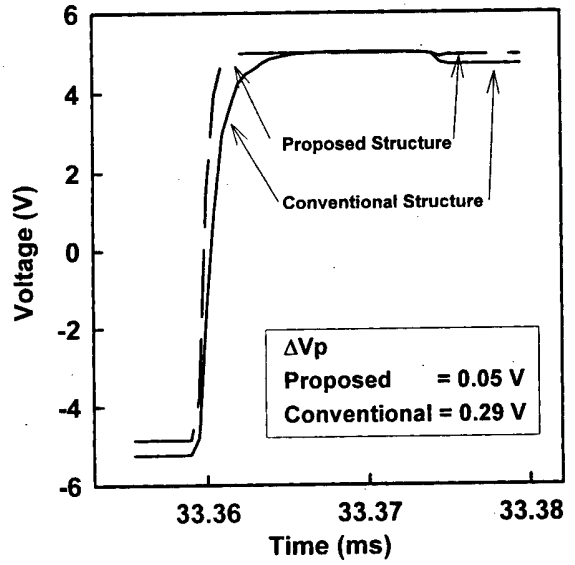

Fig. 6. A comparison of pixel charging time and ΔV_p between conventional and proposed structures (V_{signal} = 5 V). For the proposed structure the charging is faster by the smaller storage capacitance.

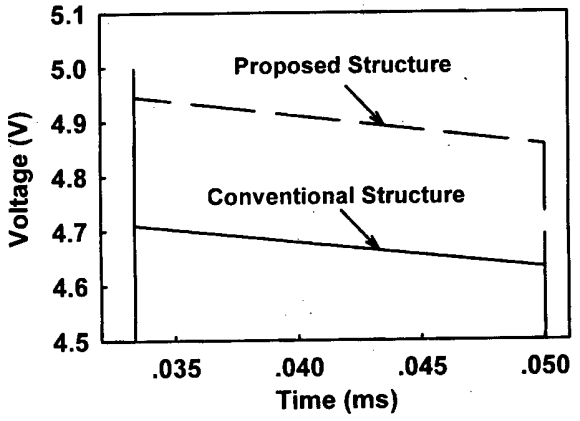

Fig. 7. Pixel discharging behavior for the proposed and conventional TFT-LCD (V_{signal} = 5 V).

voltage holding capability. The voltage holding capability is the almost same between the proposed and conventional structures.

IV. CONCLUSIONS

A new pixel structure has been proposed to have ΔV_p free TFT-LCD. A proposed pixel composed of floating common electrode, dual TFTs and two opposite polarity data lines. By the PSPICE simulation, it was proved that the kickback voltage of the proposed structure is negligible. And also, charging and discharging characteristics is simulated for the conventional and proposed structures. Proposed structure gives two times faster charging time compared to the conventional structure due to smaller storage capacitance still sustaining the same discharging behavior and suppressing the pixel voltage fluctuation. Above results means that proposed structure has high quality image with low flicker and high uniformity by the abandon of kickback voltage.

ACKNOWLEDGMENTS

This work was supported by G-7 project of Korea.

REFERENCES

[1] B. S. Bae, J. H. Lee, J. H. Huh, W. G. Lee, S. Y. Joo, J. H. Souk, K. N. Kim, J. I. Ryu, K. H. Yoo and J. Jang, SID 98 Digest, 305 (1998).

[2] K. H. Lee, B. Y. Moon, Y. C. Chung, J. H. Yoo, S. H. Lee and J. Jang, J. Korean Phys. Soc. **28**, S110 (1995).

[3] S. K. Kim, K. S. Lee, J. Jang, I. H. Kim and C. H. Hong, J. Korean Phys. Soc. **28**, S116 (1995).

[4] S. Y. Yoon, K. H. Kim, J. H. Lee and J. Jang, J. Korean Phys. Soc. **30**, S213 (1997).

[5] Y. Nanno, Y. Mino, E. Takeda and S. Nagata, Proceeding of the SID **34**, 295 (1990).

[6] E. Takeda. Y. Nan-no, Y. Mino, A. Otsuka, S. Ishihara and S. Nagata, Proceedings of the SID **31**, 87 (1990).

[7] K. Y. Jung and O. K. Kwon, The 3rd Korean Conference on the Semiconductors, 207 (1996).

[8] M. Adachi, T. Matsumoto, K. Tanaka, K. Kato, H. Morimoto, S. Yasuda and K. Awane, SID 92 Digest, 785 (1992).

[9] K. Suzuki and M. Shibnsawa, Japan Display 92 Proc., 447 (1992).

Journal of the Korean Physical Society, Vol. 34, June 1999, pp. S555~S557

Deposition of SiC Thin Films by PECVD

Nam-Ihn CHO and Svetlana VLASKINA
Center for Science and Advanced Technology, Sun Moon University, Asan 336-840

Chang Kyo KIM
Department of Electrical Engineering, Soonchunhyang University, Asan 336-741

The SiC films were deposited on Si substrate by the decomposition of CH_3SiCl_3 (methylthrichlorosilane) molecules in a high frequency discharge field. From the Raman spectra, it is conjectured that the deposited film are formed into the polycrystalline structure. The photon absorption measurement reveal that the band gap of the electron energy state are to be 2.4 eV for SiC, and 2.6 eV for $Si_{0.4}C_{0.6}$, respectively. In the high power density regime, methyl-radicals decompose easily and increases the carbon concentration in plasma and result in the growing films.

I. INTRODUCTION

Chemical vapor deposition (CVD) on the heated substrate is a widely used technique for the preparation of SiC films on the Si substrates in the industrial application [1]. However, in this processes, the substrate temperature must be raised to near 1400 °C to form a cohesive film. Such a high temperature, being close to the melting temperature of silicon, makes the process very critical. It is possible to decrease the temperature by using plasma activation during the film growth process.

Recently, plasma enhanced CVD (PECVD) has been attracted much attentions for the production of the high-quality SiC films at the low temperature [2]. It has been expected that the SiC film which is made using PECVD process may not contain much distribution of the void in the interface of the structure. It is a reason of the temperature on the substrate that make the silicon in the substrate actively to be out-diffused into the deposited SiC film to compensate dilute carbon component through the chemical reaction. But the deposited SiC films on the substrate reveal amorphous or polycrystalline states because of the lattice mismatch and the different thermal expansion coefficients between the SiC film and the Si substrate. Therefore, there are many researches in the laboratory and the industrial scale to promote crystalline properties of the deposited SiC films. Among the known facts about PECVD process, the most important parameter that can make critical effects on the deposited film is the reaction gases in the plasma environment. The reaction gases that the previous other studies used are produced from the mixtures of $SiCl_4$, CH_4, C_2H_2, H_2, *etc.* To deposit plasma induced films, the source gases must be decomposed and reacted each other by the radio frequencies (RF) to form SiC molecular before to be cohered on the substrate. In this process, it can make a domain that the silicon and the carbon occupy exclusively in the microscopic volume. However, there is another type reaction gas which can be used in the PECVD process like CH_3SiCl_3 (methylthrichlorosilane). This gas is directly decomposed into H_2, Cl_2, SiC, *etc.*, through the interaction with RF discharge field. Among the decomposed gases, SiC components are deposited on and the others are evaporated out from the substrate. The CH_3SiCl_3 gas have enough physical properties candidated for the reaction material in the PECVD process. The present study is aimed to obtain informations, from the PECVD process using the CH_3SiCl_3 reaction gas, that can be applied for manufacturing the electronic devices.

II. EXPERIMENTS

Depositions of SiC films on Si substrate have been performed with a PECVD system, operating at a frequency of 13.56 MHz. The turbo-molecular pump and rotary pump were combined to maintain the base pressure with low 10^{-7} torr in the plasma reaction chamber. Before the precipitation of the SiC films, whole accessories of the PECVD vacuum chamber and substrate were etched in hydrogen atmosphere. Molecules of the feed gases (CH_3SiCl_3) were delivered by the hydrogen gas to the RF discharge field, and decomposition of C and Si atoms from the plasma induced by the RF source. The halogen lamp were used to control the substrate temperature, and the temperature during the growth of the films was fixed at 250 °C.

The thickness of the films have been estimated from the view of scanning electron microscopy (SEM) on the cleaved lateral cross section of the sample. In order to

investigate the structure properties, Raman spectroscopy was carried out in an ambient condition. In the Raman scattering measurement, the peaks which are contributed due to the Si substrate can be easily classified from that of the SiC film. The scan of the wave number in the measurement was ranged 400~1700 cm^{-1} to identify the bonding phases formed in the deposited film. Photoluminescence (PL) spectra of the film excited by nitrogen laser at the nitrogen temperature were also used to identify the exciton properties which are contributed from the shallow defect levels. The PL measurement has been carried out on the film which were positioned in the vacuum cryostat maintained at the liquid nitrogen temperature. Even though the luminescence photons accompanying with phonon noise, it was expected that the principal peaks in the spectra could be identified. The SiC film that has been used in the Raman experiment was not employed in the PL measurement to exclude the laser annealing effects. The incident light source which create the exciton in the structure were nitrogen gas laser. The wavelength of the laser were 3370 Å which have the enough energy to exit an electron from valance band to conduction band, not depending on the crystal polytype. The monochrometer used in the PL measurement was the same as that in the Raman scattering experiment.

Optical absorption of the SiC film has been observed to understand the inter-band or intra-band transition behavior of the carriers. The irradiated photon energies were ranged 1.0~6.0 eV to examine all the absorption transitions of the carriers in the SiC film. The incident photons were not polarized during the measurement because it had been expected that the deposited SiC film on the substrate can not form the directional channels in the structure for the as-grown states.

III. RESULTS AND DISCUSSION

Fig. 1 shows a Raman spectrum of the deposited SiC film which were grown on the Si substrate with the temperature of 250 °C. The peaks shown in the spectrum have a full width at half maximum (FWHM) of ~50 cm^{-1} which is broad compared to that of the single crystal. From this result, it can be concluded that the deposited film by PECVD at the low temperature has been formed in the poly-crystalline structure. Also it can be understood that in the poly-crystalline structure, the momentum conservation is relaxed from the single crystal, leading to the participation of the photon which have the small changed momentum on broadening line shape in the Raman spectrum. The centroid of the peak position, generally, are shifted relative to the that of the crystals reflecting on stress of strain or the long ranged defects like crevice in the poly-crystalline structure. However, a general sketch can be made on the Raman spectrum for the SiC deposited film on the Si substrate. The strongest

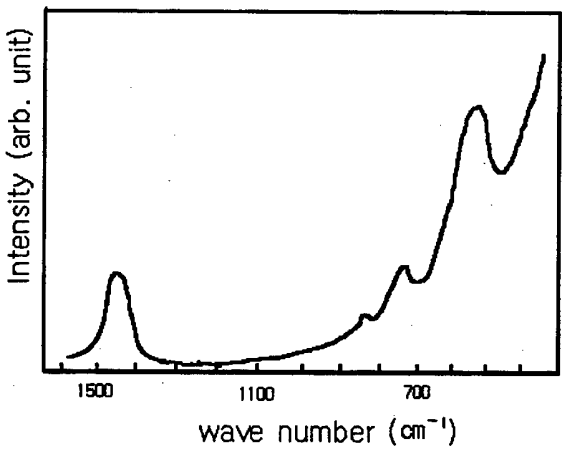

Fig. 1. Raman spectra of SiC films.

peak located at 511 cm^{-1} mode is due to the scatted photon came from the Si substrate. The peak appeared at the 1445 cm^{-1} seem to be the contribution from the second order optical phonon mode of the SiC film. The peaks positioned at 715 cm^{-1} and 836 cm^{-1} are estimated to be the characteristic modes of transverse optical (TO) and longitudinal optical (LO), respectively. There are many different features of the peaks in the spectrum of the SiC film which were made using PECVD methode at low temperature. The peak position of the presumed LO mode in this spectrum deviated from the known data for the single crystal (about 970 cm^{-1}). Also, the peak intensity of LO mode is smaller than that of TO mode, and there is no any shoulder which can be filtered from the base line. Generally, for the SiC crystals, the peak intensities in the Raman spectrum due to LO mode is larger than TO mode, and according to the relative directions between the polarization of the incident laser and the lattice symmetries of the crystal, TO mode with small peak which are positioned around the main peak appears distinctly. The reasonable conjecture for this feature in this experiment is that, because there are many distorted polytype in the SiC film which can be formed with SiC molecular, the phonon modes can be made in different fashion unlike with the crystal. So the base line overlaps the weak peaks and unexpected intensities of the peaks appear with the established peaks. This is the same as the discussion which was explained for the broadened FWHM of the peaks [3,4].

Fig. 2 shows the absorption measurement for the SiC film as a function of the photon energy. Generally, it has been known that a carrier in the SiC crystals transits between the inter-band accompanying with the phonon. In the amorphous or poly-crystal state, there are a lot of shallow levels near the band edges caused by presence of the defects in the structure. And, the bonding strength between the atoms is weaker in the amorphous state than in the crystal. So absorption trend of the deposited SiC film shows the smooth increase as shown in Fig. 2. The

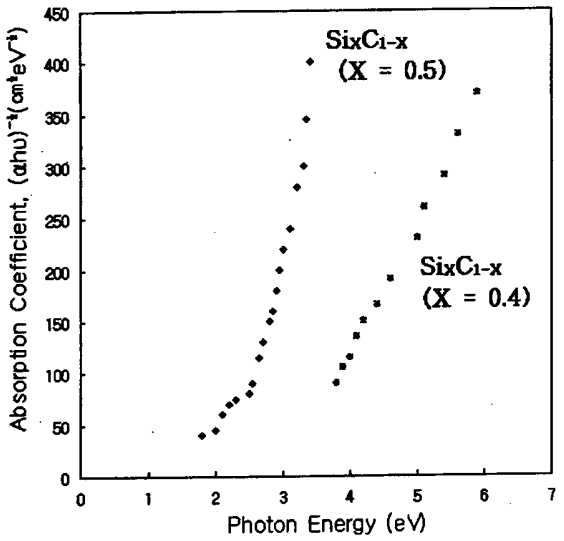

Fig. 2. Absorption spectra of SiC films.

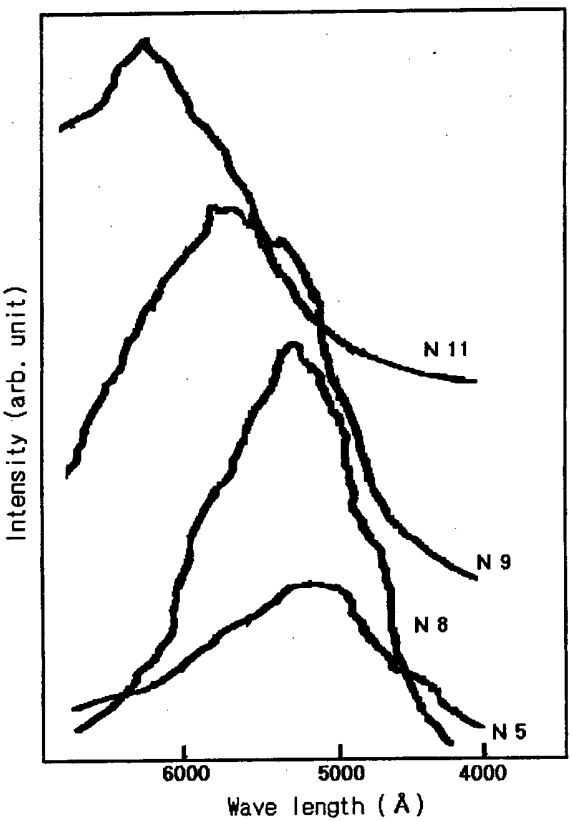

Fig. 3. Photoluminescence spectra exited by nitrogen laser.

band gap of the deposited SiC film was deduced to be 2.4 eV (and 2.6 eV) for the SiC (and $Si_{0.4}C_{0.6}$). In the high power density regime, methyl- radicals decompose easily and increases the carbon concentration in plasma and result in the growing films. The compositional ratios of the chemical compounds in the structure were determined from the results of the Auger spectrums.

In Fig. 3, PL spectra measured for the SiC films at liquid nitrogen temperature are shown. The PL spectra reveal bad resolution overlapped with the phonon noise, but the peak positions of the maximum intensity due to each exciton contribution can be identified to be 6300, 5800, 5300, and 5100 Å in the spectra. The band gap energy of 2.39 eV which was obtained from the absorption measurement is corresponds to the value 5166 Å of the wavelength. So the exciton peak at 5100 Å is attributed to the $Si_{0.4}C_{0.6}$ component and the other peaks are given from SiC components. It is supposed that formation of the excition of the quasi-particles is not due to any other impurities but the hydrogen because PECVD has been established in the hydrogen atmosphere. Nevertheless, from the PL spectra, it can not be identified what the hydrogen formed in the impurity defect level near the band edge [5].

IV. CONCLUSIONS

In order to know the possibilities for obtaining the parameter which can be applied in the manufacturing semiconductor device using CH_3SiCl_3, a PECVD technology was carried out at low temperature to deposit the SiC film on the Si substrate. From the spectroscopic analyses for the SiC film, it was found that the deposited structure was in the poly-crystalline phase, and the band gap in the electronic energy state were to be 2.4 eV (and 2.6 eV) for the SiC (and $Si_{0.4}C_{0.6}$). It has been expected that the PECVD process for making the SiC film on the Si substrate can be realized in the device application field.

ACKNOWLEDGMENTS

This work was supported by the Korea Science and Engineering Foundation through Semiconductor Equipment Research Center at Hoseo University, and also supported by the Korean Ministry of Information and Communication through the University Basic Research Program.

REFERENCES

[1] H. Matsunami, J. Korean Phys. Soc. **30**, S186 (1997).
[2] T. Uemeto, Jpn. J. Appl. Phys. **34**, L9 (1995).
[3] H. Harima, S. Nakashima, and T. Uemura, J. Appl. Phys. **78**, 3 (1995).
[4] Z. C. Feng, C. C. Tin, R. Hu, J. Willams, Thin Solid Films **226**, 1 (1995).
[5] W. J. Choyke, Z. C. Feng, J.A. Powell, J. Appl. Phy. **64**, 3163 (1988).

Journal of the Korean Physical Society, Vol. 34, June 1999, pp. S558~S561

Fabrication and Characterization of High Voltage Ni/6H-SiC and Ni/4H-SiC Schottky Barrier Diodes

Ho-Seung LEE, Sang-Wuk LEE and Dong Hyuk SHIN

Department of Physics, Dongguk University, Seoul 100-715

Hyun-Chang PARK

Department of Electronic Engineering, Dongguk University, Seoul 100-715

Woong JUNG

Department of Semiconductor Sciences, Dongguk University, Seoul 100-715

Ni/SiC Schottky diodes have been fabricated using 4H-SiC and 6H-SiC epitaxial wafers. The n-type epitaxial layers grown on n^+ substrates have a doping concentration of 4.0×10^{16} cm^{-3} and a thickness of 10 μm. Oxide edge termination has been adopted in order to obtain high breakdown voltage and low leakage current. The fabricated Ni/4H-SiC and Ni/6H-SiC Schottky barrier diodes show excellent rectifying characteristics up to the maximum measured temperature of 550 °C. In case of oxide terminated Schottky barrier diodes, breakdown voltages of 973 V (Ni/4H-SiC diode) and 920 V (Ni/6H-SiC diode), and a very low leakage current of less than 1 nA at -800 V have been observed at room temperature. On Schottky barrier diodes without edge termination, breakdown voltages were 430 V (Ni/4H-SiC) and 160 V (Ni/6H-SiC), respectively. At room temperature, Schottky barrier height (SBH), ideality factor, and specific on-resistance were 1.55 eV, 1.3, 3.6×10^{-2} $\Omega\cdot cm^2$ for Ni/4H-SiC Schottky barrier diodes, and 1.24 eV, 1.2, 2.6×10^{-2} $\Omega\cdot cm^2$ for Ni/6H-SiC Schottky barrier diodes, respectively. These results show that both Ni/4H-SiC and Ni/6H-SiC Schottky barrier diodes are very promising for high temperature and high voltage applications.

I. INTRODUCTION

Silicon carbide (SiC) is a wide bandgap semiconductor with excellent physical properties that make it suitable for power devices operating at adverse environment. The large bandgap of SiC leads to extremely low leakage currents and large breakdown voltages and allows device operation at high temperatures [1–3]. Of the many polytypes of silicon carbide, 4H-SiC and 6H-SiC have bandgaps of 3.2 eV and 3.0 eV, respectively. The room temperature electron mobilities of 443 $cm^2/V\cdot s$ (4H-SiC) and 320 $cm^2/V\cdot s$ (6H-SiC) are commonly used based on the fit of the Caughey and Thomas relation to the experimental data of Hall measurements made on n-type epilayers doped in the range of 1×10^{16} to 3×10^{19} cm^{-3} [4,5]. Many SiC devices depend crucially on metal contacts whose electrical properties are dominated by the Schottky barrier height, Φ_B. Thus the knowledge of Φ_B values allows selection of metals appropriate for high Φ_B rectifying contacts and ohmic contacts with low contact resistivity. Schottky barrier diode is a majority carrier device which does not have the storage effect of minority carriers and is therefore suitable for high frequency power devices with low power losses [6]. In power supply systems, operation at higher frequencies is attractive because of the reduction in size and power losses in the passive components which leads to a more efficient, compact system design. To accomplish higher frequency operation in power circuits, it is essential to use power rectifiers with improved switching performance [7].

In this study, we made Ni/4H-SiC and Ni/6H-SiC Schottky barrier diodes using silicon carbide epi wafers and investigated their electrical properties. Oxide edge termination has been employed to improve the breakdown characteristics and to reduce the reverse leakage current. Electrical properties have been measured under forward and reverse bias at room temperatures and at elevated temperatures up to 550 °C.

II. EXPERIMENTS

As the starting material, we used commercially available (Cree Researh Inc. Durham, NC, USA) n-type 4H-SiC and 6H-SiC wafers with 10 μm thick n^+ 4H-SiC and 6H-SiC epilayers doped to 4.0×10^{16} cm^{-3}. They have Si-face tilted 3.5 to 8 degrees from the (0001) direction. The n-type substrates have doping concetrations of (3~8)

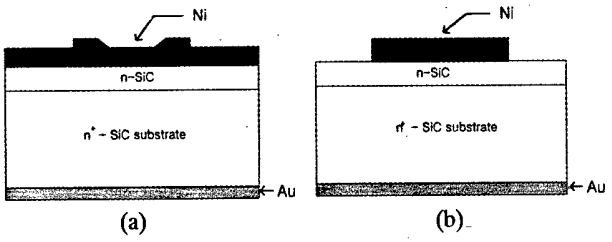

Fig. 1. Schematic cross-section of Ni/SiC Schottky barrier diodes. (a) Oxide terminated structure and (b) Structure without edge termination.

10^{18} cm^{-3}. Fig. 1 shows the schematic cross-section of the Ni/SiC Schottky barrier diodes with and without oxide edge termination. For oxide-terminated diodes, the general process of the device fabricatoin is 1) cleaning, 2) oxidation, 3) removal of oxide from backside of the wafer 4) Ohmic contact on the backside, 5) formation of the oxide windows, 6) deposition of Ni and Ni pad formation by lithography, 7) wire bonding, and 8) testing.

The cleaning of the surface is very important since any natural oxide layer or contaminant in the interface between metal and semiconductor will deteriorate the performance of the devices. We used RCA method [8] to clean the surface. After the cleaning, oxide layer was grown by wet thermal oxidation. For 4H-SiC, oxidation was carried out for 10 hours at 1350 °C and for 6H-SiC, oxidation was done at 1300 °C for 6 hours in order to get oxide thickness of 2000 Å [9]. The oxide thicknesses were measured using an ellipsometer.

The oxide on the backside of the wafer was removed using 10 % HF while protecting the front surface with photoresist. In order to form ohmic contact at the backside, 2000 Å of Au was deposited and annealed at 720 °C for 15 minutes [10].

The oxide window was formed by lithography and etched in 10 % HF solution. The sizes of the oxide windows are 80×80 cm^2, 180×180 cm^2, and 280×280 cm^2 for the oxide edge termination structure. Ni was evaporated at a pressure of 8.7×10^{-7} Torr to a thickness of 2000 Å. After defining the Ni pads by lithography, remaining Ni was etched by the Ni-etching solution of HNO_3:CH_3COOH:H_2SO_4:H_2O=5:5:2:10. For devices without edge termination, circles of Ni pads with 300um diameter were evaporated using shadow mask.

The Schottky barrier height (SBH), ideality factor (n), and the breakdown voltage (V_{BR}) have been determined from I-V and C-V measurements. From I-V measurement, Schottky barrier height and ideality factor are obtained from the following equations [7,11].

$$V_{BR} \simeq \left(\frac{E_{CR}^2 \epsilon_s}{2q}\right)\frac{1}{N_d} \tag{1}$$

$$J = J_o\left[\exp\left(\frac{qV_F}{nkT}\right) - 1\right] \tag{2}$$

$$J_o = A^* T^2 \exp\left(-\frac{q\Phi_B}{kT}\right) \tag{3}$$

where the parameter E_{CR} is the maximum breakdown electric field, ϵ_s is the dielectric constant, q is the electron charge, N_d is the doping concentration, J_o is the reverse saturation current density, V_F is the forward bias voltage, n is the ideality factor, k is the Boltzmann constant, T is the absolute temperature, A^* is the effective Richardson constant, and Φ_B is the Schottky barrier height. The specific on-resistance (R_{on}) is the total resistance in series and is given by the following equation.

$$V_F = \frac{kT}{q}\ln\left(\frac{J_F}{J_o}\right) + R_{on}J_F \tag{4}$$

From C-V measurement, Schottky barrier height and doping concentration are obtained from the following equations [7,11].

$$\frac{1}{C^2} = \frac{2(V_{bi} + V_R)}{q\epsilon_s N_d a^2} \tag{5}$$

$$\Phi_B = V_n + V_b i + \frac{kT}{q} - \Delta\Phi \tag{6}$$

where V_{bi} is the built-in potential, V_n is the potential difference between Fermi level and the conduction energy (E_c), $\Delta\Phi$ is the reduction by image force lowering, and a is the area of the diode.

III. RESULTS AND DISCUSSION

Fig. 2 shows the I-V characteristics of the oxide terminated Ni/4H-SiC Schottky barrier diode at room temperature. The breakdown voltage is 973 V. This breakdown voltage is much larger than that of the diode without termination which is 430 V (Fig. 3). The doping concentration ($N_d \simeq 4.3\times10^{16}$ cm^{-3}) was determined from the C-V measurement. Using this value, the theoretical breakdown voltage from Eq. (1) is 1100 V. Therefore the

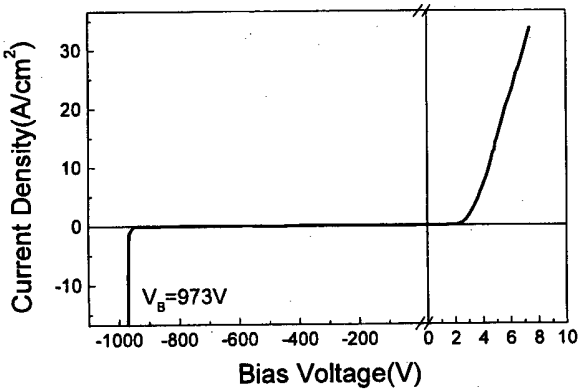

Fig. 2. I-V characteristics of oxide-terminated Ni/4H-SiC Schottky diode at room temperature.

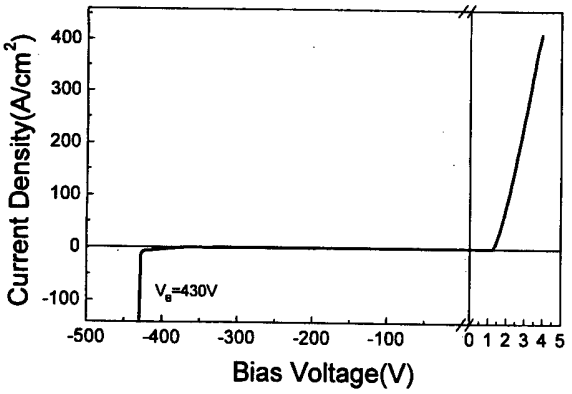

Fig. 3. I-V characteristics of Ni/4H-SiC Schottky diode without oxide termination at room temperature.

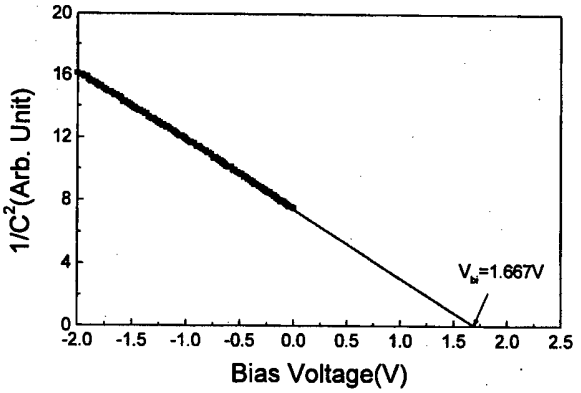

Fig. 5. C-V characteristics of Ni/4H-SiC Schottky diode without oxide termination.

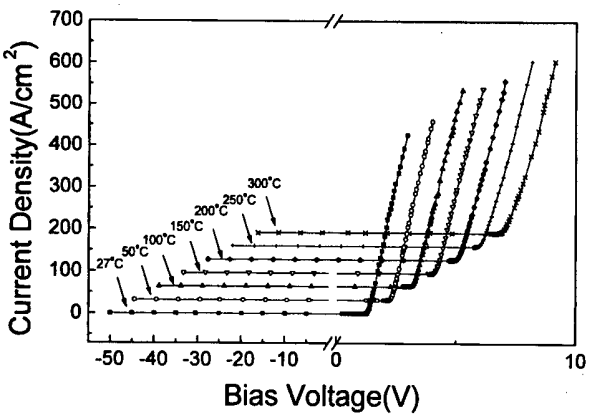

Fig. 4. I-V characteristics of Ni/4H-SiC Schottky diode without oxide termination at elevated temperatures.

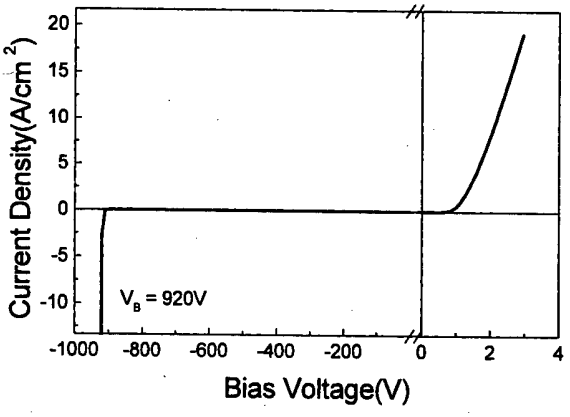

Fig. 6. I-V characteristics of oxide-terminated Ni/6H-SiC Schottky diode at room temperature.

oxide edge termination is an effective method of obtaining high breakdown voltage that approaches the theoretical value. The ideality factor of the oxide terminated device is 1.3 and the Schottky barrier height is 1.55 eV.

Fig. 4 shows the high temperature I-V characteristics of Ni/4H-SiC Schottky diode without oxide termination. The rectifying characteristics of the diode changes little even at 300 °C. The C-V curve of the non-terminated Ni/4H-SiC Schottky barrier diode is shown in Fig. 5. Schottky barrier height from Eq. (6) is 1.81 eV. This value is slightly different from the value determined from I-V measurement. Itoh, *et al.* reported similar results [12]. It is considered that the disregard of the image force lowering is responsible for the discrepancy. The measured specific on-resistance is 0.0056 $\Omega \cdot cm^2$ and the forward current density is 400 A/cm^2 at 4 V.

Fig. 6 shows the I-V characteristics of the oxide-terminated Ni/6H-SiC Schottky diode at room temperature. The maximum breakdown voltage is 920 V and the leakage current is less than 1 nA until 800 V. Comparing this value with the breakdown voltage of 160 V for the diode without termination, the effectiveness of the oxide edge termination is quite clear. The specific on-resistance is 0.026 $\Omega \cdot cm^2$ and the forward current density is 30 A/cm^2 at 4 V. The ideality factor and the Schottky barrier height are 1.2 and 1.24 eV, respectively. This barrier height agrees quite well with the results of Waldrop *et al.* (1.27 eV) and Lang *et al.* (1.7 eV) [13,14]. Compared with the devices without edge ter-

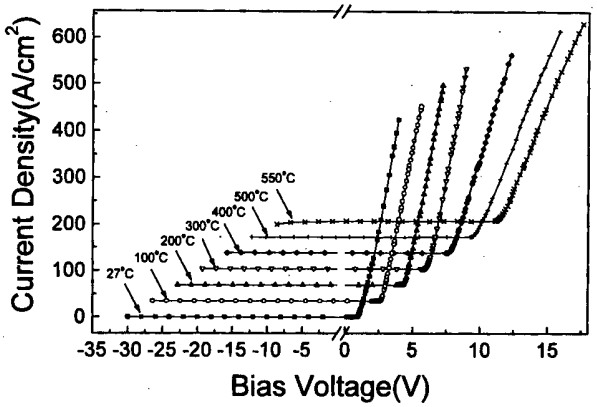

Fig. 7. I-V characteristics of Ni/6H-SiC Schottky diode without oxide termination at elevated temperatures.

Table 1. Summary of characteristics of Ni/SiC Schottky diodes.

	Ni/4H-SiC		Ni/6H-SiC	
	w/o Termination	Oxide Termination	w/o Termination	Oxide Termination
Breakdown voltage (V)	430	973	160	920
Schottky barrier height (eV)	1.59, 1.81 (CV)	1.55	1.22	1.24
Ideality factor	1.08	1.3	1.24	1.2
Turn-on voltage (V)	1.3	1.5	1.1	1.1
R_{on} (ohm·cm^2)	0.0056	0.036	0.006	0.026

mination, the oxide terminated diodes have somewhat deteriorated forward I-V characteristics with higher on-resistance and lower current density. This may have been caused by residual contaminants or oxide layer that has not been completely removed from the interface between Ni and silicon carbide.

Fig. 7 shows the I-V characteristics of the oxide-terminated Ni/6H-SiC Schottky diode at elevated temperatures. The rectifying characteristics of the diodes change little for temperatures up to 550 °C. The electrical properties of the Ni/4H-SiC and Ni/6H-SiC Schotkky diodes with and without oxide edge termination are summarized in Table 1.

IV. CONCLUSIONS

We have fabricated Ni/4H-SiC and Ni/6H-SiC Schottky diodes using epitaxial silicon carbide wafers. Thermal oxide has been used to make edge termination structures. The fabricated Ni/SiC Schottky barrier diodes have a maximum breakdown voltage of 973 V and an operating temperature of 550 °C. Forward current density is over 400 A/cm^2 with an on-state resistance as low as 0.0056 $\Omega \cdot$ cm^2. The observed maximum breakdown voltage approaches the theoretical value of 1100 V and therefore indicates the effectiveness of the oxide edge termination. The slight deterioration of the forward I-V characteristics with higher on-resistance and lower current density may have been caused by residual contaminants or oxide layer that has not been completely removed from the interface between Ni and silicon carbide. This problem may be solved by more carefully monitoring the oxide window etching and cleaning processes. The results demonstrate clearly that silicon carbide can be used for high voltage power devices which can operate at very high temperatures.

ACKNOWLEDGMENTS

This research was supported by the Korean Ministry of Science & Technology through the Power Semiconductor Devices Development Program (1998) and by the Basic Science Research Institute Program, Korean Ministry of Education, 1998, Project No. BSRI-98-2443.

REFERENCES

[1] H. Morkoç, S. Strite and G. B. Gao, J. Appl. Phys. **76**, 1363 (1994).

[2] W. J. Choyke, *Materials for High-Temperature Semiconductor Devices* (National Academy Press Washington, D. C., 1995), p. 15.

[3] H. S. Lee, S. W. Lee, M. Y. Kwak, Y. S. Choi, D. H. Shin, H. C. Park and W. Jung, Ungyong mulli (Korean J. of Appl. Phys.) **11**, 504 (1998).

[4] C. J. Scozzie, F. B. McLean and J. M. McGarrity, J. Appl. Phys. **81**, 7687 (1997).

[5] F. B. McLean, C. W. Tipton, J. M. McGarrity and C. J. Scozzie, J. Appl. Phys. **79**, 545 (1996).

[6] J. R. Waldrop, J. Appl. Phys. **75**, 4548 (1994).

[7] B. J. Baliga, *Power Semiconductor Devices* (PWS Publishing Company., 1996), p. 128.

[8] J. N. Shenoy, G. L. Chindalore and M. R. Melloch, J. Elec. Mat. **24**, 303 (1995).

[9] J. E. Song, T. H. Kim, S. K. Kim and D. H. Shin, Ungyong mulli (Korean J. of Appl. Phys.) **8**, 346 (1995).

[10] J. E. Song, T. H. Kim and D. H. Shin, J. Korean Phys. Soc. **30**, S239 (1997).

[11] S. Sze, *Physics of Semiconductor Devices* (John Wiley & Sons, 2nd ed. 1981), p. 245.

[12] A. Itoh, O. Takemura, T. Kimoto and H. Matsunami, *Silicon Carbide and Related Materials 1995*, S. Nakashima, H. Matsunami, S. Yoshida and H. Harima eds. (Institute of Physics Publishing, Bristol and Philadelphia, 1995), Institute of Physics Conference Series Number 142, p. 685.

[13] J. R. Waldrop and R. W. Grant, J. Appl. Phys. **72**, 4757 (1992).

[14] M. Lang, T. Isaac-Smith, C. C. Tin and J. R. Williams, Silicon Carbide and Related Materials 1995, S. Nakashima, H. Matsunami, S. Yoshida and H. Harima eds. (Institute of Physics Publishing, Bristol and Philadelphia 1995), Institute of Physics Conference Series Number 142, p. 681.

Journal of the Korean Physical Society, Vol. 34, June 1999, pp. S562~S566

Growth of Nanocrystalline Silicon Carbide Thin Films by Plasma Enhanced Chemical Vapor Deposition

S. W. LEE, Y. S. CHOI, J. Y. MOON, S. S. AHN, H. Y. KIM and D. H. SHIN

Department of Physics, Dongguk University, Seoul 100-715

Nanocrystalline silicon carbide thin films have been deposited by plasma enhanced chemical vapor deposition (PECVD) using SiH_4, CH_4, and H_2 gases. The effects of gas mixing ratio (CH_4/SiH_4), deposition temperature, and RF power on the film properties have been studied. The growth rate, refractive index, and the optical energy gap depends critically on the growth conditions. The dependence of the growth rate on the gas flow ratio is quite different from the results obtained for the growth using C_2H_2 gas instead of CH_4. As the deposition temperature is increased from 300 °C to 600 °C, hydrogen and carbon content in the film decreases and as a result the optical gap decreases. At the deposition temperature of 600 °C and RF power of 150 W, the film structure is nanocrystalline. As the result of the nanocrystallization the dark conductivity is greatly improved. The nanocrystalline silicon carbide thin films may be used for large area optoelectronic devices such as solar cells and thin film electroluminescence devices.

I. INTRODUCTION

Hydrogenated amorphous silicon carbide (a-$Si_{1-x}C_x$:H) is a potential material for large area optoelectronic devices in a wide spectral range due to the continuously controllable optical and electrical properties. There are many possible applications such as solar cells, thin film light emitting diodes (TFLEDs) and thin film electroluminescence devices (TFELDs) for flat panel displays (FPDs). Because of the capability of the material to emit light in the full visible wavelength range, it is an especially promising material for large area color display devices [1–3]. However, the poor electrical properties of a-$Si_{1-x}C_x$:H films make it difficult to fabricate optoelectronic devices. The dark conductivity of a-$Si_{1-x}C_x$:H films is usually $10^{-10}\ \Omega^{-1}cm^{-1}$ or below [4,5]. If it is possible to grow nanocrystalline silicon carbide (nc-SiC:H) thin films at conditions similar to that for the growth amorphous silicon carbide, the electrical properties can be improved so that large area, thin film optoelectronic devices may be fabricated.

It is well known that the carbon content and the degree of hydrogenation affect the characteristics of a-$Si_{1-x}C_x$:H films. The ratio of silane and hydrocarbon in the gas phase during PECVD process have strong influence on the structure and the optical and electrical properties [5–8]. H_2 dilution promotes diamond-like C-C bonding in the form of sp^3 over graphite-like sp^2 and affects energy gap [9,10]. Therefore we can control the optical and electrical properties as well as the band gap energy by varying the gas composition and growth conditions such as RF power density and substrate temperature.

In this work, we examined the growth rate, refractive index, and optical energy gap (E_{opt}) as a function of the gas mixing ratio of the reaction gases diluted in H_2 in the PECVD process. The effects of temperature and RF power on the film structure have been observed by Fourier transform infrared (FT-IR) spectra and transmission electron microscopy.

II. EXPERIMENTS

The samples studied in this work were prepared by plasma enhanced chemical vapor deposition (PECVD) using SiH_4 (5 % in H_2) and CH_4 (5 % in H_2) as source gases. The horizontal quartz reactor has an inner diameter of 58 mm. A boron nitride heater was used to heat the substrate. Plasma was generated using an inductively coupled RF source at 13.56 MHz with a maximum RF power of 500 W.

The $Si_{1-x}C_x$:H films were deposited on Si(100) or Corning 7059 glass with a size of 1.6×1.6 cm^2. The substrates were cleaned using trichloroethylene, acetone and methanol. The flow rate of SiH_4 (5 % in H_2) was fixed at 100 sccm and the flow rate of CH_4 (5 % in H_2) was varied from 0 to 150 sccm so that the gas mixing ratio y=CH_4/SiH_4 was controlled between 0 and 1.5. H_2 dilution ratio was 95 %. The substrate temperature and RF power were varied from 300 °C to 700 °C and from 50 W to 300 W, respectively. The pressure during growth was maintained at 0.4 Torr and the deposition time was 2.5 hours.

We used a step measurement system (α-step) and an

ellipsometer to measure the thickness of the films. Optical properties of the films were measured using UV/VIS spectrophotometer (HP8452A) and FT-IR spectrometer (Bomem). The optical energy gap, E_{opt}, was estimated using the Tauc's relation, $\alpha h\nu = B(h\nu - E_{opt})^2$, where B is a constant. Transmission electron microscopy and selected area diffraction (SAD) were used to study the microstructure of the films.

III. RESULTS AND DISCUSSIONS

The growth rate of the $Si_{1-x}C_x$:H films is shown in figure 1. The growth conditions are summarized in Table 1. The growth rate drops sharply at first as we begin to add carbon in the film and then it increases slowly until the gas mixing ratio reaches 1.0. Beyond that, the growth rate decreases again slowly. The increase of the growth rate with the gas flow ratio is consistent with the results of other works [8,11]. The decrease of the growth rate above y=1.0 can be explained by the fact that the total pressure was kept constant and therefore the amount of Si source gas in the reactor begins to decrease considerably for gas mixing ratio above 1.0. The unique feature of our result is the sharp decrease of the growth rate for y=0.2 from that for y=0.0. For comparison, Nakayama

Table 1. Parameters used for PECVD growth. The parameters used by Nakayama *et al.* are shown for comparison.

	This work	Nakayama *et al.*
Reaction gas	SiH_4 : 5 sccm	SiH_4 : 100 sccm
	CH_4 : 0~7.5 sccm	C_2H_2 : 0~100 sccm
H_2 dilution	95 %	300 sccm
Pressure	0.4 Torr	0.45 Torr
RF power	50~300 W	150 W
Temperature	300~700 °C	300 °C

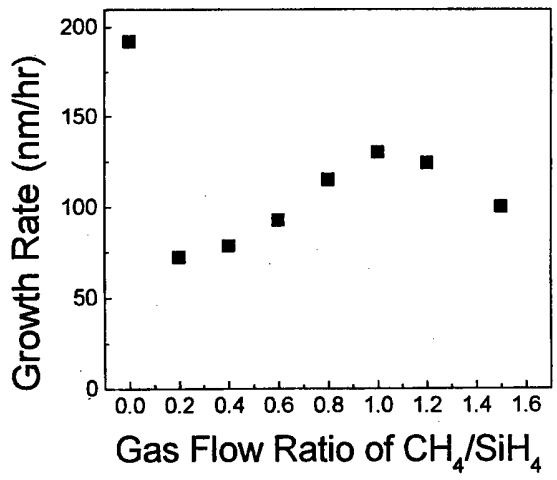

Fig. 1. Growth rate of $Si_{1-x}C_x$:H films as a function of gas mixing ratio.

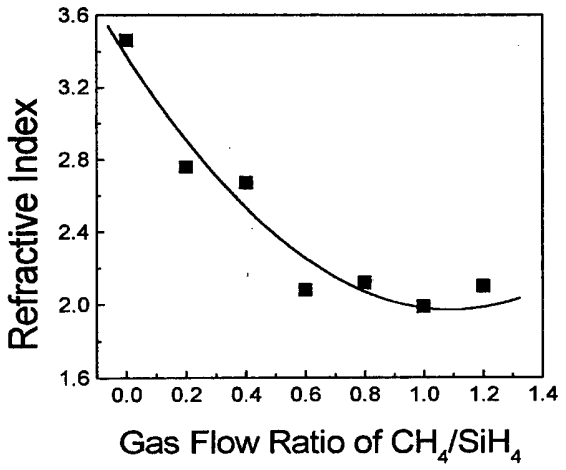

Fig. 2. Refractive index of $Si_{1-x}C_x$:H thin films as a function of gas mixing ratio.

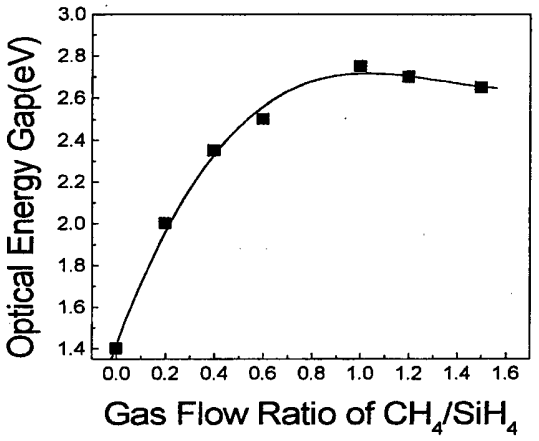

Fig. 3. Optical energy gap of $Si_{1-x}C_x$:H thin films as a function of gas mixing ratio.

et al. and Kuhman *et al.* reported that the growth rate was lowest when y=0.0. The different results may be explained by the fact that different carbon source gases were used. They used C_2H_2 gas while we used CH_4 gas. The thermal dissociation energy of CH_4 is larger than that of C_2H_2. Hence the addition of CH_4 gas may cause the growth rate to drop initially. However, as more CH_4 gas becomes available in the reactor chamber, the growth rate increase slowly.

As the gas mixing ratio is changed from 0.0 to 1.5, the refractive index of the film decreases from 3.5 to 2.0 (Fig. 2) while the optical energy gap, E_{opt}, increase from 1.40 eV to 2.78 eV (Fig. 3). The refractive index of 3.5 and E_{opt} of 1.4 eV for y=0.0 are typical of a-Si:H films. The changes of the refractive index and E_{opt} with the gas mixing ratio, y, is consistent with the results of other works [8,11]. Since it has been demonstrated that the actual carbon content in the $Si_{1-x}C_x$:H film is nearly proportional to the gas mixing ratio, y, the relation between the refractive index and the carbon content of the film and

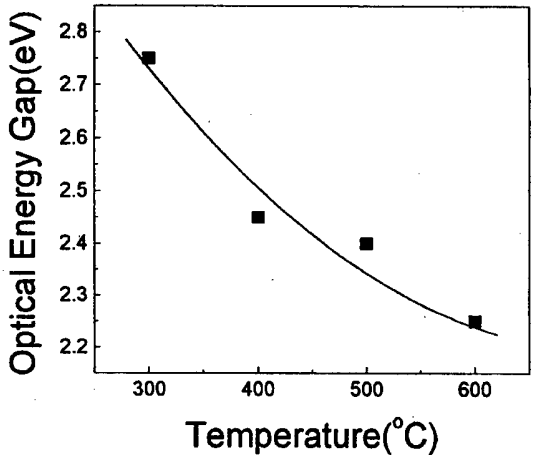

Fig. 4. Optical energy gap of $Si_{1-x}C_x$:H thin films as a function of growth temperature.

the relation between E_{opt} and the carbon content of the film can be directly established [9].

The effect of growth temperature upon the film structure has been examined while fixing the gas mixing ratio and RF power at 1.0 and 50 W, respectively. When the temperature is increased from 300 °C to 600 °C, the optical gap is decreased from 2.75 eV to 2.25 eV (Fig. 4). It is considered that the large change of E_{opt} with the growth temperature is due to the structural changes as well as to the changes in carbon content of the film. Figure 5 shows IR absorption spectra of the films grown at 300, 400, 500 and 600 °C. The observed peaks are attributed to Si-H_n stretching mode (2100 cm^{-1}) [12,13], Si-C stretching mode (780 cm^{-1}) [14–16], and C-H_n wagging or rocking mode (1030 cm^{-1}) [14,15]. As the temperature increases, Si-H_n stretching mode and C-H_n wagging mode decreases. This means that the amount of hydrogen and carbon in the film is reduced. Wickramanayaka *et al.* [17] reported that hydrogen content in a-SiC:H thin films is reduced as the annealing temperature is increased from 100 °C to 600 °C. They suggest that the sites previously occupied by hydrogen atoms form dangling bonds and the dangling bonds introduce large density of states which causes the E_{opt} to decrease significantly. Figure 5 also shows that the C-H_n wagging or rocking mode decreases as the growth temperature is increased. Since the optical gap is dependent on the carbon content in $S_{1-x}C_x$:H thin films, it is supposed that the carbon content is also decreased. As the hydrogen content is reduced, the E_{opt} was reduced to 2.25 eV when the growth temperature was 600 °C at an RF power of 50 W. However, the Si-C bonding was increased. This indicates therefore that despite the reduction of carbon content, the structure of the film begins to have crystalline phase of silicon carbide.

Figure 6 and 7 show the optical gap and the IR absorption spectra of the films grown at 600 °C with different RF power. As RF power is increased from 50 W to 125 W, E_{opt} is increased from 2.25 eV to 3.0 eV. The IR absorption spectra shows that as the RF power is increased, the peak due to Si:C stretching mode becomes

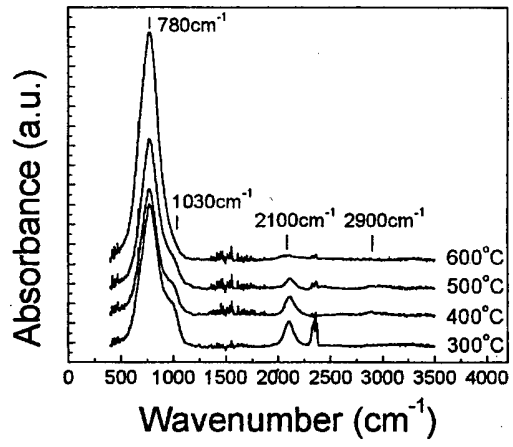

Fig. 5. IR absorption spectra of $Si_{1-x}C_x$:H thin films grown at different temperatures.

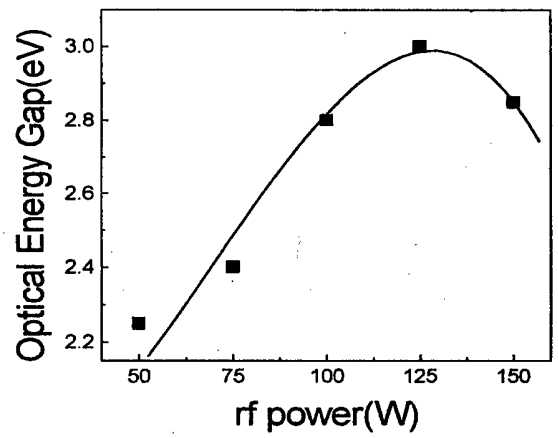

Fig. 6. Optical energy gap as a function of RF power. Growth temperature is 600 °C.

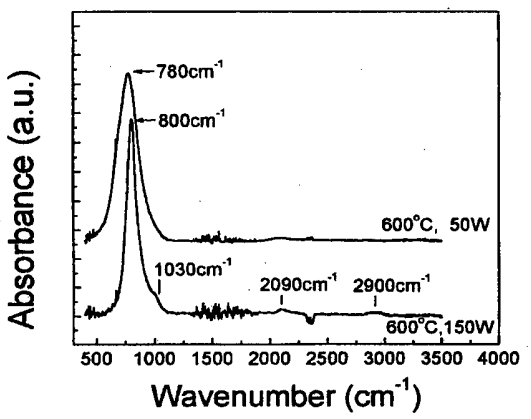

Fig. 7. IR absorption spectra of $Si_{1-x}C_x$:H thin films grown with different RF power. Growth temperature is 600 °C.

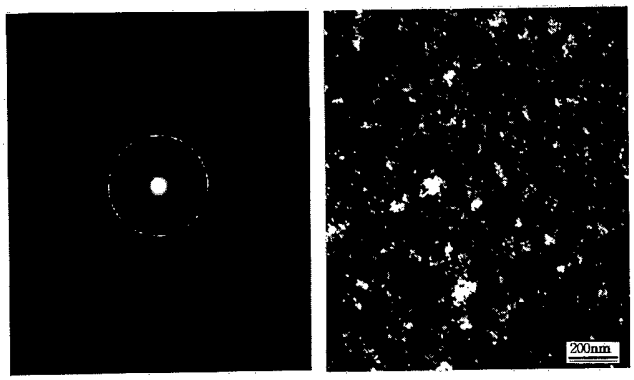

(a) (b)

Fig. 8. (a) Selected area electron diffraction (SAD) pattern of $Si_{1-x}C_x$:H thin film grown at 700 °C with RF power of 300 W. (b) Transmission electron micrograph of the same sample.

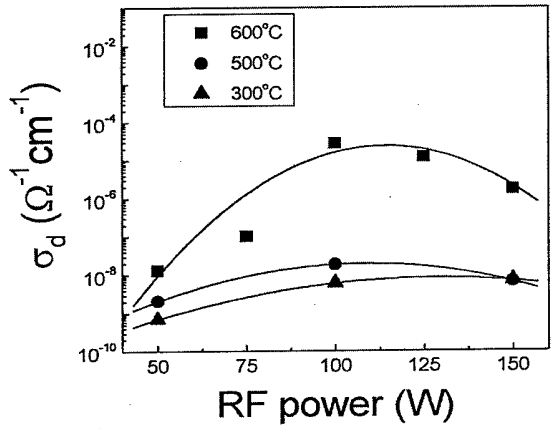

Fig. 9. Dark conductivity of $Si_{1-x}C_x$:H thin films as a funtion of RF power and growth temperature.

sharper and stronger. The FWHM of Si-C stretching mode narrowed down from 204 cm^{-1} to 102 cm^{-1} and the peak shifted slightly from 780 cm^{-1} to 800 cm^{-1}. Chen *et al.* [18] suggested that the peak at 800 cm^{-1} is due to SiC TO phonon mode. These observations indicate that more carbon atoms in the film are forming Si-C bonding, changing the structure of the film from amorphous to nanocrystalline. Therefore, both higher growth temperature and higher RF power tend to increase the crystallinity of the film. However, the latter tends to increase the carbon content and the optical gap of the film while the former tends to decrease the carbon content and the optical gap of the film. These observations can be used to control the optical gap and the film structure simultaneously.

Figure 8(a) show the electron diffraction pattern of the film grown at 700 °C with an RF power of 300 W. The SAD pattern suggests that the film consists of amorphous matrix with small crystalline grains. The transmission electron micrograph of the same film shows clearly that the film structure is nanocrystalline with grain sizes ranging from a few nanometers to a hundred nanometers (Figure 8(b)). The films grown at lower temperatures and at lower RF power are thought to have similar structures with smaller grain sizes.

Figure 9 shows the improvement of dark conductivity due to the crystallization of the $Si_{1-x}C_x$:H films. The typical dark conductivity of a-$Si_{1-x}C_x$:H film grown at 300 °C is 7.0×10^{-10} Ω^{-1} cm^{-1} while the dark conductivity of nc-$Si_{1-x}C_x$:H film grown at 600 °C is as high as 3.1×10^{-5} Ω^{-1} cm^{-1}. It is evident that the nanocrystallization of the $Si_{1-x}C_x$:H films greatly improves the electrical properties of the films.

IV. CONCLUSIONS

We have deposited amorphous and nanocrystalline silicon carbide thin films by plasma enhanced chemical vapor deposition (PECVD) using SiH_4, CH_4, and H_2 gases. The effects of gas mixing ratio (CH_4/SiH_4), deposition temperature, and RF power on the film properties have been studied. The growth rate, refractive index, and the optical energy gap, E_{opt}, depends critically on the growth conditions. When CH_4 gas is used as carbon source gas, the dependence of the growth rate on the gas flow ratio is quite different from the results obtained for the growth using C_2H_2 gas. As the deposition temperature is increased from 300 °C to 600 °C, hydrogen and carbon content in the film decreases and as a result the optical gap, E_{opt}, decreases. At the deposition temperatures over 500 °C and RF power of 150 W, the film structure is nanocrystalline. It is thought that the film consists of amorphous matrix with small crystalline grains ranging in size from a few nanometers to a hundred nanometers. As the result of the nanocrystallization the dark conductivity is improved by more than four orders of magnitude.

ACKNOWLEDGMENTS

This research was supported in part by the Korean Ministry of Science & Technology through the Future Oriented Technology Development Program (F-01, 1998) and by the Basic Science Research Institute Program, Korean Ministry of Education, 1998, Project No. BSRI-98-2443.

REFERENCES

[1] T. Ma, J. Xu, K. Chen, J. Du, W. Li and X. Huang, Appl. Phys. Lett. **72**, 13 (1998).

[2] Y.-A. Chen, C.-F. Chiou, W.-C. Tsay, L.-H. Laih, J.-W. Hong and C.-Y. Chang, IEEE Trans. Electron Divices **44**, 1360 (1997).

[3] J.-W. Lee and K. S. Lim, Appl. Phys. Lett. **68**, 1031 (1996).

[4] W. K. Choi, F. L. Loo, F. C. Loh and K. L. Tan, J. Appl. Phys. **80**, 1611 (1996).
[5] H.-K. Tsai, W.-L. Lin, W. J. Sah and S.-C. Lee, J. Appl. Phys. **64**, 1910 (1988).
[6] V. Mastelaro, A. M. Flank, M. C. A. Fantini, D. R. S. Bittencourt, M. N. P. Carreo and I. Pereyra, J. Appl. Phys. **79**, 1324 (1996).
[7] W. K. Choi, Y. M. Chan, C. H. Ling, Y. Lee, R. Gopalakrishinan and K. L. Tan, J. Appl. Phys. **77**, 827 (1995).
[8] D. Kuhman, S. Grammatica and F. Jansen, Thin Solid Films **177**, 253 (1989).
[9] A. Desalvo, F. Giorgis, C. F. Pirri, E. Tresso, P. Rava, R. Galloni, R. Rizzoli and C. Summonte, J. Appl. Phys. **81**, 7973 (1997).
[10] M. L. de Oliveira, S. S. Camargo, Jr. and F. L. Freire, Jr., J. Appl. Phys. **71**, 1531 (1992).
[11] Y. Nakayama, S. Akita, M. Nakano and T. Kawamura, J. Non-Cryst. Solids **97/98**, 1447 (1987).
[12] M. H. Brodsky, M. Cardona, J. J. Cuomo, Phys. Rev. **B16**, 3556 (1977).
[13] A. A. Langford, M. L. Fleet, B. P. Nelson, W. A. Lanford and N. Maley, Phys. Rev. **B45**, 13367 (1992).
[14] J. Bullot and M. P. Schmidt, Phys. Status Solidi **B143**, 345 (1987).
[15] F. Demichelis, C. F. Pirri, E. Tresso and T. Stapinski, J. Appl. Phys. **71**, 5641 (1992).
[16] Y. M. Li and B. F. Fieselmann, Appl. Phys. Lett. **59**, 1720 (1991).
[17] S. Wickramanayaka, Y. Nakanishi and Y. Hatamaka, J. Appl. Phys. **77**, 2061 (1995).
[18] K.-L. Cheng, H.-C. Cheng, C.-C. Lu, C. Lee and T.-R. Yew, Jpn. J. Appl. Phys. **34**, 5527 (1995).

Journal of the Korean Physical Society, Vol. 34, June 1999, pp. S567~S570

Monte Carlo Simulation on Electron Transport in $Si_{1-y}C_y$ Alloy Layers

S. H. IHM, J. H. SEOK, C. H. LEE, H. J. Lee and J. Y. KIM*

Semiconductor Physics Research Center (SPRC) and Department of Semiconductor Science and Technology, Chonbuk National University, Jeonju 561-756

S. K. CHUN

Department of Electronic Materials and Devices Engineering, Inha University, Inchon 402-751

We investigated electron transport in strained $Si_{1-y}C_y$ alloy layers grown on Si(100) substrates using the Monte Carlo simulation. The electron mobility higher than that of bulk Si over a wide range of temperatures from 40 K to 300 K is mainly attributed to the valley splitting induced by the tensile strain in the $Si_{1-y}C_y$ layer. For lower temperatures less than 100 K the mobility increases sharply depending on the carbon fraction up to about 0.6 %. Beyond the fraction, however, it keeps almost constant regardless of increasing the carbon fraction. On the other hand, we observe a monotonic mobility increase with increasing the carbon fraction for a higher temperature regime.

I. INTRODUCTION

Carbon-containing group IV materials such as $Si_{1-y}C_y$, $Ge_{1-y}C_y$, and $Si_{1-x-y}Ge_xC_y$ alloys are new materials and have recently attracted much attention because of their advantages than bulk Si and $Si_{1-x}Ge_y$ alloy and their potential for high speed devices [1–3]. Epitaxially grown $Si_{1-x}Ge_y$ layer results in a strained crystal, which has advantages since properties that are forbidden in bulk silicon become allowed. However, the inherent lattice mismatch (4.2 %) between Si and Ge makes it difficult to grow epitaxial $Si_{1-x}Ge_y$ layer thicker than a 'so-called' critical thickness without possessing strain-reliving dislocations. To circumvent this problem, doping of small amount of carbon into $Si_{1-x}Ge_y$ alloy was suggested since carbon can compensate the existing strain between Si and Ge. It is thus possible to grow much thicker epitaxial layer beyond the critical thickness. In addtion, the growth of strained $Si_{1-y}C_y$ alloy on Si allows the realization of tensile strained layers which can be used for confining electrons in the Si channel. In order to have an electron channel in SiGe material system it is needed to grow tensile strained Si layer on thick SiGe layer with graded Ge composition (typically about 1 μm). However, $Si_{1-y}C_y$/Si heterostructure can effectively confine electrons without such a thick layer as in SiGe system, so that it is a very useful structure for device applications.

This study is to investigate in-plane electron transport in strained $Si_{1-y}C_y$ layer using a Monte Carlo simulation technique. Recently published papers show different experimental results on the Hall electron mobility in epitaxial $Si_{1-y}C_y$ alloy layer [1,2,4]. The higher Hall electron mobility in the alloy layer than that of bulk Si were reported by Eberl *et al.* while Osten *et al.* reported opposite results. Although Ershov *et al.* reported an electron mobility enhancement in this system, it is not sufficient to fully support the recent experimetal results [5].

II. MONTE CARLO SIMULATION

To investigate the electron transport in $Si_{1-y}C_y$ alloy

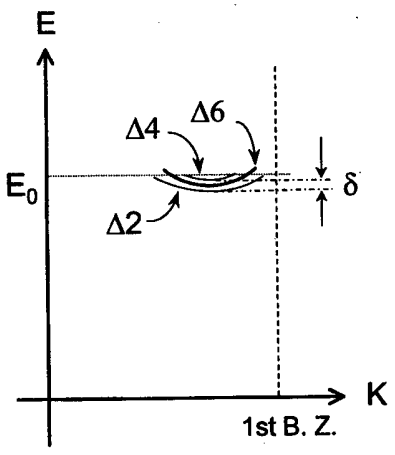

Fig. 1. Energy splitting of degenerate Δ_6 valleys into Δ_2 and Δ_4 valleys due to the tensile strain in $Si_{1-y}C_y$ layer grown on a Si(100) substrate. δ indicates the valley separation.

*E-mail: jykim@moak.chonbuk.ac.kr, Fax: +82-652-270-3585
To whom correspondence should be addressed.

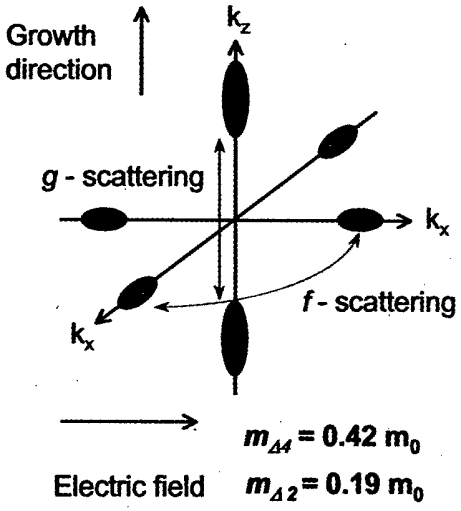

Fig. 2. Constant energy surfaces along the k-axes in tensile strained $Si_{1-y}C_y$ layer grown on a Si(100) substrate. Effective masses in each valley along the [100] direction are given.

Table 1. Parameters used in the simulation.

Parameters	Value	Units
Effective mass (m^*) along electric field m_{Δ_4}	0.42	m_0
m_{Δ_2}	0.19	m_0
Dielectric constant	11.7	
Nonparabolicity (α)	0.5	eV^{-1}
Sound velocity (μ)	9.04	10^5 cm/s
Density (ρ)	2.33	g/cm^3
Acoustic deformational potential	9.5	eV
Nonpolar optical deformation potential	4.51	eV/cm
f-phonon ($f1$, $f2$, $f3$)	0.019, 0.041, 0.059	eV
g-phonon ($g1$, $g2$, $g3$)	0.012, 0.019, 0.062	eV
Valley separation	$6y$	eV
Doping concentration (n)	10^{17}	cm^{-3}
Number of real collisions	5,000,000	

we used a Monte Carlo simulation method [6,7]. Fig. 1 shows the splitting of the sixfold degeneracy of the conduction band into the lowered twofold Δ_2 and raised fourfold Δ_4 valleys. The energy splitting between Δ_2 and Δ_4 valleys due to the tensile strain is approximately given by δ=6y eV where y indicates the doped carbon concentration [5]. The effective mass for bulk Si conduction band valley is 0.98 m_0 in the direction of the major axis of an ellipsoid, whereas that along the minor axis is 0.19 m_0. Fig. 2 shows the constant energy surfaces of the two and fourfold valleys, the growth direction, and the applied electric field. The twofold valleys have an effective mass of 0.19 m_0 and the fourfold valleys an effective mass of 0.42 m_0 along the electric field, respectively. We notice that the effective mass of Δ_4 valleys is larger than that of average effective mass of bulk Si of 0.33 m_0 along the electric field. Scattering mechanisms considered in the Monte Carlo study are intravalley acoustic and optical phonon scattering, intervalley f-($f1$, $f2$, $f3$) and g-phonon ($g1$, $g2$, $g3$) scattering, and alloy scattering, and ionized impurity scattering. The representative f- and g-scattering are also shown in the figure. The band nonparabolicity is also included. Experimental studies show that the growth window of carbon-containing epitaxial layers is narrow and thus carbon concentration of less than 1 % is taken into account in this study. To have

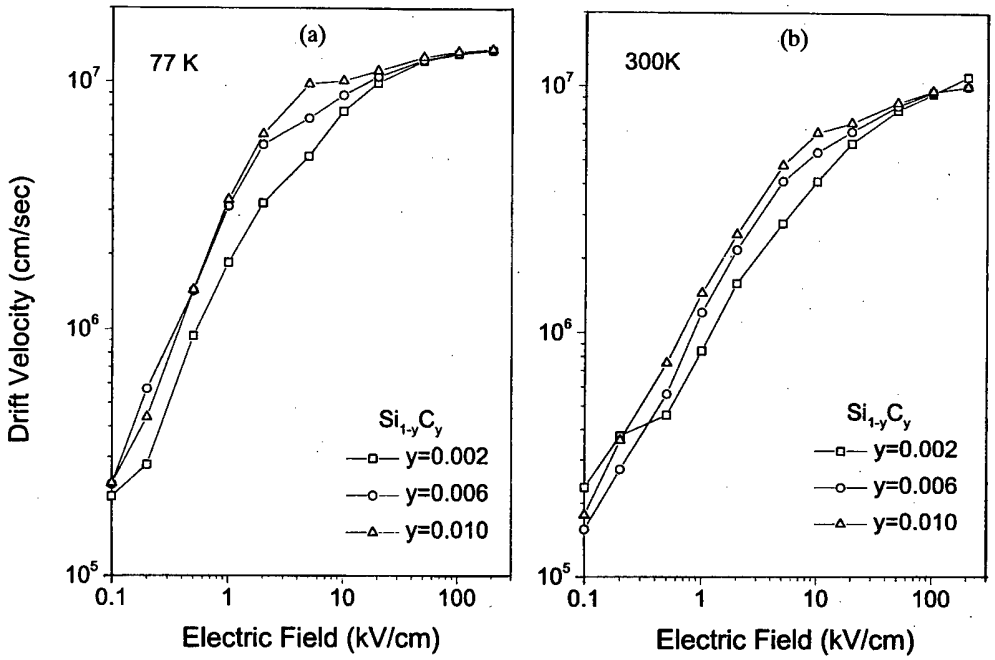

Fig. 3. Drift electron velocity with various carbon concentration simulated at (a) 77 K and (b) 300 K.

relatively accurate simulation results, we allowed 5×10^6 times of real scattering collisions for each electric field during the simulations. All of the simulation parameters used are summarized in Table 1.

III. RESULTS AND DISCUSSION

Fig. 3 shows the drift velocity with increasing electric field as a function of carbon concentration simulated at (a) 77 K and (b) 300 K. We used the value of U_0=0.55 eV for the alloy potential which corresponds to the conduction band offset for the Si/β-SiC system [5]. The relatively rapid increase of drift velocity is observed for low fields at 77 K while the relatively slow increase at 300 K. As the carbon doping increases, the velocity-field characteristic shows a minor increase of the drift velocity over the intermediate field range from 1 to 10 kV/cm.

The drift electron mobility with temperature is shown in Fig. 4. As the carbon increases, the mobility increases. However, the increasing rate of the mobility is different depending on measurement temperatures. It increases rapidly with increasing carbon fraction y up to about 0.6 % and then keeps almost constant with further increase of carbon concentration for lower temperatures less than about 100 K. However, it increases gradually for higher temperature regime greater than about 200 K. Since most electrons stay in lower valleys which have lower effective mass of 0.19 m_0 smaller than the value of 0.33 m_0 of bulk Si, the mobility is increased as we add carbon. That is, electron repopulation induces the mobility increase in this temperature regime. For higher temperature regime the mobility increases monotonically. Although the valley separation leads to the reduced intervalley scattering and thus increases the mobility, the higher fourfold valleys which have larger average effective mass of 0.42 m_0 get more electrons as temperature increases. This suppresses the rapid mobility increase in the higher temperature regime. Electron-phonon inter-

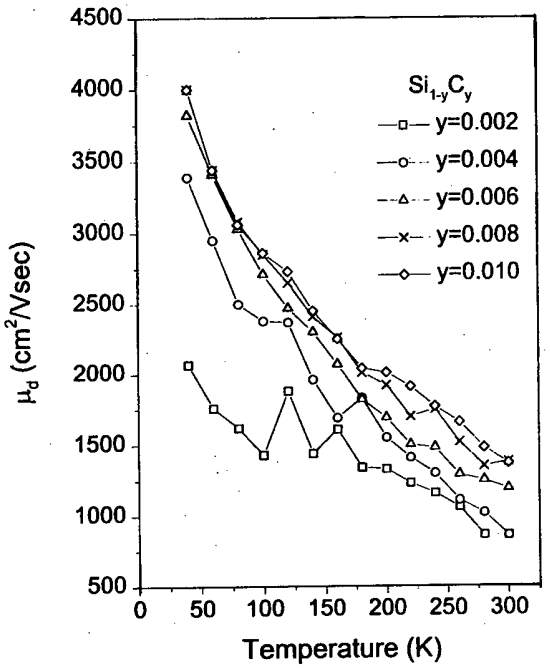

Fig. 4. Electron mobility as functions of carbon concentration and temperature.

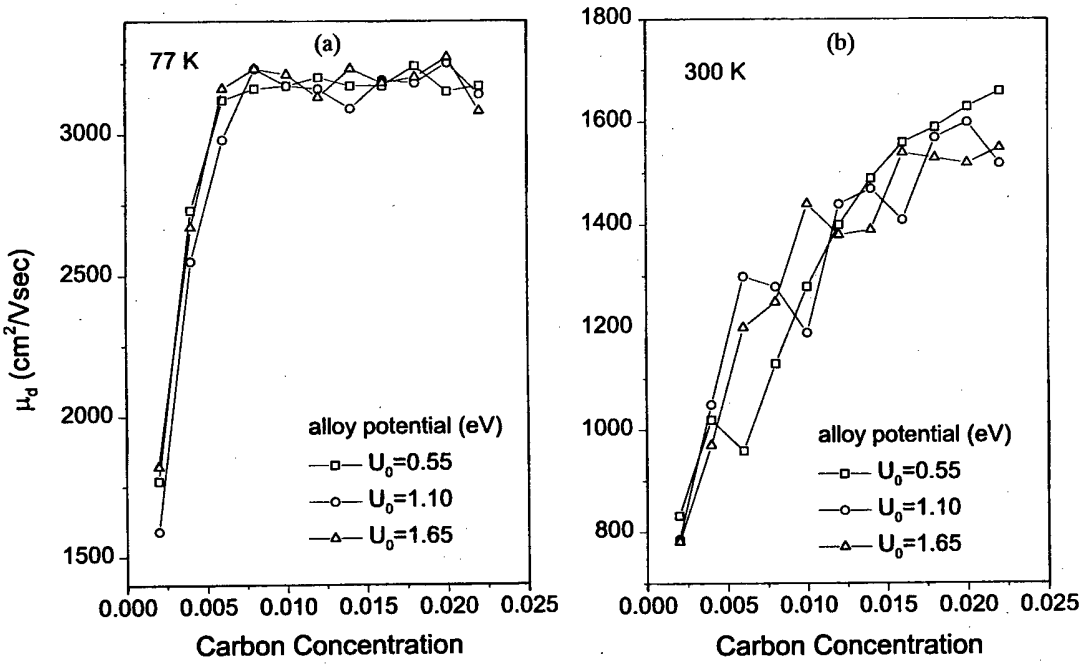

Fig. 5. Electron mobility as functions of alloy potential and carbon concentration simulated at (a) 77 K and (b) 300 K.

action at high temperatures also contributes to the slow mobility enhancement. The mobility simulation results with y=0.002 carbon shows fluctuations between 100 K and 180 K although the entire trend of the curve is not different from other reported results. But the fluctuation decreases as carbon doping increases. It is believed to be from the small valley separation for y=0.002 carbon sample. As mensioned in the introduction, two previous experimental results showed different values of Hall mobility over the temperature range from 30 to 300 K. The characteristic of drift mobility versus temperature in this study is in a good agreement with Eberl *et al.*'s experimental results. Defect-free crystal growth may be critical to achieve such a high electron mobility in $Si_{1-y}C_y$ alloy layers [8].

Alloy potential is not *a priori* known. The effect of alloy potential was thus studied with different values of alloy potential as shown in Fig. 5(a) and (b). As we mentioned in the above, the mobility increases very sharply with the carbon fraction up to 0.6 %, but it stops to increase and saturates beyond 0.6 % carbon fraction regardless of the magnitude of alloy potential. We cannot observe any maximum peak in the characteristic between the electron mobility and the carbon fraction for smaller values of U_0 as Ershov *et al.* reported [5].

IV. CONCLUSIONS

We studied electron transport in strained $Si_{1-y}C_y$ alloy layers grown on Si(100) substrates using the Monte Carlo simulation. The increased electron mobility compared to that of bulk Si over the wide range of temperatures from 40 K to 300 K is mainly attributed to the valley splitting induced by the tensile strain in the $Si_{1-y}C_y$ layer. The valley separation leads to electron repopulation, reduced effective mass in the lower valleys, and reduced intervalley scattering, so that the overall mobility is increased. For lower temperatures less than 100 K the mobility increases rapidly with increasing carbon fraction, but it stops to increase beyond 0.6 % carbon concentration. On the other hand, we observe a monotonic mobility increase with increasing y for a higher temperature regime. We noticed that defect-free crystal growth is essential to achieve high electron mobility in the $Si_{1-y}C_y$ alloy layer.

ACKNOWLEDGMENTS

This work was supported by the Korea Science and Engineering Foundation (KOSEF) through the Semiconductor Physics Research Center (SPRC) at Chonbuk National University. Part of this work has been supported by research funds of Chonbuk National University.

REFERENCES

[1] K. Eberl, K. Brunner and W. Winter, Thin Solid Films **294**, 98 (1997).
[2] H. J. Osten and P. Gaworzewski, J. Appl. Phys. **82**, 4977 (1997).
[3] O. G. Schmidt and K. Eberl, Phys. Rev. Lett. **80**, 3396 (1998).
[4] W. Faschinger, S. Zerlauth, G. Bauer and L. Palmetshofer, Appl. Phys. Lett. **67**, 3933 (1995).
[5] M. Ershov and V. Ryzhii, J. Appl. Phys. **76**, 1924 (1994).
[6] Carlo Jacoboni and Paolo Lugli, *The Monte Carlo Method for Semiconductor Device Simulation* (Springer-Verlag, Wien, 1989).
[7] Carlo Jacoboni and Lino Reggiani, Rev. Mod. Phys. **55**, 645 (1983).
[8] K. Eberl (private communications).

Journal of the Korean Physical Society, Vol. 34, June 1999, pp. S571~S576

Monte Carlo Study of Impact Ionization in 0.1 μm n-MOSFETs

Insook LEE

LG Corporate Institute of Technology, Seoul 137-724

We have investigated impact ionization characteristics as a function of temperature and substrate impurity concentration, N_{sub}, in 0.1 μm n-MOSFETs, by using the full-band Monte Carlo device simulator that solves the Poisson equation and the Boltzmann transport equation self-consistently. We focused on some interesting features of impact ionization in short channel device structures, which are not obvious from the arguments based on the conjectures from bulk properties. Suppressed hot carrier effects at low temperature mainly due to both quasi-ballistic transport and temperature dependent band gap were confirmed in 0.1 μm n-MOSFETs. Our simulation results also indicate that impact ionization rate decreases with rising substrate impurity concentration in 0.1 μm n-MOSFETs, which is consistent with the experimental findings but is just opposite to the trends in long channel devices. We believe that this is mainly because the very short pinch-off region due to shallow junctions (~50 nm) results in marked nonlocal heating effects despite the small applied V_{ds} and thus, the narrower field peak with rising N_{sub} makes its capability of producing hot carriers decreased.

I. INTRODUCTION

The rapid progress of VLSIs has been driven by the push towards miniaturization of their component such as a MOSFET to increase the storage capacity with low power consumption. As device sizes become smaller, the complexity of VLSI process and device structure continues to grow and a huge increase comes in facilities and manufacturing costs. Therefore, a device simulator can play a very important role to accomplish precise device design of VLSIs under the strong requirement on the reduction of budget and time. However, carriers in such a small-sized device where the device dimension approaches the distance between scattering events in the semiconductor crystal are less affected by collisions during the transit; thus, non-equilibrium transport effects become appreciable. In this circumstance, the device simulator based on the drift-diffusion (DD) model [1] which does not include non-equilibrium transport [2] starts to lose its validity. More rigorous physical models are needed to facilitate the modeling of associated microscopic transport mechanisms and there is a growing demand for a device simulator by which a non-equilibrium carrier transport in a small-sized device can be handled.

To simulate non-equilibrium carrier motion in a semiconductor device, both deterministic numerical methods and stochastic Monte Carlo particle methods incorporating a more complete solution to the Boltzmann transport equation (BTE) have been demonstrated [3]. One example of the former approach is the hydrodynamic (HD) model. In sub-micron semiconductor devices which are characterized by relatively large electric fields as well as relatively sharp spatial variations of the electric fields and carrier concentrations, the carriers can be easily heated by applied electric fields. This carrier heating results in a carrier energy distribution that deviates significantly from its equilibrium shape, which violates a basic assumption in the DD model. The HD model qualitatively extends beyond the DD model by allowing carrier mobilities to be functions of the average carrier energy rather than the local electric field, and allowing the carrier temperature to be different from the lattice temperature. While both the DD and the HD models provide the low-order approximate solutions to the BTE, the Monte Carlo method provides the most efficiently implemented and physically adaptive technique currently available to determine exact numerical solutions to the electron motion in semiconductor devices. In small devices where the distances between scattering events are comparable to device dimension, only an exact solution of the BTE will suffice because of the extreme non-equilibrium transport. Thus, as the miniaturization of semiconductor devices continues, the DD and the HD models must break down for they are only a truncated version of a full solution of the BTE.

Recently, short channel MOSFETs down to the 0.1 μm region have been the focus of intensive research. As device size shrinks, the drain voltage is reduced as well. However, the supply voltage is not reduced as aggressively as the gate length and thus, hot carrier effects could still exist in 0.1 μm devices and even more violent than in sub-micron devices. Thus, correct knowledge of impact

ionization is essential for precise analyses and predictions of device characteristics such as reliability and degradation of short channel semiconductor devices. In spite of its importance, large discrepancy in the energy dependence of the impact ionization rate even in Si has been existed in the past [4], mainly because meaningful studies of impact ionization become possible only if the correct ionization rate is coupled with the correct transport analyses [5,6]. When the ionization rate modeled empirically via, say, the Keldysh formula is incorporated in the BTE, the realistic band structure of semiconductor needs to be taken into account in both the ionization rate and the BTE. Thus, only the full-band Monte Carlo method currently provides the way to solve this subtle problem with a satisfactory accuracy. In this work, we employed the full-band Monte Carlo device simulator DAMOCLES [7] that has been developed in IBM and solves the Poisson equation and the BTE self-consistently, to study the impact ionization in n-channel Si-MOSFETs designed for 0.1 μm operation.

We focused on some interesting features of impact ionization in short channel device structures, which are not obvious from the arguments based on the conjectures from bulk properties. Recent MC simulations [8] have revealed that the experimental findings on suppressed hot carrier effects at low temperature in sub 0.1 μm MOSFETs are mainly due to both quasi-ballistic transport and temperature dependent band gap. Experimental studies [9] have been performed to examine the influences of substrate doping on hot carrier characteristics of small geometry n-MOSFETs and the results indicate that the dependence of impact ionization rate on substrate impurity concentration is reversed in long channel and short channel devices. In this study, we have performed MC simulations to investigate hot carrier effects associated with impact ionization in typical n-MOSFETs with gate length of 0.1 μm as a function of temperature and substrate impurity concentration, N_{sub}, respectively. Our results reproduced the anomalous temperature dependence at low drain bias and the experimental trend of the N_{sub} dependence on hot carrier effects in 0.1 μm n-MOSFETs. In our MC simulations, an ensemble of 8,000 $\sim$ 10,000 particles is used with a time step of 10^{-16} sec. The statistical enhancement procedures [6] were employed in both energy and real space to improve computational efficiency so that electrons with energy much greater than the ionization threshold energy could be handled in 0.1 μm n-MOSFETs. However, the short range carrier-carrier scattering has not been considered due to its intensive computation time, which would not change the resultant qualitative features [10]. The important device parameters of the n-MOSFET studied in this work are listed in Table 1. In the next two sections, simulation results on anomalous temperature and substrate impurity concentration dependence of impact ionization are presented and discussed. Finally, concluding remarks are given in Section IV.

Table 1. Important device parameters of a 0.1 μm n-MOSFET.

l_g : gate length	100 nm
x_j : junction depth	50 nm
t_{ox}: gate oxide thickness	4 nm
N_{sub} : substrate impurity concentration	5 $\times 10^{17}$ cm^{-3}

II. TEMPERATURE DEPENDENCE OF IMPACT IONIZATION

The low temperature operation of deep sub-micron devices is very attractive owing to the capability of improving the device performance and suppressing the short channel effect. But it has been said that one of the major obstacles to operate MOSFETs at low (77 K) temperature is the enhanced hot carrier effects. As temperature lowered, electrons gain more energy as a result of the reduced electron-phonon scatterings and thus, the high energy tail of the electron energy distribution (EED) is enhanced [11]. However, this temperature dependency is actually weak in devices and, in some cases (*i.e.*, under low drain voltage), even reversed [8]. This *anomalous* behavior implies that the hot carrier effect is less significant in deep sub-micron devices operated at low temperature. Therefore, it is very important to evaluate the impact ionization phenomena at low temperature in very short channel devices. In order to investigate this hot carrier dependence on temperature, we have performed full-band Monte Carlo device simulations and have clearly reproduced the experimental trends.

Figure 1 shows the calculated electron impact ionization generation rates along the interface of the 0.1

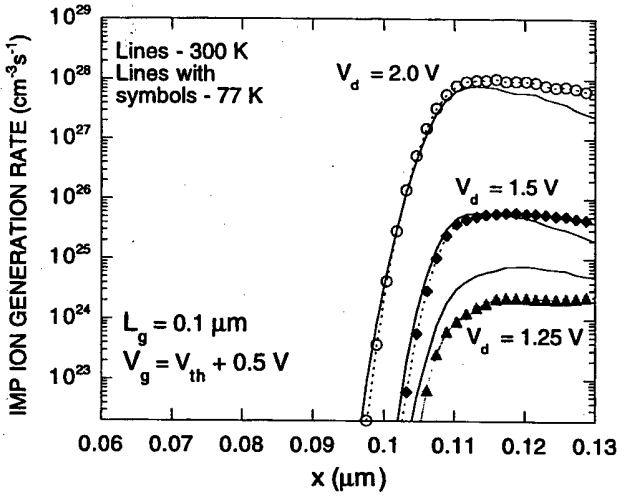

Fig. 1. Calculated electron impact ionization generation rates along the interface of the 0.1 μm n-MOSFET under the three different drain voltages, V_d=2.0 V, 1.5 V and 1.25 V and at T=77 K and 300 K. The gate voltage is fixed at $V_g = V_{th}$ + 0.5 V. At low temperature, the band-gap widening effect was taken into account (see Fig. 4).

μm n-MOSFET under the three different drain voltages, V_d = 2.0 V, 1.5 V and 1.25 V from the top in the figure for two different temperatures, T = 77 K and 300 K, respectively. The gate voltage is fixed at $V_g = V_{th} + 0.5$ V. At large bias, the impact ionization generation rate increases with reduced temperature. However, as the bias approaches the ionization threshold (E_{th}), *i.e.*, at V_d = 1.25 V, the room temperature ionization rate becomes higher than the low temperature ionization rate. Thus, the so called *cross-over* [12] occurs in the 0.1 μm n-MOSFET. Note also that under low bias at low temperature the ionization rate keeps its high value even deep inside the drain and thus, the degradation due to impact ionization affects almost the whole drain region under this condition. The corresponding electric fields and electron energies as a function of distance along the channel are shown in Fig. 2. At low temperature, the electric field strength near the drain is only slightly relaxed compared with the case at room temperature. Even though the electric field profile is almost independent of temperature, the average energy is higher at low temperature due to the reduced electron-phonon scattering rate.

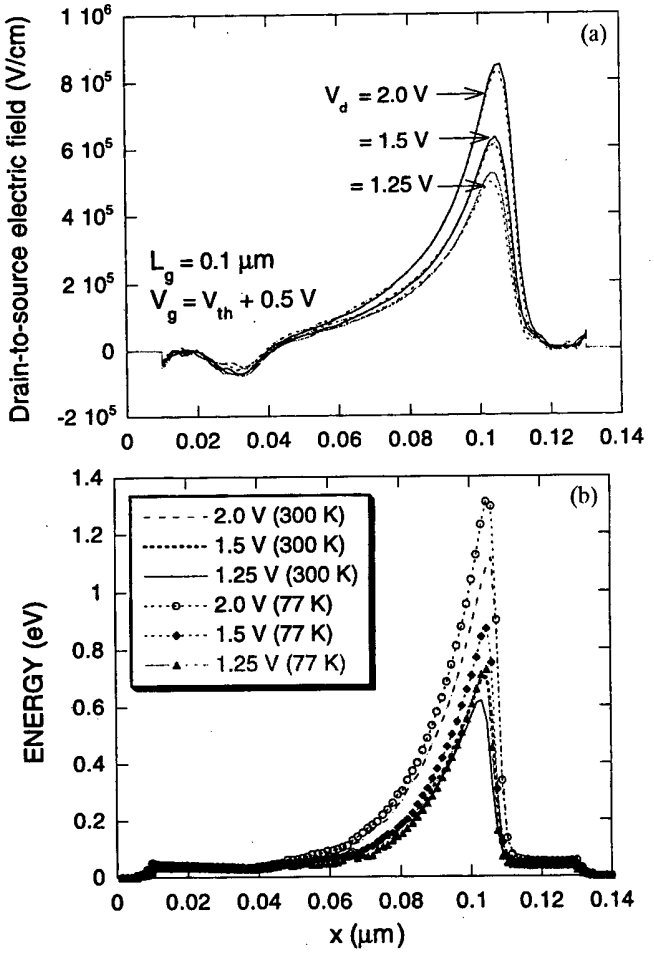

Fig. 2. (a) Electric field and (b) electron energy along the interface under the three different drain voltages, V_d=2.0 V, 1.5 V and 1.25 V. In (a) solid curves represent the electric field at T=300 K and dotted curves represent the electric field at T=77 K, respectively. The electric field strength near the drain is slightly relaxed at the low temperature, compared with the case at room temperature. In (b) curves without symbols indicate electron energy at T=300 K and curves with symbols indicate electron energy at T=77 K, respectively.

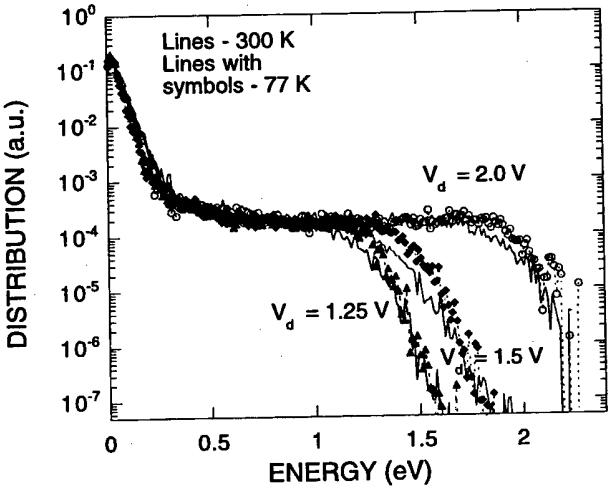

Fig. 3. Electron energy distribution at the channel/drain junction for the three different drain voltages simulated at T=77 K and 300 K.

Figure 3 shows the EED integrated over the channel/drain junction for the three different drain voltages simulated at T = 77 K and 300 K. We see that the EED is almost independent of temperature, with a marginally higher high-energy tail at low temperature. In the 0.1 μm MOSFET, the pinch-off region gets very narrow due to shallow junctions ($\sim$ 50 nm) [13] and thus, the field in this region becomes markedly high despite the small applied V_{ds}. High-fields in the pinch-off region support nearly ballistic transport. Then, the increase of phonon scattering with increased temperature has little effect on the nearly ballistic distribution in the high-field region. Under this quasi-ballistic transport, the number of electrons in the energy range, $E_{th} \leq E \leq qV_{ds}$, becomes less dependent on electron energy or temperature in the 0.1 μm n-MOSFET, which results in nearly flat and almost temperature independent middle energy range up to qV_{ds} in the EED. However, in bulk, where the high electric fields extends for long distances and equilibrium transports prevail, the distribution is determined only by the field and the phonon scattering rate. Therefore, the dependence of impact ionization generation rate on temperature is reversed in long channel and short channel devices. In Fig. 3 the marginally higher high-energy tail at low temperature compensates for the decrease in the number of electrons to have enough energy for impact ionization, due to the slight band-gap widening (so about 65 meV higher ionization threshold as shown in Fig. 4). As the bias V_{ds} is lowered towards the ionization threshold where hot electrons decay exponentially, the slightly higher ionization threshold at low temper-

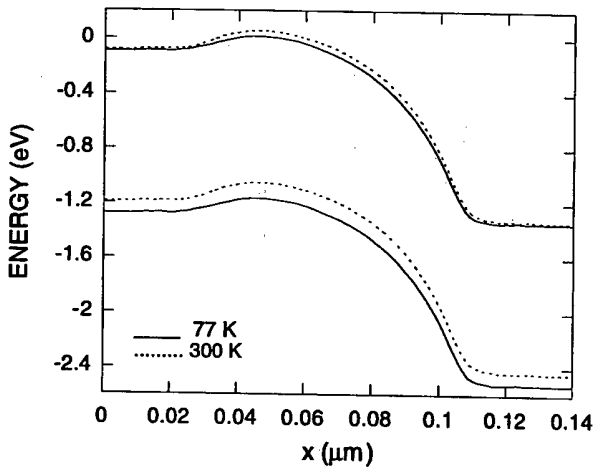

Fig. 4. Calculated conduction band and valence band along the interface at T=77 K and 300 K. The band-gap widening effect is apparent at low temperature.

ature greatly decreases the number of hot electrons for impact ionization and reduces the ionization rate at V_{ds} near the ionization threshold. The decrease of substrate current at low temperature becomes more significant in lower drain voltage. But at large bias, the slight decrease in hot electrons due to the band-gap widening is negligible compared with the higher high-energy tail at low temperature. Therefore, the suppression of hot carrier effect in 0.1 mm devices at low temperature could be mainly ascribed to both the quasi-ballistic transport characteristics and the band-gap energy widening.

III. N_{sub} DEPENDENCE OF IMPACT IONIZATION

In this section, simulation results on the N_{sub} dependence of impact ionization is discussed. Intensive research on short channel MOSFETs down to 0.1 μm has been based on a scaling method. In this method, gate oxide thickness, t_{ox}, and junction depth, x_j, are both reduced, while the substrate impurity concentration, N_{sub}, is increased. There are, of course, some limits to these scaling parameters. For example, increasing N_{sub} is limited because of excessive junction leakage current caused by tunneling. Moreover, increasing N_{sub} increases threshold voltage and reduces drivability characteristics such as transistor transconductance and drain current. Then, the gains achieved by device miniaturization are lost. Under these circumstances, it is essential to understand the influence of each scaling parameter, such as t_{ox} or N_{sub}, on device characteristics, and to investigate the limits of the scaling method. Many studies on the influence of ultra thin gate oxides on recent small geometry MOSFET characteristics have been done, but only a few investigations of the influence of substrate doping on device characteristics of such MOSFETs have been reported [9]. Generally, it has been assumed that very high substrate doping would degrade hot carrier reliability because higher electric field at drain/substrate junctions is expected due to the narrower depletion width. However, the experimental study on the influence of high substrate doping on hot carrier characteristics has shown that the dependence of substrate current and impact ionization rate upon substrate impurity concentration is reversed in long channel and short channel devices. In the long channel case, hot carrier effects are enhanced with rising substrate impurity concentration, while they are reduced in the case of short channel devices, for N_{sub} values lower than 1 or 2×10^{18} cm^{-3}. Thus, hot carrier degradation in short channel devices may not be a serious problem any more as long as the substrate impurity concentration is high, which is the opposite of what has been assumed so far.

Here, we have performed full-band Monte Carlo device simulations of impact ionization as a function of substrate doping to provide a microscopic explanation for this phenomenon in short channel MOSFETs. Figure 5

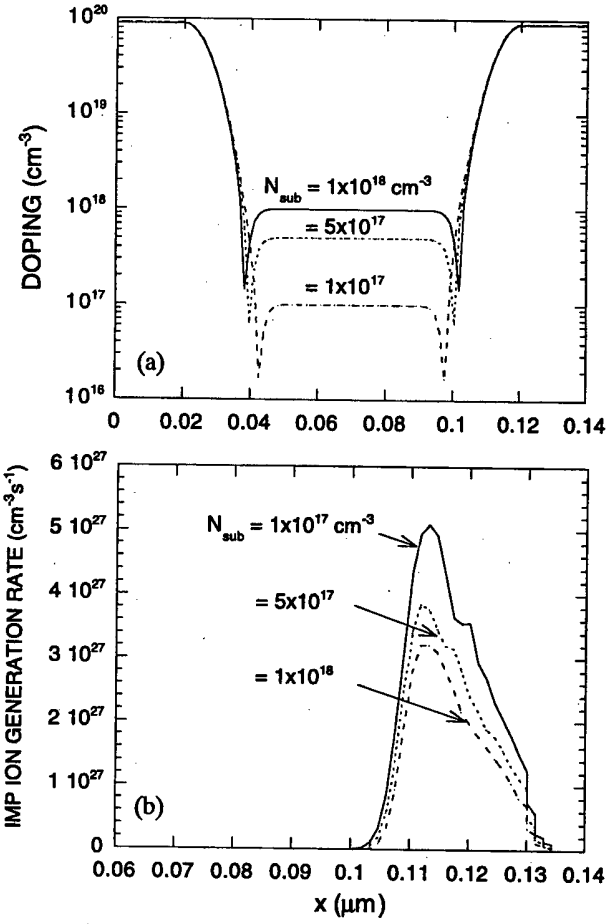

Fig. 5. (a) Doping profile and (b) electron impact ionization generation rates along the interface of the 0.1 μm n-MOSFET for the three different substrate doping levels. The drain voltage is set at V_d=2.0 V and the gate voltage is fixed at V_g=V_{th}+0.5 V (T=300 K).

shows doping profiles and electron impact ionization generation rates along the interface of 0.1 μm n-MOSFETs with three different substrate doping levels, 10^{17}, 5×10^{17}, and 10^{18} cm^{-3}, respectively, at $T = 300$ K. The drain and gate voltages are set to be $V_d = 2.0$ V and $V_g = V_{th} + 0.5$ V, respectively, as in Ref. 9 to compare both results directly. Note that the effective channel length increases slightly as the substrate doping increases, due to the reduction of junction depth as shown in Fig. 5(a). In Fig. 5(b), simulation results show that impact ionization generation rates decrease with increasing substrate impurity concentration, which is consistent with experimental findings [9]. Figure 6 shows the calculated electric field and average electron energy along the interface for the three different substrate doping levels. In the channel region, the electric field and average electron energy are higher for lower substrate doping. On the other hand, the peak field and peak energy near the substrate/drain junction are higher for higher substrate doping. However, higher peak energy does not necessarily result in higher impact ionization generation rate because impact ionization depends on individual electron energy, not on average electron energy. In the case here, the ionization rate is higher for lower substrate doping with lower peak energy. From Fig. 5(b) and Fig. 6(a) (or from Fig. 1 and Fig. 2(a)), we also noticed that most of the ionization events occur beyond the high-field region, just inside the channel/drain junction. It is in this region where the hot channel electrons reach their maximum kinetic energy but the average energy is well below its peak value because of cold electrons existing in the drain. Monte Carlo scaling analysis has shown that this spatial retardation is independent of channel length [14]; thus, the resultant hot carrier and spatial retardation effects, intrinsically nonlocal property, which cannot be handled by any local model such as models based on the first few moments of the BTE, will most likely become very important in 0.1 μm MOSFETs or below.

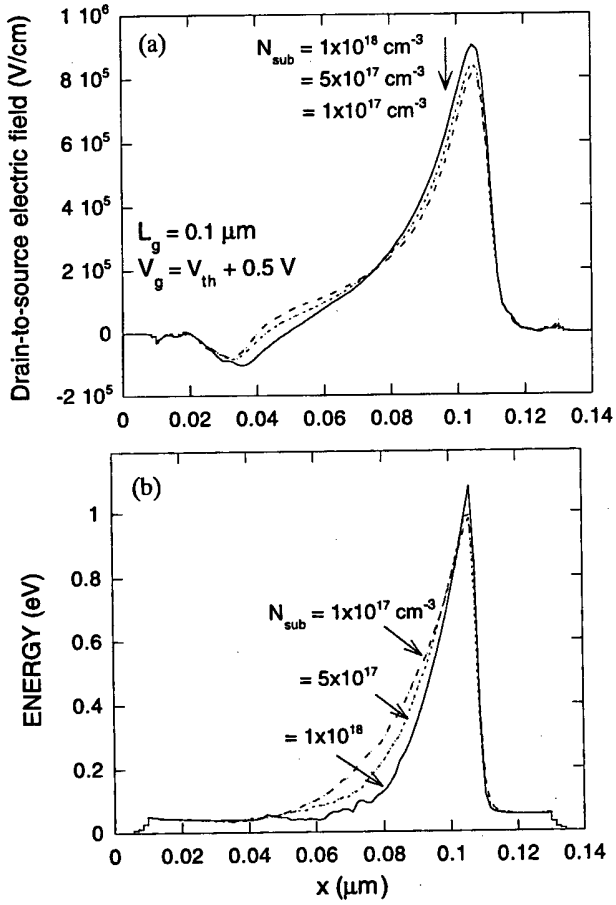

Fig. 6. (a) Electric field and (b) electron energy along the interface for the three different substrate doping levels. The drain voltage is set at V_d=2.0 V and the gate voltage is fixed at V_g=V_{th}+0.5 V (T=300 K). In the high field region, the peak field and peak energy is higher for higher substrate doping.

Electron energy distributions at the channel/drain junction for the corresponding substrate doping levels are shown in Fig. 7. The incoming hot electrons from channel cannot reach the equilibrium state with the resident cold electrons right away, so the EED is shown to be quite far away from the Boltzmann distribution. The distribution function exhibits three distinct regions. At low energy we see the drain cold electrons. The hot electrons from the channel cover nearly flat middle energy range up to $q\,V_{ds}$ after which they decay with nearly thermal ($T_e \approx T_L$) tails. Figure 7 shows that the number of hot electrons decreases as substrate impurity concentration increases. With rising substrate doping, both the junction depth and the pinch-off region become narrower owing to the relation of $l_{po} = 1.7\times10^{-2} t_{ox}^{1/8} x_j^{1/3} L_{eff}^{1/5}$, for $L_{eff} < 0.5$ μm) [13]. The very short pinch-off region results in marked nonlocal heating effects despite the small applied V_{ds} in short channel MOSFETs. The narrowness of field peak compared to the energy relaxation length with rising N_{sub} makes its capability of producing hot

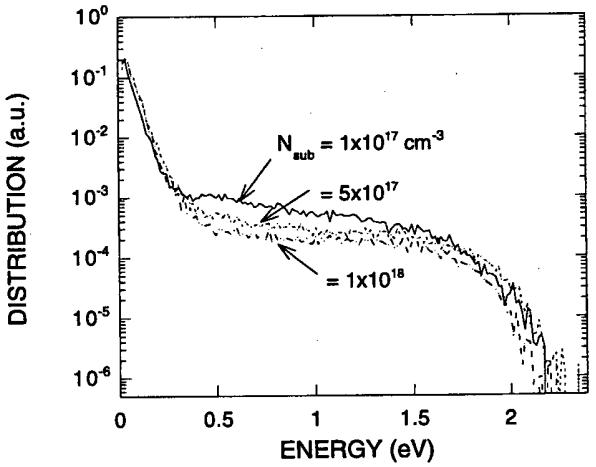

Fig. 7. Electron energy distribution at the channel/drain junction for the three substrate doping levels. As the substrate doping increases, the number of hot carriers decreases.

carriers decreased. Thus, the shape of the energy curve around the peak energy region gets sharper and narrower, even though the value of peak energy is higher for higher substrate doping. As a consequence, the number of hot electrons for impact ionization decreases as the substrate doping rises.

Recently, Fischetti *et al.* expressed their strong and profound skepticism about the validity of models that treat hot electron transport with oversimplified models [15] which cannot handle hot electron effects mainly because they are extremely small fluctuations of a large system. Apparently, the anomalous temperature dependence and the reversed N_{sub} dependence of impact ionization rate in short channel devices cannot be revealed by employing DD or HD models due to their strong nonlocal behavior and the quasi-ballistic transport.

IV. CONCLUSIONS

We have investigated the influence of temperature and high substrate impurity concentration on impact ionization in 0.1 μm n-MOSFETs, by employing the full-band MC device simulator. In regard of temperature dependence of impact ionization rate, hot carrier generation falls at low temperature and low drain bias, and hot carrier effects are suppressed mainly because of the quasi-ballistic transport characteristics and the band-gap energy widening at low temperature. Thus, the low temperature operation of deep sub-micron devices is very attractive owing to the reduced hot carrier effects as well as the capability of improving the device performance and suppressing the short channel effect.

The dependence of impact ionization rate on substrate impurity concentration in short channel devices is the reverse of that in long channel devices for N_{sub} values in the range of $10^{17} \sim 10^{18}$. In this concentration range, the impact ionization rates of short channel devices decrease with rising substrate impurity concentration, which suggests that hot carrier degradation in short channel devices may not be a serious problem any more as long as the substrate impurity concentration is high. We believe the cause of the decreased impact ionization rate with rising N_{sub} in short channel devices is the reduction in the number of hot electrons due to the marked nonlocal carrier heating in the very narrow pinch-off region of high field, which are just opposite to the trend in long channel devices.

We also emphasized that the full-band Monte Carlo method currently provides the only way to solve this hot carrier problem, including the anomalous temperature dependence and the reversed N_{sub} dependence of impact ionization rate in short channel devices, with a satisfactory accuracy.

ACKNOWLEDGMENTS

The author is grateful to Dr. C. S. Kim for his consistent encouragement of this work and thank Drs. G. Y. Jin, J. K. Ahn, and K. S. Yeom for their helpful discussions. We also acknowledge Mr. S. C. Choi and Mr. Y. J. Jeon for their MEDICI calculations and computing support.

REFERENCES

[1] W. VanRoosbroeck, Bell Syst. Tech. J. **29**, 560 (1950).

[2] J. R. Barker and D. K. Ferry, Solid-State Electron. **23**, 519 (1980).

[3] W. Lee, S. E. Laux, M. V. Fischetti, G. Baccarani, A. Gnudi, J. M. C. Stork, J. A. Mandelman, E. F. Crabbé, M. R. Wordeman and F. Odeh, IBM J. Res. Develop. **36**, 208 (1992).

[4] See, for example, E. Cartier, M. V. Fischetti, E. A. Eklund and F. R. McFeely, Appl. Phys. Lett. **62**, 3339 (1993).

[5] N. Sano, M. Tomizawa and A. Yoshi, in *Hot Carriers in in Semiconductors*, edited by K. Hess, J. -P. Leburton and U. Ravaioli (Plenum Press, New York, 1996), p. 337.

[6] S. E. Laux. M. V. Fischetti and D. J. Frank, IBM J. Res. Develop. **34**, 466 (1990).

[7] S. E. Laux and M. V. Fischetti, in *Some New Directions in Science on Computers*, edited by G. V. Bhanot, S. Chen and P. E. Seiden (World Scientific, New York, in press), and references therein.

[8] N. Sano, M. Tomizawa and A. Yoshi, IEEE Trans. Electron Devices **ED-42**, 2211 (1995), and references therein.

[9] M. Ono, M. Saito, T. Yoshitomi, C. Fiegna, T. Ohguro, H. S. Momose and H. Iwai, IEEE Trans. Electron Devices **42**, 1510 (1995).

[10] J. Bude and M. Mastrapasqua, IEEE Electron Device Lett. **16**, 439 (1995).

[11] F. Capasso, in *Semiconductors and Semimetals*, edited by D. W. Tsang (Academic, New York, 1986), Vol. 22, p. 1.

[12] D. Esseni, L. Selmi, E. Sangiorgi and B. Ricco, IEEE Electron Device Lett. **16**, 506 (1995).

[13] J. Chung, M. -C. Jeng, G. May, P. K. Ko and C. Hu, IEDM Tech. Dig., 200 (1988).

[14] R. B. Hulfachor, J. J. Ellis-Monaghan and K. W. Kim, in *Future Trends in Microelectronics*, edited by S. Luryi, J. Xu and A. Zaslavsky, NATO ASI Series E (Kluwer Academic Publishers, Boston, 1996), Vol. 323, p. 227.

[15] M. V. Fischetti and S. E. Laux, J. Appl. Phys. **78**, 1058 (1995).

Journal of the Korean Physical Society, Vol. 34, June 1999, pp. S577~S581

Frequency Chirping Characteristics of All Optical Wavelength Converter based on Cross-Gain and Cross-phase Modulation in Semiconductor Optical Amplifiers

Hanlim LEE, Yonggyoo KIM and Jichai JEONG*

Department of Radio Engineering, Korea University, Seoul 136-701

We develop a complete large-signal dynamic model of semiconductor optical amplifier (SOA)-based wavelength converters using cross-gain modulation (XGM) and cross-phase modulation (XPM). The large-signal dynamic model has been implemented using the modified transfer matrix method (TMM). This model takes account of longitudinal variations of carrier-induced refractive index, α-parameter, internal reflection, photon density, and amplified spontaneous emission (ASE) noise at each small section. Therefore, we can accurately estimate frequency chirping, optical pulse patterns, and extinction ratio of the wavelength-converted signal in SOAs. Frequency chirping and extinction ratio have been calculated for various parameters such as signal and CW power, and facet reflectivity.

I. INTRODUCTION

For all optical networks using wavelength division multiplexing (WDM), it is necessary to use wavelength converters for frequency reuse and wavelength/spatial routing. Among several promising techniques to implement all optical wavelength converters [1–4], XGM and XPM methods feature high conversion efficiency as well as insensitivity to polarization of input signals.

Although a lot of theoretical studies on wavelength converters have been carried out, only a few attempts have been made to consider longitudinal variations in carrier and photon densities in SOAs using multi-section rate equations [4–6]. They discussed crosstalk and intermodulation distortion [5], dynamics of wavelength conversion [4], and pulse shapes and chirping in MQW SOAs [6]. For accurate estimation of chirping in the wavelength-converted signal, we should include the parameters; facet power reflectivity, carrier-induced α-parameter change, extinction ratio, and ASE noise.

In this paper, a large-signal analysis for SOAs was performed using a time developed transfer matrix method (TMM) to calculate converted optical pulse waveforms and chirping in SOAs by self-consistently solving the pulse propagation equation and rate equation. It may help understand and design SOAs considering frequency chirping, extinction ratio, required facet reflectivity, and ASE noise.

This paper is organized as follows. In Section II, the modified TMM based large-signal dynamic SOA model is described in detail. We include facet reflection and variation of the α-parameter along the cavity to calculate chirping accurately. In Section III, simulation results and discussions of the XGM and XPM method are presented. Frequency chirping and extinction ratio depending on the facet reflectivity and α-parameter are investigated. Finally, conclusions are given in Section IV.

*E-mail: jcj@kuccnx.korea.ac.kr, Fax: 02-924-9710

II. SOA MODEL AND SIMULATION

The time developed TMM has been proposed for the purpose of characterizing multi- electrode DFB laser [7]. This model can describe not only forward field but also backward field which is generated by facet reflection and internal reflection at each small section. For the time dependent implementation of TMM based SOA model, we use the modified transfer matrix.

$$\begin{bmatrix} A_{i+1}(t+\Delta t) \\ B_i(t+\Delta t) \end{bmatrix} \begin{bmatrix} a_{11} - \frac{a_{12}(t)a_{21}(t)}{a_{22}(t)} & \frac{a_{12}(t)}{a_{22}(t)} \\ -\frac{a_{21}(t)}{a_{22}(t)} & \frac{1}{a_{22}(t)} \end{bmatrix} \begin{bmatrix} A_i(t) \\ B_{i+1}(t) \end{bmatrix} \quad (1)$$

where A and B are normalized slowly varying envelopes of forward and backward fields such that $|A|^2$ and $|B|^2$ represent the optical power and a_{ij} is the element of conventional transfer matrix at i-column and j-row. Fig. 1 shows the schematic diagram of the modified TMM-based dynamic SOA model. Assuming that various parameters remain unchanged through the each section for Δt, we can calculate output amplitudes $A_{w,i+1}$ and $B_{w,i}$ at a time $t + \Delta t$ from input amplitudes $A_{w,i}$ and $B_{w,i+1}$ at a time t by Eq. (1).

In order to apply this method to SOAs, we have modified the propagation part of transfer matrix using the pulse propagation [8,9]:

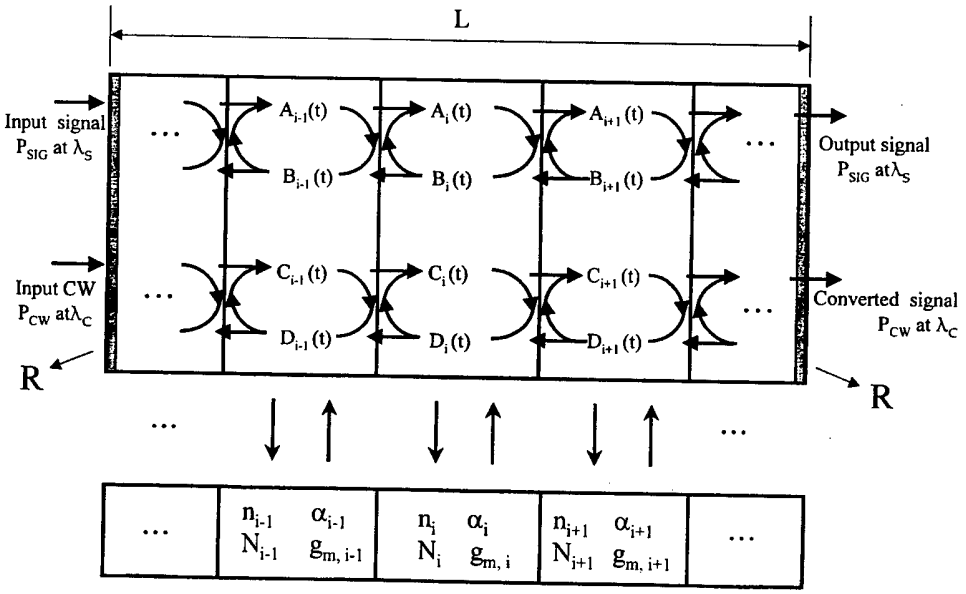

Fig. 1. Schematic diagram of the modified TMM-based dynamic SOA model. This model can explain not only the XGM but also XPM method.

$$\frac{\partial A_w(z,t)}{\partial z}+\frac{1}{v_g}\frac{\partial A_w(z,t)}{\partial t}=-\frac{i}{2}\alpha\Gamma g_{m_w}A_w(z,t) \quad (2)$$
$$.+\frac{1}{2}g_w A_w(z,t)+\mu_w(z,t)$$

where index w refers to different optical input signals, and α is the chirp parameter which accounts for carrier-induced index changes. v_g is the group velocity, Γ is the confinement factor, g_{m_w} is the material gain, and g_w is the net gain. The spontaneous emission noise is represented by two statistically independent Gaussian distributed random process $\mu_w(z,\ t)$ [9] that satisfies the correlation

$$<\mu_w(z,t)\mu_w^*(z',t')>=\beta\Gamma R_{SP}\delta(t-t')\delta(z-z') \times(v_g E_w A_{cross}) \quad (3)$$

where β is the spontaneous coupling factor, R_{SP} is the spontaneous emission (c_2N^2), $\delta(x)$ is defined as the δ function, E_w is photon energy, and A_{cross} is the cross sectional area of the active layer.

For considering interaction between carrier density N and photon density S, we divide the SOA into a number of small sections, and solve the rate equation in each section as

$$\frac{\partial N_i}{\partial t}=\frac{I}{qV}-N_i(c_1+c_2N_i+c_3+N_i^2) -\sum_{w=1,2}v_g\Gamma g_{m_w,i}S_{w,i} \quad (4)$$

where index i corresponds to different sections, I is the injection current, V is the active volume, q is the electronic charge, and c_1, c_2, and c_3 are related to recombination constants. The average photon density $S_{w,i}$ is calculated from forward field $A_{w,i}$ and backward field $B_{w,i}$. In order to model the asymmetric gain profile, the gain spectrum is assumed to be cubic and the material gain is approximated to [10]

$$g_{mi}(N_i,\lambda_w)=\frac{a_0(N_i-N_0)-a_1(\lambda_w-\lambda_p)^2+a_3(\lambda_w-\lambda_p)^3}{1+\epsilon(S_{1,i}+S_{2,i})} \quad (5)$$

where a_0, a_1, and a_3 are gain constants, λ_p is the gain peak wavelength, and ϵ is the gain compression factor.

Table 1. Device parameters used in the simulation.

Description	Symbol	Value	Unit
Confinement factor	Γ	0.3	·
SOA length	L	1000×10^{-6}	m
Active layer width	w	1×10^{-6}	m
Active layer width	d	0.15×10^{-6}	m
Spontaneous coupling factor	β	2×10^{-5}	·
Recombination rate	c_1	1×10^{8}	s^{-1}
	c_2	2.5×10^{-17}	m^3/s
	c_3	9.4×10^{-41}	m^6/s
Material gain constant	a_0	2.5×10^{-20}	m^2
	a_1	0.074×10^{20}	m^{-3}
	a_2	3.0×10^{-32}	m^4
	a_3	3.155×10^{25}	m^{-4}
Carrier density at transparency	N_0	1.1×10^{24}	m^{-3}
Wavelength at transparency	λ_0	1.605×10^{-6}	m
Group velocity	v_g	7.5×10^{7}	m/s
Nonlinear gain comperssion	ϵ	1.3×10^{-23}	m^3
Differential refractive index	dn/dN	-1.2×10^{-26}	m^3
loss in active layer	α_a	140×10^{2}	m^{-1}
Loss in claddings	α_c	20×10^{2}	m^{-1}
Scattering loss	α_{seat}	10×10^{2}	m^{-1}

The net gain is given by

$$g_i = \Gamma(g_{mi} - \alpha_a) - (1-\Gamma)\alpha_c - \alpha_{scat} \quad (6)$$

The α-parameter for each small section is taken into consideration since the parameter is directly related to frequency chirping due to self-phase modulation (SPM) and cross-phase modulation (XPM) in SOAs. The α-parameter $\{\alpha(\lambda, N) = (-4\pi/\lambda)(dn/dN)/(dg/dN)\}$ was calculated from gain variation from Eq. (5). We can obtain the α-parameter in the range of 2 to 12. These agree well with other experimental measurement [11].

The input signal is modulated at 2.5 Gb/s NRZ pattern using super Gaussian pulse with m=3. Typical buried-heterostructure (BH) SOA operating in the 1.55 μm is considered for our simulation and the device parameters are summarized in Table 1.

III. SIMULATION RESULTS AND DISCUSSIONS

1. XGM Method

An input signal at λ_S (1550 nm) modulates the gain in SOAs due to the gain saturation. A continuous wave (CW) signal at λ_{CW} (1535 nm) is modulated by the gain variation, so it contains the same data information as the input signal. Fig. 2 shows simulated output pulses and their chirping for the facet power reflectivity of 0 % (R=0 %). The wavelength-converted signal (CW signal) undergoes blue shift (6.5 GHz) during the rising edge and red shift (−7.4 GHz) during the falling edge. Thus converted signal has positive chirping which causes pulse broadening when converted signal is transmitted through the standard fiber [12]. This result is comparable to other simulation one [6].

Fig. 3 shows peak chirping (solid lines) and extinction ratio (dashed lines) of converted signal as a function of the average input signal power for different reflectivity. As the input signal power increases, both the peak chirping and extinction ratio of converted signal increase regardless of facet reflectivity. For R=0.01 %, chirping and extinction ratio are similar to those for R=0 %. However, for R=0.05 %, chirping significantly changes while the extinction ratio has similar characteristics to R=0 %. Particularly, the reflectivity of larger than 0.05 % increases the frequency chirping a lot. So, SOAs should have the facet reflectivity of less than 0.05 %. In Fig. 3, the fluctuation of chirping and extinction ratio for R=0.01 % and 0.05 % is due to the interference between reflected waves and traveling waves. Because the difference between "noise-free" chirping and "average" chirping obtained by multiple runs is negligible, for simplicity we calculated the peak chirping under condition of β= 0.

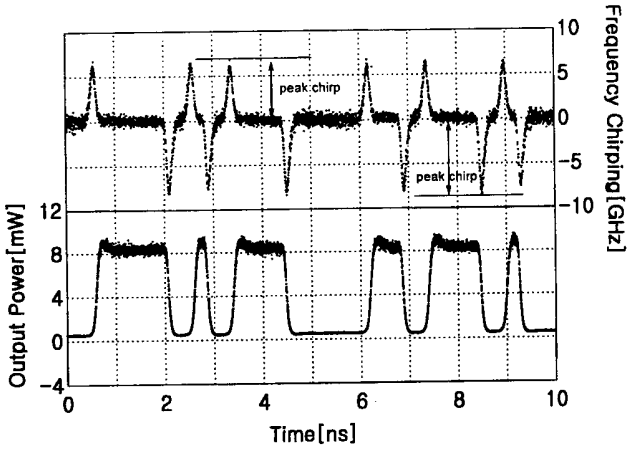

Fig. 2. Pulse pattern and chirping of converted signal in the XGM method. R=0 %, P_{SIG}=(−15 to −5 dBm), P_{CW}=−15 dBm, and I=160 mA.

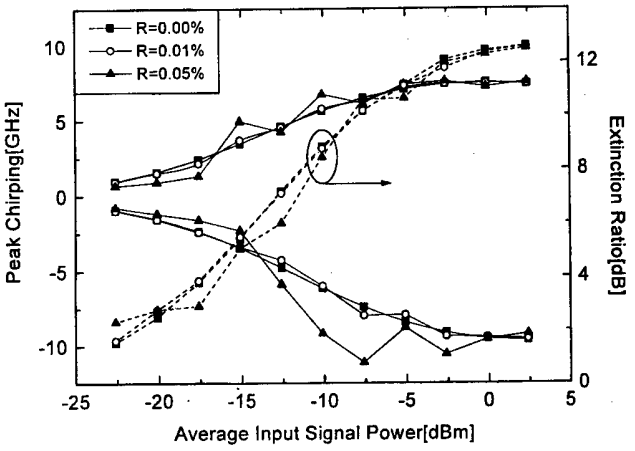

Fig. 3. Peak chirping (solid lines) and extinction ratio (dashed lines) of converted signal by the XGM method as a function of the average input signal power for different facet reflectivities (0 %, 0.01 % and 0.05 %). P_{CW}=−15 dBm, and I=160 mA.

We performed further investigation on chirping and extinction ratio with input signal and CW power for R=0.01 % and found that peak chirping and extinction ratio were reduced with increasing the CW power and decreasing the signal power. Therefore, we optimized chirping and extinction ratio by adjusting between the CW and signal power. In Fig. 4, the dashed region indicates the optimum power region, where the extinction ratio is larger than 10 dB, the peak chirping is in between −8 GHz and 7 GHz.

2. XPM Method

For the XPM method, wavelength conversions rely on carrier-induced refractive index change in the active region of SOAs. An input signal at λ_S (1565 nm) that depletes the carrier density modulates the refractive in-

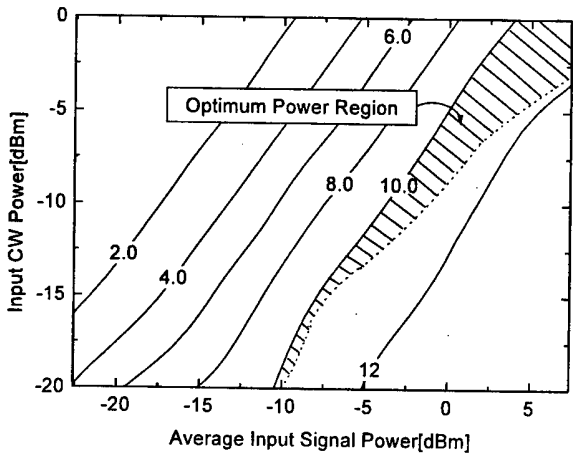

Fig. 4. Contour plot of the constant extinction ratio with signal powers and CW powers for the XGM method. R=0.01 %, and I=160 mA.

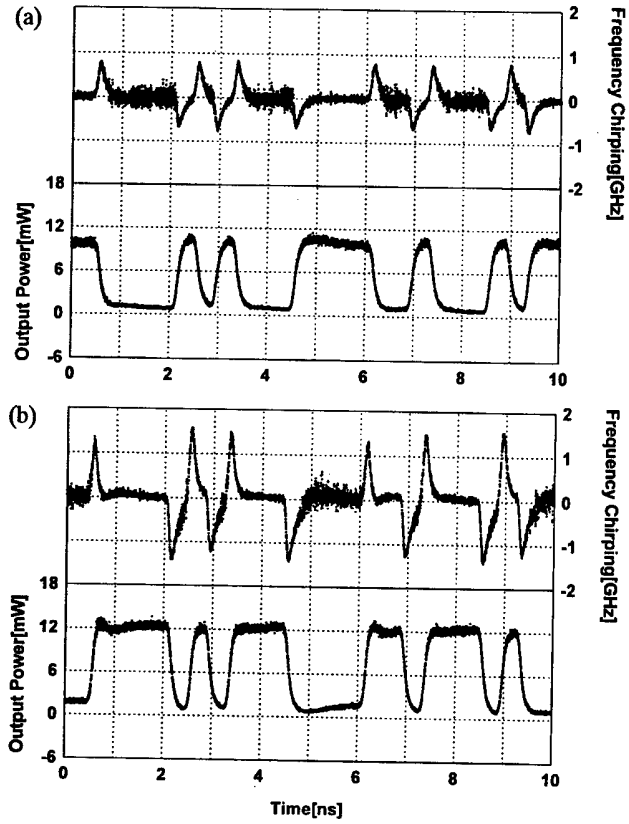

Fig. 5. Pulse pattern and chirping of converted signal by the XPM method. P_{SIG}=(−23.5 dBm to −16.5 dBm) and P_{CW}=−20 dBm: (a) in-phase operation (I_1=97 mA and I_2=116 mA) and (b) out-of-phase operation (I_1=125 mA and I_2=75 mA).

dex and thereby results in the phase modulation of the CW signal at λ_{CW} (1545 nm) coupled into the converter. We are to analyze the XPM wavelength conversion using symmetric Mach-Zehnder interferometer type SOAs [13] with minor modification (Mach-Zehnder interferometer with two SOAs) of the XGM method. The XPM method has the distinct characteristics due to the positive and negative slope of SOA's characteristics. Using the positive slope, converted signal is not inverted, compared to the input signal. Fig. 5(a) shows the optical pulse pattern and chirping of converted signal for the in-phase operation. Note that converted signal undergoes a red shift (−0.73 GHz) during the rising edge and a blue shift (0.77 GHz) during the falling edge. This leads to the pulse compression due to negative chirping in the anomalous dispersion region. This is an outstanding characteristic of the in-phase operation. Fig. 5(b) shows optical pulse patterns and chirping of converted signal for the out-of-phase operation. In this case, the chirping become large and is opposite to the in-phase operation. Still, this peak chirping is significantly smaller than that of the XGM method. For both the in-phase and out-of-phase operations, the extinction ratio is improved from 7 dB to 10 dB under our simulation condition.

IV. CONCLUSIONS

We presented a complete large-signal dynamic model of SOA-based wavelength converters using the modified TMM. To accurately calculate frequency chirping, which affects transmission performance of wavelength-converted signal, we included facet reflectivity, extinction ratio, longitudinal variation of the α-parameter due to spatial hole burning, and ASE noise. In the XGM method, we determined the optimum power region with small chirping and large extinction ratio for R=0.01 % and found that the reflectivity of larger than 0.05 % increased the chirping a lot. In the XPM method, we obtained the negative chirping effect for in-phase operation and found that frequency chirping was significantly smaller than that in the XGM method. In conclusion, our complete large-signal dynamic model provides an accurate and powerful tool to analyze frequency chirping and extinction ratio of wavelength-converted signal in SOAs.

REFERENCES

[1] R. Ludwig and G. Raybon, Electron. Lett. **30**, 338 (1994).

[2] T. Durhuus, R. J. S. Pedersen, B. Mikkelsen, K. E. Stubkjaer, M. Oberg and S. Nilsson, IEEE Photon. Technol. Lett. **5**, 86 (1993).

[3] T. Durhuus, B. Mikkelsen, C. Joergensen and K. E. Stubkjaer, J. Lightwave Technol. **14**, 942 (1996).

[4] M. Asghari, I. H. White and R. V. Penty, J. Lightwave Technol. **15**, 1181 (1997).

[5] T. Durhuus, B. Mikkelsen and K. E. Stubkjaer, J. Lightwave Technol. **10**, 1056 (1992).

[6] P. J. Annetts, M. Asghari and I. H. White, IEEE J. Select. Topics Quantum Electron. **3**, 320 (1997).

[7] M. G. Davis and R. F. O'Dowd, IEEE J. of Quantum Electron. **30**, 2458 (1994).
[8] G. P. Agrawal and N. A. Olsson, IEEE J. of Quantum Electron. **25**, 2297 (1989).
[9] L. M. Zhang, S. F. Yu, M. C. Nowell, D. D. Marcenac, J. E. Carroll and R. G. S. Plumb, IEEE J. of Quantum Electron. **30**, 1389 (1994).
[10] A. E. Willner and W. Shieh, J. Lightwave Technol. **13**, 771 (1995).
[11] N. Storkfelt, B. Mikkelsen, D. S. Olesen, M. Yamaguchi and K. E. Stubkjaer, IEEE Photon. Technol. Lett. **3**, 632 (1991).
[12] J. S. Perino, J. M. Wiesenfield and B. Glance, Electron. Lett. **30**, 256 (1994).
[13] C. Joergensen, S. L. Danielsen, T. Durhuus, B. Mikkelsen, K. E. Stubkjaer, N. Vodjdani, F. Ratovelomanana, A. Enard, G. Glastre, D. Rondi and R. Blondeau, IEEE Photon. Technol. Lett. **8**, 521 (1996).

Journal of the Korean Physical Society, Vol. 34, June 1999, pp. S582~S586

Analysis of Four-Wave Mixing in Semiconductor Optical Amplifiers for Optical Frequency Conversion and Optical Phase Conjugation

Yonggyoo KIM, Hanlim LEE and Jichai JEONG*

Department of Radio Engineering, Korea University, Seoul 136-701

We report a complete large-signal dynamic model of wavelength converter and optical phase conjugator based on four-wave mixing (FWM) in semiconductor optical amplifier (SOA). In SOA model using time developed transfer matrix method (TMM), we take into account of not only forward traveling waves but also backward traveling waves and include longitudinal variation of carrier-induced refractive index, α-parameter, gain, carrier density, photon density, reflection, and ASE noise at each small section. Therefore, we can accurately estimate optical pulse patterns, frequency chirping, and extinction ratio of conjugate signal, which affect transmission performance. In order to investigate the effects of frequency chirping on transmission performance, eye-opening penalty (EOP) has been calculated.

I. INTRODUCTION

Four-wave mixing (FWM) in semiconductor optical amplifiers (SOAs) has two applications. One is frequency conversion and the other is optical phase conjugation (OPC). Optical frequency converters are expected to become key components in future all optical networks based on wavelength division multiplexing (WDM) technology to avoid wavelength blocking and increase flexibility and capacity of WDM-based networks. And OPC is a good candidate to compensate for dispersion and Kerr effects in optical fibers [1]. Frequency conversion using FWM is very attractive since it is transparent to the data format, includes multi-frequency conversion [2], and compensates for dispersion by phase conjugation. However, this technique suffers from the small conversion efficiency and signal degradation caused by the amplified spontaneous emission (ASE) in the devices. By cavity geometry modification [3] or tandem SOA configuration [4], these drawbacks can be overcome.

Although many theoretical studies on FWM in SOAs have been carried out, most of them concentrated on conversion efficiency and signal to noise ratio (SNR) [3–5]. Extinction ratio and frequency chirping, however, are very important parameters in determining transmission performance of FWM signal through optical fiber. So, we have thrown our effort into accurately calculating extinction ratio and frequency chirping of FWM signal. In this paper, we performed a large-signal dynamic analysis for SOAs using modified transfer matrix method (TMM) to calculate optical waveforms and frequency chirping of conjugate signal in SOAs by self-consistently solving the pulse propagation equations and rate equation of carrier density. We can accurately estimate frequency chirping and extinction ratio, compared with analytical model, including the parameters: longitudinal variation of α-parameter, carrier-induced refractive index, gain, spatial hole burning, and ASE noise. Facet reflectance and extinction ratio of input signal wave also were included in our simulations. Therefore, it can help in understanding and designing FWM frequency converter and OPC.

*E-mail: jcj@kuccnx.korea.ac.kr, Fax: (02) 924-9710

II. LARGE-SIGNAL DYNAMIC SOA MODEL USING TIME DEVELOPED TMM

The time developed TMM has been proposed for the purpose of characterizing multielectrode distributed-feedback (DFB) laser [6]. This model can be considered not only forward traveling waves but also backward traveling waves which are generated by internal and facet reflection. Also, we include longitudinal variation of carrier-induced refractive index, gain, spatial hole burning, ASE noise and α-parameter at each small section and spectrally dependent gain and confinement factor at each individual wave.

Fig. 1 shows the schematic diagram of our simulation. Two optical waves, a pump (ω_p) and a signal wave ($\omega_s = \omega_p - \Delta\omega$) are injected into the SOA. The beating of both waves leads to new frequency components, FWM wave ($\omega_c = \omega_p + \Delta\omega$). We can convert ω_s into ω_c.

In order to develop a time-dependent TMM in the schematic diagram of our simulation in Fig. 1, we use the modified transfer matrix [6].

$$\begin{bmatrix} A_{w,i+1}(t+\Delta t) \\ B_{w,i}(t+\Delta t) \end{bmatrix} = \begin{bmatrix} a_{11}(t) - \frac{a_{12}(t)a_{21}(t)}{a_{22}(t)} & \frac{a_{12}(t)}{a_{22}(t)} \\ -\frac{a_{21}(t)}{a_{22}(t)} & \frac{1}{a_{22}(t)} \end{bmatrix} \times \begin{bmatrix} A_{w,i}(t) \\ B_{w,i+1}(t) \end{bmatrix} \quad (1)$$

where A and B are normalized slowly varying envelopes of forward and backward fields such that $|A|^2$ and $|B|^2$ represent the optical power. The input signal power is $|A_s|^2$ at the first section and the output signal power is the $|A_c|^2$ at the last section. And, $a_{mn}(t)$ is the element of steady-state transfer matrix. Assuming that various parameters remain unchanged through the each section for Δt, we can calculate output amplitudes $A_{w,i+1}$ and $B_{w,i}$ at a time $t+\Delta t$ from input amplitudes $A_{w,i}$ and $B_{w,i+1}$ at a time t by Eq. (1).

The pulse propagation equations, including FWM, ASE noise, and backward traveling waves, can be derived in the follows [3,7]

$$\frac{\partial A_p}{\partial z} + \frac{1}{v_g}\frac{\partial A_p}{\partial t} = G_p A_p(z,t) + \mu_p(z,t) \quad (2)$$

$$\frac{\partial A_{s,c}}{\partial z} + \frac{1}{v_g}\frac{\partial A_{s,c}}{\partial t} = G_{s,c}A_{s,c}(z,t) + F_{s,c}\{A_p^2(z,t)A_{c,s}(z,t) + 2A_p(z,t)B_p(z,t)B_{c,s}(z,t)\} + \mu_{s,c}(z,t) \quad (3)$$

$$G_{p,s,c} = \left(\frac{1}{2}\bar{g}_{p,s,c} - \frac{i}{2}\alpha\Gamma_{p,s,c}g_{p,s,c}\right) \Big/ \left(1 + \sum_{w=p,s,c}(|A_w|^2 + |B_w|^2)/P_{Sat}\right) \quad (4)$$

$$F_{s,c} = -\left(\frac{1}{2}\bar{g}_{s,c} - \frac{1}{2}\alpha\Gamma_{s,c}g_{s,c}\right)h_{CDP}(\mp\Delta\omega)/P_{Sat} - \frac{1}{2}(1-i\alpha_{CH})(\bar{g}_{s,c}\epsilon_{CH1} + g_{s,c}\epsilon_{CH2})h_{CH}(\pm\Delta\omega) - \frac{1}{2}(1-i\alpha_{SHB})\bar{g}_{s,c}\epsilon_{SHB}h_{SHB}(\mp\Delta\omega) \quad (5)$$

where index p, s, and c present pump, signal, and conjugate wave, $\Delta\omega = \omega_p - \omega_s$ denotes frequency detuning for pump and signal wave, v_g is group velocity, P_{Sat} is saturation power, ϵ_{SHB} is spectral hole burning (SHB) parameters, and ϵ_{CH1} and ϵ_{CH2} are carrier heating (CH) parameters. We consider wavelength dependent Γ, confinement factor, which is calculated from the effective index method [8,9]. The effect of spontaneous emission is represented by three statistically independent white-Gaussian distributed random process $\mu_w(z,t)$ [10]. The autocorrelation function for the process is given by

$$<\mu_w(z,t)\mu_w^*(z',t')> = (v_g E_w A_{cross})(\Gamma_w \beta N/\tau_s)\delta(t-t')\delta(z-z') \quad (6)$$

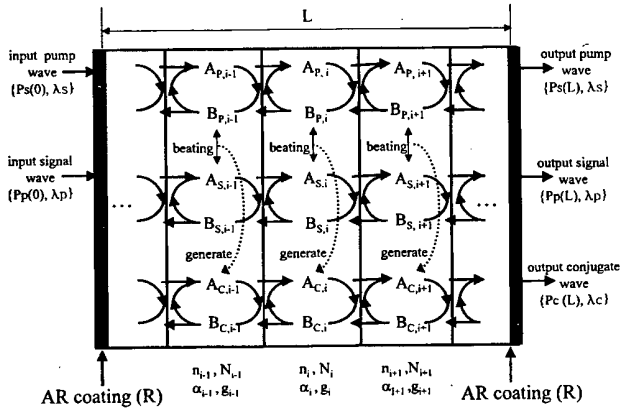

Fig. 1. Schematic diagram of the time-developed TMM-based large signal dynamic SOA model.

where E_w is photon energy, A_{cross} is the cross sectional area of the active layer, β is spontaneous coupling factor, and $\delta(x)$ is the Dirac distribution function. The frequency response $h_y(\Delta\omega)$ (y=carrier density pulsation (CDP), CH, and SHB) of the individual nonlinear processes are given by,

$$\begin{aligned} H_{CDP}^{-1}(\Delta\omega) &= (1-i\Delta\omega\tau_2)(1-\Delta\omega\tau_s) \\ H_{CH}^{-1}(\Delta\omega) &= (1-i\Delta\omega\tau_2)(1-\Delta\omega\tau_1) \\ H_{SHB}^{-1}(\Delta\omega) &= (1-i\Delta\omega\tau_2) \end{aligned} \quad (7)$$

where τ_s, τ_1, and τ_2 are parameters related to carrier lifetime. The propagation equations are coupled by the conventional rate equation for the carrier density.

In order to model asymmetric gain profile, the gain spectrum is assumed to be cubic [11]. The net gain is calculated by [10]

$$\bar{g}_{i,w} = \Gamma_w(g_{i,w} - \alpha_a) - (1-\Gamma_w)\alpha_c - \alpha_{scat} \quad (8)$$

We take consideration into the different α-parameter for each small section and each wavelength. It is very important since it is directly related to frequency chirping due to self-phase modulation (SPM) and cross-phase modulation (XPM) in SOAs. The α-parameter $\{\alpha = (-4\pi/\lambda)(dn/dN)/(dg/dN)\}$ is calculated from material gain.

The computing algorithm implementing the large signal and dynamic SOA model is illustrated in Fig. 2. The input signal is modulated at 2.5 Gb/s NRZ pattern using super Gaussian pulse shape with m=3. Simulation and nonlinear (FWM) SOA parameters are summarized

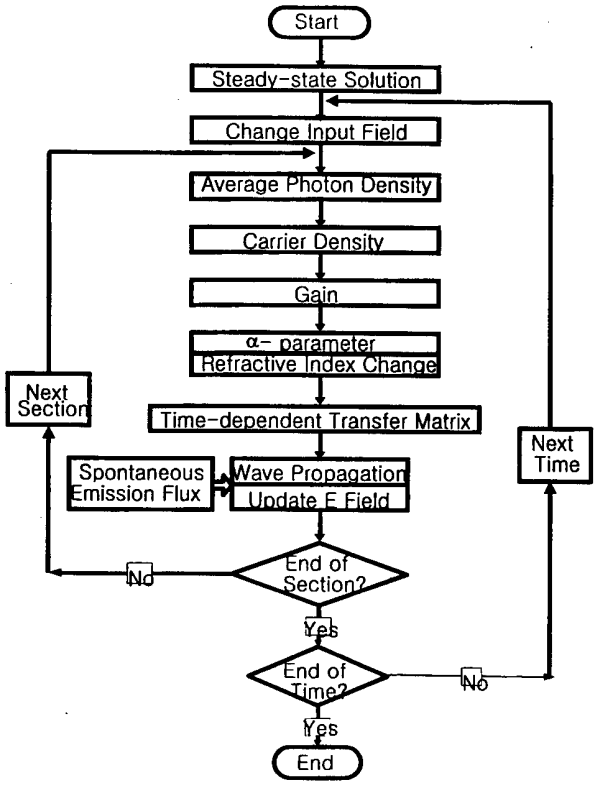

Fig. 2. Flow chart of the procedure for the time-developed TMM-based large signal dynamic SOA model.

in Table 1. We have simulated the saturation condition with high pump power. It is general condition of wavelength converter and OPC using FWM in SOAs in order to reduce the effects of ASE noise [5].

Table 1. Device and nonlinear (FWM) SOA parameters.

Symbol	Description	Value	Unit
L	SOA length	500×10^{-6}	m
w	Active layer width	1×10^{-6}	m
d	Active layer thickness	0.15×10^{-6}	m
V	Active layer volume	0.75×10^{-16}	m^3
c_1	Recombination rate	1×10^{8}	s^{-1}
c_2		2.5×10^{-17}	m^3/s
c_3		9.4×10^{-41}	m^6/s
a_0	Material gain constant	2.5×10^{-20}	m^2
a_1		0.074×10^{20}	m^{-3}
a_2		3.0×10^{-32}	m^4
a_3		3.155×10^{25}	m^{-4}
N_0	Carrier density at transparency	1.1×10^{24}	m^{-3}
λ_0	Wavelength at transparency	1.605×10^{-6}	m
v_g	Group velocity	7.5×10^{7}	m/s
dn/dN	Differential refractive index	-1.2×10^{-26}	m^3
α_a	Loss in active layer	140×10^{2}	m^{-1}
α_c	Loss in claddings	20×10^{2}	m^{-1}
α_{scat}	Scattering loss	10×10^{2}	m^{-1}
β	spontaneous coupling factor	1×10^{-5}	·
I	Injection current	100×10^{-3}	A
P_S	Saturation power	3×10^{-3}	W
ϵ_{CH1}	Carrier heating parameter	5.5	W^{-1}
ϵ_{CH2}	Carrier heating parameter at unsaturation carrier density	3.8	W^{-1}
ϵ_{SHB}	Spectral hole burning parameter	2.1	W^{-1}
α_{CH}	Linewidth enhancement factor by CH	-2.3	·
α_{SHB}	Linewidth enhancement factor by SHB	0	·
τ_S	Carrier lifetime	160×10^{-12}	s
τ_2	Spectral hole buring time	500×10^{-15}	s
τ_1	Carrier heating time	112×10^{-15}	s

III. SIMULATION RELATED WITH FREQUENCY CHIRPING AND EXTINCTION RATIO OF CONJUGATE SIGNAL

Fig. 3(a) shows input signal pulse pattern with positive frequency chirping and Fig. 3(b) and (c) show output conjugate signal pulse pattern and frequency chirping with pump power of 3 dBm and 9 dBm). From Fig. 3, we found that the spectral inversion of conjugate signal resulted from the phase conjugation. Using this effect, It is possible to perfectly compensate for signal distortion by GVD and SPM on optical transmission [1]. Extinction ratio decreases after wavelength conversion since low signal power level has higher conversion efficiency than high signal power level. In addition, we can see that ASE noise is smaller at high pump power than at low pump power by comparing Fig. 3(b) with (c) since gain saturation make ASE noise reduce at high pump power. Especially low signal power level undergoes more frequency chirping by ASE noise than high signal power level.

We performed further investigation on parasitic frequency chirp and extinction ratio of conjugate signal. Parasitic frequency chirp occurs during wavelength conversion inside SOAs. It is responsible for refractive index modulation by carrier density variation in SOAs. Parasitic frequency chirp can obstruct the perfect compensation for signal distortion. Fig. 4 shows extinction ratio and parasitic peak chirp of output conjugate signal where the extinction ratio of input signal is 10 dB. When either pump power or signal power is fixed, extinction ratio decreases with decreasing the pump power to probe power ratio (P/Q). It results from smaller difference of conversion efficiency between low signal power level and high signal power level at low P/Q ratio. Parasitic frequency chirp is minimized at higher P/Q ratio. Frequency chirping is a monotonically increasing function of α-parameter and extinction ratio. However, Frequency chirping is more strongly dependent on α-parameter than extinction ratio. As a result, signals undergo larger frequency chirping for high P/Q ratio with large α-parameter and low extinction ratio than for low P/Q ratio with small α-parameter and high extinction ratio. This result agrees

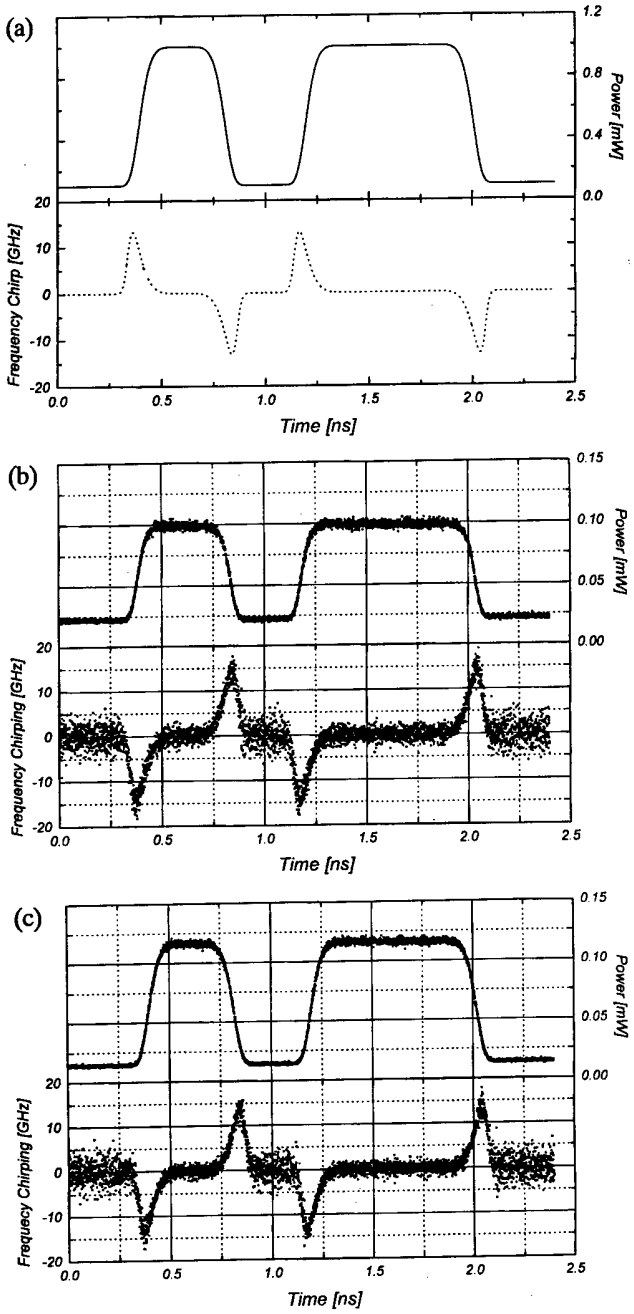

Fig. 3. (a) Input optical pulse pattern (solid line) and frequency chirping (dotted line) (λ_s=1555 nm). (b) Output optical pulse pattern (upper) and frequency chirping (lower) for the pump power of 3 dBm (λ_c=1545 nm, R=0.01 %). (c) Output optical pulse pattern (upper) and frequency chirping (lower) for pump power of 9 dBm (λ_c=1545 nm, R=0.01 %).

well with other experiment results [2]. Extinction ratio and parasitic frequency chirp can be achieved higher than 8 dB and lower than 1 GHz with the pump power of greater than 4 dBm, and the signal power of lower than −6.6 dBm. For the high pump power, extinction ratio increases and parasitic frequency chirp decreases.

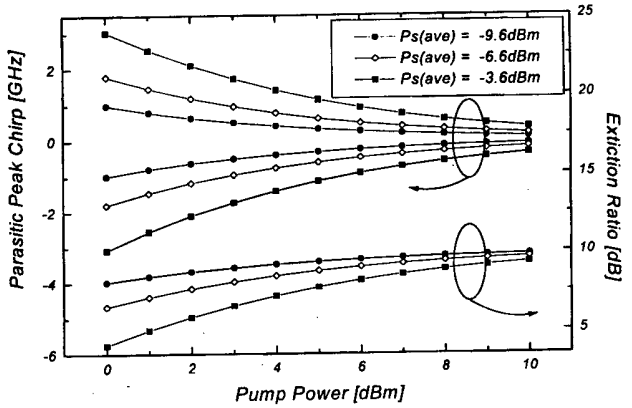

Fig. 4. Extinction ratio and parasitic peak chirp as a function of pump power with different average input signal power (extinction ratio of input signal=10 dB, λ_s=1555 nm, λ_c=1545 nm, R=0.01 %).

The pump power should be chosen as large as possible to improve transmission performance.

IV. SIMULATION OF TRANSMISSION PERFORMANCE USING SOA

To investigate the effects of parasitic chirp on transmission performance, we simulate transmission performance by solving nonlinear schrodinger equation using split-step Fourier method (SSFM) [12].

Fig. 5 shows schematic diagram of the transmission link used in our simulation. The optical fiber is assumed to be SMF with the standard parameters as shown in Table 2. The waveform distortion in fiber is compensated for the system configuration in Fig. 5: Signal wave is transmitted through SMF1. During transmission, the wave is distorted due to GVD and SPM. EDFA1 then compensates for fiber loss of SMF1. Next, SOA converts the signal wave to phase conjugate wave and EDFA2

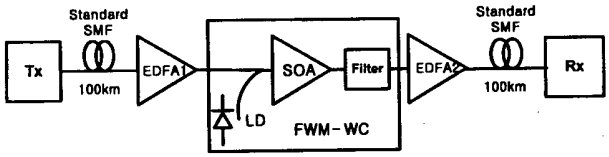

Fig. 5. Schematic diagram of transmission link.

Table 2. Parameter values used in transmission simulation.

Symbol	Description	Value	Unit
α	Fiber loss	0.266	dBm/km
D	Average normal dispersion	17.76	ps/nm/km
β_2	Second order dispersion	0.05936	ps/nm^{2}km
A_{eff}	Effective core area	90	μm^2
γ	Nonlinear coefficient	2.3×10^{-20}	m^2/W

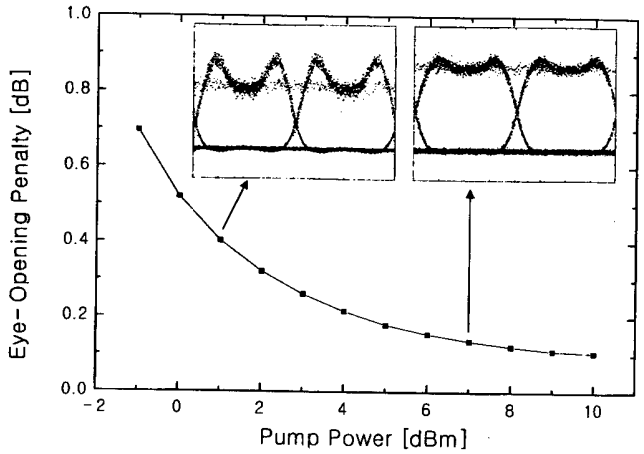

Fig. 6. Eye-opening penalty and eye diagram dependent on pump power (Input signal has no chirp, average Ps=-6.6 dBm, extinction ratio of input signal=10 dB, λ_s=1550 nm, λ_c=1552 nm, EDFA gain=26.6 dB).

compensates for small efficiency of FWM process. Finally, conjugate wave is transmitted through SMF2 and distortion can be compensated during transmission.

Fig. 6 shows eye-opening penalty (EOP) and eye-diagram dependent on SOA pump power. For the high pump power, GVD and SPM are almost compensated by OPC. Therefore, EOP is very low. On the other hand, we can not completely compensate for the low pump power due to large parasitic frequency chirp in SOAs. From these results, we can confirm that the pump power should be large to improve transmission performance.

V. CONCLUSIONS

We presented a complete large-signal dynamic model of SOA considering FWM and ASE noise, backward traveling wave. We took consideration into the effects of facet reflectivity, longitudinal variation of the α-parameter due to spatial hole burning, wavelength dependent gain and confinement factor, and extinction ratio of input signal wave. Therefore, our complete large-signal dynamic model may compute an accurate frequency chirping and extinction ratio, which affect transmission performance of conjugate signal. High pump power can contribute extinction ratio to maximize and parasitic frequency chirp to minimize. Therefore, low EOP can be achieved. Our SOA model supplies an accurate and powerful tool to analyze frequency chirping and extinction ratio of conjugate signal.

REFERENCES

[1] Shigeki Watanabe and Masataka Shirasaki, J. Lightwave Technol. **14**, 243 (1996).

[2] David F. Geraghty, Robert B. Lee, Marc Berdiell, Mehrdad Ziari, Atul Mathur and Kerry J. Vahala, IEEE J. of Select. Topics Quantum Electron. **3**, 1146 (1997).

[3] F. Girardin, J. Eckner, G. Guekos, R. Dall'Ara, A. Mecozzi, A. D'Ottavi, F. Martelli, S. Scotti and P. Spano, IEEE Photon. Technol. Lett. **9**, 746 (1997).

[4] K. Nesset, D. D. Marcenac and A. E. Kelly, Electron. Lett. **33**, 148 (1997).

[5] Stefan Diez, Carsten Schmidt, Reinhold Ludwig, Hans G. Weber, Kristof Obermann and Stefan Kindt, Igor Koltchanov and Klaus Petermann, IEEE J. of Select. Topics Quantum Electron. **3**, 1131 (1997).

[6] M. G. Davis and R. F. O'Dowd, IEEE J. of Quantum Electron. **30**, 2458 (1994).

[7] Jacques W. D. Chi, Alan Shore and Jean Le Bihan, IEEE J. of Quantum Electron. **33**, 2011 (1997).

[8] Jens Buus, IEEE J. Quantum Electron. **18**, 1083 (1982).

[9] G. P. Agrawal and N. K. Dutta, *Semiconductor Lasers* (New York, Van Nostrand, 1993).

[10] K. Petermann, *Laser Diode Modulation and Noise* (Dordrecht, Germany, Kluwer, 1988).

[11] Alan E. Willner and Willian Shieh, J. Lightwave Technol. **13**, 771 (1995).

[12] G. P. Agrawal, *Nonlinear Fiber Optics* (New York, Academic Press, 1989).

(본 학회지는 한국과학기술단체총연합회의 재정지원으로 이루어졌습니다.)

Journal of the Korean Physical Society

제 34권 보충호

1999년 6월 23일 인쇄
1999년 6월 30일 발행

<비 매 품>

발행인 민 석 기
편집인 황 정 남
인쇄인 도서출판 한 림 원 김 용 우
발행소 사단법인 한국물리학회

135-703 서울특별시 강남구 역삼동 635-4
과학기술회관 제 901호
전화 : 556-4737, FAX : 554-1643
지로번호 7512122